Handbook of POROUS MEDIA

THIRD EDITION

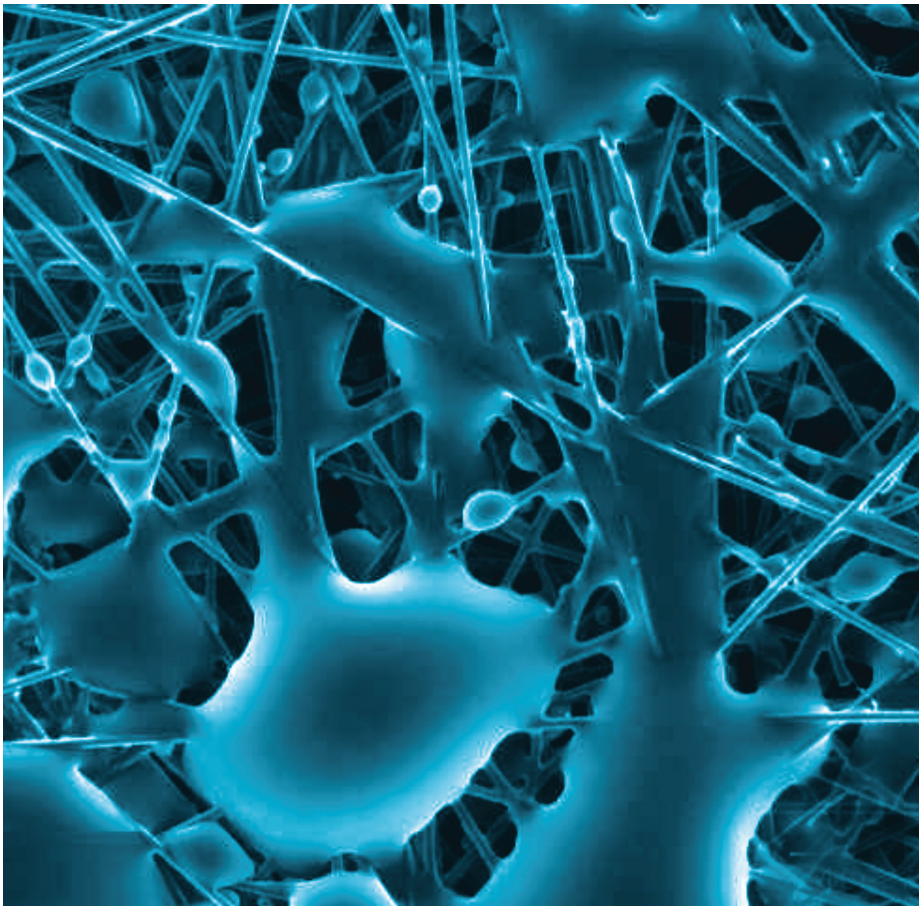

edited by

Kambiz Vafai

CRC Press
Taylor & Francis Group

Handbook of
POROUS MEDIA
THIRD EDITION

Handbook of
POROUS MEDIA
THIRD EDITION

edited by
Kambiz Vafai

CRC Press
Taylor & Francis Group
Boca Raton London New York

CRC Press is an imprint of the
Taylor & Francis Group, an **informa** business

MATLAB® and Simulink® are trademarks of The MathWorks, Inc. and are used with permission. The MathWorks does not warrant the accuracy of the text or exercises in this book. This book's use or discussion of MATLAB® and Simulink® software or related products does not constitute endorsement or sponsorship by The MathWorks of a particular pedagogical approach or particular use of the MATLAB® and Simulink® software.

CRC Press
Taylor & Francis Group
6000 Broken Sound Parkway NW, Suite 300
Boca Raton, FL 33487-2742

© 2015 by Taylor & Francis Group, LLC
CRC Press is an imprint of Taylor & Francis Group, an Informa business

No claim to original U.S. Government works
Version Date: 20150429

International Standard Book Number-13: 978-1-4398-8557-4 (eBook - PDF)

This book contains information obtained from authentic and highly regarded sources. Reasonable efforts have been made to publish reliable data and information, but the author and publisher cannot assume responsibility for the validity of all materials or the consequences of their use. The authors and publishers have attempted to trace the copyright holders of all material reproduced in this publication and apologize to copyright holders if permission to publish in this form has not been obtained. If any copyright material has not been acknowledged please write and let us know so we may rectify in any future reprint.

Except as permitted under U.S. Copyright Law, no part of this book may be reprinted, reproduced, transmitted, or utilized in any form by any electronic, mechanical, or other means, now known or hereafter invented, including photocopying, microfilming, and recording, or in any information storage or retrieval system, without written permission from the publishers.

For permission to photocopy or use material electronically from this work, please access www.copyright.com (http://www.copyright.com/) or contact the Copyright Clearance Center, Inc. (CCC), 222 Rosewood Drive, Danvers, MA 01923, 978-750-8400. CCC is a not-for-profit organization that provides licenses and registration for a variety of users. For organizations that have been granted a photocopy license by the CCC, a separate system of payment has been arranged.

Trademark Notice: Product or corporate names may be trademarks or registered trademarks, and are used only for identification and explanation without intent to infringe.

Visit the Taylor & Francis Web site at
http://www.taylorandfrancis.com

and the CRC Press Web site at
http://www.crcpress.com

Contents

Preface ix
Editor xv
Contributors xvii

SECTION I General Characteristics and Modeling of Porous Media

Chapter 1 Multiscale Modeling of Porous Medium Systems 3
Amanda L. Dye, James E. McClure, William G. Gray, and Cass T. Miller

Chapter 2 Advanced Theories of Two-Phase Flow in Porous Media 47
S. Majid Hassanizadeh

Chapter 3 Characterization of Fractures and Fracture Network of Porous Media 63
Muhammad Sahimi

Chapter 4 Thin Porous Media 89
Marc Prat and Tristan Agaësse

Chapter 5 Magnetically Stabilized and Fluidized Beds in Science and Technology: A Review 113
Teresa Castelo-Grande, Paulo A. Augusto, Angel M. Estevéz, Domingos Barbosa, Jesus Ma. Rodríguez, Audelino Álvaro, and Cármen Torrente

Chapter 6 Lift Generation in Highly Compressible Porous Media: From Red Cells to Skiing to Soft Lubrication 157
Qianhong Wu

SECTION II Transport in Porous Media

Chapter 7 Theoretical Analysis of Transport in Porous Media: Multi-Equation and Hybrid Models for a Generic Transport Problem with Nonlinear Source Terms 245
Yohan Davit and Michel Quintard

Chapter 8 Porous Media Theory for Membrane Transport Phenomena 321
A. Nakayama, Y. Sano, T. Nishimura, and K. Nagase

Chapter 9 Effective Transport Properties of Porous Media by Modeling 357
Moran Wang

Chapter 10 Effective Transport through Porous Media under Nonequilibrium Relaxation Conditions 391
Faruk Civan

Chapter 11 Modeling Approach for Gradient-Based Motion of Microorganisms in Porous Media and Applications in Biosystems 439
Zineddine Alloui and Tri Nguyen-Quang

SECTION III Turbulence in Porous Media

Chapter 12 Feedback Control for Promoting or Suppressing the Transition to Weak Turbulence in Porous Media Convection 459
Peter Vadasz

Chapter 13 Advances in Modeling Turbulence Phenomena in Heterogeneous Media: Reactive Systems 471
Marcelo J.S. de Lemos

SECTION IV Heat Transfer of Nanofluids in Porous Media

Chapter 14 Effects of Nanofluids on Convection in Porous Media 493
D.A. Nield and A.V. Kuznetsov

Chapter 15 Analyzing Nanofluids Suspension Using the Porous Media Interface Heat Transfer Model 513
Peter Vadasz

SECTION V Thermal Transport in Porous Media

Chapter 16 Thermal Transport in Highly Porous Cellular Materials 535
Raymond Viskanta

Chapter 17 Convection of a Bingham Fluid in a Porous Medium 559
D. Andrew S. Rees

Chapter 18 High-Heat-Flux Distributed Capillary Artery Evaporators 597
Gisuk Hwang, Chanwoo Park, and Massoud Kaviany

Chapter 19 Impinging Jets in Porous Media 631
Bernardo Buonomo, Oronzio Manca, and Sergio Nardini

Chapter 20 Thermohydromechanical Behavior of Poroelastic Media 663
A. P. S. Selvadurai

Chapter 21 Thermogravitational Diffusion in a Porous Medium Saturated by a Binary Fluid 713
Abdelkader Mojtabi, Marie Catherine Charrier-Mojtabi, Bilal ElHajjar, and Yazdan Pedram Razi

SECTION VI Geological Applications in Porous Media

Chapter 22 Digital Petrophysics: Imaging, Modeling, and Experimental Challenges Related to Porous Media in Oil Fields 769
Peter Tilke

Chapter 23 Modeling of Subsurface CO_2 Migration at Geological Carbon Sequestration Sites in Deep Saline Aquifers 791
Sumit Mukhopadhyay

Chapter 24 Groundwater Flows and Velocity Measurements 841
Shigeo Kimura

Chapter 25 Geostatistical Simulation and Reconstruction of Porous Media 869
Pejman Tahmasebi and Muhammad Sahimi

Chapter 26 Microbially Induced Carbonate Precipitation in the Subsurface: Fundamental Reactions and Transport Processes 891
James Connolly and Robin Gerlach

Preface

Over the past four decades, there has been increased attention in the research of transport phenomena in porous media due to its importance in many engineering and industrial sectors. Major advances have been made in modeling fluid flow, heat, and mass transfer through a porous medium, including clarification of several important physical phenomena. For example, the non-Darcy effects on momentum, energy, and mass transport in porous media have been studied in depth for different geometrical configurations and boundary conditions. Much of the research in porous media for the past couple of decades has utilized what is now commonly known as the Brinkman–Forchheimer-extended Darcy or the generalized model.

Key topics that have received considerable interest include porosity variation, thermal dispersion, the effects of non-local thermal equilibrium between the fluid phase and the solid phase, partially filled porous configurations, geomechanical effects, and anisotropic porous media, among others. Advanced measurement techniques have also been developed, including more efficient measurement of effective thermal conductivity, flow and heat transfer measurement, and flow visualization. The main objective of this handbook is to compile and present the pertinent recent research information related to fluid flow, mechanics of the porous media skeleton, and heat and mass transfer, including practical applications for the analysis and design of engineering devices and systems involving porous media. The previous editions as well as the present edition of the *Handbook of Porous Media* are aimed at providing researchers with the most relevant and up-to-date advances in the modeling and analysis of flow, heat, and mass transfer in porous media. The third edition of the *Handbook of Porous Media*, which addresses a considerably different set of topics as compared to the first and second editions, includes recent studies related to current and future challenges and advances in fundamental aspects of porous media, forced and double diffusive convection in porous media, turbulent flow, heat transfer of nanofluids in porous media, geological applications, dynamic modeling of convective transport through porous media, and a number of other important topics.

It is essential to be aware that different models can be found in the literature and in the present handbook in the area of fluid flow, heat, and mass transfer in porous media. An in-depth analysis of these models is essential in resolving uncertainty in utilizing them (see Tien and Vafai, 1989; Hadim and Vafai, 2000; Vafai and Hadim, 2000). Additionally, competing models for multiphase transport models in porous media were analyzed in detail (see Vafai and Sözen, 1990). In that work, a critical analysis of various multiphase models including the phase change process was presented. These previous studies provide some clarification and insight for understanding several suitable aspects of modeling of transport phenomena in porous media utilized in the literature and this handbook.

In another study, a detailed analysis of variations among transport models for fluid flow and heat transfer in porous media was presented (see Alazmi and Vafai, 2000a). In this work, the essential models for fluid flow and heat transfer in porous media for four major categories were analyzed. An important aspect of modeling in porous media relates to interface conditions between a porous medium and a fluid layer. As such, the analysis of fluid flow and heat transfer in the neighborhood of an interface region for the current interfacial models was presented (see Alazmi and Vafai, 2000b). The determination of the appropriate thermal boundary conditions for the solid and fluid phases within a porous medium is also an important aspect of modeling in porous media. This type of modeling is necessary when the prescribed wall heat flux boundary conditions and local thermal nonequilibrium effects are present. As such, Alazmi and Vafai (2000c) presented and analyzed different pertinent forms of constant heat flux boundary conditions.

Developments in modeling transport phenomena in porous media have advanced several relevant areas, such as in biology (see Khaled and Vafai, 2003; Khanafer, and Vafai, 2006, 2007).

In these studies, various biological areas such as diffusion in brain tissues, diffusion during the tissue generation process, the use of magnetic resonance imaging (MRI) to characterize tissue properties, blood perfusion in human tissues, blood flow in tumors, bioheat transfer in tissues, and bioconvection have been synthesized. Another area includes the applications of nanofluids in porous media. Most recently, nanofluids have received a great interest because of their role in the enhancement of thermal properties. For example, Khanafer et al. (2003) conducted one of the first studies related to natural convection of nanofluids in a differentially heated cavity. A critical synthesis of the variants within the thermophysical properties of nanofluids was presented by Khanafer and Vafai (2011). In this work, correlations for effective thermal conductivity and viscosity were synthesized and developed in terms of suitable physical parameters based on the reported experimental data.

Different turbulent models for transport through porous media were analyzed in detail by Vafai et al. (2005). In this work, various features, strengths, and weaknesses of the essential turbulent models for flow through porous media have been analyzed, and the formulation of a generalized model leading to a more promising model is established and discussed. Further advances in porous media include modeling of the free surface fluid flow and heat transfer through porous media. This topic is important in a number of engineering applications such as geophysics, die filling, metal processing, agricultural and industrial water distribution, oil recovery techniques, and injection molding. Accordingly, a comprehensive analysis of the free surface fluid flow and heat transfer through porous media is presented in a work by Alazmi and Vafai (2004).

This handbook is targeted at researchers and practicing engineers, as well as beginners in this field. A leading expert in the related subject area presents each topic. An attempt has been made to present the topics in a cohesive, concise yet complementary way with a common format. Nomenclature common to various sections was used as much as possible.

This third edition of the *Handbook of Porous Media* is divided into six sections with a total of 26 chapters. The subject matter in Section I covers general characteristics and modeling of porous media such as multiscale modeling of porous media, two-phase flow, compressible porous media, and dispersion in porous media. Section II covers fundamental topics of transport in porous media, including theoretical models of transport, membrane transport phenomena, modeling transport properties, and transport in biomedical applications. Section III covers several important aspects of turbulence in porous media, including advances in modeling turbulence phenomena in heterogeneous porous media. Heat transfer of nanofluids in porous media is presented in Section IV. Section V covers thermal transport in porous media, including forced convection, double diffusive convection, high-heat flux applications, and thermal behavior of poroelastic media. Finally, Section VI covers geological applications in porous media, including modeling and experimental challenges related to oil fields, CO_2 migration, groundwater flows, and velocity measurements.

Over the past several decades, computational models for simulating subsurface flow problems have provided an impressive, ever-expanding ability to represent processes at a high resolution. Chapter 1 provides the thermodynamically constrained averaging theory (TCAT) approach to multi-scale modeling of porous medium systems that includes systematic averaging of conservation equations, thermodynamics, and phase and interface kinematics. By developing the definitions of all larger-scale variables in terms of smaller-scale precursors, the TCAT approach overcomes the limitations of rational thermodynamics approaches, which neglect smaller-scale thermodynamics and kinematics. Because the TCAT model yields general forms of closure relations defined in terms of averaged forms of precisely defined microscale quantities, both microscale experimental and simulation approaches provide a means to fully close the model and verify critical aspects of the macroscale theory. Lattice Boltzmann simulations and microfluidic experiments are used to validate critical aspects of the theory and inform the closure processes.

Chapter 2 provides a unifying approach to the theory of capillarity based on rational thermodynamics. Theoretical, experimental, and computational results have shown that the difference in fluid pressures is a function of the boundary conditions and dynamic properties of the system, such as flow rate or dynamic viscosities. Capillary pressure can be seen as an intrinsic property of the

fluid-solid system and independent of the dynamics of the system. Therefore, specific interfacial area (area of fluid–fluid interfaces per unit volume of the porous medium) as a new state variable is introduced in this chapter to account for the fact that capillary pressure is an interfacial phenomenon and not a volumetric one. Most recently, the problem of disposal of radioactive wastes has become a critical problem of national and international concern. Geological formations are considered as an acceptable storage area for radioactive nuclear wastes, as their permeability is typically low. Many of such formations are, however, highly fractured, even several hundred meters below the surface. Groundwater that flows through the fractures at such depths would be the carrier of any nuclear waste and contaminants that might leak out of the storage area and enter the flow system. Therefore, the characterization and modeling of fractures and fracture networks are discussed in Chapter 3.

Chapter 4 aims to illustrate why thin porous media are different from traditional porous media and identify the generic problems. This is performed through the consideration of a variety of selected examples extracted from studies on fuel cells, particle filtration, drying and salt efflorescence formation. A brief review of other situations involving thin porous media is also proposed in this chapter. Magnetically stabilized and fluidized beds have been the subject of moderate research and applications for several decades. More recently, this technique is being rediscovered and applied to important areas of research, for example, environmental technologies, especially biotechnology and biomedical applications. Chapter 5 presents a review of the applications of magnetically stabilized beds, including a description of its main principles and background theory. In Chapter 6, a comprehensive review of the recent studies on the lift generation in soft porous media is provided and includes four specific sections: the motion of red blood cells over the endothelial glycocalyx layer and its implications to soft porous lubrication, lift generation in highly compressible porous media under rapid compression, lift mechanics of skiing or snowboarding, and, finally, from red blood cells to skiing to soft porous lubrication. Chapter 7 reviews models for scalar transport in saturated porous media with nonlinear bulk and surface sources and sinks. Single- and multi-equation models for both equilibrium and nonequilibrium, integro-differential descriptions of time nonlocality, and hybrid approaches that couple partial differential equations acting at different scales are presented. As an example, this chapter shows how effective parameters can be calculated directly over a three-dimensional image of a bead-packing obtained using x-ray computed microtomograph.

A porous medium approach based on the volume averaging theory can be used to investigate solute diffusion and ultrafiltration processes associated with hemodialysis using a hollow fiber membrane dialyzer. An appropriate set of the governing equations based on the three-concentration model (i.e., the blood, dialysate, and membrane phases) has been derived using a porous media concept and is presented in Chapter 8. Available experimental data are found to agree well with the presented analytical estimates generated from the porous media theory. Furthermore, three-dimensional numerical models are proposed in this chapter for possible optimization of hollow fiber systems, such as dialyzers and desalination modules.

The prediction of effective transport properties of porous media is very important not only to the analysis and optimization of material performance, but also to new material designs. Chapter 9 first examines the difficulties in predicting porous media characteristics by summarizing and critiquing the existing major analytical approaches dealing with effective property modeling. The focus then shifts to recent advances in numerical modeling that are able to predict more accurately and efficiently the effective properties of porous materials with complex internal microstructures. A random generation-growth algorithm is highlighted in Chapter 9 for reproducing porous microstructures, statistically equivalent to the actual ones, based on the geometrical and morphological information obtained from measurements and experimental estimations. Chapter 10 presents a review of the outstanding approaches presented in the literature and several improved approaches developed for the formulation of effective transport through porous media under nonequilibrium relaxation conditions. Typical applications of these approaches are presented for different processes occurring in porous media. These include the separation of dissolved gas from oil and water, displacement of immiscible fluid phases in porous media, transport of dispersed wetting/nonwetting

phases through porous media, permeability impairment in porous media by precipitate deposition, and the modification of the popular gradient laws such as the Darcy, Fourier, and Fick laws for porous media flow, heat conduction, and diffusion, respectively, under unsteady-state conditions. The improvements and developments introduced are shown to describe the nonequilibrium dynamics of the porous media processes better than the previous approaches presented in the literature.

In Chapter 11, a deterministic model is suggested that describes the collective behavior of a microorganism population with a general form of stimuli gradient-based taxis in porous media. This population has a mass density slightly heavier than the density of water and forms a suspension. The suspended cells are active in motion with a thermotaxis behavior (temperature gradient follower). The model is basically comprised of the Darcy equation for the fluid motion in porous media, the equation of cell conservation for the microorganism population, and the equation of conservation for the considered stimuli. To take into account the density effects, Boussinesq's approximation is used. Linear stability analysis shows that temperature has interesting effects on the bioconvection pattern of the thermotactic microorganisms. The last part of the chapter discusses different potential applications of this model in porous media in the fields of life sciences and engineering, as well as for various natural biological systems. The topic of using feedback control to promote or suppress the transition to chaos in porous media convection is reviewed in Chapter 12. The feedback control is used to provide a comparison between an analytical expression for the transition point to chaos and numerical results. In addition, it is shown that such a feedback control can be applied as a practical means for controlling (suppressing or promoting) chaos by using a Magyari transformation. The latter shows that the main effect the feedback control has on the solution is equivalent to altering the initial conditions. The theoretical and practical significance of such equivalent alteration of the initial conditions is presented and discussed in this chapter. Chapter 13 provides an overview of recent development in modeling and simulating turbulent reactive flow in porous media, and the advantages of having a combustion process inside an inert porous matrix are well documented. In Chapter 14, the effects of nanofluids on convection in porous media are presented. Property variations that are the consequence of the fact that nanofluids are suspensions and the processes that occur due to the smallness of the nanoparticles are discussed in this chapter. The applications to forced convection, natural convection, and mixed convection in various geometries are then reviewed.

Chapter 15 reviews the controversial results for nanofluids and provides an explanation that settles the conflict between the apparent enhancement of the effective thermal conductivity in some experiments and the lack of enhancement in other experiments. Theoretical results combined with experimental data are reviewed in this chapter to conclude that while there is no improvement in the effective thermal conductivity of nanofluids beyond Maxwell's effective medium theory (Maxwell, 1891), there is substantial heat transfer augmentation via nanofilms.

Chapter 16 is concerned with heat transfer in closed- and open-cell foams at any temperature level. Porous cellular materials are of great interest since they present an unequalled combination of physical, mechanical, electrical, and thermal properties and find numerous applications in aerospace, chemical, mechanical, and energy engineering. The account is restricted to materials with a random structure and with submillimeter and/or larger mean pore (cell) diameters. The solid and fluid are assumed to be inert, and there are no chemical reactions in the fluid and is no phase change. In this chapter, the most recent literature related to the phenomena using the volume-averaged transport equations employing phenomenological closure coefficients is discussed. Chapter 17 gives an introduction to the flow and convection of Bingham fluids in a porous medium. For such yield-stress, fluids flow arises when the local body force, such as an externally imposed pressure gradient or buoyancy force, exceeds the threshold. Network models are derived and solved and plausible macroscopic Darcy–Bingham laws are given. Nonlinear convection is computed, and the resulting patterns are found to depend on the underlying microstructure of the medium. Recent advances in distributed (and modulated) wick structures, which have resulted in increased critical heat flux (CHF) and decreased superheat are reviewed in Chapter 18. Heat sinks use liquid-vapor, phase

change in wicks submerged in liquid (pool boiling) or in phase separation (single-pipe, loop heat pipes, and vapor chambers) for high heat flux applications with exceptional mechanical reliability and minimal power consumption. The maximum heat transfer rate, that is, CHF, and the related superheat are associated with the thermal-hydraulic bottlenecks within or near the wicks. The hydrodynamic instability, capillary-viscous flow, and wick thermal resistance limits are discussed in this chapter.

Jet impingement of a cold fluid is an efficient method for the cooling of a heated surface. This is one of the techniques employed in heat transfer enhancement technologies. Chapter 19 discusses impinging jets in porous media. The main contributions on the impinging jet in a porous medium are summarized in this chapter with some information on jet geometry, thermal conditions on the target plate, flow regime, and local thermal equilibrium (LTE) and nonequilibrium (LTNE). The classical problem in geomechanics dealing with the stress-induced isothermal flow of a fluid through a deformable porous medium, usually referred to as the process of soil consolidation, is a cornerstone in the development of the subject of *soil mechanics* and is generally regarded as the start of multiphasic treatment of the mechanics of porous media. Chapter 20 considers the thermo-hydro-mechanical behavior of poroelastic media. Chapter 21 determines the effect of conducting bounding plates on the stability properties of a horizontal porous layer saturated by a binary fluid. As such, this provides a better approximation of how experiments are set up in the laboratory compared to the usual fixed temperature or heat flux boundary conditions. Recently, mechanical vibrations are also used to control thermoconvective or thermosolutal flows in incompressible fluids in order to optimize heat and mass transfer processes. An overview of the digital imaging workflow with an emphasis on x-ray computed tomography (CT) is presented in Chapter 22. This is followed by a discussion of the various elements of the digital petrophysics workflow that includes imaging, image processing, and the modeling of transport properties. A review of experimental approaches to image dynamic multiphase interactions at the microscopic level during drainage and imbibition follows. Finally, some of the difficulties involved in relating studies done at the pore scale to the phenomena observed at the macroscopic reservoir scale are addressed in this chapter.

In Chapter 23, the difficulties associated with modeling the flow and transport processes associated with CO_2 injection into subsurface formations, more specifically into deep saline aquifers (DSA), are reviewed. The progress made in recent years in addressing these challenges and the resulting analytical and numerical models for CO_2 migration in geologic sequestration in scenarios are outlined. Chapter 24 reviews groundwater flows and their measurement techniques, as tested and reported in the literature. Groundwater constitutes more than 99% of the whole volume of nonsalty liquid phase water present on Earth, and it is considered the most important source of water for living beings. At the start of this chapter, the basic aspects of groundwater hydrology and Darcy's law are discussed. Some of the unique concepts of aquifer properties, that is, hydraulic conductivity, transmissivity, and storativity, are introduced in connection with well tests. The remainder of the chapter focuses on groundwater velocity measurement techniques at both large and small scales, since velocity is the most important property that determines subsurface transport processes. One particular problem in modeling large-scale porous media, such as oil, gas, and geothermal reservoirs, and the simulation of fluid flow therein is the identification of the flow paths that consist of interwell zones with significant permeabilities. Chapter 25 discusses the geostatistical simulation and reconstruction of porous media. Finally, Chapter 26 aims to describe the major pore-scale processes associated with microbially induced carbonate precipitation (MICP), placing these in the context of porous media reactive transport modeling approaches. First, MICP is divided into biological, physical, and geochemical sub processes. Next, their interactions are discussed at the pore scale, and finally it is determined how these processes and interactions affect local and system-wide reactive transport. This chapter as a whole is intended to serve as an overview of the current knowledge within the MICP field in regards to pore-scale processes. The processes are represented in equation form where possible to provide mathematical relationships that are useful for modeling.

In each of these chapters, whenever applicable, relevant aspects of experimental work or numerical techniques are discussed. The experts in the field have reviewed each chapter of this handbook. Overall, there were many reviewers who were involved. As such, the authors and I are very thankful for the valuable and constructive comments that were received.

Kambiz Vafai

REFERENCES

Alazmi, B. and Vafai, K., 2000a, Analysis of variants within the porous media transport models, *ASME Journal of Heat Transfer*, 122, 303–326.

Alazmi, B. and Vafai, K., 2000b, Analysis of fluid flow and heat transfer interfacial conditions between a porous medium and a fluid layer, *International Journal of Heat and Mass Transfer*, 44, 1735–1749.

Alazmi, B. and Vafai, K., 2000c, Constant wall heat flux boundary conditions in porous media under local thermal non-equilibrium conditions, *International Journal of Heat and Mass Transfer*, 45, 3071–3087.

Alazmi, B. and Vafai, K., 2004, Analysis of variable porosity, thermal dispersion and local thermal non-equilibrium effects on free surface flows through porous media, *Journal of Heat Transfer*, 126, 389–399.

Hadim, H. and Vafai, K., 2000, Overview of current computational studies of heat transfer in porous media and their applications—Forced convection and multiphase transport, in W. J. Minkowycz and E. M. Sparrow, eds., *Advances in Numerical Heat Transfer*, Vol. 2, Chapter 9, pp. 291–330, Taylor & Francis, New York.

Khaled, A.-R.A. and Vafai, K., 2003, The role of porous media in modeling flow and heat transfer in biological tissues, *International Journal of Heat and Mass Transfer*, 46, 4989–5003.

Khanafer, K. and Vafai, K., 2006, The role of porous media in biomedical engineering as related to magnetic resonance and drug delivery, *Heat and Mass Transfer*, 42, 939–953.

Khanafer, K. and Vafai, K., 2007, Macromolecular transport in arterial walls: Current and future, in *Emerging Topics in Heat and Mass Transfer in Porous Media*, pp. 219–235, Springer.

Khanafer, K. and Vafai, K., 2011, A critical synthesis of thermophysical characteristics of nanofluids, *International Journal of Heat and Mass Transfer*, 54, 4410–4428.

Khanafer, K., Vafai, K., and Lightstone, M., 2003, Buoyancy-driven heat transfer enhancement in a two-dimensional enclosure utilizing nanofluids, *International Journal of Heat and Mass Transfer*, 46, 3639–3653.

Maxwell, J.C., 1891, *Treatise on Electricity and Magnetism*.

Tien, C.L. and Vafai, K., 1989, Convective and radiative heat transfer in porous media, *Advances in Applied Mechanics*, 27, 225–282.

Vafai, K. and Hadim, H., 2000, Overview of current computational studies of heat transfer in porous media and their applications—Natural convection and mixed convection, in W. J. Minkowycz and E. M. Sparrow, eds., *Advances in Numerical Heat Transfer*, Vol. 2, Chapter 10, pp. 331–371, Taylor & Francis, New York.

Vafai, K. and Sönzen, M., 1990, A comparative analysis of multiphase transport models in porous media, *Annual Review of Heat Transfer*, 3, 145–162.

Vafai, K. et al., 2005, Synthesis of models for turbulent transport through porous media, in W.J. Minkowycz and E.M. Sparrow, eds., *Handbook of Numerical Heat Transfer*, John Wiley & Sons, New York.

MATLAB® is a registered trademark of The MathWorks, Inc. For product information, please contact:

The MathWorks, Inc.
3 Apple Hill Drive
Natick, MA 01760-2098 USA
Tel: 508-647-7000
Fax: 508-647-7001
E-mail: info@mathworks.com
Web: www.mathworks.com

Editor

Kambiz Vafai received his BSc (highest honors) in mechanical engineering from the University of Minnesota and MSc and PhD in mechanical engineering from the University of California, Berkeley. He is a prolific author who is honored by his peers worldwide. He is distinguished professor of mechanical engineering at the University of California, Riverside, California, where he previously held the presidential chair. Before joining the University of California, Dr. Vafai was a full professor at The Ohio State University, where he received outstanding research awards in the assistant, associate, and full professor categories. He is fellow of several societies. Prof. Vafai is the recipient of the American Society of Mechanical Engineers (ASME) Classic Paper Award and the ASME Memorial Award. He was given the International Society of Porous Media (InterPore) Highest Award. He is also the recipient of the 75th Anniversary Medal of the ASME Heat Transfer Division. He holds 12 U.S. patents associated with electronic cooling and thermal and fluid flow applications. He is one of the highest cited authors in his fields of research according to ISI Highly Cited and Google Scholar metrics. His research interests are porous media, multiphase transport, aircraft brake design, micro cantilever biosensors, biofilms, electronics cooling, macromolecule transport in arteries, cooling enhancement, modeling of tissue and organs, natural convection in complex configurations, insulations, high heat flux design, free surface flows, flat-shaped heat pipes, power electronics, and thermal design and modeling and optimization in general.

Contributors

Tristan Agaësse
Institut de Mécanique des Fluides de Toulouse
Université de Toulouse
Toulouse, France

Zineddine Alloui
Department of Common Core of Sciences and Techniques
University of Batna
Batna, Algeria

Audelino Álvaro
Departamento de Ingeniería Química y Textil
Universidad de Salamanca
Salamanca, Spain

Paulo A. Augusto
Departamento de Engenharia Química
Universidade do Porto
Porto, Portugal

and

Departamento de Ingeniería Química y Textil
Universidad de Salamanca
Salamanca, Spain

Domingos Barbosa
Departamento de Engenharia Química
Universidade do Porto
Porto, Portugal

Bernardo Buonomo
Dipartimento di Ingegneria Industriale e dell'Informazione
Seconda Università degli Studi di Napoli
Aversa, Italy

Teresa Castelo-Grande
Departamento de Engenharia Química
Universidade do Porto
Porto, Portugal

Marie Catherine Charrier-Mojtabi
Laboratoire Phase
Toulouse, France

and

University of Evry
Evry, France

Faruk Civan
Mewbourne School of Petroleum and Geological Engineering
The University of Oklahoma
Norman, Oklahoma

James Connolly
Center for Biofilm Engineering
Montana State University
Bozeman, Montana

Yohan Davit
Institut de Mécanique des Fluides de Toulouse
Université de Toulouse
Toulouse, France

Marcelo J.S. de Lemos
Departamento de Energia
Aeronautics Institute of Technology
Sao Paulo, Brazil

Amanda L. Dye
Environmental Sciences and Engineering
University of North Carolina
Chapel Hill, North Carolina

Bilal ElHajjar
Mechanical Laboratory
Evry-Val-D'Esonne University
Île-de-France, France

Angel M. Estevéz
Departamento de Ingeniería Química y Textil
Universidad de Salamanca
Salamanca, Spain

Robin Gerlach
Department of Chemical and Biological Engineering
and
Center for Biofilm Engineering
Montana State University
Bozeman, Montana

William G. Gray
Environmental Sciences and Engineering
University of North Carolina
Chapel Hill, North Carolina

S. Majid Hassanizadeh
Department of Earth Sciences
Utrecht University
Utrecht, the Netherlands

Gisuk Hwang
Department of Mechanical Engineering
Wichita State University
Wichita, Kansas

Massoud Kaviany
Department of Mechanical Engineering
University of Michigan
Ann Arbor, Michigan

Shigeo Kimura
Institute of Nature and Environmental Study
Kanazawa University
Kakuma, Japan

A.V. Kuznetsov
Department of Mechanical and Aerospace Engineering
North Carolina State University
Raleigh, North Carolina

Oronzio Manca
Dipartimento di Ingegneria Industriale e dell'Informazione
Seconda Università degli Studi di Napoli
Aversa, Italy

James E. McClure
Advanced Research Computing
Virginia Polytechnic Institute and State University
Blacksburg, Virginia

Cass T. Miller
Environmental Sciences and Engineering
University of North Carolina
Chapel Hill, North Carolina

Abdelkader Mojtabi
Institut de Mécanique des Fluides
Toulouse, France

Sumit Mukhopadhyay
Lawrence Berkeley National Laboratory
Berkeley, California

K. Nagase
Department of Mechanical Engineering
Shizuoka University
Hamamatsu, Japan

A. Nakayama
Department of Mechanical Engineering
Shizuoka University
Hamamatsu, Japan

and

School of Civil Engineering and Architecture
Wuhan Polytechnic University
Wuhan, People's Republic of China

Sergio Nardini
Dipartimento di Ingegneria Industriale e dell'Informazione
Seconda Università degli Studi di Napoli
Aversa, Italy

Tri Nguyen-Quang
Engineering Department
Dalhousie University
Bible Hill, Nova Scotia, Canada

D.A. Nield
Department of Engineering Science
University of Auckland
Auckland, New Zealand

T. Nishimura
Department of Mechanical Engineering
Shizuoka University
Hamamatsu, Japan

Chanwoo Park
Department of Mechanical and Aerospace Engineering
University of Missouri
Columbia, Missouri

Marc Prat
Institut de Mécanique des Fluides de Toulouse
CNRS, Université de Toulouse
Toulouse, France

Michel Quintard
Institut de Mécanique des Fluides de Toulouse
Université de Toulouse
Toulouse, France

Yazdan Pedram Razi
Silicon Valley University
San Jose, California

D. Andrew S. Rees
Department of Mechanical Engineering
University of Bath
Bath, United Kingdom

Jesus Ma. Rodríguez
Departamento de Ingeniería Química y Textil
Universidad de Salamanca
Salamanca, Spain

Muhammad Sahimi
Mork Family Department of Chemical Engineering & Materials Science
University of Southern California
Los Angeles, California

Y. Sano
Graduate School of Natural Science and Technology
Okayama University
Okayama, Japan

A. P. S. Selvadurai
Department of Civil Engineering and Applied Mechanics
McGill University
Montréal, Québec, Canada

Pejman Tahmasebi
Mork Family Department of Chemical Engineering & Materials Science
University of Southern California
Los Angeles, California

Peter Tilke
Schlumberger-Doll Research Center
Cambridge, Massachusetts

Cármen Torrente
Departamento de Ingeniería Química y Textil
Universidad de Salamanca
Salamanca, Spain

Peter Vadasz
Department of Mechanical Engineering
Northern Arizona University
Flagstaff, Arizona

and

Department of Mechanical and Aeronautical Engineering
University of Pretoria
Pretoria, South Africa

Raymond Viskanta
School of Mechanical Engineering
Purdue University
West Lafayette, Indiana

Moran Wang
Department of Engineering Mechanics and CNMM
Tsinghua University
Beijing, China

Qianhong Wu
Department of Mechanical Engineering
Villanova University
Villanova, Pennsylvania

Section I

General Characteristics and Modeling of Porous Media

1 Multiscale Modeling of Porous Medium Systems

Amanda L. Dye, James E. McClure, William G. Gray, and Cass T. Miller

CONTENTS

1.1 Introduction 3
1.2 Overview 5
1.3 Theory 6
1.3.1 Averaging Theorems 6
1.3.2 Conservation and Balance Equations 7
1.3.3 Entropy Balance 9
1.3.4 Thermodynamic Formalism 10
1.3.5 Evolution Equations 13
1.3.6 Entropy Inequality 15
1.4 Model Formulation 16
1.5 Microscale Considerations 18
1.6 Lattice Boltzmann Modeling 20
1.6.1 Formulation 20
1.6.2 Verification and Parameter Estimation 24
1.6.3 Validation 24
1.7 Computational Geometry Methods 27
1.8 TCAT Closure Relations 27
1.8.1 Simulations 27
1.8.2 Capillary Pressure–Saturation–Interfacial Area Relation 30
1.8.3 Disconnected Nonwetting Phase 32
1.8.4 Dynamic Relaxation 35
1.9 Discussion and Conclusions 37
Nomenclature 38
Acknowledgments 42
References 42

1.1 INTRODUCTION

The use of computers over the last 60 years for simulating subsurface flow problems has provided an impressive, ever-expanding ability to model processes at a high resolution. Whereas in the 1960s a computational grid with 500 fixed nodes would have pushed the boundaries of computer power [59], simulations today involve millions of spatial grid points and adaptive meshes [40,57]. The availability of this power for solving equations that purport to describe physical and chemical processes in porous media is wasted, however, if the equations being used to describe

the systems are inadequate. Most assuredly, the ability to solve equations that are posed has been vastly improved. Unfortunately, the equations that are being solved have not developed to the same degree.

For example, the primary equation for describing momentum transport of fluids in porous media is Darcy's law, a correlation of data from a highly idealized set of experiments (e.g., homogeneous medium, single-fluid phase, steady state) published in 1856 [9,16,17]. The results of these experiments have been presumed to apply to transient, multiphase flows in heterogeneous systems at different scales. This extension of the experiment to systems clearly beyond their scope has resulted in equations with ill-defined and poorly understood variables. A clear path for rigorously extending the form of Darcy's equation to flows well beyond those considered by Darcy, such as high-velocity flow and flows with cross coupling between the fluid phases, does not exist. Furthermore, inclusion of physical phenomena such as capillary pressure, contact angles, and evolution of interfaces between phases has been a heuristic effort justified somewhat by dabbling in physical understanding rather than a comprehensive rigorous derivation of equations that describe the processes (e.g., [34,49,53]).

Averaging of equations from the microscale to a larger scale is one general approach that has been employed in an effort to obtain equations that have a firm theoretical basis. Underlying averaging theory is the mathematical theorems that allow transformation of the scale of equations. Theorems for transformation of conservation equations for phases have been employed for almost 50 years [3,4,60,68]. Theorems that allow averaging of equations for interfaces between phases and for common curves, where three interfaces meet, were developed subsequently [22,30], and the forms of all these equations have been unified [27]. Four principal variants of averaging theory that make use of these theorems have been employed. The first emphasizes averaging of microscale conservation equations for phases and then makes heuristic arguments to close the equation system (e.g., [6,29,68]).

A second approach pioneered by Whitaker, and employed by adherents to this approach, is commonly referred to as the method of volume averaging (MVA). Applications of MVA typically make use of averaging theorems applied to conservation equations for phases only. This approach begins with closed microscale equations, which are then averaged to a larger scale. The new terms that arise are closed typically by derivation of closure equations solved for a periodic unit cell and the solution of closure variables to map from the smaller scale to the larger scale (e.g., [8,15,21,54–56,61,69,71]).

The third approach makes use of averaging of conservation equations in conjunction with rational thermodynamics (ACRT). ACRT averages equations for phases, interfaces, and common curves. Then, based on a set of axioms concerning system behavior, thermodynamic relations are obtained directly at the larger scale; and the equation set is closed based on exploitation of an entropy inequality (e.g., [7,31,33,64]).

These preceding methods have shortcomings primarily in that the first two methods do not account for interface dynamics and require assumptions about the forms for deviations between microscale and larger-scale values. The approaches make very limited use of thermodynamic information. ACRT suffers in that the larger-scale thermodynamic relations in fact are expressed in terms of quantities that are not based on fundamental thermodynamic variables [5,42,44,66]. Additionally, these models have been abused by using erroneous closure conditions for the interface stress tensor and the interface dynamics (e.g., [50,51]). Thus, complete and correct models based on averaged conservation equations, thermodynamics, and phase distribution kinematics are missing.

In an effort to overcome the problems of these earlier methods, a fourth method, referred to as thermodynamically constrained averaging theory (TCAT), has been formulated. This method is the basis of this contribution. Here, we outline the elements of TCAT and show how it can be used to obtain model equations that overcome many theoretical difficulties.

1.2 OVERVIEW

Conservation equations and thermodynamic relations applicable to porous medium systems are well understood at the microscale where the boundaries between all phases are resolved and evolved dynamically. However, many porous medium systems are described at a scale above the microscale, where a point refers to the averaged conditions in some representative averaging region. We will call this larger scale the macroscale. The TCAT has been developed to formulate macroscale models such that all variables are expressed explicitly in terms of microscale precursors [24,28]. TCAT also assures consistency with the second law of thermodynamics. It has been shown that use of the TCAT procedure leads to the occurrence of variables such as volume fractions, interfacial tensions, and density of interfacial area between the fluid and solid phases for the case of single-fluid porous medium systems. For multifluid systems, common curve lengths per volume, interfacial tensions, curvatures, and contact angles also arise naturally in the formulation [39]. On physical grounds, these variables can be argued to be of importance; their magnitudes relate to possibilities for interactions and exchanges between phases. However, these variables do not appear explicitly in traditional porous medium models.

Despite the theoretical appeal of TCAT models, a problem remains; solvable models require the explicit identification of closure relations that have only been specified in general functional forms by the theoretical work advanced to date. The constitutive relations employed for a particular system must be consistent with the general functional dependences inferred and must also be clearly stipulated and parameterized. Closed models are needed both to facilitate solution of an equation set and to allow for validation of TCAT models by comparison with system behavior observed at the corresponding scale.

In recent years, some needed closed forms have been motivated by small-scale experimental and computational methods. Of particular interest here is the high-resolution microscale modeling approach known as the lattice Boltzmann method (LBM). This method can be used to generate both a detailed understanding of microscale transport phenomena within the pores of a porous medium system and also the macroscale variables that can be obtained as integrated forms of the microscale variables. These macroscale variables can be employed in posited general forms of closure relations [20,32,52,65]. Computational experiments thus provide a basis for the development of closed models making use of equations developed using the TCAT procedure. Because TCAT models are new, multiscale modeling of specific forms of TCAT closure relations has not yet been completed for many theorized model formulations.

In this chapter, we examine a TCAT model for two-fluid-phase flow in a porous medium system. In Section 1.3, we provide the theoretical elements that are combined to establish the TCAT approach. In Section 1.4 we propose a set of closed equations that describes two-fluid-phase flow in a porous medium. For this set to be solvable, values or functional forms of some coefficients and equations of state must be specified. In Section 1.5, we discuss how knowledge of the smaller-scale system behavior, obtained through complementary experimental and LBM studies, can provide insights for specification of the needed forms and coefficients. Section 1.6 provides details concerning the formulation, verification, and validation of the LBM approach used to simulate two-fluid-phase flow in a porous medium system. The resultant model is used to investigate various aspects of the flow system that the TCAT model suggests warrant attention, such as an appropriate formulation of capillary pressure. The need to obtain information about geometric features of the porous medium system, such as the curvature of interfaces between phases and the extent of those interfaces, is discussed in Section 1.7. In Section 1.8, specific closure relations for a two-fluid-phase system are obtained from analysis of LBM simulations. This serves as an illustration of how robust models and formulations can be advanced by rigorous theoretical analysis in conjunction with computer simulation for a range of phenomena.

1.3 THEORY

TCAT is a systematic procedure for changing the scale of conservation, balance, and thermodynamic equations from the microscale to a larger scale. For use in porous media, the TCAT method involves averaging over a representative averaging volume to obtain equations for phases, interfaces between phases, common curves, and common points, which are referred to generically as entities. TCAT has been developed by considering each of these entities separately. Here, we will make use of the similarities of the equations and averaging theorems for each of the different entity types to develop the equations. The following six sections present the essential TCAT components: averaging theorems, conservation equations, entropy balance, thermodynamic equations, evolution equations, and the entropy inequality. The full details of these equations and the procedures used to manipulate them can be found in [28]. Here, we emphasize the equations that are particularly useful in macroscale porous medium flow modeling. These results form the bases for model formulation and closure considerations, which are considered subsequently.

1.3.1 Averaging Theorems

For porous medium analysis, it is not possible to model large systems at a microscale where the flow profile within the pores is described. Neither is it always informative to model the system at a megascale where only an average value of a quantity within the full system is determined. As a compromise between these two extremes, it is important to be able to model natural systems and laboratory systems at an intermediate length scale, referred to as the macroscale, where a filtered form of quantities in the system is used. At the microscale, the phases within a system are visualized as being juxtaposed and separated by interfaces. At a microscale location, a point lies within a single phase or on an interface or a common curve. From a macroscale perspective, all phases, interfaces, and common curves may be present at a location with each having a geometric density. A phase has a volume fraction measure, an interface has an interfacial area per volume measure, and a common curve has a length per volume measure. A similar density can be developed for common points, which do not occur in the systems considered in this chapter.

The conservation and balance equations that describe a system are most easily formulated directly in terms of microscale quantities. To transform the microscale equations to the macroscale, mathematical relations are needed. These have the effect of changing averages of derivatives of microscale quantities into derivatives of macroscale quantities. These theorems [3,22,23,27,30,37,43,47,60,67] are most readily applied when the length scales of the microscale and macroscale are widely separated. Microscale phase conservation equations are 3D transient forms. Interface conservation equations are 2D at the microscale. Common curves and common points are, respectively, one and zero dimensional at the microscale. On transformation to the macroscale, all these equations become 3D as the properties of interest vary in space regardless of the type of entity to which they belong.

The spatial averaging theorems are applied, respectively, to the divergence and gradient operators according to

$$\left\langle \nabla^{(n)} \cdot \mathbf{f}_\alpha \right\rangle_{\Omega_\alpha,\Omega} = \nabla \cdot \left\langle \mathbf{l}_\alpha^{(n)} \cdot \mathbf{f}_\alpha \right\rangle_{\Omega_\alpha,\Omega} - \left\langle \left(\nabla^{(n)} \cdot \mathbf{l}_\alpha^{(n)} \right) \cdot \mathbf{f}_\alpha \right\rangle_{\Omega_\alpha,\Omega} + \sum_{\kappa \in \mathcal{J}_{c\alpha}} \left\langle \mathbf{n}_\alpha \cdot \mathbf{f}_\alpha \right\rangle_{\Omega_\kappa,\Omega} \tag{1.1}$$

and

$$\left\langle \nabla^{(n)} f_\alpha \right\rangle_{\Omega_\alpha,\Omega} = \nabla \cdot \left\langle \mathbf{l}_\alpha^{(n)} f_\alpha \right\rangle_{\Omega_\alpha,\Omega} - \left\langle \left(\nabla^{(n)} \cdot \mathbf{l}_\alpha^{(n)} \right) f_\alpha \right\rangle_{\Omega_\alpha,\Omega} + \sum_{\kappa \in \mathcal{J}_{c\alpha}} \left\langle \mathbf{n}_\alpha f_\alpha \right\rangle_{\Omega_\kappa,\Omega}, \tag{1.2}$$

where (n) is the number of primes that appears in the superscript, the integration domain is of dimensionality $3 - n$, and the averaging operator is indicated using angle brackets. Thus, for example, for a surface of dimensionality 2, $(n) = (1)$, so the microscale surface gradient operator, ∇', uses a single $'$ to indicate that it is a surface operator. For a phase, $n = 0$ and $\mathbf{l}_\alpha^{(0)} = \mathbf{l}$. For a common point, $n = 3$ and $\mathbf{l}_\alpha^{(3)} = \mathbf{0}$. Note that all variables and operators are defined in the nomenclature section.

In addition to the spatial averaging theorems, a temporal averaging theorem is employed that relates the spatial average of a time derivative of a function to the time derivative of the spatial average of the function. This theorem is stated

$$\left\langle \frac{\partial^{(n)} f_\alpha}{\partial t} \right\rangle_{\Omega_\alpha,\Omega} = \frac{\partial}{\partial t}\left\langle f_\alpha \right\rangle_{\Omega_\alpha,\Omega} + \nabla\cdot\left\langle \left(\mathbf{l} - \mathbf{l}_\alpha^{(n)}\right)\right\rangle\cdot \mathbf{v}_\alpha f_\alpha\rangle_{\Omega_\alpha,\Omega} + \left\langle \nabla^{(n)}\cdot\mathbf{l}_\alpha^{(n)}\cdot\mathbf{v}_\alpha f_\alpha\right\rangle_{\Omega_\alpha,\Omega} - \sum_{\kappa\in\mathcal{J}_{c\alpha}^-}\left\langle \mathbf{n}_\alpha\cdot\mathbf{v}_\kappa f_\alpha\right\rangle_{\Omega_\kappa,\Omega}, \tag{1.3}$$

where

(n) is the number of primes that appears in the superscript
the integration domain, Ω_α, is of dimensionality $3 - n$

Equations 1.1 and 1.3 are the primary averaging theorems that are used to convert microscale conservation equations for phases, interfaces, common curves, and common points to their macroscale forms.

1.3.2 Conservation and Balance Equations

The conservation equations at the macroscale can all be derived from the microscale total energy equation by application of the averaging theorems followed by the restriction that the equation obtained must apply in any inertial coordinate system. In the development here, we will not consider species transport or interphase mass transfer of individual species. We state the microscale total energy equation for entity α as

$$\begin{aligned}\mathcal{E}_\alpha :=& \frac{\partial^{(n)}}{\partial t}\left(E_\alpha + \rho_\alpha\frac{\mathbf{v}_\alpha\cdot\mathbf{v}_\alpha}{2} + \Psi_\alpha\right) + \nabla^{(n)}\cdot\left[\left(E_\alpha + \rho_\alpha\frac{\mathbf{v}_\alpha\cdot\mathbf{v}_\alpha}{2} + \Psi_\alpha\right)\mathbf{v}_\alpha\right]\\ &- h_\alpha - \rho_\alpha\frac{\partial^{(n)}\psi_\alpha}{\partial t} - \rho_\alpha\mathbf{g}_\alpha\cdot\left(\mathbf{l} - \mathbf{l}_\alpha^{(n)}\right)\cdot\mathbf{v}_\alpha\\ &- \sum_{\kappa\in\mathcal{J}_{c\alpha}^+}\left[\left(\frac{E_\kappa}{\rho_\kappa} + \frac{\mathbf{v}_\kappa\cdot\mathbf{v}_\kappa}{2} + \psi_\kappa\right)M_{\kappa\to\alpha} + \mathbf{v}_\kappa\cdot\mathbf{T}_{\kappa\to\alpha} + Q_{\kappa\to\alpha}\right]\\ &- \nabla^{(n)}\cdot\left(\mathbf{l}_\alpha^{(n)}\cdot\mathbf{t}_\alpha\cdot\mathbf{v}_\alpha + \mathbf{l}_\alpha^{(n)}\cdot\mathbf{q}_\alpha\right) = 0 \quad \text{for } \alpha\in\mathcal{J}; n = 3 - \dim\alpha,\end{aligned} \tag{1.4}$$

where the summation term in this equation accounts for exchanges with entities of higher dimensionality.

This equation is averaged to the macroscale using the operator $\langle\cdot\rangle_{\Omega_\alpha,\Omega}$. After application of the averaging theorems Equations 1.1 and 1.3, the macroscale energy equation that results is

$$
\begin{aligned}
\mathcal{E}^{\bar{\bar{\alpha}}} :=& \frac{\partial}{\partial t}\left[E^{\bar{\bar{\alpha}}} + \epsilon^{\bar{\bar{\alpha}}}\rho^{\bar{\bar{\alpha}}}\left(\frac{\mathbf{v}^{\bar{\alpha}}\cdot\mathbf{v}^{\bar{\alpha}}}{2} + K_E^{\bar{\bar{\alpha}}}\right) + \Psi^{\bar{\bar{\alpha}}}\right] \\
&+ \nabla\cdot\left\{\left[E^{\bar{\bar{\alpha}}} + \epsilon^{\bar{\bar{\alpha}}}\rho^{\alpha}\left(\frac{\mathbf{v}^{\bar{\alpha}}\cdot\mathbf{v}^{\bar{\alpha}}}{2} + K_E^{\bar{\bar{\alpha}}}\right) + \Psi^{\bar{\bar{\alpha}}}\right]\mathbf{v}^{\bar{\alpha}}\right\} \\
&- \epsilon^{\bar{\bar{\alpha}}}h^{\alpha} - \sum_{\kappa\in\mathcal{J}_{c\alpha}}{}^{\kappa\to\alpha}M\left(\bar{\bar{E}}^{\alpha,\kappa} + \frac{\mathbf{v}^{\bar{\bar{\alpha},\kappa}}\cdot\mathbf{v}^{\bar{\bar{\alpha},\kappa}}}{2} + K_E^{\bar{\bar{\alpha},\kappa}} + \psi^{\bar{\bar{\alpha},\kappa}}\right) \\
&- \sum_{\kappa\in\mathcal{J}_{c\alpha}}{}^{\kappa\to\alpha}\mathbf{T}\cdot\mathbf{v}^{\bar{\bar{\alpha},\kappa}} - \sum_{\kappa\in\mathcal{J}_{c\alpha}}{}^{\kappa\to\alpha}Q \\
&- \nabla\cdot\left[\epsilon^{\bar{\bar{\alpha}}}\mathbf{t}^{\bar{\bar{\alpha}}}\cdot\mathbf{v}^{\bar{\alpha}} + \epsilon^{\bar{\bar{\alpha}}}\mathbf{q}^{\bar{\bar{\alpha}}} + \epsilon^{\bar{\bar{\alpha}}}\mathbf{q}_{\mathrm{d}}^{\bar{\bar{\alpha}}}\right] + \left\langle\rho_\alpha\frac{\partial^{\square}\psi_\alpha}{\partial t}\right\rangle_{\square_\alpha} \\
&- \left\langle\rho_\alpha\mathbf{v}_\alpha\cdot\left[\mathbf{I}\cdot\mathbf{g}_\alpha\right]\right\rangle_{\square_\alpha} = \square\ \square\alpha\in\mathcal{J}\square = \square - \square\alpha
\end{aligned}
\tag{1.5}
$$

The notation used in this equation is designed to precisely indicate the macroscale quantities (with superscripts), particular kinds of averages (spatial average with no overbar on the superscript, mass density weighted with a single overbar on the superscript, specially defined with a double overbar on the superscript), and an exchange term between entities (with a super arrow indicating the transfer from one entity to the other). The definitions arise naturally in the averaging process, and the expressions in terms of microscale variables appear in the nomenclature or in far greater detail in [28]. It is useful to rewrite the first two terms in Equation 1.5 making use of the material derivative operator to obtain

$$
\begin{aligned}
\mathcal{E}_*^{\bar{\bar{\alpha}}} :=& \frac{\mathrm{D}^{\bar{\alpha}}}{\mathrm{D}t}\left[E^{\bar{\bar{\alpha}}} + \epsilon^{\bar{\bar{\alpha}}}\rho^{\alpha}\left(\frac{\mathbf{v}^{\bar{\alpha}}\cdot\mathbf{v}^{\bar{\alpha}}}{2} + K_E^{\bar{\bar{\alpha}}}\right) + \Psi^{\bar{\bar{\alpha}}}\right] \\
&+ \left[E^{\bar{\bar{\alpha}}} + \epsilon^{\bar{\bar{\alpha}}}\rho^{\alpha}\left(\frac{\mathbf{v}^{\bar{\alpha}}\cdot\mathbf{v}^{\bar{\alpha}}}{2} + K_E^{\bar{\bar{\alpha}}}\right) + \Psi^{\bar{\bar{\alpha}}}\right]\mathbf{I}:\mathbf{d}^{\bar{\bar{\alpha}}} \\
&- \epsilon^{\bar{\bar{\alpha}}}h^{\alpha} - \sum_{\kappa\in\mathcal{J}_{c\alpha}}{}^{\kappa\to\alpha}M\left(\bar{\bar{E}}^{\alpha,\kappa} + \frac{\mathbf{v}^{\bar{\bar{\alpha},\kappa}}\cdot\mathbf{v}^{\bar{\bar{\alpha},\kappa}}}{2} + K_E^{\bar{\bar{\alpha},\kappa}} + \psi^{\bar{\bar{\alpha},\kappa}}\right) \\
&- \sum_{\kappa\in\mathcal{J}_{c\alpha}}{}^{\kappa\to\alpha}\mathbf{T}\cdot\mathbf{v}^{\bar{\bar{\alpha},\kappa}} - \sum_{\kappa\in\mathcal{J}_{c\alpha}}{}^{\kappa\to\alpha}Q \\
&- \nabla\cdot\left[\epsilon^{\bar{\bar{\alpha}}}\mathbf{t}^{\bar{\bar{\alpha}}}\cdot\mathbf{v}^{\bar{\alpha}} + \epsilon^{\bar{\bar{\alpha}}}\mathbf{q}^{\bar{\bar{\alpha}}} + \epsilon^{\bar{\bar{\alpha}}}\mathbf{q}_{\mathrm{d}}^{\bar{\bar{\alpha}}}\right] + \left\langle\rho_\alpha\frac{\partial^{\square}\psi_\alpha}{\partial t}\right\rangle_{\square_\alpha} \\
&- \left\langle\rho_\alpha\mathbf{v}_\alpha\cdot\left[\mathbf{I}\cdot\mathbf{g}_\alpha\right]\right\rangle_{\square_\alpha} = \square\ \square\alpha\in\mathcal{J}\square = \square - \square\alpha
\end{aligned}
\tag{1.6}
$$

This energy equation must apply in any inertial reference coordinate system. We can replace $\mathbf{v}^{\bar{\alpha}}$ by $\mathbf{v}^{\bar{\alpha}} + \mathbf{C}$, where $\mathbf{C}$ is an arbitrary constant velocity vector, and Equation 1.6 will still apply. After making this substitution, collection of terms that multiply $\mathbf{C}$ results in an equation of the form

$$\boldsymbol{\mathcal{E}}_*^{\bar{\bar{\alpha}}} + \mathbf{C} \cdot \boldsymbol{\mathcal{P}}_*^{\bar{\bar{\alpha}}} + \frac{\mathbf{C} \cdot \mathbf{C}}{2} \mathcal{M}_*^{\bar{\bar{\alpha}}} = 0. \tag{1.7}$$

Because $\mathbf{C}$ is arbitrary, selection of $\mathbf{C} = \mathbf{0}$ confirms that Equation 1.6 still applies. If $\mathbf{C}$ is orthogonal to the terms collected to form $\boldsymbol{\mathcal{P}}_*^{\bar{\bar{\alpha}}}$, then Equation 1.7 requires that $\mathcal{M}_*^{\bar{\bar{\alpha}}} = 0$. Therefore, we must also have $\boldsymbol{\mathcal{P}}_*^{\bar{\bar{\alpha}}} = \mathbf{0}$, since Equation 1.7 must hold for any and all constant $\mathbf{C}$. The group of terms that comprises $\boldsymbol{\mathcal{P}}_*^{\bar{\bar{\alpha}}}$ is the momentum equation as follows:

$$\begin{aligned} \boldsymbol{\mathcal{P}}_*^{\bar{\bar{\alpha}}} := & \frac{\mathrm{D}^{\bar{\alpha}}}{\mathrm{D}t}\left(\epsilon^{\bar{\bar{\alpha}}} \rho^{\alpha} \mathbf{v}^{\bar{\alpha}}\right) + \epsilon^{\bar{\bar{\alpha}}} \rho^{\alpha} \mathbf{v}^{\bar{\alpha}} \mathbf{I} : \mathbf{d}^{\bar{\bar{\alpha}}} - \epsilon^{\bar{\bar{\alpha}}} \rho^{\alpha} \mathbf{g}^{\bar{\alpha}} \\ & - \sum_{\kappa \in \mathcal{J}_{c\alpha}} {}^{\kappa \to \alpha}_{M} \, \mathbf{v}^{\overline{\overline{\alpha,\kappa}}} - \sum_{\kappa \in \mathcal{J}_{c\alpha}} {}^{\kappa \to \alpha}_{\mathbf{T}} - \nabla \cdot \left(\epsilon^{\bar{\bar{\alpha}}} \mathbf{t}^{\bar{\bar{\alpha}}}\right) = 0 \quad \text{for } \alpha \in \mathcal{J}. \end{aligned} \tag{1.8}$$

The elements of $\mathcal{M}_*^{\bar{\bar{\alpha}}}$ constitute the mass conservation equation for entity α, which can be written as

$$\mathcal{M}_*^{\bar{\bar{\alpha}}} := \frac{\mathrm{D}^{\bar{\alpha}}\left(\epsilon^{\bar{\bar{\alpha}}} \rho^{\alpha}\right)}{\mathrm{D}t} + \epsilon^{\bar{\bar{\alpha}}} \rho^{\alpha} \mathbf{I} : \mathbf{d}^{\bar{\bar{\alpha}}} - \sum_{\kappa \in \mathcal{J}_{c\alpha}} {}^{\kappa \to \alpha}_{M} = 0 \quad \text{for } \alpha \in \mathcal{J}. \tag{1.9}$$

For two-fluid-phase flow, we note that the set of entities consists of the phases, interfaces, and common curve such that the index set is

$$\mathcal{J} = \{w, n, s, wn, ws, ns, wns\} \tag{1.10}$$

As an example of the connected sets, the connected set of higher- and lower-dimensional entities for the *wn* interface is

$$\mathcal{J}_{cwn}^{+} = \{w, n\} \tag{1.11}$$

and

$$\mathcal{J}_{cwn}^{-} = \{wns\}, \tag{1.12}$$

respectively. We are considering the connected set of the solid phase to include the common curve.

1.3.3 Entropy Balance

In addition to the conservation equations, an entropy balance equation may be formulated for each entity. The microscale equation denoted as $\mathcal{S}_\alpha$ is written

$$\begin{aligned} \mathcal{S}_\alpha := & \frac{\partial^{(n)} \eta_\alpha}{\partial t} + \nabla^{(n)} \cdot (\eta_\alpha \mathbf{v}_\alpha) - b_\alpha - \sum_{\kappa \in \mathcal{J}_{c\alpha}^{+}} \frac{\eta_\kappa}{\rho_\kappa} {}^{\kappa \to \alpha}_{M} - \nabla^{(n)} \cdot \left(\mathbf{I}_\alpha^{(n)} \cdot \varphi_\alpha\right) = \Lambda_\alpha \\ & \text{for } \alpha \in \mathcal{J}; n = 3 - \dim \alpha. \end{aligned} \tag{1.13}$$

Application of the averaging theorems Equations 1.1 and 1.3 to this equation yields the macroscale entropy balance given by

$$\mathcal{S}^{\bar{\bar{\alpha}}} := \frac{\partial \eta^{\bar{\bar{\alpha}}}}{\partial t} + \nabla \cdot \left(\eta^{\bar{\bar{\alpha}}} \mathbf{v}^{\bar{\alpha}} \right) - \epsilon^{\bar{\bar{\alpha}}} b^{\alpha} - \sum_{\kappa \in \mathcal{J}_{c\alpha}} {}^{\kappa \to \alpha}\!M \; \bar{\bar{\eta}}^{\alpha,\kappa} - \sum_{\kappa \in \mathcal{J}_{c\alpha}} {}^{\kappa \to \alpha}\!\Phi - \nabla \cdot \left(\epsilon^{\bar{\bar{\alpha}}} \varphi^{\bar{\bar{\alpha}}} \right) = \Lambda^{\bar{\bar{\alpha}}} \quad \text{for } \alpha \in \mathcal{J}. \tag{1.14}$$

As with the conservation equations, it will prove convenient to write this equation in terms of the material derivative such that we have

$$\mathcal{S}_{*}^{\bar{\bar{\alpha}}} := \frac{\mathrm{D}^{\bar{\alpha}} \eta^{\bar{\bar{\alpha}}}}{\mathrm{D}t} + \eta^{\bar{\bar{\alpha}}} \mathbf{I} : \mathbf{d}^{\bar{\alpha}} - \epsilon^{\bar{\bar{\alpha}}} b^{\alpha} - \sum_{\kappa \in \mathcal{J}_{c\alpha}} {}^{\kappa \to \alpha}\!M \; \bar{\bar{\eta}}^{\alpha,\kappa} - \sum_{\kappa \in \mathcal{J}_{c\alpha}} {}^{\kappa \to \alpha}\!\Phi - \nabla \cdot \left(\epsilon^{\bar{\bar{\alpha}}} \varphi^{\bar{\bar{\alpha}}} \right) = \Lambda^{\bar{\bar{\alpha}}} \quad \text{for } \alpha \in \mathcal{J}. \tag{1.15}$$

We observe that the quantities that appear in this balance equation do not appear in the conservation equations. To make use of this equation in conjunction with those conservation equations, two steps are taken. First, the inter-entity exchange terms will drop out if one sums the entropy balance equation over all entities. This gives us

$$\sum_{\alpha \in \mathcal{J}} \mathcal{S}_{*}^{\bar{\bar{\alpha}}} = \sum_{\alpha \in \mathcal{J}} \left[\frac{\mathrm{D}^{\bar{\alpha}} \eta^{\bar{\bar{\alpha}}}}{\mathrm{D}t} + \eta^{\bar{\bar{\alpha}}} \mathbf{I} : \mathbf{d}^{\bar{\alpha}} - \epsilon^{\bar{\bar{\alpha}}} b^{\alpha} - \nabla \cdot \left(\epsilon^{\bar{\bar{\alpha}}} \varphi^{\bar{\bar{\alpha}}} \right) \right] = \sum_{\alpha \in \mathcal{J}} \Lambda^{\bar{\bar{\alpha}}}. \tag{1.16}$$

From the second law of thermodynamics, we know that entropy generation due to irreversible processes is nonnegative. Therefore, we know that

$$\sum_{\alpha \in \mathcal{J}} \Lambda^{\bar{\bar{\alpha}}} \geq 0. \tag{1.17}$$

The second step in making the entropy inequality helpful in conjunction with the conservation equations is the postulation of a thermodynamic formalism that relates entropy to internal energy. An approach to this problem is provided in the next subsection.

1.3.4 Thermodynamic Formalism

The simplest thermodynamic formulation that can be employed is classical irreversible thermodynamics (CIT) [5,11,18]. We will use this formalism here because of its simplicity and the fact that it indeed describes the thermodynamic behavior of many important systems. The approach employed is to make use of the known thermodynamic relations at the microscale and then average them to the macroscale. By using this approach, we ensure that all thermodynamic quantities are well defined at the macroscale and that thermodynamic information is transferred consistently between scales. The thermodynamic formalism can be developed using a common notation for all entities except the solid. Here, we assume that the solid is elastic, and we provide the thermodynamic relations consistent with that specification.

Classical thermodynamics provides thermodynamic properties of equilibrium systems. Using the CIT approach, we make use of a local equilibrium assumption such that the thermodynamic relations are considered to apply at each point in the system even though the properties that are constant when the system is at equilibrium have spatial and temporal variation. It is important to note that the local equilibrium assumption is enforced at the microscale but is not imposed separately at a larger

scale when the larger-scale equations are obtained by averaging the smaller scale thermodynamic relations. The impact and importance of nonlocal equilibrium at the larger scale in the thermodynamic relations are obtained through the averaging process that requires consistency between scales.

The thermodynamics of fluid phases, interfaces, and common curves are all defined by the Euler form of the energy equation per region of the entity written as

$$E_\alpha = \theta_\alpha \eta_\alpha + \mu_\alpha \rho_\alpha - P_\alpha \quad \text{for } \alpha \in \mathcal{J}_{\backslash s}. \tag{1.18}$$

where

$P_\alpha = p_\alpha$ is pressure when α denotes a fluid phase
$P_\alpha = -\gamma_\alpha$ for an interface where γ_α is the interfacial tension
$P_\alpha = \gamma_\alpha$ for a common curve where γ_α is the curvilinear tension of the curve

The derivative of this equation may be written as

$$\mathrm{d}^{(n)} E_\alpha = \theta_\alpha \mathrm{d}^{(n)} \eta_\alpha + \mu_\alpha \mathrm{d}^{(n)} \rho_\alpha \quad \text{for } \alpha \in \mathcal{J}_{\backslash s}, \tag{1.19}$$

where

$\mathrm{d}^{(n)}$ is a differential operator
the superscript (n) constrains the differentiation to remain within the entity when α is of dimensionality $3 - n$

With $\mathrm{d}^{(n)}$ replaced by $\partial^{(n)}/\partial t$ in Equation 1.19, averaging theorem Equation 1.3 can be applied to obtain a macroscale thermodynamic equation involving the time derivative. If $\mathrm{d}^{(n)}$ is replaced by the gradient operator, $\nabla^{(n)}$ in Equation 1.19, the spatial averaging theorem, Equation 1.2, can be used to obtain an expression for the macroscale gradient of energy. Then summation of these two results after dotting the gradient expression with $\mathbf{v}^{\bar{\alpha}}$ yields the averaged form of the thermodynamic relation given by

$$\begin{aligned}
\mathcal{T}_*^{\bar{\alpha}} := & \frac{\mathrm{D}^{\bar{\alpha}} E^{\bar{\bar{\alpha}}}}{\mathrm{D}t} - \theta^{\bar{\bar{\alpha}}} \frac{\mathrm{D}^{\bar{\alpha}} \eta^{\bar{\bar{\alpha}}}}{\mathrm{D}t} - \mu^{\bar{\alpha}} \frac{\mathrm{D}^{\bar{\alpha}} \left(\epsilon^{\bar{\bar{\alpha}}} \rho^{\alpha} \right)}{\mathrm{D}t} \\
& + \sum_{\kappa \in \mathcal{J}_{c\alpha}} \left\langle \mathbf{n}_\alpha \cdot \left(\mathbf{v}_\kappa - \mathbf{v}^{\bar{s}} \right) P_\alpha \right\rangle_{\Omega_\kappa, \Omega} \\
& + \left\langle \eta_\alpha \frac{\mathrm{D}^{(n)\bar{s}} \left(\theta_\alpha - \theta^{\bar{\bar{\alpha}}} \right)}{\mathrm{D}t} \right\rangle_{\Omega_\alpha, \Omega} + \left\langle \rho_\alpha \frac{\mathrm{D}^{(n)\bar{s}} \left(\mu_\alpha - \mu^{\bar{\alpha}} \right)}{\mathrm{D}t} \right\rangle_{\Omega_\alpha, \Omega} \\
& - \left[\eta^{\bar{\bar{\alpha}}} \nabla \theta^{\bar{\bar{\alpha}}} - \nabla \cdot \left\langle \mathbf{l}_\alpha^{(n)} P_\alpha \right\rangle_{\Omega_\alpha, \Omega} + \epsilon^{\bar{\bar{\alpha}}} \rho^{\alpha} \nabla \mu^{\bar{\alpha}} \right] \cdot \left(\mathbf{v}^{\bar{\alpha}} - \mathbf{v}^{\bar{s}} \right) \\
& - \nabla \cdot \left\langle \left(\mathbf{I} - \mathbf{l}_\alpha^{(n)} \right) \cdot \left(\mathbf{v}_\alpha - \mathbf{v}^{\bar{\alpha}} \right) P_\alpha \right\rangle_{\Omega_\alpha, \Omega} - \left\langle \left(\mathbf{I} - \mathbf{l}_\alpha^{(n)} \right) P_\alpha \right\rangle_{\Omega_\alpha, \Omega} \cdot \mathbf{d}^{\bar{\bar{\alpha}}} \\
& - \left\langle \nabla^{(n)} \cdot \mathbf{l}_\alpha^{(n)} \cdot \left(\mathbf{v}_\alpha - \mathbf{v}^{\bar{s}} \right) P_\alpha \right\rangle_{\Omega_\alpha, \Omega} \\
& + \left\langle \eta_\alpha \left(\mathbf{v}_\alpha - \mathbf{v}^{\bar{s}} \right) \cdot \left(\mathbf{I} - \mathbf{l}_\alpha^{(n)} \right) \right\rangle_{\Omega_\alpha, \Omega} \cdot \nabla \theta^{\bar{\bar{\alpha}}} \\
& + \left\langle \rho_\alpha \left(\mathbf{v}_\alpha - \mathbf{v}^{\bar{s}} \right) \cdot \left(\mathbf{I} - \mathbf{l}_\alpha^{(n)} \right) \right\rangle_{\Omega_\alpha, \Omega} \cdot \nabla \mu^{\bar{\alpha}} = 0 \quad \forall \alpha \in \mathcal{J}_{\backslash s}
\end{aligned} \tag{1.20}$$

We emphasize that this expression makes use of the local equilibrium approximation at the microscale but does not require this condition to hold at the macroscale.

Although it is not a thermodynamic condition, the equation for the rate of change of the gravitational potential is handled similarly to the thermodynamic condition. Because $\Psi_\alpha = \rho_\alpha \psi_\alpha$, the derivative of this expression is

$$\mathrm{d}^{(n)}\Psi_\alpha - \psi_\alpha \mathrm{d}^{(n)}\rho_\alpha - \rho_\alpha \mathrm{d}^{(n)}\psi_\alpha = 0 \quad \text{for } \alpha \in \mathcal{J}. \tag{1.21}$$

The differential $\mathrm{d}^{(n)}$ may be replaced, successively, by the partial time derivative and gradient operators with the averaging theorems applied to the resulting equations. Then, if the resulting equation in terms of the gradient is dotted with $\mathbf{v}^{\bar{\alpha}}$ and added to the partial time derivative equation, the result is

$$\mathcal{T}^{\bar{\bar{\alpha}}}_{\mathcal{G}_*} := \frac{\mathrm{D}^{\bar{\alpha}}\Psi^{\bar{\bar{\alpha}}}}{\mathrm{D}t} - \psi^{\bar{\alpha}} \frac{\mathrm{D}^{\bar{\alpha}}\left(\epsilon^{\bar{\bar{\alpha}}}\rho^{\alpha}\right)}{\mathrm{D}t} - \left\langle \rho_\alpha \frac{\mathrm{D}^{(n)\bar{s}}\psi^{\bar{\alpha}}}{\mathrm{D}t} \right\rangle_{\Omega_\alpha,\Omega} - \epsilon^{\bar{\bar{\alpha}}}\rho^{\alpha}\nabla\psi^{\bar{\alpha}} \cdot \left(\mathbf{v}^{\bar{\alpha}} - \mathbf{v}^{\bar{s}}\right)$$
$$+ \left\langle \rho_\alpha \left(\mathbf{v}_\alpha - \mathbf{v}^{\bar{s}}\right) \cdot \left(\mathbf{I} - \mathbf{I}^{(n)}_\alpha\right) \right\rangle_{\Omega_\alpha,\Omega} \cdot \nabla\psi^{\bar{\alpha}} = 0 \quad \text{for } \alpha \in \mathcal{J}. \tag{1.22}$$

This equation added to Equation 1.20 provides a relation for the rate of change of macroscale internal plus potential energy for fluid phases, interfaces, and the common curve.

A potentially fertile area for additional research is the representation of solid phases at the macroscale. Here, we adopt a relatively simple model of the solid as an elastic material, which can be formulated as

$$E_s = \theta_s \eta_s + \sigma_s : \frac{\mathbf{C}_s}{j_s} + \mu_s \rho_s, \tag{1.23}$$

where

σ_s is a stress tensor
$\mathbf{C}_s$ is Green's deformation tensor
j_s is the Jacobian

The derivative of this equation may be written

$$\mathrm{d}E_s = \theta_s \, \mathrm{d}\eta_s + \sigma_s : \mathrm{d}\left(\frac{\mathbf{C}_s}{j_s}\right) + \mu_s \, \mathrm{d}\rho_s. \tag{1.24}$$

If the arbitrary differential in Equation 1.24 is replaced successively by the partial time derivative and gradient operators, the resulting equations can be averaged making use of the time and space averaging theorems. With the gradient expression dotted with $\mathbf{v}^{\bar{s}}$ added to the time derivative

expression, the resulting expression for the relation among the rates of change of macroscale thermodynamic properties of the solid is

$$\mathcal{T}_*^{\bar{\bar{s}}} := \frac{\mathrm{D}^{\bar{s}} E^{\bar{\bar{s}}}}{\mathrm{D}t} - \theta^{\bar{\bar{s}}} \frac{\mathrm{D}^{\bar{s}} \eta^{\bar{\bar{s}}}}{\mathrm{D}t} - \mu^{\bar{s}} \frac{\mathrm{D}^{\bar{s}} \left(\epsilon^{\bar{\bar{s}}} \rho^s \right)}{\mathrm{D}t} - \sum_{\kappa \in \mathcal{J}_{cs}} \left\langle \mathbf{n}_s \cdot \left(\mathbf{v}_\kappa - \mathbf{v}_s \right) \sigma_s : \frac{\mathbf{C}_s}{j_s} \right\rangle_{\Omega_\kappa, \Omega}$$
$$- \sum_{\kappa \in \mathcal{J}_{cs}} \left\langle \mathbf{n}_s \cdot \mathbf{t}_s \cdot \left(\mathbf{v}_s - \mathbf{v}^{\bar{s}} \right) \right\rangle_{\Omega_\kappa, \Omega} + \left\langle \eta_s \frac{\mathrm{D}^{\bar{s}} \left(\theta_s - \theta^{\bar{\bar{s}}} \right)}{\mathrm{D}t} \right\rangle_{\Omega_s, \Omega}$$
$$+ \left\langle \rho_s \frac{\mathrm{D}^{\bar{s}} \left(\mu_s - \mu^{\bar{s}} \right)}{\mathrm{D}t} \right\rangle_{\Omega_s, \Omega} - \nabla \cdot \left\langle \left(\mathbf{t}_s - \sigma_s : \frac{\mathbf{C}_s}{j_s} \mathbf{I} \right) \cdot \left(\mathbf{v}_s - \mathbf{v}^{\bar{s}} \right) \right\rangle_{\Omega_s, \Omega}$$
$$- \epsilon^{\bar{\bar{s}}} \mathbf{t}^s : \mathbf{d}^{\bar{s}} + \epsilon^{\bar{\bar{s}}} \sigma^{\bar{s}} : \frac{\mathbf{C}^s}{j^s} \mathbf{I} : \mathbf{d}^{\bar{s}} + \left\langle \left(\nabla \cdot \mathbf{t}_s - \nabla \sigma_s : \frac{\mathbf{C}_s}{j_s} \right) \cdot \left(\mathbf{v}_s - \mathbf{v}^{\bar{\bar{s}}} \right) \right\rangle_{\Omega_s, \Omega} = \square \tag{1.25}$$

This expression makes use of the microscale local equilibrium approximation and also accounts for the fact that a concentrated force can act on the solid surface at common curves and common points. The equation for the rate of change of gravitational potential for the solid phase is obtained from Equation 1.22.

1.3.5 Evolution Equations

Unique to the TCAT approach in comparison to other averaging methods is the incorporation of the kinematics of the space occupied by a phase, and of the shape and extent of an interface between phases and of the common curve on the solid surface into the full formulation [26,28,31]. Kinematics of irregular geometries are difficult to describe exactly, so we rely on approximations that are based on the averaging theorems, in particular Equations 1.2 and 1.3 with $f_\alpha = 1$. The gradient theorem becomes

$$0 = \nabla \epsilon^{\bar{\bar{\alpha}}} - \nabla \cdot \left\langle \mathbf{I} - \mathbf{l}_\alpha^{(n)} \right\rangle_{\Omega_\alpha, \Omega} - \left\langle \nabla^{(n)} \cdot \mathbf{l}_\alpha^{(n)} \right\rangle_{\Omega_\alpha, \Omega} + \sum_{\kappa \in \mathcal{J}_{c\alpha}} \left\langle \mathbf{n}_\alpha \right\rangle_{\Omega_\kappa, \Omega}, \tag{1.26}$$

while the time derivative theorem simplifies to

$$0 = \frac{\partial \epsilon^{\bar{\bar{\alpha}}}}{\partial t} + \nabla \cdot \left\langle \left(\mathbf{I} - \mathbf{l}_\alpha^{(n)} \right) \cdot \mathbf{v}_\alpha \right\rangle_{\Omega_\alpha, \Omega} + \left\langle \nabla^{(n)} \cdot \mathbf{l}_\alpha^{(n)} \cdot \mathbf{v}_\alpha \right\rangle_{\Omega_\alpha, \Omega} - \sum_{\kappa \in \mathcal{J}_{c\alpha}} \left\langle \mathbf{n}_\alpha \cdot \mathbf{v}_\kappa \right\rangle_{\Omega_\kappa, \Omega}. \tag{1.27}$$

These two equations provide relations among the geometric density of the entity of interest, an orientation tensor, and averages of the velocities of the entities.

It is important to recognize that the velocity of an entity is not necessarily equal to the velocity of the material in the entity except, for the case of an interfacial area or a common curve, in the directions normal to the entity. As might be expected, the velocities of the entities in their tangential directions do not appear in the preceding two equations. The challenge that arises is relating the changes of extent of one entity to that of another entity. For example, if a phase is

spherical, it is easy to relate the rate of change in the size of the sphere to the rate of change of the surface area of the sphere; for the case of complicated phase geometries, phase boundaries, and curve lengths, such a relation cannot be obtained. Nevertheless, Equations 1.26 and 1.27 provide exact relations that can be approximated to obtain appropriate macroscale relations. These results can then be studied because the larger-scale variables will be specified in terms of microscale variables.

To obtain an evolution form in terms of a material derivative moving with the macroscale solid phase velocity, we take the dot product of Equation 1.26 with $\mathbf{v}^{\bar{s}}$ and add this to Equation 1.27. After minor rearrangement, this gives

$$\frac{\mathrm{D}^{\bar{s}}\epsilon^{\bar{\bar{\alpha}}}}{\mathrm{D}t} + \nabla\cdot\left\langle\left(\mathbf{I}-\mathbf{l}_{\alpha}^{(n)}\right)\cdot\left(\mathbf{v}_{\alpha}-\mathbf{v}^{\bar{s}}\right)\right\rangle_{\Omega_{\alpha},\Omega} + \left\langle\mathbf{I}-\mathbf{l}_{\alpha}^{(n)}\right\rangle_{\Omega_{\alpha},\Omega} : \mathbf{d}^{\bar{s}} + \left\langle\nabla^{(n)}\cdot\mathbf{l}_{\alpha}^{(n)}\cdot\left(\mathbf{v}_{\alpha}-\mathbf{v}^{\bar{s}}\right)\right\rangle_{\Omega_{\alpha},\Omega} - \sum_{\kappa\in\bar{\mathcal{J}}_{\bar{\alpha}\alpha}}\left\langle\mathbf{n}_{\alpha}\cdot\left(\mathbf{v}_{\kappa}-\mathbf{v}^{\bar{s}}\right)\right\rangle_{\Omega_{\kappa},\Omega} = 0 \quad \text{for } \alpha\in\mathcal{J}. \tag{1.28}$$

Although this equation describes the evolution of the various geometric entities, it is of limited use as is because not all of the quantities expressed with the averaging operator can be evaluated in terms of the set of macroscale variables that arise in averaging conservation equations. The complex geometries and distributions of the entities also mean that robust approximate evaluations are difficult to identify. Nevertheless, these equations are important constraints on the behavior of the system. The last term on the left side of Equation 1.28 expresses the fact that the change in distribution of an entity is related to changes in the distribution of lower-dimensional entities. For the two-fluid-phase system of concern here, we make some approximations that can be revisited if significant errors in subsequent macroscale simulations or insights gained from microscale simulations suggest a need to do so.

The derivation of an approximate form of Equation 1.28 is a rather involved process and can be found in [28]. Here, we provide the equation that results when the solid deformation is much slower than fluid redistribution, and we are interested in the rate of change of the *wn* interface. Elements of the physical processes that can cause $\epsilon^{\bar{\bar{wn}}}$ to evolve are the normal velocity of the interface, interfacial curvature changes, and the movement of the common curve on the solid surface. The governing approximate equation is [26,28]

$$\frac{\mathrm{D}^{\bar{s}}\epsilon^{\bar{\bar{wn}}}}{\mathrm{D}t} + \nabla\cdot\left[\epsilon^{\bar{\bar{wn}}}\left(\mathbf{w}^{wn}-\mathbf{G}^{wn}\cdot\mathbf{v}^{\bar{s}}\right)\right] - J_{w}^{wn}\frac{\mathrm{D}^{\bar{s}}\epsilon^{\bar{\bar{w}}}}{\mathrm{D}t} - \hat{k}^{wn}\left(\epsilon_{\mathrm{eq}}^{\bar{\bar{wn}}}-\epsilon^{\bar{\bar{wn}}}\right) - \cos\varphi^{\bar{\bar{ws}},\bar{\bar{wn}}}\left(\epsilon^{\bar{\bar{ws}}}+\epsilon^{\bar{\bar{ns}}}\right)\frac{\mathrm{D}^{\bar{s}}\chi_{s}^{\bar{\bar{ws}}}}{\mathrm{D}t} = 0. \tag{1.29}$$

The terms in this equation are, in order, the rate of change of *wn* interface density, the net outward flux of $\epsilon^{\bar{\bar{wn}}}$, increase in $\epsilon^{\bar{\bar{wn}}}$ caused by a change in the volume fraction of fluid phase *w*, relaxation of $\epsilon^{\bar{\bar{wn}}}$ to an equilibrium configuration, and the change in $\epsilon^{\bar{\bar{wn}}}$ due to movement of the common curve that is the boundary of the interface. The quantity $\mathbf{G}^{wn}$ is an orientation tensor that accounts for the fact that the *wn* interface may have a preferred orientation direction.

For the common curve, more approximations are needed. These approximations are not as robust as those for the interface, but the errors are not as important if the common curve dynamics have less importance in modeling the overall system behavior. The equation that results is [26,28]

$$\frac{\mathrm{D}^{\bar{s}}\epsilon^{\bar{\bar{wns}}}}{\mathrm{D}t} + \nabla\cdot\left[\epsilon^{\bar{\bar{wns}}}\left(\mathbf{w}^{wns}-\mathbf{G}^{wns}\cdot\mathbf{v}^{\bar{s}}\right)\right] + \kappa_{\mathrm{G}}^{wns}\left(\epsilon^{\bar{\bar{ws}}}+\epsilon^{\bar{\bar{ns}}}\right)\frac{\mathrm{D}^{\bar{s}}\chi_{s}^{\bar{\bar{ws}}}}{\mathrm{D}t} - \hat{k}^{wns}\left(\epsilon_{\mathrm{eq}}^{\bar{\bar{wns}}}-\epsilon^{\bar{\bar{wns}}}\right) = 0. \tag{1.30}$$

This equation relates the rate of change of common curve length per volume, respectively, to the net outward flux of the common curve, the movement of the curve along a solid surface that leads to its expansion or contraction, and the relaxation of the common curve length to its equilibrium length due to stretching. This latter term is expected to be negligible for the case of a two-fluid system when the solid does not deform.

1.3.6 Entropy Inequality

The entropy inequality is constrained by the conservation equations, the body force potential equation, and the thermodynamic relations such that the material derivatives are eliminated as far as possible. This strategy serves to express the rate of entropy generation as a product of independent forces and fluxes, each of which is zero at equilibrium. The constrained form is expressed as

$$\sum_{\alpha\in\mathcal{J}}\left[\mathcal{S}_*^{\bar{\bar{\alpha}}}-\frac{1}{\theta^{\bar{\bar{\alpha}}}}\mathcal{E}_*^{\bar{\bar{\alpha}}}+\frac{1}{\theta^{\bar{\bar{\alpha}}}}\mathbf{v}^{\bar{\alpha}}\cdot\boldsymbol{\mathcal{P}}_*^{\bar{\bar{\alpha}}}+\frac{1}{\theta^{\bar{\bar{\alpha}}}}\left(\mu^{\bar{\alpha}}+\psi^{\bar{\alpha}}-\frac{\mathbf{v}^{\bar{\alpha}}\cdot\mathbf{v}^{\bar{\alpha}}}{2}+K_E^{\bar{\bar{\alpha}}}\right)\mathcal{M}_*^{\bar{\bar{\alpha}}}+\frac{1}{\theta^{\bar{\bar{\alpha}}}}\mathcal{T}_*^{\bar{\bar{\alpha}}}+\frac{1}{\theta^{\bar{\bar{\alpha}}}}\mathcal{T}_{\mathcal{G}^*}^{\bar{\bar{\alpha}}}\right]=\sum_{\alpha\in\mathcal{J}}\Lambda^{\bar{\bar{\alpha}}}\geq 0. \tag{1.31}$$

After substitution of the appropriate conservation and thermodynamic equations into this equation, terms can be collected and canceled. For this study, we also employ approximations consistent with an isothermal system, a rigid solid, no mass exchange between entities, and massless interfaces and common curve to obtain

$$\begin{aligned}
&\sum_{\alpha\in\mathcal{J}_{\mathrm{f}}}\frac{1}{\theta}\left(\epsilon^{\bar{\bar{\alpha}}}\mathbf{t}^{\bar{\bar{\alpha}}}+\epsilon^{\bar{\bar{\alpha}}}p^{\alpha}\mathbf{I}\right):\mathbf{d}^{\bar{\bar{\alpha}}}+\sum_{\alpha\in\mathcal{J}_{\mathrm{I}}}\frac{1}{\theta}\left[\epsilon^{\bar{\bar{\alpha}}}\mathbf{t}^{\bar{\bar{\alpha}}}-\epsilon^{\bar{\bar{\alpha}}}\gamma^{\alpha}\left(\mathbf{I}-\mathbf{G}^{\alpha}\right)\right]:\mathbf{d}^{\bar{\bar{\alpha}}}+\frac{1}{\theta}\left[\epsilon^{\overline{\overline{wns}}}\mathbf{t}^{\overline{\overline{wns}}}+\epsilon^{\overline{\overline{wns}}}\gamma^{wns}\left(\mathbf{I}-\mathbf{G}^{wns}\right)\right]:\mathbf{d}^{\overline{\overline{wns}}}\\
&+\left\{\sum_{\alpha\epsilon\mathcal{J}_{\mathrm{f}}}\frac{1}{\theta}\left\{\nabla\left(\epsilon^{\bar{\bar{\alpha}}}p^{\alpha}\right)-\epsilon^{\bar{\bar{\alpha}}}\rho^{\alpha}\nabla\left(\mu^{\bar{\alpha}}+K_E^{\bar{\bar{\alpha}}}+\psi^{\bar{\alpha}}\right)-\epsilon^{\bar{\bar{\alpha}}}\rho^{\alpha}\mathbf{g}^{\bar{\alpha}}+\sum_{\kappa\in\mathcal{J}_{c\alpha}}^{\alpha\to\kappa}\mathbf{T}\right\}\cdot\left(\mathbf{v}^{\bar{\alpha}}-\mathbf{v}^{\bar{\bar{s}}}\right)\right.\\
&-\sum_{\alpha\in\mathcal{J}_{\mathrm{I}}}\frac{1}{\theta}\left\{\nabla\cdot\left[\left(\mathbf{I}-\mathbf{G}^{\alpha}\right)\epsilon^{\bar{\bar{\alpha}}}\gamma^{\alpha}\right]+\sum_{\kappa\in\mathcal{J}_{c\alpha}}^{\kappa\to\alpha}\mathbf{T}-\sum^{\alpha\to wns}\mathbf{T}\right\}\cdot\left(\mathbf{v}^{\bar{\alpha}}-\mathbf{v}^{\bar{\bar{s}}}\right)\\
&+\frac{1}{\theta}\left\{\nabla\cdot\left[\left(\mathbf{I}-\mathbf{G}^{wns}\right)\epsilon^{\overline{\overline{wns}}}\gamma^{wns}\right]-\sum_{\kappa\in\mathcal{J}_{c\square\square}}^{\kappa\to wns}\mathbf{T}\right\}\cdot\left(\mathbf{v}^{\overline{wns}}-\mathbf{v}^{\bar{\bar{s}}}\right)\\
&+\frac{1}{\theta}\left[\frac{\square^{\bar{s}}\epsilon^{\bar{\bar{w}}}}{\square\square}-\frac{\gamma^{wn}\square^{n}\left(\epsilon^{\overline{\overline{wn}}}-\epsilon^{\overline{\overline{wn}}}_{\square\square}\right)}{\left(p_w^{wn}-p_n^{wn}\right)}\right]\left(p_w^{wn}-p_n^{wn}-\gamma^{wn}\square_{w}^{wn}\right)\\
&-\frac{1}{\theta}\left(\epsilon^{\overline{\overline{ws}}}+\epsilon^{\overline{\overline{ns}}}\right)\frac{\square^{\bar{s}}\square_{s}^{\overline{\overline{ws}}}}{\square\square}\left[\gamma_{wn}^{wns}\mathrm{c}\square\square\square^{\overline{\overline{ws}}\square n}+\gamma_{ws}^{wns}-\gamma_{ns}^{wns}+\gamma^{wns}\kappa_{\square}^{\overline{\overline{wns}}}\right]\\
&\square\sum_{\alpha\in\mathcal{J}}\square^{\bar{\bar{\alpha}}}\square\square
\end{aligned}\tag{1.32}$$

The manipulations involved in obtaining this equation are extensive, but not particularly difficult. Detailed examples of the steps involved in the algebra may be found in [28]. Equation 1.32 provides the independent force–flux pairings that are used to obtain linear relations among forces and fluxes. The entropy inequality is listed here because it is a precursor for any two-fluid-phase flow model that could be formulated with the restrictions specified preceding this equation. Because each member of the set of forces and each member of the set of fluxes is independent of all other members in their respective set, each force and flux must be zero at equilibrium. The simplest condition that this suggests is a linear relation between each flux and the forces. Here, for simplicity and with some limited generality, we will make use of these linearizations with each flux considered to be linear in only its conjugate force rather than all forces. Thus, for example, we can deduce from the third line from the bottom of Equation 1.32 that

$$\frac{\mathrm{D}^{\bar{s}}\epsilon^{\bar{\bar{w}}}}{\mathrm{D}t} - \frac{\gamma^{wn}\hat{k}_1^{wn}\left(\epsilon^{\bar{\bar{wn}}} - \epsilon_{\mathrm{eq}}^{\bar{\bar{wn}}}\right)}{\left(p_w^{wn} - p_n^{wn}\right)} = \hat{c}\left(p_w^{wn} - p_n^{wn} - \gamma^{wn}J_w^{wn}\right) \tag{1.33}$$

is an expression that describes the relaxation of the capillary pressure at the interface due to the difference in pressures between the phases at the interface. Furthermore, $\hat{c}$ must be nonnegative to ensure that the entropy inequality is not violated. If linearized approximations of fluxes in terms of conjugate forces are found to be inadequate to describe the system, more complex forms can be postulated that must still be consistent with Equation 1.32.

1.4 MODEL FORMULATION

The linearization of the force–flux pairs and substitution into the conservation equations leads to a closed set of conservation and balance equations under simple conditions of constant-density fluids, an immobile solid, an isothermal system, no mass exchange between phases, and massless interfaces and common curve. Additionally, the flow in the porous medium is considered to be slow such that the inertial terms in the momentum equation can be neglected. Mass conservation for the fluid phases is accounted for with

$$\frac{\mathrm{D}^{\bar{\alpha}}s^{\bar{\bar{\alpha}}}}{\mathrm{D}t} + s^{\bar{\bar{\alpha}}}\mathbf{I} : \mathbf{d}^{\bar{\bar{\alpha}}} = 0 \quad \text{for } \alpha \in \mathcal{J}_{\mathrm{f}}, \tag{1.34}$$

and

$$s^{\bar{\bar{n}}} = 1 - s^{\bar{\bar{w}}}. \tag{1.35}$$

The flow equations for the phases are obtained as in [25] with

$$\nabla p^{\alpha} - \rho^{\alpha}\mathbf{g} + \hat{R}_w^{\alpha}\mathbf{v}^{\bar{w}} + \hat{R}_n^{\alpha}\mathbf{v}^{\bar{n}} + \hat{R}^{p\alpha}\epsilon\nabla s^{\bar{\bar{\alpha}}} = \mathbf{0} \quad \text{for } \alpha \in \mathcal{J}_{\mathrm{f}}, \tag{1.36}$$

where the last term on the left side of the equation accounts for the impact of the gradient in the saturation on the volumetric average of a microscopic pressure field. When this term is negligible, the flow equations are similar to Darcy's law with cross coupling of the flow velocities included.

Equations 1.34 through 1.36 consist of nine scalar equation components in the 10 unknowns comprising $\mathcal{V}$ where

$$\mathcal{V} = \left\{s^{\bar{\bar{w}}}, s^{\bar{\bar{n}}}, \mathbf{v}^{\bar{w}}, \mathbf{v}^{\bar{n}}, p^{w}, p^{n}\right\}. \tag{1.37}$$

The usual procedure for making up for the deficit of equations is to require the difference in phase pressures to be equal to some function of saturation, $f(s^{\bar{\bar{w}}})$, such that

$$p^n - p^w = f(s^{\bar{\bar{w}}}). \tag{1.38}$$

This relation is demonstrably inadequate in a number of ways. No function $f(s^{\bar{\bar{w}}})$ has been found that is single valued. The function employed is based on data claimed to be collected at equilibrium, while the function itself is applied in dynamic situations. Efforts to equate $f(s^{\bar{\bar{w}}})$ to the capillary pressure merely demonstrate that, while the function is somewhat related to capillary pressure, other factors enter into the formalism due to the fact that the well-defined microscale capillary pressure is replaced by some approximate macroscale analog.

The TCAT approach suggests a more comprehensive method for closing the equation system. This method includes the fluid–fluid interfacial area per volume, $\epsilon^{\bar{\bar{wn}}}$, as an unknown. It also requires that the macroscale capillary pressure, denoted p^{wn}, and an equilibrium value for $\epsilon^{\bar{\bar{wn}}}$ be specified as functions of the problem variables. In the TCAT formulation, p^{wn} arises in the analysis as the intrinsic average over the wn interface of $\gamma_{wn}J_w$, the interfacial tension multiplied by the interfacial curvature, $J_w = \nabla' \cdot \mathbf{n}_w$. For the case where γ_{wn} is constant, this average is equal to the product of the macroscale averages γ^{wn} and J_w^{wn}. Inclusion of these variables raises the equation deficit to four, which is addressed as follows based on guidance from the entropy inequality discussed earlier and the evolution equations.

The difference in pressures of the fluid phases is modeled as

$$p^n - p^w = p^{wn} - \frac{\epsilon}{\hat{c}^{wn}} \frac{\partial s^{\bar{\bar{w}}}}{\partial t} + \frac{\gamma^{wn} \hat{k}_1^{wn} \left(\epsilon^{\bar{\bar{wn}}} - \epsilon_{\text{eq}}^{\bar{\bar{wn}}} \right)}{\hat{c}^{wn} \left(p^w - p^n \right)}, \tag{1.39}$$

where

$$p^{wn} = p^{wn} \left(s^{\bar{\bar{w}}}, \epsilon^{\bar{\bar{wn}}} \right) \tag{1.40}$$

and

$$\epsilon_{\text{eq}}^{\bar{\bar{wn}}} = \epsilon_{\text{eq}}^{\bar{\bar{wn}}} \left(p^n - p^w, s^{\bar{\bar{w}}} \right). \tag{1.41}$$

Note that in this equation set, p^{wn} depends on both saturation and the interfacial area density, and it will equal the pressure difference between the fluid phases at equilibrium. The inclusion of dependence of p^{wn} on $\epsilon^{\bar{\bar{wn}}}$ provides a better opportunity to model macroscale capillarity by approximating average interfacial curvature as a function of the volume occupied by the fluid phases and the interfacial area extent. The second and third terms on the right side of Equation 1.39 account for adjustment of the fluids during a dynamic process due, respectively, to changes in saturation and changes in interfacial area configuration.

The use of this equation set still leaves a deficit of one equation. One way that this has been handled in the past is to drop all dependences on $\epsilon^{\bar{\bar{wn}}}$ in Equations 1.39 and 1.40 such that Equation 1.41 is not needed. This approach essentially considers the relaxation to equilibrium in a system to be due solely to changes in saturation. It is typically applied in practice by adding

a term related to the rate of change of saturation to Equation 1.38 without ever considering that the interfacial area density is important. Efforts to validate this approach have not been successful (e.g., [58]).

A second approach to closure of the equation system is to include an additional equation. Such an equation is an evolution equation for the fluid–fluid interfacial area. This is obtained, most easily, as a simplified form of Equation 1.29 where the term involving the fractional wetting is neglected so that for an immobile solid

$$\frac{\partial \epsilon^{\overline{\overline{wn}}}}{\partial t} + \nabla \cdot \left(\epsilon^{\overline{\overline{wn}}} \mathbf{w}^{wn} \right) + \frac{p^{wn} \epsilon}{\gamma^{wn}} \frac{\partial s^{\overline{w}}}{\partial t} - \hat{k}^{wn} \left(\epsilon_{\text{eq}}^{\overline{\overline{wn}}} - \epsilon^{\overline{\overline{wn}}} \right) = 0, \tag{1.42}$$

where $\mathbf{w}^{wn}$ must be expressed as some function of the two-fluid-phase velocities. Additionally, we obtain the relation between $\hat{k}^{wn}$ and $\hat{k}_1^{wn}$ as

$$\hat{k}^{wn} = \left(\frac{p^{wn}}{p^n - p^w} - 1 \right) \hat{k}_1^{wn}. \tag{1.43}$$

Equations 1.34 through 1.36 supplemented by Equations 1.39 through 1.42 capture the physics of multiphase flow in porous media and account for important mechanisms that impact the system behavior not modeled in traditional models. The obvious drawback of this extended model is the additional parameters that must be determined. The values of these parameters have their roots in microscale system behavior. Therefore, if microscale equations can be solved, then the average of the solutions can be used to populate the forms of needed functions. Here, we will make use of the LBM to simulate multiphase flow and then use the results of those simulations to demonstrate some important aspects of this extended model. This demonstration suggests avenues for further research involving more general models that can be proposed based on TCAT analysis.

1.5 MICROSCALE CONSIDERATIONS

Closure of the macroscale TCAT model formulated in Equations 1.34 through 1.36 and Equations 1.39 through 1.42 requires the conversion of the general functional forms of the closure relations given by Equations 1.40 and 1.41 to specific functional forms. In addition, the closure relations given by Equations 1.42 and 1.43 contain approximations and coefficients that require evaluation. In general terms, relationships are needed among fluid pressures, fluid saturations, interfacial areas, interfacial curvatures at equilibrium, and the rate of approach to the equilibrium state. This could be dismissed as an onerous task, or it could be viewed as a necessary step if one is truly interested in obtaining a class of high-fidelity, physics-based models for two-phase flow.

Traditional two-phase-flow models require the definition of hysteretic pressure–saturation–relative permeability models and the parameters in these models, which are burdensome to determine [48]. Quite often the form of the model is assumed and the parameters estimated using surrogate means, which reduces the apparent burden. However, the difficulty with the approach in traditional models is that important aspects of the physics are being treated implicitly in the closure relation formulation, and surrogate estimates of parameters can introduce a source of error.

To advance TCAT models for two-fluid-phase flow, new methods must be developed to determine the aspects of the system that must be observed. These aspects include various types of fluid pressures depending upon the averaging region, fluid saturations, interfacial areas, curvatures of the interface, common curve lengths and curvatures, orientation tensors for interfaces and common curves, dynamic relaxation coefficients, and contact angles. The formation and characteristics of

the residual nonwetting phase are also potentially important. These detailed measures of the state of a two-fluid-phase system are of interest not only for the closure and validation of TCAT models but also because they can lead to improved fundamental understanding of the system and be used to evaluate and parameterize alternative macroscale models.

Standard macroscale experimental approaches are unable to observe many of the aspects of a two-fluid-phase porous medium system that are of interest and noted earlier, because these properties depend upon knowledge of the pore morphology and topology of the system that is not accessible by merely interpreting the total volume of each phase within the system. Likewise, destructive methods of observing the state of a two-fluid-phase system are not of much use either as they are much too inefficient to provide the level and quantity of information that it required. Thus, the information required must be obtained either through nondestructive, high-resolution experimental methods or high-resolution microscale simulation approaches.

Nondestructive, high-resolution experimental methods of observing multiphase porous medium systems have advanced greatly in recent years. In principle, many of the measures needed to close the TCAT model formulated earlier can examine and have been examined using experimental means. Two general experimental approaches are especially relevant: micromodel methods based upon image analysis [13] and high-flux photon attenuation methods [2,10,14,62,70]. Micromodel methods create a porous medium system that is thin in one dimension. Fluid displacements are then systematically studied and the state is observed using photographic and image-processing methods. While efficient and providing a means to observe all of the properties of interest, these systems are limited to those systems that are created, which are essentially 2D in nature. Because the porous medium systems of common interest are 3D in nature, and 3D systems behave much differently than 2D systems, micromodel approaches are limited in general applicability.

Alternatively, natural porous medium system can be observed using high-flux photon attenuation methods, which can be produced, for example, from a synchrotron source. This approach has the advantage of being able to study some of the details needed for TCAT model closure in real 3D systems. The disadvantages are that the facilities needed are specialized, dynamics are difficult to evaluate because of the time needed to image a system, and it is often not within reach to observe both the spatial scale of the system and the density of states needed to characterize sufficiently the equilibrium relationships sought. Therefore, while high-resolution experiments are important for advancing fundamental understanding of multiphase systems, they suffer from some drawbacks that preclude their general use for the full range of information sought.

The phase distribution morphology and topology measures needed to close the TCAT model formulated earlier can also be investigated using microscale modeling approaches. Approaches based upon idealized pore structures are embodied in pore network models, whereas discrete representation of the real porous medium systems can also be used. The key aspect of an ideal approach to microscale modeling is the ability to represent real systems of sufficient size at high resolution in a dynamic manner. Such an approach provides the means to provide all of the information needed to produce the necessary closure relations without the drawbacks associated with alternative experimental or modeling approaches. Despite the promise of microscale modeling approaches for determining closure relations, no modeling approach has yet been advanced to adequately resolve a sufficiently large porous medium system at the necessary resolution to provide a basis for determining the closure relations sought. In addition, the simulations that have been reported in the literature have not included all of the measures that arise in the TCAT model formulation detailed earlier. Thus, while microscale modeling methods hold great promise, this promise has yet to yield a sufficient foundation for formulating the closure relations that are sought.

In the following sections, we detail LBM simulation and computational geometry approaches for producing dynamic, high-resolution representations of the morphology and topology of a two-fluid-phase porous medium system. The results of these approaches can be used to motivate and guide the formulation of TCAT closure relations.

1.6 LATTICE BOLTZMANN MODELING

1.6.1 Formulation

LBMs are a class of numerical methods used to simulate fluid flow by discretely approximating the Boltzmann equation. While many LBMs exist, a desirable method has several characteristics: (1) the method should conserve mass and momentum; (2) the method should be Galilean invariant; (3) the moments modeled should be allowed to relax at different rates; (4) the approach chosen should be able to represent well-known behavior in model systems with a minimum of computational artifacts that can limit the usefulness of the results; (5) the method should be implemented using data structures, algorithms, and computational approaches that result in an efficient, scalable simulator on modern high-performance computing architectures; and (6) the simulator and computational environment must support simulations that are adequately resolved and of sufficient size to yield a representative averaging region.

An LBM simulator that possesses these characteristics was developed for multiphase porous medium systems based upon the three components common to LBMs: (1) a discrete lattice and associated sets of velocity vectors and distribution functions, (2) a collision operator expressed in terms of a set of equilibrium distribution functions that formulates the relaxation toward an equilibrium state, and (3) an evolution equation that specifies the manner in which the model state is advanced from one discrete time level to the next. We detail each of these components for the selected method in the following text.

A regular lattice space $\delta_s \mathbb{Z}_d$ is used to represent discretely phase space in d spatial dimensions. A symmetric set of discrete velocity vectors $\mathcal{E}_d = \{\mathbf{e}_i \mid i = 0,1,\ldots N\}$ characterizes the connection of each lattice site $\mathbf{x}_k \in \delta_s \mathbb{Z}_d$ to a set of neighboring lattice sites $\mathcal{X}_k = \{\mathbf{x}_{ki} \mid i = 0,1,\ldots N\}$. Additionally, a set of velocity distribution functions $\mathcal{F}_{dk} = \{f_i \mid i = 0,1,\ldots N\}$ is associated with the set $\mathcal{E}_d$ at each lattice location k. The discrete distributions and velocity vectors may be obtained from their continuous counterparts in kinetic theory based on a quadrature scheme [35]. These aspects of an LBM are often listed in shorthand form by specifying the lattice as being of a DdQq form, where $q = N + 1$ to account for standard indexing convention that starts with 0. We used a D3Q19 lattice, which specifies the discrete velocity set as

$$\mathbf{e}_i = \begin{Bmatrix} 0 & 1 & -1 & 0 & 0 & 0 & 0 & 1 & -1 & 1 & -1 & 1 & -1 & 1 & -1 & 0 & 0 & 0 & 0 \\ 0 & 0 & 0 & 1 & -1 & 0 & 0 & 1 & -1 & -1 & 1 & 0 & 0 & 0 & 0 & 1 & -1 & 1 & -1 \\ 0 & 0 & 0 & 0 & 0 & 1 & -1 & 0 & 0 & 0 & 0 & 1 & -1 & -1 & 1 & 1 & -1 & -1 & 1 \end{Bmatrix}, \tag{1.44}$$

where each column represents the components of the corresponding vector.

The 19 distributions evolve according to a multirelaxation time (MRT) form of the lattice Boltzmann equation

$$f_i(\mathbf{x}_k + \mathbf{e}_i \delta t, t_n + \delta t) - f_i(\mathbf{x}_k, t_n) = \mathcal{C}_i, \tag{1.45}$$

where δt is the time step.

The right side of Equation 1.45 is a collision term that accounts for the effects of intermolecular collisions. In practice, the form of this term is chosen to recover a desired continuum form for the microscale momentum transport equation by means of a multiscale expansion. The multirelaxation form of the collision operator is expressed in terms of moments of the distributions that are computed from the distributions using a linear transformation

$$\mathbf{m} = \mathbf{M} \cdot \mathbf{f}. \tag{1.46}$$

The vector containing the 19 distributions is $\mathbf{f}$, and $\mathbf{M}$ is a transformation matrix. Among the moments computed are the density, which relates to the fluid pressure

$$\rho = \sum_{i=0}^{N} f_i = \frac{p}{c_s^2} = 3p, \tag{1.47}$$

and the momentum

$$\mathbf{j} = \rho\mathbf{u} = \sum_{i=0}^{N} f_i \mathbf{e}_i, \tag{1.48}$$

where c_s is the speed of sound. The velocity is

$$\mathbf{u} = \frac{\mathbf{j}}{\rho}. \tag{1.49}$$

Specific details for the construction of the remaining moments including the transformation matrix $\mathbf{M}$ and its inverse are available in the literature [19]. The MRT form allows each moment to relax toward its equilibrium value at a unique rate, with the collision operator written in moment space as

$$\mathcal{C} = \mathbf{M}^{-1}\hat{\mathbf{S}}\left[\mathbf{m}_{\text{eq}}(\mathbf{x}_k, t_n) - \mathbf{m}(\mathbf{x}_k, t_n)\right]. \tag{1.50}$$

The moments relax toward their equilibrium values, denoted with the subscript "eq," at unique rates specified by the diagonal matrix $\hat{\mathbf{S}}$. A detailed account of the relaxation rates for porous medium flows is provided by Pan et al. [52]. The equilibrium value of the moments follows from this MRT formulation with additional terms present to account for surface forces, provided as follows:

$$m_{0\text{eq}} = \rho, \tag{1.51}$$

$$m_{1\text{eq}} = -11\rho + \frac{19}{\rho_0}\mathbf{j}\cdot\mathbf{j} - \sigma|\mathbf{C}|, \tag{1.52}$$

$$m_{2\text{eq}} = w_\epsilon \rho + \frac{w_{\epsilon j}}{\rho_0}\mathbf{j}\cdot\mathbf{j}, \tag{1.53}$$

$$m_{3\text{eq}} = j_x, \tag{1.54}$$

$$m_{4\text{eq}} = -\frac{2}{3}j_x, \tag{1.55}$$

$$m_{5\text{eq}} = j_y, \tag{1.56}$$

$$m_{6\mathrm{eq}} = -\frac{2}{3} j_y, \tag{1.57}$$

$$m_{7\mathrm{eq}} = j_z, \tag{1.58}$$

$$m_{8\mathrm{eq}} = -\frac{2}{3} j_z, \tag{1.59}$$

$$m_{9\mathrm{eq}} = \frac{1}{\rho_0}\left(2 j_x^2 - j_y^2 - j_z^2\right) + \frac{1}{2}\sigma \,|\, \mathbf{C} \,|\, \mathbf{n}\cdot\mathbf{n}, \tag{1.60}$$

$$m_{10\mathrm{eq}} = w_{xx} m_9, \tag{1.61}$$

$$m_{11\mathrm{eq}} = \frac{1}{\rho_0}\left(j_y^2 + j_z^2\right) + \frac{1}{2}\sigma \,|\, \mathbf{C} \,|\, \left(n_y^2 - n_z^2\right), \tag{1.62}$$

$$m_{12\mathrm{eq}} = w_{xx} m_{11}, \tag{1.63}$$

$$m_{13\mathrm{eq}} = \frac{1}{\rho_0} j_x j_y + \frac{1}{2}\sigma \,|\, \mathbf{C} \,|\, n_x n_y, \tag{1.64}$$

$$m_{14\mathrm{eq}} = \frac{1}{\rho_0} j_y j_z + \frac{1}{2}\sigma \,|\, \mathbf{C} \,|\, n_y n_z, \tag{1.65}$$

$$m_{15\mathrm{eq}} = \frac{1}{\rho_0} j_x j_z + \frac{1}{2}\sigma \,|\, \mathbf{C} \,|\, n_x n_z, \tag{1.66}$$

$$m_{16\mathrm{eq}} = 0, \tag{1.67}$$

$$m_{17\mathrm{eq}} = 0, \tag{1.68}$$

and

$$m_{18\mathrm{eq}} = 0. \tag{1.69}$$

The parameter σ is related linearly to the interfacial tension γ_{wn} [1]. The color gradient $\mathbf{C}$ and the associated unit normal vector $\mathbf{n}$ are computed from the nondimensional density field

$$\phi = \frac{\rho_w - \rho_n}{\rho_w + \rho_n}, \tag{1.70}$$

where ρ_w and ρ_n are obtained by solving a separate lattice Boltzmann equation that recovers the mass transport. The value of ϕ is constant in the bulk of each phase and varies within the transition

region in the fluid–fluid interface. Fluid–solid interactions (i.e., contact angle) are controlled by setting the value of ϕ to a constant value within the solid phase

$$\phi(\mathbf{x}_k) = \phi_s \quad \text{for } \mathbf{x}_k \in \Omega_s. \tag{1.71}$$

The color gradient is computed as

$$\mathbf{C} = \frac{3}{c_s^2 \delta_t} \sum_{i=0}^{N} w_i \mathbf{e}_i \phi(t, \mathbf{x}_k + \mathbf{e}_i \delta t), \tag{1.72}$$

and the unit normal vector is

$$\mathbf{n} = \frac{\mathbf{C}}{|\mathbf{C}|}. \tag{1.73}$$

A solution for the mass transport is provided by relying on a separate set of distributions to track the densities of the wetting and nonwetting phases, ρ_w and ρ_n, respectively. The associated distributions are computed based on these local density values, the flow velocity is determined from Equation 1.49, and the color gradient is determined from Equation 1.72. The distributions are determined by subjecting an equilibrium population to a recoloring step that minimizes the mass flux of each component in the direction of the color gradient. The redistribution step conserves the mass of each component exactly along with the total fluid momentum [41]

$$g_{iw} = w_i \left[\rho_w \left(1 + \frac{3}{c_s^2} \mathbf{e}_i \cdot \mathbf{u} \right) + \zeta \frac{\rho_w \rho_n}{\rho_w + \rho_n} \mathbf{n} \cdot \mathbf{e}_i \right], \tag{1.74}$$

and

$$g_{in} = w_i \left[\rho_n \left(1 + \frac{3}{c_s^2} \mathbf{e}_i \cdot \mathbf{u} \right) - \zeta \frac{\rho_w \rho_n}{\rho_w + \rho_n} \mathbf{n} \cdot \mathbf{e}_i \right]. \tag{1.75}$$

The parameter ζ determines the interfacial thickness, and the quadrature weights are

$$w_i = \begin{cases} \dfrac{1}{3}, & \text{for } q \in \{0\} \\ \dfrac{1}{18}, & \text{for } q \in \{1,2,3,4,5,6\} \\ \dfrac{1}{36}, & \text{for } q \in \{7,8,9,10,11,12,13,14,15,16,17,18\}. \end{cases} \tag{1.76}$$

The density values for the subsequent time step can then be computed as

$$\rho_\alpha(\mathbf{x}_k, t_n + \delta t) = \sum_{i=0}^{18} g_{i\alpha}(\mathbf{x}_k - \mathbf{e}_i \delta t, t_n) \quad \text{for } \alpha = w, n. \tag{1.77}$$

Combined with Equations 1.74 and 1.75, continuum expressions for mass conservation are thus obtained for each fluid component.

1.6.2 Verification and Parameter Estimation

The parameters that must be set in the LBM are ζ, which determines the width of the interface; σ, which controls interfacial tension; and the order parameter in the solid phase φ_s, which determines the contact angle. ζ was set to 0.9 based on previous analysis that confirmed the parameter is independent of interfacial tension and demonstrated there was no advantage to having a large interfacial thickness [46]. The parameters σ and φ_s were determined to match physical parameters of interest using a bubble test in the absence of a solid phase and a constrained bubble test in a capillary tube, respectively.

A 2D bubble test, in the absence of a solid phase, was used to measure the interfacial tension. A $40 \times 40 \times 3$ lattice was saturated with equal parts of wetting and nonwetting phases. Initially, a cylindrical shaped bubble of nonwetting phase with a defined radius was immersed in the wetting phase. Periodic boundary conditions were imposed in the x and y directions, with the z boundary being closed to flow. The system was allowed to progress to a steady state. When equilibrium was established, p_{wn} was measured as the difference in the pressure between the two phases. The values of p_n and p_w were extracted by using the phase indicator field to identify the maximum pressure value within each phase. The pressure maxima within each phase effectively excludes the interfacial region where small pressure fluctuations can occur.

In the bubble tests, equilibrium was defined when the change of dimensionless $p_n - p_w$ between time steps was less than 10^{-8}; it took approximately 40,000 time steps to achieve this criterion in the computational domain used. The difference in fluid pressures was related to the radius of curvature R through the 2D Young–Laplace equation given by

$$p_n - p_w = \frac{\gamma_{wn}}{R}. \tag{1.78}$$

Simulations for various bubble sizes were carried out, and the final radius of curvature R was calculated using imaging techniques detailed in the following text. The slope of the line relating the interfacial tension γ_{wn} and the parameter σ was found by plotting $p_n - p_w$ as a function of $1/R$ and fitting a linear function to the data points. In order to match the experimental interfacial tension, σ was determined to be 6.2×10^{-3}.

To control the contact angle with the LBM, the fluid–solid interactions with the solid phase were defined using a constrained bubble test suggested by Huang et al. [38]. In this case, a cylindrical capillary tube of radius R was used to provide a constraint on the equilibration of the bubble. With Equation 1.78 used to relate the interfacial curvature to the capillary pressure, the curvature was determined solely by the contact angle $\varphi_{ws,wn}$ between the wetting fluid–solid and wetting–nonwetting fluid interfaces according to

$$p_n - p_w = \frac{2\gamma_{wn}\cos\varphi_{ws,wn}}{R}. \tag{1.79}$$

Given the known value for σ from the previously described bubble test, the contact angle $\phi_{ws,wn}$ was determined by measuring the phase pressures and calculating $p_n - p_w$. Simulations in a capillary tube with a radius $R = 20$ were carried out for various values of ϕ_s and the corresponding $\phi_{ws,wn}$ values were calculated. The ϕ_s value that corresponded to the contact angle from a target physical system can thus be determined.

1.6.3 Validation

The computational expense required to simulate macroscale experiments has restricted the comparison of highly resolved microscale simulations with controlled experiments for two-fluid-phase flow. While some comparisons exist, virtually no comparisons exist that successfully compare these

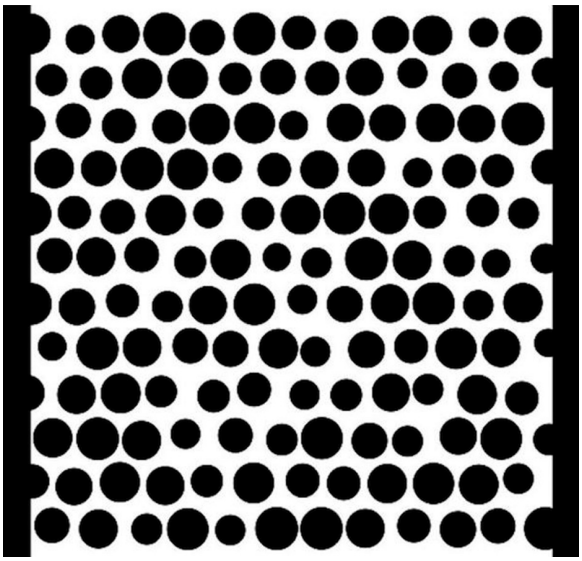

FIGURE 1.1 2D micromodel in which the solid is represented by black and the regions accessible to fluid flow by white.

systems for the full set of variables needed to close the TCAT model formulated earlier. Such comparisons of theory, experiment, and computation are a fruitful approach for advancing scientific understanding. To validate the LBM model, we performed a highly resolved microscale laboratory experiment and simulated this experiment using the LBM simulator with parameters determined for the contact angle and interfacial tension as described earlier.

The experimental methods follow the work of Pyrak-Nolte and coworkers [12]. A 2D micromodel consisting of a photosensitive polymer (photoresist) porous medium bounded by two glass slides was fabricated using lithographic methods and sealed into a cell that was 500 μm × 500 μm × 1.5 μm. Figure 1.1 is an illustration of the porous medium cell, which consisted of a distribution of cylinders with a porosity 0.52. In comparison to 3D systems, a higher porosity is necessary to ensure the connectivity of the pore space in a 2D cell. The cell was mounted horizontally on an optical microscope (Nikon SMZ-U Zoom 1:10) to avoid gravitational effects, and the microscope was interfaced to a CCD camera (Nikon D90). One outlet from the cell was connected to a wetting-fluid-phase decane reservoir, and a second outlet was connected to a nonwetting-fluid-phase nitrogen reservoir with individual and differential pressures measured using transducers (Omega PX319 and PX409). The other four boundaries of the cell were solid, no-flow boundaries. The contact angle of the decane with the photoresist material and the decane–nitrogen gas interfacial tension were measured to be 4.1° and 24.7 dynes/cm, respectively [12]. The experiment was conducted in an ultraviolet-free room with temperature maintained constant at 24°C.

A displacement experiment was performed by fully saturating the porous medium region of the cell with decane through the inlet reservoir. Primary drainage of the cell was accomplished by increasing the pressure of the nitrogen reservoir such that an increasing portion of the decane was displaced over a series of discrete pressure steps. After each pressure step, the system was allowed to equilibrate, and an image of the system and the final pressures were recorded. A series of steps leading to decane imbibition followed a partial primary drainage sequence. Following drainage, an imbibition sequence was studied by decreasing the nitrogen pressure, allowing decane to imbibe back into the cell. The experimental results are shown in Figure 1.2.

A 2D LBM simulation of the drainage and imbibition sequence was performed matching experimental conditions with a 0.5 μm grid resolution, and the computational results are also shown in Figure 1.2. In the LBM simulations, the experimental conditions were mimicked by setting a

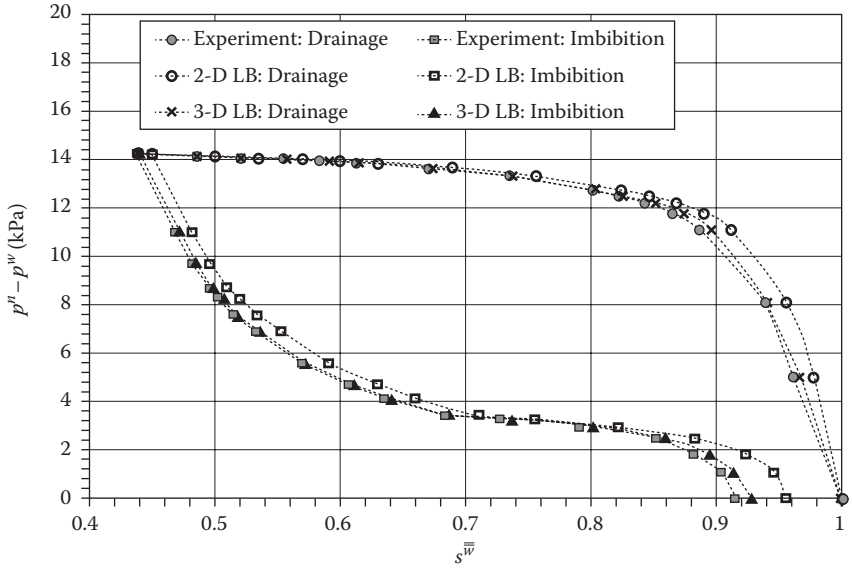

FIGURE 1.2 Pressure–saturation curves obtained from the displacement experiment and the LBM simulations for the porous geometry shown in Figure 1.1.

constant pressure boundary condition on one inlet face for one fluid and on the other inlet face for the second fluid and setting no-flow boundaries for all other horizontal boundaries. The 3D simulator employed was reduced effectively to two dimensions by having only one interior grid block in the vertical dimension and periodic boundaries in this dimension. The pressure boundary conditions for the LBM simulation were determined by scaling the external pressure applied in the experimental system using the Young–Laplace equation, Equation 1.78, to give

$$\frac{(p_n - p_w)}{\gamma_{wn}} - \frac{1}{R_z} = \frac{p_{nLB} - p_{wLB}}{D\gamma_{wnLB}}, \tag{1.80}$$

where

$p_n - p_w$ is the pressure difference between the two first-kind boundary conditions for the fluids in the cell obtained from the pressure transducer reading
γ_{wn} is the decane–nitrogen interfacial tension (24 dynes/cm)
R_z is the principal radius of curvature in the z direction
D is the lattice resolution (0.5 μm per lattice unit)
LB denotes a value in the LBM model

The lattice spacing D is introduced to scale the dimensionless LBM variables. Note that since the experiments have curvature in the z direction and the 2D simulations do not, the radius of curvature in the vertical dimension, R_z, had to be subtracted from the $p_n - p_w$ value obtained from the experimental system. This reduction of dimensionality can be viewed as an assumption that the curvature in the vertical dimension of the experimental cell is always in an equilibrium state. Given the short length scale in the vertical dimension, this approach seems reasonable.

The experimental and simulated results shown in Figure 1.2 have similar shapes with simulated saturations at a given $p_n - p_w$ typically within a few percent of the experimentally observed values. Reasons for the differences between the simulated and observed results include the following possible sources of error: potential variations in the shape of the cylindrical features that make up the porous medium with depth due to overexposure or underexposure during fabrication,

the representation of the smooth cylindrical features of the experiment with a fixed-grid discrete lattice that is inherently jagged, the use of literature values for the contact angle and interfacial tension, pressure transducer and image analysis errors, and the use of a 2D simulation to approximate a 3D experiment. To further investigate the potential sources of error between the experimental results and the LBM simulations, a 3D LBM model was used to simulate conditions, including the vertical boundary conditions, consistent with the experiments using a grid resolution of 0.25 μm in the x–y plane and 0.015 μm in the z dimension. Figure 1.2 shows that the more highly resolved 3D LBM simulation more closely represents the experimental data than the less highly resolved 2D simulation. Part of this difference is likely due to a more accurate representation of the cylindrical solid phase with an improved grid resolution. Given the known and potential sources of error, the agreement between the experimental data and the LBM simulations is judged to be acceptable and a sufficient validation of the LBM simulator to be used for the purpose of evaluating TCAT closure relations.

1.7 COMPUTATIONAL GEOMETRY METHODS

The computation of variables appearing in TCAT models requires the evaluation and integration of data from experimental observations or microscale simulations. In general, these approaches rely on three main components:

1. A sufficiently resolved source of microscale information, which may be obtained from a computational simulation or from images of an experimental system
2. A framework to numerically approximate each of the entity domains and their boundaries, including phases, interfaces, and common curves
3. A means to approximate macroscale averages based upon the underlying microscale representation of the experimental or simulated system

The regular lattice used for the LBM provides a natural way to evaluate the volumetric averages, with the dimensionless density field ϕ identifying the regions of space occupied by either phase. For the images of experimental systems, the phase positions are extracted by smoothing the image using a median filter, then selecting an isovalue that segments the pore space between wetting and nonwetting phases. This isovalue also defines the interface between the wetting and nonwetting fluids. The position of the solid phase is known, which allows all phases and interfaces to be identified explicitly. Given this information, TCAT averages can be determined in an analogous fashion for both the experimental and simulated data.

To perform averaging over an interface or a common curve, a numerical approximation must be constructed for each of these entities. The porous medium marching cubes algorithm was used to approximate Ω_{wn}, Ω_{ws}, Ω_{ns}, and Ω_{wns} [45]. For the interfaces, lists of triangles were constructed to represent each entity. Line segments that approximate the common curve were extracted at the intersection of the three surfaces. Microscale quantities were then interpolated to points on the interfaces or common curve and averaged using quadrature methods to match the respective TCAT definition of each variable. For the experimental images, a 2D analog of this approach was developed to extract the interfaces present in the system and evaluate the interfacial curvature.

1.8 TCAT CLOSURE RELATIONS

1.8.1 Simulations

The verified and validated LBM model was used to evaluate the closure relations needed for the TCAT two-fluid-phase model. Specifically, relations among fluid pressures, saturations, interfacial areas, curvatures, and dynamic evolution equations as described by Equations 1.39 through 1.43

were sought. The basic notion here is that we have shown that the 2D LBM can simulate with reasonable accuracy the 3D micromodel experiments. Since the micromodel is a valid porous medium system, we have a means to compute the detail needed to address TCAT closure relations. Although not strictly necessary, reducing the model to two dimensions greatly decreased the computational burden. Highly resolved 3D simulations would have provided a more accurate representation of the model system.

LBM simulations of drainage and imbibition were performed to mimic the micromodel experiment used to validate the model. The initial condition was a fully wetting-phase-saturated system. The simulated boundary conditions were

$$p^w(0,y,z,t) = p_b^w(t), \tag{1.81}$$

$$p^n(x_l,y,z,t) = p_b^n(t), \tag{1.82}$$

$$\left.\frac{\partial p^n}{\partial x}\right|_{0,y,z,t} = 0 \tag{1.83}$$

and

$$\left.\frac{\partial p^w}{\partial x}\right|_{x_l,y,z,t} = 0, \tag{1.84}$$

where

x_l is the length of the domain in the x direction

the subscript b denotes a boundary value, and periodic boundary conditions were used in the y and z dimensions

These conditions ensured that the wetting fluid and the nonwetting fluid entered and exited one face of the domain, matching the manner in which traditional laboratory experiments are performed. The boundary conditions were adjusted in discrete jumps in time and the simulator was run until an equilibrium state was approached, observing both the final approximate equilibrium state and the dynamics of the approach to the approximate equilibrium state. True equilibrium states were not simulated because interfacial curvature relaxation was not monitored and used as a termination criterion in the simulations. Termination was based upon a small change in fluid saturations. True equilibrium requires longer to achieve beyond the point at which fluid saturations changes are small. The LBM results were averaged over the domain, and these results were used to produce the macroscale quantities of interest in TCAT model closure.

A sequence of pressure boundary conditions was set to simulate primary drainage, main imbibition, and both imbibition and drainage scanning curves. Primary drainage was simulated until an asymptotic wetting-phase saturation was approached; main imbibition was simulated until a state where the boundary conditions were $p^n = p^w$. Figure 1.3 depicts the set of equilibrium states that were simulated, while the curves passing through the points indicate the sequence of the simulations used to reach a given equilibrium state. As was the case with the micromodel validation experiment, imbibition resulted in the formation of a disconnected, entrapped residual nonwetting phase. Examples of the simulated fluid displacement patterns for both primary drainage and main imbibition are depicted in Figures 1.4 and 1.5, respectively. The residual nonwetting phase is clearly shown

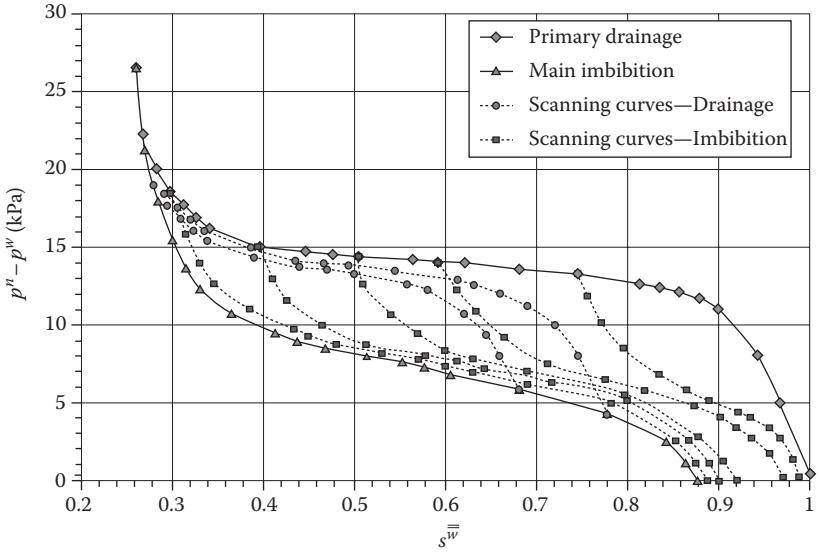

FIGURE 1.3 Pressure–saturation quasi-equilibrium states computed using the LBM.

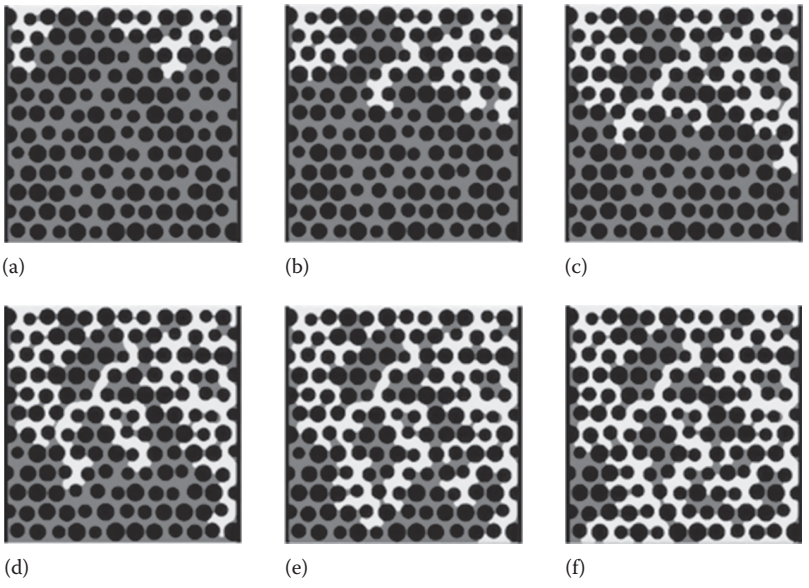

FIGURE 1.4 Fluid distributions for a set of equilibrium states along the simulated primary drainage curve shown in Figure 1.3. Black represents the solid phase, white represents the nonwetting fluid phase, and gray represents the wetting fluid phase. (a) $s^{\bar{\bar{w}}} = 0.85$, (b) $s^{\bar{\bar{w}}} = 0.709$, (c) $s^{\bar{\bar{w}}} = 0.598$, (d) $s^{\bar{\bar{w}}} = 0.482$, (e) $s^{\bar{\bar{w}}} = 0.383$, (f) $s^{\bar{\bar{w}}} = 0.272$.

by the set of disconnected nonwetting-phase (DNP) regions that remain after imbibition is complete. Each of these discrete nonwetting-phase regions formed under specific fluid pressure conditions. Therefore, each residual region at equilibrium has a distinct curvature, corresponding to a capillary pressure that was established at the time the disconnected region was formed. This observation has implications for modeling and model closure.

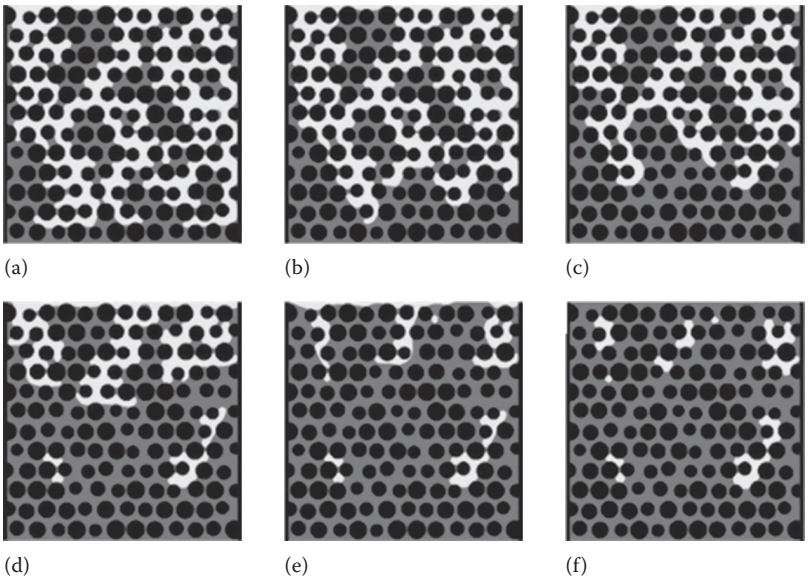

FIGURE 1.5 Fluid distributions for a set of equilibrium states along the simulated main imbibition curve shown in Figure 1.3. Black represents the solid phase, green represents the nonwetting fluid phase, and blue represents the wetting fluid phase. (a) $s^{\bar{\bar{w}}} = 0.356$, (b) $s^{\bar{\bar{w}}} = 0.43$, (c) $s^{\bar{\bar{w}}} = 0.52$, (d) $s^{\bar{\bar{w}}} = 0.705$, (e) $s^{\bar{\bar{w}}} = 0.855$, (f) $s^{\bar{\bar{w}}} = 0.895$.

1.8.2 Capillary Pressure–Saturation–Interfacial Area Relation

Traditional two-phase-flow models are closed using hysteretic pressure–saturation relations that account for nonwetting fluid entrapment but do not explicitly account for variables known from pore-scale analysis to be important, such as interfacial tensions, interfacial curvatures, and contact angles [48]. The nature of two-fluid-phase porous medium systems also suggests interfacial areas are important. The absence of important variables in closure relations for traditional models and the hysteretic nature of these relations are indicators of a modeling approach in which underlying physics has been relegated to implicit parameterization. The TCAT model formulated to describe two-fluid-phase flow posits general functional forms of closure relations that explicitly include the traditionally neglected variables. As previously noted, the determination of specific forms of these relations is an active area of current and recent research. The LBM simulations summarized earlier provide a means to investigate these closure relations with an ultimate goal being to determine specific functional forms that represent the behavior of the system.

The simulated quasi-equilibrium points were analyzed to determine the fluid pressures, p^w and p^n; the average curvature, J_w^{wn}; the saturation of the wetting phase, $s^{\bar{\bar{w}}}$; and the specific interfacial area, $\epsilon^{\bar{\bar{wn}}}$. Various subsets of the entire data set were examined to gain insight into the nature of the relation sought. In addition, subsets of the data excluding the DNP fluid were also considered. By DNP, we mean that a continuous connection to the Dirichlet boundary corresponding to the nonwetting phase cannot be traced through the system. Note that this definition implicitly has a length scale associated with it, and we take this length scale to be that associated with the averaging region over which the TCAT model is developed. Figure 1.5 shows cases in which a DNP forms during main imbibition. The goals of these simulations were to determine in a semiquantitative manner if the inclusion of interfacial area can remove the hysteresis associated with traditional models, to evaluate the role of the DNP, and to evaluate the nature of the dynamic rate of relaxation to an equilibrium state.

The data shown in Figure 1.3 were processed using the image analysis approaches described in §7 to determine the TCAT variables of interest. To close the TCAT model formulated, consistent equations of state are needed for Equations 1.40 and 1.41. Because we know that at equilibrium $p^{wn} = p^n - p^w$, a single, smooth invertible function could provide the closure information needed. Simulation results confirmed that this condition is reasonable, within a small error associated with the estimation of the curvature. The issue thus becomes identifying the necessary function from the data available or at least determining if such a well-behaved function is likely to exist given the data available. The desired function would fit the entire data set, including all scanning curves, and be single valued, and thus nonhysteretic. The pooled data for the primary drainage, main imbibition, and all scanning curves were examined for the cases in which the DNP fluid was included with the nonwetting phase fluid and for the case in which the DNP fluid was excluded. By inclusion and exclusion of the DNP, we mean that $s^{\bar{\bar{w}}}$ and $\epsilon^{\bar{\bar{wn}}}$ were computed including either all of the nonwetting phase or only the continuous, connected portion of the nonwetting phase.

A polynomial function proposed to have the form

$$\epsilon^{\bar{\bar{wn}}} + b_0 p^{(wn)^2} + p_1 s^{\bar{\bar{w}}^2} + b_2 p^{wn} s^{\bar{\bar{w}}} + b_3 p^{wn} + b_4 s^{\bar{\bar{w}}} + b_5 = 0 \tag{1.85}$$

was fit to all of the data shown in Figure 1.3 using nonlinear least squares for the cases with and without the inclusion of DNP in the computation of $s^{\bar{\bar{w}}}$ and $\epsilon^{\bar{\bar{wn}}}$. The minimized root-mean-square error between the estimated function and the data was computed according to

$$\varepsilon_{RMSE} = \sqrt{\frac{1}{3n}\sum_{i=1,n}\left[\left(\frac{p^{wni} - p^{wni*}}{p^{wn}_{\max} - p^{wn}_{\min}}\right)^2 + \left(\frac{\epsilon^{\bar{\bar{wni}}} - \epsilon^{\bar{\bar{wni*}}}}{\epsilon^{\bar{\bar{wn}}}_{\max} - \epsilon^{\bar{\bar{wn}}}_{\min}}\right)^2 + \left(\frac{s^{\bar{\bar{w}}i} - s^{\bar{\bar{wi*}}}}{s^{\bar{\bar{w}}}_{\max} - s^{\bar{\bar{w}}}_{\min}}\right)^2\right]}. \tag{1.86}$$

Additionally, the mean normalized error was calculated as

$$\varepsilon_{MAE} = \frac{1}{3n}\sum_{i=1,n}\left[\frac{\left|p^{wni} - p^{wni*}\right|}{p^{wn}_{\max} - p^{wn}_{\min}} + \frac{\left|\epsilon^{\bar{\bar{wni}}} - \epsilon^{\bar{\bar{wni*}}}\right|}{\epsilon^{\bar{\bar{wn}}}_{\max} - \epsilon^{\bar{\bar{wn}}}_{\min}} + \frac{\left|s^{\bar{\bar{w}}i} - s^{\bar{\bar{wi*}}}\right|}{s^{\bar{\bar{w}}}_{\max} - s^{\bar{\bar{w}}}_{\min}}\right]. \tag{1.87}$$

In these expressions, the sum of errors for each of the variables was computed by specifying the other two variables from the set of p^{wn}, $\epsilon^{\bar{\bar{wn}}}$, and $s^{\bar{\bar{w}}}$ and computing the root from Equation 1.85 to determine the third value; max denotes the maximum value; min denotes the minimum value; i is a data point index; n is the total number of data points in the set; and * denotes the functional value fit using Equation 1.85. Normalization of the variables was performed to rescale all the variables to a common range of [0, 1].

Nonlinear least squares yielded the coefficients tabulated in Table 1.1, and the corresponding errors are listed in Table 1.2. These results show that a simple quadratic function represents the

TABLE 1.1
Best-Fit Coefficients for Functional Form Given by Equation 1.85

	b_0	b_1	b_2	b_3	b_4	b_5
Inclusion of DNP	-1.67×10^{-5}	0.0108	–0.0011	0.0013	0.0297	–0.0398
Exclusion of DNP	-2.14×10^{-5}	0.0010	–0.0010	0.0015	0.0344	–0.0434

TABLE 1.2
Normalized Errors for Estimation of Variables Given Functional Fits Corresponding to the Coefficients Listed in Table 1.1

	$p^{wn} = p^{wn}\left(s^{\bar{\bar{w}}}, \epsilon^{\bar{\bar{wn}}}\right)$		$\epsilon^{\bar{\bar{wn}}} = \epsilon^{\bar{\bar{wn}}}\left(p^{wn}, s^{\bar{\bar{w}}}\right)$	
	ε_{RMSE}	ε_{MAE}	ε_{RMSE}	ε_{MAE}
Inclusion of DNP	0.045	0.031	0.045	0.032
Exclusion of DNP	0.031	0.022	0.028	0.015

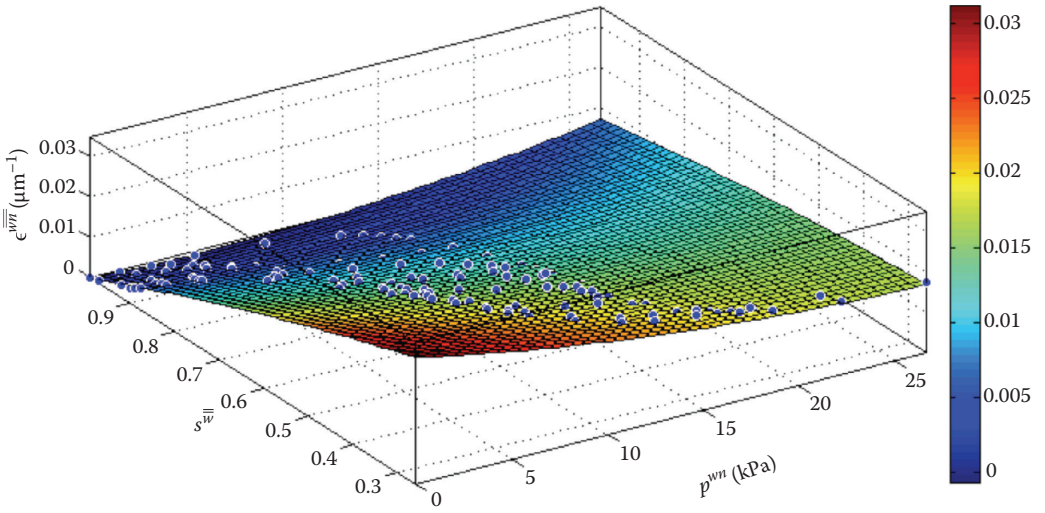

FIGURE 1.6 $\epsilon^{\bar{\bar{wn}}}$ as a function of p^{wn} and $s^{\bar{\bar{w}}}$ for the case in which DNP is excluded.

data reasonably well and that errors are reduced by excluding DNP from the fits. The surface fit to the data is shown in Figure 1.6 for the case in which DNP is removed from the analysis. The results also show that the function determined is invertible and thus hysteresis is essentially eliminated. To further demonstrate properties of the equation of state, determined for the case with DNP excluded, the relationship between the observed and predicted values of $s^{\bar{\bar{w}}}$ is shown in Figure 1.7. This figure demonstrates that the equation of state is an accurate representation of the LBM simulations.

1.8.3 Disconnected Nonwetting Phase

Results from the previous section illustrated that DNP plays an important role in the behavior of two-fluid-phase flow systems. It is important to identify this portion of the n phase and account for it appropriately in the model closure. This observation is consistent with the treatment of the nonwetting phase in traditional two-fluid-phase flow models [36,48,63], where typically some linear or nonlinear model of the fluid saturations is used to approximate the DNP. The importance of treating the DNP differently from the connected nonwetting phase was shown as a result of the equation of state fitting in the previous section, and it also seems reasonable based upon physical reasoning. Because the LBM simulations provide complete microscale detail of the fluid

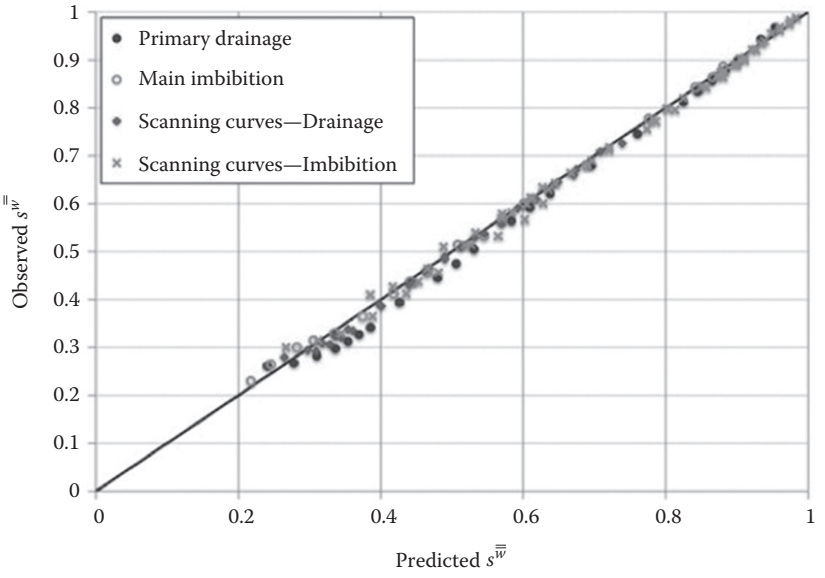

FIGURE 1.7 Error in $s^{\bar{\bar{w}}}$ resulting from the equation of state given by Equation 1.85 for the case in which DNP is excluded.

distributions, some details of the DNP are accessible based upon the simulations. For example, the saturations, curvatures, interfacial area, and geometric orientation tensor distribution of all DNP regions are available. Such information would not typically be available from traditional macroscale laboratory experiments, and it is also burdensome to collect such data even for high-resolution imaging methods because of the number of discrete equilibrium points needed to understand the formation of DNP.

We examined two aspects of DNP residual formation: (1) the maximum volume of DNP that can be formed for a given system, which occurs at $p^{wn} = 0$, along with identification of the variable(s) that enable the approximation of this formation potential, and (2) the amount of DNP at any quasi-equilibrium state. During primary drainage the nonwetting phase is connected to the boundary and thus DNP does not form. However, once imbibition starts from any partially drained state, DNP can begin to form due to snap off of the nonwetting phase. The usual case is to posit that the maximum DNP that can form in a system is a function of the minimum wetting-phase saturation that is achieved. Mechanistically, this means that the greater the fraction of the pore space that is accessed by the nonwetting phase at some point, the greater the potential to form DNP as imbibition occurs. The maximum DNP forms at the completion of the main imbibition stage, and the magnitude of this quantity depends upon the pore morphology and topology as well as the properties of the fluids and the solid. Because we have only examined a single system, pore morphology and topology factors were not evaluated in this work.

As part of the examination of the maximum DNP formation capacity, Figure 1.8 shows the relationship between the minimum wetting-phase saturation state of a system at any point in time and the maximum DNP that forms when $p^{wn} = 0$. The main imbibition and all imbibition-scanning curves were used to create this figure. These data show that a relatively smooth, monotonic, and nonlinear relationship exists between these two variables. Note that the shape is constrained by zero DNP as minimum $s^{\bar{\bar{w}}}$ approaches unity and a maximum attainable value of DNP as the minimum value of $s^{\bar{\bar{w}}}$ approaches the irreducible wetting-phase saturation. This curvilinear form is consistent with established methods of describing the DNP formation capacity [36]. Additional data could be

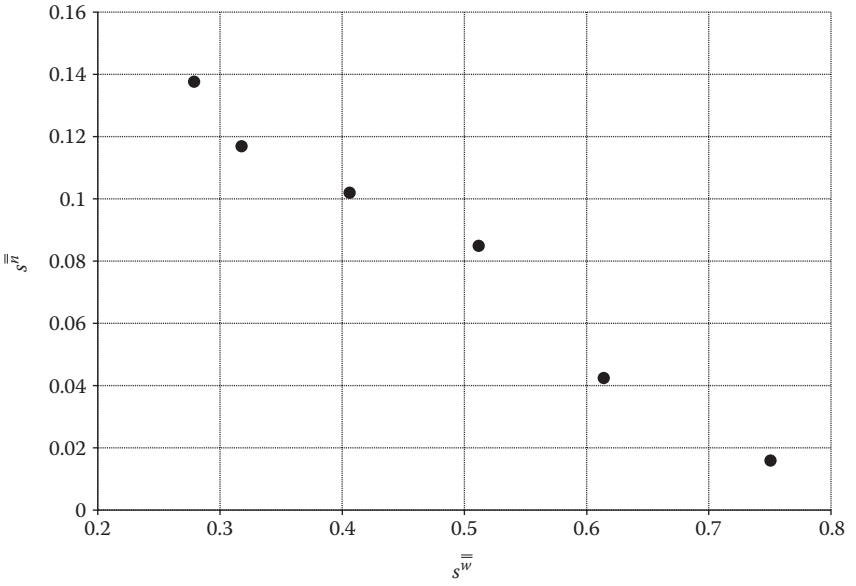

FIGURE 1.8 Maximum DNP saturation that can form as a function of the minimum wetting-phase saturation state of the system.

used to further refine this relationship, but the available data support the suggested parameterization of this relation as a function that depends upon the minimum value of $s^{\overline{\overline{w}}}$.

The second aspect of DNP is the estimation of the quantity for any equilibrium state of the system. Given the observations made earlier, two limits can be noted for any system. The lower limit is

$$\lim_{s^{\overline{\overline{w}}} \to s^{\overline{\overline{w},\min}}} s^{\overline{\overline{nd}}} = 0, \tag{1.88}$$

and the upper limit is

$$\lim_{p^n - p^w \to 0} s^{\overline{\overline{nd}}} = s^{\overline{\overline{nd},\max}}, \tag{1.89}$$

where

$s^{\overline{\overline{nd}}}$ is the saturation of the DNP
min denotes a minimum value
max denotes a maximum value

Equation 1.88 is consistent with the notion that DNP does not exist during primary drainage and a requirement that imbibition scanning curves that are reversed will be closed at the point of departure from the primary drainage curve, and Equation 1.89 is the definition of the maximum DNP. The most appropriate function to describe the DNP at intermediate saturations will depend upon characteristics of the morphology and topology of the pore space.

A remaining DNP issue that has not received attention in the literature is elucidation of the dynamics of the formation of DNP. It seems reasonable that if the dynamics of fluid saturations,

pressures, and interfacial areas are important and that DNP must be accounted for, then the dynamics of the formation and destruction of DNP must also be modeled. No method has been advanced to account for this phenomenon in a TCAT-based two-fluid-phase flow model.

1.8.4 Dynamic Relaxation

The TCAT model for two-fluid phases formulated in §4 includes dynamic changes in the relationship among capillary pressure, fluid saturations, and interfacial areas. This model formulation makes use of a general form of a state equation for capillary pressure given as Equation 1.39, a general form of an equilibrium relationship for interfacial area given by Equation 1.41, and a dynamic equation that expresses the relaxation of fluid pressures, capillary pressure, fluid saturation, and interfacial area to an equilibrium state. Because this formulation is new, aspects of this general formulation need further development and evaluation.

Consider the state equation for capillary pressure and the equilibrium relationship for interfacial area, which are restated as

$$p^{wn} = p^{wn}\left(s^{\bar{\bar{w}}}, \epsilon^{\bar{\bar{wn}}}\right) \tag{1.90}$$

and

$$\epsilon^{\bar{\bar{wn}}}_{\mathrm{eq}} = \epsilon^{\bar{\bar{wn}}}_{\mathrm{eq}}\left(p^{n} - p^{w}, s^{\bar{\bar{w}}}\right). \tag{1.91}$$

Pore-scale simulations have been used to deduce an approximate form of Equation 1.90. This smooth function can be inverted to determine $\epsilon^{\bar{\bar{wn}}}$ as a function of p^{wn} and $s^{\bar{\bar{w}}}$; alternatively a smooth quadratic function can be fit to the data to represent this inverted quantity saving the issue of multiple roots. This equation has the form

$$\epsilon^{\bar{\bar{wn}}} = F\left(p^{wn}, s^{\bar{\bar{w}}}\right). \tag{1.92}$$

When the system is not at equilibrium, we can identify an expected value of $\epsilon^{\bar{\bar{wn}}}$ that would exist if the system were at equilibrium as

$$\epsilon^{\bar{\bar{wn}}}_{\mathrm{eq}} = F\left(p^{n} - p^{w}, s^{\bar{\bar{w}}}\right). \tag{1.93}$$

It can be shown that at equilibrium,

$$p^{wn} = p^{n} - p^{w}. \tag{1.94}$$

Therefore, the difference between $\epsilon^{\bar{\bar{wn}}}$ and $\epsilon^{\bar{\bar{wn}}}_{\mathrm{eq}}$ is a measure of disequilibrium and is employed in Equation 1.30 as a driving force for evolution of the interfacial area toward equilibrium.

To evaluate the validity of Equation 1.90 as a state equation, we extracted the data from a dynamic portion of the LBM simulations as the system relaxed to an equilibrium state and compared the p^{wn} predicted by the state equation with the p^{wn} that was observed in the dynamic simulations. The results shown in Figure 1.9 demonstrate a good agreement between the capillary pressure obtained under dynamic conditions in the simulations and predictions based upon the state equation derived

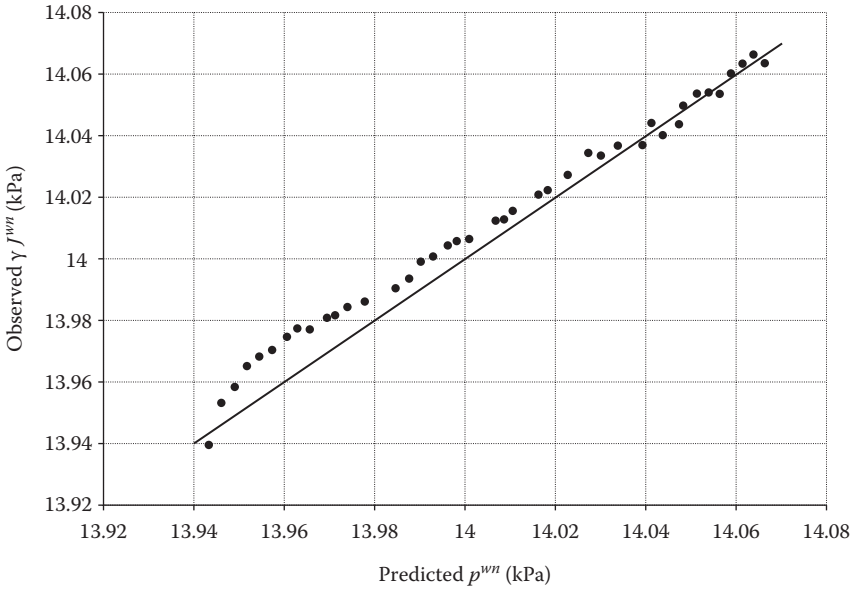

FIGURE 1.9 Observed versus predicted values of p^{wn} for points from a dynamic LBM simulation of relaxation to an equilibrium state.

using only the quasi-equilibrium data. It seems possible that the general state equation could be further improved by including not only equilibrium data but also dynamic data in its formulation. In other words, the simple quadratic form employed in this work, Equation 1.85, can likely be improved upon, but the results are encouraging in the context of the model formulation that has been proposed.

Equation 1.33 can be restated as

$$p^n - p^w = p^{wn} - \frac{\epsilon}{\hat{c}^{wn}} \frac{\partial s^{\overline{\overline{w}}}}{\partial t} + \frac{\gamma^{wn} \hat{k}_1^{wn} \left(\epsilon^{\overline{\overline{wn}}} - \epsilon_{\mathrm{eq}}^{\overline{\overline{wn}}} \right)}{\hat{c}^{wn} \left(p^w - p^n \right)}. \tag{1.95}$$

Because the LBM simulations yield dynamic information of the relaxation to an equilibrium state, these simulations can be used to determine $\hat{c}^{wn}$ and $\hat{k}_1^{wn}$ and to evaluate how well Equation 1.95 represents the simulated system. To accomplish these goals, Equation 1.95 was written as

$$\varepsilon_{\mathrm{dyn}} = p^n - p^w - p^{wn} + \frac{\epsilon}{\hat{c}^{wn}} \frac{\partial s^{\overline{\overline{w}}}}{\partial t} - \frac{\gamma^{wn} \hat{k}_1^{wn} \left(\epsilon^{\overline{\overline{wn}}} - \epsilon_{eq}^{\overline{\overline{wn}}} \right)}{\hat{c}^{wn} \left(p^w - p^n \right)}. \tag{1.96}$$

Then, $\varepsilon_{\mathrm{dyn}}$ was minimized in a least squares sense to determine $\hat{c}^{wn}$ and $\hat{k}_1^{wn}$ using cubic spline representations of all other quantities derived from the LBM simulations. The value of various groupings of terms from this equation is shown in Figure 1.10. The dynamic approach to equilibrium was represented well by Equation 1.95, and the three groupings of terms show that all components of this equation are important. It is especially telling that the interfacial area term is relatively large compared to the temporal derivative of $s^{\overline{\overline{w}}}$, because the interfacial area term has not been included in other so-called dynamic capillary pressure models, suggesting that important physics has been overlooked in these alternative approaches.

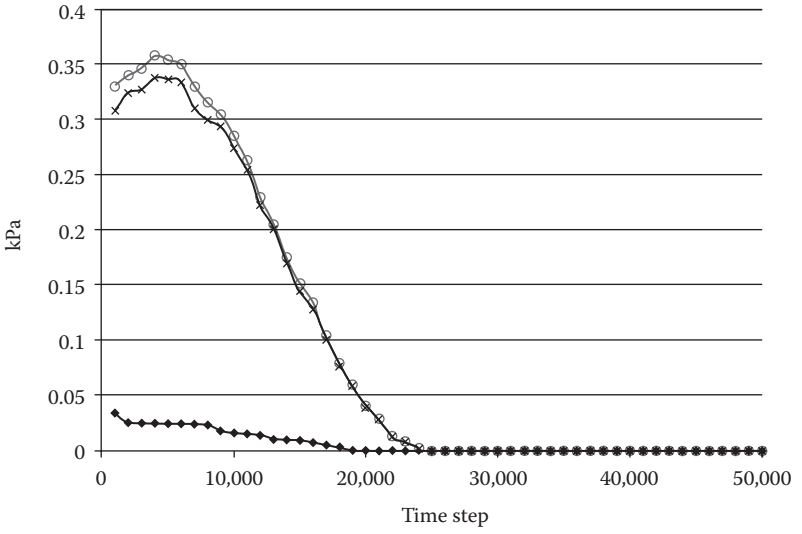

FIGURE 1.10 The line passing through the circles is the term $p^n - p^w - p^{wn}$, the line crossing through the x symbols is the term involving the interfacial area in Equation (1.96), and the line crossing through the diamonds is the term involving the temporal derivative of saturation in Equation (1.96).

1.9 DISCUSSION AND CONCLUSIONS

The elements of the TCAT theory have been summarized and used to formulate a two-fluid-phase flow model. The formulated model has many attractive features including connection across scales, a sound thermodynamic basis, inclusion of relevant physics missing from traditional models, and general forms of all closure relations needed to produce a solvable model. Because the formulated TCAT model is new and the closure relations have not yet been deduced in a specific and refined functional form, significant work remains to produce a solvable TCAT model.

Microscale simulation methods have matured to the point that they can be used to provide the sort of high-resolution simulations needed to formulate meaningful closure relations. The microscale detail from such simulations can be averaged to determine the various TCAT quantities that emerge from the model formulation. An LBM method was advanced that is capable of providing the sort of information needed to produce the closure relations sought for the formulated TCAT model. This simulator was validated by comparing to micromodel experiments, which are more costly and time consuming to perform than the desired simulations. Thus, simulation was used as a basis to investigate the closure relations sought.

Support was provided for the existence of a smooth, invertible, and unique relationship among capillary pressure, fluid saturation, and interfacial area between the fluid phases. Simulation results revealed that a simple quadratic function represented the data more accurately when the DNP was excluded from the analysis. This observation is reasonable because individual regions of DNP form over a range of capillary pressures. It seems consistent, then, to formulate and solve models that account explicitly for DNP. Such a TCAT model has not been formulated. Aspects of DNP that are important include the maximum amount that can form in a system, the amount formed under equilibrium conditions at any state point, and the role of dynamics in the formation and destruction of DNP. Significant opportunities for future work exist in these open areas of knowledge.

The LBM data were used to probe the posited dynamic form of the model. These efforts revealed an encouraging level of agreement between the posited evolution equation and microscale observations. It appears that a local equilibrium–based state equation can describe the nonequilibrium data. Also of significant interest is the importance of the deviation from equilibrium of the interfacial area state as an important component in relaxation of fluid pressures to the capillary pressure at

equilibrium. The importance of this interfacial area term has not been shown in the literature; other evolving multiphase models only include the change in fluid saturation in posited forms of a non-equilibrium equation for capillary pressure.

NOMENCLATURE

b	entropy body source density
$\mathbf{C}$	Green's deformation tensor, $\nabla_X \mathbf{x} \cdot (\nabla_X \mathbf{x})^{\mathrm{T}}$
$\mathbf{C}^s$	macroscale Green's deformation tensor, $\langle \mathbf{C}_s \rangle_{\Omega_s, \Omega_s}$
$\mathbf{C}$	constant velocity vector
$\mathbf{C}$	gradient of the dimensionless density field/color gradient
$\mathcal{C}_i$	collision operator for the LBM
$\hat{c}$	closure coefficient
c_s	speed of sound
$\mathbf{d}^{\bar{\bar{\alpha}}}$	macroscale rate of strain tensor, $[\nabla \mathbf{v}^{\bar{\alpha}} + (\nabla \mathbf{v}^{\bar{\alpha}})^{\mathrm{T}}]/2$
E	internal energy density
$E^{\bar{\bar{\alpha}}}$	macroscale energy of entity α per total volume, $\langle E_\alpha \rangle_{\Omega_\alpha, \Omega}$
$\mathcal{E}_*^{\bar{\bar{\alpha}}}$	particular material derivative form of a macroscale entity total energy conservation equation
$\mathcal{E}_d$	set of discrete velocity vectors
$\mathbf{e}_i$	discrete velocity vector i
f	general scalar function
$\mathbf{f}$	vector containing discrete distributions for the LBM
$\mathcal{F}_{dk}$	set of discrete distributions
$\mathbf{G}^\alpha$	macroscale orientation tensor for α interface or common curve, $\left\langle \mathbf{I} - \mathbf{I}_\alpha^{(n)} \right\rangle_{\Omega_\alpha, \Omega_\alpha}$
$\mathcal{G}_*^{\bar{\bar{i\alpha}}}$	particular material derivative form of a macroscale species-based body force potential balance equation
$\mathcal{G}_*^{\bar{\bar{\alpha}}}$	particular material derivative form of a macroscale entity-based body force potential balance equation
$\mathbf{g}$	body force per unit mass, acceleration
g_i^α	LBM distribution for mass transport of phase α
h	energy source density
h^α	macroscale energy source density for entity α
$\mathbf{I}$	unit tensor
$\mathbf{I}_\alpha^{(n)}$	unit tensor associated with 3 – n-dimensional entity, α, where (n) is the number of primes used
J	set of entity indices
$\mathcal{J}_{c\alpha}$	connected set of indices for entity α, = $\mathcal{J}_{c\alpha}^+ \cup \mathcal{J}_{c\alpha}^-$
$\mathcal{J}_{c\alpha}^+$	connected set of indices of dimension higher than entity α
$\mathcal{J}_{c\alpha}^-$	connected set of indices of dimension lower than entity α
$\mathcal{J}_{\mathrm{f}}$	set of fluid-phase indices
$\mathcal{J}_{\mathrm{I}}$	set of interface indices
$\mathcal{J}_{\mathrm{P}}$	set of phase indices
$\mathcal{J}_{\setminus s}$	set of entity indices except the solid phase, s
J	first curvature equal to twice the mean curvature
j	Jacobian
$\mathbf{j}$	fluid momentum
$K_{E\alpha}$	deviation kinetic energy per mass of entity α
$K_E^{\bar{\bar{\alpha}}}$	entity-based macroscale deviation kinetic energy, $\langle (\mathbf{v}_\alpha - \mathbf{v}^{\bar{\alpha}}) \cdot (\mathbf{v}_\alpha - \mathbf{v}^{\bar{\alpha}})_{\Omega_\alpha, \Omega_\alpha, \rho_\alpha} \rangle / 2$
$\hat{k}^{wn}$	parameter for rate of relaxation of interfacial area

$\hat{k}_1^{wn}$	parameter for rate of relaxation of interfacial area
$\underset{\kappa\to\alpha}{\overset{M}{\kappa\to\alpha}}$	microscale transfer rate of mass of entity κ to entity α per entity extent
M	macroscale transfer rate of mass of entity κ to entity α per entity extent
$\mathcal{M}_*^{\bar{\bar{\alpha}}}$	particular material derivative form of a macroscale entity mass conservation equation
$\mathbf{M}$	transformation matrix
$\mathbf{m}$	vector of moments obtained as a linear combination of the distributions $\mathbf{f}$
$\mathbf{n}_\alpha$	unit normal vector outward from boundary of entity α
ns	interface between n and s phases
$\boldsymbol{\mathcal{P}}_*^{\bar{\bar{\alpha}}}$	particular material derivative form of a macroscale entity momentum conservation equation
P	pressure, interfacial tension, or common curvilinear tension based upon entity qualifier
p	pressure
p^{wn}	capillary pressure of the wn interface
$\underset{\kappa\to\alpha}{\overset{Q}{\kappa\to\alpha}}$	general macroscale transfer rate of energy from entity κ to entity α
Q	general macroscale transfer rate of energy from entity κ to entity α
$\mathbf{q}$	nonadvective energy flux
$\mathbf{q}^{\bar{\bar{\alpha}}}$	macroscale nonadvective energy flux associated with entity α
R	radius
$\hat{R}$	closure scalar
r	general integration variable
$\mathcal{S}_*^{\bar{\bar{\alpha}}}$	particular material derivative form of a macroscale entity entropy balance
$s^{\bar{\bar{\alpha}}}$	saturation of fluid phase α
$\hat{\mathbf{S}}$	diagonal matrix of relaxation rates
T	transport theorem
$\underset{\kappa\to\alpha}{\overset{\mathbf{T}}{\kappa\to\alpha}}$	general microscale transfer rate of momentum from entity κ to entity α
$\mathbf{T}$	general macroscale transfer rate of momentum from entity κ to entity α
$\mathcal{T}_*^{\bar{\bar{s}}}$	particular material derivative form of a macroscale Euler equation for a solid
$\mathcal{T}_*^{\bar{\bar{\alpha}}}$	particular material derivative form of a macroscale Euler equation for an entity
$\mathcal{T}_{\mathcal{G}*}^{\bar{\bar{s}}}$	particular macroscale form of the material derivative of the body source potential of a solid phase
$\mathcal{T}_{\mathcal{G}*}^{\bar{\bar{\alpha}}}$	particular macroscale form of the material derivative of the entity body source potential
t	time
δt	time step
$\mathbf{t}$	stress tensor
$\mathbf{t}^{\bar{\bar{\alpha}}}$	macroscale stress tensor for entity α
V	set of variables
$\mathbf{v}$	velocity
$\mathbf{v}^{\overline{\overline{\alpha,\kappa}}}$	velocity of flow in an entity averaged over the boundary of the entity
W	weighting function for averaging
w_{xx}	free parameter in the MRT scheme
w_i	weight for the LBM
w	wetting phase
wn	interface between w and n phases
wns	common curve at boundary of wn, ws, and ns interfaces
ws	interface between w and s phases
$\mathbf{w}$	velocity of a domain boundary
$\mathbf{w}_{wn}$	vector velocity of normal component of wn interface, $\mathbf{v}_{wn}\cdot\mathbf{n}_w\mathbf{n}_w$

$\mathbf{X}$	position vector in a solid in the initial state
$\mathcal{X}_k$	set of neighboring lattice sites to site $\mathbf{x}_k$
$\mathbf{x}$	position vector
$\delta_s\mathbb{Z}_d$	regular lattice space in d dimensions

Greek Symbols

α	entity index
β	entity index
Γ	boundary of a domain
γ	interfacial or surface tension; common curvilinear tension
ϵ	porosity
$\epsilon^{\bar{\bar{\alpha}}}$	specific entity measure, $\langle 1 \rangle_{\Omega_\alpha,\Omega}$
ζ	parameter controlling interfacial width in LBM
η	entropy density
$\eta^{\bar{\bar{\alpha}}}$	macroscale entropy of entity α per volume, $\langle \eta_\alpha \rangle_{\Omega_\alpha,\Omega}$
θ	temperature
$\theta^{\bar{\bar{\alpha}}}$	entropy weighted macroscale temperature of entity α, $\langle \theta_\alpha \rangle_{\Omega_\alpha,\Omega_\alpha,\eta_\alpha}$
$\underline{\underline{\kappa}}_G^{wns}$	macroscale geodesic curvature
$\underline{\underline{\kappa}}_N^{wns}$	macroscale normal curvature
Λ	entropy production rate
$\Lambda^{\bar{\bar{\alpha}}}$	macroscale entropy production rate associated with entity α
μ	chemical potential
ρ	mass density
σ	LBM parameter used to control the interfacial tension
σ	solid-phase stress tensor
$\sigma^{\bar{\bar{s}}}$	macroscale solid-phase stress tensor
τ	dissipative part of the stress tensor
ϕ	dimensionless density field
ϕ_s	solid-phase value of dimensionless density field set to control contact angle
$\underset{\kappa\to\alpha}{\Phi}$	general macroscale transfer of entropy from entity κ to entity α
$\underline{\underline{\underline{\underline{\varphi}}}}^{ws,wn}$	macroscale measure of contact angle
ϕ	nonadvective entropy flux
$\varphi^{\bar{\bar{\alpha}}}$	macroscale nonadvective entropy flux associated with entity α
$\phi_{ws,wn}$	microscale contact angle
$\chi_\alpha^{\bar{\bar{k}}}$	fraction of boundary of entity α in contact with entity κ, $\langle 1 \rangle_{\Omega_\kappa,\Omega_\alpha}$
Ψ	body force potential density
$\Psi^{\bar{\bar{\alpha}}}$	entity-based macroscale body force potential density
ψ	body force potential per unit mass
$\underline{\underline{\psi}}^{\alpha,\kappa}$	macroscale average of body force potential density associated with one entity averaged over a lower-dimensional entity
Ω	averaging domain
Ω_α	domain of entity α

Superscripts

eq	equilibrium value
n	macroscale nonwetting-phase qualifier
ns	macroscale qualifier for interface between n and s phases
ss	total surface of solid-phase qualifier

s	macroscale solid-phase qualifier
T	transpose
w	macroscale wetting-phase qualifier
wn	macroscale qualifier for interface between w and n phases
wns	macroscale qualifier for common curve where wn, ws, and ns interfaces meet
ws	macroscale qualifier for interface between w and s phases
α	macroscale entity qualifier
α	intrinsic average over entity α or macroscale property of entity α
$\overline{\alpha}$	mass average over entity α
$\overline{\overline{\alpha}}$	uniquely defined average over α
–	above a superscript refers to a density-weighted macroscale average
=	above a superscript refers to a uniquely defined macroscale average
$'$	vector tangent to a surface
$''$	vector tangent to a common curve

Subscripts

eq	equilibrium value
$\mathcal{E}$	associated with the total energy conservation equation
eq	equilibrium
$\mathcal{G}$	associated with the potential energy equation
$\mathcal{M}$	associated with the mass conservation equation
n	microscale nonwetting-phase qualifier
ns	microscale qualifier for interface between n and s phases
$\mathcal{P}$	associated with the momentum conservation equation
s	microscale solid-phase qualifier
ss	refers to the total boundary of the s phase
T	total
T	associated with the thermodynamic equation
$\mathcal{T}_{\mathcal{G}}$	associated with the derivative of potential energy equation
w	microscale wetting-phase qualifier
wn	microscale qualifier for interface between w and n phases
wns	microscale qualifier for common curve where wn, ws, and ns interfaces meet
ws	microscale qualifier for interface between w and s phases
α	microscale entity qualifier
$\alpha\alpha$	refers to the total boundary of entity α

Other Mathematical Symbols

$\mathrm{D}_\alpha/\mathrm{D}t$	material derivative with microscale velocity $\mathbf{v}_\alpha$
$\mathrm{D}^{\overline{\alpha}}/\mathrm{D}t$	material derivative with macroscale velocity $\mathbf{v}^{\overline{\alpha}}$
$\mathrm{D}'^{s}/\mathrm{D}t$	material derivative on a surface where the macroscale solid is employed, $\partial'/\partial t + \mathbf{v}^{\overline{s}} \cdot \nabla'$
$\mathrm{D}''^{s}/\mathrm{D}t$	material derivative on a curve where the macroscale solid is employed, $\partial''/\partial t + \mathbf{v}^{\overline{s}} \cdot \nabla''$
$\partial'/\partial t$	partial time derivative at a point fixed on a surface
$\partial''/\partial t$	partial time derivative at a point fixed on a common curve
$\partial^{(n)}/\partial t$	partial time derivative at a point fixed on 3 – n-dimensional entity, (n) is replaced by n primes
∇'	microscale surficial del operator
∇''	microscale common curve del operator
$\nabla^{(n)}$	microscale del operator for a 3 – n-dimensional entity where (n) is the number of primes
∇_X	gradient operator with respect to $\mathbf{X}$ coordinates

∇_x gradient operator with respect to macroscale **x** coordinates
(n) denotes the number of primes that should appear
$\hat{}$ a parameter defined at the scale indicated by the subscript or superscript on the parameter

$\langle f_\alpha \rangle_{\Omega_\beta,\Omega_\gamma,W} = \left(\int_{\Omega_\beta} W f_\alpha \, d\mathfrak{r} \right) \Big/ \left(\int_{\Omega_\gamma} W \, d\mathfrak{r} \right)$, general average of microscale property f_α

$f_\alpha^\beta = \langle f_\alpha \rangle_{\Omega_\beta,\Omega_\beta}$
$f^\alpha = \langle f_\alpha \rangle_{\Omega_\alpha,\Omega_\alpha}$, intrinsic average
$f_\alpha^{\bar{\beta}} = \langle f_\alpha \rangle_{\Omega_\beta,\Omega_\beta,\rho_\alpha}$, general density-weighted average
$f^{\bar{\alpha}} = \langle f_\alpha \rangle_{\Omega_\alpha,\Omega_\alpha,\rho_\alpha}$, intrinsic density-weighted average

Abbreviations

CIT	classical irreversible thermodynamics
DNP	disconnected nonwetting phase
LBM	lattice Boltzmann method
MRT	multirelaxation time
TCAT	thermodynamically constrained averaging theory

ACKNOWLEDGMENTS

This work was supported by National Science Foundation Grant 0941235, Department of Energy Grant DE-SC0002163, and Army Research Office Grant W911NF-14-1-0287.

REFERENCES

1. B. Ahrenholz, J. Toelke, P. Lehmann, A. Peters, A. Kaestner, M. Krafczyk, and W. Durner. Prediction of capillary hysteresis in a porous material using lattice-Boltzmann methods and comparison to experimental data and a morphological pore network model. *Advances in Water Resources*, 31(9):1151–1173, 2008.
2. R. I. Al-Raoush and C. S. Wilson. Extraction of physically realistic pore network properties from three-dimensional synchrotron x-ray microtomography images of unconsolidated porous media systems. *Journal of Hydrology*, 300(1–4):44–64, 2005.
3. T. B. Anderson and R. Jackson. A fluid mechanical description of fluidized beds. *Industrial and Engineering Chemistry Fundamentals*, 6:527–539, 1967.
4. Y. Bachmat. Spatial macroscopization of processes in heterogeneous systems. *Israel Journal of Technology*, 10:391–403, 1972.
5. M. Bailyn. *A Survey of Thermodynamics*. American Institute of Physics Press, New York, 1994.
6. J. Bear. *Hydraulics of Groundwater*. McGraw-Hill, New York, 1979.
7. L. S. Bennethum and J. H. Cushman. Multiphase, multicomponent theory for multiscale swelling systems with interfaces. Part II: Constitutive theory. *International Journal of Engineering Science*, 34(2):147–169, 1996.
8. H. Bertin, M. Quintard, and V. Corpel. Two-phase flow in heterogeneous porous media III: Laboratory experiments for flow parallel to a stratified system. *Transport in Porous Media*, 5(6):543–590, 1990.
9. P. Bobeck. *The Public Fountains of the City of Dijon* (translation of *Les Fontaines Publiques de la Ville de Dijon by Henry Darcy, 1856*). Geotechnical Translations, Austin, TX, 2004.
10. M. M. Britton. Porous media studied by MRI. *eMagRes*, 2011.
11. H. B. Callen. *Thermodynamics and an Introduction to Thermostatistics*. Wiley, New York, 1985.
12. J. T. Cheng. Fluid flow in ultrafine structures. Master's thesis, Purdue University, West Lafayette, IN, 2002.
13. J. T. Cheng, L. J. Pyrak-Nolte, D. D. Nolte, and N. J. Giordano. Linking pressure and saturation through interfacial areas in porous media. *Geophysical Research Letters*, 31(8), 2004.
14. V. Cnudde and M. N. Boone. High-resolution x-ray computed tomography in geosciences: A review of the current technology and applications. *Earth–Science Reviews*, 123:1–17, 2013.

15. G. H. Crapiste, E. Rotstein, and S. Whitaker. A general closure scheme for the method of volume averaging. *Chemical Engineering Science*, 41:227–235, 1986.
16. H. Darcy. *Les Fontaines Publiques de la Ville de Dijon*. Dalmont, Paris, France, 1856.
17. H. Darcy. Determination of the laws of flow of water through sand. In R. A. Freeze and W. Back, eds., *Physical Hydrology*. Hutchinson Ross, Stroudsburg, PA, 1983.
18. K. G. Denbigh. *The Principles of Chemical Equilibrium*. Cambridge University Press, Cambridge, U.K., 1981.
19. D. d'Humiéres, I. Ginzburg, M. Krafczyk, P. Lallemand, and L. S. Luo. Multiple-relaxation-time lattice Boltzmann models in three dimensions. *Philosophical Transactions of the Royal Society of London Series A: Mathematical Physical and Engineering Sciences*, 360:437–451, 2002.
20. A. L. Dye, J. E. McClure, C. T. Miller, and W. G. Gray. Description of non-darcy flows in porous medium systems. *Physical Review E*, 87(3), 2013.
21. F. Golfier, B. D. Wood, L. Orgogozo, M. Quintard, and M. Bués. Biofilms in porous media: Development of macroscopic transport equations via volume averaging with closure for local mass equilibrium conditions. *Advances in Water Resources*, 463–485(32):3, 2009.
22. W. G. Gray and S. M. Hassanizadeh. Averaging theorems and averaged equations for transport of interface properties in multiphase systems. *International Journal of Multiphase Flow*, 15(1):81–95, 1989.
23. W. G. Gray and P. C. Y. Lee. On the theorems for local volume averaging of multiphase systems. *International Journal of Multiphase Flow*, 3:333–340, 1977.
24. W. G. Gray and C. T. Miller. Thermodynamically constrained averaging theory approach for modeling flow and transport phenomena in porous medium systems: 1. Motivation and overview. *Advances in Water Resources*, 28(2):161–180, 2005.
25. W. G. Gray and C. T. Miller. Thermodynamically constrained averaging theory approach for modeling flow and transport phenomena in porous medium systems: 5. Single-fluid-phase transport. *Advances in Water Resources*, 32(5):681–711, 2009.
26. W. G. Gray and C. T. Miller. Thermodynamically constrained averaging theory approach for modeling flow and transport phenomena in porous medium systems: 8. Interface and common curve dynamics. *Advances in Water Resources*, 33(12):1427–1443, 2010.
27. W. G. Gray and C. T. Miller. A generalization of averaging theorems for porous medium analysis. *Advances in Water Resources*, 62, 227–237, 2013.
28. W. G. Gray and C. T. Miller. *Introduction to the Thermodynamically Constrained Averaging Theory for Porous Medium Systems*. Advances in Geophysical and Environmental Mechanics and Mathematics (AGEM^2). Springer, Cham, Switzerland, 2014.
29. W. G. Gray and K. O'Neill. On the development of Darcy's law for the general equations for flow in porous media. *Water Resources Research*, 12(2):148–154, 1976.
30. W. G. Gray, A. Leijnse, R. L. Kolar, and C. A. Blain. *Mathematical Tools for Changing Spatial Scales in the Analysis of Physical Systems*. CRC Press, Boca Raton, FL, 1993.
31. W. G. Gray, A. F. B. Tompson, and W. E. Soll. Closure conditions for two-fluid flow in porous media. *Transport in Porous Media*, 47(1):29–65, 2002.
32. Z. Guo and T. S. Zhao. Lattice Boltzmann model for incompressible flows through porous media. *Physical Review E*, 66:036304-1–036304-9, 2002.
33. S. M. Hassanizadeh and W. G. Gray. General conservation equations for multi-phase systems: 1. Averaging procedure. *Advances in Water Resources*, 2(3):131–144, 1979.
34. S. M. Hassanizadeh and W. G. Gray. Toward an improved description of the physics of two-phase flow. *Advances in Water Resources*, 16(1):53–67, 1993.
35. X. He and L. S. Luo. A priori derivation of the lattice Boltzmann equation. *Physical Review E*, 55:R6333–R6336, 1997.
36. M. Hilpert, J. F. McBride, and C. T. Miller. Pore-scale modeling of hysteretic flow in porous media. In *Sixth SIAM Conference on Mathematical and Computational Issues in the Geosciences*, Boulder, CO, 2001.
37. F. A. Howes and S. Whitaker. The spatial averaging theorem revisited. *Chemical Engineering Science*, 40:1387–1392, 1985.
38. H. Huang, D. T. J. Thorne, M. G. Schaap, and M. C. Sukop. Proposed approximation for contact angles in Shan-and-Chen-type multicomponent multiphase lattice Boltzmann models. *Physical Review E*, 76(6, Part 2), 2007.
39. A. B. S. Jackson, C. T. Miller, and W. G. Gray. Thermodynamically constrained averaging theory approach for modeling flow and transport phenomena in porous medium systems: 6. Two-fluid-phase flow. *Advances in Water Resources*, 32(6):779–795, 2009.

40. L. F. Konikow and P. D. Glynn. Modeling groundwater flow and quality. In *Essentials of Medical Geology*, pp. 727–753. Springer, Netherlands, 2013.
41. M. Latva-Kokko and D. Rothman. Static contact angle in lattice Boltzmann models of immiscible fluids. *Physical Review E*, 72(4, Part 2), 2005.
42. G. Lebon, D. Jou, and J. Casas-Vázquez. *Understanding Nonequilibrium Thermodynamics*. Springer, Berlin, Germany, 2008.
43. C. Marle. Ècoulements monophasiques en milieu poreux. *Revue de L'Institut Français du Pétrole*, 22(10):1471–1509, 1967.
44. G. A. Maugin. *The Thermomechanics of Nonlinear Irreversible Behaviors: An Introduction*. World Scientific Press, Singapore, 1999.
45. J. E. McClure, D. Adalsteinsson, C. Pan, W. G. Gray, and C. T. Miller. Approximation of interfacial properties in multiphase porous medium systems. *Advances in Water Resources*, 30(3):354–365, 2007.
46. J. E. McClure, J. F. Prins, and C. T. Miller. A novel heterogeneous algorithm to simulate multiphase flow in porous media on multicore CPU-GPU systems. *Computer Physics Communication*, 185:1865–1874, 2014.
47. C. T. Miller and W. G. Gray. Thermodynamically constrained averaging theory approach for modeling flow and transport phenomena in porous medium systems: 2. Foundation. *Advances in Water Resources*, 28(2):181–202, 2005.
48. C. T. Miller, G. Christakos, P. T. Imhoff, J. F. McBride, J. A. Pedit, and J. A. Trangenstein. Multiphase flow and transport modeling in heterogeneous porous media: Challenges and approaches. *Advances in Water Resources*, 21(2):77–120, 1998.
49. N. R. Morrow. Irreducible wetting-phase saturations in porous media. *Chemical Engineering Science*, 25:1799–1815, 1970.
50. J. Niessner and S. M. Hassanizadeh. A model for two-phase flow in porous media including fluid-fluid interfacial area. *Water Resources Research*, 44(W08439), 2008.
51. J. Niessner, S. Berg, and S. M. Hassanizadeh. Comparison of two-phase Darcy's Law with a thermodynamically consistent approach. *Transport in Porous Media*, 88:133–148, 2011.
52. C. Pan, L.-S. Luo, and C. T. Miller. An evaluation of lattice Boltzmann schemes for porous medium flow simulation. *Computers & Fluids*, 35(8–9):898–909, 2006.
53. D. Pavone. A Darcy's law extension and a new capillary pressure equation for two-phase flow in porous media. In *Proceedings of the 65th Annual Technical Conference of the Society of Petroleum Engineers*, volume Rep. SPE 20474, pp. 111–119, New Orleans, LA, 1990. Society of Petroleum Engineers.
54. M. Quintard and S. Whitaker. Two-phase flow in heterogeneous porous media: The method of large-scale averaging. *Transport in Porous Media*, 3(4):357–413, 1988.
55. M. Quintard and S. Whitaker. Transport in chemically and mechanically heterogeneous porous media. I: Theoretical development of region-averaged equations for slightly compressible single-phase flow. *Advances in Water Resources*, 19(1):29–47, 1996.
56. M. Quintard and S. Whitaker. Theoretical analysis of transport in porous media. In K. Vafai, ed., *Handbook of Porous Media*, pp. 1–52. Marcel Dekker, New York, 2000.
57. N. R. Rossman and V. A. Zlotnik. Review: Regional groundwater flow modeling in heavily irrigated basins of selected states in the western United States. *Hydrogeology Journal*, 21:1173–1192, September 2013.
58. T. Sakaki, D. M. O'Carroll, and T. H. Illangasekare. Direct quantification of dynamic effects in capillary pressure for drainage-wetting cycles. *Vadose Zone Journal*, 9:424–437, 2010.
59. G. Segol. 1994. *Classic Groundwater Simulations*: *Proving and Improving Numerical Models*. Englewood Cliffs, N.J.: Prentice Hall.
60. J. C. Slattery. Flow of viscoelastic fluids through porous media. *American Institute of Chemical Engineers Journal*, 13(6):1066–1071, 1967.
61. J. C. Slattery. *Advanced Transport Phenomena*. Cambridge University Press, Cambridge, U.K., 1999.
62. P. Spanne, J. F. Thovert, C. J. Jacquin, W. B. Lindquist, K. W. Jones, and P. M. Adler. Synchrotron computed microtomography of porous-media—Topology and transports. *Physical Review Letters*, 73(14):2001–2004, 1994.
63. G. L. Stegemeier. Mechanism of entrapment and mobilization of oil in porous media. In *AIChE Symposium on Improved Oil Recovery by Surfactant and Polymer Flooding*, pp. 55–91. Academic Press Inc., New York, 1977.
64. P. W. Takhar. Unsaturated fluid transport in swelling poroviscoelastic biopolymers. *Chemical Engineering Science*, 109:98–110, 2014.

65. L. Talon, D. Bauer, N. Gland, S. Youssef, H. Auradou, and I. Ginzburg. Assessment of the two relaxation time lattice-Boltzmann scheme to simulate Stokes flow in porous media. *Water Resources Research*, 48, 2012.
66. I. Vavruch. Conceptual problems of modern irreversible thermodynamics. *Chemicke Listy*, 96(5):271–275, 2002.
67. S. Whitaker. Diffusion and dispersion in porous media. *American Institute of Chemical Engineers Journal*, 13(3):420–427, 1967.
68. S. Whitaker. Advances in theory of fluid motion in porous media. *Industrial and Engineering Chemistry*, 61(12):14–28, 1969.
69. S. Whitaker. *The Method of Volume Averaging*. Kluwer Academic Publishers, Dordrecht, the Netherlands, 1999.
70. D. Wildenschild and A. P. Sheppard. X-ray imaging and analysis techniques for quantifying pore-scale structure and processes in subsurface porous medium systems. *Advances in Water Resources*, 51:217–246, 2013.
71. B. D. Wood, F. Cherblanc, M. Quintard, and S. Whitaker. Volume averaging for determining the effective dispersion tensor: Closure using periodic unit cells and comparison with ensemble averaging. *Water Resources Research*, 39(8), August 2003.

2 Advanced Theories of Two-Phase Flow in Porous Media

S. Majid Hassanizadeh

CONTENTS

2.1 Introduction 47
2.2 Critical Evaluation of Current Two-Phase Flow Theory 49
2.2.1 Brief Description of Current Theory 49
2.2.2 Criticisms of Darcy's Law 50
2.2.3 Criticisms of Capillarity Theory 51
2.3 Thermodynamically Based Equations of Two-Phase Flow 53
2.3.1 Averaging–Thermodynamic Approach 53
2.3.2 New Two-Phase Flow Theory 54
2.3.3 Evaluation of Role of Specific Interfacial Area 56
2.3.4 Evaluation of Nonequilibrium Capillarity Effect 58
2.3.5 Comments on the Extended Darcy's Law 58
2.4 Conclusions 59
Acknowledgment 59
References 59

2.1 INTRODUCTION

Fluid-filled porous media are ubiquitous in many natural and industrial systems. The working of these systems is controlled and/or affected by the movement of fluids, solutes, particles, and heat through them. Examples of natural porous media and corresponding processes are the flow of oil, gas, and water in oil reservoirs; the potential mobilization of methane in gas hydrates; the flow of nonaqueous phase liquids (NAPLs) in contaminated aquifers; the storage of CO_2, nuclear waste, other hazardous wastes, and heat in the subsurface; the flow of fluids in biological tissues; and melting and metamorphism of snow. Examples of industrial porous media and corresponding processes are the drying of paper pulp, the adsorption of liquids in diapers and similar absorbing products, gas and water management in fuel cells, and the drying of foods, building materials, detergent tablets, and filters.

Many physical, chemical, and thermal processes (such as fluid flow, diffusion, capillarity, dissolution, adsorption, clogging, degradation, and swelling) occur in these materials. For the design, operation, and maintenance of porous media systems, it is extremely important to understand these processes, describe them quantitatively (by mathematical models), and compute solutions to the governing equations. One would expect that for such a vast range of highly important systems and for complex processes occurring therein, a well-founded science with deep roots in fundamental principles of physics and mechanics should have been developed. Indeed, governing equations embedded in mathematical models of complex porous media systems should originate from rigorous derivations following a systematic approach. But the main equations used in porous media models are relatively simple equations, often borrowed from other disciplines: Darcy's law for flow, Fick's law for solute transport, Fourier's law for heat transfer, and Hooke's law of elasticity

for deformation. These equations, which form cornerstones of conceptual and computational models of flow and transport in deformable porous media at all scales, were originally presented for simple systems. During the last century, these equations have been adopted in an ad hoc fashion in order to be applicable to complex porous media processes, but with superficial modifications only. The complexities of coupled multiphase flow and reactive transport in deformable porous media were not taken into account. It is thus no surprise that, in almost all cases, our models have failed to provide acceptable descriptions of complex porous media. There are many examples. Hereunder, I give a few examples from the energy sector.

In petroleum engineering, predictions of oil or gas production from a well are almost always significantly different from observed production. So, after some time, the model input parameters are changed to match historical production data (this is called "history matching"). Then, new predictions are made, which are usually in error again. So, the cycle is repeated. The subsurface sequestration of CO_2 involves complex processes too. In the case of injection of CO_2 into brine reservoirs, one has to deal with three-phase flow (brine, gaseous CO_2, and supercritical CO_2), dissolution of CO_2 into brine, reactions with the solid phases, and deformation of the porous medium. The design of such operations, the prediction of their performance, and safety of CO_2 sequestration are dependent on our models. Currently, there are major concerns about multiphase flow models being able to provide adequate certainty in this regard. Among other factors, this has hampered the decision-making process, while urgent measures are needed.

Another area where reliable multiphase flow models are urgently needed relates to the fate of huge reservoirs of gas hydrates. At numerous locations around the world, large quantities of methane gas are trapped inside "cages" of water ice molecules in sediments beneath the oceans and in the permafrost regions. This compound is referred to as gas hydrates and has the potential of not only being a blessing but also a curse. On the one hand, these are vast sources of energy if harvested. On the other hand, they could be destabilized as a result of the varying pressure–temperature conditions due to climate change, potentially leading to a catastrophic release of methane and causing an abrupt global warming much worse than what we are experiencing today. Various processes that need to be modeled include heat diffusion, hydration and dissociation, osmosis, sediment matrix deformation, methane oxidation, and movement of gas bubbles and water (two-phase flow). Gas bubbles will exist mainly as a discontinuous phase. But current models of two-phase flow are only valid for continuous phases. So any modeling study of the potentials for the exploitation of these resources or the threat posed by them will be done with a defective model.

The final example relates to what is considered to be the ultimate source of clean energy, namely, a "hydrogen fuel cell." In a hydrogen fuel cell, energy from oxidation of hydrogen is harnessed, producing water as the only waste. Here again, the central process is the simultaneous movement of water and gasses in layers of porous media. As some layers are hydrophobic, water is formed and moves as droplets, that is, as a discontinuous phase. So current theories of two-phase flow are inappropriate for modeling fuel cells. Many more examples from other sectors can be given.

Obviously, much is needed for improving the quality of our model predictions, including methods for characterization of the media and more robust numerical methods. But a central element, which is at the heart of any model, is the set of equations used for describing the main processes. Our current theories of multiphase flow and transport in porous media are simply outdated and insufficient for modeling systems described earlier. A central issue in formulating theories of multiphase flow is the proper choice of state variables and developing appropriate governing equations for describing the system under consideration. In current theories of two-phase flow, the state variables are considered to be two fluid pressures and the saturation of one of the phases. In this chapter, we show that these three variables are not sufficient to fully characterize the state of two-phase flow in a porous medium. One needs to add another macroscale state variable that contains information about the subscale distribution of the phases.

First, we discuss the shortcomings of current theories of two-phase flow. Then, we provide an alternative and improved theory with roots in rational thermodynamics. We introduce specific

interfacial area (area of fluid–fluid interfaces per unit volume of porous medium) as a new state variable. We present theoretical, experimental, and computational evidences to support new concepts and equations presented here.

2.2 CRITICAL EVALUATION OF CURRENT TWO-PHASE FLOW THEORY

2.2.1 Brief Description of Current Theory

Consider the flow of two or more immiscible incompressible fluids in a porous medium. The central equation in current models of multiphase flow is Darcy's law. This is an empirical equation that was originally proposed by Henry Darcy in 1856 for describing *1D steady-state flow of incompressible water in saturated homogeneous isotropic rigid sandy soil under constant temperature* in a form equivalent to the following:

$$\mathbf{q} = -\frac{\mathbf{k}}{\mu}\cdot\left(\nabla P - \rho\mathbf{g}\right) \tag{2.1}$$

where

$\mathbf{q}$ [LT^{-1}] is the fluid phase apparent velocity vector
$\mathbf{k}$ [L^2] is the intrinsic permeability tensor
μ [$ML^{-1}T^{-1}$] is the dynamic viscosity
P [$ML^{-1}T^{-2}$] is the fluid phase pressure
ρ [ML^{-3}] is the fluid mass density
$\mathbf{g}$ [LT^{-2}] is the gravity vector

In the course of the last century, this equation has been used, almost without any alteration, to describe much more complex systems, namely, *3D unsteady flow of two or more compressible fluids, with any amount of dissolved matter, in heterogeneous anisotropic deformable porous media under nonisothermal conditions*. One would expect a much more complex equation, which would account for many additional physical phenomena in such complex systems. But the so-called "generalized" Darcy's law has the same form as Equation 2.1 (Helmig, 1997):

$$\mathbf{q}^{\alpha} = -\frac{k_{r\alpha}\mathbf{k}}{\mu^{\alpha}}\cdot\left(\nabla P_{\alpha} - \rho^{\alpha}\mathbf{g}\right) \quad \alpha = w, n \tag{2.2}$$

where

subscript $\alpha(= w, n)$ refers to the fluid phase under consideration
w denotes the wetting phase, which preferably wets the porous solid
n denotes the nonwetting phase for which the solid has less affinity

The only new element in Equation 2.2 is the relative permeability $k_{r\alpha}$ [–], which scales the saturated intrinsic permeability such that the influence on the flow of one phase due to the presence of other phases is taken into account. The relative permeability is assumed to be an algebraic function of saturation only.

The governing equation for saturation is based on the principle of conservation of mass, which for incompressible fluids reduces to the conservation of volume:

$$\phi\frac{\partial S^{\alpha}}{\partial t} + \nabla\cdot\mathbf{q}^{\alpha} = 0 \quad \alpha = w, n \tag{2.3}$$

where

ϕ [–] is the porosity
S^{α} [–] is the fluid phase saturation

Equations 2.2 and 2.3 are supplemented by the so-called capillary pressure equation

$$P_n - P_w = P_c\left(S^w\right) \tag{2.4}$$

where P_c [$ML^{-1}T^{-2}$] is capillary pressure. When more fluid phases are present, Equations 2.2 through 2.4 are simply repeated for each additional phase, as if there are no other forces active, regardless of how many phases fill out the pore space.

2.2.2 Criticisms of Darcy's Law

Let us compare Equations 2.1 and 2.2. It is evident that, despite the much more complex nature of multiphase systems compared to the flow of water in saturated sand, the driving force in all cases is assumed to be $\nabla P - \rho\mathbf{g}$ for each phase. The relative permeability coefficient is given the task of accounting for the complexities of multiphase flow dynamics. Theoretically, this is the coefficient of proportionality in the linear relationship between flow velocity, $\mathbf{q}^\alpha$, and the driving force, $\nabla P_\alpha - \rho^\alpha\mathbf{g}$. It is supposed to be a known function of saturation, and its value must vary between zero and unity. Yet values of relative permeability as large as 14 have been reported in the literature; see Figure 2.1.

Furthermore, there is ample evidence that the relative permeability depends not only on saturation but also on many other variables. In particular, its dependence on capillary number ($N_c = \mu v/\sigma$, where v is the average flow velocity and σ is the fluid–fluid interfacial tension) and therefore indirectly on pressure gradient or flow velocity has been established through both computational and experimental studies. For example, Figure 2.2 from Constantinides and Payatakes (1996) shows very significant changes in the relative permeability of both phases due to changes in average capillary number. Similar results were obtained in numerical studies of Avraam and Payatakes (1995),

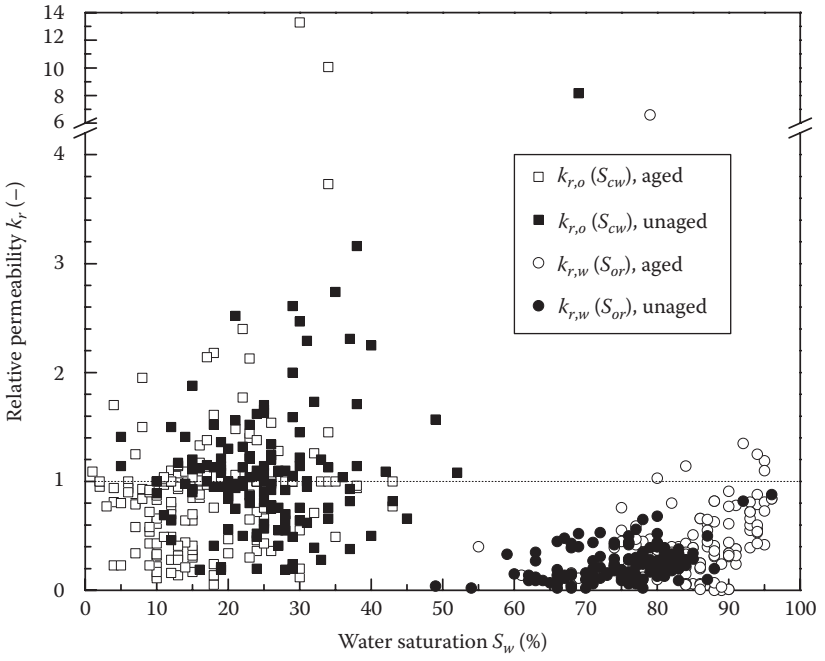

FIGURE 2.1 Relative permeability values much larger than unity are reported. (From Berg, S. et al., *Trans. Porous Media*, 74, 275–292, 2008.)

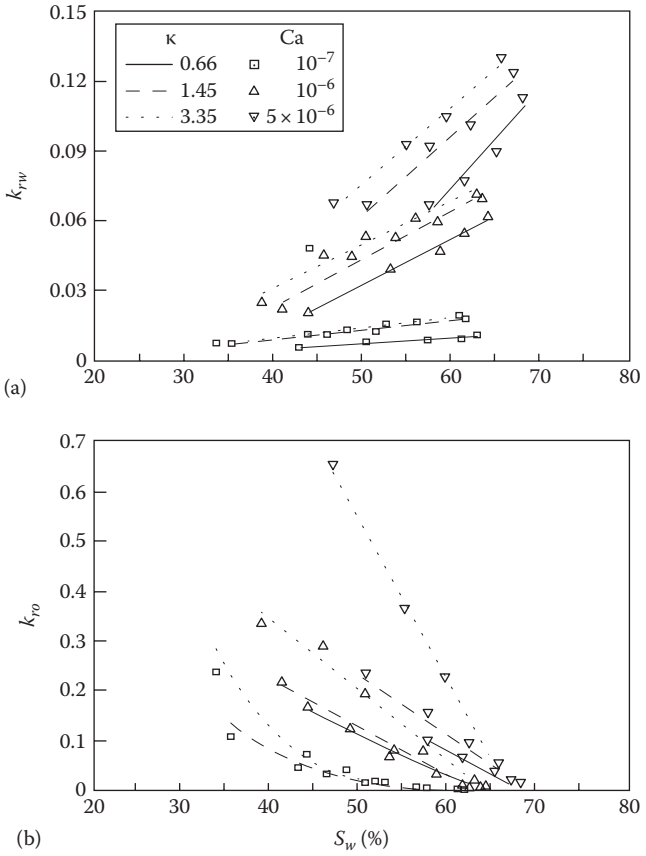

FIGURE 2.2 Relative permeability for (a) wetting phase and (b) nonwetting phase. They are not just a function of saturation but depend on capillary number, that is, indirectly on the pressure gradient or flow velocity. (From Constantinides, G.N. and Payatakes, A.C., *AIChE J.*, 42, 369, 1996.)

Ataie-Ashtiani et al. (2002), and Li et al. (2005) and in experimental works of Boom et al. (1995, 1996), Henderson et al. (1996, 2000), Skauge et al. (2001), and Bartley and Ruth (2001). Dependence of relative permeability on flow velocity or pressure gradient obviously violates the underlying assumption of linear dependence between $\mathbf{q}^{\alpha}$ and $\nabla P_{\alpha} - \rho^{\alpha}\mathbf{g}$. So either the relationship is not linear or other forces need to be included. We know of course that other forces, such as interfacial forces, are present. In fact, the pore space is simultaneously occupied by two or more phases, which are separated by fluid–fluid interfaces. The interaction between the phases takes place through these interfaces. These interfaces play a central role in many processes and effects, such as capillarity, dissolution, adsorption of surfactants, transport of colloids and microorganisms in the unsaturated zone, evaporation, drying processes, and deformation of unsaturated soil. But, in current theories of multiphase flow, interfaces and their characteristics are completely absent! One would expect forces that control the movement of interfaces to be also present in the governing equations of multiphase flow. Also, mass and heat transfer coefficients should depend on the amount of fluid–fluid interfaces.

2.2.3 Criticisms of Capillarity Theory

Major shortcomings and inconsistencies are also found in the macroscale capillary Equation 2.4. This equation was proposed empirically too; it is an ad hoc extension of the pore-scale Young–Laplace equation that is valid under equilibrium conditions. While Equation 2.4 prescribes a one-to-one

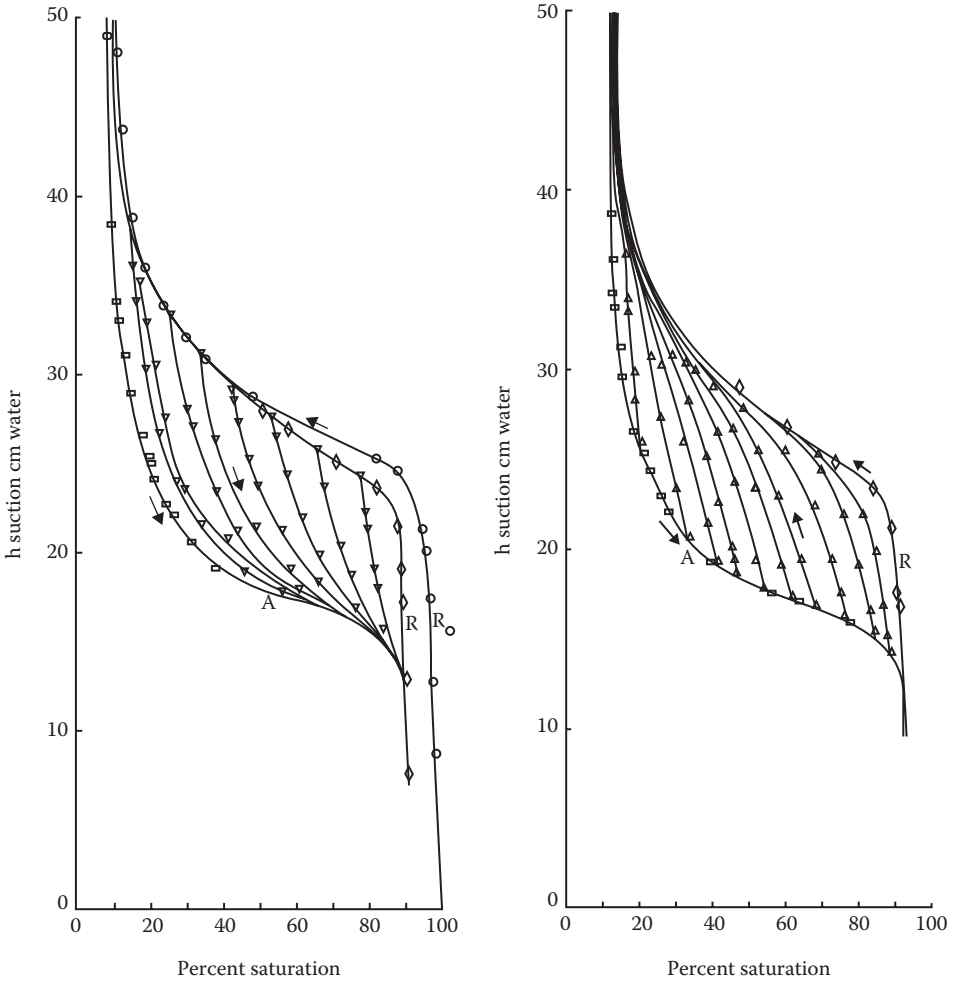

FIGURE 2.3 Equilibrium capillary pressure–saturation curves. (Adapted from Morrow, N.R. and Harris, C.C., *Soc. Petrol. Eng. J.*, 5, 15, 1965.)

relationship between fluid pressure difference and saturation, in practice, we have a strongly hysteretic and time-dependent function. In the literature, one commonly speaks of a capillary pressure–saturation curve. But, in practice, there exist many curves for the same porous medium. Typically measured capillary pressure curves are shown in Figure 2.3. It is evident that one has a primary drainage curve (i.e., reducing the wetting phase saturation from unity to some irreducible value); there is a main hysteresis loop (consisting of main drainage and imbibition curves), a large number of primary scanning loops, and a myriad of scanning loops of secondary, tertiary, and higher degrees. In fact, any point within the main hysteresis loop could be a potential equilibrium state of the porous medium.

Typical capillary pressure–saturation graphs (e.g., Figure 2.3) show that for any given saturation, the porous medium may attain a wide range of capillary pressure values. This is because a given volume of the fluid may be distributed within the pores in many different ways. Each distribution will have its own capillary pressure. This is very well evident in the images taken from quasistatic drainage and imbibition experiments in our micromodel, shown in Figure 2.4. The two images are from the same porous medium. White triangles are the solid phase. Darker areas show the nonwetting phase, whereas the wetting phase has a light color. The left image shows a stage

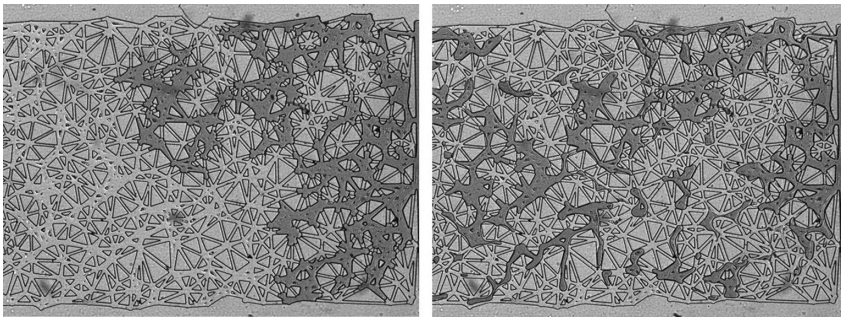

FIGURE 2.4 Images taken from quasistatic experiments in a micromodel. They are from primary drainage and main imbibition stages. (From Karadimitriou, N.K., Two-phase flow experimental studies in micromodels, PhD thesis, Utrecht University, Department of Earth Sciences, Utrecht, the Netherlands, 2013.)

during primary drainage. The right image was obtained during imbibition after main drainage had occurred. The overall wetting phase saturation in both images is 76%, but the average capillary pressure values in the left and right images are 4340 and 2200 Pa, respectively. *This makes it evident that in addition to saturation, another state variable is needed to specify the equilibrium state of the system*. In fact, we need a macroscale variable to account for the difference in fluid distributions in these two stages. We believe this variable can be linked to the area of interfaces separating the two fluids. Indeed, the total interfacial areas in the left and right images are significantly different; they are 18.32 and 30.56 mm^2, respectively.

There is another major issue with Equation 2.4. As mentioned earlier, capillary pressure–saturation curves are measured under equilibrium (no flow) conditions. They are subsequently used to simulate (very) dynamic processes! There are many situations where the timescale of the processes is much smaller than the timescale of P_c-S^w measurements. For example, in the modeling of paper pulp drying process, the capillary pressure curve for the water-adsorbing felt (which is used to absorb water out of the pulp) is measured under quasistatic conditions. It takes around 24 h to obtain it, and then it is used to model a process that takes only a fraction of a second (Iliev et al., 2012)! Another example is when there is a rainfall-induced landslide, where there are fast changes in saturation and pore pressure. Under those conditions, equilibrium P_c-S^w curve cannot be really used (see Nikooee et al., 2013 for a discussion). There are many other examples from natural and industrial porous media where equilibrium capillary pressure and relative permeability curves are used to model very fast processes. Numerous studies have shown that under flow conditions, $P_n - P_w$ is not equal to P_c. A detailed review of the literature is found in Hassanizadeh et al. (2002) and Diamantopoulos and Durner (2012). Results of our measurements of $P_n - P_w$ at a point in a column during a primary drainage process (Bottero et al., 2011) are shown in Figure 2.5. The lowest curve is the equilibrium P_c-S^w curve. The other curves are plots of $P_n - P_w$ as a function of S^w under flow conditions at various injection pressures of 20, 30, 35, and 38 kPa. Clearly, there is a huge difference between dynamic $P_n - P_w$ and the capillary pressure curve. The higher the injection pressure (and thus the saturation change with time), the larger the difference is. So the underlying premise of Equation 2.4 is simply not valid.

2.3 THERMODYNAMICALLY BASED EQUATIONS OF TWO-PHASE FLOW

2.3.1 Averaging–Thermodynamic Approach

This is a systematic framework for the derivation of physically based governing equations of flow and transport in porous media, which has its roots in the principles of rational thermodynamics. Governing equations at a given scale are composed of two ingredients: conservation laws and constitutive equations. In this approach, we use the volume averaging method to derive conservation

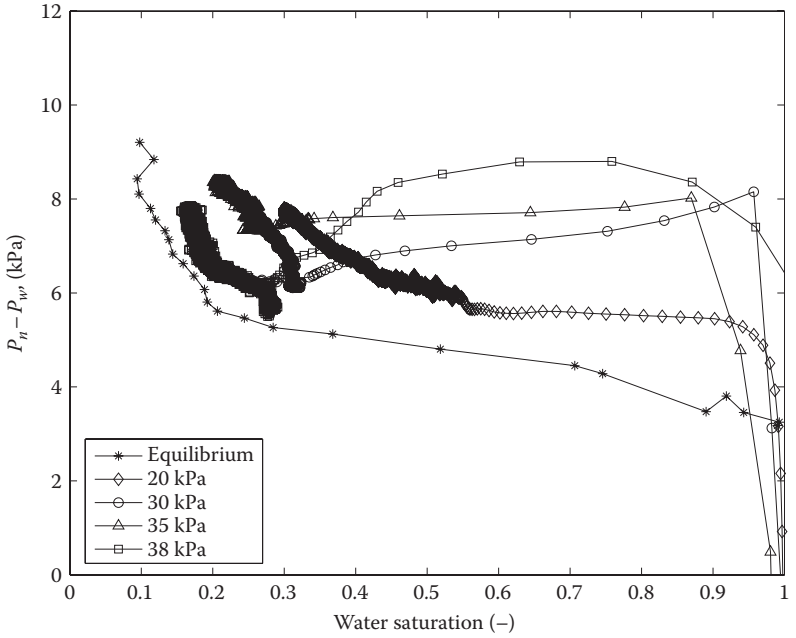

FIGURE 2.5 Curves of pressure difference $P_n - P_w$ versus saturation under dynamic conditions at various injection pressures of 20, 30, 35, and 38 kPa. The lowest curve is the equilibrium P_c-S^w curve. (From Bottero, S., Advances in theories of capillarity in porous media, PhD thesis, Utrecht University, Department of Earth Sciences, Utrecht, the Netherlands, November 2009.)

laws at the scale of interest, based on the description at a lower scale (see, e.g., Hassanizadeh and Gray, 1979a,b). Then, we employ the principle of rational thermodynamics to derive constitutive laws at the scale of interest (see, e.g., Hassanizadeh and Gray, 1980). This is based on the application of the second law of thermodynamics, which is also called the entropy inequality. The approach allows us to develop general equations for complex systems and then systematically simplify them to obtain equations for simpler systems.

2.3.2 New Two-Phase Flow Theory

Hassanizadeh and Gray (1990) have employed the averaging–thermodynamic approach to derive a new theory of two-phase flow in porous media. The new theory has four major new features, compared to the traditional approach, as explained shortly. These equations are devoid of the shortcomings of the traditional two-phase flow theory discussed earlier. First, mass balance laws are presented and then simplified equations of momentum balance.

As explained in the previous section, one would expect fluid–fluid interfaces and solid–fluid interfaces to play an important role in macroscale description of two-phase flow. Indeed, the application of volume averaging technique results in the definition of macroscale quantities not only for fluids and solid phases but also for phase interfaces. Macroscale quantities for phases are the same as the traditional ones: average mass density ρ^α and velocity vector $\mathbf{v}^\alpha$ [LT^{-1}], fluid phase saturations S^α, and pressures P^α. Similar macroscale quantities were found for interfaces: the average interfacial mass density $\Gamma^{\alpha\beta}$ ($\alpha\beta = wn, ns, ws$) [ML^{-2}], defined as the total mass of $\alpha\beta$ interfaces per area of those interfaces within a given volume; interfacial velocity vector $\mathbf{w}^{\alpha\beta}$ [LT^{-1}], average interfacial tension $\sigma^{\alpha\beta}$ [MT^{-2}]; and specific interfacial area $a^{\alpha\beta}$ [L^{-1}]. The latter is defined as the area of $\alpha\beta$ interfaces per unit volume of the porous medium.

The macroscale mass balance equations for fluid phases and interfaces are found, respectively, to be (Gray and Hassanizadeh, 1989)

$$\frac{\partial \phi S^{\alpha} \rho^{\alpha}}{\partial t} + \nabla \cdot \left(\phi S^{\alpha} \rho^{\alpha} \mathbf{v}^{\alpha} \right) = \sum_{\beta \neq \alpha} E_{\alpha}^{\alpha\beta}; \quad \alpha = w, n \tag{2.5}$$

$$\frac{\partial a^{\alpha\beta} \Gamma^{\alpha\beta}}{\partial t} + \nabla \cdot \left(a^{\alpha\beta} \Gamma^{\alpha\beta} \mathbf{w}^{\alpha\beta} \right) = E_{\alpha}^{\alpha\beta} + E_{\beta}^{\alpha\beta} + E^{\alpha\beta\gamma} \tag{2.6}$$

where

$E_{\alpha}^{\alpha\beta}$ [$ML^{-3}T^{-1}$] is the rate of exchange of mass between α-phase and αβ-interface

$E^{\alpha\beta\gamma}$ [$ML^{-3}T^{-1}$] is the rate of exchange of mass between αβ interface and αβγ common line (where the three interfaces come together)

Similar balance equations were derived by Marle (1982) and were used by Cushman and coworkers (see, e.g., Achanta et al., 1994; Bennethum and Cushman, 1996; Murad and Cushman, 1996).

Balance laws were also derived for momentum, energy, and entropy of phases and interfaces (Gray and Hassanizadeh, 1989). They were complemented by constitutive equations, and by employing the rational thermodynamics approach, Hassanizadeh and Gray (1990) derived the following simplified and linearized momentum balance equations for fluid phases and fluid–fluid interfaces, respectively:

$$\nabla P_{\alpha} - \rho_{\alpha} \mathbf{g} - \lambda_{s}^{\alpha} \nabla S^{\alpha} - \lambda_{a}^{\alpha} \nabla a^{wn} + R^{\alpha} \mathbf{v}^{\alpha} = 0; \quad \alpha = w, n \tag{2.7}$$

$$\nabla (a^{wn} \sigma^{wn}) + \Psi^{wn} \nabla S^{w} + R^{wn} \mathbf{w}^{wn} = 0 \tag{2.8}$$

where

R^{α} [$ML^{-3}T^{-1}$] and R^{wn} [$ML^{-3}T^{-1}$] are resistance coefficients

λ_{s}^{α} [$ML^{-1}T^{-2}$], λ_{a}^{α} [MT^{-2}], and Ψ^{wn} [$ML^{-1}T^{-2}$] are material coefficients (all of them may be functions of S^{w} and $a^{\alpha\beta}$)

The gravity term has been neglected in Equation 2.8.

Equations 2.5 and 2.6 can be further simplified if we assume that phase mass densities and the interfacial mass density are constant. These are reasonable assumptions for isothermal situations and in the absence of surfactants. Thus, those equations can be divided by ρ^{α} and $\Gamma^{\alpha\beta}$, respectively, to obtain the following volume balance and area balance equations:

$$\frac{\partial \phi S^{\alpha}}{\partial t} + \nabla \cdot \left(\phi S^{\alpha} \mathbf{v}^{\alpha} \right) = 0; \quad \alpha = w, n \tag{2.9}$$

$$\frac{\partial a^{wn}}{\partial t} + \nabla \cdot \left(a^{wn} \mathbf{w}^{wn} \right) = E^{wn} \tag{2.10}$$

where we limit our attention to the fluid–fluid (i.e., *wn*) interface. The term on the right-hand side of fluid phase mass balance has been neglected as we expect the rate of mass exchange between phases and interfaces to be much smaller than the advective flux of phases. The term on the right-hand side of (2.10), E^{wn} [$L^{-1}T^{-1}$], accounts for the rate of production of fluid–fluid interfaces.

This term is itself a function of saturation and specific interfacial area and their time rate of change. Expressions for such a dependency have been found through pore-network modeling by Joekar-Niasar and Hassanizadeh (2011) and by analyzing results of micromodel experiments by Karadimitriou et al. (2014a).

Next, simplified momentum balance Equations 2.7 and 2.8 are rearranged in order to obtain equations for macroscopic velocities. In the case of Equation 2.8, we assume the interfacial tension $\sigma^{\alpha\beta}$ to be constant, so that it can be absorbed into other material coefficients. Thus, we obtain the following Darcy-type equations for the movement of fluid phases and fluid–fluid interfaces:

$$\mathbf{q}^{\alpha} = -\frac{k_{r\alpha}k}{\mu^{\alpha}}(\nabla P_{\alpha} - \rho_{\alpha}\mathbf{g} - \lambda_s^{\alpha}\nabla S^{\alpha} - \lambda_a^{\alpha}\nabla a^{wn}); \quad \alpha = w, n \tag{2.11}$$

$$\mathbf{w}^{wn} = -K^{wn}(\nabla a^{wn} + \psi^{wn}\nabla S^{w}) \tag{2.12}$$

New variables in these equations are as follows: K^{wn} [L^3T^{-1}] is interfacial conductivity, and ψ^{wn} [L^{-1}] is a material coefficient, which may still depend on S^w and $a^{\alpha\beta}$.

In addition to an extended Darcy's law for the flow of fluids and the governing equations for specific interfacial area, the rational thermodynamics approach also led to a new hypothesis for the capillary pressure. Based on results of the constitutive theory, Hassanizadeh and Gray (1993a) suggested that the capillary pressure is not only a function of saturation but will also depend on specific interfacial area. They postulated that the hysteretic behavior of P_c-S^w relationship can be modeled by introducing fluid–fluid specific interfacial area $a^{\alpha\beta}$ into the P_c-S^w relationship. Based on this hypothesis, capillary pressure–saturation-specific interfacial area data points from drainage and imbibition processes under equilibrium or/and nonequilibrium conditions would fall on a unique surface. Such a surface can be described by the following formula:

$$f(P_c, S^w, a^{wn}) = 0 \tag{2.13}$$

Henceforth, we refer to this surface as the *interfacial area surface*. Also, unless otherwise stated, with the term "saturation," we refer to the wetting phase saturation.

One final result of the rational thermodynamics approach was that capillary pressure is not necessarily equal to the difference in fluid pressures. It was shown that Equation 2.4 holds under static conditions only. Under dynamic (flow) conditions, the difference in fluid pressure is not just equal to capillary pressure but includes a nonequilibrium term, given by the following equation (which is a linear approximation):

$$P_n - P_w = P_c\left(S^w, a^{wn}\right) - \tau\frac{\partial S^w}{\partial t} \tag{2.14}$$

where τ [$ML^{-1}T^{-1}$] is a material property, which may still be a function of S^w and a^{wn}. This equation is known as the dynamic capillarity formula. The second term on the right-hand side of (2.14) will vanish under equilibrium conditions, but it may be very significant under nonequilibrium conditions.

In the following sections, we discuss the significance of the set of equations developed earlier. In particular, we discuss the role of specific interfacial area and the nonequilibrium capillarity term.

2.3.3 Evaluation of Role of Specific Interfacial Area

A major feature of the new theory is the introduction of specific interfacial area, a^{wn}, as a new state variable. This is a major departure from the traditional approach where phase saturation and pressures are the only state variables. Given the fact that phenomena such as capillarity and kinetic

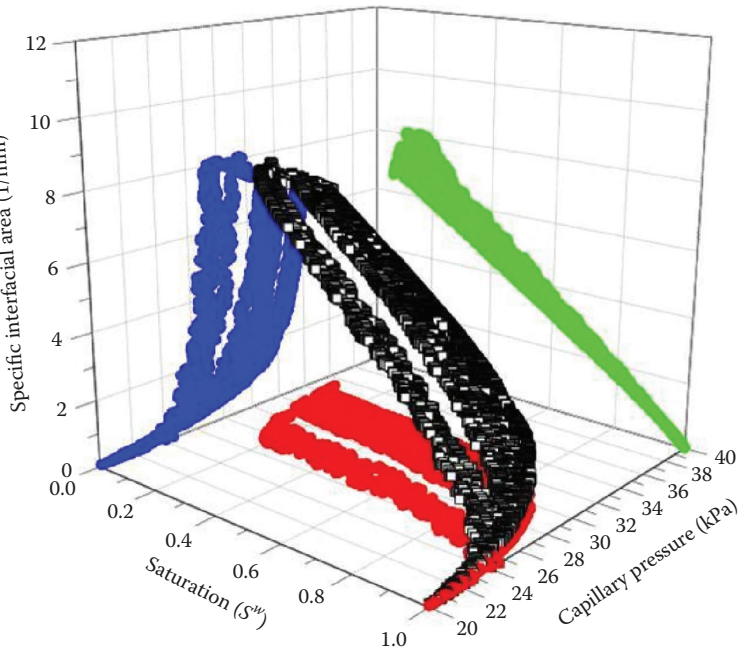

FIGURE 2.6 Schematic representation of P_c-S^w-a^{wn} surface (shown in black). Its projection onto the P_c-S^w plane creates the hysteresis domain formed by capillary pressure–saturation curves (shown in red).

mass and heat transfer occur across interfaces, we need a variable that quantifies interfacial configurations. Specific interfacial area is exactly such a variable. As evident from Equation 2.13, the capillary pressure not only is a function of saturation but also depends on the specific interfacial area, a^{wn}. This means that we do not have capillary pressure–saturation curves, but a capillary pressure–saturation-interfacial area surface, as shown in Figure 2.6. This description of capillarity suggests that the main and scanning hysteresis loops, which we see in Figure 2.3, actually represent a projection of the P_c-S^w-a^{wn} surface onto the P_c-S^w plane. This concept is illustrated in Figure 2.6.

Indeed, a growing number of numerical and experimental works show that under quasistatic conditions, drainage and imbibition P_c-S^w-a^{wn} surfaces (formed by data points from drainage and imbibition experiments, respectively) coincide with each other, within the margin of experimental error. The earliest studies were done by Reeves and Celia (1996), and Held and Celia (2001), who performed quasistatic pore-network modeling. More recent examples of computational studies that prove the existence of interfacial area surface (i.e., P_c-S^w-a^{wn} surface) are found in Joekar-Niasar et al. (2008), who also used pore-network modeling, and Porter et al. (2009), who performed lattice Boltzmann simulations. The first experimental evidence for the uniqueness of P_c-S^w-a^{wn} surface was provided by Cheng et al. (2004) and later by Chen et al. (2007) and Pyrak-Nolte et al. (2008). They performed two-phase flow experiments in a micromodel. A combination of pore-network modeling and micromodel experimental studies was performed by Joekar-Niasar et al. (2009) and Karadimitriou et al. (2013), again showing the existence of the interfacial area surface.

There are many reasons given in the literature for the occurrence of hysteresis in capillary pressure–saturation relationships (see, e.g., Bear, 1972, Morrow, 1970; Morrow and Harris, 1965). But, almost all those reasons tell us that, at the same saturation, fluid distributions are different during drainage and imbibition and interfaces have different curvatures under different conditions. Specific interfacial area is the macroscale variable that quantifies the differences in phase distributions and curvature of interfaces under various conditions. So, in Figure 2.4, the two different states (which are at the same saturation but at two different capillary pressures) are distinguished

by virtue of the differences in specific interfacial area, which are 18.32 and 30.56 mm^2 in the left and right images, respectively. In order to investigate that the inclusion of specific interfacial area will indeed model the capillary hysteretic effect, Niessner and Hassanizadeh (2008) combined the standard volume balance equation and standard Darcy's law (Equation 2.2) with new Equations 2.10 and 2.12 for specific interfacial area and a single interfacial area surface (Equation 2.13) and solved it to model drainage and imbibition processes occurring in the same domain. They compared the results with a standard model, using different capillary pressure curves for drainage and imbibition. They showed that drainage and imbibition processes can be modeled with a single interfacial area surface. In a similar work, Pop et al. (2009) showed that the horizontal redistribution of fluids in a porous medium can be properly modeled with the new theory.

The specific interfacial area is also of great significance on the modeling of kinetic heat and mass transfer processes among phases. Currently, the rate of mass transfer among two immiscible fluids is related to the fluid saturation. But, in fact, as the mass or heat transfer among two phases occurs at their interfaces, the rate of transfer must be related to the amount of interfacial area. The significance of including specific interfacial area in models of heat and mass transfer in two-phase flow has been illustrated numerically by Niessner and Hassanizadeh (2009a,b) and very recently through experiments in micromodels by Karadimitriou et al. (2014b) and Nuske et al. (2014). Recently, Nikooee et al. (2012, 2013) have shown that specific interfacial area has to be included in the description of deformation of unsaturated porous media in order to be able to model the observed hysteresis in the effective stress parameter.

2.3.4 Evaluation of Nonequilibrium Capillarity Effect

The nonequilibrium capillarity Equation 2.14 has been shown to be fully in line with experimental observations. The equation prescribes that under nonequilibrium drainage, where $-\tau\partial S^w/\partial t$ is positive, $P_n - P_w$ will be larger than P_c. This is exactly what we see in Figure 2.5, where curves of nonequilibrium $P_n - P_w$ lie higher than the drainage capillary pressure curve. Similarly, experimental studies of Oung et al. (2005) showed that under nonequilibrium imbibition, where $-\tau\partial S^w/\partial t$ is negative, $P_n - P_w$ will be smaller than P_c. Data similar to those shown in Figure 2.5 can be used to compute the value of the material coefficient τ (see Bottero et al., 2011; Oung et al., 2005). Values of τ are found to be in the order of 10^5 kg/m/s. There is a large body of experimental work on determining the validity of the nonequilibrium capillarity Equation 2.14. Examples are the works of O'Carroll et al. (2005), Camps-Roach et al. (2010), and Sakaki et al. (2010).

Some researchers, mainly mathematicians, have shown that the combination of the dynamic capillarity theory and the standard Darcy's law will make it possible to model phenomena that cannot be explained by standard capillarity theory. In particular, they have shown that it can model unstable capillary fingering and nonmonotonic saturation distributions during water infiltration into dry soil (Cuesta et al., 2000; Egorov et al., 2003; Nieber et al., 2005; van Duijn et al., 2007). Dynamic capillary effects have been also studied by means of pore-scale models (Dahle et al., 2005; Joekar-Niasar et al., 2010, 2012). Finally, a number of numerical modelers have incorporated the new capillarity Equation 2.6 in their codes (Manthey, 2006; Manthey et al., 2005).

2.3.5 Comments on the Extended Darcy's Law

As explained in the introduction, computational and experimental works have shown that the linear relationship between flow velocity, $\mathbf{q}^\alpha$, and the driving force, $\nabla P_\alpha - \rho^\alpha \mathbf{g}$, does not always hold for two-phase flow. This has been evidenced in the fact that the relative permeability could be a function of the flow velocity, among other terms. Now, Equation 2.11 suggests that other forces may play a role in the relationship between $\mathbf{q}^\alpha$ and $\nabla P_\alpha - \rho^\alpha \mathbf{g}$. Let's assume there are flow situations where the last two terms in Equation 2.11 are important. Then, if we leave them out of the equation, their

role has to be taken up by the relative permeability. This may explain why relative permeability is a function of many variables including the capillary number. Tsakiroglou at al. (2004) have shown that the relative permeability curves determined from transient and steady-state experiments are significantly different. This was also found by Joekar-Niasar et al. (2011), who showed that when all terms in Equation 2.11 are included, then the difference between transient and steady-state relative permeability curves disappear. Similar results were found in a study by Niessner et al. (2011). One final comment about Equation 2.11 needs to be made. Hassanizadeh and Gray (1993b) have shown this equation can be recast in the following forms:

$$\mathbf{q}^{\alpha} = -\rho^{\alpha} \frac{k_{r\alpha}\mathbf{k}}{\mu^{\alpha}} \cdot \left(\nabla G_{\alpha} - \mathbf{g}\right) \quad \alpha = w, n \tag{2.15}$$

where G_{α} denotes the Gibbs free energy of the fluid phase. This equation suggests that the true driving force for flow of a fluid is the gradient in Gibbs free energy (as well as gravity). In the case of single-phase flow of a fluid, and under isothermal conditions, its Gibbs free energy depends on its mass density only. Then, one can show that (2.15) reduces to the standard Darcy's law for saturated flow. But, in the case of two-phase flow, the Gibbs free energy may depend on saturation and specific interfacial area, in which case an equation similar to (2.11) has to follow.

2.4 CONCLUSIONS

For the description of two-phase flow processes, we must introduce a new state variable that accounts for the presence of fluid–fluid interfaces. We define this to be the *specific interfacial area*: the area of fluid–fluid interfaces per unit volume of the medium. The introduction of specific interfacial area allows the modeling of capillary hysteresis. It also allows for the modeling kinetic mass transfer among phases.

The driving forces in Darcy's law should be not only the pressure gradient and gravity but also gradients of saturation and specific interfacial area. The difference in fluid pressures is equal to capillary pressure but only under equilibrium conditions. Under nonequilibrium conditions, the difference in fluid pressures is a function of time rate of change of saturation, as well as saturation. This equation allows for modeling nonmonotonic saturation distributions.

ACKNOWLEDGMENT

The material presented in this chapter is based on the work of my PhD students, postdoctoral researchers, and collaborators. I am grateful for having had these coworkers. The careful reading of this chapter and extensive comments by Dr. Ehsan Nikooee and one of the anonymous reviewers is greatly appreciated.

REFERENCES

Achanta, S., J.H. Cushman, and M.R. Okos. On multicomponent, multiphase thermomechanics with interfaces. *International Journal of Engineering Science* 32(11) (1994): 1717–1738.

Ataie-Ashtiani, B., S.M. Hassanizadeh, and M.A. Celia. Effects of heterogeneities on capillary pressure–saturation–relative permeability relationships. *Journal of Contaminant Hydrology* 56(3) (2002): 175–192.

Avraam, D.G. and A.C. Payatakes. Flow regimes and relative permeabilities during steady-state two-phase flow in porous media. *Journal of Fluid Mechanics* 293 (1995): 207–236.

Bartley, J.T. and Douglas, W.R. Experimental investigation of unsteady-state relative permeability in sandpacks. *Proceedings of Society of Core Analysts Conference*, Austin, Texas, Vol. 22, 2001, pp. 1–14.

Bennethum, L.S. and J.H. Cushman. Multiscale, hybrid mixture theory for swelling systems—I: Balance laws. *International Journal of Engineering Science* 34(2) (1996): 125–145.

Berg, S., A.W. Cense, J.P. Hofman et al. Two-phase flow in porous media with slip boundary condition. *Transport in Porous Media* 74(3) (2008): 275–292.

Boom, W., K. Wit, A.M. Schulte et al. Experimental evidence for improved condensate mobility at near-wellbore flow conditions. *Society of Petroleum Engineers*: *Annual Technical Conference*, 1995, Dallas, Texas, pp. 667–675.

Boom, W., K. Wit, J.P.W. Zeelenberg et al. On the use of model experiments for assessing improved gas-condensate mobility under near-wellbore flow conditions. *SPE Annual Technical Conference*, 1996, Denver, Colorado, pp. 343–353.

Bottero, S. Advances in theories of capillarity in porous media, PhD thesis, Utrecht University, Department of Earth Sciences, Utrecht, the Netherlands, November 2009.

Bottero, S., S.M. Hassanizadeh, P.J. Kleingeld et al. Nonequilibrium capillarity effects in two-phase flow through porous media at different scales. *Water Resources Research* 47(10) (2011).

Camps-Roach, G., D.M. O'Carroll, T.A. Newson et al. Experimental investigation of dynamic effects in capillary pressure: Grain size dependency and upscaling. *Water Resources Research* 46(8) (2010).

Chen, D., L.J. Pyrak-Nolte, J. Griffin et al. Measurement of interfacial area per volume for drainage and imbibition. *Water Resources Research* 43(12) (2007).

Cheng, J-T., L.J. Pyrak-Nolte, D.D. Nolte et al. Linking pressure and saturation through interfacial areas in porous media. *Geophysical Research Letters* 31(8) (2004).

Constantinides, G.N. and A.C. Payatakes. Network simulation of steady-state two-phase flow in consolidated porous media. *AIChE Journal* 42(2) (1996): 369–382.

Cuesta, C., C.J. Van Duijn, and J. Hulshof. Infiltration in porous media with dynamic capillary pressure: Travelling waves. *European Journal of Applied Mathematics* 11(4) (2000): 381–397.

Dahle, H.K., M.A. Celia, and S.M. Hassanizadeh. Bundle-of-tubes model for calculating dynamic effects in the capillary-pressure-saturation relationship. *Transport in Porous Media* 58(1–2) (2005): 5–22.

Diamantopoulos, E. and W. Durner. Dynamic nonequilibrium of water flow in porous media: A review. *Vadose Zone Journal* 11(3) (2012).

Egorov, A.G., R.Z. Dautov, J.L. Nieber et al. Stability analysis of gravity-driven infiltrating flow. *Water Resources Research* 39(9) (2003).

Gray, W.G. and S.M. Hassanizadeh. Averaging theorems and averaged equations for transport of interface properties in multiphase systems. *International Journal of Multiphase Flow* 15(1) (1989): 81–95.

Hassanizadeh, S.M., M.. Celia, and H.K. Dahle. Dynamic effect in the capillary pressure–saturation relationship and its impacts on unsaturated flow. *Vadose Zone Journal* 1(1) (2002): 38–57.

Hassanizadeh, S.M. and W.G. Gray. General conservation equations for multiphase systems: 1. averaging procedure. *Advance in Water Research* 2 (1979a): 131–144.

Hassanizadeh, S.M. and W.G. Gray. General conservation equations for multiphase systems: 2. mass, momenta, energy and entropy equations. *Advance in Water Research* 2 (1979b): 191–203.

Hassanizadeh, S.M. and W.G. Gray. General conservation equations for multiphase systems: 3. constitutive theory for porous media flow. *Advance in Water Research* 3(1) (1980): 25–40.

Hassanizadeh, S.M. and W.G. Gray. Mechanics and thermodynamics of multiphase flow in porous media including interphase boundaries. *Advances in Water Resources* 13(4) (1990): 169–186.

Hassanizadeh, S.M. and W.G. Gray. Thermodynamic basis of capillary pressure in porous media. *Water Resources Research* 29(10) (1993a): 3389–3405.

Hassanizadeh, S.M. and W.G. Gray. Toward an improved description of the physics of two-phase flow. *Advances in Water Resources* 16(1) (1993b): 53–67.

Held, R.J. and M.A. Celia. Modeling support of functional relationships between capillary pressure, saturation, interfacial area and common lines. *Advances in Water Resources* 24(3) (2001): 325–343.

Helmig, R. *Multiphase Flow and Transport Processes in the Subsurface: A Contribution to the Modeling of Hydrosystems*. Berlin, Germany: Springer-Verlag, 1997.

Henderson, G.D., A. Danesh, B. Al-Kharusi et al. Generating reliable gas condensate relative permeability data used to develop a correlation with capillary number. *Journal of Petroleum Science and Engineering* 25(1) (2000): 79–91.

Henderson, G.D., A. Danesh, D.H. Tehrani et al. Measurement and correlation of gas condensate relative permeability by the steady-state method. *SPE Journal* 1(2) (1996): 191–202.

Iliev, O., G. Printsypar, and S. Rief. On mathematical modeling and simulation of the pressing section of a paper machine including dynamic capillary effects: One-dimensional model. *Transport in Porous Media* 92(1) (2012): 41–59.

Joekar-Niasar, V. and S.M. Hassanizadeh. Specific interfacial area: The missing state variable in two-phase flow equations? *Water Resources Research* 47(5) (2011).

Joekar-Niasar, V. and S.M. Hassanizadeh. Uniqueness of specific interfacial area–capillary pressure–saturation relationship under non-equilibrium conditions in two-phase porous media flow. *Transport in Porous Media* 94(2) (2012): 465–486.

Joekar-Niasar, V., S.M. Hassanizadeh, and H.K. Dahle. Non-equilibrium effects in capillarity and interfacial area in two-phase flow: Dynamic pore-network modelling. *Journal of Fluid Mechanics* 655 (2010): 38–71.

Joekar-Niasar, V., S.M. Hassanizadeh, and A. Leijnse. Insights into the relationships among capillary pressure, saturation, interfacial area and relative permeability using pore-network modeling. *Transport in Porous Media* 74(2) (2008): 201–219.

Joekar Niasar, V., S.M. Hassanizadeh, L.J. Pyrak-Nolte et al. Simulating drainage and imbibition experiments in a high-porosity micromodel using an unstructured pore network model. *Water Resources Research* 45(2) (2009).

Karadimitriou, N.K. Two-phase flow experimental studies in micro-models. PhD thesis, Utrecht University, Department of Earth Sciences, Utrecht, the Netherlands, 2013.

Karadimitriou, N.K., Hassanizadeh, S.M., Joekar-Niasar, V., and Kleingeld, P.J. Micromodel study of two-phase flow under transient conditions: Quantifying effects of specific interfacial area. *Water Resources Research* 50(10) (2014a): 8125–8140.

Karadimitriou, N.K., V. Joekar-Niasar, S.M. Hassanizadeh et al. A new micro-model experimental approach for two-phase flow studies: Comparison with a pore network model. *Lab on a Chip* 12 (2012): 3413–3418.

Karadimitriou, N.K., M. Musterd, P.J. Kleingeld et al. On the fabrication of PDMS micromodels by rapid prototyping, and their use in two-phase flow studies. *Water Resources Research* 49(4) (2013): 2056–2067.

Karadimitriou, N.K., P. Nuske, P.J. Kleingeld et al. Simultaneous thermal and optical imaging of two-phase flow in a micro-model. *Lab on a Chip* 14(14) (2014b): 2515–2524.

Manthey, S. Two-phase flow processes with dynamic effects in porous media—Parameter estimation and simulation. PhD thesis, Institut für Wasserbau, Fakultät Bau- und Umweltingenieurwissenschaften, Universität Stuttgart, Stuttgart, Germany, 2006.

Marle, C.M. On macroscopic equations governing multiphase flow with diffusion and chemical reactions in porous media. *International Journal of Engineering Science* 20(5) (1982): 643–662.

Morrow, N.R. Physics and thermodynamics of capillary action in porous media. *Industrial & Engineering Chemistry* 62(6) (1970): 32–56.

Morrow, N.R. and C.C. Harris. Capillary equilibrium in porous materials. *Society of Petroleum Engineers Journal* 5(1) (1965): 15–24.

Murad, M.A. and J.H. Cushman. Multiscale flow and deformation in hydrophilic swelling porous media. *International Journal of Engineering Science* 34(3) (1996): 313–338.

Niessner, J., S. Berg, and S.M. Hassanizadeh. Comparison of two-phase Darcy's law with a thermodynamically consistent approach. *Transport in Porous Media* 88(1) (2011): 133–148.

Niessner, J. and S.M. Hassanizadeh. A model for two-phase flow in porous media including fluid-fluid interfacial area. *Water Resources Research* 44(8) (2008).

Niessner, J. and S.M. Hassanizadeh. Modeling kinetic interphase mass transfer for two-phase flow in porous media including fluid–fluid interfacial area. *Transport in Porous Media* 80(2) (2009a): 329–344.

Niessner, J. and S.M. Hassanizadeh. Non-equilibrium interphase heat and mass transfer during two-phase flow in porous media—Theoretical considerations and modeling. *Advances in Water Resources* 32(12) (2009b): 1756–1766.

Nieber, J.L., R.Z. Dautov, A.G. Egorov et al. Dynamic capillary pressure mechanism for instability in gravity-driven flows: Review and extension to very dry conditions. *Transport in Porous Media* 58(1–2) (2005): 147–172.

Nikooee, E., G. Habibagahi, S.M. Hassanizadeh et al. Effective stress in unsaturated soils: A thermodynamic approach based on the interfacial energy and hydromechanical coupling. *Transport in Porous Media* 96(2) (2012): 369–396.

Nikooee, E., S.M. Hassanizadeh, and G. Habibagahi. Mechanics of unsaturated soils: From equilibrium to transient conditions. *Poromechanics V*, (2013): 2049–2058.

Nuske, P., N.K. Karadimitriou, O. Ronneberger et al. Modelling multiphase flow in a micro-model with local thermal non-equilibrium on the Darcy scale. Submitted to *International Journal of Heat and Mass Transfer*. (2014).

O'Carroll, D.M., T.J. Phelan, and L.M. Abriola. Exploring dynamic effects in capillary pressure in multistep outflow experiments. *Water Resources Research* 41(11) (2005).

Oung, O., S.M. Hassanizadeh, and A. Bezuijen. Two-phase flow experiments in a geocentrifuge and the significance of dynamic capillary pressure effect. *Journal of Porous Media* 8(3) (2005): 247–257.

Pop, I.S., C.J. van Duijn, J. Niessner, and S.M. Hassanizadeh. Horizontal redistribution of fluids in a porous medium: The role of interfacial area in modeling hysteresis. *Advances in Water Resources* 12 (2009): 383–390.

Porter, M.L., M.G. Schaap, and D. Wildenschild. Lattice-Boltzmann simulations of the capillary pressure–saturation–interfacial area relationship for porous media. *Advances in Water Resources* 32(11) (2009): 1632–1640.

Pyrak-Nolte, L.J., D.D. Nolte, D. Chen et al. Relating capillary pressure to interfacial areas. *Water Resources Research* 44(6) (2008).

Reeves, P.C. and M.A. Celia. A functional relationship between capillary pressure, saturation, and interfacial area as revealed by a pore-scale network model. *Water Resources Research* 32(8) (1996): 2345–2358.

Sakaki, T., D.M. O'Carroll, and T.H. Illangasekare. Direct quantification of dynamic effects in capillary pressure for drainage–wetting cycles. *Vadose Zone Journal* 9(2) (2010): 424–437.

Skauge, A., T. Thorsen, and A. Sylte. Rate selection for waterflooding of intermediate wet cores. *Proceedings of the International Symposium of the Society of Core Analysts*, Edinburgh, Scotland, 2001, pp. 1–14.

Tsakiroglou, C.D., D.G. Avraam, and A.C. Payatakes. Simulation of the immiscible displacement in porous media using capillary pressure and relative permeability curves from transient and steady-state experiments. *International Symposium of the Society of Core Analysts*, Abu Dhabi, United Arab Emirates, October 5–9, 2004, pp. 1–13.

van Duijn, C.J., L.A. Peletier, and I.S. Pop. A new class of entropy solutions of the Buckley-Leverett equation. *SIAM Journal on Mathematical Analysis* 39 (2007): 507–536.

3 Characterization of Fractures and Fracture Network of Porous Media

Muhammad Sahimi

CONTENTS

3.1 Introduction 63
3.2 Surveys and Data Acquisition 64
3.3 Characterization of Surface Morphology of Fractures 65
3.3.1 Self-Similar Structures 65
3.3.2 Correlation Functions 66
3.3.3 Self-Affine Rough Surfaces 67
3.3.4 Measurement of Surface Roughness 67
3.3.5 Correlation Function for a Rough Surface 69
3.4 Characterization of a Single Fracture 70
3.4.1 Aperture 70
3.4.2 Contact Area 71
3.4.3 Surface Height 71
3.4.4 Surface Roughness 71
3.5 Characterization of Fracture Networks 72
3.5.1 Fractures and Power-Law Scaling 72
3.5.2 Distribution of Fracture's Length 73
3.5.3 Distribution of Fracture's Displacement 74
3.5.4 Distribution of Fracture's Apertures 75
3.5.5 Distribution of Fracture's Orientation 76
3.5.6 Fracture Density 76
3.5.7 Connectivity of Fracture Networks 77
3.5.8 Self-Similar Structure of Fracture Networks 79
3.5.9 Interdimensional Relations 80
References 81

3.1 INTRODUCTION

Of the many problems that must be addressed by scientists who study large-scale (LS) porous media, such as oil, gas, and geothermal reservoirs, and groundwater aquifers, none is as complex as characterization and modeling of fractures, fracture networks, and fractured porous media. The economic development of a fractured oil reservoir, which is abundant in the world, cannot be planned unless the nature of the fractures (tectonic, diagenetic, or induced) and the properties of their network (connectivity, fracture length distribution, etc.) are understood and accurate models of fractures and their network are developed. The same is true in hydrology if one wishes to address the problem of contamination of groundwater flow. Most recently, the problem of disposal of radioactive wastes has

become a critical problem of national and international concern. Geological formations are considered as an acceptable storage area for radioactive nuclear wastes, as their permeability is typically low. Many of such formations are, however, highly fractured, even several hundred meters below the surface. Groundwater that flows through the fractures at such depths would be the carrier of any nuclear waste and contaminants that might leak out of the storage area and enter the flow system (Kersting et al., 1999). Hence, characterization and modeling of fractured rock has, once again, emerged as a fundamental problem of immense importance.

Despite decades of study, however, accurate determination of fracture's spatial distribution remains an active area of research. The permeability of fractures is much larger than that of the porous matrix in which they are embedded. Thus, the permeability data measured at various locations can provide insight into the spatial distribution of fractures. There is, however, an insufficient volume of such data. Borehole-wall imaging is a very reliable method of mapping the fractures and faults within boreholes. Such imaging techniques are, however, expensive and are not always included in a logging run. In addition, they are not available for many of the older oil reservoirs and other LS porous media.

In this chapter, we describe characterization of fractures and fracture networks. Over the past 25 years or so, many new techniques and models have been developed for this purpose. The improved understanding that has been gained is instrumental to obtaining more accurate predictions for flow and transport properties of LS porous media. In principle, characterization of fractures and fracture networks is divided into two distinct, but related, parts: (1) characterization of a single fracture and (2) characterization of a network of fractures. The fractures may be present *discretely*; that is, they do *not* form an interconnected network between two widely separated parts of a porous medium such as the injection and extraction wells in an oil reservoir, although they may form local clusters of interconnected fractures. Alternatively, the fractures may form a network at large length scales, which would be the main conduit for flow and transport processes.

An important result that has emerged over the past 20 years is that many properties of fractures and fracture networks follow power-law distributions, characterized by long-range correlations. In addition, it is now generally accepted that the connectivity of fractures and its effect on their network's properties may be quantified accurately by the concepts of percolation theory (Sahimi, 1994, 2011), while the internal surface of fractures, which is typically very rough, may be understood and modeled in terms of self-affine stochastic functions. Extensive discussions of modeling of fractures, fracture networks, and fractured porous media are presented by Sahimi (2011) and Adler et al. (2012).

3.2 SURVEYS AND DATA ACQUISITION

Let us first briefly describe how experimental data for various characteristics of fractures and fracture networks are obtained. There are three types of *surveys* for characterizing porous rock:

1. *Borehole surveys* (Narr and Lerche, 1984; Genter et al., 1995) in which the measurements are usually made on oriented cores. Alternatively, they can be deduced from the resistivity of various samples at different depths, usually referred to as the resistivity logs. The location, orientation, aperture, surface geometry, and other properties are recorded for each fracture, hence providing information about the fracture density and its regionalization and the orientation distribution. Such surveys do not, however, provide any insight into the extent of the fractures or their interconnectivity, as they are local.
2. *Scanline surveys* (Priest and Hudson, 1981) are extensions of borehole surveys in which one paints and collects the fractures that intersect a horizontal line on an outcrop. Each fracture is represented by its trace. The intersection abscissae and trace lengths and orientations may also be recorded. Scanline survey is usually used for pit batters and high bench walls, where one can observe long traces. Sisavath et al. (2004) developed a method

by which several important geometrical and connectivity properties of fracture networks are derived from line data, and showed that when data relative to fractures are collected along a line, such as a road or a well, estimates of major geometrical properties of the corresponding fracture networks can be obtained.

3. *Areal surveys* collect all the fracture traces that intersect a rectangle. If they continue beyond the rectangle, only the portion within the rectangle is recorded. Areal surveys are usually used for drift or tunnel walls (Rouleau and Gale, 1985; Billaux et al., 1989; Abelin et al., 1991), but they may also be used for outcrops. Odling (1992) studied an 18 m × 18 m area from ground observations; Koestler and Reksten (1982) mapped a 45 m × 230 m quarry well, and Barthélémy et al. (1996) used photographs taken from aircrafts or helicopters. Vignes-Adler et al. (1991) even used images obtained by satellites. Castaing et al. (1996) utilized a variety of techniques in order to characterize a fractured area in the western Arabian plate. The sampling scales used were anywhere from 10 m to as large as 1000 km.

Note that although samples for measuring the spatial properties of fracture networks should, in principle, be 3D, the aforementioned surveys are essentially 1D or 2D, since 3D surveys and samplings are very difficult, if not impossible, as they require geophysical imaging and mapping of the fracture surfaces in a volume of the rock. Complete 3D characterization of fracture networks is still very difficult, and therefore, very few attempts have been made in this direction. Montemagno and Pyrak-Nolte (1995) and Pyrak-Nolte et al. (1997) used x-ray computed tomography in order to characterize small fractured samples. Gertsch (1995) and Gonzalez-Garcia et al. (2000) constructed 3D fracture network from serial sectioning data. Crosta (1997) provided practical guidelines for ground-level data acquisition.

3.3 CHARACTERIZATION OF SURFACE MORPHOLOGY OF FRACTURES

Natural fractures and their networks have enormous variations in their morphology that consist of the geometry, topology, and structure of their internal surface. The geometry refers to size or aperture of fractures, as well as their shape. The topology describes how fractures are connected to one another. The structure of the internal surface of fractures is also very important because it is typically very rough and possesses complex features. The roughness of a fracture's internal surface affects, of course, its flow and transport properties (Sahimi, 2011). We should keep in mind, however, that when we speak of surface roughness, we must specify the length scales over which the roughness is measured. Even the most rugged mountains look perfectly smooth when viewed from the outer space. Therefore, surface roughness and other morphological characteristics of fractures and their networks *depend on the length scale of the observations or measurements.*

The enormous variations in the morphology of fractures and fractured porous media are such that, up until the mid-1980s, the problem of describing them meaningfully seemed hopeless. But significant experimental and theoretical developments have brightened the prospects for deeper understanding of the morphology and in particular the structure of the internal surface of fractures. Among them is the advent of powerful concepts of fractal geometry and fractal distributions, which we now describe briefly.

3.3.1 Self-Similar Structures

An intuitive definition of a self-similar fractal object is that its parts are reminiscent of the whole, implying that the object possesses *scale-invariant* properties and that above a certain length scale—the lower cutoff scale for fractality—the structure of a piece of an object can be magnified to recover its morphology at larger length scales, up to another length scale, the upper cutoff for its fractality. Below and above the two cutoff length scales, the system loses its self-similarity.

While there are disordered media that are self-similar at *any* length scale, natural porous media that exhibit self-similarity typically lose their fractal characteristics at sufficiently small or large length scales.

A simple characteristic of a self-similar fractal is its *fractal dimension* D_f, defined as follows. We cover the fractal system by non-overlapping d-dimensional spheres of Euclidean radius r, or boxes of linear size r, and count the number $N(r)$ of such spheres that completely cover the system. The fractal dimension D_f of the system is then defined by

$$D_f = \lim_{r \to 0} \frac{\ln N}{\ln(1/r)}. \tag{3.1}$$

Estimating the fractal dimension through Equation 3.1 is called the *box-counting method*. For non-fractal objects, $D_f = d$, where d is the Euclidean dimensionality of the space in which the objects are embedded. One may also define the fractal dimension D_f through the relation between the system's mass M and its characteristic length scale L. If the system is composed of particles of radius r and mass m, then

$$M = cm\left(\frac{L}{r}\right)^{D_f}, \tag{3.2}$$

where c is a geometrical constant of order 1. Since we can fix the dependence of M on m and r, we can write

$$M(L) \propto L^{D_f}. \tag{3.3}$$

Measuring M often entails using an ensemble of samples with similar structures, rather than a single sample. In this case,

$$\langle M \rangle = cm\left(\frac{L}{r}\right)^{D_f}, \tag{3.4}$$

where $\langle\cdot\rangle$ represents an average over the masses of a large number of samples with linear sizes in the range $L \pm \delta L$, centered on L. Natural fractals are usually *statistically self-similar* because, due to the heterogeneities, the self-similarity is only in an average sense. For example, if a fracture network is self-similar, it is only in an average sense; no exactly self-similar fracture network is known to exist in nature.

3.3.2 Correlation Functions

A powerful method for testing self-similarity of any disordered medium is to construct a general correlation function $C_n(\mathbf{r}^n)$ defined by

$$C_n(\mathbf{r}^n) = \left\langle \rho(\mathbf{r}_0)\rho(\mathbf{r}_0 + \mathbf{r}_1) + \cdots + \rho(\mathbf{r}_0 + \mathbf{r}_n) \right\rangle, \tag{3.5}$$

where $\rho(\mathbf{r})$ is the density at position $\mathbf{r}$, and the average is taken over all possible values of $\mathbf{r}_0$. Here, $\mathbf{r}^n$ denotes the set of points at $\mathbf{r}_1, \ldots, \mathbf{r}_n$. C_n, in the limit $n = 2$, is usually referred to as the *covariance function*. If an object is self-similar, then its correlation function defined by Equation 3.5 should

take on the same shape (aside from a constant prefactor) if all the length scales of the system are rescaled by a constant factor b. Thus, one must have

$$C_n(b\mathbf{r}_1, b\mathbf{r}_2, \ldots, b\mathbf{r}_n) = b^{-nx} C_n(\mathbf{r}_1, \ldots, \mathbf{r}_n). \tag{3.6}$$

Only a *power-law* correlation function can satisfy Equation 3.6 with $x = d - D_f$. In most cases, however, only the two-point correlation function $C_2(\mathbf{r}^2)$—also called the *direct correlation function* or the covariance function—can be computed or measured with high precisions, and therefore, we focus on this quantity. Assuming isotropy and self-similarity, $C_2(\mathbf{r}^2)$ *decays* as a power law:

$$C_2(\mathbf{r}) \sim r^{D_f - d}. \tag{3.7}$$

Thus, a logarithmic plot of $C_2(r)$ versus r should be a straight line with a slope $D_f - d$.

3.3.3 Self-Affine Rough Surfaces

The self-similarity of a fractal structure implies that its microstructure is invariant under an *isotropic* rescaling of lengths. That is, if all the lengths in all the directions are rescaled by the same scale factor, the same structure emerges again. There are, however, many fractals that preserve their scale invariance only if lengths in different directions are rescaled by direction-dependent scale factors. In other words, their scale invariance is preserved only if the lengths in the x, y, and z directions are scaled by scale factors b_x, b_y, and b_z that are not, in general, equal. This type of scale invariance implies that the fractal system is *anisotropic*. Such systems are called *self-affine* fractal, which is an object that cannot be characterized by a single fractal dimension D_f.

Among natural self-affine surfaces are those of pores and fractures of rock. Many properties of such surfaces are described by a stochastic function $f(\mathbf{x})$ with self-affine properties. For example, the surface height $h(x, y)$ at a lateral position $\mathbf{x}$ of the rough internal surface of a fracture has self-affine property (see Equation 3.22). In fact, self-affinity of many natural systems that are associated with Earth, such as various properties of rock, is quite understandable, since gravity plays a dominant role in the direction perpendicular to the Earth's surface but has very little, if any, effect in the other directions, hence generating anisotropy in the rock's structure.

Similar to self-similar structures, the self-affinity of the internal surface of fractures is only in a statistical sense. In addition, a disordered self-affine fractal surface may be thought of as the fluctuations about a straight line or a flat surface that generate rough, self-affine profiles and surfaces. If we consider the height difference between a pair of points $h(\mathbf{x}_1)$ and $h(\mathbf{x}_2)$ on a self-affine surface $h(\mathbf{x})$ that lie above or below the points separated by a distance $x_1 - x_2 = x = |\mathbf{x}|$ on a flat reference surface (or a line in 1D), then

$$\left\langle |\, h(\mathbf{x}_1) - h(\mathbf{x}_2)\, | \right\rangle \sim x^H, \tag{3.8}$$

where H is called the *roughness exponent*, often also called the *Hurst exponent*. One may generalize Equation 3.8 to higher dimensions and generate rough surfaces that are encountered in a variety of contexts, ranging from internal surface of pores of natural porous media (Sahimi, 2011) to the internal surface of fractures of rock (see Chapter 1), fracture surface of heterogeneous materials, and thin solid films (Sahimi, 2003b).

3.3.4 Measurement of Surface Roughness

In practice, self-affinity of a surface is bounded by upper and lower correlation lengths, ξ^+ and ξ^-, respectively, in both the horizontal ($\parallel$) and vertical ($\perp$) directions, hence being

restricted to the ranges, $\xi_{\parallel}^{-} < \delta x < \xi_{\parallel}^{+}$ and $\xi_{\perp}^{-} < \delta h < \xi_{\perp}^{+}$, where h is the surface's height. Then due to self-affinity, we must have

$$\frac{\xi_{\perp}^{+}}{\xi_{\perp}^{-}} = \left(\frac{\xi_{\parallel}^{+}}{\xi_{\parallel}^{-}}\right)^{H}. \tag{3.9}$$

The numerical value of the Hurst or roughness exponent H is not, however, sufficient for characterizing the roughness of a surface, as H only indicates how the roughness (or the variance in the height) varies with the transverse length scale over which it is measured (Dashtian et al., 2011a,b). A complete characterization of a rough surface would require not only H but also the *amplitudes* of the height fluctuations, as well as the transverse correlation lengths. One quantitative way of characterizing a rough surface is by measuring its width w, defined by

$$w(\ell) = \left\langle [h(\mathbf{x}) - \langle h \rangle_{\ell}]^2 \right\rangle^{1/2}, \tag{3.10}$$

where

$h(\mathbf{x})$ is the height of the surface at position $\mathbf{x}$

$\langle h \rangle_{\ell}$ is its average over a horizontal segment of length ℓ, normalized by the "volume" ℓ^{d-1} for a d-dimensional surface

Over a segment of size ℓ of the surface, and for $\ell \ll \xi_{\parallel}$, we must have

$$w(\ell) \sim \ell^{H}. \tag{3.11}$$

For $\ell \gg \xi_{\parallel}$, we must, of course, have $w = \xi_{\perp}$.

Another method of characterizing a rough surface is by the so-called *slit island* method (Mandelbrot et al., 1984), in which the rough surface is coated with another material and then polished carefully parallel to a flat reference surface to reveal a series of horizontal cuts. As the coating material is removed, islands of the surface material appear in a sea of the coating material. With further removal of the coating material, the islands will grow and merge. If we consider a region of linear sizes ℓ and height fluctuations $\Delta h = h(\mathbf{x}) - \langle h \rangle_{\ell}$, the distribution $P(\Delta h)$ of the height fluctuations is described by the following scaling law:

$$P(\Delta h) = w(\ell)^{-1} f\left[\frac{\Delta h}{w(\ell)}\right]. \tag{3.12}$$

Since $w(\ell)$ follows Equation 3.11, the implication is that the density $\rho(\ell)$ of the material in a cross section of size ℓ must scale as

$$\rho(\ell) \sim \ell^{-H}. \tag{3.13}$$

Equation 3.13 suggests that the interface between the two materials, that is, between the rough surface and the coating material, in the cross sections parallel to the reference plane is a *self-similar* fractal with a fractal dimension

$$D_f = d - H. \tag{3.14}$$

Therefore, if the fractal dimension D_f is estimated independently, then an estimate of the Hurst or roughness exponent H will also be obtained. Typically, the islands have a surface area distribution n_A such that

$$n_A \sim A^{-\tau}, \tag{3.15}$$

where n_A is the number of islands with area A in the range $[A-(1/2)\Delta A, A+(1/2)\Delta A]$. The exponent τ is related to the fractal dimension D_f through the following equation:

$$\tau = \frac{1}{d}(D_f + d), \tag{3.16}$$

so that measurement of the islands' areas yields D_f, from which the roughness exponent H is estimated.

A third method for characterization of a rough surface uses a mechanical stylus profilometer that provides, by design, 1D profiles of the surface heights. The resolution of the method is in the range 1–10 μm and was probably used for the first time by Whitehouse and Archard (1970). Since their pioneering work, the method and instrument have been refined significantly (see, e.g., Boffa et al., 1998) by using a computer to control and precisely position the device on the surface. In addition, more advanced techniques based on scanning tunneling microscopy (Mitchell and Bonnell, 1990) and atomic force microscopy (Daguier et al., 1996) have also been used for characterization of rough surfaces.

3.3.5 Correlation Function for a Rough Surface

To characterize a rough self-affine surface, we define a height correlation function $C_h(\mathbf{x})$ by

$$C_h(\mathbf{x}) = \left\langle |\, h(\mathbf{x}_0 + \mathbf{x}) - h(\mathbf{x}_0)\,|^n \right\rangle^{1/n}, \tag{3.17}$$

where the average is over all the origins $\mathbf{x}_0$. The choice of the reference surface is important. If, for example, the rough surface has been grown from a planar substrate, then the original flat surface would be the logical choice. In any case, it has been found for many rough surfaces that

$$C_h(x) = \langle C_h(\mathbf{x}) \rangle_{|\mathbf{x}|=x} \sim x^{H(n)}, \tag{3.18}$$

where the average is taken with respect to all the origins $\mathbf{x}_0$ in the smooth reference plane. In many cases, the exponents $H(n)$ take on the same value H for all n. A surface with correlation function given by Equation 3.18 is a self-affine fractal over the range of length scales in which $C_h(x)$ is computed. Typically, the case $n = 2$ is utilized for estimating H, which has proven to be a very robust and accurate method. The correlation function $C_h(x)$ satisfies a general scaling equation given by

$$C_h(x) = x^H F_n\left(\frac{x}{\xi_\parallel^+}, \frac{x}{\xi_\parallel^-}\right). \tag{3.19}$$

For $x \gg \xi_\parallel^-$, such that $x / \xi_\parallel^- \to \infty$, the scaling Equation 3.19 simplifies to

$$C_h(x) = x^H f_n\left(\frac{x}{\xi_\parallel^+}\right), \tag{3.20}$$

where the scaling function $f(y)$ has the properties that $f(y) = c$ for $y \ll 1$ and $f(y) \sim y^{-H}$ for $y \gg 1$, where c is a constant on the order of unity.

3.4 CHARACTERIZATION OF A SINGLE FRACTURE

A single fracture is characterized by several properties. In what follows, we consider each of such properties and describe their measurements.

3.4.1 Aperture

A most important property of a single fracture is its aperture that controls its flow and transport properties. However, the internal surface of a fracture is typically rough. Therefore, a given fracture is characterized by a *distribution* of the local apertures, rather than a unique aperture, which can be constructed only if the fracture's internal surface is characterized and the distribution of the contact areas in the fracture's interior is obtained. In addition, a fracture is also characterized by its length and displacement—properties that manifest their effect in a network of interconnected fractures—and therefore, experimental data for such properties and their implications will be described in the following.

Profilometer is used for the surface topographies to construct the void space of a single fracture (Keller and Bonner, 1985), but one must be careful in using the technique since many artifacts affect the constructed structure of the void space. In addition, 2D cuts provide direct estimates of the aperture that is usually visible in such cuts, and are obtained either from natural outcrops or fracture traces, notwithstanding their possible changes by natural or human activities. To preserve the open space of a single fracture, one usually injects resin into the fracture. For example, Hakami and coworkers (Hakami and Stephansson, 1993; Hakami, 1995; Hakami and Larsson, 1996) injected polyurethane into fractures in granites. The aperture field is then reconstructed by analysis of the images of the sample's sections. Measurements have also been carried out on transparent replicas of natural fracture (Yeo et al., 1998; Koyama et al., 2006; Bauget and Fourar, 2008). A dyed fluid was injected into the void space of the fracture, a calibration law was established to relate the local light absorption to the local apertures, and the distribution of the local apertures was then measured.

Both normal (Vickers et al., 1992; Hakami and Larsson, 1996; Yeo et al., 1998; Matsuki et al., 2006) and log-normal (Snow, 1970; Gale, 1982, 1987; Hakami, 1995; Pyrak-Nolte et al., 1997; Keller, 1998; Koyama et al., 2006) appear to represent the distribution accurately, hence indicating some dependence on the nature of the rock and its deformation mode. Log-normal distributions have been reported mostly for fractures that had been submitted to a normal stress. The reason is clear: with a normal stress, the apertures are shifted toward lower values because the surfaces come into close contact; see Oron and Berkowitz (1998) and Sharifzadeh et al. (2008) for more discussions.

The aperture changes under mechanical deformation. If a normal stress is applied, contact areas emerge, the local apertures are reduced, and the deformation varies nonlinearly with the stress, reflecting the changes in the void space of the fracture. The rate of deformation is largest when small stresses are applied, indicating that fracture stiffness has increased. Such phenomena were studied by Pyrak-Nolte et al. (1987) who used injection of an alloy with a low melting point into the fracture in order to obtain a cast of its void space. Studies have also been reported in which the effect of shear displacements, as well as that of various variations of normal stresses, on the aperture distribution was studied, and have demonstrated that deforming a fracture subject to a shear stress changes significantly its void space. In particular, two main features have been reported, namely, (1) *dilatancy* of the fracture—*expansion* of rock as it is *squeezed*—that increases the apertures and (2) the emergence of damage zones.

When shear stress is applied to a fracture, at first, small variations of the apertures are observed, up to a shear displacement of a few millimeters (see, e.g., Sharifzadeh et al., 2008). This is due to the fact that the motion is stopped when the asperities of the opposite surfaces of the fracture come into contact. Then there is uplift of the two halves that reflect the dilation, as the shear stress increases simultaneously up to a maximum value. Beyond this point, the shear stress decreases rapidly to a residual value that is essentially constant. At a critical value near the maximum shear stress, all the asperities in contact are sheared simultaneously, resulting in a sudden change in the distribution of

the apertures, because the roughness of the two opposite surfaces no longer matches. If the shear stress is increased further, the apertures increase results in an increase in the fracture permeability by about one order of magnitude.

3.4.2 Contact Area

In principle, one is interested in determining the contact area in fractures under in situ stress. Gentier et al. (1989), for example, generated a cast of the open space of a granite fracture by injecting into it a dyed translucent resin, which is done if the sample is under normal stress, as well as without any external load. They then removed half of the rock sample and countermolded a second thicker layer of transparent resin onto the first one, which produced a composite cast with a thin layer of dyed resin that corresponded exactly to the void space of the fracture, and a transparent thicker layer acting only as the mechanical support of the system. The distribution of the apertures was then deduced from a gray-level image of the cast illuminated by transmission. The connectivity of all the void zones of the fracture is also obtained from the skeleton of the open space. Hakami and Barton (1990) and Hakami (1992) replicated both sides of several fractures and used them as molders to cast transparent replicas of the rock samples, which were then fitted together to produce a transparent sample of the original fracture. To measure the apertures, calibrated water droplets or soft rubber pieces were spread on the fracture's lower surface, and their apparent surface areas were measured when the fracture was closed. Such methods do suffer from one problem or another.

Perhaps the most accurate and problem-free method is 3D x-ray computed tomography that allows measurements down to a few microns (Johns et al., 1993; Spanne et al., 1994; Keller, 1998; Arns et al., 2001, 2002; Bertels et al., 2001; Gouze et al., 2003). But the method is expensive and time consuming.

3.4.3 Surface Height

The key quantity to modeling a single fracture is its surface height or elevation $h(x, y)$, which controls the fracture aperture. Surface characteristics are expressed either in terms of various statistics of h itself, for example, its central-line average $\langle |h| \rangle$ (recall that $\langle h \rangle = 0$) and variance $\sigma_h^2 = \langle h^2 \rangle$, or in terms of its derivatives, such as $Z_2 = \langle \partial h/\partial x \rangle^2$. Moreover, in addition to the correlation function defined earlier, the covariance function of h is also defined as

$$C_2(\mathbf{r}) = \langle h(\mathbf{r}')h(\mathbf{r}+\mathbf{r}') \rangle = \sigma_h^2 - \gamma_h(\mathbf{r}), \tag{3.21}$$

where

the average is taken over all the positions $\mathbf{r}'$

γ_h is the semivariogram

For an isotropic surface, $C_2(\mathbf{r}) = C_2(|r|)$.

3.4.4 Surface Roughness

There is ample experimental evidence (Brown and Scholz, 1985; Brown et al., 1986; Brown, 1987a,b; Power et al., 1987; Poon et al., 1992; Cox and Wang, 1993; Schmittbuhl et al., 1993; Odling, 1994; Boffa et al., 1998; Ponson et al., 2007) that the internal surface of fractures of rock masses, and even induced fracture surface of heterogeneous materials (Sahimi, 2003b), is very rough, with the roughness following self-affine fractal statistics described earlier. More specifically, we consider the internal surface of a fracture with a single-valued function $h(x, y)$ representing the surface height and the coordinates (x, y) lying in the mean plane of the fracture. We assume the surface not to have any overhangs; that is, it is *continuously* rough. As described earlier, self-affinity of a rough surface

implies that it exhibits scale invariance under rescaling with direction-dependent rescaling such that $x \to b_x x$, $y \to b_y y$ and $h \to b_h h$. Assuming isotropy in the mean plane of the fracture, which is typically the case, and writing $b_x = b_y = b$ and $b_h = b^H$, one has

$$h(x,y) = b^{-H} h(bx, by), \tag{3.22}$$

where H is the roughness or Hurst exponent. For example, Schmittbuhl et al. (1993) measured the height of a granitic fault surface as a function of spatial positions along 1D profiles and showed that the profiles exhibit self-affinity or anisotropic scale invariance, following Equation 3.22.

The value of the roughness exponent H is not universal. Earlier studies (Sahimi, 1998, 2003b) indicated that the fracture surface of *disordered materials* is characterized by a more or less universal value of the roughness exponent, $H \simeq 0.75 - 0.8$, with very weak dependence on the orientation. It was even conjectured that $H \simeq 0.8$ represents a universal value. But more recent careful studies indicate nonuniversality and that, depending on the type of the fractured material, the roughness exponent may take on two distinct values. One, $H \simeq 0.8$, is for such materials as glass, cement, granite, and tuff (Brown, 1989; Måløy et al., 1992; Poon et al., 1992; Schmittbuhl et al., 1993; Glover et al., 1998; Auradou et al., 2005; Matsuki et al., 2006), and $H \simeq 0.5$ for sandstones (Boffa et al., 1998; Ponson et al., 2007), calcite (Gouze et al., 2003), and sintered glass beads (Ponson et al., 2006). But the estimate, $H \simeq 0.75 - 0.8$, was also reported for sandstones (Nasseri et al., 2006). As for the internal surface of rock fracture, a similar estimate, $H \simeq 0.85$, was reported by Schmittbuhl et al. (1993) for granitic faults. Vickers et al. (1992), Cox and Wang (1993), Johns et al. (1993), and Odling (1994), however, analyzed extensive data for a variety of rock joints and reported nonuniversal values of the roughness exponent H in the range $0 < H \leq 0.85$. Extensive computer simulations (Ansari-Rad et al., 2011) indicated that the roughness exponent is also strongly dependent on the anisotropy of rock, which is of course prevalent.

There is also considerable indirect experimental evidence for roughness of the internal surface of fractures. For example, if we model a single fracture as the space between two parallel flat surfaces, then the volume flow rate q is related to the distance δ between the two plates by, $q \propto \delta^3$, the so-called *cubic law*. Significant experimental deviations from the cubic law have been reported and attributed (Tsang and Witherspoon, 1981; Hakami and Larsson, 1996) to the roughness of the internal surface of fracture.

The evidence for self-affine roughness of a fracture surface described so far has been obtained from laboratory experiments and characterization. Detailed data and measurements on field-scale fractures are scarce, and the best evidence that they provide is circumstantial. The data are typically obtained from fracture traces, but they indicate mostly jumps and discontinuities, rather than a continuously rough surface. Therefore, at large length scales, the surface roughness of fractures may not be self-affine. Such length scales are truly large, however, and it is reasonable to assume that the internal surface of fractures, up to a certain length scale, is self-affine.

3.5 CHARACTERIZATION OF FRACTURE NETWORKS

A fracture network is characterized by the statistical distributions of six distinct properties of its constituent fractures: (1) length, (2) displacement, (3) aperture distribution, (4) orientation, (5) density, and (6) connectivity. Extensive experimental evidence indicates that most properties of rock fractures follow power-law statistics.

3.5.1 Fractures and Power-Law Scaling

Up until the 1980s, data collection was limited mostly to the type of 1D sampling of spacing between fractures intersected along a traverse that was described earlier. The sampling was without any

regard for, or knowledge of, the fracture's orientation or size. The analysis of the data was limited to the calculation of arithmetic averages of the properties of interest using such distributions as the log-normal or exponential. In the early 1980s, a step in the right direction was taken by several research groups when they explored the use of semivariograms as a way of analyzing fracture spacing along a scanline. Semivariograms plot the second moment of a distribution, such as that of the number of fractures per unit length of the scanline, versus the length of sampling increment over some range of the increment size. Doing so is similar to the box-counting method of estimating the fractal dimension of an object, described earlier. In fact, such semivariograms can be recast into a fractal analysis if we plot their logarithm versus logarithm of sample increment size. The slope of the resulting diagram would provide an estimate of the Hurst or roughness exponent H and, hence, an estimate of the fractal dimension of the object.

If fractal concepts are truly relevant to describing the properties of fracture networks, they would imply the existence of power-law scalings for various characteristics of the networks. Therefore, the relevant question is, why should power-law scaling be favored during the process of fracture formation? The key point in answering this question is that power laws imply the absence of a characteristic length scale in the system, and this is what one expects for natural systems, such as rock, in which the heterogeneities exist regardless of the size of the systems that one may inspect.

Strong evidence for the prevalence of power-law distributions in describing several important properties of fractures is also provided by LS computer simulation of fracture of heterogeneous materials. In such models, first proposed by Sahimi and Goddard (1986), one utilizes a disordered network, each bond of which describes the sample material on a small length scale, with fracture characteristics described by a few key parameters. Several types of forces that are typically encountered in the deformation of rock may act on the bonds, including stretching, angle changing, and torsional forces. One then deforms the network gradually by applying a specific boundary condition (e.g., shear, tensile) to the network, as a result of which the individual bonds begin to break irreversibly, hence generating microcracks in the network. If the sample's deformation continues, the microcracks will grow, join each other, and form large fractures.

Computer simulations (Sahimi and Goddard, 1986; de Arcangelis et al., 1989; Arbabi and Sahimi, 1990; Lockner and Madden, 1991; Reuschlé, 1992; Sahimi and Arbabi, 1992, 1993, 1996; Sahimi et al., 1993; Renshaw and Pollard, 1994; Davy et al., 1995; Robertson et al., 1995; Bonnet et al., 2001; for a comprehensive review, see Sahimi, 2003b) indicate power-law scaling for most, if not all, properties of the fracture network that is produced by such models, particularly when the disorder is broad, as is the case in rock. In addition, such models indicate power-law dependence of the strength of the rock sample on the length scale of interest, which is also predicted by rock mechanics. It is important to point out that a wide variety of models, both quasistatic and dynamic, and a broad class of the distribution of the heterogeneities were employed in the aforementioned works, and yet they all yielded the same type of power-law scaling for various properties of fracture networks, implying that such power laws may be a generic feature of fracture of heterogeneous rock.

3.5.2 Distribution of Fracture's Length

Suppose that $n_l(\ell)$ is the number density of fractures with lengths in the interval $[\ell, \ell + d\ell]$ (for $d\ell \ll \ell$). Then the power-law distribution of the fracture's length is defined by

$$n_l(\ell) = a_l \ell^{-a}, \tag{3.23}$$

where

a_l is a constant that depends on the density of the fracture

a is the corresponding characteristic exponent

Four types of materials have been used in laboratory experiments on fractures: clay, plaster, rock, and sand, with the last one used with or without a basal silicon putty layer. Walmann (1998) stretched a thin layer of clay to produce a system of tensile fractures with lengths that followed an exponential distribution. Walmann suggested that a power law may result from the interaction of several exponential laws. In the experiments of Reches (1986), a transition was observed from a power-law distribution to a log-normal one, as the deformation of the sample continued. Reches suggested that samples with a low fracture density should exhibit power-law distributions, whereas high-density rock should follow the log-normal distribution, although a log-normal distribution may have been caused by sample-size effects. Rossen et al. (2000) also reported power-law distributions in the fractured porous media that they studied.

Krantz (1983), Lockner et al. (1992), and Moore and Lockner (1995) analyzed the length distribution of microcracks in rock samples and found that the density of microcracks was largest close to the main fracture, which the aforementioned computer simulations also indicated, and that the small cracks tend to cluster around the large fractures. Such observations agree with those made on natural faults—the largest fractures in rock—reported by Anders and Wiltschko (1994). Hatton et al. (1993) found a power-law distribution for the length of the microcracks with $2 \leq a \leq 2.7$, with a being dependent upon the fluid content of sample, with its lower values corresponding to dry samples.

Data on the distribution of fracture's length have been obtained using 1D, 2D, and 3D samples. For all the 1D data reported, which consisted of the trace lengths of fractures that intersect a scanline (Cruden, 1977; Priest and Hudson, 1981), the length distribution was exponential. Due to its obvious difficulties, obtaining 3D data has been very difficult. Instead, most of the reported data are from 2D maps and consist of fracture traces in a plane that intersect a 3D fractured sample. Such maps have been obtained from field and seismic data and the analysis of satellite image. In most cases, the distribution of fracture's length was reported to be of power-law type, although exponential and log-normal distributions were also reported.

It has been proposed that the distribution of fracture's length is exponential, when stratification of rock plays a prominent role in restricting joint growth, whereas a power-law distribution may be representative of massive rock samples without significant mechanical effect of stratification. Bonnet et al. (2001) compiled the existing data and the corresponding exponents. Most of the data indicated that $a \geq 2$, although smaller values have also been reported. In addition, the data indicated that the prefactor a_ℓ in Equation 3.23 is *independent* of the length scale and the resolution of the observations.

Computer simulations of fracture growth have suggested that the distribution of fracture's length may evolve as the microcracks continue to grow. For example, Cowie et al. (1993) reported that the distribution of fracture's length follows an exponential law during the initial steps of the deformation of the sample when the microcracks are nucleated essentially at random. However, as they grow and begin interacting with each other, a crossover to a power-law distribution of the fracture's length developed. Cowie et al. (1993, 1995) and Cladouhos and Marrett (1996) reported that, in their computer simulations, the exponent a depended on the extent of the deformation, hence indicating that, at long times, the growth and connection of the fractures dominate the deformation process and, therefore, with increasing time, there are fewer small fractures. Sornette and Davy (1991) investigated a model of fault growth and the possibility of a universal fault length distribution.

3.5.3 Distribution of Fracture's Displacement

Another widely studied property of fractures is the distribution of the displacement (throw) on faults. The distribution is estimated by 1D and 2D sampling methods. In the 1D sampling, one records the displacement of a fault where it intersects a scanline, which may not necessarily represent the maximum displacement of the fault, as the displacement varies along the fault. Since the largest faults have the highest probability of intersecting the scanline, the method necessarily

samples such faults. If $n_d(u)$ is the number density of the fractures that have a displacement u, the data have been fitted to a power law:

$$n_d(u) = a_d u^{-\zeta}, \tag{3.24}$$

where the reported estimates of exponent ζ obtained from the 1D measurements are in the range $\zeta(d = 1) = 0.4 - 1.0$ (Gillespie et al., 1993; Nicol et al., 1996; Steen and Andresen, 1999).

If the maximum displacement $u_{\max}$ along each fault is measured, then the sampling is 2D. To carry out such measurements, one must first identify each fault. Because sampling is most often done in 2D sections from 3D samples, identification of the fault is somewhat subjective, and therefore, the measured data will not necessarily represent the maximum displacements. Despite this fact, it is generally believed that the 2D method yields reliable data. The reported data (Villemin and Sunwoo, 1987; Childs et al., 1990; Scholz and Cowie, 1990; Gauthier and Lake, 1993; Carter and Winter, 1995; Watterson et al., 1996; Yielding et al., 1996; Pickering et al., 1997; Fossen and Hesthammer, 1997) indicate an exponent in the range $\zeta(d = 2) = 1.7 - 2.4$, with an average of about 2.2, where $\zeta(d = 2)$ is defined by Equation 3.24 in which u has been replaced by $u_{\max}$. Hence, there appears to be no simple relation between the exponents obtained from the 1D and 2D sampling. The relation that is often used, namely, $\zeta(d = 2) = \zeta(d = 1) + 1$, assumes that the displacements and positions are independent, which is not necessarily true.

The lengths and maximum displacements of faults are generally correlated. If we write

$$u_{\max} = b\ell^{\chi} \tag{3.25}$$

then it is clear that $a = \zeta\chi$. Although theoretical considerations based on the theory of elasticity predict that $\chi = 1$, the experimental data (Gillespie et al., 1992; Fossen and Hesthammer, 1997) indicate that $0.5 \leq \chi \leq 2$. Aside from attributing the deviation of χ from unity to the scatter in the data, it has been suggested that χ is affected by faults intersecting one another and that linkage of fault segments may result in $\chi < 1$ (Peacock and Sanderson, 1991; Trugdill and Cartwright, 1994; Cartwright et al., 1995). Other factors, such as finite size of the samples and their heterogeneity, may also affect the numerical value of χ (Gross et al., 1997).

3.5.4 Distribution of Fracture's Apertures

The aperture determines a fracture's permeability, since the volume flow rate Q through a fracture is given by $Q \propto \delta^m$, where $m = 3$ for a fracture with a smooth surface. As already mentioned, however, for a fracture with rough surface, m can be as large as 6. One possible source for the variation in m may be the roughness of the fracture surface. The roughness of a fracture's internal surface also implies that one must define a *local* aperture that varies spatially even within a single fracture.

Note that, as described earlier, in addition to its surface roughness, there are also voids and contact areas in a fracture that further contribute to the variations of the apertures. Moreover, apertures measured at the surface may be wider than those deep inside due to stress release. In addition, for some natural porous media, no correlation has been detected between a fracture's length and its aperture. Therefore, fractures in a network may appear to have different characteristics than if they are isolated, where the aperture is expected to correlate with a fracture's length. In any event, each fracture should, in fact, be characterized by a distribution of local apertures. Assuming that an average aperture can be unambiguously defined, a fracture network is then characterized by a distribution of *average* apertures.

The distribution of the apertures, both at the scale of a single fracture and over large length scales relevant to a fracture network, is typically broad because the apertures may change over time, due to mechanical misfits of the fracture walls, chemical reactions, dissolution and precipitation,

as well as the pressure due to the depth of the overburden. In addition, since fracture apertures can be measured directly in cores or outcrops, or indirectly through fluid flow measurements, the reported data may exhibit considerable scatter. As mentioned earlier, log-normal (Snow, 1970; Gale, 1982, 1987; Hakami, 1995; Pyrak-Nolte et al., 1997), normal (Vickers et al., 1992; Hakami and Larsson, 1996; Yeo et al., 1998; Matsuki et al., 2006), and power-law distributions (Barton and Zoback, 1992; Sanderson et al., 1994; Belfield and Sovitch, 1995; Johnston and McCaffrey, 1996; Marrett, 1996), as well as unusual distributions, such as the Lévy stable distribution (Painter and Paterson, 1994; Painter et al., 1995; Sahimi et al., 1995; Painter, 1996; Belfield, 1998), have been proposed for describing the aperture distribution. The probability density for the Lévy stable distribution is given by (Hughes, 1995)

$$P(x) = \frac{1}{2\pi}\int_{-\infty}^{\infty} \cos(\omega x)\exp(-C_L\omega^{\alpha})d\omega, \tag{3.26}$$

where

C_L is a constant

α is called the *index* of the distribution that represents the fractal dimension of the set of points that are visited by a random walker whose probability density follows Equation 3.26

If $\alpha = 2$, one has a Gaussian distribution. The Lévy stable distribution corresponds to $\alpha < 2$, in which case the second moment of the distribution is *divergent*.

Assuming that the apertures follow a power-law distribution,

$$n_a(\delta) = a_\delta \delta^{-z}, \tag{3.27}$$

the exponent z has been measured and reported over a broad range of apertures. For example, Barton and Zoback (1992) reported $z \simeq 2.5$ for 1600 apertures measured in the range of millimeters to centimeters. Johnston and McCaffrey (1996) reported that $z \simeq 1.7 - 1.8$, for apertures in the range 5–50 mm, while Barton (1995b) found that $z \simeq 1.53$ for apertures in the range 1–10 mm. For smaller apertures, Belfield and Sovitch (1995) reported $z \simeq 2 - 2.4$ in the range 6–40 μm, while Wong et al. (1989) found for microcracks in granite and quartzite that $z \simeq 1.8$ for apertures in the range 0.03–10 μm. In addition, similar to fracture's displacement, attempts have been made to relate the aperture to the length of a fracture through a power-law relation (Stone, 1984; Hatton et al., 1994; Johnston, 1994; Vermilye and Scholz, 1995; Walmann et al., 1996; Renshaw and Park, 1997).

3.5.5 Distribution of Fracture's Orientation

A fracture's orientation is usually quantified by its *strike* and *dip*. The strike is the trace of the intersection of a fracture with a horizontal plane. The direction of the strike is specified by its azimuth, usually counted in degree clockwise from the north. The dip is the magnitude of the angle between a fracture and a horizontal plane, also expressed in degrees. If the strike is oriented such that the dip plunges on the right-hand side, the azimuth of the strike, which takes on a unique value between 0° and 360°, and the dip angle, which is between 0° and 90°, specify the orientation of the fracture.

3.5.6 Fracture Density

The 2D fracture density ρ_2 is defined as the sum of fracture trace lengths per unit area, while in 3D, ρ_3 is defined as the average fractured surface per unit volume of rock. If a fracture network is

isotropic (which is usually not the case), then $\rho_2 = \rho_3$. One can even define a 1D fracture density ρ_1 along a straight line as the number of fracture intersections per unit length. The 3D density may be estimated from a borehole or scanline survey with the help of a weighting of the observed fractures. However, the correct weight is important. Suppose that N fractures intersect the line and that the ith fracture intersects it with an angle ϑ_i. Then it is not difficult to show that the fracture density ρ_3 is given by

$$\rho_3 = \frac{1}{L}\sum_{i=1}^{N}\frac{1}{\sin\vartheta_i}. \tag{3.28}$$

If the angles ϑ_i are completely random, then the average value of $\sin\vartheta$ between a fracture plane and a survey line is 1/2, and between a fracture plane and a survey plane is $\pi/4$. Thus, for this particular case, one has $\rho_1 = (1/2)\rho_3$ and $\rho_2 = (1/\pi)\rho_3$.

3.5.7 Connectivity of Fracture Networks

To characterize the connectivity and clustering of intersecting fractures (and faults), one may use percolation theory. For a simple introduction to percolation theory, see Stauffer and Aharony (1994); see also Sahimi et al. (1990) and Sahimi (1993b, 1994, 1998, 2003a).

If fractures do not form a sample-spanning cluster between two widely separated points, such as injection and production wells in an oil reservoir, then the size of the clusters that they form is finite, as the network is below its percolation threshold, that is, the point at which a sample-spanning cluster is formed for the first time. In this case, the typical radius ξ_p of the clusters of the fracture is what is called the *correlation length*. If the fractures do form a sample-spanning cluster, then the correlation length is simply the typical radius of the matrix in between the fractures. Recall also that near the percolation threshold p_c, $\xi_p \sim |p - p_c|^{-\nu}$ and that ν, the *critical exponent* of ξ_p, does not depend on the connectivity of the network. Here, p is the fraction of the fractures in the sample-spanning cluster, and $\nu(d = 2) = 4/3$ and $\nu(d = 3) \simeq 0.89$.

The physical significance of ξ_p for fracture networks is that it sets the length scale for their macroscopic homogeneity: over *any* length scale $L \gg \xi_p$, the network is macroscopically homogeneous. If $\ell \ll L \ll \xi_p$, however, where ℓ is the typical or average length of a single fracture, the network is macroscopically heterogeneous. In fact, over such length scales, the sample-spanning cluster of the fractures is a statistically self-similar fractal. That is, the average number $\langle N(L)\rangle$ of fractures within a cluster of linear size $L \ll \xi_p$ follows an equation similar to Equation 3.3, where the average is taken over *all* the possible realizations (configurations) of the clusters of fractures for a fixed connectivity. At the percolation threshold p_c, the sample-spanning cluster of fractures is a fractal object at any length scale.

It has been proposed by many researchers that the connectivity of fracture network of rock may be represented by a percolation cluster *at or very close* to the percolation threshold (Chelidze, 1982; Madden, 1983; Guéguen et al., 1991; Sahimi et al., 1993; Robertson et al., 1995; Renshaw, 1998), although others (see, e.g., Barton, 1995b) have argued that the fracture networks are well connected and, therefore, well above their percolation threshold.

The question is, why should the structure of a fracture network of rock be similar to that of a percolation network at or very close to the percolation threshold? One argument that supports the hypothesis is based on what is usually referred to as the *critical path analysis* (CPA).

It was argued by Ambegaokar et al. (1971) and confirmed by extensive computer simulations that transport processes, and in particular conduction, in a highly heterogeneous material can be reduced to one in a percolation system at or very near the percolation threshold. The idea is that in a broadly disordered material, a finite volume fraction of the material possesses very small conductivity and,

hence, makes negligible contribution to the overall conductivity or other effective transport properties. Therefore, zones of low conductivity may be eliminated from the material, which would then reduce it to a percolation system (as some of the local connectivity is lost). Ambegaokar et al. (1971) described a procedure by which the equivalent percolation network is built up and showed that the resulting model is at or very near its percolation threshold. The CPA has been applied to fluid flow in laboratory scale (Katz and Thompson, 1986, 1987; Sahimi, 1993a; Friedman and Seaton, 1998), as well as LS porous media (Sahimi and Mukhopadhyay, 1996). Hunt et al. (2014) describe several applications of the CPA to problems in porous media.

When applied to fractured rock, the CPA implies that the fracture network should have the connectivity of a percolation cluster, because the fractures are the main pathways for fluid flow in the rock, as their permeabilities (or hydraulic conductances) are much larger than those of the matrix in which they are embedded, and thus, fractured rock may be envisioned as a mixture of nearly impermeable bonds, the pores, and the highly permeable bonds, the fractures, that is, a percolation network. That the fracture network in heterogeneous porous media should be similar to a percolation network at or very close to the percolation threshold may also be inferred from computer simulations of fracture propagation in highly disordered network, which were mentioned earlier.

There is also considerable indirect evidence that supports such arguments. For example, Long and Billaux (1987) found that at Fanay–Augéres site in France, only about 0.1% of the fractures contributed to fluid flow at large length scales, hence indicating the existence of a barely connected fracture network that should be similar to a percolation network at or very near its percolation threshold. Chelidze (1982) summarized the experimental results and showed that the percolation threshold for propagating and intersecting fractures is reached simultaneously with the development of a macrofracture that is sample spanning.

In practice, rock fractures are distributed at all orientations, and therefore, the fracture network does not have a regular topology. Thus, the percolation threshold of a fracture network (the minimum number of intersecting fractures between two widely separated planes) may depend on the orientation distribution of the fractures. In addition, the fracture's length typically follows a power-law distribution, and hence, the percolation threshold should depend on such a distribution (Englman et al., 1983; Robinson, 1983, 1984a,b; Charlaix et al., 1984, 1987; Balberg, 1986, Balberg et al., 1991; Huseby et al., 1997), because even a single long fracture might enable a fracture network to become sample spanning. In particular, Berkowitz (1995) and Watanabe and Takahashi (1995), who studied 2D networks, found the percolation threshold p_c to depend on the second moment of the length distribution.

With 3D orthogonal families of square fracture of unit length, Robinson (1984b) estimated that $p_c \simeq 0.19$, where p_c was defined as

$$p_c = \frac{N_c r^3}{L^3}, \tag{3.29}$$

N_c is the number of fractures at the percolation threshold, r is the half-width of the fractures, and L is the linear size of the sample. If the orientations of the fractures are uniformly distributed, then Robinson (1984b) found that $0.15 < p_c < 0.3$. If the fractures are polydisperse, then p_c is defined as (Charlaix et al., 1984)

$$p_c = \frac{N_c \langle r^2 \rangle \langle r \rangle}{L^3}. \tag{3.30}$$

In proposing Equation 3.31, Charlaix et al. (1984) suggested that one must take into account the effect of the *excluded volume*, defined as the average volume surrounding an object representing a

fracture into which the center of another object cannot lie without intersecting it. On the other hand, numerical simulations (Balberg et al., 1984) suggested that one must define p_c as

$$p_c = \frac{N_c \langle r^3 \rangle}{L^3}, \tag{3.31}$$

which is an intuitive generalization of Equation 3.30.

Charlaix et al. (1984) suggested that *at* the percolation threshold of a 3D fracture network that consists of equal flat disks of radius r with a density ρ_3 of disks per unit volume, one must have

$$\rho_3 r^3 \sim 0.15\text{–}0.3. \tag{3.32}$$

Note that r^3 essentially represents the volume of a disk. As Equation 3.30 suggests, for polydisperse disks with a distribution of disks' radii, one must replace r^3 with $\pi^2 \langle r^2 \rangle \langle r \rangle$ in Equation 3.29, which is nothing but $(1/2)\langle \text{surface} \rangle \langle \text{perimeter} \rangle$, where $\langle \cdots \rangle$ represents an average with respect to the distribution of the radii. These predictions were confirmed by Charlaix (1986) using Monte Carlo simulations. Robinson (1984b) found that for 3D networks of planar fractures, the percolation threshold, that is, the number of intersections per plane, is about 2, whereas for 2D networks of fractures with constant length, the percolation threshold, that is, the average number of fractures intersecting a given fracture, was found to be about 3.1.

Equations 3.29 through 3.31 were proposed based on the assumption that all the fractures have the same length. However, as discussed earlier, the distribution of the fracture's lengths is typically of the power-law type, and therefore, the length of the fractures can significantly affect the location of the percolation threshold of a fracture network. Hence, one must define a more general relation for the fracture connectivity.

3.5.8 Self-Similar Structure of Fracture Networks

In addition to the various properties of fracture networks for which power-law distributions and correlations have been exhibited, many investigators have studied the self-similar fractal structure of fracture networks. Such studies began in 1985 by the U.S. Geological Survey as part of the program to characterize the geologic and hydrologic framework at Yucca Mountain in Nevada (Barton and Larsen, 1985; Barton et al., 1987; summarized in Barton and Hsieh, 1989). The site has been approved by the U.S. Department of Energy as an underground repository for high-level radioactive waste (the decision was still being challenged in courts at the time of writing this review). Barton and Larsen (1985) developed the *pavement method* of clearing a subplanar surface and mapping the fracture surface, in order to measure its connectivity, trace length, density, and fractal scaling in addition to the orientation, surface roughness, and aperture.

The most significant observation of the Yucca Mountain study was that the fractured pavements had a fractal geometry and were scale invariant and that it was possible to represent the distribution of fractures ranging from 20 cm to 20 m by a single parameter, the fractal dimension D_f, calculated by the box-counting method (Equation 3.1) (in which $N(r)$ should be taken to be the number of fractures of length r). For the fracture surfaces analyzed by Barton and coworkers, $D_f \simeq 1.6\text{–}1.7$. LaPointe (1988) carried out a careful reanalysis of three fracture trace maps of Barton and Larsen (1985) and found that for the corresponding 3D fracture networks, $D_f \simeq 2.37$, 2.52, and 2.68, with an average of about $D_f \simeq 2.52$, so that the average fractal dimension of 3D the fracture networks is essentially identical with that of 3D percolation network at the percolation threshold p_c, which is about 2.53.

Velde et al. (1991) analyzed fractal patterns of fractures in granites. Vignes-Adler et al. (1991) carried out fractal analysis of fracturing in two African regions and analyzed data at several

length scales, ranging from those obtained from satellite images to ground states, and found strong evidence for the fractality of the fracture patterns, while 2D maps of fracture traces spanning nearly 10 orders of magnitude, ranging from microfractures in Archean Albites to large fractures in South Atlantic seafloors, were analyzed by Barton (1992) who reported that $D_f \simeq 1.3$–1.7. The reader should also consult Walsh and Watterson (1993) on the pitfalls of fractal analysis of fracture patterns.

A similar result was reported for the Geysers geothermal field in northeast California (Sahimi et al., 1993), one of the most significant geothermal fields in the world. The reservoir's fractures can be detected during drilling as they produce a sudden and measurable increase in the steam pressure. Analysis of the 2D data indicated a fractal dimension $D_f \simeq 1.9$, which is the same as that of 2D percolation networks at p_c. Much more recent work by Tafti et al. (2013) confirmed the earlier result of Sahimi et al. (1993).

Watanabe and Takahashi (1995) also used fractal concepts to characterize the structure of geothermal reservoirs, as did Babadagli (2001) who analyzed fractal properties of 2D samples of geothermal reservoirs in southwestern Turkey. Nolen-Hoeksema and Gordon (1987) and Chelidze and Guéguen (1990) studied the fracture patterns in Stockbridge (near Canamn, Connecticut) dolomite marble, which is very branched and appears to be a highly interconnected network. Analysis of Chelidze and Guéguen (1990) indicated that the 3D fracture network is a fractal object with $D_f \simeq 2.5$, very close to that of the sample-spanning percolation cluster at p_c.

In addition to fractures, faults, which can be thought of as fractures at the largest length scales, may also possess fractal properties. Faults are usually created when two strata or layers move with respect to each other. The interface between the two displaced layers is what constitutes a fault. Therefore, in some sense, faults are similar to fractures, and one often finds large faults in almost any kind of LS porous media. Unlike fractures, however, which are created by a variety of processes ranging from the diagenetic to mechanical processes, faults are usually manifestations of tectonic processes that rock experienced in the past. Moreover, unlike fractures that provide large permeability zones and facilitate transport of fluids in rock, faults may or may not do so. They sometimes hinder fluid transport in rock by compartmentalizing and isolating large portions of it.

Tchalenko (1970) observed that over many orders of magnitude in length scale, ranging from millimeters to hundreds of meters, shear deformation zones in rock are similar, thus suggesting strongly that the fault patterns are fractal (although Tchalenko was not aware of the fractal geometry). The work of others (Andrews, 1980; Aki, 1981; King, 1984) confirmed this suggestion. In particular, Okubo and Aki (1987) and Aviles et al. (1987) analyzed maps of the San Andreas fault system in California and obtained fractal dimensions for fault surfaces varying from 1.1 to 1.4 (see also Davy, 1993), and Barton (1995a) and Berkowitz and Hadad (1997) reanalyzed the data for Yucca Mountain and reported that $D_f \simeq 1.7 - 1.98$, which is close to the fractal dimension of 2D percolation networks at p_c.

3.5.9 Interdimensional Relations

An important question is how to extrapolate data for fracture networks from 1D to 2D and from 2D to 3D. The mapping must be based on stereological methods. Despite the fundamental importance of the subject, few thorough studies have been carried out to investigate it. In particular, Berkowitz and Adler (1998) invoked the common but highly idealistic assumption that fractures can be modeled as disks of finite radii, and predicted the distribution of fracture trace lengths on planes that intersect randomly such fractures. They also considered the extrapolation problem from 1D to 2D, and from 2D to 3D, and developed a series of analytical relationships to accomplish their goal.

A related important question is how to relate the exponents for the aforementioned various distributions that are obtained from lower-dimensional samples to those for 3D ones. For example, how

does one relate the fractal dimension of a fracture network obtained from 2D maps to 3D samples? It is common to assume that

$$D_f(d=3) = D_f(d=2) + 1, \tag{3.33}$$

which would be true for isotropic and large enough samples, in which the fractures are randomly distributed with a uniform spatial distribution. However, Equation 3.33 is not necessarily valid if there are strong correlations between the spatial positions of the fractures or if there is strong directional anisotropy. Hatton et al. (1993) proposed that

$$\kappa(d=3) = c_1\kappa(d=2) + c_2, \tag{3.34}$$

where

κ is any exponent of interest
$c_1 = 1.28 \pm 0.3$
$c_2 = -0.23 \pm 0.0.3$

Hatton et al. (1993) compared scaling exponents from acoustic emission (3D) data and direct fracture trace (2D) data in order to obtain Equation 3.34. Borgos et al. (2000) studied the problem theoretically and suggested that $c_1 = 1$ and $0 \leq c_2 \leq 1$. The main conclusion is that such equations as (3.35) represent the ideal case and are not necessarily valid for natural rock samples that are characterized by long-range correlations, directional anisotropy, and preferential fracture nucleation at the tensile surface.

REFERENCES

Abelin, H., L. Birgersson, J. Gidlund, and I. Neretnieks, A large-scale flow and tracer experiment in granite. I. Experimental design and flow distribution. *Water Resour. Res.* **27**, 3107 (1991).

Adler, P.M., J.-F. Thovert, and V.V. Mourzenko, Fractured Porous Media, Oxford University Press, London (2012).

Aki, K., A probabilistic synthesis of precursory phenomena. In *Earthquake Prediction: An Introductional Review*, D.W. Simpson and P.G. Richards (eds.) (American Geophysical Union, Washington, DC, 1981), p. 566.

Ambegaokar, V., B.I. Halperin, and J.S. Langer, Hopping conductivity in disordered systems. *Phys. Rev. B* **4**, 2612 (1971).

Anders, M.H. and D.V. Wiltschko, microfracturing, paleostress, and the growth of faults. *J. Struct. Geol.* **16**, 795 (1994).

Andrews, D.J., A stochastic fault model: 1. Static case. *J. Geophys. Res.* **85**, 3867 (1980).

Ansari-Rad, M., S.M. Vaez Allaei, and M. Sahimi, Nonuniversality of roughness exponent of quasi-static brittle fracture. *Phys. Rev. E* **85**, 021121 (2011).

Arbabi, S. and M. Sahimi, Test of universality for three-dimensional models of mechanical breakdown in disordered solids. *Phys. Rev. B* **41**, 772 (1990).

Arns, C.H., M.A. Knackstedt, W.V. Pinczewski, and E.J. Garboczi, Computation of linear elastic properties from microtomographic images: Methodology and agreement between theory and experiment. *Geophysics* **67**, 1396 (2002).

Arns, C.H., M.A. Knackstedt, W.V. Pinczewski, and W.B. Lindquist, Accurate estimation of transport properties from microtomographic images. *Geophys. Res. Lett.* **28**, 3361 (2001).

Auradou, H., G. Drazer, J.-P. Hulin, and J. Koplik, Permeability anisotropy induced by the shear displacement of rough fracture walls. *Water Resour. Res.* **41**, W09423 (2005).

Aviles, C.A., C.H. Scholz, and J. Boatwrigth, Fractal analysis applied to characteristic segments of the San Andreas Fault. *J. Geophys. Res.* **92**, 331 (1987).

Babadagli, T., Fractal analysis of 2-D fracture networks of geothermal reservoirs in south-western Turkey. *J. Volcan. Geother. Res.* **112**, 83 (2001).

Balberg, I., Connectivity and conductivity in 2-D and 3-D fracture systems. *Ann. Isr. Phys. Soc.* **8**, 89 (1986).

Balberg, I., B. Berkowitz, and G.E. Drachsler, Application of a percolation model to flow in fractured hard rocks. *J. Geophys. Res.* **B98**, 10015 (1991).

Balberg, I., C.H. Anderson, S. Alexander, and N. Wagner, Excluded volume and its relation to the onset of percolation. *Phys. Rev. B* **30**, 3933 (1984).

Barthélémy, P., C. Jacquin, J. Yao, J.-F. Thovert, and P.M. Adler, Hierarchical structures and hydraulic properties of a fracture network in the Causse of Larzac. *J. Hydrol.* **187**, 237 (1996).

Barton, C.C., Fractal analysis of the scaling and spatial clustering of fractures. In *Fractals and Their Use in the Earth Sciences*, C.C. Barton and P.R. LaPointe (eds.) (Geological Society of America, Boulder, CO, 1992).

Barton, C.C., Fractal analysis of scaling and spatial clustering of fractures. In *Fractals in Earth Sciences*, C.C. Barton and P.R. LaPointe (eds.) (Plenum, New York, 1995a), p. 141.

Barton, C.C., Bedrock geological map of Hubbard Brooks experimental forest and maps of fracture and geology in road cuts along Interstate 93, Grafton County, New Hampshire. *Rep. I-2562, U.S. Geological Survey Misc. Invest. Ser.* **2**, 1 (1995b).

Barton, C.C. and P.A. Hsieh, *Physical and Hydrological-Flow Properties of Fractures, Guidebook T385* (American Geophysical Union, Las Vegas, NV, 1989).

Barton, C.C. and E. Larsen, *Proceedings of the International Symposium on Fundamentals of Rock Joints*, O. Stephansson (ed.) (Bjorkliden, Sweden, 1985), p. 77.

Barton, C.C., T.A. Schutter, W.R. Page, and J.K. Samuel, Computer generation of fracture networks for hydrologic-flow modelling. *Trans. Amer. Geophys. Union* **68**, 1295 (1987).

Barton, C.C. and M.D. Zoback, Self-similar distribution and properties of macroscopic fractures at depth in crystalline rock in the Cajon Pass scientific drill hole. *J. Geophys. Res.* **97**, 5181 (1992).

Bauget, F. and M. Fourar, Non-fickian dispersion in a single fracture. *J. Contanm. Hydro.* **100**, 137 (2008).

Belfield, W.C., Incorporating spatial distribution into stochastic modelling of fractures: Multifractal and Lévy-stable statistics. *J. Struct. Geol.* **20**, 473 (1998).

Belfield, W.C. and J. Sovitch, Fractures statistics from horizontal wells. *J. Can. Pet. Technol.* **34**, 47 (1995).

Berkowitz, B., Analysis of fracture network connectivity using percolation theory. *Math. Geol.* **27**, 467 (1995).

Berkowitz, B. and P.M. Adler, Stereological analysis of fracture network structure in geological formations. *J. Geophys. Res.* **103**, 15339 (1998).

Berkowitz, B. and A. Hadad, Fractal and multifractal measures of natural and synthetic fracture networks. *J. Geophys. Res.* **102**, 12205 (1997).

Bertels, S., D. Dicarlo, and M.J. Blunt, *Water Resour. Res.* **37**, 649 (2001).

Billaux, D., J.P. Chiles, K. Hestir, and J.C.S. Long, Three-dimensional statistical modelling of a fractured rock mass. An example from the Fanay-Augeres mine. *Int. J. Rock Mech. Min. Sci. Geomech. Abstr.* **26**, 281 (1989).

Boffa, J.M., C. Allain, and J.P. Hulin, Experimental analysis of fracture rugosity in granular and compact rock. *Eur. Phys. J. Appl. Phys.* **2**, 281 (1998).

Bonnet, E., O. Bour, N.E. Odling, P. Davy, I. Main, P. Cowie, and B. Berkowitz, Scaling of fracture systems in geological media. *Rev. Geophys.* **39**, 347 (2001).

Borgos, H.G., P.A. Cowie, and N.H. Dawers, Practicalities of extrapolating one-dimensional fault and fracture size-frequency distributions to higher-dimensional samples. *J. Geophys. Res.* **105**, 28377 (2000).

Brown, S.R., A note on the description of surface roughness using fractal dimension. *Geophys. Res. Lett.* **14**, 1095 (1987a).

Brown, S.R., Fluid flow through rock joints: The effect of surface roughness. *J. Geophys. Res.* **B92**, 1337 (1987b).

Brown, S.R., Transport of fluid and electric current through a single fracture. *J. Geophys. Res.* **B94**, 9429 (1989).

Brown, S.R., R.L. Krantz, and B.P. Bonner, Correlation between the surfaces of natural rock joints. *Geophys. Res. Lett.* **13**, 1430 (1986).

Brown, S.R. and C.H. Scholz, Broad bandwidth study of the topography of natural rock surfaces. *J. Geophys. Res.* **B90**, 12575 (1985).

Carter, J.E. and C.L. Winter, Fractal nature of normal faults in the Española basin, Rio Grande rift, New Mexico: Implications for fault growth and brittle strain. *J. Struct. Geol.* **17**, 863 (1995).

Cartwright, J.A., B.D. Trugdill, and C.S. Mansfield, Fault growth by segment linkage: An explanation for scatter in maximum displacement and trace length data from the Canyonlands grabens of SE Utah. *J. Struct. Geol.* **17**, 1319 (1995).

Castaing, C., M.A. Halawani, F. Gervais, J.P. Chilés, A. Genter, B. Bourgine, G. Ouillon et al., Scaling relationships in intraplate fracture systems related to Red Sea rifting. *Techtonophysics* **261**, 291 (1996).

Charlaix, E., Percolation threshold of a random array of discs: A numerical simulation. *J. Phys. A* **18**, L533 (1986).
Charlaix, E., E. Guyon, and N. River, Criterion for percolation threshold in a random array of plates. *Solid State Commun.* **50**, 999 (1984).
Charlaix, E., E. Guyon, and S. Roux, Permeability of a random array of fractures of widely varying apertures. *Transp. Porous Media* **2**, 31 (1987).
Chelidze, T.L., Percolation and fracture. *Phys. Earth Planet. Int.* **28**, 93 (1982).
Chelidze, T.L. and Y. Guéguen, Evidence of fractal fracture. *Int. J. Rock Mech. Min. Sci. Geomech. Abstr.* **27**, 223 (1990).
Childs, C., J.J. Walsh, and J. Watterson, A method for estimation of the density of fault displacements below the limits of seismic resolution in reservoir formations. In *North Sea Oil and Gas Reservoirs II*, A.T. Butler (ed.) (Graham & Trotman, Norwell, MA, 1990), p. 309.
Cladouhos, T.T. and R. Marret, Are fault growth and linkage models consistent with power-law distribution of fault length? *J. Struct. Geol.* **18**, 281 (1996).
Cowie, P.A., D. Sornette, and C. Vanneste, Multifractal scaling properties of a growing fault population. *Geophys. J. Int.* **122**, 457 (1995).
Cowie, P.A., C. Vanneste, and D. Sornette, Statistical physics model for spatiotemporal evolution of faults. *J. Geophys. Res.* **98**, 21809 (1993).
Cox, B.L. and J.S.Y. Wang, Fractal surfaces: Measurements and applications in the earth sciences. *Fractals* **1**, 87 (1993).
Crosta, G., Evaluating rock mass geometry from photographic images. *Roch Mech. Rock Eng.* **30**, 35 (1997).
Cruden, D.M., Describing the size of discontinuities. *Int. J. Rock. Mech. Min. Sci. Geomech. Abstr.* **14**, 133 (1977).
Daguier, P., S. Henaux, E. Bouchaud, and F. Creuzet, Quantitative analysis of a fracture surface by atomic force microscopy. *Phys. Rev. E* **53**, 5637 (1996).
Dashtian, H., G.R. Jafari, Z. Koohi Lai, M. Masihi, and M. Sahimi, Analysis of cross correlations between well logs of hydrocarbon reservoirs. *Transp. Porous Media* **90**, 445 (2011a).
Dashtian, H., G.R. Jafari, M. Sahimi, and M. Masihi, Scaling, multifractality and long-range correlations in well log data of large-scale porous media. *Physica* **390**, 2096 (2011b).
Davy, P., On the frequency-length distribution of the San Andreas fault system. *J. Geophys. Res.* **98**, 12141 (1993).
Davy, P., A. Hansen, E. Bonnet, and S.Z. Zhang, Localization and fault growth in layered brittle-ductile systems: Implications for deformation of the continental lithosphere. *J. Geophys. Res.* **100B**, 6281 (1995).
de Arcangelis, L., A. Hansen, H.J. Herrmann, and S. Roux, Scaling laws in fracture. *Phys. Rev. B* **40**, 877 (1989).
Englman, R., Y. Gur, and Z. Jaeger, Fluid flow through a crack network in rocks. *J. Appl. Mech.* **50**, 707 (1983).
Fossen, H. and J. Hesthammer, Geometric analysis and scaling relation of deformation bands in porous sandstone from the San Rafael Desert, Utah. *J. Struct. Geol.* **19**, 1479 (1997).
Friedman, S.P. and N. Seaton, Critical path analysis of the relationship between permeability and electrical conductivity of three-dimensional pore networks. *Water Resour. Res.* **34**, 1703 (1998).
Gale, J.E., The effects of fracture type (induced versus natural) on the stress-fracture closure-fracture permeability relationships. In *Proceedings of 23rd US Symposium on Rock Mechanics*, Berkeley, CA (1982), p. 290.
Gale, J.E., *Proceedings of the 28th U.S. Symposium of Rock Mechanics*, Tucson, AZ (1987), p. 1213.
Gauthier, B.D.M. and S.D. Lake, Probabilistic modeling of faults below the limit of seismic resolution in Pelican field, North Sea, offshore United Kingdom. *Am. Assoc. Pet. Geol. Bull.* **77**, 761 (1993).
Genter, A., H. Traineau, Ch. Dezayes, Ph. Elsass, B. Ledesert, A. Meunier, and Th. Villemin, Fracture analysis and reservoir characterization of the granitic basement in the HDR Soultz Project (France). *Geotherm. Sci. Technol.* **4**, 189 (1995).
Gentier, S., D. Billaux, and L. van Vliet, Laboratory testing of the voids of a fracture. *Rock Mech. Rock Eng.* **22**, 149 (1989).
Gertsch, L.S., Three-dimensional fracture network models from laboratory-scale rock samples. *Int. J. Rock Mech. Min. Sci. Geomech. Abstr.* **32**, 85 (1995).
Gillespie, P.A., C. Howard, J.J. Walsh, and J. Watterson, Measurement and characterisation of spatial distribution of fractures. *Tectonophysics* **226**, 113 (1993).
Gillespie, P.A., J.J. Walsh, and J. Watterson, Limitations of dimension and displacement data from single faults and the consequences for data analysis and interpretation. *J. Struct. Geol.* **14**, 1157 (1992).

Glover, P. et al. Fluid flow in synthetic rough fractures and application to the Hachimantai geothermal HDR test site. *J. Geophys. Res.* **B103**, 9621 (1998).

Gonzalez-Garcia, R., O. Huseby, J.-F. Thovert, and P.M. Adler, Three-dimensional characterization of a fractured granite and transport properties. *J. Geophys. Res. B* **105**, 21387 (2000).

Gouze, P., C. Noiriel, C. Bruderer, D. Loggia, and R. Leprovost, *Geophys. Res. Lett.* **30**, 1267 (2003).

Gross, M.R., G. Gutierrez-Alonzo, T. Bai, M.A. Wacker, K.B. Collinsworth, and R.J. Behl, Influence of mechanical stratigraphy and kinematics on fault scaling relations. *J. Struct. Geol.* **19**, 171 (1997).

Guéguen, Y., C. David, and P. Gavrilenko, Percolation and fluid transport in the crust. *Geophys. Res. Lett.* **18**, 931 (1991).

Hakami, E., Joint aperture measurements—An experimental technique. In *Proceedings of International Symposium on Fractured and Jointed Rock Masses*, Lake Tahoe, CA (1992).

Hakami, E., Aperture distribution of rock fractures, PhD thesis, Royal Institute of Technology, Stockholm, Sweden (1995).

Hakami, E. and N. Barton, Aperture measurements and flow experiments using transparent replicas of rock joints. In *Rock Joint*, N. Barton and O. Stephansson (eds.) (Balkema, Rotterdam, the Netherlands, 1990), p. 383.

Hakami, E. and E. Larsson, Aperture measurements and flow experiments on a single natural fracture. *Int. J. Rock Mech. Min. Sci. Geomech. Abstr.* **33**, 395 (1996).

Hakami, E. and O. Stephansson, Experimental technique for aperture studies of intersecting joints. In *Proceedings of ISRM International Symposium on Eurock 93*, Lisboa, Portugal (1993), p. 301.

Hatton, C.G., I.G. Main, and P.G. Meredith, A comparison of seismic and structural measurements of fractal dimension during tensile subcritical crack growth. *J. Struct. Geol.* **15**, 1485 (1993).

Hatton, C.G., I.G. Main, and P.G. Meredith, Nonuniversal scaling of fracture length and opening displacement. *Nature* **367**, 160 (1994).

Hughes, B.D., *Random Walks and Random Environments*, Vol. 1 (Oxford University Press, London, U.K., 1995).

Hunt, A., R. Ewing, and B. Ghanbarian, *Percolation Theory for Flow in Porous Media* (Springer, Heidelberg, Germany, 2014).

Huseby, O., J.-F. Thovert, and P.M. Adler, Geometry and topology of fracture systems. *J. Phys. A* **30**, 1415 (1997).

Johns, R.A., J.S. Steude, L.M. Castanier, and P.V. Roberts, Nondestructive measurements of fracture aperture in crystalline rock cores using x ray computed tomography, *J. Geophys. Res. B*, **98**, 1889 (1993).

Johnston, J.D., Fractal geometries of filled fracture systems—Scaling mechanism. In *Tectonic Studies Group Special Meeting, Edinburgh* (1994); Fault Population, Extended Abstract Volume, p. 64, Geological Society of London, London, U.K.

Johnston, J.D. and K.J.W. McCaffrey, Fractal geometries of vein systems and the variation of scaling relationships with mechanism. *J. Struct. Geol.* **18**, 349 (1996).

Katz, A.J. and A.H. Thompson, Quantitative prediction of permeability in porous rock. *Phys. Rev. B* **34**, 8179 (1986).

Katz, A.J. and A.H. Thompson, Prediction of rock electrical conductivity from mercury injection measurements. *J. Geophys. Res.* **B92**, 599 (1987).

Keller, A., High resolution, non-destructive measurement and characterization of fracture apertures. *Int. J. Rock Mech. Min. Sci.* **35**, 1037 (1998).

Keller, K. and B.P. Bonner, Automatic, digital system for profiling rough surface. *Rev. Sci. Instrum.* **56**, 330 (1985).

Kersting, A.B., D.W. Efurd, D.L. Finnegan, D.J. Rokop, D.K. Smith, and J.L. Thompson, Migration of plutonium in ground water at the Nevada test site. *Nature* **397**, 56 (1999).

King, G.C.P., The accommodation of strain in the upper lithosphere of the earth by self-similar fault systems; the geometrical origin of b-value. *Pure Appl. Geophys.* **121**, 761 (1984).

Koestler, A.G. and K. Reksten, Insight into the 3D fracture network of an exposed analogue of fractured chalk reservoirs—The Lägerdorf case. In *Proceedings of Fourth North Sea Chalk Symposium*, Deauville, France (1992).

Koyama, T.N., L. Fardin, L. Jing, and O. Stephansson. Numerical simulation of shear-induced flow anisotropy and scale-dependent aperture and transmissivity evolution of rock fracture replicas. *Int. J. Rock Mech. Min. Sci.* **43**, 89 (2006).

Krantz, R.L., Microcracks in rocks: A review. *Tectonophysics* **100**, 449 (1983).

LaPointe, P.R., A method to characterize fracture density and connectivity through fractal geometry. *Int. J. Rock Mech. Min. Sci. Geomech. Abstr.* **25**, 421 (1988).

Lockner, D.A. and T.R. Madden, A multiple-crack model of brittle fracture: 1. Non-time-dependent simulations. *J. Geophys. Res.* **96**, 19623 (1991).
Lockner, D.A., D.E. Moore, and Z. Reches, Microcracks interaction leading to shear fracture. In *Proceedings of the 33rd U.S. Symposium on Rock Mechanic*, J.R. Tillerson and W.R. Wawersik (eds.) (Balkema, Brookfield, WI, 1992), p. 807.
Long, J.C.S. and D. Billaux, From field data to fracture network modeling: An example incorporating spatial structure. *Water Resour. Res.* **23**, 1201 (1987).
Madden, T.R., Microcrack connectivity in rocks: A renormalization group approach to the critical phenomena of conductivity and failure in crystalline rocks. *J. Geophys. Res.* **88**, 585 (1983).
Måløy, K.J., A. Hansen, E. Hinrichsen, and S. Roux, *Phys. Rev. Lett.* **68**, 213 (1992).
Mandelbrot, B.B., D.E. Passoja, and A.J. Paullay, Fractal character of fracture surfaces of metals. *Nature* **308**, 721 (1984).
Marret, R., Aggregate properties of fracture populations. *J. Struct. Geol.* **18**, 169 (1996).
Matsuki, K., Y. Chida, K. Sakaguchi, and P.W.J. Glover, size effect on aperture and permeability of a fracture as estimated in large synthetic fractures. *Int. J. Rock Mech. Min. Sci*. **43**, 726 (2006).
Mitchell, M.W. and D.A. Bonnell, Quantitative topographic analysis of fractal surfaces by scanning tunneling microscopy. *J. Mater. Res.* **5**, 2244 (1990).
Montemagno, C.D. and L.J. Pyrak-Nolte, Porosity of natural fracture networks. *J. Geophys. Res.* **B22**, 1397 (1995).
Moore, D.E. and D.A. Lockner, The role of microcracking in shear fracture propagation in granite. *J. Struct. Geol.* **17**, 95 (1995).
Narr, W. and I. Lerche, A method for estimating subsurface fracture density in core. *AAPG Bull.* **68**, 637 (1984).
Nasseri, M., B. Mohanty, and R. Young, *Pure Appl. Geophys.* **163**, 917 (2006).
Nicol, A., J.J. Walsh, and J. Watterson, Fault size distributions—Are they really power-law? *J. Struct. Geol.* **18**, 191 (1996).
Nolen-Hoeksema, R.C. and R.B. Gordon, Optical detection of crack patterns in the opening-mode fracture of marble. *Int. J. Rock Mech. Min. Sci. Geomech. Abstr.* **24**, 135 (1987).
Odling, N.E., Network properties of a two-dimensional natural fracture pattern. *Pure Appl. Geophys.* **138**, 95 (1992).
Odling, N.E., Natural fracture profiles, fractal dimension and joint roughness coefficients. *Rock Mech. Rock Eng.* **27**, 135 (1994).
Okubo, P.G. and K. Aki, Fractal geometry in the San Andreas Fault system. *J. Geophys. Res. B* **92**, 345 (1987).
Oron, A. and B. Berkowitz, *Water Resour. Res.* **34**, 2811 (1998).
Painter, S., Evidence for non-Gaussian scaling behavior in heterogeneous sedimentary formations. *Water Resour. Res.* **32**, 1183 (1996).
Painter, S., G. Beresford, and L. Paterson, On the distribution of seismic amplitudes and seismic reflection coefficients. *Geophysics* **60**, 1187 (1995).
Painter, S. and L. Paterson, Fractional Lévy motion as a model for spatial variability in sedimentary rock. *Geophys. Res. Lett.* **21**, 2857 (1994).
Peacock, D.C.P. and D.J. Sanderson, Displacements, segment linkage and relay ramps in normal fault zones. *J. Struct. Geol.* **13**, 721 (1991).
Pickering, G., D.C.P. Peacock, D.J. Sanderson, and J.M. Bull, Modeling tip zones to predict the throw and length characteristics of faults. *Am. Assoc. Pet. Geol. Bull.* **81**, 82 (1997).
Ponson, L., H. Auradou, P. Vié, M. Pessel, V. Lazarus, and J.P. Hulin, Failure mechanisms and surface roughness statistics of fractured Fontainebleau sandstone, *Phys. Rev. E* **76**, 036108 (2007).
Poon, C.Y., R.S. Sayles, and T.A. Jones, Surface measurement and fractal characterization of naturally fractured rocks. *J. Phys. D* **25**, 1269 (1992).
Power, W.L., T.E. Tullis, S.R. Brown, G.N. Boitnott, and C.H. Scholz, Roughness of natural fault surfaces. *Geophys. Res. Lett.* **14**, 29 (1987).
Priest, S.D. and J.A. Hudson, Estimation of discontinuity spacing and trace length using scanline surveys. *Int. J. Rock. Mech. Min. Sci. Geomech. Abstr.* **18**, 183 (1981).
Pyrak-Nolte, L.J., C.D. Montemagno, and D.D. Nolte, Volumetric imaging of aperture distributions in connected fracture networks. *Geophys. Res. Lett.* **24**, 2343 (1997).
Pyrak-Nolte, L.J., L.R. Myer, N.G.W. Cook, and P.A. Witherspoon, Hydraulic and mechanical properties of natural fractures in low permeability rock. *Proceedings of Sixth International Congress of Rock Mechanics* (1987), p. 225.
Reches, Z., Network of shear faults in the field and in experiment. *Ann. Isr. Phys. Soc.* **8**, 42 (1986).
Renshaw, C.E., Sampling bias and the scaling of hydraulic conductivity in fractured rock. *Geophys. Res. Lett.* **25**, 121 (1998).

Renshaw, C.E. and J.C. Park, Effect of mechanical interactions on the scaling of fracture length and aperture. *Nature* **386**, 482 (1997).
Renshaw, C.E. and D.D. Pollard, Numerical simulations of fracture set formation: A fracture mechanics model consistent with experimental observations. *J. Geophys. Res.* **99**, 9359 (1994).
Reuschlé, T., Fracture in heterogeneous medium: A network approach. *Terra Nova* **4**, 591 (1992).
Robertson, M.C., C.G. Sammis, M. Sahimi, and A.J. Martin, Fractal analysis of three-dimensional spatial distribution of earthquakes with a percolation interpretation. *J. Geophys. Res.* **100B**, 609 (1995).
Robinson, P.C., Connectivity of fracture systems: A percolation theory approach. *J. Phys. A* **16**, 605 (1983).
Robinson, P.C., Connectivity, flow and transport in network models of fractured media. PhD thesis, St. Catherine's College, Oxford University, England, U.K. (1984a).
Robinson, P.C., Numerical calculations of critical densities for lines and planes. *J. Phys. A* **17**, 2823 (1984b).
Rossen, W.R., Y. Gu, and L.W. Lake, Connectivity and permeability in fracture networks obeying power-law statistics. SPE Paper 59720 (2000).
Rouleau, A. and J.E. Gale, Stochastic discrete fracture simulation of groundwater flow into an underground excavation in granite. *Int. J. Rock Mech. Min. Sci. Geomech. Abstr.* **24**, 99 (1987).
Sahimi, M., Nonlinear transport processes in disordered media. *AIChE J.* **39**, 369 (1993a).
Sahimi, M., Flow phenomena in rocks: From continuum models to fractals, percolation, cellular automata and simulated annealing. *Rev. Mod. Phys.* **65**, 1395 (1993b).
Sahimi, M., *Applications of Percolation Theory* (Taylor & Francis, London, U.K., 1994).
Sahimi, M., Nonlinear and nonlocal transport in heterogeneous media: From long-range correlated percolation to fracture and materials breakdown. *Phys. Rep.* **306**, 213 (1998).
Sahimi, M., *Heterogeneous Materials I: Linear Transport and Optical Properties* (Springer, New York, 2003a).
Sahimi, M., *Heterogeneous Materials II: Nonlinear and Breakdown Properties and Atomistic Modeling* (Springer, New York, 2003b).
Sahimi, M., *Flow and Transport in Porous Media and Fractured Rock*, 2nd edn. (VCH-Wiley, Weinheim, Germany, 2011).
Sahimi, M. and S. Arbabi, Percolation and fracture in disordered solids and granular media: Approach to a fixed point. *Phys. Rev. Lett.* **68**, 608 (1992).
Sahimi, M. and S. Arbabi, Mechanics of disordered solids. III. Fracture properties. *Phys. Rev. B* **47**, 713 (1993).
Sahimi, M. and S. Arbabi, Scaling laws for fracture of heterogeneous materials and rock. *Phys. Rev. Lett.* **77**, 3689 (1996).
Sahimi, M. and S. Mukhopadhyay, Scaling properties of a percolation model with long-range correlations. *Phys. Rev. E* **54**, 3870 (1996).
Sahimi, M., G.R. Gavalas, and T.T. Tsotsis, Statistical and continuum models of fluid-solid reactions in porous media. *Chem. Eng. Sci.* **45**, 1443 (1990).
Sahimi, M. and J.D. Goddard, Elastic percolation models for cohesive mechanical failure in heterogeneous systems. *Phys. Rev. B* **33**, 7848 (1986).
Sahimi, M., H. Rassamdana, and A.R. Mehrabi, Fractals in porous media: From pore to field scale. *Proc. Mater. Res. Soc.* **367**, 203 (1995).
Sahimi, M., M.C. Robertson, and C.G. Sammis, Fractal distribution of earthquake hypocenters and its relation to fault patterns and percolation. *Phys. Rev. Lett.* **70**, 2186 (1993).
Sanderson, D.J., S. Roberts, and P.A. Gumiel, A fractal relationship between vein thickness and gold grade in drill core from La Codosera, Spain. *Econ. Geol.* **89**, 168 (1994).
Schmittbuhl, J., S. Gentier, and S. Roux, Field-measurements of the roughness of fault surfaces. *Geophys. Res. Lett.* **20**, 639 (1993).
Scholz, C.H. and P. Cowie, Determination of total strain from faulting using slip measurements. *Nature* **346**, 837 (1990).
Sharifzadeh, M., Y. Mitani, and T. Esaki, *Rock Mech. Rock Eng.* **41**, 299 (2008).
Sisavath, S., V. Mourzenko, P. Genthon, J.-F. Thovert, and P.M. Adler, Geometry, percolation and transport properties of fracture networks derived from line data. *Geophys. J. Int.* **157**, 917 (2004).
Snow, D.T., The frequency and apertures of fractures in rock. *Int. J. Rock Mech. Sci.* **7**, 25 (1970).
Sornette, D. and P. Davy, Fault growth model and the universal fault length distribution. *Geophys. Res. Lett.* **18**, 1079 (1991).
Spanne, P., J.-F. Thovert, C.J. Jacquin, W.B. Lindquist, K.W. Jones, and P.M. Adler, Synchrotron computed microtomography of porous media: Topology and transport. *Phys. Rev. Lett.* **73**, 2001 (1994).
Stauffer, D. and A. Aharony, *Introduction to Percolation Theory*, 2nd revised edn. (Taylor & Francis, London, U.K., 1994).

Steen, Ø. and A. Andresen, Effects of lithology on geometry and scaling of small faults in Triassic sandstones, east Greenland. *J. Struct. Geol.* **21**, 1351 (1999).

Stone, D., Sub-surface fracture maps predicted from borehole data. An example from the Eye-Dashwa pluton, Atikokan Canada. *Int. J. Rock Mech. Min. Sci. Geomech. Abstr.* **21**, 183 (1984).

Tafti, T.A., M. Sahimi, F. Aminzadeh, and C.G. Sammis, Use of microseismicity for determining the structure of fracture network of large-scale porous media. *Phys. Rev. E* **87**, 032152 (2013).

Tchalenko, J.S., Similarities between shear zones of different magnitudes. *Geol. Soc. Amer. Bull.* **81**, 1625 (1970).

Trugdill, B. and J. Cartwright, Relay ramp forms and normal fault linkage, Canyonlands National Park, Utah. *Geol. Soc. Am. Bull.* **106**, 1143 (1994).

Tsang, Y.W. and P.A. Witherspoon, Hydromechanical behavior of a deformable rock fracture subject to normal stress. *J. Geophys. Res.* **86**, 9287 (1981).

Velde, B., J. Dubois, D. Moore, and G. Touchard, Fractal patterns of fractures in granites. *Earth Planet. Sci. Lett.* **104**, 25 (1991).

Vermilye, J.M. and C.H. Scholz, Relation between vein length and aperture. *J. Struct. Geol.* **17**, 423 (1995).

Vickers, B.C., S.P. Neuman, M.J. Sully, and D.D. Evans, Reconstruction and geostatistical analysis of multi-scale fracture apertures in a large block of welded tuff. *Geophys. Res. Lett.* **19**, 1029 (1992).

Vignes-Adler M., A. Le Page, and P.M. Adler, Fractal analysis of fracturing in two African regions, from satellite imagery to ground scale. *Tectonophysics* **196**, 69 (1991).

Villemin, T. and C. Sunwoo, Distribution logarithmique self similaire des rejets et longueurs de failles: Exemple du bassin Houiller Lorrain. *C.R. Acad. Sci. Ser. II* **305**, 1309 (1987).

Walmann, T., Dynamics and scaling properties of fractures in clay-like materials. PhD thesis, Department of Physics, University of Oslo, Oslo, Norway (1998).

Walmann, T., A. Malthe Sørensen, J. Feder, T. Jøssang, and P. Meaking, Scaling relations for the lengths and widths of fractures. *Phys. Rev. Lett.* **77**, 5393 (1996).

Walsh, J.J. and J. Watterson, Fractal analysis of fracture pattern using the standard box-counting technique: Valid and invalid methodologies. *J. Struct. Geol.* **15**, 1509 (1993).

Watanabe, K. and H. Takahashi, Fractal geometry characterization of geothermal reservoir fracture networks. *J. Geophys. Res.* **100B**, 521 (1995).

Watterson, J., J.J. Walsh, P.A. Gillespie, and S. Easton, Scaling systematics of fault sizes on a large range fault map. *J. Struct. Geol.* **18**, 199 (1996).

Whitehouse, D.J. and J.F. Archard, The properties of random surfaces of significance in their contact. *Proc. Roy. Soc. Lond. A* **316**, 97 (1970).

Wong, T.F., J.T. Fredrich, and G.D. Gwanmesia, Crack aperture statistics and pore space fractal geometry of Westerly granite and Rutland quartzite: Implications for an elastic contact model of rock compressibility. *J. Geophys. Res.* **94**, 10267 (1989).

Yeo, I.W., M.H. De Freitas, and R.W. Zimmerman, *Int. J. Rock Mech. Min. Sci.* **35**, 1051 (1998).

Yielding, G., T. Needham, and H. Jones, Sampling of fault population using sub-surface data: A review. *J. Struct. Geol.* **18**, 135 (1996).

4 Thin Porous Media

Marc Prat and Tristan Agaësse

CONTENTS

4.1 Introduction 89
4.2 Brinkman Equation and Thin Porous Media 90
4.2.1 Brinkman Equation 90
4.2.2 Flow through an Array of Cylinders Confined between Two Plates 90
4.2.3 Filtration Cake at Early Stages 92
4.3 Two-Phase Flow in Thin Porous Media: Examples from PEMFC 95
4.4 Mixed Wettability 98
4.5 Thin Porous-Layer Assembly: The Concept of Third Layer 100
4.6 Thin Porous Media and Liquid Film Flows 104
4.7 Impact of a Thin Salt Crust on Drying 106
4.8 Brief Review of Other Situations Involving TPM 107
4.9 Research Opportunities 108
4.10 Conclusions 109
Acknowledgments 110
References 110

4.1 INTRODUCTION

Thin porous media are common and of great importance for various industries and products. These include papers and cartons, filters and filtration cakes, porous coatings, fuel cells, textiles, and diapers and wipes, to name only a few. A thin porous medium is obviously characterized by lateral dimensions much greater than its thickness. As an example, the thickness of the so-called gas diffusion layers (GDLs) of proton exchange membrane fuel cells is typically on the order of 200 μm, whereas its lateral dimension is on the order of 20 cm (see Section 4.3), leading here to a ratio lateral dimension/thickness on the order of 10^3. Suppose we wish to compute some transfer within such a system assuming that the transfer in question is governed by a known PDE within the framework of the continuum approach to porous media. Consider a uniform computational mesh with a minimum of 10 grid points over the thickness. This leads to a grid containing about 10^9 computational nodes over the whole layer. Thus, clearly adapted modeling and adequate approximations are needed to determine the transfer over the whole domain. Furthermore, relying on the traditional continuum approach to porous media can of course lead to poor results when the traditional length scale separation criterion is not met over the thickness. As an example, a GDL is only a few pore sizes thick. This type of situation, where classical length scale separation criteria are not met, is one of the distinguishing features of thin porous media. Actually, this leads to a possible and convenient stricter definition of thin porous media. Accordingly, a thin porous medium could be defined as a medium whose thickness is on the order of the pore dimension, typically less than 10 pore sizes. However, introducing such a purely geometrical definition can be considered as a bit too simplistic

since the limit between a thin porous medium and a thick porous medium can be in fact transport process dependent. This will be illustrated in Section 4.3. Thus, we believe that further studies are still needed before everyone agrees with the same definition.

At first sight, thin porous media research area can be seen as a disparate collection of quite different situations. For instance, fuel cells are electrochemical devices that seem to have very little in common with paper processing technology or paper printing or the biomedical porous coatings used at a bone–implant interface. Yet an increasing number of people agreed that sharing modeling or experimental experiences coming from the various thin porous media applications can be beneficial. In other terms, thin porous media are emerging as a possible research area where specific questions of common interest to many applications can be addressed.

This chapter is in line with this tendency. The objectives are first to show that thin porous media can behave differently from ordinary porous media. Then the idea is to identify generic aspects from the consideration of selected examples.

4.2 BRINKMAN EQUATION AND THIN POROUS MEDIA

4.2.1 Brinkman Equation

Brinkman equation is a variant of momentum conservation equation that reads, for example (Nield and Bejan 1992),

$$\nabla P = -\frac{\mu}{K}\mathbf{v} + \tilde{\mu}\nabla^2\mathbf{v}, \tag{4.1}$$

where

P is the pressure
K is the permeability
$\mathbf{v}$ is the filtration velocity
μ is the fluid dynamic viscosity
$\tilde{\mu}$ is an effective viscosity

This equation can be derived using homogenization, for example, Levy (1981), but the conclusion of the theory is that keeping the Laplacian term is only justified for unrealistically highly porous material, that is, $\varepsilon \approx 1$, where ε is the porosity. However, the homogenization technique considers spatially periodic medium far from walls. Although the Laplacian term in Equation 4.1 cannot be rigorously justified, the Brinkman equation can be an interesting approximation in the context of thin porous media because of the influence of the walls that often border the thin porous layer. This is illustrated in what follows through two examples.

4.2.2 Flow through an Array of Cylinders Confined between Two Plates

As sketched in Figure 4.1, consider a periodic array of short cylinders confined between two parallel walls as model thin porous medium. The flow within this system was studied by Tsay and Weinbaum (1991) in relation with the capillary filtration through the clefts between endothelial cells in continuous capillaries; see Tsay and Weinbaum (1991) for more details. It can be also a good model for flow in a single fracture partially occupied by particles or trapped droplets or bubbles, for example, Chauvet et al. (2012). The objective is to compute the flow through the fracture, taking into account both the presence of the cylinders and the friction on the confinement walls. As shown in details by Tsay and Weinbaum (1991), the Brinkman equation can be used to obtain a reasonably good estimate of the viscous resistance in this system.

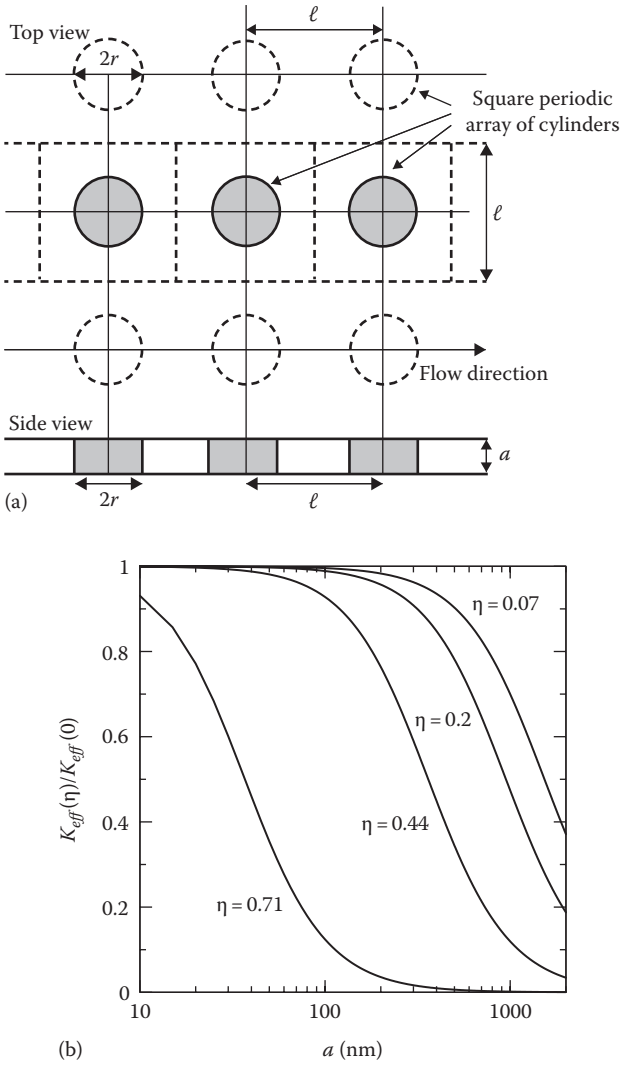

FIGURE 4.1 (a) Periodic array of cylinders (gray plots) confined between two solid plates. (b) Ratio between $K_{eff}(\eta)$ and the permeability of a Hele-Shaw slit $K(0)$.

According to the Brinkman approximation and assuming $\tilde{\mu} = \mu$, the effective permeability of the thin porous medium can be estimated as

$$K_{eff}(\eta) = K_p(\eta)\left(1 - \frac{\tanh(Da)}{Da}\right), \tag{4.2}$$

where

K_p is the permeability of the unconfined array of cylinders

η is the surface fraction of the cylinder

$\eta = \pi r^2/\ell^2$, where r is the cylinder radius (see Figure 4.1)

$Da = a/(2(K_p(\eta))^{1/2})$, where a is the spacing between the two confinement walls

The permeability K_p of a square periodic array of cylinders of infinite length can be deduced from the work of Sangani and Acrivos (1982):

$$K_p(\eta) = \frac{\ell^2}{2f(\eta)}, \tag{4.3}$$

where

ℓ is the center-to-center distance between two cylinders

$f(\eta)$ is a coefficient depending on the surface fraction of the cylinder (compacity)

Discrete values of $f(\eta)$ are provided in Sangani and Acrivos (1982). Intermediate values can be obtained from linear interpolation. The liquid flow rate q through a cross section of width ℓ can then be linked to the pressure gradient within the thin porous medium using Darcy's law:

$$\frac{q}{a\ell} = -\frac{K_{eff}(\eta)}{\mu}\frac{dP}{dx}, \tag{4.4}$$

where x is the flow direction (see Figure 4.1).

Considering as an example the case depicted in Figure 4.1a, we varied the cylinder radius r and plotted in Figure 4.1b the effective permeability K_{eff} as a function of gap distance a.

This leads to a counterintuitive result when the porous layer is sufficiently thin. As can be seen from Figure 4.1b, the effective permeability (Equation 4.2) does not depend on the presence of the cylinders when the system is very thin (gaps lower than 100 nm). At these very small scales, the effective permeability K_{eff} is actually very close to the Hele-Shaw permeability $K(0) = a^2/12$. Thus, here, the friction on the confinement walls completely dominates the flow resistance compared to the cylinder contribution. By contrast, the effective permeability becomes lower than $K(0)$ for still thin but less confined systems owing to the additional flow resistance due to the cylinders (parts of the curves on the right-hand side in Figure 4.1b).

4.2.3 Filtration Cake at Early Stages

As it is well known, particle filtration processes, for example (Elimelech et al. 1995), often lead to the formation of a filtration cake at the filter inlet. As sketched in Figure 4.2, the filtration cake is formed by particles accumulating at the inlet. The cake causes an additional flow resistance, which is important to characterize for operating a filtration system. Of particular interest is the additional resistance due to the capture of first particles at the filter surface. Detecting the beginning of cake formation can be indeed a desirable objective for cleaning the filter before any important increase of the overall pressure drop due to cake development. A filtration cake at the early stages of its development is an example of thin porous medium with a poor length scale separation between the particle size and the cake thickness. As such, a traditional continuum approach, that is, Darcy's law, is likely to lead to a

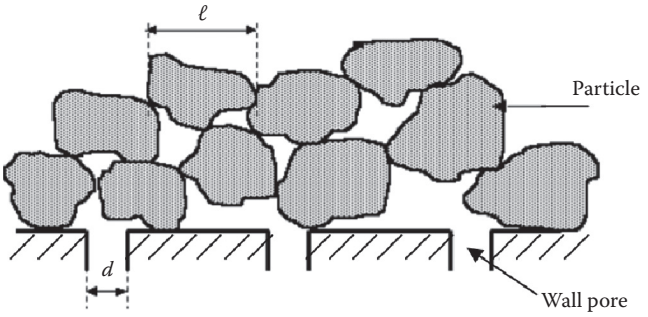

FIGURE 4.2 Sketch of particles forming a thin porous medium at the inlet of a filter or a filtration membrane.

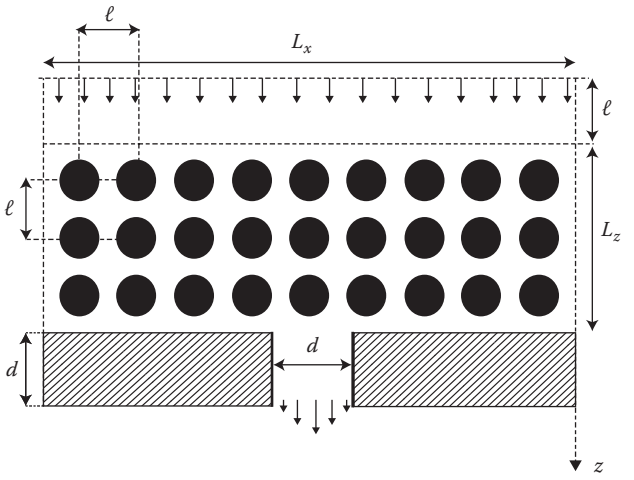

FIGURE 4.3 Model filtration cake. Particles are represented by a square array of cylinders.

poor estimate of the flow resistance due to the cake. To gain some insights into this problem, we consider the 2D model problem sketched in Figure 4.3, where the particles are represented by cylinders of radius r forming a square array. The distance between the centers of two neighboring cylinders is ℓ.

We wish to compute apparent permeability K_{app} of the system formed by the cake and the filter surface, which is considered as a wall with regularly spaced pores of width d and length also equal to d. As sketched in Figure 4.3, the distance between two wall pores is L_x, whereas the cake thickness is denoted by L_z. The apparent permeability is defined by

$$K_{app} = \frac{\mu Q}{(P_{en} - P_{ex})} \frac{L_z}{L_x}, \tag{4.5}$$

where

Q is the flow rate

P_{en} is the pressure at the entrance of the system

P_{ex} is the average pressure at the exit, that is, at the pore wall entrance, which is located at $z = L_z + \ell$

As shown in Dufrêche et al. (2002),

$$\frac{K_{app}}{K} = f\left(\frac{d}{L_x}, \frac{L_z}{L_x}\right), \tag{4.6}$$

where K is the intrinsic permeability of the cake when the scales are separated, that is, when the size r of particles is small compared to other lengths in the problem, especially the wall pore width d. The apparent permeability is smaller than the cake permeability because of streamline deformation near the wall pores; see Dufrêche et al. (2002) for more details.

By contrast, the reduced apparent permeability K_{app}/K depends not only on the macroscopic scales but also on the microscopic ones when the scales are not well separated, that is,

$$\frac{K_{app}}{K} = f\left(\frac{d}{L_x}, \frac{L_z}{L_x}, \frac{\ell}{L_x}, \eta\right), \tag{4.7}$$

where $\eta = \pi r^2/\ell^2$ is the compacity as in Section 4.2.2. As an example, we consider the case $\ell/L_x = 0.1$, which corresponds to horizontal rows of 10 cylinders over the unit cell of size L_x, for $\eta = 0.05$, which corresponds to a highly porous cake ($\varepsilon = 0.95$).

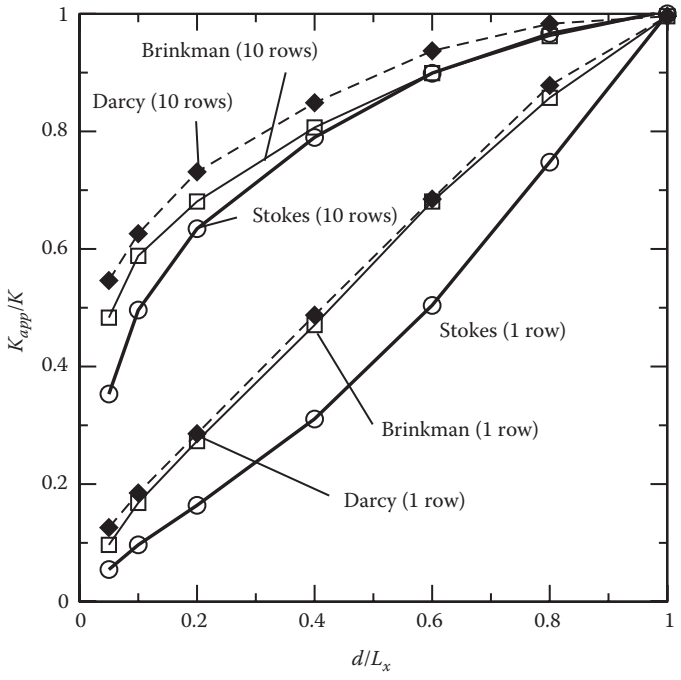

FIGURE 4.4 Reduced apparent permeability as a function of wall pore width for $\eta = 0.05$ and $\ell/L_x = 0.1$ for a thin porous layer formed by 1 or 10 rows of 10 cylinders.

The reduced apparent permeability is shown in Figure 4.4 as a function of the wall pore width. Comparison is made between the values computed from the solution of Stokes equation (considered as reference solution since pore Reynolds number is generally small in the related applications), Brinkman equation, and Darcy equation; see Noel (2006) for the method of solution corresponding to each problem. All the solutions lead to about the same result when $d = L_x$, that is, when there is no wall. Thus, the entrance/exit effects, which are captured by the Stokes equation but not the Darcy equation, are negligible here. As can be seen, both Brinkman equation and Darcy equation significantly overestimate the apparent permeability when the cake is very thin (formed by only one row of particles). As shown in Figure 4.5, the overall pressure drop is in fact dominated by the pressure drop in the passage right above the pore wall. This quite localized pressure drop cannot obviously be captured properly by the continuum approaches.

As expected, the discrepancy between the Stokes solution and the continuum approaches decreases as the cake grows. Also, it can be noted that the Brinkman equation leads to better results compared to the Darcy model. This is because the friction on the solid surface of filter is taken into account with the Brinkman equation but not with the Darcy equation. The discrepancy with Stokes solution increases with decreasing wall pore aperture. The picture is similar to the one shown in Figure 4.5. For narrow wall pores, whose size is on the order of one or two particle diameters, the length scale separation is particularly weak, and not surprisingly, the continuum approaches are unable to capture the very localized pressure drop right above the wall pore.

An alternative to the solution of the Stokes equation over the whole computational domain when the cake is not very thin, that is, it is formed by several layers of particles, is to combine continuum model and pore-scale model. This multiscale or hybrid approach consists in solving the Stokes equation in the region of the cake adjacent to the filter inlet, whereas the Darcy model is solved in the region further away from the filter inlet; see Dufrêche et al. (2003) for more details. As reported in Dufrêche et al. (2003), the coupling between the two models can be performed through a domain

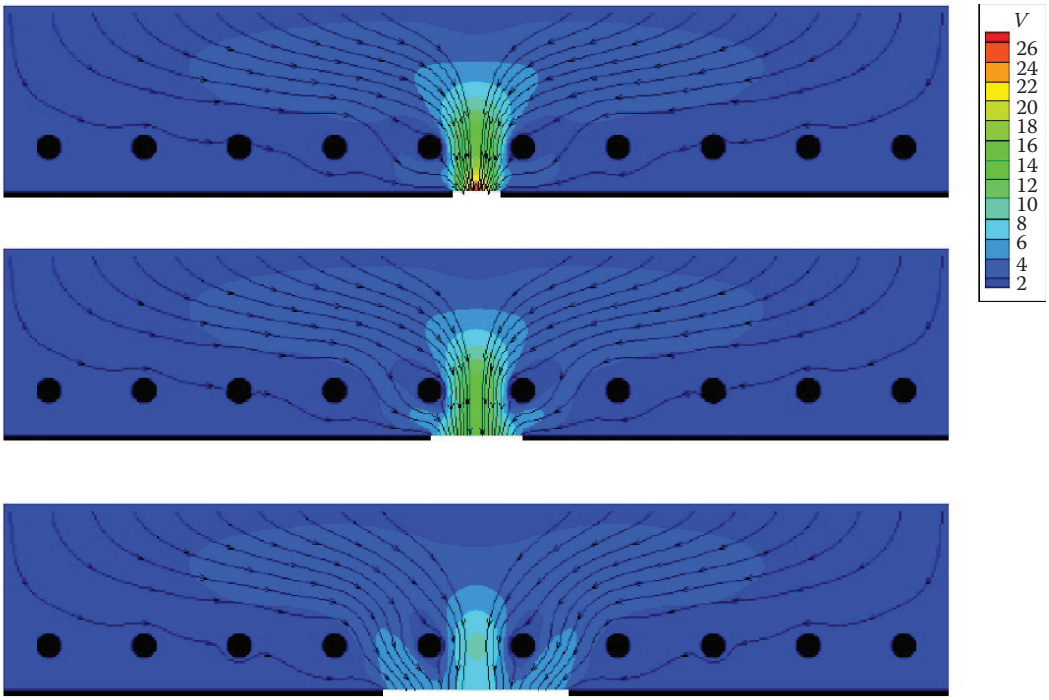

FIGURE 4.5 Velocity magnitudes (arbitrary unit) and streamlines for a cake formed by one layer of particles for different wall pore width ($d/L_x = 0.05$, 0.1, 0.2 from top to bottom), $\ell/L_x = 0.1$ and $\eta = 0.05$.

decomposition technique using the closure relationships, allowing to map a continuum field into a pore-scale field within the framework of the volume averaging technique (Whitaker 1999).

More widely, multiscale modeling, for example (Weinan 2011), could be of general interest in the studies of thin porous media (see Section 4.8).

4.3 TWO-PHASE FLOW IN THIN POROUS MEDIA: EXAMPLES FROM PEMFC

Polymer electrolyte membrane fuel cells (PEMFCs) are promising energy conversion devices operating at low temperature (around 80°C). Water is essential for the operation of PEMFC. The polymer membrane functions properly when sufficiently hydrated. However, problems can arise when there is excessive water in PEMFC. The excess water forms liquid that fills the pores in catalyst layer (CL) and GDL, two key porous components of the device. This phenomenon is called flooding. The flooding on the cathode side is caused by continuous generation of water in the cathode CL and is believed to significantly limit the oxygen diffusion in GDL (and as a result the oxygen reduction reaction in CL). Therefore, the water control in PEMFC is a crucial issue, referred to as the water management issue (Eikerling et al. 2006). A better understanding of two-phase flows in the porous layers forming the cathode is therefore highly desirable in the prospect of improving the PEMFC performance.

In the context of this chapter, the objective of this section is to briefly discuss some aspects of water invasion in GDL as an illustrative example of two-phase flow in thin porous media. As illustrated in Figure 4.6, a GDL is a 3D fibrous structure, whose thickness typically varies between 170 and 400 μm (Barbir 2005). The in-plane extension of a GDL is on the order of 10 cm. The pore sizes in GDL range from a few microns to tens of microns, and as discussed, for example, in Rebai and Prat (2009), the mean distance between two pores is about 50 μm. Using this mean distance as a

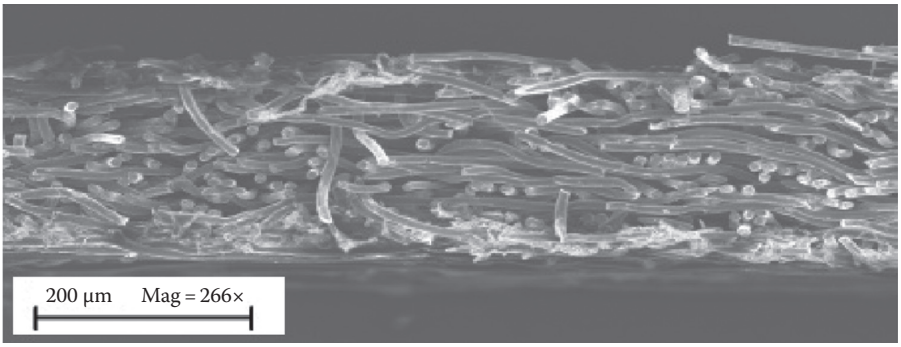

FIGURE 4.6 Example of GDL. (Image courtesy of CEA/LITEN, Grenoble, France.)

unit of length, the GDL thickness is only 4–10 units of length, thus a perfect example of thin system with a lack of length scale separation in the through-plane direction.

A GDL is generally treated with a hydrophobic fluoropolymer so as to render it hydrophobic on the grounds that this improves the PEMFC performances (see Section 4.4). Water that forms in the CL (a porous layer adjacent to the GDL) should be transported through the GDL without blocking the gas transport across the GDL. Hence, roughly, the problem is to evacuate through the GDL the water that forms in excess in the CL while minimizing the impact of liquid water in the pores on the gas access to the CL.

Water invasion in an initially dry hydrophobic porous medium is a drainage process where the invading nonwetting fluid is liquid water and the displaced wetting fluid is gas. Water invasion flow rates are sufficiently low in a PEMFC for the displacement to be analyzed as a quasistatic displacement; see Rebai and Prat (2009) for a discussion. According to Lenormand et al. (1988), the type of displacement is characterized by the formation of a fractal pattern, referred to as capillary fingering. This is illustrated in Figure 4.7. Standard continuum models, based on the concept of relative permeability and retention curve, are unable to simulate correctly this type of displacement for which there is no representative elementary volume (REV) since the phase (liquid–gas) distribution is fractal. Thus, here, there are two good reasons for not using the continuum approach to porous media: (1) the length scale separation is poor for the dry material, and (2) the two-phase invasion pattern is not compatible with a standard continuum modeling.

Among the alternatives to continuum modeling (Perré 2011), pore network (PN) models are particularly well adapted to study two-phase flows in thin systems. As discussed in Joekar-Niasar et al. (2010), they are much less computational time demanding than direct simulations while sufficiently accurate for obtaining valuable results. Thus, here, we consider that the GDL can be represented as a usual network or pores connected by throats. For simplicity, structured networks, that is, square or cubic, are considered.

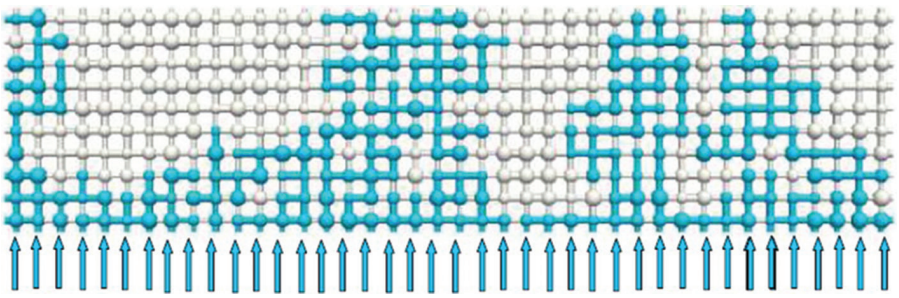

FIGURE 4.7 Two-dimensional invasion pattern in a model GDL. The liquid in blue is injected from the bottom. Liquid breakthrough occurs at the layer's top edge.

It turns out that the mechanisms leading possibly to the flooding of GDL are not completely delineated. There are two main options: phase change phenomenon (condensation) and invasion directly in liquid phase from the CL. Evaluation of the relative significance of each mechanism is still under study. Here, we simply discuss one aspect of the second scenario, that is, invasion in liquid phase from the adjacent CL. Since the expected invasion regime is capillary fingering, the invasion percolation algorithm (Wilkinson and Willemsen 1983) is well adapted to simulate the water invasion in the network. The distinguishing feature that must be discussed is the boundary condition at the inlet. The traditional boundary condition, used, for example, to compute the capillary pressure curve, is to consider that the porous layer is in contact with a liquid reservoir at uniform pressure. This traditional boundary condition seems not to be adapted to the GDL invasion problem.

It is envisioned in fact that water that forms in the adjacent CL as a result of the electrochemical reaction is produced not everywhere throughout the CL but at discrete locations (El Hannach et al. 2011). Physically, this would mean that water is produced in independent point sources within the CL. As a result of the growth of water clusters from these point sources, water will access the adjacent GDL through a series of independent points at the interface between the CL and the GDL (Ceballos and Prat 2010, Ceballos et al. 2011, and references therein). This leads to the problem of the quasistatic displacement of a wetting fluid (the gas phase in the PEMFC problem) by a nonwetting one (water in the PEMFC problem) in a porous layer with the nonwetting fluid entering in the porous layer at the inlet through a series of independent entry points. Of primary interest is then the number of droplets forming at the outlet as a function of the layer thickness and the fraction n_i of injection points at the inlet. This is because the occurrence of several droplets is generally observed in operating fuel cells. The density of droplets at the GDL surface is in fact one of the available observable data for this system. It is therefore important that models lead to results consistent with these data. The droplets correspond to the breakthrough points at the outlet (see Figure 4.8).

As an example, consider the case where all pores at the inlet are injection points ($n_i = 100\%$). This leads to the results depicted in Figure 4.9 where N_{BT} is the number of breakthrough points at the inlet. Four regions are distinguished depending on the thickness N_z of the system: (1) the ultrathin system region when the system is sufficiently thin, that is, $N_z \leq 15$, (2) the thin system characterized by a power law for larger thicknesses right after the region of ultrathin systems, (3) a transition region between the power law region and region #4, and (4) the thick systems characterized by only one breakthrough point (plateaus on the right-hand side in the figure, noticing that only the beginning of plateaus is shown).

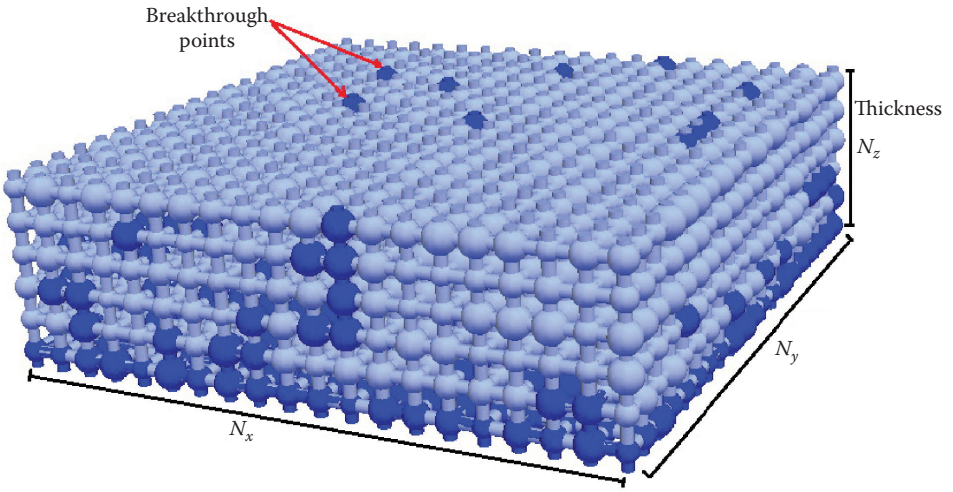

FIGURE 4.8 Illustration of the multiple breakthrough problems at the outlet of a thin porous layer.

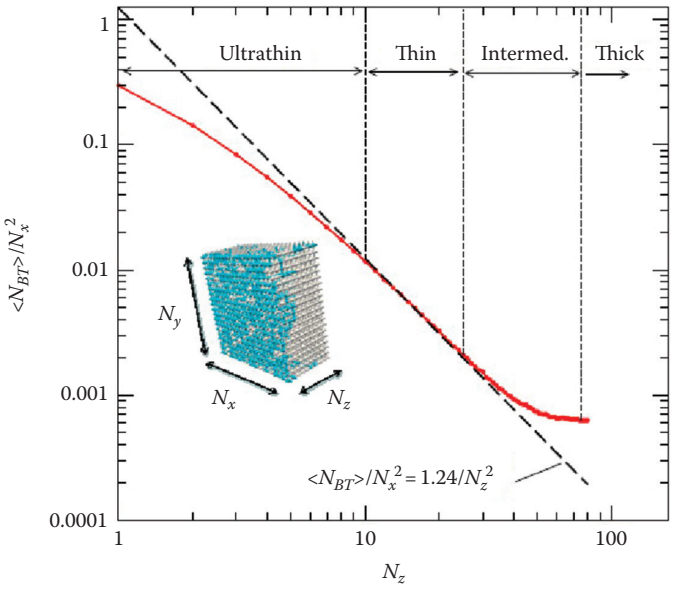

FIGURE 4.9 Probability that an outlet bond is a breakthrough point as a function of network thickness N_z when all inlet bonds are injection bonds (n_i = 100%). These results were obtained considering 40 × 40 × N_z cubic networks, Ceballos et al. (2011).

A major conclusion is that the behavior of thin systems is distinct from thicker ones. There is eventually only one breakthrough point in sufficiently thick systems because of the successive merging of various liquid paths emanating from the various injection points. By contrast, several breakthrough points are observed in sufficiently thin systems. As discussed in Ceballos and Prat (2010), the number of breakthrough points for a layer of thickness similar to a GDL thickness is consistent with the droplet density observed in an operating PEMFC (Zhang et al. 2006).

Further results are presented in Ceballos et al. (2011) and Ceballos and Prat (2013).

In summary, the illustrative result presented in this section first shows that thin system behavior can be markedly different from thicker systems. The second major conclusion is that PN models can be very well adapted to the studies of thin systems. They can offer an optimal trade-off between accuracy (no issue of length scale separation) and computational effort. (The results shown in Figure 4.9 are obtained from ensemble averaging over many realizations. It is impossible in practice to perform a similar statistical study from direct simulations, i.e., LBM simulations, etc., owing to the much higher computational times.)

4.4 MIXED WETTABILITY

Mixed wettability can be an important feature in thin porous media. Mixed wettability refers to systems in which the wettability properties change spatially within the pore space. For instance, some regions of the medium can be hydrophobic, whereas others are hydrophilic. The wettability properties can also change in time as the result, for example, of the interaction with the liquid. A system originally entirely hydrophobic can evolve into a system of a mixed wettability or even become entirely hydrophilic. The change can have a great impact on the transport properties of a thin porous medium. The control of wettability properties can therefore be a crucial issue. This is illustrated in this section from examples related to the PEMFC water management issue.

As discussed in Section 4.3, water invasion in a hydrophobic porous medium in the quasistatic limit that is expected to prevail for flows in fuel cells leads to capillary fingering. By contrast, the invasion pattern is compact in a fully hydrophilic medium (Chapuis et al. 2008). The capillary

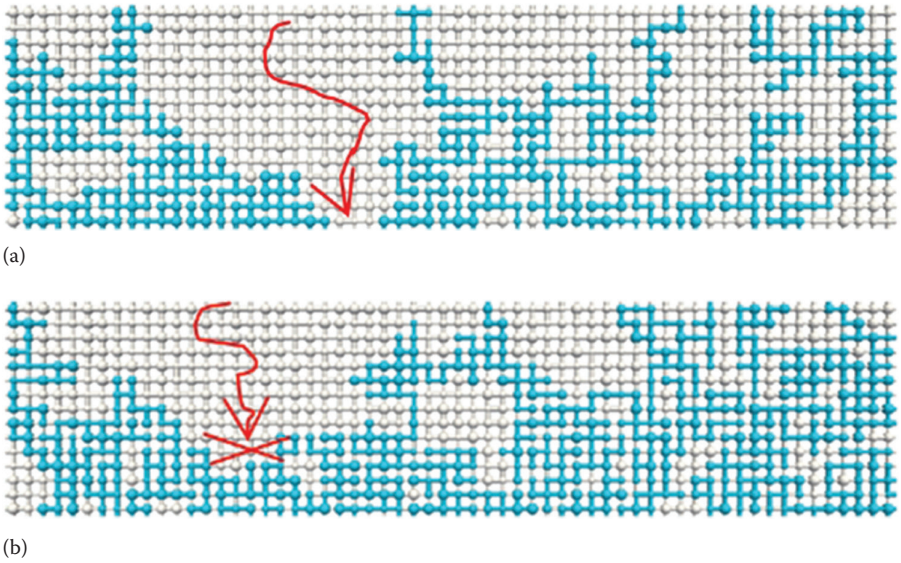

FIGURE 4.10 Schematic illustration of the impact of a change in wettability. Liquid water (in blue) is injected at the bottom and invades the layer up to breakthrough. The red arrow symbolizes the gas access between the top and bottom edges. The change in wettability in (b) leads to a more compact invasion pattern forming a barrier to the gas access.

fingering pattern leaves many pores not invaded by the liquid and therefore available for the gas transport. By contrast, the compact invasion pattern blocks rapidly the gas transport across the GDL. This explains why a hydrophobic GDL is a better option.

Suppose now that the layer is entirely hydrophobic when the system starts. Then as illustrated in Figure 4.10a, the gas access across the layer is good because, as just discussed, the capillary fingerings leave many pores not occupied by the liquid water (the gas access is in fact much better than suggested by Figure 4.10a because the gas access is much better in a 3D network than in the 2D network shown in Figure 4.10a). Suppose a progressive loss of hydrophobic agent carpeting initially the pore walls. Furthermore, assume that the loss of hydrophobic agent is not uniform but randomly localized. Thus, for simplicity, we assume that the wettability can be characterized by the fraction f of pores that are hydrophilic. The fraction of pores still hydrophobic is therefore $1\text{-}f$. As the result of the increase in the fraction of hydrophilic pores f, the invasion pattern becomes eventually more compact, which can severely limit the gas access. This is schematically illustrated in Figure 4.10b.

As reported in Pulloor Kuttanikkad et al. (2011) and Ceballos and Prat (2013), the somewhat surprising result is that the impact of hydrophobic loss is strongly nonlinear according to this model. This is illustrated in Figure 4.11, which shows the variation of the apparent overall diffusion conductivity G_D of the whole layer as a function of f. G_D is defined by

$$J = AG_D\Delta C, \tag{4.8}$$

where

J is the diffusive mass rate through the porous layer when a concentration difference ΔC is applied across the porous layer
A is the in-plane cross-sectional area of the porous layer
G_D is computed numerically using a PN model

The concentration C_0 is imposed in the first plane of pores occupied by the gas phase at the gas inlet (note that the inlet for the gas phase corresponds to the outlet for liquid water), and the

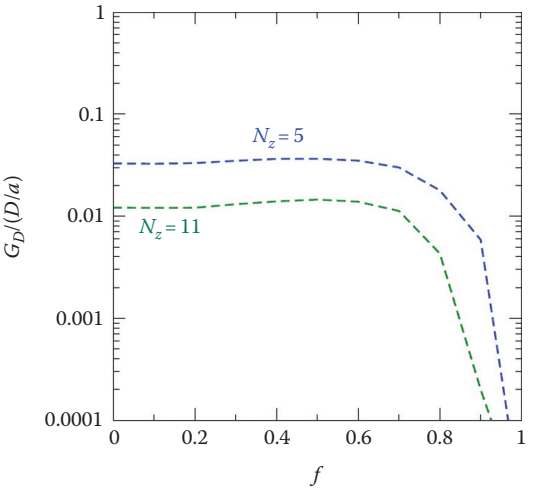

FIGURE 4.11 Variation of gas-phase diffusive conductance G_D as a function of fraction of hydrophilic pores. The computations were performed over a $20 \times 20 \times N_z$ network (N_z is the porous-layer thickness measured in lattice spacing unit). D is the binary diffusion coefficient in the free fluid, and a is the lattice spacing (distance between two pores).

concentration $C_0 - \Delta C$ in each pore occupied by the gas at the gas outlet. J is computed from the solution of the diffusion problem over the gas phase under steady-state condition. The computation is made at breakthrough, that is, at the end of water invasion. The results shown in Figure 4.11 were obtained using the invasion percolation algorithm with the reservoir condition at the water inlet for simulating the water invasion. One can refer to Ceballos and Prat (2013) for more details and to Pulloor Kuttanikkad et al. (2011) as regards the method of solution of the diffusion problem over the network.

As can be seen from Figure 4.11, the gas access is in fact not affected by the change in wettability as long as the fraction f of hydrophilic pores is lower than about 0.7. As discussed in Pulloor Kuttanikkad et al. (2011) and Ceballos and Prat (2013), this value corresponds to the percolation threshold of the hydrophilic PN. Thus, here, a significant change in wettability, that is, f varying from 0 to 0.7, has no effect on the gas access. This can be explained looking at the variation of the water invasion pattern with f as reported in the two aforementioned references. By contrast, the change in wettability has a major impact on gas accesses for f above 0.7, that is, when the network becomes sufficiently hydrophilic for the invasion pattern to become increasingly compact.

The analysis of the change in wettability can also help to analyze aging problems in PEMFC (Pulloor Kuttanikkad et al. 2011).

Naturally, the change in wettability of a given system can be different from that considered in this simple model. For example, the change can occur at smaller scales than the pore scale. The hydrophilic pore localization can also be not random with, for instance, a greater probability in the middle of the layer than at the periphery. The detailed experimental characterization of wettability variation at the scale of the microstructure is in fact an open issue as briefly discussed in Section 4.9.

4.5 THIN POROUS-LAYER ASSEMBLY: THE CONCEPT OF THIRD LAYER

Thin porous media are often made of several layers of different properties. For example, the GDL discussed in the previous sections is often used in conjunction with another thin porous medium called the microporous layer (MPL) (Weber and Newman 2005). The bilayer gas diffusion medium (GDM) consists of a coarse GDL coated with a fine MPL. Compared to the GDL, the MPL, composed of carbon powder and hydrophobic agent, has smaller pores and a lower porosity. It has been

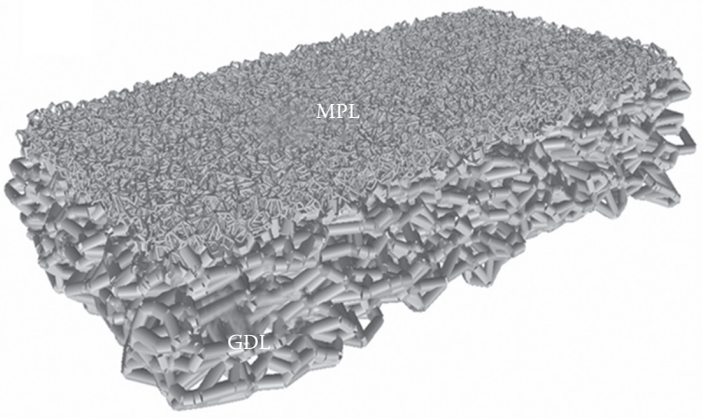

FIGURE 4.12 Computer-generated model of bilayer thin porous medium.

shown that using the bilayer GDM can increase the fuel cell performance, especially at high current density (Qi and Kaufman 2002). This type of system is illustrated in Figure 4.12.

Diapers are another example of multilayer thin porous media of practical interest (Diersch et al. 2011).

There is first a geometry problem. Owing to the fabrication processes, a multilayer thin porous medium is rarely a simple juxtaposition of different layers. Often there is interpenetration between the various layers (see Figure 4.13b). For instance, the grains of the carbon powder used to make the MPL can penetrate into the larger pores of the GDL. This leads to envision a bilayer thin porous medium as in fact as a three-layer porous medium, where the third layer is the transition region at the interface between the two layers. The extension of the concept to multilayer thin porous media is straightforward. We only consider bilayer systems in this chapter.

An illustrative example is given in Figure 4.13. The technique to generate this type of bilayer cellular porous medium is a simple extension of the methods described in Gostick (2013) for a single layer. As can be seen from Figure 4.13a, the interface between the two layers forms here an ultrathin intermediate porous layer with pores of intermediate size.

The importance of the third layer can be also illustrated as follows. As depicted in Figure 4.14, suppose the presence of a defect in the transition region between the two layers. The defect can be a single big pore or a collection of big pores larger than the pores in both the adjacent fine and coarse porous layers or a collection of hydrophilic pores. As an example, consider again the quasistatic invasion process of liquid water in the system depicted in Figure 4.14 assuming hydrophobic pores everywhere except in the defect region where the pores are hydrophilic. The invasion capillary threshold of the pores in the defect being smaller than the ones of other pores, the result is the preferential filling

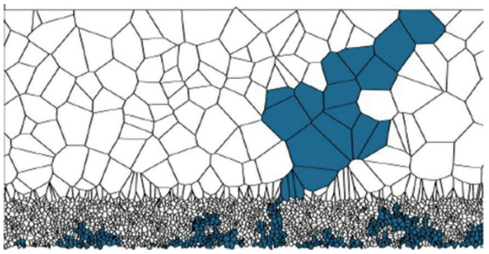

(a)

FIGURE 4.13 Bilayer thin porous medium model. (a) A porous layer with large pores is in contact with a layer with smaller pores. The interface between the two layers forms an intermediate porous layer with pores of intermediate size. The blue cells are pores invaded by a nonwetting fluid injected at the bottom of the bilayer system. (*Continued*)

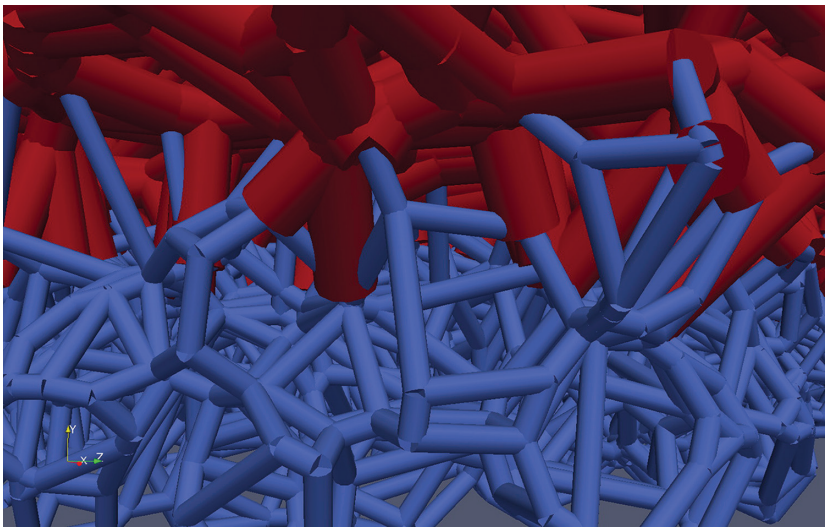

(b)

FIGURE 4.13 (*Continued*) Bilayer thin porous medium model. (b) Illustration of the interpenetration between a fibrous layer with small pores (in blue) and a coarser fibrous layer (in red).

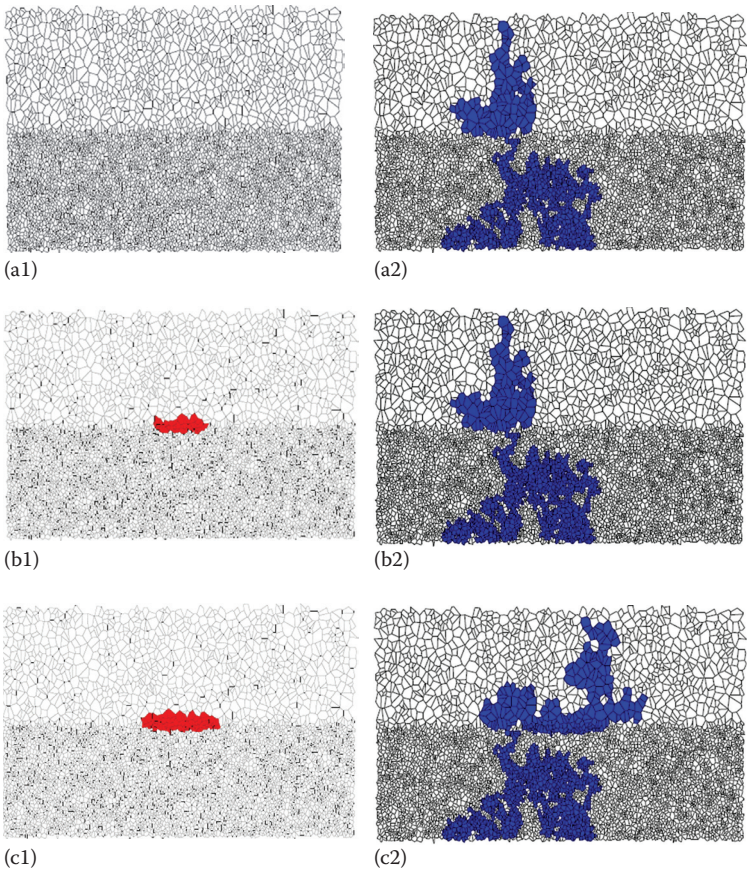

(a1) (a2)

(b1) (b2)

(c1) (c2)

FIGURE 4.14 Influence of a defect (in red) on the invasion pattern at breakthrough (in blue) in a bilayer thin porous system. Water (in blue) is injected at the bottom. (*Continued*)

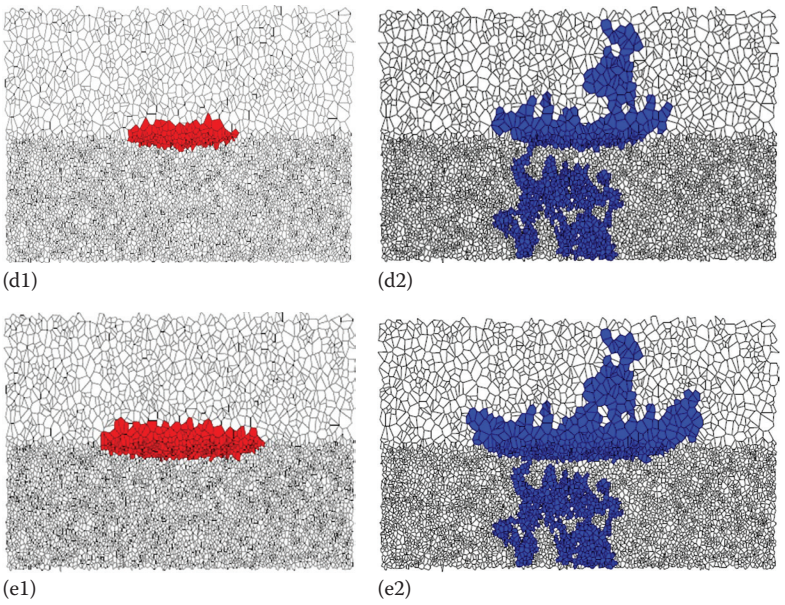

FIGURE 4.14 (*Continued*) Influence of a defect (in red) on the invasion pattern at breakthrough (in blue) in a bilayer thin porous system. Water (in blue) is injected at the bottom.

of the defect. This is illustrated in Figure 4.14 for a defective region of increasing size. The defective region is shown in red in Figure 4.14. The defective zone was created in this example by positioning an ellipse of increasing size at the interface between the two media. All pores contained in the ellipse were considered as hydrophilic. We again consider a slow (quasistatic) invasion from the bottom edge and use the standard invasion percolation algorithm. To take into account the defective zone, we simply impose a very small capillary invasion threshold in all pores located in the defective zone. This leads to the preferential invasion of the defective zone as soon as the liquid reaches the periphery of the defective zone. As can be seen from Figure 4.14, the presence of the defect can first modify the location of the breakthrough point (e.g., compare Figure 4.14a and c).

Suppose we are again interested in the gas transfer. The partial flooding of the third layer can obviously have a detrimental consequence on the gas access between the top and bottom edges of system and thus the performance of the system using this type of bilayer thin porous medium. The gas transfer is characterized from the computation of the overall gas diffusion conductivity similarly as in Section 4.4 (see Equation 4.8 and the associated text in Section 4.4). The results corresponding to the various patterns shown in Figure 4.14 are presented in Table 4.1.

TABLE 4.1
Liquid Saturation *(S)* and Overall Gas Diffusion Conductivity Corresponding to the Various Patterns Shown in Figure 4.14. G_{Dref} Is the Conductivity in the Absence of Defect (Figure 4.14a)

Pattern	S	G_D/G_{Dref}
Figure 4.14a	0.142	1
Figure 4.14b	0.142	1
Figure 4.14c	0.176	0.87
Figure 4.14d	0.161	0.96
Figure 4.14e	0.204	0.79

As expected, the gas conductivity globally decreases as the defect size increases. However, the variation can be nonmonotonous as indicated in Table 4.1. This can be easily explained from the variation of saturation and the liquid invasion pattern. For example, compare the invasion pattern in the bottom fine layer between Figure 4.14c and d. The fine layer is clearly less invaded in Figure 4.14d compared to Figure 4.14c. This explains the increase in the gas diffusion conductivity between the situation corresponding to Figure 4.14c and the one corresponding to Figure 4.14d. The change in the invasion pattern is a consequence of the change in the capillary invasion threshold occurring in the pores of the fine layer located in the interfacial region between the two layers when they become pores belonging to the defective zone.

In this section, we briefly discussed the concept of third layer, that is, the possible transition region forming the interface between two thin porous layers in contact. The impact of the so-called third layer was illustrated through PN simulations of two-phase flow in the quasistatic limit and the computation of the diffusive transport in the region free of liquid. Naturally, many other transport processes can be of interest, and other modeling techniques are certainly worth considering depending on the process to be studied. Regarding the modeling aspect, the works dedicated to the study of transport phenomena at the interface between two porous media or a porous medium and a free fluid could be a source of inspiration (D'Hueppe et al. 2012, Jamet et al. 2009, and references therein).

4.6 THIN POROUS MEDIA AND LIQUID FILM FLOWS

To illustrate the possible impact of liquid film flows on transfers in a thin porous medium, we consider the problem of slow drying of a thin porous layer initially fully saturated by a wetting liquid. Drying is ubiquitous in industry and one of the most energy-consuming unit operations (Plumb 2000). This holds also for thin porous media. For instance, the teflonization process rendering hydrophobic the GDL evoked in previous sections usually involves a drying step. Drying processes have been the subject of many works. Among the advances made over the last decade is the full recognition that liquid film flows can have a major impact on the drying process (Yiotis et al. 2004, Prat 2007, Chauvet et al. 2009, Yiotis et al. 2012). They notably contribute to significantly extend the duration of the period of intense evaporation, referred to as the constant rate period (Plumb 2000). This is so because the hydraulic connectivity to the surface is maintained via the liquid films, even when the bulk-phase connectivity ends. Also the films can be a vector for transporting species, colloidal particles, ions, etc., up to the surface of porous medium (Camassel et al. 2005).

The fact that the liquid films can extend over a significant region of a drying porous medium is illustrated in Figure 4.15. As can be seen, the liquid film region is by far the region of largest spatial extent in this example.

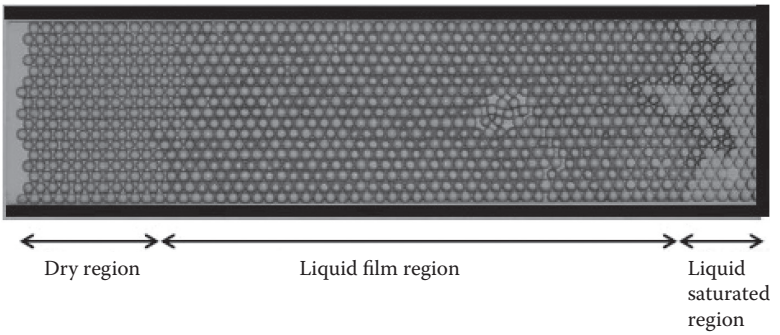

FIGURE 4.15 Phase distribution within a thin porous layer drying from the left-hand side. This medium consists of a monolayer of glass beads sandwiched between two glass plates.

As discussed in Chauvet et al. (2009), the extended liquid films are controlled by the competition between the capillary forces, the viscous forces generated by the liquid flow within the films, and the gravity forces. In a thin medium, gravity forces can be expected to be negligible. Therefore, the extent of the films is expected to be controlled by the competition between viscous forces and capillary forces. According to the currently available model of liquid films in a drying porous medium (Yiotis et al. 2004, Prat 2007), the maximum extent L_f of film regions for a perfectly wetting liquid can be estimated as

$$\frac{L_f}{r} \approx f^{-1} Ca^{-1} \chi^{-3}, \tag{4.9}$$

where

r is a mean pore size
$\chi = 1.885$
$f = 528$
$Ca = 3\mu j/\rho_\ell \gamma$ where j, μ, γ, and ρ_ℓ are the evaporation flux, the liquid dynamic viscosity, surface tension, and liquid density, respectively

A typical evaporation flux for water at the room temperature is on the order of 1 cm/day. This corresponds to $j \approx 10^{-4}$ kg/m^2/s. Application of Equation 4.9 then leads to the result shown in Figure 4.16. In accordance with Equation 4.9, the maximum size of film region varies linearly with the mean pore size. As can be seen from Figure 4.16, L_f varies about between 6 mm and 6 m when the mean pore size varies between 0.1 and 100 μm. Since the thickness of a thin porous medium is typically less than 1 mm in many applications, thus shorter than L_f, this result shows that the hydraulic conductivity to the surface of porous medium will be maintained via liquid films over practically all drying duration in such systems. Thus, it is expected that slow drying of thin porous media will be essentially characterized by a long constant rate period over which all pores will be eventually invaded in the bulk by the gas phase. After this constant rate period, a very short falling rate period corresponding to the evaporation of liquid films still present all over the pore space at the end of the constant rate period is expected. The falling rate period is expected to be short for two reasons: (1) the liquid mass corresponding to the films is small compared to the mass of liquid initially present in the medium, and (2) the external mass transfer length scale (the mass external

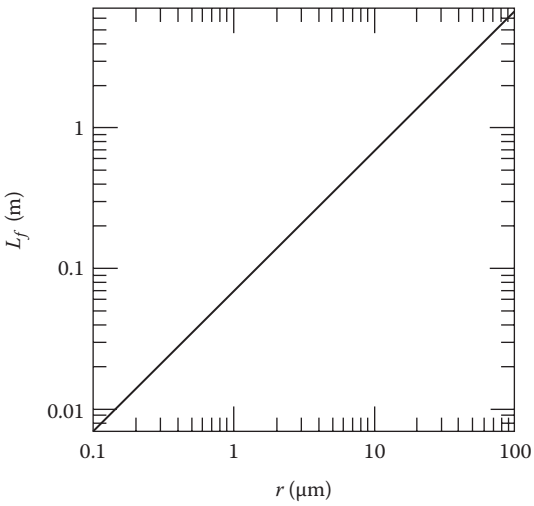

FIGURE 4.16 Film region maximum size as a function of pore mean radius for an evaporation flux of 1 cm/day.

boundary layer typically) is typically greater than the thickness of the medium (this implies that the mass transfer resistance due to the receding of film tips within the medium is weak compared to the external mass transfer resistance).

It must be pointed out that Equation 4.9 gives an overestimate of the film region maximum size. Depending on the contact angle, pore space geometry, evaporation rate (the film extent is inversely proportional to the evaporation rate), etc., the extent of film regions might be less than anticipated from Equation 4.9. However, this does not change the main conclusion since L_f in Figure 4.16 is much greater than the expected thickness of typical thin porous media.

In summary, while liquid films can be often ignored in thick porous media because the main phases of drying are dominated by the changes in the hydraulic connectivity of the network formed by the fully saturated pores, the situation can be completely different in thin porous media with drying kinetics entirely controlled by the liquid films.

4.7 IMPACT OF A THIN SALT CRUST ON DRYING

Here, we consider the special case where the liquid solution saturating a (thick) porous medium is an aqueous solution containing a dissolved salt (sodium chloride in what follows). The considered situation is sketched in Figure 4.17. As discussed in Hidri et al. (2013), this is a subject of interest in relation with soil physics, the underground storage of CO_2, civil engineering issues, and the protection of our cultural heritage, the latter because of the damages that can be induced in a porous material by the salt crystallization process. In the context of this chapter, this particular drying situation is interesting because the drying process can result in the formation of a thin porous medium at the top of the underlying porous material. Thus, this is an example of self-generation of a thin porous medium on top of a thick porous medium. The fact that the precipitation of the salt occurs on top, that is, at the evaporative surface of the porous medium, is well understood (Hidri et al. 2013 and references therein). The ions are transported by the flow induced in the liquid phase by the evaporation process. This flow is directed toward the evaporation surface where the ions accumulate until the ion concentration marking the onset of crystallization is reached. Then the salt precipitation continues, and salt efflorescence develops at the porous medium surface. As reported in Eloukabi et al. (2013) and Dueñas Velasco et al. (2013), two main types of efflorescence can be distinguished, namely, crusty and patchy. As sketched in Figure 4.17b, the crusty efflorescence forms a thin salt crust eventually covering all the surface of the porous medium. By contrast, the patchy efflorescence only partially covers the porous medium surface and is characterized by the formation of well-individualized crystallized salt structures. The impact of the two types of efflorescence on evaporation is quite different. The patchy efflorescence leads to evaporation rates comparable to the ones observed for pure water, whereas, as shown in Figure 4.18, the development of salt crust severely reduces the evaporation rate.

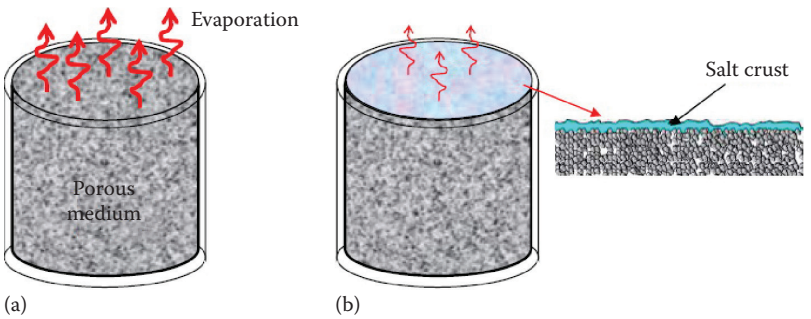

FIGURE 4.17 Sketch of drying situation discussed in this section. (a) Situation before crystals form at the surface and (b) sample with developed salt crust at the top surface.

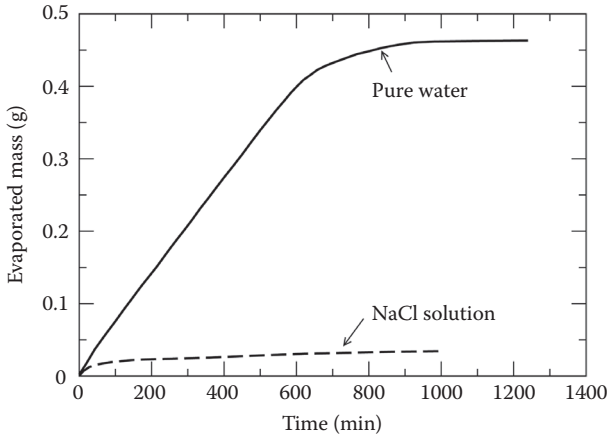

FIGURE 4.18 Evaporated mass as a function of time. Comparison between a sample initially saturated with pure water (solid line) and the same sample initially saturated with a nearly saturated NaCl solution (dashed line). These results were obtained with a porous medium consisting of sintered glass beads. The porous cylinder is 10.0 mm ± 0.2 mm long and has a diameter of 10.0 mm ± 0.25 mm. The pore sizes are distributed in the range 1.0–1.6 μm; see Dueñas Velasco et al. (2013) for more details.

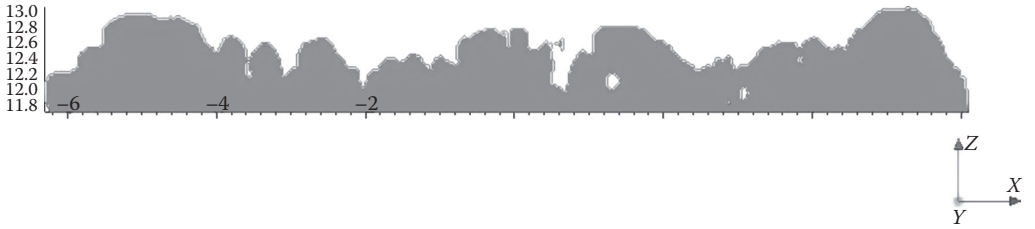

FIGURE 4.19 Topography obtained by x-ray tomography along a vertical slice of the crust formed in the experiment described in the caption of Figure 4.18; the figures along the *z*-axis are in millimeters; see Dueñas Velasco et al. (2013) for more details.

The crust is in fact not compact but forms a thin porous medium. As shown in Figure 4.19, the average thickness of the crust formed in the experiment discussed in this section is on the order of 500 μm. Crust internal porous structure is not known, and its characterization is one the numerous open questions in this field.

In summary, the salt crust discussed in this section has a great impact on the drying process. The evaporation rate is considerably reduced compared to pure water drying. The crust is an example of thin porous medium, whose internal porous structure is in fact not known. This piece of information is, however, crucial if one wishes to explain the observed evaporation rate reduction. More widely, this poses the question of the characterization of thin porous media. This point is briefly discussed in more detail in Section 4.9.

In addition to the previously mentioned references, the reader interested in this problem can also refer to Veran-Tissoires et al. (2012a,b), Veran-Tissoires and Prat (2014), Gupta et al. (2014), and references therein.

4.8 BRIEF REVIEW OF OTHER SITUATIONS INVOLVING TPM

In addition to the examples considered in previous sections, thin porous media are encountered in many other situations. Some of them are evoked in this section. Porous-layer coatings are a good example of thin porous media developed for improving heat transfer performance

(Liter and Kaviany 2001). The porous layers considered in Liter and Kaviany (2001) are typically formed by conical particle stacks. Each cone is less than 10 particle diameters in height. This type of coating can be very effective with an enhancement of the critical heat flux by a factor of three compared to a flat surface.

Another problem having received quite a lot of attention is the absorption of droplets in thin media (e.g., printing). The last stage of the ink-jet printing process, the spreading and solidification of droplets on a substrate, determines to a large extent the final print quality. In this context, the development of numerical codes aiming at simulating the printing process can be regarded as an important development tool for next generations of the ink-jet printing technology (Markicevic and Navaz 2010, Siregar et al. 2013, and references therein). Naturally, there are also basic questions that need to be answered (Shikhmurzaev and Sprittles 2013).

Beyond the droplet problem, the various operations involved in the processing of paper are also a source of interesting problems (Iliev et al. 2012, Karlsson and Oyj 2000, and references therein).

Hygiene products, such as diapers and wipes, are also a subject of investigations (Mirnyy et al. 2013). Often the transport problem in a thin porous medium cannot be decoupled from the problem of the deformation of the porous layer(s) (Mirnyy et al. 2013). This is often the case with the paper or hygiene product–related problems. Deformation of the layers can be also an issue in PEMFC (Lin et al. 2008). Owing to their small thickness, thin porous media can often deform easily. Thus, deformation of thin porous media can be regarded as a quite important issue, not only from a purely mechanical standpoint (Taber 1992), but also because of the impact of deformation on transport phenomena.

Textiles and associated processes are also a source of interesting thin porous media–related problems. This has long been identified (Cassie 1944), and this field is still a very active domain of innovative research (Yang et al. 2010). Thin porous media are also encountered in thermal insulation systems (Fricke et al. 2006, Arambakam et al. 2014).

Some bioengineering-related problems can also be considered as good examples of thin porous media problems. This notably includes the porous coatings used in order to increase the attachment of bone to metal implants (Hanzlik and Day 2013) or biomechanics problem at the scale of arterial walls, which can be addressed using techniques similar as for other classes of thin porous media (Chung and Vafai 2013).

This short list is of course far from being exhaustive.

4.9 RESEARCH OPPORTUNITIES

Research opportunities in the domain of thin porous media are numerous for several reasons. Firstly, specific applications, for example, fuel cells, filters, and hygiene products, are of course themselves often very interesting. Secondly, the field is king of emerging as a well-identified research field. This means that trying to identify theoretical, numerical, or experimental techniques or specific problems of common interest to various applications involving thin porous media is recognized as a specific field of interest. For instance, tools developed for the study of a specific application can be of wider interest and worth considering for other situations involving thin porous media. Thirdly, the fact that the porous medium is thin can be an advantage. For instance, direct numerical simulations at pore scale can be performed only over a small region of an ordinary porous sample because of the computational cost. When the system is only a few pore sizes thick, the use of direct simulations can be a possible option for understanding and characterizing transport processes at the scale of the whole system, that is, over its entire thickness. The same holds of course for less computational time demanding techniques, such as PN simulations. This was illustrated in Section 4.3. This is in contrast with the ordinary porous media where the PN simulations are often used only to compute the macroscopic parameters, that is, the relative permeabilities or the retention curve, involved in the Darcy's scale equations (Blunt et al. 2002). Similarly, the modern imaging techniques, such as x-ray microtomography, can image a given thin material over its whole thickness (Rolland du Roscoat et al. 2007).

There are many open scientific problems associated with the study of thin porous media. Some of them are in fact not specific to thin porous media. For example, fibrous materials are often encountered in thin porous systems. The GDLs of PEMFC, textiles, and paper are just three obvious examples. Yet the question of the modeling of two-phase flow in fibrous materials using the PN technique is generic and not specific to thin porous media. Despite recent advances (Gostick 2013), this is still a subject of controversy. The microstructure of a fibrous material is obviously quite different from the microstructures of mineral rocks or packings of particles mostly considered in previous works on PN modeling. The applicability of traditional PN modeling concepts to fibrous materials is therefore a question.

Naturally, there are also many specific questions. For example, it is often not possible to use an experimental setup designed for ordinary porous samples in order to characterize a thin porous medium. An example is the characterization of the retention curve of GDL. Specific setups must be developed (Gostick et al. 2008). A yet not-well-solved issue is the characterization of wettability of thin porous media, especially when the system is of mixed wettability. GDLs are most probably an example of thin porous media of mixed wettability in spite of its treatment by a hydrophobic agent. Methods can be used to characterize its mean apparent contact angle (Gurau et al. 2006). By contrast, although this piece of information would be extremely useful to modelers, the experimental characterization of the wettability variations at smaller scales within the GDL is out of reach for the moment.

On the modeling side, the lack of length scale separation over the thickness can require the development of specific models. When the lack of length scale separation is not an issue, the fact that the thickness is much smaller than the other dimensions can motivate specific modeling upscaling studies (Feng and Weinbaum 2000, Qin and Hassanizadeh 2014). Often there are also in-plane heterogeneities that need appropriate modeling to be taken into account properly.

In some multilayer thin systems, such as a PEMFC, a continuum approach can be acceptable in one layer, whereas another approach, PN modeling or direct simulation for instance, is more suitable in an adjacent layer. This type of situation requires combining models expressed at different scales. As mentioned in Section 4.2, this can be done using mixed or hybrid numerical methods; see, for instance, Sun et al. (2012) and references therein.

In brief, thin porous media can be regarded as a widely open field for innovative experimental, numerical, and theoretical studies. To a certain extent, thin porous media can be even regarded as a (virtual) laboratory for testing innovative methods whose development can be in fact motivated by the studies of thick/ordinary porous media. A given method can be tested with reduced computational times owing to the small size of thin porous media in the through-plane direction.

4.10 CONCLUSIONS

Thin porous media are first interesting because they often behave differently than thicker porous media. This was illustrated through the droplet formation problem discussed in Section 4.3. This is often so because some physical phenomena whose impact is weak or even negligible in an ordinary porous medium can become dominant in a thin medium. Liquid films in drying are an example (see Section 4.6).

As discussed in this chapter, thin porous media are encountered in many applications. Each application, for example, PEMFC, paper printing, porous coatings, insulation, and filters, possesses its own specificities, scientific questions, and bottlenecks.

However, thin porous media are also emerging as a specific research area encompassing the various applications. This is so because experimental, numerical, and theoretical problems of common interest can be identified. The possible lack of length separation over the medium thickness, the problem of coupling models at different scales, the need of developing models taking advantage of the small ratio between the medium thickness and the other spatial dimensions, the inherent in-plane and through-plane heterogeneities, the possible existence of defects between layers in multilayer thin media, and swelling and shrinking phenomena are just a few examples of generic problems.

Thin porous media are also in fact of wider interest because they offer excellent opportunities to develop and test innovative methods. Hybrid methods, that is, coupling models at various scales, are an example.

ACKNOWLEDGMENTS

The first author (M.P.) is thankful to the students and colleagues he has worked with over the years on thin porous media–related problem. Their contribution is greatly appreciated. Works on PEMFC have been developed in close collaboration with J. Pauchet from CEA. His contribution and support are also greatly appreciated. Financial supports for PEMFC-related studies from GIP ANR (Project No. ANR-06-PANH-022-02 "Chameau"), CEA, and CNRS are gratefully acknowledged.

REFERENCES

Arambakam, R., H. Vahedi Tafreshi, and B. Pourdeyhimi. 2014. Modeling performance of multi-component fibrous insulations against conductive and radiative heat transfer. *International Journal of Heat and Mass Transfer* 71: 341–348.

Barbir, F. 2005. *PEM Fuel Cells: Theory and Practice.* Elsevier Academic Press, Amsterdam, the Netherlands.

Blunt, M.J., M.D. Jackson, M. Piri, and P.H. Valvatne. 2002. Detailed physics, predictive capabilities and macroscopic consequences for pore-network models of multiphase flow. *Advances in Water Resources* 25: 1069–1089.

Camassel, B., N. Sghaier, M. Prat, and S. Ben Nasrallah. 2005. Ions transport during evaporation in capillary tubes of polygonal cross section. *Chemical Engineering Science* 60: 815–826.

Cassie, A.B.D. 1944. Physics and textiles. *Reports of Progress in Physics* 10: 141–171.

Ceballos, L. and M. Prat. 2010. Invasion percolation with multiple inlet injections and the water management problem in proton exchange membrane fuel cells. *Journal of Power Sources* 195: 825–828.

Ceballos, L. and M. Prat. 2013. Slow invasion of a fluid from multiple inlet sources in a thin porous layer: Influence of trapping and wettability. *Physical Review E* 87: 043005.

Ceballos, L., M. Prat, and P. Duru. 2011. Slow invasion of a nonwetting fluid from multiple inlet sources in a thin porous layer. *Physical Review E* 84: 056311.

Chapuis, O., M. Prat, M. Quintard, E. Chane-Kane, O. Guillot, and N. Mayer. 2008. Two-phase flow and evaporation in model fibrous media. Application to the gas diffusion layer of PEM fuel cells. *Journal of Power Sources* 178: 258–268.

Chauvet, F., P. Duru, S. Geoffroy, and M. Prat, 2009, Three periods of drying of a single square capillary tube. *Physical Review Letters* 103: 124502.

Chauvet, F., S. Geoffroy, A. Hamoumi, M. Prat, and P. Joseph. 2012. Role of gas in capillary filling of nanoslits. *Soft Matter* 8: 10738.

Chung, S. and K. Vafai. 2013. Low-density lipoprotein transport within a multi-layered arterial wall-effect of the atherosclerotic plaque/stenosis. *Journal of Biomechanics* 46: 574–585.

D'Hueppe A., M. Chandesris, D. Jamet, and B. Goyeau. 2012. Coupling a two-temperature model and a one-temperature model at a fluid-porous interface. *International Journal of Heat and Mass Transfer* 55: 2510–2538.

Diersch, H.-J.G., V. Clausnitzer, V. Myrnyy, R. Rosati, M. Schmidt, H. Beruda, B.J. Ehrnsperger, and R. Virgilio. 2011. Modeling unsaturated flow in absorbent swelling porous media: Part 2. Numerical simulation. *Transport in Porous Media* 86: 753–776.

Dueñas Velasco, M., P. Duru, M. Marcoux, and M. Prat. 2013. Efflorescence fairy ring and salt centripetal colonization at the surface of a drying porous medium containing a salt solution. Impact on drying curve. *Proceedings of Eurodrying'2013*, Paris, France, October, 2–4.

Dufrêche, J., M. Prat, and P. Schmitz. 2003. A two–scale domain decomposition method for computing the flow through a porous layer limited by a perforated plate. *International Journal Numerical Methods in Fluids* 42: 623 –639.

Dufrêche, J., M. Prat, P. Schmitz, and J.D. Sherwood. 2002. On the apparent permeability of a porous layer backed by a perforated plate. *Chemical Engineering Science* 57: 2933–2944.

Eikerling, M., A.A. Kornyshev, and A.R. Kucernak. 2006. Water in polymer electrolyte fuel cells: Friend or foe? *Physics Today* 59 (10): 38–44.

El Hannach, M., M. Prat, and J. Pauchet. 2011. Pore network modelling: Application to multiphase transport inside the cathode catalyst layer of proton exchange membrane fuel cell. *Electrochimica Acta* 56: 10796–10808.

Elimelech, M., X. Jia, J. Gregory, and R. William. 1995. *Particle Deposition & Aggregation: Measurement, Modelling and Simulation*. Butterworth-Heinemann, Boston, MA.

Eloukabi, H., N. Sghaier, S. Ben Nasrallah, and M. Prat. 2013. Experimental study of the effect of sodium chloride on drying of porous media: The crusty-patchy efflorescence transition. *International Journal of Heat and Mass Transfer* 56: 80–93.

Feng J. and S. Weinbaum. 2000. Lubrication theory in highly compressible porous media: The mechanics of skiing, from red cells to humans. *Journal of Fluid Mechanics* 422: 281–317.

Fricke, J., H. Schwab, and U. Heinemann. 2006. Vacuum insulation panel-exciting thermal properties and most challenging applications. *International Journal Thermophysics* 27: 1123–1139.

Gostick, J.T. 2013. Random pore network modeling of fibrous PEMFC gas diffusion media using Voronoi and Delaunay tessellations. *Journal of the Electrochemical Society* 160 (8): F731–F743.

Gostick, J.T., M.A. Ioannidis, M.W. Fowler, and M.D Pritzker. 2008. Direct measurement of the capillary pressure characteristics of water–air–gas diffusion layer systems for PEM fuel cells. *Electrochemistry Communications* 10: 1520–1523.

Gupta, S., H. Huinink, M. Prat, L. Pel, and K. Kopinga. 2014. Paradoxical drying due to salt crystallization. *Chemical Engineering Science* 109: 204–211.

Gurau, V., M.J. Bluemle, E.S. De Castro, Y.-M. Tsou, J.A. Mann Jr., and T.A. Zawodzinski Jr. 2006. Characterization of transport properties in gas diffusion layers for proton exchange membrane fuel cells 1. Wettability (internal contact angle to water and surface energy of GDL fibers). *Journal of Power Sources* 160: 1156–1162.

Hanzlik, J.A. and J.S. Day. 2013. Bone ingrowth in well-fixed retrieved porous tantalum implants. *The Journal of Arthroplasty* 28: 922–922.

Hidri, F., N. Sghaier, H. Eloukabi, M. Prat, and S. Ben Nasrallah. 2013. Porous medium coffee ring effect and other factors affecting the first crystallization time of sodium chloride at the surface of a drying porous medium. *Physics of Fluids* 25: 127101.

Iliev, O., G. Printsypar, and S. Rief. 2012. On mathematical modeling and simulation of the pressing section of a paper machine including dynamic capillary effects: One-dimensional model. *Transport in Porous Media* 92: 41–59.

Jamet, D., M. Chandesris, and B. Goyeau. 2009. On the equivalence of the discontinuous one- and two-domain approaches for the modeling of transport phenomena at a fluid/porous interface. *Transport in Porous Media* 78 (3): 419–438.

Joekar-Niasar, V., S.M. Hassanizadeh, and H. Dahle. 2010. Dynamic pore-network modeling of drainage in two-phase flow. *Journal of Fluid Mechanics* 655: 38–71.

Karlsson, M. and M. Oyj. 2000. Drying. Chapter 9 in *Papermaking Science and Technology: Papermaking Part 2*. Published by Finnish Engineers' Association and Tappi. 496 p., Fapet Oy, Helsinki.

Lenormand, R., E. Touboul, and C. Zarcone. 1988. Numerical models and experiments on immiscible displacements in porous media. *Journal of Fluid Mechanics* 189: 165–187.

Levy, T. 1981. Loi de Darcy ou loi de Brinkman? *C. R. Acad. Sci. Paris Série II* 292: 872–874.

Lin, J., W. Chen, Y. Su, and T. Ko. 2008. Effect of gas diffusion layer compression on the performance in a proton exchange membrane fuel cell. *Fuel* 87 (12): 2420–2424.

Litter, S.G. and M. Kaviany. 2001. Pool boiling CHF enhancement by modulated porous-layer coating: Theory and experiment. *International Journal of Heat and Mass Transfer* 44: 4287–4311.

Markicevic, B. and H.K. Navaz. 2010. The influence of capillary flow on the fate of evaporating wetted imprint of the sessile droplet in porous medium. *Physics of Fluids* 22: 122103.

Mirnyy V., V. Clausnitzer, H.J.G. Diersch, R. Rosati, M. Schmidt, and H. Beruda. 2013. Wicking in absorbent swelling porous materials. Chapter 7 in *Wicking in Porous Materials: Traditional and Modern Modeling Approaches*, eds. R. Masoodi and K.M. Pillai. CRC Press/Taylor & Francis, Boca-Raton, FL.

Nield, D.A. and A. Bejan. 1992. *Convection in Porous Media*. Springer-Verlag, NewYork.

Noel, F. 2006. Simulation directe d'écoulements à travers un réseau d'obstacles situé près d'une singularité de paroi. Application à la filtration. PhD dissertation, INPT. University of Toulouse, France.

Perré, P. 2011. A review of modern computational and experimental tools relevant to the field of drying. *Drying Technology* 29 (13): 1529–1541.

Plumb, O.A. 2000. Transport phenomena in porous media: Modeling the drying process. In *Handbook of Porous Media*, ed. K. Vafai. Marcel Dekker, NewYork.

Prat, M. 2007. On the influence of pore shape, contact angle and film flows on drying of capillary porous media. *International Journal of Heat and Mass Transfer* 50: 1455–1468.

Pulloor Kuttanikkad, S., M. Prat, and J. Pauchet. 2011. Pore-network simulations of two-phase flow in a thin porous layer of mixed wettability: Application to water transport in gas diffusion layers of proton exchange membrane fuel cells. *Journal of Power Sources* 196: 1145–1155.

Qi, Z. and A. Kaufman. 2002. Improvement of water management by a microporous sublayer for PEM fuel cells. *Journal of Power Sources* 109: 38–46.

Qin, C.Z. and S.M. Hassanizadeh. 2014. Multiphase flow through multilayers of thin porous media: General balance equations and constitutive relationships for a solid–gas–liquid three-phase system. *International Journal of Heat and Mass Transfer* 70: 693–708.

Rebai, M. and M. Prat. 2009. Scale effect and two-phase flow in a thin hydrophobic porous layer. Application to water transport in gas diffusion layers of PEM fuel cells. *Journal of Power Sources* 192: 534–543.

Rolland du Roscoat, S., M. Decain, X. Thibault, C. Geindreau, and J.-F. Bloch. 2007. Estimation of microstructural properties from synchrotron x-ray microtomography and determination of the REV in paper materials. *Acta Materialia* 55: 2841–2850.

Sangani, A.S. and A. Acrivos. 1982. Slow flow past periodic arrays of cylinders with application to heat transfer. *International Journal of Multiphase Flow* 8: 193–206.

Shikhmurzaev, Y.D. and J.E. Sprittles. 2013. Dynamic contact angle of a liquid spreading on an unsaturated wettable porous substrate. *Journal of Fluid Mechanics* 715: 273–282.

Siregar, D.P., J.G.M. Kuerten, and C.W.M. van der Geld. 2013. Numerical simulation of the drying of inkjet-printed droplets. *Journal of Colloid and Interface Science* 392: 388–395.

Sun, T., Y. Mehmani, and M.T. Balhoff. 2012. Hybrid multi scale modeling through direct substitution of pore-scale models into near-well reservoir simulators. *Energy & Fuels* 26 (9): 5828–5836.

Taber, L.A. 1992. A theory for transverse deflection of poroelastic plates. *Journal of Applied Mechanics* 59: 628–634.

Tsay, R.-Y. and S. Weinbaum. 1991. Viscous flow in a channel with periodic cross-bridging fibres: Exact solutions and Brinkman approximation. *Journal of Fluid Mechanics* 226: 125–148.

Veran-Tissoires, S., M. Marcoux, and M. Prat. 2012a. Discrete salt crystallization at the surface of a porous medium. *Physical Review Letters* 108: 054502.

Veran-Tissoires, S., M. Marcoux, and M. Prat. 2012b. Salt crystallization at the surface of a heterogeneous porous medium. *Europhysics Letters* 98: 34005.

Veran-Tissoires, S. and M. Prat. 2014. Evaporation of a sodium chloride solution from a saturated porous medium with efflorescence formation. *Journal of Fluid Mechanics* 749: 701–749.

Weber, A.Z. and J. Newman. 2005. Effects of microporous layers in polymer electrolyte fuel cells. *Journal of the Electrochemical Society* 152: A677–A688.

Weinan, E. 2011. *Principles of Multiscale Modeling*, 1st edn. Cambridge University Press, Cambridge, U.K.

Whitaker, S. 1999. *The Method of Volume Averaging*. Kluwer Academic Publishers, Dordrecht, the Netherlands.

Wilkinson, D. and J.F. Willemsen. 1983. Invasion percolation: A new form of percolation theory. *Journal of Physics A: Mathematical and General* 16: 3365–3376.

Yang, Y.-L., M.-C. Chuang, S.-L. Lou, and J. Wang. 2010. Thick-film textile-based amperometric sensors and biosensors. *Analyst* 135: 1230–1234

Yiotis, A.G., A.G. Boudouvis, A.K. Stubos, I.N. Tsimpanogiannis, and Y.C. Yortsos. 2004. The effect of liquid films on the drying of porous media. *AIChE Journal* 50 (11): 2721–2737.

Yiotis, A.G., D. Salin, E.S. Tajerand, and Y.C. Yortsos, 2012. Drying in porous media with gravity-stabilized fronts: Experimental results. *Physical Review E* 86: 026310.

Zhang, F.Y., X.G. Yang, and C.Y Wang. 2006. Liquid water removal from a polymer electrolyte fuel cell. *Journal of the Electrochemical Society* 153 (2): A225–A232.

5 Magnetically Stabilized and Fluidized Beds in Science and Technology

A Review

Teresa Castelo-Grande, Paulo A. Augusto, Angel M. Estevéz, Domingos Barbosa, Jesus Ma. Rodríguez, Audelino Álvaro, and Cármen Torrente

CONTENTS

5.1 Introduction 114
5.2 Historical Overview of MSFBs 114
5.2.1 In Biotechnology and Biomedicine 116
5.3 Principles of MSFBs 116
5.4 Particles Used in MSFBs: MSFBs as Porous Media 118
5.5 General Supporting Theory 129
5.5.1 Forces 129
5.5.1.1 Magnetic Forces 130
5.5.1.2 van der Waals Forces 130
5.5.1.3 Electrostatic Forces 131
5.5.1.4 Collisional Forces 131
5.5.1.5 Working Factors 131
5.5.2 Simulations 134
5.6 Heat and Mass Transfer 135
5.7 Applications during the Last Decade 137
5.7.1 Main Biotechnological and Biomedical Applications 137
5.7.1.1 Enzyme or Cell Immobilization/Bioreactions 137
5.7.1.2 Protein Purification/Adsorption 138
5.7.1.3 MSFB Chromatography 139
5.7.1.4 Novel Separations 140
5.7.2 Environmental Applications 140
5.7.3 Catalytic Applications for Process Engineering 146
5.7.4 Other Applications 146
5.8 Conclusion and Future Perspectives 148
References 149

5.1 INTRODUCTION

Since the beginnings of science, separation of particles and substances has been an urged need for mankind. If, in the beginnings, the separation was obviously based on manual processing, nowadays the spectrum of high-tech techniques, devices, and processes used to achieve the separation has reached impressive levels.

Most areas where separation processes are applied demand different characteristics for the process itself. Namely, in chemical engineering processing industries, many times, efficiency is a factor that drives the selection of the separation process, sometimes at the expense of the degree of purity of the final product, while in chemical and pharmaceutical processing industries, the opposite happens several times. The processing of cells, biomedical substances, and/or high-valued biotechnological product substances has always been a major issue in bioengineering and biomedicine, and approximately 5% (in the case of wholesale products) up to 90% (in the case of pharmaceuticals) of the production costs result from downstream processing (Böhm and Pittermann 2000).

Magnetic methods are very attractive concerning the purification and isolation of substances, especially when allied with magnetic tagging and carrying technologies, because they represent a low-cost, effective process (Augusto et al. 2005). This is even more the case when day-after-day new methods to create and manipulate substances to effectively behave as magnetic carriers and tags are successfully demonstrated.

Magnetically stabilized and fluidized beds (MSFBs) exhibit a unique combination of packed-bed and fluidized-bed properties (Hausmann et al. 2000) and are one of the magnetic separation techniques used during the last decades to achieve the purification of substances. In this process, the magnetic particles (magnetic carriers or other type of tags) are placed within the influence of an external magnetic field that is capable to sustain them at flow velocities higher than in packed beds. These magnetic particles present some artificially manipulated affinity that enables them to collect/react with/adsorb/attach the target substance from the media that flows through them. They represent a very important factor for the efficiency of the overall process and so, must be carefully designed. Many of them are porous media, which is important for their performance.

Typical cases of application of magnetically stabilized beds (MSBs) in these areas of research are environmentally oriented, such as aerosol filtration, water treatment, waste removal, and metal ion removal, but also biomedically driven—for example, antibody removal and processing, fermentation, and cell and enzyme immobilization—and include typical chemical engineering processes, such as ammonia synthesis, mass transfer studies and applications, countercurrent contacting gas–solids magnetic valves, coal separation, and catalytic applications, (for example, purification of caprolactam, chlorophenol dehalogenation, and CH_4–CO_2 reforming).

Mass transfer and heat transfer studies, as well as hydrodynamic and more fundamental studies, are also important and will be referred to in this chapter.

In this chapter, we address all the topics detailed earlier, giving a clear insight of MSFBs in what concerns its fundamentals, mass and heat transfer characteristics, historical overview, present and future prospects, details of the particulate media used, and the main applications.

5.2 HISTORICAL OVERVIEW OF MSFBs

The first paper published regarding magnetically fluidized beds (MFBs) was of the authorship of Kirko and Filipov (Kirko and Filipov 1960). Filipov further developed this subject by investigating the behavior of a fluidized bed of iron particles under the influence of a magnetic field and the flow of a water stream and reported it in three subsequent papers (Filipov 1961a,b, 1962) that, complemented by the works of Nekrassov and Chekin (Nekrassov and Chekin 1956, 1961), initiated the investigation and development of the MFBs and MSBs. Figure 5.1 represents the device studied and developed by Filipov. Many publications on the subject have followed this breakthrough, and we may stand out as examples the following ones: Rosensweig (Rosensweig 1979) presented the first

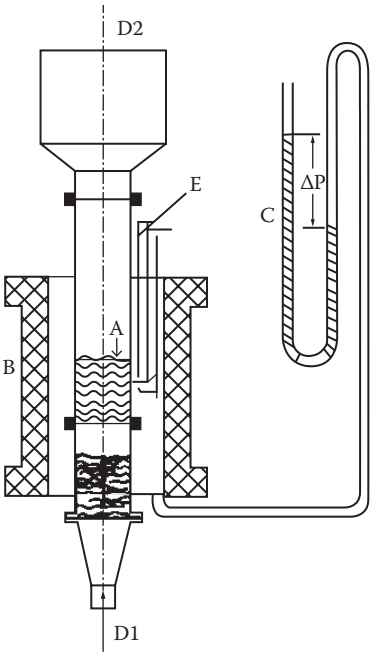

FIGURE 5.1 The first setup of an MFB for the treatment of gases. A, MFB; B, magnetic field generator; C, measure of pressure drop in the bed; D, air flow: 1, entrance, 2, exit; E, periscope. (Based on Filipov, M.V., *Izv. Acad. Nauk. Latv. SSR* 12(173), 47, 1961a; Hristov, J.Y., *Rev. Chem. Eng.*, 18, 295, 2002.)

basic description of MSB and claims that Filipov and other previous researchers apparently did not realize the importance of the orientation and uniformity of the applied field and also neglected the existence of a distinct range of superficial gas velocities between the minimum fluidization velocity and the transition velocity (Liu et al. 1991). Other researchers were very active in the field, and Zrunchev, Popova, and Grozev (Inavov and Grozev 1970; Zrunchev 1975; Zrunchev and Popova 1975) were the first to apply this technique to ammonia synthesis. Some important developments were also reported by Herschler (Herschler 1969) with the application of magnetic fields to liquid metals and to fluidized beds composed of magnetizable particles, also showing that if the magnetic field was created by an alternating current, it would induce a good mixture. Later, papers appeared studying the hydrodynamics of MSB and MFB (Penchev and Hristov 1990; Conta et al. 1998), and even some noncommon techniques like countercurrent contacting gas–solids magnetic valves (Jaraiz 1983; Jaraiz and Estevez 1987). Mass transfer in MSFB has always been a studied topic as MSFB possesses important mass transfer characteristics. Examples of this research may be seen in Neff and Rubinsky (1983) and Arnaldos et al. (1985) that studied the way heat is transferred, or in Arnaldos and Casal (1987) and Terranova and Burns (1991) where heat transfer in liquid and gas fluidized beds is detailed. Regarding applications, papers have been published studying, for example, aerosol filtration (Albert and Tien 1985; Geuzens and Thoens 1988a), bioapplications—like biotechnological applications (Terranova and Burns 1991) or bioreactors (Moffat et al. 1994; Hristov and Ivanova 1999)—and adsorption applications (e.g., waste removal (Nuñez and Kaminski 1998), metal ions removal (Anacleto and Carvalho 1996; Sedzimir 2002; Zouboulis and Katsoyiannis 2002), analytical separations (Siegell 1988; Graves 1992), and bioseparations (Graves 1992; Evans and Burns 1995). Recently, the publication rate on the subject has not diminished, and we may find, for example, publications concerning the study of fundamentals of MSBs and MFBs for coal separation (Fan et al. 2003), biological and medical applications (Özkara et al. 2004; Uzun and Denizli 2006; Al-Qodah and Al-Shannag 2007), environmental applications (Rodriguez et al. 1999;

Estevez et al. 2008), hydrodynamics (Britton et al. 2005), mass transfer studies (Hausmann et al. 2000), and catalytic applications (Graham et al. 2006; Gui and Zhang 2006; Dong et al. 2008).

Good reviews on MSFB have been published (Bologa and Syutkin 1977; Colver 1979; Siegell 1989; Sonolikar 1989; Liu et al. 1991; Saxena et al. 1994), and more recently Hristov presented a series of reviewing papers detailing the major aspects developed so far in this field (Hristov 2002, 2003a,b, 2004, 2006, 2007, 2009, 2010, 2012).

The idea of this chapter is to present a basis of understanding MSFBs and its principles and background theory and to complement the earlier cited reviews by reviewing the main applications of this technique in all areas of research and the particulate media used, in order to give a concise review of the field and current applications.

5.2.1 In Biotechnology and Biomedicine

Due to their relevance, we present in this section a historical overview of biotechnological and biomedical applications.

Several applications (laboratorial and industrial) of the MSFBs have been developed through all these years in several areas of science. In the last decades, a huge effort has been put into the biotechnological and medical applications of MSFBs; examples of this are separation of proteins (Cocker et al. 1997; Seibert and Burns 1998; Tanyolac and Özdural 2000; Tong and Sun 2003; Özkara et al. 2004; Safarik and Safarikova 2004; Ding and Sun 2005; Turkmen et al. 2006; Yao et al. 2006), antibody removal/processing and antibiotics production (Webb et al. 1996; Al-Qodah 2000), fermentation and cell/enzyme immobilization (Ivanova et al. 1996; Al-Qodaha and Al-Hassan 2000; Bahar and Celebi 2000; Böhm and Pittermann 2000; Al-Qodah and Al-Shannag 2006; Qiu et al. 2006; Van Hee et al. 2006; Betancor and Luckarift 2008), processing of valuable substances (e.g., plant cell culture processing) (Al-Qodah and Al-Shannag 2006), bilirubin removal (Uzun and Denizli 2006), cell separation (Qiu et al. 2006; Al-Qodah and Al-Shannag 2007; Karatas et al. 2007), immunoglobulin-G depletion and erythrocyte fractionation (Özkara et al. 2004; Karatas et al. 2007; Özturk et al. 2007), bioanalytical techniques (e.g., continuous affinity chromatography) (Cocker et al. 1997; Turkmen et al. 2006; Yao et al. 2006; Özturk et al. 2007), water treatment by enzymes (Arica 2000), and nucleic acid purification (Hultman et al. 1989; Yamaura et al. 2004).

5.3 PRINCIPLES OF MSFBs (AUGUSTO ET AL. 2008)

An MFB is a device in which a bed of particles suffers the influence of an external magnetic field. This magnetic field may act axially or transversely to the flow (the former is more common, although some authors defend the latter as being the most effective configuration). The interparticle forces between the particles forming the bed are increased by the action of this magnetic field that will stimulate the appearance of a magnetic force between them (as the bed consists of ferromagnetic or strong paramagnetic particles or agglomerates presenting strong magnetic characteristics), leading to an enhancement of the properties and efficiency of the fluidized beds. Distinguishing between magnetic fluidized and stabilized beds is not an easy task and actually is not even accepted without questions within the scientific community, but the majority of researchers consider that the former includes the latter, establishing that MSBs are fluidized beds in which the bubbling effect, usually present in ordinary fluidized beds, is suppressed (caused by the influence of the magnetic field and thus of the interparticle magnetic forces), thus *stabilizing* the bed. This bubbling effect may or may not be present in MFBs, and therefore the definition of MFBs includes the cases of MSBs, where the field is not uniform, and even odd cases as the magnetic valve for solids (Jaraiz et al. 1984) and the magnetic distribution downcomer (Jaraiz et al. 1984). Many authors prefer to ally both definitions in order to avoid controversy, referring to MSFBs, or to magnetic field–assisted fluidization (Hristov 2002, 2003a,b, 2004, 2006, 2007, 2009, 2010, 2012), and in this chapter, we will adopt the former

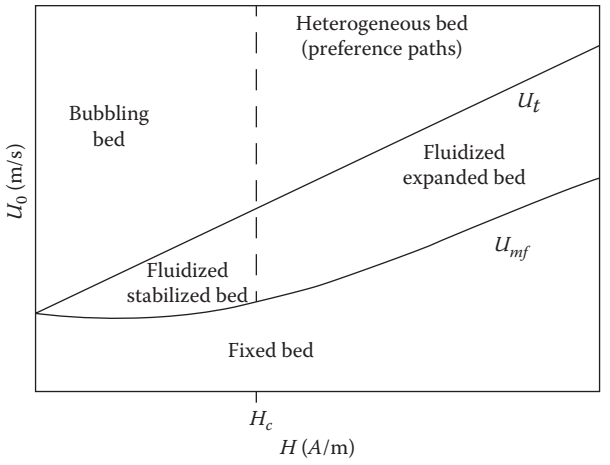

FIGURE 5.2 Regions of behavior of an MSB depending on the velocity and magnetic field values. (Adapted from Augusto, P.A. et al., *Defect Diffusion Forum*, 273–276, 46, 2008.)

noncontroversial denomination of MSFB, in order to indicate that we are generally speaking about both forms of magnetic bed systems.

The magnetic field in MSFBs is usually fixed—does not usually vary with time (stable)—and its magnitude is high enough to strengthen the immobilization of the magnetic bed of particles and to avoid the appearance of bubbles, as far as a specified velocity is not reached. In fact, for these systems, a graphical depiction of the velocity of the gas (U_0) versus the magnitude of the magnetic field, like the one depicted in Figure 5.2, may be divided into five different regions:

(I) *Fixed bed*—in this region, for a certain magnitude of the externally acting magnetic field, the bed behaves as a fixed bed, as long as the velocity is maintained below a specified value the velocity of fluidization U_{mf}.

(II) *Fluidized stabilized bed*—this is the region where the system behaves as a fluidized bed, but stabilized (with no bubble creation), as long as the magnetic field is maintained below a certain magnitude and velocities between the velocity of fluidization U_{mf} and the velocity of transition U_t.

(III) *Fluidized expanded bed*—in this region, the system behaves as an expanded stabilized bed (with no bubble creation) and expands as a piston for increasing velocities, as long as the magnetic field is maintained above a certain magnitude and velocities between the velocity of fluidization U_{mf} and the velocity of transition U_t.

(IV) *Bubbling bed*—this is the region where the system behaves as an ordinary fluidized bed containing bubbles and exists as long as the magnetic field is maintained below a certain magnitude and velocities above the velocity of transition U_t.

(V) *Heterogeneous bed*—in this region, it is observed that the system starts creating preference paths for the fluid to flow, as the particles tend to align with the field, and this phenomenon appears when the magnetic field is maintained above a certain magnitude and velocities above the velocity of transition U_t.

In Figure 5.3, we present a graphical depiction of the bed behavior in each of these regions.

Increasing the velocity too much will lead to the collapse of the bed and particles will be dragged by the flow—this is called elutriation and the corresponding velocity, velocity of elutriation. On the other hand, if the magnetic field is increased too much, regardless of the value of the velocity, the magnetic particles in the bed start to align with the field creating also the earlier cited preference paths, which allow a tunneling effect of the flow, and pressure drops abruptly.

There are several important characteristics of the MSFBs that make them the best option for several applications, and many of them are referred through this chapter in several sections.

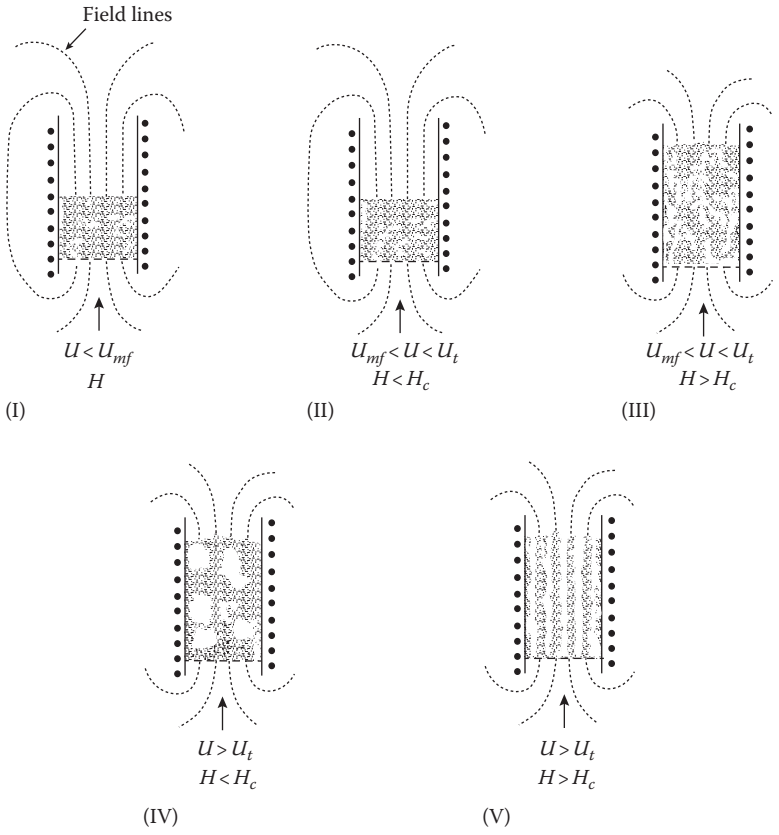

FIGURE 5.3 Different behaviors of an MSFB (I) fixed bed, (II) fluidized stabilized bed, (III) fluidized expanded bed, (IV) bubbling bed, and (V) heterogeneous bed.

Nonetheless, we may point out, as a general characteristic, its capability to maintain the stabilization of the bed (suppressing bubbling and slugging) for much higher velocities than ordinary fluidized beds (maintaining the fixed bed behavior much longer) while keeping a low pressure drop at all times (a characteristic that is typical of fluidized beds). MSFB does also enable the processing of solutions containing suspended solids while maintaining solids mixing at the same time. Important in biomedical and biotechnological applications is also their ability to process biological cultures in a gentle and harmless way (Hristov 2009, 2010).

5.4 PARTICLES USED IN MSFBs: MSFBs AS POROUS MEDIA

Particles used in MSFBs can be both porous and nonporous. Nonporous magnetic particles seem to be more resistant to diffusion limitations, friction, and fouling than porous beds (Halling and Dunnill 1980). Several nonporous particles have been used, as, for example, iron, cobalt, and their oxides, and the methods of their preparation have been classified into four groups: direct use of a coupling agent, adsorption, encapsulation, and formation of a thin film of polymer layer. However, porous particles are the most interesting media, especially for biotechnological, biomedical, and environmental applications, and in many situations, such applications would be impossible to perform with nonporous magnetic particles. The main feature of the magnetic porous particles, when used as media for MSFBs, is their adsorption capability, which, when properly controlled, acts directly in the separation/purification of important substances. This is supported by their spreading

use for water contaminants and protein adsorption. MSFBs are replacing existing packed-bed operating systems, as they present the advantage of a low constant pressure drop that is independent of the flow rate. Besides the ability to process feed streams with suspended solids (as described previously), magnetic stabilization of fluidized beds also reduces axial dispersion and enhances separations (Lucchesi et al. 1979; Rosensweig 1979; Rosensweig et al. 1981; Siegell 1984, 1987, 1989; Burns and Graves 1985; Geuzens and Thoens 1988b; Rosensweig and Ciprios 1991; Wallace et al. 1991; Sajc et al. 1994;).

The porous particles are usually polymeric (generally have a magnetite core and polymer shell) and contain biological/organic active centers that help in the adsorption/separation of biological/organic media. Details of these particle beads will be described in what follows. Magnetic porous particles present a high magnetic susceptibility and large reactive polymer surface area and pores on which functional molecules such as enzymes, antibodies, antigens, cells, drugs, biotins, and many others can be immobilized (Ugelstad et al. 1992; Ding et al. 1998; Qiu et al. 2006). These magnetic particles have many advantages as carriers of cell immobilization due to controlled surface area and porous structure, good thermal resistance, and reasonable chemical inertness (Qiu et al. 2006). At the end, these particles can be reused. These polymer beads can be formed either by suspension polymerization and branch treatment with acid and base or by seed-swelling polymerization in the presence of the magnetite core (Bahar and Celebar 2000).

Nonetheless, except for the general cases of adsorption and enzyme (and others) immobilization, the importance of the porosity (or nonporosity) is negligible, and in many of the remaining applications, the porous structure is not even characterized, as it is not of high relevance.

In Table 5.1, we present a summary of some of the particles used in MSFBs and their main characteristics.

As seen from Table 5.1 and from literature, magnetic particles used in MSFBs may assume many forms and compositions, but the mostly used are composed of a central core made of magnetite, maghemite, or any other kind of strong paramagnetic or ferromagnetic material covered by some kind of polymeric adsorbent or resin, usually functionalized and surface modified, in order to present higher adsorption and activated sites responsible for the interaction with the target media—see Figure 5.4. This interaction may be direct on the substances to be removed/modified/purified or indirect, via the previous attachment of biological or organic material to the surface of the beads (e.g., enzymes, zeolites), which then interact with the desired target substances. Some reviews on these magnetic beads may be found in the literature (e.g., Hristov 1999; Tanyolac and Özdural 2000).

A more specific analysis of the contents of Table 5.1 must be made. When theoretical, hydrodynamic, fluidization, and optimization studies are carried out, we may find different kinds of particles, but these are most naturally based on iron or magnetite cores, usually *in brut*—nonfunctionalized and not possessing any superimposed polymeric layer—and, although in several studies the particles possess a micron range, in many others, they present sizes in the range of the millimeters.

Particles used for bioadsorption (proteins, cells, etc.) usually present a magnetite core on which a layer of polymer is deposited and to which another substance is added that performs as a cross-linking agent or promotes covalent bonds to attach the defined target; they usually have a range of sizes between 100 and 200 μm.

In magnetic affinity chromatography, which is closely related to magnetic protein absorption and enzyme immobilization, the general structure of the particles is more or less the same as in the previous case, where the particle incorporates an immobilized component that is active to interact and capture the desired specific target.

Biocatalysts applications usually use a similar structure for the particulate media, which, in this case, contains an attached immobilized enzyme *glued* by some kind of resin; the overall structure reaches the order of magnitude of the millimeters, although many applications use particles with sizes as low as hundreds of microns.

TABLE 5.1
Particulate Media Used in MSFBs

Particle	Type	Size	Application	References
PVA + magnetite polystyrene + hematite	NP (?)	1.31–14.8 μm (Fe_3O_4) 6.46 μm (PVA + Fe_3O_4) 1.05–4.4 μm (Polystyrene + Fe_2O_3)	Investigations on magnetization behavior	Eichholz et al. (2014)
Nonmagnetic	NP (?)	3 mm	Simulation of flow behavior of liquid and particles	Wang et al. (2012)
Magnetite + activated carbon; magnetite + zeolite	P/NP	0.9–1.0 mm (activated carbon + Fe_3O_4) 1.1 mm (zeolite + Fe_3O_4)	Hydrothermal behavior	Al-Qodah et al. (2001)
Spherical beads of glass plated with Fe_3O_4	NP	160–200 μm	Yield stress experiments	Atodiresei and Badescu (2004)
Ferrite (ferromagnetic powder) + microsphere balloons (NaB Silicate) + calcium alginate	NP (?)	1.5–2.16 mm	Prediction of voidage distribution in the bed	Somchamni (2000)
Magnetite steel powders	PNP	35, 50, 65 μm (Fe_3O_4) 35, 50, 80, 110 μm (steel powders)	Stabilization of gas fluidization of magnetic particles in a cross flow magnetic field	Espin et al. (2011)
Steel shots (Fe > 98.5%)	PNP	0.2–0.5 mm; 0.5–1.0 mm	Hydrodynamic studies	Ursu et al. (2010)
Polyoxymethylene (POM) spheres	?	6 mm	Particle dynamics; magnetic particle tracking; modeling	Neuwirth et al. (2013)
Synthetic magnetic particles	?	35–65 μm	Effect of magnetic field orientation	Quintanilla et al. (2014)
Magnetite	?	425 μm	Influence of magnetic field on fluidization	Seibert and Burns (1998)
Experimental polymeric adsorbent + magnetite	?	55 μm	Effect of hydrodynamics and magnetic stabilization on fluidized-bed adsorption	Böhm and Pittermann (2000)
Fe_3O_4 + alginate	?	63–125; 125–180; 180–250 μm	Hydrodynamics in biochemical applications	Atodiresei and Badescu (2004)
MIEX—anion-exchange resin with a macroporous polyacrylic matrix in the chloride form, with iron oxide incorporated in the matrix	P	Diversified (usually between 100 and 600 μm)	Removal of natural organic matters (e.g., humic acid)	Chen et al. (2010)
Ba ferrite (BaO-6Fe_2O_3) coated with polyurethane	P	1–3 mm	Mixed magnetic and nonmagnetic fluidization experiments in magnetic beds	Yu et al. (2005)

(*Continued*)

TABLE 5.1 (*Continued*)
Particulate Media Used in MSFBs

Particle	Type	Size	Application	References
Mixture of Fe_3O_4 + coarse particles (SiO_2 + ZnO + TiO_2 + Al_2O_3) + coarse magnets (steel spheres)	NP	Fe_3O_4—30 nm; SiO_2—20 nm; ZnO—20 nm; TiO_2—10 nm; Al_2O_3—20 nm; steel spheres—2mm	Behavior studies	Zhou et al. (2011)
Ion-exchange resin + maghemite	P (?)	500–630 μm	Mass transfer studies	Hausmann et al. (2004)
Magnetite + activated carbon; magnetite + zeolite	P	1.1 mm	Mass transfer studies on G-L-S airlift fermenter	Al-Qodah et al. (2000)
Agarose-stabilized magnetic colloids	P	70–130 μm	Protein adsorption (BSA)	Ding and Sun (2005)
CB—modified magnetite agarose support	P	80–240 μm	Protein adsorption (lysozyme)	Tong and Sun (2003)
Magnetic Mowital microbeads (magnetite core + PVA + Mowital)	P	125–250 μm	Protein adsorption (BSA)	Tanyolac and Ozdural (2000)
Mag-poly(EGDMA-MAH) beads	P	50–100 μm; 155–250 μm	Affinity adsorption (immunoglobulin G)	Ozkara et al. (2004); Karatas et al. (2007)
mPHEMA beads	P	80–120 μm	Adsorption (removal of anti-dsDNA antibodies system)	Odabas et al. (2005)
Fe_3O_4 + activated carbon	P	200–500 μm	Yeast cells adsorption (separation)	Al-Qodah and Al-Shannag (2006)
mPHMEA + CB (Fe_3O_4)	P	80–120 μm	Protein adsorption (lysozyme)	Basar et al. (2007)
m-poly (HEMA-EGDMA) (silanized magnetic beads)	P	150–250 μm	Affinity adsorption (immunoglobulin G)	Ozturk et al. (2007)
HSA immobilized mPHEMA particles (Fe_3O_4) couples to CNBr—activated	P	80–120 μm	Protein removal/ adsorption (bilirubin)	Uzun and Denizli (2006)
Magnetite + activated carbon; magnetite + zeolite	NP	0.7 mm	Removal of yeast cells from cell suspensions/ adsorption/filtration	Al-Qodah and Al-Shannag (2007)
P(GMA-co-MMA) beads with covalent immobilized *p*-amino-benzamidine for trypsin; (Fe_3O_4)	P (?)	?	Protein adsorption/ separation (trypsin)	Bayramoglu et al. (2014)
mPHEMA beads (Fe_3O_4)—CB covalently immobilized via nucleophilic substitution	P (?)	100–140 μm	Affinity chromatography protein adsorption (β-casein)	Tuzmen et al. (2010)
PAM beads—immobilized soy bean trypsin inhibitor	P (?)	60–600 μm	Affinity separation of trypsin and chymotrypsin (adsorption)	Cocker et al. (1997)

(*Continued*)

TABLE 5.1 (*Continued*)
Particulate Media Used in MSFBs

Particle	Type	Size	Application	References
mPHEMA PEI-attached + Cu^{2+} chelated	P (?)	100–140 μm	Affinity separation of cytochrome C (adsorption)	Turkmen et al. (2006)
Magnetic poly(GMA-DVB-MAA) microspheres (oleic acid cores Fe_3O_4 + polymerization) + lipase immobilization	P	10–20 μm	Catalysis (synthesis of hexyl acetate and etherification conversion)	Lei et al. (2009)
Alginate + immobilization; *Saccharomyces cerevisiae*	P (?)	3.2 mm	Ethanol fermentation of glucose	Liu et al. (2009)
Magnetic polystyrene particles + immobilized glucoamylase	?	125 μm	Biocatalysts/bioreactor (maltose hydrolysis)	Bahar and Celebi (2000)
Fe_3O_4/polystyrene (St-acrylic acid) magnetic porous beads + immobilized *Thiobacillus thioparus*	P	500–650 μm	Removal of sulfide (bio-desulfurization of industrial wastewaters)	Qiu et al. (2006)
Poly(GMA-MMA) with horseradish peroxidase immobilized	?	75–100 μm	Treatment of phenolic wastewaters (phenol and *p*-chlorophenol)	Bayramo and Arica (2008)
Haldor Topsoe catalyst + epoxy resin + *S. cerevisiae* immobilized	NP (?)	1.0–2.0 mm	Glucose conversion to ethanol (biocatalysts/ bioreactor) transverse field	Ivanova et al. (2010)
(Magnetite + activated carbon + epoxy resin; magnetite + zeolite + epoxy resin) + *S. cerevisiae* immobilized	NP	0.7 mm	Removal of yeast cells from cell suspensions/ adsorption/filtration	Al-Hassan et al. (1991)
Penicillium chrysogenum immobilized in Fe_3O_4 + activated carbon or zeolite	NP (?)	900 μm	Antibiotic products (penicillin) with three-stage reactor	Al-Qodah (2000)
Magnetic mesoporous silica nanoparticles (MMSNPs-CPTS-IDA-Cu^{2+}) with Cu^{2+} chelated laccase immobilization	P	287 nm	Phenol degradation in cooking wastewater	Wang et al. (2012)
Magnetic anion–exchange resin with acrylic matrix, NDMB	P	100–150 μm	Dissolved organic matter removal (adsorption—ion exchange)	Wang et al. (2014)
MIEX	P	150–180 μm	Removal of organic matter (pretreatment of MBR) in wastewater and reuse	Zhang et al. (2008)

(*Continued*)

TABLE 5.1 (*Continued*)
Particulate Media Used in MSFBs

Particle	Type	Size	Application	References
Fe_2O_3 catalyst	?	450–600 μm	Reduction of NO by NH_3 over Fe_2O_3 catalyst	Petrova et al. (2011)
Magnetic steel	NP	1.18–1.68 mm	Removal of iron oxide particles in gas stream	Rodriguez et al. (1999)
MIEX	P	150–180 μm	Removal of dissolved organic carbon	Chen et al. (2010b)
Magnetite powder; magnetite powder + glass beads; magnetite powder + silica gel; magnetite powder + sand; magnetite powder + natural fiber	P (?)	1–5 μm	Treatment of metal-contaminated aqueous waste	Cotten et al. (1999)
Magnetic polyamide-epichlorohydrin resin (magnetic ferrite)	?	63–125 μm	Wastewater decontamination (removal of actinide and heavy metals from wastewaters)	Kochen and Navratil (1997)
Fe_3O_4 + Degussa P25	?	40 μm 30–100 nm	Photocatalytic degradation of formaldehyde coupled with sound-magnetic assistance	Si et al. (2013)
Co–Ni bimetallic catalyst	P	<100 nm	Hydrogen production via methane oxidative CO_2 reforming	Chen et al. (2010)
Co/Al_2O_3 catalyst	P	40–150 nm	CH_4–CO_2 catalytic reforming	Hao et al. (2008)
$NiCo/Al_2O_3$ catalyst	P	4–10 μm	Co-methanation for synthetic natural gas production	Li et al. (2013)
Na_2SiO_2/Fe_3O_4 catalyst	P	87.6 nm	Biodiesel production (transesterification reaction of cottonseed oil)	Guo et al. (2013)

Porous (P)/Nonporous (NP).

In environmental applications, the configuration of the particles (beads) changes accordingly to the desired goal; thus, ion-exchanged resins are incorporated with a core of magnetite when removal of organic materials and other substances is in order, while in environmental catalysis, catalysts integrated in magnetite core particles or pure Co–Ni core catalysts are often applied; the size ranges do not even reach the unity of hundred of microns as nanosized particles are nowadays often seen in this application.

Different approaches have also been used in some of the previous applications, for example, by using polymeric core particles covered with a shell made out of magnetite or some paramagnetic/ferromagnetic material or by using a mixed mode of particles. In fact, as mentioned previously,

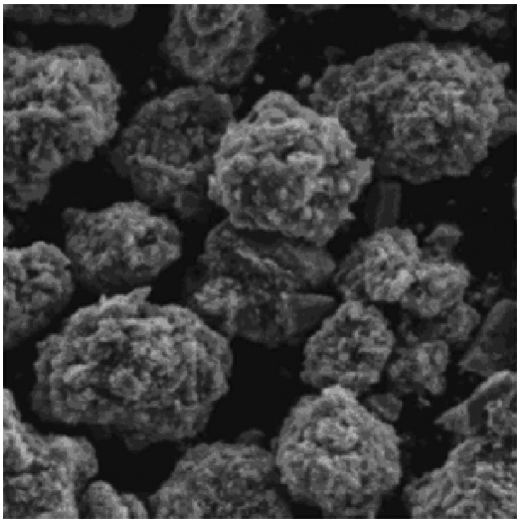

FIGURE 5.4 Fe_3O_4/alginate particles with a sphericity of 0.87. (From Böhm, B. and Pittermann, B., *Chem. Eng. Technol*., 23, 309, 2000. With permission.)

MSFBs require, in order to work, the use of particles/substances possessing high enough values concerning the magnitude of their magnetic properties.

In general, two main systems have been used: one that uses 100% magnetic particles and another that uses a mixture of magnetic and nonmagnetic particles. In the recently developed applications, the systems applying only magnetic particles have proven to be superior, concerning the fulfillment of all the goals of separation and reaction (Seibert and Burns 1998; Hristov 1999).

These magnetic beads are usually prepared by depositing the polymeric substance/resin/alginate on the magnetic cores and then applying some kind of chemical reagent or thermal technique that modifies the surface of the beads in order for it to be fully functionalized, according to the specific goals.

Specific details differ from application to application as may be seen from the large number of papers published so far.

In what follows, we will present some of the most common preparation methods.

Shornchamni (2000), in her PhD thesis, focused on the prediction of the voidage distribution in MSFBs using alginate-ferromagnetic particles in the experiments; for the preparation of these particles, it used the following procedure: for preparing 100 g of particles, 70.74 g of water is weighted and inserted in a 250 cm^3 beaker, which is placed under the mixer; 1.26 g of alginate is weighted and slowly added as powder into the mixing water contained in the beaker, obtaining a 1.75% alginate solution; then 20 g of ferromagnetic powder (ferrite) and 8 g of microsphere balloons (sodium borosilicate) are added slowly to the alginate solution, and mixing is maintained during 4 h; and the perfectly mixed suspension is then placed in a particle generator (see Figures 5.5 and 5.6).

In another hydrodynamic testing (Seibert and Burns 1998), the functionalization of the polymeric adsorbent is achieved by treating its surface with a concentrated base (1.0 M NaOH), creating carboxylic acid groups that will allow the particles to be used as a cationic exchanger to adsorb horse heart myoglobin.

For protein adsorption (bovine serum albumin [BSA]), Ding and Sun used agarose-stabilized magnetic colloids that were synthesized by a modified coprecipitation method (Ding and Sun 2005)—Figure 5.7. The procedure was as follows: 7.2 g $FeSO_4$ and 14.0 g $FeCl_3$ were dissolved in 150 mL water, and the solution was added to a 500 mL round-bottom glass flask; the solution was heated to 90°C in a water bath and 40 mL of 25% ammonia was slowly added; after 5 min reaction under stirring at 1000 rpm, 20 mL of 4% agarose solution was slowly added to the flask, and the

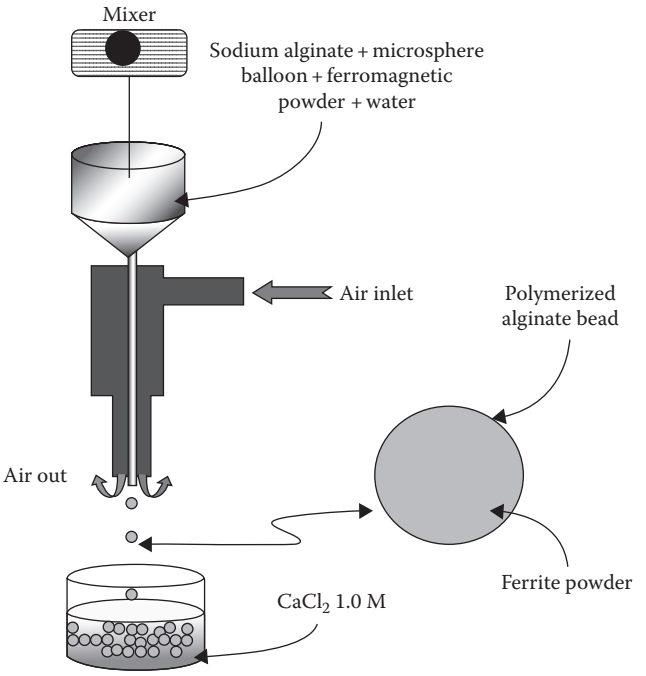

FIGURE 5.5 Particle production schematic diagram. (From Sornchamni, T., The prediction of voidage distribution in a nonuniform magnetically assisted fluidized bed: Theory and experiment, Oregon State University, Corvallis, OR, Master of Science thesis, 2000.)

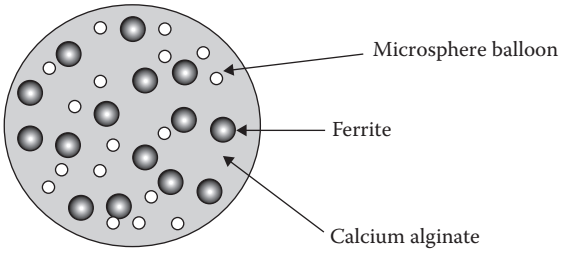

FIGURE 5.6 The ferromagnetic particle obtained. (From Sornchamni, T., The prediction of voidage distribution in a nonuniform magnetically assisted fluidized bed: Theory and experiment, Oregon State University, Corvallis, OR, Master of Science thesis, 2000.)

reaction continued for 1 h at 90°C; then, the magnetic colloids in the suspension were collected as precipitate under magnetic field and washed with water to remove soluble salts; the magnetic precipitate was stored at room temperature for further use; then, the water-in-oil emulsification method was utilized to prepare the magnetic agarose gel–coated glass bead (Ding and Sun 2005); a 500 mL round-bottom glass flask equipped with a half-moon paddle fitting to the flask bottom was used to prepare water-in-oil emulsion; soybean oil (240 mL) containing 5% Span 80 was added to the vessel and heated to 90°C in a water bath; then, 8 g of preheated glass beads and magnetic colloids (2 g) were suspended in 40 mL of 4% agarose solution at 90°C; the suspension was slowly poured into the oil phase stirred at 1400 rpm; and after 5 min, the vessel was rapidly cooled below 15°C with cold water in the water bath, and the magnetic pellicular support (MPS) was recovered by the permanent magnet and washed with water and acetone to remove any adsorbed oil. The MPS was then cross-linked and reduced and coupled with diethylaminoethyl (DEAE) (Ding and Sun 2005): the MPS

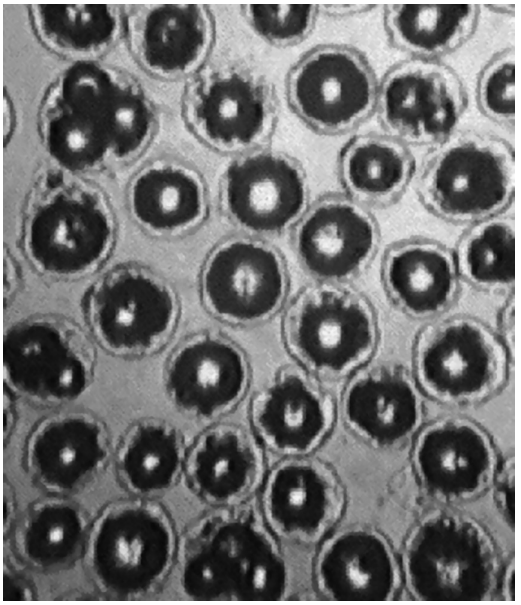

FIGURE 5.7 Optical photograph of the MPS (×160). (From Ding, Y. and Sun, Y., *Chem. Eng. Sci*., 60, 917, 2005. With permission.)

particle was drained to remove the interparticle fluid, and the drained solid phase was mixed with a solution 3 mol/L DEAE–HCl (2/3 of the volume) in a 250 mL flask; after agitation at 170 rpm in a water bath of 40°C for 30 min, NaOH was introduced to a final concentration of 1.5 mol/L, and the agitation was continued for an additional 1 h; and then, the solid phase was routinely washed with deionized water, 25% ethanol, and 0.5 mol/L NaCl solution.

For immunoglobulin-G purification, Karatas et al. (Karatas et al. 2007) used mag-poly(EGDMA-MAH) particles that were produced in the following way (Karatas et al. 2007): 5.0 g of l-histidine methyl ester and 0.2 g of hydroquinone were dissolved in 100 mL of dichloromethane solution, and this solution was cooled down to 0°C; then about 12.7 g triethylamine was added to the solution, and about 5.0 mL of methacryloyl chloride was poured slowly into this solution and then this solution was stirred magnetically at room temperature for 2 h; at the end of the chemical reaction period, hydroquinone and unreacted methacryloyl chloride were extracted with 10% NaOH solution; aqueous phase was evaporated in a rotary evaporator; and the residue (i.e., MAH) was crystallized in an ether–cyclohexane mixture and then dissolved in ethyl alcohol. Then, magnetic poly(EGDMA-MAH) beads were prepared by suspension polymerization as follows (Karatas et al. 2007): the stabilizer, poly(vinyl alcohol) (200 mg), was dissolved in 50 mL deionized water for the preparation of the continuous phase; the dispersion phase was prepared by mixing EGDMA (8.0 mL), MAH (1.0 g), magnetite particles (1.0 g), and toluene (12.0 mL) in a test tube; the initiator, benzoyl peroxide (BPO) (100 mg), was dissolved in this homogeneous solution; the dispersion phase was added to the continuous medium in a glass-sealed polymerization reactor (100 mL) placed in a water bath equipped with a temperature-control system; the polymerization reactor was heated to 65°C by stirring the polymerization medium at 600 rpm; the polymerization was conducted at 65°C for 4 h and at 90°C for 2 h; after completion of polymerization, the reactor content was cooled to room temperature; a washing procedure was applied after polymerization to remove the diluent and any possible unreacted monomers and other ingredients from the beads; the mag beads were separated by a permanent magnet and then resuspended in ethyl alcohol; the suspension was stirred for about 1 h at room temperature, and the beads were separated by filtration; and the mag beads were washed twice with ethyl alcohol and then four times with deionized water using the same procedure.

Finally, Cu^{2+} ions were incorporated by chelation in a batch system (Karatas et al. 2007); an aqueous Cu^{2+} solution (20 mL) was treated with the mag beads for 2 h (equilibrium adsorption time); the flask was magnetically stirred at an agitation rate of 100 rpm at room temperature (25°C); the initial concentration of the metal ion was 30 ppm. The medium pH was 5.0; nitrate salt was used for the preparation of standard Cu^{2+} solutions.

For enzyme encapsulation, the major techniques are covalent binding, ionic and hydrophobic adsorption, aggregation, and entrapment. A review on enzyme encapsulation and its materials is presented in Betancor and Luckarift (2008). Lei et al. (Lei et al. 2009) prepared magnetic poly(glycidyl methacrylate [GMA]-divinylbenzene [DVB]-methacrylic acid [MAA]) microspheres with active epoxy groups by the suspension polymerization of GMA and MAA in the presence of oleic acid–coated magnetic Fe_3O_4 nanoparticles, using DVB as a cross-linking agent—Figures 5.8 and 5.9. The procedure was as follows (Lei et al. 2009): the oleic acid–coated Fe_3O_4 (OA–Fe_3O_4)

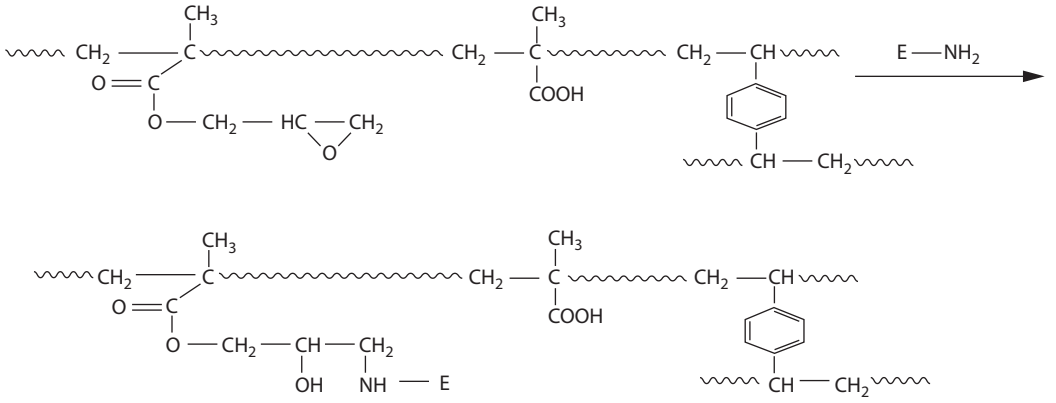

FIGURE 5.8 Scheme of the magnetic microspheres and the reaction for covalent immobilization lipase. (From Lei, L. et al., *J. Magn. Magn. Mater.*, 321, 252, 2009. With permission.)

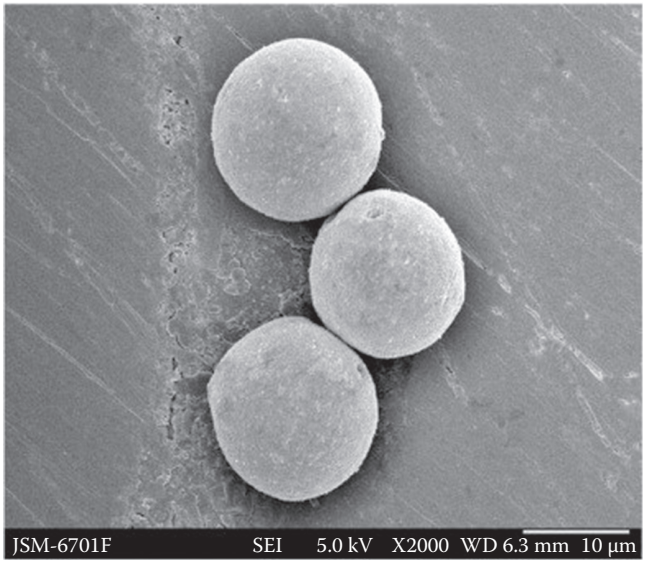

FIGURE 5.9 SEM micrograph of the magnetic microspheres—magnification 2000×. (From Lei, L. et al., *J. Magn. Magn. Mater.*, 321, 252, 2009. With permission.)

nanoparticles were prepared by the conventional coprecipitation method with some modifications; 0.196 mol $FeCl_3 \cdot 6H_2O$ and 0.098 mol $FeCl_2 \cdot 4H_2O$ were dissolved in 600 mL deionized water in a 2.0 l beaker under nitrogen gas with vigorous stirring at 80°C; then, 30 mL $NH_3 \cdot H_2O$ (25 wt%) was added to the solution, and 20 mL oleic acid was added dropwise into the suspension within 20 min; after several minutes, the resulting Fe_3O_4 magnetic fluid was isolated from the solution by a magnet and washed several times with deionized water to remove the excess of oleic acid; then, the magnetic microspheres were prepared by suspension polymerization; a starch solution saturated with sodium chloride and a few methylene blue was used as aqueous phase; the organic phase contained a mixture of the monomers (GMA/MAA ¼ 6:1), DVB (25% of the total weight of the monomers), initiator BPO (1% of the total weight of the monomers), and 0.3 g magnetic OA–Fe_3O_4 nanoparticles; the ratio of aqueous phase to organic phase was controlled to be 3:1; suspension polymerization was carried out in a 100 mL three-necked flask with a nitrogen inlet, a refluxing condenser and mechanical stirrer; the three-necked flask was placed in a water bath, stirred at 450 rpm; the suspension polymerization was undergone at 55°C for 0.5 h, 65°C for 4 h, 75°C for 3 h, and then for 2 h at 85°C; subsequently, the copolymer microspheres were separated by a magnet and then washed several times with heated distilled water and isopropyl alcohol, respectively; and the copolymer microspheres were then extracted by using methanol for 24 h and dried at room temperature under vacuum.

Hematite-coated Fe_3O_4 particles used as arsenic adsorbents for drinking water were prepared by the following procedure (Simeonidis et al. 2011)—Figure 5.10: magnetite (Fe_3O_4) powder (size distribution under 40 μm) was milled in a high-energy planetary ball mill at rotational speeds 200–400 rpm to produce iron oxide nanostructures; the milling stage was performed under a protective argon atmosphere with the ball-to-powder weight ratio of 10:1 for milling times varying from 0.5 to 150 h; heptane (50%–150% of powder weight) was introduced in the grinding bowl as a lubricant agent; in the slurry mixture obtained after milling, a size selection process, including washing with ethanol/deionized water and centrifugation cycles, was performed; the material was kept for 1 month at ambient conditions before its use in arsenic adsorption experiments. Since specific surface area is a criterion for high adsorption efficiency, magnetite nanoparticles as small as 30 nm were also prepared (Simeonidis et al. 2011) through the employment of ball milling in the presence of surfactants; for the preparation of these samples, oleic acid (12% of powder weight) was also added; and to enable nanoparticles dispersion in aqueous solutions, organic surfactants were substituted by cetyltrimethylammonium bromide.

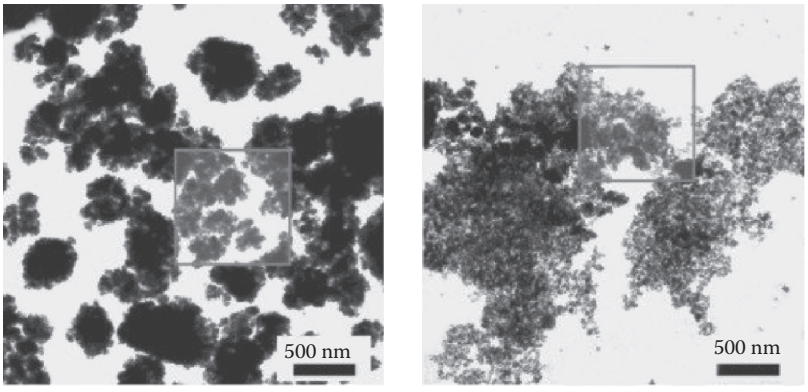

FIGURE 5.10 TEM images and electron diffraction patterns, corresponding to the pointed areas, of Fe_3O_4 powder ball milled for 100 h in the absence (a) and the presence (b) of oleic acid. (From Simeonidis, K. et al., *Chem. Eng. J.*, 168, 1008, 2011. With permission.)

Nanomagnetic particles are nowadays heavily studied for several applications, ranging from medical sciences to environmental remediation. The main practical developments were achieved during the last decade, and MSFBs are also a current example of an application using these nanostructures. There are still many issues concerning their applications, namely, their agglomeration, force balance behavior (switches between Navier–Stokes flow and Brownian flow), and safety. The main advantage on *going nano* for MSFBs is the high superficial area/volume ratio, which make them very attractive, especially for environmental (Hao et al. 2008; Chen et al. 2010; Wang et al. 2012; Guo et al. 2013; Li et al. 2013) and biotechnological applications (Simeonidis et al. 2011).

Production of nanomagnetic particles has been thoroughly investigated during recent years, namely, the attempt to produce monodispersed, biocompatible, and stable iron oxide nanoparticles. The most common methods to achieve their synthesis are coprecipitation, thermal decomposition, hydrothermal methods, micro emulsion, and sonic methods.

5.5 GENERAL SUPPORTING THEORY

5.5.1 Forces

The forces acting in a nonnegligible way in an MSFB may be divided into four main categories: gravitational forces, buoyancy forces, drag forces, and interparticle forces. These four main categories of forces interact in such a way that they reach a balance in a magnetic particle of the bed, until elutriation is achieved.

Drag forces: F_d, are expressed by Stoke's equation

$$F_d = 6\pi\mu r_{part}(U_f - U_p) \tag{5.1}$$

for laminar flows or by Newton's equation

$$F_d = C_d A \frac{\rho_f (U_p - U_f)^2}{2} \tag{5.2}$$

for turbulent flows, being

- μ the viscosity of the fluid
- r_{part} the radius of the bed particle
- U_p the velocity of the particle (zero in the case of MSBs)
- U_f the velocity of the fluid
- C_d the drag coefficient of the particle (Shames 2002)
- A the cross-sectional area of the particle in the direction of the flow

Gravitational forces: F_g, are expressed by the well-known equation

$$F_g = -\rho_p V_p g \tag{5.3}$$

being

- g the acceleration of gravity
- ρ_p the density of the particle
- V_p its volume

The buoyancy forces: F_b, may be expressed by

$$F_b = \rho_f V_p g \tag{5.4}$$

being ρ_f the density of the fluid.

Interparticle forces: F_{ip} represents a class of important forces for MSFBs, and it is important to begin by distinguishing between their natures. The most active interparticle force within the particles of an MSFBs is the magnetic force (Fan and Zhu 1998), but other nonnegligible forces may also be considered, as it is the case of short-range interparticle forces like van der Waals electrostatic and even collisional forces.

5.5.1.1 Magnetic Forces

The main factor for the stabilization of the bed is the magnetic forces acting on it due to the presence of a magnetic field generated by current-bearing coils structured according to Helmholtz. In a homogeneous magnetic field, these forces are function of the magnetic susceptibility of the particles composing the bed and of the field gradient.

From Rosensweig (Rosensweig 1985), we know that the magnetic force, F_m, can be expressed by

$$F_m = \frac{1}{4\pi} M \nabla(\mu_0 H) \tag{5.5}$$

where

μ_0 is the magnetic permeability of the vacuum
H is the magnetic field intensity
M is the magnetization

If all particles are oriented according to the direction of the magnetic field, for the x direction, Equation 5.5 reduces into

$$F_m = \frac{1}{4\pi} \chi_m \mu_0 H \frac{dH}{dx} \tag{5.6}$$

being

χ_m the mass magnetic susceptibility of the particles
dH/dx its gradient over the x direction

5.5.1.2 van der Waals Forces

These forces exist not only between atoms and molecules but also between solid particles. If we assume the particles to be spherical, then these forces, F_{vw}, may be expressed by (Hamaker 1937)

$$F_{vw} = \frac{A_{12} a}{6 l^2} \tag{5.7}$$

being

A_{12} the Hamaker constant
l the distance between the surfaces of the two solid particles
a the relative radius defined as

$$\frac{1}{a} = \frac{1}{a_1} + \frac{1}{a_2} \tag{5.8}$$

where a_1 and a_2 are the radii of the spherical solid particles.

5.5.1.3 Electrostatic Forces

Electrostatic effects are always present, but they are more noticeable when working with a gas–solid two-phase flow. The simple contact or collision of the particles with each other, or with other surfaces, is enough to trigger the electrostatic charging of the particles. This force, F_e, acts along a straight line from one charged object to the other and is expressed by

$$F_e = \frac{q_1 q_2}{4\pi\varepsilon r^2} \tag{5.9}$$

being

q_1 and q_2 the charges of the solid particles
r the distance between them
ε the permittivity of the surrounding medium

5.5.1.4 Collisional Forces

Collisions between particles of the bed exist when they move, even if they soon get stabilized. For elastic spheres, the maximum collisional force in a collinear impact between them is expressed by

$$F_{col} = \frac{4}{3} E\sqrt{a}\left(\frac{15mU^2}{16E\sqrt{a}}\right)^{3/5} \tag{5.10}$$

being

U the relative velocity of the two particles
a the relative radius as defined by Equation 5.8
E the contact module
m the relative mass of the particles

defined as

$$\frac{1}{m} = \frac{1}{m_1} + \frac{1}{m_2} \tag{5.11}$$

5.5.1.5 Working Factors

The equilibrium in an MSFB is reached (the bed particles do not move—*get stabilized*) as long as we maintain

$$F_b + F_d + F_{ip} - F_g = 0 \tag{5.12}$$

being that

$$F_{ip} = F_m + F_{vw} + F_e + F_{col} \tag{5.13}$$

In the work of Van Hee and coworkers (Van Hee et al. 2006), this overall balance is seen as a driving force that helps to select the particle–particle separation technique in biotechnological applications, by defining a window of opportunity as depicted in Figure 5.11.

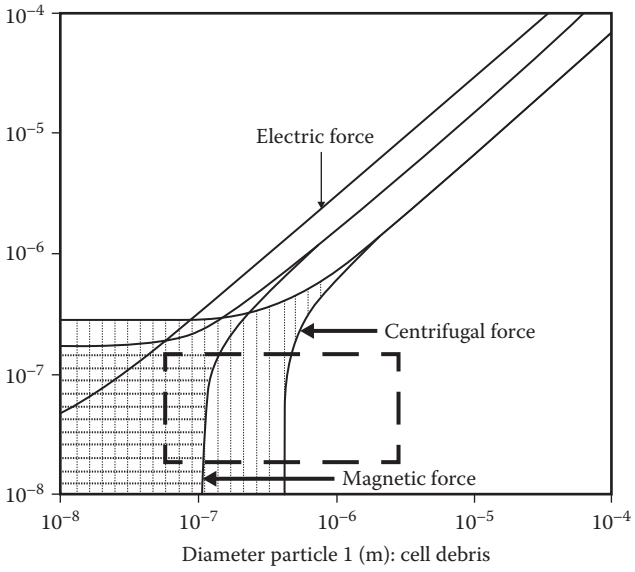

FIGURE 5.11 An overview of the particle–particle separation limits for the centrifugal force, the electric force, and the magnetic force for extreme particle–particle separation problems that are encountered in biotechnology. (From Van Hee, P. et al., *Biotechnol. Bioeng.*, 94, 689, 2006. With permission.)

The minimum fluidization velocity may be computed by using the following equations taken out from the theory of Ergun (Estevez et al. 1995):

$$\frac{\Delta p d_p \Phi_S \varepsilon_m^3}{\rho \mu_0^2 L(1-\varepsilon_m)} = 150\frac{(1-\varepsilon_m)\nu_1}{\mu_0 d_p \Phi_S} + 1.75 \tag{5.14}$$

$$Ar = 150\frac{(1-\varepsilon_{mf})^3}{\varepsilon_{mf}^3}\mathrm{Re}_{mf}\,\Phi_S + 1.75\frac{(1-\varepsilon_{mf})^2}{\varepsilon_{mf}^3}\mathrm{Re}_{mf}^2\,\Phi_S^2 \tag{5.15}$$

where

Δp is the pressure drop
d_p is the diameter of the particles
Φ_S is the sphericity
ε_m is the porosity
ε_{mf} is the porosity at minimum fluidization
ρ is the density of the particle
μ_0 is the magnetic permeability of the vacuum
L is the length of the bed
Ar is the Archimedes number
Re_{mf} is the Reynolds number at minimum fluidization

Rosensweig and coworkers (Rosensweig et al. 1981a,b) have studied the arrangement of the particles in an MSFB and have concluded that it can be quantitatively correlated to a number they denominated by E_G, which is adimensional and given by

$$E_G = \frac{24\rho_S g d_p}{\mu_0 H_p^2} \tag{5.16}$$

where

ρ_s is the density of the particles
g is the acceleration due to the gravity
d_p is the diameter of the particles
μ_0 is the permeability of the vacuum
H_p is the apparent applied magnetic field acting on the particles due to their magnetization

When $E_G < 1$, the particles align with the field lines and form chain-like structures that create the tunneling effect (due to the strong magnetization felt). When $E_G > 10$, the structure appears random, compact, and with no preferred orientation. When $1 < E_G < 10$, the bed is partially structured.

Extra forces or equations required to be considered when MSFBs are applied in biotechnology and medicine.

In some of the applications of MSFBs in the areas of biotechnology and biomedicine, the overall equations are able to describe the basic process, but they must be also complemented by another kind of support theory.

This is the case for mass transfer, for example, the equations that regulate the diffusion of a certain compound into and within a porous magnetic compound that forms the bed. We may use the dispersion model, given by

$$\frac{\partial c_i}{\partial t} + u\frac{\partial c_i}{\partial z} - D_{ax}\frac{\partial^2 c_i}{\partial z^2} = \nu(c_i) \tag{5.17}$$

and applying this general equation to our specific problem, we may obtain

$$t = \frac{\sum t_i c_i \Delta t_i}{\sum c_i \Delta t_i}; \quad \sigma^2 = \frac{\sum \left(t_i - \bar{t}\right)^2 c_i \Delta t_i}{\sum c_i \Delta t_i} = \frac{\sum t_i^2 c_i \Delta t_i}{\sum c_i \Delta t_i} - \bar{t}^2; \quad C_\theta = \frac{1}{2\sqrt{\pi\theta\left(\frac{D_{ax}}{uL}\right)}} e^{\left[\frac{-(1-\theta)^2}{4\theta\left(\frac{D_{ax}}{uL}\right)}\right]} \tag{5.18}$$

One of the most complementing theories is the one concerning chemical or biological reactions and/or adsorptions, as many applications are based on a chemical or biological reaction. As these processes vary widely, the reaction and/or adsorption equations will also vary accordingly. We may point out as an example the adsorption of *Saccharomyces cerevisiae* in activated carbon or zeolites governed by the sorption isotherm,

$$Y = \frac{AX}{B + X} \tag{5.19}$$

being

X the free cell concentration in 10^7 cells/g support
Y the adsorbed cell concentration in 10^6 cells/g support
A and B the coefficients that describe the maximum possible cell loading and the sorptive immobilization constant of yeast cells on these magnetic particles (Al-Hassan et al. 1991)

First-order rate equations such as

$$\ln A = \ln A_0 - K_i t \tag{5.20}$$

are very often observed for the description of reactions (e.g., in the immobilization of horseradish peroxidase [HRP] for phenol degradation; Bayramoglu and Arica 2008), where K_i is the inactivation rate constant and A_0 and A are the initial activity and the activity after time t (min).

5.5.2 Simulations

Mathematical modeling of fluidized beds is based on the previous equations of mass and force balances. However, recent developments use complex computer fluid dynamics (CFD) procedures, which assume that not only the fluid but also the disperse phase may be modeled as two interpenetrating continua (Sobral and Cunha 2005).

In modeling this process, the equation of motion for the liquid phase is based on the Navier–Stokes motion and is given by (Wang et al. 2013)

$$\frac{\partial\left(\rho_l \varepsilon_l\right)}{\partial t} + \nabla \cdot \left(\rho_l \varepsilon_l u_l\right) = 0 \tag{5.21}$$

$$\frac{\partial\left(\rho_l \varepsilon_l u_l\right)}{\partial t} + \nabla \cdot \left(\rho_l \varepsilon_l u_l u_l\right) = -\varepsilon_l \nabla P + \varepsilon_l \nabla \cdot \tau_l + \varepsilon_l \rho_l g - F_{pl} \tag{5.22}$$

being

g the acceleration of gravity
P the liquid pressure
ε_l the liquid volume fraction
τ_l the viscous stress tensor
ρ_l the density of liquid

The coupling term F_{pl} between particle phase and liquid phase is estimated as the sum of the drag on each particle within the corresponding fluid control volume. The stress tensor of liquid phase can be represented by (Wang et al. 2013)

$$\tau_l = \mu_l \left[\nabla u_l + \left(\nabla u_l\right)^T\right] - \frac{2}{3}\mu_l \left(\nabla \cdot u_l\right) I \tag{5.23}$$

being μ_l the viscosity of liquid phase.
The equation of motion of the particles may be written as (Wang et al. 2013)

$$m_i \frac{dv_i}{dt} = -V_p \nabla P + m_i g + f_{di} + f_{mi} + \sum_{j=1}^{N} \left(f_{lj} + f_{cj} + F_{mj}\right) \tag{5.24}$$

$$I_p \frac{d\omega_i}{dt} = \sum_{j=1}^{N} T_{pij} \tag{5.25}$$

being

m_i and v_i the mass and velocity of particle i
V_p the volume of a particle
T_p the torque arising from the tangential components of the contact force
I_p and ω the moment of inertia and angular velocity of a particle, respectively

The terms of the right-hand side of Equation 5.24 are the liquid pressure gradients, gravity, drag force exerted from the fluid, virtual mass force, lubrication force, contact force, and magnetic force introduced by the external magnetic field, respectively.

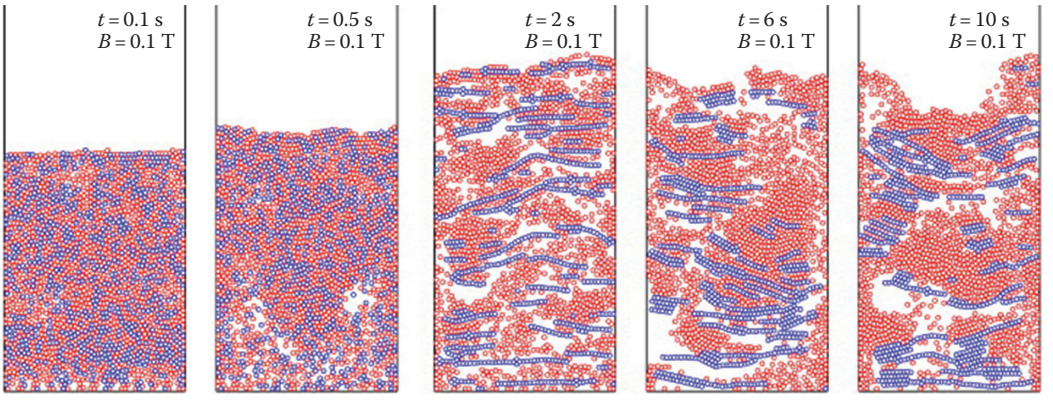

FIGURE 5.12 Instantaneous snapshots of particles at magnetic density of 0.1 T. (From Wang, S. et al., *Powder Technol*., 245, 314, 2013. With permission.)

These interparticle forces and torques are summed over the N particles in contact with particle i. The contact force between particles is calculated based on the soft-particle method (Wang et al. 2013).

Figure 5.12 represents the simulations results for a uniform transverse magnetic field.

Several other recent developments concerning CFD and modern simulation theoretical support of MSFBs may be seen in Wang et al. (2012, 2013), Sobral and Cunha (2003, 2005), Cunha et al. (2013), and Eichholz et al. (2014).

5.6 HEAT AND MASS TRANSFER

MSFBs clearly show advantages in applications where the limiting or one of the limiting steps is the diffusion of mass in the fluid phase or in the particle because, as it was described earlier, it will allow higher flow rates of the liquid/gas phase and smaller particles in the solid phase without elutriating (the particles are retained by the influence of the magnetic field).

In fact, in a conventional fluidized bed with small particles, if the flow rate of the liquid/gas phase is increased too much, the particles are carried away from the device. Hence, there is a compromise between the size of the particles and the flow rate of the fluid.

A liquid (gas)–solid contactor using a magnetic field for increasing the retention of solids would allow high flow rates, and therefore a good mixing and a decrease of the mass transfer resistances in the liquid (gas) phase and, at the same time, will prevent particles to be taken out of the contactor (Novell 1984; Estevez et al. 1995).

However, we must be aware that the mass transfer effects highly depend on the application we are studying, for example, in ion exchange it was observed that mass transfer was not improved by applying magnetic fields (Haussmann et al. 2000), regardless of their good behavior, as depicted in Figure 5.13.

Some authors (Lucchesi et al. 1979) have compared the heat transfer characteristics of packed beds with and without the presence of magnetic field. For this, they had to heat up the gas before entering the bed for both cases and then read the temperature of the outlet gases. The results are presented in Figure 5.14. This figure represents the heat transfer observed in both systems expressed in terms of two adimensional numbers: Nusselt versus Reynolds. As it may be seen, until the minimum fluidization velocity is reached, the two curves coincide, and afterward the heat transfer coefficient increases faster with increasing Reynolds number in the MSB than in the conventional packed bed. So, we may conclude that an MSB promotes a more effective fluid–solid contact. However, we must be also aware, as for mass transfer, that this does not mean that heat transfer is improved for all applications. In fact, for example, Arnaldos and coworkers (Arnaldos et al. 1985; Arnaldos and Casal 1987) have performed several studies regarding this subject and

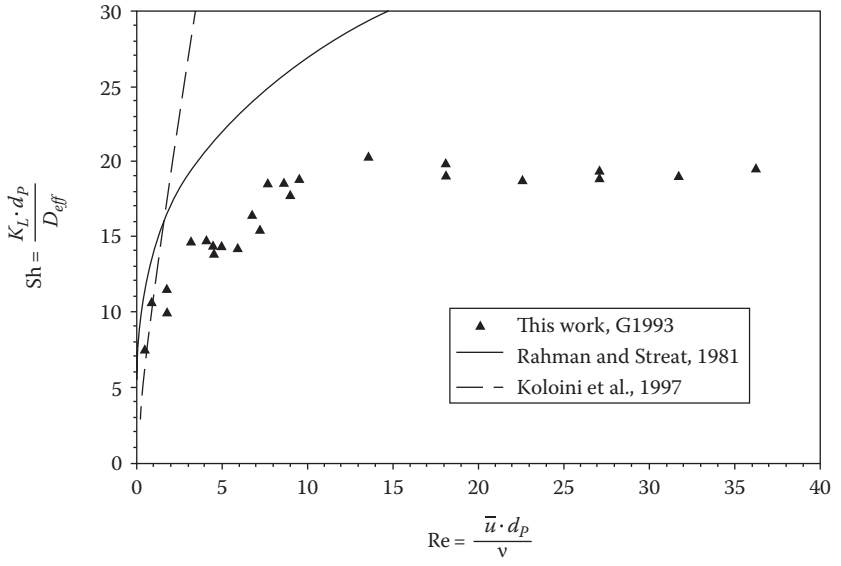

FIGURE 5.13 Liquid to particle mass transfer in a fluidized bed of magnetized G-1993 particles with an applied magnetic field of 7.5 mT, compared to the theoretical behavior of packed beds. (Based on Haussmann, R. et al., *Chem. Eng. Sci*., 55, 1477, 2000. With permission.)

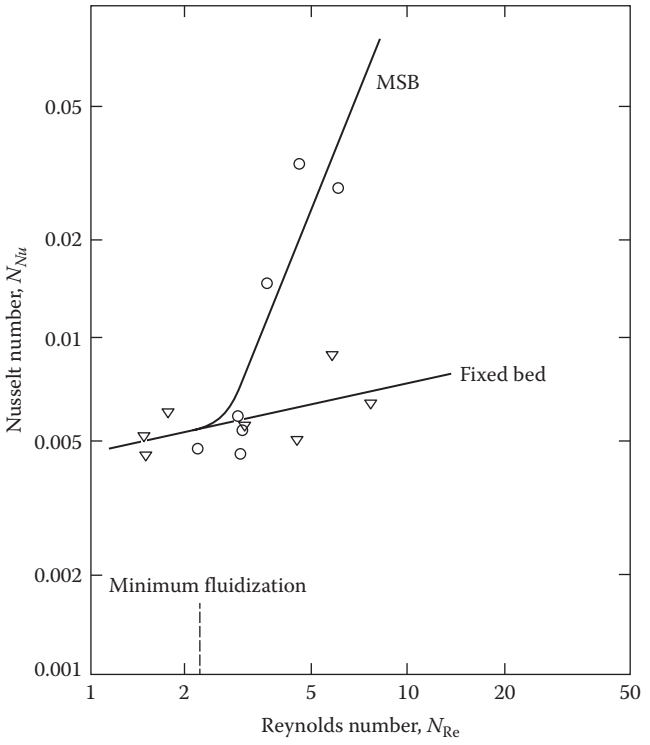

FIGURE 5.14 Gas-particle heat transfer. Comparison between an MSB and a common packed bed. Nusselt versus Reynolds numbers. (Based on Lucchesi, P.J. et al., *Proceedings of the 10th World Petroleum Congress*, Vol. 4, Bucharest, Romania, 1979, pp. 419–425.)

arrived at different conclusions depending on the application. We may even point out that in some experimental setups, the heat transfer worsens because of the lack of bubbling and hence mixing (Levenspiel and Kamholz 1981).

Al-Qodah and coworkers (Al-Qodah et al. 2001) studied the effect of a transverse magnetic field on the hydrothermal behavior of fluidized beds with immersed uniform surfaces.

For good reviews on this topic, the interested reader is addressed to the reviews made by Hristov (2010).

5.7 APPLICATIONS DURING THE LAST DECADE

In Section 5.2 of this chapter, an overview of the historical and traditional applications of MSFBs was presented, including chemical and chemical engineering processes (ammonia synthesis, mass transfer studies and applications, countercurrent contacting gas–solids magnetic valves, coal separation, catalytic applications), environmental applications (aerosol filtration, water treatment, waste removal, metal ions removal), biotechnological applications, bioreactors and bioseparations (separation of proteins, antibody removal/processing and antibiotics production, fermentation and cell/enzyme immobilization, processing of valuable substances [e.g., plant cell culture processing], bilirubin removal, cell separation, immunoglobulin-G depletion and erythrocyte fractionation, bioanalytical techniques [e.g., continuous affinity chromatography], water treatment by application of enzymes, nucleic acids purification), and analytical separations.

In this section, we will focus on the main applications that were studied in the last decade (in some cases, in the last two decades). These have been mainly centered on environmental, catalytic and biotechnological applications, or fundamental studies. Nanoparticles have also been introduced during the last decade and some new and old applications studied using this type of particles.

5.7.1 Main Biotechnological and Biomedical Applications

In the last couple of years, the number of applications of MSFBs in biotechnology and biomedicine has witnessed a significant increase. In fact, until recently, the most known applications of MSFBs in these areas were all directed toward bioreaction, by the use of immobilized enzymes; toward magnetic ion-exchange systems, for protein purification or analytical procedures (such as chromatographic methods); and toward protein adsorption.

In this section, we will review these already established processes and point out also some recently developed applications that stand out by their importance.

5.7.1.1 Enzyme or Cell Immobilization/Bioreactions

Biocatalysts use enzymes or cells as catalyzers in order to catalyze a remarkable spectrum of reactions. However, enzymes present a problem of solubility, and therefore a recovering process (which is always difficult) at the end of the reaction step must be usually incorporated in common bioreactions. Thus, enzyme immobilization is very often the best solution to adopt in order to avoid enzymes to dissolve and flow with the final stream, and thus avoiding product contamination, poor stability, and limited reuse (Webb et al. 1996; Betancor and Luckarift 2008). However, many methods used for enzyme immobilization are not suitable as they lead to the reduction of its activity (by causing structural damages) (Betancor and Luckarift 2008).

Immobilization of enzymes or cells in MSFBs has been a very well accepted method and its high potential has been known for a long time (e.g., Webb et al. 1996). Although the majority of enzyme and cell supports in these applications are nonporous, there are some cases where porous media are used.

The operating principles of enzyme or cell immobilization in MSFBs are quite simple. The first step is concerned with the selection of the appropriate enzyme/cell and reaction process. Betancor and Luckarift (2008) refer several cases concerning their encapsulation in silica supports.

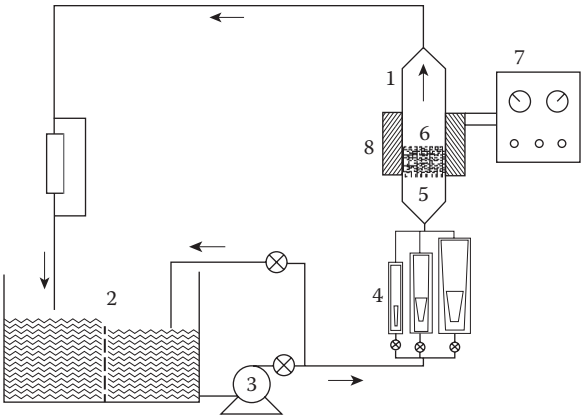

FIGURE 5.15 Experimental setup of an enzyme-immobilized MSFB: 1, MSFB column; 2, recirculation tank; 3, pump; 4, rotameters; 5, distributor; 6, enzyme-immobilized magnetic particle bed; 7, power supply; 8, magnetic coil. (From Webb, C. et al., *Chem. Eng. J.*, 61, 241, 1996. With permission.)

Just for exemplification, we may refer to the use of glucoamylase for the hydrolysis of maltodextrin (Bahar and Celebi 2000), *S. cerevisiae* for ethanol fermentation (Ivanova et al. 1996; Liu et al. 2009), lipase to catalyze the hydrolysis of triacylglycerol to glycerol and fatty acids (Lei et al. 2009), *Thiobacillus thioparus* for biodesulfurization of industrial water (Qiu et al. 2006), HRP for the treatment of phenolic wastewater in continuous systems (Bayramoglu and Arica 2008), and *Penicillium chrysogenum* for antibiotics production (Al-Qodah 2000).

Enzymes/cells are then immobilized in a magnetic support. These magnetic supports may present many compositions but usually are based on a ferromagnetic core, covered with a layer of a certain polymer and/or some sort of epoxy resin that attaches the enzymes/cells. Examples of magnetic supports were referred in Section 5.4 and may be seen in the following references: Betancor and Luckarift (2008), Webb et al. (1996), Al-Qodah and Al-Hassan (2000), Bahar and Celebi (2000), Liu et al. (1991, 2009); Lei et al. (2009), Qiu et al. (2006), Al-Hassan et al. (1991), Ivanova et al. (1996), Bayramoglu and Arıca (2008), Al-Qodah (2000), Safarik and Safarikova (2004), Hristov and Fachikov (2007), Van Hee et al. (2006), and Hristov (1999).

These encapsulated enzymes and their magnetic support matrices are then inserted in an MSFB where they sustain higher flow velocities and present all the advantages of these kinds of beds, as referred in a previous section, which assume particular importance in the case of enzyme-/cell-based reactors.

A typical flow process using magnetic stabilized and fluidized immobilized enzyme beds is depicted in Figure 5.15.

Many examples of immobilized enzymes/cells applications may be found in the literature, and we may refer as typical examples ethanol and fermentation (Ivanova et al. 1996; Al-Qodah and Al-Hassan 2000; Liu et al. 2009), antibiotics production (Al-Qodah 2000), phenol and *p*-chlorophenol removal from wastewaters (Bayramoglu and Arica 2008) or its biodesulfurization (Qiu et al. 2006), synthesis of hexyl acetate (Lei et al. 2009), glucose production (Bahar and Celebi 2000), and starch hydrolysis (Webb et al. 1996).

5.7.1.2 Protein Purification/Adsorption

Protein purification by adsorption is also one of the few *classical* applications of MSFBs in biological and health sciences. Its use is only moderate mainly due to the great efficiency of another well-known competitive method—affinity chromatography. However, when particulate solids are present (early stages of the separation/purification processes), MSFB is presently the most effective method.

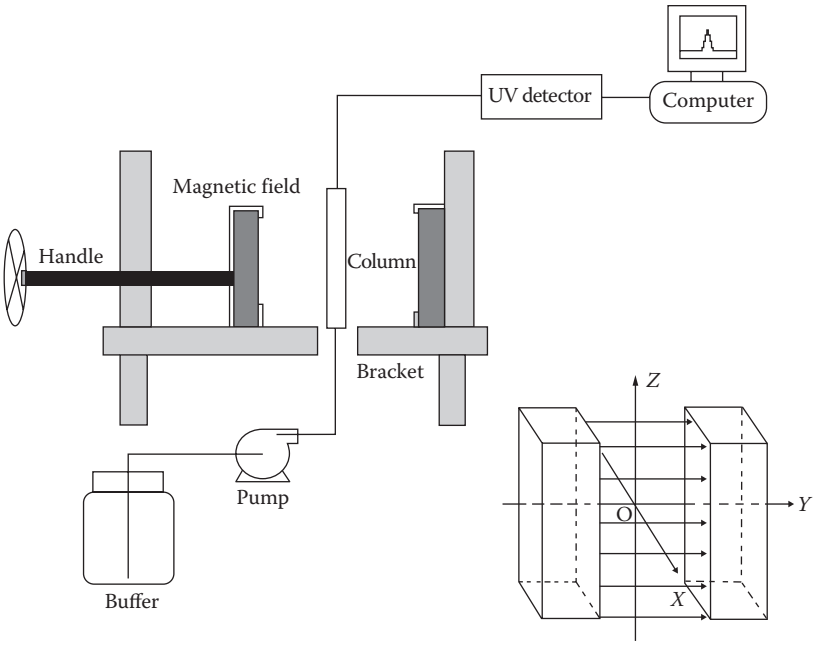

FIGURE 5.16 Experimental setup of an MSFB for protein adsorption. (From Tong, X.D. and Sun, Y., *Biotechnol. Prog.*, 19, 1721, 2003. With permission.)

Protein purification/adsorption by MSFBs depends on the special creation of certain porous nanomagnetic beads that are capable to adsorb the target protein within. These nanomagnetic beads vary largely on their compositions, and details about many of them, mainly how to manufacture and functionalize, can be found in the work of Safarik and Safarikova (Safarik and Safarikova 2004). As previously stated, these nanomagnetic beads are based on a ferromagnetic core covered by a polymeric layer, which is then functionalized (polymers possess a huge variety of surface functional groups that can be tailored to be used in different applications; Turkmen et al. 2006). Polymer chains are then attached onto the surface of the polymeric surface of the porous nanomagnetic beads and form tentacle-type supports that enhance the protein adsorption capability (Turkmen et al. 2006).

These magnetic adsorbents are then inserted in an MSFB setup, as shown in Figure 5.16.

Several proteins are and have been purified by this method; many of them are detailed in the work of Safarik and Safarikova (Safarik and Safarikova 2004). As typical examples, we may refer the cytochrome-c adsorption (Turkmen et al. 2006), lysozyme adsorption (with the kind of beads described earlier or with dye-affinity mPHEMA beads) (Tong and Sun 2003; Basar et al. 2007), BSA adsorption (Tanyolac and Özdural 2000; Ding and Sun 2005), and horse heart myoglobin (Seibert and Burns 1998).

5.7.1.3 MSFB Chromatography

A technique called MSFB chromatography was initiated several decades ago, and it has been developed up to an efficient level. Recently, a novel chromatographic technique using continuous super macroporous monolith has been used for the direct purification of products.

This chromatographic technique is useful in the selective separation of protein and enzymes, and in fact, its difference from the applications detailed in the previous section is often very diffuse, and they may be, in these cases, considered to belong to the same area of applications. There are two typical operation setups: one based on the use of nanomagnetic particles covered by a functionalized porous polymeric layer that are assembled in a magnetic bed structure (Cocker et al. 1997) and

the other being composed of a super macroporous cryogel column containing embedded ferromagnetic nanoparticles that are acted by the external magnetic field and that allow flows similar to those in common chromatographic columns, presenting at the same time several pores that selectively delay the target substances (Yao et al. 2006).

Typical examples of application of MSFB chromatography in biotechnology are the chromatographic application to BSA (Yao et al. 2006), the affinity separation of trypsin from chymotrypsin (Cocker et al. 1997), the affinity purification of trypsin from crude pancreas extract (Bayramoglu et al. 2014), or the dye-ligand affinity chromatography for β-casein purification (Tuzmen et al. 2010).

5.7.1.4 Novel Separations

In this section, we will detail some recent applications of MSFBs in the areas of concern of this work. Some of them could be inserted and considered as being part of the applications described previously; however, due to their importance, they are referred in this separate section.

Immunoglobulin-G separation (Özkara et al. 2004; Karatas et al. 2007; Özturk et al. 2007) and *antibody removal* (Odabas et al. 2005) have been a recent application of MSFBs. They represent an important step concerning clinical analysis and treatment of diseases like lupus and cancer. They are based in the same process as described for protein purification, and while in immunoglobulin-G, functionalized mag-poly(EGDMA-MAH) beads are used, in the antibody removal, functionalized mPHEMA beads are the usual choice.

Separation of cells and nucleic acids are also important applications of MSFBs, and as before, the process is very similar to the previously shown for protein purification (Al-Qodah and Al-Shannag 2006, 2007). A schematic drawing of such a process setup is depicted in Figure 5.17 for the case of yeast cells, where magnetic beads are composed of a magnetite (Fe_3O_4) core, and covered by a stable layer of activated carbon whose function is to adsorb the cells from the suspension.

Unusual applications like the *bilirubin removal* (Uzun and Denizli 2006) may also be found in recent literature, where typical mPHEMA particles are used with human serum albumin immobilized on them. The process setup is similar to the ones used for protein purification.

Applications exist where *Fe_3O_4/alginate complexes* (as the one shown in Figure 5.4) are used (Böhm and Pittermann 2000), as, for example, in *chlorophenol dehalogenation* (Graham et al. 2006). In this application, the process setup is not the conventional one, as may be seen in Figure 5.18.

5.7.2 Environmental Applications

Some environmental applications are closely connected with other areas of application. This is the case of enzyme immobilization—seen in the previous subchapter—for biocatalysis to achieve the removal/transformation of contaminants, which is, of course, also an environmental application. Other environmental applications are pointed in what follows.

One of the major achievements of MSFBs in the environmental area is the use of specially manufactured (see Section 5.4) porous/nonporous magnetic particles that interact and adsorb contaminants from water media; these particles allied with the special features given by MSFBs, concerning diffusional, mass and heat transfer performance, and higher flow rates, provide an efficient combination for environmental treatment of water, wastewater, leachates, and other environmental remediation entities. As seen previously, these particles usually possess an iron oxide core, which is covered by some sort of polymeric layer, that is functionalized (reacted, e.g., with NaOH) in order to present active organic groups; these organic groups are able to selectively attract contaminants that are desired to be removed from watery media. Another major application uses, instead, ion-exchange resins as recovering layer for the same environmental goals.

In several cases, simple ferromagnetic particles are able to perform very effectively the adsorption of heavy metals and their contaminants, thus eliminating the expensive step of covering and functionalization.

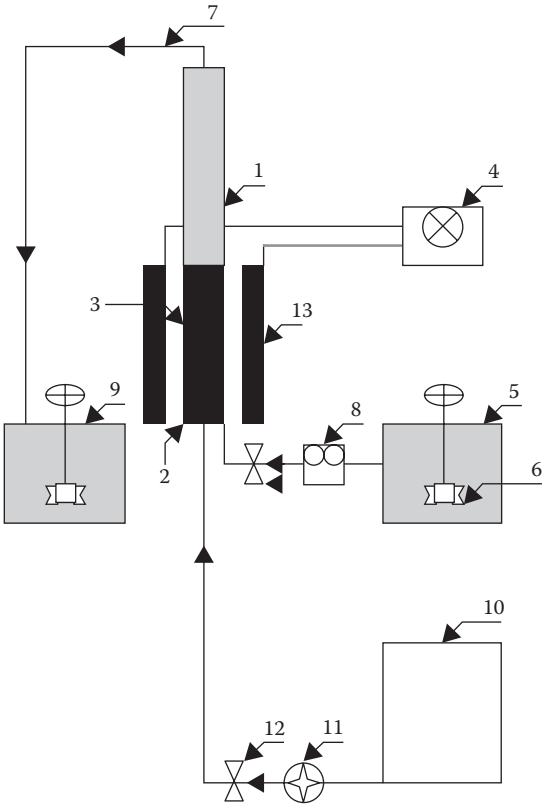

FIGURE 5.17 Schematic of the experimental setup of the application of MSFBs to the removal of yeast cells. 1, column; 2, supporting grid; 3, magnetic particles; 4, power supply; 5, feed tank; 6, mixer; 7, effluent stream; 8, peristaltic pump; 9, effluent receiver; 10, distilled water; 11, centrifugal pump; 12, valve; 13, magnetic system. (From Al-Qodah, Z. and Al-Shannag, M., *Lett. Appl. Microbiol*., 43, 652, 2006. With permission.)

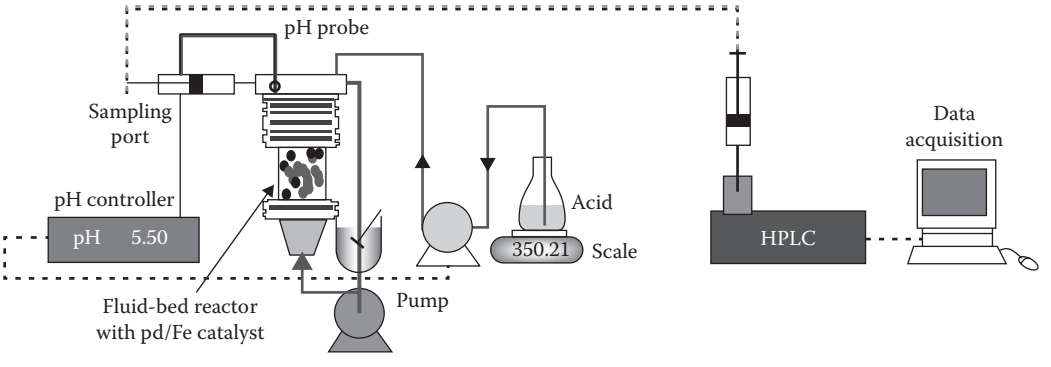

FIGURE 5.18 Schematic of the experimental setup of the application of MSFBs with Fe_3O_4/alginate complexes to the chlorophenol dehalogenation. (From Graham, L.J. et al., *AIChE J*., 52, 1083, 2006. With permission.)

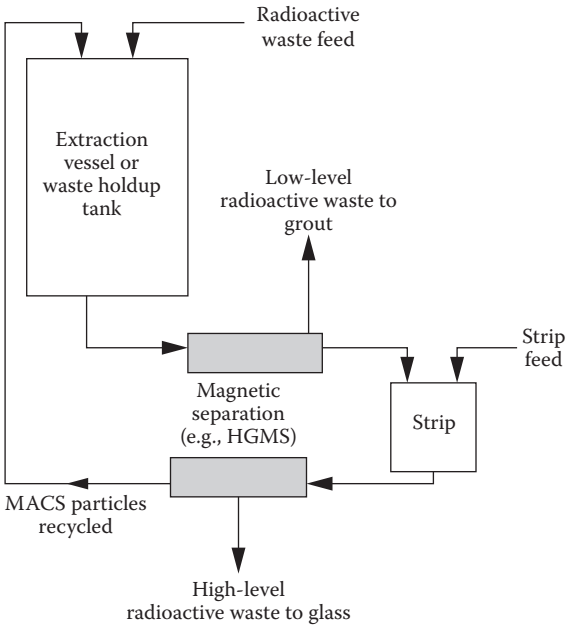

FIGURE 5.19 Concept diagram of MACS process. (From Nuñez, L. and Kaminski, M.D., *J. Magn. Magn. Mater.*, 194, 102, 1999. With permission.)

Waste removal with MSFBs dates back to several decades ago, and we may stand out the work of, for example, Nuñez and Kaminski (1998) that developed a magnetically assisted chemical separation (MACS) method for removal of transuranic elements via magnetic particles covered by various adsorbent/absorbents (clinoptilolite, Transylvanian volcanic tuff, resorcinol formaldehyde, crystalline silica–titanate, etc.). In Figure 5.19, it is depicted the schematic diagram of such process. In this process, small superparamagnetic magnetic carriers (30 nm to 25 μm) provide a simple way to remove these contaminants from solutions under a wide range of chemical conditions; the magnetic carriers are coated with a material that has affinity for the targeted transuranic elements. These magnetic carriers are poured into a tank containing a contaminated solution, where they complex the contaminants. The magnetic carriers and their bound radionuclides are removed after extraction. The magnetic carriers are magnetically separated by one of three methods: (1) placing a magnetic field around the treatment tank, (2) pumping the solution through a magnetic filter (e.g., commercially available high-gradient magnetic separation units), or (3) introducing a magnet into the tank. The contaminant-laden coating is removed by using a small volume of a stripping agent. The magnetic carriers are then regenerated. The concentrated solution containing the contaminant can either be disposed of or treated further to recover the radionuclides (Nuñez and Kaminski 1999).

The magnetic carriers are composed of rare earths or superparamagnetic materials embedded in a polymeric matrix. The surface of the polymeric materials is treated to retain selective chemical extractants (e.g., octyl(phenyl)-*N*,*N*-diisobutyl-carbamoylmethyl-phosphine oxide, trioctylphosphine oxide, di-2-ethylhexyl phosphoric acid, tributyl phosphate, amines, phosphinic acid, crown ethers, cryptands, polyethylene glycols, polyethyleneimine, silicotitanates) (from Nuñez and Kaminski 1999).

Aerosol removal, namely, iron oxide, has also been the subject of study (Rodriguez et al. 1999). In this research, a MSFB is used to achieve the removal of iron oxide particles present in an airstream. In Figure 5.20, a diagram of the process is given. The procedure applied was the following (Rodriguez et al. 1999): prior to each filtration experiment, the air supply from the compressor

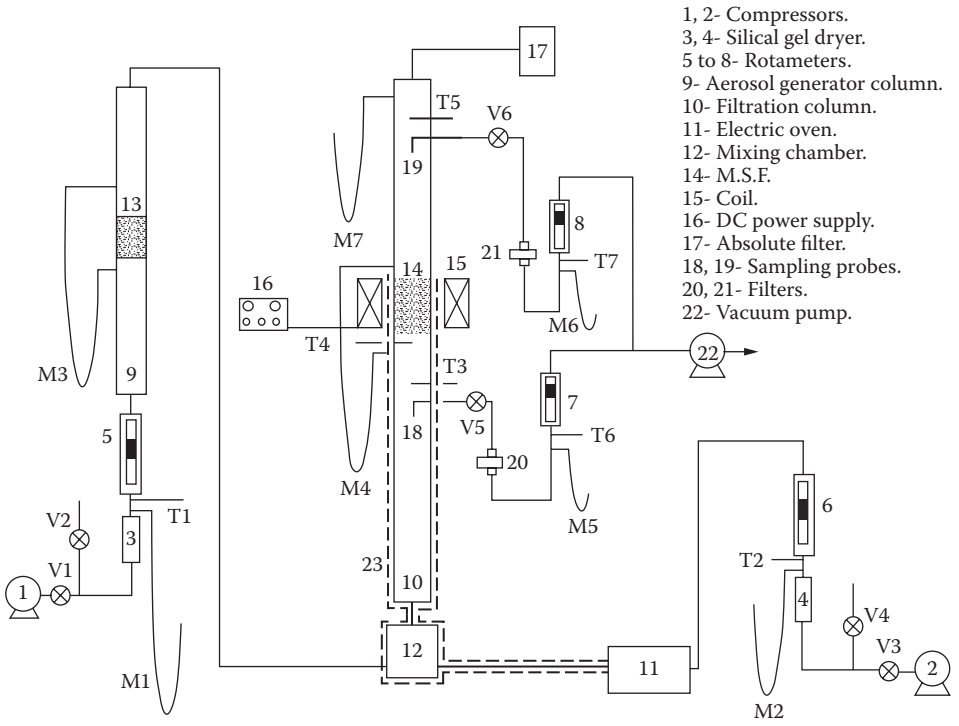

FIGURE 5.20 Diagram of experimental apparatus. (From Rodriguez, J.M. et al., *Ind. Eng. Chem. Res*., 38, 276, 1999. With permission.)

was filtered and dried. The air supply was used to operate the aerosol generator. After the mixture reached a good consistency, the dust with the grain of the fluidized bed, that is, the dust suspension, was allowed to pass through a decanting—mixing chamber. In this chamber, the dust is mixed with hot gas that entered from the other compressor that is connected to a heat exchanger. After that, the dust suspension was allowed to pass through the mass spectrometry facility (MSF). Dust samples were taken simultaneously at both the inlet and the exit of the MSF. The dust that was not collected in the MSF was collected in a chamber with water placed at the exit of the equipment. This chamber enabled the collection of those particles that were not held by the granular filter. The magnetic field was systematically varied to determine its influence on the filtration efficiency. The samples were taken every 30 min, and each experiment lasted for approximately 3 h.

Heavy metal ion removal has been the subject of deep studies and applications. As examples, we may stand out the work of Li and Zhang (Li and Zhang 2000a,b) for chromium and nickel removal from spent electroplating solutions by an MSB of iron–zinc. The feasibility of MSFBs to heavy metal ion removal heavily depends on the particles used, while, on the other hand, the processing procedure is usually the same: the water flow is passed through an MSFB made out by specifically prepared magnetic particles, designed to specifically adsorb the contaminant we are interested in removing; thus, purer water is obtained at the exit stream.

The main bottleneck is the manufacture of the particles and the optimization of their design and performance.

One of the most common manufacturing processes is to achieve the *connection* between the heavy metal ion and the iron oxide particles. Then, we are able to apply successfully an MSFB. Several examples of studies leading to these *connections* are found in literature, namely, (Hristov and Fachikov 2007) cementation of metal ions by other metals for metal recovery such as copper, silver, and gold. (Sedzimir 2002). Copper cementation by iron chips and scrap is a process widely

applied to copper removal from natural and industrial wastewaters (Stefanowicz et al. 1997). Gross (2005) investigated in detail magnetically stabilized iron–zinc admixture beds for copper cementation; precipitations of gold on mild steel (Zhang et al. 1996) and nickel (Vorobyova et al. 2002), mercury on iron and zinc (Anacleto and Carvalho 1996), tin and lead on iron (Makhloufi et al. 2000; Lee et al. 2003), chromium (Li and Zhang 2000b; Niu et al. 2005) and nickel (Li and Zhang 2000b) from spent electroplating solutions by MSBs of iron–zinc mixtures, nitrates deposition on iron particles (Hao et al. 2005a,b), arsenic removal by iron-coated sands and iron oxide–loaded polymers (Zouboulis and Katsoyiannis 2002) and magnetite (Ohe et al. 2005), and uranium from groundwater on iron surfaces (mild steel) (Scott et al. 2005).

Another very common procedure is to manufacture particles (usually iron oxides) that are able to adsorb heavy metal ions. Several reviews on the subject have been written, such as Hritcu et al. (2012) and Petrova et al. (2011). Arsenic removal is an example of a much studied case, for example, Estevez and coworkers (Estevez et al. 2008) described the testing of several iron oxide–based particles for its adsorption, while Simeonidis and coworkers (Simeonidis et al. 2011) report several absorption isotherms.

Adsorption is also very common for other contaminants, for which we may apply (presently or potentially in the future) MSFBs as a possible effective treatment technology. Examples of these are the use of activated carbon/nanoscale zerovalent iron for removal of trihalomethanes from drinking waters (Xiao et al. 2014) or the quite common use of ion-exchange resins for removal of organic matter (Chen et al. 2010b; Wang et al. 2014)—already a common application of MSFBs as a pretreatment stage in wastewater treatment (Zhang et al. 2008) or as a full treatment. In Figure 5.21, it is presented a schematic diagram of the use of a fluidized bed MIEX® contactor as pretreatment of a submerged membrane hybrid system.

Recently, other environmental applications have emerged. This is the case of the selective catalytic reduction of NO by NH_3 over Fe_2O_3 catalyst (Yao et al. 2010). A depiction of the schematic diagram of this process is given in Figure 5.22. Another process is based on the usual connection between environmental and biotechnological applications by using, in this particular situation, immobilized laccase on magnetic mesoporous silica nanoparticle for degradation of phenol in cooking wastewaters (Wang et al. 2012); the schematic diagram of this process is depicted in Figure 5.23.

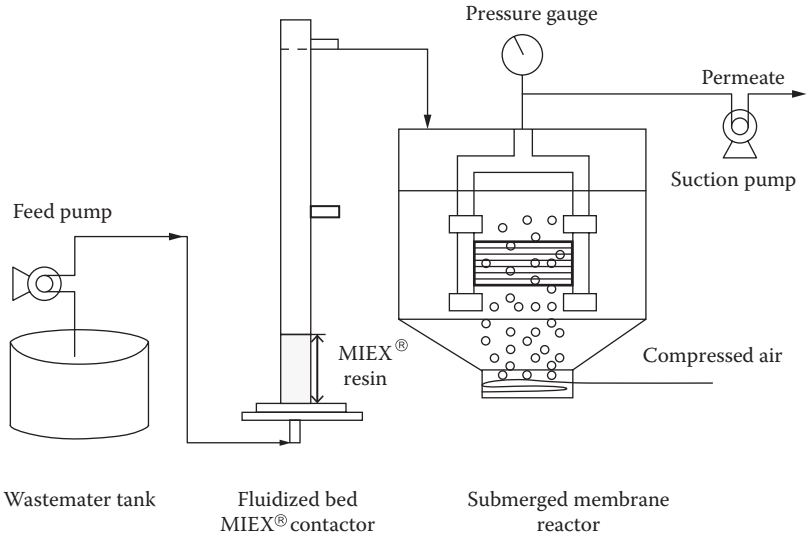

FIGURE 5.21 Schematic diagram of submerged membrane hybrid system with fluidized bed MIEX contactor as pretreatment. (From Zhang, R. et al., *Desalination*, 227, 85, 2008. With permission.)

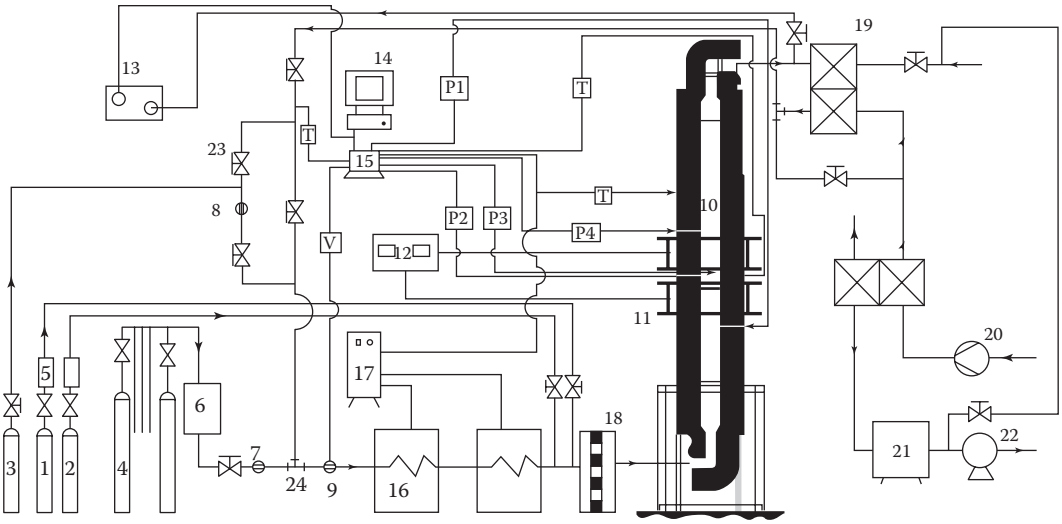

FIGURE 5.22 Schematic diagram of testing apparatus for NO removal from flue gas in an MFB. 1, NO; 2, NH_3; 3, purified air; 4, N_2; 5, mass flow rate controller; 6, N_2 collector tank; 7, N_2 thermal mass flow meter; 8, air thermal mass flow meter; 9, target flow meter; 10, fluidized bed reactor; 11, Helmholtz coils; 12, D.C. stabilized voltage supply; 13, flue gas analyzer; 14, computer; 15, Agilent 34970A data acquisition instrument; 16, electric heater; 17, temperature control cabinet; 18, mixing chamber composed of perforated plates; 19, spiral heat exchanger; 20, vortex fan; 21, bag collector; 22, Lortz vacuum pump; 23, valve; 24, tee; T, temperature; P, pressure; V, volume flow rate. (From Yao, G. et al., *Energy*, 35, 2295, 2010. With permission.)

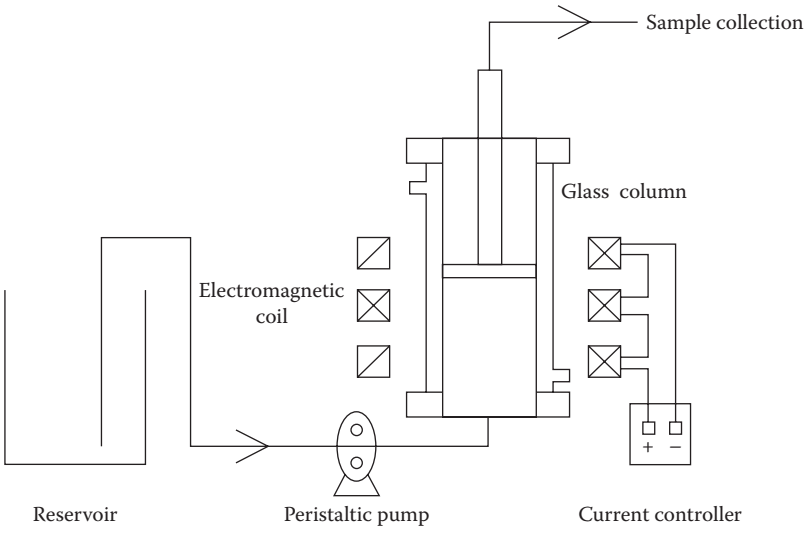

FIGURE 5.23 Schematic diagram of the use of MFB with immobilized laccase on magnetic mesoporous silica nanoparticle for degradation of phenol in cooking wastewaters. (From Wang, F. et al., *Bioresour Technol*., 110, 120, 2012. With permission.)

5.7.3 Catalytic Applications for Process Engineering

Since the work of Filipov (Filipov 1961), MSFB reactors have been applied and explored mainly for pure investigation purposes. Articles on gas–solid and liquid–solid reactors have been published with some frequency, as, for example, it is the case of Hu and Wu (1987), Saxena and Shrivastava (1991), Hristov (1998), and Miura et al. (2001).

In the last decade, we may stand, as an example, the purification of caprolactam in an MSB reactor that was reported by Meng and coworkers (Meng et al., 2003); in this process, the hydrogenation of unsaturated caprolactam into the saturated form, by amorphous nickel alloy catalyst (that constitutes an MSFB), is carried out to allow its removal from raw material used in nylon-6 production. A schematic diagram of the process is given in Figure 5.24.

Chlorophenol dehalogenation, by using composite palladium–iron catalyst in an MSFB, was achieved and reported by Graham and coworkers (Graham et al. 2006), while selective acetylene hydrogenation by using a core–shell magnetic Pd-Al_2O_3 catalyst in an MSFB is described by Dong and coworkers (Dong et al. 2008). Another Pd-based catalyst ($Pd/La_{1-x}Pb_xMnO_3$) was used recently by Lu to synthesize diphenyl carbonate (Lu et al. 2013).

Also recently, CH_4–CO_2 reforming was carried out using MSFBs. The catalyst used and immobilized in the MSFBs is based on $NiCo/Al_2O_3$ (Chen et al. 2010; Li et al. 2013) or simply in Co/Al_2O_3 (Hao et al. 2008). An example of one of the apparatus used for this application is presented in Figure 5.25.

Olefin oligomerization by the use of a magnetic $NiSO_4/Al_2O_3$ catalyst and a light fluid catalytic cracking gasoline feedstock in both fixed bed and MSB reactor was studied by Peng and coworkers (Peng et al. 2009).

A recent review by Zhong et al. (Zhong et al. 2013) overviews the most recent and important applications in the area of reaction engineering and introduces a particular focus on industrial applications.

5.7.4 Other Applications

The search for the fundamental working principles and clear hydrodynamics insight of MSFBs has been the object of research since the dawning of this technology. In fact, it is quite common to step into articles detailing studies performed on this subject. Examples are Quintanilla et al. (2014), Neuwirth et al. (2013), Ursu et al. (2010), Espin et al. (2011), Somchamni (2000), Atodiresei and Badescu (2004), Al-Qodah et al. (2001), Wang et al. (2012, 2013), Eichholz et al. (2014), Cunha et al. (2013), Sobral and Cunha (2003, 2005), Seibert and Burns (1998), Böhm and

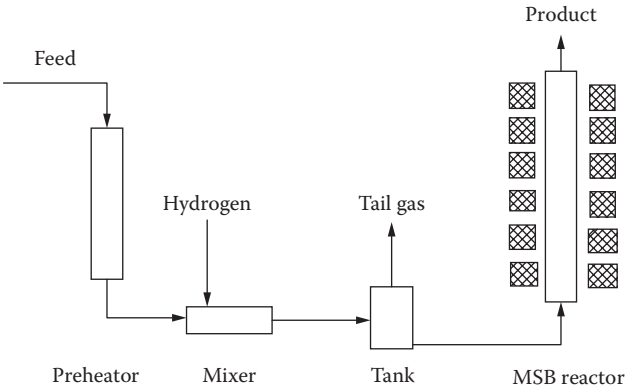

FIGURE 5.24 Flow scheme of the reaction system in caprolactam purification. (From Meng, X. et al., *Catalysis Today*, 79, 21, 2003. With permission.)

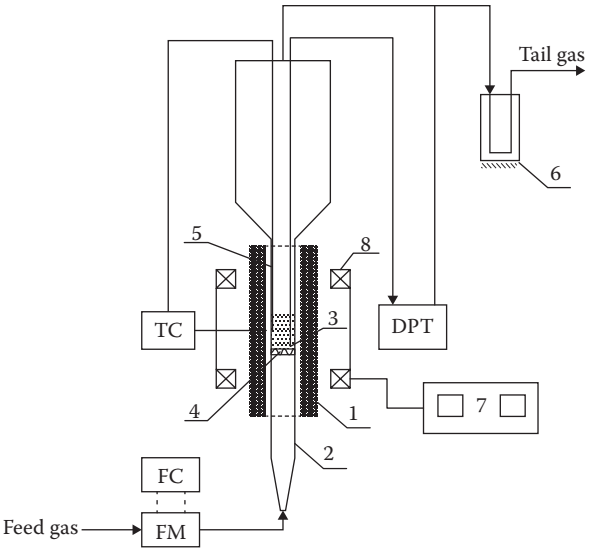

FIGURE 5.25 Schematic diagram of MFB apparatus: FM, flow meter; FC, flow controller; TC, temperature controller; DPT, differential pressure transducer; 1, heat furnace; 2, fluidized bed reactor; 3, pressure port; 4, gas distributor; 5, thermocouple; 6, ice trap; 7, power supply; 8, magnetic solenoids. (From Li, J. et al., *Ind. Eng. Chem. Res*., 52, 6647, 2013. With permission.)

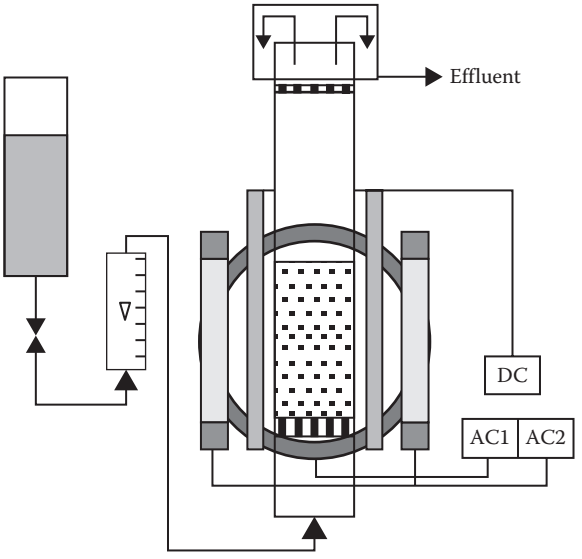

FIGURE 5.26 Schematic diagram of the MSFB used for yield stress experiments. (From Atodiresei, M. and Badescu, V. J. *Magn. Magn. Mater*., 272, 2359, 2004. With permission.)

Pittermann (2000), and Atodiresei and Badescu (2004). In these studies, regular MSFBs are used; however, the system is usually adapted to enhance the parameters under study. Figure 5.26 shows a process diagram of such a study; in this case, the aim is to analyze the yield stress in a fluidized bed stabilized with a compound magnetic field, where the design was changed in order to include the possibility to apply vertical and uniform magnetic fields and a rotating horizontal orientated magnetic field.

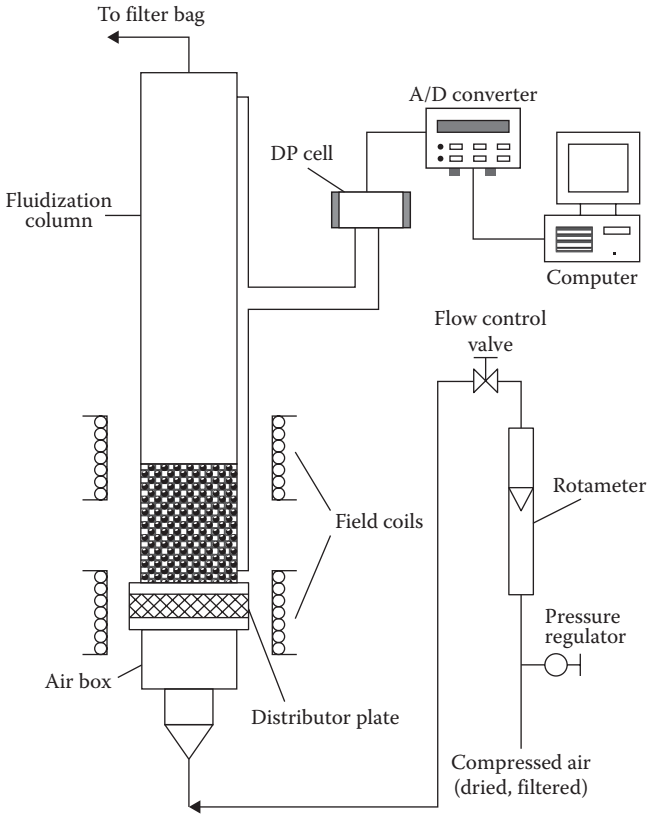

FIGURE 5.27 Schematic diagram of the experimental setup used for Geldart group studies. (From Rhodes, M.J. et al., *Chem. Eng. Sci*., 56, 5429, 2001. With permission.)

Mass transfer has also been the object of several studies, as we have detailed in a previous section.

The study of Geldart Group B to A transition, by using an MSFB, is reported by Rhodes and coworkers (Rhodes et al. 2001); the schematic diagram of the experimental setup used is represented in Figure 5.27, while the biodiesel production by MSFB is reported by Guo and coworkers (Guo et al. 2013); and Si et al. (Si et al. 2013) give details of the photocatalytic degradation of formaldehyde in a fluidized bed, with the novel use of sound-magnetic assistance.

Quite recently nanoparticles have been tested successfully in several applications. As examples, we may stand out the works of Safarik et al. (2012), Philippova et al. (2011), Van Ommen and Pfeffer (2010), Tabnaoui et al. (2013), Zeng et al. (2007), Xiao et al. (2014), Wang et al. (2012), Hao et al. (2008), Yu et al. (2005), Zhou et al. (2011), Chen et al. (2010), and Guo et al. (2013).

5.8 CONCLUSION AND FUTURE PERSPECTIVES

MSFBs have been the subject of study and development for more than six decades. Usual classical applications were aimed specially on chemical engineering processing, although environmental applications were also present in the past. Biotechnological and biomedical applications of MSFBs have only appeared more recently and boomed the impact of MSFBs. In this chapter, we have reviewed the main features of MSFBs, including the background theory, simulations, and main operating principles. Mass and heat transfer topics were also reviewed as one of the major advantages of the technique under focus. A large section was dedicated to the particulate material used in these beds, and although part of them is nonporous, the majority shows porosity, which in some cases is fundamental to achieve efficient results or even any results at all. The major applications

were reviewed, including some recent developments. This has included environmental applications like aerosol treatment, waste removal, metal ions adsorption and removal, phenol degradation, and NO_x reduction. We have also described the main biotechnological and biomedical applications of MSFBs (classical and recent), namely, enzyme immobilization for bioreactions, protein separation, magnetic chromatography, immunoglobulin G separation, antibody removal, separation of cells and nucleic acids, bilirubin removal, and environmental improvements. Catalytic use of MSFBs was also reviewed, namely, its application for purification of caprolactam, chlorophenol dehalogenation, selective acetylene hydrogenation, and more recently, CH_4–CO_2 reforming. Other applications like hydrodynamics, mass and heat transfer, and other fundamental studies were also detailed, as well as nonconventional applications such as particulate group transitions studies, biodiesel production, and photocatalytic degradation of formaldehyde by using sound-magnetic assistance.

The spectrum of future MSFBs applications is vast. This is specially the case in biotechnological and biomedical applications of MSFBs, and also in its environmental applications, as they are usually mainly dependent upon the development of appropriated magnetic beads, and nowadays these magnetic beads are more and more cheap and easier to fabricate and functionalize.

Nanoparticles are also expected to slowly revolutionize MSFBs, as their introduction implies the revisit of many of the classical applications and also means the development of new applications.

REFERENCES

Albert, R. V. and Tien, C. 1985. Particle collection in magnetically stabilized fluidized filters. *AIChE Journal* 31: 288–295.

Al-Hassan, I. V. et al. 1991. Non-porous magnetic supports for cell immobilization. *Journal of Fermentation and Bioengineering* 71: 1–6.

Al-Qodah, Z. 2000. Antibiotics production in a fluidized bed reactor utilizing a transverse magnetic field. *Bioprocess Engineering* 22: 299–308.

Al-Qodah, Z., Al-Busoul, M., and Al-Hassan, M. 2001. Hydrothermal behavior of magnetically stabilized fluidized beds. *Powder Technology* 115: 58–67.

Al-Qodah, Z. and Al-Hassan, M. 2000. Phase holdup and gas-to-liquid mass transfer coefficient in magneto stabilized G-L-S airlift fermenter. *Chemical Engineering Journal* 79: 41–52.

Al-Qodah, Z. and Al-Shannag, M. 2006. Separation of yeast cells from aqueous solutions using magnetically stabilized fluidized beds. *Letters in Applied Microbiology* 43: 652–658.

Al-Qodah, Z. and Al-Shannag, M. 2007. Application of magnetically stabilized fluidized beds for cell suspension filtration from aqueous solutions. *Separation Science and Technology* 42: 421–438.

Anacleto, A. L. and Carvalho, J. R. 1996. Mercury cementation from chloride solutions using iron, zinc and aluminium. *Mineral Engineering* 9(4): 385–397.

Angel, M. E., Jesus, M. R., Audelino, A., Paulo, A. A., Oroncio, J., Castelo-Grande, T., and Barbosa, D. 2008. Preparation, characterization, and testing of magnetic carriers for arsenic removal from water. *IEEE Transactions on Magnetics* 44: 1–8.

Arica, M. Y. 2000. Immobilization of polyphenol oxidase on carboxymethylcellulose hydrogels beads: Preparation and characterization. *Polymer International* 49: 775–781.

Arnaldos, J. and Casal, J. 1987. Study and modelling of mass transfer in magnetically stabilized beds. *International Journal of Heat and Mass Transfer* 30(7): 1525–1529.

Arnaldos, J., Casal, J., Lucas, A., and Puigjaner, L. 1985. *Powder Technology* 44: 57–62.

Atodiresei, M. and Badescu, V. 2004. Yield stress in a fluidized bed stabilized with a compound magnetic field. *Journal of Magnetism and Magnetic Materials* 272–276: 2359–2361.

Augusto, P. A., Castelo-Grande, T., and Augusto, P. 2005. Magnetic classification in health sciences and in chemical engineering. 111(2–3): 85–90.

Augusto, P. A., Castelo-Grande, T., Estevéz, A. M., Barbosa, D., Rodríguez, J. M., Álvaro, A., and Sanchéz, J. 2008. Magnetically stabilized and fluidized beds: Heat and mass transfer. *Defect and Diffusion Forum* 273–276: 46–51.

Bahar, T. and Celebi, S. S. 2000. Performance of immobilized glucoamylase in a magnetically stabilized fluidized bed reactor (MSFBR). *Enzyme and Microbial Technology* 26: 28–33

Basar, N., Uzun, L., Guner, A., and Denizli, A. 2007. Lysozyme purification with dye-affinity beads under magnetic field. *International Journal of Biological Macromolecules* 41: 234–242.

Bayramoglu, G. and Arıca, M. Y. 2008. Enzymatic removal of phenol and p- chlorophenol in enzyme reactor: Horseradish peroxidase immobilized on magnetic beads. *Journal of Hazardous Materials* 156: 148–155.

Bayramoglua, G., Ozalp, V. C., Altintas, B., and Arica, M. Y. 2014. Preparation and characterization of mixed-mode magnetic adsorbent with *p*-amino-benzamidine ligand: Operated in a magnetically stabilized fluidized bed reactor for purification of trypsin from bovine pancreas. *Process Biochemistry* 49: 520–528.

Betancor, L. and Luckarift, H. R. 2008. Bioinspired enzyme encapsulation for biocatalysis. *Trends in Biotechnology* 26(10): 566–572.

Böhm, B. and Pittermann, B. 2000. Magnetically stabilized fluidized beds in biochemical engineering ± investigations in hydrodynamics. *Chemical Engineering Technology* 23(4): 309–312.

Bologa, M. K. and Syutkin, S. V. 1977. Effect of an electromagnetic field on the structure and hydrodynamic characteristics of a fluidized bed. *Electroanna Obrabotka Materialov* (*Russia*) 1: 37–42.

Britton, M. M., Sederman, A. J., Taylor, A. F., Scott, S. K., and Gladden, L. F. 2005. Magnetic resonance imaging of flow-distributed oscillations. *Journal of Physical Chemistry A* 109: 8306–8313.

Burns, M. A. and Graves, D. J. 1985. Continuous affinity chromatography using a magnetically stabilized fluidized bed. *Biotechnology Progress* 1: 95–103.

Chen, J. P., Wang, L. K., Yang, L., and Lim, S.-F. 2006. Emerging biosorption, adsorption, ion exchange, and membrane technologies. In *Handbook of Environmental Engineering,* Volume 5: Advanced Physicochemical Treatment Technologies, eds. L. K. Wang, Y. -T. Hung, and N. K. Shammas, Totowa, NJ: The Humana Press Inc.

Chen, J. P., Yang, L., Wun-Jern, N. G., Wang, L. K., and Thong, S.-L. Ion exchange. In *Handbook of Environmental Engineering,* Volume 4: Advanced Physicochemical Treatment Processes, eds. L. K. Wang, Y. -T. Hung, and N. K. Shammas, Totowa, NJ: The Humana Press Inc.

Chen, L., Zhu, Q., Hao, Z., Zhang, T., and Xie, Z. 2010. Development of a Co-Ni bimetallic aerogel catalyst for hydrogen production via methane oxidative CO_2 reforming in a magnetic assisted fluidized bed. *International Journal of Hydrogen Energy* 35: 8494–8502.

Cocker, T. M., Fee, C. J., and Evans, R. A. 1997. Preparation of magnetically susceptible polyacrylamide/magnetite beads for use in magnetically stabilized fluidized bed chromatography. *Biotechnology and Bioengineering* 53(1): 80–87.

Colver, G. M. 1979. The influence of electric and magnetic fields on air-fluidized beds. In *Proceedings of the NSF Workshop on Fluidization and Fluid-Particle Systems: Research Needs and Priorities,* ed. H. Littman, p. 57. Washington, DC: National Science Foundation.

Conta, P., Gonthier, Y., Bernis, A., and Lacour, G. 1998. Etude et modélisation du comportement hydrodynamique d'un lit fluidisé gaz-solide stabilize. *Powder Technology* 99: 201–209.

Cotten, G. B., Navratil, J. D., and Bradley, H. March 1999. Magnetic adsorption method for the treatment of metal contaminated aqueous waste. In *Waste Management '99 Conference*, Tucson, AZ.

Cunha, F. R., Sobral, Y. D., and Gontijo, R. G. 2013. Stabilization of concentration waves in fluidized beds of magnetic particles. *Powder Technology* 241: 219–229.

Ding, X. B., Sun, Z. H., Wan, G. X., and Jiang, Y. Y. 1998. Preparation of thermosensitive magnetic particles by dispersion polymerization. *Reactive and Functional Polymers* 38: 11–15.

Ding, Y. and Sun, Y. 2005. Small-sized dense magnetic pellicular support for magnetically stabilized fluidized bed adsorption of protein. *Chemical Engineering Science* 60: 917–924

Dong, M., Pan, Z., Peng, Y., Meng, X., Mu, X., and Zong, B. 2008. Selective acetylene hydrogenation over core–shell magnetic Pd-supported catalysts in a magnetically stabilized bed. *AIChE Journal* 54(5): 1358–1364.

Eichholz, C., Knoll, J., Lerche, D., and Nirschl, H. 2014. Investigations on the magnetization behavior of magnetic composite particles. *Journal of Magnetism and Magnetic Materials* 368: 139–148.

Espin, M. J., Valverde, J. M., Quintanilla, M. A. S., and Castellanos, A. 2011. Stabilization of gas-fluidized beds of magnetic powders by a cross-flow magnetic field. *Journal of Fluid Mechanics* 680: 80–113.

Estevez, A. M. et al. 1995. Behavior of magnetizable composites in a liquid-solid magnetofluidized bed. Potential use as a bioreactor. *Chemical and Biochemical Engineering Quarterly* 9(2): 67–77.

Evans, L. L. and Burns, M. A. 1995. Countercurrent gradient chromatography: A continuous focusing technique. *Biotechnology and Bioengineering* 48(5): 461–475.

Fan, L. S. and Zhu, C. H. 1998. Fundamentals of a magnetically stabilized fluidized bed for coal separation. *Principles of Gas-Solid Fluidization.* New York: Cambridge University Press.

Fan, M., Chen, Q., Zhao, Y., Luo, Z., and Guan, Y. 2003. *Coal Preparation* 23: 47–55.

Filipov, M. V. 1961a. A fluidized bed of ferromagnetic particles and the action of magnetic field on it. *Izv Acad Nauk Latv SSR* 12(173): 47–51.

Filipov, M. V. 1961b. The resistance and expansion of a magnetite fluidized bed in a magnetic field. *Troudii Inst Latv SSR* 12: 215–236.

Filipov, M. V. 1962. Some properties of a suspended bed of ferromagnetic particles in a magnetic field. *"Voprosii magn. Gdrodinamiki I dinamiki plasmii"* (Riga) 637–642.

Geuzens, P. and Thoenes, D. 1988a. *Chemical Engineering Communication* 67: 229–242.

Geuzens, P. and Thoens, D. 1988b. *Chemical Engineering Communication* 67: 217.

Graham, L. J., Atwater, J. E., and Jovanovic, G. N. 2006. Chlorophenol dehalogenation in a magnetically stabilized fluidized bed reactor. *AIChE Journal* 52(3): 1083–1093.

Graves, D. J. 1992. Bioseparations in magnetically stabilized fluidized bed. In *Preparative and Production Scale Chromatography*, eds. G. Ganetsos and P. E. Barker, pp. 187–207. New York: Marcel Dekker.

Gross, F. 2005. Intensification of copper recovery from solutions: Cementation in fixed and fluidized beds, mono and bi-component, affected by a magnetic field. Grenoble, France (in French): Doctoral Dissertation, INPG, Grenoble, France.

Gui, K. and Zhang, Q. 2006. Study on the mechanism of the flue gas desulphurization in magnetically fluidized bed. In *Proceedings of 11th Workshop on Transport Phenomena in Two-Phase Flow,* ed. J. Hristov, pp. 61–68.

Guo, P., Huang, F., Huang, Q., and Zheng, C. 2013. Retraction notice to biodiesel production using magnetically stabilized fluidized bed reactor. *Renewable Energy* 55: 561.

Halling, P. J. and Dunnill, P. 1980. Magnetic supports for immobilized enzymes and bioaffinity adsorbents. *Enzyme Microbiology Technology* 2: 1–10.

Hamaker, H. C. 1937. The London van der Waals attraction between spherical particles. *Physica IV* 10: 1058.

Hao, Z., Xu, X., Jin, J., He, P., Liu, Y., and Wang, D. 2005a. Simultaneous removal of nitrate and heavy metals by iron metal. *Journal of Zhejiang University of Science* 6B(5): 307–310.

Hao, Z., Xu, X., and Wang, D. 2005b. Reductive denitrification of nitrate by scrap iron fillings. *Journal of Zhejiang University of Science* 6B(3): 182–186.

Hao, Z., Zhu, Q., Jiang, Z., and Li, H. 2008. Fluidization characteristics of aerogel Co/Al_2O_3 catalyst in a magnetic fluidized bed and its application to CH_4–CO_2 reforming. *Powder Technology* 183: 46–52.

Hausmann, R., Hofmann, C., Franzreb, M., and Holl, W. H. 2000. *Chemical Engineering Science* 55: 1477–1482.

Hausmann, R., Reichert, C., Franzreb, M., and Holl, W. H. 2004. Liquid-phase mass transfer of magnetic ion exchangers in magnetically influenced fluidized beds II. AC fields. *Reactive & Functional Polymers* 60: 17–26.

Herschler, A. 1969. Method for the production and control of fluidized beds. U.S. Patent 3439899.

Hristov, J. Y. 1998. Fluidization of ferromagnetic particles in a magnetic field Part 2: Field effects on preliminarily gas fluidized bed. *Powder Technology* 97(1): 35–44.

Hristov, J. Y. 1999. Remarks on the equipment and the operating modes of fluidized magnetizable particle bed bioreactors (liquid-solid systems). In *Proceedings of the Second Conference "Magnetic Separations in Biosciences and Biotechnologies"*, eds. I. Safarik and M. Safarikova, pp. 97–107. Ceske Budejovice.

Hristov, J. Y. 2002. Magnetic field assisted fluidization—A unified approach. Part 1. Fundamentals and relevant hydrodynamics of gas-fluidized beds (batch solids mode). *Reviews in Chemical Engineering* 18(4–5): 295–509.

Hristov, J. Y. 2003a. Magnetic field assisted fluidization—A unified approach. Part 2. Solids batch gas-fluidized beds: Versions and rheology. *Reviews in Chemical Engineering* 19(1): 1–132.

Hristov, J. Y. 2003b. Magnetic field assisted fluidization–A unified approach. Part 3. Heat transfer—a critical re-evaluation of the results. *Reviews in Chemical Engineering* 19(3): 229–355.

Hristov, J. Y. 2004. Magnetic field assisted fluidization–A unified approach. Part 4. Moving gas—fluidized beds. *Reviews in Chemical Engineering* 20(5–6): 377–550.

Hristov, J. Y. 2006. Magnetic field assisted fluidization—A unified approach. Part 5. A hydrodynamic treatise on liquid—solid fluidized beds. *Reviews in Chemical Engineering* 22(4–5): 195–375.

Hristov, J. Y. 2007. Magnetic field assisted fluidization—A unified approach. Part 6. Topics of gas-liquid-solid fluidized bed hydrodynamics. *Reviews in Chemical Engineering* 23(6): 373–526.

Hristov, J. Y. 2009. Magnetic field assisted fluidization—A unified approach. Part 7. Mass transfer: Chemical reactors, basic studies and practical implementations thereof. *Reviews in Chemical Engineering* 25(1–3): 1–254.

Hristov, J. Y. 2010. Magnetic field assisted fluidization—A unified approach. Part 8. Mass transfer: Magnetically assisted bioprocesses. *Reviews in Chemical Engineering* 26(3–4): 55–128.

Hristov, J. Y. 2012. Magnetic field assisted fluidization—A unified approach. Part 9. Mechanical processing with emphasis on separations. *Reviews in Chemical Engineering* 28(4–6): 243–308.

Hristov, J. Y. and Fachikov, L. 2007. An overview of separation by magnetically stabilized beds: State-of-the-art and potential applications. *China Particuology* 5: 11–18.

Hristov, J. Y. and Ivanova, V. 1999. Magnetic field assisted bioreactors. In *Recent Research Developments in Fermentation and Bioengineering*, Vol. 2, pp. 41–95. Trivandrum, India: SignPost Research.

Hritcu, D., Dodi, G., and Popa, M. I. 2012. Heavy metal ions adsorption on chitosan-magnetite microspheres. *International Review of Chemical Engineering* (*I.RE.CH.E.*) 4(3). Special Section on Open Door Initiative (ODI)—2nd edn, 364–368.

Hu, T. T. and Wu, J. Y. 1987. Study on the characteristics of a biological fluidized bed in a magnetic field. *Chemical Engineering Research and Design* 65: 238.

Hultman, T., Stal, S., Hornes, E., and Uhlen, M. 1989. Direct phase sequencing of genomic and plasmid DNA using magnetic beads as solid support. *Nucleic Acid Research* 17: 4937–4946.

Inavov, D. G. and Grozev, G. T. 1970. Determination of the critical velocity of fluidization of ferrochrome catalyst in a magnetic field. *Zh. Prikl. Khim. (Russia)* 43: 2200–2204.

Ivanova, V., Hristov, J., Dobreva, E., Al-Hassan, Z., and Penchev, I. 1996. Performance of a magnetically stabilized bed reactor with immobilized yeast cells. *Applied Biochemistry and Biotechnology* 59: 187–198.

Jaraiz, E. M. and Estevez, A. M. 1987. Design concepts for collar-type magnetic valve for small-size solids (MVS): Theory and experiments. *Powder Technology* 53: 1–9.

Jaraiz, E. M., Levenspiel, O., and Fitzgerald, T. J. 1983. The uses of magnetic fields in the processing of solids. *Chem Engng Science* 38: 107–114.

Jaraiz, E. M., Wang, Y., Zhang, G. T., and Levenspiel, O. 1984. Theory and operational characteristics of the magnetic valve for solids. Part 1. Grate design. *AIChE Journal* 30: 951–959.

Karatas, M., Akgol, S., Yavuz, H., Say, R., and Denizli, A. 2007. Immunoglobulin G depletion from human serum with metal-chelated beads under magnetic field. *International Journal of Biological Macromolecules* 40: 254–260.

Kirko, I. M. and Filipov, M. V. 1960. The features of a suspended bed of ferromagnetic particles in a magnetic field. *J. Techn. Fiziki (Russia)* 30(9): 1081–1084.

Kochen, R. L. and J. D. Navratil. July 29, 1997. Method for regenerating magnetic polyamine-epichlorohydrin resin. U. S. Patent 5652190 .

Lee, M.-S., Ahn, J.-G., and Ahn, J.-W. 2003. Recovery of copper, tin and lead from the spent nitric etching solutions of printed circuit board and regeneration of the etching solution. *Hydrometallurgy* 70(1–3): 23–29.

Lei, L., Bai, Y., Li, Y., Yi, L., Yang, Y., and Xia, C. 2009. Study on immobilization of lipase onto magnetic microspheres with epoxy groups. *Journal of Magnetism and Magnetic Materials* 321: 252–258.

Levenspiel, O. and Kamholz, K. 1981. Enhancing the characteristics of magnetically stabilized fluidized beds. U.S. Patent 4272893.

Li, G. and Zhang, M. 2000a. Research on the performance of liquid-solid AC magnetic field fluid bed. *Journal of Huainan Institute of Technology* 20(3): 36–40 (in Chinese).

Li, G. and Zhang, M. 2000b. Research on the recovery of chromium and nickel from electroplating spent solution by magnetic field liquid bed. *Journal of Hefei University of Technology* 23(5): 757–760 (in Chinese).

Li, J., Zhou, L., Zhu, Q., and Li, H. 2013. Enhanced methanation over aerogel $NiCo/Al_2O_3$ catalyst in a magnetic fluidized bed. *Industrial and Engineering Chemistry Research* 52: 6647–6654.

Liu, C. Z., Wang, F., and Ou-Yang, F. 2009. Ethanol fermentation in a magnetically fluidized bed reactor with immobilized *Saccharomyces cerevisiae* in magnetic particles. *Bioresource Technology* 100: 878–882.

Liu, Y. A., Hamby, R. K., and Colberg, R. D. 1991. Fundamental and practical developments of magnetofluidized beds: A review. *Powder Technology* 64: 3–41.

Lucchesi, P. J., Hatch, W. H., Mayer, F. X., and Rosensweig, R. E. 1979. Magnetically stabilized beds-new gas solids contacting technology. In *Proceedings of the 10th World Petroleum Congress,* Vol. 4, pp. 419–425. Bucharest, Romania.

Makhloufi, L., Saidani, B., and Hammache, H. 2000. Removal of lead ions from acidic aqueous solutions by cementation on iron. *Water Resources* 34(9): 2517–2524.

Meng, X., Mu, X., Zong, B., Min, E., Zhu, Z., Fu, S., and Luo, Y. 2003. Purification of caprolactam in magnetically stabilized bed reactor. *Catalysis Today* 79–80: 21–27.

Miura, H., Takahashi, T., Ichikawa, J., and Kawase, Y. 2001. Bed expansion in liquid–solid two-phase fluidized beds with Newtonian and non-Newtonian fluids over the wide range of Reynolds numbers. *Powder Technology* 117(3): 239–246.

Moffat, G., Williams, R. A., Webb, C., and Stirling, R. 1994. Selective separations in environmental and industrial processes using magnetic carrier technology. *Mineral Engineering* 7: 1039–1056.

Neff, J. and Rubinsky, B. 1983. The effect of a magnetic field on the heat transfer. *International Journal of Heat and Mass Transfer* 16: 1885–1889.

Nekrassov, Z. I. and Chekin, V. V. 1956. *Izv. Acad. Nauk (Russia)—Metall and Fuels* 1: 56–59.

Nekrassov, Z. I. and Chekin, V. V. 1961. *Izv. Acad. Nauk. (Russia)—Metall and Fuels* 6: 25–29.

Neuwirth, J., Antonyuk, S., and Heinrich, S. 2013. Particle dynamics in the fluidized bed: Magnetic particle tracking and discrete particle modeling. *AIP Conference Proceedings* 1542: 1098.

Niu, S., Liu, Y., Xu, X., and Lou, Z. 2005. Removal of hexavalent chromium from aqueous solution by iron nanoparticles. *Journal of Zhejiang University of Science* 6B(10): 1022–1027.

Novell, E. C. 1984. *Ingeniería Química. 2. Fenómenos de transporte,* p. 283. Alhambra, Madrid.

Nuñez, L. and Kaminski, M. D. 1998. Magnetically assisted chemical separation process. *Filtration & Separation* 35: 349–352.

Nuñez, L. and Kaminski, M. D. 1999. Transuranic separation using organophosphorus extractants adsorbed onto superparamagnetic carriers. *Journal of Magnetism and Magnetic Materials* 194(1–3): 102–107.

Odabas, M., Ozkayar, N., Ozkara, S., Unal, S., and Denizli, A. 2005. Pathogenic antibody removal using magnetically stabilized fluidized bed. *Journal of Chromatography* B 826: 50–57.

Ohe, K., Tagai, Y., Nakamura, S., Ohshima, T., and Baba, Y. 2005. Adsorption behaviour of arsenic (III) and arsenic (IV) using magnetite. *Journal of Chemical Engineering of Japan* 38(8): 671–676.

Ozkara, S., Akgol, S., Cüanak, Y., and Denizli, A. 2004. A novel magnetic adsorbent for immunoglobulin-G purification in a magnetically stabilized fluidized bsed. *Biotechnology Progress* 20: 1169–1175.

Ozturk, N., Gunay, M. E., Akgol, S., and Denizli, A. 2007. Silane-modified magnetic beads: Application to immunoglobulin G separation. *Biotechnology Progress* 23: 1149–1156.

Penchev, I. P. and Hristov, J. Y. 1990. *Powder Technology* 61: 103–118.

Peng, Y., Dong, M., Meng, X., Zong, B., and Zhang, J. 2009. Light FCC gasoline olefin oligomerization over a magnetic $NiSo_4/\gamma\text{-}Al_2O_3$ catalyst in a magnetically stabilized bed. *AIChE Journal* 717–725.

Petrova, T. M., Fachikov, L., and Hristov, J. 2011. The magnetite as adsorbent for some hazardous species from aqueous solutions: A review. *International Review of Chemical Engineering (I.RE.CH.E.)* 3(2).

Philippova, O., Barabanova, A., Molchanov, V., and Khokhlov, A. 2011. Magnetic polymer beads: Recent trends and developments in synthetic design and applications. *European Polymer Journal* 47: 542–559.

Qiu, G., Li, Y., and Zhaoa, K. 2006. *Thiobacillus thioparus* immobilized by magnetic porous beads: Preparation and characteristic. *Enzyme and Microbial Technology* 39: 770–777.

Quintanilla, M., Espin, M., and Valverde, J. M. 2014. Effect of magnetic field orientation on fluidized beds of magnetic particles: Theory and experiment. *Particuology* 12: 54–63.

Rhodes, M. J., Wang, X. S., Forsyth, A. J., Gan, K. S., and Phadtajaphan, S. 2001. Use of a magnetic fluidized bed in studying Geldart Group B to A transition. *Chemical Engineering Science* 56: 5429–5436.

Rodríguez, J. M., Macias-Machin, A., Alvaro, A., Sánchez, J. R., and Estevez, A. M. 1999. Removal of iron oxide particles in a gas stream by means of a magnetically stabilized granular filter. *Industrial and Engineering Chemistry Research* 38: 276–283.

Rosensweig, R. E. 1979. *Science* 204: 57.

Rosensweig, R. E. 1985. *Ferrohydrodynamics.* Cambridge, U.K.: Cambridge University Press.

Rosensweig, R. E. and Ciprios, G. 1991. *Powder Technology* 64: 115.

Rosensweig, R. E., Jerauld, G. R., and Zahn, M. 1981a. Structure of magnetically stabilized fluidized solids. In *Continuum Models of Discrete Systems,* eds. O. Brulin and R. K. T. Hsieh, pp. 137–144. Amsterdam, the Netherlands: North-Holland.

Rosensweig, R. E., Siegell, J. H., Lee, W. K., and Mikus, T. 1981b. Magnetically stabilized fluidized solids. *AIChE Symposium Series* 77(205): 8–16.

Safarik, I., Horska, K., Pospiskova, K., and Safarikova, M. 2012. Magnetically responsive activated carbons for bio and environmental applications. *International Review of Chemical Engineering (I.RE.CH.E.)* 4(3): 346–352. Special Section on Open Door Initiative (ODI)—2nd edn.

Safarik, I. and Safarikova, M. 2004. *BioMagnetic Research and Technology* 2(7): 17.

Sajc, L. M., Jovanovic, Z. R., Vunjak-Novakovic, G., Jovanovic, G. N., Pesic, R. D., and Vukovic, D. V. 1994. *Transactions of the Institution of Chemical Engineering* 72: 236–240.

Saxena, S. C., Ganzha, V. L., Rahman, S. H., and Dolidovich, A. F. 1994. *Advances in Heat Transfer* 25: 151–249.

Saxena, S. C. and Shrivastava, S. 1991. Some hydrodynamic investigations of a magnetically stabilized air-fluidized bed of ferromagnetic particles. *Powder Technology* 57–67.

Scott, T. B., Allen, G. C., Heard, P. J., Lewis, A. C., and Lee, D. F. 2005. The extraction of uranium from groundwaters on iron surfaces. *Proceedings of Royal Society A* 461(2057): 1247–1259.

Sedzimir, J. A. 2002. Precipitation of metals by metals (cementation)—Kinetics, equilibria. *Hydrometallurgy* 64(3): 161–167.

Seibert, K. D. and Burns, M. A. 1998. Effect of hydrodynamic and magnetic stabilization on fluidized-bed adsorption. *Biotechnology Progress* 14: 749–755.

Shames, I. 2002. *Mechanics of Fluids.* McGraw-Hill.

Si, C., Zhou, J., Gao, H., and Liu, G. 2013. Photocatalytic degradation of formaldehyde in a fluidized bed with sound-magnetic assistance. *Advanced Powder Technology* 24: 295–300.

Siegell, J. H. 1984. *Separation Science Technology* 19: 213.

Siegell, J. H. 1987. *Powder Technology* 52: 139–148.

Siegell, J. H. 1988. Applications of crossflow magnetically stabilized fluidized beds. *Chemical Engineering Communications* 67(1): 43–54.

Siegell, J. H. 1989. *Powder Technology* 57: 213–220.

Simeonidisa, K., Gkinisa, T. H., Tresintsi, S., Martinez-Boubetac, C., Vourliasa, G., Tsiaoussisa, I., Stavropoulos, G., Mitrakas, M., and Angelakeris, M. 2011. Magnetic separation of hematite-coated Fe_3O_4 particles used as arsenic adsorbents. *Chemical Engineering Journal* 168: 1008–1015.

Sobral, Y. D. and Cunha, F. R. 2003. A stability analysis of a magnetic fluidized bed. *Journal of Magnetism and Magnetic Materials* 258–259: 464–467.

Sobral, Y. D. and Cunha, F. R. 2005. Hierarchy of concentration waves in magnetic fluidized beds. *Journal of Magnetism and Magnetic Materials* 289: 111–114.

Sonolikar, R. L. 1989. Magneto-fluidized beds. *In Transport in Fluidized Particle Systems,* pp. 359–422. New York: Elsevier.

Sornchamni, T. 2000. The prediction of voidage distribution in a non-uniform magnetically assisted fluidized bed: Theory and experiment. Oregon State University, Corvallis, OR: Master of Science Thesis.

Stefanowicz, T., Napieralska-Zagozda, S., and Osinska, M. 1997. Copper recovery by cementation method. *Hydrometallurgy* 47(1): 69–90.

Tabnaoui, S., Pereiro, I., Fermigier, M., Descroix, S., Viovy, J. L., and Malaquin, L. October 27–31, 2013. Magnetic fluidized bed in microfluidics: Hydrodynamic characterization and validation to immunocapture. In *17th International Conference on Miniaturized Systems for Chemistry and Life Sciences*, pp. 1394–1396. Freiburg, Germany.

Tanyolac, D. and Ozdural, A. R. 2000. A new low cost magnetic material: Magnetic polyvinylbutyral microbeads. *Reactive & Functional Polymers* 43: 279–286.

Terranova, B. E. and Burns, M. A. 1991. Continuous cell suspension processing using magnetically stabilized fluidized beds. *Biotechnology and Bioengineering* 37: 110–120.

Tong, X.-D. and Sun, Y. 2003. Application of magnetic agarose support in liquid magnetically stabilized fluidized bed for protein adsorption. *Biotechnology Progress* 19: 1721–1727.

Turkmen, D., Yavuz, H., and Denizli, A. 2006. Synthesis of tentacle type magnetic beads as immobilized metal chelate affinity support for cytochrome c adsorption. *International Journal of Biological Macromolecules* 38: 126–133.

Tuzmen, N., Akdogan, F., Kalburcu, T., Akgo, S., and Denizli, A. 2010. Development of the magnetic beads for dye ligand affinity chromatography and application to magnetically stabilized fluidized bed system. *Process Biochemistry* 45: 556–562.

Ugelstad, J., Berge, A., and Ellingsen, T. 1992. Preparation and application of new monosized polymer particle. *Progress Polymer Science* 17: 526–529.

Ursu, A.-V., Nistor, I. D., Gros, F., Aruş, A. V., Isopencu, G., and Mareş, A. M. 2010. Hydrodynamic aspects of fluidized bed stabilized in magnetic field. *U.P.B. Scientific Bulletin Series B* 72(3).

Uzun, L. and Denizli, A. 2006. Bilirubin removal performance of immobilized albumin in a magnetically stabilized fluidized bed. *Journal of Biomaterials Science, Polymer Edition* 17(7): 791–806.

van Hee, P., Hoeben, M. A., van der Lans, R. G. J. M., and van der Wielen, L. A. M. 2006. Strategy for selection of methods for separation of bioparticles from particle mixtures *Biotechnology and Bioengineering* 94(4): 689–709.

van Ommen, J. R. and Pfeffer, R. 2010. Fluidization of nanopowders: Experiments, modeling, and applications. In *Proceedings of the 13th International Conference on Fluidization—New Paradigm in Fluidization Engineering,* pp. 1–8. ECI Digital Archives.

Vorobyova, T. N., Poznyak, S. K., Rimskaya, A. A., and Sviridov, V. V. 2002. Side processes at gold cementation on nickel and copper. *Metal Finishing* 100(1): 26–36.

Wallace, A. K. et al. 1991. *Powder Technology* 64: 125.

Wang, F., Hua, Y., Guo, C., Huang, W., and Liu, C.-Z. 2012a. Enhanced phenol degradation in coking wastewater by immobilized laccase on magnetic mesoporous silica nanoparticles in a magnetically stabilized fluidized bed. *Bioresource Technology* 110: 120–124.

Wang, J., Li, H., Li, A., Shuang, C., and Zhou, Q. 2014. Dissolved organic matter removal by magnetic anion exchange resin and released ion elimination by electrolysis. *Chemical Engineering Journal* 253: 237–242.

Wang, S., Guo, S., Gao, J., Lan, X., Dong, Q., and Li, X. 2012b. Simulation of flow behavior of liquid and particles in a liquid–solid fluidized bed. *Powder Technology* 224: 365–373.

Wang, S., Shen, Y., Ma, Y., Gao, J., Lan, X., Dong, Q., and Cheng, Q. 2013. Study of hydrodynamic characteristics of particles in liquid–solid fluidized bed with uniform transverse magnetic field. *Powder Technology* 245: 314–323.

Webb, C., Kang, H.-K., Moffat, G., Williams, R. A., Estévez, A.-M., Cuéllar, J., Jaraíz, E., and Galán, M.-A. 1996. *The Chemical Engineering Journal* 61: 241–246.

Wei, L., Zhiping, D. U., and Hua, Y. et al. 2013. Synthesis of diphenyl carbonate over the magnetic catalysts Pd/La1-xPbxMnO$_3$ (x = 0.2-0.7)[J]. *Chin. J. Chem. Eng*. 21(1): 8–13.

Xiao, J., Yue, Q., Gao, B., Sun, Y., Kong, J., Gao, Y., Li, Q., and Wang, Y. 2014. Performance of activated carbon/nanoscale zero-valent iron for removal of trihalomethanes (THMs) at infinitesimal concentration in drinking water. *Chemical Engineering Journal* 253: 63–72.

Yamaura, M., Camilo, R. L., Sampaio, L. C., Macedo, M. A., Nakamura, M., and Toma, H. E. 2004. Preparation and characterization of (3- aminopropyl)triethoxysilane-coated magnetite nanoparticles. *Journal of Magnetism and Magnetic Materials* 279: 210–217.

Yao, G., Wang, F., Wang, X., and Gui, K. 2010. Magnetic field effects on selective catalytic reduction of NO by NH_3 over Fe_2O_3 catalyst in a magnetically fluidized bed. *Energy* 35: 2295–2300.

Yao, K., Yun, J., Shen, S., Wang, L., He, X., and Yu, X. 2006. Characterization of a novel continuous supermacroporous monolithic cryogel embedded with nanoparticles for protein chromatography. *Journal of Chromatography A* 1109: 103–110.

Yu, Q., Dave, R. N., Zhu, C., Quevedo, J. A., and Pfeffer, R. 2005. Enhanced fluidization of nanoparticles in an oscillating magnetic field. *AIChE Journal* 51: 1971–1979.

Zeng, P., Zhoua, T., Chena, G., and Zhub, Q. 2007. Behavior of mixed ZnO and SiO_2 nano-particles in magnetic field assisted fluidization. *China Particuology* 5: 169–173.

Zhang, H. G., Doyle, J. A., Kenna, C. C., La Brooy, S. R., Hefter, G. T., and Ritchie, I. M. 1996. A kinetic and electrochemical study of the cementation of gold onto mild steel from acidic thiourea solutions. *Electrochimica Acta* 41(3): 389–395.

Zhang, R., Vigneswarana, S., Ngoa, H., and Nguyen, H. 2008. Fluidized bed magnetic ion exchange (MIEX®) as pre-treatment process for a submerged membrane reactor in wastewater treatment and reuse. *Desalination* 227: 85–93.

Zhou, L., Diao, R., Zhou, T., Wanga, H., Kage, H., and Mawatari, Y. 2011. Behavior of magnetic Fe_3O_4 nanoparticles in magnetically assisted gas-fluidized beds. *Advanced Powder Technology* 22: 427–432.

Zouboulis, A. I. and Katsoyiannis, I. A. 2002. Arsenic removal using iron oxide loaded alginate beads. *Industrial Engineering Chemistry Research* 41(24): 6149–6155.

Zrunchev, I. A. 1975. *Annals of Reports of UCTM (Sofia)* 22(4): 171–181.

Zrunchev, I. A. and Popova, T. F. 1975. *Annals of Reports of UCTM (Sofia)* 22(3): 105–110.

6 Lift Generation in Highly Compressible Porous Media
From Red Cells to Skiing to Soft Lubrication

Qianhong Wu

CONTENTS

6.1 On the Motion of the Red Blood Cell over the Endothelial Glycocalyx Layer and Its Implications to Soft Porous Lubrication 160
6.2 Lift Generation in Highly Compressible Porous Media under Rapid Compression: A Systematic, Experimental, and Theoretical Study 160
6.3 Lift Mechanics of Skiing or Snowboarding 160
6.4 From Red Blood Cells to Skiing to Soft Porous Lubrication 160
6.5 On the Motion of the Red Cell over the Endothelial Glycocalyx Layer and Its Implications to Soft Porous Lubrication 161
6.5.1 Endothelial Glycocalyx Layer 161
6.5.1.1 Molecular Sieve for Plasma Proteins 161
6.5.1.2 Mechanotransducer for Fluid Shear Stress 162
6.5.1.3 Highly Compressible Porous Hydrodynamic Interface in the Motion of Red and White Cells in Capillaries 162
6.5.2 Lubrication Theory for Highly Compressible Porous Media 164
6.5.2.1 New Reynolds Equation 164
6.5.2.2 Darcy Permeability 166
6.5.2.3 Results and Discussion 166
6.6 Lift Generation in Highly Compressible Porous Media under Rapid Compression: A Systematic, Experimental, and Theoretical Study 170
6.6.1 Dynamic Compression of Highly Compressible Porous Media with Application to Snow Compaction and Skiing 170
6.6.1.1 Experiments 171
6.6.1.2 Theory 176
6.6.1.3 Remarks on the Dynamic Compression of Snow 188
6.6.1.4 On the Characterization of Lifting Forces during the Rapid Compaction of Deformable Porous Media 190
6.6.1.5 Dynamic Compression of Soft Porous Media: From Finite to Infinite Domain 206
6.7 Lift Mechanics of Downhill Skiing or Snowboarding 217
6.7.1 Theoretical Formulation 218
6.7.1.1 Darcy Permeability of Snow 218
6.7.1.2 Pore Pressure 219

6.7.1.3 Lift Force from Solid Phase 224
6.7.1.4 Force and Moment Balance 225
6.7.2 Results and Discussion 226
6.7.2.1 Rectangular Snowboard or Ski ($g(x) = 1$) 226
6.8 From Red Blood Cells to Snowboarding to a New Concept for a Train Track 234
References 239

In a recent study, Feng and Weinbaum (2000), hereafter referred to as F&W, laid the foundation for a new type of lubrication theory that is applicable for porous medium whose structure is so compressible that the normal forces generated by the elastic compression of the matrix are negligible compared to the pressure forces generated within the porous layer. This new theory shows that there is an unexpected and remarkable dynamic similarity between the motion of a red cell gliding at <20 μm/s on a compressed endothelial glycocalyx layer (EGL) of sulfated proteoglycans and glycoproteins that lines the endothelial cells (ECs) of our capillaries (Figures 6.1 and 6.2a) and a human skier or snowboarder skiing on soft snow powder (Figures 6.3 and 6.46), even though their difference in mass is of the order 10^{15}. F&W predicted that the excess pore pressure generated by a planing surface moving on any compressible porous medium scales as $\alpha^2 = h^2/K$, where h is the layer thickness and K is the Darcy permeability and α is of an order 10^2 or larger for both red blood cells gliding on the EGL as shown in Figure 6.2a and human skiing as shown in Figure 6.3. Thus, the lift forces generated can be four or more orders of magnitude greater than the classical lubrication theory. The huge enhancement in the lift arises from the fact that as the matrix compresses, there is a dramatic increase in the lubrication pressure because of the marked increase in the hydraulic resistance that the fluid encounters as it tries to escape from the confining boundaries through the thin compressed porous layer.

At velocities >20 μm/s, the red blood cell rises out of the EGL and there is an intervening thin fluid lubricating layer between the EGL and RBC membranes. The compression of the EGL is

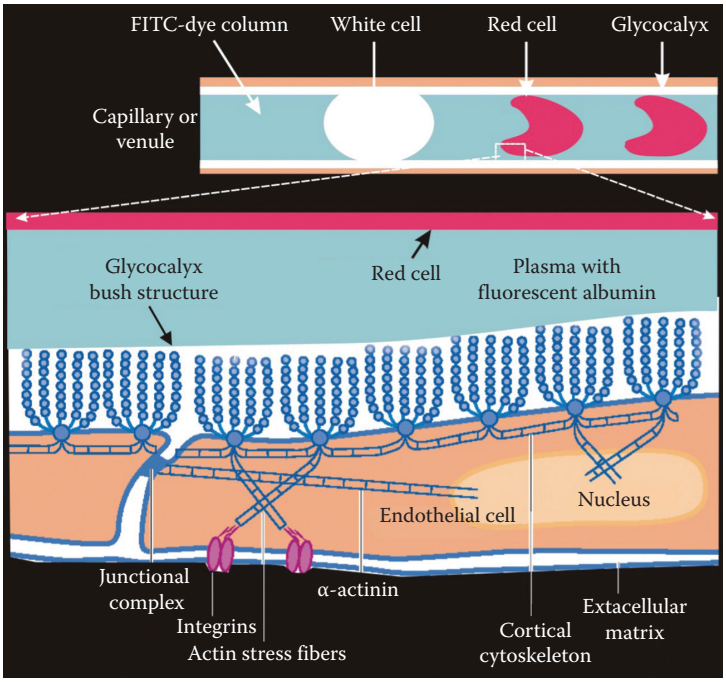

FIGURE 6.1 Schematic of the Vink and Duling (1996) experiment that shows the motion of blood cells over the bush-like EGL rooted from the underlying ACC of the endothelium.

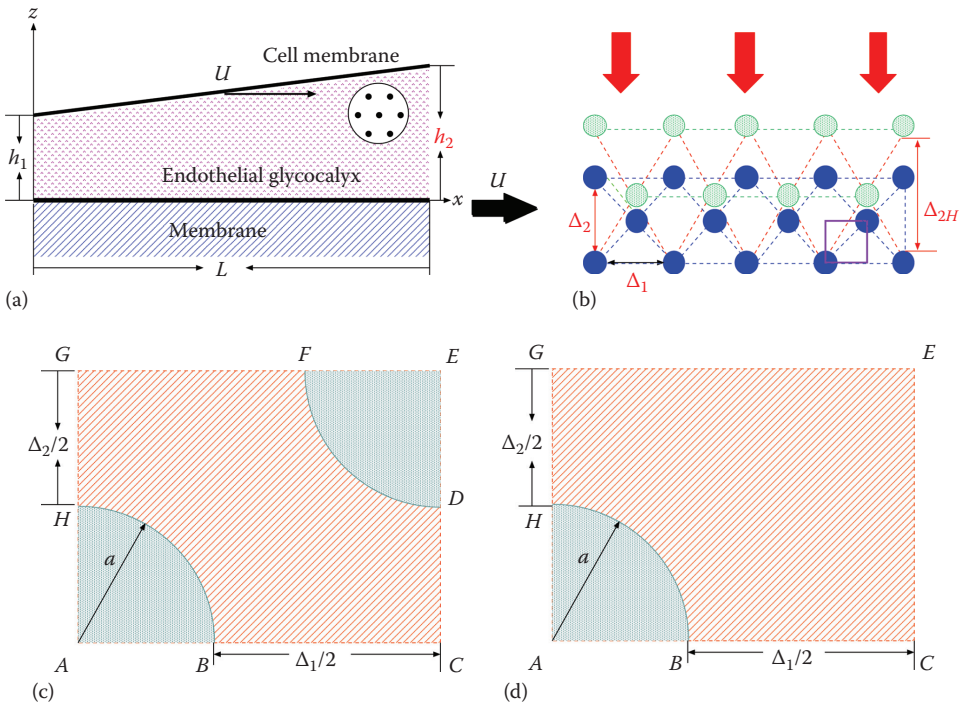

FIGURE 6.2 (a) Schematic illustration of the present model for sliding motion of a rigid planar surface over a thin layer of fiber matrix. (b) Blowup of the inset in (a) shows an idealized model for the fiber matrix that is composed of doubly periodic array of cylindrical fibers of radius a. During compression, only the vertical fiber spacing Δ_2 changes and Δ_1 remains unchanged. (c) A unit cell for a deformed hexagonal fiber array in which the Stokes equation is solved for the local Darcy permeability. (d) A unit cell showing the deformed rectangular fiber array. (Reprinted from Feng, J. and Weinbaum, S., *J. Fluid Mech.*, 422, 282, 2000. With permission from Cambridge University Press.)

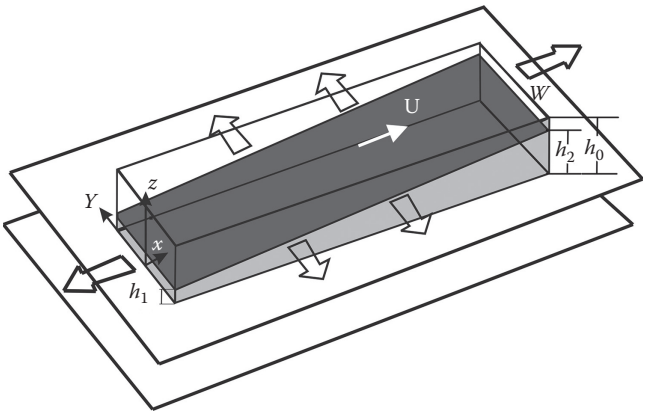

FIGURE 6.3 Schematic illustration of a snowboard or ski compressing a thin layer of fresh powder. Note the escape of air at lateral edges. (Reprinted from Feng, J. and Weinbaum, S., *J. Fluid Mech.*, 422, 282, 2000. With permission from Cambridge University Press.)

caused by the enhanced fluid pressure generated in the thin intervening fluid layer. F&W theory is not directly applicable to this case.

In a more recent paper, Weinbaum et al. (2003) provided a new perspective on the various roles of the EGL in the microcirculation. Based on the quasiperiodic ultrastructural model proposed in Squire et al. (2001), Weinbaum et al. (2003) showed that the flexural rigidity, *EI*, of the core proteins in the bush-like structures comprising the endothelial glycocalyx, as shown in Figure 6.1, is sufficiently stiff for these structures to serve as a molecular sieve and a mechanical transducer of fluid shearing stresses. On the other hand, they show that the buckling forces for the core proteins are one to two orders of magnitude smaller than the hydraulic forces generated during the arrest of the motion of red blood cells. When the red cell velocity is <20 μm/s, the sliding friction between the red cell membrane and the endothelial glycocalyx is proportional to the normal force applied on the solid phase and, therefore, is greatly reduced.

In the past decade, since the pioneering work of Weinbaum and colleagues, significant efforts have been made to understand the lift generation in highly compressible porous media and its broad applications, from biological systems to sports sciences (human skiing or snowboarding), as well as a new concept of soft porous lubrication. In this chapter, a comprehensive review of the recent studies on the lift generation in soft porous media is provided, including the following four sections:

6.1 ON THE MOTION OF THE RED BLOOD CELL OVER THE ENDOTHELIAL GLYCOCALYX LAYER AND ITS IMPLICATIONS TO SOFT POROUS LUBRICATION

In this section, the biological background for the motion of red blood cells over the EGL that covers the inner surface of our blood vessels will be presented. The lubrication theory for highly compressible porous media developed by F&W (2000) will be introduced. This theory is applied to explain the frictionless motion of red blood cells gliding over the EGL, as well as the enhanced lift phenomena for human skiing and snowboarding.

6.2 LIFT GENERATION IN HIGHLY COMPRESSIBLE POROUS MEDIA UNDER RAPID COMPRESSION: A SYSTEMATIC, EXPERIMENTAL, AND THEORETICAL STUDY

In this section, a novel experimental and theoretical approach is presented for the dynamic compression of snow. The purpose of this study is to provide the first experimental examination of the F&W theory. The technical approach and the general idea further lead to a systematic study of the lift generation inside a highly compressible porous medium under rapid compression. This study has a very broad application potential in squeeze damping and soft lubrication.

6.3 LIFT MECHANICS OF SKIING OR SNOWBOARDING

In this section, the lubrication theory for highly compressible porous media is extended to the lift mechanics of downhill skiing and snowboarding. The lift contribution from both the transiently trapped air and the ice crystals is considered. This theory, although applied to the mechanics of skiing, provides a general theoretical framework for applying soft porous media in soft lubrication.

6.4 FROM RED BLOOD CELLS TO SKIING TO SOFT POROUS LUBRICATION

In this section, the concept of lift generation inside a highly compressible porous medium, as a lesson learned from the motion of red cells inside our blood vessels, is applied to the design of a future-generation train that can glide on a track whose permeability and elastic properties are similar to

goose down. This biomimetic application is an example of employing highly compressible porous media for soft lubrication.

The aforementioned four topics entail the track of the development of the lift generation in soft porous media, from biological systems to biomimetic applications.

6.5 ON THE MOTION OF THE RED CELL OVER THE ENDOTHELIAL GLYCOCALYX LAYER AND ITS IMPLICATIONS TO SOFT POROUS LUBRICATION

6.5.1 Endothelial Glycocalyx Layer

At the luminal side of the ECs lies a hydrated layer, the EGL. The EGL is a negatively charged layer of proteoglycans, plasma proteins, and glycosaminoglycans (GAGs) coating the surface of microvessels (Henry and Duling, 1999; Fu and Tarbell, 2013). Its thickness was found to be in the order of 0.1–1 μm by different visualization techniques and in different types of vessels.

Electron microscopy (EM) in vitro: Using EM, Adamson and Clough (1992) performed in vitro studies of frog mesentery microvessels, demonstrating the EGL thickness to be 0.1 μm. In a later study using EM, van den Berg et al. (2003) used a new approach to stabilize the anionic carbohydrate structures on the EGL of the rat left ventricular myocardial capillaries by Alcian Blue 8GX. The EGL thickness was estimated to be 0.2–0.5 μm.

In vivo: The first in vivo observation of the EGL was made by Vink and Duling (1996), who used a 70 kD FITC-dextran plasma tracer and showed that the EGL thickness of hamster cremaster microvessels is 0.4–0.5 μm. Figure 6.1 is a schematic of the Vink and Duling (1996) experiment, which shows the motion of blood cells over the bush-like EGL rooted from the underlying actin cortical cytoskeleton (ACC) of the endothelium. Recently, Gao et al. (2010) obtained similar EGL thickness estimates, ~0.5 μm, in rat mesenteric postcapillary venules by employing FITC-dextran labeling with intravital microscopy. Another technique for estimating the EGL thickness was developed by Long et al. (2004) and Smith et al. (2003) who used high-resolution, near-wall, intravital fluorescent microparticle image velocimetry (μ-PIV). The EGL thickness in mouse cremaster muscle was estimated to be 0.5 μm.

Confocal microscopy: Most recently, Yen et al. (2012) applied high-sensitive, high-resolution, confocal microscopy and in situ/in vivo single microvessel and ex vivo aorta immunostaining, revealing that the thickness of the EGL on rat mesenteric and mouse cremaster capillaries and postcapillary venules is 1–1.5 μm, while the EGL thickness is 2–2.5 μm on rat and mouse aorta. This new technique treated the limits of the poor spatial resolution of intravital optical microscopies.

While the existence of the EGL was first identified nearly 50 years ago (Luft, 1966), its ultrastructural and crucial functions were just recently realized. The fundamental insight of this chapter is the outgrowth of several recent discoveries concerning the role of the EGL as a molecular sieve for plasma proteins, as a mechanotransducer of fluid shear stress, and as a highly compressible porous hydrodynamic interface in the motion of red and white cells in capillaries (Squire et al., 2001; Weinbaum et al., 2007; Reitsma et al., 2011; Curry and Adamson, 2012; Fu and Tarbell, 2013).

6.5.1.1 Molecular Sieve for Plasma Proteins

Michel (1997) and Weinbaum (1998) have proposed that the GAG side chains in this fiber matrix constitute the primary molecular sieve that determines the colloidal osmotic pressure that is felt across the capillary wall. In Hu and Weinbaum (1999), a new microstructural model and interpretation of the classical Starling equation (Starling, 1896) for water movement across capillaries is presented. The new model predicts that the driving forces for water exchange are the hydrostatic and oncotic pressure differences across the thin EGL rather than the global difference in these pressures between plasma and tissue, as had universally been believed for over a century. Recent studies by

Constantinescu et al. (2011) experimentally verified this theory that shows that the EGL contributes to the vascular barrier against transvascular lipoprotein leakage in the microcirculation, as demonstrated in an experiment where diet-induced hyperlipidemia reduced the thickness of the glycocalyx and thus led to enhanced leakage of the chylomicrons across the capillary wall.

6.5.1.2 Mechanotransducer for Fluid Shear Stress

Another vital function of the EGL is to provide a mechanotransduction mechanism via which fluid shear stresses can be communicated to the cortical cytoskeleton of the EC (see Figure 6.1) in initiating intracellular signaling, as proposed by Weinbaum et al. (2003). Due to the existence of this porous layer, the fluid flow inside most region of the EGL is a plug flow dominated by the Darcy law. The fluid shear stress acting on the ECs is greatly attenuated. However, the bending moment applied at the tip of the core proteins of the EGL, as shown in Figure 6.1, is transmitted with little attenuation to the cortical cytoskeleton beneath the EC membrane due to the finite flexural rigidity of the core proteins. Furthermore, the bending arm provided by the core proteins leads to an amplification of the stress acting on the actin cortical scaffold and increases their deformation. Thi et al. (2004) performed a series of experiments and proved this hypothesis by observing if the glycocalyx layer was directly involved in the reorganization of the ACC and the redistribution of various linker proteins in response to fluid shear.

6.5.1.3 Highly Compressible Porous Hydrodynamic Interface in the Motion of Red and White Cells in Capillaries

One of the fundamental mysteries of microcirculation is how an 8 μm in diameter red blood cell is able to glide over the EGL and survive 10^5 passages through microcirculation during a typical lifetime of 120 days without being damaged or undergoing hemolysis. This longevity is quite remarkable in that the red blood cell can travel at velocities that approach 100 times its diameter a second and can also pass, at much lower velocities, through muscular sphincters of a few μm diameters at the entrance to arterioles. A possible mechanism behind the mystery was proposed by F&W, in their classical paper published in the *Journal of Fluid Mechanics*. In this paper, the authors developed a new lubrication theory for highly compressible porous media, which shows that (1) the excess pore pressure generated by a planing surface moving on any compressible porous media, as shown in Figures 6.2a and 6.3, scales as $\alpha^2 = h_2^2/K$, where α is the Brinkman parameter, h_2 is the porous layer thickness at the leading edge, and K is the local Darcy permeability, and (2) α is of an order 10^2 or larger for red blood cells gliding on the EGL. Thus, the lift forces generated can be four or more orders of magnitude greater than the classical lubrication theory. Adhesive proteins in the opposing membranes of the red cells and ECs would be in constant contact were it not for this large pressure (lift) forces generated within the EGL that prevent opposing membranes from touching. (3) The same mechanism applies to a human skiing or snowboarding on fresh snow powder, which has an unexpected, remarkable hydrodynamic similarity to the motion of a red blood cell gliding over the compressed EGL, even though their difference in mass is of the order 10^{15}. Interestingly, α is of the same order for both cases. (4) The huge enhancement in the lift arises from the fact that as the matrix compresses, there is a dramatic increase in the lubrication pressure because of the marked increase in hydraulic resistance that the fluid encounters as it escapes from the confining boundaries through the thin porous layer. Weinbaum et al. (2003) also predicted that the elastic restoring force of the core proteins of the EGL is at most five percent of the pore pressure when the red cell is moving at velocities of even a few μm/s. Thus, the friction drag from the solid phase will be dramatically reduced since most of the load is supported, not by the fibers, but by the fluid pore pressure.

From the structural point of view, the EGL is a remarkable, resilient fibrous porous medium that functions exquisitely to provide a protective lubricating layer and prevents adhesive molecular interaction between proteins in the red blood cell membrane and their ligands in the plasmalemma membrane of the EC. Besides the aforementioned elastohydrodynamic model proposed by Weinbaum and coworkers (F&W; Weinbaum et al., 2003; Wu et al., 2004), who attributed this protective function

to the dramatically enhanced hydrodynamic lifting force generated inside the EGL as a red blood cell glides over it, Secomb and coworkers (1998, 2001a, 2001b) believe it is due to the oncotic pressure, while Damiano and coworkers (2002, 2005) believe it is due to mechanoelectrochemical effects of the EGL. Pries et al. (1997) first introduced the concept that even a minute difference between the concentration of plasma proteins adsorbed to the EGL and that of free plasma proteins in the capillary lumen would be sufficient to generate an oncotic (or colloid osmotic) pressure that would be sufficient to exclude red blood cells from the EGL region near the vessel wall under standard flow conditions in capillaries. This concept was then applied in Secomb et al. (1998, 2001) to develop a model for red blood cell motion in an EGL-lined capillary. They argued that the pressure in the lubrication layer between the red blood cell and the vessel wall, along with the oncotic pressure imposed by the EGL, determines the magnitude of the normal lifting force on the red cell membrane. In contrast, the mechanoelectrochemical model of Damiano and coworkers (2002, 2005) ascribes the repulsive forces to the electrochemical potential gradient between the compressed EGL and the lumen side of the blood vessel. It consists of electrostatic and chemical gradient components. The former accounts for the interactions of the fixed-bound charges on the matrix with the counterions in solution, whereas the latter arises as a result of the higher concentration of bound GAGs, glycoproteins, and proteoglycans in the EGL relative to the concentration of corresponding blood-borne constituents in the lumen. The model predicts that a fixed-charge density of the EGL of 1 mEq/L would result in the magnitude of the stress traction exerted by the layer on passing red cells of 20–30 dyn/cm^2. This result is consistent with the magnitude necessary to account for the exclusion of red blood cells by the EGL observed in skeletal muscle capillaries in vivo (Secomb, 2001) but differs from the predictions by Fu et al. (2003) who show that the charge density of the EGL is ~25–30 mEq/L.

In contrast to snow, the EGL appears to be completely resilient and returns to its equilibrium position in a fraction of a second after the passage of the cell. Three alternate hypotheses have been advanced for the ability of the EGL to restore itself. Weinbaum et al. (2003) proposed that it is due to the flexural rigidity, EI, of the core proteins, the major structural component of the EGL. Here, E and I are the Young modulus and moment of inertia of the core proteins, respectively. The elastohydrodynamic theory of Weinbaum et al. (2003) and Han et al. (2006), based on a detailed ultrastructural model deduced from the electron microscopic images in Squire et al. (2001) of the EGL, predicted the EI of the core proteins to be 490–700 pN·nm^2 and accounted for the restoring force of the EGL as a function of the compression. Secomb (2001) proposed that this weak restoring force is due to an oncotic pressure associated with proteins trapped by fibers in the EGL, and Damiano and Stace (2002) ascribe the structural rigidity of the EGL to the electrochemical forces associated with fixed charges attached to the GAGs.

To date, there is no conclusion with respect to which of the three mechanisms or the combination of them determines the structural integrity and super lubrication feature of the EGL. This is mainly because the experimental verification of these theories is almost impossible because the dimensions of the red cells are obviously too small to obtain detailed pressure measurements, the EGL itself is very fragile and no thicker than one micron, and living cells are contamination prone presenting too many uncontrollable variables. Despite this, the lessons learned from the microcirculation could have significant potential in biomimetic applications. Especially, the lift generation in highly compressible porous media, as proposed in F&W, could have important applications in employing soft porous media in soft lubrication.

During the last decade, evidence has been presented indicating that the EGL plays an important role in vascular homeostasis (Van den Berg and Vink, 2006; Brands et al., 2007; Nieuwdrop et al., 2007; Davies, 2009). Modifications of the EGL structures in the vasculature by enzymes such as pronase, heparinase, and hyaluronidase were found to result in an increased leakage of fluid and solutes across the EGL and the vessel wall (Huxley and Williams, 2000; Bruegger et al., 2005; Singh et al. 2007; Lopez-Quintero et al., 2009), edema formation (van den Berg et al., 2003), impairment in flow-induced endothelial nitric oxide (NO) production (Mochizuki et al., 2003; Nieuwdorp et al., 2006), and increased adhesion of leukocytes (Henry and Duling, 2000; Constantinescu et al., 2003;

Lipowsky et al., 2011). At the arteriolar level, a damaged EGL is associated with impaired shear stress–dependent NO production (Florian et al., 2003; Mochizuki et al., 2003; Kelly et al., 2006; Pahakis et al., 2007), while at the capillary level, perturbation of the EGL can result in reduction of functional capillary density and an inability to recruit glycocalyx volume by agonists. Since cardiovascular disease is the leading cause of death and illness in developed countries and the EGL is actively involved in a variety of vascular functions, such as regulation of vascular tone, fluid and solute exchange, hemostasis, coagulations, and inflammatory responses (Van Den Berg and Vink, 2007), assessment of the state of the EGL as a diagnostic marker for early endothelial dysfunction might become a valuable method for the detection of increased cardiovascular risk in humans.

6.5.2 Lubrication Theory for Highly Compressible Porous Media (Feng and Weinbaum, 2000)

6.5.2.1 New Reynolds Equation

In 2000, the foundation was laid for a new type of lubrication theory for highly compressible porous media in which one could generate lift forces that are several orders of magnitude greater than in the classical lubrication theory (Feng and Weinbaum, 2000). The analysis in F&W was based on a generalized Reynolds equation derived using an effective-medium theory, in which the large local variations in the Darcy permeability in the compressed fiber layer were determined from local solutions of the Stokes equations for the local flow through a compressed 2-D fiber array. This approximate model was applied in F&W to both the endothelial glycocalyx and fresh snow powder. The fundamental new insights gained from this analysis provided the basis for the first rational theoretical and experimental approach for understanding the mechanics of skiing and, equally important, provided the basis for a new type of soft lubricating bearing that might have the potential for indefinite life, since the lift forces generated so greatly exceed conventional lubrication layer forces.

The initial study in F&W was motivated by the red blood cell pop-out phenomenon; however, the critical intuition for understanding this behavior arose from crude measurements of the depth of ski tracks in freshly fallen snow at a ski resort in the northern Catskills, by the senior author of the paper. Nearly every experienced skier will tell you that skiing on dry powder is like skiing on air. Both dry snow powder and the endothelial glycocalyx share the common properties of being highly porous and easily compressed. Snow will compress tenfold when it has to bear the static load of the skier. The crude measurements, just alluded to, readily confirmed that the skier would rise off the packed base and create a thin layer of partially compressed snow, which would be fully crushed when the skier returned and stepped in his or her former tracks. Rough estimates of the lift forces produced using conventional lubrication theory and a classic Reynolds equation were at least three orders of magnitude smaller than the forces required to lift a 70 kg human with his or her skis. It is also intuitively obvious that the basic mechanism is fundamentally different than water skiing, where the density of the water is typically 10 times greater than snow, the angle of attack much greater, and the basic lift mechanism due to inertia. Herein, we briefly summarize the salient equations and results of the new lubrication theory for highly compressible porous media developed in F&W.

First of all, a 2-D rigid boundary as shown in Figure 6.3 is considered, which moves arbitrarily with velocity $\mathbf{U} = (U_x, U_y, U_z)$ over a fiber layer that is thin compared to the characteristic dimensions of the moving boundary in the x and y directions. An effective-medium theory based on the Brinkman (1947) equation is used to describe the flow in the fiber layer:

$$\mu\left(\nabla^2 - \frac{1}{K}\right)\vec{u} = \nabla P, \tag{6.1}$$

where

μ is the dynamic viscosity of the fluid

K is the Darcy permeability of the porous medium

This is a modification of the Stokes equation in which a distributed force described by the Darcy law is added to the overall force balance to describe the resistance of the matrix fibers. In most, if not all previous applications of Equation 6.1, the Darcy permeability K has been treated as uniform. There have been no previous attempts to our knowledge that have tried to include large amplitude local deformations of the matrix and the resulting spatial variation of K in the solution of Equation 6.1.

In F&W, an order of magnitude analysis is performed and it is shown that by using the standard lubrication theory arguments, Equation 6.1 can be rewritten in dimensionless form and reduced to the simplified equations

$$\frac{\partial p}{\partial x} = \left(\frac{\partial^2}{\partial^2 z} - \alpha^2 \right) u \tag{6.2}$$

$$\frac{\partial p}{\partial y} = \left(\frac{\partial^2}{\partial^2 z} - \alpha^2 \right) v, \tag{6.3}$$

where $\alpha = h/K^{1/2}$ is a spatially varying permeability parameter and $p = P/(\mu U_x L/h_2^2)$. Here L is the length of the planning surface in the x direction; h_2 is the thickness of the porous layer at the leading edge. These can be readily solved for the u and v velocity profiles across the fiber layer. These profiles satisfy the no slip conditions on both the stationary lower boundary and the moving upper boundary. The velocity of the upper boundary satisfies the Eulerian relationship

$$U_z = \frac{\partial h}{\partial t} + U_x \frac{\partial h}{\partial x} + U_y \frac{\partial h}{\partial y}. \tag{6.4}$$

When the velocity profiles just described are integrated across the fiber layer and the continuity equation is applied, one obtains, after some algebraic manipulation, a generalized Reynolds equation whose full form is given by the following equation:

$$\frac{\partial}{\partial x}\left[f + \frac{1}{\alpha^2}\frac{\partial p}{\partial x}(2f - h) \right] + \frac{L^2}{W^2}\frac{\partial}{\partial y}\left[\frac{W}{L}\frac{U_y}{U_x} f + \frac{1}{\alpha^2}\frac{\partial p}{\partial y}(2f - h) \right] = \frac{\partial h}{\partial x} + \frac{L}{W}\frac{U_y}{U_x}\frac{\partial h}{\partial y} - \frac{1}{\varepsilon_x}\frac{U_z}{U_x}, \tag{6.5}$$

where

L and W are the length and width of the planing surface, respectively

h is the local thickness of the porous layer normalized by the undeformed porous layer thickness, H

$\varepsilon_x = H/L$

$f = (\cosh \alpha h - 1)/\alpha \sinh \alpha h$

The applications in F&W examine several specialized cases of this equation. One is a simple slider bearing that is sketched in Figure 6.2a. The second is the 2-D planform sketched in Figure 6.3, which is our basic geometry for a ski or snowboard. The third is an axisymmetric model for red blood cell motion.

For the case of 1-D flow shown in Figure 6.2a, where $\mathbf{U} = U\mathbf{i}$, the new generalized Reynolds equation (6.5) reduces to

$$\frac{d}{dx}\left[f + \frac{1}{\alpha^2}\frac{dp}{dx}(2f - h) \right] = \frac{dh}{dx}. \tag{6.6}$$

For the 2-D planform shown in Figure 6.3, where $\mathbf{U} = U\mathbf{i}$, Equation 6.5 reduces to

$$\frac{\partial}{\partial x}\left[f + \frac{1}{\alpha^2}\frac{\partial p}{\partial x}(2f - h) \right] + \frac{L^2}{W^2\alpha^2}(2f - h)\frac{\partial^2 p}{\partial y^2} = \frac{\partial h}{\partial x}. \tag{6.7}$$

Here, L/W, the aspect ratio of the planform, is an important new parameter. The solutions of Equation 6.7 for an elongated planform, such as a ski, can differ greatly from the solutions of (6.6) since $L^2/W^2 \gg 1$ and the second term in (6.7) is of $O(L^2/W^2)$ larger than the first. In F&W, Equation 6.6 is used to describe a 1-D slider bearing with a deformable porous layer or the flow through the endothelial glycocalyx surrounding a red blood cell in a tightly fitting capillary. In the latter application, there is no lateral leakage because the capillary wall surrounds the red blood cell and the fiber layer is a continuous axisymmetric fluid-filled fiber annulus. In contrast to (6.6), Equation 6.7 describes the flow beneath a 2-D planing surface in the thin lubrication layer limit, where Equations 6.2 and 6.3 apply and there is a continuous leakage of fluid along the lateral boundaries as shown in Figure 6.3.

In the limit α equals zero, $f = h/2 - \alpha^2 h^3/24$, and Equations 6.6 and 6.7 reduce to the classical equations of the lubrication theory for 1-D and 2-D flow, respectively. Other than the new form of the generalized Reynolds equation, the key new feature of Equations 6.6 and 6.7 is that the permeability parameter α is spatially varying and depends on the local compression of the matrix. This will be described shortly.

6.5.2.2 Darcy Permeability

In this section, we will very briefly describe the model that was developed in F&W to determine K and hence α as a function of the local compression.

The basic model for the local deformation of the fibers is sketched in Figure 6.2b. It is assumed that in the undeformed state, the fibers form a 2-D periodic array whose resistance is isotropic in the x and z directions and that the flow is perpendicular to the fiber axes. Under compression due to the motion of the upper boundary, F&W assume that the spacing of the fibers in the vertical direction, Δ_2, scales linearly with the displacement of the upper boundary, whereas the spacing in the horizontal direction, Δ_1, remains unchanged since there is little compression in this direction. The deformed matrix is shown by the dark circles in Figure 6.2b. In F&W, two initially undeformed fiber arrays are considered, a hexagonal array, Figure 6.2c, and a square array, Figure 6.2d. New infinite series solutions of the Stokes equations for the deformed array are obtained and the periodicity boundary condition is satisfied using the combined analytical–numerical boundary technique employed in Sangani and Acrivos (1982) for an isotropic fiber array. The forces on the fibers are evaluated using contour integration and the hydraulic resistance of the matrix determined as a function of its compression.

The results for K as a function of the porous layer compression were applied to both the endothelial glycocalyx and columnar snow crystals. This simple model for K was intended to capture the essential physics of the compression process until more realistic experiments could be conducted.

6.5.2.3 Results and Discussion

The results of the theory depart dramatically from classical lubrication theory as the value of the permeability parameter α is increased. We shall first examine the predictions of the 1-D analysis obtained by solving Equation 6.6 and then examine the more complicated 2-D solutions for Equation 6.7. In both cases, it is assumed that the simple inclined planar surface does not deform under loading.

Figure 6.4 shows the solutions for the pressure distribution under a simple slipper bearing as either the parameter α is increased, Figure 6.4a, or the compression ratio $k = h_2/h_1$, the ratio leading to trailing edge gap heights, is increased when α is large, Figure 6.4b. These curves illustrate two very important points. First, in Figure 6.4a, one observes that the dimensionless pressure increases modestly for values of α up to 5 and then grows by nearly four orders of magnitude as α increases to 100. The growth in pressure scales roughly as α^2. Second, in Figure 6.4b, one observes a dramatic change in shape and magnitude of the pressure profiles as k is increased at large α. The latter change is due to the large decrease in K that results from the compression of the matrix as one approaches the trailing edge as k increases. This distortion of the pressure profile leads to a large shift in the position of the pressure maximum.

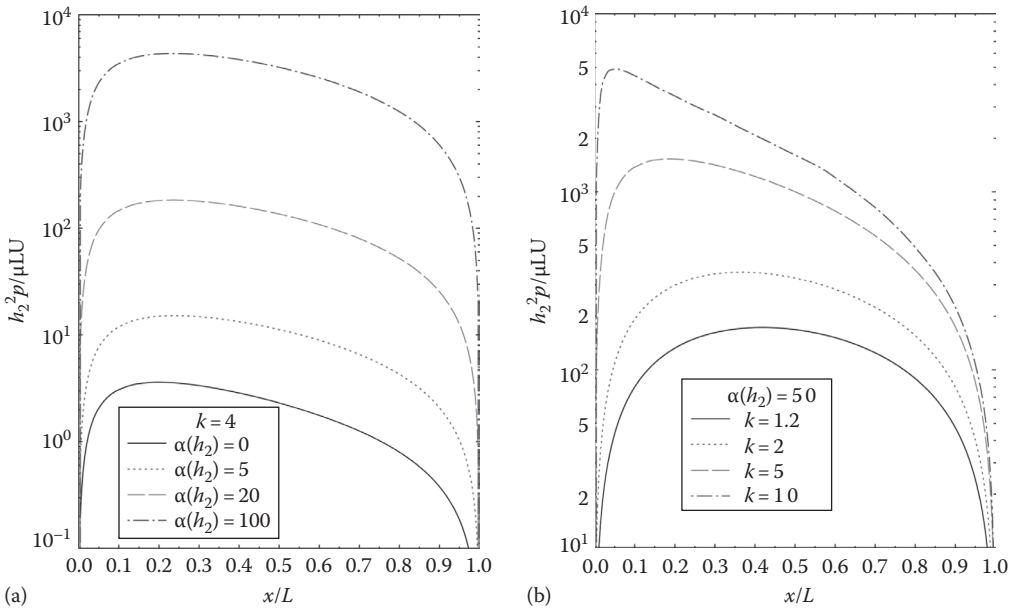

FIGURE 6.4 Dimensionless pressure distribution in a compressed fiber matrix. (a) $k = 4$ and $\alpha(h_2)$ varied. (b) $\alpha(h_2) = 50$ and k varied. $\Delta_1 = 7$ nm; $\Delta_{2H} = 13$ nm; the fiber radius, $a = 0.6$ nm; the compression ratio, $k = h_2/h_1$. (Reprinted from Feng, J. and Weinbaum, S., *J. Fluid Mech.*, 422, 282, 2000. With permission from Cambridge University Press.)

The dramatic changes in the pressure profiles as α is increased are accompanied by equally striking changes in the u velocity profiles shown in Figure 6.5. These profiles are plotted from left to right: at the trailing edge, the position of the maximum pressure, and the leading edge. The results for classical lubrication theory, $\alpha = 0$, are given by the solid line. For a large α, one observes that a 1-D plug flow develops at all locations, that there is a thin fiber boundary layer at the upper and lower surfaces, and that there is little motion over most of the matrix except near boundaries and as one approaches the leading and trailing edges. The fluid motion at the trailing edge ($x/L = 0$) is the most intriguing. It is directed backward due to the very steep adverse pressure gradient that develops at the trailing edge. The streamline thus shows a pattern of dividing streamlines developing beneath the moving surface, which separates the fluid going forward and backward, and that there is no through flow as would occur in traditional lubrication theory. One of the major surprises of the analysis was the close similarity in the values of α for both the red cells and the human skier. In both cases the value of α is of the order of 100. This dynamic similarity will be discussed shortly.

Representative solutions to Equation 6.7 for the centerline pressure profiles beneath a 2-D planing surface are compared in Figure 6.6 with the 1-D profiles, $L/W = 0$, just presented in Figure 6.4 for $\alpha = 0$ and 100. The value of $L/W = 10$ is in between a snowboard, where L/W is typically 5, and a ski, where L/W is typically 20. In general, the pressure buildup is two orders of magnitude smaller than for the 1-D case because of the large leakage of fluid that occurs at the lateral edges. In fact the primary pressure relaxation occurs at these lateral boundaries. As noted earlier, this pressure loss, described by the second term in Equation 6.7, is of order $(L/W)^2$ larger than the leading term describing the stream-wise flow. The 2-D plot of the entire pressure distribution in Figure 6.7 reveals a very important simplification that is the cornerstone for the new theoretical approach outlined in the lift mechanics of skiing developed later in this chapter. Despite the complexity of the profiles in the x direction, the transverse profiles all appear to be parabolic in shape in the y direction. This suggests that the governing

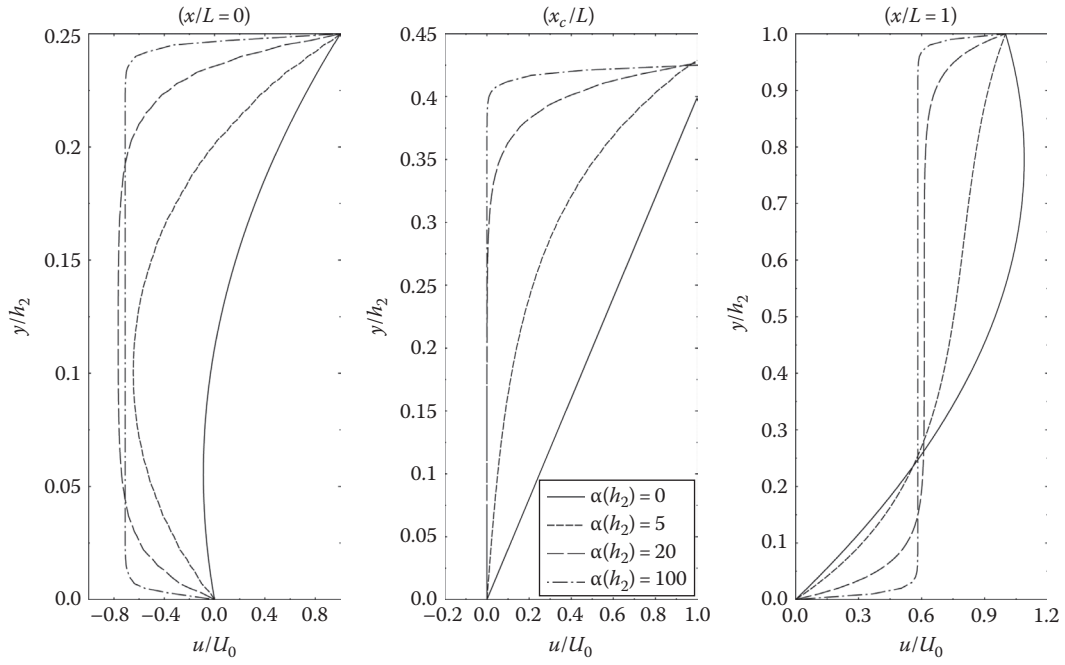

FIGURE 6.5 Normalized horizontal velocity profiles in fiber matrix for representative $\alpha(h_2)$. Three sets of profiles are shown, which correspond to the leading and trailing edges and the position where the pressure reaches its maximum, x_m/L. (Reprinted from Feng, J. and Weinbaum, S., *J. Fluid Mech.*, 422, 282, 2000. With permission from Cambridge University Press.)

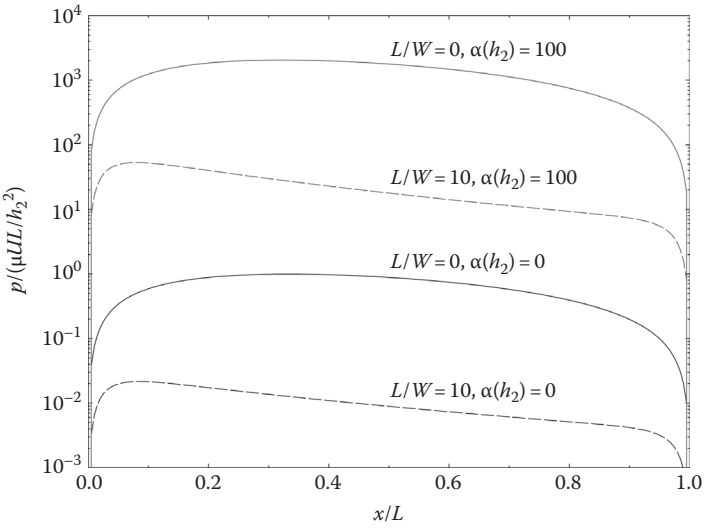

FIGURE 6.6 Comparison of the pressure distribution on the centerline of a ski or snowboard for $L/W = 10$ and on an infinitely wide surface, $L/W = 0$, with no leakage of air at the lateral edges. In both cases $k = h_2/h_1 = 2$. The thickness of the compressed snow powder at the leading edge is assumed to be 2 cm and the value of α at this location $\alpha(h_2) = 100$, a value typical of moderately packed fresh snow. (Reprinted from Feng, J. and Weinbaum, S., *J. Fluid Mech.*, 422, 282, 2000. With permission from Cambridge University Press.)

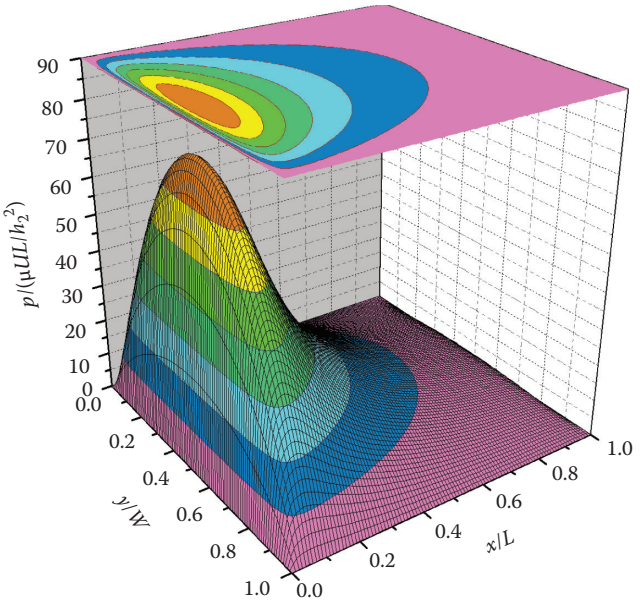

FIGURE 6.7 Pressure distribution and equal pressure contours under a snowboard. The aspect ratio is $L/W = 10$ and the thickness of undeformed snow powder is 2 cm. $\alpha(h_2) = 100$. (Reprinted from Feng, J. and Weinbaum, S., *J. Fluid Mech.*, 422, 282, 2000. With permission from Cambridge University Press.)

equations for the flow in the transverse plane might have a feature that is very similar to the classic solutions for a 2-D stagnation-point flow where the inviscid pressure field is also parabolic.

Figure 6.8 is a summary plot of the total dimensionless lift force generated for an either 1-D or 2-D planar surface as a function of α at the leading edge. For a 0.4 μm thick endothelial glycocalyx with a fiber spacing of 7 nm, $\alpha = 160$. The values of α for skiing (dark circles) are determined by the requirement that the porous medium (snow) is compressed until the lift forces just balance the weight of the skier with his or her skis. This critical value of α depends on the compression ratio k. By bending one's ankles, one can change the tilt angle or compression ratio and produce a much larger compression at the trailing edge. This in turn reduces the required value of α at the leading edge. One notes that the total lift force scales roughly as α^2 for $\alpha > 5$. The remarkable observation is that the tiny red cell is bracketed by the predicted values of α for the human skier whose mass is 10^{15} times larger.

In summary, motivated by recent in vivo studies in the microcirculation and a rapidly growing recognition of the importance of the EGL, F&W developed a generalized lubrication theory for highly compressible porous layers based on an effective-medium approach. This theory predicts orders of magnitude variation in the Darcy permeability within the porous layer. The predictions of this theory support Vink and Duling's (1996) in vivo experimental observations for the pop-out phenomenon of the red blood cells gliding over the EGL. It gives the first explanation for the phenomena of why a 70 kg human can glide over a soft powder snow layer without sinking to the base as would occur if the motion is arrested. This research has far broader implications beyond the red blood cells moving in our capillaries and human skiing or snowboarding since it has the potential to revolutionize the design of lubricating bearings. In particular, it could lead to a new generation of soft bearings with far greater lift forces and much longer life.

On the other hand, while the theory for the pop-out phenomenon of the red blood cell developed in F&W illustrates the striking similarity between a red blood cell and a human skiing, it does not provide a rigorous basis for evaluating the accuracy of the theory or its limitations since the dimensions of the red blood cells are obviously too small to obtain the detailed pressure measurements

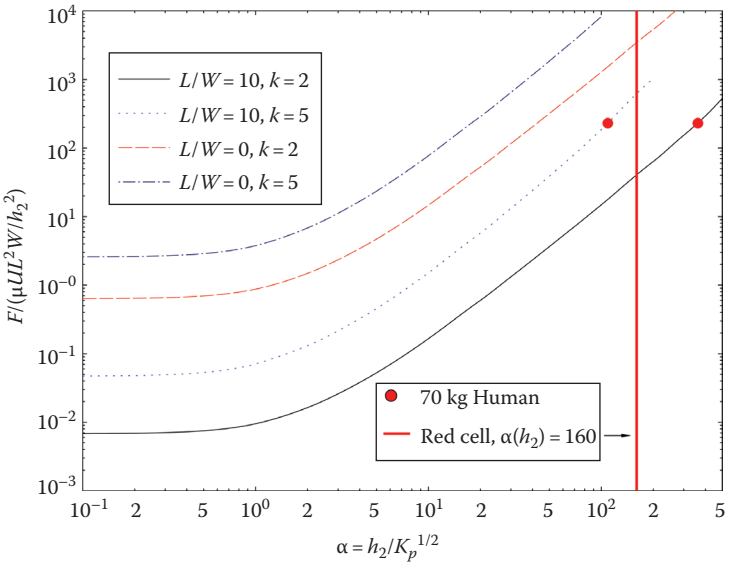

FIGURE 6.8 Increase in the dimensionless lift force as the value of α at the leading edge, $\alpha(h_2)$, increases. For a red cell, $L/W = 0$, $h_2 = 0.4$ μm, $\Delta_1 = 7$ nm, and $\alpha(h_2) = 160$. For a human skiing on a planar surface with $L/W = 10$, the chosen value of α is required such that the lift force supports a 70 kg person. The critical value of α depends on the compression ratio, $k = h_2/h_1$, of the surface. If $h_2 = 2$ cm, $\alpha(h_2) \sim 400$ for $k = 2$ and $\alpha(h_2) \sim 100$ for $k = 5$. (Reprinted from Feng, J. and Weinbaum, S., *J. Fluid Mech.*, 422, 282, 2000. With permission from Cambridge University Press.)

that would be needed for this assessment. This motivated the study described in the following section to experimentally verify the lift generation inside a soft porous medium under rapid discussion, as predicted by F&W.

6.6 LIFT GENERATION IN HIGHLY COMPRESSIBLE POROUS MEDIA UNDER RAPID COMPRESSION: A SYSTEMATIC, EXPERIMENTAL, AND THEORETICAL STUDY

6.6.1 Dynamic Compression of Highly Compressible Porous Media with Application to Snow Compaction and Skiing

Whereas it would be very difficult to measure the excess pore pressure that develops during red blood cell motion, an equivalent experiment can easily be performed for snow in order to verify the F&W theory. Extensive literature exists on the behavior of snow during uniaxial compression (Mellor, 1977; Shapiro et al., 1997). These studies, however, focused on the load bearing capacity of snow as a more permanent supporting structure and the changing microstructure of the snow as a function of aging and load applications. In sharp contrast, when one is observing skiing on unpacked snow (not piste snow or prepared, already compressed surfaces), one is interested in the short-lived initial compression and the changing distribution of the load between the excess pore pressure and the compression of the solid phase before creep begins. To the extent of our knowledge, no one has ever attempted to measure the draining pressure that builds up in snow on a timescale characteristic of skiing or snowboarding. This timescale varies from 0.05 to 0.2 s for skiing velocities of 10 to 30 m/s, depending on the length of the ski.

Wu et al. (2005a) developed a new experimental and theoretical approach that allowed for the examination of the dynamic properties of snow on the timescales encountered during skiing or

snowboarding. The time-dependent pore-pressure response of initially unloaded snow to rapid compression was observed using a novel porous-walled cylinder–piston apparatus. Meanwhile, the mechanical properties of the solid phase of snow were determined in the absence of inertia and the excess pore pressure. In the dynamic experiments, the authors measured the excess pore pressure that built up beneath the piston surface under a rapid compaction as well as its subsequent decay due to the venting of the air from the snow at the porous wall of the cylinder. In the quasistatic experiments where the air was slowly and continuously drained to avoid a buildup in pore pressure, the compressive properties of the solid phase (snow crystals) as a function of instantaneous deformation were measured. Two snow types were used during these experiments: freshly fallen snow and 2-day old snow sampled at different depths in a wind-packed snow layer. A theoretical model was developed using a consolidation approach in order to describe the pore-pressure relaxation within the porous layer. As shown later, the theoretical predictions were in excellent agreement with the experimental results, as long as the initial Darcy permeability K_0 was chosen in the right range.

6.6.1.1 Experiments

6.6.1.1.1 Method

6.6.1.1.1.1 Dynamic Compression Experiments A schematic of the experimental setup is shown in Figure 6.9. The design of this experimental setup consists of a cylindrical sidewall that is porous and is attached to a solid base plate. The design also includes a light piston that can carry additional fixed weights and can slide freely along the inner surface of the cylindrical porous sidewall while providing a uniform loading to the porous medium. The apparatus was designed so that there is no leakage of snow through the porous sidewall or through the clearance gap between the piston and the cylinder. In order to form the desired cylindrical surface, Rigimesh® was used, which filtered out all particles with size greater than 0.120 mm. Rigimesh is an arrangement of several screens sintered together for more rigidity. The mesh provides a negligible airflow resistance, which was evident in tests without snow inside the cylinder. These tests indicated no pressure buildup during a free fall of the piston with a weight. This apparatus has not been designed to realistically reproduce the boundary conditions that one encounters in human skiing or snowboarding, where the undeformed snow near the edges of the compressed snow layer provides additional resistance and a permeable snow base is present. The gap between the piston and the cylinder is less than 1 mm. Snow leakage through this gap during the compression is negligible.

Four high-frequency response subminiature pressure transducers fabricated by Kulite Semiconductor Products, model XCS-062-5-D, were installed on the apparatus to measure the time-dependent pore-pressure distribution inside the snow layer and its spatial variation under rapid compression. One transducer was fixed at the center of the piston; two were installed on the piston

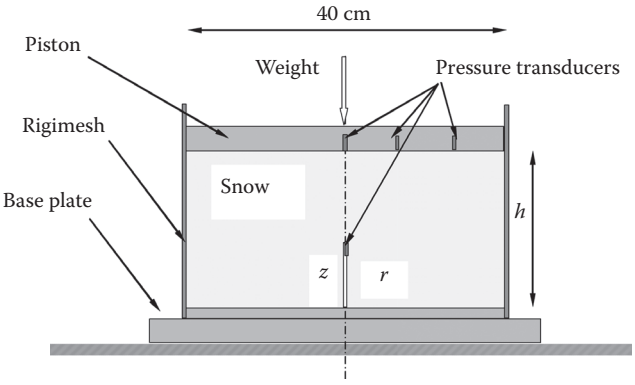

FIGURE 6.9 Schematic of dynamic snow compression apparatus. (Reprinted from Wu, Q. et al., *J. Fluid Mech.*, 542, 281, 2005a. With permission from Cambridge University Press.)

at distances $R/3$ and $2R/3$ away from the center, respectively, where R is the radius of the piston; and the fourth was installed along the centerline of the cylinder with an adjustable height. The inner diameter of the transducer is 1 mm, which is small enough to guarantee good spatial resolution of the local pressure measurement. The pressure transducers were powered by a 9 V battery and calibrated in a small portable pressure chamber with controllable pressure. The electrical outputs were filtered and amplified by EC&G preamplifiers and signal conditioners and then collected by an Iotech 488/8 data acquisition system with 16 bit resolution (an Iotech Filter 488/8 and an ADC488/8SA). Finally, the signals were transferred to a computer for further processing. Pressure was measured relative to the ambient pressure.

The transient pore-pressure responses to rapid deformation and spatial variation were measured by the instrumented apparatus shown in Figure 6.9. The measurement of spatial pressure variation is necessary in order to address the question as to whether a weak "pressure bulb" or a pressure "shock wave" forms beneath the ski or snowboard as a result of compaction. By using prescribed pressure–density curves, Johnson (1991) developed a simple momentum model to compute the pressure attenuation of a shock wave in snow. It was not initially clear whether the snow beneath a snowboard or ski was relatively uniformly compressed or whether such a "pressure bulb" was produced. By observing the pressure distribution measurement along the centerline of the cylinder, this nonuniformity in density can be seen. The theory in Johnson is applied to pressure waves whose amplitude is several orders of magnitude larger than the excess pore pressure developed during skiing, which is several kPa.

The apparatus was filled with snow to a height of approximately 10 cm by using a flat surface snow shovel. In order to ensure that a uniform height/depth of snow was reached in all radial positions of the apparatus, excessive snow was removed by using a long sharp steel blade. The piston was weighted, placed back, and then released under gravity to compress the snow. Setting up the equipment and apparatus and initial tests lasted several hours. The apparatus worked as expected. No snow leakages were observed through the cylindrical sidewall of the container or through its clearance with the piston. The pressure transducers also functioned as expected in the field measurements without problems.

The depth of the snow layer before and after the compression and its mass were measured to determine the initial and final snow density and porosity.

6.6.1.1.1.2 Static Compression Experiment When first developed, the F&W theory was intended to apply to highly compressible porous media in the limit where the structure is so compressible that the normal forces generated by the compression of the solid phase are negligible compared to the pore-pressure forces generated within the porous media. Intuitively, this assumption is only true for alpine skiing on fine-grained dense snow at velocities greater than 20 m/s for a ski length of 2 m. This is because under such conditions, the duration of contact time of the ski with snow is very short (less than 0.1 s) and the air is still transiently trapped inside the porous medium. However, in the dynamic compression experiment discussed herein, the piston is always in contact with snow; thus, the partially compressed solid phase can contribute significantly to the lift force. Furthermore, as the air inside the snow drains through the porous sidewall, the resistant force of the snow crystals increases until it finally supports the entire load. Hence, measuring the quasi-steady force generated when the snow is subject to incrementally increasing compressive forces provided the key insight into the mechanical properties of the solid phase in the absence of piston inertia and excess pore pressure.

In the static compression experiments, the load was added gradually to the piston so that the air in the pores can slowly escape without elevating the pore pressure. This was in contrast to the dynamic experiments in which the air in the pores was temporarily trapped before it escaped. By performing these experiments, it was possible to separate out the inertial effects associated with the acceleration and deceleration of the piston. Due to the length of the time interval between

the load increments (>1 s), air was allowed to escape; however, the bonding of the snow crystals did not occur until the final deformation was achieved and the motion was arrested. The apparatus described in the dynamic compression experiments was used to determine the relationship between applied quasistatic stress and displacement. This made it possible for a relatively realistic estimate of the stress that was applied by the solid phase as the compression proceeded. The deformation of the snow sample was measured immediately after load application, hence excluding creep deformation.

6.6.1.1.2 Snow Samples

The experiments were carried out in March 2002 and 2003 at Hunter Mountain in upstate NY, near the village of Tannersville. Two different types of snow samples were tested.

6.6.1.1.2.1 Wind-Packed Snow Natural snow, two days old, was used in the March 2002 experiments. The snow was dense and wind packed, with fine grains. These characteristics could be attributed to the low temperature (−10°C), windy weather conditions, and the deposition of snow. The ice crystal was in needle shape, typical for the low temperature and windy weather condition. The snow sample had a relatively low porosity and Darcy permeability, as predicted by numerous researchers, that is, Jordan et al. (1999).

6.6.1.1.2.2 Fresh Snow The experiments in March 2003 were performed at the same location as that in the year 2002. Naturally freshly fallen snow was used. The weather conditions were mild and breezy and the ambient temperature was −4°C. The snow was quite soft and fluffy and the ice crystals had a characteristic hexagonal shape. The fresh snow is featured by relatively high porosity and Darcy permeability (Jordan et al., 1999).

6.6.1.1.3 Experimental Results

6.6.1.1.3.1 Dynamic Compression Experiments

6.6.1.1.3.1.1 Wind-Packed Snow Six dynamic compression experiments with wind-packed snow were performed. A representative time-dependent trace of the pore-pressure signals at the center of the piston during the dynamic compression process is shown in Figure 6.10a, for a piston weight of 5.9 kg, comparable to an average normal stress of 456.6 Pa applied on the top surface of the snow layer. It is evident from this figure that the pore pressure inside the snow powder becomes greater than the applied normal stress rapidly. From this observation, it is clear that the air is transiently trapped before it escapes, as suggested by F&W. The compression ratio, $\Delta h/h_0$, was 0.22 in this experiment with an initial height $h_0 = 11.43$ cm. The pore air pressure rises rapidly to its maximum value of 744 Pa within about 0.15 s and then falls back to zero within 1 s. The normal stress in the solid phase at its new equilibrium supports the applied normal force at the end of the experiment.

The timescale of compression is in the same range as the typical timescale of skiing (0.05–0.2 s), assuming a ski or snowboard length between 1.6 and 2 m and a downhill speed between 10 and 30 m/s. This initial experiment was performed on the first design of the apparatus, which had only a single central pressure transducer.

6.6.1.1.3.1.2 Fresh Snow Twelve dynamic snow compression experiments with fresh snow were performed with a load of 10 kg, equivalent to an average normal stress of 778.2 Pa applied on the snow layer. In order to further process the signals, a digital Butterworth low-pass filter design was used. The results of a representative test on the time-dependent pressure signals are shown in Figure 6.10b and c. In Figure 6.10b, signals acquired from the three equally spaced pressure transducers on the piston are shown, where ch#9 refers to the pressure transducer at the center of the piston and ch#1 and ch#2 refer to the pressure transducers on the piston at distances $R/3$ and $2R/3$

away from the center, respectively. Figure 6.10c shows signals obtained from the pressure transducers along the centerline of the cylinder, where ch#10 is the pressure transducer mounted along the centerline, 4.25 cm above the base of the cylinder.

As shown in Figure 6.10b and c, the pore pressure builds up to its maximum value within approximately 0.1 s and then relaxes on a timescale (~0.1 s) that is considerably shorter than the soft wind-packed snow experiment (~1 s). The peak value of pressure at the center of the piston was 300 Pa, roughly 45% of the average normal pressure applied on the bottom surface of the piston. Due to the fresh snow having a large value of K, too large for the excess pore pressure to support the full

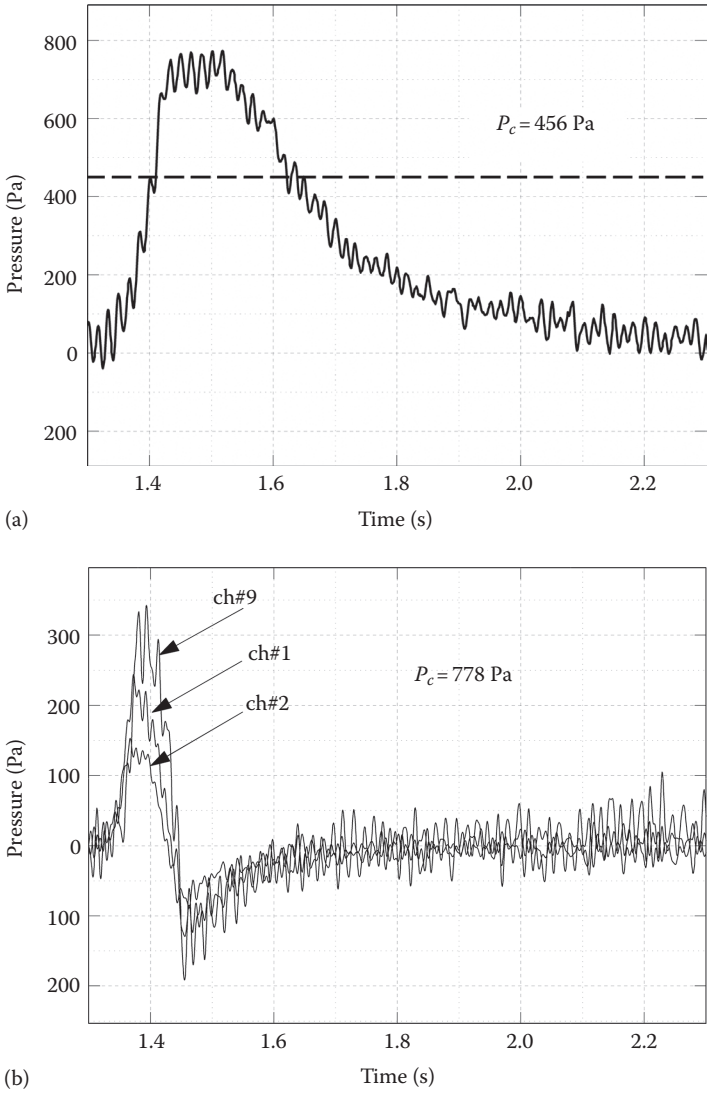

FIGURE 6.10 Time-dependent pressure signals obtained from the dynamic compression experiments: (a) Wind-packed snow, load = 5.9 kg, equivalent to average normal stress of 456.6 Pa, $h_0 = 11.43$ cm, $h_f/h_0 = 0.78$, and $P_{max} = 744$ Pa, with signals that are from the central pressure transducer on the piston. (b) Fresh snow, $h_0 = 8.29$ cm, $h_f/h_0 = 0.83$, and load = 10 kg, equivalent to average normal stress of 778.2 Pa, with signals that are from the three equally spaced pressure transducers on the piston, ch#9 refers to the pressure transducer at the center of the piston, and ch#1 and ch#2 refer to the pressure transducers on the piston at distances R/3 and 2R/3 away from the center, respectively, where R is the radius of the piston. (*Continued*)

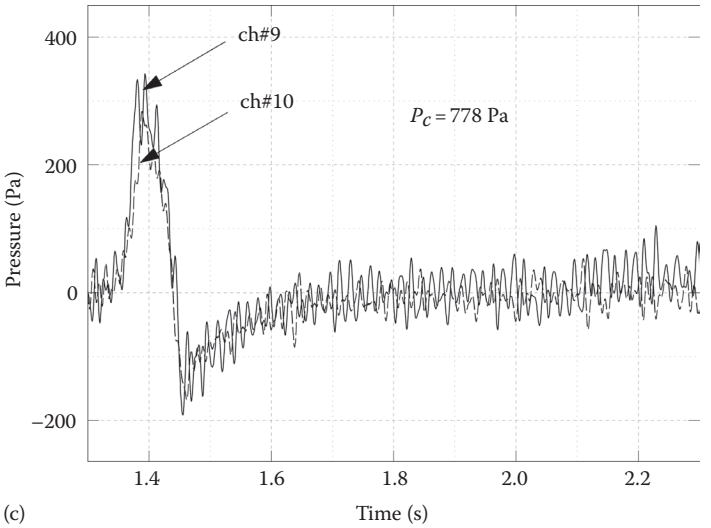

FIGURE 6.10 (*Continued*) Time-dependent pressure signals obtained from the dynamic compression experiments: (c) Fresh snow, $h_0 = 8.29$ cm, $h_f/h_0 = 0.83$, and load = 10 kg, with signals that are from the pressure transducers along the centerline of the cylinder where ch#10 is the pressure transducer mounted along the centerline with 4.25 cm above the base of the cylinder. (Reprinted from Wu, Q. et al., *J. Fluid Mech.*, 542, 281, 2005a. With permission from Cambridge University Press.)

weight of the piston, and the dimensions of the piston being too small, there is no extended pressure relaxation phase for the fresh snow. It is also shown in Figure 6.10b and c that a vacuum is created before the pore pressure finally returned to atmospheric pressure. In this experiment, the initial snow layer thickness is $h_0 = 8.29$ cm and the compression ratio is $\Delta h/h_0 = 0.17$. The porosity was 0.8, a characteristic for fresh snow (Jordan et al., 1999).

6.6.1.1.3.2 Static Compression Experiments After finishing dynamic compression experiments in the field, static experiments were performed on the same type of snow samples using the same apparatus. It was noticed that a small load increment, such as 0.5 kg, could not compress the snow sample, whereas a slightly larger increment, such as 2 kg, could. This is due to the bonding between the snow crystals that creates a threshold for the resistance of compression. A typical incremental loading curve sequence for a static compression test on natural fresh snow with an initial porosity of 0.8 is shown in Figure 6.11.

Both the applied load F and the displacement Δh have been nondimensionalized by their corresponding maximum values. The data for the incremental loading experiments in Yong and Fukue (1977) performed on natural coarse-grained snow with an initial porosity of 0.6 were also plotted for comparison. They were obtained by applying loads incrementally to a snow sample under drained conditions, over a period of two and a half minutes, until a final load intensity of 0.5 kg/cm^2 was reached (Yong and Fukue, 1977). It is evident from looking at the figure that the static experimental results by Wu et al. (2005a) are very similar to the results gathered by Yong and Fukue (1977).

The results shown in Figure 6.11 indicate that the supporting force from the solid phase of the snow sample increases almost linearly with increase in deformation. This is because after the initial instantaneous compression, the bonding of the snow crystal structure becomes increasingly stronger. A resistive force, provided by the microfracture of the partially sintered snow crystals, increases with the applied load until a new bonding equilibrium is achieved. In the experimental study presented herein, the maximum compression was <22% of the undeformed height of the snow layer. This is significantly less than the final critical compaction that would be

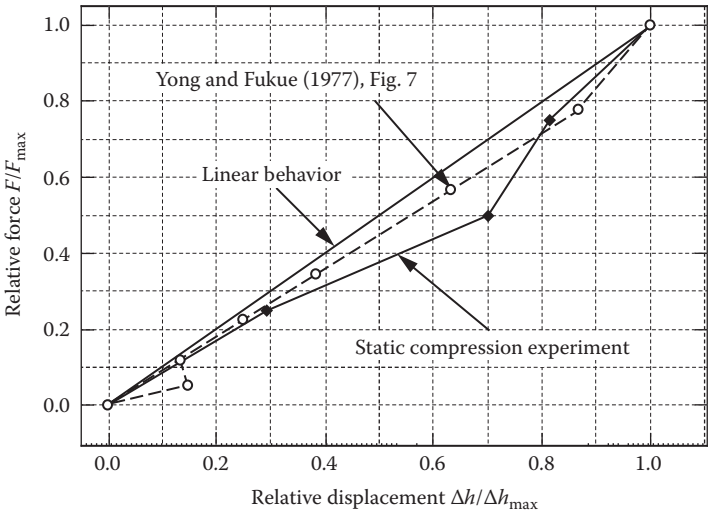

FIGURE 6.11 Force/displacement relation obtained in the quasistatic compression experiment with snow. (Reprinted from Wu, Q. et al., *J. Fluid Mech.*, 542, 281, 2005a. With permission from Cambridge University Press.)

achieved for large applied loads that could lead to critical (maximum) density (0.875 g/cm^3). The experimentally determined force–displacement profile, Figure 6.11, was later used to estimate the increasing force that the ice crystals would exert on the falling piston during the dynamic snow compression experiments.

6.6.1.2 Theory

6.6.1.2.1 Theoretical Model

In Wu et al. (2005a), a theoretical model was developed to predict the pore-pressure distribution during the dynamic compression of snow. By applying Newton's law, the motion of the falling piston can be modeled. As shown in Figure 6.9, the piston was released from rest and starts falling toward a solid planar surface. The distance between the piston and the ground is presumed to be uniform in the radial direction so that Δh, the displacement, is independent of r and varies only with time. A balance of the forces acting on the piston requires that

$$m\frac{d^2h}{dt^2} = -mg + F_{air} + F_{solid}, \tag{6.8}$$

where

m is the mass of the piston
F_{air} is the dynamic pore-pressure force on the piston due to the pore pressure
F_{solid} is the resistance force due to the solid phase (ice crystals) of snow

This model is similar to the Terzaghi consolidation theory (Terzaghi, 1943), which can be applied to both soil mechanics and biomechanics in order to describe the decay of pore pressure in porous media. F_{solid} was approximated from the static compression experiment described in the previous section, where the porous medium is compressed slowly so that the trapped air has enough time to

escape and the entire load is supported by the solid phase. The resistance–deformation relation in Figure 6.3 can be written in the following form:

$$\frac{F}{F_{\max}} = f\left(\frac{\Delta h}{\Delta h_{\max}}\right). \tag{6.9}$$

The dynamic pore-pressure force $F_{air}(t)$ is obtained by integrating the time-dependent pressure acting over the piston:

$$F_{air}(t) = \int_0^R 2\pi r P(r, h, t)\, dr, \tag{6.10}$$

where

R is the radius of the cylinder

$P(r, h, t)$ is found by solving for the instantaneous pore-pressure distribution inside the snow sample

The flow in this device is time dependent, but the instantaneous flow is approximately described by a quasi-steady axisymmetric flow within the cylinder, which satisfies the Darcy law:

$$\mathbf{q} = -\frac{K}{\mu}\nabla P, \tag{6.11}$$

where

μ is the fluid viscosity

K is the Darcy permeability

$\mathbf{q}$ is the specific flux vector with components q_r, q_θ, and q_z in the directions of the cylindrical r, θ, and z coordinates, respectively

In a consolidating porous medium where the porous matrix endures deformation during the process of transient fluid flow, $\mathbf{q}$ is the relative specific flux with respect to the solid grains. In the experimental study presented herein, the displacement of the ice crystals was less than 22% of the 10 cm thickness of the snow layer, while the characteristic discharge distance for the air is equal to the radius of the cylinder, which is 20 cm. As a result, the ice crystal velocity is negligible compared to the air velocity and $\mathbf{q}$ is assumed to be specific flux with respect to a fixed coordinate system

$$\mathbf{q} = \phi \mathbf{V}_1, \tag{6.12}$$

where

$\mathbf{V_1}$ is the local velocity vector (velocity of air within the pores)

ϕ is the porosity

$$\phi = \frac{U_v}{U_i}, \tag{6.13}$$

where

U_i is the volume of the porous medium

U_v is the volume of void space within U_i

Relationship (6.12) is sometimes called the Dupuit–Forchheimer equation (Bear, 1972).

Figure 6.10c indicates the pressure variation in the vertical direction is negligible, which implies no pressure bulb exists in the vertical direction and the snow is compressed uniformly. If the snow layer thickness is assumed to be h at any time t and initially $h = h_0$, $\phi = \phi_0$, one obtains from Equation 6.13

$$\phi = 1 - \frac{h_0}{h}(1 - \phi_0). \tag{6.14}$$

From continuity we require that

$$\nabla \cdot \left(\rho_a \mathbf{q}\right) + \frac{\partial\left(\rho_a \phi\right)}{\partial t} = 0, \tag{6.15}$$

where ρ_a is the density of the air. This describes the transient deformation of a consolidating medium. In the dynamic compression experiments, the pressure under the piston never surpasses 3 kPa above ambient pressure, and the pressure generation inside the porous layer with respect to the ambient pressure is approximately 3%. Thus, the Mach number is $\ll 1$, and the air can be treated as incompressible. In fact, in the current application, the isothermal compressibility defined as $\tau_t = -(1/v)(\partial v/\partial P) = -(1/h)(\partial h/\partial P)$ is of the order of 10^{-4} Pa^{-1}. Equation 6.15 then simplifies to

$$\nabla \cdot \mathbf{q} + \frac{\partial \phi}{\partial t} = 0. \tag{6.16}$$

From Equations 6.11 and 6.16, one obtains

$$\nabla^2 P - \frac{\mu}{K}\frac{\partial \phi}{\partial t} = 0. \tag{6.17}$$

This can be written in cylindrical coordinate system as

$$\frac{1}{r}\frac{\partial}{\partial r}\left(r\frac{\partial P}{\partial r}\right) + \frac{\partial^2 P}{\partial z^2} + \frac{\mu}{K}\frac{h_0(\phi_0 - 1)}{h^2}\frac{dh}{dt} = 0. \tag{6.18}$$

Using quasistatic and homogeneous assumptions, one finds that the source term in this equation, $(\mu/K)(h_0(\phi_0 - 1)/h^2)dh/dt$, is a function of time only.

Introducing dimensionless variables, P', r', z', h', and t', as follows,

$$P' = \frac{P}{P_c}, \quad r' = \frac{r}{R}, \quad z' = \frac{z}{h_0}, \quad h' = \frac{h}{h_0}, \quad t' = \frac{t}{t_c}, \tag{6.19a,b,c,d}$$

where

$$t_c = \frac{\mu R^2(\phi_0 - 1)}{P_c K}, \quad P_c = \frac{mg}{\pi R^2}, \tag{6.19e,f}$$

one substitutes (6.19) into Equation 6.18 and obtains a dimensionless equation for $P'(r', z', t')$:

$$\frac{1}{r'}\frac{\partial}{\partial r'}\left(r'\frac{\partial P'}{\partial r'}\right) + 4\beta^2\frac{\partial^2 P'}{\partial z'^2} + \frac{1}{h'^2}\frac{dh'}{dt'} = 0, \tag{6.20}$$

where $\beta = R/2h_0$.

At the base planar boundary, $z = 0$, the no-penetration condition requires that

$$q\,|_{z=0} = 0 \Rightarrow \frac{\partial P'}{\partial z'}\,|_{z'=0} = 0. \tag{6.21a}$$

At $z = h(t)$, the lower surface of the piston, the no-penetration condition requires that the flow must have a uniform downward velocity dh/dt at any location r:

$$q|_{z=h} = \frac{dh}{dt} = -\frac{K}{\mu}\frac{\partial P}{\partial z} \Rightarrow \frac{\partial P'}{\partial z'}\,|_{z'=h'} = -\frac{1}{4\beta^2(\phi_0 - 1)}\frac{dh'}{dt'}. \tag{6.21b}$$

Because of the symmetry of the flow with respect to the z axis and the nature of the pressure boundary conditions, it is evident that

$$\frac{\partial P'}{\partial r'}\,|_{r'=0} = 0, \quad P'\,|_{r'=1} = 0. \tag{6.21c,d}$$

The boundary-value problem (6.20 and 6.21) for the quasistatic pressure distribution inside the snow layer depends on two parameters, β and ϕ_0, and has the following solution:

$$P'(r', z', t') = \sum_{k=1}^{\infty} a_k J_0(\lambda_k r')\cosh\frac{\lambda_k}{2\beta}z' + \frac{1}{4h'^2}\frac{dh'}{dt'}(1 - r'^2), \tag{6.22}$$

where

$$a_k = \frac{-\dfrac{1}{2\beta(\phi_0 - 1)}\dfrac{dh'}{dt'}\displaystyle\int_0^1 r' J_0(\lambda_k r')dr'}{\lambda_k \sinh\left(\dfrac{\lambda_k}{2\beta}h'\right)\displaystyle\int_0^1 r' J_0^2(\lambda_k r')dr'} \tag{6.23}$$

and

$$J_0(\lambda_k) = 0. \tag{6.24}$$

Applying Equation 6.19 in Equation 6.10, one rewrites the dynamic pore-pressure force, $F_{air}(t)$, acting on the piston in the following dimensionless form:

$$F_{air}'(t') = \frac{F_{air}(t)}{mg} = 2\int_0^1 P'(r', h', t')r'dr', \tag{6.25}$$

Substituting Equation 6.22 into Equation 6.25, $F_{air}'(t')$ is given by

$$F_{air}'(t') = \left\{ -\frac{1}{\beta(\phi_0 - 1)} \sum_{k=1}^{\infty} \frac{\left[\int_0^1 r' J_0(\lambda_k r') dr'\right]^2}{\lambda_k \int_0^1 r' J_0^2(\lambda_k r') dr'} \coth\left(\frac{\lambda_k}{2\beta} h'\right) + \frac{1}{8h'^2} \right\} \frac{dh'}{dt'}. \tag{6.26}$$

In the dynamic consolidation process being discussed, the Darcy permeability of the snow, K, and the porosity, ϕ, are the two basic mechanical properties. The porosity ϕ is related to the snow density ρ_s and ice density ρ_i by the relationship $\phi = 1 - \rho_s/\rho_i$. The permeability of snow has been measured for a wide variety of conditions known as Bader's (1939) classifications (fresh, old, wind packed, depth hoar). However, there has only been limited success in the creation of theoretical models to predict the permeability of snow; see summary in Jordan et al. (1999). A principle difficulty is that ice crystals can take on a variety of shapes, from planar dendritic (hexagonal) to columnar within each classification (Arons and Colbeck, 1995). Temperature plays a major role in the shape of the newly formed snow crystals. Studies of ice crystals in natural clouds (Ono, 1970) have shown that there are at least two basic transitions as the temperature is lowered. The primary transition, from plane hexagonal to needle-type columnar, occurs at −3.5°C. The second transition, from needle- or sheath-type columnar back to a stellar or more complex planar dendritic form, occurs at approximately −10°C. The dimensions of the various ice crystals are summarized in the classic paper by Auer and Veal (1970). Due to the great variety of shapes that occur, ice crystals are commonly described by a general parameter. This parameter is the surface area to mass ratio or specific surface area (Fassnacht et al., 1999).

Despite the difficulty in modeling the permeability of snow, there are some semiempirical or empirical relationships. In the current study, one adopted Shimitzu's (1970) empirical expression for relating permeability to crystal size:

$$K = 0.077 \exp(-0.0078\rho_s) D^2, \tag{6.27}$$

where

D is the mean diameter of the snow particle

ρ_s is the density of snow

Jordan et al. (1999) experimentally demonstrated that snow permeability, K, follows Shimitzu's Equation 6.27 rather closely. In the current application, during the compression process, the density of the snow layer changes due to the motion of the upper boundary. For a snow layer with an initial uniform density, ρ_{s0}, the deformation-dependent average snow density, $\rho_s(h)$, is expressed as

$$\frac{\rho_s(h)}{\rho_{s0}} = \frac{h_0}{h}. \tag{6.28}$$

Assuming that the mean diameter of the ice crystal, D, remains a constant value and the Darcy permeability of the undeformed snow is K_0, Equations 6.27 and 6.28 can then be used to obtain

$$K = 0.077 \exp\left[\frac{h_0}{h} \ln \frac{K_0}{0.077 d^2}\right] D^2. \tag{6.29}$$

By employing the dimensionless variables sought out in Equation 6.19 and substituting Equations 6.9, 6.25, and 6.26 back into (6.8), one obtains

$$\gamma \frac{d^2h'}{dt'^2}\left\{-\frac{1}{\beta(\phi_0-1)}\sum_{k=1}^{\infty}\frac{\left[\int_0^1 r'J_0(\lambda_k r')dr'\right]^2}{\lambda_k\int_0^1 r'J_0^2(\lambda_k r')dr'}\coth\left(\frac{\lambda_k}{2\beta}h'\right)+\frac{1}{8h'^2}\right\}\frac{dh'}{dt'}-f\left(\frac{1-h'}{1-h_f'}\right)+1=0, \qquad (6.30)$$

where $\gamma=\left(t_g/t_c\right)^2$, $t_g=\sqrt{h_0/g}$, and h_f' is the final position of the piston. γ is the square of the ratio of two timescales: the gravitational timescale t_g and the viscous draining timescale t_c. Because γ is very small, the leading term in Equation 6.30 can be anticipated to be important at very short times. After that short time period, the movement of the piston is governed by the remaining terms on the left-hand side of Equation 6.30. This is a singular perturbation problem in which a small parameter is used to multiply the highest-order derivative term. At $t = 0$,

$$h'\,|_{r'=0}=1, \quad \frac{dh'}{dt'}\,|_{t'=0}=0. \qquad (6.31a,b)$$

The differential Equation 6.30 was solved numerically while subject to the initial conditions given by (6.31a, b). Once $h'(t)$ was obtained, the pore-pressure distribution was found by substituting the numerical result for $h'(t)$ into Equation 6.22.

6.6.1.2.2 Comparison between Theoretical Results and Experimental Data

6.6.1.2.2.1 Wind-Packed Snow The wind-packed snow sample had an initial porosity ϕ_0 of 0.6; the initial thickness of the snow layer before compaction, $h_0 = 11.43$ cm; and the final thickness after compaction, $h_f = 0.78h_0$. The applied load was 5.9 kg; the mean diameter of the snowflake, D, was estimated to be 0.42 mm based on the measurements in Jordan et al. (1999). For solid-volume fractions >0.2, the dynamic viscosity, μ, of the trapped air inside the snow could not be assumed to be simply the air viscosity at the same temperature. However, it is reasonable to assume that μ is unchanged in the experiment, with a value of $\mu = 1.667 \times 10^{-5}$ N · s/m^2, while K varies with compression. Implementing these parameter values into Equation 6.30, the time-dependent displacement and velocity of the piston for different values of the initial Darcy permeability K_0 can be obtained. The results are plotted in Figure 6.12a and b, respectively. The initial values of K_0 vary between 0.25×10^{-9} m^2 and 1.0×10^{-9} m^2, which are typical values that can be observed for wind-packed snow (Jordan et al., 1999; Albert et al., 2000, 2002; Albert and Shultz, 2002). The inverse of K is a measure of the resistance that the air encounters as it flows through the porous medium or, equivalently, the damping force of the trapped air that acts on the piston. It is expected that as K_0 decreases, it will take longer for the air to escape due to the increased resistance that it encounters. It is also expected that the velocity of the falling piston decreases as the air damping force increases. The theoretical predictions for the motion of the piston capture these features in Figure 6.12.

The time-dependent pore-pressure P/P_{max}, computed at the location of the central pressure transducer on the underside of the piston, is predicted theoretically using different values of initial permeability, K_0. The results are compared to the experimental data, as shown in Figure 6.13. The theoretical predictions for the time-dependent generation and decay of the excess pore pressure are represented by the solid curves in this figure. It is observed from the figure that the pressure relaxation time increases as K_0 decreases. The theoretical prediction that provides the best fit to the experimental data corresponds to an initial Darcy permeability, K_0, of 0.5×10^{-9} m^2. Although the choice of K_0 varies substantially with the snow sample, this value of K_0 is typical of

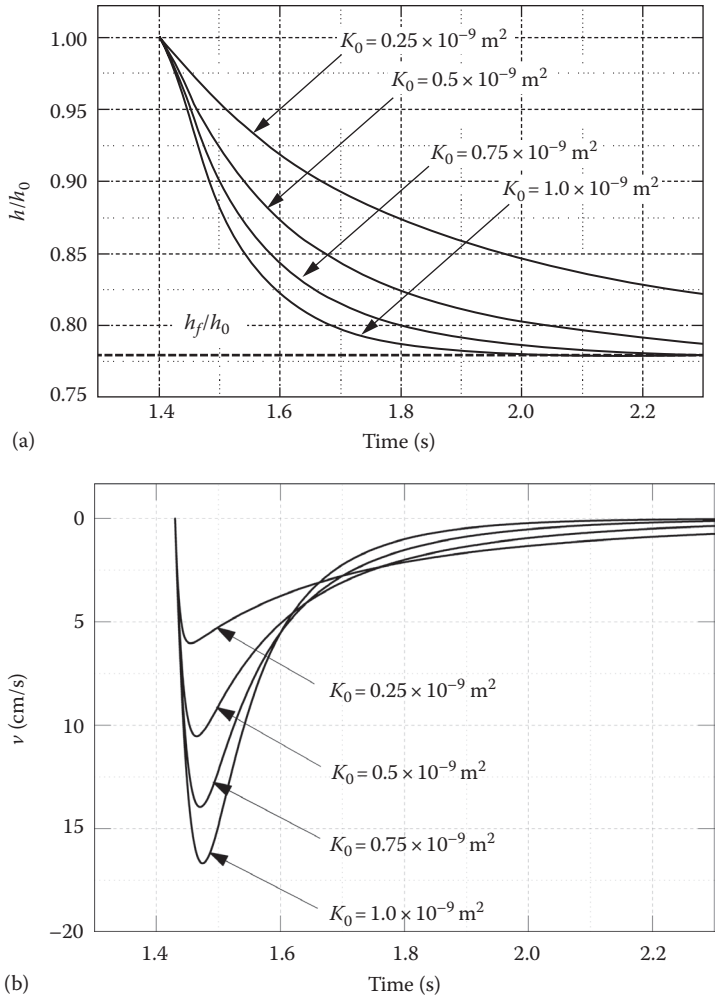

FIGURE 6.12 Theoretical predictions for the time-dependent (a) displacement h/h_0 and (b) velocity of the piston for different values of the initial Darcy permeability K_0 of wind-packed snow, where the initial thickness of the snow layer $h_0 = 11.43$ cm and the initial snow porosity $\varphi_0 = 0.6$. The dashed line in (a) denotes the measured thickness of the snow layer after the compaction, $h_f/h_0 = 0.78$. (Reprinted from Wu, Q. et al., *J. Fluid Mech.*, 542, 281, 2005a. With permission from Cambridge University Press.)

the measurements that are found for wind-packed fine snow (Jordan et al., 1999; Albert et al., 2000, 2002, Albert and Shultz, 2002). For example, the experiments performed by Albert et al. (2000) for wind-blown snow in the top 0–20 cm indicate a K_0 of $0.5 \sim 0.9 \times 10^{-9}$ m^2, whereas the best fit, as shown in Figure 6.13, indicates K_0 values between 0.5 and 0.75×10^{-9} m^2 for similar snow conditions, consistent with the Albert et al.'s published data.

In Figure 6.13, a rapid rise in pore pressure is observed before a decay that occurs on a timescale of roughly 0.7 s. In comparison, a 1.5 m snowboard traveling at 15 m/s would be in contact with a given patch of snow for 0.1 s. It is clear from Figure 6.13 that after 0.1 s, the excess pore pressure has only started to relax, and thus, much of the weight of the snowboarder is expected to be supported by the air that is still trapped in the partially compressed snow layer. The successful agreement between the predicted pore-pressure relaxation with the experimental measures shown in Figure 6.13 would not have been possible if the experimentally measured relation for the force exerted by the solid phase, Equation 6.9, were not reasonably accurate.

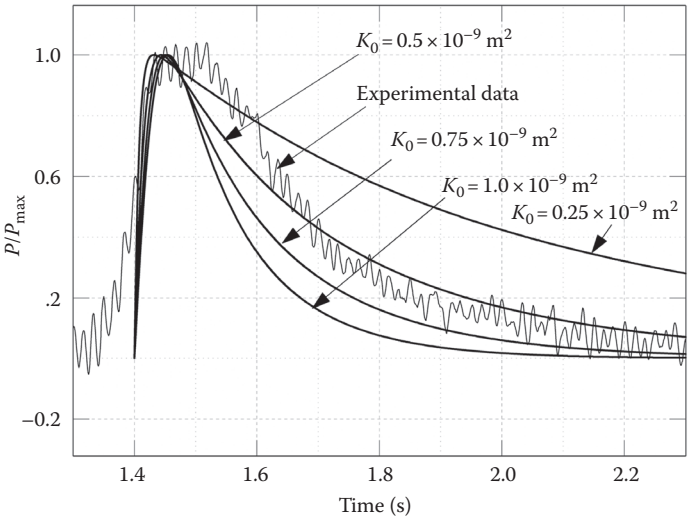

FIGURE 6.13 Comparison between the theoretical predictions of the time-dependent pressure and the experimental data for various values of the initial Darcy permeability K_0. The test sample was wind-packed snow with initial thickness $h_0 = 11.43$ cm, $h_f/h_0 = 0.78$, applied mass $m = 5.9$ kg, and $P_{max} = 744$ Pa. (Reprinted from Wu, Q. et al., *J. Fluid Mech.* 542, 281, 2005a. With permission from Cambridge University Press.)

The dynamic compression experiments performed in wind-packed snow demonstrate that a sudden compression of the wind-packed snow can generate peak pore pressures that are substantially larger than the average applied normal stress, as shown in Figure 6.10. The lumped parameter model based on the consolidation theory developed herein has the ability to reproduce the major features of the experimental data. Furthermore, the model provides key insights into the relative importance of the individual forces observed during the compression process. The results are summarized in Figure 6.14, which shows the time variation of the three forces that appear in Equation 6.8. These forces are normalized by the applied weight, mg. Thus, their summation at any time must equal unity. It is evident that the force due to the pore pressure builds up very quickly in the initial stages of the compression and is counterbalanced solely by the inertial force of the piston. When pressure approaches P_{max}, the piston achieves its maximum downward velocity, the inertial force vanishes, and the solid-phase force starts to increase. As previously noted in Equation 6.30, the highest derivative term that describes the inertia is multiplied by a small parameter, γ. This term is only important for short periods of times on the order $\sqrt{\gamma t_c}$. The solid-phase force continues to increase until it fully supports the piston weight, which corresponds to the time when the pore air is completely vented. For brevity, Figure 6.14 only shows the initial 0.9 s of the compression process, the stage when the inertial force completely vanishes and all of the weight is supported by the solid phase that is not shown.

It is evident from Figure 6.14 that at $t = 1.5$ s, the snow has been compressed up to only ~ 40% of its final deformation. It is at this point that the pore pressure supplies more than 80% of the total lift, the solid-phase lifting force is about 20%, and the inertial force is negligible. Despite the fact that the present experiments do not realistically reproduce the exact conditions that one encounters in skiing or snowboarding, the contact time of a 1.5 m snowboard moving at 15 m/s with the snow layer underneath is in the range where the pore pressure is the dominant lifting force. The concept of lift generation in a highly compressible porous medium under rapid compression, as proposed by F&W, is thus qualitatively verified.

Due to the dimensions of the piston, the timescales for the motion of the piston are more representative of a snowboard than a ski. For the application of skis, the relaxation time will be significantly shorter because of the narrow width that will allow trapped air to escape laterally. Consequently, the

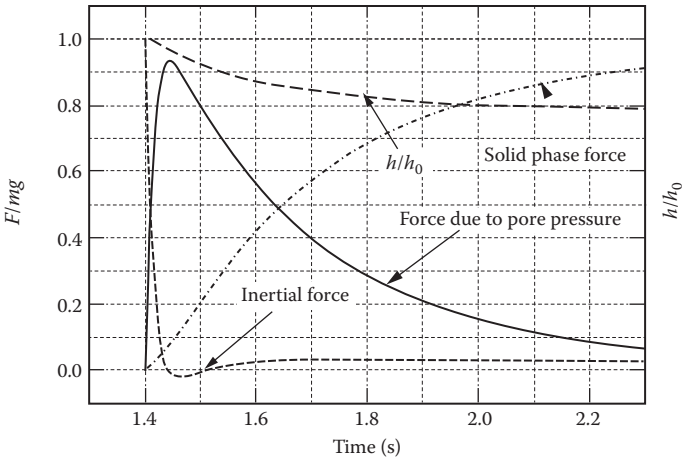

FIGURE 6.14 Time-dependent forces during dynamic compression of wind-packed snow. (Reprinted from Wu, Q. et al., *J. Fluid Mech.*, 542, 281, 2005a. With permission from Cambridge University Press.)

solid phase is expected to carry a substantially greater portion of the load under a ski than it would under a snowboard. This will be confirmed later in this chapter when a realistic model for downhill skiing or snowboarding is analyzed.

From Equation 6.20 in the previous section, the pressure relaxation in the porous cylinder–piston device is found to depend on the parameter, $\beta = R/2h_0$, where β denotes the ratio of the weight-bearing area to the ventilation perimeter–area. In Figure 6.15, the theoretical predictions for the time-dependent pressure distribution, P', at the center of the piston are plotted for different values of β, where $h_f/h_0 = 0.78$ and $K_0 = 0.5 \times 10^{-9}$ m^2. It shows that for values of $\beta > 1$, an increase in β will consequently increase the peak value of the pressure and therefore lengthen the pressure relaxation time. This is because the ventilation area is too small and the trapped air cannot easily escape. However, it is also observed in this figure that for values of $\beta < 1$, an increase in β will decrease the duration of pore-pressure relaxation. This is because for values of $\beta \ll 1$, the air only vents in the

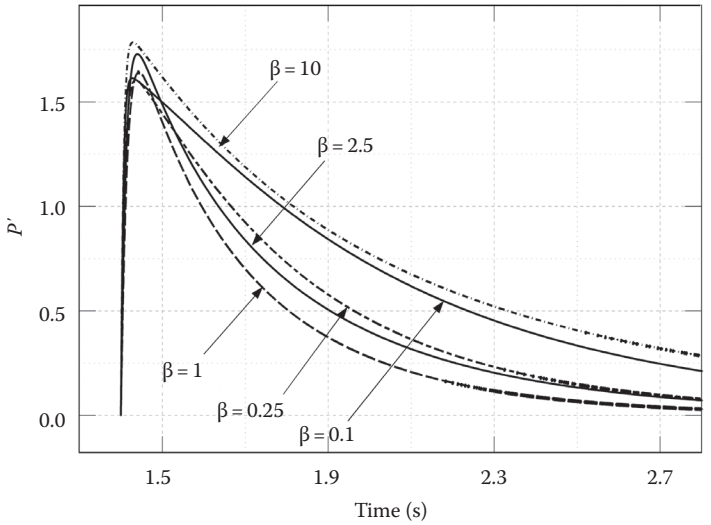

FIGURE 6.15 Theoretical predictions for the time-dependent pressure distribution, P', at the center of the piston for different values of β, where $h_f/h_0 = 0.78$ and $K_0 = 0.5 \times 10^{-9}$ m^2. (Reprinted from Wu, Q. et al., *J. Fluid Mech.*, 542, 281, 2005a. With permission from Cambridge University Press.)

vicinity of the piston, and therefore the full height of the snow column does not contribute to the drainage of the air. As a result, there is a different venting behavior for the small and large β limits with a transition that occurs at roughly β = 1.

The dynamic compression experiment of wind-packed snow and the consolidation theory developed to describe the compression process, as reported in Wu et al. (2005a), were the first study of its type. It captures the key physics of the response of soft porous media under rapid compression, leading to a series of studies on this topic in the past decade. Some of these studies (Barabadi et al., 2009; Akaydin et al., 2011; Crawford et al., 2011a,b, 2012) will be reviewed later in this chapter. On the other hand, because it is the first study of its kind, both the experiments and their comparison to the theoretical predictions have several major limitations. For example, there was no repeatability study reported and the comparison between experiments and the theory was based on normalized pressure response, Figure 6.13. Intuitively, different values of the initial Darcy permeability lead to different magnitudes of pore-pressure response. It should be noted that $K_0 = 0.5 \times 10^{-9}$ m^2 provides a reasonable good fit for the normalized pore-pressure response and the dimensional pore-pressure prediction based on this value of the Darcy permeability also matches the experimental data. Wu and colleagues noticed this limitation and performed experiments with fresh snow the following year.

6.6.1.2.2.2 Fresh Snow For the fresh snow sample, the following parameters were used: the initial porosity, φ_0, was 0.8; the thickness, h_0, of the snow layer before compaction was 8.29 cm; and the final thickness, h_f, after compaction was $0.83h_0$. The applied mass was 10 kg. The mean diameter, D, of the ice crystal was estimated to be 1 mm, and the undeformed Darcy permeability, K_0, was estimated to be ~10^{-8} m^2 for this sample (Jordan et al., 1999). The solid fraction, $(1 - \phi_0)$, was 0.2. Due to the fact that fresh snow is more porous and its Darcy permeability is 20–30 times greater than wind-packed snow, it is expected that the piston will be poorly damped by the trapped air in its downward descent, as noted earlier in Figure 6.10b and c. The peak value of pressure at the center of the piston during the compaction process is only about 45% of the average normal pressure applied on the bottom surface of the piston. A vacuum pressure is then created before the pore pressure finally returns to atmospheric level, indicating a rebound of the piston.

It is widely accepted that snow is a collection of ice grains interconnected in an intricate 3-D structure. The grain bonds between sintered snow crystals play an important role in determining the mechanical properties of snow, which are structure dependent. During the rapid compression, the bonds between the snow grains are broken abruptly and it is not expected that a significant damping effect from the snow crystals would occur. Equation 6.9, obtained from the static experiment, which has no memory effect, predicts the resistance force from the snow sample quite accurately. However, if the piston rebounds over a relatively longer time period after its maximum compression, as observed in the dynamic compression of soft fresh snow, the partially sintered snow sample is aerated and experiences an expansion process. During this process, the relative motion between the ice grains has to overcome this bonding effect, and an additional damping force from the debonding of the sintered snow crystals is applied. Intuitively, this damping force is modeled as linearly proportional to the deformation rate since this is the rate at which bonds are being broken. Thus, this debonding force was approximated by $\eta(dh/dt)mg$, where η, the debonding coefficient, is determined by requiring that the theoretical prediction for the piston rebound process fits the experimental data once K_0 is determined from the downward phase of the piston motion.

Based on the preceding analysis, the dynamic compression process and its rebound were divided into two consecutive motions: first, a compression ending at Δh_{max} and second, a rebound to the final equilibrium position. For the compression phase, the only unknown parameter is the value of the initial Darcy permeability, K_0, and for the rebound phase, the only unknown is the snow damping parameter, η.

Figure 6.16 shows the comparison between the experimental data (ch#9 in Figure 6.10b) and the theoretical predictions during the initial compression phase for the time-dependent pressure at the

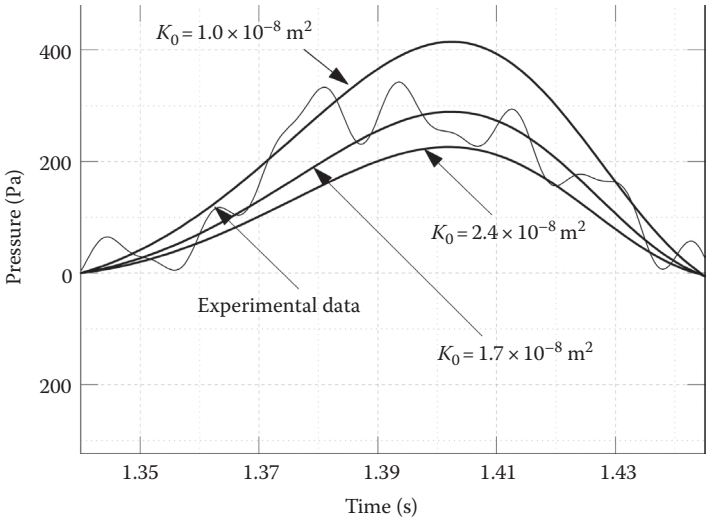

FIGURE 6.16 Theoretical predictions for the time-dependent pressure at the center of the piston and its comparison with the dynamic experimental data. The initial values of snow permeability, K_0, are 1.0×10^{-8} m^2, 1.7×10^{-8} m^2, and 2.4×10^{-8} m^2, respectively. The initial porosity $\varphi_0 = 0.8$, the initial thickness $h_0 = 8.29$ cm, $h_f/h_0 = 0.83$, and load = 10 kg. (Reprinted from Wu, Q. et al., *J. Fluid Mech.*, 542, 281, 2005a. With permission from Cambridge University Press.)

center of the piston. Various values of the initial Darcy permeability, K_0, are used. These values of K_0 are typical for fresh snow (Jordan et al., 1999). Due to the fact that $1/K$ reflects the distributed Darcy resistance of the ice crystals as the air flows through the snow layer, it is expected that the pore pressure will decrease as K_0 increases. From Figure 6.16, one notes that $K_0 = 1.7 \times 10^{-8}$ m^2 provides the best fit to the experimental data. Also shown in this figure is that the pressure relaxation time for fresh snow (~0.1 s) is significantly shorter than that for the wind-packed snow (~0.7 s). This is because the former has a much higher K_0 (1.7×10^{-8} m^2) and a lower solid fraction (0.2).

During the rebound phase, with the undeformed initial Darcy permeability determined in the compression phase, $K_0 = 1.7 \times 10^{-8}$ m^2, and the dependence of K on deformation following Shimizu's relationship, Equation 6.27, the only unknown parameter is the debonding coefficient, η. Figure 6.17 shows the comparison between the theoretical predications for the time-dependent pressure at the center of the piston with the experimental data (ch#9 in Figure 6.10b). Different values of η are applied and the results showed that for small values of η (e.g., $\eta = 1$ s/m), the damping force is insufficient to dissipate the inertia of the piston and the theory predicts oscillations. For large values of η (e.g., $\eta = 20$ s/m), the damping force from the debonding of the snow crystals is too large and the theoretical predictions for the pore air pressure are lower than the experimental data. The value of η that provides a best fit to the experimental data is $\eta = 15$ s/m.

Theoretical predictions for the radial pressure distribution beneath the piston surface for $K_0 = 1.7 \times 10^{-8}$ m^2 and $\phi_0 = 0.8$ are compared with the experimental data at $t = 1.40$ s, when the peak pressure is achieved, as shown in Figure 6.18. Excellent agreement between the experiment and the theory is observed. The radial pressure distribution is almost parabolic. This is expected because the pressure gradient in the radial direction is dominant, and a simple plug-flow model would predict a parabolic pressure distribution in this direction.

The pressure distribution along the centerline of the cylinder (not shown here) was also computed at $t = 1.40$ s, when the peak value of pressure is achieved. The theoretical prediction for the peak value of pressure at $z = 4.25$ cm is 276 Pa, which is very close to the experimental value (280 Pa) at the same position. One also observed a very small pressure gradient in the vertical z direction. This is expected because the air can only escape in the r direction where the pressure drop is much larger.

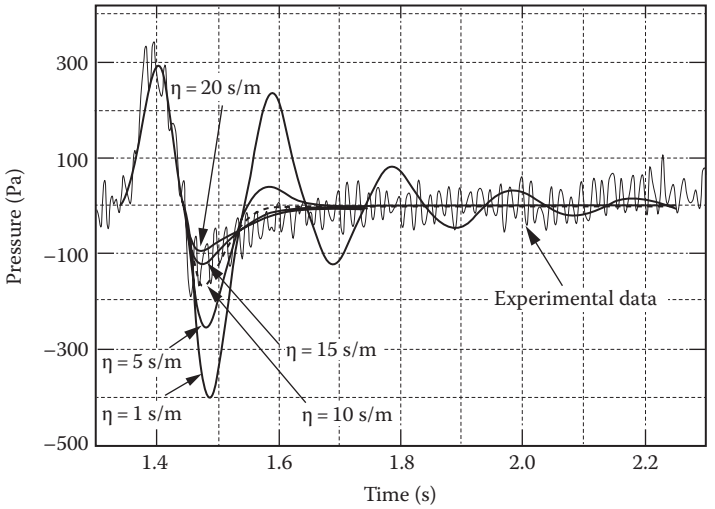

FIGURE 6.17 Theoretical predictions of the time-dependent pressure at the center of the piston and its comparison with the dynamic experimental data for fresh snow. The initial values of snow permeability $K_0 = 1.7 \times 10^{-8}\,m^2$ and the debonding coefficient η were chosen as η = 1 s/m, 5 s/m, 10 s/m, 15 s/m, and 20 s/m, respectively. The initial porosity $\varphi_0 = 0.8$, the initial thickness $h_0 = 8.29$ cm, $h_f/h_0 = 0.83$, and load = 10 kg. (Reprinted from Wu, Q. et al., *J. Fluid Mech.*, 542, 281, 2005a. With permission from Cambridge University Press.)

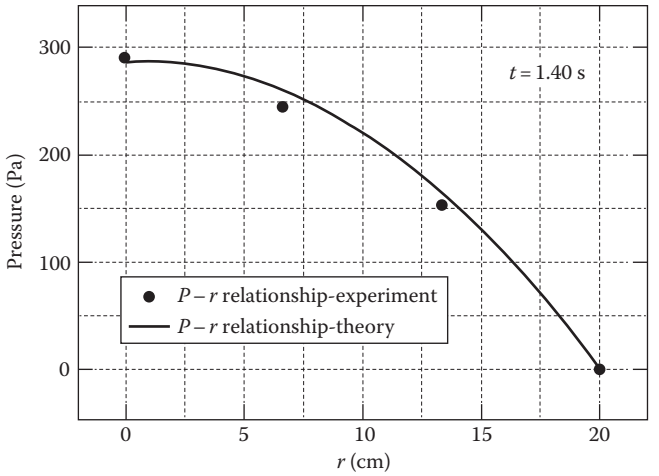

FIGURE 6.18 Theoretical predictions for the radial pressure distribution beneath the piston surface and its comparison with the experimental data at $t = 1.40$ s, when the peak value of pressure is achieved. The initial Darcy permeability of snow is $K_0 = 1.7 \times 10^{-8}\,m^2$, the initial porosity $\varphi_0 = 0.8$, the initial thickness $h_0 = 8.29$ cm, $h_f/h_0 = 0.83$, and load = 10 kg. (Reprinted from Wu, Q. et al., *J. Fluid Mech.*, 542, 281, 2005a. With permission from Cambridge University Press.)

The slight pressure difference along the centerline of the cylinder also negates the possibility of nonuniform compression and the pressure wave propagation on the timescale of interest.

Figure 6.19 shows the time-dependent variation of the normalized inertial, pore-pressure, solid-phase, and debonding forces for the compression of fresh snow. In contrast to the wind-packed snow compression, as shown in Figure 6.14, it is clear that fresh snow is too porous to trap air efficiently. It is also clear that the damping effect from the pore air pressure is insufficient to dissipate the piston inertia on the rebound. The damping force from the debonding of the sintered crystals is required

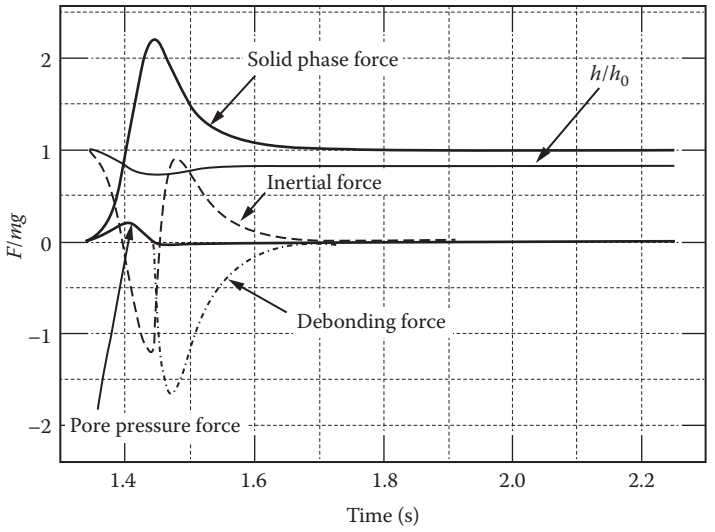

FIGURE 6.19 Time-dependent forces during dynamic compression of fresh snow. (Reprinted from Wu, Q. et al., *J. Fluid Mech.*, 542, 281, 2005a. With permission from Cambridge University Press.)

to balance the piston inertia. The fast relaxation time for the pore air pressure (0.1 s) can also be attributed to the high permeability and porosity of the fresh snow.

6.6.1.3 Remarks on the Dynamic Compression of Snow

6.6.1.3.1 Summary and Discussions

Wu et al. (2005a) developed a novel experimental and theoretical approach for examining the dynamic lift forces that are generated during the initial compaction of both fresh snow powder and wind-packed, older snow in a layer whose thickness is typical of a snow blanket that is left after a single snowfall in an urban environment. The dynamic compression experiments provide the first measurements of the excess pore pressure that builds up inside a snow layer after a sudden compression, as well as its subsequent decay due to the venting of the air from the snow at the edges of the porous cylinder. In the static experiments, the force exerted by the solid phase (snow) as a function of its instantaneous deformation was able to be separated out from the pore pressure and the inertial force of the piston. The theoretical consolidation model provides excellent agreement with the experimental results, as long as the initial Darcy permeability K_0 is chosen in the right range and the debonding effects of the sintered snow crystals are considered in the piston rebound. This was the first time that such forces have been considered.

This research is in large measure the outgrowth of the lubrication theory developed in F&W for flow in highly compressible porous media. The objective was to understand the dynamic pore pressures that might build up in a new snow layer on the timescale of skiing or snowboarding. The idealized experimental apparatus is not intended to realistically reproduce the boundary conditions that one encounters in skiing or snowboarding in which other factors have to be considered, including the permeability of the base layer on which the latest snowfall rests, shear forces in the snow at the edge of the planform, and the lateral displacement and momentum of the displaced snow especially during turns and maneuvering. However, this initial study does qualitatively and quantitatively explore the time variation of the various dynamic forces that one encounters when a weighted planar surface is suddenly dropped on a snow layer. The study demonstrated that on the timescale of importance for skiing or snowboarding on fine-grained wind-packed snow, the pressure of the transiently trapped air provides a significant fraction of the total lift even for small compressions. For skiing or snowboarding on fresh snow, the solid

phase will carry a significantly greater portion of the load since the excess pore pressure will be insufficient to carry most of the load.

An interesting observation is that when the motion of a red cell is arrested, the timescale for the drainage of the fluid from the EGL is estimated experimentally to be ~0.5 s (Vink and Duling, 1996; Weinbaum et al., 2003). This was determined by examining the amount of time it takes for the gap between the red cell and EC membranes to vanish. This characteristic time is very similar to the pressure relaxation time that was found in the dynamic compression study with wind-packed snow. The experimental and theoretical approach presented in this chapter therefore provides an intriguing analogy for the drainage of the ESL following red blood cell arrest.

The theoretical approach developed in this session, as far as we are aware, has never been applied before to snow. It is based on the consolidation theory first proposed by Terzaghi (1943) and later refined in the more general theory of Biot (1941, 1957) for 2-D and 3-D compression of a porous medium. The dynamic compression experiments indicate that the timescale of the buildup in pore pressure of the air after dropping the piston varies between 0.05 and 0.1 s depending on the permeability of the snow and that the decay time can be as long as 5 times longer than this if the pore pressure is large enough to bear the entire weight of the piston. However, the critical frequency for the propagation of pressure waves in a porous medium of infinite depth appears to be of the order 100 kHz if one employs the present data in the theory by Albert (1993) and Johnson (1982). Thus, the imposition of the pressure field through the fast compressive wave and the multiple reflections of this wave occur on a much shorter timescale than the viscous phenomena investigated herein. The pore-pressure buildup and relaxation within the cylinder thus exhibit a time-dependent quasi-steady behavior that is governed by the Darcy law.

6.6.1.3.1.1 Limitations The phenomena of pore pressure increase due to sudden compression on soft porous media, and that of slow pressure venting due to viscous effects is a new concept for porous medium flow. The application to snow compaction and the potential application to human skiing were chosen for their originality. The general idea of lift generation in soft porous media under rapid compression could have very broad application potential in squeeze damping and soft porous lubrication. Since the study discussed so far only focused on two types of samples, wind-blown snow and fresh snow, one would ask: "How would other soft porous materials with varying mechanical properties behave when subjected to sudden compressive forces?"

Furthermore, when the theory in F&W was first developed, it was intended to apply to highly compressible porous media in the limit where the structure is so compressible that the normal forces generated by the compression of the solid phase were negligible, as compared to the pore-pressure forces generated within the porous media. In the dynamic compression study by Wu et al. (2005a), the authors took into account the lift generation from both the transiently trapped air and the solid phase; however, the viscous damping force from the solid phase was only considered in the rebound process in fresh snow dynamic compression experiments, while it was neglected in both wind-packed snow and the compression phase of the fresh snow experiments. More recently, Skotheim and Mahadevan (2005) theoretically investigated the fluid-induced deformation of soft interface and the resultant lift generation due to the draining of the fluid and the elastic response of the solid structures. The viscous damping effect of the solid phase was also neglected. No previous work, to our knowledge, comprehensively treated the damping effects from both the trapped fluid and the solid structure. One would ask: "How would the viscoelastic property of the solid phase affect the lift generation in a soft porous medium?"

Third, in Wu et al.'s experiments (2005a), the motion of the dropping piston was only predicted theoretically. The comparison between the theoretical model and the experimental data was only based on the pore air pressure response. If the damping effects from both the solid phase and the pore air pressure need to be determined, another criterion besides the pressure response would be necessary. What is that criterion?

The following session will be dedicated to treating these limitations.

6.6.1.4 On the Characterization of Lifting Forces during the Rapid Compaction of Deformable Porous Media

Barabadi et al. (2009) and Crawford et al. (2011a,b, 2012) redesigned the experimental setup in Wu et al. (2005a) by introducing a guiding system for the dropping of the piston. The new apparatus was fully instrumented with pressure, acceleration, and displacement sensors. A more comprehensive set of experimental data obtained from trials conducted on various synthetic fibrous porous materials were obtained. The consolidation theory developed by Wu et al. (2005a) was modified to include the damping force from the solid phase, $\eta(dh/dt)mg$, where η is the damping coefficient and dh/dt and mg are the velocity and weight of the piston, respectively. Matching between the experimental data and the theoretical predictions was made, not only on the pore air pressure generation but also on the motion of the piston. This allows one to determine the initial Darcy permeability, $K_{0,}$ of the porous medium that is related to the damping effect of the pore air pressure, as well as the damping coefficient of the solid phase, η. By performing detailed analyses of the pore air pressure distribution and the viscoelastic behavior of the solid phase, a quantitative approach was developed in characterizing different aspects that affect the lift generation in a soft porous medium.

6.6.1.4.1 Experiments

6.6.1.4.1.1 Experimental Setup In order to obtain critical insight into the behavior of soft porous media in response to rapid compaction, a porous-walled cylinder–piston apparatus was designed, fabricated, and tested in the Cellular Biomechanics and Sports Science Laboratory at Villanova University. The design of this apparatus was based on the setup in Wu et al. (2005a), but with substantial improvements. The previous experimental setup was a fairly accurate design and the experimental results were reasonable. However, it had several major limitations:

1. The piston that provides sudden compaction on the porous medium was released manually in the previous studies. This technique showed inconsistent drop rates for similar initial conditions. In addition, since the cylindrical sidewall was not transparent, when the piston was manually released, it was not clear if the material was precompressed before the piston was released or if there was an air gap between the bottom surface of the piston and the top surface of the porous layer.
2. There was no direct measurement of the time-dependent displacement of the piston in the previous study. One only manually measured the initial and final thicknesses of the porous medium in Wu et al. (2005a).
3. The previous experiments were only performed on two types of snow. Other types of porous media and particularly synthetic fibers have not yet been tested.

Considering these limitations, a new, modified experimental setup was built. A schematic of the apparatus is shown in Figure 6.20. The cylindrical sidewall was 120 mm high and 383.8 mm in diameter attached to a solid base plate. It was constructed from Rigimesh, a single, rigid, porous metal sheet made by Pall Corporation. The selection of the type of the Rigimesh was based on the following considerations: first, it needed to be rigid enough to maintain its structural integrity without any deformation; second, its pore size had to be small enough to prevent any material from escaping the cylinder, yet large enough to allow air to pass through the sidewall freely. Rigimesh A 304L, with pore size being 280 μm and the total percentage of the open pore area being 37%, was selected for the current study. This configuration ensures no pressure buildup was observed when dropping the piston with no material inside the cylinder, indicating no resistance provided by the side wall.

A light piston that can be loaded with fixed weights on top of it can slide freely along the inner surface of the cylinder. A linear bearing from the top of the piston was added to the design in order

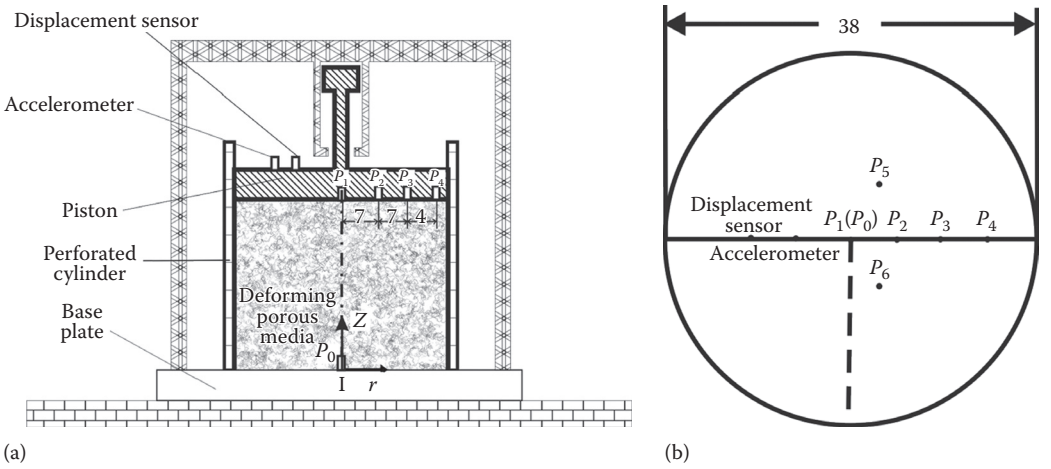

FIGURE 6.20 (a) Experimental setup for compression of porous fibers and (b) top surface of the piston showing the pressure sensor locations, unit in centimeter, not to scale. (Reprinted from *Exp. Therm. Fluid Sci.*, 36, Crawford, R., Nathan, R., Wang, L., and Wu, Q., Experimental study on the lift generation inside a random synthetic porous layer under rapid compaction, 205–216, Copyright 2012, with permission from Elsevier.)

to prevent any misplacement of the piston during the free fall, to minimize friction, as well as to create consistency between all of the experiments. A glider was attached to the rod that can glide through a vertical gliding path to create a uniform loading. In order to allow the trapped air to flow out of the cylinder only through the porous side walls in the radially outward direction, the apparatus was designed with a small clearance gap between the piston and the cylinder sidewall.

In order to examine the motion of the piston, a dual-axis accelerometer (ADXL203) with a range of ±1.7 g and a sensitivity of 1000 mV/g was installed on the top surface of the piston to measure the inertia of the piston. The accelerometer tracked the vertical acceleration of the piston and monitored the horizontal acceleration to confirm no lateral movement while dropping. A laser displacement sensor (Micro-Epsilon, model ILD1300-200) was used to measure the time-dependent displacement of the piston as well as the initial and final thickness of the porous filling material. The laser displacement sensor has a range of 200 mm and a dynamic resolution of 200 μm. The previous cylinder–piston configuration in Wu et al. (2005a) presented the potential for inconsistent drops due to manually releasing the piston. An unsteady hand caused the piston to move up and down in the tiniest bit resulting in precompression of the material or the presence of an air gap between the piston head and the top surface of the porous material. Both affected the initial acceleration and velocity of the compressing piston. In the current study, a one-way release mechanism with mechanical triggering was developed to ensure consistent drop heights and even loading on the porous filling materials. A fibrous material with certain porosity was first placed in the cylinder. It naturally bulged and expanded because its top boundary was not confined. A string, one end of which was hooked up to the triggering mechanism mounted on the top frame with the other end attached to the piston head, was used to lower the piston to the designed position, 12 cm away from the base. At this position, the piston fit inside the cylindrical wall and the top surface of the porous medium was flat. The piston very slightly compressed the porous material and confined it underneath. Its position was precisely controlled by the laser displacement sensor. Since the piston was still hooked up by the string, the material was only compressed very slightly and generated a minimal solid-phase lifting force, as shown later in the static experiments. Once the releasing system was triggered, the piston dropped instantaneously and compressed the porous materials underneath.

To study the pore-pressure generation inside the porous material, six micro pressure transducers were placed underneath the piston surface and one on the base plate, as shown in Figure 6.20b. A high-frequency response MEMS-based pressure transducer, P_1 (Kulite Semiconductor

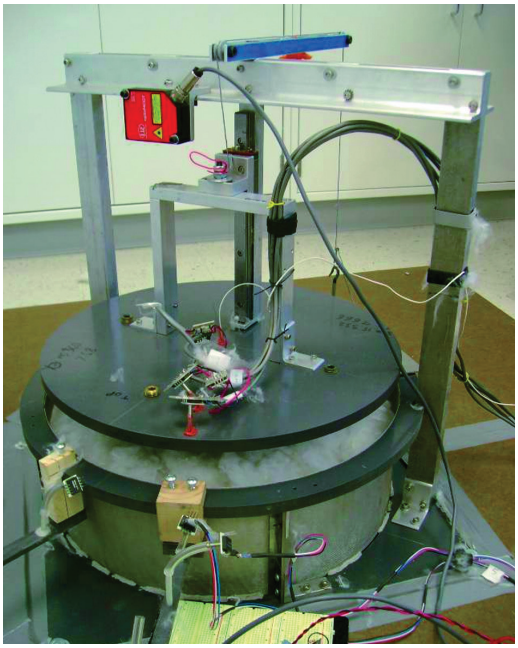

FIGURE 6.21 Cylinder–piston apparatus. (Reprinted from *Exp. Therm. Fluid Sci.*, 36, Crawford, R., Nathan, R., Wang, L., and Wu, Q., Experimental study on the lift generation inside a random synthetic porous layer under rapid compaction, 205–216, Copyright 2012, with permission from Elsevier.)

Products, model MIC-062), was mounted at the center on the piston's bottom surface, and three other pressure transducers, P_2, P_3, and P_4 (SI Micro, model SM5652-015-G-3-L), were installed radially at 7, 14, and 18 cm from the center. These three pressure transducers along with P_1 provided a detailed description of the radial pressure distribution. Two other pressure sensors, P_5 and P_6, were placed at a radius of 7 cm sharing a circumference with pressure sensor P_2 to verify the axisymmetry of the pore-pressure distribution underneath the piston. An additional pressure sensor, P_0, was placed at the center of the base plate and was compared with the reading from P_1 to provide information on the axial pressure variation. The largest inner diameter of the pressure transducers was 0.203 cm, resulting in a satisfying spatial resolution in local pressure measurements. All the pressure signals were measured relative to the ambient atmospheric pressure. Because the speed of sound is the product of signal frequency and the signal wavelength, in order to get uncorrelated measurement signals, for a rough estimate with 4 cm spacing between the pressure sensors and the speed of sound in air, the signal frequency should be more than 8.25 kHz. In the experiments discussed herein, one chose the sampling frequency to be 18 kHz; thus, there is no correlated measurement signal.

The signals from the pressure transducers, accelerometer, and displacement sensor were captured by a USB chassis NI cDAQ9172 data acquisition system and a plug-in module NI9205 with 16 bit resolution and a maximum sampling rate of 250 k samples/second. A LabVIEW® program was written to acquire, filter, and store the data in ASCII format for further processing with MATLAB®. All sensors were calibrated in the lab before running the experiment.

Figure 6.21 shows the real picture of the new experimental setup.

6.6.1.4.1.2 Material Characterization Two kinds of polyester fibers with different densities termed material A and material B were used for the experiments. Material A was used in Egyptian pillows. Material B was a filling material used in stuffed animals (Build-a-Bear). These two materials were chosen due to their significantly different solid-phase stiffness. Hand feeling indicates

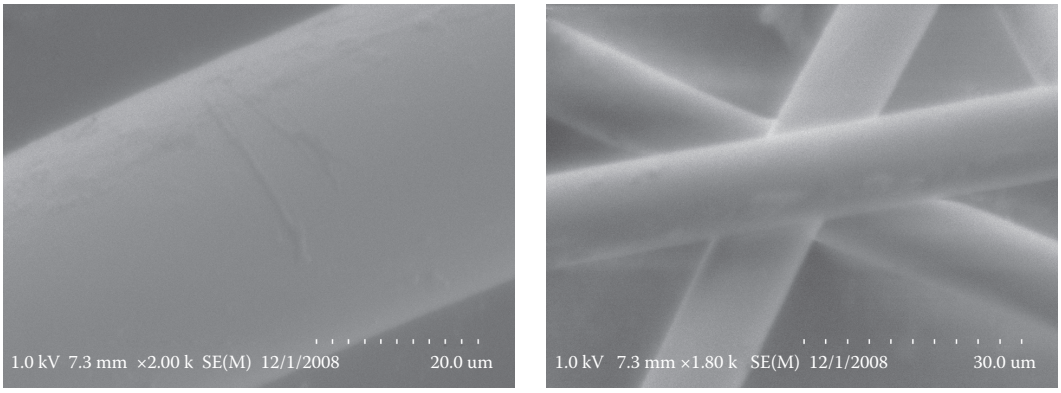

(a) (b)

FIGURE 6.22 (a) SEM image for material A at 1 kV and 2000×. (b) SEM image for material B at 1 kV and 1800×. (Reprinted from *Exp. Therm. Fluid Sci.*, 36, Crawford, R., Nathan, R., Wang, L., and Wu, Q., Experimental study on the lift generation inside a random synthetic porous layer under rapid compaction, 205–216, Copyright 2012, with permission from Elsevier.)

that material A is much stiffer than material B. This is confirmed in a quasistatic compression experiment shown later in this chapter.

A Hitachi s-4800 high-resolution scanning electron microscope (SEM) was used to investigate the microstructures of materials A and B. Due to the fibers being curved in loops, special care was taken to secure them onto the SEM specimen holder. Conductive carbon tape was first placed on the SEM specimen holder to grasp the fibers. A small amount of the fibers was then pressed onto the carbon tape using a pair of tweezers to secure them in a desirable position. For material A, a small amount of silver paint was used to further secure the fiber position as well as to provide better electrical conductivity and to reduce the charging effect. No silver paint was needed for material B because its diameter was smaller and it was easier to attach its fibers onto the conductive carbon tape. Neither fiber could be attached onto the conductive carbon tapes flatly along its whole length. Therefore, they were at slightly different heights and only one portion of a fiber was focused on when a photo was taken. To avoid electron charging effect on the polyester fibers, the acceleration voltages of the SEM were kept at 5 kV or less. The SEM images, as shown in Figure 6.22, showed that the fibers of material A were of constant diameter (40 μm) with smooth surfaces. In contrast, fibers of material B were of a smaller diameter (13 μm) and with more surface irregularities, as shown in Figure 6.22b.

In order to obtain a 3-D perception on the porous materials, such as the space between fibers, the fiber shape, and the homogeneity of the fibrous materials, a Zeiss stereomicroscope (model STEMI SV-11 APO) equipped with a Leica DC480 digital camera was used to characterize the materials. A 1.5 mm in diameter material specimen was investigated. For each material, observations were made as the focal plane moved from the bottom toward the top of the sample. For example, Figure 6.23a shows the bottom layer of the material A, while Figure 6.23b shows the top layer of material B. In both of these figures, the whole view from left to right is about 3.21 mm and from top to bottom about 2.55 mm. For material A, since the fiber diameter is about 40 μm, as shown in Figure 6.22a, the space between the fibers was estimated in Figure 6.23a to be 0.7 mm (700 μm) or less. The fibers were curved and intertwined, making it almost impossible to identify the beginning and the end of each fiber. Thus, the length of the fibers could not be easily identified. However, if the fibers are long enough, it is obvious that the overall length of the fibers is not a significant factor as long as there are many intertwining points where the fibers interlock with each other. It is the interlocking distance that plays an important role to the mechanical properties, assuming that the fiber stiffness and strength are kept the same. No difference was observed as the focal plane moved

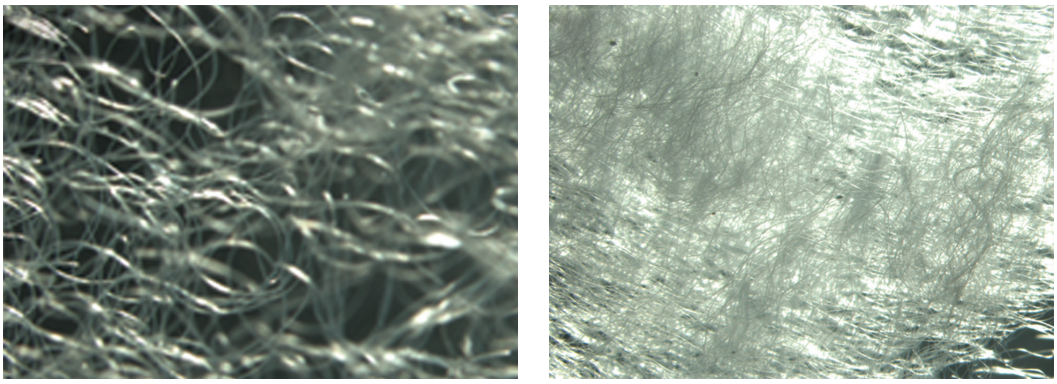

(a) (b)

FIGURE 6.23 Stereomicroscopy images for (a) material A at bottom layer and (b) material B at top layer. (Reprinted from *Exp. Therm. Fluid Sci.*, 36, Crawford, R., Nathan, R., Wang, L., and Wu, Q., Experimental study on the lift generation inside a random synthetic porous layer under rapid compaction, 205–216, Copyright 2012, with permission from Elsevier.)

from the bottom toward the top of the sample, indicating the material was spatially homogeneous. Figure 6.23b shows that material B contains many very fine and dense fibers. From this figure, the space between the fibers of material B was estimated to be 200 μm or less based on its fiber diameter determined from the SEM study. Material B has straighter fibers without too much of the twists and turns. Therefore, there will be less interlocking mechanisms among the fibers. This is consistent with the SEM study that shows that material B was easier to be flattened onto the conductive carbon tape due to its smaller diameter, less curving, and less interlocking mechanism. Spatial homogeneity is observed for material B as well.

The porosities of materials A and B were quantified using the following equation:

$$\phi = \frac{V_{void}}{V_{total}} = 1 - \frac{\rho}{\rho_{fiber}} \tag{6.32}$$

where ρ and ρ_{fiber} are the densities of the porous medium and its solid phase, respectively. To determine ρ_{fiber}, water displacement was employed in which a sample of the porous material A or B was weighed to 0.01 g and placed in a graduated centrifuge tube with a known volume of water. After the material was fully saturated, air bubbles were removed by spinning the tubes at high speed in a centrifuge (Fisher Scientific accuSpin, model 400 Benchtop Centrifuge). Since the fibers are 100% polyester, water absorption by the fiber itself is negligible (Lynch, 1974). A reading of the final volume of the water was then taken. The change in the water volume inside the centrifuge tube indicated the volume of the solid phase, which was then used to calculate ρ_{fiber} with its mass being given as 0.01 g. For material A, ρ_{fiber} is 0.771 g/ccm with standard deviation being 0.034 g/ccm. For material B, ρ_{fiber} is 0.872 g/ccm with standard deviation being 0.027 g/ccm.

For a given porosity, φ, using Equation 6.32, the density of the porous material, ρ, was calculated. Since the volume of the porous-walled cylinder–piston apparatus was known, the mass needed for the test for the given porosity could be determined.

6.6.1.4.1.3 Experimental Methods and Results

6.6.1.4.1.3.1 Static Experiments Static experiments, as discussed in Wu et al. (2005a), were performed with fibrous materials A and B. The cylinder was first filled with the desired material at a specific porosity, 0.98. The material was spread out by hand to ensure even distribution throughout

the cylinder. The piston was then loaded incrementally in small steps from an initial height of 12 cm until maximum compression of the material was reached and subsequently unloaded in the same manner. For each step of loading, the experiment was not continued until the piston reached equilibrium. This ensured that the static loads were completely supported by the solid phase of the porous medium and that the contribution of any resulting inertial forces due to acceleration or deceleration of the piston was eliminated. The applied load and the resulting compression of the porous material were recorded. Five experiments were performed under the same conditions to examine the repeatability of the experiment and determine its uncertainty. After each time, the porous sample was refluffed to return it to its original, natural state.

The load–compression relationships for these two materials, fitted with a fifth-order polynomial, are plotted in Figure 6.24a. These relationships were nonlinear due to the inelastic nature of the materials.

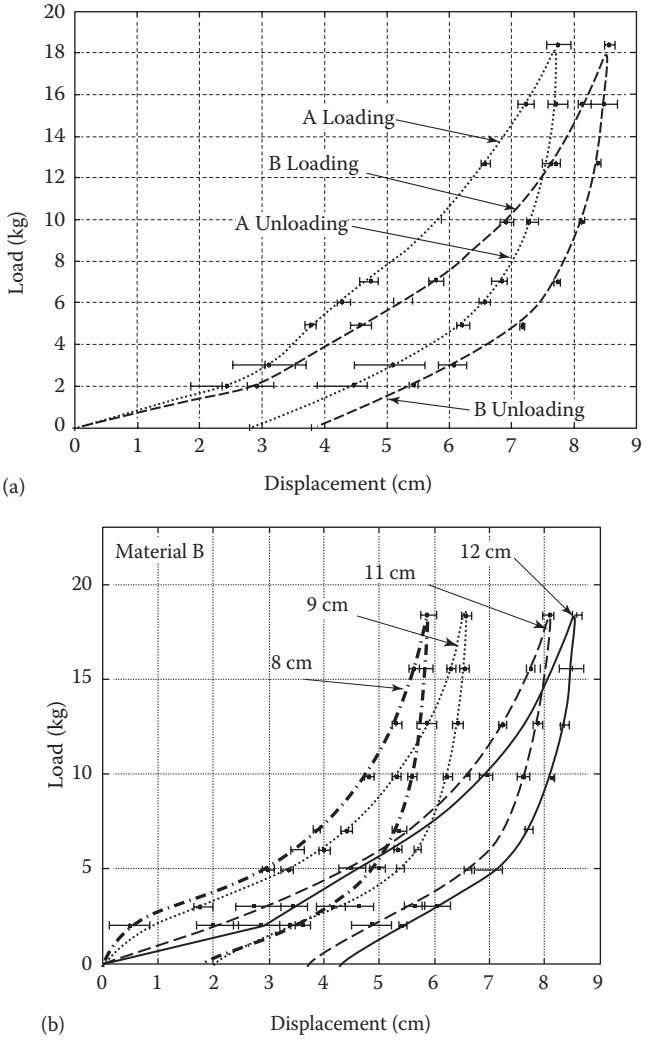

FIGURE 6.24 Static experiments for (a) materials A and B for initial porous layer thickness being 12 cm and (b) material B for various initial porous layer thicknesses. (Reprinted from *Exp. Therm. Fluid Sci.*, 36, Crawford, R., Nathan, R., Wang, L., and Wu, Q., Experimental study on the lift generation inside a random synthetic porous layer under rapid compaction, 205–216, Copyright 2012, with permission from Elsevier.)

Stiffness is defined as the ratio of applied force to compression. It can be seen in Figure 6.24a that material B compresses more under the same load as compared to material A. Thus, material A was stiffer than material B. This was consistent with material A having a larger fiber diameter (40 μm) than material B (13 μm), with both of these polyester fibrous materials extruded at the same temperature.

During the unloading stage of the static experiment, permanent deformation was observed, confirming the inelastic nature of these materials. This viscoelastic behavior is determined by the frictions between fibers as well as that between fibers and the confined cylindrical side wall. The latter plays the dominant role because the relative motion between the fibrous material and the cylindrical side wall is more substantial. During the decompression phase of the static experiment, the pores on the cylindrical wall tangle and grab the fibers, causing more permanent deformation of the fibrous material. This behavior has recently been studied by Al-Chidiac et al. (2009) who experimentally demonstrated that the hysteresis effect is considerably less in the case of laterally unconfined axial compression/decompression as compared to the case when the porous material is confined in the cylindrical wall. Because of this effect, refluffing of the material must be performed to break the bonds on the sidewall without bringing new orientation to the system globally. The residual deformation of material A was smaller than that of material B due to the fact that material A contains fibers with larger diameters and thus a greater capacity to restore to its original thickness.

Another consideration was to perform static experiments for the same porous material (e.g., material B with initial porosity, $\phi_0 = 0.98$), but with different initial loading thicknesses (e.g., $h_0 = 8$ cm, 9 cm, 11 cm, and 12 cm, respectively), Figure 6.24b. It can be observed from this figure that for the same loading on the piston, a thicker porous layer tends to compress more and thus behaves softer. The hysteresis effect, corresponding to the permanent compression after all the loading was removed at the end of the experiment, was larger for the thicker porous layers as well.

6.6.1.4.1.3.2 Dynamic Experiments The dynamic compaction experiments were performed on the two porous materials A and B. While filling the cylinder with the fibers, care was taken to ensure that the fiber was spread out evenly by hand and that the fibers were put in layers inside the cylinder. The piston with applied loads was then suddenly released by a triggering mechanism to provide a rapid compaction on the porous material underneath. The time-varying pore-pressure buildup was captured by the pressure sensors. The displacement of the piston was recorded simultaneously by the displacement sensor.

Figure 6.25a and b shows the dynamic pressure response beneath the piston at different radial distances r from the center for material B (initial porosity, $\varphi_0 = 0.97$, loading = 7.0 kg) and material A ($\varphi_0 = 0.97$, loading = 9.25 kg), respectively. As shown in Figure 6.25a, the pressure builds up in about 0.15 s and then relaxes in 0.1 s. The maximum pore pressure registers at the center and the magnitude of the maximum pore pressure decreases with increasing radial distance from the center. Minimum pressure is registered at the radially outermost location from the center. It is this pressure gradient that forces the air flow outward in the radial direction.

In Figure 6.25, a negative pressure is observed just after the pressure relaxation is complete for material A, yet this behavior was absent for material B. This negative pressure corresponds to the rebound of the piston. It occurs due to the lack of damping effects from both the trapped air and the solid phase. Thus, after the air is completely purged out, the piston was pushed up and a partial vacuum was created. The rebound effect is better described in Figure 6.26a and b, where the time-dependent displacements of the piston corresponding to the dynamic compaction experiments described in Figure 6.25 are presented. The displacements are normalized by the initial thickness of the porous layer. Rebound behavior for material A is clearly demonstrated in Figure 6.26b.

The time-dependent displacement of the piston was measured by the laser sensor, and its acceleration was captured by the accelerometer. Since these measurements occurred simultaneously, it is most instructive if the acceleration obtained from the direct measurement is compared with the time derivative of the piston displacement. This comparison is shown in Figure 6.27a for material B ($\varphi_0 = 0.97$, loading = 7.0 kg) and 6.27b for material A ($\varphi_0 = 0.97$, loading = 9.25 kg). From these two

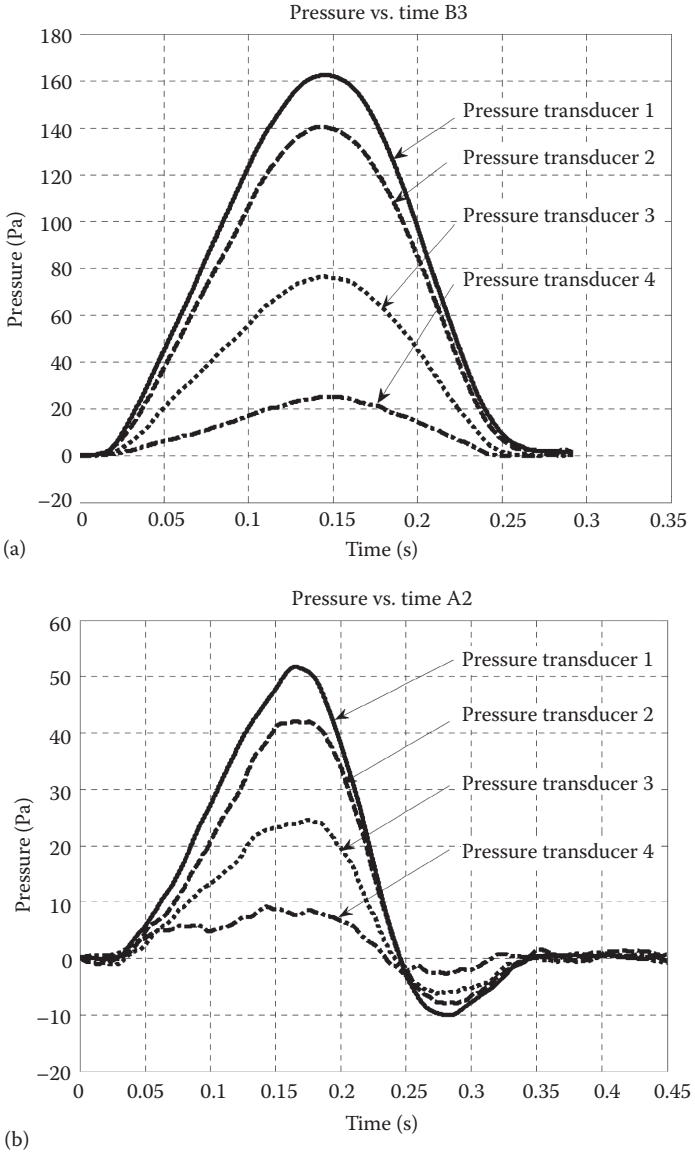

FIGURE 6.25 Representative dynamic pressure response for (a) material B ($\phi_0 = 0.97$) with 7.0 kg loading and (b) material sample A ($\phi_0 = 0.97$) with 9.25 kg loading. (Reprinted from Barabadi, B. et al., *J. Heat Transfer*, 131, 101006. Copyright 2009, with permission from American Society of Mechanical Engineers.)

figures, it can be clearly seen that the readings of the accelerometer and the time derivative of the displacement data match very well. Thus, one is confident about the experimental method and results.

A representative normalized radial pressure distribution recorded by the pressure transducers 1–4 is plotted in Figure 6.28. The testing material is A ($\varphi_0 = 0.97$, loading = 9.25 kg). It was plotted at the time when peak pressure was achieved at these locations. As is evident from this figure, the pressure distribution in the r direction is very close to parabolic, confirming the observation in Wu et al. (2005a).

In order to examine the repeatability of the measurement, six sets of experiments were performed under the same condition. The data were normalized by the maximum pressure obtained by pressure transducer 1 at the center of the piston, P_{max}. The error bars in Figure 6.28 indicate the range of the variation of the pressure measurements. In terms of standard deviation, the actual error is about 4%.

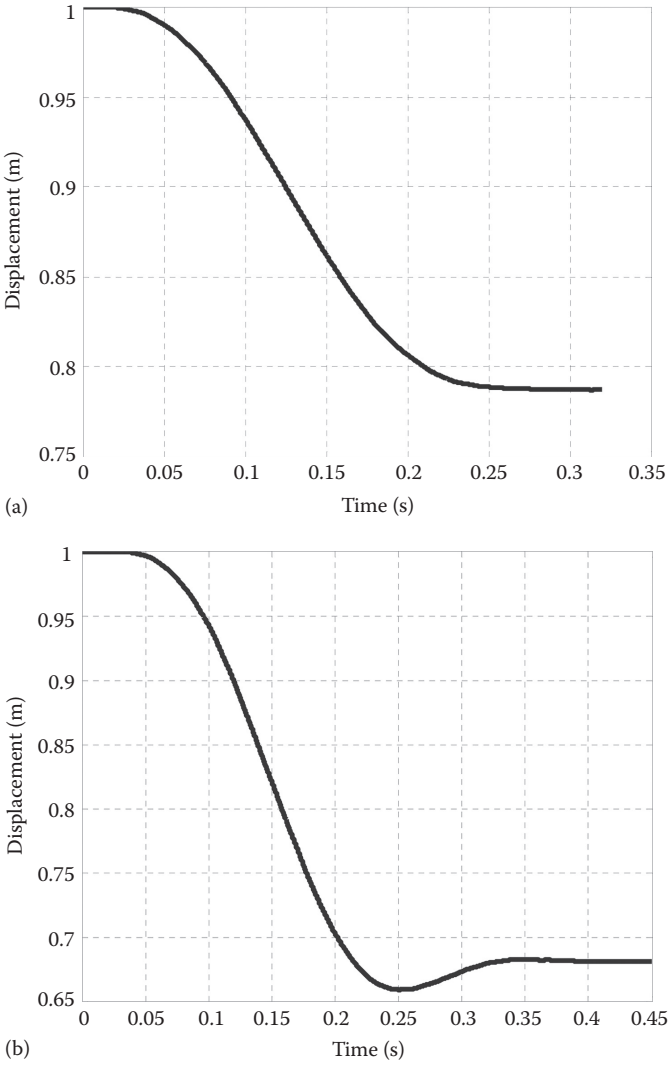

FIGURE 6.26 Representative time-dependent displacement of the piston during the dynamic compaction experiment in Figure 6.25 for (a) material B ($\phi_0 = 0.97$) with 7.0 kg loading and (b) material A ($\phi_0 = 0.97$) with 9.25 kg loading. (Reprinted from Barabadi, B. et al., *J. Heat Transfer*, 131, 101006. Copyright 2009, with permission from American Society of Mechanical Engineers.)

Comparing the pressure profiles obtained from P_2, P_5, and P_6 in Figure 6.20, which were all at the same radial distance from the center of the piston, confirmed the assumption of an axisymmetric pressure distribution inside the porous layer. The less than 6% standard deviation in readings obtained from these three pressure sensors is attributed to the disparities in the homogeneity of the material due to manually fluffing the fibrous material.

6.6.1.4.2 Theoretical Formulation

The consolidation theory developed in Wu et al. (2005a) is modified and applied to describe the motion of the piston and the resulting pore-pressure response. The modification is reflected in two aspects.

First, the solid-phase lifting force, F_{solid}, in the momentum Equation 6.8 about the motion of the piston, is now expressed as the summation of two contributing components, $F_{solid} = F_{solid-elastic} + F_{solid-damping}$,where $F_{solid-elastic}$ and $F_{solid-damping}$ are the elastic and viscous damping

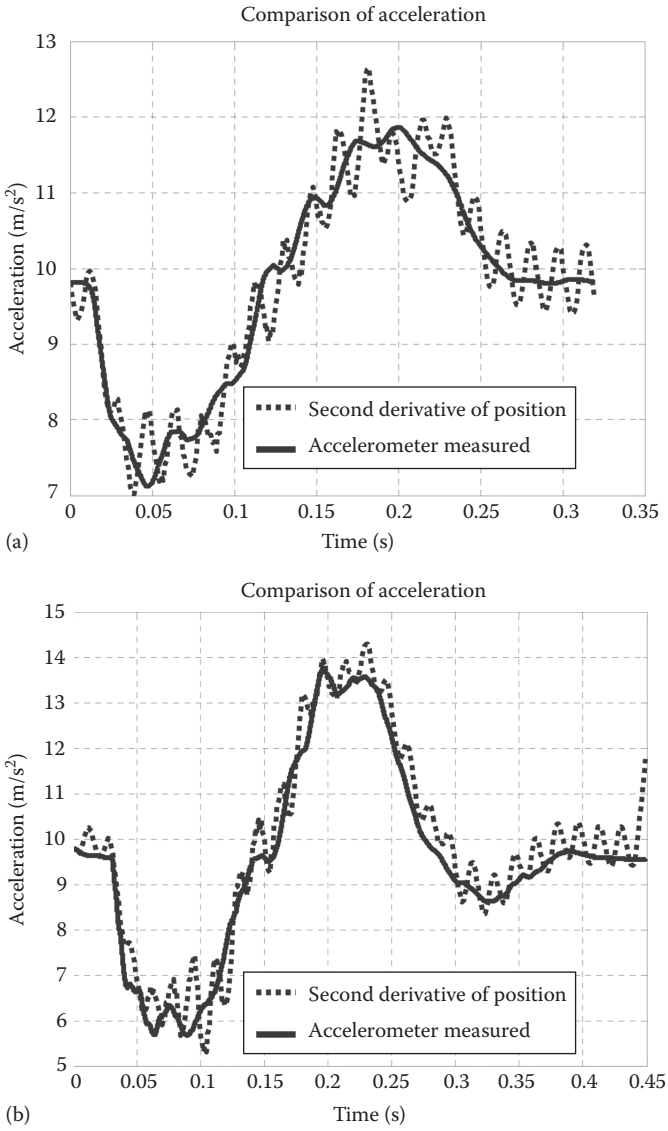

FIGURE 6.27 Comparison between the acceleration obtained from the direct measurement using accelerometer and the time derivative of the piston displacement described in Figure 6.26 for (a) material B (ϕ_0 = 0.97) with 7.0 kg loading and (b) material A(ϕ_0 = 0.97) with 9.25 kg loading. (Reprinted from Barabadi, B. et al., *J. Heat Transfer*, 131, 101006. Copyright 2009, with permission from American Society of Mechanical Engineers.)

forces exerted by the solid phase, respectively. The former is equivalent to a spring and the latter is equivalent to a dashpot.

The elastic force is determined by the quasistatic experiment, Figure 6.24, in which the piston was loaded slowly and incrementally so that the air in the pores could slowly escape without elevating pore pressure. The empirical expression, Equation 6.9, is now expressed as

$$\frac{F_{solid-elastic}}{F_{\max}} = f\left(\frac{\Delta h}{\Delta h_{\max}}\right), \tag{6.33}$$

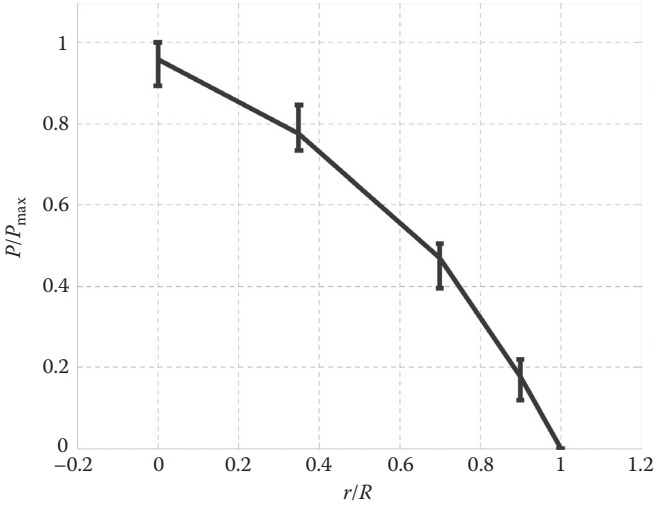

FIGURE 6.28 Representative radial pressure measured by the pressure transducers 1–4 as shown in Figure 6.20. The testing material is A ($\phi_0 = 0.97$) with 9.25 kg loading. It is plotted at the time when peak pressure is achieved at these locations. The data have been normalized by the maximum pressure obtained by pressure transducer 1 at the center of the piston, P_{max}. The error bars in the graph indicate the range of the variation of the pressure measurements in multiple sets of experiments. (Reprinted from Barabadi, B. et al., *J. Heat Transfer*, 131, 101006. Copyright 2009, with permission from American Society of Mechanical Engineers.)

where $F_{max} = mg$ and Δh_{max} is the final displacement of the piston when the full load mg is applied. This takes different forms for loading and unloading processes, as shown in Figure 6.24.

As can be seen from the stereomicroscopy images shown in Figure 6.23, the fibers of porous materials A and B are connected and twisted in an intricate 3-D structure. The bonds between the fibers play an important role in determining the mechanical properties of each material. During the rapid compression, these bonds between the fibers are broken. It is the friction between these fibers that creates significant damping forces, which, by intuition, are proportional to the velocity of the compaction. As the piston rebounds after its maximum compression, the compressed fiber sample is aerated and expands. During this process, the relative motion between the fibers has to overcome the connections between the fibers, and a damping force from the debonding of the compressed fibers is applied. This force is intuitively expected to be proportional to velocity as well since this is the rate at which the bonds are being broken. Thus, the damping force from the solid phase is expressed as

$$F_{solid-damping} = -mg\left(\eta_i \frac{dh}{dt}\right), \tag{6.34}$$

where η_i is the damping coefficient and the index "i" indicates the damping coefficient during compression (η_d) and rebound (η_u). η_i is to be determined by comparing the theoretical predictions of the time-dependent pressure distribution and piston displacement with the corresponding experimental data. The negative sign indicates that the direction of the damping force is always opposite to that of the motion of the piston.

F_{air} is determined by using the consolidation theory developed in Wu et al. (2005a), Equation 6.26, where the variation of the Darcy permeability of the porous layer during the compression process was determined using the Carman–Kozeny semiempirical relationship. This is the second modification of the Wu et al. (2005a) theory.

The Carman–Kozeny relationship is expressed as

$$K = \frac{D^2}{180}\frac{\varphi^3}{(1-\varphi)^2}, \tag{6.35}$$

where D is denoted as the mean diameter of the solid particles. During the compression process, if the mean diameter, D, remains the same and the Darcy permeability of the undeformed porous medium is K_0, the following equation can be obtained from (Equations 6.14 and 6.35)

$$K = K_0 \frac{\left(1-\frac{h_0}{h}(1-\varphi_0)\right)^3}{\left(\frac{h_0}{h}\right)^2 \varphi_0^3}. \tag{6.36}$$

Substituting this equation into Equation 6.19e, the characteristic time, t_c, can readily be obtained, which, along with Equation 6.19, is further used in Equation 6.22 to determine the pore-pressure distribution, $P(r, z, t)$. $P(r, z, t)$ is then substituted into Equations 6.25 and 6.26 to obtain $F_{air}(t)$.

Once the expression for the lifting forces from both the pore air pressure and the solid phase is determined, Equation 6.8 can be integrated subject to initial conditions (6.31a,b) numerically. The solution for $h(t)$ is then substituted into (Equation 6.22) to determine the pore-pressure distribution.

6.6.1.4.3 Comparison between Theoretical Results and Experimental Data

In the previous study by Wu et al. (2005a), the comparison between experiment and theory on the pore-pressure response was employed to determine the initial Darcy permeability of the porous medium. Since there was no direct measurement of the displacement of the piston, the comparison of the motion of the piston was not represented. The problem with this approach is that there might have been some solid damping force that contributed to the lift generation that was not described. In Barabadi et al. (2009) and Crawford et al. (2011a, 2012), the time-dependent displacement of the piston was recorded directly, Figure 6.26. This made it possible for one to compare the experimental results with the theoretical prediction based on the motion of the piston and the pore-pressure response. Thus, the initial Darcy permeability K_0 and the solid damping coefficient η_i of a porous medium could be determined.

The Darcy permeability, K, denotes how easily the air can pass through a porous structure. The inverse of K is a measure of the resistance that the air encounters as it flows through the porous medium or, equivalently, the damping force of the trapped air that acts on the piston. In the snow compaction study by Wu et al. (2005a), the damping force of the solid phase was only considered when there was a rebound of the piston. In the fiber compression experiments discussed herein, if the same idea is followed and the fiber damping force during compression is neglected, the experimental data match either the theoretical predictions for the time-dependent motion of the piston or that for the pore-pressure response, but not at the same time. This is better explained in Figure 6.29a for material B ($\varphi_0 = 0.97$, loading = 7.0 kg), where the initial Darcy permeability of the fibrous material needs to be chosen to be 1.33×10^{-9} m^2 so that the theoretical prediction matches the experimental data for the motion of the piston. If this value of the Darcy permeability is substituted into Equation 6.22, it is found that the theoretical prediction for the peak pore pressure at the center of the piston is eight times larger than the experimental result, Figure 6.29b. Also, the pore-pressure peak happens approximately 0.04 s earlier ($t = 0.11$ s) for the theory, as compared to the experiment ($t = 0.15$ s). This discrepancy indicates that the value of the Darcy permeability is obviously overestimated. This is due to the neglect of the fiber damping force during the compression process. If only the air damping is considered, in order to match the displacement data, a smaller Darcy permeability is needed. With this lower permeability, air cannot escape easily and more pressure is built up.

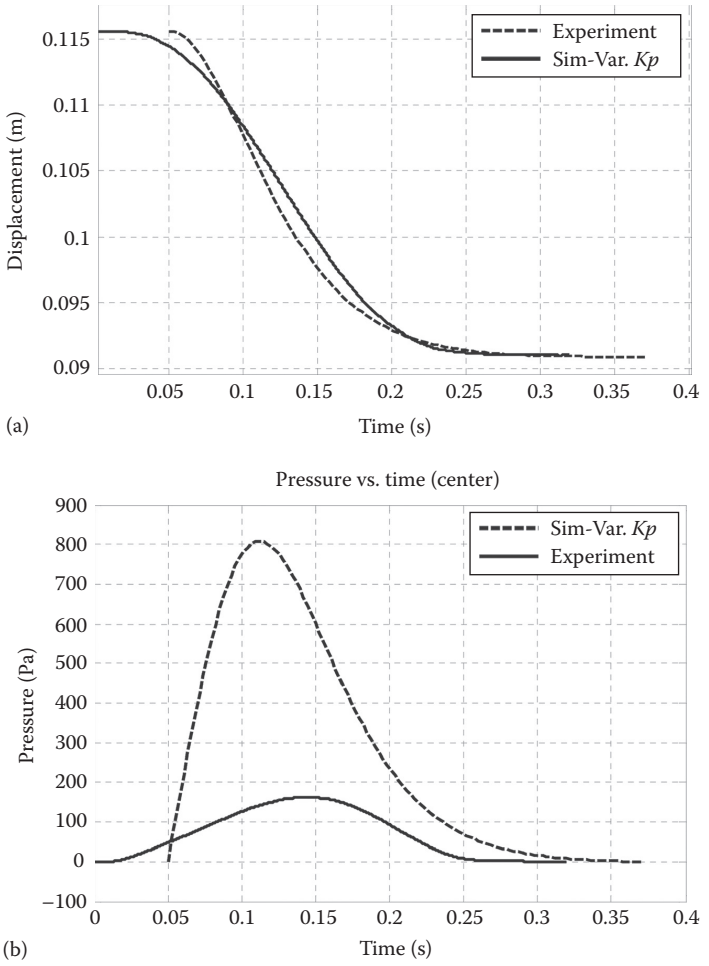

FIGURE 6.29 Comparison between experimental results (solid line) and theoretical simulation (dash line) for the dynamic compaction experiments with material B ($\varphi_0 = 0.97$) at 7.0 kg loading: (a) displacement of the piston and (b) pore pressure at the center of the piston. The simulation was based on no solid damping effects during compression. (Reprinted from Barabadi, B. et al., *J. Heat Transfer*, 131, 101006. Copyright 2009, with permission from American Society of Mechanical Engineers.)

Figure 6.29 leads to the conclusion that the fiber damping force plays a significant role in the lift generation. In order to match the theoretical predictions to the experimental data, both the initial Darcy permeability, K_0, and the solid damping coefficient η_i have to be adjusted in the simulation. This match was found by trial and error. It is shown in Figure 6.30 that if the permeability of the fiber is assumed to be a constant during the compression, the best fit between experiments and theory requires $K = 6.25 \times 10^{-9}$ m^2, $\eta_d = 4.73$ s/m, and $\eta_u = 300$ s/m. If the permeability changes as a function of compression based on the Carman–Kozeny equation (6.36), the initial Darcy permeability was determined to be $K_0 = 8.79 \times 10^{-9}$ m^2 and $\eta_d = 4.73$ s/m and $\eta_u = 300$ s/m.

It is clearly demonstrated in Figure 6.30 that varying permeability provides a better match. However, even with varying permeability, the theoretical model still predicts a faster pressure buildup compared with the experimental data. This behavior can be attributed to the following three reasons: First, the change in permeability does not exactly follow the Carman–Kozeny equation. Actually, this was later confirmed by Akaydin et al. (2011) and Crawford et al. (2011b). Second, the

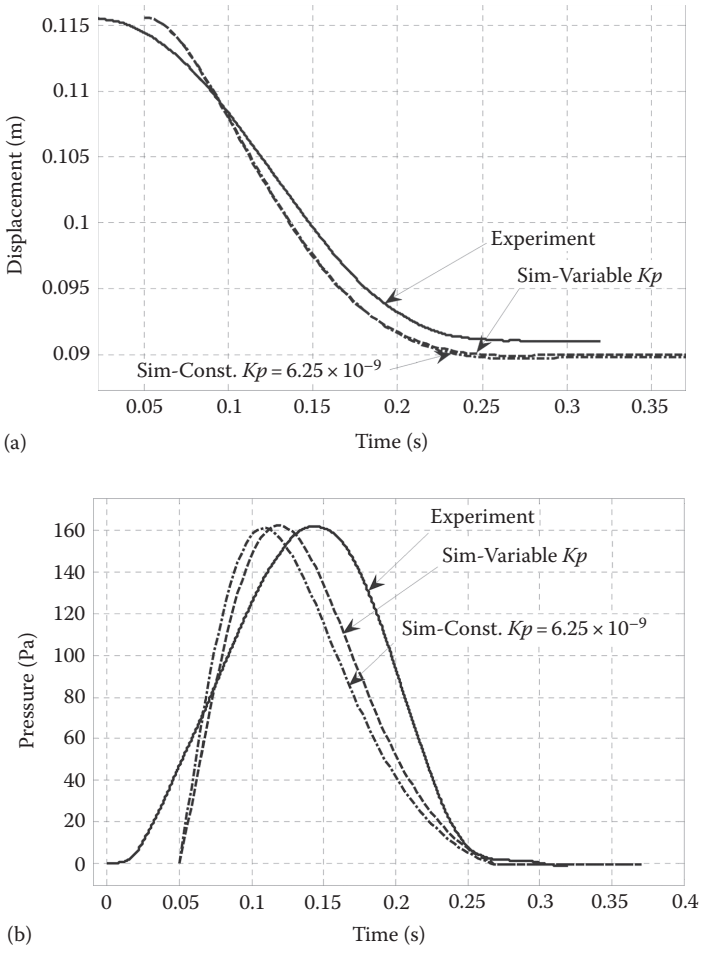

FIGURE 6.30 Comparison between experimental results and theoretical simulation for the dynamic compaction experiments with material B ($\phi_0 = 0.97$) at 7.0 kg loading: (a) displacement of the piston and (b) pore pressure at the center of the piston. Two simulations are provided: one for constant permeability at $K = 6.25 \times 10^{-9}$ m^2 and the other for varying permeability following equation (6.36) with initial value of permeability $K_0 = 8.79 \times 10^{-9}$. In both cases, the solid damping coefficients in compression and expansion are determined as $\eta_d = 4.73$ s/m and $\eta_u = 300$ s/m, respectively. (Reprinted from Barabadi, B. et al., *J. Heat Transfer*, 131, 101006. Copyright 2009, with permission from American Society of Mechanical Engineers.)

solid damping coefficient varies during the compression process. Third, the empirical relationship obtained from the quasistatic experiment does not precisely describe the elastic lifting force from the solid phase during the rapid compaction.

In order to verify if the approach presented herein is appropriate, simulations were performed for material B ($\varphi_0 = 0.973$) with different loading conditions, 8.71 kg, Figure 6.31. Interestingly, it was found that the best fit for both the motion of the piston and the pore-pressure distribution requires $K_0 = 8.79 \times 10^{-9}$ m^2, $\eta_d = 3.33$ s/m, $\eta_u = 300$ s/m, and the same value of permeability K_0 and rebound coefficient η_u as that obtained in 7.0 kg loading condition. The solid damping coefficient during the compression was relatively small. This is not surprising because the bonds between fibers are more easily broken with an increased load. The cross-checking was repeated for other loading conditions of material B, and consistent matches were obtained, assuring the validity of the theoretical and experimental methods presented herein.

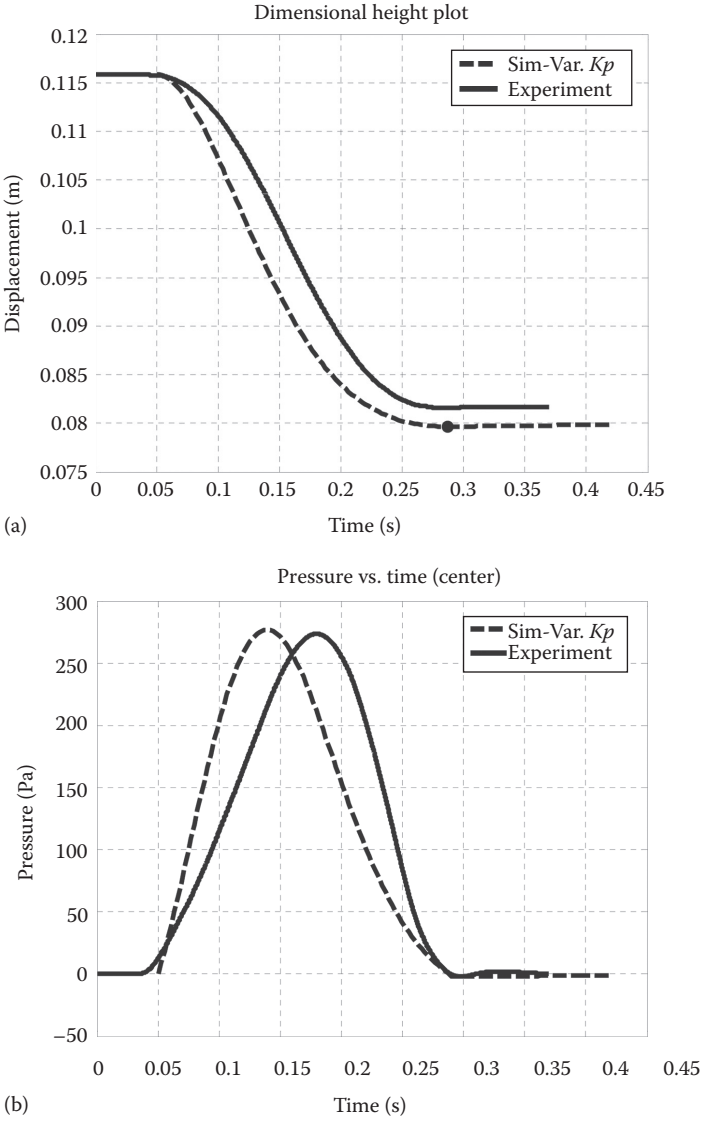

FIGURE 6.31 Comparison between experimental results and theoretical simulation for the dynamic compaction experiments with material B ($\phi_0 = 0.97$) at 8.71 kg loading: (a) displacement of the piston and (b) pore pressure at the center of the piston. The initial value of Darcy permeability $K_0 = 8.79 \times 10^{-9}$, and the solid damping coefficients in compression and expansion are $\eta_d = 3.33$ s/m and $\eta_u = 300$ s/m, respectively. (Reprinted from Barabadi, B. et al., *J. Heat Transfer*, 131, 101006. Copyright 2009, with permission from American Society of Mechanical Engineers.)

The same approach was also applied for the dynamic compression with material A ($\varphi_0 = 0.97$, loading = 9.25 kg). It was found that if Equation 6.36 was employed for the variation of the permeability, the initial Darcy permeability was determined to be $K_0 = 1.301 \times 10^{-7}$ m^2, and the solid damping coefficients for the compression and expansion were $\eta_d = 3.82$ s/m and $\eta_u = 7.7$ s/m, respectively. Comparing this with what was found for material B where $K_0 = 8.79 \times 10^{-9}$ m^2, $\eta_d = 4.73$ s/m, and $\eta_u = 300$ s/m, it is obvious that the damping effects of B from the pore air pressure are much higher than that of material A. This observation is consistent with the SEM and stereomicroscopy study presented previously. The fiber diameter of material A is three times larger than material B. Since

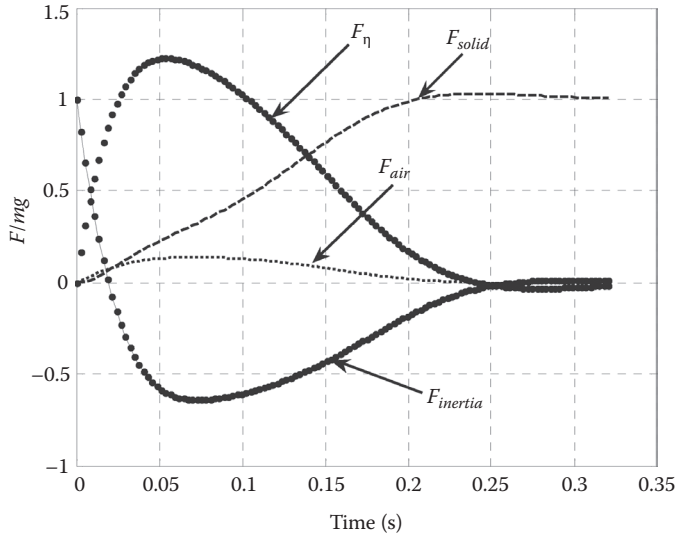

FIGURE 6.32 Time-dependent forces during dynamic compression of fiber B ($\phi_0 = 0.97$) at 7.0 kg loading. (Reprinted from Barabadi, B. et al., *J. Heat Transfer*, 131, 101006. Copyright 2009, with permission from American Society of Mechanical Engineers.)

the Darcy permeability of a porous medium is proportional to the square of the fiber dimension, as shown in Equation 6.35, the permeability of A is expected to be higher than B. Furthermore, it was observed that the fibers of material A are stiffer. This implies the contribution of the solid-phase elastic forces is more significant for material A.

The lumped parameter model based on the consolidation theory developed herein can reproduce the major features of the experimental data and provide further insight into the relative importance of the individual forces during the compression process. This insight is summarized in Figure 6.32, which shows the time variation of the four forces that appear in Equation 6.8 for fibrous material B ($\varphi_0 = 0.97$, loading = 7.0 kg). The forces were normalized by the applied weight, *mg*. The figure indicates that the solid damping effect is dominant and the damping force from the trapped air (in Figure 6.32 expressed as F_{air}) plays a minor role in damping the inertial force of the piston (in Figure 6.32 expressed as $F_{inertia}$). During the compression process, the elastic solid-phase force (in Figure 6.32 expressed as F_{solid}) continues to increase until it fully supports the piston weight; this point occurs when the air pore pressure is completely vented and the velocity of the piston reaches zero.

In the experimental setup of Barabadi et al. (2009), the frictional force between the piston and the cylinder is high as evidenced in Figure 6.32 where the pore-pressure lifting force is much smaller than one expects. It is also reflected in the time-dependent pore-pressure response. For example, in the dynamic compression with material B ($\varphi_0 = 0.97$, loading = 4.17 kg), the maximal dimensionless velocity of the piston, $v^* = v/(2h_0 g)^{0.5}$, was experimentally measured to be 24%, and the dimensionless maximal pore pressure at the center of the piston, $P^* = P/(mg/(\pi d^2/4))$, was 67%. Here, h_0 is the initial thickness of the porous layer, m is the applied load (kg), and d is the diameter of the piston. The lower-pressure generation was mainly caused by the fact that with a 0.7 mm gap between the piston and the cylinder, the piston was too tightly fitted in the cylinder. It caused huge wall friction and significantly decreased the piston velocity, leading to smaller pore-pressure generation. In a later study by Crawford et al. (2012), a relatively bigger radial clearance gap, 1.7 mm, was created between the piston and the sidewall. Since the overall gap area, 2.012×10^{-3} m^2, is only 3% of the pore area on the side wall, air leakage through this gap is still negligible. For similar loading, v^* was measured to be 25.2%, and P^* at the center of the piston was as high as 74%.

6.6.1.4.4 Remarks on the Dynamic Compression of Fibrous Materials

The dynamic compression of fibrous materials developed in Barabadi et al. (2009) and Crawford et al. (2012) provided a systematic, experimental, and theoretical approach for examining the dynamic lift forces that are generated during the rapid compaction of soft porous media. Notably, the redesign of the experimental setup and the application of a displacement sensor allowed the measurement of the motion of the piston. By comparing the theoretical predictions to the experimental data on the motion of the piston as well as the pore-pressure response, one was able to separate the solid-phase damping force from that of the transiently trapped air. This experimental and theoretical approach has provided an important method in characterizing the relative contributions of the different forces involved in the lift generation in a porous medium. To our knowledge, it is the first time that such forces have been considered.

The phenomena of lift generation in soft porous media discussed so far, from red blood cells gliding over the EGL to human skiing/snowboarding on fresh powder snow, all share a common feature: only the soft porous medium beneath the loading surface is compressed. Pore pressure is generated underneath the loading surface and relaxes in the undeformed surrounding porous layer. There were no studies on the lift generation in a soft porous medium, however, that considered the contribution of the surrounding porous structure to the total lift, including the dynamic compression experiments discussed earlier. This is a major limitation of the study discussed herein. It leads to the questions: "What is the role of the surrounding porous material to the total lift? How will the pore pressure distribute if a deforming porous medium is surrounded by undeformed porous structures?" In the following session, Crawford et al. (2011a) will answer these questions by experimentally examining the change in lift generation if surrounding porous materials are considered.

6.6.1.5 Dynamic Compression of Soft Porous Media: From Finite to Infinite Domain

In the dynamic compression experiments by Wu et al. (2005a), Barabadi et al. (2009), and Crawford et al. (2012) using a porous-walled cylinder–piston apparatus, the air that was trapped inside a porous layer underneath the loaded piston was forced out through the porous wall (Figures 6.9 and 6.20) to the ambient, that is, "finite domain." It oversimplifies the real applications where transiently trapped fluid is squeezed out to the surrounding porous structures, that is, "infinite domain." In Crawford et al. (2011a), the authors experimentally treated this shortcoming. A soft, polyester, fibrous, porous material, C, was chosen for the study. Its microstructure was characterized using a SEM. Its porosity was measured using the water displacement method and its permeability was determined using a permeameter. The cylinder–piston apparatus in Crawford et al. (2012) was first used in the quasistatic experiment to examine the material's stiffness and was then used in the dynamic compaction experiments in the "infinite domain." Detailed pressure distribution was examined. The results indicated that the air lifting force is enhanced by 25%–30% for the "infinite domain" over the "finite domain" due to the existence of the surrounding porous material. The pore pressure, however, relaxes rapidly in the undeformed surroundings. These observations improved our understanding of the dynamic response of soft porous media under rapid compression. Detailed results of the dynamic compression in the "infinite domain" by Crawford et al. (2011a) are summarized in the following Sections 6.6.1.5.1 and 6.6.1.5.2 (Figures 6.33 through 6.42).

6.6.1.5.1 Material Characterization

6.6.1.5.1.1 Microstructures Lift generation in a highly compressible porous medium, as a function of porosity, loading conditions, material stiffness, and porous layer thickness, was largely examined in Crawford et al. (2012) for the "finite domain" compression. The study in Crawford et al. (2011a) discussed herein is focused on the difference between the "finite domain" and "infinite domain" cases; hence, only one soft porous material was investigated. It was shown by Crawford et al. (2012) that a softer material with smaller fiber diameters has a greater potential to generate lift. Considering this observation, pillow-filling material constructed of 100% polyester, that is, "material C," was used in this study.

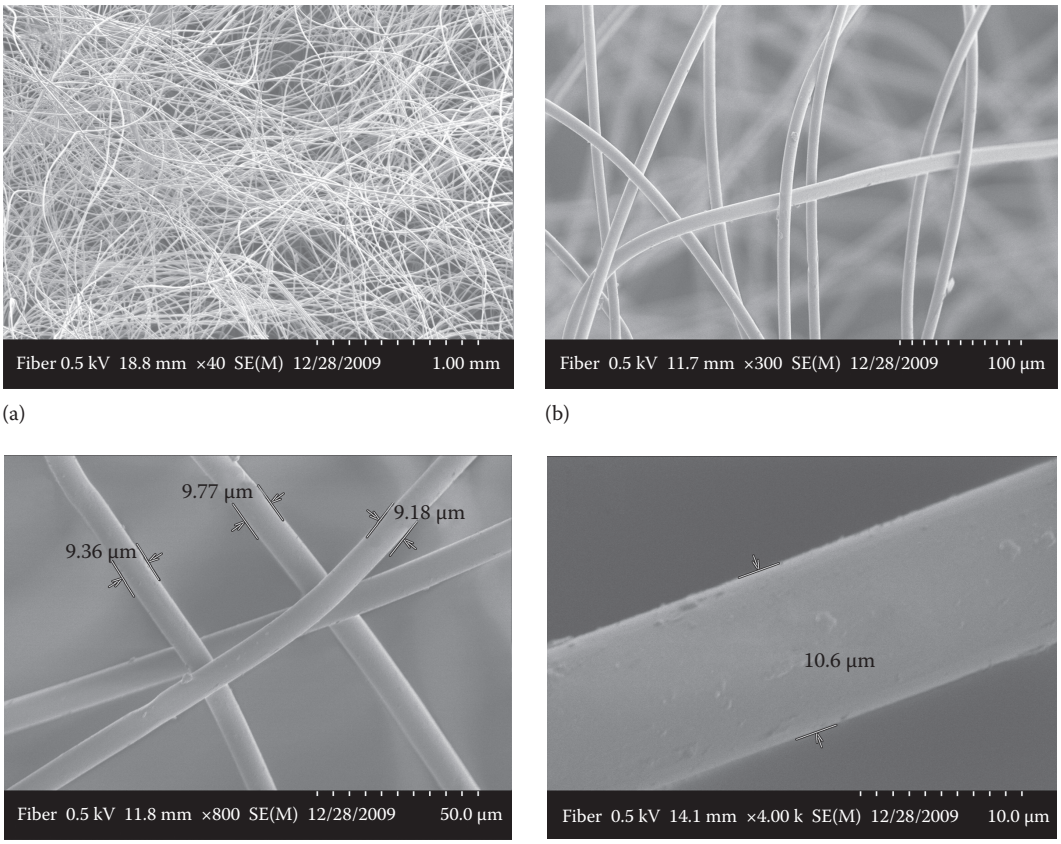

FIGURE 6.33 SEM images of material C at (a) 40×, (b) 300× (c) 800×, and (d) 4000×. (Reprinted from Crawford, R. et al., *J. Porous Media*, 14, 51. Copyright 2011a, with permission from Begell House Publishers.)

A Hitachi S-4800 high-resolution SEM was first used to identify the diameter of the fibers and the material's overall surface features. Conductive carbon double-stick tape was used to attach the fibers onto a 20 mm diameter SEM holder. Therefore, the overall fiber area was 20 mm in diameter and 5 mm in height. Since the fibers were elastic and curved, not all of the fibers could be stuck to the carbon tape. In order to prevent the fibers from falling off the SEM specimen holder, special care was taken to secure the fibers onto the holder. A small amount of silver paint was used to secure several points on the outer edges of the fibers, which also provided better electrical conductivity to reduce the charging effect. The SEM was operated at only 0.5 kV to avoid the electron charging effect on the polyester fibers. Figure 6.33a is an image of a SEM picture at 40× that shows the overall waviness, interconnection, and fiber length of the fibers of material C. Because most of the fibers were curved and long, it was difficult to determine the actual fiber length due to the challenge of identifying the beginning and end of the fibers. As indicated in Figure 6.33a, the length of the fibers seemed to be greater than the diagonal length of the image that was measured at 5 mm. The fibrous material can be compressed so that all of the fibers are close together, yet there are still sufficient gaps to see through. The holes that were capable of seeing through ranged from 0.01 to 1 mm on the *x*-*y* plane based on the image setting in Figure 6.33a. Careful investigation through the holes indicated that there were more fibers in another layer underneath the holes. However, these fibers could not be seen easily due to the lack of contrast and intensity. Figure 6.33b is a SEM picture of the top layer of the fibers taken at 300×.

Because some of the fibers in the background were out of focus at this SEM setting, it indicated that the fibers had some gaps in the vertical direction (z direction). The gaps of the fibers that were on the x-y plane can be as high as 100 μm in this top layer of the fibers. Figure 6.33c is a SEM image taken at 800×. The image shows three measurements of the fiber diameters for three different fibers, all of which were slightly less than 10 μm. At this magnification, the surfaces of the fibers are shown to be quite clean and smooth. When increasing the magnification to 4000×, as shown in Figure 6.33d, there are more surface features that are revealed. Small surface roughness on the fibers at different locations can be observed. The measurement of the fiber diameter in this Figure 6.33d is 10.6 μm, a value that is consistent with the previous measurements that were taken at a magnification of 800×. By observing all of Figure 6.33a through d, it can be concluded that the overall fiber surfaces are smooth and clean, all with consistent diameters. The extrusion process for these fibers provided this favorable reproducibility.

6.6.1.5.1.2 Porosity and Permeability The porosities of the fibrous material were quantified using Equation 6.32, where the densities of the solid fibers were determined using water displacement method, $\rho_{fiber} = 0.70$ g/cc. With ρ_{fiber} determined in Equation 6.32, the porosity of the porous material becomes a single, linear function of the density of the porous material, ρ. Or equivalently, ρ was solely determined for a desired porosity, ϕ. The mass of the material can then be calculated with the specific density, ρ.

Crawford et al. (2011b) designed, fabricated, and tested a special permeability measurement apparatus that was used to examine the change of permeability as a function of compression (or equivalently the decrease in the porosity) for material C. The apparatus, shown in Figure 6.34, consists of a cylindrical tube fitted with a double-head cylinder inside. Air is pumped through the sample material inside the tube and then divided into two streams at the exit. One can adjust the valves on the two substreams at the exit to eliminate the pressure difference in the radial direction of the tube. The Darcy law, Equation 6.11, is applied to evaluate the permeability once the pressure drop from the inlet to the outlet and the volume flow rate of the air are measured. The result of this experiment is shown in Figure 6.35, which indicates that for porosity $0.78 < \phi < 0.98$, the Darcy permeability K ranges from 1.7×10^{-10} m^2 to 5.3×10^{-9} m^2. It is observed that in the

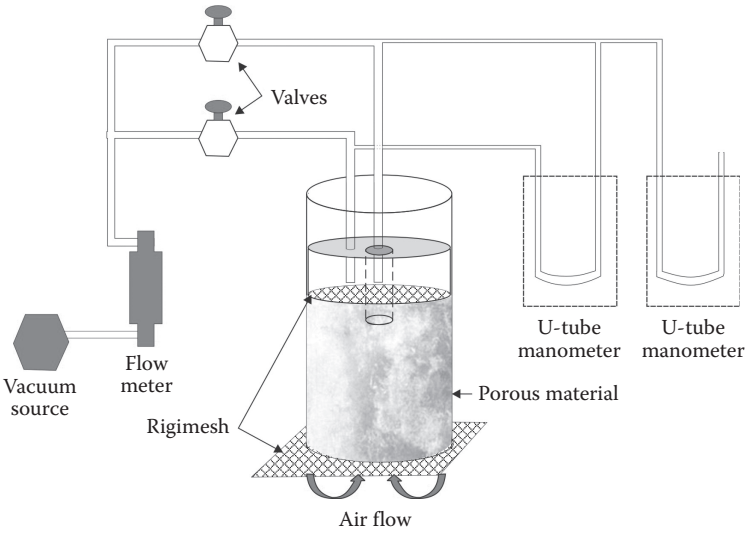

FIGURE 6.34 Experimental setup for the permeameter. (Reprinted from *Chem. Eng. Sci.*, 66, Crawford, R., Jones, G. F., You, L., and Wu, Q., Compression-dependent permeability measurement for random soft porous media and its implications to lift generation, 294–302, Copyright 2011b, with permission from Elsevier.)

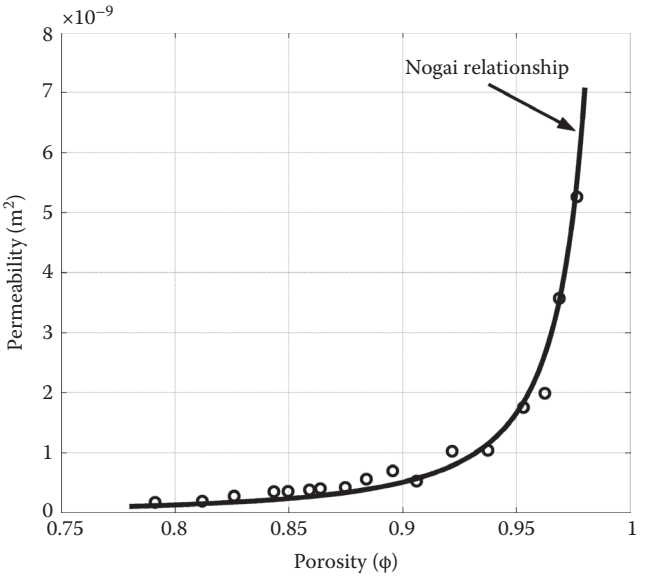

FIGURE 6.35 Permeability as a function of porosity for material C. The experimental data are fitted with the Nogai relationship, Equation 6.37 (Nogai 1978). (Reprinted from Crawford, R. et al., *J. Porous Media*, 14, 51. Copyright 2011a, with permission from Begell House Publishers.)

very porous region, a slight compression of the porous medium causes a sharp decrease in the permeability; the rate of change in the permeability slows down significantly after the porosity of the porous medium reaches values that are below 0.9. It was found that the Nogai relationship (Nogai et al., 1978) provided the best description for the change of permeability as a function of compression:

$$K = \chi \frac{\phi^3}{(1-\phi)^{\kappa}} \tag{6.37}$$

where χ and κ were experimentally determined values, $\chi = 2.3 \times 10^{-11}$ m^2 and $\kappa = 1.48$.

6.6.1.5.1.3 Mechanical Properties Using the porous-walled cylinder–piston apparatus, shown in Figure 6.21, static compression experiments were performed to determine the stiffness of the material C (fiber diameter, D = 10 μm) (Crawford et al., 2011a). For the purpose of comparison, materials A (fiber diameter, D = 40 μm) and B (fiber diameter, D = 13 μm) were also tested. The result is shown in Figure 6.36.

It indicated that material C was the most compliant and material A was the stiffest. This is consistent with the microstructure observations that material A has a larger fiber diameter (40 μm) than materials B (13 μm) and C (10 μm). Since the three polyester fibrous materials were all extruded at the same temperature, the fiber diameter plays the major role in determining their stiffness. As described earlier in this chapter, the stiffness plays an important role in the behavior of soft porous materials. Stiffer materials compress less under the same loading.

Figure 6.36 also shows that permanent deformation occurred at the end of the unloading phase of the static experiment, confirming the inelastic nature of the materials as well as the effects of the side wall friction. The viscoelastic behavior of a fibrous material is determined by the friction between fibers as well as that between fibers and the confined cylindrical side wall. The latter is expected to play a more important role as the relative motion between the fibrous material and the cylindrical side wall is more substantial. During the decompression phase of the static experiment,

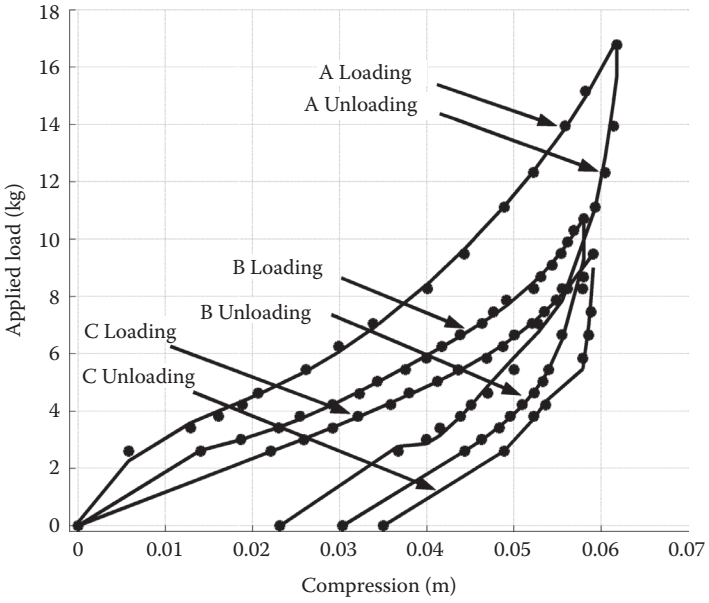

FIGURE 6.36 Static experimental results for materials A and B at 0.98 porosity and material C at 0.97 porosity. (Reprinted from Crawford, R. et al., *J. Porous Media*, 14, 51. Copyright 2011a, with permission from Begell House Publishers.)

the pores on the cylindrical wall tangle and grab the fibers, causing more permanent deformation of the fibrous material. This behavior was extensively studied by Al-Chidiac et al. (2009) who experimentally demonstrated that the hysteresis effect is considerably less in the case of laterally unconfined axial compression/decompression as compared to the case when the porous material is confined in the cylindrical wall.

6.6.1.5.2 Dynamic Experiments

6.6.1.5.2.1 Methods The porous-walled cylinder–piston apparatus introduced earlier in this chapter, developed by Crawford et al. (2012) and shown in Figure 6.21, was adopted for this study. This setup differed, however, because of the implementation of undeformed porous media surrounding the cylinder–piston apparatus, as shown in Figures 6.37 and 6.38. The same material was placed both inside and outside of the cylinder–piston apparatus. For the outside, this material was evenly distributed in the four cells that surround the cylinder. The roof of the cells, made of highly permeable porous netting, held the material at a certain height. The volume of the cells could then subsequently be determined, which allowed the different porosities of the surrounding porous media to be obtained.

A certain amount of dead weight was loaded onto the piston, which was released by a triggering mechanism and created a sudden compression on the porous medium underneath. The motion of the piston was guided by a linear guide rail with minimal friction. The gap between the moving piston and the cylindrical sidewall was small enough to eliminate air leakage through it, yet large enough to prevent sliding friction.

The motion of the piston was captured by the dual-axis accelerometer (ADXL203) as well as the high-resolution laser displacement sensor (Micro-Epsilon, model ILD1300-200). The pore-pressure generation inside the compressed porous material was captured by the four micro pressure transducers P_{0-4}, as shown in Figures 6.20 and 6.37.

Three SI micro pressure transducers, P_{10}, P_{11}, and P_{12}, were installed outside of the cylinder–piston apparatus on the edge of the porous wall. They were placed at a distance 2, 5, and 8 cm from

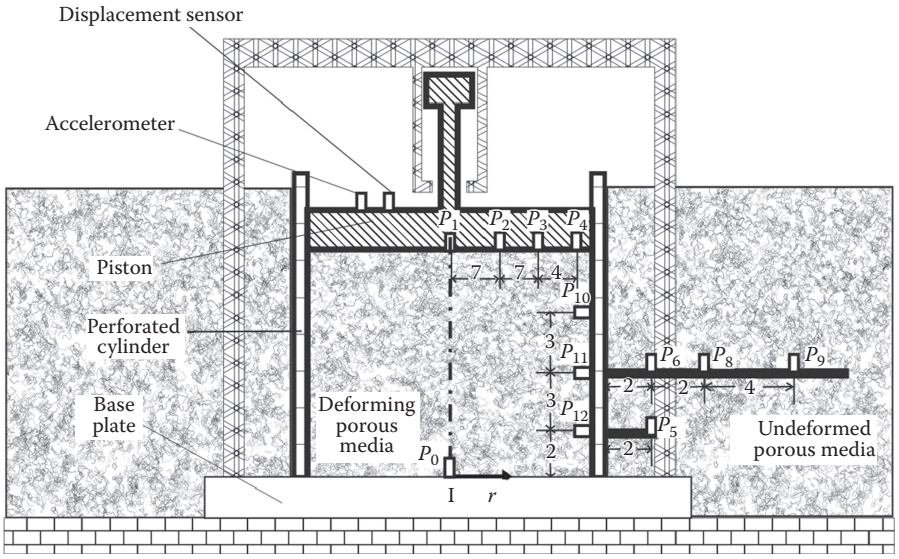

FIGURE 6.37 Experimental setup for static and dynamic compaction experiments of fibrous material (dimensions in centimeter). (Reprinted from Crawford, R. et al., *J. Porous Media*, 14, 51. Copyright 2011a, with permission from Begell House Publishers.)

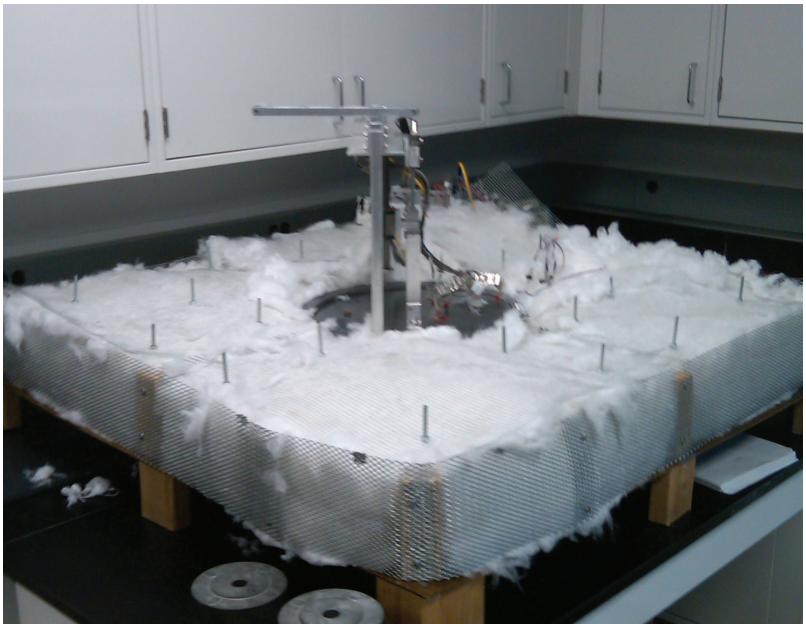

FIGURE 6.38 Image of the cylinder–piston apparatus with an infinite domain. (Reprinted from Crawford, R. et al., *J. Porous Media*, 14, 51. Copyright 2011a, with permission from Begell House Publishers.)

the base of the cylinder–piston apparatus, respectively, as shown in Figure 6.37. These pressure sensors provided critical measurements of the pore-pressure distribution at the interface between the deformed and the undeformed porous domains. Another three SI micro pressure transducers, P_6, P_8, and P_9, were placed outside the cylinder–piston apparatus at a distance of 2, 4, and 8 cm away from the cylindrical porous wall and at a height of 5 cm from the base. The readings from P_{11}, P_6, P_8, and P_9 provided the radial pressure distribution in the radial direction outside the cylinder.

One final pressure transducer, P_5, was placed directly beneath P_6 at a height of 2 cm from the base. Readings obtained from P_5 and P_6 provided information on the vertical pressure distribution in the undeformed porous domain outside the cylinder.

The electrical outputs of the sensors were captured by the NI cDAQ9172 data acquisition system and processed by LabVIEW and MATLAB.

Material C, with a desired porosity of 0.97, was first spread out evenly inside the cylinder–piston apparatus. The piston was then lowered to the chosen drop height of 12 cm, where it gently touched the top surface of the porous material prior to rapid compaction. Weights were then placed on top of the piston up to a load of 17 kg. The same material that was used inside the cylinder–piston was then placed outside the cylinder in the surrounding cells. The height of the cells was adjusted so that the thickness of the undeformed porous material surrounding the cylinder–piston apparatus was equal to or greater than that of the deforming porous layer inside the apparatus. The porosity of the outside material was precisely controlled in the range between 0.95 and 0.97.

Following each experimental trial, the porous material underneath the piston was refluffed to ensure that there was no initial precompression before the test. Multiple trials were conducted under the same initial conditions to examine the repeatability and uncertainty of the experiment.

6.6.1.5.2.2 Results and Discussion Material C, with a porosity of 0.97 and initial thickness of 12 cm, was placed in the cylinder–piston apparatus. The same material, with a porosity of 0.95 and thickness of 14 cm, was placed outside of the apparatus. The applied load on top of the piston was 8.274 kg.

To better understand the difference in the lift generation in a highly compressible porous layer from the "finite domain" compression to the "infinite domain" compression, dynamic compression experiments with and without surrounding porous media were performed under the same loading conditions. A comparison of the pore-pressure generation is shown in Figure 6.39a, where "Fin" stands for "finite domain" compression while "Inf" stands for "infinite domain" compression. Two prominent observations were obtained from this figure: (1) The duration for the air being trapped inside the porous layer, corresponding to the duration of the pore-pressure generation, was much longer for the "infinite domain" case. This is because the surrounding porous medium provided extra resistance to the air as it passed through. (2) At the center of the piston, higher pore pressure, P_1, is observed for the "finite domain" compression, while at other radial positions, P_2, P_3, and P_4, higher pressure was generated for the "infinite domain" compression. This seems to be puzzling as one expects the "infinite domain" compression to always generate higher pore pressure. The answer to this question lies in the fact that there are two competing mechanisms that determine the pore-pressure generation. On the one hand, the surrounding porous structure prevents the air from escaping and thus facilitates the pore-pressure buildup. While on the other hand, with more air being trapped, higher air lifting force is generated, leading to a decrease in the velocity of the piston as it travels downward, as demonstrated in Figure 6.39b. Slower impact, along with the resulting slower change in the permeability of the porous material, leads to less pore-pressure generation.

In Figure 6.39c, the radial pressure distributions obtained from pressure transducers P_1–P_4, at the time when peak pressure was reached for the "finite domain" and "infinite domain" compressions, are compared. A parabolic pressure distribution is observed for both cases, with the highest pressure registered at the center of the piston and lowest pressure at the edge of the cylinder. The pressure at the edge of the cylinder, however, was zero gage pressure for the "finite domain" and about 200 Pa for the "infinite domain" compression. In order to obtain the total force from the pore air pressure, the pore pressure underneath the piston surface can be integrated based on the radial pressure distribution presented in Figure 6.39c. One finds that the imposed surrounding porous structure allowed for the lifting force from the pore air pressure to be enhanced by roughly 30%, 63.4 N for the "infinite domain," which is about 78% of the applied load, and 49.4 N for the "finite domain" compression, which is about 61% of the applied load. This observation confirmed that the

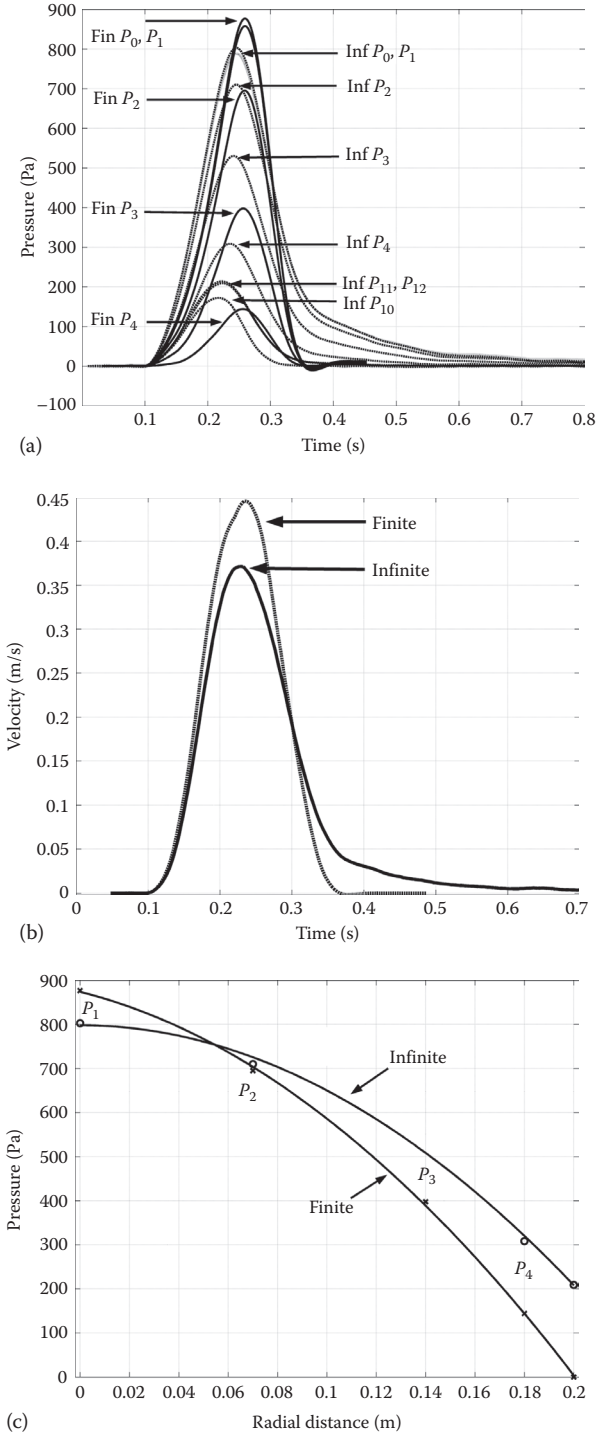

FIGURE 6.39 (a) Pressure profiles, (b) velocity profiles, and (c) radial peak pressure profiles comparing the finite and infinite domains. Both had initial conditions inside the cylinder–piston apparatus of material C at a porosity of 0.97, a load of 8.274 kg, and a material thickness of 0.12 m. The infinite domain conditions were 0.95 porosity and 0.14 m material thickness. (Reprinted from Crawford, R. et al., *J. Porous Media*, 14, 51. Copyright 2011a, with permission from Begell House Publishers.)

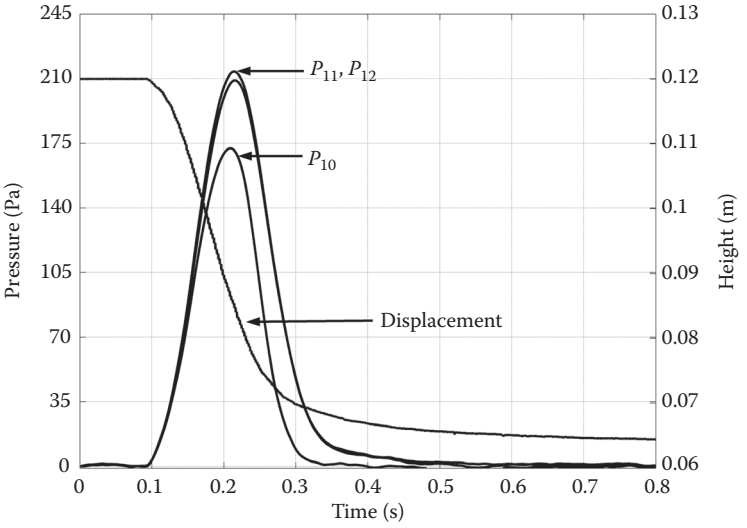

FIGURE 6.40 Pressure profile on the cylinder–piston apparatus wall. The initial conditions inside the cylinder–piston apparatus for this experiment were material C at 0.97 porosity, 8.274 kg load, and 0.12 m material thickness. The infinite domain conditions were 0.95 porosity and 0.14 m material thickness. (Reprinted from Crawford, R. et al., *J. Porous Media*, 14, 51. Copyright 2011a, with permission from Begell House Publishers.)

lift generation inside a deformable porous medium is noticeably enhanced due to the existence of the surrounding porous structures.

A closer examination of the pressure distribution along the cylindrical sidewall for the "infinite domain" compression is provided in Figure 6.40. Pressures at P_{11} and P_{12} are very close to each other, around 25% of the peak pressure at P_1, while pressure at P_{10} is much lower than P_{11} and P_{12}, around 20% of P_1. The mechanism for the similarity in the pressure profile between P_1 and P_0, as discussed before, explains why pressures at P_{11} and P_{12} are very close to each other. The reason why pressure at P_{10} is lower is because this pressure sensor was placed at 8 cm away from the base and was closer to the upper atmospheric boundary. Especially, with the motion of the piston, the distance between this pressure sensor and the atmosphere decreased. Continuous leakage of the air to the atmosphere caused lower-pressure buildup at P_{10}. In Figure 6.40, the displacement of the piston is also plotted, which indicated that at around $t = 0.24$ s, the piston passed the pressure sensor P_{10}, exposing it to the atmosphere and causing the pressure at this position to relax to zero gage pressure much earlier than the other two. The pressure sensors P_{11} and P_{12}, however, were 5 and 2 cm away from the base, far from the upper atmospheric boundary, and the piston never passed either of these two. Thus, higher, identical pressures were generated.

After the air was forced out of the cylinder–piston apparatus, it entered the surrounding undeformed porous structures. The flow pattern is the potential Darcy flow in an infinite domain. In Figure 6.41, the pore-pressure generation captured by pressure sensors located outside the cylindrical wall at 5 cm away from the base, P_{11}, P_6, P_8, and P_9, is plotted. As shown in Figure 6.41a, pore pressure built up simultaneously at these locations and decreased radially, with the highest pressure registered near the cylindrical wall. Figure 6.41b shows the radial pressure distribution outside the cylinder at the time when peak pressure was achieved. It can be seen that the pressure decreases by almost threefold as moving from P_{11}, which is on the edge of the cylindrical wall, to P_9, which is 8 cm away from the cylindrical wall. The fast pressure relaxation justified the experimental setup imposing an undeformed surrounding porous structure that extended by 1.0 m away from the cylindrical wall to act as an infinite porous medium.

The general pressure behavior is consistent with the theoretical prediction by Wu et al. (2005a) for the "finite domain" compression and by Wu et al. (2014a) for the "infinite domain" compression.

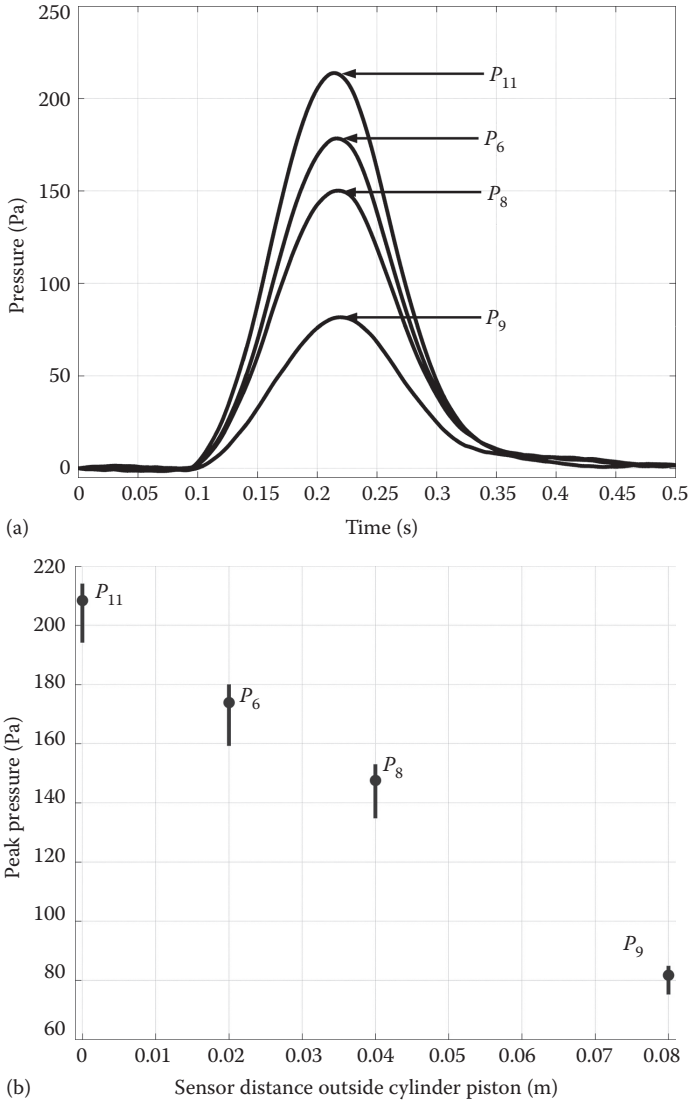

FIGURE 6.41 (a) Pressure profiles in the infinite domain and (b) peak pressures radially outside the cylinder–piston apparatus showing consistency between trials. The initial conditions inside the cylinder–piston apparatus for this experiment were material C at 0.97 porosity, 8.274 kg load, and 0.12 m material thickness. The infinite domain conditions were 0.95 porosity and 0.14 m material thickness. (Reprinted from Crawford, R. et al., *J. Porous Media*, 14, 51. Copyright 2011a, with permission from Begell House Publishers.)

In Wu et al. (2014a), an analytical approach was developed to characterize the pore-pressure distribution for the "infinite domain" compression. In this theory, two porous domains were considered: the inside ($r < R$) deforming porous medium with negligible vertical pressure gradient and the outside undeformed porous medium with vertical pressure gradient. At any instant, the pore pressure on the edge of the cylinder is uniform vertically and provides a pressure source for the potential flow in the outside undeformed porous medium. The experimental data obtained in the current study agree well with the theoretical predictions in Wu et al. (2014a).

Figure 6.41b also shows the repeatability of these experiments. Five experiments were performed for the same initial conditions. High repeatability was obtained with a standard deviation less than 4%.

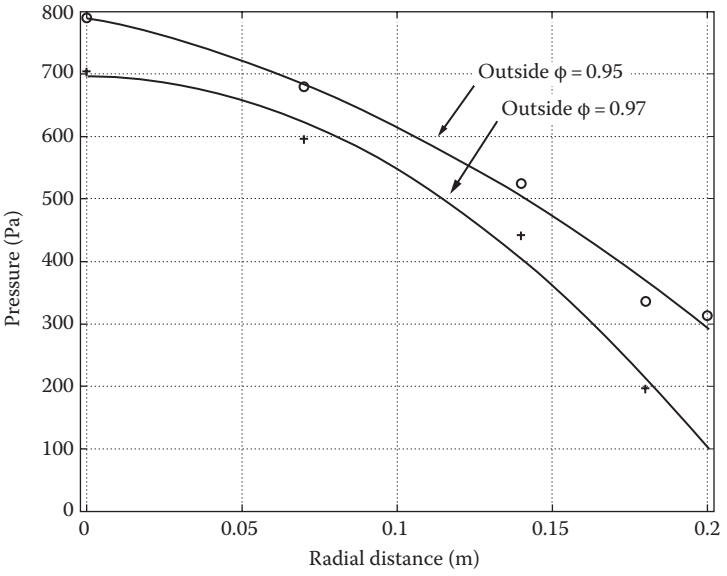

FIGURE 6.42 Radial pressure distribution underneath the piston surface at 0.1 s after it was released, comparing two different infinite domain porosities 0.95 and 0.97. The initial conditions inside the cylinder–piston apparatus for this experiment were material C at 0.97 porosity, 16.785 kg load, and 0.12 m material thickness. The infinite domains had a material thickness of 0.14 m. (Reprinted from Crawford, R. et al., *J. Porous Media*, 14, 51. Copyright 2011a, with permission from Begell House Publishers.)

Various layer thicknesses of the surrounding material, ranging from 12 to 14 cm, were examined with no change in the pressure generation observed. This is expected because the added porous material introduces negligible resistance to the air compared to the overall volume of the porous medium. In addition, pore pressure relaxes very quickly outside of the cylindrical wall, making the velocity of the air very small as it approaches the upper boundary.

One expects that the porosity of the surrounding porous material plays a significant role in the lift generation under the loading piston, which was confirmed in Figure 6.42 for the radial pressure distribution underneath the piston surface at 0.1 s after the release of the piston. The applied loading was 16.785 kg. The initial thickness of the porous layer inside the cylinder was 12 cm and the initial porosity was 0.97. The thickness of the surrounding porous medium was 14 cm and its porosity was either 0.95 or 0.97. It was observed that by lowering the porosity of the surrounding material by 2%, an increased resistance was encountered by the transiently trapped air as it passed through the porous layer, resulting in a higher generated pore pressure. By integrating the pressure generated underneath the piston, it can be concluded the enhancement in the air lifting force changes from 50.1 to 63.8 N, an increase of 27%.

In this section, a systematic, experimental, and theoretical approach was introduced for examining the lift generation inside a highly compressible porous medium under rapid compression. The original idea of performing the dynamic compression experiments with snow, as discussed in Section 6.2.1, was to verify the F&W theory. The technical approach was further developed extensively to fibrous materials in Section 6.2.2. Most recently, Wu and colleagues (Wu et al., 2014b) have successfully separated the solid-phase lifting force from the inertial force as well as the pore-pressure lifting force during the dynamic compression process. This study conclusively demonstrated that the theoretical approach in describing the pore-pressure generation as presented earlier this section is correct. The study also provided a lumped viscoelastic model to characterize the solid-phase lifting force as well as the sidewall friction.

The fundamental insights obtained from the dynamic compression of soft porous media could have very broad application potentials in soft porous lubrication or soft porous damping. In the

following two sessions, the application of soft porous media for soft lubrication will be introduced. This includes the lifting mechanics of downhill skiing and a next-generation train running on a soft porous track with minimal sliding frictions.

6.7 LIFT MECHANICS OF DOWNHILL SKIING OR SNOWBOARDING

Downhill skiing or snowboarding, in its simplest form, can be described as the motion of a human sliding down an inclined plane on a porous layer. The extensive classic literature pertaining to the science of skiing and snowboarding is summarized in Lind and Sanders (1996). A major contribution to this literature is the pioneering work of Colbeck (1991, 1992, 1994a,b, 1995), which focused on the reduced frictional force that results from the micron-thick fluid film that forms on the underside of a ski or snowboard due to frictional heating. As mentioned earlier in this chapter, a major breakthrough in the skiing mechanics research area occurred in the year 2000, when F&W developed a new lubrication theory for highly compressible porous media. This theory provided a new perspective on the lift mechanics of downhill skiing or snowboarding and answered a fundamental question, which was why a 70 kg human can glide through a soft snow layer without sinking into the base, as would occur if the motion was arrested. Later studies by Wu and colleagues (Wu et al. 2005a,b; Barabadi et al., 2009; Crawford et al., 2011a,b, 2012), as summarized earlier in this chapter, conclusively proved the feasibility of the enhanced lift concept that was proposed by F&W.

Despite the progress, the F&W theory, when applied to the lift mechanics of skiing or snowboarding, has several major limitations. These limitations include the following:

1. In the analysis performed by F&W, the lubrication limit was assumed and the inertia of the air escaping from the lateral edges of a ski or snowboard was neglected. This omission, however, was not justified.
2. In the analysis by F&W, the local variations of the Darcy permeability in the compressed fiber layer were determined from solutions of the Stokes equations for the local average flow through a compressed 2-D fiber array. This approximate model was applied in F&W to both the EGL and fresh powder snow. In the case of snow, this approximation was only intended to capture the essential physics of the compression process due to the wide variety of shapes and sizes of snow crystals from planar dendritic (hexagonal) to columnar within each snow classification (Arons and Colbeck, 1995).
3. When the theory in F&W was first developed, it was intended to apply to highly compressible porous media in the limit where the structure was so compressible that the normal forces generated by the compression of the solid phase were negligible, compared to the pore-pressure forces generated within the porous media. In the snow experiments performed by Wu et al. (2005a), which were discussed earlier in this chapter, it was shown that this might be true for snowboarding on fine-grained less permeable (wind-packed) snow at velocities greater than 15 m/s for a 1.5 m snowboard. Under such conditions, the duration of the contact time of the snowboard with the snow is sufficiently short (less than 0.1 s) such that the air is transiently trapped inside the snow, which might provide the major component of the lift force, as shown in Figure 6.14. However, for snowboarding on more permeable (fresh) snow in which the porous medium is too porous or for skiing where the dominant pressure relaxation length, the width of the ski W, is too small, the air cannot be efficiently trapped inside the porous medium, and the compressed snow crystals would consequently support much of the load, as shown in Figure 6.19.
4. The F&W analysis focused on the pore-pressure generation underneath a planing surface, but the resultant force and moment analysis were absent. This analysis, however, is critical for examining the overall lift mechanics involved in downhill skiing or snowboarding including control and stability.

Herein, a comprehensive lift mechanics theory for downhill skiing or snowboarding (Wu et al., 2006; Wu and Sun, 2011) is introduced. The theory, treating all of the limitations of the F&W theory listed earlier, combines the lift mechanisms from both the transiently trapped air and the solid phase (ice crystals). The pore air pressure distribution beneath the planing surface is based on a consolidation theory deduced from the F&W theory along with a porous medium stagnation-point flow theory developed by Wu et al. (2005b). The local change of the Darcy permeability due to the compression of the snow layer is obtained from Shimizu's classical empirical relationship, Equation 27. The local resistance force from the solid phase (ice crystals) is based on the static experiments of Wu et al. (2005), as shown in Equation 6.9. A force and moment analysis about the skier or snowboarder was employed to determine the compression ratio of the snow layer at both the leading and trailing edges, which were dependent on the skiing velocity, the friction coefficient between the snow and the bottom surface of the ski or snowboard, the location of the center of mass (CM), and the snow types. This analysis was then used to examine the mechanism for the control and stability in response to the horizontal and vertical shifts in the CM of the individual.

6.7.1 Theoretical Formulation

6.7.1.1 Darcy Permeability of Snow

As described earlier in this chapter, limited success has been made in the creation of theoretical models to predict the permeability of snow. In the study of lift mechanics of downhill skiing or snowboarding (Wu et al., 2006; Wu and Sun, 2011) discussed herein, Shimizu's (1970) empirical expression, Equation 6.27, is applied for characterizing the change of the Darcy permeability of snow as a function of its compression.

When a fresh snow layer of depth, h_0, with nondeformed Darcy permeability, K_0, is compressed by a planar surface, the density, ρ_s, of the snow layer changes due to the motion of the upper boundary. It is assumed that the bottom surface of the ski or snowboard is planar and that there is no lateral tilt or edging; this can be seen in both Figures 6.3 and 6.43. Assuming that the snow layer is uniformly compacted in the vertical direction, whereas in the horizontal plane there is no crystal movement, the deformation-dependent Darcy permeability of snow based on Equation 6.29 simplifies to

$$K = 0.077 \exp\left[\left(1 - \left(\frac{1-1}{k}\right) \cdot \left(\frac{1-x}{L}\right)^{-1}\right) \ln\left(\frac{K_2}{0.077 d^2}\right)\right] d^2, \tag{6.38a}$$

where

L is the length of the ski or snowboard

$k = h_2/h_1$ is the compression ratio

h_2 and h_1 are the local thickness of the snow layer at the leading ($x = L$) and trailing ($x = 0$) edges of the planing surface, respectively

K_2 is the Darcy permeability of the snow underneath the leading edge

$$K_2 = 0.077 \exp\left[\left(\frac{h_0}{h_2}\right) \ln\left(\frac{K_0}{0.077 d^2}\right)\right] d^2 \tag{6.38b}$$

To demonstrate how the Darcy permeability, K, varies with position, x, and the compression ratio, $k = h_2/h_1$, the variation of K from the leading to the trailing edge for different compression ratios, k, is plotted in Figure 6.44. In this figure, the snow layer at the leading edge is assumed to be undeformed, $h_2 = h_0 = 10$ cm (typical value in the snow compaction measurements [Wu et al., 2005a]);

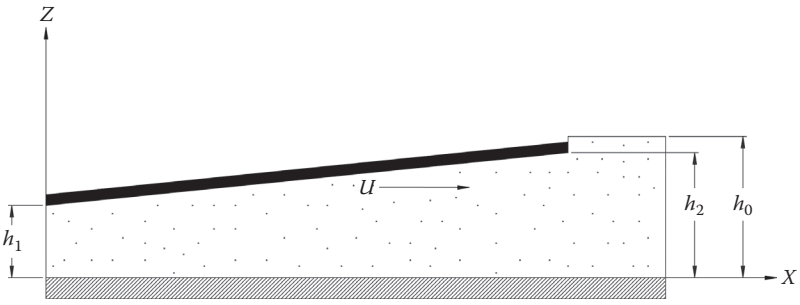

FIGURE 6.43 Schematic illustration of a snowboard or ski compressing a layer of snow powder. (Reprinted from Wu, Q. et al., *Med. Sci. Sports Exerc*., 38, 1132, Copyright 2006, with permission from American College of Sports Medicine.)

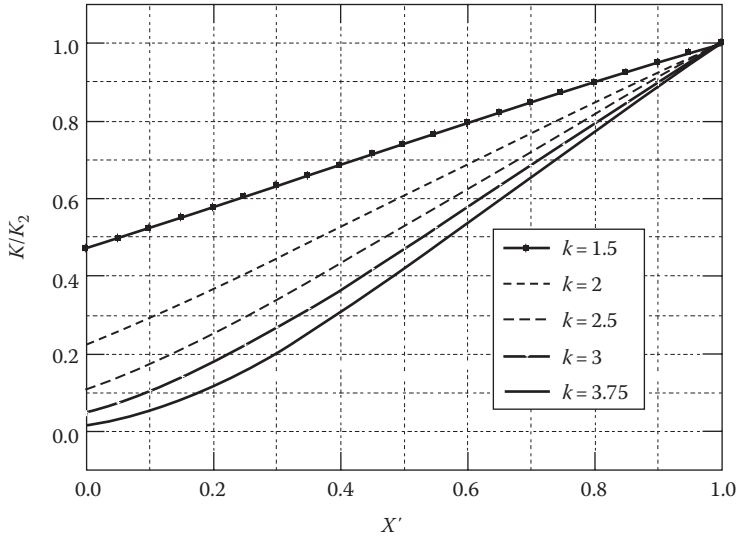

FIGURE 6.44 Spatial variation of K from leading to trailing edge for different compression ratios, k. The snow layer at the leading edge is undeformed, $h_2 = h_0 = 10$ cm; the diameter of the snow crystal, $d = 0.001$ m; and the permeability of the snow beneath the leading edge of the planing surface, $K_2 = K_0 = 1.7 \times 10^{-8}$ m^2. (Reprinted from Wu, Q. et al., *Med. Sci. Sports Exerc*., 38, 1132, Copyright 2006, with permission from American College of Sports Medicine.)

the mean diameter of the ice crystal d is 1.0 mm and the permeability of the snow underneath the leading edge of the planing surface is $K_2 = K_0 = 1.7 \times 10^{-8}$ m^2 (typical value of fresh snow [Wu et al., 2005a]). A monotonic variation of the Darcy permeability K is observed in this figure, due to the compression of the snow. It is expected that a large decrease in K from the leading to trailing edge at the higher values of k will produce a pronounced asymmetry with respect to x in the pressure distribution, as well as an increase in the maximum pressure.

6.7.1.2 Pore Pressure

6.7.1.2.1 Governing Equation

In F&W, a 2-D rigid boundary moving arbitrarily with velocity $\boldsymbol{U} = (U_x, U_y, U_z)$ over a fiber layer was considered, as shown in Figure 6.3. An effective-medium theory based on the Brinkman equation (Equation 6.1) was used to define the flow in the fiber layer. For a large Brinkman parameter, $\alpha = h_2/K^{0.5}$, F&W predicted that a 1-D plug flow in the axial direction develops at all locations,

as shown in Figure 6.5, where a thin fiber boundary layer is observed at the upper and lower surfaces and there is little motion over most of the porous media, with the exception of the motion near boundaries and as one approaches the leading and trailing edges. For a 10 cm thick snow layer, α is in the order of 10^3. It is evident that the x velocity component u satisfies the Darcy law and that the profile approaches a uniform plug flow outside the thin fiber interaction layers adjacent to the bottom of the ski or the ground. Thus,

$$u = -\frac{K}{\mu}\frac{\partial P}{\partial x}. \tag{6.39}$$

Since the length of a ski or snowboard is much larger than its width, the air velocities will be much larger in the transverse y, z plane than in the x direction. This holds true in all locations except at the upper boundary where there is a very thin fiber interaction boundary layer due to the motion of the ski or snowboard. In Figure 6.7, F&W provided a solution for the pressure field beneath a snowboard, which clearly demonstrated parabolic pressure distributions at any axial location, the same as one finds for a classical 2-D stagnation-point flow. This key insight inspired Wu et al. (2005b) to propose that the flow in the transverse plane can be viewed, to a first approximation, as a stagnation-point flow in a porous medium, where the vertical velocity of the moving board is equivalent to the incoming flow in the classical 2-D stagnation-point flow.

In the analysis of Wu et al. (2005b), a new fundamental dimensionless parameter group υ/KA emerges for a stagnation-point flow in a porous medium, where υ is the kinematic viscosity and A is the characteristic velocity gradient imposed by the external flow. In the case of skiing or snowboarding, $A = -U_z(x, y, h)/h$. Here, the vertical velocity of the upper boundary $U_z(x, y, h)$ in the general case is given by

$$U_z(x,y,h) = U_x\frac{\partial h}{\partial x} + U_y\frac{\partial h}{\partial y}, \tag{6.40}$$

where

$h(x, y)$ is the local gap height

U_x, U_y are the velocities of the ski or snowboard in the x, y directions

Thus,

$$A = -\frac{U_z(x,y,h)}{h} = \frac{U_x}{h}\frac{\partial h}{\partial x} + \frac{U_y}{h}\frac{\partial h}{\partial y}. \tag{6.41}$$

In Wu et al. (2005b), the structure of a new type of boundary layer is observed. This boundary layer evolves as υ/KA varies from zero, the classical limit of the Hiemenz (1911) and Homann (1936) solutions, to $\upsilon/KA \gg 1$, the classical Brinkman (1947) limit where inertial effects are negligible. It shows that for the case of skiing or snowboarding, $\upsilon/KA \gg 1$; thus, the viscous boundary layer is vanishingly thin and one is left with an outer flow for the velocity field given by

$$v = -\frac{K}{\mu}\frac{\partial P}{\partial y}, \tag{6.42}$$

$$w = -Az. \tag{6.43}$$

The velocity profile in the y direction is a uniform plug flow that increases linearly with distance y from the centerline ($y = 0$) of a ski or snowboard. In contrast, the downward velocity w decreases linearly with z.

Substituting Equations 6.39, 6.42, and 6.43 into the continuity equation

$$\frac{\partial u}{\partial x}+\frac{\partial v}{\partial y}+\frac{\partial w}{\partial z}=0, \tag{6.44}$$

one obtains

$$\nabla^2 P=-\frac{\mu}{K}A-\frac{1}{K}\nabla P\cdot\nabla K. \tag{6.45}$$

This is the new simplified governing equation for the pore pressure in skiing or snowboarding. The two terms on the right-hand side have a simple interpretation. The first term, proportional to A, is the force due to the angle of attack and the lateral edging of the ski or snowboard, which can be seen in the definition of A in Equation 6.41. The second term arises from the variation in the Darcy permeability due to the compression of the snow. Both the first and the second terms include lateral tilt or edging that is reflected in the partial derivative with respect to y. If both terms vanish, one is left with a potential equation for a Darcy flow without any forcing.

6.7.1.2.2 No Lateral Tilt or Edging Governing Equation

In the case where there is no lateral tilt to the ski or snowboard, both the local thickness of the snow layer and the local Darcy permeability are only functions of x, $h = h(x)$, $K = K(x)$. Knowing $A = (U/h)\,dh/dx$, where $U = U_x$, Equation 6.45 can be simplified to

$$\frac{\partial^2 P}{\partial x^2}+\frac{\partial^2 P}{\partial y^2}=-\frac{\mu A}{K}-\frac{1}{K}\frac{\partial P}{\partial x}\frac{dK}{dx}. \tag{6.46}$$

The analysis performed by F&W and Wu et al. (2005b) shows a parabolic pressure distribution in the y direction, which can be expressed as

$$P(x,y)=\frac{4}{w(x)^2}\left[P_0-P_c(x)\right]y^2+P_c(x), \tag{6.47}$$

where

$P_c(x)$ is the centerline pressure corresponding to the cross section at the location x

P_0 is pressure at the edge of the planing surface, which is extremely close to the atmospheric pressure due to the fact that the porosity of the compressed snow abruptly changes at the lateral edges where the compression ends and the hydrodynamic resistance falls swiftly

$w(x)$ is the local width of the planing surface, as shown in Figure 6.45

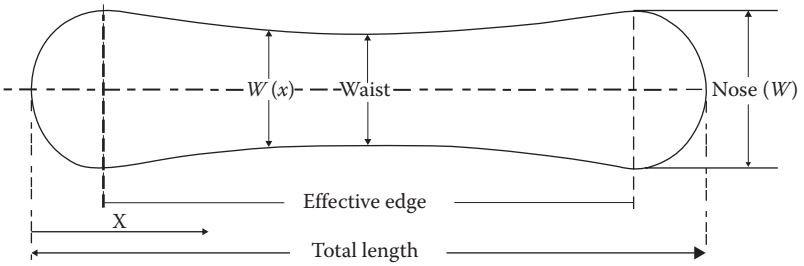

FIGURE 6.45 Geometric snowboard dimensions described using common nomenclature (top view). (Reprinted from Wu, Q. and Sun, Q., *Med. Sci. Sports Exerc.*, 43, 1955, Copyright 2011, with permission from American College of Sports Medicine.)

In comparison to the ideal case where the planing surface is of constant width in the axial direction, shown in Figure 6.3, commercially available skis/snowboards have complex geometries and variable width in order to reduce weight and improve performance while maintaining the strength and rigidity of the planing surface. If the nose width is W, one defines the width factor of a snowboard as $g(x) = w(x)/W$. $f(x)$ characterizes the variation of width from the leading to the trailing edge.

By substituting Equation 6.47 into the generalized governing Equation 6.46 and evaluating it at $y = 0$, the governing equation for the centerline pressure distribution beneath a ski or snowboard can be obtained:

$$\frac{d^2P_c(x)}{dx^2} + \frac{1}{K(x)}\frac{dK(x)}{dx}\frac{dP_c(x)}{dx} - \frac{8}{w(x)^2}\left[P_c(x) - P_0\right] + \frac{\mu A(x)}{K(x)} = 0. \tag{6.48}$$

Introducing dimensionless variables

$$p' = \frac{P - P_0}{P_0}, \quad p_c{}' = \frac{P_c - P_0}{P_0}, \quad x' = \frac{x}{L}, \quad y' = \frac{y}{W/2}, \quad h' = \frac{h}{h_2}, \quad K' = \frac{K}{K_2}, \tag{6.49a,b,c,d,e,f}$$

one obtains a dimensionless equation for $p_c'(x')$:

$$\frac{d^2p_c'(x')}{dx'^2} + \frac{1}{K'(x')}\frac{dK'(x')}{dx'}\frac{dp_c'(x')}{dx'} - \frac{8}{\varepsilon g(x')^2}p_c'(x') + \frac{\theta_L}{K'(x')h'(x')} = 0, \tag{6.50}$$

where

$$\varepsilon = \left(\frac{W}{L}\right)^2, \quad \theta_L = \frac{\mu}{P_0}\left(\frac{U}{h_2}\frac{dh}{dx}\right)\frac{L^2}{K_2}. \tag{6.51}$$

At the leading and trailing edges of the planing surface, the pressure is close to the atmospheric pressure:

$$p_c'(0) = p_c'(1) = 0. \tag{6.52}$$

Equation 6.50, which is subject to the boundary conditions of Equation 6.52, is a nonlinear, two-point boundary-value problem that contains two dimensionless parameters, ε and θ_L. ε denotes the ratio of the square of two characteristic pressure relaxation lengths in the y and x directions. In general, due to the large leakage of air that occurs at the lateral edges, the primary pressure relaxation occurs at these lateral boundaries. One expects a decrease in ε will decrease the pore pressure beneath the planing surface due to the increased lateral air drainage. This is consistent with the predictions in F&W, where for $L/W \gg 1$, the solutions of the generalized Reynolds equation (6.7) for an elongated platform, such as a ski, differ greatly from the solutions of Equation 6.6 in F&W when $L^2/W^2 \gg 1$, since the second term in (6.7) is $O(L^2/W^2)$ larger than the first. θ_L in Equation 6.50 is a combination of two dimensionless parameters, $\mu A\|_{x=L}/P_0$ and L^2/K_2. A is the vertical velocity gradient. For a given tilt angle, either an increase in the forward velocity U or a decrease in the snow layer thickness at the leading edge h_2 will increase the value of A. It is clear that this increase of A will increase the pore pressure since a faster compression generates a higher pore air pressure. The inverse of K is a measure of the resistance that the air encounters as it flows through the porous medium. One expects that as K_2 decreases, the maximum pore pressure will increase since the air will encounter an increased resistance when escaping.

6.7.1.2.3 $\varepsilon \ll 1$ (Ski)

Equation 6.50, subject to the boundary conditions (6.52), can be solved numerically. However, for $\varepsilon \ll 1$, a simple asymptotic solution can be obtained that is a good approximation for skiing. For a ski, $L = 2$ m, $W = 0.1$ m, and $\varepsilon = 2.5 \times 10^{-3}$. Inspection of Equation 6.50 reveals that

$$\frac{d^2 p_c'(x')}{dx'^2} \sim \mathrm{O}(1), \quad \frac{1}{K'(x')}\frac{dK'(x')}{dx'}\frac{dp_c'(x')}{dx'} \sim \mathrm{O}(1), \quad \frac{8}{\varepsilon g(x')} p_c'(x') \sim \mathrm{O}(800). \tag{6.53a,b,c}$$

Equation 6.50 can be rewritten as

$$\varepsilon \frac{d^2 p_c'(x')}{dx'^2} + \varepsilon \frac{1}{K'(x')}\frac{dK'(x')}{dx'}\frac{dp_c'(x')}{dx'} - 8p_c'(x') + \frac{\theta_W}{K'(x')h'(x')} = 0, \tag{6.54}$$

where

$$\theta_W = \left(\frac{\mu A\big|_{x=L}}{P_0}\right) \cdot \left(\frac{W^2}{K_2}\right).$$

In Equation 6.54, the small dimensionless parameter ε multiplies both the highest derivative term $d^2 p_c'(x')/dx'^2$ and the nonlinear term $(1/K'(x'))(dK'(x')/dx')(dp_c'(x')/dx')$. It can be readily solved using a singular perturbation method:

$$\begin{aligned} p_c'(x')_{composite} = {} & \frac{\theta_W}{8K'(x')h'(x')} \\ & - \frac{\theta_W}{8K'h'\big|_{x'=0}} \exp\left(\frac{-\sqrt{\left(\frac{1}{K'(x')}\frac{dK'(x')}{dx'}\right)_{x'=0}^2 + \frac{32}{\varepsilon}} - \left(\frac{1}{K'(x')}\frac{dK'(x')}{dx'}\right)_{x'=0}}{2} x' \right) \\ & - \frac{\theta_W}{8K'h'\big|_{x'=1}} \exp\left(\frac{-\sqrt{\left(\frac{1}{K'(x')}\frac{dK'(x')}{dx'}\right)_{x'=1} + \frac{32}{\varepsilon}} + \left(\frac{1}{K'(x')}\frac{dK'(x')}{dx'}\right)_{x'=1}}{2} (1-x') \right). \end{aligned} \tag{6.55}$$

Once $p_c'(x')$ in Equations 6.50 or 6.55 is determined, the 2-D pressure distributions beneath a snowboard or ski surface can be found by applying Equations 6.47 and 6.49:

$$p'(x',y') = \left(1 - \left(\frac{y'}{g(x')}\right)^2\right) p_c'(x'). \tag{6.56}$$

The average dimensionless pressure generated by the trapped air inside the compressed snow layer is obtained by integrating the pore pressure over the entire surface:

$$P_{ava}' = \iint\limits_{ski\ or\ snowboard} p'(x',y')dx'dy' = \frac{2}{3}\left[\int_0^1 p_c'(x')g(x')dx' \Big/ \int_0^1 g(x')dx'\right]. \tag{6.57}$$

6.7.1.3 Lift Force from Solid Phase

The solid-phase (ice crystals) lifting force is obtained from the quasistatic, drained experiments performed by Wu et al. (2005a), as shown in Equation 6.9 and Figure 6.11. In these static experiments, the loading area of the piston cancels out and Equation 6.9 reduces to

$$\frac{P_{solid}}{P_{\max}} = f\left(\frac{\Delta h}{\Delta h_{\max}}\right). \tag{6.58}$$

As shown in Figure 6.46, the skier descends directly down the fall line and the angle of the inclined slope is α_h. In the case where there is no lateral tilting or edging, the snow is compressed uniformly at any location x, and the local pressure from the ice grains is given by Equation 6.58, where $P_{\max} = P_{mg} = mg \cos \alpha_h/LW$, $\Delta h = h_0 - h(x)$, $\Delta h_{\max} = h_0 - h_{\min}$, and $h_{\min}$ corresponds to the thickness of the snow layer where maximum compression is achieved. P_{mg} is the ice crystal pressure when the pore air pressure vanishes. Note that for snowboarding, m is the mass of the snowboarder with his or her equipment, while for skiing, it is half of this total mass because of two skis. Equation 6.58 can be written as

$$\frac{P_{solid}(x)}{P_{mg}} = f\left(\frac{1-\dfrac{h(x)}{h_0}}{1-\dfrac{h_{\min}}{h_0}}\right). \tag{6.59}$$

The maximum deformation that can be achieved for a given patch of snow corresponds to a density as high as $\rho_{s,\max} = 0.875$ g/cm^3 (Mellor, 1977; Wu et al., 2005a). Thus, the minimum snow porosity $\phi_{\min} = 1 - \rho_{s,\max}/\rho_i = 0.06$, where the ice density $\rho_i = 0.931$ g/cm^3. If the undeformed porosity of the snow layer is ϕ_0, $h_{\min}/h_0 = (1 - \phi_0 + \phi_{\min})/1 = 1.06 - \phi_0$. By defining $p_s'(x') = P_{solid}(x)/P_0$, Equation 6.59 reduces to

$$p_s'(x') = \frac{P_{solid}(x')}{P_0} = \left(\frac{P_{mg}}{P_0}\right) \cdot f\left(0.94\left[\frac{1-\lambda}{k} - \left(\frac{\lambda-\lambda}{k}\right)x'\right] / \left(\phi_0 - 0.06\right)\right), \tag{6.60}$$

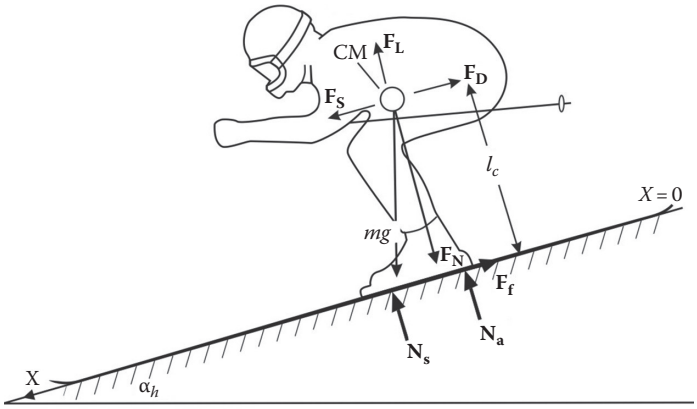

FIGURE 6.46 A skier descends directly down the fall line. The various forces that act upon the skier in this situation are shown. The weight **mg** is resolved into two forces: $\mathbf{F_S}$ parallel to the slope and $\mathbf{F_N}$ normal to the slope. $\mathbf{N_a}$ is the lift force due to the pore air pressure; $\mathbf{N_s}$ is the ice crystals' lift force. $\mathbf{F_f}$ is the snow friction force; $\mathbf{F_D}$ is the wind resistance or aerodynamic drag force that is directed up the slope. An aerodynamic lift force $\mathbf{F_L}$ is also present. All of the forces are shown at the points at which they act. (Reprinted from Wu, Q. et al., *Med. Sci. Sports Exerc.*, 38, 1132, Copyright 2006, with permission from American College of Sports Medicine.)

where $\lambda = h_2/h_0$ and $f(x')$ is the empirical relationship, Equation 6.59. The average pressure generated by the solid phase is then given by

$$P_{avs}{}' = \left(\int_0^L P_{solid}(x) w(x) dx \Big/ \int_0^L w(x) dx \right) / P_0 = \int_0^1 p_s{}'(x') g(x') dx' \Big/ \int_0^1 g(x') dx'. \tag{6.61}$$

6.7.1.4 Force and Moment Balance

For a skier/snowboarder gliding with velocity U (Ux, Uy, Uz) over a snow layer as shown in Figure 6.46, the sudden compaction of the snow leads to the generation of pore air pressure inside the compressed layer, $\mathbf{N_a}$, as well as the solid-phase lifting force from the ice crystals, $\mathbf{N_s}$. The normal component of the weight $\mathbf{mg}$, $\mathbf{F_N}$, is balanced by the summation of $\mathbf{N_a}$ and $\mathbf{N_s}$,

$$mg \cos \alpha_h = N_a + N_s, \tag{6.62}$$

where α_h is the angle of the inclined slope. This can also be written in the form of an average pressure by dividing each term by the board area A_s. If the total dimensionless average pressure arising from both the trapped air and the solid phase is defined as $P'_{av} = ((N_a + N_s)/A_s)/P_0 = P'_{ava} + P'_{avs}$, and the total dimensionless loading pressure exerted by the skier or snowboarder is defined as $P'_{avload} = P_{mg}/P_0$, where $P_{mg} = mg\cos\alpha_h/A_s$, Equation 6.62 reduces to

$$P'_{avload} = P'_{av} = P'_{ava} + P'_{avs}. \tag{6.63}$$

This can also be written as

$$f_{air} + f_{solid} = 1, \tag{6.64}$$

where $f_{air} = P'_{ava}/P'_{avload}$ and $f_{solid} = P'_{avs} + P'_{avload}$.

Similarly, the sum of all torques about the CM must also be zero, as shown in Figure 6.46,

$$N_a(x_{ccr} - x_a) + F_f l_c = N_s(x_s - x_{ccr}), \tag{6.65}$$

where

F_f is the snow friction force $F_f = \eta \cdot Ns$, where η is the coefficient of friction
l_c is the normal distance of the CM from the ski surface
x_{ccr}, x_a, and x_s are the x coordinates of the CM, center of $\mathbf{N_a}$, and center of $\mathbf{N_s}$, respectively

The setup of the coordinate system is shown in Figure 6.3.

The moment balance, Equation 6.65, can be written as

$$f_{air} \cdot x_s{}' + f_{solid} \cdot x_a{}' - f_f \cdot l_c = x'_{ccr}, \tag{6.66}$$

where $x'_{ccr} = x_{ccr}/L$, $x'_a = x_a/L$, $x_s{}' = x_s/L$, $l_c{}' = l_c/L$, and $F_f{}' = F_{ff} mg\cos\alpha_h$.

When a skier glides down a slope at velocity U over an undeformed snow layer of thickness h_0 and a Darcy permeability K_0 without changing his or her location of CM, the tilt angle γ (or the compression ratio from the leading to trailing edge, $k = h_2/h_1$) and the compression ratio at the leading edge, $\lambda = h_2/h_0$, need to be adjusted to satisfy the force and moment balance, Equations 6.64 and 6.66.

6.7.2 Results and Discussion

The lift generation inside a compressible snow layer and its distribution between the trapped air and the ice crystals strongly depend on the geometry of the planing surface, L/W; the speed of the skier or snowboarder, U; the frictional coefficient η; the location of CM (x_{ccr}', l_c); and the properties of snow (K_0, ϕ_0, D). This is reflected in Equation 6.50 where the pore air pressure generated as the planing surface glides over the compressed snow layer depends on two dimensionless parameters, ε and θ_L. Wu et al. (2006) and Wu and Sun (2011) thoroughly examined the lift mechanisms of skiing or snowboarding as a function of these parameters. In the case of snowboarding, the following parameters are used: $L/W = 4.3$ or $\varepsilon = (1/4.3)^2 = 0.054$, a typical value for a 1.16 m long snowboard. In the case of skiing representative values, $L = 1.7$ m, $L/W = 17$, or $\varepsilon = (1/17)^2 = 0.0035$ are used. Two typical snow types, wind-packed and fresh snow, are considered. These two snow types bracket the range of permeability for most skiing conditions and are also the snow conditions for which Wu et al. (2005a) conducted their field experiments to determine the mechanical properties of snow under dynamic compression. The thickness of the fresh undeformed snow layer was assumed to be $h_0 = 10$ cm. The mass of the snowboarder with his or her equipment is 80 kg; the angle of the inclined slope $\alpha_h = 15°$. Unless specifically mentioned otherwise, the location of the skier's CM is assumed as $x_c' = 0.45$ for snowboarding and $x_c' = 0.40$ for skiing, the normal distance of the center of gravity from the ski or snowboard surface $l_c = 80$ cm, the coefficient of sliding friction $\eta = 0.04$, and the velocity of the skier is 20 m/s.

For a given compression ratio, λ, at the leading edge, Figures 6.3 and 6.43, an increase in the tilt angle (increasing k) will lead to the increase in both the lift force from the transiently trapped air and the ice crystals. Since the applied load is fixed, the compression ratio k from the leading to the trailing edge is uniquely determined based on the force balance, using Equation 6.63 or 6.64. The compression ratio, λ, at the leading edge can be adjusted to obtain a series of (λ, k) that satisfy the force balance. Each (λ, k) combination generates a value of $x_c' = f_{solid} \cdot x_s' + f_{air} \cdot x_a' - F_f \cdot l_c'$. When and only when ($x_c' - x_{ccr}'$) vanishes, the moment balance Equation 6.65 or 6.66 is achieved.

6.7.2.1 Rectangular Snowboard or Ski ($g(x) = 1$)

A rectangular board as shown in Figure 6.3 is first discussed.

6.7.2.1.1 Representative Results

Figure 6.47a shows the change of ($x_c' - x_{ccr}'$) as a function of λ for snowboarding at 20 m/s on a wind-packed snow layer of 10 cm thick. It is clear from this figure that multisolutions, corresponding to multiple zero values of ($x_c' - x_{ccr}'$), exist for this problem. In other words, there are several equilibrium positions for a given CM location. This observation reveals the nonlinear nature of the stability and control of skiing and snowboarding. As a skier glides on a snow layer with an initial penetration depth at the leading edge, in order to achieve force and moment balance, he or she has to adjust the snow compression ratios both at the leading and trailing edges to the closest equilibrium location (λ, k) predicted in Figure 6.47a. Shifting from one equilibrium position to another occurs by varying λ. This change is accompanied by a transfer of lift forces from the air to the solid phase or vice versa, as well as a change in the angle of attack of the snowboard. Figure 6.47b shows the contribution of trapped air to the total lift, f_{air}, at different equilibrium positions. From this figure, it can be seen that less compression at the leading edge (larger λ) leads to a higher air lifting force, f_{air}.

It is evident from Figure 6.47b that the lift contribution from the trapped air, f_{air}, ranges from 31.1% to 58.4% for the several possible neutral equilibrium positions predicted in Figure 6.47a. The centerline pore-pressure distributions and the associated solid-phase pressure beneath the surface of the snowboard for typical neutral equilibrium positions, (λ, k) = (0.715, 1.085), (0.685, 1.065). and (0.565, 1.015), are plotted in Figure 6.48. One notices that with more compression at the leading edge, λ decreases, leading to the increase in the solid-phase pressure p_s' and thus decrease in the pore air pressure p'. Since less pore pressure is needed, less tilt angle is required; thus, k decreases.

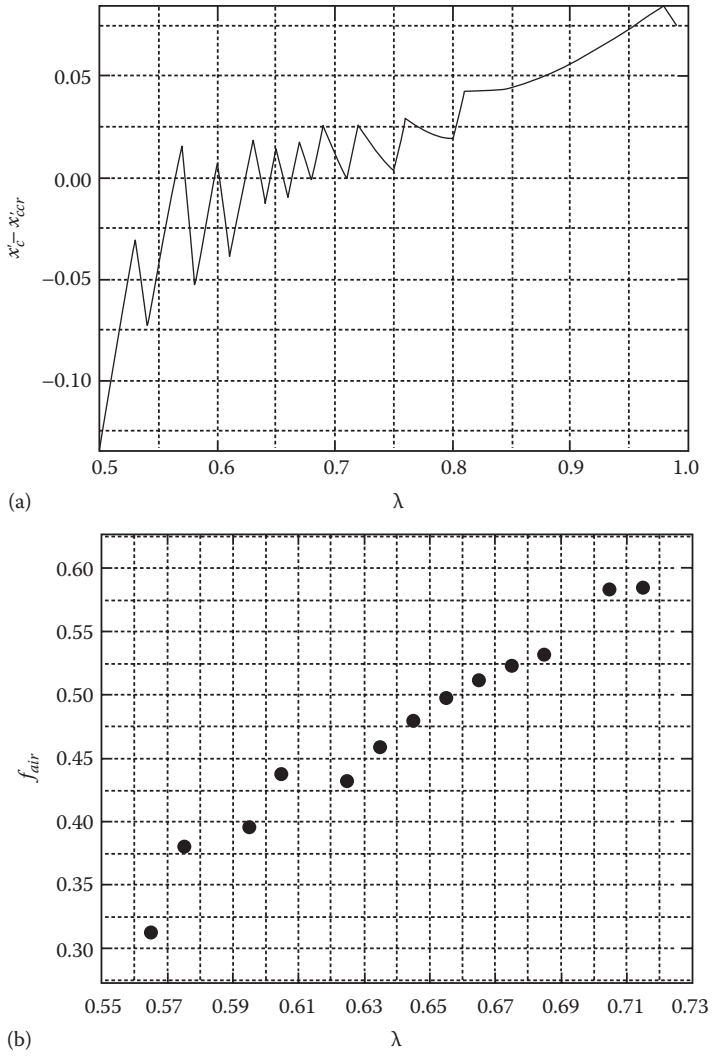

FIGURE 6.47 (a) $x'_c - x'_{ccr}$, is a function of the precompression ratio of snow at the leading edge, λ, for a rectangular snowboard. Note $x'_c - x'_{ccr} = 0$ corresponds to the neutral equilibrium position. (b) The contribution of trapped air to the total lift, f_{air}, at different equilibrium positions predicted in Figure 6.47a. (Reprinted from Wu, Q. and Sun, Q., *Med. Sci. Sports Exerc*., 43, 1955, Copyright 2011, with permission from American College of Sports Medicine.)

Along with this decrease is the shift of peak pore pressure away from the trailing edge toward the middle of the snowboard, and the pore air pressure profile becomes flatter.

6.7.2.1.2 Parametric Study

6.7.2.1.2.1 U = 10, 20, and 30 m/s As one increases his or her velocity, the contact time of the planing surface with the snow layer decreases, and the air which is trapped inside the snow has less time to escape before the pore pressure decays, and thus, a smaller compression to generate the required lift force is needed. This intuition is confirmed in Figure 6.49a where the lift contribution from the trapped air, f_{air}, for several possible neutral equilibrium positions is plotted as one snowboards on a wind-packed snow layer at velocities of 10, 20, and 30 m/s. For U = 10 m/s, f_{air} ranges from 24.4% to 42.8%, $\lambda = h_2/h_0$ ranges from 0.525 to 0.625, $k = h_2/h_1$ ranges from 1.015 to

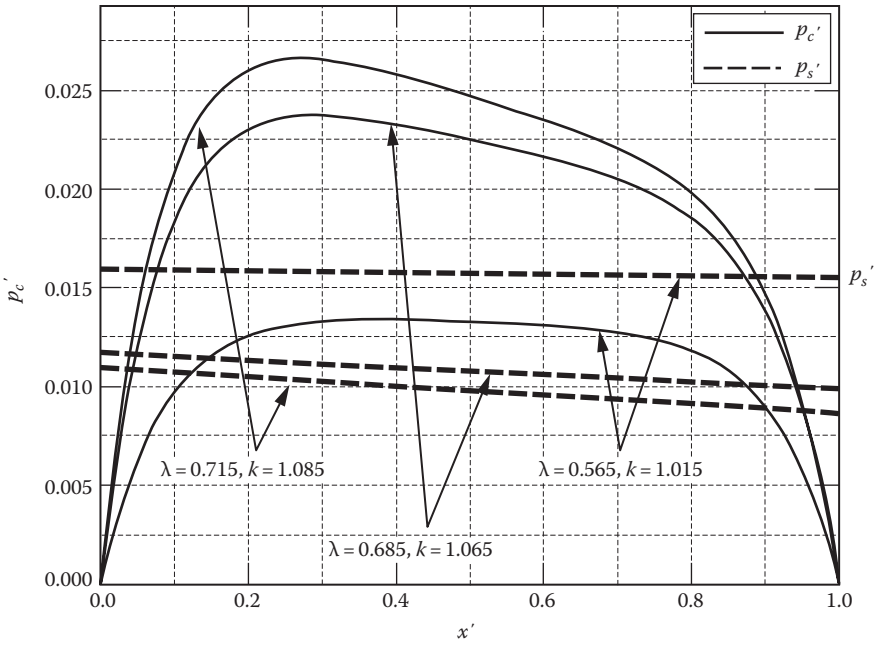

FIGURE 6.48 Dimensionless centerline pore-pressure distribution p' and the associated solid-phase pressure p_s' underneath a rectangular snowboard for different equilibrium positions: (λ, k) = (0.715, 1.085), (0.685, 1.065), and (0.565, 1.015), predicted in Figure 6.47. (Reprinted from Wu, Q. and Sun, Q., *Med. Sci. Sports Exerc*., 43, 1955, Copyright 2011, with permission from American College of Sports Medicine.)

1.065, and $\lambda/k = h_1/h_0$ ranges from 0.517 to 0.587; for U = 20 m/s, f_{air} ranges from 31.1% to 58.4%, $\lambda = h_2/h_0$ ranges from 0.565 to 0.715, $k = h_2/h_1$ ranges from 1.015 to 1.105, and $\lambda/k = h_1/h_0$ ranges from 0.557 to 0.647; and for U = 30 m/s, f_{air} ranges from 38.2% to 68.5%, $\lambda = h_2/h_0$ ranges from 0.585 to 0.775, $k = h_2/h_1$ ranges from 1.015 to 1.095, and $\lambda/k = h_1/h_0$ ranges from 0.576 to 0.708. It is clear that an increase in velocity leads to an increase in the trapped air's contribution to the total lift and a decrease in the compression of the snow layer.

The results presented herein are consistent with the experimental measurements discussed earlier in this chapter (Wu et al., 2005a) for the dynamic compression of wind-packed snow in a porous-walled cylinder–piston apparatus that suggests that for snowboarding on fine-grained less permeable (wind-packed) snow at velocities greater than 10 m/s, the lift forces generated by the trapped air in the compressed snow layer should provide a significant fraction of the total lift.

6.7.2.1.2.2 Friction (U = 20 m/s, η = 0.02, 0.04, and 0.08) Before the development of the lift mechanics of downhill skiing or snowboarding by Wu et al. (2006), most of the literature on ski or snowboard friction was focused on the presence of a micron-thick fluid film that forms beneath the running surface as a melted water lubrication layer (Colbeck and Warren, 1991; Colbeck, 1992, 1994a,b, 1995). Wu et al. (2006), for the first time, investigated the effects of the surface smoothness on the lift generation underneath a ski or snowboard. This study was further extended by Wu and Sun (2011).

Figure 6.49b shows the lift contribution from the trapped air, f_{air}, for various values of friction coefficient, η, as one glides over a 10 cm wind-packed snow layer at a velocity U = 20 m/s. The values of η, 0.02–0.08, are chosen to span a broad range of thermal, bottom snowboard surface and ice crystal conditions (Lind and Sanders, 1996). For η = 0.02, f_{air} ranges from 43.1% to 64.5%, $\lambda = h_2/h_0$

ranges from 0.625 to 0.755, $k = h_2/h_1$ ranges from 1.035 to 1.115, and $\lambda/k = h_1/h_0$ ranges from 0.604 to 0.677; for $\eta = 0.04$, f_{air} ranges from 31.1% to 58.4%, $\lambda = h_2/h_0$ ranges from 0.565 to 0.715, $k = h_2/h_1$ ranges from 1.015 to 1.105, and $\lambda/k = h_1/h_0$ ranges from 0.57 to 0.647; and for $\eta = 0.08$, f_{air} ranges from 32.1% to 47.1%, $\lambda = h_2/h_0$ ranges from 0.525 to 0.615, $k = h_2/h_1$ ranges from 1.010 to 1.035, and $\lambda/k = h_1/h_0$ ranges from 0.520 to 0.590. It is clear from this figure that a decrease in the sliding friction leads to an increase in the trapped air's contribution to the total lift and decrease in the compression ratios at the leading and trailing edges, $\lambda = h_2/h_0$ and $\lambda/k = h_1/h_0$. These results indicate that for downhill skiing and snowboarding, a decrease in the sliding friction not only reduces the snow frictional drag force that the skier encounters as he or she glides down the slope at a given

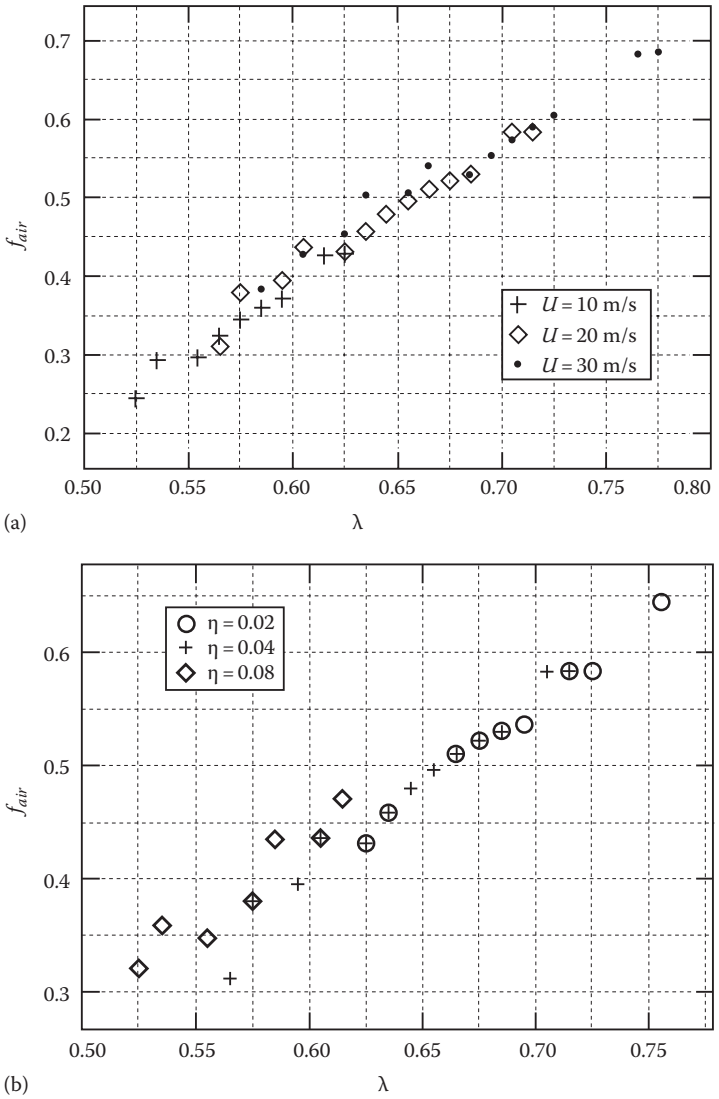

FIGURE 6.49 The lift contribution from the trapped air, f_{air}, for different possible neutral equilibrium positions as one snowboards on a 10 cm, wind-packed snow layer: (a) At velocities of 10, 20, and 30 m/s, $\eta = 0.04$, $x'_{ccr} = 0.45$, and $l_c = 1.0$ m. (b) With different friction coefficient $\eta = 0.02$, 0.04, and 0.08, $U = 20$ m/s, $x'_{ccr} = 0.45$, and $l_c = 1.0$ m. (*Continued*)

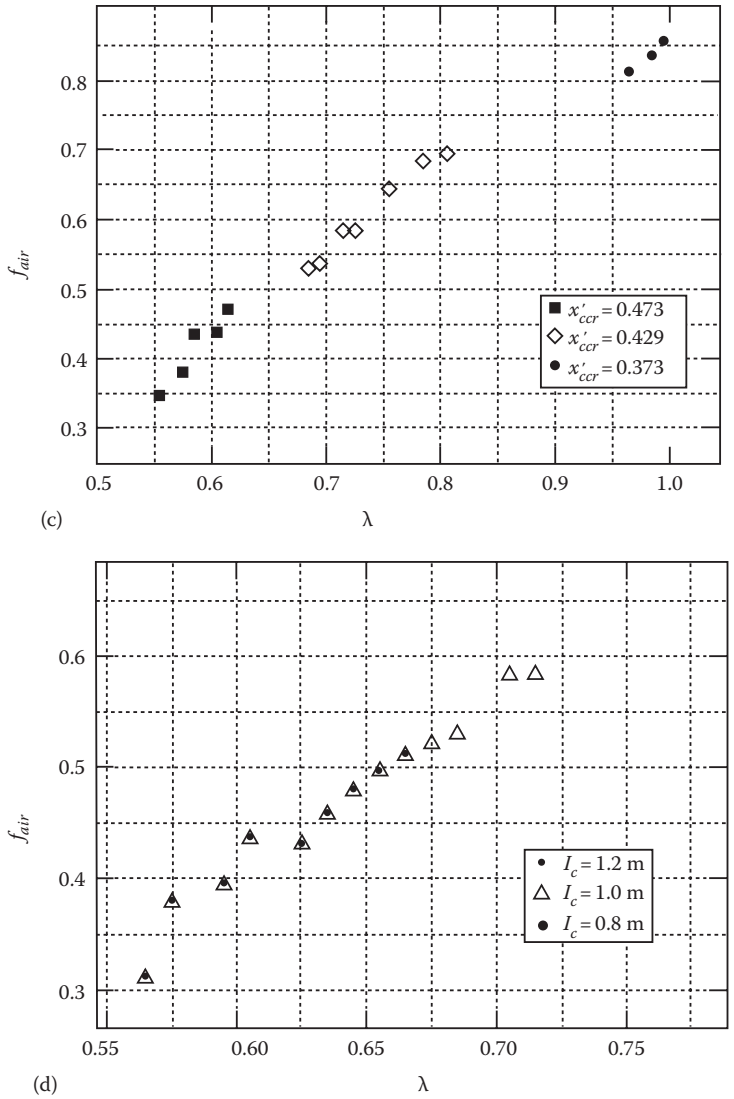

FIGURE 6.49 (*Continued*) The lift contribution from the trapped air, f_{air}, for different possible neutral equilibrium positions as one snowboards on a 10 cm, wind-packed snow layer: (c) With different axial CM locations, x'_{ccr} = 0.373, 0.429, and 0.473; U = 20 m/s; η = 0.04; and l_c = 1.0 m. (d) With different vertical CM locations, l_c = 0.8 m, 1.0 m, and 1.2 m; U = 20 m/s,; η = 0.04; and x'_{ccr} = 0.45. (Reprinted from Wu, Q. and Sun, Q., *Med. Sci. Sports Exerc*., 43, 1955, Copyright 2011, with permission from American College of Sports Medicine.)

speed but also increases the trapped air's contribution to the total lift. It provides a new insight into the role of friction in skiing and snowboarding performance. For a smooth air cushioned glide, a low value of η is desired. This can be obtained by waxing the bottom surface of the snowboard or ski.

6.7.2.1.2.3 Shift of x_c' Critical insights about the stability and control of skiing or snowboarding were obtained by Wu et al. (2006) and Wu and Sun (2011), who showed that a snowboarder can stay in equilibrium positions by altering his or her CM. For snowboarding, this is achieved by shifting their weight from the front to the rear foot. Under most conditions, this shift in x'_{cr} is small and varies between roughly 0.37 and 0.47. However, as shown in Figure 6.49c, it has a dramatic impact on

the distribution of the lifting forces between the air and solid (ice crystal) phases. When one places more of their weight on their rear foot while snowboarding, x_{cr}' decreases and approaches the lower limit of 0.373, whereas when one shifts their weight to the front foot, x_{cr}' increases and approaches the upper limit of 0.473. When $x_{cr}' = 0.473$, f_{air} ranges from 34.6% to 47.1%, $\lambda = h_2/h_0$ ranges from 0.555 to 0.615, $k = h_2/h_1$ ranges from 1.015 to 1.035, and $\lambda/k = h_1/h_0$ ranges from 0.547 to 0.594. The contribution of the trapped air pressure is small, and larger snow compression at the leading and trailing edges is needed to generate enough lift to support the skier. In contrast, when $x_{cr}'= 0.373$, f_{air} ranges from 81.3% to 85.7%, $\lambda = h_2/h_0$ ranges from 0.965 to 0.995, $k = h_2/h_1$ ranges from 1.31 to 1.35, and $\lambda/k = h_1/h_0$ is around 0.737. The contribution of the trapped air pressure is large, and the tilt angle and the snow compression ratio at the leading and trailing edges are smaller.

Figure 6.49c shows the neutral stability condition in which both the force and moment balance equations are satisfied. If one shifts their weight (changes x_{cr}') and does not change their angle of attack, the equilibrium condition is broken. In order to avoid falling and return to a new neutral stability condition, one must adjust the snow compression ratios at both the leading and trailing edges, corresponding to the changes in the λ and λ/k as prescribed in Figure 6.49c.

6.7.2.1.2.4 Shift of l_c The vertical displacement of the CM will also affect the snowboarder's stability. Similar to the shift of x_{cr}' in Figure 6.49c, if one raises or lowers his or her CM vertically through up–turn–down or down–turn–up body motions without changing their compression ratios at the leading and trailing edges, the initial neutral force and moment balance are broken. In order to maintain stability, one has to input a muscular moment or change the compression ratios of the snow layer to get back to a new neutral moment balance position. The latter requires no muscular input and is accompanied by a transfer of lift forces between the trapped air and the solid ice crystals as well as changes of snow compressions at the leading and trailing edges. Figure 6.49d shows the lift contribution from the trapped air, f_{air}, for different values of l_c, $l_c = 0.8$ m, 1.0 m, and 1.2 m, as one glides over a 10 cm wind-packed snow layer at a velocity $U = 20$ m/s. For $l_c = 1.2$ m, f_{air} ranges from 31.2% to 51.1%, $\lambda = h_2/h_0$ ranges from 0.565 to 0.665, $k = h_2/h_1$ ranges from 1.015 to 1.055, and $\lambda/k = h_1/h_0$ ranges from 0.557 to 0.630; for $l_c = 1.0$ m, f_{air} ranges from 31.1% to 58.4%, $\lambda = h_2/h_0$ ranges from 0.565 to 0.715, $k = h_2/h_1$ ranges from 1.015 to 1.085, and $\lambda/k = h_1/h_0$ ranges from 0.557 to 0.659; and for $l_c = 0.8$ m, f_{air} ranges from 31.2% to 64.5%, $\lambda = h_2/h_0$ ranges from 0.565 to 0.755, $k = h_2/h_1$ ranges from 1.015 to 1.115, and $\lambda/k = h_1/h_0$ ranges from 0.557 to 0.677. It is clear that as one vertically lowers his or her CM from $l_c = 1.2$ m to 0.8 m, the potential trapped air's contribution to the total lift increases and the solid-phase lift contribution decreases accordingly. Meanwhile, the required compression at the leading and trailing edges decreases. As shown in Figure 6.49d, for the same precompression at the leading edge, λ, the same lifting force could be obtained from the pore air pressure with different l_c. However, a smaller l_c requires less compression at the trailing edge.

6.7.2.1.2.5 Skiing versus Snowboarding As predicted by F&W, a larger snow compression is necessary for skiing than for snowboarding in order to generate the required lifting forces to support the weight of the skier or snowboarder. This is due to the fact that the width of a ski is 1/3 that of a snowboard, and thus larger pore-pressure relaxation happens at the lateral edges. In Figure 6.50, comparisons are made for the lift contribution from the trapped air, f_{air}, for skiing and snowboarding as one glides over a 10 cm wind-packed snow layer at a velocity $U = 20$ m/s. For snowboarding, $L = 1.16$ m, $W = 0.27$ m, $x_{cr}' = 0.45$, and $l_c = 1$ m, while for skiing, $L = 1.7$ m, $W = 0.1$ m, $x_{cr}' = 0.4$, and $l_c = 0.8$ m. As shown in this figure, multiple equilibrium positions are found in the case of snowboarding, with f_{air} ranging from 31.1% to 58.4%, $\lambda = h_2/h_0$ ranging from 0.565 to 0.715, $k = h_2/h_1$ ranging from 1.015 to 1.105, and $\lambda/k = h_1/h_0$ ranging from 0.57 to 0.647. In contrast, limited equilibrium conditions are found for the case of skiing. For the same precompression ratio at the leading edge, $\lambda = 0.685$, f_{air} is 53% for snowboarding and is 43.4% for skiing, $k = h_2/h_1$ is 1.065 for snowboarding and is 1.285 for skiing, and $\lambda/k = h_1/h_0$ is 0.643 for snowboarding and is 0.533 for skiing. It is clear that for the same required compression at the

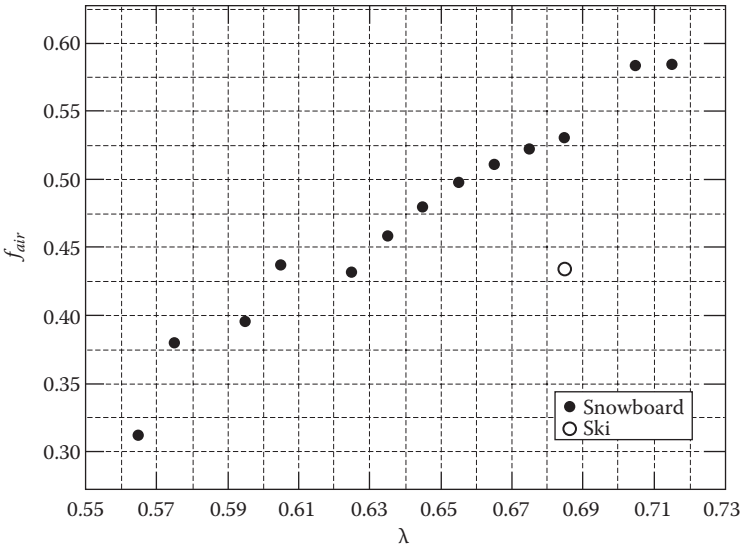

FIGURE 6.50 The lift contribution from the trapped air, f_{air}, for skiing and snowboarding as one glides over a 10 cm wind-packed snow layer at a velocity $U = 20$ m/s. For snowboarding, $L = 1.16$ m, $W = 0.27$ m, $x_{cr}' = 0.45$, and $l_c = 1$ m, while for skiing, $L = 1.7$ m, $W = 0.1$ m, $x_{cr}' = 0.4$, and $l_c = 0.8$ m. (Reprinted from Wu, Q. and Sun, Q., *Med. Sci. Sports Exerc.*, 43, 1955, Copyright 2011, with permission from American College of Sports Medicine.)

leading edge, the tilt angle γ of the planing surface (or the compression ratio from the leading to trailing edge, $k = h_2/h_1$) is much larger in skiing than in snowboarding, and thus, the snow layer at the trailing edge of the ski is more compressed, causing more pore air lift for snowboarding than for skiing. The difference in f_{air} is not great considering the large difference in L/W. This is because the skier's CM is both closer to the trailing edge and to the board and the tilt angle γ needs to be increased to satisfy the moment balance equation. By doing so, the center of pore air pressure shifts toward the trailing edge enhancing the pore-pressure contribution to the total lift and compensates in part for the pressure leakage at the lateral edges.

6.7.2.1.2.6 Less Permeable Wind-Packed Snow versus Highly Permeable Fresh Snow Because the Darcy permeability of fresh snow is roughly 34 times larger than wind-packed snow, air cannot be trapped efficiently in fresh snow. At a given speed, a much larger compression of the fresh snow layer and a larger contribution from the solid phase are needed to generate the required lift. Wu et al. (2006) shows that, for a given speed, the trapped air's contribution to the total lift is much larger in the less permeable wind-packed snow than in the highly permeable fresh snow. The values of h/h_0 at both the leading and trailing edges decrease by roughly a factor of two.

6.7.2.1.3 Real Snowboard or Ski (g(x)≠1)

A commercially available snowboard, **A**, was selected for the study (Wu and Sun, 2011). The characteristic dimensions of the snowboard are as follows: total length = 1.38 m, effective edge length = 1.175 m, nose length = 0.308 m, and waist length = 0.264 m, Figure 6.45. For the same gliding condition, multisolutions are obtained. In other words, there are several equilibrium positions for a given CM location as observed in the previous section for rectangular skis or snowboards. Figure 6.51a shows the contribution of trapped air to the total lift, f_{air}, at different equilibrium positions. It is evident that the lift contribution from the trapped air, f_{air}, ranges from 30% to 60% for the different possible neutral equilibrium positions. It can also be seen that less compression at the leading edge (larger λ) leads to higher air lifting force, f_{air}.

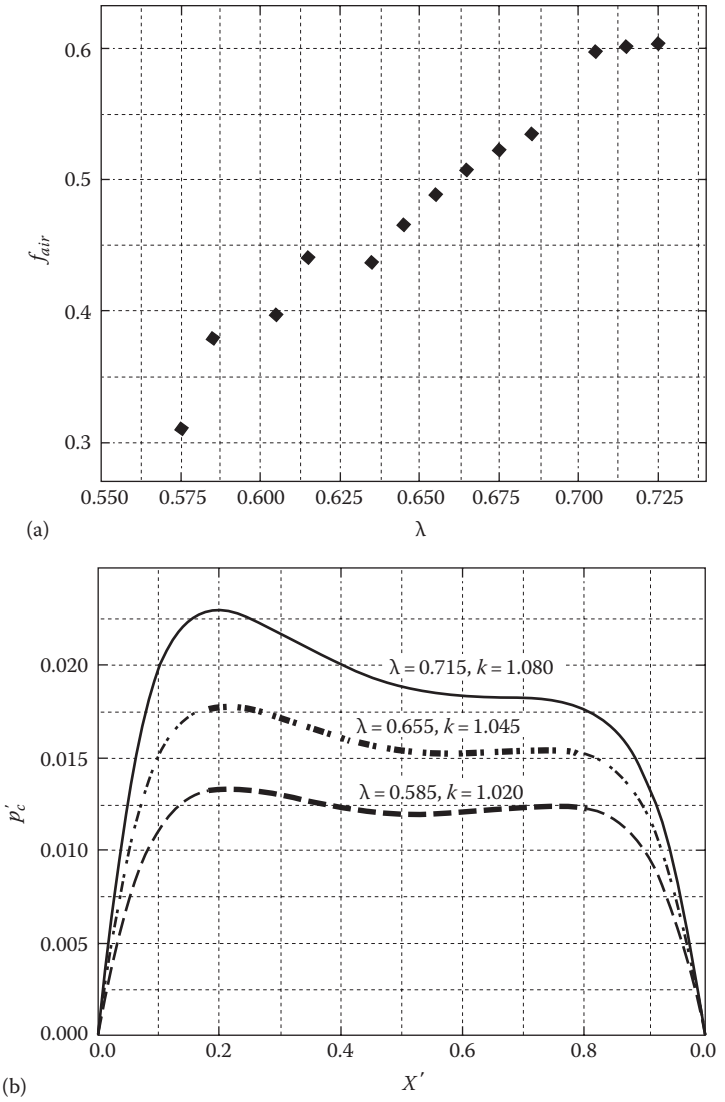

FIGURE 6.51 (a) The contribution of trapped air to the total lift, f_{air}, underneath a commercially available snowboard, **A**, η = 0.04, U = 20 m/s, $x_{ccr}{}'$ = 0.45, and l_c = 1.0 m. (b) Centerline pore-pressure distribution underneath the snowboard, **A**, at three typical neutral equilibrium positions. (Reprinted from Wu, Q. and Sun, Q., *Med. Sci. Sports Exerc*., 43, 1955, Copyright 2011, with permission from American College of Sports Medicine.)

In Figure 6.51b, the centerline pore-pressure distributions beneath the surface of snowboard **A** for typical neutral equilibrium positions are plotted, (λ, k) = (0.585, 1.020), (0.655, 1.045), and (0.715, 1.080). It is observed from this figure that there are two pressure peaks along the length of the snowboard occurring near the nose section where the width of the snowboard is at a maximum. This is in sharp contrast with the results predicted in the previous section for rectangular snowboards where a single pressure peak was observed. This behavior can be attributed to the fact that the increased width of the snowboard at the nose prolongs the outflow of the trapped air in the lateral direction; hence, for the timescale that the snowboard is in contact with the snow, higher pore pressure is generated at these two sections. Based on similar reasoning, a narrower section of the snowboard in the vicinity of the waist section that is near to the center of the snowboard entails

a rapid pressure relaxation and hence a drop in the pore air pressure buildup. Evidently, the pore pressure reaches a maximum near the trailing edge where maximum snow compression occurs. It is also noteworthy that as the compression ratio at the leading edge decreases, the compression ratio from the leading to the trailing edge, k, decreases. In other words, if the snow at the leading edge is compressed enough, very little tilt angle is needed to generate the required lifting forces.

In summary, a new theoretical analysis of the lift forces generated during downhill skiing or snowboarding was developed by Wu and colleagues (Wu et al., 2006; Wu and Sun, 2011). The theory incorporates the lift contribution from both the transiently trapped air and the compressed ice crystals. It is an extension of the classical lubrication theory for highly compressible porous media developed in F&W. The prediction based on this theory agrees with the more qualitative experiments presented earlier in this chapter (Wu et al., 2005a) where the pore pressures generated in snow were measured for the first time using a porous cylinder–piston apparatus.

The significant enhancement in lift generated by a planing surface as it glides over a soft porous medium is a new concept. The application to human skiing or snowboarding was first suggested in F&W. This concept was also applied in the design of a future-generation train that can glide on a soft porous track whose mechanical properties are similar to goose down pillows (Wu et al., 2004). The key insight in the latter application is that lift can be greatly enhanced and drag due to friction in the solid phase can be reduced if the lateral loss of pore pressure at the side walls of the track is eliminated. If this could be achieved, the authors predicted that it would be possible to support a 50 ton train car moving on a porous material with permeability properties that do not differ greatly from fresh snow at velocities greater than approximately 10 m/s. A detailed discussion of this application is introduced in the following section.

6.8 FROM RED BLOOD CELLS TO SNOWBOARDING TO A NEW CONCEPT FOR A TRAIN TRACK

Ever since the motion of red blood cells was first observed in capillaries, biological scientists have wondered how the highly flexible red blood cell can move with so little friction in tightly fitting microvessels. In 1996, Vink and Duling conclusively demonstrated in vivo that our microvessels are lined with a uniform highly compressible EGL. The experiment by Vink and Duling (1996) is shown in Figure 6.1, which indicates that at velocities greater than 20 μm/s, the red blood cells appear to glide above the EGL and there is a narrow intervening fluid gap. At velocities less than 20 μm/s, however, the red blood cells entered the EGL, and when motion was arrested, the red cells crushed the glycocalyx and filled nearly the entire lumen of the capillary (Vink and Duling, 1996). In F&W, a generalized lubrication theory is developed to describe the pressure and lift forces generated during this motion. This theory, which applies to 1-D or 2-D planar lifting surfaces, shows that the principal difference between a red blood cell squeezing through a tightly fitting capillary and a human snowboarding is the substantial loss of pore pressure that occurs due to leakage at the lateral edges of the snowboard. The analysis in F&W shows that the behavior is governed by three dimensionless groups: a dimensionless permeability parameter, $\alpha = h/K^{1/2}$, the tilt angle of the planning surface, and its length-to-width ratio L/W. For $\alpha \gg 1$, the lift forces increase as α^2. The dramatic increase in lift is due to the fact that the fluid is transiently trapped within the soft porous material and cannot escape on the timescale of the motion.

It is well known that sliding friction produced while skiing on snow is greatly reduced by the presence of μm thick fluid films that form beneath the ski due to frictional heating (Colbeck, 1994a,b). This film greatly reduces friction drag in cross-country skiing much like the thin fluid film that exists between the red blood cell membrane and the edge of the EGL when the red blood cell is moving at velocities greater than 20 μm/s. At velocities less than 20 μm/s, the basic mechanism by which the red blood cell is able to reduce its drag once it enters the glycocalyx is described in Weinbaum et al. (2003), where it is shown that the normal force required to compress the core proteins in the glycocalyx is two orders of magnitude smaller than the lift force due to the fluid draining pressure.

Whereas it would be very difficult to measure the excess pore pressure that develops during red blood cell motion, an equivalent experiment can be easily performed for snow. In 2005, Wu and colleagues (Wu et al., 2005a) developed a novel experimental and theoretical approach to examine the pore-pressure generation inside a snow layer during rapid compression as discussed earlier in this chapter. Figure 6.13 shows a representative result for the time-dependent variation of the pore pressure at the location of the central pressure transducer on the underside of the piston after it is released from rest. Natural wind-packed soft snow, with an ambient temperature of −10°C, was used in this experiment. A rapid rise in pore pressure is observed, which is followed by a decay that occurs on a timescale of roughly 0.8 s. The characteristic time to drain the air can be ascertained from a simple drainage model, $t_c = \mu\pi R^2/(8P_cK)$,where $P_c = mg/\pi R^2$. In the current application, it becomes evident that $t_c \approx 1$ s for $K = 5.0 \times 10^{-10}$ m^2 and $m = 5.9$ kg. Since the length of time that a 1.5 m snowboard would be in contact with a given patch of snow is 0.15 s, if it was traveling at 10 m/s, it is clear from the Figure 6.13 that after 0.15 s, the excess pore pressure has only started to relax and much of the weight of the snowboarder would be supported by the air that is still trapped in the partially compressed snow layer.

The behavior just described suggests that it might be possible to support very heavy loads on very soft porous materials, provided the time of passage of the planing surface is small compared to the time that it would take for the confined air or fluid to drain from the porous medium beneath it. The calculations in F&W, Wu et al. (2006), and Wu and Sun (2011) show that the air trapped in snow can easily support the weight of a 70 kg snowboarder when $K_0 < 10^{-8}$ m^2. For a snowboard whose surface area is 0.5 m^2, the pore pressure required is approximately 1/75 of an atmosphere or 1.4 kPa. The tilt angle of the snowboard will depend on its velocity U. The feasibility of supporting a 50 ton high-speed train car, whose planform is 25 m long ($L = 25$ m) and 2 m wide ($W = 2$ m), can be ascertained from the fact that the average excess pore pressure required will be 9.8 kPa, or only seven times that of the snowboard. This is easily within the realm of possibility for a porous material whose permeability is on the order of 10^{-8} m^2 or smaller, provided the loss of pressure through lateral leakage is eliminated. Furthermore, if the deformation of the solid phase is small, that is, $\Delta h/\Delta h_{\max} \ll 1$, the load bearing force of the solid phase will be small and sliding friction will be greatly reduced. For these purposes, a synthetic material with the mechanical properties of goose down was found to be ideal (Wu et al., 2004). The material also possessed the important additional advantage of a small degree of restorative force after compression, whereas snow had no elastic recoil.

In order to measure the dynamic compression properties of goose down, the same porous cylinder apparatus shown in Figure 6.9 was used in Wu et al. (2004) to perform dynamic compression experiments on the goose down. The results were then compared to the theoretical model, Equation 6.22. It is noteworthy that one value of K, 1.6×10^{-8} m^2, provided a best fit for the experimental data as shown in Figure 6.52. The principal difference between the curves in Figures 6.13 and 6.52 is that there is no extended relaxation phase for the goose down since the dimensions of the piston are too small and the value of K too large for the excess pore pressure to support most of the piston weight. The maximum pore pressure is only 400 Pa, about half of what is required. However, if $t_c = \mu\pi R^2/(8P_cK)$, the diameter of the piston were 25 m (the length of a train car), and the time to travel this distance were 3 s (velocity only 8.3 m/s), the maximum pore pressure would increase to 50 kPa. These scaling arguments predict that a planform with a length of 25 m and a width of 2 m would have a maximum possible lift of approximately 250 metric tons for K of order 10^{-8} m^2.

Figure 6.53 shows a schematic of the proposed lift enhancing goose down–filled train track reported in Wu et al. (2004). The top surface on which the planform glides is a highly flexible porous sheet through which the pore pressure in the porous medium is transmitted. To prevent lateral leakage of pressure, the sidewalls of the track are made of an impermeable membrane that is supported by an outer set of rigid sidewalls. As a result, the only significant leakage of pressure occurs at the front and back ends of the planform where the pressure is that of the ambient air. At low speeds, the train relies upon its wheels as the primary means of locomotion because its velocity is not sufficient for its weight to be supported by the trapped air in the long, slender, rectangular

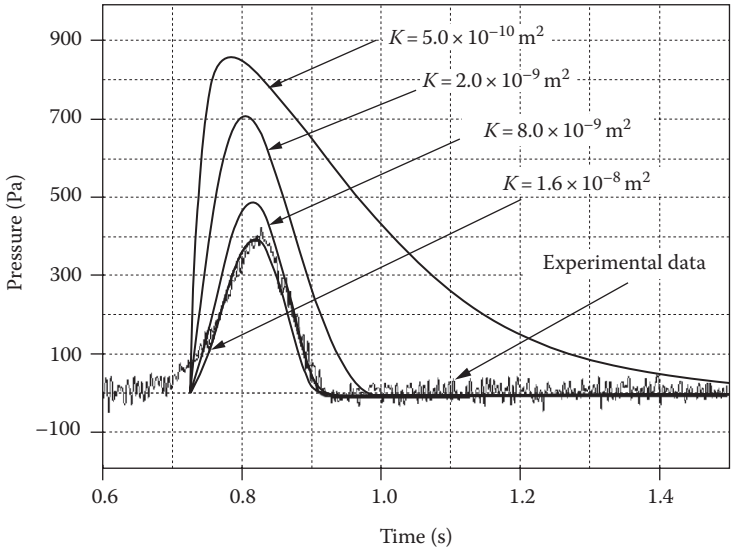

FIGURE 6.52 Time-dependent pressure at the center of the piston and its comparison with the predictions of Equation 6.22 during dynamic compression experiments with goose down, $m = 6.4$ kg, $h_0 = 12.77$ cm, $\Delta h_{max}/h_0 = 0.35$, and $P_{max} = 400$ Pa. (Reprinted from Wu, Q., Andreopoulos, Y., and Weinbaum, S., *Phys. Rev. Lett.,* 93, 2004. Copyright 2004, with permission from American Physical Society.)

goose down pillow beneath it. Once its velocity has increased to a value sufficient to support its weight, however, its wheels are raised.

The performance of the enhanced lift, 50 ton train car is plotted in Figure 6.54, where the track height h_2 at the leading edge is 10 cm. These theoretical predictions are based on the solution of the generalized Reynolds equation (6.6), which, in the large α limit, reduces to

$$\frac{d}{dx}\left(-\frac{1}{\alpha^2}\frac{dp}{dx}h\right) = \frac{dh}{dx}, \tag{6.67}$$

where $p = P/(\mu LU/h_2^2)$. For each U, the compression ratio $k = h_2/h_1$ of the leading to trailing edge heights is determined so that the weight of the train car is supported. It should be noted that even for this coarser goose down where $K = 1.6 \times 10^{-8}$ m^2, h_2/h_1 will be less than 1.4 and the slope = tan β < 0.001 if the car velocity is >10 m/s. Moreover, the performance curves are highly nonlinear, and at

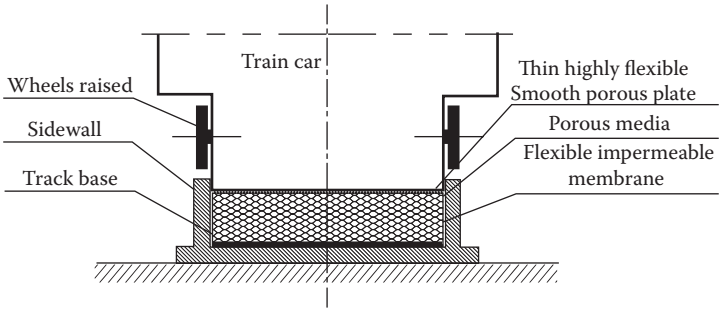

FIGURE 6.53 Sketch of the new train model in the transverse plane (not to scale). (Reprinted from Wu, Q., Andreopoulos, Y., and Weinbaum, S., *Phys. Rev. Lett.,* 93, 2004. Copyright 2004, with permission from American Physical Society.)

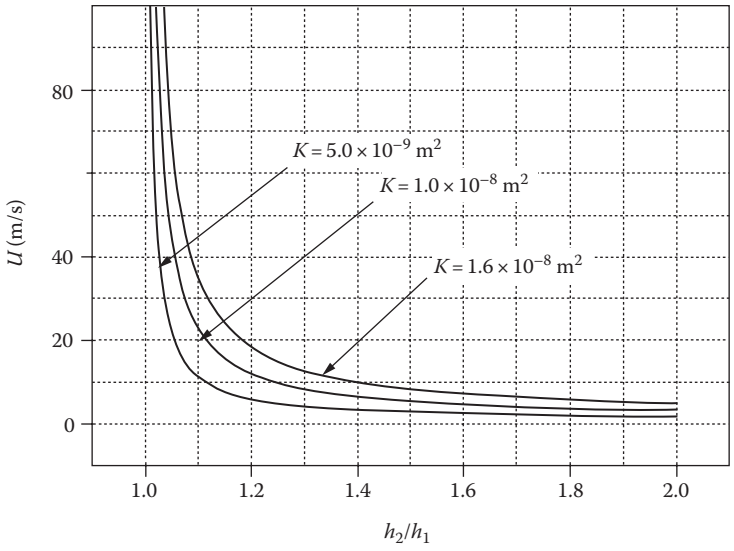

FIGURE 6.54 The velocity U required to support a train car of 50 metric tons gliding on a porous track as a function of h_2/h_1 for various K. Note that for $U > 35$ m/s, $h_2/h_1 < 1.1$, $L = 25$ m, $W = 2$ m, and $h_2 = 0.10$ m. (Reprinted from Wu, Q., Andreopoulos, Y., and Weinbaum, S., *Phys. Rev. Lett.,* 93, 2004. Copyright 2004, with permission from American Physical Society.)

high speeds in excess of 35 m/s, there is a less than 10% compression of the track at the trailing edge. For such small compressions, static compression experiments with the goose down indicate that the lift force generated by the solid phase will be <2% of the lift force due to the pore pressure.

The force diagram in Figure 6.55 provides an overview of the global force balance on the moving train car. In this figure, U is the velocity of the train car; N_a and N_s are the normal forces due to air and goose down, respectively; T is the force due to solid sliding friction where $T = \eta \cdot N_s$ and η is the sliding friction coefficient; and D is the aerodynamic drag where $D = C_D A\rho U^2/2$ and the mass of the train is W/g. Using this model, it is estimated that for $U = 50$ m/s and $\eta = 0.15$, the force due to sliding friction will be about 1/5 of the aerodynamic drag on a streamlined train car, and the pore-pressure lift force will be more than 300 times greater than the sliding friction force, which comparatively is 50 times the total drag. This total drag includes T, D, and the planform drag $(N_a + N_s)\sin\beta$, which is due to the very small tilt angle β of the planing surface. It should be noted that $N_s \sin\beta$ is negligible and $N_a \sin\beta$ is only 8% of T. Sliding friction can never approach rolling friction where the friction coefficient is only 0.001. The objective of this new train track, however, is simply to reduce sliding friction to a level where it is small compared to other drag forces. With proper design, the new train

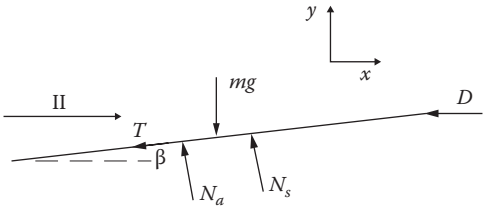

FIGURE 6.55 Forces on train car. Here, U is its velocity; N_a and N_s are the normal forces due to air and goose down, respectively; T is the force due to solid sliding friction; and D is the aerodynamic drag. (Reprinted from Wu, Q., Andreopoulos, Y., and Weinbaum, S., *Phys. Rev. Lett*., 93, 2004. Copyright 2004, with permission from American Physical Society.)

car should be able to negotiate turns with remarkable ease and little sidewall friction. Both sides of the car planform could be arched inward (concave) to turn in either direction on a curved track of adequate turning radius, unless the planform is able to deform in its own plane. Sidewall friction can be nearly entirely eliminated by having retractable horizontal wheels in the sidewalls near the front and back edges of the planform. These wheels will resist the appreciable centripetal forces that will occur during high-speed turns where the track must be banked accordingly.

In a later study by Mirbod et al. (2009), the idea of the next-generation high-speed train track as shown in Figure 6.53 was extended to an airborne jet train that would be suspended several centimeters above the ground by a soft porous track. The design was intended to supersede current forms of transportation such as Maglev trains and commercial aircraft by only needing engines with 10,000 lbf of thrust to reach a cruising speed of up to 700 km/h. By operating within the fastest tier of commercial travel, the prosed AJT would offer a less expensive alternative to both Maglev trains, whose price is derived from the high cost of track operation, and commercial air travel, whose larger engines require more fuel.

Originally learned as a lesson from the microcirculation, the concept of lift generation in a highly compressible porous medium was applied to the human skiing and the design of a futuristic train track for their novelty. The enhanced lifted phenomenon is also observed in other biomechanical applications. For example, much like the low frictional conditions a red blood cell or skier experiences, evolution designed joints in mammals to function with minimal friction. Articular cartilage, soft tissue connected together to form a porous structure, lubricates joints using the hydrodynamic pressure of the interstitial synovial fluid that is generated as the porous cartilage is under compression (McCutchen, 1959, 1962). Ateshian and Wang (1995) theoretically predicted that a loaded migrating surface could be supported indefinitely by interstitial synovial fluid, and thus the sliding friction is decreased tremendously. This theory was experimentally examined by Krishnan et al. (2005), who, after performing cyclical, dynamic loading tests on cartilage, found that the pressurization of the interstitial fluid subsided over time and that the friction coefficients increased as a result. Recently, Caligaris and Ateshian (2008) demonstrated experimentally that the speed of the migrating contact area needed to exceed the diffuse velocity of the interstitial fluid in order to keep high pore pressure and low friction coefficient. These studies show results consistent with the dynamic compression of soft porous media discussed in this chapter. The current study, thus, could provide critical insights for the biomechanics study of soft tissue as well as the design of artificial knees.

Another example of the application of deformable soft porous media is squeeze damping. Common problems in rotor dynamics include steady-state synchronous vibrations and subsynchronous rotor instability (Zeidan et al., 1996). Squeeze film dampers have been used to alleviate high vibrations and rotational instability in rotating shafts by creating a cushion when two boundaries come together and squeeze the fluid. Current technology involves applying viscous fluids between the rotating component and the stationary housing to create damping. The drawback of regular squeeze fluid dampers, however, is their ineffectiveness in generating enough damping. The need for porous medium bearings to employ the lift generation concept becomes apparent for its superior performance. It was theoretically predicted that porous squeeze film dampers could significantly reduce vibrations and instability by enhanced fluid damping force generated in the porous layer (Zhang et al., 1992; Lin, 1996; Lin et al., 2001). In addition, since porous film squeeze dampers are less sensitive to sudden imbalances in the system, for example, blade loss in a turbine, they help to improve the dynamic response of the rotor-support system and lessen the potential damage to an engine or aircraft. Finally, since no reservoir or pump is required to continually replenish the fluid once a porous bearing is assembled and filled with the operating fluid, the requirement for maintenance is minimal.

The comprehensive experimental and theoretical study presented in this chapter laid the foundation for understanding the dynamic response of soft porous media to rapid deformation and its broad applications.

REFERENCES

Adamson, R. H. and G. Clough. 1992. Plasma proteins modify the endothelial cell glycocalyx of frog mesenteric microvessels. *Journal of Physiology (London)* 445: 473–486.

Akaydin, H. D., Pierides, A., Weinbaum, S., and Y. Andreopoulos. 2011. Permeability of soft porous media under one-dimensional compaction. *Chemical Engineering Science* 66(1): 1–14.

Albert, M., Shultz, E., and F. Perron. 2000. Snow and firn permeability at Siple Dome, Antarctica. *Annals of Glaciology* 31: 353–356.

Al-Chidiac, M., Andreopoulos, Y., and S. Weinbaum. 2009. Dynamic compaction of soft compressible porous materials: Experiments and air-solid phase interaction. *Journal of Porous Media* 12(11): 1019–1035.

Arons, E. M. and S. C. Colbeck. 1995. Geometry of heat and mass transfer in dry snow: A review of theory and experiment. *Reviews of Geophysics* 33: 463–492.

Ateshain, G. and H. Wang. 1995. A theoretical solution for the frictionless rolling contact of cylindrical biphasic articular cartilage layers. *Journal of Biomechanics* 28(11): 1341–1355.

Auer, A. H. and D. L. Veal. 1970. The dimensions of ice crystals in natural clouds. *Atmospheric Sciences* 27: 919–926.

Bader, H., Haefeli, R., Bucher, E. et al. 1939. "Der Schnee und seine Metamorphose." 1954. "Snow and its metamorphism." *SIPRE Translation, US Army Corps of Engineers, Snow Ice and Permafrost Research Establishment* 14: 313.

Barabadi, B., Nathan, R., Jen, K., and Q. Wu. 2009. On the characterization of lifting forces during the rapid compaction of deformable porous media. *Journal of Heat Transfer* 131: 101006.

Bear, J. 1972. *Dynamics of Fluids in Porous Media.* New York: Elsevier.

Biot, M. A. 1941. General theory of three-dimensional consolidation. *Journal of Applied Physics* 12: 155–164.

Biot, M. A. and D. G. Willis. 1957. The elastic coefficients of the theory of consolidation. *Journal of Applied Mechanics* 24: 594–601.

Brands, J., van Teeffelen, J. W., van den Berg, B., and H. Vink. 2007. Role for glycocalyx perturbation in atherosclerosis development and associated microvascular dysfunction. *Future Lipidology* 2: 527–534.

Brinkman, H. C. 1947. A calculation of the viscous force exerted by a flowing fluid in a dense swarm of particles. *Applied Science Research A* 1: 27–34.

Bruegger, D., Jacob, M., Rehm, M. et al. 2005. Atrial natriuretic peptide induces shedding of endothelial glycocalyx in coronary vascular bed of guinea pig hearts. *American Journal of Physiology: Heart and Circulatory Physiology* 289: H1993–H1999.

Caligaris, M. and G. Ateshian. 2008. Effects of sustained interstitial fluid pressurization under migrating contact area, and boundary lubrication by synovial fluid, on cartilage friction. *Osteoarthritis Cartilage* 16(10): 1220–1227.

Colbeck, S. C. 1992. Review of the processes that control snow friction. U.S. Army Cold Regions Research and Engineering Laboratory, Monograph April, 40.

Colbeck, S. C. 1994a. A review of the friction of snow skis. *Journal of Sports Sciences* 12: 285.

Colbeck, S. C. 1994b. Bottom temperatures of skating ski on snow. *Medicine and Science in Sports and Exercise* 26: 258–262.

Colbeck, S. C. 1995. Electrical charging of skis gliding on snow. *Medicine and Science in Sports and Exercise* 27: 136–141.

Colbeck, S. C. and G. C. Warren. 1991. The thermal response of downhill skis. *Journal of Glaciology* 37: 228–235.

Constantinescu, A. A., Spaan, J. A. E., Arkenbout, E. K., Vink, H., and J. W. G. E. VanTeeffelen. 2011. Degradation of the endothelial glycocalyx is associated with chylomicron leakage in mouse cremaster muscle microcirculation. *Thrombosis and Haemostasis* 105: 3.

Constantinescu, A. A., Vink, H., and J. A. E. Spaan. 2003. Endothelial cell glycocalyx modulates immobilization of leukocytes at the endothelial surface. *Atherosclerosis, Thrombosis, and Vascular Biology* 23: 1541–1547.

Crawford, R., Nathan, R., Jen, K.P., and Q. Wu. 2011a. Dynamic compression of soft porous media: From finite to infinite domain. *Journal of Porous Media* 14: 51–64.

Crawford, R., Jones, G. F., You, L., and Q. Wu. 2011b. Compression-dependent permeability measurement for random soft porous media and its implications to lift generation. *Chemical Engineering Science* 66: 294–302.

Crawford, R., Nathan, R., Wang, L., and Q. Wu. 2012. Experimental study on the lift generation inside a random synthetic porous layer under rapid compaction. *Experimental Thermal and Fluid Science* 36: 205–216.

Curry, F. E. and R. H. Adamson. 2012. Endothelial glycocalyx: Permeability barrier and mechanosensor. *Annals of Biomedical Engineering* 40(4): 828–839.

Damiano, E. R. and T. M. Stace. 2002. A mechano-electrochemical model of radial deformation of the capillary glycocalyx. *Biophysical Journal* 82: 1670–1690.

Damiano, E. R. and T. M. Stace. 2005. Flow and deformation of the capillary glycocalyx in the wake of a leukocyte. *Physics of Fluids* 17: 031509–031517.

Davies, P. F. 2009. Hemodynamic shear stress and the endothelium in cardiovascular pathophysiology. *Nature Clinical Practice: Cardiovascular Medicine* 6(1): 16–26.

Fassnacht, S. R., Innes, J., Kouwem, N., and E. D. Soulis. 1999. The specific surface area of fresh dendritic snow crystals. *56th Eastern Snow Conference Fredericton*, Edmundston, New Brunswick, Canada.

Feng, J. and S. Weinbaum. 2000. Lubrication theory in highly compressible porous media: the mechanics of skiing, from red cells to humans. *Journal of Fluid Mechanics* 422: 282–317.

Florian, J. A., Kosky, J. R., Ainslie, K. et al. 2003. Heparan sulfate proteoglycan is a mechanosensor on endothelial cells. *Circulation Research* 93: E136–E142.

Fu, B. M., Chen, B, and Chen, W. 2003. An electrodiffusion model for effects of surface glycocalyx layer on microvessel permeability. *American Journal of Physiology: Heart and Circulatory Physiology* 284: H1240–H1245.

Fu, B. M., Han, Y., Weinbaum, S., Spaan, J. A. E., and H. Vink. 2006. Large-deformation analysis of the elastic recoil of fiber layers in a Brinkman medium with application to the endothelial glycocalyx. *Journal of Fluid Mechanics* 554: 217–235.

Fu, B. M. and Tarbell, J. M. 2013. Mechano-sensing and transduction by endothelial surface glycocalyx: Composition, structure, and function. *Wiley Interdisciplinary Reviews: Systems Biology and Medicine* 5(3): 381–390.

Gao, L. and H. H. Lipowsky. 2010. Composition of the endothelial glycocalyx and its relation to its thickness and diffusion of small solutes. *Microvascular Research* 80: 394–401.

Henry, C. B. and B. R. Duling. 1999. Permeation of the luminal capillary glycocalyx is determined by hyaluronan. *American Journal of Physiology* 277: 508–514.

Henry, C. B. and B. R. Duling. 2000. TNF-alpha increases entry of macromolecules. *American Journal of Physiology: Heart and Circulatory Physiology* 279: H2815–H2823.

Hiemenz, K. 1911. Die grenzschicht an einem in den gleichformigen fluessigkeitsstrom eingetauchten geraden kreiszylinder. *Dinglers Polytechnisches Journal* 326: 321.

Homann, F. 1952. The effect of high viscosity on the flow around a cylinder and around a sphere. *NACA TM* 1334.

Hu, X. and S. Weinbaum. 1999. A new view of Starling's hypothesis at the microstructural level. *Microvascular Research* 58: 281–304.

Huxley, V. H. and D. A. Williams. 2000. Role of a glycocalyx on coronary arteriole permeability to proteins: Evidence from enzyme treatments. *American Journal of Physiology* 278(4): H1177–1185.

Johnson, J. B. 1982. On the application of Biot's theory to acoustic wave propagation in snow. *Cold Regions Science Technology* 6: 49–60.

Johnson, J. B. 1991. Simple model of shock-wave attenuation in snow. *Journal of Glaciology* 37: 303–312.

Jordan, R., Hardy, J., Perron Jr., F., and D. Fisk. 1999. Air permeability and capillary rise as measures of the pore structure of snow: an experimental and theoretical study. *Hydrological Process* 13(12): 1733–1753.

Kelly, R., Ruane-O'Hora, T., Noble, M. I., Drake-Holland, A. J., and Snow, H. M. 2006. Differential inhibition by hyperglycaemia of shear stress- but not acetylcholine-mediated dilatation in the iliac artery of the anaesthetized pig. *Journal of Physiology* 573: 133–145.

Krishnam, R., Mariner, E., and G. Ateshian. 2005. Effect of dynamic loading on the frictional response of bovine articular cartilage. *Journal of Biomechanics* 38: 1665–1673.

Lin, J., Lu, R., and C. Yang. 2001. Derivation of porous squeeze-film Reynolds equations using Brinkman model and its application. *Journal of Physics D: Applied Physics* 34: 3217–3223.

Lin, R. 1996. Squeeze film behavior in a hemispherical porous bearing using the Brinkman model. *Tribology Transactions* 39: 769–778.

Lind, D. and S. P. Sanders. 1996. *The Physics of Skiing—Skiing at The Triple Point*. New York: Woodbury.

Lipowsky, H. H., Gao, L., and A. Lescanic. 2011. Shedding of the endothelial glycocalyx in arterioles, capillaries, and venules and its effect on capillary hemodynamics during inflammation. *American Journal of Physiology: Heart and Circulatory Physiology* 301: H2235–H2245.

Long, D. S., Smith, M. L., Pries, A. R., Ley, K., and E. R. Damiano. 2004. Microviscometry reveals reduced blood viscosity and altered shear rate and shear stress profiles in microvessels after hemodilution. *Proceedings of the National Academic Science USA* 101: 10060–10065.

Lopez-Quintero, S. V., Amaya, R., Pahakis, M., and J. M. Tarbell. 2009. The endothelial glycocalyx mediates shear-induced changes in hydraulic conductivity. *American Journal of Physiology and Heart Circulatory Physiology* 296: H1451–H1456.

Luft, J. 1966. Fine structure of capillary and endocapillary layer as revealed by ruthenium red. *Federation Process* 2: 1773–1783.

Lynch, C. T. 1974. *Handbook of Material Science*, Volume III: Nonmetallic Materials and Applications. Boca Raton, FL: CRC Press Inc.

McCutchen, C. 1959. Mechanism of animal joints: sponge-hydrostatic and weeping bearings. *Nature* 184: 1284–1285.

McCutchen, C. 1962. The frictional properties of animal joints. *Wear* 5: 1–17.

Mei, C. C. and L. Auriault. 1991. The effect of weak inertia on flow through a porous medium. *Journal of Fluid Mechanics* 222: 647–663.

Mellor, M. 1964. Properties of snow. USA Cold Regions Research and Engineering Laboratory Monograph III-A1.

Mellor, M. 1977. Engineering properties of snow. *Journal of Glaciology* 19: 15–66.

Michel, C. C. 1997. Starling: The formulation of his hypothesis of microvascular fluid exchange and its significance after 100 years. *Experimental Physiology* 82: 1–30.

Mirbod, P., Andreopoulos, Y., and S. Weinbaum. 2009. Application of soft porous materials to a high-speed train track. *Journal of Porous Media* 12(11): 1037–1052.

Mirbod, P., Andreopoulos, Y., and S. Weinbaum. 2009a. On the generation of lift forces in random soft porous media. *Journal of Fluid Mechanics* 619: 147–166.

Mochizuki, S., Vink, H., Hiramatsu, O. et al. 2003. Role of hyaluronic acid in shear induced endothelium derived nitric oxide release. *American Journal of Physiology* 285: H722–H726.

Nieuwdorp, M., Holleman, F., Groot, E. de et al. 2007. Perturbation of hyaluronan metabolism predisposes patients with type 1 diabetes mellitus to atherosclerosis. *Diabetologia* 50: 1288–1293.

Nieuwdorp, M., van Haeften, T., Gouverneur, M., and H. Mooij. 2006. Loss of endothelial glycocalyx during acute hyperglycemia coincides with endothelial dysfunction and coagulation activation in vivo. *Diabetes* 55: 480–486.

Nogai, T. and M. Ihara. 1978. Study on air permeability of fiber assemblies oriented unidirectionally. *Journal of Textile Machinery Society of Japan* 31(12): T166–T170.

Ono, A. 1970. Growth mode of ice crystals in natural clouds. *Journal of Atmospheric Sciences* 27: 649–658.

Pahakis, M. Y., Kosky, J. R., Dull, R. O., and J. M. Tarbell. 2007. The role of endothelial glycocalyx components in mechanotransduction of fluid shear stress. *Biochemical and Biophysical Research Communications* 355(1): 228–233.

Pascovici, M., Cicone, T., and V. Marian. 2009. Squeeze process under impact, in highly compressible porous layers, imbibed with liquids. *Tribology International* 42: 1433–1438.

Perla, R. and B. Glenne. 1981. Skiing. In *Handbook of Snow*. Toronto, Ontario, Canada: Pergamon.

Pries, A. R., Secomb, T. W., Jacobs, H., Sperandio, M., Osterloh, K., and P. Gaehtgens. 1997. Microvascular blood flow resistance: Role of endothelial surface layer. *American Journal of Physiology: Heart and Circulatory Physiology* 273: H2272–H2279.

Reitsma, S., Egbrink, M. G. A., Vink, H. et al. 2011. Endothelial glycocalyx structure in the intact carotid artery: A two-photon laser scanning microscopy study. *Journal of Vascular Research* 48: 297–306.

Sangani, A. and A. Acrivos. 1982. Slow flow past periodic arrays of cylinders with application to heat transfer. *International Journal of Multiphase Flow* 8: 343–360.

Secomb, T. W., Hsu, R., and A. R. Pries. 1998. A model for red blood cell motion in glycocalyx-lined capillaries. *American Journal of Physiology* 274: H1016–H1022.

Secomb, T. W., Hsu, R., and A. R. Pries. 2001. Motion of red blood cells in a capillary with an endothelial surface layer: effect of flow velocity. *American Journal of Physiology* 281: H629–H636.

Shapiro, L. H., Johnson, J. B., Sturm, M., and G. L. Blaisdell. 1977. Snow mechanics review of state of knowledge and applications. *USA Cold Regions Research and Engineering Laboratory, Hanover, NH, Research Report* 97-3.

Shimizu, H. 1970. Air permeability of deposited snow. *The Institute of Low Temperature Science* 22: 1–32.

Shoop, S. and R. Alger. 1998. Snow deformation beneath a vertically loaded plate formation of pressure bulb with limited lateral displacement. In *Proceedings of the Intonation Conference on Cold Regions Engineering*. Duluth, MN.

Singh, A., Satchell, S. C., Neal, C. R., McKenzie, E. A., Tooke, J. E., and P. W. Mathieson. 2007. Glomerular endothelial glycocalyx constitutes a barrier to protein permeability. *Journal of American Society of Nephrology* 18(11): 2885–2893.

Skotheim, J. M. and L. Mahadevan. 2005. Soft lubrication: the elastohydrodynamics of nonconforming and conforming contacts. *Physics of Fluids* 17: 092101-1–09191-23.

Smith, M. L., Long, D. S., Daminao, E. R., and K. Ley. 2003. Near-wall Micro-PIV reveals a hydrodynamically relevant endothelial surface layer in venules *in vivo*. *Biophysical Journal* 85: 637–645.

Squire, J. M., Chew, M., Nneji, G., Neal, C., Barry, J., and C. Michel. 2001. Quasi-periodic substructure in the microvessel endothelial glycocalyx: A possible explanation for molecular filtering? *Journal of Structural Biology* 136(3): 239–255.

Starling, E. H. 1896. On the absorption of fluids from the convective tissue spaces. *Journal of Physiology* 19: 312–326.

Terzaghi, K. 1943. *Theoretical Soil Mechanics*. New York: Wiley.

Thi, M. M., Tarbell, J. M., Weinbaum, S., and D. C. Spray. 2004. The role of the glycocalyx in reorganization of the actin cytoskeleton under fluid shear stress: A "bumper-car" model." *Proceedings of National Academy of Sciences* 101(47): 16483–16485.

van den Berg, B. and H. Vink. 2006. Glycocalyx perturbation: cause or consequence of damage to the vasculature? *American Journal of Physiology: Heart and Circulatory Physiology* 290: H2174–H2175.

van den Berg, B. M., Vink, H., and J. A. E. Spaan. 2003. The endothelial glycocalyx protects against myocardial edema. *Circulation Research* 92: 592–594.

Vink, H. and B. R. Duling. 1996. Identification of distinct luminal domains for macromolecules, erythrocytes, and leukocytes within mammalian capillaries. *Circulation Research* 79(3): 581–589.

Wang, W. and K. Parker. 1995. The effect of deformable porous surface layers on the motion of a sphere in a narrow cylindrical tube. *Journal of Fluid Mechanics* 283: 287–305.

Weinbaum, S., Tarvell, J. M., and E. R. Damiano. 2007. The structure and function of the endothelial glycocalyx layer. *Annual Review of Biomedical Engineering* 9: 121–167.

Weinbaum, S., Zhang, X., Han, Y., Vink, H., and S. C. Cowin. 2003. Mechanotransduction and flow across the endothelial glycocalyx. *Proceedings of National Academy of Sciences* 100(13): 7988–7995.

Wu, Q., Andreopoulos, Y., and S. Weinbaum. 2004. From red cells to snowboarding: A new concept for a train track. *Physical Review Letters* 93: 194–501.

Wu, Q., Andreopoulos, Y., Xanthos, S., and S. Weinbaum. 2005a. Dynamic compression of highly compressible porous media with application to snow compaction. *Journal of Fluid Mechanics* 542: 281–304.

Wu, Q., Igci, Y., Andrepoulos, Y., and S. Weinbaum. 2006. Lift mechanics of downhill skiing and snowboarding. *Medicine and Science in Sports and Exercises* 38(6): 1132–1146.

Wu, Q., Nathan, R., and R. Crawford. 2014a. Theoretical study on the dynamic compression of soft porous media: From finite to infinite domain. *Journal of Fluid Mechanics* (in review).

Wu, Q., Santhanam, S., Nathan, R., and T. Gacka. 2014b. How to model the lift generation in a highly compressible porous media? *Journal of Fluid Mechanics* (in review).

Wu, Q. and Q. Sun. 2011. A comprehensive skiing mechanics theory with implications to snowboard optimization. *Medicine and Science in Sports and Exercise* 43(10): 1955–1963.

Wu, Q., Weinbaum, S. and Y. Andrepoulos. 2005b. Stagnation point flow in a porous medium. *Chemical Engineering Sciences* 123–134.

Yen, W. Y., Cai, B., Zeng, M., Tarbell, J. M., and B. M. Fu. 2012. Quantification of the endothelial surface glycocalyx on rat and mouse blood vessels. *Microvascular Research* 83: 337–346.

Zeidan, F., San Andres, L., and J. Vance. 1996. Design and application of squeeze film dampers in rotating machinery. *Proceedings of the Twenty-Fifth Turbomachinery Symposium*, Houston, TX, pp. 169–188.

Zhang, S., Yan, L., and Q. Li. 1992. Development of porous squeeze film damper bearings for improving the blade loss dynamics of rotor-support systems. *Journal of Vibration and Acoustics* 114: 347–353.

Section II

Transport in Porous Media

7 Theoretical Analysis of Transport in Porous Media

Multi-Equation and Hybrid Models for a Generic Transport Problem with Nonlinear Source Terms

Yohan Davit and Michel Quintard

CONTENTS

7.1 Introduction 247
7.2 Pore-Scale Equations 249
7.2.1 Momentum and Scalar Transport 249
7.2.2 Nondimensionalization 250
7.2.3 Operator Notation 251
7.3 Volume Averaging Methodology 252
7.3.1 Definitions and Theorems 252
7.3.2 Upscaling Algorithm 254
7.3.3 Resolution Algorithm 255
7.4 Macroscale and Hybrid Models 255
7.4.1 Two-Equation Models 256
7.4.1.1 Two-Equation Transient 256
7.4.1.2 Two-Equation Quasi-Stationary 257
7.4.1.3 Two-Equation Quasi-Stationary with Fluxes 257
7.4.1.4 Two-Equation Variant 259
7.4.1.5 Telegrapher's Equation 259
7.4.1.6 Link with Multirate Approaches 259
7.4.2 One-Equation Models 259
7.4.3 Hybrid Models 260
7.4.4 Domains of Validity 262
7.4.4.1 LE versus LNE 262
7.4.4.2 Hybrid Model 262
7.4.4.3 Conservative Forms and Variations of Effective Parameters 262
7.5 Derivation of the Two-Equation Models 263
7.5.1 Averaging 263
7.5.2 Perturbation 265
7.5.3 Approximations 266
7.5.3.1 Spatial Frequency Approximation 266
7.5.3.2 Amplitude Approximation 268
7.5.3.3 Simplified Form 268

7.5.4 Closure 268
7.5.4.1 Two-Equation Transient Closure 268
7.5.4.2 Two-Equation Quasi-Stationary Closure 269
7.5.4.3 Transient Closure Problems 270
7.5.4.4 Stationary Closure Problems 273
7.5.5 Macroscale Models 274
7.5.5.1 Two-Equation Fully Transient 274
7.5.5.2 Two-Equation Quasi-Stationary 278
7.5.5.3 Two-Equation Quasi-Stationary with Fluxes 279
7.5.5.4 Two-Equation Variants 283
7.6 Derivation of the One-Equation LE Model 283
7.6.1 Approximations 283
7.6.2 Closure 284
7.6.2.1 LE Quasi-Stationary Closure 284
7.6.2.2 Closure Problems 284
7.6.3 Macroscale Model 285
7.7 Derivation of the One-Equation Nonequilibrium Models 286
7.7.1 Averaging 286
7.7.2 Perturbation 287
7.7.3 Approximations 287
7.7.3.1 Spatial Frequency Approximation 287
7.7.3.2 Amplitude Approximation 288
7.7.3.3 Approximate Form 288
7.7.4 Closure 289
7.7.4.1 Closure Problems 289
7.7.5 Macroscale Model 291
7.8 Derivation of the Hybrid Models 293
7.8.1 Averaging 293
7.8.2 Perturbations 293
7.8.3 Approximations 293
7.8.3.1 Spatial Frequency Approximation 293
7.8.3.2 Amplitude Approximation 293
7.8.3.3 Hybrid Approximations 294
7.8.3.4 Quasi-Stationarity 294
7.8.3.5 Approximate Form 294
7.8.4 Closure 294
7.8.5 Hybrid Model 295
7.9 Computation of Effective Parameters in Realistic Media 296
7.9.1 Distribution Coefficient ξ 296
7.9.2 Closure Problems and Numerical Methods 296
7.9.3 Challenges Associated with X-Ray Tomography Images 299
7.9.4 Results for the Cubic-Centered Unit Cell 300
7.9.5 Results for the X-Ray Tomography Unit Cell 301
7.10 Example Problems 301
7.10.1 Effect of Constant Source Terms in a Stratified Medium 301
7.10.1.1 Effective Parameters 302
7.10.1.2 Zero-Dimensional Case with Heterogeneous Sources, $R_0' = 0$ 303
7.10.1.3 One-Dimensional Case with Homogeneous Sources, $\Omega_0' = 0$ 306
7.10.2 Model Selection and Domains of Validity 307
7.11 Discussion and Conclusion 313
References 315

7.1 INTRODUCTION

Many challenges we face today in porous media sciences relate to a crucial need to better describe transport phenomena in heterogeneous multiscale systems. A typical multiscale problem is illustrated in Figure 7.1a, where the pore-scale properties, such as the indicator field describing the phase geometry, vary *rapidly* with the spatial coordinates relative to the length scale of the macroscopic domain. This can be interpreted as

$$\ell \ll L. \tag{7.1}$$

This inequality (7.1) implies a significant numerical and physical complexity. The numerical complexity arises from the necessity to compute coupled processes occurring over a broad spectrum of spatial and temporal scales. The physical complexity follows from the scale dependence of the partial differential equations that are used to describe transport phenomena. For example, Stokes equations at the pore-scale transition to Darcy's law at the macroscale. Another example is solute advection and diffusion at the pore-scale, which yield dispersion effects at a coarser scale. During solute biodegradation in soils, a stochastic reaction rate at the molecular level may be described via a Monod reaction rate at the cellular scale (due to metabolic limitations), which may become a Monod reaction rate at the biofilm scale (but with different parameters encompassing diffusion limitations), which in turn may be described by a first-order reaction rate at the Darcy scale (e.g., due to low solute concentration). This cascade of reaction rates illustrates the complexity of the problem and is schematized in Figure 7.2.

A common approach to tackling these theoretical and numerical issues is to determine a scale of interest and adopt a macroscopic or effective viewpoint in which high-frequency fluctuations have been filtered out (see Figure 7.1b). Early examples of such ideas include Maxwell's work on the conductivity of dilute suspensions [1] and Einstein's analysis of the viscosity of a dilute suspension of neutrally buoyant hard spheres [2]. One of the first fundamental analyses related to porous media was devised in the 1950s by Taylor and Aris in [3,4]. It was concerned with solute transport in a tube (Poiseuille flow) and deriving an asymptotic equation that would describe the transport of the average cross-section concentration. Taylor and Aris showed that this average satisfies a 1D advection–dispersion equation and that the dispersion coefficient is proportional to the square of the

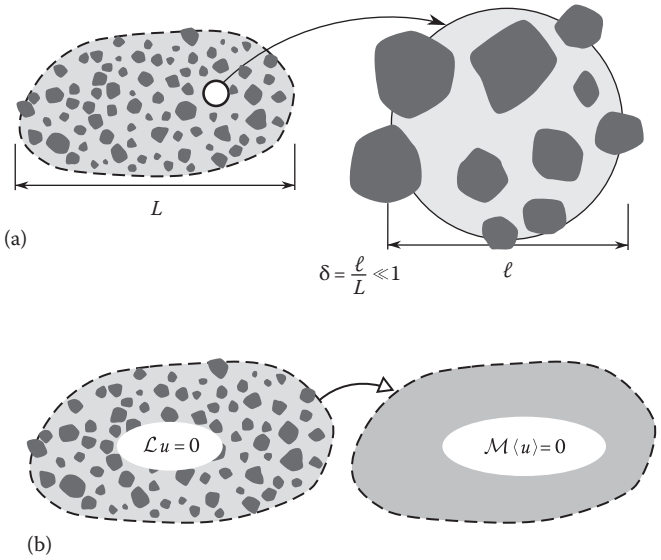

FIGURE 7.1 Schematic illustration of (a) a hierarchy of scales in a porous medium; and (b) the homogenization procedure where the micro-scale differential operator, $\mathcal{L}$, applying to u, is transformed into a macro-scale operator, $\mathcal{M}$, applying to the average value $\langle u \rangle$.

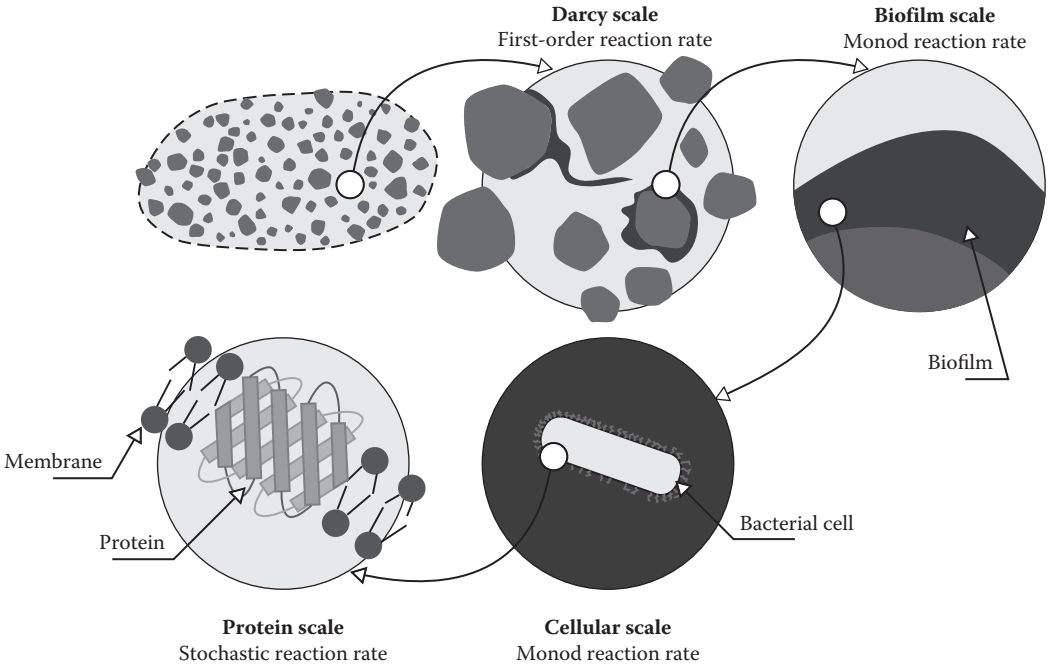

FIGURE 7.2 Multiscale system with microbial biodegradation illustrating the scaledependence of the reaction rate.

Péclet number. This result is valid only in the long-time limit, the relevant timescale being the time for a molecule of solute to travel across the tube by molecular diffusion. Therefore, this analysis is particularly useful when the diameter of the tube is much smaller than the total length. More generally, effective viewpoints require a notion of separation of scales, such as the inequality (7.1) (see [5] or [6] for a broader historical perspective).

Nowadays, effective theories and upscaling techniques have a wide spectrum of applications in Earth, biological, and engineered systems, for example, for describing flow in aquifers [7], petroleum reservoirs [8], composite materials [9], biological tissues [10], networks of large-scale bodies such as buildings [11], reservoirs with large faults [12], reactive transport in the subsurface [13], transport in the brain microvascular network [14], optimal design [15], or shape optimization [16]. In many of these applications, problems involving two or more phases, sources, and sinks are ubiquitous.

In the remainder of this work, we will focus on a prototypical transport problem, as described in Section 7.2, and develop a variety of macroscale representations. This contribution proposes a synthetic presentation of previous upscaling results scattered in different papers, with additional ingredients, in particular a second-order closure and the treatment of nonlinear homogeneous (bulk) and heterogeneous (surface) sources. As such, it is an extension of a previous handbook chapter [17] on the subject.

This chapter is organized as follows. In Section 7.2, we set up the microscale problem. In Section 7.3, we detail the method of volume averaging with closure that will be used for the homogenization of partial differential equations. We then present the macroscale models in Section 7.4. The mathematical developments that yield these macroscale models are derived in Section 7.5 for two-equation models, in Section 7.6 for the one-equation local equilibrium (LE) model, in Section 7.7 for one-equation nonequilibrium models, and in Section 7.8 for the hybrid models. In Section 7.9, we show how effective parameters can be calculated directly by using a 3D reconstruction of a bead packing obtained via x-ray computed microtomography. In Section 7.10, we give several example applications of our models, with a focus on two-equation models. Finally, in Section 7.11, we conclude and discuss example open problems in the field.

7.2 PORE-SCALE EQUATIONS

Here, we present the microscale equations that are used to describe momentum and scalar transport in saturated porous media with homogeneous and heterogeneous nonlinear sources and sinks. The porous medium consists of a solid porous structure, phase σ, fully saturated by a fluid, phase β (see Figure 7.3).

7.2.1 Momentum and Scalar Transport

In many situations, the relaxation of the flow problem is much faster than the relaxation of the transport problem. Therefore, we consider a steady mass and momentum conservation in the fluid phase that can be written as

$$\nabla \cdot \mathbf{v}_\beta = 0 \text{ in } \mathcal{V}_\beta, \tag{7.2a}$$

$$\mathbf{v}_\beta = 0 \text{ on } \mathcal{A}_{\beta\sigma}, \tag{7.2b}$$

$$\rho_\beta \mathbf{v}_\beta \cdot \nabla \mathbf{v}_\beta = -\nabla p_\beta + \rho_\beta \mathbf{g} + \mu_\beta \nabla^2 \mathbf{v}_\beta \text{ in } \mathcal{V}_\beta, \tag{7.2c}$$

for a Newtonian flow, with constant density (i.e., not depending on pressure, temperature, and concentration).

We further consider the following transient scalar transport problem:

$$a_\beta \rho_\beta \left[\partial_t u_\beta + \nabla \cdot \left(\mathbf{v}_\beta u_\beta \right) \right] = \nabla \cdot \left(\mathbf{A}_\beta \cdot \nabla u_\beta \right) + R_\beta \left(u_\beta \right) \text{ in } \mathcal{V}_\beta, \tag{7.3a}$$

$$\text{BC1} \quad u_\beta - u_\sigma = 0 \text{ on } \mathcal{A}_{\beta\sigma}, \tag{7.3b}$$

$$\text{BC2} \quad -\mathbf{n}_{\beta\sigma} \cdot \left(\mathbf{A}_\beta \cdot \nabla u_\beta - \mathbf{A}_\sigma \cdot \nabla u_\sigma \right) = \Omega \left(u_\sigma \right) \text{ on } \mathcal{A}_{\beta\sigma}, \tag{7.3c}$$

$$\text{BC3} \quad \text{Domain boundary conditions}, \tag{7.3d}$$

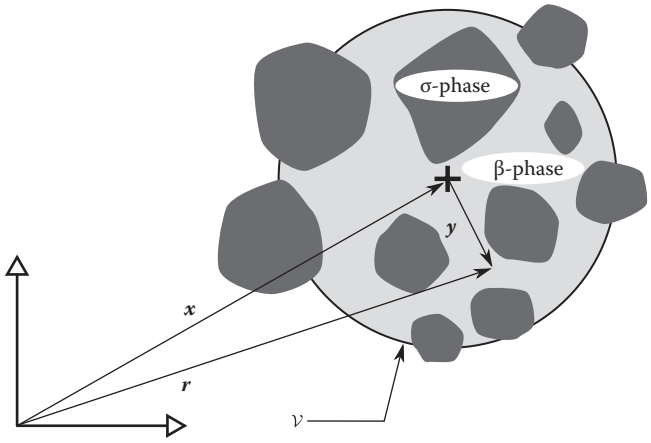

FIGURE 7.3 Averaging volume and the corresponding notations.

$$\text{IC} \quad u_\beta\left(t=0\right)=u_\sigma\left(t=0\right)=0, \tag{7.3e}$$

$$a_\sigma\rho_\sigma\partial_t u_\sigma=\nabla\cdot\left(\mathbf{A}_\sigma\cdot\nabla u_\sigma\right)+R_\sigma\left(u_\sigma\right)\ \text{in}\ \mathcal{V}_\sigma, \tag{7.3f}$$

where

ρ_α [kg · m^{-3}] is the constant mass density of phase α
$\mathbf{n}_{\beta\sigma}$ is the unit vector normal to $\mathcal{A}_{\beta\sigma}$ pointing from β to σ
BC3 is a set of unspecified domain boundary conditions

For upscaling, we usually assume that effective parameters and closure variables do not depend on these boundaries, so that BC3 can be left unspecified. We have also introduced homogeneous R_α and heterogeneous Ω sources/sinks.

This problem may describe heat transport in porous media (see, e.g., [18]) where $u \equiv$ T [K] is the temperature, $\mathbf{A} \equiv k\mathbf{I}$ [W · m^{-1} · K^{-1}] the thermal conductivity, and $a \equiv c_p$ [J · K^{-1} · m^{-3}] the specific heat capacity (assumed to be constant in the following developments). Another example problem is the diffusion of a solute in multiphase or multiregion systems. Mass conservation yields a similar type of problem where $u \equiv \omega$ is the mass fraction, $\mathbf{A} \equiv \rho\mathbf{D}$ [kg · m^{-3} · m^2 · s^{-1}] is the diffusion tensor times the mass density, and a_β, $a_\sigma = 1$. Homogeneous and heterogeneous sources, $R_\beta(u_\beta)$ and $\Omega(u_\sigma)$, may be the consequence of various processes, including chemical or biochemical reactions, radioactive decay, or microwave heating.

7.2.2 Nondimensionalization

Using the characteristic microscale length, ℓ, for spatial nondimensionalization, this system of equations reads

$$\nabla'\cdot\mathbf{v}'_\beta=0\ \text{in}\ \mathcal{V}_\beta, \tag{7.4a}$$

$$\mathbf{v}'_\beta=0\ \text{on}\ \mathcal{A}_{\beta\sigma}, \tag{7.4b}$$

$$\mathrm{Re}_\beta^\ell\mathbf{v}'_\beta\cdot\nabla'\mathbf{v}'_\beta=-\nabla p'_\beta+\nabla^2\mathbf{v}'_\beta\ \text{in}\ \mathcal{V}_\beta, \tag{7.4c}$$

for momentum and total mass conservation. The scalar transport problem reads

$$\partial_{t'}u'_\beta+\nabla'\cdot\left(\mathrm{Pe}_\beta^\ell\mathbf{v}'_\beta u'_\beta\right)=\nabla'\cdot\left(\mathbf{A}'_\beta\cdot\nabla u'_\beta\right)+R'_\beta\left(u'_\beta\right)\ \text{in}\ \mathcal{V}_\beta, \tag{7.5a}$$

$$\text{BC1} \quad u'_\beta-u'_\sigma=0\ \text{on}\ \mathcal{A}_{\beta\sigma}, \tag{7.5b}$$

$$\text{BC2} \quad -\mathbf{n}_{\beta\sigma}\cdot\left(\mathbf{A}'_\beta\cdot\nabla' u'_\beta-\Gamma_A\mathbf{A}'_\sigma\cdot\nabla' u'_\sigma\right)=\Omega'(u'_\sigma)\ \text{on}\ \mathcal{A}_{\beta\sigma} \tag{7.5c}$$

$$\text{BC3} \quad \text{Domain boundary conditions}, \tag{7.5d}$$

$$\text{IC} \quad u'_\beta\left(t'=0\right)=u'_\sigma\left(t'=0\right)=0, \tag{7.5e}$$

$$\Gamma_a\partial_{t'}u'_\sigma=\nabla'\cdot\left(\Gamma_A\mathbf{A}'_\sigma\cdot\nabla u'_\sigma\right)+R'_\sigma\left(u'_\sigma\right)\ \text{in}\ \mathcal{V}_\sigma, \tag{7.5f}$$

with

$$u'_\alpha = \frac{u_\alpha}{u_0}, \quad \mathbf{v}'_\beta = \frac{\mathbf{v}_\beta}{\left\|\left\langle \mathbf{v}_\beta \right\rangle^\beta\right\|}, \quad p'_\beta = \frac{\left(p_\beta - \rho_\beta \mathbf{g}\cdot\mathbf{r}\right)\ell}{\mu_\beta \left\|\left\langle \mathbf{v}_\beta \right\rangle^\beta\right\|}, \quad \mathbf{A}'_\alpha = \frac{\mathbf{A}_\alpha}{\left\|\mathbf{A}_\beta\right\|}, \quad t' = \frac{t}{\tau} \text{ with } \tau = \frac{\ell^2 \left(a_\beta \rho_\beta\right)}{\left\|\mathbf{A}_\beta\right\|},$$

and

$$\mathrm{Pe}^\ell_\beta = \frac{\left\|\left\langle \mathbf{v}_\beta \right\rangle^\beta\right\| \ell \left(a_\beta \rho_\beta\right)}{\left\|\mathbf{A}_\beta\right\|}, \quad R'_\alpha(u'_\alpha) = \frac{R_\alpha(u_\alpha)\ell^2}{u_0 \left\|\mathbf{A}_\beta\right\|}, \quad \Omega'(u'_\sigma) = \frac{\Omega(u_\sigma)\ell}{u_0 \left\|\mathbf{A}_\beta\right\|}, \quad \Gamma_a = \frac{a_\sigma \rho_\sigma}{a_\beta \rho_\beta}, \quad \Gamma_A = \frac{\left\|\mathbf{A}_\sigma\right\|}{\left\|\mathbf{A}_\beta\right\|}.$$

We have used $\|\langle \mathbf{v}_\beta \rangle^\beta\|$, which is the norm of a spatially averaged value of the velocity (see Section 7.3 for a precise definition of the spatial averaging operators). For space, we have used the microscale length ℓ, that is, $\mathbf{x}' = \mathbf{x}/\ell$, so that we have the following relationship between the macro- and microscale Péclet numbers:

$$\mathrm{Pe}^L_\beta = \frac{\left\|\left\langle \mathbf{v}_\beta \right\rangle^\beta\right\| L \left(a_\beta \rho_\beta\right)}{\left\|\mathbf{A}_\beta\right\|} = \delta^{-1} \mathrm{Pe}^\ell_\beta$$

with $\delta = \dfrac{\ell}{L}$. Similarly, we have the microscale Reynolds number as

$$\mathrm{Re}^\ell_\beta = \frac{\rho_\beta \left\|\left\langle \mathbf{v}_\beta \right\rangle^\beta\right\| \ell}{\mu_\beta},$$

and the macroscale one as

$$\mathrm{Re}^L_\beta \equiv \frac{\rho_\beta \left\|\left\langle \mathbf{v}_\beta \right\rangle^\beta\right\| L}{\mu_\beta} = \delta^{-1} \mathrm{Re}^\ell_\beta.$$

To improve readability, we eliminate the $'$ notation for the dimensionless variables and consider that BC3 and IC are implicit in the remainder of this chapter.

7.2.3 Operator Notation

To facilitate presentation and highlight the structure of the mathematical problems, we further use an operator notation, that is, calligraphic symbols $\mathcal{L}$ for the bulk and $\mathcal{B}$ for the boundaries. This yields

$$\partial_t u_\beta = \mathcal{L}_\beta u_\beta + R_\beta\left(u_\beta\right) \text{ in } \mathcal{V}_\beta, \tag{7.6a}$$

$$\text{BC1} \quad u_\beta - u_\sigma = 0 \text{ on } \mathcal{A}_{\beta\sigma}, \tag{7.6b}$$

$$\text{BC2} \quad \mathcal{B}_\beta u_\beta - \mathcal{B}_\sigma u_\sigma = \Omega\left(u_\sigma\right) \text{ on } \mathcal{A}_{\beta\sigma}, \tag{7.6c}$$

$$\Gamma_a \partial_t u_\sigma = \mathcal{L}_\sigma u_\sigma + R_\sigma\left(u_\sigma\right) \text{ in } \mathcal{V}_\sigma, \tag{7.6d}$$

with

$$\mathcal{L}_\beta u_\beta = \nabla\cdot\left(\mathbf{A}_\beta\cdot\nabla u_\beta - \mathrm{Pe}_\beta^\ell \mathbf{v}_\beta u_\beta\right),\quad \mathcal{L}_\sigma u_\sigma = \nabla\cdot\left(\Gamma_A \mathbf{A}_\sigma\cdot\nabla u_\sigma\right), \tag{7.7}$$

$$\mathcal{B}_\beta u_\beta = -\mathbf{n}_{\beta\sigma}\cdot\left(\mathbf{A}_\beta\cdot\nabla u_\beta\right),\quad \mathcal{B}_\sigma u_\sigma = -\mathbf{n}_{\beta\sigma}\cdot\left(\Gamma_A \mathbf{A}_\sigma\cdot\nabla u_\sigma\right). \tag{7.8}$$

Now that we have defined the transport problem at the microscale, we present, in the next section, the volume averaging methodology that will be used to perform upscaling and obtain several macroscale descriptions for this microscale problem.

7.3 VOLUME AVERAGING METHODOLOGY

The analysis of multiscale systems has produced a variety of upscaling tools. These include *homogenization theory* (see [19–22]), *variants of volume averaging and mixture theories* (see [23–29]), the *Taylor–Aris–Brenner method of moments* (see [30–32]), and *stochastic approaches* (see [33–36]). Although the methodologies are different, the goal of all these approaches is to answer the same questions: Can we obtain a macroscale representation? If yes, what is its domain of validity? How do we define macroscale quantities? How do we treat boundary conditions?

In this work, we use the particular type of volume averaging that is presented in Whitaker's book [37], the idea of which is to obtain the macroscale equations by averaging the microscale equations in space and then using scaling approximations. Before detailing the algorithm, we must first define the averaging operators along with several fundamental theorems.

7.3.1 Definitions and Theorems

For any tensor ψ (including scalars, vectors, and dyadics), we define the volume average as (see [24,27,38–41])

$$\psi_m\left(\boldsymbol{x},t\right) \equiv \int_{\mathbb{R}^n} m\left(\xi\right)\psi\left(\boldsymbol{x}-\xi,t\right)dV_\xi \equiv m\star\psi, \tag{7.9}$$

where

$\star$ denotes the spatial convolution

$m:\mathbb{R}^n\rightarrow\mathbb{R}$ is a smoothing kernel that has compact support in $\mathbb{R}^n$ and is normalized so that $\int_{\mathbb{R}^n} m\left(\xi\right)dV_\xi \equiv 1$

In practice, we are often interested in problems for which the spatial dimension, n, is such that $n\leq 3$ with a particular emphasis on $n=3$ and sets measured as *volumes*. A standard choice for the kernel is

$$m\left(\xi\right) = \begin{cases} \dfrac{1}{V} & \text{if } \|\xi\| \leq R \\ 0 & \text{if } \|\xi\| > R \end{cases}, \tag{7.10}$$

so that

$$\psi(\boldsymbol{x},t) \equiv \frac{1}{V}\int_{\boldsymbol{r}\in\mathcal{V}(\boldsymbol{x})} \psi(\boldsymbol{r},t)\,dV_r, \tag{7.11}$$

where

$\mathcal{V}(\boldsymbol{x}) \equiv \mathcal{B}_r(\boldsymbol{x})$ is the closed ball with radius R centered at point $\boldsymbol{x}$ (see Figure 7.3)

V its volume $\left(V \equiv \int_{\mathcal{V}(\boldsymbol{x})} dV\right)$

In multiphase systems, we also often define the phase and intrinsic averages. For phase α (the set $\mathcal{V}_\alpha$ within the averaging volume $\mathcal{V}$, see Figure 7.3 where α = σ or β), these correspond to the following:

$$\text{Phase average:}\quad \langle\psi_\alpha\rangle = \frac{1}{V}\int_{\mathcal{V}_\alpha}\psi_\alpha dV, \tag{7.12}$$

$$\text{Intrinsic average:}\quad \langle\psi_\alpha\rangle^\alpha = \frac{1}{V_\alpha}\int_{\mathcal{V}_\alpha}\psi_\alpha dV, \tag{7.13}$$

where $V_\alpha \equiv \int_{\mathcal{V}_\alpha} dV$. With these notations, we have the simple relationship

$$\langle\psi_\alpha\rangle = \varepsilon_\alpha\langle\psi_\alpha\rangle^\alpha, \tag{7.14}$$

where $\varepsilon_\alpha = V_\alpha/V$ is the volume fraction of phase α.

As mentioned earlier, the method relies on averaging of partial differential equations. Therefore, it is often useful to interchange the spatial integration and the differential operators, an operation that follows a specific set of rules. For sufficiently smooth tensor fields ψ_α (see discussion in [42]) defined in phase α, we have (proofs are available in, among others [25,39,40,43–45])

$$\langle\nabla\cdot\psi_\alpha\rangle = \nabla\cdot\langle\psi_\alpha\rangle + \frac{1}{V}\int_{\mathcal{A}_{\beta\sigma}}\boldsymbol{n}_\alpha\cdot\psi_\alpha dA, \tag{7.15}$$

$$\langle\nabla\psi_\alpha\rangle = \nabla\langle\psi_\alpha\rangle + \frac{1}{V}\int_{\mathcal{A}_{\beta\sigma}}\boldsymbol{n}_\alpha\psi_\alpha dA, \tag{7.16}$$

$$\langle\partial_t\psi_\alpha\rangle = \partial_t\langle\psi_\alpha\rangle - \frac{1}{V}\int_{\mathcal{A}_{\beta\sigma}}(\boldsymbol{n}_\alpha\cdot\boldsymbol{w}_\alpha)\psi_\alpha dA. \tag{7.17}$$

where

$\mathcal{A}_{\beta\sigma}$ represents the interphase boundary

$\boldsymbol{n}_\alpha$ denotes the outward unit normal vector to the boundary of phase α

$\boldsymbol{w}_\alpha$ is the velocity of the corresponding boundary

In the remainder of this work, we assume that boundaries are immobile so that

$$\left\langle \partial_t \psi_\alpha \right\rangle = \partial_t \left\langle \psi_\alpha \right\rangle. \tag{7.18}$$

We further define decompositions of the microscale fields in terms of an average value, $\langle \psi_\alpha \rangle^\alpha$, and a perturbation, $\tilde{\psi}_\alpha$, as

$$\psi_\alpha = \left\langle \psi_\alpha \right\rangle^\alpha + \tilde{\psi}_\alpha. \tag{7.19}$$

We will also use a weighted or mixture intrinsic average over both phases

$$\left\langle \psi \right\rangle^{\beta\sigma} = \frac{\varepsilon_\beta}{\varepsilon_\beta + \varepsilon_\sigma \Gamma_a} \left\langle \psi_\beta \right\rangle^\beta + \frac{\varepsilon_\sigma \Gamma_a}{\varepsilon_\beta + \varepsilon_\sigma \Gamma_a} \left\langle \psi_\sigma \right\rangle^\sigma, \tag{7.20}$$

with the corresponding perturbation decomposition

$$\psi_\alpha = \left\langle \psi \right\rangle^{\beta\sigma} + \hat{\psi}_\alpha. \tag{7.21}$$

7.3.2 Upscaling Algorithm

The detailed algorithm for the volume averaging with closure methodology is detailed in Figure 7.4 for a linear problem at the microscale and can be summarized as follows. The first steps involve averaging the microscale initial boundary value problem (IBVP), using the perturbative decomposition,

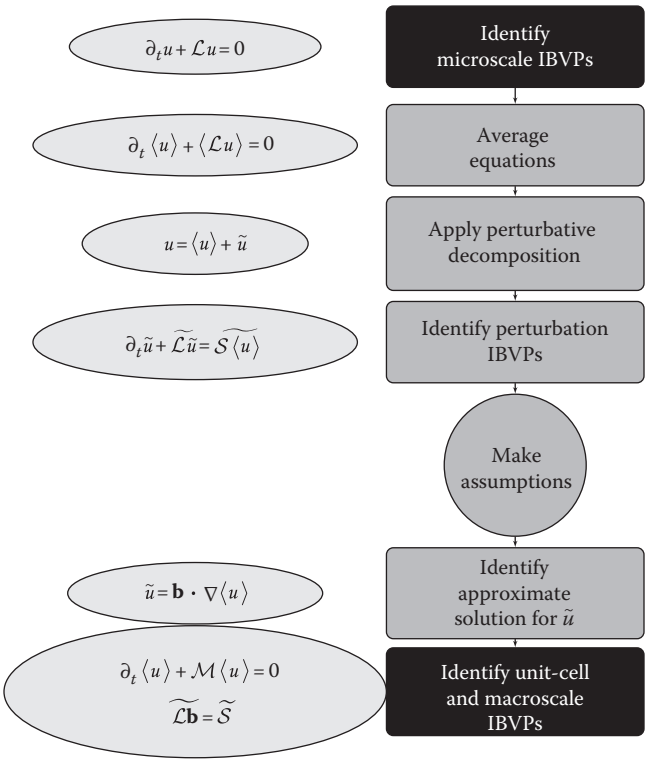

FIGURE 7.4 Volume averaging algorithm for a linear operator $\mathcal{L}$ at the micro-scale, with $\mathcal{M}$ the corresponding macro-scale operator and $\mathcal{S}$ the sources.

and obtaining the perturbation IBVP. Then we make several assumptions in order to obtain an approximate solution to the perturbation IBVP. This approximate solution is further introduced in the unclosed form of the macroscale equations to obtain a homogenized problem.

Although varying from problem to problem, approximations often involve a separation of scales, a notion that states that variables exhibit two dominant (one slow, one fast) spatial frequencies. This approximation is connected to the notion of representative volume element (RVE), which relies on the quasi-stationarity of the medium's geometry (for hierarchical systems, see [7,46–48] and further discussions in [42,49]). We also often use the hypothesis of time quasi-stationarity, which is based on the fact that processes at the scale of the RVE relax quickly compared to macroscopic timescales, and assume that the porous medium of interest can be approximated by a locally periodic structure. The effects of this latter approximation are often difficult to evaluate, especially for images of non-periodic media (e.g., subsurface) and for large values of the Péclet number. We further discuss the limitations of periodic unit cells in Section 7.9.

7.3.3 Resolution Algorithm

The solution procedure depends on the type of macroscale model that has been derived. In the local case, effective parameters can be expressed as functions of closure variables that are calculated separately using auxiliary problems. Many academic works have focused on 2D with analytical (e.g., stratified media) or numerical approaches (see [17,50]). Advances in imaging techniques, such as x-ray microtomography, combined with the computing power of today's workstation make it possible to solve closure problems in realistic 3D unit cells. Even commercially available softwares (see, e.g., Avizo Fire® [51] or GeoDict® [52]) offer tools for both image processing and calculations of effective properties such as diffusivities or permeabilities. We also refer to the special issue [53] for a broader perspective on digital rock physics, benchmarking of codes, and applications in the geosciences.

If the problem is nonlocal (see [54–58]), however, the numerical solution is generally much more tedious to obtain. For example, in the special case of time nonlocality, which generally takes the form of integrodifferential equations with temporal convolutions, the solution at a given time may strongly depend upon solutions at earlier times, therefore complicating numerical schemes and resolutions. For spatial nonlocality, discretization of integrodifferential descriptions, such as fractional derivatives or spatial convolutions, yields dense linear systems that are more difficult to inverse than sparse matrices produced by purely local models. Other types of nonlocal spatial representations are hybrid models for which microscale and averaged equations are solved simultaneously. For instance, the solution in part of the domain is computed at the microscale, while only an averaged behavior is considered in the rest of the domain (see Sections 7.4 and 7.8 for further discussion on hybrid models).

The volume averaging methodology presented here can be used to obtain macroscale equations for a number of transport problems. Depending on the set of approximation that is used, we can obtain different macroscale representations. These are presented in the next section for the microscale problem in Section 7.2.

7.4 MACROSCALE AND HYBRID MODELS

In this section, we summarize and discuss the macroscale models without presenting the mathematical developments. We focus on scalar transport and assume that the velocity field is known pointwise and satisfies $\nabla \cdot \langle \mathbf{v}_\beta \rangle = 0$ and a no-slip boundary condition at the fluid–solid interface. We present three classes of macroscale models, each corresponding to different types of upscaling assumptions, that can be used to describe scalar transport in porous media: two-equation, one-equation, and hybrid models. Two-equation models rely on a phase/domain decomposition approach, where each equation describes the behavior of the intrinsic average of a phase and both are coupled

via exchange terms. One-equation representations describe an average value over both phases, using either LE or time-asymptotic assumptions. Hybrid models couple a description of one phase at the macroscale with the description of the other phase at the microscale model. All these models can be further declined in several categories, corresponding to different upscaling assumptions. We will discuss these variants with an emphasis on fully transient and quasi-stationary models and their domains of validity. We further emphasize that results are presented with a *second-order closure* for the linear part of the operator and that we show how to deal with *nonlinear sources/sinks*. For simplicity, we consider here a homogeneous porous medium and a nonconservative form of the equations. We will discuss in the end of this section possible extensions to conservative forms and varying effective parameters.

7.4.1 Two-Equation Models

Two-equation models have been introduced in various different forms by different communities. In the geosciences, for instance, these are often termed mobile/mobile, mobile/immobile, dual-continua, dual-porosity, or two-region models (see, e.g., [59–61]). In volume averaging, we use the terminology *two-equation* that refers to the mathematical structure of the problem, rather than the scale of application or the variable of interest. Such models have been studied in various works using Whitaker's methodology (see [62–69]), variants of the volume averaging technique [70–72], and formal multiscale asymptotics (see [50,73]). The different types of two-equation models are as follows.

7.4.1.1 Two-Equation Transient

The fully transient two-equation model (see, e.g., [66]) reads

$$\underbrace{\begin{bmatrix}\varepsilon_\beta & 0\\ 0 & \varepsilon_\sigma\Gamma_a\end{bmatrix}\partial_t\begin{bmatrix}\langle u_\beta\rangle^\beta\\ \langle u_\sigma\rangle^\sigma\end{bmatrix}}_{\text{Rate of change}}+\underbrace{\partial_t\begin{bmatrix}\mathbf{V}^\star_{\beta\beta} & \mathbf{V}^\star_{\beta\sigma}\\ \mathbf{V}^\star_{\sigma\beta} & \mathbf{V}^\star_{\sigma\sigma}\end{bmatrix}\cdot\star\begin{bmatrix}\nabla\langle u_\beta\rangle^\beta\\ \nabla\langle u_\sigma\rangle^\sigma\end{bmatrix}}_{\text{Advection}}$$

$$=\underbrace{\partial_t\begin{bmatrix}\mathbf{A}^\star_{\beta\beta} & \mathbf{A}^\star_{\beta\sigma}\\ \mathbf{A}^\star_{\sigma\beta} & \mathbf{A}^\star_{\sigma\sigma}\end{bmatrix}:\star\begin{bmatrix}\nabla\nabla\langle u_\beta\rangle^\beta\\ \nabla\nabla\langle u_\sigma\rangle^\sigma\end{bmatrix}}_{\text{Dispersion}}+\underbrace{\partial_t\begin{bmatrix}\square & +\square\\ +\square & \square\end{bmatrix}\star\begin{bmatrix}\langle u_\beta\rangle^\beta\\ \langle u_\sigma\rangle^\sigma\end{bmatrix}}_{\text{irst order exchange}}$$

$$+\underbrace{\begin{bmatrix}\varepsilon_\beta & 0\\ 0 & \varepsilon_\sigma\end{bmatrix}\begin{bmatrix}\square_\beta\langle u_\beta\rangle^\beta\\ \square_\sigma\langle u_\sigma\rangle^\sigma\end{bmatrix}}_{\text{ource sin}}\underbrace{\partial_t\begin{bmatrix}a_\square\star & 0\\ 0 & a_\square\end{bmatrix}\star\begin{bmatrix}\square\langle u_\sigma\rangle^\sigma\\ \square\langle u_\sigma\rangle^\sigma\end{bmatrix}}_{\text{face source sin}}\square \tag{7.22}$$

where $\star$ denotes the time convolution, $f\star g=\int_0^t f(\tau)g(t-\tau)d\tau$, and the algebra is written in terms of block matrices. For instance, we have

$$\partial_t\begin{bmatrix}\mathbf{V}^\star_{\beta\beta} & \mathbf{V}^\star_{\beta\sigma}\\ \mathbf{V}^\star_{\sigma\beta} & \mathbf{V}^\star_{\sigma\sigma}\end{bmatrix}\cdot\star\begin{bmatrix}\nabla\langle u_\beta\rangle^\beta\\ \nabla\langle u_\sigma\rangle^\sigma\end{bmatrix}=\begin{bmatrix}\partial_t\mathbf{V}^\star_{\beta\beta}\cdot\star\nabla\langle u_\beta\rangle^\beta+\partial_t\mathbf{V}^\star_{\beta\sigma}\cdot\star\nabla\langle u_\sigma\rangle^\sigma\\ \partial_t\mathbf{V}^\star_{\sigma\beta}\cdot\star\nabla\langle u_\beta\rangle^\beta+\partial_t\mathbf{V}^\star_{\sigma\sigma}\cdot\star\nabla\langle u_\sigma\rangle^\sigma\end{bmatrix},$$

with $\partial_t\mathbf{V}^\star_{\beta\beta}\cdot\star\nabla\langle u_\beta\rangle^\beta=\partial_t V^\star_{\beta\beta,i}\star\partial_i\langle u\rangle$.

Equation 7.22 exhibits the following:

- Advective terms that represent both the physical velocity and the coupling between the two phases.
- Diffusive terms.
- A first-order exchange term of the form $\partial_t h^\star \star \left(\langle u_\beta \rangle^\beta - \langle u_\sigma \rangle^\sigma \right)$.
- Bulk sources/sinks $R_\alpha \left(\langle u_\alpha \rangle^\alpha \right)$.
- Surface sources/sinks $\Omega \left(\langle u_\sigma \rangle^\sigma \right)$ with a coefficient ξ that distributes the surface effects between each phase. This distribution coefficient was already introduced in [17] and used to develop a local nonequilibrium (LNE) model taking into account radiation effects through a generalized radiation transfer equation in [74].

For all operator types, the convolution products account for the relaxation times of the effective parameters, therefore capturing a broad range of characteristic times. Such convolutions are particularly useful to describe the short-time regime (see [75–78]). This is easily shown for a sinusoidal excitation in a simple stratified system (see [79]) where the nonlocal model recovers the exact solution for all excitation frequencies. In practice, if the topology of the microscale problem is unknown and if the relaxation of effective parameters cannot be calculated over a representative unit cell, the kernels may also be approximated using empirical functions (see [80,81]).

7.4.1.2 Two-Equation Quasi-Stationary

A simpler version of the two-equation model is quasi-stationary (see, e.g., [76]) and reads

$$\underbrace{\begin{bmatrix} \varepsilon_\beta & 0 \\ 0 & \varepsilon_\sigma \Gamma_a \end{bmatrix} \partial_t \begin{bmatrix} \langle u_\beta \rangle^\beta \\ \langle u_\sigma \rangle^\sigma \end{bmatrix}}_{\text{Rate of change}} + \underbrace{\begin{bmatrix} \mathbf{V}_{\beta\beta} & \mathbf{V}_{\beta\sigma} \\ \mathbf{V}_{\sigma\beta} & \mathbf{V}_{\sigma\sigma} \end{bmatrix} \cdot \begin{bmatrix} \nabla \langle u_\beta \rangle^\beta \\ \nabla \langle u_\sigma \rangle^\sigma \end{bmatrix}}_{\text{Advection}}$$

$$= \underbrace{\begin{bmatrix} \mathbf{A}_{\beta\beta} & \mathbf{A}_{\beta\sigma} \\ \mathbf{A}_{\sigma\beta} & \mathbf{A}_{\sigma\sigma} \end{bmatrix} : \begin{bmatrix} \nabla\nabla \langle u_\beta \rangle^\beta \\ \nabla\nabla \langle u_\sigma \rangle^\sigma \end{bmatrix}}_{\text{Dispersion}} + \underbrace{\begin{bmatrix} - & + \\ + & - \end{bmatrix} \begin{bmatrix} \langle u_\beta \rangle^\beta \\ \langle u_\sigma \rangle^\sigma \end{bmatrix}}_{\text{first order exchange}}$$

$$+ \underbrace{\begin{bmatrix} \varepsilon_\beta & 0 \\ 0 & \varepsilon_\sigma \end{bmatrix} \begin{bmatrix} \gamma_\beta \left[\langle u_\beta \rangle^\beta \right] \\ \gamma_\sigma \left[\langle u_\sigma \rangle^\sigma \right] \end{bmatrix}}_{\text{source sink}} - \underbrace{\begin{bmatrix} a_{\Gamma} & 0 \\ 0 & a_{\Gamma} \end{bmatrix} \begin{bmatrix} \left[\langle u_\sigma \rangle^\sigma \right] \\ \left[\langle u_\sigma \rangle^\sigma \right] \end{bmatrix}}_{\text{surface source sink}} \tag{7.23}$$

This model differs from the previous one in that the temporal convolution products have disappeared. This approximation is valid when the times for the relaxation of the effective parameters $\mathbf{V}^\star$, $\mathbf{A}^\star$, $h^\star$, and $\xi^\star$ are much smaller than the characteristic times corresponding to the average variables $\nabla\langle u \rangle$, $\nabla\nabla\langle u \rangle$, $\langle u_\beta \rangle^\beta - \langle u_\sigma \rangle^\sigma$ and $\Omega \left(\langle u_\sigma \rangle^\sigma \right)$ (see [79]).

7.4.1.3 Two-Equation Quasi-Stationary with Fluxes

The two-equation model is often written by grouping terms of similar mathematical types, for example, advective and diffusive parts of the operators. Two-equation models may also be written

in a way that emphasizes the physical, rather than mathematical, nature of the different terms. For the quasi-stationary version, this reads

$$\varepsilon_\beta\left[\underbrace{\partial_t\left\langle u_\beta\right\rangle^\beta}_{\text{Rate of change}}+\mathrm{Pe}_\beta^\ell\nabla\cdot\left(\underbrace{\left\langle \mathbf{v}_\beta\right\rangle^\beta\left\langle u_\beta\right\rangle^\beta}_{\text{Convection}}+\underbrace{\theta_\beta}_{\text{Velocity fluctuation effects}}\right)\right]$$

$$=\nabla\cdot\left[\varepsilon_\beta\mathbf{A}_\beta\cdot\left(\underbrace{\nabla\left\langle u_\beta\right\rangle^\beta}_{\text{Diffusion}}+\underbrace{\zeta_\beta}_{\text{Surface effects}}\right)\right]-\underbrace{\mathsf{J}_{\beta\sigma}}_{\text{Interfacial flux}}+\underbrace{\varepsilon_\beta R_\beta\left(\left\langle u_\beta\right\rangle^\beta\right)}_{\text{Bulk reaction rate}},\tag{7.24}$$

and

$$\varepsilon_\sigma\Gamma_a\underbrace{\partial_t\left\langle u_\sigma\right\rangle^\sigma}_{\text{Rate of change}}=\nabla\cdot\left[\varepsilon_\sigma\Gamma_A\mathbf{A}_\sigma\cdot\left(\underbrace{\nabla\left\langle u_\sigma\right\rangle^\sigma}_{\text{Diffusion}}+\underbrace{\zeta_\sigma}_{\text{Surface effects}}\right)\right]-\underbrace{\mathsf{J}_{\sigma\beta}}_{\text{Interfacial flux}}+\underbrace{\varepsilon_\sigma R_\sigma\left(\left\langle u_\sigma\right\rangle^\sigma\right)}_{\text{Bulk reaction rate}}.\tag{7.25}$$

For instance, the term $h(\langle u_\beta\rangle^\beta-\langle u_\sigma\rangle^\sigma)$ is often wrongly interpreted as the interfacial flux in the mathematical version of the two-equation model, whereas it is only part of the flux:

$$\mathsf{J}_{\beta\sigma}=\underbrace{h\left(\left\langle u_\beta\right\rangle^\beta-\left\langle u_\sigma\right\rangle^\sigma\right)}_{\text{First-order exchange}}+\underbrace{a_v\xi\Omega\left(\left\langle u_\sigma\right\rangle^\sigma\right)}_{\text{Flux component from the surface source}}$$

$$\underbrace{+\mathcal{O}\left(\begin{bmatrix}\nabla\left\langle u_\beta\right\rangle^\beta\\ \nabla\left\langle u_\sigma\right\rangle^\sigma\end{bmatrix}\right)+\mathcal{O}\left(\begin{bmatrix}\nabla\nabla\left\langle u_\beta\right\rangle^\beta\\ \nabla\nabla\left\langle u_\sigma\right\rangle^\sigma\end{bmatrix}\right)}_{\text{Higher-order corrections}}.\tag{7.26}$$

This shows that the flux is affected by the source/sink term on the interface, $a_v\xi\Omega(\langle u_\sigma\rangle^\sigma)$, and higher-order corrections in $\begin{bmatrix}\nabla\langle u_\beta\rangle^\beta & \nabla\langle u_\sigma\rangle^\sigma\end{bmatrix}^T$ and $\begin{bmatrix}\nabla\nabla\langle u_\beta\rangle^\beta & \nabla\nabla\langle u_\sigma\rangle^\sigma\end{bmatrix}^T$.

We further emphasize that the surface terms translate tortuosity effects, both for the advective and diffusive operators:

$$\zeta_\beta\simeq\underbrace{\left\langle\nabla\mathbf{a}_\beta\right\rangle^\beta}_{\text{Advective tortuosity}}\left(\left\langle u_\beta\right\rangle^\beta-\left\langle u_\sigma\right\rangle^\sigma\right)$$

$$+\underbrace{\left\langle\nabla\begin{bmatrix}\mathbf{b}_{\beta\beta} & \mathbf{b}_{\beta\sigma}\end{bmatrix}^\beta\right\rangle}_{\text{Diffusive tortuosity}}\cdot\begin{bmatrix}\nabla\left\langle u_\beta\right\rangle^\beta\\ \nabla\left\langle u_\sigma\right\rangle^\sigma\end{bmatrix}.\tag{7.27}$$

Similarly, velocity fluctuations lead to enhanced dispersion effects and corrections of the advective terms:

$$\theta_\beta\equiv\left\langle\tilde{\mathbf{v}}_\beta\tilde{u}_\beta\right\rangle^\beta\simeq\underbrace{\left\langle\tilde{\mathbf{v}}_\beta\mathbf{a}_\beta\right\rangle^\beta}_{\text{Velocity correction}}\left(\left\langle u_\beta\right\rangle^\beta-\left\langle u_\sigma\right\rangle^\sigma\right)$$

$$+\underbrace{\left\langle\tilde{\mathbf{v}}_\beta\begin{bmatrix}\mathbf{b}_{\beta\beta} & \mathbf{b}_{\beta\sigma}\end{bmatrix}^\beta\right\rangle}_{\text{Hydrodynamic dispersion}}\cdot\begin{bmatrix}\nabla\left\langle u_\beta\right\rangle^\beta\\ \nabla\left\langle u_\sigma\right\rangle^\sigma\end{bmatrix}.\tag{7.28}$$

7.4.1.4 Two-Equation Variant

The relaxation times for $\mathbf{V}^\star$, $\mathbf{A}^\star$, $h^\star$, and $\xi^\star$ are different. For example, $\mathbf{V}^\star$ and $\mathbf{A}^\star$ may relax much faster than $\xi^\star$ and $h^\star$ (e.g., for fractured media, see [76,82,83] Chapter 4), in which case we obtain a macroscale model of the form (see, e.g., [84])

$$\begin{aligned}
&\begin{bmatrix} \varepsilon_\beta & 0 \\ 0 & \varepsilon_\sigma \Gamma_a \end{bmatrix} \partial_t \begin{bmatrix} \langle u_\beta \rangle^\beta \\ \langle u_\sigma \rangle^\sigma \end{bmatrix} + \begin{bmatrix} \mathbf{V}_{\beta\beta} & \mathbf{V}_{\beta\sigma} \\ \mathbf{V}_{\sigma\beta} & \mathbf{V}_{\sigma\sigma} \end{bmatrix} \cdot \begin{bmatrix} \nabla \langle u_\beta \rangle^\beta \\ \nabla \langle u_\sigma \rangle^\sigma \end{bmatrix} \\
&= \begin{bmatrix} \mathbf{A}_{\beta\beta} & \mathbf{A}_{\beta\sigma} \\ \mathbf{A}_{\sigma\beta} & \mathbf{A}_{\sigma\sigma} \end{bmatrix} : \begin{bmatrix} \nabla\nabla \langle u_\beta \rangle^\beta \\ \nabla\nabla \langle u_\sigma \rangle^\sigma \end{bmatrix} + \partial_t \begin{bmatrix} -h^\star & +h^\star \\ +h^\star & -h^\star \end{bmatrix} \star \begin{bmatrix} \langle u_\beta \rangle^\beta \\ \langle u_\sigma \rangle^\sigma \end{bmatrix} \\
&\quad + \begin{bmatrix} \varepsilon_\beta & 0 \\ 0 & \varepsilon_\sigma \end{bmatrix} \left[\begin{bmatrix} \square_\beta \langle u_\beta \rangle^\beta \square \\ \square_\sigma \langle u_\sigma \rangle^\sigma \square \end{bmatrix} - \partial_t \begin{bmatrix} a_\square^\star & 0 \\ 0 & a_\square \square \square t \square^\star \square \end{bmatrix} \star \begin{bmatrix} \square \langle u_\sigma \rangle^\sigma \square \\ \square \langle u_\sigma \rangle^\sigma \square \end{bmatrix} \right] \square
\end{aligned} \tag{7.29}$$

The fully transient model can therefore be adapted to the timescales of interest using any combination of convolution products that is suited to the timescales of the physical problem.

7.4.1.5 Telegrapher's Equation

Other nonequilibrium models have been proposed in the literature. For instance, it has been shown in [85,86] that the two-equation model is equivalent under certain conditions to a dual-phase-lagging heat conduction model. Similarly, other types of equations may potentially reproduce some of the features of LNE situations, for instance, equations with fractional derivatives that have already been used to describe dispersion in porous media [87].

7.4.1.6 Link with Multirate Approaches

The two-equation quasi-stationary model with a linear exchange term, Equation 7.23, features only one characteristic time for describing the fluid–solid relaxation. This limitation can be overcome using temporal convolution products, as is done in Equation 7.22, although these can be impractical for numerical implementations. Alternatively, simplified models have been designed to incorporate more characteristic times in the macroscale equations, such as the multirate mass transfer (MRMT) models (see, e.g., [80,88]). These models can be derived by an N-phase decomposition of the fields, defined either by geometrical considerations (for instance, grains with large and small diameters) or through a more sophisticated mathematical approach, for example, using the properties of the eigenvalue spectrum for the diffusion process in the solid phase. This leads to N-equation models (similarly to what is discussed for MRMT in [88]), which may capture more accurately the temporal behavior without the inconvenience of convolution products. They can also be presented by considering the variant of the two-equation model Equation 7.29 that retains only the convolution associated with the linear exchange term (see further discussions based on volume averaging in [84]).

7.4.2 One-Equation Models

One-equation models describe the behavior of a mixture average over the different phases. They do not capture timescales associated with exchange phenomena so that they require a form of relaxation between the phases. For multiphase systems, these can be primarily obtained using the LE or time-asymptotic LNE approximations. The LE assumption states that (see [17])

$$\langle u_\beta \rangle^\beta \cong \langle u_\sigma \rangle^\sigma \cong \langle u \rangle^{\beta\sigma}. \tag{7.30}$$

Combined with the quasi-stationarity assumption, this yields a model of the form

$$\underbrace{\left(\varepsilon_\beta + \Gamma_a \varepsilon_\sigma\right) \partial_t \left\langle u \right\rangle^{\beta\sigma}}_{\text{Rate of change}} + \underbrace{\varepsilon_\beta \mathrm{Pe}_\beta^\ell \left\langle \mathbf{v}_\beta \right\rangle^\beta \cdot \nabla \left\langle u \right\rangle^{\beta\sigma}}_{\text{Advection}}$$
$$= \underbrace{\mathbf{A}^{\mathrm{LE}} : \nabla\nabla \left\langle u \right\rangle^{\beta\sigma}}_{\text{Dispersion}} + \underbrace{\varepsilon_\beta R_\beta \left(\left\langle u \right\rangle^{\beta\sigma} \right) + \varepsilon_\sigma R_\sigma \left(\left\langle u \right\rangle^{\beta\sigma} \right)}_{\text{Bulk source/sink}} - \underbrace{a_v \Omega \left(\left\langle u \right\rangle^{\beta\sigma} \right)}_{\text{Surface source/sink}}. \tag{7.31}$$

On the contrary, the LNE transient one-equation model does not make the assumption, Equation 7.30, but rather considers a long-time relaxation and reads

$$\left(\varepsilon_\beta + \Gamma_a \varepsilon_\sigma\right) \partial_t \left\langle u \right\rangle^{\beta\sigma} + \varepsilon_\beta \mathrm{Pe}_\beta^\ell \left\langle \mathbf{v}_\beta \right\rangle^\beta \cdot \nabla \left\langle u \right\rangle^{\beta\sigma}$$
$$= \mathbf{A}^{\mathrm{LNE}} : \nabla\nabla \left\langle u \right\rangle^{\beta\sigma} + \varepsilon_\beta R_\beta \left(\left\langle u \right\rangle^{\beta\sigma} \right) + \varepsilon_\sigma R_\sigma \left(\left\langle u \right\rangle^{\beta\sigma} \right) - a_v \Omega \left(\left\langle u \right\rangle^{\beta\sigma} \right). \tag{7.32}$$

The LNE model can be derived at least in two different ways, either as the asymptotic behavior of the two-equation model or via a special perturbation decomposition. The asymptotic method was studied in detail in [63,89,90]. The more direct one-step derivation can be obtained by averaging over the two phases simultaneously and using a nonconventional perturbation decomposition (see [79,91,92]). We further remark that we have the relationship

$$\mathbf{A}^{\mathrm{LNE}} = \mathbf{A}^{\mathrm{LE}} + \text{correction}, \tag{7.33}$$

with $\|\mathbf{A}^{\mathrm{LNE}}\| \geq \|\mathbf{A}^{\mathrm{LE}}\|$. This stems from the fact that the nonequilibrium effects induce additional dispersion effects that the LE model fails to capture. Examples and comparisons of models with direct numerical simulations at the microscale can be found in [93,94]. We also have the following relationship between the LE dispersion tensor and the two-equation effective parameters:

$$\mathbf{A}^{\mathrm{LE}} = \mathbf{A}_{\beta\beta} + \mathbf{A}_{\beta\sigma} + \mathbf{A}_{\sigma\beta} + \mathbf{A}_{\sigma\sigma}. \tag{7.34}$$

7.4.3 Hybrid Models

Hybrid models combine the resolution of coupled micro- and macroscale models as a compromise between computational cost and accuracy. Here, we focus on the simple model derived in Section 7.8, which is based on the assumption that the diffusion in the solid phase is much smaller than in the fluid phase, that is,

$$\Gamma_A \ll 1. \tag{7.35}$$

We obtain the following macroscale model for phase β:

$$\varepsilon_\beta \left[\underbrace{\partial_t \left\langle u_\beta \right\rangle^\beta}_{\text{Rate of change}} + \underbrace{\nabla \cdot \left(\mathrm{Pe}_\beta^\ell \left\langle \mathbf{v}_\beta \right\rangle^\beta \left\langle u_\beta \right\rangle^\beta \right)}_{\text{Advection}} \right] = \underbrace{\nabla \cdot \left(\mathbf{A}^{\mathrm{HYB}} \cdot \nabla \left\langle u_\beta \right\rangle^\beta \right)}_{\text{Dispersion}} - \underbrace{\mathbf{J}_{\beta\sigma}}_{\text{Interfacial flux}} + \underbrace{R^{\mathrm{HYB}}}_{\text{Bulk source/sink}}, \tag{7.36}$$

$$\text{BC} \quad \text{Macro scale domain boundary}, \tag{7.37}$$

$$\text{IC} \quad \langle u_\beta \rangle^\beta \left(t = 0\right) = 0, \tag{7.38}$$

where $J_{\beta\sigma}$ is the interfacial flux, and

$$\Gamma_a \partial_t u_\sigma = \mathcal{L}_\sigma u_\sigma + R_\sigma \left(u_\sigma\right) \text{ in } \mathcal{V}_\sigma, \tag{7.39}$$

$$\text{BC1} \quad u_\sigma = \langle u_\beta \rangle^\beta \text{ on } \mathcal{A}_{\beta\sigma}, \tag{7.40}$$

$$\text{BC2} \quad \text{Macro scale domain boundary}, \tag{7.41}$$

$$\text{IC} \quad u_\sigma \left(t = 0\right) = 0, \tag{7.42}$$

at the microscale.

Coupling of the micro- and macroscale fields occurs via both $J_{\beta\sigma}$ and BC1, hence the word hybrid (or mixed). Solving the hybrid model requires (1) solving the closure problem to estimate the dispersion tensor in Equation 7.36 and then (2) solving the coupled hybrid problem expressed by Equations 7.36 through 7.40.

There exist various ways to deal with hybrid problems, corresponding to different computational costs and levels of accuracy. Figure 7.5 represents a schematic view of these strategies in the case of a 1D macroscale problem. The most direct approach consists in transforming the 3D pore-scale problem, Figure 7.5a, in a 1D averaged equation for the β-phase, plus a series of 3D pore-scale problems for the σ-phase, Figure 7.5b. We can reduce the computational cost via additional assumptions regarding the solid phase. For example, if phase σ consists of monodisperse grains, the problem for one grain can be used to calculate $J_{\beta\sigma}$ in Equation 7.36, Figure 7.5c. To further facilitate solution, we can reduce the number of hybrid grains and extrapolate values of $J_{\beta\sigma}$, Figure 7.5d, at the macroscale. Several other simplifications may further improve the efficiency of hybrid models, for example, by solving the problem over a few representative grains in the polydisperse case or by using analytical/semianalytical solutions at the microscale.

We have also presented an example variant formulation in Figure 7.5e, where the domain is decomposed in two regions. This allows us to solve the original pore-scale problem in a smaller portion where average representations may fail to describe scalar transport. Such an approach may be useful to describe sharp fronts [95], or to deal with specific macroscale boundary conditions and microscale singularities (see, e.g., [96]).

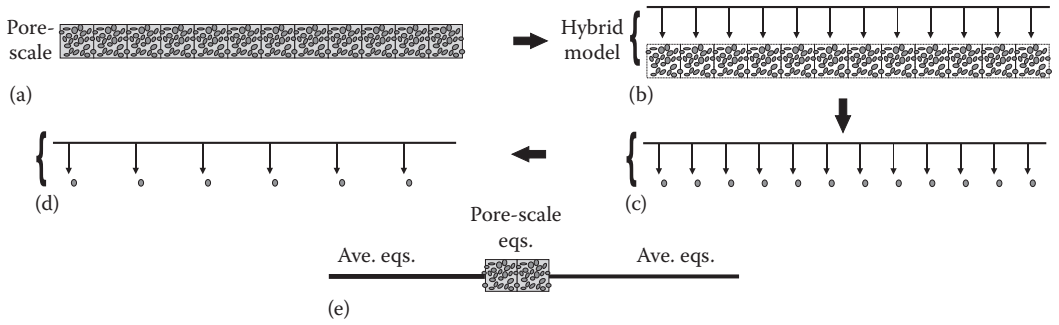

FIGURE 7.5 Schematic illustration of hybrid models.

7.4.4 Domains of Validity

7.4.4.1 LE versus LNE

LE models are based on the assumption that microscale gradients are relatively small, so that both phases can be treated in exactly the same way and $\langle u_\beta \rangle^\beta \simeq \langle u_\sigma \rangle^\sigma$ (see discussion and additional references in [17]). When this is not the case, for instance, if there exists a strong gradient at the interface between phases, the situation is termed LNE. LE situations are described via the one-equation LE model, and LNE situations via the one-equation LNE, two-equation, or hybrid models.

Nonequilibrium effects are often the consequence of properties contrast between phases and boundary conditions. For the case presented in Section 7.2, very large or small ratios of diffusivities may induce nonequilibrium effects. This is the case for heat wave propagation with a smaller diffusivity in the solid phase, a case for which the temperature profile exhibits a well-known tailing effect. The relaxation processes involve a range of different timescales/eigenvalues that are captured more or less accurately by the different macroscale models.

For each macroscale representation, we can usually identify regions of parameter space that describe the validity of the LE, LNE, or other hypotheses. In general, the LE approximation will be verified if $\Gamma_a = \mathcal{O}(1)$, $\Gamma_A = \mathcal{O}(1)$, $\mathrm{Pe}_\beta^\ell < 1$, and the characteristic times for sources/sinks are larger than transport times (see [17,97] for a more detailed description of domains of validity). An example of a more complicated diagram of validity involving a larger set of dimensionless parameters can be found in [98] or in [79,99] for temporal regimes.

These simple estimates of the various time and length scales that are interpreted as order of magnitude estimates of dimensionless parameters may be sufficient in many practical instances to decide whether a nonequilibrium analysis is needed or not. However, this is not always possible to decide on the basis of an order of magnitude analysis as attempted in [100]. The matter is in general more complex and depends on, among others, the geometry and topology of the unit cell [97]; the boundary conditions and the type of problem [101–103]; the processes involved, for instance, natural convection [104]; phase change [105,106]; and the coupling with reactive transport [107,108].

7.4.4.2 Hybrid Model

The hybrid model described earlier has been used in many applications including flows in fractured porous media (see a review in [82], original articles [109–111] for a derivation using homogenization theory). The advantage of such a hybrid model is that the whole spectrum of eigenvalues/characteristic times for the diffusion problem in the phase σ is captured, without the use of tedious convolution products. Another important advantage is that it can be used for highly nonlinear problems, such as combustion or pyrolysis fronts in the solid phase [112]. Hybrid models are also often utilized to derive expressions for the exchange coefficient via the introduction of approximate analytical solutions: parabolic profiles, such as in [113], or piecewise linear profiles [114] (see also [76] for a discussion on various proposals). On the other hand, hybrid models have strong limitations, including their significant computational cost. For the approach presented earlier, we have also assumed that $\Gamma_A \ll 1$ and $\tilde{u}_\beta \ll \left\langle u_\beta \right\rangle^\beta$. If these constraints are not satisfied, the hybrid model will not provide an accurate representation compared with two-equation models as discussed in [115].

7.4.4.3 Conservative Forms and Variations of Effective Parameters

In this chapter, we primarily consider a homogeneous porous medium with constant effective parameters and nonconservative versions of the macroscale models. If effective parameters vary in space, the macroscale models can be written in a conservative way without too much difficulty. However, this means that we must specify how these variations occur and, possibly, compute numerous unit-cell problems, therefore increasing computational cost. In some cases, we can use probability density functions to describe the variation of effective parameters (see [116]).

7.5 DERIVATION OF THE TWO-EQUATION MODELS

We have presented in the previous section a perspective on the various models. In this section, we provide details about the mathematical development of these models, in particular the way approximate solutions of the coupled micro- and macroscale equations are obtained (the so-called *closure*).

7.5.1 Averaging

Applying the spatial averaging operators to Equations 7.6a through d with an immobile porous structure yields

$$\varepsilon_\beta \partial_t \langle u_\beta \rangle^\beta = \langle \mathcal{L}_\beta u_\beta \rangle + \langle R_\beta (u_\beta) \rangle, \tag{7.43}$$

$$\varepsilon_\sigma \Gamma_a \partial_t \langle u_\sigma \rangle^\sigma = \langle \mathcal{L}_\sigma u_\sigma \rangle + \langle R_\sigma (u_\sigma) \rangle. \tag{7.44}$$

We further use the perturbation decompositions $u_\beta = \langle u_\beta \rangle^\beta + \tilde{u}_\beta$ and $u_\sigma = \langle u_\sigma \rangle^\sigma + \tilde{u}_\sigma$, along with the linearity of the spatial operators $\mathcal{L}_\beta$ and $\mathcal{L}_\sigma$, to obtain

$$\varepsilon_\beta \partial_t \langle u_\beta \rangle^\beta = \langle \mathcal{L}_\beta \langle u_\beta \rangle^\beta \rangle + \langle \mathcal{L}_\beta \tilde{u}_\beta \rangle + \langle R_\beta (u_\beta) \rangle, \tag{7.45}$$

$$\varepsilon_\sigma \Gamma_a \partial_t \langle u_\sigma \rangle^\sigma = \langle \mathcal{L}_\sigma \langle u_\sigma \rangle^\sigma \rangle + \langle \mathcal{L}_\sigma \tilde{u}_\sigma \rangle + \langle R_\sigma (u_\sigma) \rangle. \tag{7.46}$$

These equations use operator notations that are rather abstract but have the advantage of being compact and emphasizing the mathematical structure of the problem. In the literature, a more physical interpretation has often been used based on the averaging theorems and scaling constraints. To facilitate physical interpretation, we present here these developments, although subsequent analysis will be mainly based on Equations 7.45 and 7.46. The first term on the right-hand side (RHS) of Equation 7.45 reads

$$\langle \mathcal{L}_\beta u_\beta \rangle = \langle \nabla \cdot (\mathbf{A}_\beta \cdot \nabla u_\beta - \mathrm{Pe}_\beta^\ell \mathbf{v}_\beta u_\beta) \rangle. \tag{7.47}$$

Applying the averaging theorems to the divergence operator and the no-slip boundary condition leads to

$$\begin{aligned} \langle \mathcal{L}_\beta u_\beta \rangle = {} & \nabla \cdot \langle \mathbf{A}_\beta \cdot \nabla u_\beta \rangle - \nabla \cdot \langle \mathrm{Pe}_\beta^\ell \mathbf{v}_\beta u_\beta \rangle \\ & + \frac{1}{V} \int_{\mathcal{A}_{\beta\sigma}} \mathbf{n}_{\beta\sigma} \cdot (\mathbf{A}_\beta \cdot \nabla u_\beta) \, dA, \end{aligned} \tag{7.48}$$

where the last term on the RHS is the average surface flux. We can further apply the averaging theorems to the gradient operator in the first term on the RHS of Equation 7.48, so that we have

$$\nabla \cdot \langle \mathbf{A}_\beta \cdot \nabla u_\beta \rangle = \nabla \cdot \left[\mathbf{A}_\beta \cdot \left(\nabla \langle u_\beta \rangle + \frac{1}{V} \int_{\mathcal{A}_{\beta\sigma}} \mathbf{n}_{\beta\sigma} u_\beta dA \right) \right]. \tag{7.49}$$

This equation involves the phase-average $\langle u_\beta \rangle$ that we can transform into the intrinsic-average $\langle u_\beta \rangle^\beta$ using $\langle u_\beta \rangle = \varepsilon_\beta \langle u_\beta \rangle^\beta$ so that

$$\nabla \langle u_\beta \rangle = \langle u_\beta \rangle^\beta \nabla \varepsilon_\beta + \varepsilon_\beta \nabla \langle u_\beta \rangle^\beta . \tag{7.50}$$

Similarly, we obtain $\langle u_\beta \rangle^\beta$ in the interfacial term $\frac{1}{V}\int_{\mathcal{A}_{\beta\sigma}} \mathbf{n}_{\beta\sigma} u_\beta dA$ using the average plus perturbation decomposition $u_\beta = \langle u_\beta \rangle^\beta + \tilde{u}_\beta$,

$$\begin{aligned}
\frac{1}{V}\int_{\mathcal{A}_{\beta\sigma}} \mathbf{n}_{\beta\sigma} u_\beta \, dA &= \frac{1}{V}\int_{\mathcal{A}_{\beta\sigma}} \mathbf{n}_{\beta\sigma} \tilde{u}_\beta dA + \frac{1}{V}\int_{\mathcal{A}_{\beta\sigma}} \mathbf{n}_{\beta\sigma} \langle u_\beta \rangle^\beta \, dA, \\
&\simeq \frac{1}{V}\int_{\mathcal{A}_{\beta\sigma}} \mathbf{n}_{\beta\sigma} \tilde{u}_\beta dA + \left(\frac{1}{V}\int_{\mathcal{A}_{\beta\sigma}} \mathbf{n}_{\beta\sigma} dA \right) \langle u_\beta \rangle^\beta \\
&\simeq \frac{1}{V}\int_{\mathcal{A}_{\beta\sigma}} \mathbf{n}_{\beta\sigma} \tilde{u}_\beta dA - \langle u_\beta \rangle^\beta \nabla \varepsilon_\beta .
\end{aligned} \tag{7.51}$$

We have used the symbol $\simeq$ to emphasize the approximation that $\langle u_\beta \rangle^\beta$ can be extracted from the surface integral (all the aforementioned simplifications have been discussed at length for the cases of ordered and disordered media in [39,40,117–119]). We also have that $\frac{1}{V}\int_{\mathcal{A}_{\beta\sigma}} \mathbf{n}_{\beta\sigma} dA = -\nabla \varepsilon_\beta$, from a simple application of the averaging theorems to the β-phase indicator function, γ_β (unity in the β-phase and zero elsewhere)

$$\begin{aligned}
\langle \nabla \gamma_\beta \rangle &= \nabla \langle \gamma_\beta \rangle + \frac{1}{V}\int_{\mathcal{A}_{\beta\sigma}} \mathbf{n}_{\beta\sigma} dA \\
&= \nabla \varepsilon_\beta + \frac{1}{V}\int_{\mathcal{A}_{\beta\sigma}} \mathbf{n}_{\beta\sigma} dA = 0
\end{aligned} \tag{7.52}$$

Therefore, we can eliminate terms $\langle u_\beta \rangle^\beta \nabla \varepsilon_\beta$ when adding Equations 7.51 and 7.50 into Equation 7.49 to obtain

$$\nabla \cdot \langle \mathbf{A}_\beta \cdot \nabla u_\beta \rangle \simeq \nabla \cdot \left[\varepsilon_\beta \mathbf{A}_\beta \cdot \left(\nabla \langle u_\beta \rangle^\beta + \frac{1}{V_\beta}\int_{\mathcal{A}_{\beta\sigma}} \mathbf{n}_{\beta\sigma} \tilde{u}_\beta dA \right) \right]. \tag{7.53}$$

We have also extracted $\mathbf{A}_\beta$ from the integrals using the assumption that the porous medium is homogeneous. The second term on the RHS of Equation 7.48 can be treated as follows:

$$\nabla \cdot \langle \mathrm{Pe}_\beta^\ell \mathbf{v}_\beta u_\beta \rangle \simeq \nabla \cdot \left(\mathrm{Pe}_\beta^\ell \langle \mathbf{v}_\beta u_\beta \rangle \right), \tag{7.54}$$

with

$$\langle \mathbf{v}_\beta u_\beta \rangle \simeq \varepsilon_\beta \langle \mathbf{v}_\beta \rangle^\beta \langle u_\beta \rangle^\beta + \langle \tilde{\mathbf{v}}_\beta \tilde{u}_\beta \rangle, \tag{7.55}$$

that can be proven using $\langle \tilde{\mathbf{v}}_\beta \rangle \simeq 0$ and $\langle \tilde{u}_\beta \rangle \simeq 0$ (see [17,37]). Therefore, Equation 7.48 may be approximated by

$$\begin{aligned}\langle \mathcal{L}_\beta u_\beta \rangle \simeq \nabla \cdot \left[\varepsilon_\beta \mathbf{A}_\beta \cdot \left(\nabla \langle u_\beta \rangle^\beta + \frac{1}{V_\beta} \int_{\mathcal{A}_{\beta\sigma}} \mathbf{n}_{\beta\sigma} \tilde{u}_\beta dA \right) \right] \\ + \frac{1}{V} \int_{\mathcal{A}_{\beta\sigma}} \mathbf{n}_{\beta\sigma} \cdot \left(\mathbf{A}_\beta \cdot \nabla u_\beta \right) dA \\ - \nabla \cdot \left(\mathrm{Pe}_\beta^\ell \langle \tilde{\mathbf{v}}_\beta \tilde{u}_\beta \rangle \right) - \nabla \cdot \left(\varepsilon_\beta \mathrm{Pe}_\beta^\ell \langle \mathbf{v}_\beta \rangle^\beta \langle u_\beta \rangle^\beta \right). \end{aligned} \tag{7.56}$$

Using this result, we can rewrite the average equation over the phase β as

$$\begin{aligned}\varepsilon_\beta \Bigg[\underbrace{\partial_t \langle u_\beta \rangle^\beta}_{\text{Rate of change}} + \underbrace{\nabla \cdot \left(\mathrm{Pe}_\beta^\ell \langle \mathbf{v}_\beta \rangle^\beta \langle u_\beta \rangle^\beta \right)}_{\text{Convection}} + \underbrace{\nabla \cdot \left(\mathrm{Pe}_\beta^\ell \langle \tilde{\mathbf{v}}_\beta \tilde{u}_\beta \rangle^\beta \right)}_{\text{Velocity fluctuation effects}} \Bigg] \\ = \nabla \cdot \left[\varepsilon_\beta \mathbf{A}_\beta \cdot \left(\underbrace{\nabla \langle u_\beta \rangle^\beta}_{\text{Diffusion}} + \underbrace{\frac{1}{V_\beta} \int_{\mathcal{A}_{\beta\sigma}} \mathbf{n}_{\beta\sigma} \tilde{u}_\beta dA}_{\text{Surface effects}} \right) \right] \\ \underbrace{+ \frac{1}{V} \int_{\mathcal{A}_{\beta\sigma}} \mathbf{n}_{\beta\sigma} \cdot \left(\mathbf{A}_\beta \cdot \nabla u_\beta \right) dA}_{\text{Interfacial flux}} + \underbrace{\langle R_\beta (u_\beta) \rangle}_{\text{Average reaction rate}} . \end{aligned} \tag{7.57}$$

For the solid phase, similar manipulations of the average and differential operators yield an identical expression, minus the convection and velocity fluctuation terms:

$$\begin{aligned}\varepsilon_\sigma \Gamma_a \underbrace{\partial_t \langle u_\sigma \rangle^\sigma}_{\text{Rate of change}} = \nabla \cdot \left[\varepsilon_\sigma \Gamma_A \mathbf{A}_\sigma \cdot \left(\underbrace{\nabla \langle u_\sigma \rangle^\sigma}_{\text{Diffusion}} + \underbrace{\frac{1}{V_\sigma} \int_{\mathcal{A}_{\sigma\beta}} \mathbf{n}_{\sigma\beta} \tilde{u}_\sigma dA}_{\text{Surface effects}} \right) \right] \\ \underbrace{+ \frac{1}{V} \int_{\mathcal{A}_{\beta\sigma}} \mathbf{n}_{\sigma\beta} \cdot \left(\Gamma_A \mathbf{A}_\sigma \cdot \nabla u_\sigma \right) dA}_{\text{Interfacial flux}} + \underbrace{\langle R_\sigma (u_\sigma) \rangle}_{\text{Average reaction rate}} . \end{aligned} \tag{7.58}$$

We remark that these equations use approximations, in particular the fact that average quantities are quasi-linear within the REV. This is a form of spatial localization that allows us to extract such variables from the differential operators and integrals. These equations provide insight into the physics of the problem, as we can clearly identify, for example, fluxes and surface effects. Mathematically, however, it is convenient to use Equations 7.45 and 7.46 to derive the perturbation problem.

7.5.2 Perturbation

We now focus on the equations that describe the behavior of the perturbations. Recall that these perturbations are defined as $\tilde{u}_\beta = u_\beta - \langle u_\beta \rangle^\beta$ and $\tilde{u}_\sigma = u_\sigma - \langle u_\sigma \rangle^\sigma$. Therefore, the perturbation equations are obtained by performing the following operations: (Equation 7.6a minus ε_β^{-1} times Equation 7.45) and (Equation 7.6d minus ε_σ^{-1} times Equation 7.46). This results in the following two problems:

$$\partial_t \tilde{u}_\beta - \widetilde{\mathcal{L}_\beta \tilde{u}_\beta} - \widetilde{R_\beta (u_\beta)} = \widetilde{\mathcal{L}_\beta \langle u_\beta \rangle^\beta} \text{ in } \mathcal{V}_\beta, \tag{7.59}$$

$$\Gamma_a \partial_t \tilde{u}_\sigma - \widetilde{\mathcal{L}_\sigma \tilde{u}_\sigma} - \widetilde{R_\sigma\left(u_\sigma\right)} = \widetilde{\mathcal{L}_\sigma \left\langle u_\sigma \right\rangle^\sigma} \text{ in } \mathcal{V}_\sigma, \tag{7.60}$$

where we have organized the equations with the microscale differential operators on the left-hand side (LHS) and the macroscale source terms on the RHS. We have also used the following notation for the perturbation differential operators:

$$\widetilde{\mathcal{L}_\beta \phi_\beta} = \mathcal{L}_\beta \phi_\beta - \left\langle \mathcal{L}_\beta \phi_\beta \right\rangle^\beta = \nabla \cdot \left(\mathbf{A}_\beta \cdot \nabla \phi_\beta - \mathrm{Pe}_\beta^\ell \mathbf{v}_\beta \phi_\beta \right) - \left\langle \nabla \cdot \left(\mathbf{A}_\beta \cdot \nabla \phi_\beta - \mathrm{Pe}_\beta^\ell \mathbf{v}_\beta \phi_\beta \right) \right\rangle^\beta, \tag{7.61}$$

in the phase β and

$$\widetilde{\mathcal{L}_\sigma \phi_\sigma} = \mathcal{L}_\sigma \phi_\sigma - \left\langle \mathcal{L}_\sigma \phi_\sigma \right\rangle^\sigma = \nabla \cdot \left(\Gamma_A \mathbf{A}_\sigma \cdot \nabla \phi_\sigma \right) - \left\langle \nabla \cdot \left(\Gamma_A \mathbf{A}_\sigma \cdot \nabla \phi_\sigma \right) \right\rangle^\sigma, \tag{7.62}$$

in the phase σ. Similarly, the reaction rate perturbation functions are defined by

$$\widetilde{R_\beta\left(\phi_\beta\right)} = R_\beta\left(\phi_\beta\right) - \left\langle R_\beta\left(\phi_\beta\right) \right\rangle^\beta, \tag{7.63}$$

$$\widetilde{R_\sigma\left(\phi_\sigma\right)} = R_\sigma\left(\phi_\sigma\right) - \left\langle R_\sigma\left(\phi_\sigma\right) \right\rangle^\sigma. \tag{7.64}$$

The corresponding boundary conditions are obtained by introducing the average plus perturbation decomposition in Equations 7.6b and c:

$$\tilde{u}_\beta - \tilde{u}_\sigma = -\left(\left\langle u_\beta \right\rangle^\beta - \left\langle u_\sigma \right\rangle^\sigma \right) \text{ on } \mathcal{A}_{\beta\sigma}, \tag{7.65}$$

$$\mathcal{B}_\beta \tilde{u}_\beta - \mathcal{B}_\beta \tilde{u}_\sigma = -\left(\mathcal{B}_\beta \left\langle u_\beta \right\rangle^\beta - \mathcal{B}_\sigma \left\langle u_\sigma \right\rangle^\sigma \right) + \Omega\left(u_\sigma\right) \text{ on } \mathcal{A}_{\beta\sigma}, \tag{7.66}$$

with

$$-\left(\mathcal{B}_\beta \left\langle u_\beta \right\rangle^\beta - \mathcal{B}_\sigma \left\langle u_\sigma \right\rangle^\sigma \right) = \mathbf{n}_{\beta\sigma} \cdot \left(\mathbf{A}_\beta \cdot \nabla \left\langle u_\beta \right\rangle^\beta - \Gamma_A \mathbf{A}_\sigma \cdot \nabla \left\langle u_\sigma \right\rangle^\sigma \right). \tag{7.67}$$

7.5.3 Approximations

So far, except during the digression that resulted in Equations 7.57 and 7.58, we have not made scaling approximations. Further progress, however, requires such approximations that we present in this section.

7.5.3.1 Spatial Frequency Approximation

Effective medium theories usually require a notion of separation of length scales. In our approach, this can be expressed as spatial localization constraints imposed upon averaged fields. Roughly speaking, we assume that average quantities are quasi-linear within the REV since they vary over

the macroscopic length scale, L. This simplification allows us to extract average quantities from microscale differential operators and integrals. For instance, consider that

$$\left\langle \nabla\cdot\left(\Gamma_A\mathbf{A}_\sigma\cdot\nabla\langle u_\sigma\rangle^\sigma\right)\right\rangle^\sigma = \nabla\cdot\left[\Gamma_A\mathbf{A}_\sigma\cdot\left(\nabla\langle u_\sigma\rangle^\sigma+\frac{1}{V_\sigma}\int_{\mathcal{A}_{\sigma\beta}}\mathbf{n}_{\sigma\beta}\langle u_\sigma\rangle^\sigma dA\right)\right] + \frac{1}{V}\int_{\mathcal{A}_{\beta\sigma}}\mathbf{n}_{\sigma\beta}\cdot\left(\Gamma_A\mathbf{A}_\sigma\cdot\nabla\langle u_\sigma\rangle^\sigma\right)dA. \tag{7.68}$$

We assume that $\langle u_\sigma\rangle^\sigma$ and $\nabla\langle u_\sigma\rangle^\sigma$ vary slowly in space so that we have

$$\frac{1}{V_\sigma}\int_{\mathcal{A}_{\sigma\beta}}\mathbf{n}_{\sigma\beta}\langle u_\sigma\rangle^\sigma dA \simeq \left(\frac{1}{V_\sigma}\int_{\mathcal{A}_{\sigma\beta}}\mathbf{n}_{\sigma\beta}dA\right)\langle u_\sigma\rangle^\sigma \simeq 0, \tag{7.69}$$

for a homogeneous porous medium (constant porosity). Similarly,

$$\frac{1}{V}\int_{\mathcal{A}_{\beta\sigma}}\mathbf{n}_{\sigma\beta}\cdot\left(\Gamma_A\mathbf{A}_\sigma\cdot\nabla\langle u_\sigma\rangle^\sigma\right)dA \simeq \left(\frac{1}{V}\int_{\mathcal{A}_{\beta\sigma}}\mathbf{n}_{\sigma\beta}\cdot\Gamma_A\mathbf{A}_\sigma dA\right)\cdot\nabla\langle u_\sigma\rangle^\sigma \simeq 0. \tag{7.70}$$

Therefore, we obtain

$$\widetilde{\mathcal{L}_\sigma\langle u_\sigma\rangle^\sigma} = \nabla\cdot\left(\Gamma_A\mathbf{A}_\sigma\cdot\nabla\langle u_\sigma\rangle^\sigma\right) - \left\langle\nabla\cdot\left(\Gamma_A\mathbf{A}_\sigma\cdot\nabla\langle u_\sigma\rangle^\sigma\right)\right\rangle^\sigma \simeq 0. \tag{7.71}$$

For the phase β, we have

$$\widetilde{\mathcal{L}_\beta\langle u_\beta\rangle^\beta} \simeq -\mathrm{Pe}_\beta^\ell\tilde{\mathbf{v}}_\beta\cdot\nabla\langle u_\beta\rangle^\beta \equiv \widetilde{\mathcal{L}_\beta}\langle u_\beta\rangle^\beta. \tag{7.72}$$

These approximations can be further justified by considering Taylor expansions of the form

$$\langle u_\sigma\rangle^\sigma|_{\mathbf{x}+\mathbf{y}} = \langle u_\sigma\rangle^\sigma|_{\mathbf{x}} + \delta\mathbf{y}\cdot\nabla_L\langle u_\sigma\rangle^\sigma|_{\mathbf{x}} + \delta^2\mathbf{yy}:\nabla_L\nabla_L\langle u_\sigma\rangle^\sigma|_{\mathbf{x}} + \mathcal{O}\left(\delta^3\right), \tag{7.73}$$

where

- $\mathbf{x}$ is the center of the averaging volume
- $\mathbf{y}$ is the vector pointing inside the averaging volume
- ∇_L is rescaled with the macroscale length L so that $\left\|\nabla_L\langle u_\sigma\rangle^\sigma\right\| = \mathcal{O}(1)$ and $\delta = \dfrac{\ell}{L}$

In volume averaging, we often neglect terms involving $\mathbf{y}$ using $\delta \ll 1$ (see [39,40,117–119]).

7.5.3.2 Amplitude Approximation

In addition to these upscaling assumptions, we need to linearize the system to obtain a closure and an approximate form of the perturbations. We assume that perturbations are small enough so that

$$R_i\left(u_i\right) \simeq R_i\left(\left\langle u_i \right\rangle^i\right) \quad \text{and} \quad \Omega\left(u_A\right) \simeq \Omega\left(\left\langle u_\sigma \right\rangle^\sigma\right). \tag{7.74}$$

Such approximations are nonstandard, as volume averaging usually requires only *spatial* frequency approximations for linear operators. This is, however, a frequent approximation for nonlinear operators featuring changes in density, viscosity, diffusivities, and others (see example in [120] for the case of multicomponent mixtures). We emphasize that this approximation is very limiting and may break down relatively easily for large microscale gradients. This also implies that the closure problems are systematically independent from the reaction rates, an assumption that is known to hold when the Damköhler number is smaller than ≈ 10 (see [93]).

7.5.3.3 Simplified Form

We can now use approximations discussed earlier to obtain an approximate form of Equations 7.59 and 7.60 along with the boundary conditions (Equations 7.65 and 7.66). This yields

$$\partial_t \tilde{u}_\beta - \widetilde{\mathcal{L}_\beta \tilde{u}_\beta} = -\mathrm{Pe}_\beta^\ell \tilde{\mathbf{v}}_\beta \cdot \nabla \left\langle u_\beta \right\rangle^\beta \text{ in } \mathcal{V}_\beta, \tag{7.75}$$

$$\Gamma_a \partial_t \tilde{u}_\sigma - \widetilde{\mathcal{L}_\sigma \tilde{u}_\sigma} = 0 \text{ in } \mathcal{V}_\sigma, \tag{7.76}$$

with the set of boundary conditions

$$\tilde{u}_\beta - \tilde{u}_\sigma = -\left(\left\langle u_\beta \right\rangle^\beta - \left\langle u_\sigma \right\rangle^\sigma\right) \text{ on } \mathcal{A}_{\beta\sigma}, \tag{7.77}$$

$$\mathcal{B}_\beta \tilde{u}_\beta - \mathcal{B}_\beta \tilde{u}_\sigma = \mathbf{n}_{\beta\sigma} \cdot \left(\mathbf{A}_\beta \cdot \nabla \left\langle u_\beta \right\rangle^\beta - \Gamma_A \mathbf{A}_\sigma \cdot \nabla \left\langle u_\sigma \right\rangle^\sigma\right) + \Omega\left(\left\langle u_\sigma \right\rangle^\sigma\right) \text{ on } \mathcal{A}_{\beta\sigma}, \tag{7.78}$$

where sources appear on the RHS. At this point in the developments, we have obtained a linear IBVP for the perturbation. This problem still involves $\langle u_\sigma \rangle^\sigma$ and $\langle u_\beta \rangle^\beta$ so that the micro- and macroscale problems are still coupled.

7.5.4 Closure

Fortunately, there is only a weak coupling between the micro- and macroscale problems, and we can use the linearity of the spatial operators to decompose the perturbations into several components corresponding to each of the macroscopic source terms: $\langle u_\sigma \rangle^\sigma - \langle u_\beta \rangle^\beta$, $\nabla \langle u_\beta \rangle^\beta$, $\nabla \langle u_\sigma \rangle^\sigma$, and $\Omega(\langle u_\sigma \rangle^\sigma)$.

7.5.4.1 Two-Equation Transient Closure

A generic form of the solution reads

$$\begin{bmatrix} \tilde{u}_\beta \\ \tilde{u}_\sigma \end{bmatrix} = \partial_t \begin{bmatrix} \mathbf{a}_\beta^\star \\ \mathbf{a}_\sigma^\star \end{bmatrix} \star \left(\left\langle u_\beta \right\rangle^\beta - \left\langle u_\sigma \right\rangle^\sigma\right) + \partial_t \begin{bmatrix} \mathbf{b}_{\beta\beta}^\star & \mathbf{b}_{\beta\sigma}^\star \\ \mathbf{b}_{\sigma\beta}^\star & \mathbf{b}_{\sigma\sigma}^\star \end{bmatrix} \cdot \star \begin{bmatrix} \nabla \left\langle u_\beta \right\rangle^\beta \\ \nabla \left\langle u_\sigma \right\rangle^\sigma \end{bmatrix}$$
$$+ \partial_t \begin{bmatrix} \mathbf{W}_{\beta\beta}^\star & \mathbf{W}_{\beta\sigma}^\star \\ \mathbf{W}_{\sigma\beta}^\star & \mathbf{W}_{\sigma\sigma}^\star \end{bmatrix} : \star \begin{bmatrix} \nabla\nabla \left\langle u_\beta \right\rangle^\beta \\ \nabla\nabla \left\langle u_\sigma \right\rangle^\sigma \end{bmatrix} + \partial_t \begin{bmatrix} \mathbf{c}_\beta^\star \\ \mathbf{c}_\sigma^\star \end{bmatrix} \star \Omega\left(\left\langle u_\sigma \right\rangle^\sigma\right), \tag{7.79}$$

where $\star$ denotes a time convolution and

$$\begin{bmatrix} \mathsf{a}_\beta^\star \\ \mathsf{a}_\sigma^\star \end{bmatrix}, \quad \begin{bmatrix} \mathbf{b}_{\beta\beta}^\star & \mathbf{b}_{\beta\sigma}^\star \\ \mathbf{b}_{\sigma\beta}^\star & \mathbf{b}_{\sigma\sigma}^\star \end{bmatrix}, \quad \begin{bmatrix} \mathbf{W}_{\beta\beta}^\star & \mathbf{W}_{\beta\sigma}^\star \\ \mathbf{W}_{\sigma\beta}^\star & \mathbf{W}_{\sigma\sigma}^\star \end{bmatrix}, \quad \text{and} \quad \begin{bmatrix} \mathsf{c}_\beta^\star \\ \mathsf{c}_\sigma^\star \end{bmatrix}$$

are mapping variables. $\mathsf{a}_\alpha^\star$ and $\mathsf{c}_\alpha^\star$ are scalars, $\mathbf{b}_{\alpha\gamma}^\star$ are vectors, and $\mathbf{W}_{\alpha\gamma}^\star$ are dyadics. We have also used the convenient block notations

$$\begin{bmatrix} \mathbf{b}_{\beta\beta}^\star & \mathbf{b}_{\beta\sigma}^\star \\ \mathbf{b}_{\sigma\beta}^\star & \mathbf{b}_{\sigma\sigma}^\star \end{bmatrix} \cdot \star \begin{bmatrix} \nabla \langle u_\beta \rangle^\beta \\ \nabla \langle u_\sigma \rangle^\sigma \end{bmatrix} = \begin{bmatrix} \mathbf{b}_{\beta\beta}^\star \cdot \star \nabla \langle u_\beta \rangle^\beta + \mathbf{b}_{\beta\sigma}^\star \cdot \star \nabla \langle u_\sigma \rangle^\sigma \\ \mathbf{b}_{\sigma\beta}^\star \cdot \star \nabla \langle u_\beta \rangle^\beta + \mathbf{b}_{\sigma\sigma}^\star \cdot \star \nabla \langle u_\sigma \rangle^\sigma \end{bmatrix}, \tag{7.80}$$

and

$$\begin{bmatrix} \mathbf{W}_{\beta\beta}^\star & \mathbf{W}_{\beta\sigma}^\star \\ \mathbf{W}_{\sigma\beta}^\star & \mathbf{W}_{\sigma\sigma}^\star \end{bmatrix} : \star \begin{bmatrix} \nabla\nabla \langle u_\beta \rangle^\beta \\ \nabla\nabla \langle u_\sigma \rangle^\sigma \end{bmatrix} = \begin{bmatrix} \mathbf{W}_{\beta\beta}^\star : \star \nabla\nabla \langle u_\beta \rangle^\beta + \mathbf{W}_{\beta\sigma}^\star : \star \nabla\nabla \langle u_\sigma \rangle^\sigma \\ \mathbf{W}_{\sigma\beta}^\star : \star \nabla\nabla \langle u_\beta \rangle^\beta + \mathbf{W}_{\sigma\sigma}^\star : \star \nabla\nabla \langle u_\sigma \rangle^\sigma \end{bmatrix}, \tag{7.81}$$

with

$$\mathbf{b}^\star \cdot \star \nabla \langle u \rangle = \mathsf{b}_i^\star \star \partial_i \langle u \rangle = \int_0^t \mathsf{b}_i^\star (\tau) \partial_i \langle u \rangle (t - \tau) d\tau \quad \text{and} \quad \mathbf{W}^\star : \star \nabla\nabla \langle u \rangle = \mathsf{W}_{ij}^\star \star \partial_{ji} \langle u \rangle.$$

This is not obvious yet why we have chosen this specific decomposition Equation 7.79. It will become straightforward later on that this allows us to uncouple the micro- and macroscale problems.

7.5.4.2 Two-Equation Quasi-Stationary Closure

A simplification of this transient problem consists in considering that the timescales for the relaxation of the mapping variables are much faster than the variations of the corresponding macroscale quantities, $\langle u_\beta \rangle^\beta - \langle u_\sigma \rangle^\sigma$, $\left[\nabla \langle u_\beta \rangle^\beta \ \nabla \langle u_\sigma \rangle^\sigma \right]^T$, $\left[\nabla\nabla \langle u_\beta \rangle^\beta \ \nabla\nabla \langle u_\sigma \rangle^\sigma \right]^T$, and $\Omega(\langle u_\sigma \rangle^\sigma)$. When this holds, we can ignore the transient behavior of the mapping variables and use the following form:

$$\begin{bmatrix} \tilde{u}_\beta \\ \tilde{u}_\sigma \end{bmatrix} = \begin{bmatrix} \mathsf{a}_\beta \\ \mathsf{a}_\sigma \end{bmatrix} \left(\langle u_\beta \rangle^\beta - \langle u_\sigma \rangle^\sigma \right) + \begin{bmatrix} \mathbf{b}_{\beta\beta} & \mathbf{b}_{\beta\sigma} \\ \mathbf{b}_{\sigma\beta} & \mathbf{b}_{\sigma\sigma} \end{bmatrix} \cdot \begin{bmatrix} \nabla \langle u_\beta \rangle^\beta \\ \nabla \langle u_\sigma \rangle^\sigma \end{bmatrix}$$

$$+ \begin{bmatrix} \mathbf{W}_{\beta\beta} & \mathbf{W}_{\beta\sigma} \\ \mathbf{W}_{\sigma\beta} & \mathbf{W}_{\sigma\sigma} \end{bmatrix} : \begin{bmatrix} \nabla\nabla \langle u_\beta \rangle^\beta \\ \nabla\nabla \langle u_\sigma \rangle^\sigma \end{bmatrix} + \begin{bmatrix} \mathsf{c}_\beta \\ \mathsf{c}_\sigma \end{bmatrix} \Omega \left(\langle u_\sigma \rangle^\sigma \right). \tag{7.82}$$

Roughly speaking, in the limit where a function f relaxes infinitely fast toward a constant C with $f(t = 0) = 0$, we have $\partial_t f \star \langle u \rangle \simeq C \partial_t H \star \langle u \rangle = C \, \delta \star \langle u \rangle = C \langle u \rangle$, where H is the unit-step function and δ is a Dirac distribution.

7.5.4.3 Transient Closure Problems

The IBVPs corresponding to the mapping variables, which are often termed closure problems, can be obtained by introducing Equations 7.82 and 7.79 into Equations 7.75 through 7.78. To facilitate solution with the time convolutions, we can work in Laplace space where $\mathcal{T}f(t) = \underline{f}(p)$ denotes the Laplace transform and p is the Laplace variable (although it is not mandatory to do so, see, e.g., [78]). Applying this transform to Equation 7.79 with zero initial conditions yields

$$\begin{bmatrix} \underline{\tilde{u}}_\beta \\ \underline{\tilde{u}}_\sigma \end{bmatrix} = p \begin{bmatrix} \underline{\mathbf{a}}^\star_\beta \\ \underline{\mathbf{a}}^\star_\sigma \end{bmatrix} \left(\langle \underline{u}_\beta \rangle^\beta - \langle \underline{u}_\sigma \rangle^\sigma \right) + p \begin{bmatrix} \underline{\mathbf{b}}^\star_{\beta\beta} & \underline{\mathbf{b}}^\star_{\beta\sigma} \\ \underline{\mathbf{b}}^\star_{\sigma\beta} & \underline{\mathbf{b}}^\star_{\sigma\sigma} \end{bmatrix} \cdot \begin{bmatrix} \nabla \langle \underline{u}_\beta \rangle^\beta \\ \nabla \langle \underline{u}_\sigma \rangle^\sigma \end{bmatrix}$$

$$+ p \begin{bmatrix} \underline{\mathbf{W}}^\star_{\beta\beta} & \underline{\mathbf{W}}^\star_{\beta\sigma} \\ \underline{\mathbf{W}}^\star_{\sigma\beta} & \underline{\mathbf{W}}^\star_{\sigma\sigma} \end{bmatrix} : \begin{bmatrix} \nabla\nabla \langle \underline{u}_\beta \rangle^\beta \\ \nabla\nabla \langle \underline{u}_\sigma \rangle^\sigma \end{bmatrix} + p \begin{bmatrix} \underline{\mathbf{c}}^\star_\beta \\ \underline{\mathbf{c}}^\star_\sigma \end{bmatrix} \square \left(\langle \underline{u}_\sigma \rangle^\sigma \right). \tag{7.83}$$

Similarly, Equations 7.75 through 7.78 become

$$p\underline{\tilde{u}}_\beta - \widetilde{\mathcal{L}_\beta \underline{\tilde{u}}_\beta} = -\mathrm{Pe}^\ell_\beta \tilde{\mathbf{v}}_\beta \cdot \nabla \langle \underline{u}_\beta \rangle^\beta \text{ in } \mathcal{V}_\beta, \tag{7.84}$$

$$\Gamma_a p\underline{\tilde{u}}_\sigma - \widetilde{\mathcal{L}_\sigma \underline{\tilde{u}}_\sigma} = 0 \text{ in } \mathcal{V}_\sigma, \tag{7.85}$$

along with the set of boundary conditions

$$\underline{\tilde{u}}_\beta - \underline{\tilde{u}}_\sigma = -\left(\langle \underline{u}_\beta \rangle^\beta - \langle \underline{u}_\sigma \rangle^\sigma \right) \text{ on } \mathcal{A}_{\beta\sigma}, \tag{7.86}$$

$$\mathcal{B}_\beta \underline{\tilde{u}}_\beta - \mathcal{B}_\beta \underline{\tilde{u}}_\sigma = \mathbf{n}_{\beta\sigma} \cdot \left(\mathbf{A}_\beta \cdot \nabla \langle \underline{u}_\beta \rangle^\beta - \Gamma_A \mathbf{A}_\sigma \cdot \nabla \langle \underline{u}_\sigma \rangle^\sigma \right) + \underline{\Omega} \left(\langle u_\sigma \rangle^\sigma \right) \text{ on } \mathcal{A}_{\beta\sigma}. \tag{7.87}$$

We are looking for solutions that hold for any value of $\langle u_\beta \rangle^\beta - \langle u_\sigma \rangle^\sigma$, $\nabla \langle u_\beta \rangle^\beta \ldots$ This means that we can separate problems involving the different macroscopic source terms by identifying terms corresponding to the different source terms. In Laplace space, this leads to

$$p\underline{\mathbf{a}}^\star_\beta - \widetilde{\mathcal{L}_\beta \underline{\mathbf{a}}^\star_\beta} = 0 \text{ in } \mathcal{V}_\beta, \tag{7.88a}$$

$$\text{BC1} \quad \underline{\mathbf{a}}^\star_\beta - \underline{\mathbf{a}}^\star_\sigma = -\frac{1}{p} \text{ on } \mathcal{A}_{\beta\sigma}, \tag{7.88b}$$

$$\text{BC2} \quad \mathcal{B}_\beta \underline{\mathbf{a}}^\star_\beta - \mathcal{B}_\sigma \underline{\mathbf{a}}^\star_\sigma = 0 \text{ on } \mathcal{A}_{\beta\sigma}, \tag{7.88c}$$

$$\Gamma_a p\underline{\mathbf{a}}^\star_\sigma - \widetilde{\mathcal{L}_\sigma \underline{\mathbf{a}}^\star_\sigma} = 0 \text{ in } \mathcal{V}_\sigma. \tag{7.88d}$$

Applying the inverse Laplace transform $\mathcal{T}^{-1}$ to these expressions yields the following:

7.5.4.3.1 Problem 2eq-Transient-I

$$\partial_t \mathbf{a}^\star_\beta - \widetilde{\mathcal{L}_\beta \mathbf{a}^\star_\beta} = 0 \text{ in } \mathcal{V}_\beta, \tag{7.89a}$$

$$\text{BC1} \quad \mathbf{a}^\star_\beta - \mathbf{a}^\star_\sigma = -H(t) \text{ on } \mathcal{A}_{\beta\sigma}, \tag{7.89b}$$

$$\text{BC2} \quad \mathcal{B}_\beta \mathsf{a}^\star_\beta - \mathcal{B}_\sigma \mathsf{a}^\star_\sigma = 0 \text{ on } \mathcal{A}_{\beta\sigma}, \tag{7.89c}$$

$$\text{Periodicity 1} \quad \mathsf{a}^\star_\alpha\left(\mathbf{x}+\mathbf{l}_i\right) = \mathsf{a}^\star_\alpha\left(\mathbf{x}\right) \text{with } \alpha = \beta,\sigma, \tag{7.89d}$$

$$\text{Periodicity 2} \quad \mathcal{J}_\alpha \mathsf{a}^\star_\alpha\left(\mathbf{x}+\mathbf{l}_i\right) = \mathcal{J}_\alpha \mathsf{a}^\star_\alpha\left(\mathbf{x}\right) \text{with } \alpha = \beta,\sigma, \tag{7.89e}$$

$$\text{Average} \quad \left\langle \mathsf{a}^\star_\alpha \right\rangle = 0 \text{ with } \alpha = \beta,\sigma, \tag{7.89f}$$

$$\Gamma_a \partial_t \mathsf{a}^\star_\sigma - \widetilde{\mathcal{L}_\sigma \mathsf{a}^\star_\sigma} = 0 \text{ in } \mathcal{V}_\sigma, \tag{7.89g}$$

where we have used the flux notation

$$\mathcal{J}_\beta \phi_\beta = -\mathbf{A}_\beta \cdot \nabla \phi_\beta + \mathrm{Pe}^\ell_\beta \mathbf{v}_\beta \phi_\beta, \tag{7.90}$$

$$\mathcal{J}_\sigma \phi_\sigma = -\Gamma_A \mathbf{A}_\sigma \cdot \nabla \phi_\sigma. \tag{7.91}$$

We have also completed the problem with periodicity conditions ($\mathbf{l}_i$ are the periodicity vectors, with $i = 1, 2, 3$ for $\mathbf{x} \in \mathbb{R}^3$) and have introduced the average conditions $\left\langle \mathsf{a}^\star_\alpha \right\rangle = 0$, which are derived from $\left\langle \tilde{u}_\alpha \right\rangle \simeq 0$. Indeed, recall that $u_\alpha = \left\langle u_\alpha \right\rangle^\alpha + \tilde{u}_\alpha$, so that averaging yields $\left\langle u_\alpha \right\rangle^\alpha = \left\langle \left\langle u_\alpha \right\rangle^\alpha \right\rangle^\alpha + \left\langle \tilde{u}_\alpha \right\rangle^\alpha$. The localization (frequency assumption) leads to $\left\langle \left\langle u_\alpha \right\rangle^\alpha \right\rangle^\alpha \simeq \left\langle u_\alpha \right\rangle^\alpha$, so that $\left\langle \tilde{u}_\alpha \right\rangle \simeq 0$. On introducing Equation 7.79 in $\left\langle \tilde{u}_\alpha \right\rangle \simeq 0$ and identifying terms that are $\mathcal{O}\left(\left\langle u_\beta \right\rangle^\beta - \left\langle u_\sigma \right\rangle^\sigma\right)$, we obtain $\left\langle \mathsf{a}^\star_\alpha \right\rangle = 0$.

An identical procedure for the other source terms leads to the following sequence of closure problems:

7.5.4.3.2 Problem 2eq-Transient-II

$$\partial_t \mathbf{b}^\star_{\beta\beta} - \widetilde{\mathcal{L}_\beta \mathbf{b}^\star_{\beta\beta}} + \widetilde{\mathcal{J}_\beta \mathsf{a}^\star_\beta} = \mathbf{A}_\beta \cdot \widetilde{\nabla \mathsf{a}^\star_\beta} - \mathrm{Pe}^\ell_\beta \tilde{\mathbf{v}}_\beta H\left(t\right) \text{ in } \mathcal{V}_\beta, \tag{7.92a}$$

$$\text{BC1} \quad \mathbf{b}^\star_{\beta\beta} - \mathbf{b}^\star_{\sigma\beta} = 0 \text{ on } \mathcal{A}_{\beta\sigma}, \tag{7.92b}$$

$$\text{BC2} \quad \mathcal{B}_\beta \mathbf{b}^\star_{\beta\beta} - \mathcal{B}_\sigma \mathbf{b}^\star_{\sigma\beta} = \mathbf{n}_{\beta\sigma} \cdot \left[\mathbf{A}_\beta\left(H\left(t\right) + \mathsf{a}^\star_\beta\right) - \Gamma_A \mathbf{A}_\sigma \mathsf{a}^\star_\sigma\right] \text{ on } \mathcal{A}_{\beta\sigma}, \tag{7.92c}$$

$$\text{Periodicity 1} \quad \mathbf{b}^\star_{\alpha\beta}\left(\mathbf{x}+\mathbf{l}_i\right) = \mathbf{b}^\star_{\alpha\beta}\left(\mathbf{x}\right) \text{with } \alpha = \beta,\sigma, \tag{7.92d}$$

$$\text{Periodicity 2} \quad \mathcal{J}_\alpha \mathbf{b}^\star_{\alpha\beta}\left(\mathbf{x}+\mathbf{l}_i\right) = \mathcal{J}_\alpha \mathbf{b}^\star_{\alpha\beta}\left(\mathbf{x}\right) \text{ with } \alpha = \beta,\sigma, \tag{7.92e}$$

$$\text{Average} \quad \left\langle \mathbf{b}^\star_{\alpha\beta} \right\rangle = 0 \text{ with } \alpha = \beta,\sigma, \tag{7.92f}$$

$$\Gamma_a \partial_t \mathbf{b}^\star_{\sigma\beta} - \widetilde{\mathcal{L}_\sigma \mathbf{b}^\star_{\sigma\beta}} + \widetilde{\mathcal{J}_\sigma \mathsf{a}^\star_\sigma} = \Gamma_A \mathbf{A}_\sigma \cdot \widetilde{\nabla \mathsf{a}^\star_\sigma} \text{ in } \mathcal{V}_\sigma. \tag{7.92g}$$

7.5.4.3.3 Problem 2eq-Transient-III

$$\partial_t \mathbf{b}^\star_{\beta\sigma} - \widetilde{\mathcal{L}_\beta \mathbf{b}^\star_{\beta\sigma}} - \widetilde{\mathcal{J}_\beta \mathbf{a}^\star_\beta} = -\mathbf{A}_\beta \cdot \widetilde{\nabla \mathbf{a}^\star_\beta} \text{ in } \mathcal{V}_\beta, \tag{7.93a}$$

$$\text{BC1} \quad \mathbf{b}^\star_{\beta\sigma} - \mathbf{b}^\star_{\sigma\sigma} = 0 \text{ on } \mathcal{A}_{\beta\sigma}, \tag{7.93b}$$

$$\text{BC2} \quad \mathcal{B}_\beta \mathbf{b}^\star_{\beta\sigma} - \mathcal{B}_\sigma \mathbf{b}^\star_{\sigma\sigma} = \mathbf{n}_{\beta\sigma} \cdot \left[-\mathbf{A}_\beta \mathbf{a}^\star_\beta + \Gamma_A \mathbf{A}_\sigma \left(-H(t) + \mathbf{a}^\star_\sigma \right) \right] \text{ on } \mathcal{A}_{\beta\sigma}, \tag{7.93c}$$

$$\text{Periodicity 1} \quad \mathbf{b}^\star_{\alpha\sigma}(\mathbf{x} + \mathbf{l}_i) = \mathbf{b}^\star_{\alpha\sigma}(\mathbf{x}) \text{ with } \alpha = \beta, \sigma, \tag{7.93d}$$

$$\text{Periodicity 2} \quad \mathcal{J}_\alpha \mathbf{b}^\star_{\alpha\sigma}(\mathbf{x} + \mathbf{l}_i) = \mathcal{J}_\alpha \mathbf{b}^\star_{\alpha\sigma}(\mathbf{x}) \text{ with } \alpha = \beta, \sigma, \tag{7.93e}$$

$$\text{Average} \quad \left\langle \mathbf{b}^\star_{\alpha\sigma} \right\rangle = 0 \text{ with } \alpha = \beta, \sigma, \tag{7.93f}$$

$$\Gamma_a \partial_t \mathbf{b}^\star_{\sigma\sigma} - \widetilde{\mathcal{L}_\sigma \mathbf{b}^\star_{\sigma\sigma}} - \widetilde{\mathcal{J}_\sigma \mathbf{a}^\star_\sigma} = -\Gamma_A \mathbf{A}_\sigma \cdot \widetilde{\nabla \mathbf{a}^\star_\sigma} \text{ in } \mathcal{V}_\sigma. \tag{7.93g}$$

7.5.4.3.4 Problem 2eq-Transient-IV

$$\partial_t \mathbf{W}^\star_{\beta\beta} - \widetilde{\mathcal{L}_\beta \mathbf{W}^\star_{\beta\beta}} + \widetilde{\mathcal{J}_\beta \mathbf{b}^\star_{\beta\beta}} = \mathbf{A}_\beta \cdot \widetilde{\nabla \mathbf{b}^\star_{\beta\beta}} + \mathbf{A}_\beta \mathbf{a}^\star_\beta \text{ in } \mathcal{V}_\beta, \tag{7.94a}$$

$$\text{BC1} \quad \mathbf{W}^\star_{\beta\beta} - \mathbf{W}^\star_{\sigma\beta} = 0 \text{ on } \mathcal{A}_{\beta\sigma}, \tag{7.94b}$$

$$\text{BC2} \quad \mathcal{B}_\beta \mathbf{W}^\star_{\beta\beta} - \mathcal{B}_\sigma \mathbf{W}^\star_{\sigma\beta} = \mathbf{n}_{\beta\sigma} \cdot \left(\mathbf{A}_\beta \mathbf{b}^\star_{\beta\beta} - \Gamma_A \mathbf{A}_\sigma \mathbf{b}^\star_{\sigma\beta} \right) \text{ on } \mathcal{A}_{\beta\sigma}, \tag{7.94c}$$

$$\text{Periodicity 1} \quad \mathbf{W}^\star_{\alpha\beta}(\mathbf{x} + \mathbf{l}_i) = \mathbf{W}^\star_{\alpha\beta}(\mathbf{x}) \text{ with } \alpha = \beta, \sigma, \tag{7.94d}$$

$$\text{Periodicity 2} \quad \mathcal{J}_\alpha \mathbf{W}^\star_{\alpha\beta}(\mathbf{x} + \mathbf{l}_i) = \mathcal{J}_\alpha \mathbf{W}^\star_{\alpha\beta}(\mathbf{x}) \text{ with } \alpha = \beta, \sigma, \tag{7.94e}$$

$$\text{Average} \quad \left\langle \mathbf{W}^\star_{\alpha\beta} \right\rangle = 0 \text{ with } \alpha = \beta, \sigma, \tag{7.94f}$$

$$\Gamma_a \partial_t \mathbf{W}^\star_{\sigma\beta} - \widetilde{\mathcal{L}_\sigma \mathbf{W}^\star_{\sigma\beta}} + \widetilde{\mathcal{J}_\sigma \mathbf{b}^\star_{\sigma\beta}} = \Gamma_A \mathbf{A}_\sigma \cdot \widetilde{\nabla \mathbf{b}^\star_{\sigma\beta}} + \Gamma_A \mathbf{A}_\sigma \mathbf{a}^\star_\sigma \text{ in } \mathcal{V}_\sigma. \tag{7.94g}$$

7.5.4.3.5 Problem 2eq-Transient-V

$$\partial_t \mathbf{W}^\star_{\beta\sigma} - \widetilde{\mathcal{L}_\beta \mathbf{W}^\star_{\beta\sigma}} + \widetilde{\mathcal{J}_\beta \mathbf{b}^\star_{\beta\sigma}} = \mathbf{A}_\beta \cdot \widetilde{\nabla \mathbf{b}^\star_{\beta\sigma}} - \mathbf{A}_\beta \mathbf{a}^\star_\beta \text{ in } \mathcal{V}_\beta, \tag{7.95a}$$

$$\text{BC1} \quad \mathbf{W}^\star_{\beta\sigma} - \mathbf{W}^\star_{\sigma\sigma} = 0 \text{ on } \mathcal{A}_{\beta\sigma}, \tag{7.95b}$$

$$\text{BC2} \quad \mathcal{B}_\beta \mathbf{W}^\star_{\beta\sigma} - \mathcal{B}_\sigma \mathbf{W}^\star_{\sigma\sigma} = \mathbf{n}_{\beta\sigma} \cdot \left(\mathbf{A}_\beta \mathbf{b}^\star_{\beta\sigma} - \Gamma_A \mathbf{A}_\sigma \mathbf{b}^\star_{\sigma\sigma} \right) \text{ on } \mathcal{A}_{\beta\sigma}, \tag{7.95c}$$

$$\text{Periodicity 1} \quad \mathbf{W}^{\star}_{\alpha\sigma}\left(\mathbf{x}+\mathbf{l}_i\right)=\mathbf{W}^{\star}_{\alpha\sigma}\left(\mathbf{x}\right) \text{ with } \alpha=\beta,\sigma, \tag{7.95d}$$

$$\text{Periodicity 2} \quad \mathcal{J}_{\alpha}\mathbf{W}^{\star}_{\alpha\sigma}\left(\mathbf{x}+\mathbf{l}_i\right)=\mathcal{J}_{\alpha}\mathbf{W}^{\star}_{\alpha\sigma}\left(\mathbf{x}\right) \text{ with } \alpha=\beta,\sigma, \tag{7.95e}$$

$$\text{Average} \quad \left\langle \mathbf{W}^{\star}_{\alpha\sigma}\right\rangle=0 \text{ with } \alpha=\beta,\sigma, \tag{7.95f}$$

$$\Gamma_a\partial_t\mathbf{W}^{\star}_{\sigma\sigma}-\widetilde{\mathcal{L}_{\sigma}\mathbf{W}^{\star}_{\sigma\sigma}}+\widetilde{\mathcal{J}_{\sigma}\mathbf{b}^{\star}_{\sigma\sigma}}=\Gamma_A\mathbf{A}_{\sigma}\cdot\widetilde{\nabla\mathbf{b}^{\star}_{\sigma\sigma}}-\Gamma_A\mathbf{A}_{\sigma}\mathbf{a}^{\star}_{\sigma} \text{ in } \mathcal{V}_{\sigma}. \tag{7.95g}$$

7.5.4.3.6 Problem 2eq-Transient-VI

$$\partial_t\mathsf{c}^{\star}_{\beta}-\widetilde{\mathcal{L}_{\beta}\mathsf{c}^{\star}_{\beta}}=0 \text{ in } \mathcal{V}_{\beta}, \tag{7.96a}$$

$$\text{BC1} \quad \mathsf{c}^{\star}_{\beta}-\mathsf{c}^{\star}_{\sigma}=0 \text{ on } \mathcal{A}_{\beta\sigma}, \tag{7.96b}$$

$$\text{BC2} \quad \mathcal{B}_{\beta}\mathsf{c}^{\star}_{\beta}-\mathcal{B}_{\sigma}\mathsf{c}^{\star}_{\sigma}=H\left(t\right) \text{ on } \mathcal{A}_{\beta\sigma}, \tag{7.96c}$$

$$\text{Periodicity 1} \quad \mathsf{c}^{\star}_{\alpha}\left(\mathbf{x}+\mathbf{l}_i\right)=\mathsf{c}^{\star}_{\alpha}\left(\mathbf{x}\right) \text{ with } \alpha=\beta,\sigma, \tag{7.96d}$$

$$\text{Periodicity 2} \quad \mathcal{J}_{\alpha}\mathsf{c}^{\star}_{\alpha}\left(\mathbf{x}+\mathbf{l}_i\right)=\mathcal{J}_{\alpha}\mathsf{c}^{\star}_{\alpha}\left(\mathbf{x}\right) \text{ with } \alpha=\beta,\sigma, \tag{7.96e}$$

$$\text{Average} \quad \left\langle \mathsf{c}^{\star}_{\alpha}\right\rangle=0 \text{ with } \alpha=\beta,\sigma, \tag{7.96f}$$

$$\Gamma_a\partial_t\mathsf{c}^{\star}_{\sigma}-\widetilde{\mathcal{L}_{\sigma}\mathsf{c}^{\star}_{\sigma}}=0 \text{ in } \mathcal{V}_{\sigma}. \tag{7.96g}$$

In most cases, these problems are coupled via flux terms. They appear when developing the derivatives of products. For example,

$$\begin{aligned}\mathcal{L}_{\sigma}\left[\mathsf{a}_{\sigma}\left(\left\langle u_{\beta}\right\rangle^{\beta}-\left\langle u_{\sigma}\right\rangle^{\sigma}\right)\right]=&\nabla\cdot\left(\Gamma_A\mathbf{A}_{\sigma}\cdot\nabla\mathsf{a}_{\sigma}\right)\left(\left\langle u_{\beta}\right\rangle^{\beta}-\left\langle u_{\sigma}\right\rangle^{\sigma}\right)\\&+2\left(\Gamma_A\mathbf{A}_{\sigma}\cdot\nabla\mathsf{a}_{\sigma}\right)\cdot\nabla\left(\left\langle u_{\beta}\right\rangle^{\beta}-\left\langle u_{\sigma}\right\rangle^{\sigma}\right)\\&+\Gamma_A\mathbf{A}_{\sigma}\mathsf{a}_{\sigma}:\nabla\nabla\left(\left\langle u_{\beta}\right\rangle^{\beta}-\left\langle u_{\sigma}\right\rangle^{\sigma}\right),\end{aligned} \tag{7.97}$$

therefore implying a coupling between a and $\mathbf{b}$ for $\mathcal{O}\left(\nabla\left\langle u_{\alpha}\right\rangle^{\alpha}\right)$ and between a and $\mathbf{W}$ for $\mathcal{O}\left(\nabla\nabla\left\langle u_{\alpha}\right\rangle^{\alpha}\right)$.

7.5.4.4 Stationary Closure Problems

The corresponding stationary closure problems for a, $\mathbf{b}$, $\mathbf{W}$, and c are obtained by removing the time derivatives and replacing $H(t)$ by 1 in the transient problems earlier. The notations are similar, except that we remove the upper $\star$ symbol from the variables.

7.5.5 Macroscale Models

Recall the average equations

$$\varepsilon_\beta \partial_t \langle u_\beta \rangle^\beta - \left\langle \mathcal{L}_\beta \langle u_\beta \rangle^\beta \right\rangle - \varepsilon_\beta R_\beta \left(\langle u_\beta \rangle^\beta \right) = \left\langle \mathcal{L}_\beta \tilde{u}_\beta \right\rangle, \tag{7.98}$$

$$\Gamma_a \varepsilon_\sigma \partial_t \langle u_\sigma \rangle^\sigma - \left\langle \mathcal{L}_\sigma \langle u_\sigma \rangle^\sigma \right\rangle - \varepsilon_\sigma R_\sigma \left(\langle u_\sigma \rangle^\sigma \right) = \left\langle \mathcal{L}_\sigma \tilde{u}_\sigma \right\rangle, \tag{7.99}$$

that are obtained by introducing the linearization of the reaction rate and the localization assumptions in Equations 7.45 and 7.46. We further explicitly detail the terms $\left\langle \mathcal{L}_\beta \langle u_\beta \rangle^\beta \right\rangle$ and $\left\langle \mathcal{L}_\sigma \langle u_\sigma \rangle^\sigma \right\rangle$ as

$$\begin{aligned} \left\langle \mathcal{L}_\beta \langle u_\beta \rangle^\beta \right\rangle &= \left\langle \nabla \cdot \left(\mathbf{A}_\beta \cdot \nabla \langle u_\beta \rangle^\beta - \mathrm{Pe}_\beta^\ell \mathbf{v}_\beta \langle u_\beta \rangle^\beta \right) \right\rangle \\ &\simeq \nabla \cdot \left(\varepsilon_\beta \mathbf{A}_\beta \cdot \nabla \langle u_\beta \rangle^\beta - \mathrm{Pe}_\beta^\ell \langle \mathbf{v}_\beta \rangle \langle u_\beta \rangle^\beta \right) \equiv \langle \mathcal{L}_\beta \rangle \langle u_\beta \rangle^\beta, \end{aligned} \tag{7.100}$$

$$\begin{aligned} \left\langle \mathcal{L}_\sigma \langle u_\sigma \rangle^\sigma \right\rangle &= \left\langle \nabla \cdot \left(\Gamma_A \mathbf{A}_\sigma \cdot \nabla \langle u_\sigma \rangle^\sigma \right) \right\rangle \\ &\simeq \nabla \cdot \left(\varepsilon_\sigma \Gamma_A \mathbf{A}_\sigma \cdot \nabla \langle u_\sigma \rangle^\sigma \right) \equiv \langle \mathcal{L}_\sigma \rangle \langle u_\sigma \rangle^\sigma, \end{aligned} \tag{7.101}$$

so that

$$\varepsilon_\beta \partial_t \langle u_\beta \rangle^\beta - \langle \mathcal{L}_\beta \rangle \langle u_\beta \rangle^\beta - \varepsilon_\beta R_\beta \left(\langle u_\beta \rangle^\beta \right) = \left\langle \mathcal{L}_\beta \tilde{u}_\beta \right\rangle, \tag{7.102}$$

$$\Gamma_a \varepsilon_\sigma \partial_t \langle u_\sigma \rangle^\sigma - \langle \mathcal{L}_\sigma \rangle \langle u_\sigma \rangle^\sigma - \varepsilon_\sigma R_\sigma \left(\langle u_\sigma \rangle^\sigma \right) = \left\langle \mathcal{L}_\sigma \tilde{u}_\sigma \right\rangle. \tag{7.103}$$

These equations are not in a closed form, since they involve the perturbations via the terms $\left\langle \mathcal{L}_\beta \tilde{u}_\beta \right\rangle$ and $\left\langle \mathcal{L}_\sigma \tilde{u}_\sigma \right\rangle$. The next step of the volume averaging process is to introduce the approximate analytical forms of the perturbations (Equations 7.79 and 7.82 in Equations 7.102 and 7.103).

7.5.5.1 Two-Equation Fully Transient

For the transient closure, we obtain

$$\begin{aligned} \left\langle \mathcal{L}_\beta \tilde{u}_\beta \right\rangle &= \left\langle \mathcal{L}_\beta \partial_t \mathsf{a}_\beta^\star \star \left(\langle u_\beta \rangle^\beta - \langle u_\sigma \rangle^\sigma \right) \right\rangle \\ &+ \left\langle \mathcal{L}_\beta \partial_t \begin{bmatrix} \mathbf{b}_{\beta\beta}^\star \\ \mathbf{b}_{\beta\sigma}^\star \end{bmatrix} \cdot \star \begin{bmatrix} \nabla \langle u_\beta \rangle^\beta \\ \nabla \langle u_\sigma \rangle^\sigma \end{bmatrix} \right\rangle \\ &+ \left\langle \mathcal{L}_\beta \partial_t \begin{bmatrix} \mathbf{W}_{\beta\beta}^\star \\ \mathbf{W}_{\sigma\beta}^\star \end{bmatrix} : \star \begin{bmatrix} \nabla\nabla \langle u_\beta \rangle^\beta \\ \nabla\nabla \langle u_\sigma \rangle^\sigma \end{bmatrix} \right\rangle \\ &+ \left\langle \mathcal{L}_\beta \partial_t \mathsf{c}_\beta^\star \star \Omega \left(\langle u_\sigma \rangle^\sigma \right) \right\rangle, \end{aligned} \tag{7.104}$$

using Equation 7.79. We now treat each term on the RHS of Equation 7.104 separately. For the first term, we obtain

$$\begin{aligned}\left\langle \mathcal{L}_\beta \partial_t \mathbf{a}_\beta^\star \star \left(\langle u_\beta \rangle^\beta - \langle u_\sigma \rangle^\sigma \right) \right\rangle \simeq\ & \partial_t \left\langle \mathcal{L}_\beta \mathbf{a}_\beta^\star \right\rangle \star \left(\langle u_\beta \rangle^\beta - \langle u_\sigma \rangle^\sigma \right) \\ & - \partial_t \left\langle \mathcal{J}_\beta \mathbf{a}_\beta^\star \right\rangle \cdot \star \nabla \left(\langle u_\beta \rangle^\beta - \langle u_\sigma \rangle^\sigma \right) \\ & + \partial_t \left\langle \mathbf{A}_\beta \cdot \nabla \mathbf{a}_\beta^\star \right\rangle \cdot \star \nabla \left(\langle u_\beta \rangle^\beta - \langle u_\sigma \rangle^\sigma \right), \end{aligned} \tag{7.105}$$

where terms in $\nabla\nabla$ have disappeared since $\left\langle \mathbf{a}_\alpha^\star \right\rangle = 0$. The second term on the RHS of Equation 7.104 yields

$$\begin{aligned}\left\langle \mathcal{L}_\beta \partial_t \begin{bmatrix} \mathbf{b}_{\beta\beta}^\star \\ \mathbf{b}_{\beta\sigma}^\star \end{bmatrix} \cdot \star \begin{bmatrix} \nabla \langle u_\beta \rangle^\beta \\ \nabla \langle u_\sigma \rangle^\sigma \end{bmatrix} \right\rangle \simeq\ & \partial_t \left\langle \mathcal{L}_\beta \begin{bmatrix} \mathbf{b}_{\beta\beta}^\star \\ \mathbf{b}_{\beta\sigma}^\star \end{bmatrix} \right\rangle \cdot \star \begin{bmatrix} \nabla \langle u_\beta \rangle^\beta \\ \nabla \langle u_\sigma \rangle^\sigma \end{bmatrix} \\ & - \partial_t \left\langle \mathcal{J}_\beta \begin{bmatrix} \mathbf{b}_{\beta\beta}^\star \\ \mathbf{b}_{\beta\sigma}^\star \end{bmatrix} \right\rangle : \star \begin{bmatrix} \nabla\nabla \langle u_\beta \rangle^\beta \\ \nabla\nabla \langle u_\sigma \rangle^\sigma \end{bmatrix} \\ & \square \partial_t \left\langle \mathbf{A}_\beta \cdot \nabla \begin{bmatrix} \mathbf{b}_{\beta\beta}^\star \\ \mathbf{b}_{\beta\sigma}^\star \end{bmatrix} \right\rangle : \star \begin{bmatrix} \nabla\nabla \langle u_\beta \rangle^\beta \\ \nabla\nabla \langle u_\sigma \rangle^\sigma \end{bmatrix}. \end{aligned} \tag{7.106}$$

The third term on the RHS of Equation 7.104 can be written as

$$\left\langle \mathcal{L}_\beta \partial_t \begin{bmatrix} \mathbf{W}_{\beta\beta}^\star \\ \mathbf{W}_{\sigma\beta}^\star \end{bmatrix} : \star \begin{bmatrix} \nabla\nabla \langle u_\beta \rangle^\beta \\ \nabla\nabla \langle u_\sigma \rangle^\sigma \end{bmatrix} \right\rangle \simeq \partial_t \left\langle \mathcal{L}_\beta \begin{bmatrix} \mathbf{W}_{\beta\beta}^\star \\ \mathbf{W}_{\sigma\beta}^\star \end{bmatrix} \right\rangle : \star \begin{bmatrix} \nabla\nabla \langle u_\beta \rangle^\beta \\ \nabla\nabla \langle u_\sigma \rangle^\sigma \end{bmatrix} \tag{7.107}$$

Finally, the last term on the RHS of Equation 7.104 reads

$$\left\langle \mathcal{L}_\beta \partial_t \mathbf{c}_\beta^\star \star \Omega \left(\langle u_\sigma \rangle^\sigma \right) \right\rangle \simeq \partial_t \left\langle \mathcal{L}_\beta \mathbf{c}_\beta^\star \right\rangle \star \Omega \left(\langle u_\sigma \rangle^\sigma \right). \tag{7.108}$$

We can combine these equations to obtain an approximate form of Equation 7.104:

$$\begin{aligned}\left\langle \mathcal{L}_\beta \tilde{u}_\beta \right\rangle \simeq\ & \partial_t \left\langle \mathcal{L}_\beta \mathbf{a}_\beta^\star \right\rangle \star \left(\langle u_\beta \rangle^\beta - \langle u_\sigma \rangle^\sigma \right) + \partial_t \left\langle \mathcal{L}_\beta \begin{bmatrix} \mathbf{b}_{\beta\beta}^\star \\ \mathbf{b}_{\beta\sigma}^\star \end{bmatrix} \right\rangle \cdot \star \begin{bmatrix} \nabla \langle u_\beta \rangle^\beta \\ \nabla \langle u_\sigma \rangle^\sigma \end{bmatrix} \\ & + \left\langle -\mathcal{J}_\beta \mathbf{a}_\beta^\star + \mathbf{A}_\beta \cdot \nabla \mathbf{a}_\beta^\star \right\rangle \cdot \star \nabla \left(\langle u_\beta \rangle^\beta - \langle u_\sigma \rangle^\sigma \right) \\ & + \partial_t \left\langle \mathcal{L}_\beta \begin{bmatrix} \mathbf{W}_{\beta\beta}^\star \\ \mathbf{W}_{\sigma\beta}^\star \end{bmatrix} - \mathcal{J}_\beta \begin{bmatrix} \mathbf{b}_{\beta\beta}^\star \\ \mathbf{b}_{\beta\sigma}^\star \end{bmatrix} + \mathbf{A}_\beta \cdot \nabla \begin{bmatrix} \mathbf{b}_{\beta\beta}^\star \\ \mathbf{b}_{\beta\sigma}^\star \end{bmatrix} \right\rangle : \star \begin{bmatrix} \nabla\nabla \langle u_\beta \rangle^\beta \\ \nabla\nabla \langle u_\sigma \rangle^\sigma \end{bmatrix} \\ & + \partial_t \left\langle \mathcal{L}_\beta \mathbf{c}_\beta^\star \right\rangle \star \square \left(\langle u_\sigma \rangle^\sigma \right). \end{aligned} \tag{7.109}$$

The closed macroscale model for the phase β can be written as

$$\varepsilon_\beta \partial_t \langle u_\beta \rangle^\beta - \langle \mathcal{L}_\beta \rangle \langle u_\beta \rangle^\beta - \varepsilon_\beta R_\beta \left(\langle u_\beta \rangle^\beta \right) = -\nabla \cdot \left(\partial_t \mathbf{d}^\star_{\beta\beta} \star \langle u_\beta \rangle^\beta \right) - \nabla \cdot \left(\partial_t \mathbf{d}^\star_{\beta\sigma} \star \langle u_\sigma \rangle^\sigma \right) + \nabla \cdot \left(\partial_t \mathbf{B}^\star_{\beta\beta} \cdot \star \nabla \langle u_\beta \rangle^\beta \right) + \nabla \cdot \left(\partial_t \mathbf{B}^\star_{\beta\sigma} \cdot \star \nabla \langle u_\sigma \rangle^\sigma \right) + \partial_t h^\star_\beta \star \left(\langle u_\beta \rangle^\beta - \langle u_\sigma \rangle^\sigma \right) + a_v \partial_t \xi^\star_\beta \star \Omega \left(\langle u_\sigma \rangle^\sigma \right), \quad (7.110)$$

where $a_v = A_{\sigma\beta}/V$ is the specific surface.

The effective velocity-like terms, $\mathbf{d}_{\beta\beta}$ and $\mathbf{d}_{\beta\sigma}$, are

$$\mathbf{d}^\star_{\beta\beta} = -\left\langle \mathcal{L}_\beta \mathbf{b}^\star_{\beta\beta} - \mathcal{J}_\beta \mathbf{a}^\star_\beta + \mathbf{A}_\beta \cdot \nabla \mathbf{a}^\star_\beta \right\rangle, \quad (7.111)$$

$$\mathbf{d}^\star_{\beta\sigma} = -\left\langle \mathcal{L}_\beta \mathbf{b}^\star_{\beta\sigma} + \mathcal{J}_\beta \mathbf{a}^\star_\beta - \mathbf{A}_\beta \cdot \nabla \mathbf{a}^\star_\beta \right\rangle. \quad (7.112)$$

Similarly, dispersion-like effective parameters, $\mathbf{B}_{\beta\beta}$ and $\mathbf{B}_{\beta\sigma}$, may be written as

$$\mathbf{B}^\star_{\beta\beta} = \left\langle \mathcal{L}_\beta \mathbf{W}^\star_{\beta\beta} - \mathcal{J}_\beta \mathbf{b}^\star_{\beta\beta} + \mathbf{A}_\beta \cdot \nabla \mathbf{b}^\star_{\beta\beta} \right\rangle, \quad (7.113)$$

$$\mathbf{B}^\star_{\beta\sigma} = \left\langle \mathcal{L}_\beta \mathbf{W}^\star_{\beta\sigma} - \mathcal{J}_\beta \mathbf{b}^\star_{\beta\sigma} + \mathbf{A}_\beta \cdot \nabla \mathbf{b}^\star_{\beta\sigma} \right\rangle. \quad (7.114)$$

The first-order exchange and distribution coefficients read

$$h^\star_\beta = \left\langle \mathcal{L}_\beta \mathbf{a}^\star_\beta \right\rangle \quad \text{and} \quad \xi^\star_\beta = a_v^{-1} \left\langle \mathcal{L}_\beta \mathbf{c}^\star_\beta \right\rangle. \quad (7.115)$$

For the other phase, we obtain an equivalent expression

$$\varepsilon_\sigma \Gamma_a \partial_t \langle u_\sigma \rangle^\sigma - \langle \mathcal{L}_\sigma \rangle \langle u_\sigma \rangle^\sigma - \varepsilon_\sigma R_\sigma \left(\langle u_\sigma \rangle^\sigma \right) = -\nabla \cdot \left(\partial_t \mathbf{d}^\star_{\sigma\beta} \star \langle u_\beta \rangle^\beta \right) - \nabla \cdot \left(\partial_t \mathbf{d}^\star_{\sigma\sigma} \star \langle u_\sigma \rangle^\sigma \right) + \nabla \cdot \left(\partial_t \mathbf{B}^\star_{\sigma\beta} \cdot \star \nabla \langle u_\beta \rangle^\beta \right) + \nabla \cdot \left(\partial_t \mathbf{B}^\star_{\sigma\sigma} \cdot \star \nabla \langle u_\sigma \rangle^\sigma \right) + \partial_t h^\star_\sigma \star \left(\langle u_\beta \rangle^\beta - \langle u_\sigma \rangle^\sigma \right) + a_v \partial_t \xi^\star_\sigma \star \Omega \left(\langle u_\sigma \rangle^\sigma \right), \quad (7.116)$$

with velocity-like terms

$$\mathbf{d}^\star_{\sigma\beta} = -\left\langle \mathcal{L}_\sigma \mathbf{b}^\star_{\sigma\beta} - \mathcal{J}_\sigma \mathbf{a}^\star_\sigma + \Gamma_A \mathbf{A}_\sigma \cdot \nabla \mathbf{a}^\star_\sigma \right\rangle, \quad (7.117)$$

$$\mathbf{d}^\star_{\sigma\sigma} = -\left\langle \mathcal{L}_\sigma \mathbf{b}^\star_{\sigma\sigma} + \mathcal{J}_\sigma \mathbf{a}^\star_\sigma - \Gamma_A \mathbf{A}_\sigma \cdot \nabla \mathbf{a}^\star_\sigma \right\rangle, \quad (7.118)$$

and dispersion-like terms

$$\mathbf{B}^{\star}_{\sigma\beta} = \left\langle \mathcal{L}_{\sigma}\mathbf{W}^{\star}_{\sigma\beta} - \mathcal{J}_{\sigma}\mathbf{b}^{\star}_{\sigma\beta} + \Gamma_{A}\mathbf{A}_{\sigma}\cdot\nabla\mathbf{b}^{\star}_{\sigma\beta}\right\rangle, \tag{7.119}$$

$$\mathbf{B}^{\star}_{\sigma\sigma} = \left\langle \mathcal{L}_{\sigma}\mathbf{W}^{\star}_{\sigma\sigma} - \mathcal{J}_{\sigma}\mathbf{b}^{\star}_{\sigma\sigma} + \Gamma_{A}\mathbf{A}_{\sigma}\cdot\nabla\mathbf{b}^{\star}_{\sigma\sigma}\right\rangle. \tag{7.120}$$

The first-order exchange and distribution coefficients read

$$h^{\star}_{\sigma} = \left\langle \mathcal{L}_{\sigma}\mathbf{a}^{\star}_{\sigma}\right\rangle \quad \text{and} \quad \xi^{\star}_{\sigma} = a_{v}^{-1}\left\langle \mathcal{L}_{\sigma}\mathbf{c}^{\star}_{\sigma}\right\rangle. \tag{7.121}$$

The macroscale expressions can be slightly simplified by remarking that these effective parameters are not independent. In particular, we have that

$$-h^{\star}_{\beta} = h^{\star}_{\sigma} \equiv h^{\star}, \tag{7.122}$$

$$-\xi^{\star}_{\beta} = H\left(t\right) + \xi^{\star}_{\sigma} \equiv \xi^{\star}. \tag{7.123}$$

These relations can be easily proven via flux considerations. For example,

$$h^{\star}_{\beta} = \left\langle \mathcal{L}_{\beta}\mathbf{a}^{\star}_{\beta}\right\rangle \simeq \frac{1}{V}\int_{\mathcal{A}_{\beta\sigma}} \mathbf{n}_{\beta\sigma}\cdot\left(\mathbf{A}_{\beta}\cdot\nabla\mathbf{a}^{\star}_{\beta}\right)dA, \tag{7.124}$$

$$h^{\star}_{\sigma} = \left\langle \mathcal{L}_{\sigma}\mathbf{a}^{\star}_{\sigma}\right\rangle \simeq \frac{1}{V}\int_{\mathcal{A}_{\beta\sigma}} \mathbf{n}_{\sigma\beta}\cdot\left(\Gamma_{A}\mathbf{A}_{\sigma}\cdot\nabla\mathbf{a}^{\star}_{\sigma}\right)dA, \tag{7.125}$$

with

$$\mathbf{n}_{\beta\sigma}\cdot\left(\mathbf{A}_{\beta}\cdot\nabla\mathbf{a}^{\star}_{\beta} - \Gamma_{A}\mathbf{A}_{\sigma}\cdot\nabla\mathbf{a}^{\star}_{\sigma}\right) = 0, \tag{7.126}$$

on the boundary, so that $-h^{\star}_{\beta} = h^{\star}_{\sigma}$. For $\xi^{\star}$, we must consider a jump in the flux value that yields $-\xi^{\star}_{\beta} = H\left(t\right) + \xi^{\star}_{\sigma} \equiv \xi^{\star}$.

We can therefore rewrite the system of equations as

$$\begin{aligned}\varepsilon_{\beta}\partial_{t}\left\langle u_{\beta}\right\rangle^{\beta} - \left\langle \mathcal{L}_{\beta}\right\rangle\left\langle u_{\beta}\right\rangle^{\beta} - \varepsilon_{\beta}R_{\beta}\left(\left\langle u_{\beta}\right\rangle^{\beta}\right) &= -\nabla\cdot\left(\partial_{t}\mathbf{d}^{\star}_{\beta\beta}\star\left\langle u_{\beta}\right\rangle^{\beta}\right) - \nabla\cdot\left(\partial_{t}\mathbf{d}^{\star}_{\beta\sigma}\star\left\langle u_{\sigma}\right\rangle^{\sigma}\right)\\ &\quad + \nabla\cdot\left(\partial_{t}\mathbf{B}^{\star}_{\beta\beta}\cdot\star\nabla\left\langle u_{\beta}\right\rangle^{\beta}\right) + \nabla\cdot\left(\partial_{t}\mathbf{B}^{\star}_{\beta\sigma}\cdot\star\nabla\left\langle u_{\sigma}\right\rangle^{\sigma}\right)\\ &\quad - \partial_{t}h^{\star}\star\left(\left\langle u_{\beta}\right\rangle^{\beta} - \left\langle u_{\sigma}\right\rangle^{\sigma}\right) - a_{v}\partial_{t}\xi^{\star}\star\Omega\left(\left\langle u_{\sigma}\right\rangle^{\sigma}\right),\end{aligned} \tag{7.127}$$

$$\begin{aligned}\varepsilon_{\sigma}\Gamma_{a}\partial_{t}\left\langle u_{\sigma}\right\rangle^{\sigma} - \left\langle \mathcal{L}_{\sigma}\right\rangle\left\langle u_{\sigma}\right\rangle^{\sigma} - \varepsilon_{\sigma}R_{\sigma}\left(\left\langle u_{\sigma}\right\rangle^{\sigma}\right) + a_{v}\Omega\left(\left\langle u_{\sigma}\right\rangle^{\sigma}\right) &= -\nabla\cdot\left(\partial_{t}\mathbf{d}^{\star}_{\sigma\beta}\star\left\langle u_{\beta}\right\rangle^{\beta}\right) - \nabla\cdot\left(\partial_{t}\mathbf{d}^{\star}_{\sigma\sigma}\star\left\langle u_{\sigma}\right\rangle^{\sigma}\right)\\ &\quad + \nabla\cdot\left(\partial_{t}\mathbf{B}^{\star}_{\sigma\beta}\cdot\star\nabla\left\langle u_{\beta}\right\rangle^{\beta}\right) + \nabla\cdot\left(\partial_{t}\mathbf{B}^{\star}_{\sigma\sigma}\cdot\star\nabla\left\langle u_{\sigma}\right\rangle^{\sigma}\right)\\ &\quad + \partial_{t}h^{\star}\star\left(\left\langle u_{\beta}\right\rangle^{\beta} - \left\langle u_{\sigma}\right\rangle^{\sigma}\right) + a_{v}\partial_{t}\xi^{\star}\star\Omega\left(\left\langle u_{\sigma}\right\rangle^{\sigma}\right).\end{aligned} \tag{7.128}$$

Note that we have grouped terms involving the time convolution on the RHS of the fully transient model. We can write these equations in a more compact nonconservative way as

$$\begin{aligned}
&\begin{bmatrix} \varepsilon_\beta & 0 \\ 0 & \varepsilon_\sigma \Gamma_a \end{bmatrix} \partial_t \begin{bmatrix} \langle u_\beta \rangle^\beta \\ \langle u_\sigma \rangle^\sigma \end{bmatrix} + \partial_t \begin{bmatrix} \mathbf{V}^\star_{\beta\beta} & \mathbf{V}^\star_{\beta\sigma} \\ \mathbf{V}^\star_{\sigma\beta} & \mathbf{V}^\star_{\sigma\sigma} \end{bmatrix} \cdot\star \begin{bmatrix} \nabla \langle u_\beta \rangle^\beta \\ \nabla \langle u_\sigma \rangle^\sigma \end{bmatrix} \\
&= \partial_t \begin{bmatrix} \mathbf{A}^\star_{\beta\beta} & \mathbf{A}^\star_{\beta\sigma} \\ \mathbf{A}^\star_{\sigma\beta} & \mathbf{A}^\star_{\sigma\sigma} \end{bmatrix} :\star \begin{bmatrix} \nabla\nabla \langle u_\beta \rangle^\beta \\ \nabla\nabla \langle u_\sigma \rangle^\sigma \end{bmatrix} + \partial_t \begin{bmatrix} -\square & +\square \\ +\square & -\square \end{bmatrix} \star \begin{bmatrix} \langle u_\beta \rangle^\beta \\ \langle u_\sigma \rangle^\sigma \end{bmatrix} \\
&\quad + \begin{bmatrix} \varepsilon_\beta & 0 \\ 0 & \varepsilon_\sigma \end{bmatrix} \begin{bmatrix} \square_\beta \left[\langle u_\beta \rangle^\beta \right] \\ \square_\sigma \left[\langle u_\sigma \rangle^\sigma \right] \end{bmatrix} - \partial_t \begin{bmatrix} a_{\square}\square^\star & 0 \\ 0 & a_{\square}\left[\square\, t \,\square^\star\right] \end{bmatrix} \star \begin{bmatrix} \square \left[\langle u_\sigma \rangle^\sigma \right] \\ \square \left[\langle u_\sigma \rangle^\sigma \right] \end{bmatrix} \square
\end{aligned} \tag{7.129}$$

with

$$\begin{bmatrix} \mathbf{V}^\star_{\beta\beta} & \mathbf{V}^\star_{\beta\sigma} \\ \mathbf{V}^\star_{\sigma\beta} & \mathbf{V}^\star_{\sigma\sigma} \end{bmatrix} = \begin{bmatrix} \mathrm{Pe}^\ell_\beta \langle \mathbf{v}_\beta \rangle H(t) + \mathbf{d}^\star_{\beta\beta} & \mathbf{d}^\star_{\beta\sigma} \\ \mathbf{d}^\star_{\sigma\beta} & \mathbf{d}^\star_{\sigma\sigma} \end{bmatrix}, \tag{7.130}$$

$$\begin{bmatrix} \mathbf{A}^\star_{\beta\beta} & \mathbf{A}^\star_{\beta\sigma} \\ \mathbf{A}^\star_{\sigma\beta} & \mathbf{A}^\star_{\sigma\sigma} \end{bmatrix} = \begin{bmatrix} \varepsilon_\beta \mathbf{A}_\beta H(t) + \mathbf{B}^\star_{\beta\beta} & \mathbf{B}^\star_{\beta\sigma} \\ \mathbf{B}^\star_{\sigma\beta} & \varepsilon_\sigma \Gamma_A \mathbf{A}_\sigma H(t) + \mathbf{B}^\star_{\sigma\sigma} \end{bmatrix}. \tag{7.131}$$

7.5.5.2 Two-Equation Quasi-Stationary

For the quasi-stationary version of the two-equation model, we can write

$$\begin{aligned}
&\varepsilon_\beta \left[\partial_t \langle u_\beta \rangle^\beta + \nabla \cdot \left(\mathrm{Pe}^\ell_\beta \langle \mathbf{v}_\beta \rangle^\beta \langle u_\beta \rangle^\beta \right) \right] + \nabla \cdot \left(\mathbf{d}_{\beta\beta} \langle u_\beta \rangle^\beta \right) + \nabla \cdot \left(\mathbf{d}_{\beta\sigma} \langle u_\sigma \rangle^\sigma \right) \\
&\quad = \nabla \cdot \left[\left(\varepsilon_\beta \mathbf{A}_\beta + \mathbf{B}_{\beta\beta} \right) \cdot \nabla \langle u_\beta \rangle^\beta \right] + \nabla \cdot \left(\mathbf{B}_{\beta\sigma} \cdot \nabla \langle u_\sigma \rangle^\sigma \right) \\
&\qquad - h \left(\langle u_\beta \rangle^\beta - \langle u_\sigma \rangle^\sigma \right) + \varepsilon_\beta R_\beta \left(\langle u_\beta \rangle^\beta \right) - a_v \xi \Omega \left(\langle u_\sigma \rangle^\sigma \right),
\end{aligned} \tag{7.132}$$

$$\begin{aligned}
&\varepsilon_\sigma \Gamma_a \partial_t \langle u_\sigma \rangle^\sigma + \nabla \cdot \left(\mathbf{d}_{\sigma\beta} \langle u_\beta \rangle^\beta \right) + \nabla \cdot \left(\mathbf{d}_{\sigma\sigma} \langle u_\sigma \rangle^\sigma \right) \\
&\quad = \nabla \cdot \left(\mathbf{B}_{\sigma\beta} \cdot \nabla \langle u_\beta \rangle^\beta \right) + \nabla \cdot \left[\left(\varepsilon_\sigma \Gamma_A \mathbf{A}_\sigma + \mathbf{B}_{\sigma\sigma} \right) \cdot \nabla \langle u_\sigma \rangle^\sigma \right] \\
&\qquad + h \left(\langle u_\beta \rangle^\beta - \langle u_\sigma \rangle^\sigma \right) + \varepsilon_\sigma R_\sigma \left(\langle u_\sigma \rangle^\sigma \right) - a_v \left(1 - \xi \right) \Omega \left(\langle u_\sigma \rangle^\sigma \right).
\end{aligned} \tag{7.133}$$

Effective velocities are

$$\mathbf{d}_{\beta\beta} = -\left\langle \mathcal{L}_\beta \mathbf{b}_{\beta\beta} - \mathcal{J}_\beta \mathbf{a}_\beta + \mathbf{A}_\beta \cdot \nabla \mathbf{a}_\beta \right\rangle, \quad \mathbf{d}_{\beta\sigma} = -\left\langle \mathcal{L}_\beta \mathbf{b}_{\beta\sigma} + \mathcal{J}_\beta \mathbf{a}_\beta - \mathbf{A}_\beta \cdot \nabla \mathbf{a}_\beta \right\rangle, \tag{7.134}$$

$$\mathbf{d}_{\sigma\beta} = -\left\langle \mathcal{L}_\sigma \mathbf{b}_{\sigma\beta} - \mathcal{J}_\sigma \mathbf{a}_\sigma + \Gamma_A \mathbf{A}_\sigma \cdot \nabla \mathbf{a}_\sigma \right\rangle, \quad \mathbf{d}_{\sigma\sigma} = -\left\langle \mathcal{L}_\sigma \mathbf{b}_{\sigma\sigma} + \mathcal{J}_\sigma \mathbf{a}_\sigma - \Gamma_A \mathbf{A}_\sigma \cdot \nabla \mathbf{a}_\sigma \right\rangle, \tag{7.135}$$

and dispersion-like terms are

$$\mathbf{B}_{\beta\beta} = \left\langle \mathcal{L}_\beta \mathbf{W}_{\beta\beta} - \mathcal{J}_\beta \mathbf{b}_{\beta\beta} + \mathbf{A}_\beta \cdot \nabla \mathbf{b}_{\beta\beta} \right\rangle, \quad \mathbf{B}_{\beta\sigma} = \left\langle \mathcal{L}_\beta \mathbf{W}_{\beta\sigma} - \mathcal{J}_\beta \mathbf{b}_{\beta\sigma} + \mathbf{A}_\beta \cdot \nabla \mathbf{b}_{\beta\sigma} \right\rangle, \tag{7.136}$$

$$\mathbf{B}_{\sigma\beta} = \left\langle \mathcal{L}_\sigma \mathbf{W}_{\sigma\beta} - \mathcal{J}_\sigma \mathbf{b}_{\sigma\beta} + \Gamma_A \mathbf{A}_\sigma \cdot \nabla \mathbf{b}_{\sigma\beta} \right\rangle, \quad \mathbf{B}_{\sigma\sigma} = \left\langle \mathcal{L}_\sigma \mathbf{W}_{\sigma\sigma} - \mathcal{J}_\sigma \mathbf{b}_{\sigma\sigma} + \Gamma_A \mathbf{A}_\sigma \cdot \nabla \mathbf{b}_{\sigma\sigma} \right\rangle. \quad (7.137)$$

The first-order exchange and distribution coefficients read

$$h = -\left\langle \mathcal{L}_\beta \mathsf{a}_\beta \right\rangle \quad \text{and} \quad \xi = -a_v^{-1} \left\langle \mathcal{L}_\beta \mathsf{c}_\beta \right\rangle. \quad (7.138)$$

A more compact nonconservative version of these equations reads

$$\begin{bmatrix} \varepsilon_\beta & 0 \\ 0 & \varepsilon_\sigma \Gamma_a \end{bmatrix} \partial_t \begin{bmatrix} \langle u_\beta \rangle^\beta \\ \langle u_\sigma \rangle^\sigma \end{bmatrix} + \begin{bmatrix} \mathbf{V}_{\beta\beta} & \mathbf{V}_{\beta\sigma} \\ \mathbf{V}_{\sigma\beta} & \mathbf{V}_{\sigma\sigma} \end{bmatrix} \cdot \begin{bmatrix} \nabla \langle u_\beta \rangle^\beta \\ \nabla \langle u_\sigma \rangle^\sigma \end{bmatrix}$$
$$= \begin{bmatrix} \mathbf{A}_{\beta\beta} & \mathbf{A}_{\beta\sigma} \\ \mathbf{A}_{\sigma\beta} & \mathbf{A}_{\sigma\sigma} \end{bmatrix} : \begin{bmatrix} \nabla\nabla \langle u_\beta \rangle^\beta \\ \nabla\nabla \langle u_\sigma \rangle^\sigma \end{bmatrix} + \begin{bmatrix} -h & +h \\ +h & -h \end{bmatrix} \begin{bmatrix} \langle u_\beta \rangle^\beta \\ \langle u_\sigma \rangle^\sigma \end{bmatrix}$$
$$+ \begin{bmatrix} \varepsilon_\beta & 0 \\ 0 & \varepsilon_\sigma \end{bmatrix} \left[\begin{bmatrix} \square_\beta \left[\langle u_\beta \rangle^\beta \right] \\ \square_\sigma \left[\langle u_\sigma \rangle^\sigma \right] \end{bmatrix} - \begin{bmatrix} a_\square & 0 \\ 0 & a_\square \end{bmatrix} \begin{bmatrix} \square \left[\langle u_\sigma \rangle^\sigma \right] \\ \square \left[\langle u_\sigma \rangle^\sigma \right] \end{bmatrix} \right] \quad (7.139)$$

with

$$\begin{bmatrix} \mathbf{V}_{\beta\beta} & \mathbf{V}_{\beta\sigma} \\ \mathbf{V}_{\sigma\beta} & \mathbf{V}_{\sigma\sigma} \end{bmatrix} = \begin{bmatrix} \mathrm{Pe}_\beta^\ell \langle \mathbf{v}_\beta \rangle + \mathbf{d}_{\beta\beta} & \mathbf{d}_{\beta\sigma} \\ \mathbf{d}_{\sigma\beta} & \mathbf{d}_{\sigma\sigma} \end{bmatrix}, \quad (7.140)$$

and

$$\begin{bmatrix} \mathbf{A}_{\beta\beta} & \mathbf{A}_{\beta\sigma} \\ \mathbf{A}_{\sigma\beta} & \mathbf{A}_{\sigma\sigma} \end{bmatrix} = \begin{bmatrix} \varepsilon_\beta \mathbf{A}_\beta + \mathbf{B}_{\beta\beta} & \mathbf{B}_{\beta\sigma} \\ \mathbf{B}_{\sigma\beta} & \varepsilon_\sigma \Gamma_A \mathbf{A}_\sigma + \mathbf{B}_{\sigma\sigma} \end{bmatrix}. \quad (7.141)$$

7.5.5.3 Two-Equation Quasi-Stationary with Fluxes

In the previous equations, we have grouped together terms that are of similar mathematical types. For instance, this was done for terms involving convolutions, or advective and diffusive parts of the spatial operators. Two-equation models can also be interpreted in a more physical way where the macroscale equations for each phase are decomposed in advection–dispersion equations with multiphase corrections and an interfacial flux that contains different types of mathematical operators. To obtain this formulation for the steady closure, we use Equations 7.57 and 7.58, which can be written, using the spatial amplitude and frequency approximations, as

$$\varepsilon_\beta \left[\underbrace{\partial_t \langle u_\beta \rangle^\beta}_{\text{Rate of change}} + \underbrace{\nabla \cdot \left(\mathrm{Pe}_\beta^\ell \langle \mathbf{v}_\beta \rangle^\beta \langle u_\beta \rangle^\beta \right)}_{\text{Convection}} + \underbrace{\nabla \cdot \left(\mathrm{Pe}_\beta^\ell \left\langle \tilde{\mathbf{v}}_\beta \tilde{u}_\beta \right\rangle^\beta \right)}_{\text{Velocity fluctuation effects}} \right] = \nabla \cdot \left[\varepsilon_\beta \mathbf{A}_\beta \cdot \left(\underbrace{\nabla \langle u_\beta \rangle^\beta}_{\text{Diffusion}} + \underbrace{\frac{1}{V_\beta} \int_{\mathcal{A}_{\beta\sigma}} \mathbf{n}_{\beta\sigma} \tilde{u}_\beta dA}_{\text{Surface effects}} \right) \right]$$
$$\underbrace{+ \frac{1}{V} \int_{\mathcal{A}_{\beta\sigma}} \mathbf{n}_{\beta\sigma} \cdot \left(\mathbf{A}_\beta \cdot \nabla \tilde{u}_\beta \right) dA}_{\text{Interfacial flux}} + \underbrace{\varepsilon_\beta \square_\beta \left(\langle u_\beta \rangle^\beta \right)}_{\text{Overage reaction rate}} \quad (7.142)$$

and

$$\underbrace{\varepsilon_\sigma \Gamma_a \ \partial_t \left\langle u_\sigma \right\rangle^\sigma}_{\text{Rate of change}} = \nabla \cdot \left[\varepsilon_\sigma \Gamma_A \mathbf{A}_\sigma \cdot \left(\underbrace{\nabla \left\langle u_\sigma \right\rangle^\sigma}_{\text{Diffusion}} + \underbrace{\frac{1}{V_\sigma} \int_{\mathcal{A}_{\sigma\beta}} \mathbf{n}_{\sigma\beta} \tilde{u}_\sigma dA}_{\text{Surface effects}} \right) \right]$$

$$+ \underbrace{\frac{1}{V} \int_{\mathcal{A}_{\sigma\beta}} \mathbf{n}_{\sigma\beta} \cdot \left(\Gamma_A \mathbf{A}_\sigma \cdot \nabla \tilde{u}_\sigma \right) dA}_{\text{Interfacial flux}} + \underbrace{\varepsilon_\sigma R_\sigma \left(\left\langle u_\sigma \right\rangle^\sigma \right)}_{\text{Average reaction rate}}. \tag{7.143}$$

We first focus on the interfacial flux in Equation 7.142, which reads

$$\mathsf{J}_{\beta\sigma} \equiv -\frac{1}{V} \int_{\mathcal{A}_{\beta\sigma}} \mathbf{n}_{\beta\sigma} \cdot \left(\mathbf{A}_\beta \cdot \nabla \tilde{u}_\beta \right) dA. \tag{7.144}$$

We also have

$$\mathsf{J}_{\beta\sigma} \equiv \frac{1}{V} \int_{\mathcal{A}_{\beta\sigma}} \mathbf{n}_{\sigma\beta} \cdot \left(\Gamma_A \mathbf{A}_\sigma \cdot \nabla \tilde{u}_\sigma \right) dA + a_v \Omega \left(\left\langle u_\sigma \right\rangle^\sigma \right), \tag{7.145}$$

using the reactive boundary condition with $a_v = \dfrac{A_{\beta\sigma}}{V}$ and therefore

$$\mathsf{J}_{\beta\sigma} = -\mathsf{J}_{\sigma\beta} + a_v \Omega \left(\left\langle u_\sigma \right\rangle^\sigma \right). \tag{7.146}$$

We can use the steady closure

$$\tilde{u}_\beta = \mathsf{a}_\beta \left(\left\langle u_\beta \right\rangle^\beta - \left\langle u_\sigma \right\rangle^\sigma \right) + \begin{bmatrix} \mathbf{b}_{\beta\beta} & \mathbf{b}_{\beta\sigma} \end{bmatrix} \cdot \begin{bmatrix} \nabla \left\langle u_\beta \right\rangle^\beta \\ \nabla \left\langle u_\sigma \right\rangle^\sigma \end{bmatrix}$$

$$+ \begin{bmatrix} \mathbf{W}_{\beta\beta} & \mathbf{W}_{\beta\sigma} \end{bmatrix} : \begin{bmatrix} \nabla\nabla \left\langle u_\beta \right\rangle^\beta \\ \nabla\nabla \left\langle u_\sigma \right\rangle^\sigma \end{bmatrix} + \mathsf{c}_\beta \Omega \left(\left\langle u_\sigma \right\rangle^\sigma \right), \tag{7.147}$$

to obtain

$$\begin{aligned}
\mathsf{J}_{\beta\sigma} = &-\left[\frac{1}{V}\int_{\mathcal{A}_{\beta\sigma}}\mathbf{n}_{\beta\sigma}\cdot\left(\mathbf{A}_\beta\cdot\nabla\mathsf{a}_\beta\right)dA\right]\left(\left\langle u_\beta\right\rangle^\beta-\left\langle u_\sigma\right\rangle^\sigma\right)\\
&-\left[\frac{1}{V}\int_{\mathcal{A}_{\beta\sigma}}\mathbf{n}_{\beta\sigma}\cdot\left[\mathbf{A}_\beta\cdot\left(\nabla\mathbf{b}_{\beta\beta}+\mathsf{a}_\beta\mathbf{I}\right)\right]dA\right]\cdot\nabla\left\langle u_\beta\right\rangle^\beta\\
&-\left[\frac{1}{V}\int_{\mathcal{A}_{\beta\sigma}}\mathbf{n}_{\beta\sigma}\cdot\left[\mathbf{A}_\beta\cdot\left(\nabla\mathbf{b}_{\beta\sigma}-\mathsf{a}_\beta\mathbf{I}\right)\right]dA\right]\cdot\nabla\left\langle u_\sigma\right\rangle^\sigma\\
&-\left[\frac{1}{V}\int_{\mathcal{A}_{\beta\sigma}}\mathbf{n}_{\beta\sigma}\cdot\left[\mathbf{A}_\beta\cdot\left(\nabla\mathbf{W}_{\beta\beta}+\mathbf{b}_{\beta\beta}\mathbf{I}\right)\right]dA\right]:\nabla\nabla\left\langle u_\beta\right\rangle^\beta\\
&-\left[\frac{1}{V}\int_{\mathcal{A}_{\beta\sigma}}\mathbf{n}_{\beta\sigma}\cdot\left[\mathbf{A}_\beta\cdot\left(\nabla\mathbf{W}_{\beta\sigma}+\mathbf{b}_{\beta\sigma}\mathbf{I}\right)\right]dA\right]:\nabla\nabla\left\langle u_\sigma\right\rangle^\sigma\\
&-\left[\frac{1}{V}\int_{\mathcal{A}_{\beta\sigma}}\mathbf{n}_{\beta\sigma}\cdot\left(\mathbf{A}_\beta\cdot\nabla\square_\beta\right)dA\right]\square\left(\left\langle u_\sigma\right\rangle^\sigma\right),
\end{aligned}\tag{7.148}$$

which for a homogeneous porous medium can be put as

$$\begin{aligned}
\mathsf{J}_{\beta\sigma} = &\underbrace{h\left(\left\langle u_\beta\right\rangle^\beta-\left\langle u_\sigma\right\rangle^\sigma\right)}_{\text{First-order exchange}}+\underbrace{a_v\xi\Omega\left(\left\langle u_\sigma\right\rangle^\sigma\right)}_{\text{Flux component from the surface source}}\\
&-\left\langle\nabla\cdot\left(\mathbf{A}_\beta\cdot\nabla\mathbf{b}_{\beta\beta}\right)+\mathbf{A}_\beta\cdot\nabla\mathsf{a}_\beta\right\rangle\cdot\nabla\left\langle u_\beta\right\rangle^\beta\\
&-\left\langle\nabla\cdot\left(\mathbf{A}_\beta\cdot\nabla\mathbf{b}_{\beta\sigma}\right)-\mathbf{A}_\beta\cdot\nabla\mathsf{a}_\beta\right\rangle\cdot\nabla\left\langle u_\sigma\right\rangle^\sigma\\
&-\left\langle\nabla\cdot\left(\mathbf{A}_\beta\cdot\nabla\mathbf{W}_{\beta\beta}\right)+\mathbf{A}_\beta\cdot\nabla\mathbf{b}_{\beta\beta}\right\rangle\cdot\nabla\nabla\left\langle u_\beta\right\rangle^\beta\\
&-\left\langle\nabla\cdot\left(\mathbf{A}_\beta\cdot\nabla\mathbf{W}_{\beta\sigma}\right)+\mathbf{A}_\beta\cdot\nabla\mathbf{b}_{\beta\sigma}\right\rangle\cdot\nabla\nabla\left\langle u_\sigma\right\rangle^\sigma.
\end{aligned}\tag{7.149}$$

We also have the relationship

$$\mathsf{J}_{\sigma\beta} = -\mathsf{J}_{\beta\sigma}+a_v\Omega\left(\left\langle u_\sigma\right\rangle^\sigma\right).\tag{7.150}$$

The surface effect term reads

$$\zeta_\beta \equiv \frac{1}{V_\beta}\int_{\mathcal{A}_{\beta\sigma}} \mathbf{n}_{\beta\sigma}\tilde{u}_\beta dA \simeq \frac{1}{V_\beta}\int_{\mathcal{A}_{\beta\sigma}} \mathbf{n}_{\beta\sigma}\mathsf{a}_\beta dA\left(\langle u_\beta\rangle^\beta - \langle u_\sigma\rangle^\sigma\right) + \frac{1}{V_\beta}\int_{\mathcal{A}_{\beta\sigma}} \mathbf{n}_{\beta\sigma}\left[\mathbf{b}_{\beta\beta} \quad \mathbf{b}_{\beta\sigma}\right] dA\cdot\begin{bmatrix}\nabla\langle u_\beta\rangle^\beta\\ \nabla\langle u_\sigma\rangle^\sigma\end{bmatrix} + \frac{1}{V_\beta}\int_{\mathcal{A}_{\beta\sigma}} \mathbf{n}_{\beta\sigma}\mathsf{c}_\beta dA\Omega\left(\langle u_\sigma\rangle^\sigma\right), \tag{7.151}$$

that we approximate as

$$\zeta_\beta \simeq \underbrace{\langle\nabla\mathsf{a}_\beta\rangle^\beta}_{\text{Advective tortuosity}}\left(\langle u_\beta\rangle^\beta - \langle u_\sigma\rangle^\sigma\right) + \underbrace{\left\langle\nabla\left[\mathbf{b}_{\beta\beta} \quad \mathbf{b}_{\beta\sigma}\right]\right\rangle^\beta}_{\text{Diffusive tortuosity}}\cdot\begin{bmatrix}\nabla\langle u_\beta\rangle^\beta\\ \nabla\langle u_\sigma\rangle^\sigma\end{bmatrix} + \underbrace{\langle\nabla\mathsf{c}_\beta\rangle^\beta}_{\text{Reactive tortuosity}}\Omega\left(\langle u_\sigma\rangle^\sigma\right). \tag{7.152}$$

Similarly, we have

$$\zeta_\sigma \simeq \underbrace{\langle\nabla\mathsf{a}_\sigma\rangle^\sigma}_{\text{Advective tortuosity}}\left(\langle u_\beta\rangle^\beta - \langle u_\sigma\rangle^\sigma\right) + \underbrace{\left\langle\nabla\left[\mathbf{b}_{\sigma\beta} \quad \mathbf{b}_{\sigma\sigma}\right]\right\rangle^\sigma}_{\text{Diffusive tortuosity}}\cdot\begin{bmatrix}\nabla\langle u_\beta\rangle^\beta\\ \nabla\langle u_\sigma\rangle^\sigma\end{bmatrix} + \underbrace{\langle\nabla\mathsf{c}_\sigma\rangle^\sigma}_{\text{Reactive tortuosity}}\Omega\left(\langle u_\sigma\rangle^\sigma\right). \tag{7.153}$$

Further, the velocity fluctuation effects may be written as

$$\theta_\beta \equiv \left\langle\tilde{\mathbf{v}}_\beta\tilde{u}_\beta\right\rangle^\beta \simeq \underbrace{\left\langle\tilde{\mathbf{v}}_\beta\mathsf{a}_\beta\right\rangle^\beta}_{\text{Flux velocity correction}}\left(\langle u_\beta\rangle^\beta - \langle u_\sigma\rangle^\sigma\right) + \underbrace{\left\langle\tilde{\mathbf{v}}_\beta\left[\mathbf{b}_{\beta\beta} \quad \mathbf{b}_{\beta\sigma}\right]\right\rangle^\beta}_{\text{Hydrodynamic dispersion}}\cdot\begin{bmatrix}\nabla\langle u_\beta\rangle^\beta\\ \nabla\langle u_\sigma\rangle^\sigma\end{bmatrix} + \underbrace{\left\langle\tilde{\mathbf{v}}_\beta\mathsf{c}_\beta\right\rangle^\beta}_{\text{Flux reactive correction}}\Omega\left(\langle u_\sigma\rangle^\sigma\right). \tag{7.154}$$

We neglect terms involving $\Omega(\langle u_\sigma\rangle^\sigma)$ assuming that $\nabla\Omega(\langle u_\sigma\rangle^\sigma)$ are small when considering $\nabla\cdot\boldsymbol{\zeta}$ and $\nabla\cdot\theta$ and keeping in mind that the most restrictive assumption is $\Omega(u_\sigma) \simeq \Omega\ (\langle u_\sigma\rangle^\sigma)$. Therefore, we obtain the following macroscale equations:

$$\varepsilon_\beta\left[\underbrace{\partial_t\langle u_\beta\rangle^\beta}_{\text{Rate of change}} + \mathrm{Pe}_\beta^\ell\nabla\cdot\left(\underbrace{\langle\mathbf{v}_\beta\rangle^\beta\langle u_\beta\rangle^\beta}_{\text{Convection}} + \underbrace{\theta_\beta}_{\text{Velocity fluctuation effects}}\right)\right] = \nabla\cdot\left[\varepsilon_\beta\mathbf{A}_\beta\cdot\left(\underbrace{\nabla\langle u_\beta\rangle^\beta}_{\text{Diffusion}} + \underbrace{\zeta_\beta}_{\text{Surface effects}}\right)\right] + \underbrace{\varepsilon_\beta R_\beta\left(\langle u_\beta\rangle^\beta\right)}_{\text{Average reaction rate}} - \underbrace{\mathsf{J}_{\beta\sigma}}_{\text{Interfacial flux}}. \tag{7.155}$$

and

$$\varepsilon_\sigma \Gamma_a \underbrace{\partial_t \left\langle u_\sigma \right\rangle^\sigma}_{\text{Rate of change}} = \nabla \cdot \left[\varepsilon_\sigma \Gamma_A \mathbf{A}_\sigma \cdot \left(\underbrace{\nabla \left\langle u_\sigma \right\rangle^\sigma}_{\text{Diffusion}} + \underbrace{\zeta_\sigma}_{\text{Surface effects}} \right) \right] - \underbrace{\mathsf{J}_{\sigma\beta}}_{\text{Interfacial flux}} + \underbrace{\varepsilon_\sigma R_\sigma \left(\left\langle u_\sigma \right\rangle^\sigma \right)}_{\text{Average reaction rate}} . \quad (7.156)$$

We remark that higher-order exchange terms are often overlooked in the literature, as well as the additional advective terms. There is no clear answer as to the relative effect of these terms, although several examples have shown that they may significantly affect the macroscale fields [67,121], at least for simple unit cells.

7.5.5.4 Two-Equation Variants

The hypothesis regarding the timescales for the relaxation of the mapping variables can be made independently for each effective parameter. Physically, this stems from the fact that there may be significant differences between characteristic times for relaxation of these mapping variables. In particular, it has been shown that the exchange parameters $h^\star$ and $\xi^\star$ [76] may exhibit a longer relaxation than other effective parameters. Therefore, it may be interesting to consider the following variant of the two-equation transient model:

$$\begin{aligned}
&\begin{bmatrix} \varepsilon_\beta & 0 \\ 0 & \varepsilon_\sigma \Gamma_a \end{bmatrix} \partial_t \begin{bmatrix} \left\langle u_\beta \right\rangle^\beta \\ \left\langle u_\sigma \right\rangle^\sigma \end{bmatrix} + \begin{bmatrix} \mathbf{V}_{\beta\beta} & \mathbf{V}_{\beta\sigma} \\ \mathbf{V}_{\sigma\beta} & \mathbf{V}_{\sigma\sigma} \end{bmatrix} \cdot \begin{bmatrix} \nabla \left\langle u_\beta \right\rangle^\beta \\ \nabla \left\langle u_\sigma \right\rangle^\sigma \end{bmatrix} \\
&= \begin{bmatrix} \mathbf{A}_{\beta\beta} & \mathbf{A}_{\beta\sigma} \\ \mathbf{A}_{\sigma\beta} & \mathbf{A}_{\sigma\sigma} \end{bmatrix} : \begin{bmatrix} \nabla\nabla \left\langle u_\beta \right\rangle^\beta \\ \nabla\nabla \left\langle u_\sigma \right\rangle^\sigma \end{bmatrix} + \partial_t \begin{bmatrix} -h^\star & +h^\star \\ +h^\star & -h^\star \end{bmatrix} \star \begin{bmatrix} \left\langle u_\beta \right\rangle^\beta \\ \left\langle u_\sigma \right\rangle^\sigma \end{bmatrix} \\
&+ \begin{bmatrix} \varepsilon_\beta & 0 \\ 0 & \varepsilon_\sigma \end{bmatrix} \begin{bmatrix} \square_\beta \left[\left\langle u_\beta \right\rangle^\beta \right] \\ \square_\sigma \left[\left\langle u_\sigma \right\rangle^\sigma \right] \end{bmatrix} - \partial_t \begin{bmatrix} a\square^\star & 0 \\ 0 & a\square\square\square + \square^\star \end{bmatrix} \star \begin{bmatrix} \square \left[\left\langle u_\sigma \right\rangle^\sigma \right] \\ \square \left[\left\langle u_\sigma \right\rangle^\sigma \right] \end{bmatrix} \square
\end{aligned} \quad (7.157)$$

7.6 DERIVATION OF THE ONE-EQUATION LE MODEL

7.6.1 Approximations

The LE model is based on the idea that gradients at the microscale are sufficiently small, so that we can use the following approximation (see [17,37]):

$$\left\langle u_\beta \right\rangle^\beta \simeq \left\langle u_\sigma \right\rangle^\sigma \simeq \left\langle u \right\rangle^{\beta\sigma} . \quad (7.158)$$

We use this approximation for any value of the spatial variable $\mathbf{x}$ and any time t, so that we also have

$$\nabla \left\langle u_\beta \right\rangle^\beta \simeq \nabla \left\langle u_\sigma \right\rangle^\sigma \simeq \nabla \left\langle u \right\rangle^{\beta\sigma} , \quad (7.159)$$

$$\nabla\nabla \left\langle u_\beta \right\rangle^\beta \simeq \nabla\nabla \left\langle u_\sigma \right\rangle^\sigma \simeq \nabla\nabla \left\langle u \right\rangle^{\beta\sigma} , \quad (7.160)$$

$$\partial_t \left\langle u_\beta \right\rangle^\beta \simeq \partial_t \left\langle u_\sigma \right\rangle^\sigma \simeq \partial_t \left\langle u \right\rangle^{\beta\sigma} . \quad (7.161)$$

7.6.2 Closure

7.6.2.1 LE Quasi-Stationary Closure

With these approximations, we can now simplify the more general closure proposed in Section 7.5. LE is already a restrictive constraint, and it is often not compatible with a fully transient closure. We therefore focus on the following stationary form of the perturbations that is derived directly from Equation 7.82:

$$\begin{bmatrix}\tilde{u}_\beta\\ \tilde{u}_\sigma\end{bmatrix}=\begin{bmatrix}\mathbf{b}_\beta^{\mathrm{LE}}\\ \mathbf{b}_\sigma^{\mathrm{LE}}\end{bmatrix}\cdot\nabla\langle u\rangle^{\beta\sigma}+\begin{bmatrix}\mathbf{W}_\beta^{\mathrm{LE}}\\ \mathbf{W}_\sigma^{\mathrm{LE}}\end{bmatrix}:\nabla\nabla\langle u\rangle^{\beta\sigma}+\begin{bmatrix}\mathbf{c}_\beta^{\mathrm{LE}}\\ \mathbf{c}_\sigma^{\mathrm{LE}}\end{bmatrix}\Omega\left(\langle u\rangle^{\beta\sigma}\right),\tag{7.162}$$

with the relationships $\mathbf{b}_\beta^{\mathrm{LE}}=\mathbf{b}_{\beta\beta}+\mathbf{b}_{\beta\sigma}$, $\mathbf{b}_\sigma^{\mathrm{LE}}=\mathbf{b}_{\sigma\beta}+\mathbf{b}_{\sigma\sigma}$, $\mathbf{W}_\beta^{\mathrm{LE}}=\mathbf{W}_{\beta\beta}+\mathbf{W}_{\beta\sigma}$, and $\mathbf{W}_\sigma^{\mathrm{LE}}=\mathbf{W}_{\sigma\beta}+\mathbf{W}_{\sigma\sigma}$.

7.6.2.2 Closure Problems

The corresponding closure problems are as follows (see also [17]):

7.6.2.2.1 Problem LE-Stationary-I

$$-\widetilde{\mathcal{L}_\beta\mathbf{b}_\beta^{\mathrm{LE}}}=-\tilde{\mathbf{v}}_\beta\text{ in }\mathcal{V}_\beta,\tag{7.163a}$$

$$\text{BC1}\quad \mathbf{b}_\beta^{\mathrm{LE}}-\mathbf{b}_\sigma^{\mathrm{LE}}=0\text{ on }\mathcal{A}_{\beta\sigma},\tag{7.163b}$$

$$\text{BC2}\quad \mathcal{B}_\beta\mathbf{b}_\beta^{\mathrm{LE}}-\mathcal{B}_\sigma\mathbf{b}_\sigma^{\mathrm{LE}}=\mathbf{n}_{\beta\sigma}\cdot\left(\mathbf{A}_\beta-\Gamma_A\mathbf{A}_\sigma\right)\text{ on }\mathcal{A}_{\beta\sigma},\tag{7.163c}$$

$$\text{Periodicity 1}\quad \mathbf{b}_\alpha^{\mathrm{LE}}\left(\mathbf{x}+\mathbf{l}_i\right)=\mathbf{b}_\alpha^{\mathrm{LE}}\left(\mathbf{x}\right)\text{ with }\alpha=\beta,\sigma,\tag{7.163d}$$

$$\text{Periodicity 2}\quad \mathcal{J}_\alpha\mathbf{b}_\alpha^{\mathrm{LE}}\left(\mathbf{x}+\mathbf{l}_i\right)=\mathcal{J}_\alpha\mathbf{b}_\alpha^{\mathrm{LE}}\left(\mathbf{x}\right)\text{ with }\alpha=\beta,\sigma,\tag{7.163e}$$

$$\text{Average}\quad \left\langle\mathbf{b}_\alpha^{\mathrm{LE}}\right\rangle=0\text{ with }\alpha=\beta,\sigma,\tag{7.163f}$$

$$-\widetilde{\mathcal{L}_\sigma\mathbf{b}_\sigma^{\mathrm{LE}}}=0\text{ in }\mathcal{V}_\sigma.\tag{7.163g}$$

7.6.2.2.2 Problem LE-Stationary-II

$$-\widetilde{\mathcal{L}_\beta\mathbf{W}_\beta^{\mathrm{LE}}}+\widetilde{\mathcal{J}_\beta\mathbf{b}_\beta^{\mathrm{LE}}}=\mathbf{A}_\beta\cdot\widetilde{\nabla\mathbf{b}_\beta^{\mathrm{LE}}}\text{ in }\mathcal{V}_\beta,\tag{7.164a}$$

$$\text{BC1}\quad \mathbf{W}_\beta^{\mathrm{LE}}-\mathbf{W}_\sigma^{\mathrm{LE}}=0\text{ on }\mathcal{A}_{\beta\sigma},\tag{7.164b}$$

$$\text{BC2}\quad \mathcal{B}_\beta\mathbf{W}_\beta^{\mathrm{LE}}-\mathcal{B}_\sigma\mathbf{W}_\sigma^{\mathrm{LE}}=\mathbf{n}_{\beta\sigma}\cdot\left(\mathbf{A}_\beta\mathbf{b}_\beta^{\mathrm{LE}}-\Gamma_A\mathbf{A}_\sigma\mathbf{b}_\sigma^{\mathrm{LE}}\right)\text{ on }\mathcal{A}_{\beta\sigma},\tag{7.164c}$$

$$\text{Periodicity 1}\quad \mathbf{W}_\alpha^{\mathrm{LE}}\left(\mathbf{x}+\mathbf{l}_i\right)=\mathbf{W}_\alpha^{\mathrm{LE}}\left(\mathbf{x}\right)\text{ with }\alpha=\beta,\sigma,\tag{7.164d}$$

$$\text{Periodicity 2}\quad \mathcal{J}_\alpha\mathbf{W}_\alpha^{\mathrm{LE}}\left(\mathbf{x}+\mathbf{l}_i\right)=\mathcal{J}_\alpha\mathbf{W}_\alpha^{\mathrm{LE}}\left(\mathbf{x}\right)\text{ with }\alpha=\beta,\sigma,\tag{7.164e}$$

$$\text{Average}\quad \left\langle\mathbf{W}_\alpha^{\mathrm{LE}}\right\rangle=0\text{ with }\alpha=\beta,\sigma,\tag{7.164f}$$

$$-\widetilde{\mathcal{L}_\sigma\mathbf{W}_\sigma^{\mathrm{LE}}}+\widetilde{\mathcal{J}_\sigma\mathbf{b}_\sigma^{\mathrm{LE}}}=\Gamma_A\mathbf{A}_\sigma\cdot\widetilde{\nabla\mathbf{b}_\sigma^{\mathrm{LE}}}\text{ in }\mathcal{V}_\sigma.\tag{7.164g}$$

7.6.2.2.3 Problem LE-Stationary-III

$$-\widetilde{\mathcal{L}_\beta \mathsf{c}_\beta^{\mathrm{LE}}} = 0 \text{ in } \mathcal{V}_\beta, \tag{7.165a}$$

$$\text{BC1} \quad \mathsf{c}_\beta^{\mathrm{LE}} - \mathsf{c}_\sigma^{\mathrm{LE}} = 0 \text{ on } \mathcal{A}_{\beta\sigma}, \tag{7.165b}$$

$$\text{BC2} \quad \mathcal{B}_\beta \mathsf{c}_\beta^{\mathrm{LE}} - \mathcal{B}_\sigma \mathsf{c}_\sigma^{\mathrm{LE}} = 1 \text{ on } \mathcal{A}_{\beta\sigma}, \tag{7.165c}$$

$$\text{Periodicity 1} \quad \mathsf{c}_\alpha^{\mathrm{LE}}\left(\mathbf{x}+\mathbf{l}_i\right) = \mathsf{c}_\alpha^{\mathrm{LE}}\left(\mathbf{x}\right) \text{ with } \alpha = \beta,\sigma, \tag{7.165d}$$

$$\text{Periodicity 2} \quad \mathcal{J}_\alpha \mathsf{c}_\alpha^{\mathrm{LE}}\left(\mathbf{x}+\mathbf{l}_i\right) = \mathcal{J}_\alpha \mathsf{c}_\alpha^{\mathrm{LE}}\left(\mathbf{x}\right) \text{ with } \alpha = \beta,\sigma, \tag{7.165e}$$

$$\text{Average} \quad \left\langle \mathsf{c}_\alpha^{\mathrm{LE}} \right\rangle = 0 \text{ with } \alpha = \beta,\sigma, \tag{7.165f}$$

$$-\widetilde{\mathcal{L}_\sigma \mathsf{c}_\sigma^{\mathrm{LE}}} = 0 \text{ in } \mathcal{V}_\sigma. \tag{7.165g}$$

7.6.3 Macroscale Model

The macroscale model is obtained by summing up Equations 7.132 and 7.133, an operation that leads to

$$\left(\varepsilon_\beta + \varepsilon_\sigma \Gamma_a\right)\partial_t \left\langle u \right\rangle^{\beta\sigma} + \nabla\cdot\left(\varepsilon_\beta \mathrm{Pe}_\beta^\ell \left\langle \mathbf{v}_\beta \right\rangle^\beta \left\langle u \right\rangle^{\beta\sigma}\right) = \nabla\cdot\left(\mathbf{A}^{\mathrm{LE}}\cdot\nabla\left\langle u \right\rangle^{\beta\sigma}\right) + R^{\mathrm{LE}}, \tag{7.166}$$

where we have used the notations

$$\mathbf{A}^{\mathrm{LE}} = \varepsilon_\beta \mathbf{A}_\beta + \mathbf{B}_{\beta\beta} + \mathbf{B}_{\beta\sigma} + \varepsilon_\sigma \Gamma_A \mathbf{A}_\sigma + \mathbf{B}_{\sigma\beta} + \mathbf{B}_{\sigma\sigma}, \tag{7.167}$$

which can also be written as

$$\mathbf{A}^{\mathrm{LE}} = \mathbf{A}_{\beta\beta} + \mathbf{A}_{\beta\sigma} + \mathbf{A}_{\sigma\beta} + \mathbf{A}_{\sigma\sigma}, \tag{7.168}$$

for the effective dispersion tensor, and

$$R^{\mathrm{LE}} = \varepsilon_\beta R_\beta\left(\left\langle u \right\rangle^{\beta\sigma}\right) + \varepsilon_\sigma R_\sigma\left(\left\langle u \right\rangle^{\beta\sigma}\right) - a_v \Omega\left(\left\langle u \right\rangle^{\beta\sigma}\right) \tag{7.169}$$

for the effective reaction rate, which includes both homogeneous and heterogeneous sources. It is also interesting to note that velocity-like terms have disappeared since we have the relationship

$$\mathbf{d}_{\beta\beta} + \mathbf{d}_{\beta\sigma} + \mathbf{d}_{\sigma\beta} + \mathbf{d}_{\sigma\sigma} = 0 \tag{7.170}$$

that can be easily proven by remarking that terms involving the mapping variable a cancel out and that the remaining terms are opposite average fluxes (see Equations 7.124 through 7.126 for similar developments). We also have

$$\begin{aligned}\mathbf{B}_{\beta\beta} + \mathbf{B}_{\beta\sigma} + \mathbf{B}_{\sigma\beta} + \mathbf{B}_{\sigma\sigma} = &\left\langle \mathcal{L}_\beta \mathbf{W}_\beta - \mathcal{J}_\beta \mathbf{b}_\beta + \mathbf{A}_\beta\cdot\nabla\mathbf{b}_\beta \right\rangle \\ &+ \left\langle \mathcal{L}_\sigma \mathbf{W}_\sigma - \mathcal{J}_\sigma \mathbf{b}_\sigma + \Gamma_A \mathbf{A}_\sigma\cdot\nabla\mathbf{b}_\sigma \right\rangle,\end{aligned} \tag{7.171}$$

which can be simplified in

$$\mathbf{B}_{\beta\beta} + \mathbf{B}_{\beta\sigma} + \mathbf{B}_{\sigma\beta} + \mathbf{B}_{\sigma\sigma} = \left\langle \mathbf{A}_\beta \cdot \nabla \mathbf{b}_\beta \right\rangle + \left\langle \Gamma_A \mathbf{A}_\sigma \cdot \nabla \mathbf{b}_\sigma \right\rangle - \left\langle \mathbf{v}_\beta \mathbf{b}_\beta \right\rangle, \tag{7.172}$$

where the second-order terms in $\mathbf{W}$ disappear from the macroscale equation because

$$\left\langle \mathcal{L}_\beta \mathbf{W}_\beta - \mathcal{J}_\beta \mathbf{b}_\beta \right\rangle + \left\langle \mathcal{L}_\sigma \mathbf{W}_\sigma - \mathcal{J}_\sigma \mathbf{b}_\sigma \right\rangle = 0,$$

and we have

$$\mathbf{A}^{\mathrm{LE}} = \underbrace{\varepsilon_\beta \mathbf{A}_\beta + \varepsilon_\sigma \Gamma_A \mathbf{A}_\sigma}_{\text{Weighted arithmetic mean}} + \underbrace{\left\langle \mathbf{A}_\beta \cdot \nabla \mathbf{b}_\beta \right\rangle + \left\langle \Gamma_A \mathbf{A}_\sigma \cdot \nabla \mathbf{b}_\sigma \right\rangle}_{\text{Tortuosity}} - \underbrace{\left\langle \mathbf{v}_\beta \mathbf{b}_\beta \right\rangle}_{\text{Hydrodynamic dispersion}}. \tag{7.173}$$

7.7 DERIVATION OF THE ONE-EQUATION NONEQUILIBRIUM MODELS

There are primarily two ways to develop the one-equation nonequilibrium model. One is based on direct averaging and using a special perturbation decomposition. This is the method that we will present in this chapter. The other approach is based on an asymptotic analysis of the two-equation models in terms of spatial moments. This equivalence has been discussed in [94].

7.7.1 Averaging

We define an average over both phases as

$$\left\langle u \right\rangle^{\beta\sigma} = \frac{\varepsilon_\beta}{\varepsilon_\beta + \varepsilon_\sigma \Gamma_a} \left\langle u_\beta \right\rangle^\beta + \frac{\varepsilon_\sigma \Gamma_a}{\varepsilon_\beta + \varepsilon_\sigma \Gamma_a} \left\langle u_\sigma \right\rangle^\sigma, \tag{7.174}$$

and the corresponding perturbation decompositions are

$$u_\beta = \left\langle u \right\rangle^{\beta\sigma} + \hat{u}_\beta, \quad u_\sigma = \left\langle u \right\rangle^{\beta\sigma} + \hat{u}_\sigma. \tag{7.175}$$

The one-equation macroscale equation is obtained from the phase-average equations derived in Section 7.5 as

$$\varepsilon_\beta \partial_t \left\langle u_\beta \right\rangle^\beta = \left\langle \mathcal{L}_\beta u_\beta \right\rangle + \left\langle R_\beta \left(u_\beta \right) \right\rangle, \tag{7.176}$$

$$\varepsilon_\sigma \Gamma_a \partial_t \left\langle u_\sigma \right\rangle^\sigma = \left\langle \mathcal{L}_\sigma u_\sigma \right\rangle + \left\langle R_\sigma \left(u_\sigma \right) \right\rangle, \tag{7.177}$$

and summing them yields

$$\left(\varepsilon_\beta + \varepsilon_\sigma \Gamma_a \right) \partial_t \left\langle u \right\rangle^{\beta\sigma} = \left\langle \mathcal{L}_\beta u_\beta \right\rangle + \left\langle \mathcal{L}_\sigma u_\sigma \right\rangle + \left\langle R_\beta \left(u_\beta \right) \right\rangle + \left\langle R_\sigma \left(u_\sigma \right) \right\rangle. \tag{7.178}$$

We can then apply the average plus perturbation decompositions, so that we have

$$\begin{aligned} \left(\varepsilon_\beta + \varepsilon_\sigma \Gamma_a \right) \partial_t \left\langle u \right\rangle^{\beta\sigma} = {} & \left\langle \mathcal{L}_\beta \left\langle u \right\rangle^{\beta\sigma} \right\rangle + \left\langle \mathcal{L}_\sigma \left\langle u \right\rangle^{\beta\sigma} \right\rangle \\ & + \left\langle \mathcal{L}_\beta \hat{u}_\beta \right\rangle + \left\langle \mathcal{L}_\sigma \hat{u}_\sigma \right\rangle + \left\langle R_\beta \left(u_\beta \right) \right\rangle + \left\langle R_\sigma \left(u_\sigma \right) \right\rangle. \end{aligned} \tag{7.179}$$

7.7.2 Perturbation

We consider the microscale operators that are given by Equations 7.6a and 7.6d and use the perturbation decomposition to obtain

$$\partial_t \langle u \rangle^{\beta\sigma} + \partial_t \hat{u}_\beta = \mathcal{L}_\beta \langle u \rangle^{\beta\sigma} + \mathcal{L}_\beta \hat{u}_\beta + R_\beta(u_\beta) \text{ in } \mathcal{V}_\beta, \tag{7.180a}$$

$$\Gamma_a \partial_t \langle u \rangle^{\beta\sigma} + \Gamma_a \partial_t \hat{u}_\sigma = \mathcal{L}_\sigma \langle u \rangle^{\beta\sigma} + \mathcal{L}_\sigma \hat{u}_\sigma + R_\sigma(u_\sigma) \text{ in } \mathcal{V}_\sigma. \tag{7.180b}$$

The perturbation equations for phase β can be obtained by the operation ($(\varepsilon_\beta + \varepsilon_\sigma \Gamma_a)$ times Equations 7.180a minus Equation 7.179), which yields

$$\begin{aligned}(\varepsilon_\beta + \varepsilon_\sigma \Gamma_a)\partial_t \hat{u}_\beta = {} & (\varepsilon_\beta + \varepsilon_\sigma \Gamma_a)\mathcal{L}_\beta \langle u \rangle^{\beta\sigma} - \left\langle \mathcal{L}_\beta \langle u \rangle^{\beta\sigma} \right\rangle - \left\langle \mathcal{L}_\sigma \langle u \rangle^{\beta\sigma} \right\rangle \\ & + (\varepsilon_\beta + \varepsilon_\sigma \Gamma_a)\mathcal{L}_\beta \hat{u}_\beta - \langle \mathcal{L}_\beta \hat{u}_\beta \rangle - \langle \mathcal{L}_\sigma \hat{u}_\beta \rangle \\ & + (\varepsilon_\beta + \varepsilon_\sigma \Gamma_a) R_\beta(u_\beta) - \langle R_\beta(u_\beta) \rangle - \langle R_\sigma(u_\sigma) \rangle. \end{aligned} \tag{7.181}$$

A similar operation can be performed for the other phase ($(\varepsilon_\beta + \varepsilon_\sigma \Gamma_a)$ times Equations 7.180b minus Γ_a times Equation 7.179 minus) and leads to

$$\begin{aligned}(\varepsilon_\beta + \varepsilon_\sigma \Gamma_a)\Gamma_a \partial_t \hat{u}_\sigma = {} & (\varepsilon_\beta + \varepsilon_\sigma \Gamma_a)\mathcal{L}_\sigma \langle u \rangle^{\beta\sigma} - \Gamma_a \left\langle \mathcal{L}_\beta \langle u \rangle^{\beta\sigma} \right\rangle - \Gamma_a \left\langle \mathcal{L}_\sigma \langle u \rangle^{\beta\sigma} \right\rangle \\ & + (\varepsilon_\beta + \varepsilon_\sigma \Gamma_a)\mathcal{L}_\sigma \hat{u}_\sigma - \Gamma_a \langle \mathcal{L}_\beta \hat{u}_\beta \rangle - \Gamma_a \langle \mathcal{L}_\sigma \hat{u}_\beta \rangle \\ & + (\varepsilon_\beta + \varepsilon_\sigma \Gamma_a) R_\sigma(u_\sigma) - \Gamma_a \langle R_\beta(u_\beta) \rangle - \Gamma_a \langle R_\sigma(u_\sigma) \rangle. \end{aligned} \tag{7.182}$$

We further have the set of boundary conditions as

$$\hat{u}_\beta - \hat{u}_\sigma = 0 \text{ on } \mathcal{A}_{\beta\sigma}, \tag{7.183}$$

$$\mathcal{B}_\beta \hat{u}_\beta - \mathcal{B}_\beta \hat{u}_\sigma = \mathbf{n}_{\beta\sigma} \cdot (\mathbf{A}_\beta - \Gamma_A \mathbf{A}_\sigma) \cdot \nabla \langle u \rangle^{\beta\sigma} + \Omega(u_\sigma) \text{ on } \mathcal{A}_{\beta\sigma}, \tag{7.184}$$

that is simply obtained by using the average plus perturbation decomposition.

7.7.3 Approximations

7.7.3.1 Spatial Frequency Approximation

Similar to approximations detailed in Section 7.5.3, we will assume that we can neglect terms involving the intra-REV spatial variable, **y**, so the first term on the RHS of Equation 7.181 is

$$\begin{aligned}\left\langle \mathcal{L}_\beta \langle u \rangle^{\beta\sigma} \right\rangle &= \left\langle \nabla \cdot \left(\mathbf{A}_\beta \cdot \nabla \langle u \rangle^{\beta\sigma} - \text{Pe}_\beta^\ell \mathbf{v}_\beta \langle u \rangle^{\beta\sigma} \right) \right\rangle \\ &\simeq \langle \mathcal{L}_\beta \rangle \langle u \rangle^{\beta\sigma}, \end{aligned} \tag{7.185}$$

and the first term on the RHS of Equation 7.182 is

$$\left\langle \mathcal{L}_\sigma \langle u \rangle^{\beta\sigma} \right\rangle \simeq \langle \mathcal{L}_\sigma \rangle \langle u \rangle^{\beta\sigma}. \tag{7.186}$$

7.7.3.2 Amplitude Approximation

We further linearize our system using the zero-order Taylor expansions

$$R_i\left(u_i\right) \simeq R_i\left(\left\langle u\right\rangle^{\beta\sigma}\right), \tag{7.187}$$

$$\Omega\left(u_A\right) \simeq \Omega\left(\left\langle u\right\rangle^{\beta\sigma}\right). \tag{7.188}$$

We emphasize that such approximations are nonstandard, as the analysis of linear systems only requires approximation on the frequencies of the signals (see discussion in Section 7.5.3).

7.7.3.3 Approximate Form

Applying all these approximations to Equation 7.181 leads to

$$\begin{aligned}
&\left(\varepsilon_\beta + \varepsilon_\sigma \Gamma_a\right)\partial_t \hat{u}_\beta - \left(\varepsilon_\beta + \varepsilon_\sigma \Gamma_a\right)\mathcal{L}_\beta \hat{u}_\beta + \left(\left\langle \mathcal{L}_\beta \hat{u}_\beta\right\rangle + \left\langle \mathcal{L}_\sigma \hat{u}_\sigma\right\rangle\right) \\
&\quad = \left(\varepsilon_\beta + \varepsilon_\sigma \Gamma_a\right)\mathcal{L}_\beta \left\langle u\right\rangle^{\beta\sigma} - \varepsilon_\beta \left\langle \mathcal{L}_\beta\right\rangle^{\beta} \left\langle u\right\rangle^{\beta\sigma} - \varepsilon_\sigma \left\langle \mathcal{L}_\sigma\right\rangle^{\sigma} \left\langle u\right\rangle^{\beta\sigma} \\
&\qquad + \left(\varepsilon_\beta + \varepsilon_\sigma \Gamma_a\right)R_\beta\left(\left\langle u\right\rangle^{\beta\sigma}\right) - \varepsilon_\beta R_\beta\left(\left\langle u\right\rangle^{\beta\sigma}\right) - \varepsilon_\sigma R_\sigma\left(\left\langle u\right\rangle^{\beta\sigma}\right).
\end{aligned} \tag{7.189}$$

For Equation 7.182, we have

$$\begin{aligned}
&\left(\varepsilon_\beta + \varepsilon_\sigma \Gamma_a\right)\Gamma_a \partial_t \hat{u}_\sigma - \left(\varepsilon_\beta + \varepsilon_\sigma \Gamma_a\right)\mathcal{L}_\sigma \hat{u}_\sigma + \Gamma_a\left(\left\langle \mathcal{L}_\beta \hat{u}_\beta\right\rangle + \left\langle \mathcal{L}_\sigma \hat{u}_\beta\right\rangle\right) \\
&\quad = \left(\varepsilon_\beta + \varepsilon_\sigma \Gamma_a\right)\mathcal{L}_\sigma \left\langle u\right\rangle^{\beta\sigma} - \varepsilon_\beta \Gamma_a \left\langle \mathcal{L}_\beta\right\rangle^{\beta} \left\langle u\right\rangle^{\beta\sigma} - \varepsilon_\sigma \Gamma_a \left\langle \mathcal{L}_\sigma\right\rangle^{\sigma} \left\langle u\right\rangle^{\beta\sigma} \\
&\qquad + \left(\varepsilon_\beta + \varepsilon_\sigma \Gamma_a\right)R_\sigma\left(u_\sigma\right) - \varepsilon_\beta \Gamma_a R_\beta\left(\left\langle u\right\rangle^{\beta\sigma}\right) - \varepsilon_\sigma \Gamma_a R_\sigma\left(\left\langle u\right\rangle^{\beta\sigma}\right).
\end{aligned} \tag{7.190}$$

The first line on the RHS of Equation 7.189 can be decomposed to make source terms explicit

$$\begin{aligned}
&\left(\varepsilon_\beta + \varepsilon_\sigma \Gamma_a\right)\mathcal{L}_\beta \left\langle u\right\rangle^{\beta\sigma} - \varepsilon_\beta \left\langle \mathcal{L}_\beta\right\rangle^{\beta} \left\langle u\right\rangle^{\beta\sigma} - \varepsilon_\sigma \left\langle \mathcal{L}_\sigma\right\rangle^{\sigma} \left\langle u\right\rangle^{\beta\sigma} \\
&\quad = \left(\varepsilon_\beta + \varepsilon_\sigma \Gamma_a\right)\widetilde{\mathcal{L}}_\beta \left\langle u\right\rangle^{\beta\sigma} + \varepsilon_\sigma \Gamma_a \left\langle \mathcal{L}_\beta\right\rangle^{\beta} \left\langle u\right\rangle^{\beta\sigma} - \varepsilon_\sigma \left\langle \mathcal{L}_\sigma\right\rangle^{\sigma} \left\langle u\right\rangle^{\beta\sigma}.
\end{aligned} \tag{7.191}$$

We have that

$$\begin{aligned}
&\left(\varepsilon_\beta + \varepsilon_\sigma \Gamma_a\right)\widetilde{\mathcal{L}}_\beta \left\langle u\right\rangle^{\beta\sigma} + \varepsilon_\sigma \Gamma_a \left\langle \mathcal{L}_\beta\right\rangle^{\beta} \left\langle u\right\rangle^{\beta\sigma} - \varepsilon_\sigma \left\langle \mathcal{L}_\sigma\right\rangle^{\sigma} \left\langle u\right\rangle^{\beta\sigma} \\
&\quad = -\left[\left(\varepsilon_\beta + \varepsilon_\sigma \Gamma_a\right)\mathrm{Pe}_\beta^\ell \tilde{\mathbf{v}}_\beta + \varepsilon_\sigma \Gamma_a \mathrm{Pe}_\beta^\ell \left\langle \mathbf{v}_\beta\right\rangle^{\beta}\right] \cdot \nabla \left\langle u\right\rangle^{\beta\sigma} + \varepsilon_\sigma \left(\Gamma_a \mathbf{A}_\beta - \Gamma_A \mathbf{A}_\sigma\right) : \nabla\nabla \left\langle u\right\rangle^{\beta\sigma},
\end{aligned} \tag{7.192}$$

with $\widetilde{\mathcal{L}}_\beta \left\langle u\right\rangle^{\beta\sigma} \equiv -\mathrm{Pe}_\beta^\ell \tilde{\mathbf{v}}_\beta \cdot \nabla \left\langle u\right\rangle^{\beta\sigma}$. Similarly for the first line on the RHS of Equation 7.190, we have

$$\begin{aligned}
&\left(\varepsilon_\beta + \varepsilon_\sigma \Gamma_a\right)\mathcal{L}_\sigma \left\langle u\right\rangle^{\beta\sigma} - \varepsilon_\beta \Gamma_a \left\langle \mathcal{L}_\beta\right\rangle^{\beta} \left\langle u\right\rangle^{\beta\sigma} - \varepsilon_\sigma \Gamma_a \left\langle \mathcal{L}_\sigma\right\rangle^{\sigma} \left\langle u\right\rangle^{\beta\sigma} \\
&\quad = \varepsilon_\beta \Gamma_a \mathrm{Pe}_\beta^\ell \left\langle \mathbf{v}_\beta\right\rangle^{\beta} \cdot \nabla \left\langle u\right\rangle^{\beta\sigma} - \varepsilon_\beta \left(\Gamma_a \mathbf{A}_\beta - \Gamma_A \mathbf{A}_\sigma\right) : \nabla\nabla \left\langle u\right\rangle^{\beta\sigma}.
\end{aligned} \tag{7.193}$$

Equation 7.189 can therefore be written as

$$\begin{aligned}&\left(\varepsilon_\beta+\varepsilon_\sigma\Gamma_a\right)\partial_t\hat{u}_\beta-\left(\varepsilon_\beta+\varepsilon_\sigma\Gamma_a\right)\mathcal{L}_\beta\hat{u}_\beta+\left\langle\mathcal{L}_\beta\hat{u}_\beta\right\rangle+\left\langle\mathcal{L}_\sigma\hat{u}_\sigma\right\rangle\\&=-\left[\left(\varepsilon_\beta+\varepsilon_\sigma\Gamma_a\right)\mathrm{Pe}_\beta^\ell\tilde{\mathbf{v}}_\beta+\varepsilon_\sigma\Gamma_a\mathrm{Pe}_\beta^\ell\left\langle\mathbf{v}_\beta\right\rangle^\beta\right]\cdot\nabla\left\langle u\right\rangle^{\beta\sigma}\\&\quad+\varepsilon_\sigma\left(\Gamma_a\mathbf{A}_\beta-\Gamma_A\mathbf{A}_\sigma\right):\nabla\nabla\left\langle u\right\rangle^{\beta\sigma}+\varepsilon_\sigma\left[\Gamma_aR_\beta\left(\left\langle u\right\rangle^{\beta\sigma}\right)-R_\sigma\left(\left\langle u\right\rangle^{\beta\sigma}\right)\right],\end{aligned}\tag{7.194}$$

and Equation 7.190 as

$$\begin{aligned}&\left(\varepsilon_\beta+\varepsilon_\sigma\Gamma_a\right)\Gamma_a\partial_t\hat{u}_\sigma-\left(\varepsilon_\beta+\varepsilon_\sigma\Gamma_a\right)\mathcal{L}_\sigma\hat{u}_\sigma+\Gamma_a\left(\left\langle\mathcal{L}_\beta\hat{u}_\beta\right\rangle+\left\langle\mathcal{L}_\sigma\hat{u}_\sigma\right\rangle\right)\\&=\varepsilon_\beta\Gamma_a\mathrm{Pe}_\beta^\ell\left\langle\mathbf{v}_\beta\right\rangle^\beta\cdot\nabla\left\langle u\right\rangle^{\beta\sigma}-\varepsilon_\beta\left(\Gamma_a\mathbf{A}_\beta-\Gamma_A\mathbf{A}_\sigma\right):\nabla\nabla\left\langle u\right\rangle^{\beta\sigma}\\&\quad-\varepsilon_\beta\left[\Gamma_aR_\beta\left(\left\langle u\right\rangle^{\beta\sigma}\right)-R_\sigma\left(\left\langle u\right\rangle^{\beta\sigma}\right)\right],\end{aligned}\tag{7.195}$$

with the set of boundary conditions

$$\hat{u}_\beta-\hat{u}_\sigma=0\ \text{ on }\ \mathcal{A}_{\beta\sigma},\tag{7.196}$$

$$\mathcal{B}_\beta\hat{u}_\beta-\mathcal{B}_\beta\hat{u}_\sigma=\mathbf{n}_{\beta\sigma}\cdot\left(\mathbf{A}_\beta-\Gamma_A\mathbf{A}_\sigma\right)\cdot\nabla\left\langle u\right\rangle^{\beta\sigma}+\Omega\left(\left\langle u\right\rangle^{\beta\sigma}\right)\text{on }\mathcal{A}_{\beta\sigma}.\tag{7.197}$$

7.7.4 Closure

In general, the transient closure is incompatible with the time-asymptotic limit so that we only consider the stationary closure:

$$\begin{aligned}\begin{bmatrix}\tilde{u}_\beta\\\tilde{u}_\sigma\end{bmatrix}&=\begin{bmatrix}\mathbf{b}_\beta^{\mathrm{LNE}}\\\mathbf{b}_\sigma^{\mathrm{LNE}}\end{bmatrix}\cdot\nabla\left\langle u\right\rangle^{\beta\sigma}+\begin{bmatrix}\mathbf{W}_\beta^{\mathrm{LNE}}\\\mathbf{W}_\sigma^{\mathrm{LNE}}\end{bmatrix}:\nabla\nabla\left\langle u\right\rangle^{\beta\sigma}\\&\quad+\begin{bmatrix}\mathbf{c}_\beta^{\mathrm{LNE}}\\\mathbf{c}_\sigma^{\mathrm{LNE}}\end{bmatrix}\Omega\left(\left\langle u\right\rangle^{\beta\sigma}\right)+\begin{bmatrix}\mathbf{r}_\beta^{\mathrm{LNE}}\\\mathbf{r}_\sigma^{\mathrm{LNE}}\end{bmatrix}\left[\Gamma_aR_\beta\left(\left\langle u\right\rangle^{\beta\sigma}\right)-R_\sigma\left(\left\langle u\right\rangle^{\beta\sigma}\right)\right].\end{aligned}\tag{7.198}$$

7.7.4.1 Closure Problems

We can now introduce Equation 7.198 in Equations 7.194 through 7.197 and identify the mapping variables corresponding to each source term. This leads to the following four problems.

7.7.4.1.1 Problem LNE-Stationary-I

$$\begin{aligned}&-\mathcal{L}_\beta\mathbf{b}_\beta^{\mathrm{LNE}}+\frac{1}{\varepsilon_\beta+\varepsilon_\sigma\Gamma_a}\left(\left\langle\mathcal{L}_\beta\mathbf{b}_\beta^{\mathrm{LNE}}\right\rangle+\left\langle\mathcal{L}_\sigma\mathbf{b}_\beta^{\mathrm{LNE}}\right\rangle\right)\\&\qquad=-\mathrm{Pe}_\beta^\ell\tilde{\mathbf{v}}_\beta-\frac{\varepsilon_\sigma\Gamma_a}{\varepsilon_\beta+\varepsilon_\sigma\Gamma_a}\mathrm{Pe}_\beta^\ell\left\langle\mathbf{v}_\beta\right\rangle^\beta\text{ in }\mathcal{V}_\beta,\end{aligned}\tag{7.199a}$$

$$\text{BC1} \quad \mathbf{b}_\beta^{\text{LNE}} - \mathbf{b}_\sigma^{\text{LNE}} = 0 \text{ on } \mathcal{A}_{\beta\sigma}, \tag{7.199b}$$

$$\text{BC2} \quad \mathcal{B}_\beta \mathbf{b}_\beta^{\text{LNE}} - \mathcal{B}_\sigma \mathbf{b}_\sigma^{\text{LNE}} = \mathbf{n}_{\beta\sigma} \cdot \left(\mathbf{A}_\beta - \Gamma_A \mathbf{A}_\sigma \right) \text{on } \mathcal{A}_{\beta\sigma}, \tag{7.199c}$$

$$\text{Periodicity 1} \quad \mathbf{b}_\alpha^{\text{LNE}} \left(\mathbf{x} + \mathbf{l}_i \right) = \mathbf{b}_\alpha^{\text{LNE}} \left(\mathbf{x} \right) \text{ with } \alpha = \beta, \sigma, \tag{7.199d}$$

$$\text{Periodicity 2} \quad \mathcal{J}_\alpha \mathbf{b}_\alpha^{\text{LNE}} \left(\mathbf{x} + \mathbf{l}_i \right) = \mathcal{J}_\alpha \mathbf{b}_\alpha^{\text{LNE}} \left(\mathbf{x} \right) \text{ with } \alpha = \beta, \sigma, \tag{7.199e}$$

$$\text{Average} \quad \varepsilon_\beta \left\langle \mathbf{b}_\beta^{\text{LNE}} \right\rangle^\beta + \varepsilon_\sigma \left\langle \mathbf{b}_\sigma^{\text{LNE}} \right\rangle^\sigma = 0, \tag{7.199f}$$

$$-\mathcal{L}_\sigma \mathbf{b}_\sigma^{\text{LNE}} + \frac{\Gamma_a}{\varepsilon_\beta + \varepsilon_\sigma \Gamma_a} \left(\left\langle \mathcal{L}_\beta \mathbf{b}_\sigma^{\text{LNE}} \right\rangle + \left\langle \mathcal{L}_\sigma \mathbf{b}_\sigma^{\text{LNE}} \right\rangle \right) = \frac{\varepsilon_\beta \Gamma_a}{\varepsilon_\beta + \varepsilon_\sigma \Gamma_a} \text{Pe}_\beta^\ell \left\langle \mathbf{v}_\beta \right\rangle^\beta \text{ in } \mathcal{V}_\sigma. \tag{7.199g}$$

7.7.4.1.2 Problem LNE-Stationary-II

$$-\mathcal{L}_\beta \mathbf{W}_\beta^{\text{LNE}} + \frac{1}{\varepsilon_\beta + \varepsilon_\sigma \Gamma_a} \left(\left\langle \mathcal{L}_\beta \mathbf{W}_\beta^{\text{LNE}} \right\rangle + \left\langle \mathcal{L}_\sigma \mathbf{W}_\beta^{\text{LNE}} \right\rangle \right)$$

$$= -\mathcal{J}_\beta \mathbf{b}_\beta^{\text{LNE}} + \frac{1}{\varepsilon_\beta + \varepsilon_\sigma \Gamma_a} \left(\left\langle \mathcal{J}_\beta \mathbf{b}_\beta^{\text{LNE}} \right\rangle + \left\langle \mathcal{J}_\sigma \mathbf{b}_\sigma^{\text{LNE}} \right\rangle \right) + \varepsilon_\sigma \left(\Gamma_a \mathbf{A}_\beta - \Gamma_A \mathbf{A}_\sigma \right), \tag{7.200a}$$

$$\text{BC1} \quad \mathbf{W}_\beta^{\text{LNE}} - \mathbf{W}_\sigma^{\text{LNE}} = 0 \text{ on } \mathcal{A}_{\beta\sigma}, \tag{7.200b}$$

$$\text{BC2} \quad \mathcal{B}_\beta \mathbf{W}_\beta^{\text{LNE}} - \mathcal{B}_\sigma \mathbf{W}_\sigma^{\text{LNE}} = \mathbf{n}_{\beta\sigma} \cdot \left(\mathbf{A}_\beta \mathbf{b}_\beta^{\text{LNE}} - \Gamma_A \mathbf{A}_\sigma \mathbf{b}_\sigma^{\text{LNE}} \right) \text{on } \mathcal{A}_{\beta\sigma}, \tag{7.200c}$$

$$\text{Periodicity 1} \quad \mathbf{W}_\alpha^{\text{LNE}} \left(\mathbf{x} + \mathbf{l}_i \right) = \mathbf{W}_\alpha^{\text{LNE}} \left(\mathbf{x} \right) \text{ with } \alpha = \beta, \sigma, \tag{7.200d}$$

$$\text{Periodicity 2} \quad \mathcal{J}_\alpha \mathbf{W}_\alpha^{\text{LNE}} \left(\mathbf{x} + \mathbf{l}_i \right) = \mathcal{J}_\alpha \mathbf{W}_\alpha^{\text{LNE}} \left(\mathbf{x} \right) \text{ with } \alpha = \beta, \sigma, \tag{7.200e}$$

$$\text{Average} \quad \varepsilon_\beta \left\langle \mathbf{W}_\beta^{\text{LNE}} \right\rangle^\beta + \varepsilon_\sigma \left\langle \mathbf{W}_\sigma^{\text{LNE}} \right\rangle^\sigma = 0, \tag{7.200f}$$

$$-\mathcal{L}_\sigma \mathbf{W}_\sigma^{\text{LNE}} + \frac{\Gamma_a}{\varepsilon_\beta + \varepsilon_\sigma \Gamma_a} \left(\left\langle \mathcal{L}_\beta \mathbf{W}_\beta^{\text{LNE}} \right\rangle + \left\langle \mathcal{L}_\sigma \mathbf{W}_\beta^{\text{LNE}} \right\rangle \right)$$

$$= -\mathcal{J}_\sigma \mathbf{b}_\sigma^{\text{LNE}} + \frac{\Gamma_a}{\varepsilon_\beta + \varepsilon_\sigma \Gamma_a} \left(\left\langle \mathcal{J}_\beta \mathbf{b}_\beta^{\text{LNE}} \right\rangle + \left\langle \mathcal{J}_\sigma \mathbf{b}_\sigma^{\text{LNE}} \right\rangle \right) - \varepsilon_\beta \left(\Gamma_a \mathbf{A}_\beta - \Gamma_A \mathbf{A}_\sigma \right). \tag{7.200g}$$

7.7.4.1.3 Problem LNE-Stationary-III

$$-\mathcal{L}_\beta \mathbf{c}_\beta^{\text{LNE}} + \frac{1}{\varepsilon_\beta + \varepsilon_\sigma \Gamma_a} \left(\left\langle \mathcal{L}_\beta \mathbf{c}_\beta^{\text{LNE}} \right\rangle + \left\langle \mathcal{L}_\sigma \mathbf{c}_\beta^{\text{LNE}} \right\rangle \right) = 0 \text{ in } \mathcal{V}_\beta, \tag{7.201a}$$

$$\text{BC1} \quad \mathsf{c}_\beta^{\text{LNE}} - \mathsf{c}_\sigma^{\text{LNE}} = 0 \text{ on } \mathcal{A}_{\beta\sigma}, \tag{7.201b}$$

$$\text{BC2} \quad \mathcal{B}_\beta \mathsf{c}_\beta^{\text{LNE}} - \mathcal{B}_\sigma \mathsf{c}_\sigma^{\text{LNE}} = 1 \text{ on } \mathcal{A}_{\beta\sigma}, \tag{7.201c}$$

$$\text{Periodicity 1} \quad \mathsf{c}_\alpha^{\text{LNE}}\left(\mathbf{x} + \mathbf{l}_i\right) = \mathsf{c}_\alpha^{\text{LNE}}\left(\mathbf{x}\right) \text{ with } \alpha = \beta, \sigma, \tag{7.201d}$$

$$\text{Periodicity 2} \quad \mathcal{J}_\alpha \mathsf{c}_\alpha^{\text{LNE}}\left(\mathbf{x} + \mathbf{l}_i\right) = \mathcal{J}_\alpha \mathsf{c}_\alpha^{\text{LNE}}\left(\mathbf{x}\right) \text{ with } \alpha = \beta, \sigma, \tag{7.201e}$$

$$\text{Average} \quad \varepsilon_\beta \left\langle \mathsf{c}_\beta^{\text{LNE}} \right\rangle^\beta + \varepsilon_\sigma \left\langle \mathsf{c}_\sigma^{\text{LNE}} \right\rangle^\sigma = 0, \tag{7.201f}$$

$$-\mathcal{L}_\sigma \mathsf{c}_\sigma^{\text{LNE}} + \frac{\Gamma_a}{\varepsilon_\beta + \varepsilon_\sigma \Gamma_a}\left(\left\langle \mathcal{L}_\beta \mathsf{c}_\beta^{\text{LNE}} \right\rangle + \left\langle \mathcal{L}_\sigma \mathsf{c}_\sigma^{\text{LNE}} \right\rangle\right) = 0 \text{ in } \mathcal{V}_\sigma. \tag{7.201g}$$

7.7.4.1.4 *Problem LNE-Stationary-IV*

$$-\mathcal{L}_\beta \mathsf{r}_\beta^{\text{LNE}} + \frac{1}{\varepsilon_\beta + \varepsilon_\sigma \Gamma_a}\left(\left\langle \mathcal{L}_\beta \mathsf{r}_\beta^{\text{LNE}} \right\rangle + \left\langle \mathcal{L}_\sigma \mathsf{r}_\sigma^{\text{LNE}} \right\rangle\right) = \varepsilon_\sigma \text{ in } \mathcal{V}_\beta, \tag{7.202a}$$

$$\text{BC1} \quad \mathsf{r}_\beta^{\text{LNE}} - \mathsf{r}_\sigma^{\text{LNE}} = 0 \text{ on } \mathcal{A}_{\beta\sigma}, \tag{7.202b}$$

$$\text{BC2} \quad \mathcal{B}_\beta \mathsf{r}_\beta^{\text{LNE}} - \mathcal{B}_\sigma \mathsf{r}_\sigma^{\text{LNE}} = 1 \text{ on } \mathcal{A}_{\beta\sigma}, \tag{7.202c}$$

$$\text{Periodicity 1} \quad \mathsf{r}_\alpha^{\text{LNE}}\left(\mathbf{x} + \mathbf{l}_i\right) = \mathsf{r}_\alpha^{\text{LNE}}\left(\mathbf{x}\right) \text{ with } \alpha = \beta, \sigma, \tag{7.202d}$$

$$\text{Periodicity 2} \quad \mathcal{J}_\alpha \mathsf{r}_\alpha^{\text{LNE}}\left(\mathbf{x} + \mathbf{l}_i\right) = \mathcal{J}_\alpha \mathsf{r}_\alpha^{\text{LNE}}\left(\mathbf{x}\right) \text{ with } \alpha = \beta, \sigma, \tag{7.202e}$$

$$\text{Average} \quad \varepsilon_\beta \left\langle \mathsf{r}_\beta^{\text{LNE}} \right\rangle^\beta + \varepsilon_\sigma \left\langle \mathsf{r}_\sigma^{\text{LNE}} \right\rangle^\sigma = 0, \tag{7.202f}$$

$$-\mathcal{L}_\sigma \mathsf{r}_\sigma^{\text{LNE}} + \frac{\Gamma_a}{\varepsilon_\beta + \varepsilon_\sigma \Gamma_a}\left(\left\langle \mathcal{L}_\beta \mathsf{r}_\beta^{\text{LNE}} \right\rangle + \left\langle \mathcal{L}_\sigma \mathsf{r}_\sigma^{\text{LNE}} \right\rangle\right) = -\varepsilon_\beta \text{ in } \mathcal{V}_\sigma. \tag{7.202g}$$

7.7.5 Macroscale Model

Applying the frequency and amplitude approximations to Equation 7.179 leads to

$$\begin{aligned}\left(\varepsilon_\beta + \varepsilon_\sigma \Gamma_a\right) \partial_t \left\langle u \right\rangle^{\beta\sigma} = {} & \left\langle \mathcal{L}_\beta \right\rangle \left\langle u \right\rangle^{\beta\sigma} + \left\langle \mathcal{L}_\sigma \right\rangle \left\langle u \right\rangle^{\beta\sigma} + \left\langle \mathcal{L}_\beta \hat{u}_\beta \right\rangle + \left\langle \mathcal{L}_\sigma \hat{u}_\sigma \right\rangle \\ & + R_\beta\left(\left\langle u \right\rangle^{\beta\sigma}\right) + R_\sigma\left(\left\langle u \right\rangle^{\beta\sigma}\right).\end{aligned} \tag{7.203}$$

Using Equation 7.198 in Equation 7.203, we have

$$\begin{aligned}
&\left(\varepsilon_\beta + \varepsilon_\sigma \Gamma_a\right) \partial_t \left\langle u \right\rangle^{\beta\sigma} + \nabla \cdot \left(\mathrm{Pe}_\beta^\ell \left\langle \mathbf{v}_\beta \right\rangle \left\langle u \right\rangle^{\beta\sigma} \right) \\
&- \nabla \cdot \left[\left(\varepsilon_\beta \mathbf{A}_\beta + \varepsilon_\sigma \Gamma_A \mathbf{A}_\sigma + \mathbf{B}^{\mathrm{LNE}} \right) \cdot \nabla \left\langle u \right\rangle^{\beta\sigma} \right] \\
&= \varepsilon_\beta R_\beta \left(\left\langle u \right\rangle^{\beta\sigma} \right) + \varepsilon_\sigma R_\sigma \left(\left\langle u \right\rangle^{\beta\sigma} \right) \\
&+ M^{\mathrm{LNE}} \left(\Gamma_a R_\beta \left(\left\langle u \right\rangle^{\beta\sigma} \right) - R_\sigma \left(\left\langle u \right\rangle^{\beta\sigma} \right) \right) + N^{\mathrm{LNE}} \Omega \left(\left\langle u \right\rangle^{\beta\sigma} \right),
\end{aligned} \tag{7.204}$$

with

$$\begin{aligned}
\mathbf{B}^{\mathrm{LNE}} &= \left\langle \mathcal{L}_\beta \mathbf{W}_\beta^{\mathrm{LNE}} - \mathcal{J}_\beta \mathbf{b}_\beta^{\mathrm{LNE}} + \mathbf{A}_\beta \cdot \nabla \mathbf{b}_\beta^{\mathrm{LNE}} \right\rangle \\
&+ \left\langle \mathcal{L}_\sigma \mathbf{W}_\sigma^{\mathrm{LNE}} - \mathcal{J}_\sigma \mathbf{b}_\sigma^{\mathrm{LNE}} + \Gamma_A \mathbf{A}_\sigma \cdot \nabla \mathbf{b}_\sigma^{\mathrm{LNE}} \right\rangle.
\end{aligned} \tag{7.205}$$

Cancelling opposite fluxes leads to

$$\mathbf{B}^{\mathrm{LNE}} = \left\langle \mathbf{A}_\beta \cdot \nabla \mathbf{b}_\beta^{\mathrm{LNE}} \right\rangle + \left\langle \Gamma_A \mathbf{A}_\sigma \cdot \nabla \mathbf{b}_\sigma^{\mathrm{LNE}} \right\rangle - \left\langle \mathbf{v}_\beta \mathbf{b}_\beta^{\mathrm{LNE}} \right\rangle. \tag{7.206}$$

We also remark that a similar operation yields

$$M^{\mathrm{LNE}} = \left\langle \mathcal{L}_\beta \mathbf{r}_\beta^{\mathrm{LNE}} \right\rangle + \left\langle \mathcal{L}_\sigma \mathbf{r}_\sigma^{\mathrm{LNE}} \right\rangle = 0, \tag{7.207}$$

$$N^{\mathrm{LNE}} = \left\langle \mathcal{L}_\beta \mathbf{c}_\beta^{\mathrm{LNE}} \right\rangle + \left\langle \mathcal{L}_\sigma \mathbf{c}_\sigma^{\mathrm{LNE}} \right\rangle = -a_v. \tag{7.208}$$

Therefore, we obtain the following transient nonequilibrium model:

$$\left(\varepsilon_\beta + \varepsilon_\sigma \Gamma_a\right) \partial_t \left\langle u \right\rangle^{\beta\sigma} + \nabla \cdot \left(\mathrm{Pe}_\beta^\ell \left\langle \mathbf{v}_\beta \right\rangle \left\langle u \right\rangle^{\beta\sigma} \right) = \nabla \cdot \left(\mathbf{A}^{\mathrm{LNE}} \cdot \nabla \left\langle u \right\rangle^{\beta\sigma} \right) + R^{\mathrm{LNE}}, \tag{7.209}$$

with

$$\mathbf{A}^{\mathrm{LNE}} = \varepsilon_\beta \mathbf{A}_\beta + \varepsilon_\sigma \Gamma_A \mathbf{A}_\sigma + \left\langle \mathbf{A}_\beta \cdot \nabla \mathbf{b}_\beta^{\mathrm{LNE}} \right\rangle + \left\langle \Gamma_A \mathbf{A}_\sigma \cdot \nabla \mathbf{b}_\sigma^{\mathrm{LNE}} \right\rangle - \left\langle \mathbf{v}_\beta \mathbf{b}_\beta^{\mathrm{LNE}} \right\rangle, \tag{7.210}$$

and the effective reaction rate is

$$R^{\mathrm{LNE}} = \varepsilon_\beta R_\beta \left(\left\langle u \right\rangle^{\beta\sigma} \right) + \varepsilon_\sigma R_\sigma \left(\left\langle u \right\rangle^{\beta\sigma} \right) - a_v \Omega \left(\left\langle u \right\rangle^{\beta\sigma} \right). \tag{7.211}$$

We remark here that the source terms appear simply in the macroscale model as volume or surface averages.

7.8 DERIVATION OF THE HYBRID MODELS

Hybrid models (also referred to as mixed models) combine macro- and microscale descriptions of a porous medium. There are many different possible hybrid descriptions of a single problem, and here, we will just give a simple example of one such model in the case where the ratio of diffusivities verifies

$$\Gamma_A \ll 1, \tag{7.212}$$

which corresponds to a much larger diffusion coefficient in the fluid phase. Our goal is to obtain a macroscale equation for the phase β coupled with a microscale equation for the solid phase σ.

7.8.1 Averaging

Since our goal is to obtain a macroscopic description only for the phase β, we average as in Section 7.5.1 for phase β and simply obtain

$$\varepsilon_\beta \partial_t \langle u_\beta \rangle^\beta = \left\langle \mathcal{L}_\beta \langle u_\beta \rangle^\beta \right\rangle + \left\langle \mathcal{L}_\beta \tilde{u}_\beta \right\rangle + \left\langle R_\beta \left(u_\beta \right) \right\rangle. \tag{7.213}$$

7.8.2 Perturbations

The perturbation equation is obtained by subtracting ε_β^{-1} times Equation 7.213 from Equation 7.6a, an operation that yields

$$\partial_t \tilde{u}_\beta - \widetilde{\mathcal{L}_\beta \tilde{u}_\beta} - \widetilde{R_\beta \left(u_\beta \right)} = \widetilde{\mathcal{L}_\beta \langle u_\beta \rangle^\beta} \text{ in } \mathcal{V}_\beta. \tag{7.214}$$

The corresponding boundary conditions result from the introduction of the average plus perturbation decompositions in Equations 7.6b and c:

$$\tilde{u}_\beta - u_\sigma = -\langle u_\beta \rangle^\beta \text{ on } \mathcal{A}_{\beta\sigma}, \tag{7.215}$$

$$\mathcal{B}_\beta \tilde{u}_\beta - \mathcal{B}_\beta u_\sigma = -\mathcal{B}_\beta \langle u_\beta \rangle^\beta + \Omega \left(u_\beta \right) \text{ on } \mathcal{A}_{\beta\sigma}. \tag{7.216}$$

Unfortunately, this problem is not well suited to a hybrid formulation since the boundary conditions strongly couple the micro- and macroscale problem. To circumvent this issue, we use the following approximations.

7.8.3 Approximations

7.8.3.1 Spatial Frequency Approximation

Similar to what was done previously, we use a frequency approximation so that

$$\widetilde{\mathcal{L}_\beta \langle u_\beta \rangle^\beta} \simeq -\mathrm{Pe}_\beta^\ell \tilde{\mathbf{v}}_\beta \cdot \nabla \langle u_\beta \rangle^\beta \equiv \widetilde{\mathcal{L}_\beta} \langle u_\beta \rangle^\beta. \tag{7.217}$$

7.8.3.2 Amplitude Approximation

The nonlinear reaction rates are approximated, using $\tilde{u}_\beta \ll \langle u_\beta \rangle^\beta$, so that

$$\Omega \left(u_\beta \right) \simeq \Omega \left(\langle u_\beta \rangle^\beta \right), \quad R_\beta \left(u_\beta \right) \simeq R_\beta \left(\langle u_\beta \rangle^\beta \right). \tag{7.218}$$

7.8.3.3 Hybrid Approximations

First, the flux boundary condition can be written as

$$\mathcal{B}_\beta \tilde{u}_\beta = -\mathcal{B}_\beta \left\langle u_\beta \right\rangle^\beta \text{ on } \mathcal{A}_{\beta\sigma}, \tag{7.219}$$

in the limit where $\Gamma_A \to 0$ and the interfacial source/sink does not influence the dispersion tensor (this is usually correct for Damkhöler numbers smaller than ≈ 10; see [93]). We will assume that these conditions hold only in the perturbation problem for the phase β, that is, that the BC does not modify the standard form of the dispersion coefficients, although it plays a role in the exchanged flux between the two phases. We will further simplify the system by considering the amplitude approximation $\tilde{u}_\beta \ll \left\langle u_\beta \right\rangle^\beta$, on the boundary $\mathcal{A}_{\beta\sigma}$. This yields

$$u_\sigma = \left\langle u_\beta \right\rangle^\beta \text{ on } \mathcal{A}_{\beta\sigma}. \tag{7.220}$$

We remark that this boundary condition is of a mixed type since it involves a macroscale value on the RHS and a microscale value on the LHS. Further, it is unclear how much the approximation $\tilde{u}_\beta \ll \left\langle u_\beta \right\rangle^\beta$ affects the results for the reactive case.

7.8.3.4 Quasi-Stationarity

We assume that the timescale for the relaxation of the phase β is much faster than in phase σ, which is consistent with the limit $\Gamma_A \to 0$, so that Equation 7.214 becomes

$$-\widetilde{\mathcal{L}_\beta \tilde{u}_\beta} - \widetilde{R_\beta\left(u_\beta\right)} = \widetilde{\mathcal{L}_\beta \left\langle u_\beta \right\rangle^\beta} \text{ in } \mathcal{V}_\beta. \tag{7.221}$$

7.8.3.5 Approximate Form

With the amplitude approximation, we have $\widetilde{R_\beta\left(u_\beta\right)} \simeq 0$. Therefore, we can write the perturbation problem as

$$-\widetilde{\mathcal{L}_\beta \tilde{u}_\beta} = -\mathrm{Pe}_\beta^\ell \tilde{\mathbf{v}}_\beta \cdot \nabla \left\langle u_\beta \right\rangle^\beta \text{ in } \mathcal{V}_\beta, \tag{7.222a}$$

$$\text{BC1} \quad \mathcal{B}_\beta \tilde{u}_\beta = -\mathbf{n}_{\beta\sigma} \cdot \left(\mathbf{A}_\beta \cdot \nabla \left\langle u_\beta \right\rangle^\beta \right) \text{ on } \mathcal{A}_{\beta\sigma}. \tag{7.222b}$$

7.8.4 Closure

We look for a solution of the type

$$\tilde{u}_\beta = \mathbf{b}_\beta^{\mathrm{HYB}} \cdot \nabla \left\langle u_\beta \right\rangle^\beta \tag{7.223}$$

and obtain the following closure problems:

$$-\widetilde{\mathcal{L}_\beta \mathbf{b}_\beta^{\mathrm{HYB}}} = -\mathrm{Pe}_\beta^\ell \tilde{\mathbf{v}}_\beta \text{ in } \mathcal{V}_\beta, \tag{7.224a}$$

$$\mathcal{B}_\beta \mathbf{b}_\beta^{\mathrm{HYB}} = \mathbf{n}_{\beta\sigma} \cdot \mathbf{A}_\beta \text{ at } \mathcal{A}_{\beta\sigma}, \tag{7.224b}$$

$$\text{Periodicity} \quad \mathbf{b}_\beta^{\text{HYB}}\left(\mathbf{x}+\mathbf{l}_i\right)=\mathbf{b}_\beta^{\text{HYB}}\left(\mathbf{x}\right), \tag{7.224c}$$

$$\text{Average} \quad \left\langle \mathbf{b}_\beta^{\text{HYB}} \right\rangle = 0. \tag{7.224d}$$

7.8.5 Hybrid Model

We can reformulate the macroscale equation in a way similar to Equation 7.57, that is,

$$\varepsilon_\beta\left[\underbrace{\partial_t\left\langle u_\beta\right\rangle^\beta}_{\text{Rate of change}}+\underbrace{\nabla\cdot\left(\text{Pe}_\beta^\ell\left\langle \mathbf{v}_\beta\right\rangle^\beta\left\langle u_\beta\right\rangle^\beta\right)}_{\text{Convection}}+\underbrace{\nabla\cdot\left(\text{Pe}_\beta^\ell\left\langle\tilde{\mathbf{v}}_\beta\tilde{u}_\beta\right\rangle^\beta\right)}_{\text{Velocity fluctuation effects}}\right]$$

$$=\underbrace{\nabla\cdot\left[\varepsilon_\beta\Gamma_A\mathbf{A}_\beta\cdot\left(\nabla\left\langle u_\beta\right\rangle^\beta+\underbrace{\frac{1}{V_\beta}\int_{\mathcal{A}_{\beta\sigma}}\mathbf{n}_{\beta\sigma}\tilde{u}_\beta dA}_{\text{Surface effects}}\right)\right]}_{\text{Diffusion}}$$

$$+\underbrace{\frac{1}{V}\int_{\mathcal{A}_{\beta\sigma}}\mathbf{n}_{\beta\sigma}\cdot\left(\Gamma_A\mathbf{A}_\beta\cdot\nabla u_\beta\right)dA}_{\square\text{nterfacialflu}\square}+\underbrace{\varepsilon_\beta\square_\beta\left(\left\langle u_\beta\right\rangle^\beta\right)}_{\square\text{verage reaction rate}}\square \tag{7.225}$$

While we have neglected the interfacial flux for estimating the dispersion tensor in the phase β, we do not neglect this flux in the averaged balance equations, as it is important to ensure conservation of properties (e.g., mass or energy). Neglecting it in the closure problems just means that we assume that it does not influence significantly the closure variables, not that we neglect it altogether.

The macroscale equation may be written as

$$\varepsilon_\beta\left[\partial_t\left\langle u_\beta\right\rangle^\beta+\nabla\cdot\left(\text{Pe}_\beta^\ell\left\langle\mathbf{v}_\beta\right\rangle^\beta\left\langle u_\beta\right\rangle^\beta\right)\right]=\nabla\cdot\left(\mathbf{A}^{\text{HYB}}\cdot\nabla\left\langle u_\beta\right\rangle^\beta\right)-\mathsf{J}_{\beta\sigma}+R^{\text{HYB}}, \tag{7.226}$$

with

$$\mathbf{A}^{\text{HYB}}=\varepsilon_\beta\mathbf{A}_\beta+\underbrace{\frac{1}{V}\int_{\mathcal{A}_{\beta\sigma}}\mathbf{n}_{\beta\sigma}\mathbf{b}_\beta dA}_{\text{Tortuosity}}-\underbrace{\text{Pe}_\beta^\ell\left\langle\tilde{\mathbf{v}}_\beta\mathbf{b}_\beta\right\rangle}_{\text{Dispersion}}, \tag{7.227}$$

$$R^{\text{HYB}}=-a_v\Omega\left(\left\langle u_\beta\right\rangle^\beta\right)+\varepsilon_\beta R_\beta\left(\left\langle u_\beta\right\rangle^\beta\right), \tag{7.228}$$

$$\mathsf{J}_{\beta\sigma}=-\frac{1}{V}\int_{\mathcal{A}_{\beta\sigma}}\mathbf{n}_{\beta\sigma}\cdot\left(\mathbf{A}_\beta\cdot\nabla u_\beta\right)dA=\frac{1}{V}\int_{\mathcal{A}_{\beta\sigma}}\mathbf{n}_{\beta\sigma}\cdot\left(\Gamma_A\mathbf{A}_\sigma\cdot\nabla u_\sigma\right)dA. \tag{7.229}$$

Solving the macroscale equation, Equation 7.226, requires the knowledge of $\mathsf{J}_{\beta\sigma}$, which may be calculated by solving the following coupled pore-scale equations:

$$\Gamma_a\partial_t u_\sigma=\mathcal{L}_\sigma u_\sigma+R_\sigma\left(u_\sigma\right)\text{ in }\mathcal{V}_\sigma, \tag{7.230}$$

$$\text{BC1} \quad u_\sigma = \left\langle u_\beta \right\rangle^\beta \text{ on } \mathcal{A}_{\beta\sigma}, \tag{7.231}$$

$$\text{IC} \quad u_\sigma\left(t = 0\right) = 0. \tag{7.232}$$

7.9 COMPUTATION OF EFFECTIVE PARAMETERS IN REALISTIC MEDIA

The computation of effective properties by solving closure problems started in the 1980s with relatively simple unit cells [122–124], to become a standard practice for complex 3D images in several commercial softwares. This chapter [17] presents several results for thermal dispersion coefficients, heat exchange coefficient, and distribution coefficient for 1D, 2D, and 3D simple unit cells. Given the renewed interest on the distribution coefficient [50,74] and the sparsity of published results, we will focus on this effective property in this section and provide results for 3D images of porous media.

7.9.1 Distribution Coefficient ξ

The calculation of the distribution coefficient ξ requires to solve the closure problem 2eq-stationary-VI. This problem is integrodifferential and requires a specific change of variables; see [17,65,125]. Preliminary results for ξ were given in [17] for stratified systems and simple unit cells (Chang's unit cell, simple cubic arrays of spheres, in-line and staggered arrays of cylinders). Recent results in [74] for equilateral triangle arrays of cylinders are consistent with early results in [17] and showed that ξ is a fundamental parameter in nonequilibrium models with heat sources at the fluid–solid interface. Here, we study the behavior of ξ for more realistic porous structures obtained via x-ray microtomography.

The porous medium that we study consists of glass beads packed into a plastic column. The 3D structure was obtained via x-ray computed microtomography (Phoenix nanotom®). The segmentation of gray-scale images was performed in Avizo®, using basic filtering and thresholding methods. A cubic region of interest was then selected in the center of the bead packing, which is presented in Figure 7.6a. Another simpler structure (Figure 7.6b,c), a cubic-centered array of spheres, was also used in the simulations for two different purposes:

1. To validate the finite volume (FV) numerical method with a Cartesian mesh. To this end, we compare results for a_v and ξ obtained using an FV approach on a Cartesian grid, with results obtained using the finite element (FE) method with an unstructured mesh.
2. To illustrate the effect of the geometries on values of the effective parameters.

7.9.2 Closure Problems and Numerical Methods

For the theoretical part of this chapter, we focused on a generic transport problem. Here, we illustrate the application to a heat transfer in a porous medium with $a = c_p$ and $u = T$. The steady-state version of problem 2eq-transient-VI Equation 7.96 can be written in dimensionalized form for a heat transfer problem as

$$\rho_\beta c_{p\beta}\mathbf{v}_\beta \cdot \nabla \mathsf{c}_\beta = k_\beta \nabla^2 \mathsf{c}_\beta - a_v \varepsilon_\beta^{-1} \xi_\beta \text{ in } \mathcal{V}_\beta, \tag{7.233a}$$

$$\text{BC1} \quad \mathsf{c}_\beta - \mathsf{c}_\sigma = 0 \text{ on } \mathcal{A}_{\beta\sigma}, \tag{7.233b}$$

$$\text{BC2} \quad -\mathbf{n}_{\beta\sigma} \cdot \left(k_\beta \nabla \mathsf{c}_\beta - k_\sigma \nabla \mathsf{c}_\sigma\right) = 1 \text{ on } \mathcal{A}_{\beta\sigma}, \tag{7.233c}$$

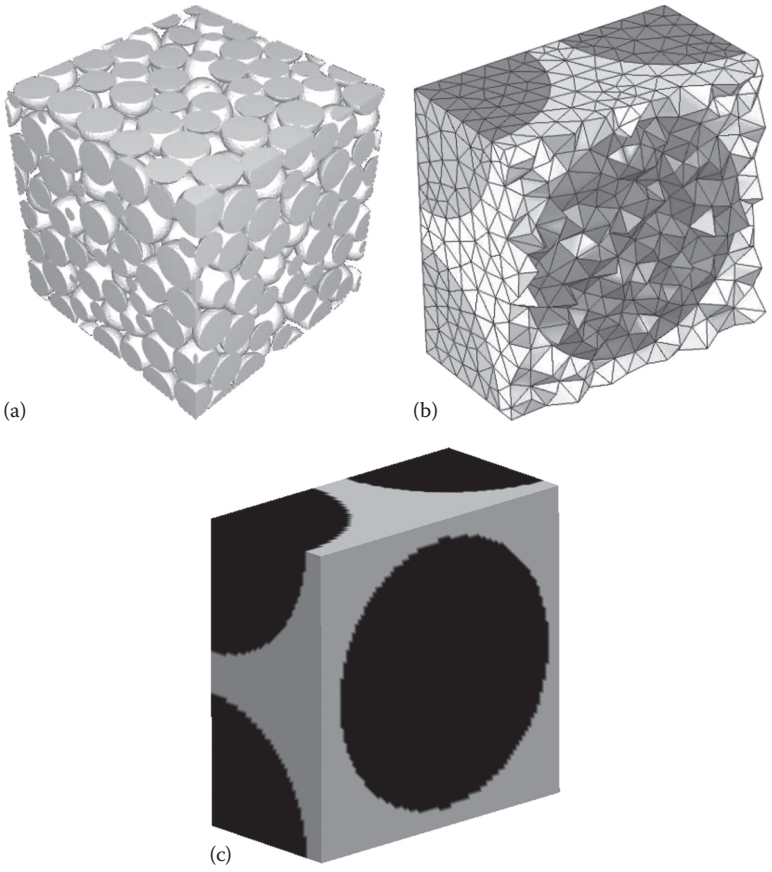

FIGURE 7.6 Geometries and meshes used for numerical calculations for (a) a 3D reconstruction of a bead packing obtained using x-ray microtomography, (b) an unstructured mesh used for the FE method, and (c) a Cartesian grid used for the FV method.

$$\text{Periodicity 1} \quad \mathsf{c}_\alpha\left(\mathbf{x}+\mathbf{l}_i\right)=\mathsf{c}_\beta\left(\mathbf{x}\right) \text{ with } \alpha=\beta,\sigma, \tag{7.233d}$$

$$\text{Periodicity 2} \quad \mathcal{J}_\alpha\mathsf{c}_\alpha\left(\mathbf{x}+\mathbf{l}_i\right)=\mathcal{J}_\alpha\mathsf{c}_\alpha\left(\mathbf{x}\right) \text{ with } \alpha=\beta,\sigma, \tag{7.233e}$$

$$\text{Average} \quad \left\langle \mathsf{c}_\alpha \right\rangle = 0 \text{ with } \alpha=\beta,\sigma, \tag{7.233f}$$

$$0 = k_\sigma\nabla^2\mathsf{c}_\sigma - a_v\varepsilon_\sigma^{-1}\xi_\sigma \text{ in } \mathcal{V}_\sigma, \tag{7.233g}$$

where the parameters ξ_β and ξ_σ are defined explicitly by

$$\xi_\beta = \frac{1}{A_{\beta\sigma}}\int_{\mathcal{A}_{\beta\sigma}} \mathbf{n}_{\beta\sigma}\cdot k_\beta\nabla\mathsf{c}_\beta dA = a_v^{-1}\left\langle\nabla\cdot\left(k_\beta\nabla\mathsf{c}_\beta\right)\right\rangle, \tag{7.234}$$

$$\xi_\sigma = \frac{1}{A_{\sigma\beta}}\int_{\mathcal{A}_{\sigma\beta}} \mathbf{n}_{\sigma\beta}\cdot k_\sigma\nabla\mathsf{c}_\sigma dA = a_v^{-1}\left\langle\nabla\cdot\left(k_\sigma\nabla\mathsf{c}_\sigma\right)\right\rangle = -1-\xi_\beta. \tag{7.235}$$

As in the theoretical part, we write the *distribution coefficient* as $\xi = -\xi_\beta$.

A practical way to solve this problem, based on the fact that ξ is constant over a unit cell, is to follow the procedure outlined in [65] and use the following change of variables:

$$c_\beta = c_\beta^0 + \xi c_\beta^1, \quad c_\sigma = c_\sigma^0 + \xi c_\sigma^1. \tag{7.236}$$

This leads to two independent closure problems that are given as

$$\rho_\beta c_{p\beta} \mathbf{v}_\beta \cdot \nabla c_\beta^0 = k_\beta \nabla^2 c_\beta^0 \text{ in } \mathcal{V}_\beta, \tag{7.237a}$$

$$\text{BC1} \quad c_\beta^0 - c_\sigma^0 = 0 \text{ on } \mathcal{A}_{\beta\sigma}, \tag{7.237b}$$

$$\text{BC2} \quad -\mathbf{n}_{\beta\sigma} \cdot \left(k_\beta \nabla c_\beta^0 - k_\sigma \nabla c_\sigma^0 \right) = 1 \text{ on } \mathcal{A}_{\beta\sigma}, \tag{7.237c}$$

$$\text{Periodicity 1} \quad c_\alpha^0 \left(\mathbf{x} + \mathbf{l}_i \right) = c_\alpha^0 \left(\mathbf{x} \right) \text{ with } \alpha = \beta, \sigma, \tag{7.237d}$$

$$\text{Periodicity 2} \quad \mathcal{J}_\alpha c_\alpha^0 \left(\mathbf{x} + \mathbf{l}_i \right) = \mathcal{J}_\alpha c_\alpha^0 \left(\mathbf{x} \right) \text{ with } \alpha = \beta, \sigma, \tag{7.237e}$$

$$\text{Average} \quad \left\langle c_\sigma^0 \right\rangle^\sigma = 0 \text{ with } \alpha = \beta, \sigma, \tag{7.237f}$$

$$0 = k_\sigma \nabla^2 c_\sigma^0 + a_v \varepsilon_\sigma^{-1} \text{ in } \mathcal{V}_\sigma, \tag{7.237g}$$

and

$$\rho_\beta c_{p\beta} \mathbf{v}_\beta \cdot \nabla c_\beta^1 = k_\beta \nabla^2 c_\beta^1 - a_v \varepsilon_\beta^{-1} \text{ in } \mathcal{V}_\beta, \tag{7.238a}$$

$$\text{BC1} \quad c_\beta^1 - c_\sigma^1 = 0 \text{ on } \mathcal{A}_{\beta\sigma}, \tag{7.238b}$$

$$\text{BC2} \quad -\mathbf{n}_{\beta\sigma} \cdot \left(k_\beta \nabla c_\beta^1 - k_\sigma \nabla c_\sigma^1 \right) = 0 \text{ on } \mathcal{A}_{\beta\sigma}, \tag{7.238c}$$

$$\text{Periodicity 1} \quad c_\alpha^1 \left(\mathbf{x} + \mathbf{l}_i \right) = c_\alpha^1 \left(\mathbf{x} \right) \text{with } \alpha = \beta, \sigma, \tag{7.238d}$$

$$\text{Periodicity 2} \quad \mathcal{J}_\alpha c_\alpha^1 \left(\mathbf{x} + \mathbf{l}_i \right) = \mathcal{J}_\alpha c_\alpha^1 \left(\mathbf{x} \right) \text{ with } \alpha = \beta, \sigma, \tag{7.238e}$$

$$\text{Average} \quad \left\langle c_\sigma^1 \right\rangle^\sigma = 0 \text{ with } \alpha = \beta, \sigma, \tag{7.238f}$$

$$0 = k_\sigma \nabla^2 c_\sigma^1 + a_v \varepsilon_\sigma^{-1} \text{ in } \mathcal{V}_\sigma. \tag{7.238g}$$

The condition imposed on the phase average, $\langle c_\beta \rangle = 0$, is not automatically satisfied by these two closure problems so that we have

$$\xi = -\frac{\langle c_\beta^0 \rangle^\beta}{\langle c_\beta^1 \rangle^\beta}. \tag{7.239}$$

We also remark that the two previous problems are well posed in the sense that they satisfy the solvability conditions/Fredholm alternative. In our case, looking at the adjoint problem is equivalent

to averaging the closure problems in space (see, e.g., [42]). For instance, averaging the bulk equations in Problem 7.237 and using the periodicity conditions yields

$$\frac{1}{V}\int_{\mathcal{A}_{\beta\sigma}} \mathbf{n}_{\beta\sigma}\cdot\left(k_\beta \nabla \mathsf{c}_\beta^0\right) dA = 0 \text{ in } \mathcal{V}_\beta, \quad \frac{1}{V}\int_{\mathcal{A}_{\beta\sigma}} \mathbf{n}_{\beta\sigma}\cdot\left(k_\sigma \nabla \mathsf{c}_\sigma^0\right) dA = a_v \text{ in } \mathcal{V}_\sigma, \tag{7.240}$$

which is *consistent* with the boundary condition

$$\mathrm{BC} - \mathbf{n}_{\beta\sigma}\cdot\left(k_\beta \nabla \mathsf{c}_\beta^0 - k_\sigma \nabla \mathsf{c}_\sigma^0\right) = 1 \text{ on } \mathcal{A}_{\beta\sigma}. \tag{7.241}$$

The two IBVPs 7.237 and 7.238 are local in space and can be solved via standard FV or FE methods. In this chapter, we use an FV method based on a voxel description of the material, which is the most direct way of using tomographic data. Equations are discretized on a Cartesian grid with the numerical scheme proposed in [125,126]. We remark that a Cartesian grid may not provide an accurate value of the specific area a_v, since the discretization of a surface by a piecewise constant function leads to an error that is independent of the mesh size. In order to evaluate the extent of this effect on the computation of ξ, we also compare results with those obtained via an FE method (COMSOL Multiphysics®) with unstructured grids in the case of the cubic-centered unit cell.

7.9.3 Challenges Associated with X-Ray Tomography Images

Beyond the difficulties associated with image filtering and segmentation, the calculation of effective parameters using x-ray images of porous media poses a number of challenges, including the choice of boundary conditions. In the theoretical developments presented in this work, we have used periodic boundary conditions. The geometry obtained via x-ray tomography, however, is usually not periodic. Although we can still use periodic conditions for the PDEs, this may yield erroneous results, for instance, if the operation produces a nonpercolating porous medium, as is illustrated in Figure 7.7a. A possible solution to this problem is to periodize the unit cell via geometrical transformations, for example, by translation and symmetry operations, as is illustrated in Figure 7.7b.

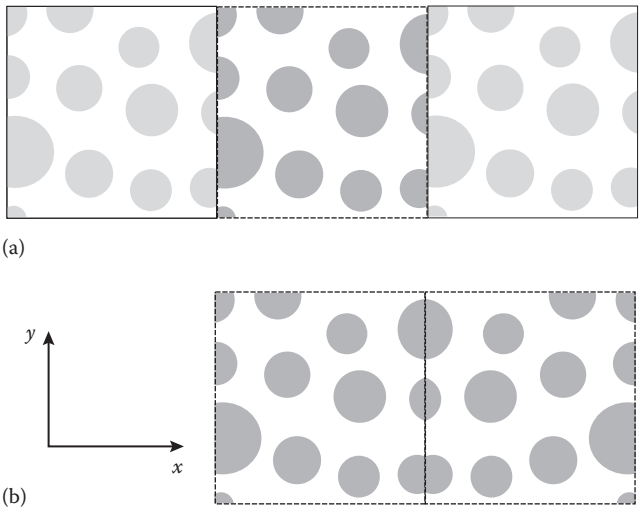

FIGURE 7.7 Schematics illustrating problems with boundary conditions. (a) Application of periodic boundary conditions to a nonperiodic geometry resulting in a nonpercolating porous medium. (b) Symmetry operation leading to a periodic unit-cell.

TABLE 7.1
Properties of the Set of Images and Comparison with Cubic-Centered Array

Image	1	2	3	CC
l_r	1.49	2.24	5.97	—
ε_β	0.309	0.339	0.357	0.319

This procedure is also not ideal since it modifies the original structure and may result in the loss of important features, such as anisotropy. These problems are even more crucial if advection effects are relatively large, as errors do not localize in the vicinities of the boundary. For h and ξ, in the diffusive regime, the impact of boundary conditions is usually small, so that we can use directly periodic boundary conditions.

Another important challenge associated with tomography techniques is the size of the images that can readily reach $1{,}000^3$ voxels and may go up to $10{,}000^3$, so that the computational cost associated with the numerical resolution of the closure problems with a similar spatial resolution can be enormous. If we restrict calculation to a region of interest, we must make sure that the size of the unit cell is much larger than the average spatial correlation length; otherwise values of the effective parameters may not be representative. In the case of the medium presented in Figure 7.6a, the correlation length corresponds to a few grain diameters, l_σ, and the size of the unit cell can be characterized using l_r, the ratio $l_r = l_{uc}/l_\sigma$, with l_{uc} as the size of the unit cell. Properties of the geometries are presented in Table 7.1.

7.9.4 Results for the Cubic-Centered Unit Cell

In [17], it was shown that ξ exhibits only a weak dependence upon the Péclet number, so that we focus here on the effects of the thermal conductivity ratio $\Gamma_k = k_\sigma/k_\beta$. Results are presented in Figure 7.8 for the FV and FE methods with various meshes.

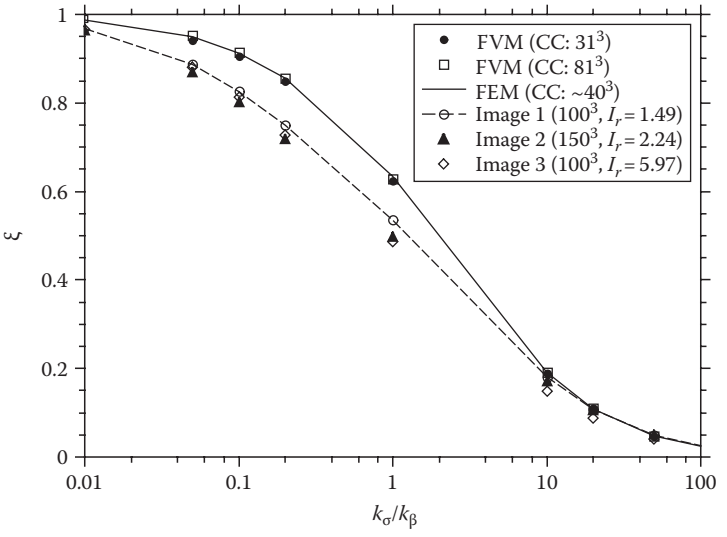

FIGURE 7.8 Distribution coefficient versus k_σ/k_β for the cubic-centered array of spheres (CC) and the tomographic data (images 1, 2, and 3). Images 1 and 2 are two subsets of the image presented in Figure 7.6a with a mesh size identical to the voxel size, while image 3 corresponds to the entire images in Figure 7.6a with a mesh size four times larger than the voxel size.

TABLE 7.2
Specific Area, a_v, for the Cubic-Centered Unit Cell

	FV (31^3)	FV (81^3)	FE ($\approx 40^3$)	Theoretical
a_v	5.955	5.978	4.045	4.081

First, we remark that the convergence with the mesh size is relatively fast, and even the coarser Cartesian grid (e.g., 31^3) provides good results. This shows that the Cartesian grid is suited to the resolution of such problems and that errors in the estimation of a_v (see Table 7.2) do not significantly impact results for ξ. Our interpretation of this result is that the integration procedure is consistent for all parameters, so that the errors cancel out during the evaluation of intensive variables. If one is interested in an accurate estimate of extensive variables, more sophisticated numerical schemes (see, e.g., [127]) can be used. These results also show that the FV approach can be used for the calculation of ξ over the geometry presented in Figure 7.6a.

7.9.5 Results for the X-Ray Tomography Unit Cell

Results of calculations over several subset of the original image, characterized by different values of l_r, are plotted in Figure 7.8. These show that the impact of l_r is relatively mild for this particular disordered structure, and we obtained reasonably good results for $l_r \geq 2$. The mesh size was equal to the tomograph voxel size for images 1 and 2, two subsets of the image presented in Figure 7.6a. Image 3 is the entire volume presented in Figure 7.6a, with a mesh size four times larger than the voxel size (i.e., 100^3 since the original image is 400^3). Although results are not presented here, we verified numerical convergence by performing additional calculations for image 3 with identical mesh and voxel sizes, that is, with a 400^3 grid. We observed a maximum relative error of about 1% between the 400^3 and 100^3 grids.

The goal of this section was to show that closure parameters can be solved over complex unit cells, so that we can determine effective parameters for realistic porous media. In the next section, we consider simpler unit cells, sometimes with analytical solutions, to characterize the behavior of the different models.

7.10 EXAMPLE PROBLEMS

In the theoretical part of this work, we have shown that there is a variety of macroscale models associated with a single microscale problem. Choosing among these models for a specific application is often based on an order of magnitude analysis of dimensionless parameters. However, this is often feasible only for simple conceptual cases, such as a 1D infinite medium, where the effects of boundary and initial conditions are abnormally weak. In this section, we provide several examples illustrating the importance of such conditions, with a particular focus on the two-equation quasi-stationary and one-equation LNE models.

7.10.1 Effect of Constant Source Terms in a Stratified Medium

The domain considered here is a periodic stratified geometry, as detailed in Figure 7.9, with $l_\beta + l_\sigma = 1$. We consider the following heat transfer problem:

$$\frac{\partial T'_\beta}{\partial t'} = \Delta' T'_\beta + R'_0 \text{ in } \mathcal{V}_\beta, \tag{7.242a}$$

$$\text{BC1} \quad T'_\beta - T'_\sigma = 0 \text{ on } \mathcal{A}_{\beta\sigma}, \tag{7.242b}$$

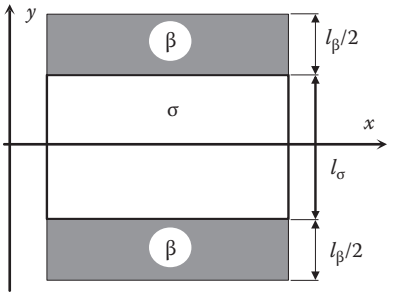

FIGURE 7.9 Unit cell for a stratified medium.

$$\text{BC2} \quad -\mathbf{n}_{\beta\sigma}\cdot\left(\nabla' T'_\beta - \Gamma_k \nabla' T'_\sigma\right) = -\Omega'_0 \text{ on } \mathcal{A}_{\beta\sigma}, \tag{7.242c}$$

$$\text{Periodicity} \quad T'_\beta\left(\frac{1}{2}\right) = T'_\beta\left(-\frac{1}{2}\right) \quad \text{and} \quad \frac{\partial T'_\beta}{\partial y'}\left(\frac{1}{2}\right) = \frac{\partial T'_\beta}{\partial y'}\left(-\frac{1}{2}\right), \tag{7.242d}$$

$$\text{IC} \quad T'_\beta\left(t=0\right) = T'_\sigma\left(t=0\right) = 0, \tag{7.242e}$$

$$\Gamma_{\rho c_p}\frac{\partial T'_\sigma}{\partial t'} = \nabla'\cdot\left(\Gamma_k \nabla' T'_\sigma\right) + R'_0 \text{ in } \mathcal{V}_\sigma, \tag{7.242f}$$

where we have used the ratio of the thermal diffusivities, $\Gamma_k = k_\sigma/k_\beta$, and $\Gamma_{\rho c_p} = \rho_\sigma c_{p\sigma}/\rho_\beta c_{p\beta}$. Here, Ω'_0 and R'_0 are constant bulk and surface sources, respectively. Note the minus sign in front of Ω'_0 in BC2 so that $\Omega'_0 > 0$ is a heat source.

We emphasize that this system of equations is underdetermined since boundary conditions on the LHS and RHS have not been imposed so far. Here, we consider (1) the case where the system is infinite in the x-direction, so that fields are uniform in the x-direction and averaging in the y-direction leads to a 0D macroscale problem, and (2) the case where we impose Dirichlet boundary conditions and average in the y-direction, so that the macroscale problem is 1D.

7.10.1.1 Effective Parameters

For this geometry, we can solve the closure problems analytically in order to obtain the following expressions for the exchange coefficient

$$h = \frac{12}{\varepsilon_\beta + \varepsilon_\sigma \Gamma_k} \tag{7.243}$$

and the distribution coefficient

$$\xi = \frac{\varepsilon_\sigma}{\varepsilon_\beta \Gamma_k + \varepsilon_\sigma}. \tag{7.244}$$

The evolution of ξ against the phase volume fraction and the thermal conductivity ratio is illustrated in Figure 7.10a. This figure shows the distribution of the boundary source depending on the relative conductivity of both phases and emphasizes that even for very large or very small ratios, this source affects both phases. The evolution of h against the phase volume fraction and the thermal conductivity ratio is illustrated in Figure 7.10b.

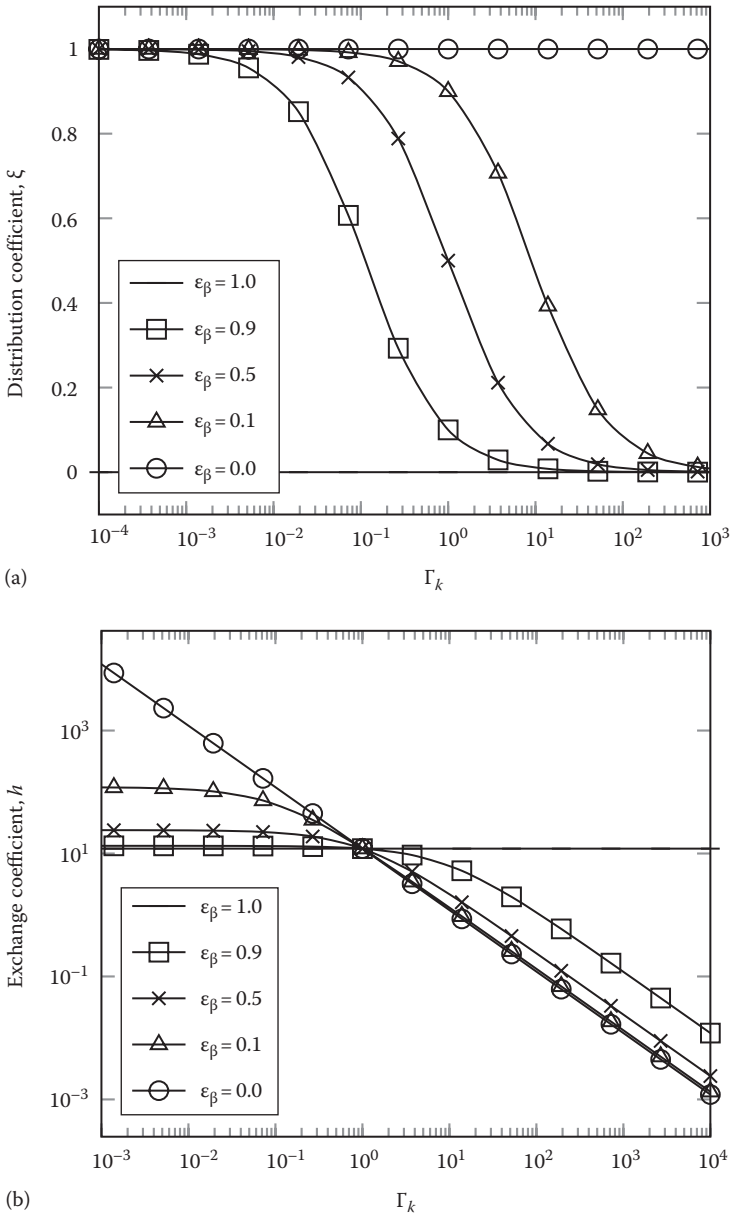

FIGURE 7.10 Evolution of (a) ξ and (b) h against the thermal conductivity ratio for various volume fractions.

7.10.1.2 Zero-Dimensional Case with Heterogeneous Sources, $R_0' = 0$

We consider here the case of an infinitely long stratified system. We focus on the two-equation quasi-stationary model at the macroscale and on the impact of heterogeneous sources ($R_0' = 0$). On averaging in the y-direction, the quasi-stationary two-equation model corresponding to this system only evolves in time so that we have

$$\varepsilon_\beta \frac{d\left\langle T_\beta' \right\rangle^\beta}{dt'} = -h\left(\left\langle T_\beta' \right\rangle^\beta - \left\langle T_\sigma' \right\rangle^\sigma\right) + a_v \xi \Omega_0', \tag{7.245}$$

$$\varepsilon_\sigma \Gamma_{\rho c_p} \frac{d\left\langle T'_\sigma \right\rangle^\sigma}{dt'} = h\left(\left\langle T'_\beta \right\rangle^\beta - \left\langle T'_\sigma \right\rangle^\sigma\right) + a_v\left(1-\xi\right)\Omega'_0, \tag{7.246}$$

with zero uniform temperatures at $t = 0$. The analytical solution of this problem is given as

$$\left\langle T'_\beta \right\rangle^\beta\left(t'\right) = \frac{\varepsilon_\sigma \Gamma_{\rho c_p}}{\left(\varepsilon_\sigma \Gamma_{\rho c_p} + \varepsilon_\beta\right)^2}\left[\varepsilon_\sigma \Gamma_{\rho c_p}\xi - \varepsilon_\beta\left(1-\xi\right)\right]\frac{a_v\Omega'_0}{h}\left(1 - e^{-\frac{h\left(\varepsilon_\sigma \Gamma_{\rho c_p} + \varepsilon_\beta\right)}{\varepsilon_\beta \varepsilon_\sigma \Gamma_{\rho c_p}} t'}\right) + \frac{a_v\Omega'_0}{\left(\varepsilon_\sigma \Gamma_{\rho c_p} + \varepsilon_\beta\right)} t', \tag{7.247}$$

$$\left\langle T'_\sigma \right\rangle^\sigma\left(t'\right) = -\frac{\varepsilon_\beta}{\left(\varepsilon_\sigma \Gamma_{\rho c_p} + \varepsilon_\beta\right)^2}\left[\varepsilon_\sigma \Gamma_{\rho c_p}\xi - \varepsilon_\beta\left(1-\xi\right)\right]\frac{a_v\Omega'_0}{h}\left(1 - e^{-\frac{h\left(\varepsilon_\sigma \Gamma_{\rho c_p} + \varepsilon_\beta\right)}{\varepsilon_\beta \varepsilon_\sigma \Gamma_{\rho c_p}} t'}\right) + \frac{a_v\Omega'_0}{\left(\varepsilon_\sigma \Gamma_{\rho c_p} + \varepsilon_\beta\right)} t'. \tag{7.248}$$

From a fundamental viewpoint, this problem is interesting because it mixes the effects of both the heat exchange and the distribution coefficients. The sign of $\left\langle T'_\beta \right\rangle^\beta - \left\langle T'_\sigma \right\rangle^\sigma$ will essentially depend on ξ, which distributes the heat between the two phases. We can study this effect by subtracting Equation 7.248 from Equation 7.247,

$$\left\langle T'_\beta \right\rangle^\beta - \left\langle T'_\sigma \right\rangle^\sigma = \frac{\left[\varepsilon_\sigma \Gamma_{\rho c_p}\xi - \varepsilon_\beta\left(1-\xi\right)\right]}{\varepsilon_\sigma \Gamma_{\rho c_p} + \varepsilon_\beta}\frac{a_v\Omega'_0}{h}\left(1 - e^{-\frac{h\left(\varepsilon_\sigma \Gamma_{\rho c_p} + \varepsilon_\beta\right)}{\varepsilon_\beta \varepsilon_\sigma \Gamma_{\rho c_p}} t'}\right), \tag{7.249}$$

and look at the limit as $t \to \infty$:

$$\lim_{t\to\infty}\left(\left\langle T'_\beta \right\rangle^\beta - \left\langle T'_\sigma \right\rangle^\sigma\right) = \frac{\left[\varepsilon_\sigma \Gamma_{\rho c_p}\xi - \varepsilon_\beta\left(1-\xi\right)\right]}{\varepsilon_\sigma \Gamma_{\rho c_p} + \varepsilon_\beta}\frac{a_v\Omega'_0}{h}. \tag{7.250}$$

This difference is proportional to the heat source and will decrease if the exchange between the phases is large. The influence of the distribution coefficient is more complex and influences the sign of this difference. Indeed, we have

$$\lim_{t\to\infty}\left(\left\langle T'_\beta \right\rangle^\beta - \left\langle T'_\sigma \right\rangle^\sigma\right) = 0 \Rightarrow \varepsilon_\sigma^2 \frac{\rho_\sigma c_{p\sigma}}{k_\sigma} = \varepsilon_\beta^2 \frac{\rho_\beta c_{p\beta}}{k_\beta}, \tag{7.251}$$

showing that the change in the sign of the temperature difference does not occur for equal diffusivities or equal conductivities but instead for equal Fourier numbers. We also see that the volume fraction (or relative thickness in the stratified case) of the phases plays an important role. In the nonstratified case, the sign change will also occur for $\varepsilon_\sigma \Gamma_{\rho c_p}\xi - \varepsilon_\beta(1-\xi) = 0$, but ξ must be obtained from the solution of the related closure problem.

To compare micro- and macroscale results, we now solve the problem given by Equations 7.242 numerically using an FE approach (COMSOL Multiphysics®). Results are presented in Figure 7.11. For the curves corresponding to $\Gamma_k = 20$ and $\Gamma_k = 0.05$, the important difference between the thermal conductivity of both phases produces a temperature field with the largest temperatures corresponding to the largest thermal conductivity. For $\Gamma_k = 1.2$, however, the conductivity of phase σ is only slightly larger than the conductivity of phase β so that the largest temperature corresponds to the thinnest stratum.

We compare these results with those obtained via the quasi-stationary two-equation model in Figure 7.12 where the averaged temperature fields were reconstructed discretely using quadrature

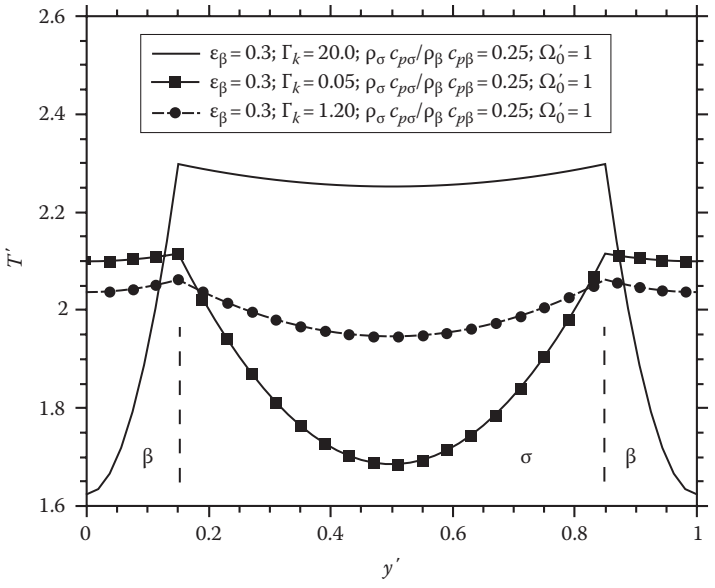

FIGURE 7.11 Pore-scale temperature field for different values of the pore-scale parameters as $t' \to \infty$.

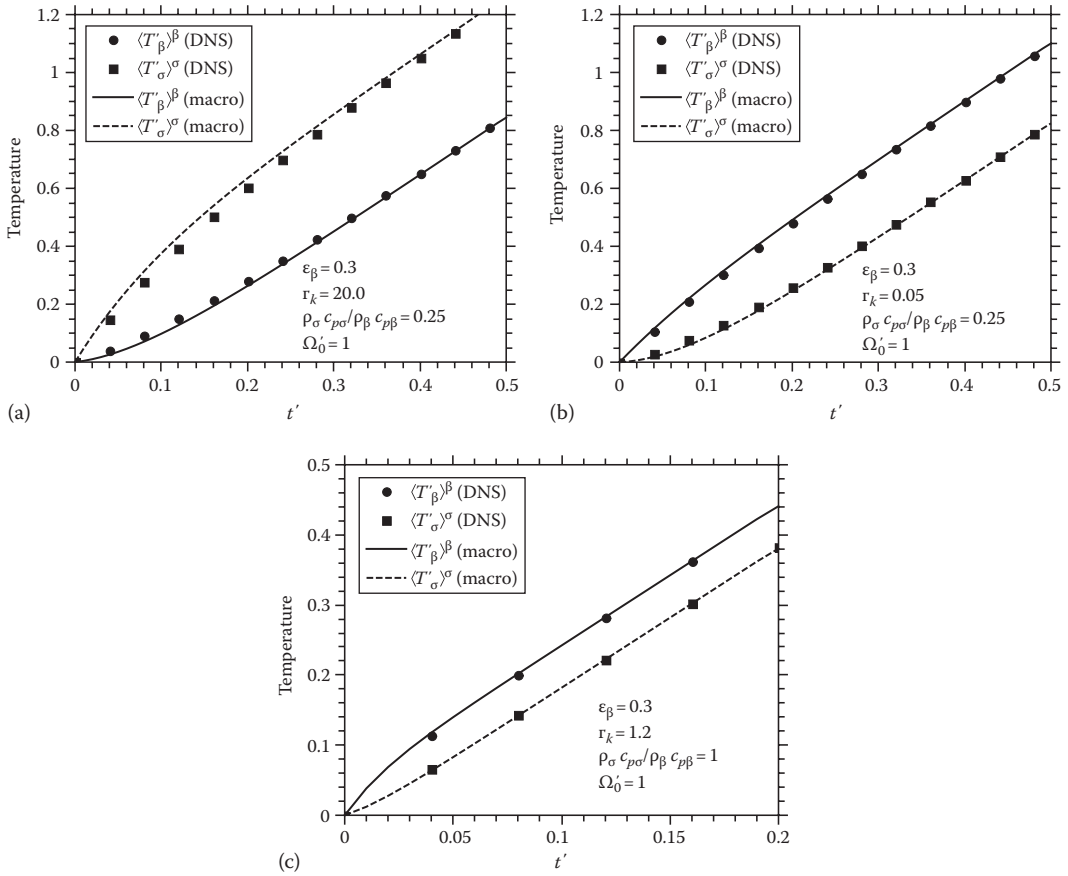

FIGURE 7.12 Evolution of $\left\langle T'_\beta \right\rangle^\beta$ and $\left\langle T'_\sigma \right\rangle^\sigma$ versus time for different parameters. (a) $\Gamma_k = 20$ and $(\rho c_p)_\sigma/(\rho c_p)_\beta = 0.25$; (b) $\Gamma_k = 0.05$ and $(\rho c_p)_\sigma/(\rho c_p)_\beta = 0.25$; and (c) $\Gamma_k = 1.2$ and $(\rho c_p)_\sigma/(\rho c_p)_\beta = 1$.

formulas. Typically, after a short transient evolution, the average temperature difference reaches a constant value. This evolution is perfectly captured by the two-equation quasi-stationary model, with only a small difference in the short-time limit where the steady closure fails to capture all characteristic times. The fact that the temperature difference is perfectly captured by the two-equation model means that both the exchange and the distribution coefficients are accurately calculated from the closure problems.

7.10.1.3 One-Dimensional Case with Homogeneous Sources, $\Omega_0' = 0$

Corrector results are reconstructions of the microscale fields from the average models, using the average temperature fields and the mapping variables. Here, our goal is to compare corrector results for the two-equation quasi-stationary and one-equation models with results of numerical simulations at the microscale. We consider the case of a homogeneous constant source of heat in both phases with a stratified system as presented in Figure 7.9. We study only the steady temperatures, so that analytical solutions are easily obtained for the average equations.

The stationary microscale problem becomes

$$0 = \Delta T_\beta' + R_0' \text{ in } \mathcal{V}_\beta, \tag{7.252a}$$

$$\text{BC1} \quad T_\beta' - T_\sigma' = 0 \text{ on } \mathcal{A}_{\beta\sigma}, \tag{7.252b}$$

$$\text{BC2} \quad \mathbf{n}_{\beta\sigma} \cdot \left(\nabla' T_\beta' - \Gamma_k \nabla' T_\sigma'\right) = 0 \text{ on } \mathcal{A}_{\beta\sigma}, \tag{7.252c}$$

$$\text{BC3} \quad \text{Periodicity} \tag{7.252d}$$

$$\text{IC} \quad T_\beta'\left(t = 0\right) = T_\sigma'\left(t = 0\right) = 0, \tag{7.252e}$$

$$0 = \Gamma_k \Delta' T_\sigma' + R_0' \text{ in } \mathcal{V}_\sigma, \tag{7.252f}$$

with $l_\beta = l_\sigma = 1/2$.

On averaging in the y-direction, the quasi-stationary two-equation model reads

$$0 = \varepsilon_\beta \frac{d^2 \left\langle T_\beta' \right\rangle^\beta}{dx'^2} - h\left(\left\langle T_\beta' \right\rangle^\beta - \left\langle T_\sigma' \right\rangle^\sigma\right) + \varepsilon_\beta R_0', \tag{7.253}$$

$$0 = \varepsilon_\sigma \Gamma_k \frac{d^2 \left\langle T_\sigma' \right\rangle^\sigma}{dx'^2} + h\left(\left\langle T_\beta' \right\rangle^\beta - \left\langle T_\sigma' \right\rangle^\sigma\right) + \varepsilon_\sigma R_0', \tag{7.254}$$

with zero uniform temperatures at $t = 0$ and boundaries $\left\langle T_\beta' \right\rangle^\beta = \left\langle T_\sigma' \right\rangle^\sigma = 0$ for $x = 0$ and $x = 5$. We remark that, for simplicity, we have used a standard first-order two-equation model here, not the

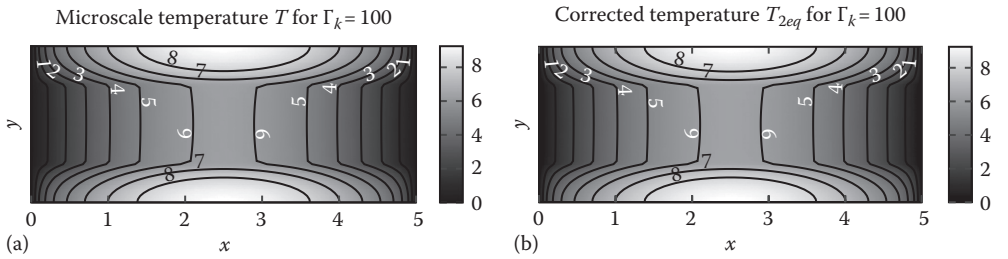

FIGURE 7.13 Results for (a) the microscale and (b) the corrector for the two-equation model.

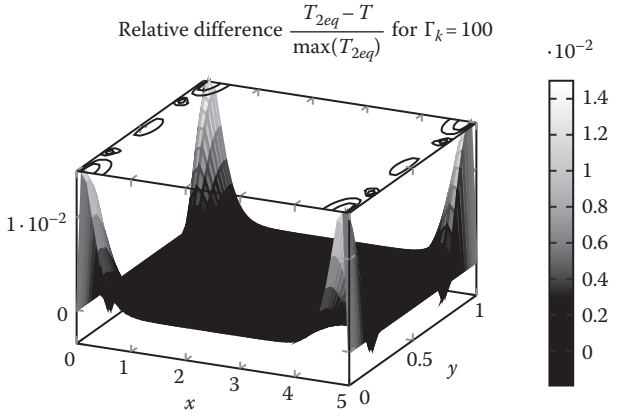

FIGURE 7.14 Relative difference between corrector-type and microscale results.

more general second-order closure used in this chapter. A microscale field was reconstructed by solving analytically the two-equation model and using

$$T_{\beta,2eq} = \langle T'_\beta \rangle^\beta (x) + \mathsf{a}_\beta (y) \left(\langle T'_\beta \rangle^\beta - \langle T'_\sigma \rangle^\sigma \right)(x), \tag{7.255}$$

$$T_{\sigma,2eq} = \langle T'_\sigma \rangle^\sigma (x) + \mathsf{a}_\sigma (y) \left(\langle T'_\beta \rangle^\beta - \langle T'_\sigma \rangle^\sigma \right)(x), \tag{7.256}$$

where a_β and a_σ are the closure variables (second-order polynomials in y here). Equations 7.252a through f were solved numerically using an FE approach. Comparison of the direct numerical solutions of the microscale result and the corrector results is plotted in Figure 7.13. A plot of the relative difference is given in Figure 7.14, showing that the error localizes close to the boundaries and the maximum is about one percent.

For comparison purposes, it is interesting to consider the cases of the one-equation quasi-stationary LE and LNE models, which in this case are equivalent. The corrector yields only a 1D field so that the one-equation model necessarily fails to recover the correct microscale solutions. This also suggests that even for a stationary problem, the two-equation models may provide a much better approximation (excellent here) of the solution than a one-equation model and therefore a more secure way of solving problems when a doubt exists about potential nonequilibrium effects.

7.10.2 Model Selection and Domains of Validity

In this section, we show that the choice of a specific macroscale model is a complex matter. A model may suddenly fail to describe accurately transport because of changes in the transport conditions,

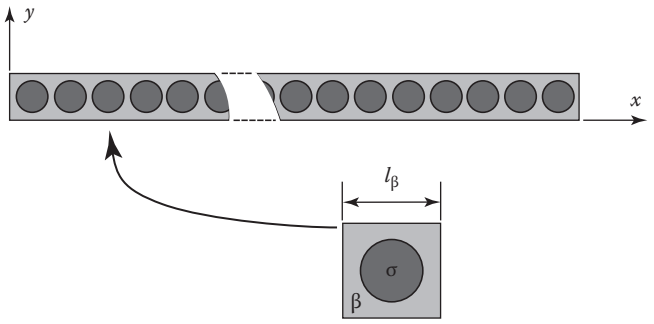

FIGURE 7.15 Array of cylinders.

for example, effect of heterogeneities, source terms, or proximity with a boundary condition. To illustrate this behavior, we further develop an example that was initially proposed in [128] for a 1D macroscale model. We perform pore-scale numerical simulations over an array of cylinders, as illustrated in Figure 7.15, consisting of n_{UC} unit cells of length l_β. We first solve Stokes equations, Equations 7.2a and 7.2c, to obtain the velocity field, v_β, and the corresponding intrinsic β-phase velocity, $U_\beta = \langle v_\beta \rangle^\beta$. Then we use the velocity field to solve Equations 7.3a through 7.3f for heat transfer, that is, $u_\alpha = T_\alpha$ (for $\alpha = \beta, \sigma$), where T is the temperature and $a_\alpha = c_{p\alpha}$ is the specific heat capacity. The initial and boundary conditions read as follows:

- No sources or sinks.
- Impervious and adiabatic lateral walls.
- $T_\beta = T_\sigma = 1$ at $x = 0$ and $T_\beta = T_\sigma = 0$ at $x = n_{UC} l_\beta$. We will see later that this Dirichlet condition significantly affects heat transfer and the discussion.
- $T_\beta(x, t) = T_\sigma(x, t) = 0$ at $t = 0$.

Once we have obtained the microscale solution, we calculate the average temperature fields $\langle T_\beta \rangle^\beta$ and $\langle T_\sigma \rangle^\sigma$ and compare them with the numerical solutions of the three macroscale models: the two-equation quasi-stationary, one-equation LE, and one-equation LNE models. The two-equation model is

$$\varepsilon_\beta \rho_\beta c_{p\beta} \frac{\partial \langle T_\beta \rangle^\beta}{\partial t} + \varepsilon_\beta \rho_\beta c_{p\beta} U_\beta \frac{\partial \langle T_\beta \rangle^\beta}{\partial x} = \frac{\partial}{\partial x}\left(K^*_{\beta\beta} \frac{\partial \langle T_\beta \rangle^\beta}{\partial x} + K^*_{\beta\sigma} \frac{\partial \langle T_\sigma \rangle^\sigma}{\partial x} \right) - h\left(\langle T_\beta \rangle^\beta - \langle T_\sigma \rangle^\sigma \right), \tag{7.257}$$

$$\varepsilon_\sigma \rho_\sigma c_{p\sigma} \frac{\partial \langle T_\beta \rangle^\beta}{\partial t} = \frac{\partial}{\partial x}\left(K^*_{\sigma\beta} \frac{\partial \langle T_\beta \rangle^\beta}{\partial x} + K^*_{\sigma\sigma} \frac{\partial \langle T_\sigma \rangle^\sigma}{\partial x} \right) + h\left(\langle T_\beta \rangle^\beta - \langle T_\sigma \rangle^\sigma \right), \tag{7.258}$$

with boundary conditions

$$\langle T_\beta \rangle^\beta = \langle T_\sigma \rangle^\sigma = 1 \quad \text{at } x = 0, \tag{7.259}$$

$$\left\langle T_\beta \right\rangle^\beta = \left\langle T_\sigma \right\rangle^\sigma = 0 \quad \text{at } x = n_{UC} l_\beta, \tag{7.260}$$

$$\left\langle T_\beta \right\rangle^\beta = \left\langle T_\sigma \right\rangle^\sigma = 0 \quad \text{at } t = 0. \tag{7.261}$$

The one-equation LE model reads

$$\left(\rho c_p\right)^* \frac{\partial T_{\mathrm{LE}}}{\partial t} + \varepsilon_\beta \rho_\beta c_{p\beta} U_\beta \frac{\partial T_{\mathrm{LE}}}{\partial x} = \frac{\partial}{\partial x}\left(K^*_{\mathrm{LE}} \frac{\partial T_{\mathrm{LE}}}{\partial x} \right), \tag{7.262}$$

where $(\rho c_p)^* = \varepsilon_\beta \rho_\beta c_{p\beta} + \varepsilon_\sigma \rho_\sigma c_{p\sigma}$, and the one-equation LNE model is

$$\left(\rho c_p\right)^* \frac{\partial T_{\mathrm{LNE}}}{\partial t} + \varepsilon_\beta \rho_\beta c_{p\beta} U_\beta \frac{\partial T_{\mathrm{LNE}}}{\partial x} = \frac{\partial}{\partial x}\left(K^*_{\mathrm{LNE}} \frac{\partial T_{\mathrm{LNE}}}{\partial x} \right), \tag{7.263}$$

where the mixture temperature, T_{LNE}, is given as

$$T_{LNE} = \frac{\varepsilon_\beta \rho_\beta c_{p\beta} \left\langle T_\beta \right\rangle^\beta + \varepsilon_\sigma \rho_\sigma c_{p\sigma} \left\langle T_\sigma \right\rangle^\sigma}{\varepsilon_\beta \rho_\beta c_{p\beta} + \varepsilon_\sigma \rho_\sigma c_{p\sigma}}, \tag{7.264}$$

and

$$K^*_{\mathrm{LNE}} = K^*_{\mathrm{LE}} + \frac{1}{h} \frac{\left(\varepsilon_\beta \rho_\beta c_{p\beta} \varepsilon_\sigma \rho_\sigma c_{p\sigma}\right)^2}{\left(\varepsilon_\beta \rho_\beta c_{p\beta} + \varepsilon_\sigma \rho_\sigma c_{p\sigma}\right)^2} U_\beta U_\beta. \tag{7.265}$$

The closure problems giving the effective parameters in these equations were solved following the numerical procedures in [65] with the following parameters:

$$n_{UC} = 480, \quad \frac{\rho_\sigma c_{p\sigma}}{\rho_\beta c_{p\beta}} = 1, \quad \varepsilon_\beta = 0.615, \quad \frac{k_\sigma}{k_\beta} = 0.01. \tag{7.266}$$

The resulting values are

$$\frac{K^*_{\beta\beta}}{k_\beta} \simeq 0.4455, \quad \frac{K^*_{\sigma\beta}}{k_\beta} = \frac{K^*_{\beta\sigma}}{k_\beta} \simeq 0.1757 \times 10^{-2}, \quad \frac{K^*_{\sigma\sigma}}{k_\beta} \simeq 0.3845 \times 10^{-2}, \quad \frac{h l_\beta^2}{k_\beta} \simeq 0.25, \tag{7.267}$$

for a Péclet number $\mathrm{Pe}_l \simeq 0.556$, defined as $\mathrm{Pe}_l = \dfrac{\rho_\beta c_{p\beta} U_\beta l_\beta}{k_\beta}$. We also found a value of K^*_{LNE} very close, as expected, to $K^*_{\beta\beta} + K^*_{\sigma\beta} + K^*_{\beta\sigma} + K^*_{\sigma\sigma}$, that is,

$$\frac{K^*_{\mathrm{LE}}}{k_\beta} = 0.453, \quad \frac{K^*_{\mathrm{LNE}}}{k_\beta} = 0522. \tag{7.268}$$

For Figure 7.16, we define the characteristic time t_{ad} as

$$t_{ad} = \frac{k_\beta t}{\rho_\beta c_{p\beta} l_\beta^2}, \tag{7.269}$$

and x is scaled by l_β. For the shortest time plotted in Figure 7.16a, we observe a progression of the thermal front only over a few unit cells. In principle, the close proximity of the boundary on the LHS and the corresponding boundary effects cannot be captured by homogenized models, although the two-equation model still captures essential features. For the second time, illustrated in Figure 7.16b, the temperature fields have had time to spread but still exhibit LNE effects. For the third time, illustrated in Figure 7.16c, the time-asymptotic regime has been reached. Finally, for the fourth time, illustrated in Figure 7.16c, the fields have reached steady state, which is strongly affected by the Dirichlet condition on the RHS boundary. We remark that the two-equation model provides accurate results for all times.

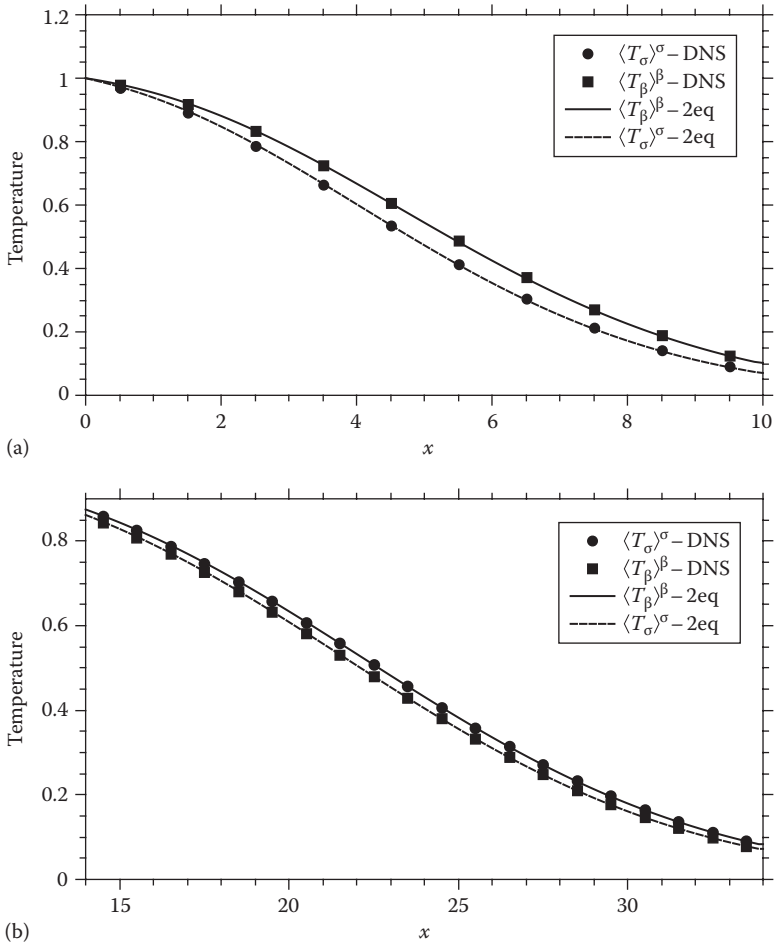

FIGURE 7.16 Comparison of the averaged phase temperatures for direct numerical simulation (symbols) and the two-equation quasi-stationary model (solid lines). Results are plotted against the dimensionless spatial variable, x, for different dimensionless times: (a) $t_{ad} = 5 \times 10^{-5}$, (b) $t_{ad} = 2.5 \times 10^{-4}$. (*Continued*)

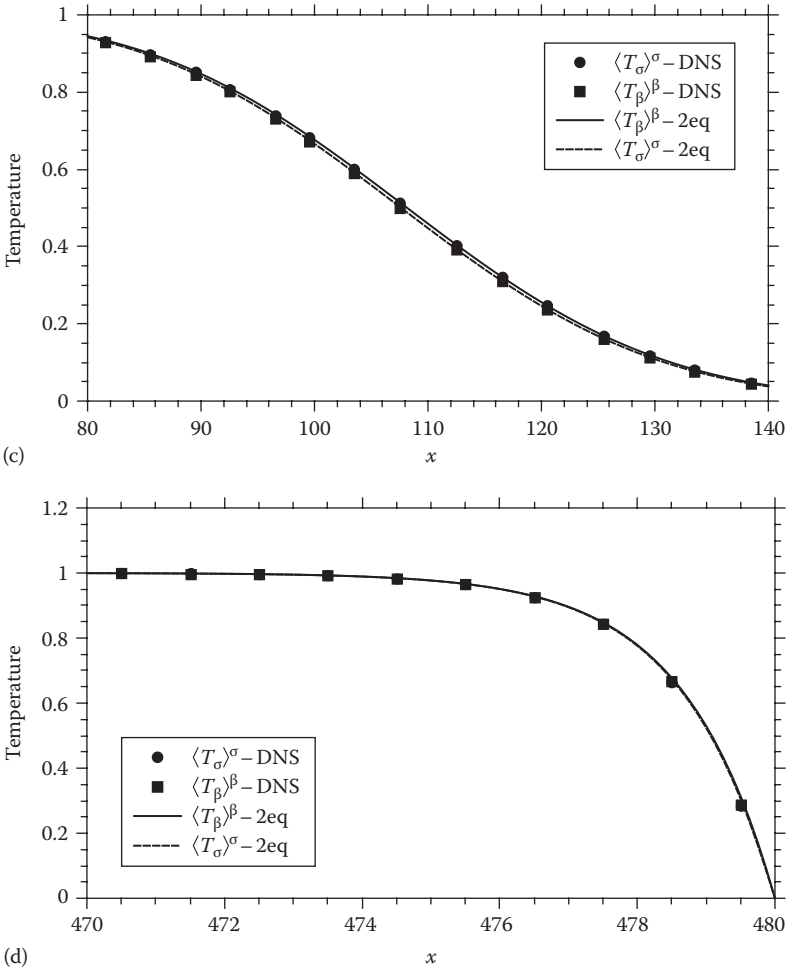

FIGURE 7.16 (*Continued*) Comparison of the averaged phase temperatures for direct numerical simulation (symbols) and the two-equation quasi-stationary model (solid lines). Results are plotted against the dimensionless spatial variable, x, for different dimensionless times: (c) $t_{ad} = 1.25 \times 10^{-3}$, and (d) steady state $t_{ad} \to \infty$.

We now study results obtained using the one-equation representations and compare results with those obtained with the two-equation model, which is used as a reference (results for the mixture temperature difference between DNS and the two-equation model are small, on the order of numerical accuracy, as indicated by the results plotted in Figure 7.17). To quantify differences, we calculate the mixture temperature, $T^{\beta\sigma}$, defined as

$$T^{\beta\sigma} = \frac{\varepsilon_\beta \rho_\beta c_{p\beta} \langle T_\beta \rangle^\beta + \varepsilon_\sigma \rho_\sigma c_{p\sigma} \langle T_\sigma \rangle^\sigma}{\varepsilon_\beta \rho_\beta c_{p\beta} + \varepsilon_\sigma \rho_\sigma c_{p\sigma}}, \tag{7.270}$$

using results from the two-equation quasi-stationary model. We then consider the differences $T_{\mathrm{LE}} - T_{2eq}^{\beta\sigma}$ and $T_{\mathrm{LNE}} - T_{2eq}^{\beta\sigma}$ that are plotted in Figure 7.17. We remark that, at the early stages in Figure 7.17a and b, the temperature obtained via the one-equation models is significantly different from the mixture temperature obtained using the two-equation model. Between the two one-equation models, the one based on the LE assumption seems to provide slightly better results in

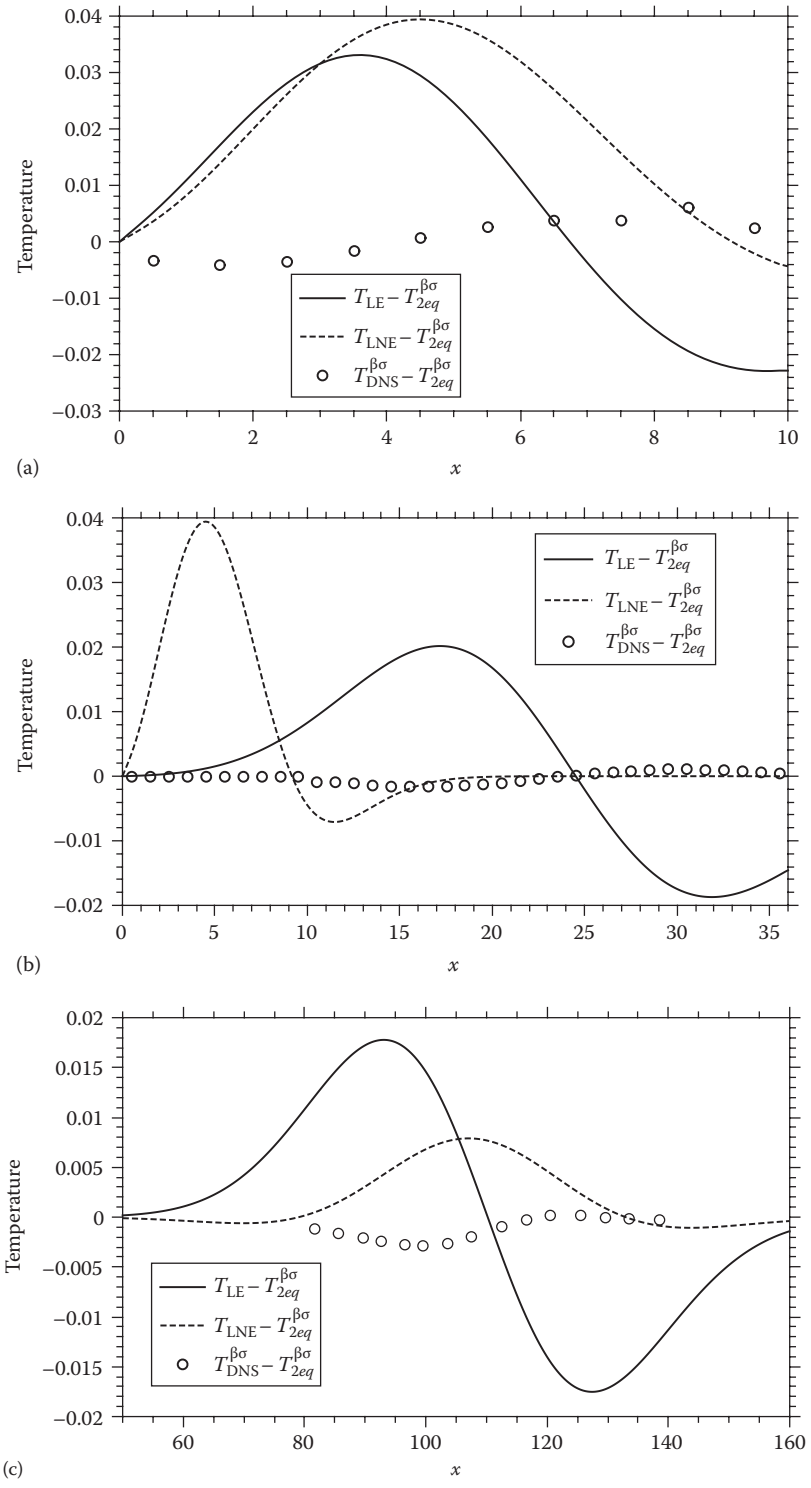

FIGURE 7.17 Differences between the mixture temperature $T_{2eq}^{\beta\sigma}$ calculated from the two-equation model and the results of the one-equation LE model, the LNE model, and the DNS. Results are plotted against the dimensionless spatial variable, x, for different dimensionless times: (a) $t_{ad} = 5 \times 10^{-5}$, (b) $t_{ad} = 2.5 \times 10^{-4}$, (c) $t_{ad} = 1.25 \times 10^{-3}$. (*Continued*)

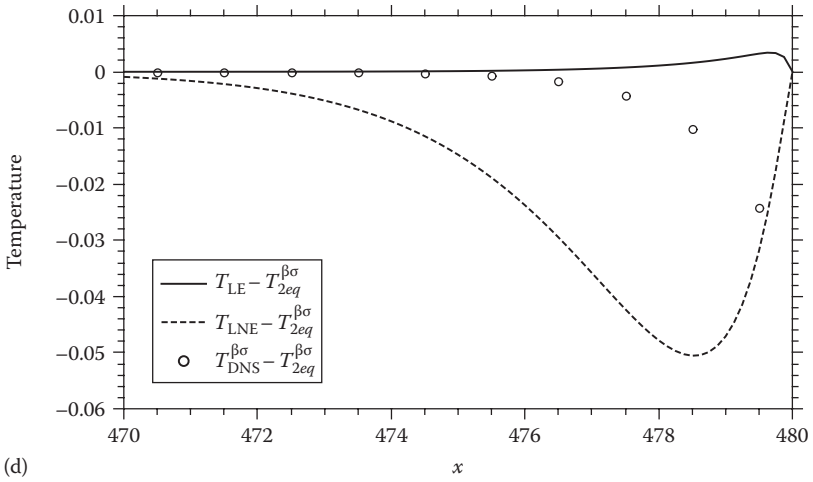

FIGURE 7.17 (*Continued*) Differences between the mixture temperature $T_{2eq}^{\beta\sigma}$ calculated from the two-equation model and the results of the one-equation LE model, the LNE model, and the DNS. Results are plotted against the dimensionless spatial variable, x, for different dimensionless times: (d) steady state $t_{ad} \to \infty$.

the early stages. As time increases, however, the asymptotic regime is reached and the one-equation LNE model provides a better estimation than the one-equation LE model (see Figure 7.17c). Finally, at *steady state*, the LE model provides surprisingly good results (see Figure 7.17d). On the other hand, the one-equation LNE model fails to capture accurately the temperature as it induces too much spreading. This stems from the fact that this particular *steady state* is strongly affected by the Dirichlet boundary condition, which imposes an LE-like situation. This situation is specific to the 1D configuration and the absence of heat sources/sinks (contrary to the problem treated in Section 7.10.2). We also emphasize that the two-equation model provides good results in all cases and conclude that, if a doubt exists as to the behavior of the system, the model of choice clearly is the two-equation representation.

7.11 DISCUSSION AND CONCLUSION

A single transport problem at the microscale usually leads to a multiplicity of macroscale models. Depending on the physical parameters of the problem, the boundary conditions, the tolerance, and the computational cost that are acceptable, we can use a variety of different macroscale models. In this work, we discussed models for scalar transport in porous media (see summary in Figure 7.18): one- and two-equation models both equilibrium and nonequilibrium, integrodifferential descriptions of time nonlocality, and hybrid approaches that couple partial differential equations acting at different scales. We presented the corresponding mathematical developments, discussed the domains of validity of the different models, and highlighted several fundamental features by comparing computations at the pore-scale with results of the homogenized models. As an example, we also showed how effective parameters can be calculated directly over a 3D image of a bead packing obtained using x-ray computed microtomography.

This contribution is, in many ways, an update of the previous handbook chapter by Quintard and Whitaker [17]. Quintard and Whitaker focused on two-equation quasi-stationary and one-equation LE models. Here, we have presented the one-equation LNE model; we have extended the models to the fully transient cases and to nonlinear bulk and surface sources/sinks; and we have discussed hybrid micro–macro strategies using a simple example. We have also derived the models using a second-order closure, a technical point that had never been performed before (although the idea was proposed in [129] to deal with the different problem of two-phase flow in heterogeneous porous media). We showed that this leads to additional terms in both the macro- and microscale equations.

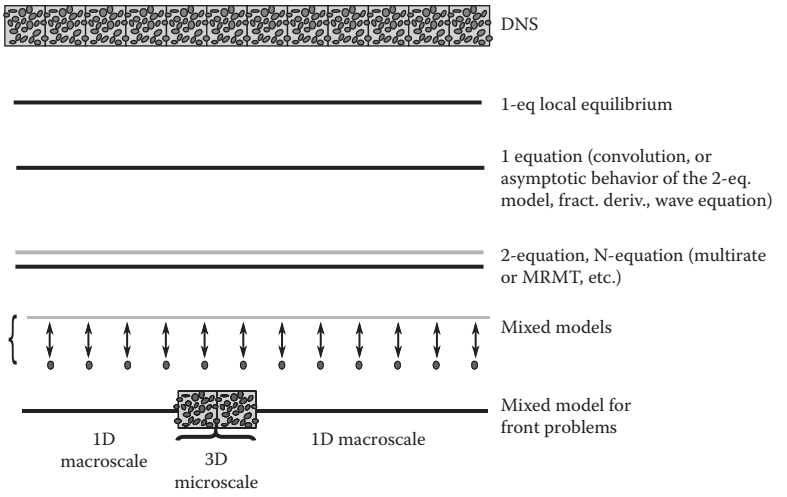

FIGURE 7.18 Schematic representation summarizing the different models reviewed in this chapter.

The different examples presented in Section 7.10 emphasize the difficulty to predict if one-equation models can be used accurately. The answer depends upon the topology of the problem, initial and boundary conditions, and the presence of sources/sinks. On the other hand, the two-equation model provides excellent results in most cases, even when in LNE conditions. Therefore, we recommend it as a model of choice if a doubt exists as to the behavior of the system. In particular, it may be used to examine domains of validity for various classes of problems, thus providing reference results for assessing the viability of one-equation models.

There are many other open problems in the field, in particular those involving strong nonlinear coupling between mass, momentum, and energy transfers. Bulk or surface heat sources in the energy equations may be uncoupled from heat transfer, for example, in the case of the cooling of nuclear reactor debris beds where the heat source is produced by radioactivity. They may also lead to strongly nonlinear coupled problems, as is the case for smoldering or combustion in porous media. Highly nonlinear reaction terms, such as Arrhenius equations, or the potential existence of sharp combustion fronts may require more complicated closures [107], direct numerical simulations, or hybrid models [95].

Similarly, weak coupling of thermodynamic quantities, that is, density, viscosity, thermal diffusion, or mass diffusion coefficients, can produce complex behaviors. From an averaging viewpoint, one way to treat such problems is to assume that perturbations are relatively small so that

$$\rho\left(T_\beta, p_\beta\right) \simeq \rho\left(\left\langle T_\beta \right\rangle^\beta, \left\langle p_\beta \right\rangle^\beta\right) + \tilde{T}_\beta \frac{\partial \rho}{\partial T} + \tilde{p}_\beta \frac{\partial \rho}{\partial p}, \tag{7.271}$$

or even

$$\rho\left(T_\beta, p_\beta\right) \simeq \rho\left(\left\langle T_\beta \right\rangle^\beta, \left\langle p_\beta \right\rangle^\beta\right). \tag{7.272}$$

An important consequence, however, is that the closure problems will still be coupled to these parameters and may therefore depend nonlinearly on $\langle c_\beta \rangle^\beta$ and $\langle T_\beta \rangle^\beta$.

One-sided coupling may be treated relatively easily. This is the case, for instance, when modeling thermodiffusion with only Soret effect (see [128]) where the thermal upscaling problem may be treated

independently of the species transport problem. Most of the time, however, coupling is quite complicated and it is difficult to find a complete closure. This, of course, leaves the door opened to empirical or semiempirical models that are in fact used in many models in porous media physics. To illustrate such problems, consider transport in porous media with intense phase change, such as boiling occurring when cooling hot debris bed in nuclear reactor after a loss-of-coolant accident (LOCA). So far, closures have been proposed in which the momentum transport is treated independently. Practical models make use of generalized Darcy's laws or Forchheimer extensions [130–132]. These models remain largely heuristic and are not entirely supported by upscaling developments [133–136], which in fact are made without taking into account the specifics of the phase repartition when boiling occurs in the porous medium. The need for nonequilibrium heat transfer model for LOCA modeling has been recognized long ago [137,138]. The macroscale model can be written as a three-temperature model. A limited closure can be found for such a model assuming a quasi-static gas–liquid interface [106]. Calculations of the effective properties suggest a significant difference between the values for a wet solid surface, the so-called *slg* configuration, which occurs when boiling is not important, compared to an *slg* configuration with a vapor film near the solid surface. Moreover, pore-scale nucleate boiling does not fit with the idea of a quasi-static interface. Therefore, it is expected that both two-phase and energy models should be impacted by the phase change process taking place within the pores. Experimental evidence interpreted through a three-temperature model [139] suggests that there is indeed an impact of the two-phase configuration on the effective properties and that, at least for the heat exchange coefficients, Nukiyama curves [140] specific to porous media configurations should be introduced.

Further, several problems of paramount importance have not been addressed in this chapter, in particular numerical methods that are used to solve closure problems, evolving microscale structures, the development of experimental techniques for imaging porous media, and image processing, including thresholding and meshing difficulties associated with 3D imaging techniques. Absorption x-ray computed microtomography can be used to obtain the phase distribution and calculate effective parameters, as is illustrated for a bead packing in this work, but image processing and meshing of such structures poses a number of challenges (see, e.g., [141]).

REFERENCES

1. J. Maxwell, *A Treatise on Electricity and Magnetism*, MacMillan & Co./ Oxford at the Clarendon Press, London, U.K., 1873.
2. A. Einstein, Eine neue bestimmung der moleküldimensionen, *Annalen der Physik* 324(2) (1906) 289–306.
3. G. Taylor, Dispersion of soluble matter in solvent flowing slowly through a tube, *Proceedings of the Royal Society A* 219 (1953) 186–203.
4. R. Aris, On the dispersion of a solute in a fluid flowing through a tube, *Advances in Water Resources* 235 (1956) 67–77.
5. A. Scheidegger, *The Physics of Flow through Porous Media*, University of Toronto Press, Toronto, Ontario, Canada, 1957.
6. K. Markov, Elementary micromechanics of heterogeneous media, in: *Heterogeneous Media: Modeling and Simulation in Science*, Engineering and Technology, Springer, Boston, MA, 2000.
7. J. Bear, *Dynamics of Fluids in Porous Media*, Elsevier, New York, 1972.
8. L.W. Lake, *Enhanced Oil Recovery*, Prentice Hall, Englewood Cliffs, NJ, 1989.
9. G. Milton, *The Theory of Composites*, University Press, Cambridge, U.K., 2002.
10. B. Wood, S. Whitaker, Multi-species diffusion and reaction in biofilms and cellular media, *Chemical Engineering Science* 55 (2000) 3397–3418.
11. F. Valdés-Parada, J. Varela, J. Alvarez-Ramirez, Upscaling pollutant dispersion in the Mexico City Metropolitan Area, *Physica A* 391 (2012) 606–615.
12. N. Henn, M. Quintard, B. Bourbiaux, S. Sakthikumar, Modelling of conductive faults with a multiscale approach, *Oil & Gas Science and Technology* 59(2) (2004) 197–214.
13. C.S.D. DePaolo, P. Lichtner, Reactive transport modeling: An essential tool and a new research approach for the earth sciences, *Earth and Planetary Science Letters* 240 (2005) 539–558.

14. S. Lorthois, F. Cassot, Fractal analysis of vascular networks: Insights from morphogenesis, *Journal of Theoretical Biology* 262(4) (2010) 614–633.
15. M. Bendsoe, N. Kikuchi, Generating optimal topologies in structural design using a homogenization method, *Computer Methods in Applied Mechanics and Engineering* 71(2) (1988) 197–224.
16. G. Allaire, *Shape Optimization by the Homogenization Method*, Springer-Verlag, New York, 2002.
17. M. Quintard, S. Whitaker, Theoretical analysis of transport in porous media, in: *Handbook of Heat Transfer in Porous Media*, Marcel Decker Inc., New York, 2000, pp. 1–52.
18. R. Bird, W. Stewart, E. Lightfoot, *Transport Phenomena*, John Wiley & Sons, New York, 1960.
19. E. Sanchez-Palencia, Solutions périodiques par rapport aux variables d'espaces et applications, *C.R. Academic Science Paris, Séries A–B* 271 (1970) A1129–A1132.
20. H.I. Ene, E. Sanchez-Palencia, Equations et phénomènes de surface pour l'écoulement dans un modèle de milieu poreux, *Journal of Mécanique* 14 (1975) 73–108.
21. A. Bensoussan, J.-L. Lions, G. Papanicolaou, *Asymptotic Analysis for Periodic Structures*, Studies in Mathematics and its Applications 5, North-Holland Publishing Company, Amsterdam, the Netherlands, 1978.
22. U. Hornung (Ed.), *Homogenization and Porous Media*, Springer-Verlag, Heidelberg, Germany, 1997.
23. R.G. Mokadam, Thermodynamic analysis of the Darcy law, *Journal of Applied Mechanics* 28(2) (1961) 208–212. doi:10.1115/1.3641653.
24. C. Marle, Application de la méthode de la thermodynamique des processus irréversible à l'écoulement d'un fluide à travers un milieux poreux, *Bulletin RILEM* 29 (1965) 1066–1071.
25. C.M. Marle, Ecoulements monophasiques en milieu poreux, *Revue de l'Institut Français du Pétrole* 22(10) (1967) 1471–1509.
26. M. Hassanizadeh, W.G. Gray, General conservation equations for multi-phase systems: 1. Averaging procedure, *Advance Water Resources* 2 (1979) 131–144.
27. C.M. Marle, On macroscopic equations governing multiphase flow with diffusion and chemical reactions in porous media, *International Journal of Engineering Science* 20(5) (1982) 643–662.
28. L.S. Bennethum, J.H. Cushman, Multiscale, hybrid mixture theory for swelling systems. I. Balance laws, *International Journal of Engineering Science* 34(2) (1996) 125–145.
29. R.M. Bowen, Theory of mixtures, in: *Continuum Physics*, Academic Press, New York, 1976.
30. H. Brenner, Dispersion resulting from flow through spatially periodic porous media, *Transactions of the Royal Society* 297(1430) (1980) 81–133.
31. H. Brenner, P. Adler, Dispersion resulting from flow through spatially periodic porous media II. Surface and intraparticle transport, *Philosophical Transactions of the Royal Society of London*: *Series A, Mathematical and Physical Sciences* 307(1498) (1982) 149–200.
32. P.K. Kitanidis, Analysis of macrodispersion through volume-averaging: Moment equations, *Stochastic Hydrology and Hydraulics* 6(1) (1992) 5–25.
33. G. Matheron, *Les variables régionalisées et leur estimation: une application de la théorie des fonctions aléatoires aux sciences de la nature*, Masson, Paris, France, 1965.
34. L.W. Gelhar, Stochastic subsurface hydrology from theory to applications, *Water Resources Research* 22(9) (1986) 129–139.
35. G. Dagan, *Flow and Transport in Porous Formations*, Springer-Verlag, Heidelberg, Germany, 1989.
36. G. Dagan, S.P. Neuman, *Subsurface Flow and Transport*: *A Stochastic Approach*, Cambridge University Press, Cambridge, U.K., 1997.
37. S. Whitaker, *The Method of Volume Averaging*, Kluwer Academic Publishers, Dordrecht, the Netherlands, 1999.
38. P. Baveye, G. Sposito, The operational significance of the continuum hypothesis in the theory of water movement through soils and aquifers, *Water Resources Research* 20 (1984) 521–530.
39. M. Quintard, S. Whitaker, Transport in ordered and disordered porous media II: Generalized volume averaging, *Transport in Porous Media* 14 (1994) 179–206.
40. M. Quintard, S. Whitaker, Transport in ordered and disordered porous media I: The cellular average and the use of weighting functions, *Transport in Porous Media* 14 (1994) 163–177.
41. S. Pride, J. Berryman, Connecting theory to experiment in poroelasticity, *Journal of the Mechanics and Physics of Solids* 46(4) (1998) 719–747.
42. Y. Davit, C.G. Bell, H.M. Byrne, L.A. Chapman, L.S. Kimpton, G.E. Lang, K.H. Leonard et al., Homogenization via formal multiscale asymptotics and volume averaging: How do the two techniques compare? *Advances in Water Resources* 62 (2013) 178–206.
43. W. Gray, P. Lee, On the theorems for local volume averaging of multiphase systems, *International Journal of Multiphase Flow* 3 (1977) 333–342.

44. J. Cushman, Proofs of the volume averaging theorems for multiphase flow, *Advances in Water Resources* 5 (1982) 248–253.
45. W. Gray, *Mathematical Tools for Changing Spatial Scales in the Analysis of Physical Systems*, CRC Press, Boca Raton, FL, 1993.
46. R. Hill, Elastic properties of reinforced solids: Some theoretical principles, *Journal of the Mechanics and Physics of Solids* 11(5) (1963) 357–372.
47. H. J. Cushman, *The Physics of Fluids in Hierarchical Porous Media: Angstroms to Miles*, Academic Publishers, Dordrecht, the Netherlands, 1997.
48. M. Sahimi, *Flow and Transport in Porous Media and Fractured Rocks: From Classical Methods to Modern Approaches*, VCH, New York, 1995.
49. B. Wood, Technical note: Revisiting the geometric theorems for volume averaging and the meaning of disorder in porous media, *Advances in Water Resources* SI Whitaker 62 (December 2013) 340–352.
50. C. Moyne, H.A. Souto, Multi-scale approach for conduction heat transfer: One-and two-equation models, part 2: Results for a stratified medium, *Computational and Applied Mathematics* 33(2) (2013) 433–449.
51. D. Lichau, S. Zhang, N. Combaret, F. Gamba, P. Barthelemy, From 3D images to simulations, practical issues and software tools, international conference on flows and mechanics in natural porous media from pore to field scale. Pore2field, IFP Energies nouvelles.
52. T. Hutzenlaub, J. Becker, R. Zengerle, S. Thiele, How coarsening the 3d reconstruction of a porous material influences diffusivity and conductivity values, *ECS Electrochemistry Letters* 2(2) (2013) F14–F17.
53. J. Caers, A special issue on benchmark problems, datasets and methodologies for the computational geosciences, *Computers & Geosciences* 50 (2013) 1–3.
54. D. Koch, J. Brady, A non-local description of advection-diffusion with application to dispersion in porous media, *Journal of Fluid Mechanics Digital Archive* 180 (1987) 387–403.
55. J. Koch, J. Brady, Anomalous diffusion in heterogeneous porous media, *Physics of Fluids* 31 (1988) 965–973.
56. J. Cushman, B. Hu, A resumé of nonlocal transport theories, *Stochastic Hydrology and Hydraulics* 9(2) (1995) 105–116.
57. B. Wood, The role of scaling laws in upscaling, *Advances in Water Resources* 32 (2009) 723–736.
58. B. Wood, F. Valdés-Parada, Volume averaging: Local and nonlocal closures using a green's function approach, *Advances in Water Resources* 51 (2012) 139–167.
59. G. Barenblatt, I. Zheltov, I. Kochina, Basic concepts in the theory of seepage of homogeneous liquids in fissured rocks, *Journal of Applied Mathematics* (USSR) 24(5) (1960) 852–864.
60. K.H. Coats, B.D. Smith, Dead-end pore volume and dispersion in porous media, *Society of Petroleum Engineers Journal* 4(1) (March 1964) 73–84.
61. H. Gerke, M. Genuchten, A dual-porosity model for simulating the preferential movement of water and solutes in structured porous media, *Water Resources Research* 29(2) (1993) 305–319.
62. R.G. Carbonell, S. Whitaker, Heat and mass transfer in porous media, in: J. Bear, M.Y. Corapcioglu (Eds.), *Fundamentals of Transport Phenomena in Porous Media*, Martinus Nijhof Publishers, Dordrecht, 1984, pp. 121–198.
63. F. Zanotti, R.G. Carbonell, Development of transport equations for multiphase systems—I: General development for two-phase systems, *Chemical Engineering Science* 39 (1984) 263–278.
64. J. Levec, R.G. Carbonell, Longitudinal and lateral thermal dispersion in packed beds—I: Theory, *AIChE Journal* 31 (1985) 581–590.
65. M. Quintard, M. Kaviany, S. Whitaker, Two-medium treatment of heat transfer in porous media: Numerical results for effective properties, *Advances in Water Resources* 20 (2–3) (1997) 77–94.
66. C. Moyne, Two-equation model for a diffusive process in porous media using the volume averaging method with an unsteady state closure, *Advances in Water Resources* 20(2–3) (1997) 63–76.
67. F. Cherblanc, A. Ahmadi, M. Quintard, Two-domain description of solute transport in heterogeneous porous media: Comparison between theoretical predictions and numerical experiments, *Advances in Water Resources* 30(5) (2007) 1127–1143.
68. F. Cherblanc, A. Ahmadi, M. Quintard, Two-medium description of dispersion in heterogeneous porous media: Calculation of macroscopic properties, *Water Resources Research* 39(6) (2003) 6–1.
69. A. Souadnia, S. Didierjean, C. Moyne, Transient dispersion in porous media: A comparison between exact and approximate solutions in a case study, *Transport in Porous Media* 47 (2002) 245–277.
70. C. Hsu, A closure model for transient heat conduction in porous media, *Journal of Heat Transfer* 121 (1999) 733–739.
71. A. Nakayama, F. Kuwahara, M. Sugiyama, G. Xu, A two-energy equation model for conduction and convection in porous media, *International Journal of Heat and Mass Transfer* 44(22) (2001) 4375–4379.

72. C.T. DeGroot, A.G. Straatman, Closure of non-equilibrium volume-averaged energy equations in high-conductivity porous media, *International Journal of Heat and Mass Transfer* 54(23–24) (2011) 5039–5048.
73. C. Moyne, H.A. Souto, Multi-scale approach for conduction heat transfer: One-and two-equation models, part 1. *Theory, Computational and Applied Mathematics* 33(1) (2014) 1–18.
74. V. Leroy, B. Goyeau, J. Taine, Coupled upscaling approaches for conduction, convection, and radiation in porous media: Theoretical developments, *Transport in Porous Media* 98(2) (2013) 323–347.
75. J. Parker, A. Valocchi, Constraints on the validity of equilibrium and first-order kinetic transport models in structured soils, *Water Resources Research* 22(3) (1986) 399–407.
76. P. Landereau, B. Noetinger, M. Quintard, Quasi-steady two-equation models for diffusive transport in fractured porous media: Large-scale properties for densely fractured systems, *Advances in Water Resources* 24 (2001) 863–876.
77. Y. Davit, M. Quintard, Comment on "frequency-dependent dispersion in porous media", *Physical Review E* 86 (2012) 013201.
78. F. Valdés-Parada, J. Alvarez-Ramirez, Reply to "comment on 'frequency-dependent dispersion in porous media'", *Physical Review E* 86 (2012) 013202.
79. Y. Davit, B. Wood, G. Debenest, M. Quintard, Correspondence between one- and two-equation models for solute transport in two-region heterogeneous porous media, *Transport in Porous Media* 95(1) (2012) 213–238.
80. R. Haggerty, S. McKenna, L. Meigs, On the late-time behavior of tracer test breakthrough curves, *Water Resources Research* 36(12) (2000) 3467–3479.
81. J. Luo, O. Cirpka, M. Fienen, W. Wu, T. Mehlhorn, J. Carley, P. Jardine, C. Criddle, P. Kitanidis, Accurate predictions based on mechanistic models require knowledge of the spatial distribution of the hydraulic, chemical, and biological properties, *Journal of Contaminant Hydrology* 83 (2006) 27–41.
82. Z.-X. Chen, Transient flow of slightly compressible fluids through double-porosity, double-permeability systems—A state-of-the-art review, *Transport in Porous Media* 4 (1989) 147–184.
83. P. Landereau, Modèles macroscopiques pour les ecoulements monophasiques en milieux poreux fracturés: Application aux tests de puits (macroscopic models for one-phase flow in fractured porous media: Application to well tests), PhD, Ecole Nationale Supérieure des Arts et Métiers, Bordeaux, France.
84. G. Porta, S. Chaynikov, M. Riva, A. Guadagnini, Upscaling solute transport in porous media from the pore scale to dual-and multicontinuum formulations, *Water Resources Research* 49(4) (2013) 2025–2039.
85. L. Wang, X. Wei, Equivalence between dual-phase-lagging and two-phase-system heat conduction processes, *International Journal of Heat and Mass Transfer* 51(7) (2008) 1751–1756.
86. L. Wang, M. Xu, X. Wei, Dual-phase-lagging and porous-medium heat conduction processes, in: *Emerging Topics in Heat and Mass Transfer in Porous Media*, Springer, Netherlands, 2008, pp. 1–37.
87. J. Sabatier, O.P. Agrawal, J.T. Machado, *Advances in Fractional Calculus: Theoretical Developments and Applications in Physics and Engineering*, Springer, Netherlands, 2007.
88. R. Haggerty, S.M. Gorelick, Multiple-rate mass transfer for modelling diffusion and surface reactions in media with pore-scale heterogeneity, *Water Resources Research* 31(10) (1995) 2383–2400.
89. F. Zanotti, R.G. Carbonell, Development of transport equations for multiphase systems—II: Application to one-dimensional axi-symmetric flows of two-phases, *Chemical Engineering Science* 39 (1984) 279–297.
90. F. Zanotti, R.G. Carbonell, Development of transport equations for multiphase systems—III: Application to heat transfer in packed beds, *Chemical Engineering Science* 39 (1984) 299–311.
91. M. Quintard, F. Cherblanc, S. Whitaker, Dispersion in heterogeneous porous media: One-equation non-equilibrium model, *Transport in Porous Media* 44(1) (2001) 181–203.
92. C. Moyne, S. Didierjean, H.P.A. Souto, O.T.D. Silveira, Thermal dispersion in porous media: One-equation model, *International Journal of Heat and Mass Transfer* 43(20) (2000) 3853–3867.
93. Y. Davit, G. Debenest, B.D. Wood, M. Quintard, Modeling non-equilibrium mass transport in biologically reactive porous media, *Advances in Water Resources* 33 (2010) 1075–1093.
94. Y. Davit, M. Quintard, G. Debenest, Equivalence between volume averaging and moments matching techniques for mass transport models in porous media, *International Journal of Heat and Mass Transfer* 53(21–22) (2010) 4985–4993.
95. G. Debenest, V. Mourzenko, J. Thovert, Smouldering in fixed beds of oil shale grains: Governing parameters and global regimes, *Combustion Theory and Modelling* 9(2) (2005) 301–321.

96. J. Batsale, C. Gobbé, M. Quintard, Local non-equilibrium heat transfer in porous media, in: *Recent Research Developments in Heat, Mass and Momentum Transfer*, Research Signpost, India, 1996, pp. 1–24.
97. M. Quintard, S. Whitaker, One- and two-equation models for transient diffusion processes in two-phase systems, in: *Advances in Heat Transfer*, Academic Press, New York, 1993, pp. 369–464.
98. F. Golfier, M. Quintard, F. Cherblanc, C. Harvey, B. Zinn, B. Wood, Comparison of theory and experiment for solute transport in highly heterogeneous porous medium, *Advances in Water Resources* 30 (2007) 2235–2261.
99. Y. Davit, H. Byrne, J. Osborne, J. Pitt-Francis, D. Gavaghan, M. Quintard, Hydrodynamic dispersion within porous biofilms, *Physical Review E* 87 (2013) 012718.
100. S. Whitaker, Improved constraints for the principle of local thermal equilibrium, *Industrial and Engineering Chemistry* 30 (1991) 983–997.
101. K. Vafai, M. Sozen, Analysis of energy and momentum transport for fluid flow through a porous bed, *Journal of Heat Transfer* 112 (1990) 690–699.
102. A. Amiri, K. Vafai, Analysis of dispersion effects and non-thermal equilibrium, non-Darcian, variable porosity incompressible flow through porous media, *International Journal of Heat and Mass Transfer* 37(6) (1994) 939–954.
103. P. Vadasz, Explicit conditions for local thermal equilibrium in porous media heat conduction, *Transport in Porous Media* 59(3) (2005) 341–355.
104. D. Rees, I. Pop, 6—Local thermal non-equilibrium in porous medium convection, in: D. Ingham, I. Pop (Eds.), *Transport Phenomena in Porous Media III*, Pergamon, Oxford, U.K., 2005, pp. 147–173.
105. M. Soezen, K. Vafai, Analysis of the non-thermal equilibrium condensing flow of a gas through a packed bed, *International Journal of Heat Mass Transfer* 33 (1990) 1247–1261.
106. F. Duval, F. Fichot, M. Quintard, A local thermal non-equilibrium model for two-phase flows with phase-change in porous media, *International Journal of Heat and Mass Transfer* 47(3) (2004) 613–639.
107. M. Fatehi, M. Kaviany, Role of gas-phase reaction and gas-solid thermal nonequilibrium in reverse combustion, *International Journal of Heat Mass Transfer* 40(11) (1997) 2607–2620.
108. A.A.M. Oliveira, M. Kaviany, Nonequilibrium in the transport of heat and reactants in combustion in porous media, *Progress in Energy and Combustion Science* 27(5) (2001) 523–545.
109. O.A. de Swaan, Analytical solutions for determining naturally fractured reservoir properties by well testing, *SPE Journal* 16(3) (1976) 117–122.
110. H. Kazemi, Pressure transient analysis of naturally fractured reservoirs with uniform fracture distribution, *Society of Petroleum Engineers Journal* 9(4) (December 1969) 451–462.
111. T. Arbogast, Analysis of the simulation of single phase flow through a naturally fractured reservoir, *SIAM Journal of Numerical Analysis* 26 (1989) 12–29.
112. F. Mermoud, F. Golfier, S. Salvador, L. Van de Steene, J. Dirion, Experimental and numerical study of steam gasification of a single charcoal particle, *Combustion and Flame* 145(1) (2006) 59–79.
113. J. Warren, P. Root, The behavior of naturally fractured reservoirs, *Society of Petroleum Engineers Journal* 3(3) (September 1963) 245–255.
114. H. Kazemi, L.S. Merril, K.L. Porterfield, P.R. Zeman, Numerical simulation of water-oil flow in naturally fractured reservoirs, *Society of Petroleum Engineers Journal* 16(6) (December 1976) 317–326.
115. G. Debenest, M. Quintard, Transport in highly heterogeneous porous media: From direct simulation to macro-scale two-equation models or mixed models, *Chemical Product and Process Modeling* 3(1) (2008) 1–23 (Article 19).
116. M. Kfoury, R. Ababou, B. Noetinger, M. Quintard, Matrix-fracture exchange in a fractured porous medium: Stochastic upscaling, *Comptes Rendus Mécanique* 332 (2004) 679–686.
117. M. Quintard, S. Whitaker, Transport in ordered and disordered porous media V: Geometrical results for two-dimensional systems, *Transport in Porous Media* 15 (1994) 183–196.
118. M. Quintard, S. Whitaker, Transport in ordered and disordered porous media IV: Computer generated porous media for three-dimensional systems, *Transport in Porous Media* 15 (1994) 51–70.
119. M. Quintard, S. Whitaker, Transport in ordered and disordered porous media III: Closure and comparison between theory and experiment, *Transport in Porous Media* 15 (1994) 31–49.
120. M. Quintard, L. Bletzacker, D. Chenu, S. Whitaker, Nonlinear, multicomponent, mass transport in porous media, *Chemical Engineering Science* 61(8) (2006) 2643–2669.
121. F. Golfier, M. Quintard, S. Whitaker, Heat and mass transfer in tubes: An analysis using the method of volume averaging, *Journal of Porous Media* 5 (2002) 169–185.
122. A. Eidsath, R.G. Carbonell, S. Whitaker, L.R. Herrmann, Dispersion in pulsed systems III: Comparison between theory and experiment for packed beds, *Chemical Engineering Science* 38 (1983) 1803–1816.

123. M. Quintard, Diffusion in isotropic and anisotropic porous systems: Three-dimensional calculations, *Transport in Porous Media* 11 (1993) 187–199.
124. P. Adler, *Porous Media: Geometry and Transport*, Butterworth-Heineman, Stoneham, U.K., 1994.
125. M. Quintard, S. Whitaker, Convection, dispersion, and interfacial transport of contaminants: Homogeneous porous media, *Advances in Water Resources* 17 (1994) 221–239.
126. M. Quintard, Diffusion in isotropic and anisotropic porous systems: Three-dimensional calculations, *Transport in Porous Media* 11 (1993) 187–199.
127. G.L. Vignoles, M. Donias, C. Mulat, C. Germain, J.-F. Delesse, Simplified marching cubes: An efficient discretization scheme for simulations of deposition/ablation in complex media, *Computational Materials Science* 50(3) (2011) 893–902.
128. H. Davarzani, M. Marcoux, M. Quintard, Theoretical predictions of the effective thermodiffusion coefficients in porous media, *International Journal of Heat and Mass Transfer* 53 (2010) 1514–1528.
129. M. Quintard, S. Whitaker, Two-phase flow in heterogeneous porous media i: The influence of large spatial and temporal gradients, *Transport in Porous Media* 5 (1990) 341–379.
130. H. Hardee, R. Nilson, Natural convection in porous media with heat generation, *Nuclear Science Engineering* (United States) 63(2) (1977) 119–132.
131. I. Catton, M. Chung, Two-phase flow in porous media with phase change steam injection and post-dryout heat transfer, in: M. Quintard, M. Todorovic (Eds.), *Heat and Mass Transfer in Porous Media*, Elsevier, New York, 1992, pp. 675–702.
132. F. Fichot, F. Duval, N. Trégourès, C. Béchaud, M. Quintard, The impact of thermal non-equilibrium and large-scale 2d/3d effects on debris bed reflooding and coolability, *Nuclear Engineering and Design* 236(19) (2006) 2144–2163.
133. S. Whitaker, Flow in porous media II: The governing equations for immiscible two-phase flow, *Transport in Porous Media* 1 (1986) 105–125.
134. J.L. Auriault, Nonsaturated deformable porous media: Quasistatics, *Transport in Porous Media* 2 (1987) 45–64.
135. S. Majid Hassanizadeh, W.G. Gray, Toward an improved description of the physics of two-phase flow, *Advances in Water Resources* 16(1) (1993) 53–67.
136. M. Panfilov, I. Panfilova, Phenomenological meniscus model for two-phase flows in porous media, *Transport in Porous Media* 58(1–2) (2005) 87–119.
137. W. Amarasooriya, T. Theofanous, Premixing of steam explosions: A three-fluid model, *Nuclear Engineering and Design* 126 (1991) 23–39.
138. G. Berthoud, M. Valette, Development of a multidimensional model for the premixing phase of a fuel-coolant interaction, *Nuclear Engineering and Design* 149 (1994) 409–418.
139. A. Bachrata, F. Fichot, G. Repetto, M. Quintard, J. Fleurot, Quench front progression in a superheated porous medium: Experimental analysis and model development, *Journal of Energy and Power Engineering* 7 (2013) 514–523.
140. S. Nukiyama, The maximum and minimum values of the heat Q transmitted from metal to boiling water under atmospheric pressure, *International Journal of Heat and Mass Transfer* 9(12) (1966) 1419–1433.
141. D. Wildenschild, A. Sheppard, X-ray imaging and analysis techniques for quantifying pore-scale structure and processes in subsurface porous medium systems, *Advances in Water Resources* 51 (2013) 217–246.

8 Porous Media Theory for Membrane Transport Phenomena

A. Nakayama, Y. Sano, T. Nishimura, and K. Nagase

CONTENTS

8.1 Introduction 321
8.2 Volume-Averaging Theory 322
8.3 Mathematic Model of Hollow Fiber Membrane Systems 324
8.4 Macroscopic Governing Equations for Hollow Fiber Membrane Systems 326
8.5 Three-Concentration Model for Hollow Fiber Membrane Systems 327
8.6 Application of the Three-Concentration Model for Dialyzer 329
8.6.1 Velocity Fields 329
8.6.2 Solute Concentration Fields 331
8.6.3 Clearance 333
8.6.4 Closed-Form Solutions for the Case of Pure Diffusion 334
8.6.5 Closed-Form Solutions for the Case of Symmetric Flow Rates 335
8.6.6 Comparison of the Present Analytic Results and Available Experimental Data 337
8.7 Application of the Three-Concentration Model for Reverse Osmosis Module 339
8.7.1 Concentration Polarization and Three-Concentration Model 340
8.7.2 Salt Concentration Fields 342
8.7.3 Comparison of the Present Analytic Results and Available Experimental Data 347
8.8 3D Numerical Models for Membrane Systems 351
8.9 Concluding Remarks 353
Acknowledgment 353
Nomenclature 353
References 355

8.1 INTRODUCTION

Hollow fiber dialyzers, that is, artificial kidney systems, are widely used in the therapy of hemodialysis, which is a method for removing waste products such as creatinine and urea, as well as free water from the blood when the kidneys are in renal failure. In this dialyzer, a bundle of hollow fibers of ultrafiltration membranes are used so as to remove metabolic end products from the human body. Mass diffusion and ultrafiltration processes through such membranes are most commonly described by the Kedem–Katchalsky model (1958), which estimates the volume and solute flows of nonelectrolyte solutions across membranes. In this 1D model, the total solute flux vector perpendicular to the membranes is evaluated in consideration of the solute diffusion rate through the membranes due to the difference of the concentration as well as the ultrafiltration flow induced by the transmembrane pressure and osmotic pressure.

Hollow fibers are also used in reverse osmosis modules for water purification. Such hollow fiber reverse osmosis modules are most extensively used for both domestic and industrial water

purification, since they are capable of providing high specific surface area and recovery factor. Various membrane transport models are available for mathematically describing transport phenomena through membranes with concentration polarization. Sekino (1993, 1995) was the first to introduce what is known as the friction–concentration–polarization model. The Sekino model was adopted by Al-Bastaki and Abbas (1999, 2000), Kumano et al. (2008), and Marcovecchio et al. (2010) for estimating desalination performance of actual modules. Chatterjee et al. (2004), Gupta (1985, 1987) and Murthy and Gupta (1994, 1998) replaced this concentration polarization by applying the three-parameter, nonlinear, Spiegler–Kedem model (1966) to analyze the performances of radial flow hollow fiber reverse osmosis modules.

In the Spiegler–Kedem model (1966), the so-called reflection coefficient is introduced as another parameter in addition to two parameters commonly used in the solution–diffusion model, namely, hydrodynamic permeability and solute permeability. The Spiegler–Kedem model is believed to be more accurate for describing transport phenomena through membranes with polarization. However, in this Spiegler–Kedem model (1966), the solute flux across the membrane is assumed to be 1D, as in the Kedem–Katchalsky model (1958). Thus, it fails to describe the complex 3D mass and momentum transfer taking place within a reverse osmosis module.

The concept of local volume-averaging theory (VAT) widely used in the study of porous media (Cheng 1978, Vafai and Tien 1981, Quintard and Whitaker 1993, Nakayama 1995, Kuwahara et al. 1996, Nakayama and Kuwahara 2008, Yang and Nakayama 2010) is quite useful under these situations, in which thousands of small-scale elements exist in a large space. In the VAT, we use a grid system, which is just fine enough to resolve macroscopic flow and concentration fields. We do not grid small-scale elements but model them as a porous medium. A variety of models for the fiber membrane systems have been proposed so far. Yet the theory of porous media appears to be most appropriate for treating transport phenomena within hollow fiber systems since it is of 3D and contains fewer assumptions as compared to existing models.

In this chapter, we shall prove that the VAT itself is capable of describing such complex 3D flow and concentration fields prevailing within hollow fiber membrane dialyzer systems and hollow fiber reverse osmosis desalination systems. Therefore, there is no need to prescribe any particular membrane mass transport model. In fact, the VAT in a general 3D form, when applied to a 1D mass transport system, naturally reduces to an appropriate membrane mass transport equation for a hollow fiber devise.

In what follows, a rigorous mathematical development based on the VAT (Sano and Nakayama 2012) is presented to obtain two complete sets of the 3D volume-averaged governing equations appropriate for fiber membrane dialyzer and reverse osmosis desalination systems, respectively. In these models, three individual concentrations are assigned according to the porous media theory for individual phases, namely, the lumen-side fluid phase within the hollow fibers, the shell-side fluid phase outside the hollow fibers, and the membrane phase. This three-concentration equation model derived through the porous media approach can be used to estimate performances of both hollow fiber membrane dialyzers and hollow fiber reverse osmosis modules.

First, we shall present 1D analytic solutions for both hollow fiber dialyzer and reverse osmosis module. We shall compare the analytic results against available experimental data so as to examine the validity of the three-concentration equation model derived through the porous media approach. Subsequently, the 3D numerical computations will be proposed to capture individual concentration fields within a module. The present numerical methods based on the three-concentration model can be used for possible optimization of various hollow fiber systems.

8.2 VOLUME-AVERAGING THEORY

In what follows, the porous media approach, that is, the VAT, is introduced to derive a complete set of the volume-averaged governing equations for the case of fiber membrane dialyzer systems. The corresponding set of the volume-averaged governing equations can easily be obtained for the

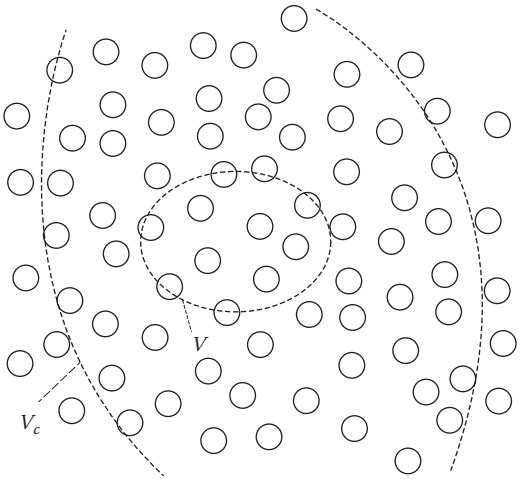

FIGURE 8.1 Control volume in a porous medium.

case of reverse osmosis module as well, when we identify the brine (i.e., salt water) as the shell-side phase and the permeate (filtered water) as the lumen-side phase, respectively. The procedure introduced by Nakayama and Kuwahara (2008) for a general bioheat transfer model may readily be extended for the case of countercurrent dialysis system. A local control volume V is considered in a fluid-saturated porous medium, as shown in Figure 8.1, whose length scale $V^{1/3}$ is much smaller than the macroscopic characteristic length $V_c^{1/3}$, but, at the same time, much greater than the microscopic characteristic length. Under this condition, the volume average of a certain variable ϕ is defined as

$$\langle \phi \rangle = \frac{1}{V} \int_{V_f} \phi \, dV \tag{8.1}$$

Another average, that is, the intrinsic average, is given by

$$\langle \phi \rangle^f = \frac{1}{V_f} \int_{V_f} \phi \, dV \tag{8.2}$$

where V_f is the volume space that the fluid of interest (either blood or dialysate for the case of dialyzer) occupies. Obviously, two averages are related as $\langle \phi \rangle = \varepsilon_f \langle \phi \rangle^f$, where $\varepsilon_f = V_f/V$ is the local volume fraction of the fluid space.

A variable may be decomposed into its intrinsic average and the spatial deviation from it:

$$\phi = \langle \phi \rangle^f + \tilde{\phi} \tag{8.3}$$

This spatial decomposition is similar to the Reynolds decomposition used in the theory of turbulence, which splits the quantity into its time average part and fluctuating part. Naturally, its spatial deviation $\tilde{\phi}$ is defined such that its spatial average equals zero $\langle \tilde{\phi} \rangle = 0$. All dependent variables in the

microscopic governing equations for the blood, dialysate, and membrane phases will be decomposed in this manner. We may utilize the following spatial average relationships:

$$\langle \phi_1 \phi_2 \rangle^f = \langle \phi_1 \rangle^f \langle \phi_2 \rangle^f + \langle \tilde{\phi}_1 \tilde{\phi}_2 \rangle^f \tag{8.4}$$

$$\left\langle \frac{\partial \phi}{\partial x_i} \right\rangle = \frac{\partial \langle \phi \rangle}{\partial x_i} + \frac{1}{V} \int_{A_{int}} \phi n_i dA \tag{8.5a}$$

$$\left\langle \frac{\partial \phi}{\partial x_i} \right\rangle^f = \frac{1}{\varepsilon_f} \frac{\partial \varepsilon_f \langle \phi \rangle^f}{\partial x_i} + \frac{1}{V_f} \int_{A_{int}} \phi n_i dA \tag{8.5b}$$

and

$$\left\langle \frac{\partial \phi}{\partial t} \right\rangle = \frac{\partial \langle \phi \rangle}{\partial t} \tag{8.6}$$

where A_{int} represents the interfaces between the fluid and membrane matrix within the local control volume. Note n_i is the unit vector pointing outward from the fluid side to the membrane matrix side.

8.3 MATHEMATIC MODEL OF HOLLOW FIBER MEMBRANE SYSTEMS

Although we define three individual phases, namely, the shell-side phase, lumen-side phase, and membrane phase, strictly focusing on the case of a hollow fiber dialyzer, the definitions and formulations presented in Sections 8.3 through 8.5 may easily be translated for the case of reverse osmosis desalination module.

Figure 8.2 schematically shows a hollow fiber membrane countercurrent dialyzer, in which only outer fibers are shown for clarity. In the VAT, we define individual velocities and species concentrations to three individual phases, namely, the blood, dialysate, and membrane phases. Each phase is treated as a continuum filling the entire internal space of the dialyzer container. Thus, three phases

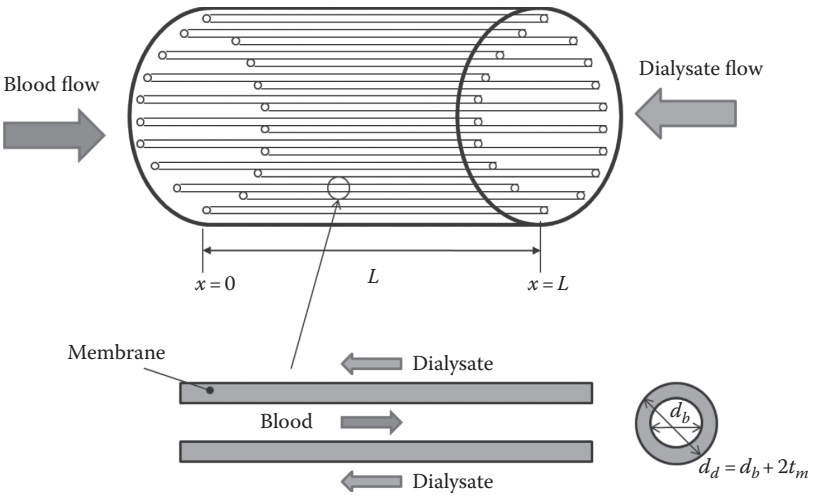

FIGURE 8.2 Dialyzer system.

share the same space but with different volume fractions. Assigning the subscripts b, d, and m to the blood phase, dialysate phase, and membrane phase, respectively, the following relations can be found for the volume fractions ε_b, ε_m, ε_d and the specific area of the blood compartment a_b and that of the dialysate compartment a_d:

$$\varepsilon_b = \frac{N(\pi/4)d_b^{\,2}}{A} \tag{8.7a}$$

$$\varepsilon_m = \frac{(\pi/4)\left(\left(d_b + 2t_m\right)^2 - d_b^{\,2}\right)}{(\pi/4)d_b^{\,2}}\varepsilon_b = 4\frac{t_m}{d_b}\left(1 + \frac{t_m}{d_b}\right)\varepsilon_b \tag{8.7b}$$

$$\varepsilon_d = 1 - \left(1 + 4\frac{t_m}{d_b}\left(1 + \frac{t_m}{d_b}\right)\right)\varepsilon_b \tag{8.7c}$$

$$a_b = \frac{4\varepsilon_b}{d_b}, \quad a_d = \frac{4\varepsilon_b}{d_b}\left(1 + 2\frac{t_m}{d_b}\right) \tag{8.8a,b}$$

Note that N is the number of hollow fibers, while A is the cross-sectional area of the dialyzer container. The membrane thickness and the inner and outer diameters of the hollow fiber are indicated by t_m, d_b, and $d_d = d_b + 2t_m$, respectively.

Another important parameter in addition to the foregoing geometrical parameters is the permeability of the membrane, which controls the ultrafiltration velocity. Referring to Figure 8.3, we may consider the radial Darcy flow through the membrane of the intrinsic permeability of the membrane K_m and follow the Kedem–Katchalsky model in terms of the ultrafiltration velocity J_V, the transmembrane pressure difference Δp, and the osmotic pressure difference Π as follows:

$$J_V = L_p\left(\Delta p - \Pi\right) \tag{8.9}$$

where

$$L_p = \frac{1}{(\mu/K_m)(d_b/2)\ln\left(1 + \left(2t_m/d_b\right)\right)} \tag{8.10}$$

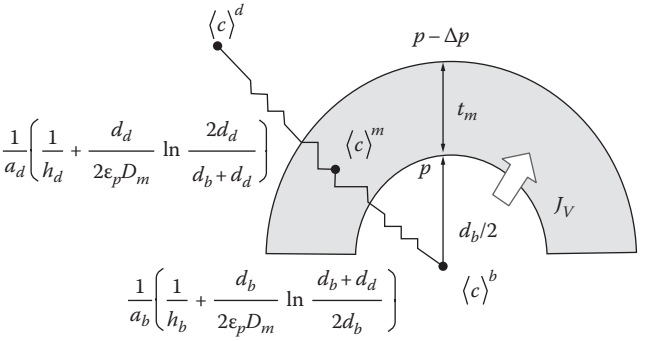

FIGURE 8.3 Ultrafiltration through a membrane.

is the hydraulic permeability of the porous membrane. In the case of hollow fiber membrane countercurrent dialyzer, the ingredients in the dialysate are blended such that the osmotic pressure difference Π vanishes:

$$J_V = L_p \Delta p \tag{8.11}$$

The intrinsic permeability of the membrane based on the capillary tube model with cylindrical pores of the diameter d_p and porosity ε_p may be evaluated from

$$K_m = \frac{\varepsilon_p d_p^2}{32} \tag{8.12}$$

It should be pointed out that a number of membrane descriptions based on the Kedem–Katchalsky model and its derivatives have been reported in the literature (e.g., Waniewski 2006). Lu and Lu (2010) introduced a half channel model in which two parallel straight channels are considered for two fluids of different viscosities. They carried out an analysis for mass transfer through the porous membranes. Flat-plate membrane dialyzers were considered analytically by Tu et al. (2006, 2009) for both concurrent and countercurrent dialysis systems. Their theoretical predictions agree qualitatively with their experimental results. Yeh (2009) presented an analysis analogous to conventional heat exchanger analysis to consider the effect of external recycle on the performance of dialysis in double-pass rectangular membrane modules. Similar analyses were reported by Legallais et al. (2000), Palaty et al. (2006), Galach et al. (2003), Yeh et al. (1998), and Sigdell (1982). On the other hand, Ding et al. (2004) accounted for both radial and axial gradients of the blood and dialysate sides, which were neglected in most of previous investigations. In recent years, some numerical attempts have been made to simulate the fluid and solute transport processes in fiber membrane systems (Kumar and Upadhyay 2000, Shirazian, et al. 2009, Wang et al. 2010). However, it appears to be impossible to resolve the details of flow and concentration within the dialyzer containing thousands of hollow fibers and dialysate compartments, even using a supercomputer available today, due to tremendous computational memory and CPU time required. Thus, the only possible way to describe complex momentum and mass transfer within hollow fiber membrane systems is to appeal to a local volume-averaging procedure based on the VAT, as illustrated in the next section.

8.4 MACROSCOPIC GOVERNING EQUATIONS FOR HOLLOW FIBER MEMBRANE SYSTEMS

The microscopic governing equations, namely, the continuity, momentum, and species mass transfer equations, can be written as follows:

$$\frac{\partial u_j}{\partial x_j} = 0 \tag{8.13}$$

$$\rho \frac{\partial u_i}{\partial t} + \rho \frac{\partial u_j u_i}{\partial x_j} = -\frac{\partial p}{\partial x_i} + \mu \frac{\partial^2 u_i}{\partial x_j^2} \tag{8.14}$$

$$\frac{\partial c}{\partial t} + \frac{\partial u_j c}{\partial x_j} = D \frac{\partial^2 c}{\partial x_j^2} \tag{8.15}$$

These governing equations may be written for three individual phases. Then, all dependent variables for these three phases, namely, lumen-side phase (blood), shell-side phase (dialysate),

and membrane phase, are decomposed according to Equation 8.3. Subsequently, these microscopic equations are integrated over the local control volume, exploiting the foregoing spatial average relationships, as given by Equations 8.4 through 8.6. The set of the macroscopic governing equations thus obtained for the lumen phase (blood) flow may be given as follows:

$$\frac{\partial \varepsilon_b \langle u_j \rangle^b}{\partial x_j} + \int_{A_{int}} u_j n_{bj} dA = 0 \tag{8.16}$$

$$\rho \frac{\partial \langle u_i \rangle^b}{\partial t} + \rho \frac{\partial \langle u_j \rangle^b \langle u_i \rangle^b}{\partial x_j} = -\frac{\partial \langle p \rangle^b}{\partial x_i} + \frac{\partial}{\partial x_j}\left(\mu \frac{\partial \langle u_i \rangle^b}{\partial x_j} + \frac{\mu}{V_b} \int_{V_{bint}} u_i dA - \rho \langle \tilde{u}_i \tilde{u}_j \rangle^b \right)$$

$$+ \frac{1}{V_b} \int_{A_{bint}} \left(\mu \frac{\partial u_i}{\partial x_j} - p\delta_{ij} \right) n_{bj} dA - \frac{1}{V_b} \int_{A_{bint}} \rho u_j u_i n_{bj} dA \tag{8.17}$$

$$\frac{\partial \varepsilon_b \langle c \rangle^b}{\partial t} + \frac{\partial \varepsilon_b \langle u_j \rangle^b \langle c \rangle^b}{\partial x_j} = \frac{\partial}{\partial x_j}\left(\varepsilon_b D_b \frac{\partial \langle c \rangle^b}{\partial x_j} + \frac{D_b}{V} \int_{A_{bint}} c n_{bj} dA - \rho \varepsilon_b \langle \tilde{c} \tilde{u}_j \rangle^b \right)$$

$$+ \frac{1}{V} \int_{A_{bint}} D_b \frac{\partial c}{\partial x_j} n_{bj} dA - \frac{1}{V} \int_{A_{bint}} c u_j n_{bj} dA \tag{8.18}$$

where the superscripts b are assigned to indicate the blood phase intrinsic average quantities as defined by Equation 8.2. As already noted, n_{bi} is the unit vector pointing outward from the blood side to the membrane side.

8.5 THREE-CONCENTRATION MODEL FOR HOLLOW FIBER MEMBRANE SYSTEMS

These macroscopic equations may be modeled as follows:

$$\frac{\partial \varepsilon_b \langle u_j \rangle^b}{\partial x_j} + \omega = 0 \tag{8.19}$$

$$\rho \frac{\partial \langle u_i \rangle^b}{\partial t} + \rho \frac{\partial \langle u_j \rangle^b \langle u_i \rangle^b}{\partial x_j} = -\frac{\partial \langle p \rangle^b}{\partial x_i} + \mu \frac{\partial^2 \langle u_i \rangle^b}{\partial x_j^{\,2}} - \frac{\mu}{K_{b_{ij}}} \varepsilon_b \langle u_j \rangle^b \tag{8.20}$$

$$\frac{\partial \varepsilon_b \langle c \rangle^b}{\partial t} + \frac{\partial \varepsilon_b \langle u_j \rangle^b \langle c \rangle^b}{\partial x_j} = \frac{\partial}{\partial x_j}\left(\varepsilon_b D_b \frac{\partial \langle c \rangle^b}{\partial x_j} + \varepsilon_b D_{bdis_{jk}} \frac{\partial \langle c \rangle^b}{\partial x_k} \right) - a_b h_{tb} \left(\langle c \rangle^b - \langle c \rangle^m \right) - \omega \langle c \rangle^b \tag{8.21}$$

where

$$\omega = a_b J_V = \frac{1}{V} \int_{A_{bint}} u_j n_{bj} dA \tag{8.22}$$

is the perfusion rate (1/s) that is the product of the specific area a_b and ultrafiltration velocity J_V, describing the ultrafiltration volume rate of the blood per unit volume of the dialyzer, bleeding off to the dialysate compartment through the membrane. The axial permeability component $K_{b_{xx}} = \varepsilon_b d_b^2/32$ was estimated assuming a laminar fully developed flow in a tube, while the transverse components $K_{b_{yy}} = K_{b_{zz}}$ may virtually be set to zero, since it is unlikely that the filtrated blood reenters into the other fibers. The effective mass transfer coefficient h_{tb} for the case of negligible tortuosity within the membrane is defined, referring to Figure 8.3, as

$$\frac{1}{h_{tb}} = \frac{1}{h_b} + \frac{d_b}{2\varepsilon_p D_m} \ln\left(1 + \frac{t_m}{d_b}\right) \tag{8.23}$$

where D_m is the solute diffusion coefficient in water.

Likewise, the set of the macroscopic equations for the dialysate (shell) flow may be written with sub- and superscripts d as

$$\frac{\partial \varepsilon_d \langle u_j \rangle^d}{\partial x_j} - \omega = 0 \tag{8.24}$$

$$\rho \frac{\partial \langle u_i \rangle^d}{\partial t} + \rho \frac{\partial \langle u_j \rangle^d \langle u_i \rangle^d}{\partial x_j} = -\frac{\partial \langle p \rangle^d}{\partial x_i} + \mu \frac{\partial^2 \langle u_i \rangle^d}{\partial x_j^2} - \frac{\mu}{K_{d_{ij}}} \varepsilon_d \langle u_j \rangle^d \tag{8.25}$$

$$\frac{\partial \varepsilon_d \langle c \rangle^d}{\partial t} + \frac{\partial \varepsilon_d \langle u_j \rangle^d \langle c \rangle^d}{\partial x_j} = \frac{\partial}{\partial x_j}\left(\varepsilon_d D_d \frac{\partial \langle c \rangle^d}{\partial x_j} + \varepsilon_d D_{d dis_{jk}} \frac{\partial \langle c \rangle^d}{\partial x_k}\right) - a_d h_{td}\left(\langle c \rangle^d - \langle c \rangle^m\right) + \omega \langle c \rangle^m \tag{8.26}$$

where

$$\frac{1}{h_{td}} = \frac{1}{h_d} + \frac{d_b}{2\varepsilon_p D_m}\left(1 + 2\frac{t_m}{d_b}\right) \ln\left(\frac{1 + 2\left(t_m/d_b\right)}{1 + \left(t_m/d_b\right)}\right) \tag{8.27}$$

The axial permeability component may be evaluated using the hydraulic diameter concept as $K_{d_{xx}} = \varepsilon_d(\varepsilon_d {d_b}^2/\varepsilon_b d_d)^2/32$. Although the ultrafiltration takes place radially outward from the lumen to shell compartments through the membranes, the macroscopic velocity resulting from such microscopically radial flow vanishes within the membrane continuum. Thus, as for the membrane phase, we only need to consider the species concentration equation:

$$\frac{\partial \varepsilon_m \langle c \rangle^m}{\partial t} = \frac{\partial}{\partial x_j}\left(\varepsilon_m D_{m_{jk}} \frac{\partial \langle c \rangle^m}{\partial x_k}\right) + a_b h_{tb}\left(\langle c \rangle^b - \langle c \rangle^m\right) + \omega \langle c \rangle^b + a_d h_{td}\left(\langle c \rangle^d - \langle c \rangle^m\right) - \omega \langle c \rangle^m \tag{8.28}$$

where $D_{mxx} \gg D_{myy} = D_{mzz}$ such that the transverse diffusion may be neglected as compared with the axial one. This completes our closure procedure. The present three-concentration model consists of the continuity, momentum, and concentration equations for the blood and dialysate compartments and the concentration equation for the membrane along with the ultrafiltration velocity relationship, namely, (8.9) and (8.22). These partial differential equations can be solved numerically for given initial and boundary conditions using a standard numerical procedure such as those based on primitive variables (e.g., Nakayama 1995). Such 3D calculation results will be presented later.

8.6 APPLICATION OF THE THREE-CONCENTRATION MODEL FOR DIALYZER

In what follows, we shall consider the steady 1D case and derive an analytic solution to verify the validity of the present three-concentration model.

8.6.1 Velocity Fields

For this case, Equations 8.11, 8.19 through 8.22, 8.24 through 8.26, and 8.28 reduce to

$$\frac{du_b}{dx} = -\frac{du_d}{dx} = -\omega = -a_b J_V = -a_b L_p \left(\langle p \rangle^b - \langle p \rangle^d \right) \tag{8.29}$$

$$-\frac{d\langle p \rangle^b}{dx} - \frac{\mu}{K_{b,xx}} u_b = 0 \tag{8.30}$$

$$-\frac{d\langle p \rangle^d}{dx} - \frac{\mu}{K_{d,xx}} u_d = 0 \tag{8.31}$$

$$\frac{d}{dx} u_b \langle c \rangle^b = -a_b h_{tb} \left(\langle c \rangle^b - \langle c \rangle^m \right) - \omega \langle c \rangle^b \tag{8.32}$$

$$\frac{d}{dx} u_d \langle c \rangle^d = -a_d h_{td} \left(\langle c \rangle^d - \langle c \rangle^m \right) + \omega \langle c \rangle^m \tag{8.33}$$

$$a_b h_{tb} \left(\langle c \rangle^b - \langle c \rangle^m \right) + \omega \langle c \rangle^b + a_d h_{td} \left(\langle c \rangle^d - \langle c \rangle^m \right) - \omega \langle c \rangle^m = 0 \tag{8.34}$$

where the axial Darcian velocities of the blood and dialysate flows are denoted by

$$u_b = \varepsilon_b \langle u \rangle^b \quad \text{and} \quad u_d = \varepsilon_d \langle u \rangle^d \tag{8.35a,b}$$

The inertia and macroscopic diffusion (Brinkman) terms in the momentum equations are neglected since the blood and dialysate flows within the dialysate case are most likely to be laminar and fully developed except the small regions near the entrances. In all three-concentration equations, the macroscopic diffusion terms are dropped, since such effects on the solute mass transfer would be negligibly small as compared with those of the interfacial mass transfer and ultrafiltration. The continuity Equation 8.29 gives

$$u_b + u_d = C_u = \text{const.} \tag{8.36}$$

Note that u_b is positive, while u_d is negative. Moreover, the dialysate inlet velocity is often higher than the blood inlet velocity, so that the constant C_u is likely to be negative. Subtracting Equation 8.31 from (8.30) and then substituting Equation 8.29 along with the foregoing Equation 8.36 to eliminate u_d and the transmembrane pressure ($\langle p \rangle^b - \langle p \rangle^d$), we obtain the second-order ordinary differential equation for u_b as follows:

$$\frac{d^2 u_b}{dx^2} = a_b L_p \mu \left(\frac{1}{K_{b,xx}} + \frac{1}{K_{d,xx}} \right) \left(u_b - \frac{C_u}{1+\alpha} \right) \tag{8.37}$$

which can readily be solved as

$$u_b(x^*) = \frac{C_u}{1+\alpha} + \frac{\left(u_b(0) - \frac{C_u}{1+\alpha}\right)\sinh\left(B(1-x^*)\right) + \left(\frac{\alpha C_u}{1+\alpha} - u_d(1)\right)\sinh Bx^*}{\sinh B} \tag{8.38}$$

where

$$\alpha = \frac{K_{dxx}}{K_{bxx}} \tag{8.39a}$$

is the permeability ratio (i.e., lumen and shell resistance ratio) and

$$B = L\sqrt{a_b L_p \mu\left(\frac{1}{K_{bxx}} + \frac{1}{K_{dxx}}\right)} = \frac{L}{d_b}\sqrt{8\varepsilon_b \frac{K_m\left(\left(1/K_{bxx}\right) + \left(1/K_{dxx}\right)\right)}{\ln\left(1 + \left(2t_m/d_b\right)\right)}} \tag{8.39b}$$

is the dimensionless parameter associated with the membrane permeability. Moreover,

$$x^* = \frac{x}{L} \tag{8.39c}$$

is the dimensionless coordinate, where L is the length of the dialyzer case, as indicated in Figure 8.2. In Equation 8.38, the inlet Darcian velocities of the blood $u_b(0)$ and that of the dialysate $u_d(1)$ are used since they are the ones that are usually provided. The unknown constant C_u may be determined from the continuity relationship, that is, Equation 8.29:

$$\omega(x^*) = -\frac{du_b}{dx} = a_b L_p\left(\langle p\rangle^b - \langle p\rangle^d\right) = \frac{B}{L}\frac{\left(u_b(0) - \frac{C_u}{1+\alpha}\right)\cosh\left(B(1-x^*)\right) - \left(\frac{\alpha C_u}{1+\alpha} - u_d(1)\right)\cosh Bx^*}{\sinh B} \tag{8.40}$$

which can be solved for C_u for given transmembrane pressure at $x = 0, \left(\langle p\rangle^b - \langle p\rangle^d\right)\Big|_{x^*=0}$, as

$$C_u = \frac{1+\alpha}{\alpha + \cosh B}\left(u_b(0)\left(\cosh B - \frac{\sinh B}{B}\beta\right) + u_d(1)\right) \tag{8.41}$$

where

$$\beta = \frac{La_b L_p\left(\langle p\rangle^b - \langle p\rangle^d\right)\Big|_{x^*=0}}{u_b(0)} = \frac{8\varepsilon_b K_m L}{\mu u_b(0) d_b^{\,2}\ln\left(1 + \left(2t_m/d_b\right)\right)}\left(\langle p\rangle^b - \langle p\rangle^d\right)\Big|_{x^*=0} \tag{8.42}$$

is another important dimensionless parameter, that is, the dimensionless transmembrane pressure at the inlet.

8.6.2 Solute Concentration Fields

Having established the velocity field, we shall consider the concentration fields. Equation 8.34 may readily be solved for the membrane concentration $\langle c\rangle^m$ as

$$\langle c\rangle^m = \frac{a_b h_{tb} + \omega}{a_b h_{tb} + a_d h_{td} + \omega}\langle c\rangle^b + \frac{a_d h_{td}}{a_b h_{tb} + a_d h_{td} + \omega}\langle c\rangle^d \tag{8.43}$$

which can be substituted into Equation 8.33 as

$$\frac{d}{dx}u_d\langle c\rangle^d = \frac{a_d h_{td}\left(a_b h_{tb} + \omega\right)}{a_b h_{tb} + a_d h_{td} + \omega}\left(\langle c\rangle^b - \langle c\rangle^d\right) + \omega\langle c\rangle^m \tag{8.44}$$

It is interesting to note that this foregoing equation along with Equation 8.43 is quite similar to the Kedem–Katchalsky model as introduced by Waniewski et al. (1991), Galach et al. (2003), and many others, which for the case of negligible osmotic pressure and solute reflection coefficient can be written as

$$\frac{d}{dx}u_d\langle c\rangle^d = a_b\left(P_m\left(\langle c\rangle^b - \langle c\rangle^d\right) + J_V\langle c\rangle^m\right) \tag{8.45}$$

and

$$\langle c\rangle^m = \left(1 - \frac{1}{Pe} + \frac{1}{\exp(Pe) - 1}\right)\langle c\rangle^b + \left(\frac{1}{Pe} - \frac{1}{\exp(Pe) - 1}\right)\langle c\rangle^d \tag{8.46}$$

where P_m is the effective membrane diffusivity permeability (i.e., the overall mass transfer coefficient with respect to the inner membrane surface area) and

$$Pe = \frac{J_V}{P_m} \tag{8.47a}$$

is the Peclet number based on the filtration velocity. Comparison of Equations 8.44 and 8.45 reveals that this Peclet number corresponds to

$$Pe = \frac{\left(a_b h_{tb} + a_d h_{td} + \omega\right)\omega}{a_d h_{td}\left(a_b h_{tb} + \omega\right)} \tag{8.47b}$$

which for the case of very thin membrane with $h_{tb} = h_{td}$ gives

$$\frac{\omega}{a_b h_{td}} = \frac{\sqrt{4 + Pe^2} + Pe - 2}{2Pe} \tag{8.48}$$

Thus, Equation 8.43 based on the present three-concentration model may be written as

$$\langle c\rangle^m = \frac{Pe - 2 + \sqrt{4 + Pe^2}}{2Pe}\langle c\rangle^b + \left(1 - \frac{Pe - 2 + \sqrt{4 + Pe^2}}{2Pe}\right)\langle c\rangle^d \tag{8.49}$$

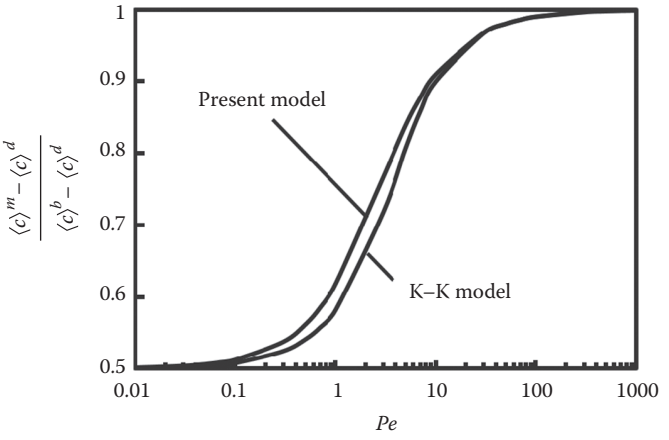

FIGURE 8.4 Comparison of the present model and the Kedem–Katchalsky model.

which naturally yields $\langle c\rangle^m = \left(\langle c\rangle^b + \langle c\rangle^d\right)/2$ for small ultrafiltration velocity (i.e., $Pe \ll 1$) and $\langle c\rangle^m = \langle c\rangle^b$ for large ultrafiltration velocity (i.e., $Pe \gg 1$). In Figure 8.4, Equation 8.49 based on the present three-concentration model is compared against Equation 8.46 based on the Kedem–Katchalsky model, in terms of $\left(\langle c\rangle^m - \langle c\rangle^d\right)/\left(\langle c\rangle^b - \langle c\rangle^d\right)$. The figure shows a fairly good agreement with each other.

Substitution of Equation 8.43 into the solute transport Equation 8.32 yields

$$\frac{d}{dx}u_b\langle c\rangle^b = -\frac{a_b h_{tb} a_d h_{td}}{a_b h_{tb} + a_d h_{td} + \omega}\left(\langle c\rangle^b - \langle c\rangle^d\right) - \omega\langle c\rangle^b \tag{8.50}$$

Furthermore, adding Equations 8.32 and 8.33, we have

$$u_b\langle c\rangle^b + u_d\langle c\rangle^d = u_b(1)\langle c\rangle^b(1) + u_d(1)\langle c\rangle^d(1) = \left(C_u - u_d(1)\right)\langle c\rangle^b(1) = \text{const.} \tag{8.51}$$

where the solute concentration in the dialysate at the inlet $\langle c\rangle^d(1)$ is assumed to be zero. Upon noting $\langle c\rangle^b du_b/dx = -\omega\langle c\rangle^b$, the foregoing two equations can be combined to give

$$\frac{d}{dx}\langle c\rangle^b = -\left(\frac{a_b h_{tb} a_d h_{td}}{a_b h_{tb} + a_d h_{td} + \omega}\right)\frac{C_u\langle c\rangle^b - \left(C_u - u_d(1)\right)\langle c\rangle^b(1)}{u_b\left(C_u - u_b\right)} \tag{8.52}$$

For a given solute concentration in the blood at the inlet $\langle c\rangle^b(0)$, this equation can be solved to give

$$\frac{\langle c\rangle^b(x^*)}{\langle c\rangle^b(0)} = \frac{1 - \left(u_d(1)/C_u\right)\left(1 - e^{f(1)-f(x^*)}\right)}{1 - \left(u_d(1)/C_u\right)\left(1 - e^{f(1)}\right)} \tag{8.53a}$$

Hence,

$$\frac{\langle c\rangle^d(x^*)}{\langle c\rangle^b(0)} = \frac{u_b(1) - \left(1 - \left(u_d(1)/C_u\right)\left(1 - e^{f(1)-f(x^*)}\right)\right)u_b(x^*)}{\left(1 - \left(u_d(1)/C_u\right)\left(1 - e^{f(1)}\right)\right)\left(C_u - u_b(x^*)\right)} \tag{8.53b}$$

where

$$f(x^*) = a_b h_{tb} a_d h_{td} L \int_0^{x^*} \frac{dx^*}{\left(a_b h_{tb} + a_d h_{td} + \omega(x^*)\right) u_b(x^*)\left(1 - \left(u_b(x^*)/C_u\right)\right)}$$

$$= \frac{1}{Pe_m} \int_0^{x^*} \frac{dx^*}{\left(1 + \dfrac{Pe_m}{2 + \dfrac{a_d h_{td}}{a_b h_{tb}} + \dfrac{a_b h_{tb}}{a_d h_{td}}} \left(\dfrac{\omega(x^*) L}{u_b(0)}\right)\right) \dfrac{u_b(x^*)}{u_b(0)} \left(1 - \dfrac{u_b(x^*)}{C_u}\right)}$$

$$\cong \frac{1}{Pe_m} \int_0^{x^*} \frac{dx^*}{\left(1 + \dfrac{Pe_m}{\square} \left(\dfrac{\omega(x^*) L}{u_b(0)}\right)\right) \dfrac{u_b(x^*)}{u_b(0)} \left(1 - \dfrac{u_b(x^*)}{C_u}\right)} \tag{8.54}$$

The dimensionless function $f(x^*)$ can be evaluated numerically using any standard integration scheme such as the Runge–Kutta–Gill method (see, e.g., Nakayama 1995). The modified Peclet number, Pe_m (which is the last of the five important dimensionless parameters, namely, $u_d(1)/u_b(0)$, α, B, β, and Pe_m), is defined as

$$Pe_m = \left(\frac{1}{a_b h_{tb}} + \frac{1}{a_d h_{td}}\right) \frac{u_b(0)}{L} \cong \frac{{d_b}^2 u_b(0)}{8 \varepsilon_b \varepsilon_p D_m L} \ln\left(1 + 2\frac{t_m}{d_b}\right) \tag{8.55}$$

since

$$\frac{1}{a_b h_{tb}} + \frac{1}{a_d h_{td}} = \frac{1}{a_b h_b} + \frac{1}{a_d h_d} + \frac{{d_b}^2}{8 \varepsilon_b \varepsilon_p D_m} \ln\left(1 + 2\frac{t_m}{d_b}\right) \cong \frac{{d_b}^2}{8 \varepsilon_b \varepsilon_p D_m} \ln\left(1 + 2\frac{t_m}{d_b}\right) \tag{8.56}$$

When the blood velocity is fixed, Pe_m may simply be regarded as a dimensionless total mass transfer resistance. The perfusion rate $\omega(x^*)$ and the blood Darcian velocity $u_b(x^*)$ are given by Equations 8.38 and 8.40, respectively. For the case of small metabolite clearances, we have $\omega(x^*) \ll a_b h_{tb} + a_d h_{td}$. Then, Equation 8.54 simplifies to

$$f(x^*) = \frac{1}{Pe_m} \int_0^{x^*} \frac{dx^*}{\dfrac{u_b(x^*)}{u_b(0)}\left(1 - \dfrac{u_b(x^*)}{C_u}\right)} \tag{8.57}$$

8.6.3 Clearance

Our primary interest, that is, the clearance of the solute from blood to dialysate CL, is given by

$$CL = A \frac{u_b(0)\langle c \rangle^b(0) - u_b(1)\langle c \rangle^b(1)}{\langle c \rangle^b(0)} = A u_b(0) \left(1 - \frac{C_u - u_d(1)}{u_b(0)\left(1 - \dfrac{u_d(1)}{C_u}\left(1 - e^{f(1)}\right)\right)}\right) \tag{8.58}$$

The clearance CL is often used for the scale for the dialysis time. For the initial total blood volume V_b for recirculation, we may define the dimensionless dialysis time as

$$t^* = \frac{CL}{V_b} t \tag{8.59}$$

which is often designated as KT/V by dialyzer practitioners and is usually set to around 1.2 or more. The temporal description of the balance of total solute mass may be given by

$$\frac{d}{dt}\left(V_b - A\left(u_b(0) - u_b(1)\right)t\right)\langle c\rangle^b = -CL\langle c\rangle^b \tag{8.60}$$

Thus, after dialyzing for the time period $t^* = CLt/V_b$, the solute concentration $\langle c\rangle^b(1;t^*)$ will be reduced to

$$\frac{\langle c\rangle^b(1;t^*)}{\langle c\rangle^b(0;0)} = \left(1 - \gamma t^*\right)^{((1/\gamma)-1)} \tag{8.61}$$

where

$$\gamma = \frac{A\left(u_b(0) - u_b(1)\right)}{CL} = \frac{1 - \dfrac{C_u - u_d(1)}{u_b(0)}}{1 - \dfrac{C_u - u_d(1)}{u_b(0)\left(1 - \dfrac{u_d(1)}{C_u}\left(1 - e^{f(1)}\right)\right)}} \tag{8.62}$$

For the case of the removal of small metabolites such as urea, γ is small. Then, Equation 8.61 reduces to the following conventional formula:

$$\frac{\langle c\rangle^b(1;t^*)}{\langle c\rangle^b(0;0)} = e^{-t^*} \tag{8.63}$$

which may be used for a rough estimation.

8.6.4 Closed-Form Solutions for the Case of Pure Diffusion

There exist some special cases in which closed analytic solutions are possible. We shall investigate such cases, namely, the case of no ultrafiltration (i.e., pure diffusive clearance) and the case of symmetry flow rates (i.e., $C_u = 0$). For this case of no ultrafiltration, we have $K_m = 0$; hence,

$$B = 0, \quad \beta = 0, \quad u_b(x^*) = u_b(0), \quad \text{and} \quad u_d(x^*) = u_d(1) \tag{8.64a–d}$$

$$f(x^*) = \frac{C_u x^*}{Pe_m u_d(1)} = \frac{\left(\dfrac{1}{u_b(0)} + \dfrac{1}{u_d(1)}\right)L}{\left(\dfrac{1}{a_b h_{tb}} + \dfrac{1}{a_d h_{td}}\right)} x^* \tag{8.65}$$

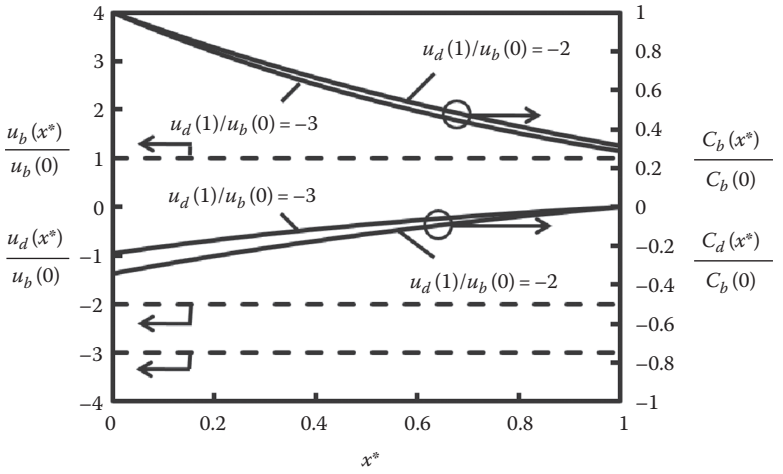

FIGURE 8.5 Velocity and solute variations along the axial coordinate for the case of pure diffusion.

Thus, the pure diffusive clearance CL_0 is given by

$$CL_0 = Au_b(0)\frac{\exp\left(\dfrac{1+\dfrac{u_b(0)}{u_d(1)}}{Pe_m}\right)-1}{\exp\left(\dfrac{1+\dfrac{u_b(0)}{u_d(1)}}{Pe_m}\right)+\dfrac{u_b(0)}{u_d(1)}} = Au_b(0)\frac{\exp\left(\dfrac{\dfrac{1}{u_b(0)}+\dfrac{1}{u_d(1)}}{\dfrac{1}{a_b h_{tb}}+\dfrac{1}{a_d h_{td}}}L\right)-1}{\exp\left(\dfrac{\dfrac{1}{u_b(0)}+\dfrac{1}{u_d(1)}}{\dfrac{1}{a_b h_{tb}}+\dfrac{1}{a_d h_{td}}}L\right)+\dfrac{u_b(0)}{u_d(1)}} \tag{8.66}$$

For $Pe_m = 0.68$ and $\alpha = 2.53$, the velocity and solute concentration variations along the length of the dialyzer are indicated in Figure 8.5, in which the two cases, that is, $u_d(1)/u_b(0) = -2$ and -3, are treated. Higher dialysate velocity $-u_d(1)/u_b(0)$ results in lowering solute concentrations at both exits.

8.6.5 Closed-Form Solutions for the Case of Symmetric Flow Rates

For this case, we set the transmembrane pressure for given B associated with the membrane permeability as

$$\beta = \frac{B}{\sinh B}\left(\cosh B + \frac{u_d(1)}{u_b(0)}\right) \tag{8.67}$$

such that Equation 8.41 yields

$$u_b(x^*) + u_d(x^*) = C_u = 0 \tag{8.68}$$

For the case of removal of small metabolites, we have $\omega(x^*) \ll a_b h_{tb} + a_d h_{td}$. Hence,

$$\frac{d}{dx}\langle c\rangle^b = \left(\frac{a_b h_{tb} a_d h_{td}}{a_b h_{tb} + a_d h_{td} + \omega}\right)\frac{u_d(1)\langle c\rangle^b(1)}{u_b{}^2} \cong \frac{1}{Pe_m}\left(\frac{u_b(0)u_d(1)\langle c\rangle^b(1)}{L}\right)\frac{1}{u_b{}^2} \tag{8.69}$$

where

$$u_b(x^*) = \frac{u_b(0)\sinh\left(B(1-x^*)\right) - u_d(1)\sinh Bx^*}{\sinh B} \tag{8.70}$$

Equation 8.69 with (8.70) may readily be integrated for given solute concentration in the blood at the inlet $\langle c\rangle^b(0)$:

$$\frac{\langle c\rangle^b(x^*)}{\langle c\rangle^b(0)} = 1 + \frac{\dfrac{1}{Pe_m}\dfrac{u_d(1)}{u_b(0)}\dfrac{\sinh B}{B\left(e^{-B}+\dfrac{u_d(1)}{u_b(0)}\right)}\left(\dfrac{2\sinh B}{e^{B}+\dfrac{u_d(1)}{u_b(0)}-\left(e^{-B}+\dfrac{u_d(1)}{u_b(0)}\right)e^{2Bx^*}}-1\right)}{1-\dfrac{1}{Pe_m}\dfrac{u_d(1)}{u_b(0)}\dfrac{\sinh B}{B\left(e^{-B}+\dfrac{u_d(1)}{u_b(0)}\right)}\left(\dfrac{2\sinh B}{e^{B}+\dfrac{u_d(1)}{u_b(0)}-\left(e^{-B}+\dfrac{u_d(1)}{u_b(0)}\right)e^{2B}}-1\right)} \tag{8.71}$$

$$CL = Au_b(0)\left(1 + \frac{\left(u_d(1)/u_b(0)\right)}{1-\dfrac{1}{Pe_m}\dfrac{u_d(1)}{u_b(0)}\dfrac{\sinh B}{B\left(e^{-B}+\dfrac{u_d(1)}{u_b(0)}\right)}\left(\dfrac{2\sinh B}{e^{B}+\dfrac{u_d(1)}{u_b(0)}-\left(e^{-B}+\dfrac{u_d(1)}{u_b(0)}\right)e^{2B}}-1\right)}\right) \tag{8.72}$$

Figure 8.6 shows the axial variations of the velocity and solute concentration fields for the cases of $B = 0.21$ (i.e., $\beta = 0.52$), $-u_d(1)/u_b(0) = 0.5$, and $\alpha = 2.53$, with $Pe_m = 0.68$ and 1.69. As can be seen

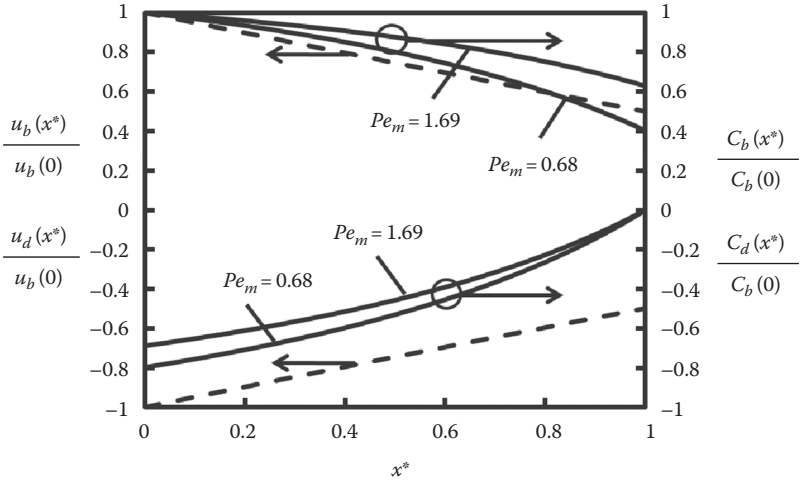

FIGURE 8.6 Velocity and solute variations along the axial coordinate for the case of symmetric flow rates.

from the figure, an increase in the modified Peclet number (i.e., dimensionless mass transfer resistance) retards reduction of the solute concentration in the blood at the exit.

8.6.6 Comparison of the Present Analytic Results and Available Experimental Data

For given dimensionless system parameters, namely, the lumen and shell permeability ratio α and the membrane permeability dimensionless parameter B, we only need to specify the inlet velocity ratio $-u_d(1)/u_b(0)$, the modified Peclet number Pe_m (i.e., dimensionless mass transfer resistance), and the dimensionless transmembrane pressure at the blood inlet β. However, in many practical cases, the total ultrafiltration rate $A\left(u_b(0)-u_b(1)\right)$ is provided instead of the transmembrane pressure. For such cases of given total ultrafiltration rate, we evaluate the transmembrane pressure at the blood inlet β using Equation 8.41 as follows:

$$\beta=\frac{B}{\sinh B}\left(\cosh B+\frac{u_d(1)}{u_b(0)}-\frac{\alpha+\cosh B}{1+\alpha}\left(1+\frac{u_d(1)}{u_b(0)}-\frac{\left(A\left(u_b(0)-u_b(1)\right)\right)}{Au_b(0)}\right)\right) \tag{8.73}$$

Jaffrin et al. (1990) carried out a series of experiments with a Hospal Filtral 12 AN69HF module using saline in substitution of the blood. Clearances for the two solutes, namely, creatinine (113 daltons) and vitamin B_{12} (1355 D), are predicted by the present model and are compared with their experimental data. Fortunately, detailed information is available for these two solutes. Geometric characteristics of the membrane module are provided by the manufacturer as follows:

$$L=20\text{ cm},\quad N=8500,\quad d_b=220\ \mu\text{m},\quad t_m=45\ \mu\text{m},\quad A=11.94\text{ cm}^2$$

while the hydraulic permeability of the membrane L_p and the overall mass transfer coefficient P_m are provided by Ding et al. (2004) as follows:

$$L_p=5.63\times10^{-11}\text{ m/s Pa},\quad P_m(\text{Creatinine})=4.172\times10^{-6}\text{ m/s},\quad P_m(\text{Vitamin B}_{12})=1.675\times10^{-6}\text{ m/s}$$

Thus, the modified Peclet number Pe_m is evaluated using the overall mass transfer coefficient P_m as

$$Pe_m=\left(\frac{1}{a_bh_{tb}}+\frac{1}{a_dh_{td}}\right)\frac{u_b(0)}{L}=\frac{u_b(0)}{a_bLP_m} \tag{8.74}$$

Figure 8.7 shows the pure diffusive clearances CL_0 as a function of the inlet blood flow rate $Au_b(0)$ when the dialysate inlet volume flow rate is $Au_d(1)=-500$ mL/min. The figure shows good agreement between the present analysis and the experiment reported by Jaffrin et al. (1990). For the case of $Au_b(0)=200$ mL/min and $Au_d(1)=-500$ mL/min, a series of clearances are calculated for given total ultrafiltration rate $A\left(u_b(0)-u_b(1)\right)$, by assigning the dimensionless transmembrane pressure β according to Equation 8.84. In Figure 8.8, the predicted $(CL-CL_0)/CL_0$ are plotted against the predicted ultrafiltration volume flow rate $A\left(u_b(0)-u_b(1)\right)$ with the experimental data obtained by Jaffrin et al. (1990). It is interesting to note that both analysis and experiment suggest that an almost linear relationship exists between $(CL-CL_0)/CL_0$ and $A\left(u_b(0)-u_b(1)\right)$.

The temporal variation of creatinine concentration in the same dialyzer is evaluated for the case of ultrafiltration volume flow rate $A\left(u_b(0)-u_b(1)\right)=60$ mL/min and the initial total blood volume $V_b=42000$ mL (N.B. $CL=164.8$ mL/min and $\gamma=0.364$) and is plotted in Figure 8.9 along with the

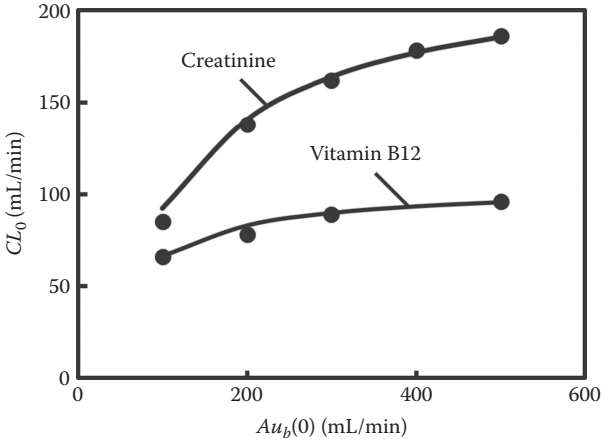

FIGURE 8.7 Effect of blood flow velocity on the pure diffusive clearance of solutes (●, experiment by Jaffrin et al. (1990); —, present model; $L = 20$ cm, $N = 8500$, $d_b = 220$ μm, $t_m = 45$ μm, $A = 11.94$ cm^2, $L_p = 5.63 \times 10^{-11}$ m/s Pa, P_m(creatinine) $= 4.172 \times 10^{-6}$ m/s, P_m(vitamin B_{12}) $= 1.675 \times 10^{-6}$ m/s).

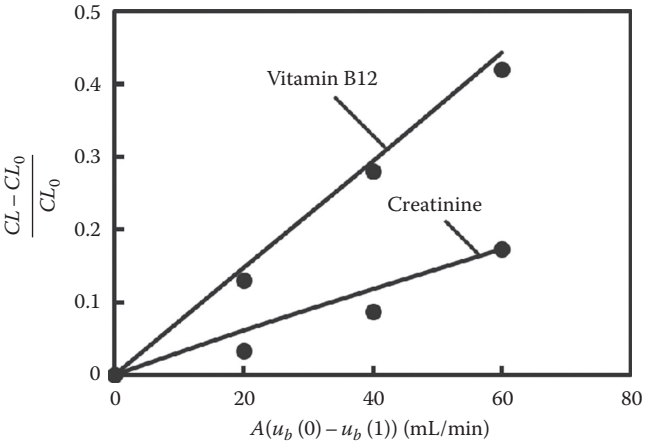

FIGURE 8.8 Effect of ultrafiltration flow rate on the clearance enhancement (●, experiment by Jaffrin et al. [26]; —, present model; $L = 20$ cm, $N = 8500$, $d_b = 220$ μm, $t_m = 45$ μm, $A = 11.94$ cm^2, $L_p = 5.63 \times 10^{-11}$ m/s Pa, P_m(creatinine) $= 4.172 \times 10^{-6}$ m/s, P_m(vitamin B_{12}) $= 1.675 \times 10^{-6}$ m/s, $Au_b(0) = 200$ mL/min, $Au_d(1) = -500$ mL/min).

conventional exponential decay curve. It can be seen from the figure that the solute concentrations decrease rapidly for an initial recirculation period (say $t^* = KT/V < 1$) and then diminish further gradually. The dynamic curve based on the present model reveals that the estimation based on the exponential decay curve may not be accurate especially for the case of removal of comparatively large metabolites.

Closed-form solutions were obtained for the two special cases, namely, pure diffusion clearance and symmetry flow rates. In order to verify the validity of the present three-concentration model, numerical integrations were carried out using the Runge–Kutta–Gill method, and the results were compared with available experimental data. Comparison between the analysis and experiment reveals that the present model is fully capable of describing complex transport process associated with countercurrent dialyzer systems.

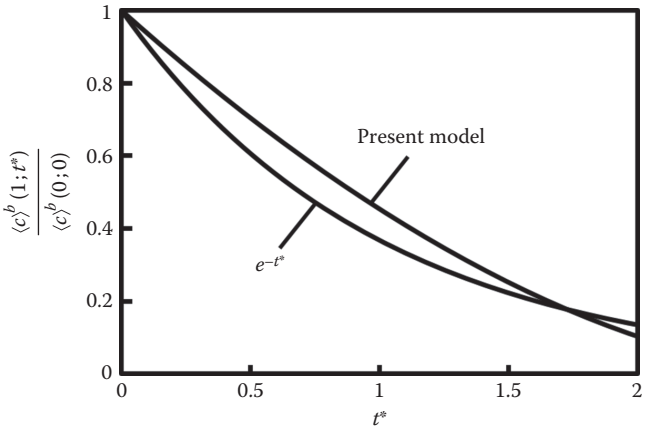

FIGURE 8.9 Temporal variation of the solute concentration (creatinine A ($u_b(0) - (u_b(1)) = 60$ mL/min, $V_b = 42000$ mL, $CL = 164.8$ mL/min, $\gamma = 0.364$).

8.7 APPLICATION OF THE THREE-CONCENTRATION MODEL FOR REVERSE OSMOSIS MODULE

The foregoing three-concentration model used for the dialyzer may readily be exploited for analyzing the performance of the reverse osmosis desalination modules after some modification (Nakayama and Sano 2012). A radial flow hollow fiber reverse osmosis module is illustrated in Figure 8.10, in which the fibers are packed in the module. The fibers may be in parallel to or wound around the feeder core tube, in which the feed stream enters. The fiber bores are sealed at one end and open at the other such that the permeate can flow out axially to be collected. The concentrated brine, on the other hand, flows out radially to be collected at the outer side of the fiber bundle, as indicated in the figure.

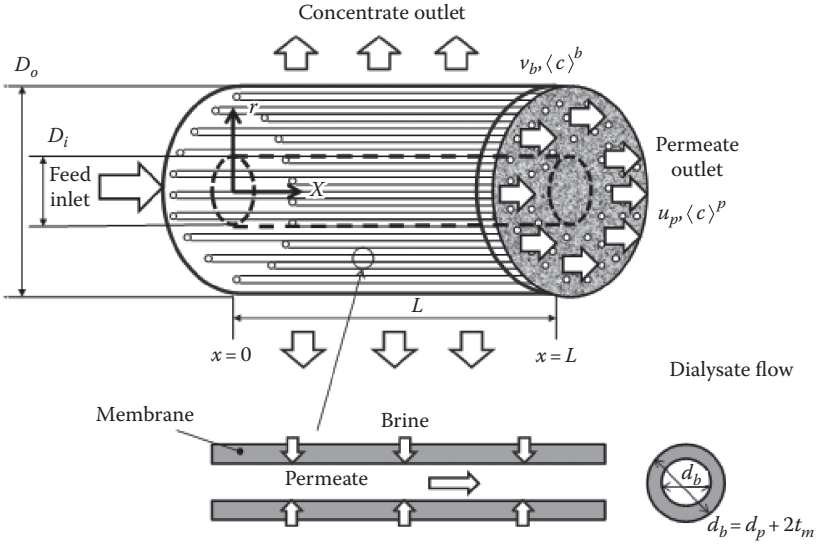

FIGURE 8.10 Radial flow hollow fiber reverse osmosis module.

8.7.1 Concentration Polarization and Three-Concentration Model

The concentration polarization takes place within the membrane, as illustrated in Figure 8.11, so that the solute concentration in the membrane surface at the shell side remains higher than those of brine (reject) and permeate streams. In all previous analyses, certain membrane mass transport models such as the Sekino solution–diffusion model and the Spiegler–Kedem model, are introduced to characterize the mass transfer through the membrane. Thus, some relationships between the salt concentration of the polarized membrane surface and those of the brine and permeate are prescribed in advance, with the help of the membrane parameters, such as hydrodynamic permeability, solute permeability, and reflection coefficient. In these membrane mass transport models including the Spiegler–Kedem model and the Kedem–Katchalsky model, the solute flux vector is 1D, aligning normal to the membrane outer and inner surfaces. Hence, they fail to describe the complex 3D mass and momentum transfer taking place within a bundle of hollow fibers.

The three-concentration model established for the hollow fiber membrane systems is of 3D and hence may easily be applied for the case of radial flow hollow fiber reverse osmosis module. In this model based on the VAT (Nakayama et al. 2006, Nakayama and Kuwahara 2008), all 3D mass and momentum conservation equations for three individual phases, namely, the shell-side fluid, lumen-side fluid, and membrane phases, are considered just as in the study of countercurrent dialyzer systems, presented in Equations 8.19 through 8.28. In what follows, we shall derive the desalination version of three-concentration membrane transport model and then investigate the concentration polarization phenomena associated with hollow fiber reverse osmosis desalination systems.

The volume-averaged governing Equations 8.19 through 8.28 obtained for the dialyzer may readily be translated for the case of the radial flow hollow fiber reverse osmosis module. The steady-state assumption is valid when the timescale for the temporal variation of the average feed pressure is sufficiently large as compared with the residence time of the fluid, that is, $\pi\left(D_0^2 - D_i^2\right)L/4Q_{feed}$, which is of the order 10–100 s for the present case. In most cases of radial flow hollow fiber reverse osmosis modules, this condition is satisfied, and the steady-state (or quasi-steady-state) assumption holds most of the time during operation. Thus, the unsteady terms in the volume-averaged equations are dropped, as in the case of the countercurrent dialyzer. The macroscopic governing equations for the steady case of reverse osmosis desalination phenomena,

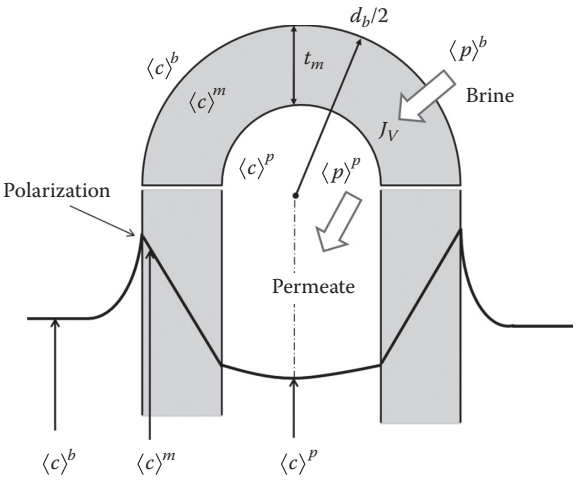

FIGURE 8.11 Concentration polarization in the membrane surface.

namely, the continuity, momentum, and concentration equations for the three individual phases, run as follows:

For the brine phase,

$$\frac{\partial \varepsilon_b \langle u_j \rangle^b}{\partial x_j} + \omega = 0 \tag{8.75}$$

$$\frac{\partial \langle p \rangle^b}{\partial x_i} = -\frac{\mu_b}{K_{b_{ij}}} \varepsilon_b \langle u_j \rangle^b - \varepsilon_b{}^2 \rho_b b_{bij} \sqrt{\langle u_k \rangle^b \langle u_k \rangle^b} \langle u_j \rangle^b \tag{8.76}$$

$$\frac{\partial \varepsilon_b \langle u_j \rangle^b \langle c \rangle^b}{\partial x_j} = -\omega \langle c \rangle^b - a_b h_b \left(\langle c \rangle^b - \langle c \rangle^m \right) \tag{8.77}$$

For the permeate phase,

$$\frac{\partial \varepsilon_p \langle u_j \rangle^p}{\partial x_j} - \omega = 0 \tag{8.78}$$

$$\frac{\partial \langle p \rangle^p}{\partial x_i} = -\frac{\mu_p}{K_{p_{ij}}} \varepsilon_p \langle u_j \rangle^p - \varepsilon_p{}^2 \rho_p b_{pij} \sqrt{\langle u_k \rangle^p \langle u_k \rangle^p} \langle u_j \rangle^p \tag{8.79}$$

$$\frac{\partial \varepsilon_p \langle u_j \rangle^p \langle c \rangle^p}{\partial x_j} = (1-\sigma) \omega \langle c \rangle^m - a_b h_m \left(\langle c \rangle^p - \langle c \rangle^m \right) \tag{8.80}$$

For the membrane phase,

$$\frac{\partial}{\partial x_j} \left(\varepsilon_m D_{m_{jk}} \frac{\partial \langle c \rangle^m}{\partial x_k} \right) + \omega \langle c \rangle^b + a_b h_b \left(\langle c \rangle^b - \langle c \rangle^m \right) - (1-\sigma) \omega \langle c \rangle^m + a_b h_m \left(\langle c \rangle^p - \langle c \rangle^{\boldsymbol{m}} \right) = 0 \tag{8.81}$$

where

$$\omega = a_b J_V = \frac{1}{V} \int_{A_{b_{\text{int}}}} u_j n_{b_j} dA = a_b L_p \left\{ \left(\langle p \rangle^b - \langle p \rangle^p \right) - \sigma \frac{iR \langle T \rangle^m}{M} \left(\langle c \rangle^m - \langle c \rangle^p \right) \right\} \tag{8.82}$$

Equations 8.75 through 8.77 describe the continuity, momentum, and salt mass balance equations for the brine phase (shell-side phase), while Equations 8.78 through 8.80 describe the continuity, momentum, and salt mass balance equations for the permeate phase (lumen-side phase), respectively. This 3D tonsorial set of the macroscopic governing equations along with the salt mass balance Equation 8.81 for the membrane phase will be used for full 3D numerical calculations.

As for the operating conditions, the feed pressure, flow rate, and salt concentration are given along with the pressure at the permeate outlet. The appropriate boundary conditions for the set of the foregoing partial differential equations may readily be generated from these feed values, as the geometrical configuration of the desalination module is provided.

The sub- and superscripts b, p, and m are assigned to the brine, permeate, and membrane phases, respectively, such that a_b and a_p are the specific surface area of the brine (shell) side area (i.e., the total outer wall surface area of the hollow fibers per unit volume) and that of the permeate (lumen) side area (i.e., the total inner wall surface area of the hollow fibers per unit volume). Moreover, ε_b, ε_p, and ($\varepsilon_m = 1-\varepsilon_b-\varepsilon_p$) are the volume fractions of the brine, permeate, and membrane phases, respectively. The surface integral, $\omega \equiv 1/V\int_{A_{b\text{int}}} u_j n_{b_j} dA$ as defined in Equation 8.82, is the total permeate volume flow rate per unit volume (i.e., the permeate stream production rate per unit volume), which is the product of the specific area of the membrane surface a_b and the total permeate volume flux J_V through the membrane. The membrane is characterized in terms of three parameters, namely, the hydraulic permeability L_p, the solute permeability h_m, and the reflection coefficient σ. Moreover, the osmotic pressure is given by $\left(iR\langle T\rangle^m/M\right)\left(\langle c\rangle^m - \langle c\rangle^p\right)$, where i (= 2), R (= 8341 J/kg kmol K), M (= 58.8), and $\langle T\rangle^m$ are the number of ions for ionized solutes (i.e., the vant Hoff factor), ideal gas constant, molecular weight of solute, and feed brine temperature, respectively. As closing the equations to obtain Equations 8.75 through 8.77, the surface integral terms over the membrane wall surface are modeled as follows:

$$\frac{1}{V_b}\int_{A_{b\text{int}}}\left(\mu_b\frac{\partial u_i}{\partial x_j} - p\delta_{ij}\right)n_{bj}dA - \frac{\partial}{\partial x_j}\left(\rho\langle\tilde{u}_i\tilde{u}_j\rangle^b\right) = -\frac{\mu}{K_{b_{ij}}}\varepsilon_b\langle u_j\rangle^b - \varepsilon_b{}^2\rho_b b_{bij}\sqrt{\langle u_k\rangle^b\langle u_k\rangle^b}\langle u_j\rangle \tag{8.83}$$

$$\frac{1}{V}\int_{A_{b\text{int}}} cu_j n_{bj}dA = \omega\langle c\rangle^b \tag{8.84}$$

$$\frac{1}{V}\int_{A_{b\text{int}}} D_b\frac{\partial c}{\partial x_j}n_{bj}dA = a_b h_b\left(\langle c\rangle^b - \langle c\rangle^m\right) \tag{8.85}$$

For this case of desalination module, n_{bi} is the unit vector pointing outward from the brine side to membrane side, while $A_{b\text{int}}$ is the interfacial area between the brine and membrane phases. A similar modeling procedure can be taken for the surface integral terms for the permeate phase to obtain Equations 8.78 through 8.80.

Only the difference between the present set of the governing equations and that introduced for the dialyzer is the introduction of the reflection coefficient σ, which represents the rejection capability of a membrane (i.e., $\sigma = 0$ for no rejection and $\sigma = 1$ for perfect rejection). As one sets $\sigma = 0$, the set of the equations naturally reduces to that originally proposed for the analysis of dialyzer systems.

8.7.2 Salt Concentration Fields

In what follows, an approximate analytical treatment is presented prior to the 3D numerical calculations. The set of the foregoing equations based on the three-concentration model may be simplified further to investigate the concentration polarization phenomena associated with radial hollow fiber reverse osmosis modules. We note that the macroscopic diffusion within the membrane is negligibly small as compared with the interfacial mass transfer terms since the hollow fibers are not consolidated. (Note that the ratio of the interfacial mass transfer to the mass diffusion in the membrane

phase corresponds with the Sherwood number $h_m L/D_m$, which is usually much greater than 1.) Thus, the differential Equation 8.81 reduces to an algebraic equation:

$$\omega\langle c\rangle^b + a_b h_b\left(\langle c\rangle^b - \langle c\rangle^m\right) - (1-\sigma)\omega\langle c\rangle^m + a_b h_m\left(\langle c\rangle^p - \langle c\rangle^m\right) = 0 \tag{8.86a}$$

The first two terms on the left-hand side of the equation correspond with the salt coming from the brine side through the brine/membrane interface, while the last two terms correspond with the salt coming from the permeate side through the permeate/membrane interface. Note that the last two terms are negative, since the salt permeates through the membrane interface from the membrane side to the permeate side. Equation 8.86a may be solved for $\langle c\rangle^m$ as

$$\langle c\rangle^m = \frac{(a_b h_b + \omega)\langle c\rangle^b + a_b h_m \langle c\rangle^p}{a_b h_b + a_b h_m + (1-\sigma)\omega} \tag{8.86b}$$

The mass transfer coefficient h_b between the brine and membrane (i.e., shell side) may be estimated according to Sekino (1995):

$$\frac{h_b d_b}{D_b} = 0.048\left(\frac{\rho_b \varepsilon_b \left|\langle \vec{u}\rangle^b\right| d_b}{\mu_b}\right)^{0.6}\left(\frac{\mu_b}{\rho_b D_b}\right)^{1/3} \tag{8.87}$$

The total mass transfer resistance between the membrane and permeate, on the other hand, is approximated by $1/a_b h_m$ as in Equation 8.80, since the mass transfer coefficient between the permeate and membrane (i.e., lumen side) is much higher than the solute permeability of the membrane h_m:

$$\frac{1}{a_b h_m} + \frac{1}{a_p h_p} \cong \frac{1}{a_b h_m} \tag{8.88}$$

In the radial flow hollow fiber reverse osmosis module, the volume-averaged permeate flow velocities are aligned axially, while the volume-averaged brine flow velocities are radially directed outward from the core tube. Thus, one may assume these velocity vectors' components (u, v) as

$$\varepsilon_b \langle u_i\rangle^b = (0, v_b) \tag{8.89a}$$

and

$$\varepsilon_p \langle u_i\rangle^p = (u_p, 0) \tag{8.89b}$$

where v_b and u_p are the apparent radial flow velocity of the brine and the apparent axial flow velocity of the permeate, respectively. Thus, the macroscopic governing Equations 8.75 through 8.80 reduce to For the brine phase,

$$\frac{1}{r}\frac{\partial r v_b}{\partial r} = -\omega \tag{8.90}$$

$$\frac{\partial \langle p \rangle^b}{\partial r} = -\frac{150(1-\varepsilon_b)^2}{\varepsilon_b^3 d_b^2}\mu_b v_b - 1.75\frac{1-\varepsilon_b}{\varepsilon_b^3 d_b}\rho_b v_b^2 \tag{8.91}$$

$$\frac{1}{r}\frac{\partial r v_b \langle c \rangle^b}{\partial r} = -\omega \langle c \rangle^b - h_{bv}\left(\langle c \rangle^b - \langle c \rangle^m\right) \tag{8.92}$$

For the permeate phase,

$$\frac{\partial u_p}{\partial x} = \omega \tag{8.93}$$

$$\frac{\partial \langle p \rangle^p}{\partial x_i} = -\frac{32\mu_p}{\varepsilon_p d_p{}^2} u_p \tag{8.94}$$

$$\frac{\partial u_p \langle c \rangle^p}{\partial x} = (1-\sigma)\omega \langle c \rangle^m - h_{mv}\left(\langle c \rangle^p - \langle c \rangle^m\right) \tag{8.95}$$

where $h_{bv} = a_b h_b$ and $h_{mv} = a_b h_m$ are the volumetric mass transfer coefficients. The Hagen–Poiseuille permeate flow is assumed to prevail in the hollow fibers, while the radial brine flow through fibers is approximated by the flow through a porous medium, introducing the Ergun equation.

Noting $u_p(0, r) = 0$ at the closed end, Equation 8.93 may be integrated as

$$u_p(x, r) = \int_0^x \omega dx = \bar{\omega} x \tag{8.96a}$$

such that

$$\bar{u}_p(r) = \frac{1}{2}\bar{\omega} L \tag{8.96b}$$

where

$$\bar{\varphi}(r) = \frac{1}{L}\int_0^L \varphi dx \tag{8.97}$$

is in general the value averaged over the module length L such that

$$\bar{\omega}(r) = a_b L_p \left\{\left(\overline{\langle p \rangle^b} - \overline{\langle p \rangle^p}\right) - \sigma\frac{iR\langle T \rangle^m}{M}\left(\overline{\langle c \rangle^m} - \overline{\langle c \rangle^p}\right)\right\} \tag{8.98}$$

Noting $\langle p \rangle^p(L, r) = p_{atm}$ (i.e., atmospheric pressure) at the permeate outlet, Equation 8.94 with (8.96a) yields

$$\langle p \rangle^p(x, r) = p_{atm} + \frac{32\mu_p}{2\varepsilon_p d_p{}^2}\bar{\omega}\left(L^2 - x^2\right) \tag{8.99a}$$

such that

$$\overline{\langle p\rangle^{p}}(r) = p_{atm} + \frac{32\mu_{p}}{3\varepsilon_{p}{d_{p}}^{2}}\bar{\omega}L^{2} \tag{8.99b}$$

Then, one may integrate Equation 8.95, noting (8.96a) and $u_p(0, r) = 0$, and find

$$\langle c\rangle^{p}(x,r) = \overline{\langle c\rangle^{p}}(r) = \frac{(1-\sigma)\bar{\omega}\overline{\langle c\rangle^{m}} - h_{mv}\left(\overline{\langle c\rangle^{p}} - \overline{\langle c\rangle^{m}}\right)}{\bar{\omega}} \tag{8.100a}$$

or

$$\overline{\langle c\rangle^{p}}(r) = \frac{(1-\sigma)\bar{\omega} + h_{mv}}{\bar{\omega} + h_{mv}}\overline{\langle c\rangle^{m}} \tag{8.100b}$$

Thus, using this and Equation 8.86b, one may express the concentration of the permeate $\overline{\langle c\rangle^{p}}$ and that of the polarized membrane $\overline{\langle c\rangle^{m}}$ in terms of the concentration of the brine $\overline{\langle c\rangle^{b}}$ alone as

$$\overline{\langle c\rangle^{p}} = \frac{\left((1-\sigma)\bar{\omega} + h_{mv}\right)\left(\bar{\omega} + h_{bv}\right)}{\left(\bar{\omega} + h_{mv}\right)\left(\bar{\omega} + h_{bv}\right) - \sigma\bar{\omega}^{2}}\overline{\langle c\rangle^{b}} \tag{8.101}$$

and

$$\overline{\langle c\rangle^{m}} = \frac{\left(\bar{\omega} + h_{mv}\right)\left(\bar{\omega} + h_{bv}\right)}{\left(\bar{\omega} + h_{mv}\right)\left(\bar{\omega} + h_{bv}\right) - \sigma\bar{\omega}^{2}}\overline{\langle c\rangle^{b}} \tag{8.102}$$

Equations 8.100b and 8.101 readily give the intrinsic salt rejection $R_{in} = \left(\overline{\langle c\rangle^{m}} - \overline{\langle c\rangle^{p}}\right)\Big/\overline{\langle c\rangle^{m}}$ and the solute concentration ratio $\overline{\langle c\rangle^{p}}/\overline{\langle c\rangle^{b}}$ as

$$R_{in} = \frac{\sigma}{1 + \left(1/\left(J_V/h_m\right)\right)} \tag{8.103a}$$

and

$$\frac{\overline{\langle c\rangle^{p}}}{\overline{\langle c\rangle^{b}}} = 1 - \frac{\dfrac{\sigma}{\left(J_V/h_b\right)}}{\left(1 + \dfrac{1}{\left(J_V/h_b\right)}\right)\left(1 + \dfrac{1}{\left(J_V/h_m\right)}\right) - \sigma} \tag{8.103b}$$

where the relations $\bar{\omega}/h_{bv} = J_V/h_b$ and $\bar{\omega}/h_{mv} \cong J_V/h_m$ are used. In Figures 8.12 and 8.13, these results for the intrinsic rejection and solute concentration ratio (with $J_V/h_b = 0.1$) are compared against those of the Spiegler–Kedem model (1966), which run as

$$R_{in} = \frac{\sigma\left(1 - \exp\left(-(1-\sigma)\left(J_V/h_m\right)\right)\right)}{1 - \sigma\exp\left(-(1-\sigma)\left(J_V/h_m\right)\right)} \tag{8.104a}$$

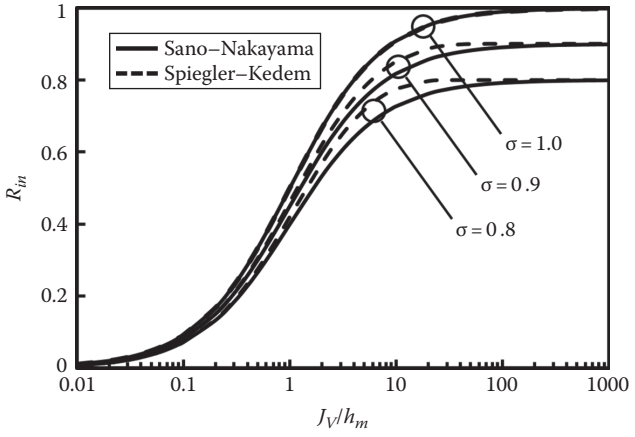

FIGURE 8.12 Intrinsic salt rejection.

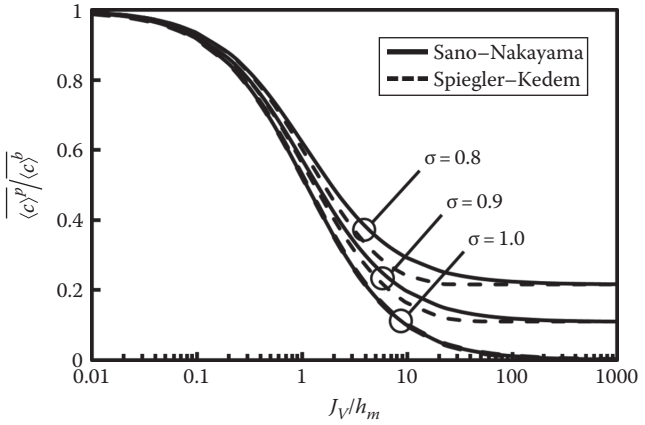

FIGURE 8.13 Observed salt rejection.

and

$$\frac{\langle c\rangle^p}{\langle c\rangle^b} = \frac{(1-\sigma)\exp(J_V/h_b)}{(1-\sigma)\exp(J_V/h_b) + \sigma\left(1-\exp\left(-(1-\sigma)(J_V/h_m)\right)\right)} \tag{8.104b}$$

The present expressions (8.103a,b) based on the three-concentration model appear to be much simpler than those of the Spiegler–Kedem model (8.104a,b), which involves exponential functions. The two models, despite the difference in their appearances, agree fairly well with each other. It is interesting to note that the membrane transport characteristics are automatically described in the present set of the governing equations. Thus, no additional membrane transport models are needed in the present approach.

Having simplified the governing equations as given by Equations 8.101 and 8.102, Equations 8.90 through 8.92 for the brine are integrated from $x = 0$ to $x = L$. Then, the foregoing Equations 8.96b, 8.99b, 8.101, and 8.102 are substituted into these integrated equations and (8.98), to obtain the following set of the equations written solely in terms of the brine phase quantities:

$$\frac{d\overline{v_b}}{dr} = -\frac{\overline{v_b}}{r} - \overline{\omega} \tag{8.105}$$

$$\frac{d\overline{\langle p\rangle^b}}{dr} = -\frac{150\left(1-\varepsilon_b\right)^2}{\varepsilon_b^{\,3} d_b^{\,2}}\mu_b \overline{v_b} - 1.75\frac{1-\varepsilon_b}{\varepsilon_b^{\,3} d_b}\rho_b \overline{v_b}^{\,2} \tag{8.106}$$

$$\frac{d\overline{\langle c\rangle^b}}{dr} = \frac{\sigma\bar{\omega}^2 h_{bv}}{\left(\bar{\omega}+h_{mv}\right)\left(\bar{\omega}+h_{bv}\right)-\sigma\bar{\omega}^2}\frac{\overline{\langle c\rangle^b}}{\overline{v_b}} \tag{8.107}$$

where

$$\bar{\omega} = a_b L_p\left\{\left(\overline{\langle p\rangle^b} - p_{atm} - \frac{32\mu_p}{3\varepsilon_p d_p^{\,2}}\bar{\omega}L^{*2}\right) - \frac{iR\langle T\rangle^m}{M}\frac{\sigma^2\bar{\omega}\left(\bar{\omega}+h_{bv}\right)}{\left(\bar{\omega}+h_{mv}\right)\left(\bar{\omega}+h_{bv}\right)-\sigma\bar{\omega}^2}\overline{\langle c\rangle^b}\right\} \tag{8.108}$$

$L^*(r) = \sqrt{L^2 + (2W\pi r)^2}$ is the effective length of the hollow fibers, which may be wound W times at the radius r. The first-order ordinary differential Equations 8.105 through 8.107 with the algebraic Equation 8.108 may readily be integrated to find $\overline{v_b}(r)$, $\overline{\langle p\rangle^b}(r)$, and $\overline{\langle c\rangle^b}(r)$, using any standard integration scheme such as the Runge–Kutta–Gill method (see, e.g., Nakayama 1995). The algebraic Equation 8.108 may be rearranged to form a cubic equation for $\bar{\omega}$, which may readily be shot for a positive root. The boundary conditions at $r = D_i/2$ for the three first-order differential equations are given by

$$\overline{v_b}\Big|_{r=D_i/2} = \frac{Q_{feed}}{\pi D_i L}, \quad \overline{\langle p\rangle^b}\Big|_{r=D_i/2} = p_{feed}, \quad \overline{\langle c\rangle^b}\Big|_{r=D_i/2} = c_{feed} \tag{8.109a–c}$$

One may integrate these equations to the end at $r = D_o/2$, to find the permeate production rate Q_p as

$$Q_p = Q_{feed} - \pi D_o L\,\overline{v_b}\Big|_{r=D_o/2} \tag{8.110}$$

Subsequently, the bulk mean salt concentration of the permeate stream flowing out of the module, c_p, may be estimated from

$$c_p = \frac{Q_{feed}c_{feed} - \pi D_o L\,\overline{v_b}\Big|_{r=D_o/2}\overline{\langle c\rangle^b}\Big|_{r=D_o/2}}{Q_p} \tag{8.111}$$

8.7.3 Comparison of the Present Analytic Results and Available Experimental Data

Chatterjee et al. (2004) and Sekino (1993) numerically investigated reverse osmosis separation processes in the Toyobo Hollosep modules, solving the set of the friction–concentration–polarization model equations written in the axisymmetric coordinates by finite difference methods. Sekino (1993) used the two-parameter solution–diffusion membrane model, whereas Chatterjee et al. (2004) introduced the three-parameter Spiegler–Kedem membrane model. The specifications of Toyobo Hollosep module and its operating conditions are listed in Table 8.1.

The present analysis based on Equations 8.105 through 8.108 enables one to estimate the permeate salinity, permeate flow rate, and recovery factor, without resorting to exhaustive finite difference calculations. In Figure 8.14, such estimates on the permeate flow rate Q_p and the ratio of the

TABLE 8.1
Specifications of the Toyobo Hollosep Module and Its Operating Conditions

d_b	163×10^{-6} m
d_p	70×10^{-6} m
L_p	2.73×10^{-13} m/s Pa
h_m	8.12×10^{-10} m/s
ε_b	0.45
$\varepsilon_p = \varepsilon_b(d_p/d_b)^2$	0.083
D_i	0.04 m
D_o	0.19 m
L	0.99 m
S	361 m^2
$a_b \cong a_p = 4S/\pi(D_o^2 - D_i^2)L$	1.35×10^4/m
W	2
σ	0.9–1.0
Q_{feed}	$2–25 \times 10^{-4}$ m^3/s
c_{feed}	30–45 kg/m^3 (35 kg/m^3)
p_{feed}	5.0–6.5 MPa (5.5 MPa)
p_{atm}	0.1 MPa
$\langle T \rangle^m$	298 K
ρ_b	1060 kg/m3
μ_b	1.09×10^{-3} Pa s
μ_p	0.90×10^{-3} Pa s
D_b	5.0×10^{-9} m^2/s
R	8341 J/kg kmol K
M	58.8
i	2

$$h_b = \frac{0.048 D_b}{d_b}\left(\frac{\rho_b v_b d_b}{\mu_b \nu_b}\right)^{0.6}\left(\frac{\mu_b}{\rho_b D_b}\right)^{1/3}, L^*(r) = \sqrt{L^2 + (2W\pi r)^2}$$

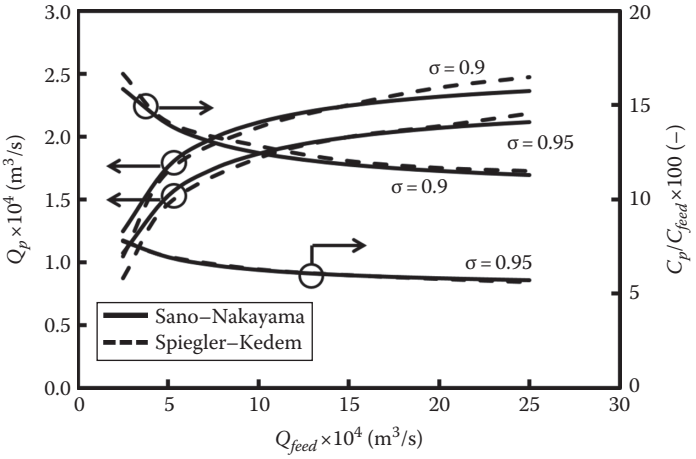

FIGURE 8.14 Variations of permeate variables with feed brine flow rate.

concentrations of the produced permeate to the feed brine c_p/c_{feed} are presented against the feed brine flow rate Q_{feed} for the case of the Toyobo Hollosep module, $c_{feed} = 3.5$ kg/m^3 and $p_{feed} = 5.5$ MPa, with the other specifications as listed in Table 8.1. The reflection coefficient σ is set to 0.9 and 0.95 to show the effects of rejection capability of a membrane on Q_p and c_p/c_{feed}. The present results agree well with the finite difference calculation results obtained by Chatterjee et al. (2004) with the Spiegler–Kedem model (1966).

The radial developments of the variables $\overline{v_b}(r)$, $\overline{\langle p \rangle^b}(r)$, $\overline{\langle c \rangle^b}(r)$, and $\overline{\omega}(r)$ for the case of $\sigma = 0.9$, $Q_{feed} = 15 \times 10^{-4}$ m^3/s, $c_{feed} = 35$ kg/m^3, and $p_{feed} = 5.5$ MPa are presented in Figure 8.15a and b. The radial velocity of the brine decreases from 0.0121 to 0.002 m/s as the pressure drops by 0.075 atmospheric pressure toward the outlet. The permeate volume flow rate per unit volume ω (i.e., the permeate production rate per unit volume) decreases only slightly from 0.0097/m to 0.0072/m, while the rejected salt concentration of the brine increases from 35.0 to 40.4 kg/m^3, indicating both effective salt rejection and uniform production of the permeate within the whole module.

Sekino (1993) reported various sets of experimental data obtained using the aforementioned Toyobo Hollosep module. He investigated the individual effects of c_{feed}, p_{feed} and the recovery factor $Rc \equiv Q_p/Q_{feed}$ on Q_p and c_p/c_{feed}. The present analytic results with $\sigma = 1$ are compared against his experimental data in Figure 8.16a through c, which show reasonable agreement with the experimental data. The results for fixed Rc were obtained iteratively to find the boundary value Q_{feed} that yields

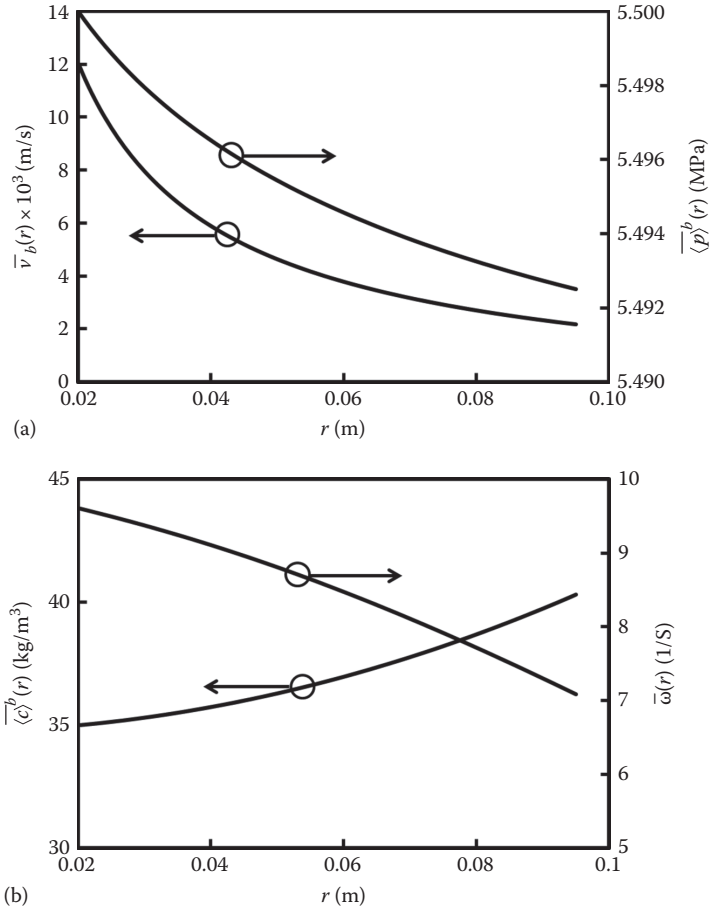

FIGURE 8.15 Radial variations of brine variables ($\sigma = 0.9$, $Q_{feed} = 15 \times 10^{-4}$ m^3/s, $c_{feed} = 35$ kg/m^3, $p_{feed} = 5.5$ MPa). (a) Velocity and pressure. (b) Concentration and permeate production rate per unit volume.

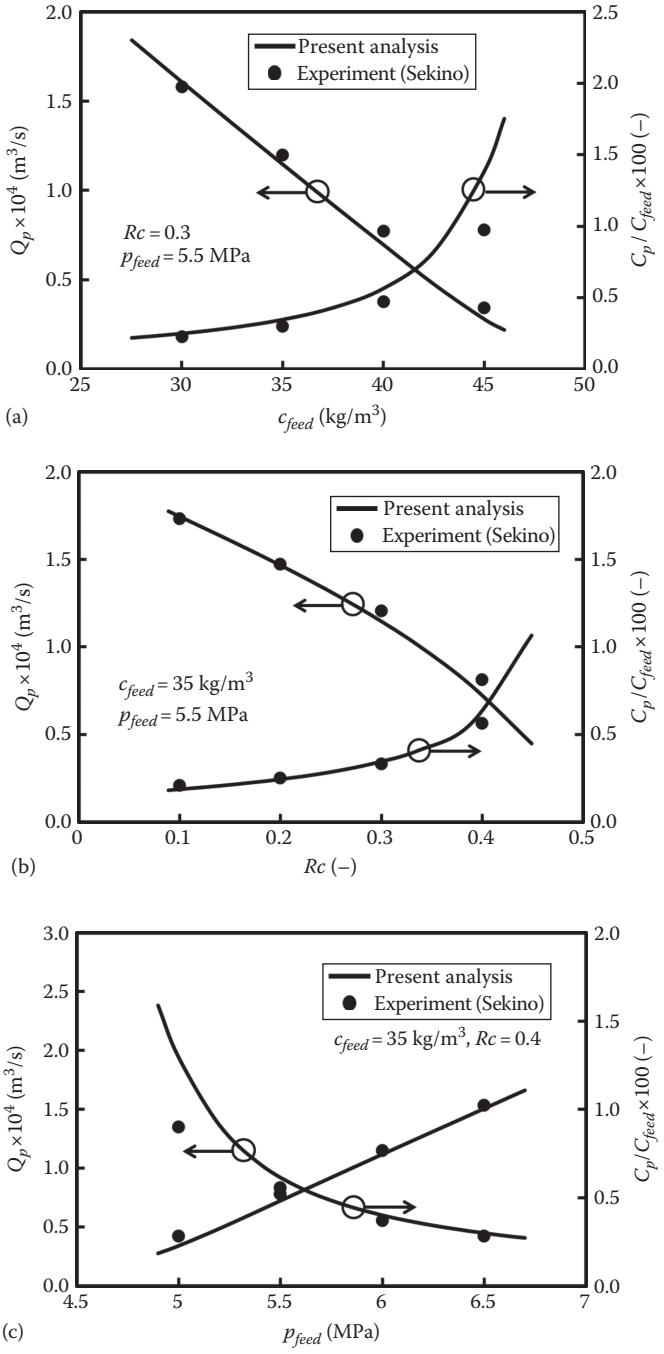

FIGURE 8.16 Comparison between the present analysis and the Sekino experimental data. (a) Effects of c_{feed} on Q_p and c_p/c_{feed}. (b) Effects of Rc on Q_p and c_p/c_{feed}. (c) Effects of p_{feed} on Q_p and c_p/c_{feed}.

$Q_p = RcQ_{feed}$. Thus, one can readily and accurately estimate all transport characteristics associated with radial flow hollow fiber reverse osmosis modules, simply by solving Equations 8.105 through 8.108 for given specifications.

It has been shown that the three-concentration model originally introduced for the analysis of countercurrent hemodialyzer system (Sano and Nakayama 2012) is able to describe transport

processes through membranes with concentration polarization, as observed in hollow fiber reverse osmosis desalination systems (Nakayama and Sano 2013). The volume-averaged governing equations based on the three-concentration model were integrated to form three distinctive first-order ordinary equations in terms of the average velocity, pressure, and salt concentration of the brine phase. The equations along with an algebraic equation for the permeate volume flow rate per unit volume were solved to find permeate salinity, permeate flow rate, and pressure drops in a hollow fiber reverse osmosis module. The analytic results based on the three-concentration model are found to agree well with the finite difference calculation results of Chatterjee et al. as well as the experimental data of Sekino. As will be shown shortly, the present three-concentration model in a 3D form can easily be implemented in a numerical solution code and can be used to design efficient hollow fiber membrane systems.

8.8 3D NUMERICAL MODELS FOR MEMBRANE SYSTEMS

Comparison of the analytic results against available experimental data revealed the validity of the present three-concentration model based on the VAT. Subsequently, the set of the macroscopic governing equations, namely, the continuity, momentum, and concentration equations, for the two fluid phase compartments and the concentration equation for the membrane along with the membrane velocity and hydraulic–osmotic pressure difference can be discretized and then can be solved numerically for given initial and boundary conditions.

A standard finite difference code based on SIMPLE algorithm (Patankar 1980) may be used to discretize the volume-averaged governing equations, as given by Equations 8.19 through 8.28 for the dialyzer (or by Equations 8.75 through 8.81 for the desalination module), so as to accomplish such numerical investigations. Since the continuity Equations 8.19 and 8.24 contain ω, it would not be straightforward to formulate the pressure correction equation (i.e., discretized continuity equation). This problem can readily be overcome, as we introduce the following combined velocity vector:

$$\left\langle u_i \right\rangle \equiv \varepsilon_b \left\langle u_i \right\rangle^b + \varepsilon_d \left\langle u_i \right\rangle^d \tag{8.112}$$

such that

$$\frac{\partial \left\langle u_j \right\rangle}{\partial x_j} = 0 \tag{8.113}$$

As we express the governing equations for the dialysate, Equations 8.24 through 8.26, in terms of this combined velocity vector $\langle u_i \rangle$, a usual discretization procedure can be used to formulate the pressure correction equations from the discretized continuity equation and momentum equation.

A 3D numerical model for a dialyzer is shown in Figure 8.17, in which the dialysate enters from the tube connected vertically near the right end of the container and leaves from the tube connected vertically near its left end.

In Figure 8.18, a 3D velocity field in the dialysate phase is illustrated in terms of local velocity vectors. The dialysate fluid particles pass deep through the bundles of hollow fibers and change the direction to flow horizontally, before making sharp turn to exit from the container. In Figure 8.19, the waste (creatinine) concentration fields of dialysate and blood phases on the vertical symmetrical plane are illustrated in terms of the dimensionless concentration normalized by the value at the blood phase inlet. The creatinine concentration in the blood phase decreases as it flows from left to right, while the dialysate carries the waste in the blood phase as it flows from right to left. The figures indicate that the waste concentration of blood going out from the right end is quite nonuniform. The blood in lower layers away from the entrance of the dialysate is less purified than that in upper layers close to it.

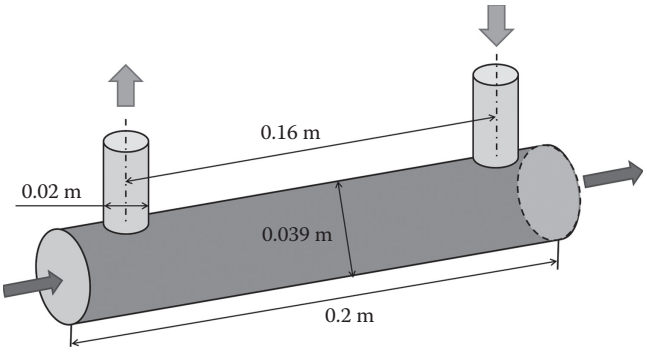

FIGURE 8.17 Numerical model for a dialyzer.

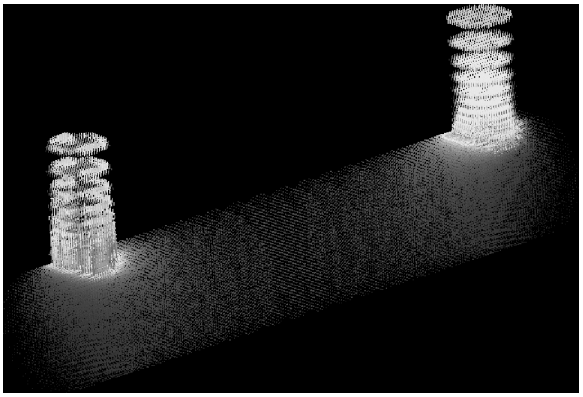

FIGURE 8.18 Velocity field in the dialysate phase.

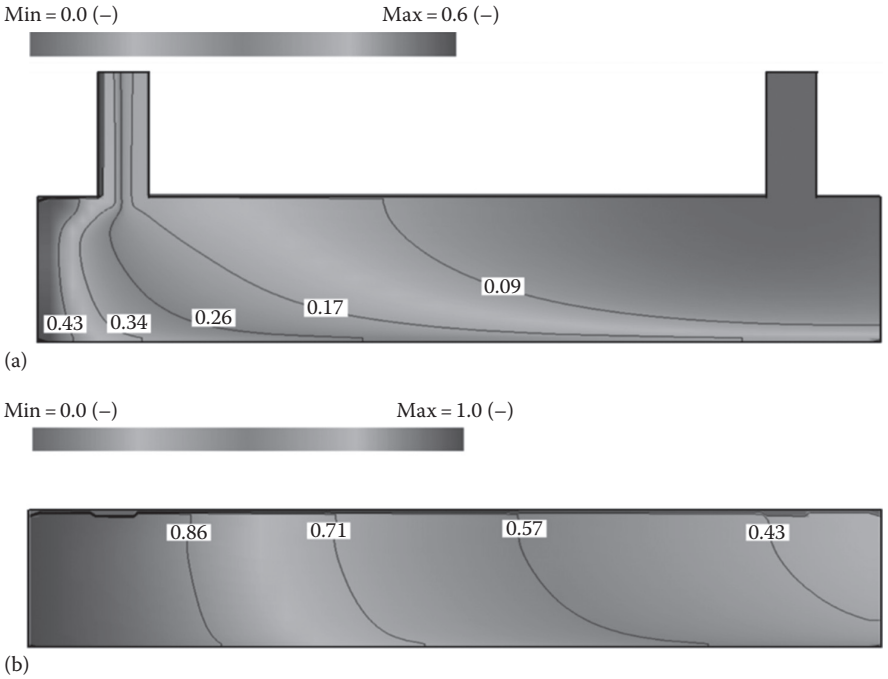

FIGURE 8.19 Concentration fields in (a) dialysate and (b) blood phases.

The sample results obtained from the present numerical model indicate that such numerical simulations based on the three-concentration model can be used for possible optimization of various hollow fiber membrane systems. Such a numerical investigation is underway.

8.9 CONCLUDING REMARKS

A three-concentration model based on the VAT has been proposed to investigate membrane transport processes associated with hollow fiber dialyzers and radial flow hollow fiber reverse osmosis module. The dialysate flows over the shell side, while the blood flows over the lumen side (i.e., inside the hollow fiber) for the case of the hollow fiber dialyzers. For the case of the radial flow hollow fiber reverse osmosis module, on the other hand, the brine flows over the shell side radially outward, while the permeate flows over the lumen side. A general set of macroscopic governing equations valid for all these hollow fiber systems has been derived for the three individual phases, namely, the lumen-side flow phase, shell-side flow phase, and membrane phase. Available experimental data are found to agree well with the present analytical estimates generated from the three-concentration model. Furthermore, 3D numerical models based on the SIMPLE algorithm are proposed for possible optimization of hollow fiber systems, such as dialyzers and desalination modules. The full set of the volume-averaged governing equations derived in a tensor form are numerically solved to reveal the details of the velocity and concentration fields of individual phases. The numerical models may be used for optimization of various hollow fiber membrane systems.

ACKNOWLEDGMENT

This study was supported by JSPS Grant-in-Aid for Scientific Research (B) 22360088.

NOMENCLATURE

A	Cross-sectional area of the dialyzer case (m^2)
A_{int}	Interface between the fluid and membrane phases (m^2)
$a_{b,d}$, $a_{b,p}$	Specific surface area (1/m)
B	Dimensionless parameter associated with membrane permeability (–)
$b_{b,p}$	Forchheimer coefficient (1/m)
c	Solute concentration (kg/m^3)
c_p	Bulk mean salt concentration of the permeate flowing out of the module
C_u	Integration constant (m/s)
CL	Clearance (m^3/s)
CL_0	Pure diffusive clearance (m^3/s)
D_b	Diffusivity of the brine (m^2/s)
$D_{b,d,m}$	Solute diffusion coefficient (m^2/s)
$D_{bdis_{jk}}$	Dispersion tensor of the blood flow (m^2/s)
$D_{ddis_{jk}}$	dispersion tensor of the dialysate flow (m^2/s)
$D_{i,o}$	Inner and outer diameters of the fiber bundle (m)
$d_{b,d}$, $d_{b,p}$	Inner and outer diameters of the hollow fiber (m)
d_p	Diameter of cylindrical pore of the membrane(m)
$f(x^*)$	Dimensionless function (–)
h	Mass transfer coefficient (m/s)
h_b	Mass transfer coefficient of the brine (shell side) (m/s)
h_m	Solute permeability of the membrane (m/s)
h_t	Effective mass transfer coefficient (m/s)
i	vant Hoff factor
J_V	Ultrafiltration velocity or permeate volume flux through the membrane (m/s)

$K_{b,d,m}$, $K_{b,p}$	Permeability (m^2)
L	Effective length of the dialyzer case or effective length of the desalination module (m)
L_p	hydraulic permeability of the membrane (m/s Pa)
M	Molecular weight of the solute (–)
n_i	Unit vector pointing outward from the fluid side to the membrane side (–)
P_m	Effective membrane diffusivity permeability (overall mass transfer coefficient) (m/s)
Pe	$Pe = J_V/P_m$: Peclet number (–)
Pe_m	$Pe_m = u_b(0)/a_b LP_m$: modified Peclet number (–)
p	Pressure (Pa)
Q_{feed}	Feed brine flow rate (m^3/s)
Q_p	Permeate flow rate (m^3/s)
r	Radial coordinate (m)
R	Universal gas constant (J/kg kmol K)
R_{in}	Intrinsic rejection (–)
Rc	Recovery
t	Time (s)
t_m	Membrane thickness (m)
$\langle T \rangle^m$	Temperature of the feed brine (K)
u_b	Darcian velocity of the blood (m/s)
u_d	Darcian velocity of the dialysate (m/s)
u_p	Darcian velocity of the permeate (m/s)
u_i	Velocity vector (m/s)
V	Representative elementary volume (m^3)
V_b	Initial total volume of blood (m^3)
W	Number of wound of hollow fibers (–)
x	axial coordinate (m)
x^*	$x^* = x/L$: dimensionless axial coordinate (–)

Greek Symbols

α	Permeability ratio (–)
β	Dimensionless transmembrane pressure at the blood inlet (–)
γ	$\gamma = A\left(u_b\left(0\right) - u_b\left(1\right)\right)/CL$: dimensionless parameter (–)
$\varepsilon_{b,d,m}$, $\varepsilon_{b,p,m}$	Volume fraction (–)
ε_p	Porosity of the membrane (–)
μ	Viscosity (Pa s)
Π	Osmotic pressure (Pa)
ρ	Density (kg/m^3)
σ	Reflection coefficient (–)
ω	Permeate volume flow rate per unit volume (1/s)

Special Symbols

$\tilde{\phi}$	Deviation from intrinsic average
$\langle \phi \rangle$	Darcian average
$\langle \phi \rangle^{b,d,m}$, $\langle \phi \rangle^{b,p,m}$	Intrinsic average

Subscripts and Superscripts

b	Blood or brine
d	Dialysate

dis	Dispersion
f	Fluid
feed	Feed brine
m	Membrane
p	Permeate

REFERENCES

Al-Bastaki, N. M. and Abbas, A., 1999, Modeling an industrial reverse osmosis unit, *Desalination*, 126: 33–39.

Al-Bastaki, N. M. and Abbas, A., 2000, Predicting the performance of RO membranes, *Desalination*, 132: 181–187.

Chatterjee, A., Ahluwalia, A., Senthilmurugan S., and Gupta, S. K., 2004, Modeling of a radial flow hollow fiber module and estimation of model parameters using numerical techniques, *Journal of Membrane Science*, 236: 1–16.

Cheng, P., 1978, Heat transfer in geothermal systems, *Advances in Heat Transfer*, 14: 1–105 (Academic Press, New York).

Ding, W.-P., He, L.-Q., Zhao, G., Zhang, H.-F., Shu Z.-Q., and Gao, D.-Y., 2004, Double porous media model for mass transfer of hemodialyzers, *International Journal of Heat and Mass Transfer*, 47: 4849–4855.

Galach, M., Ciechanowska, A., Sabalinska, S., Waniewski, J., Wojcicki, J., and Werynski, A., 2003, Impact of convective transport on dialyzer clearance, *Journal of Artificial Organs*, 6: 42–48.

Gupta, S. K., 1985, Analytical design equations for reverse osmosis systems, *Industrial and Engineering Chemistry Process Design and Development*, 24: 1240–1244.

Gupta, S. K., 1987, Design and analysis of a radial-flow hollow-fiber reverse-osmosis system, *Industrial and Engineering Chemistry Research*, 26: 2319–2323.

Jaffrin, M. Y., Ding, L., and Laurent, J. M., 1990, Simultaneous convective and diffusive mass transfer in a hemodialyzer, *The Journal of Biomechanical Engineering*, 112: 212–219.

Kedem, O. and Katchalsky, A., 1958, Thermodynamics analysis of the permeability of biological membranes to non-electrolytes, *Biochimica et Biophysica Acta*, 27: 229–246.

Kumano, A., Sekino, M., Matsui, Y., Fujiwara, N., and Fujiwara, N., 2008, Study of mass transfer characteristics for a hollow fiber reverse osmosis module, *Journal of Membrane Science*, 324: 136–141.

Kumar, V. and Upadhyay, S. N., 2000, Computer simulation of membrane processes: Ultrafiltration and dialysis units, *Computers and Chemical Engineering*, 23: 1713–1724.

Kuwahara, F., Nakayama, A., and Koyama, H., 1996, A numerical study of thermal dispersion in porous media, *Journal of Heat Transfer-Transactions of the ASME*, 118: 756–761.

Legallais, C., Catapano, G., Von Harten, B., and Baurmeister, U., 2000, A theoretical model to predict the vitro performance of hemodiafilters, *Journal of Membrane Science*, 168: 3–15.

Lu, J.-F. and Lu, W.-Q., 2010, A numerical simulation for mass transfer through the porous membrane of parallel straight channels, *International Journal of Heat and Mass Transfer*, 53: 2404–2413.

Marcovecchio, M. G., Scenna, N. J., and Aguirre, P. A., 2010, Improvements of a hollow fiber reverse osmosis desalination model: Analysis of numerical results, *Chemical Engineering Research and Design*, 88: 789–802.

Murthy, Z. V. P. and Gupta, S. K., 1994, Sodiumcyanide separation and parameter estimation for reverse osmosis thin film composite polyamide membrane, *J. Membrane Science*, 154: 89–103.

Murthy, Z. V. P. and Gupta, S. K., 1998, Thin film composite polyamide membrane parameters estimation for phenol-water system by reverse osmosis, *Separation Science and Technology*, 33: 2541–2557.

Nakayama, A., 1995, *PC-Aided Numerical Heat Transfer and Convective Flow*, CRC Press, Boca Raton, FL.

Nakayama, A. and Kuwahara, F., 2008, A general bioheat transfer model based on the theory of porous media, *International Journal of Heat and Mass Transfer*, 51: 3190–3199.

Nakayama, A., Kuwahara, F., and Kodama, Y., 2006, An equation for thermal dispersion flux transport and its mathematical modelling for heat and fluid flow in a porous medium, *Journal of Fluid Mechanics*, 563: 81–96.

Nakayama, A. and Sano, Y., 2013, An application of the Sano–Nakayama membrane transport model in hollow fiber reverse osmosis desalination systems, *Desalination*, 311: 95–102.

Palaty, Z., Zakova, A., and Petrik, P., 2006, A simple treatment of mass transfer data in continuous dialyzer, *Journal of Membrane Science*, 45: 806–811.

Patankar, S. V., 1980, *Numerical Heat Transfer and Fluid Flow*, Hemisphere, Washington, DC.

Quintard, M. and Whitaker, S., 1993, One and two equation models for transient diffusion processes in two-phase systems, *Advances in Heat Transfer*, 23: 369–465.

Sano, Y. and Nakayama, A., 2012, A porous media approach for analyzing a countercurrent dialyzer system, *Journal of Heat Transfer-Transactions of the ASME*, 134(7): 072602.

Sekino, M., 1993, Precise analytical model of hollow fiber reverse osmosis module, *Journal of Membrane Science*, 85: 241–252.

Sekino, M., 1995, Study of an analytical model for hollow fiber reverse osmosis module systems, *Desalination*, 100: 85–97.

Sigdell, J. E., 1982, Calculation of combined diffusive and convective mass transfer, *The International Journal of Artificial Organs*, 5(6): 361–372.

Shirazian, S., Moghadassi, A., and Moradi, S., 2009, Numerical simulation of mass transfer in gas-liquid hollow fiber membrane contactors for laminar flow conditions, *Simulation Modelling Practice and Theory*, 17: 708–718.

Spiegler, K. S. and Kedem, O., 1966, Thermodynamics of hyperfiltration (reverse osmosis): Criteria for efficient membranes, *Desalination*, 1: 311–326.

Tu, J.-W., Ho, C.-D., and Chuang, C.-J., 2009, Effect of ultrafiltration on the mass-transfer efficiency improvement in a parallel-plate countercurrent dialysis system, *Desalination*, 242: 70–83.

Tu, J.-W., Ho, C.-D., and Yeh, H.-M., 2006, The analytical and experimental studies of the parallel-plate concurrent dialysis system coupled with ultrafiltration, *Journal of Membrane Science*, 281: 676–684.

Vafai, K. and Tien, C. L., 1981, Boundary and inertia effects on flow and heat transfer in porous media, *International Journal of Heat and Mass Transfer*, 24: 195–203.

Wang, Y., Brannock, M., Cox, S., and Leslie, G., 2010, CFD simulations of membrane filtration zone in a submerged hollow fiber membrane bioreactor using a porous media approach, *Journal of Membrane Science*, 363: 57–66.

Waniewski, J., 2006, Mathematical modelling of fluid and solute transport in hemodialysis and peritoneal dialysis, *Journal of Membrane Science*, 274: 24–37.

Waniewski, J., Werynski, A., Ahrenholtz, P., Lucjanek, O., Judycki, W., and Esther, G., 1991, Theoretical basis and experimental verification of the impact of ultrafiltration on dialyzer clearance, *Artificial Organs*, 15: 70–77.

Yang, C. and Nakayama, A., 2010, A synthesis of tortuosity and dispersion in effective thermal conductivity, *International Journal of Heat and Mass Transfer*, 53(15–16): 3222–3230.

Yeh, H. M., 2009, Numerical analysis of mass transfer in double-pass parallel-pale dialyzers with external recycle, *Computers and Chemical Engineering*, 33: 815–821.

Yeh, H. M., Cheng, T.-W., and Wu, H.-H., 1998, Membrane ultrafiltration in hollow-fiber module with the consideration of pressure declination along the fibers, *Separation and Purification Technology*, 13: 171–180.

9 Effective Transport Properties of Porous Media by Modeling

Moran Wang

CONTENTS

9.1 Introduction 357
9.2 Theoretical Models and Challenges 359
9.3 Numerical Methods 361
9.3.1 Structure Characterization and Reproduction Algorithms 361
9.3.1.1 Granular Structure 363
9.3.1.2 Fibrous Structure 366
9.3.1.3 Netlike Structure 367
9.3.2 Solutions of the Governing Laws 367
9.3.2.1 Governing Equations 368
9.3.2.2 Lattice Boltzmann Method 369
9.3.2.3 Benchmarks 372
9.4 Modeling Results and Discussion 373
9.4.1 Effective Transport Properties Compared with Experiments 373
9.4.1.1 Thermal Conductivity 374
9.4.1.2 Electric Conductivity 377
9.4.1.3 Dielectric Permittivity 378
9.4.1.4 Elastic Moduli 379
9.4.2 Structure Effects 381
9.4.2.1 Size Effects 381
9.4.2.2 Anisotropy Effects 382
9.4.2.3 Morphology Effects 383
9.5 Conclusions 384
Acknowledgments 385
References 385

9.1 INTRODUCTION

For many engineering materials, it has been known since long time ago that there is a rather weak correlation between the properties of the ingredients and those of the resulting products, as revealed by the pioneer works of Griffith[1] on material strength, and independently of Peirce[2] on the weakest link theorem. That is, constituents with improved quality cannot assure a better product, and the internal structure—the way the constituents are arranged in the material system—is just as, if not more, important. On the other hand, the inclusion of different components into a material can be beneficial, acting as reinforcement or supplements to improve the performance of the material—alloys and fiber-reinforced composite are just such examples. Nevertheless, analysis and prediction of behaviors of composites are in general much more intricate. Once mixed together, the components of different types will more or less interact with each other, and the properties at the interfacial

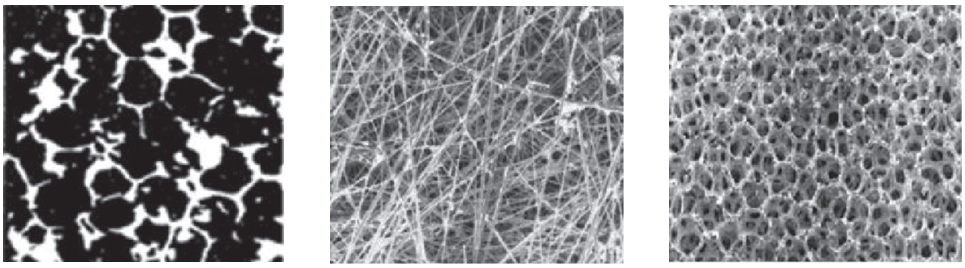

FIGURE 9.1 Three types of porous structures: (a) typical cross section of sand soil, (b) fibrous layer in PEM fuel cells, and (c) porous open-cell foam.

region will exhibit a transition from one component to the other.[3–6] Such effects usually turn even more complicated when the components are at different phase states, such as in a semifrozen soil system.[7,8] The porous multiphase materials are increasingly used in various fields, but analysis and investigation efforts are severely lagging behind.[9,10]

The challenges in studying porous media come mainly from the inherent variety and randomness of their internal microstructures and the coupling between the components of different phases.[11] Figure 9.1 shows three typical such material structures having extensive and important applications. Figure 9.1a shows a typical cross section of sand soil with granular structure.[12–14] For soil, the black stands for the solid phase and the white is the void. The similar structures can be found in wood[15,16] or food.[17–20] For some cases of food, like the bread, since there are lots of granular pores in the flour, the white becomes the solid frame and the black is the pore/voids. The next type is a fibrous structure as shown in Figure 9.1b of another solid–void mixture with the solid in a slender and oriented form, usually existing in polymeric and biomaterials.[21] For a long time, the porous transport layer (PTL) in PEM fuel cell has been thought to possess a granular porous structure; however, very recent investigations have demonstrated that the PTL actually possesses a fibrous structure that exhibits quite different transport behaviors from those with granular structures.[22,23] Another example of fibrous materials is the advanced fiber-reinforced composites where fibers are utilized to enhance the mechanical and thermal properties of the composites up to surprisingly high levels.[24–28] Figure 9.1c shows a cross section of an open-cell foam material.[29–32] It has a netlike porous structure that leads, for metal–foam materials, to the interesting combination of high porosity and low density yet very high thermal and electric conductivities. Such foam materials, typically two-phase systems of solid and void, have played critical roles in advanced aircraft designs, for instance, to improve the catalytic surfaces and enhance the heat exchanger systems.

Given the complexities of the porous systems, the concept of effective properties has become widely accepted.[9–11,33–46] Porous materials are multicomponent and/or multiphase (state) systems. As such, the behaviors of the material are dictated by each and every component of different phases, that is, its overall macroscopic property is not equal to that of any single constituent, rather a collective one contributed by all components forming the system. Therefore, the effective property is actually the equivalent property of a hypothetical simple material (homogeneous with single component and phase), which yields the same response as that of the complex one at the same given conditions and excitations.[9,33–35] Note that, however, this mapping between the complex material system and its equivalent simple material is not unique. The different components and phases in the complex system will exhibit diverse and varying behaviors under different ambient conditions and external excitations.[9,34,47,48] The system overall properties are thus the functions of these external factors as well, thus leading to different equivalent simple systems.[9,33,34,47] Research and investigation of the effective properties of complex materials are important because not only do the porous media/materials have so many significant applications, but it can also shed new light on, and drive further developments of, the related mathematical, physical, and engineering theories.[47–58]

This chapter summarizes the existing achievements in prediction methods for the effective transport properties of porous media. The "effective transport properties" here are associated with three implications: (1) they are steady-state (equilibrium) macroscopic properties without moving parts. Even though in some cases where nanoscale inclusions play an important role, such as in nanocomposites,[40,42,59–64] only the contributions of the nanoscale inclusions to the macroscopic properties are concerned by using the *corresponding effective properties* of the inclusions. So the continuum theories are still valid for the whole system. (2) The properties concerned are limited to pure physical properties only, and no chemical reactions are taken into account. (3) The multiphase systems are in stable and equilibrium state with no phase change, and only very small or negligible deformations or convections, when appropriate, are allowed. Thus, the overall objectives for this chapter are (1) to examine the existing models and methodologies to highlight the recent significant progresses and to discuss the promising directions; (2) through further analysis, to bridge the microstructures and the effective physical properties for complex multiphase materials; (3) using examples, to explore the interanalogies between various properties governed by partial differential equations (PDEs) in similar form so that one can adopt the established methodologies to other untilled or unfledged questions; and (4) when possible, to connect the theoretical results with engineering applications. Through analytical predictions and numerical modeling, certain optimization approaches and design schemes for novel materials could be acheived for engineering applications, and in turn, the new observations and experiences from the practice would accelerate the development of new theories and methodologies.

9.2 THEORETICAL MODELS AND CHALLENGES

A substantial number of theoretical (or analytical) models for effective physical properties have been proposed in the past of more than 100 years.[65] Some of them have been intended for highly specific applications, while others have wider applicability. Nonetheless, most of them focus on the compositions and barely dealt with the internal geometry or microstructures beyond very simple geometrical arrangements, in spite of the critical importance of those factors on the effective properties of a complex material. Apparently, theoretical approaches are still preferred owing to their predictive or estimative power, low cost of easy use, and reasonable accuracy for certain specific cases, especially when the microstructure can be simplified.

Most, if not all, of the existing analytical models for the effective physical properties in the literature are based on, or derived from, several basic models. Here, we list six representative ones in Table 9.1, each of which has led to a model family and played very important roles in analyzing materials properties. Of them, the parallel and series models are the simplest for two-phase systems and are often used as benchmarks for new model validations. They often offer upper and lower bounds for many properties of two-phase heterogonous materials, as proven by Wiener for effective conductivity.[66,67] In the case of elastic modulus, they are often called the Voigt and the Reuss models, respectively.[68,69] The parallel model also serves as the first-order approximation to the calculation of the coefficient of thermal expansion.[70] Next, the effective medium theory (EMT) model tackles materials with a completely random distribution of all the components.[66,71] Note that the expression for EMT model is an implicit form of what was proposed by Bruggeman,[72,73] and it takes other forms for spherical and ellipsoidal inclusions for conductivity[74–76] and elastic moduli.[77] The Maxwell models are likely the most widely used ones in the literature, with the assumptions of a dispersion of small particles within a continuous matrix phase and the particles being far apart from each other so that the local distortions to the transport characteristics around each particle do not interfere with their neighbors.[78] The Maxwell model, which is actually also a special case of the EMT models, has led to a huge derived variations in dealing with transport phenomena, such as the well-known Maxwell–Eucken model,[79] the Maxwell–Garnett model,[80,81] and their submodels.[82–87] The Hamilton–Crosser model introduces a shape factor (n) into the expression so as to deal with cases of nonspherical particle inclusions.[88] But when $n = 3$,

TABLE 9.1
Fundamental Analytical Models for Effective Properties of Two-Component Materials

Model	Structure Schematic[a]	Expressions[b]	Reference
Parallel model	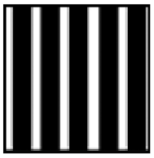	$\lambda_e = (1-\phi)\lambda_1 + \phi\lambda_2$	For conductivity[66, 67] For elastic modulus[68, 69] For thermal expansion coefficient[70]
Series model	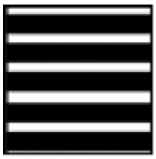	$\lambda_e = [(1-\phi)/\lambda_1 + \phi/\lambda_2]^{-1}$	Same as parallel model
EMT model		$(1-\phi)\dfrac{\lambda_1-\lambda_e}{\lambda_1+2\lambda_e} + \phi\dfrac{\lambda_2-\lambda_e}{\lambda_2+2\lambda_e} = 0$	[71–73]
Maxwell model	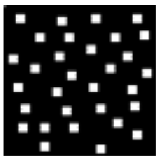	$\dfrac{\lambda_e}{\lambda_1} = 1 + \dfrac{3(\alpha-1)\phi}{(\alpha+2)-(\alpha-1)\phi}$	[78]
Hamilton model		$\dfrac{\lambda_e}{\lambda_1} = \dfrac{\alpha+(n-1)+(n-1)(\alpha-1)\phi}{\alpha+(n-1)+(1-\alpha)\phi}$	[88]
Reciprocity model	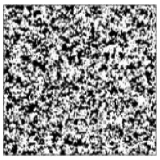	$\dfrac{\lambda_e}{\lambda_1} = \dfrac{1+(\sqrt{\alpha}-1)\phi}{1+(\sqrt{1/\alpha}-1)\phi}$	[74,89]

[a] Assuming the heat flow is in the vertical direction.

[b] λ_1 is the property of the continuous phase; λ_2 is the property of the dispersed phase; λ_e is the corresponding effective property; ϕ is the volume fraction of the dispersed phase; α is the property ratio ($\alpha = \lambda_2/\lambda_1$); and n is the shape factor of the dispersed phase.

it turns into the case of spherical particles and back to the Maxwell model, while $n = 6$ is for cylindrical particles. The reciprocity model was based on the reciprocity theorem[89] that assumes that a microstructure of two components remains statistically equivalent when exchanging the volume fractions of the components.[90,91] Although the idea of this model appears quite different from other models, its predictions agreed rather well with experimental data,[89] and the very same expression was also derived from the Maxwell–Garnett-type approximation by including the shape distribution effects.[74]

These basic models provide acceptable predictions of the effective properties for simple or simplified problems, but the applicability and the accuracy of them are clearly very limited.

Three approaches have been proposed by different researchers at different cases to more or less improve their capability by (1) introducing empirical parameters to account for certain structure characteristics,[92–96] (2) combining two or more basic models for more complex structures,[19,97–100] and (3) using a network formed by huge number of parallel and series models.[101–104]

Although theoretical models for predictions of effective properties of complex materials have been extensively explored, the inherent limitations in these models greatly restraint their capability. The following limitations in the existing theoretical models, and thus the challenges in developing new ones, are summarized:

1. Most existing theoretical models are based on simplified physics with certain overidealized assumptions. This may make the models easy and quick to use, but the simplifications also restrict the models to only simple structures.
2. Any efforts in combining the models for more complex structures will lead to escalating in model complexity and computational costs. Most modifications to improve the accuracy of the models will in turn narrow their applicability.
3. The empirical parameters introduce factors with no physical significance, whose values have to be determined case by case, thus rendering the models more difficult to use.
4. Most existing theoretical models can only handle simple structures and thus become powerless once encountering complex materials. Consequently, none of the existing models is able to tackle directly the effects of morphological changes in the microstructure on the materials properties.
5. The existing theoretical models are largely incapable of dealing with the issue of phase interactions in multiphase systems, such as in a liquid–solid wetting process, the liquid phase distribution, and their collective influence on the overall effective properties of the materials.
6. Even for the relatively successful theoretical models, they can only calculate the properties of existing materials, rather than make predictions for new material. Therefore, they are not of much value in optimizations or design for novel materials.

9.3 NUMERICAL METHODS

Given the limited power of the existing theoretical models in dealing with complex materials, the numerical methods are becoming increasingly important and more widely used in material science and engineering.[105,106] Especially, the rapid development of computational techniques in the past decades has tremendously enhanced our numerical capacities in modeling the multiphysical behaviors of multiphase materials and enabled more accurate and robust approaches in prediction and design of more novel material systems. As stated repeatedly before, the effective properties of a complex material are determined by the collective contributions of the individual components and by their internal structures. As a result, a complete numerical determination of the effective properties of multiphase media has to include such two major steps as first to reproduce properly the multiphase microstructures using computer algorithms and then to solve the relevant transport governing equations (PDEs) with acceptable efficiency and accuracy.

9.3.1 Structure Characterization and Reproduction Algorithms

Considering the random and irregular microstructures of multiphase materials, at least five major structural characteristics can be identified:

1. *Heterogeneity*: Multiphase complex materials are made of two or more components/phases that are rarely distributed uniformly, and each component has its own properties and proportion and thus contributes toward the effective system properties differently.[107,108]

2. *Interactions*: As a result of mixture, both the phase distributions and interphase interactions become highly essential for the overall material behaviors.[3,4]
3. *Structure geometrical varieties*: The microstructures of the complex media can be roughly divided into three distinct types: particle-like, fiber-like, and netlike. As the property and geometry, distributions, interconnections, and couplings are totally different between each type, no generalized algorithms have been established to tackle such variations.
4. *Randomness*: Microstructures of multiphase materials mostly have strong stochastic characteristics, that is, the shape, location, and orientation of the structure elements, and the connections between them are all random to certain degree. For this reason, there are nearly no two materials, or even no two pieces of the same material, that possess exactly the same microstructure in every detail. The concept of the *equivalent* structures becomes more meaningful, that is, structures formed based on certain statistical information from the original material and yielded the same effective properties. Such statistical information from real microstructures makes an equivalent structure realizable using computer algorithms.[109]
5. *Multiscale hierarchy*: As there is rapid development of the microscopy technique, more observations and measurements have indicated that the microstructures of porous materials are actually of hierarchal multiscale, meaning each single "element" at one scale level can show a porous microstructure of its own at a still lower level.[110,111] The multiscale microstructure and its effects on materials properties are a very interesting and important topic for material design.

Several methods have been proposed to reconstruct the microstructures of multiphase materials using computers, and they can be divided into two classes/levels based on the methodologies. The methods at the primary level are the so-called apparent-similarity methods. The random location of obstacles is the simplest one for two-phase granular microstructures. Each imaginary obstacle stands for a particle when the particle geometry details are negligible.[112,113] For instance, Tacher et al.[114] presented a discrete reduced-distance method to generate spherical/elliptical two-phase granular porous media. Based on Tacher's work, Pilotti[115] developed a grain sedimentation algorithm. Yang et al.[116] and Li et al.[117] used the assemblies of 3D spheres with random size to reconstruct the microstructures of porous media. All these methods indeed created two-phase structures with random size and details. However, none of them can deal well with the interactions between the grains, thus unsuitable for energy/electric transfer problems that are extremely sensitive to contacts.

Given the significant influences of the geometric details such as the element shapes, orientations, and connections, on the materials properties, a few newer methods aimed at approaching the real structures in more geometric details have been proposed, the so-called detail-similar methods. As the microscopy instruments and the observation technologies are well developed now, the image mapping has become a highly powerful tool for this purpose.[118,119] Better reconstruction processes have been used to generate two-phase[120,121] and multicomponent[122,123] random structures of porous materials based on the digital microtomographic information and statistical correlation functions. A similar algorithm has been found in the soil research, termed as the Markov chain Monte Carlo method, which created 2D structures with satisfactory agreement using the scanned images of real soil samples.[13,124] More about these reconstruction methods based on image mapping can be found in some review papers[108,123,125] and books.[126,127] For fibrous porous materials, Pan and his colleagues have done a series of analysis to theoretically characterize the microstructure using the statistical density distribution function approaches.[21,128]

The stochastic and statistical characteristics are two key natures in the microstructures of complex multiphase materials, as discussed earlier. Such stochastic characteristics reveal two things: (1) Even in the real world, it is hard to find two materials that have exactly the same microstructure

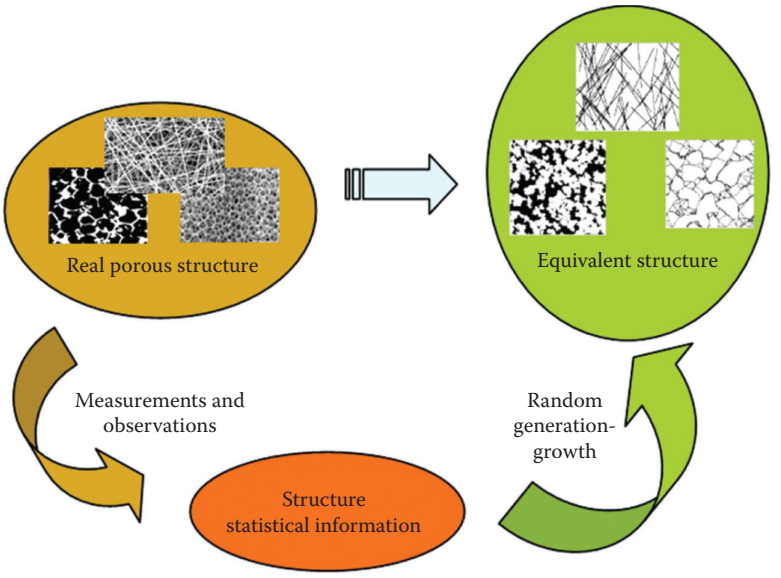

FIGURE 9.2 Microstructure reproduction schematic of the RGG method.

in every detail. This indicates that it is not necessary to duplicate in computer algorithm the microstructure of real materials in the exact duplicate. (2) Random factors have to be incorporated into the reproduction process. The statistical characteristics also indicate two clues: (1) we can reproduce an equivalent microstructure for each real structure, where only the effective factors contributing to the materials properties are taken into account; (2) the equivalent microstructure owns the same major geometric statistical features as the real one but not in every detail. Based on these characteristics and inspired by the cluster growth theory,[129] Wang et al.[8,130–132] proposed a multiparameter RGG method to reproduce the random multiphase microstructures using given statistical information. The basic idea of the method is shown in Figure 9.2. The RGG method is designed to reproduce structural assemblies of elements with random sizes, locations and orientations, and connections, each of which grows from also randomly distributed seeds, and the growth is guided by a few given probabilistic growth rates. For different types of microstructures (granular, fibrous, or netlike), the algorithms will be different but still bear the same principles.

9.3.1.1 Granular Structure

The RGG algorithm for granular media, also termed as the quartet structure generation set (QSGS)[8,130] in which four parameters are identified for controlling the internal porous structure, can be described as follows.

Before initiation, one has to determine among the different phases in a system a nongrowing phase, and the rests are the growing ones. For generality, we call the growing phase as the nth phase, where $n = 2$ to N, the total number of phases in the system. Customarily and without losing generality, the discrete phases are normally taken as the growing phases. For example, rocks and moisture are the growing phases in unsaturated sands, whereas gas is the growing phase in polyurethane (PU) foams. Then the growing process follows the following steps:

(**I**) Randomly locate the cores of the first growing phase in a grid system based on a core distribution probability, c_d, whose value is no greater than the volume fraction of the phase. Each cell in the grid will be assigned a random number by a uniform distribution function within (0, 1). Each cell whose random number is no greater than c_d will be chosen as a core. (**II**) Expand every element of the growing phase to its neighboring cells in all directions based on each given directional growth

probability, D_i, where i represents the direction. Again, for each growing element, new random numbers will be assigned to its neighboring cells. The neighboring cell in direction i will become part of the growing phase if its random number is no greater than D_i. (**III**) Repeat the growing process of (**II**) until the volume fraction of the first growing phase reaches its given value ϕ^2 (if the growing phase is gas, ϕ^2 is more often expressed as the porosity ε). (**IV**) As to the next growing phase, there are two cases to consider depending on its interaction with the existing phase(s). If this phase is an equivalent discrete phase as the existing growing phase, such as multicomponent mixture, it grows from separate seeds, which is very similar as the first growing phase described in (**I**) through (**III**). Otherwise, we have to consider the constraint by and interaction with the existing phase(s). For such cases, the nth phase ($n > 2$) will grow based on a phase interaction growth probability, $I_i^{n,m}$, which represents the growth probability of the nth phase on the mth phase along the ith direction. (**V**) Stop the nth phase growth once its volume fraction reaches the given value ϕ^n. (**VI**) Repeat the next phase growth as described in (**IV**) and (**V**) until n = N. (**VII**) The spaces not occupied at the end represent the nongrowing phase.

Thus, the four parameters (c_d, D_i, ϕ^n, and $I_i^{n,m}$) essentially control the microstructural characteristics of the generated porous media based on our QSGS process. The parameters can be determined through the statistical analysis of measured data, such as from the x-ray microtomography technique or through first-principle modeling such as molecular dynamics simulations. Each parameter has physical significance, rather than just an empirical factor.

The core distribution probability c_d is defined as the probability of a cell to become a core of the first growing phase on which growth or expansion of the first phase originates. The value of c_d indicates the number density of growing cores for the first growing phase, to reflect the statistical distribution of the first growing phase throughout the system. For a given porosity, the average volume of each solid particle V_s could be related with c_d as $V_s = (1 - \varepsilon)V/(N_c \cdot c_d)$, where V represents the total volume of system and N_c the total cell number. The $c_d$value thus also controls the degree of structure details of a system; a smaller c_d leads to a finer description of the microstructures including particle/pore shapes and interparticle/pore connections. However, a small c_d value will also decrease the statistical particle numbers for a given grid size and thus increase the computation fluctuation.

The directional growth probability D_i is defined as the probability for a yet-to-be-occupied cell to merge into a neighboring cell in the ith direction to become part of the growing phase. An appropriate arrangement of the directional growth probabilities may lead to an isotropic structure. In other words, the growth probabilities can be adjusted to control the degree of anisotropy. For 2D cases specially, each square cell has eight growing directions to its neighbors, as seen in Figure 9.3. There are four main directions (1, 2, 3, 4) and four diagonal directions (5, 6, 7, 8). To obtain an isotropic structure in such systems, we set both the main directional growth probabilities D_{1-4} and the diagonal directional growth probabilities D_{5-8} into respective constants in each group and set both constants in a fixed ratio. For instance, by designating the probabilities ratio, D_{1-4}:D_{5-8} = 4, we get

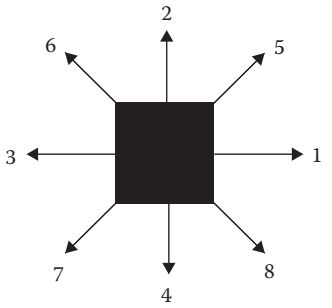

FIGURE 9.3 Eight growth directions of each cell for 2D granular systems.

the directional growth probability consistent with the equilibrium density distribution function for isotropic materials.[133] For 3D structures, a similar probability ratio was used,[134] yet more validations are needed in the future work. The relative value instead of the absolute value of D_i actually controls the anisotropy of structure.

For multiphase porous media systems ($n \geq 3$), the interactions between different discrete phases become even more complex, and we have to consider the effects of such interactions during the phase growth. Such effects are important especially, for instance, in unsaturated porous media soaked by a liquid that wets other phases in the system differentially. In such systems, the growth order of the various phases is important. Generally, the solid phase is selected as the first growing phase, and then the liquid phase grows under the influences of phase interactions. The phase interaction growth probability, $I_i^{n,m}$, that is, the growth probability of nth phase on the surface of mth phase along the ith direction, is hence introduced to account for this influence by assigning different values to $I_i^{n,m}$ for different materials. The value of the phase interaction growth probability $I_i^{n,m}$ could be determined by analyzing the scanned pictures of phase distributions or by calculating from the wetting properties directly.

Figure 9.4 shows six schematic illustrations of the porous structures generated using the QSGS method, where the stochastic characteristics are depicted very realistically in the figures. The first four figures represent two-phase cases, where the white area corresponds to the growing phase (solid) and the black the nongrowing phase (gas). The parameters for Figure 9.4a are $c_d = 0.01$, $\phi^s = 0.3$, and $D_{1,3} = D_{2,4} = 4D_{5-8}$. Figure 9.4b shows the case with a larger solid volume fraction ϕ^s, that is, both the volume and the interparticle connections of the solid phase increased. The comparison between Figure 9.4b and c shows the effect of the core distribution probability c_d on the generated microstructure, and a higher value of c_d leads to a more uniform phase distribution of

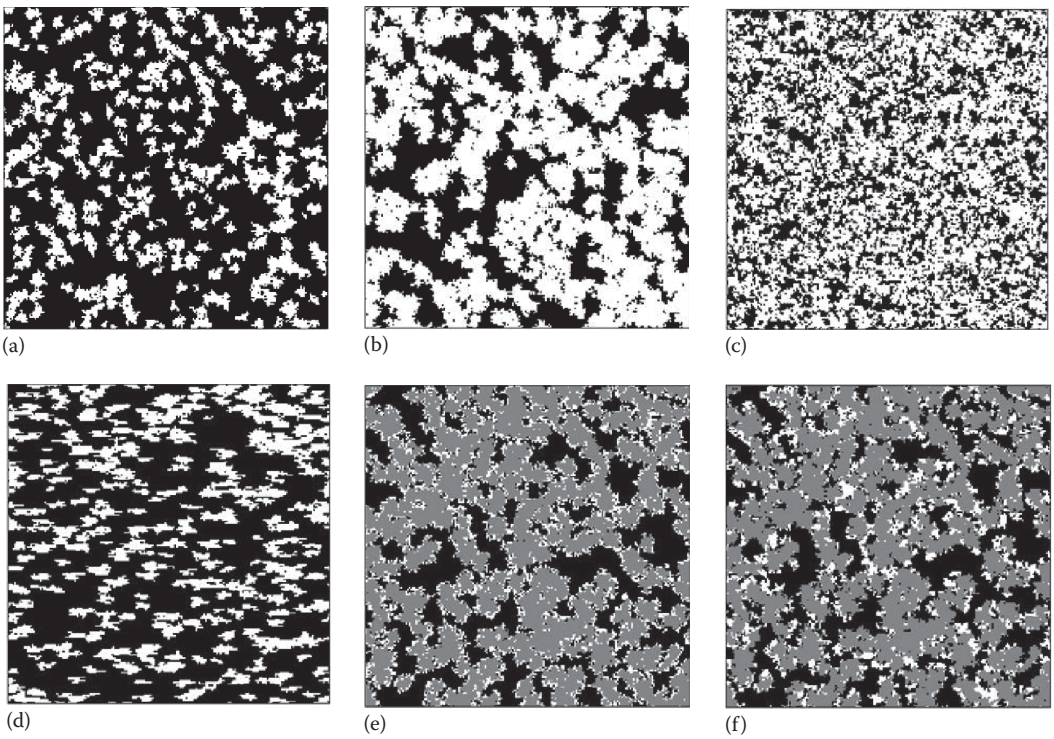

FIGURE 9.4 Schematics of the generated porous structures using QSGS method in 200 × 200 grids. (a) $c_d = 0.01$, $\phi^s = 0.3$, (b) $c_d = 0.01$, $\phi^s = 0.6$, (c) $c_d = 0.1$, $\phi^s = 0.6$, (d) $c_d = 0.01$, $\phi^s = 0.3$, $D_{1,3}$:$D_{2,4} = 10$, (e) $I_i^{l,l} : I_i^{l,s} = 1$, and (f) $I_i^{l,l} : I_i^{l,s} = 10$.

the medium. When the directional growth probability is not the same in every direction, the isotropy will be destroyed. Figure 9.4d shows the generated anisotropic structure, where the horizontal growth probability is 10 times of the vertical one, $D_{1,3} = 10D_{2,4}$ and $D_{2,4} = 4D_{5-8}$. Figure 9.4e and f show the phase distributions of three-phase porous medium using different phase interaction probabilities. The black is the nongrowing phase (gas), the gray is the first growing phase (solid), and the white is the second growing phase (liquid). The phase interaction probability dictates the distribution status of the second growing phase. A high value of liquid–solid interaction means a strong wetting property of the liquid on the solid surface so that the liquid will distribute like a film on the solid surface, as shown in Figure 9.4e. On the contrary, a strong liquid–liquid interaction probability leads to a high degree of liquid aggregation, and the liquid exists as droplets or liquid bridges on the solid particles (see Figure 9.4a through f).

Compared with most of the previous reconstruction methods, the QSGS method has the following merits: (1) Both stochastic and statistical features are incorporated into the generation-growth process, and therefore the generated microstructure is closer to a real one. (2) Each of the parameters in the algorithm has a distinct physical meaning, instead of just being an empirical coefficient. (3) The multibody connection problem is thus solved. (4) The method is efficient without turning to any iteration process. (5) The algorithm can be extended straightforwardly to 3D and/or multiphase cases and is suitable for parallel computing.

9.3.1.2 Fibrous Structure

The RGG algorithm for fibrous structures is much easier if one assumes that each fiber is represented by a straight line with given diameter d and length l and located by its core position and orientation angle θ, as illustrated in Figure 9.5a. Similar assumptions can be found in many previous studies.[135] The generation process for 2D structures is conducted as follows.[131]

(**I**) Randomly locate the fiber cores based on a core distribution probability, c_d, and the core position distribution function, F. The core distribution probability c_d is defined as the probability of a point to become a core of the fiber, and this $c_d$value is related to the fiber number density. The core position distribution function F could be a uniform, a normal, or any other distribution function of position (x, y). (**II**) Randomly assign an orientation angle θ to each fiber core and θ ranges within $[-\theta_{\text{lim}}, \theta_{\text{lim}}]$. (**III**) Grow fibers from each core along both directions of the orientation θ for fiber length and crosswise for fiber thickness. (**IV**) Stop growth once fiber dimensions, d and l, reach the specified values, or the overall porosity attains the given level ε. Thus, there are six parameters, c_d, F, θ_{lim}, d, l, and ε, collectively controlling the resulting structure.

Figure 9.5b shows an example of a generated fibrous structure in 200 × 200 grids for c_d = 0.0025, $d = \delta_x$ $l = 100\delta_x$, $\theta_{\text{lim}} = \pi/2$, and a uniform distribution. The fibers are in dark and the

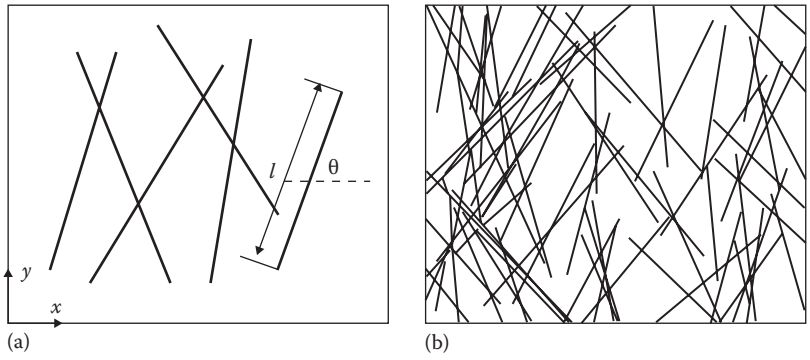

FIGURE 9.5 RGG method for fibrous structure and a reconstructed structure. (a) Growing fibers with parameters. (b) A reconstructed fibrous structure.

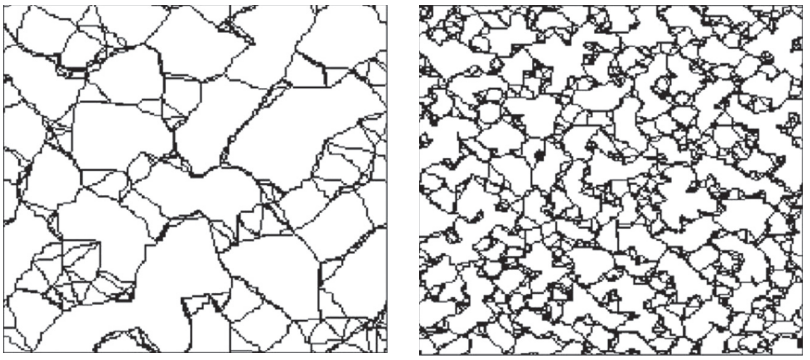

FIGURE 9.6 A reproduced netlike random microstructure of a two-phase system. The dark is the solid and the white the air. (a) $\varepsilon = 0.8888$ and (b) $\varepsilon = 0.7373$.

continuous phase in white. This 2D algorithm has been extended to 3D by simply adding another orientation angle to control the fiber growth direction in the 3D space.[136]

9.3.1.3 Netlike Structure

The netlike structures, such as the open-cell foam, are a little more complex, and few approaches available in the public can tackle such structures with an acceptable accuracy. Calmidi and Mahajan[137] and Bhattacharya et al.[31] depicted this type of structure using an array of hexagonal cells with lump formed at the intersection. Boomsma and Poulikakos[138] modeled such structures in three dimensions in the form of tetrakaidecahedral cells with cubic nodes at the intersection. However, such existing models have to use an empirical parameter to account for the effects of the intercell connections.

Under the same idea of RGG method, the main process of reconstruction for netlike structures for a 2D two-phase (2d2p) case can be described as follows:

(**I**) Stochastically distribute the cores as the net nodes on a lattice system based on a given probability c_d, similar to the other generation processes. (**II**) For each net node, search outward to the neighboring nodes and randomly select N_n of them as the link nodes; here, N is determined based on the features of specific porous media. Genetic algorithm or other searching algorithms could be used for this process. (**III**) Grow link lines from a net node to each of its N link nodes. Again, the random rejection–acceptance rule is applied to the process, and in the end every node will connect with other nodes with N_n link lines so as to form such a network. Figure 9.6 shows two reproduced netlike structures on a 200×200 grid with $N_n = 4$.

9.3.2 Solutions of the Governing Laws

After the microstructures are reconstructed, the governing equations for transport in the materials need to be solved numerically for the effective properties of multiphase material systems. The conventional PDE solvers, such as finite difference method, finite element method, boundary element method, and finite analytic method, have been applied to tackle the governing equations in multiphase media of heat transfer[139–146] and electric field transports.[147–156] However, the structural complexities bring in two difficulties. The first is the requirement of *grid refinements* for complex structures: the accuracy of such conventional numerical methods is strongly dependent on the grid size, so that an extrafine grid is needed whenever the transport process is complex in physics and/or in geometry. Consequently, when dealing with multiphase transport problems in porous media with

complex geometries, the extreme complexities and the corresponding computation intensity will in practice confine the computational domain in a very limited area. The second is the *conjugate constraints* at interfaces between different phases: for steady electric field transport through multiphase structures, for instance, electric potential and flux continuities have to be ensured at the interfaces when solving the governing equations, thus demanding enormously high computational resources for a porous medium with innumerable interfaces in the structure.

Recently, the stochastic methods for representing the perturbations in porous media have gained much attention.[157,158] Shoshany et al.[159] and Barta and Dieska[160] modeled the thermal conductivity of porous materials using the Monte Carlo method to reflect the structural fluctuations during the process. Yue et al.[161,162] developed a lattice gas automata method to predict the electric transport properties in 2D multiphase porous media. Owing to its easy implementation of multiple interparticle interactions and complex geometry boundary conditions[134,163] and that in general the conservation laws can hold automatically without additional computational efforts,[164–167] the lattice Boltzmann method (LBM) has recently been developed successfully for modeling of hydrodynamics,[106,163,164] thermodynamics,[168–170] and electrodynamics[167,171–174] in complex systems, and the effective properties can be consequently calculated.

9.3.2.1 Governing Equations

Let us consider thermal or electric transport through a multiphase material system as shown in Figure 9.7. To determine the effective conductivities, a set of transport governing equations need to be solved. Considering a steady and pure thermal or electric transport process without contact resistance, radiation, phase change, or other influences from the source, the governing equations can be summarized as follows.

Once the EMT is applicable,[175] the thermal or electric transports in a multiphase medium are governed by a Laplace equation[150,155]:

$$\nabla \cdot \left(\lambda_n \nabla \Phi \right) = 0 \tag{9.1}$$

where λ_n is the local conductivity of the nth phase, which could be thermal conductivity or electric conductivity/dielectric permittivity for a given case, and, correspondingly, Φ would be the thermal potential/temperature[39–145,176] or the electric potential.[147–155,177]

Two points in Equation 9.1 should be noted: First, only steady-state transport is described by the equation, because the unsteady terms have no contribution to the effective properties.

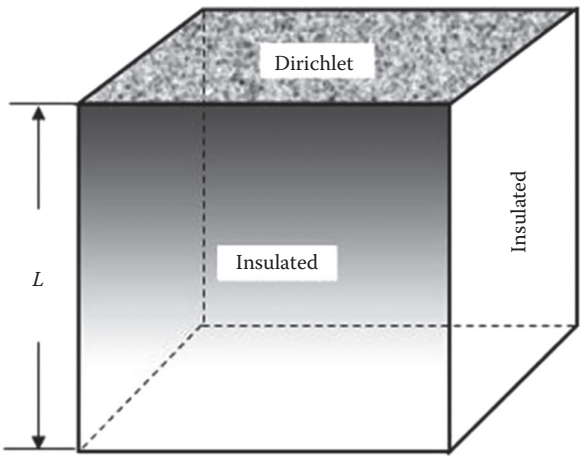

FIGURE 9.7 Schematic diagram of domain and boundaries.

Second, the local property (λ_n) should not be moved outside of the divergence operator since it changes its value with the position, leading to incorrect predictions.[178]

At the interfaces between two phases (i and j) in equilibrium, the continuities of both potential and flux have to be satisfied, that is,

$$\Phi_{\text{int},i} = \Phi_{\text{int},j} \tag{9.2}$$

$$\lambda_i \nabla\Phi\big|_{\text{int},i} = \lambda_j \nabla\Phi\big|_{\text{int},j} \tag{9.3}$$

where the subscript "int" corresponds to the interfaces between phase i and j. Equation 9.1 thus governs the distribution of potential Φ in the multiphase material, subject to the interface constraints in Equations 9.2 and 9.3. After the potential field is derived, the effective conductivity can be determined as

$$\lambda_{eff} = \frac{qL}{\Delta\Phi} \tag{9.4}$$

where q is the steady flux through the material between the potential differences ($\Delta\Phi$) over a thickness L.

Very similar governing equations have been derived for mechanical elastic properties with the assumptions of steady small elastic strain in the direction of the force with negligible multidimensional deformation effects.[179,180] For the mechanics equation, λ_n in Equation 9.1 represents the local mechanical modulus, either Young's modulus or shear modulus, Φ the displacement in the direction of force, and q the stress in a given direction. Unlike the other transport properties, such a governing equation for mechanical moduli has rarely been employed to numerical calculation of the effective properties of multiphase materials. The likely first attempt has shown successful applications.[181]

9.3.2.2 Lattice Boltzmann Method

The LBM is intrinsically a *mesoscopic* computational fluid dynamics (CFD) approach based on the evolution of statistical distribution on lattices and has achieved considerable success in simulating fluid flows and associated transport phenomena.[164,166] For more details about the LBM, one can consult excellent book[165] and review papers.[106,164] The most important advantages of LBM include the easy implementation of both multiple interparticle interactions and complex geometry boundary conditions.[134,163,182,183] Conservations can generally hold automatically without additional computational efforts.[165,167,170,184]

The original lattice Boltzmann model for single time Bhatnagar–Gross–Krook (BGK) relaxation collision operator is used to solve the Navier–Stokes (NS) equation for fluid flow.[164] The evolution equation is

$$f_\alpha(\mathbf{r} + \mathbf{e}_\alpha\delta_t, t + \delta_t) - f_\alpha(\mathbf{r}, t) = -\frac{1}{\tau_v}\left[f_\alpha(\mathbf{r}, t) - f_\alpha^{eq}(\mathbf{r}, t)\right] \tag{9.5}$$

with a local equilibrium distribution function

$$f_\alpha^{eq} = \omega_\alpha \rho_f \left[1 + 3\frac{\mathbf{e}_\alpha \cdot \mathbf{u}}{c^2} + 9\frac{(\mathbf{e}_\alpha \cdot \mathbf{u})^2}{2c^4} - \frac{3\mathbf{u}^2}{2c^2}\right] \tag{9.6}$$

and

$$\tau_\nu = 3\nu\frac{\delta_t}{\delta_x^2} + 0.5 \tag{9.7}$$

where
- τ_ν is the viscosity-based dimensionless relaxation time
- ν is the kinematic viscosity
- δ_x is the lattice constant
- δ_t is the time step

It has been proved that through the Chapman–Enskog multiscale expansion, the Lattice BGK equation is consistent with the incompressible NS equation[164,185]:

$$\frac{\partial \mathbf{u}}{\partial t} + \mathbf{u}\cdot\nabla\mathbf{u} = -\nabla p_f + \nabla\cdot(\nu_f\nabla\mathbf{u}) \tag{9.8}$$

Inspired by this process and by treating the generalized governing equation (Equation 9.1) as a special case of NS equation, the lattice evolution equation can be expressed as[169,170]

$$g_\alpha\left(\mathbf{r}+\mathbf{e}_\alpha\delta_t, t+\delta_t\right) - g_\alpha\left(\mathbf{r},t\right) = -\frac{1}{\tau_n}\left[g_\alpha\left(\mathbf{r},t\right) - g_\alpha^{eq}\left(\mathbf{r},t\right)\right] \tag{9.9}$$

where
- g_α^{eq} gis the local equilibrium distribution in each direction
- $\mathbf{e}_\alpha$ is the discrete lattice velocity
- τ_n the dimensionless relaxation time for local phase

The equilibrium distribution of the evolution variable, g_α, for the 2D nine-speed (D2Q9) model is

$$g_\alpha^{eq} = \begin{cases} 0 & \alpha = 0 \\ \Phi/6 & \alpha = 1,2,3,4 \\ \Phi/12 & \alpha = 5,6,7,8 \end{cases} \tag{9.10}$$

the microscopic velocity

$$\mathbf{e}_\alpha = \begin{cases} (0,0) & & \alpha = 0 \\ \left(\cos\theta_\alpha, \sin\theta_\alpha\right)c & \theta_\alpha = (\alpha-1)\pi/2 & \alpha = 1,2,3,4 \\ \sqrt{2}\left(\cos\theta_\alpha, \sin\theta_\alpha\right)c & \theta_\alpha = (\alpha-5)\pi/2 + \pi/4 & \alpha = 5,6,7,8 \end{cases} \tag{9.11}$$

and the dimensionless relaxation time

$$\tau^n = \frac{3}{2}\frac{\lambda_n}{c^2\delta_t} + 0.5 \tag{9.12}$$

where
- δ_t is the time step
- c is the lattice speed whose value in theory can take any positive value provided the resulting τ_n value is within (0.5, 2)[167,170]

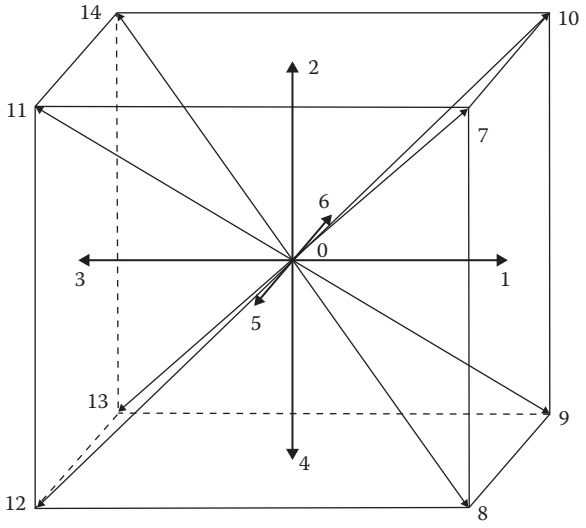

FIGURE 9.8 The lattice direction system (α) for D3Q15 model.

For a 3D fifteen-speed (D3Q15) model shown in Figure 9.8, there are

$$g_\alpha^{eq} = \begin{cases} 0 & \alpha = 0 \\ \Phi/9 & \alpha = 1\text{–}6 \\ \Phi/24 & \alpha = 7\text{–}14 \end{cases} \tag{9.13}$$

$$\mathbf{e}_\alpha = \begin{cases} (0,0,0) & \alpha = 0 \\ (\pm 1,0,0)c,(0,\pm 1,0)c,(0,0,\pm 1)c & \alpha = 1\text{–}6 \\ (\pm 1,\pm 1,\pm 1)c & \alpha = 7\text{–}14 \end{cases} \tag{9.14}$$

and

$$\tau_n = \frac{9}{5}\frac{\lambda_n}{c^2\delta_t} + 0.5 \tag{9.15}$$

Both the potential and flux can then be calculated according to[186]

$$\Phi = \sum_\alpha g_\alpha \quad \text{and} \quad q = \left(\sum_\alpha \mathbf{e}_\alpha g_\alpha\right) \tag{9.16}$$

Once the potential field is solved, the effective conductivity, λ_{eff}, can be determined as

$$\lambda_e = \frac{L \cdot \int q \cdot dA}{\Delta\Phi \int dA} \tag{9.17}$$

For the Dirichlet boundary treatment, we follow the bounce-back rule of nonequilibrium distribution proposed by Zou and He[187]: $g_\alpha - g_\alpha^{eq} = -\left(g_\beta - g_\beta^{eq}\right)$, where α and β represent the opposite directions and the equilibrium distribution can be calculated based on the local boundary temperature. For the insulated boundaries, a specular reflection treatment is implemented to prevent flux from leaking along the insulate surfaces. It has been proved that the current boundary treatments have second-order accuracies.[187]

9.3.2.3 Benchmarks

The lattice Boltzmann algorithm and codes were numerically validated by two basic structures of dual-component systems: the parallel mode and the series mode. Assuming the conductivity of each component is k_1 and k_2, respectively, the theoretical solutions predict the effective conductivities as $(k_1 + k_2)/2$ for the parallel mode and $1/(1/2k_1 + 1/2k_2)$ for the series mode.[66,67] Table 9.2 lists the calculated effective thermal conductivities by the present model in comparison with the theoretical solutions for different values of k_1/k_2. We keep k_1 as 1.0 while changing k_2 from 10 to 10,000. Such a large contrast between k_1 and k_2 leads to a longer computational time for any algorithms to converge, yet provides a more strict test on the LB model. The deviations in Table 9.2 between the predictions are no greater than 0.006% for the parallel mode and 0.765% for the series mode even under such large conductivity contrasts, showing a good accuracy of the LBM.

Next, the LBM was validated by simulating the transport process in functionally graded materials with continuously varying properties. Consider the cube problem with given property gradations only along the z-axis, which is position dependent only. Let the potential at the top surface maintain at Φ_T and that at the bottom $\Phi_B = 0$. The conductivity at the bottom surface is λ_0. Three cases are considered with, respectively, the property variations in the z-direction: the quadratic, $\lambda = \lambda_0(1 + \beta z)^2$; the exponential, $\lambda = \lambda_0 e^{2\beta z}$; and the trigonometric, $\lambda = \lambda_0(a_1\cos\beta z + a_2\sin\beta z)^2$. The corresponding steady analytical solutions of the potential distribution for these cases are[144] the quadratic, $\Phi = \sqrt{\lambda_0}\,(1+\beta L)z\Phi_T \Big/ \left(\sqrt{\lambda} L\right)$; the exponential, $\Phi = \Phi_T(1 - e^{-2\beta z})/(1 - e^{-2\beta L})$; and the trigonometric, $\Phi = \sqrt{\lambda_0}\,(a_1\cos\beta L + a_2\sin\beta L)\Phi_T \sin\beta z \Big/ \left(\sqrt{\lambda}\sin\beta L\right)$.

Figure 9.9 compares the potential distributions of the three analytical solutions, with our numerical predictions using the present LBM. The dimensionless parameters used are $\lambda_0 = 10$, $\beta = 2$, $\Phi_T = 1$, $L = 1$, and $a_1 = a_2 = 1$. The solid lines are the analytical solutions and the symbols are our numerical predictions. Three-dimensional grids of $200 \times 200 \times 200$ dimension are used in the simulations. The excellent agreements in the figure thus validate the present algorithm and the computation codes.

On the computational efficiency, the LBM has been compared with the conventional CFD methods by simulating the same conjugate heat transfer problem in thick straight-wall channels.[170] The results indicated that the conventional CFD (performed by Fluent 6.22) needs at least 5–10 times finer grid divisions to reach the same accuracy as the LBM. Such an advantage of LBM will become much more apparent in dealing with complex geometry, a key feature of porous media.

TABLE 9.2
Comparisons between Our Predicted Results and Existing Theoretical Solutions, $k_1 = 1.0$

Results / k_1:k_2	Parallel Mode			Series Mode		
	Theoretical Value	Present Predictions	Relative Deviations (%)	Theoretical Value	Present Predictions	Relative Deviations (%)
1:10	5.500	5.500	0.000	1.818	1.815	0.165
1:100	50.50	50.50	0.000	1.980	1.976	0.202
1:500	250.5	250.5	0.000	1.996	1.991	0.250
1:1000	500.5	500.5	0.000	1.998	1.993	0.250
1:10000	5000.5	5000.2	0.006	1.9998	2.0151	0.765

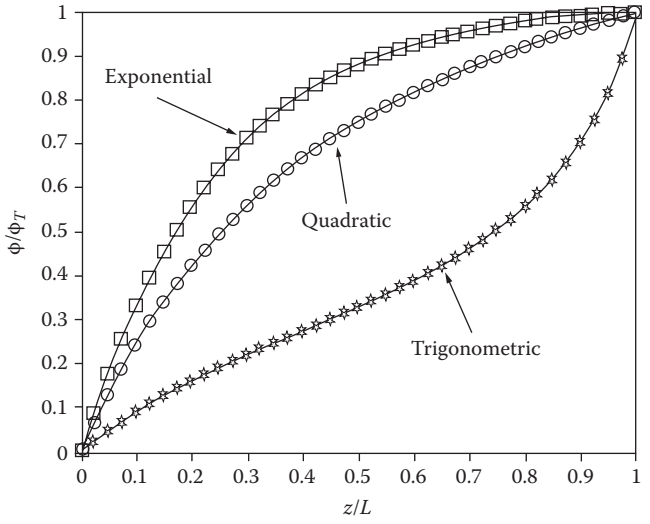

FIGURE 9.9 Potential profiles in the z-direction. The parameters used are $\lambda_0 = 10$, $\beta = 2$, $\phi_T = 1$, $L = 1$, and $a_1 = a_2 = 1$. The solid lines are analytical solutions and the symbols are numerical predictions.

9.4 MODELING RESULTS AND DISCUSSION

It is one of the most fundamental goals in materials science to establish connections between the macro behaviors of a material and the corresponding properties of each inclusion. Inherently, two major issues appeared—the internal morphology of the material formed by the constituents and the interactions among themselves. However, even for simple cases, bringing these two factors into a theoretical treatment often poses as a challenge except for highly regular structures. Once materials become more complex with irregular internal morphology and formed by constituents of different phases, dealing with such issues turns into a daunting task.

However, in the set of novel mesoscopic numerical methods introduced in the last section, two steps were performed to tackle the issues: First, the equivalent multiphase microstructures were reproduced by a multiparameter RGG method based on the statistical information of real structures from experiments or existing data. Second, the related governing equations on transport processes were numerically solved by a high-efficiency LBM. Such methods enable us not only to calculate the properties of the existing structures of materials but also to predict those of new or even materials nonexistent in nature.

This section is to demonstrate the power of the new methods by dealing with several transport problems. For each problem, the methodology is first validated by comparing the yield predictions with the existing experimental data from the literature. Subsequently, the major structure effects on the effective properties of these materials are systematically studied, including the morphology effects, anisotropy effects, and size effects.

9.4.1 Effective Transport Properties Compared with Experiments

As stated earlier, since some different physical processes share the same governing equations (Equations 9.1 through 9.3) under certain assumptions, our new mesoscopic methods are employed below for predictions of various physical properties, including the thermal conductivity, the electric conductivity/dielectric permittivity, and the elastic moduli. The calculated results were compared with the existing experimental data.

9.4.1.1 Thermal Conductivity

Among all physical properties of multiphase material systems, the thermal and electric conductivities are the mostly studied ones due to their significance and wide applications. There are large numbers of experimental data available for validation purpose.

9.4.1.1.1 For Granular Structure

Consider a Cu/solder composite, where the Cu particles are uniformly dispersed in the solder mass.[188] To reproduce the 2D microstructure of this two-phase granular composite using the QSGS,[8] the solder is selected as the nongrowing (first) phase and the Cu particles are the growing (second) phase. The structure is considered as isotropic. Since the Cu particle size was not provided in the literature[188] where the experimental data are collected, the parameter in QSGS on the growing phase size has to be estimated as $c_d = 0.01$. The component thermal conductivities are $k_{Cu} = 398.0$ W/m · K and $k_{solder} = 78.1$ W/m · K.[188] Figure 9.10 shows the effective thermal conductivities calculated by the new mesoscopic method, as a function of Cu volume fraction, ϕ_2, compared with the experimental data from Ref. [188]. The numerical results agree with the experimental data fairly well.

Unsaturated soil represents a typical case of three-phase granular material systems. Customarily, the porosity, ε, is defined as the total volume fraction of both air and the liquid. The degree of saturation, S, is the liquid volume fraction within the fluids. Therefore, the solid phase, the liquid phase, and the gas phase have the volume fractions of $(1 - \varepsilon)$, εS, and $\varepsilon(1 - S)$, respectively. To reconstruct a three-phase isotropic microstructure, the parameters used in QSGS are $c_d = 0.01$ and $I_i^{3,2} = I_i^{3,3}$ for each i direction. Figure 9.11 shows the predicted effective thermal conductivities versus the degree of saturation S at $\varepsilon = 0.52$ for moist porous brick sands, in both the frozen and unfrozen states. The thermal conductivities used in the simulations are $k_s = 2.85$ W/m · K, $k_w = 0.5924$ W/m · K, $k_g = 0.0249$ W/m · K, and $k_{ice} = 2.38$ W/m · K.[189,190] A 200×200 grid is used in the simulations, yielding the random fluctuation within 3%. The numerical results are compared with the experimental data.[7,189] Once again, good agreements are obtained with the experimental data for both frozen and unfrozen cases.

9.4.1.1.2 For Fibrous Composites

It has been attractive to use carbon fiber for its excellent performance acting as fillers in composite materials to improve the thermal, electrical, and mechanical performances. One typical example is for

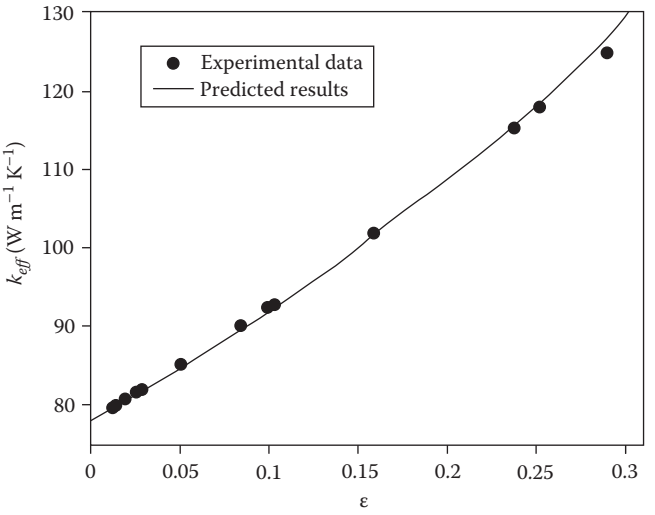

FIGURE 9.10 Comparisons between predictions and experimental data for Cu/solder material. The parameters are $k_{Cu} = 398.0$ W/m · K and $k_{solder} = 78.1$ W/m · K. (The experimental data are from Lee, H.J. and Taylor, R.E., *J. Appl. Phys*., 47(1), 148, 1976.)

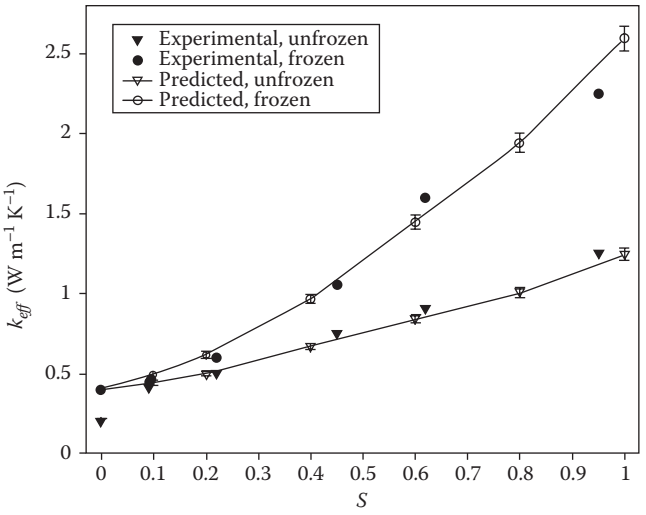

FIGURE 9.11 Comparisons between predicted and experimental effective thermal conductivities of unsaturated porous sands in frozen and unfrozen states. The parameters are $\varepsilon = 0.52$, $k_s = 2.85$ W/m·K, $k_w = 0.5924$ W/m·K, $k_g = 0.0249$ W/m·K, and $k_{ice} = 2.38$ W/m·K. (The experimental data are from Sepaskhah, A.R. and Boersma, L., *Soil Sci. Soc. Am. J.*, 43(3), 439, 1979; Singh, A.K. et al., *J. Phys. D Appl. Phys.*, 23(6), 698, 1990.)

nanofluids. [24,191,192] It has been reported that by just adding 1% volume faction of carbon nanofibers into oil to form a nanofiber-in-oil suspension, the thermal conductivity of the oil was enhanced up to 150%.[24] However, the extremely high aspect ratio and the very small volume fraction of the nanofibers brought big challenges in reconstruction of such a fibrous structure. The predictions became fluctuated due to the low fiber loadings. In another case, Frusteri et al.[27,28] have recently measured the thermal conductivity of a phase change material containing carbon fibers. The fiber loading is much higher (up to 10 wt.%). Here, we compare their experimental data with our mesoscopic numerical predictions. Because little structure information was provided with the experimental measurements, we have to estimate the statistical parameters for structure reproductions. To reduce the computational load, the microstructure was reconstructed in a 60 × 60 × 60 3D grid system. To reflect the high aspect ratio without losing the fiber-end transport effects, the fibers were generated with $L = 120$ by performing a periodic treatment when the growth met the boundaries. The width of each fiber was assumed as one unit grid size, and the orientation angle of the fibers was uniformly random so that the structure was isotropic. The thermal properties used in our simulations are $k_f = 180$ W/m·K and $k_m = 0.47$ W/m·K.[28] Figure 9.12 shows good agreement between our predictions and the measured data when the volume fraction is lower than 6%. When the fiber fraction is high, the interfiber contacts will affect the effective thermal property. Because no thermal contact resistance[193] is considered in our model, the predicted thermal conductivities are a little higher than, but still comparable with, the experimental data when the fiber fraction is high. The numerical relative errors due mainly to the fiber distribution randomness are at the same level as those of experimental measurements.

9.4.1.1.3 For Netlike Structure

Foam materials have shown good transport and mechanical performances at high porosities, because of the porous netlike microstructures. Their effective properties were severely underestimated when the traditional theoretical models were applied. Several new numerical approaches for regular structures have been proposed for such materials, but with some empirical parameters to account for the gap between the assumed regular structures and the actual materials.[30,31, 94,195] The RGG method has been used to reconstruct the netlike random microstructures of the foam materials on a 50 × 50 × 50 grid,[132] which could limit the fluctuations in the predictions to roughly smaller than 5%.

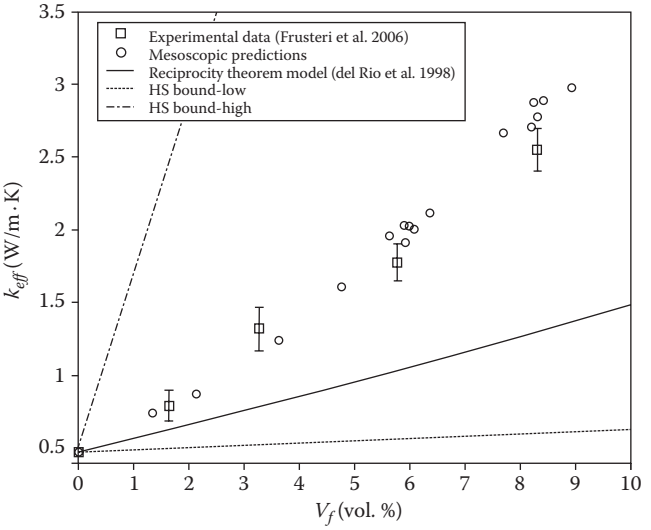

FIGURE 9.12 Measured and predicted effective thermal conductivities of phase change materials containing carbon fibers. The properties used are $k_f = 180$ W/m · K and $k_m = 0.47$ W/m · K.

The predicted effective thermal conductivities of reticulated vitreous carbon (RVC) foams with water or air as the fluid media are compared with the existing experimental data[31] in Figure 9.13. The component thermal conductivities used in the simulations are $k_{RVC} = 8.5$ W/m · K, $k_{water} = 0.615$ W/m · K, and $k_{air} = 0.026$ W/m · K .[194] The RVC–water predictions agree well with the experimental data, while the RVC–air predictions are a little lower. We noticed that the ambient temperature was 25°C when performing the experimental measurements[31]; therefore, the underestimation of the effective thermal conductivity of RVC–air foams could result from the neglected thermal radiation. The effects of thermal radiation may become more significant when the overall effective thermal conductivity of the media is relatively low.

To evaluate the contribution of the radiation heat transfer, a simple relationship was proposed to introduce the radiation effect into the thermal conductivity, k_{rd}, for the PU foams as[195]

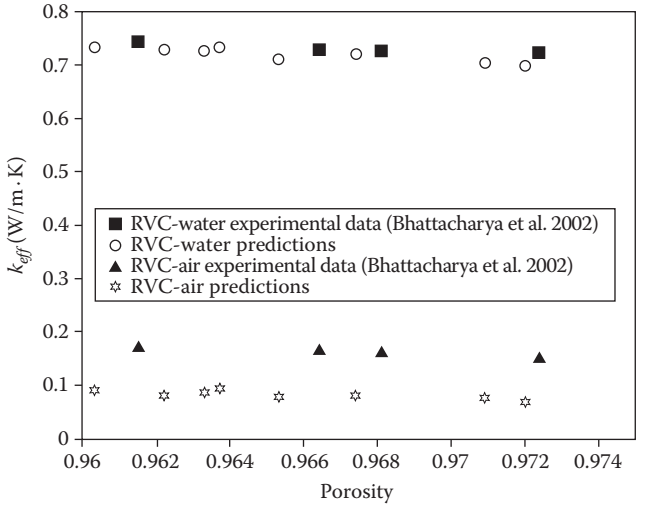

FIGURE 9.13 Comparisons of effective thermal conductivities in RVC foams.

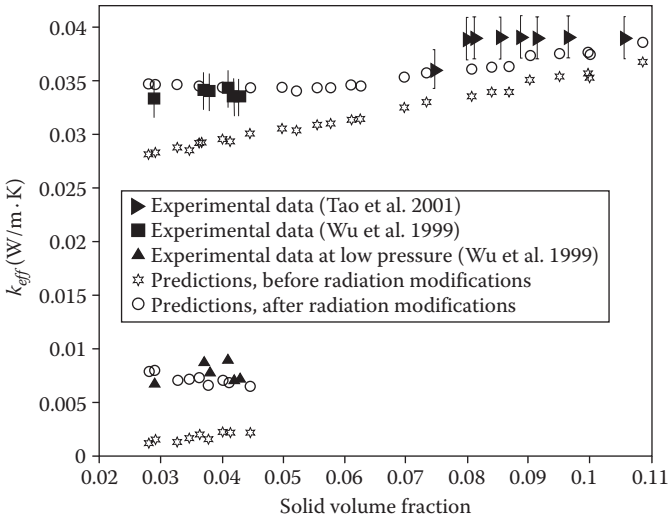

FIGURE 9.14 Comparisons of effective thermal conductivities against the solid volume fraction in PU foams. The solid symbols are experimental data, the stars are predicted results before radiation modifications, and the circles are predictions after modifications.

$k_{rd} = 16\sigma T^3/3(42.038\rho_s V_s + 121.55)$, where σ is the Stefan–Boltzmann constant (5.67×10^{-8} W/m^2 K^4), T the mean temperature, ρ_s the solid density, and V_s the solid volume fraction.

Figure 9.14 shows the predictions of effective thermal conductivities of PU foams at 286 K with and without the radiation modification, in comparison with experimental data.[30,195] The parameters used in the simulations are the thermal conductivity of PU solid $k_{PU} = 0.262$ W/m · K, the thermal conductivity of air at 286 K and under standard pressure $k_{air,sp} = 0.0252$ W/m · K and then at 286 K and under a lower pressure (nearly 2 Pa) $k_{air,lp} = 5 \times 10^{-7}$ W/m · K, and the PU solid density $\rho_s \approx 800$ kg/m^3.[132] After the radiation modification, the predicted effective thermal conductivities agree pretty well with the experimental data for PU foams under both standard air pressure and the lower air pressure as seen in Figure 9.14. The results also show that the importance of radiation contribution decreases with an increasing solid volume fraction so that the two simulation results converge at high solid volume fraction.

9.4.1.2 Electric Conductivity

For the two-phase case, we compare our predicted effective electric conductivities of Al_2O_3/Y-TZP composite materials with the measurements by Sanchez-Herencia et al.[196] Figure 9.15a shows the results of effective electric conductivity versus volume fraction of Al_2O_3 for single-layer composites. The electric conductivities of the Al_2O_3 and Y-TZP components used in the simulations are 3.7×10^{-7} and 1.0×10^{-2} S/cm, respectively.[196] When we use a logarithmic scale for the y-axis, the effective electric conductivity exhibits a nearly bilinear trend, with the intersecting point falling around the point where the volume fraction of Al_2O_3 is 0.8. Before the intersecting point, the effective electric conductivity decreases with the volume fraction of Al_2O_3 at a low rate, whereas after the point, the rate of decrease becomes much steeper. Such a trend is consistent with the previous report.[196] Unlike the previous predictions[197] however, the change of the effective conductivity is smooth and continuous with no singular point, making more physical sense. Our predictions agree well also with the experimental data when the Al_2O_3 volume fraction is below 0.8, yet the predictions are much greater than the measured values once the Al_2O_3 volume fraction approaches 0.9. The reason for the discrepancy, as pointed out in Ref. [197], might lie in the systematic error of the experimental equipment or the lacunae existing in the materials.

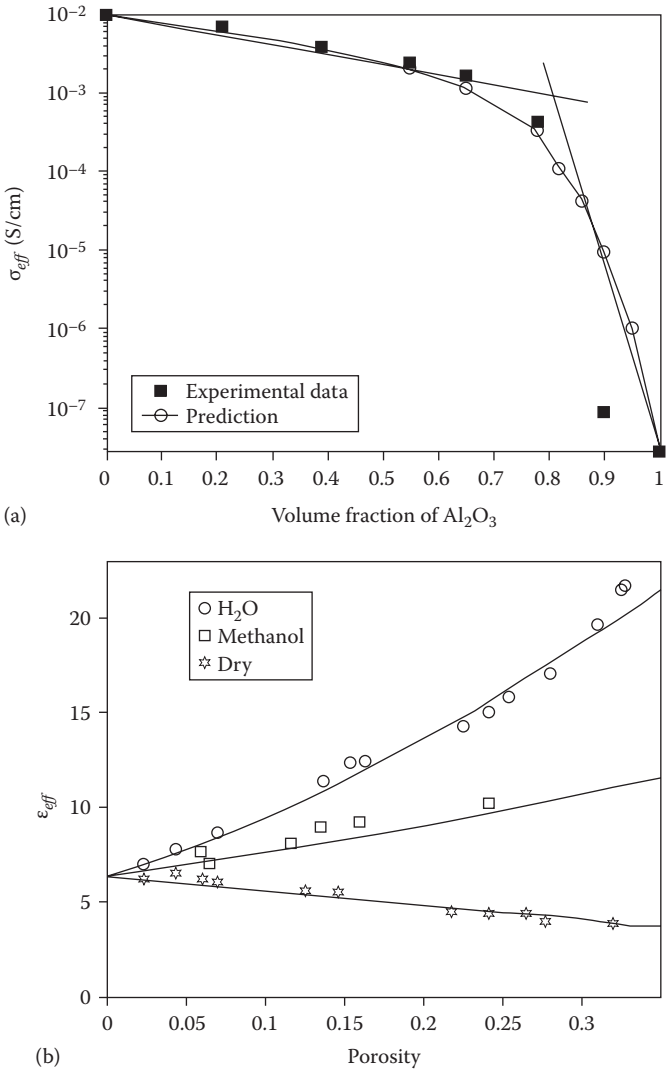

FIGURE 9.15 (a) Effective electric conductivities variation with volume fraction of Al_2O_3 for the granular Al_2O_3/Y-TZP composites. (The experimental data are from Sanchez-Herencia, A.J. et al., *J. Eur. Ceramic Soc.*, 20(10), 1611, 2000.) (b) Effective dielectric permittivity versus porosity for porous glass (two-phase cases) where $c_d = 0.01\phi^{glass}$, $\varepsilon_r^{water} = 80, \varepsilon_r^{Methanol} = 30, \varepsilon_r^{air} = 1,$ and $\varepsilon_r^{glass} = 6.4$. The symbols are the experimental data [198], and the lines are the predicted results. (Data from Sen, P.N. et al., *Geophysics*, 46(5), 781, 1981.)

9.4.1.3 Dielectric Permittivity

Consider a glass porous structure, either dry or saturated fully by a liquid, that is, a two-phase case. Sen et al. measured the dielectric constant of such porous systems in three cases: dry, water saturated, and methanol saturated.[198] We reproduce the porous structures by QSGS[8] with $c_d = 0.01\phi^{glass}$ on 200 × 200 grids and calculate the effective dielectric constant by LBM with the component dielectric properties: $\varepsilon_r^{water} = 80, \varepsilon_r^{Methanol} = 30, \varepsilon_r^{air} = 1,$ and $\varepsilon_r^{glass} = 6.4$.[198] Figure 9.15b shows the predicted effective dielectric constant versus the porosity for the three cases, compared with the experimental data. The symbols represent the experimental data[198] and the solid lines are the predicted values. The numerical results show good agreements with the experimental data.

9.4.1.4 Elastic Moduli

The theoretical models are more widely used in calculations of mechanical elastic moduli of multiphase materials. Very little effort however has been made for a completely numerical modeling of effective moduli of porous media. Since the displacement field under the pure elastic deformation can also be governed by Equation 9.1 under certain assumptions listed in Section 3.2.1, the same methodology can be extended to the estimation of the effective elastic moduli.

First, the equivalent microstructures need to be reproduced based on the experimental information. For instance, Tilbrook et al.[199] provided a series of microstructural images of alumina–epoxy composite samples. Pores are clearly observable in the composites, although the porosity details are not reported. Their results show roughly that the porosity decreases with the alumina volume fraction $\phi^{Al_2O_3}$ when $\phi^{Al_2O_3} \geq 50\%$ but increase with $\phi^{Al_2O_3}$ otherwise. Since it is reported in the study that the porosity was at most 5% in the Al_2O_3–epoxy composites, a bilinear relationship was proposed between the porosity and the volume fraction of alumina: $\varepsilon = 0.1 \cdot \phi^{Al_2O_3}$ when $v_f^{Al_2O_3} < 50\%$ and $\varepsilon = 0.1 \cdot (1 - \phi^{Al_2O_3})$ when $v_f^{Al_2O_3} \geq 50\%$. Figure 9.16 shows six generated random microstructures

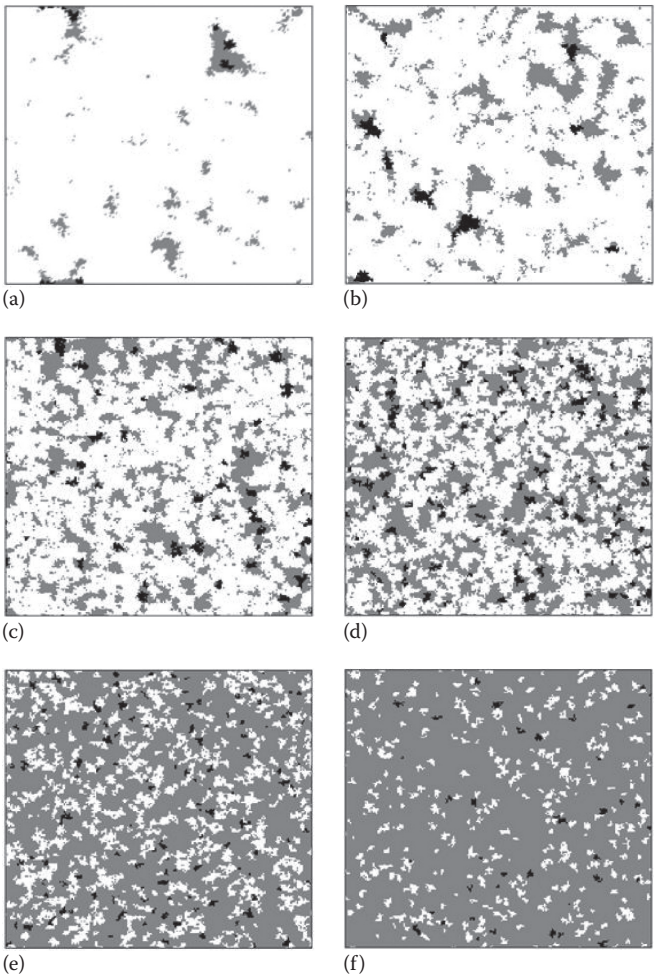

FIGURE 9.16 Reproduced three-phase microstructures of alumina–epoxy composites with pores inside. The parameters used are $c_d^{Al_2O_3} = 0.1 \cdot \phi^{Al_2O_3}(1 - \phi^{Al_2O_3})$ and $c_d^{pore} = (1 - \phi^{Al_2O_3}) \cdot c_d^{Al_2O_3}$ for $\phi^{Al_2O_3} \geq 50\%$ or $c_d^{pore} = \phi^{Al_2O_3} \cdot c_d^{Al_2O_3}$ for $\phi^{Al_2O_3} < 50\%$. The light phase is alumina, the gray phase is epoxy, and the dark spots are pores. (a) 95% alumina, 0.5% pore, (b) 85% alumina, 1.5% pore, (c) 70% alumina, 3% pore, (d) 55% alumina, 4.5% pore, (e) 25% alumina, 2.5% pore, (f) 10% alumina, 1.0% pore.

of such Al_2O_3–epoxy–pore composites using our approach on a 200 × 200 grid system, where the light phase is alumina, the gray phase is epoxy, and the dark spots are pores. Compared with the microstructure images of the actual composites (see Figure 9.1 in Ref. [199]), the generated ones here capture well the structural details and the stochastic characteristics.

Figure 9.17a provides the predicted effective Young's modulus compared with the experimental data of Tilbrook et al.[199] The properties of alumina and epoxy are listed in Table 9.3. The elastic properties of the material in pores are assigned to a small value, such as 10^{-5} GPa. For such a large contrast in the elastic moduli between the two solid components ($E^{Al_2O_3}/E^{epoxy}$ = 390:3.4), the HS bounds failed to provide tight constraints, whereas the present method still yields accurate predictions without resorting to any empirical parameters. If the porosity data were given, the prediction accuracy could be further improved. When the direction of the external force and the displacement varies from normal to parallel to the top surface, the same governing equation, Equation 9.1, is still

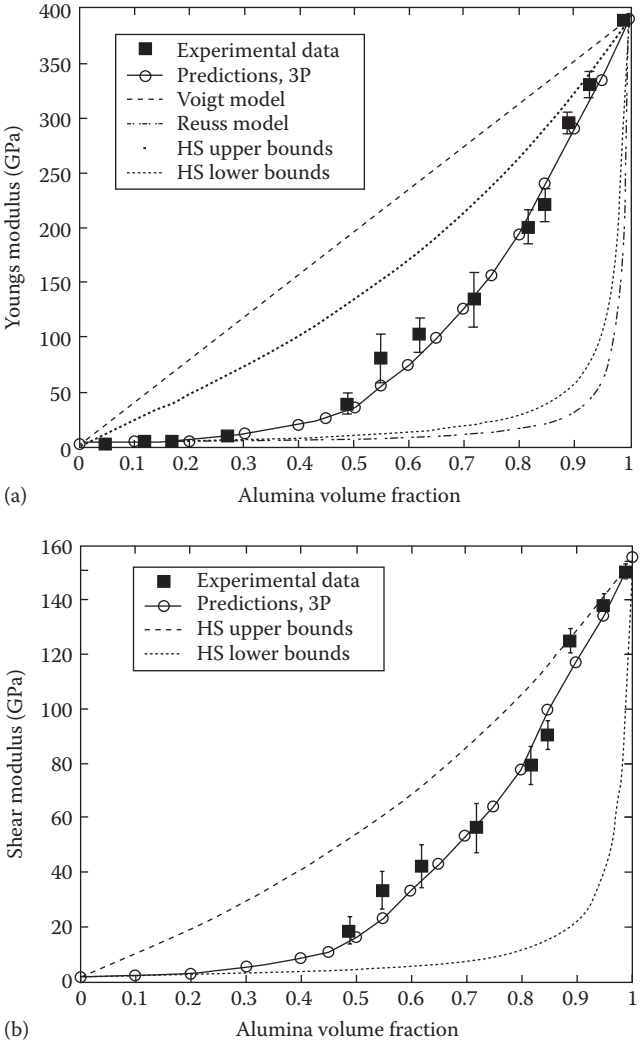

FIGURE 9.17 Comparisons of three-phase (epoxy, Al_2O_3, air) predictions of effective elastic modulus, as a function of alumina volume fraction, for epoxy–Al_2O_3 composites with experimental data[199] and various theoretical modeling results. (a) Young's modulus (b) shear modulus. (Data from Tilbrook, M.T. et al., *Mater. Sci. Eng. Struct. Mater. Prop. Microstruct. Process.,* 393(1–2), 170, 2005.)

TABLE 9.3
Elastic Properties of Composite Materials

Property	Al_2O_3	Epoxy
E (GPa)	390	3.4
K (GPa)	260	3.8
G (GPa)	156	1.26

roughly valid under the assumptions listed in Section 3.2.1 to describe the small shear displacement with varying local shear modulus of composite materials. Figure 9.17b shows the predicted effective shear modulus of the alumina–epoxy composites versus the alumina volume fraction for the same aforementioned three-phase microstructures. The used shear moduli of Al_2O_3 and epoxy are listed in Table 9.3. Again, with the dispersed pores/voids considered, the predicted effective shear modulus of the Al_2O_3–epoxy composites is consistent with the experimental measurements.[199] After Young's moduli and the shear moduli were calculated, Poisson's ratio was also calculated and compared with the experimental data.[181]

9.4.2 Structure Effects

9.4.2.1 Size Effects

Size or scale effect is a prevalent phenomenon in materials properties, that is, many properties thought to be intrinsic turn out to vary when the material dimension is altered. Several researchers have reported that the effective thermal conductivities of porous media may vary for different average pore/particle sizes by their experiments even though the components and the porosities of the media are same.[200–203] For the solid–air porous system, finer solid particles often led to a higher effective thermal conductivity at the same porosity.[202,203] The existing theoretical models can hardly explain this phenomenon, and few analyses have been found to explore the mechanism.

Here, we control the average pore/particle size by changing the values of c_d. Based on the definition of c_d, a greater value of c_d leads to a smaller average size of pores/particles at a given porosity ε. Figure 9.18a demonstrates two generated structures at $\varepsilon = 0.5$. The structure for a higher c_d looks more uniform and has a higher surface-to-volume ratio. The rough surfaces of the generated structure appear to be typical of natural granular porous media. These complexities of structure may exhaust the computational resources of classical PDE solvers but have little effect on the computational efficiency of the LBM calculations.

Based on the porous structures generated for different values of c_d, the particle size effect on the effective properties of porous media has been investigated using the present method.[8] To highlight the point without repeating the preceding contents, we used a general property below to focus on the scale effect. For the granular solid particle materials, Figure 9.18b shows the calculated effective properties versus the solid volume fraction for two different values of c_d. Suppose the solid particles have a higher value of the property at $\lambda_s = 3.0$ and the property of the other phase is much lower $\lambda_g = 0.025$. No unit is specified here since it depends on the physical type. The theoretical solutions for parallel mode and series mode are also provided in the same figure. The results show that this effective property of the random porous media lies in between the values of parallel mode and series mode and a larger average particle size leads to a lower effective property over the full range of the porosity except at 0 and 1. The largest difference between the results of the effective property at different values of c_d occurs where the solid volume fraction is somewhere within 0.5–0.8.

A recent research studied the effective thermal conductivity of granular porous materials with or without consideration of the thermal contact resistance.[204] Their results showed that the effective

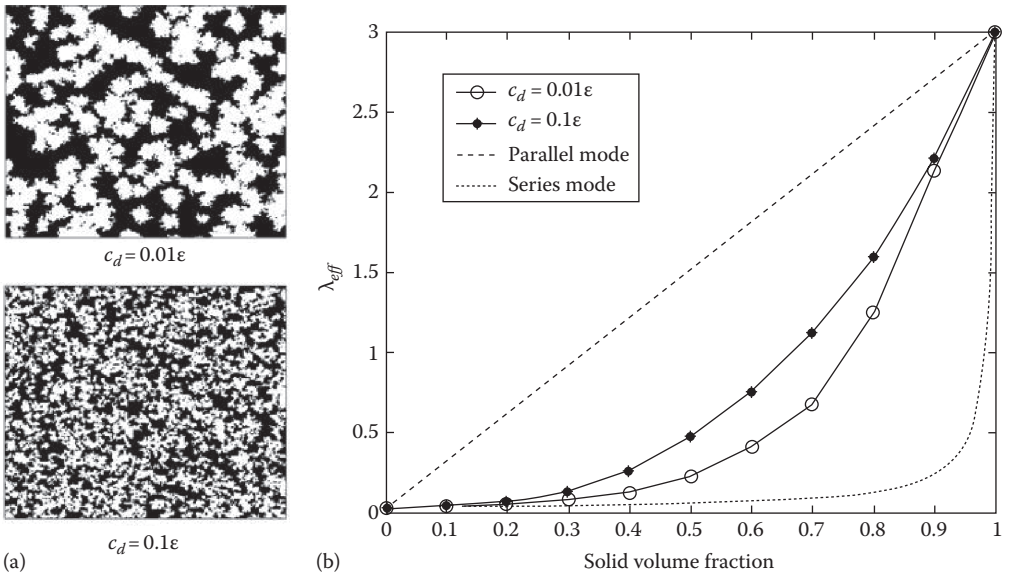

FIGURE 9.18 Isotropic microstructures and the predicted effective property versus solid volume fraction for different grain sizes at ε = 0.5. The dark is gas and the white is solid. (a) Microstructures with different grain sizes (b) predicted effective property of porous media.

thermal conductivity decreased slightly with the averaged grain size for negligible thermal contact resistance, consistent with existing observations in engineering materials studies. When the thermal contact resistance was significant, the effective thermal conductivity decreases sharply as the grain size gets smaller, which agreed with the experimental measurements on nanoporous materials where the particles were not able to contact well with each other and the resistance dominates the thermal transport.

9.4.2.2 Anisotropy Effects

Although materials with directional features are common, most previous work has focused on the isotropic cases, except some studies that attempted to bring this property–direction dependence into general formulation.[23,40,107,205] Still a few researchers have generated anisotropic porous materials by using ellipse groups with different axis lengths or orientation angles.[114] Based on the present QSGS process, an anisotropic microstructure can be easily generated by varying values of the directional growth probability, D_i, for the granular porous media. No additional efforts are needed to handle the interparticle connections. Figure 9.19a shows the generated structures for different ratio values of D_x/D_y, where D_x is along the horizontal main directions (directions 1 and 3 in Figure 9.3) and D_y is the vertical main directions (directions 2 and 4 in Figure 9.3). The growth probabilities in the four diagonal directions are always set as a quarter of the minimum value of those in the main directions. The other parameters are $c_d = 0.01$ and $\varepsilon = 0.5$, and the grid used is 200 × 200. The generated microstructures show quite different characteristics for different values of directional growth probabilities. The anisotropy increases with the D_x/D_y ratio. The directional growth probabilities are determined based on the macrostructure statistical information and can thus be estimated by the measurement data from actual porous structures.

After the anisotropic microstructures are generated with the D_x/D_y ratio varying from 0.01 to 100, we predict the effective properties along the y-direction. Figure 9.19b shows the numerical results where $\varepsilon = 0.5$, $c_d = 0.01\varepsilon$, $\lambda_s = 3.0$, and $\lambda_g = 0.025$. The results indicate that the effective properties along the y-direction decrease monotonically with the D_x/D_y ratio. For a given porosity, the effective

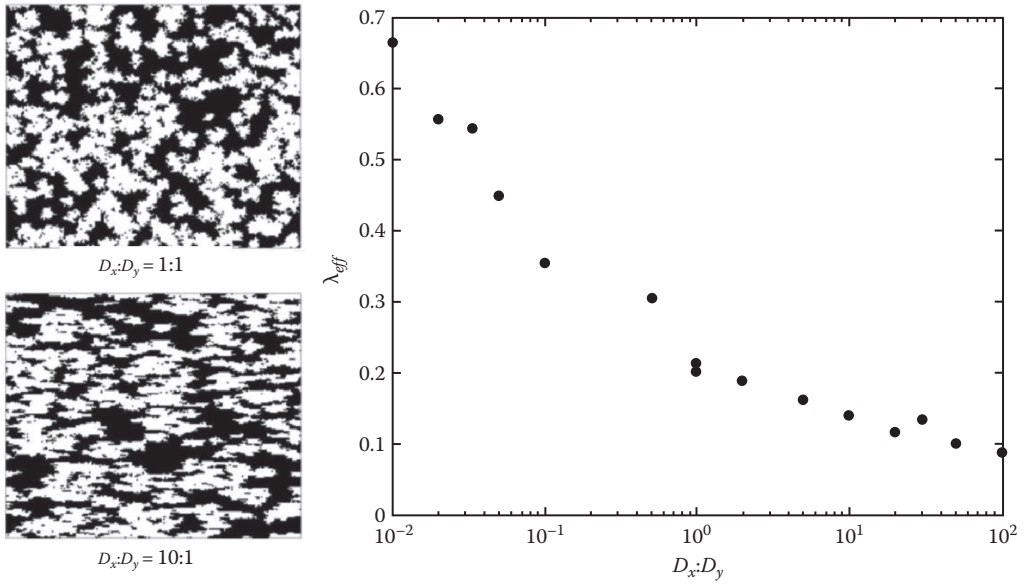

FIGURE 9.19 Microstructures and the predicted effective property of anisotropic porous media for different directional growth probabilities with $c_d = 0.01$ and $\varepsilon = 0.5$. The dark is gas and the white is solid.

property is enhanced along the direction with higher growth probability and meanwhile weakened along the direction with lower growth probability.

Another typical anisotropic structure is the aligned fiber material. The 2d2p fibrous structures have been studied, for instance, by changing the orientation angle bounds of fibers.[131] Generally, the effective properties of fibrous material would be enhanced along the alignment direction and weakened along the perpendicular direction.

9.4.2.3 Morphology Effects

The morphology here refers to the internal structural features of a material. For random microstructures, there are at least three typical structure types: granular, fibrous, and netlike. For different structure types, the effective properties usually differ drastically even for the same components and fractions. Due to the complexity of the problem, very few researches have focused on the morphology effect on the effective properties, especially, via theoretical approaches. Tekce et al.[206] measured the thermal conductivity of copper reinforced polymer composites with different filler shapes and found that the fiber shape may lead the better conductivities than the sphere and plate shapes at the same filler fractions. Since the RGG method can reproduce all the three different types of microstructures, the present mesoscopic method provides a way to study such effects.

Consider 2d2p materials with different morphologies reproduced using the RGG method on a 200 × 200 grid for different dispersed component volume fractions. Again, a nominal property without any unit is used here. The component property for the dispersed phase is set at 100 units and that for the continuous phase at 1 unit. The effective properties for the three random microstructures are compared with the theoretical bounds as well as those of a structured sphere array in Figure 9.20. The results indicate that (1) the effective properties of the sphere array case are almost the same as the HS lower bounds, for there are no contacts between the dispersed particles in both cases, and (2) the granular structure leads to the lowest properties for the same dispersed phase volume fraction. Without considering the contact resistance and connect manner, the fibrous structure seems to be the optimal one for the highest properties. Such results may have important significances for material or structure designs.

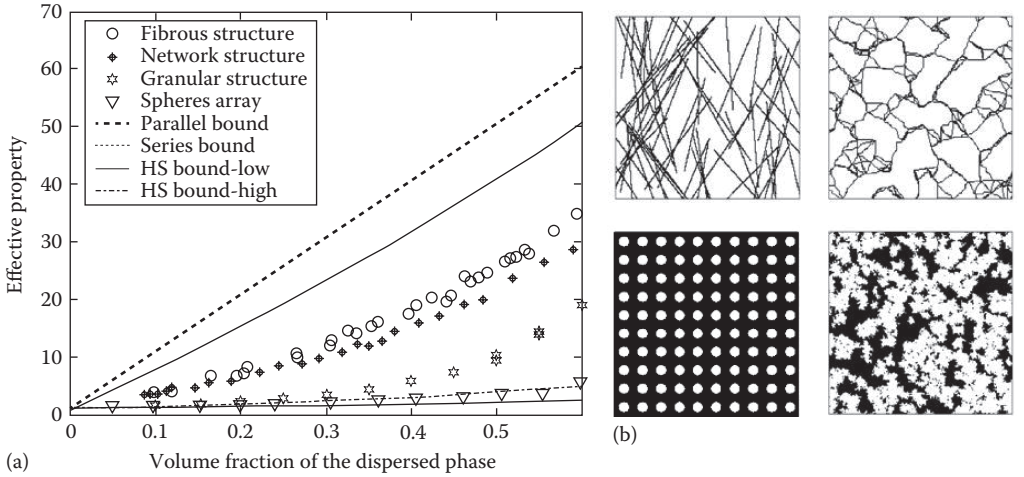

FIGURE 9.20 The effective properties versus volume fractions of the dispersed phases for different morphologies. (a) All structures are assumed isotropic. For the spheres array, 10 × 10 spheres were used; for the granular structure, $c_d = 0.01\phi^s$; for the netlike structure, $n_{node} = 4$; for the fibrous structure, the fiber's length is set 100 grid size, and the width is 1. (b) Schematics of the four structures. For fibrous and netlike structures, the dark is solid (dispersed phase); for array and granular random structures, the white is solid.

9.5 CONCLUSIONS

It has always been one of the most important but challenging goals to establish connections between the effective properties of multiphase materials and their internal microstructures. Inherently, two major issues are involved—the internal morphology of the material formed by the constituents and the interactions among themselves. However, even for simple cases, bringing these two factors into a theoretical treatment often poses a challenge. Once materials become more complex with irregular internal morphology and formed by constituents of different phases, prediction of the system behavior turns into a daunting task.

This chapter first surveys and summarizes the existing major analytical models dealing with the effective property predictions for heterogeneous materials. Besides the classical fundamental models, with or without the modified or added empirical parameters, the combined models and the network schemes of basic models have also attracted much attention in recent years. However, despite quick, often rough, estimation and/or small computation costs, the theoretical models are unable to reflect the effects of connections and interactions of the constituents on the effective properties of multiphase material systems. The capability of each model is largely empirical and the models cannot be used for new material designs.

The numerical methods using computer simulations provide an alternative in dealing with the effective properties of complex multiphase materials. After reviewing the previous numerical methods and summarizing the challenges due to complex geometries and conjugate effects, we highlight the recent progress in the mesoscopic methods that can predict more accurately and efficiently the thermal, electrical, and mechanical properties of multiphase materials with complex internal structures. Two major parts are involved: (1) a multiparameter RGG algorithm for reproducing multiphase microstructures based on the macroscopic statistical information of real structures and (2) a high-efficiency lattice Boltzmann model for solving the relevant governing equations with conservation and continuity constrains automatically satisfied for a closed system. The theoretical analysis indicates that such numerical methods are applicable to calculate effective thermal conductivity, electric conductivity, dielectric permittivity, and even elastic moduli for stable and equilibrium multiphase systems.

Various applications have validated the feasibility, effectiveness, and robustness of the mesoscopic methods by comparing the predictions with existing experimental data for different cases. Since the microstructure reconstructions are controllable by adjusting the statistical parameters, the mesoscopic numerical method has been used to investigate the effects of structure geometries and phase interactions on the effective properties for complex materials. For two-phase systems, the size effect of particles, the anisotropy effect of microstructures, and the morphology effect are therefore studied. For multiphase systems, different phase interactions, which influence the aggregations of the liquid phase, are taken into account for the effective properties of materials. By comparisons between the experimental data and the numerical results, the existing experimental techniques are also examined, concluding that the methods based on hot wire or hot probe are all 2D measurement technologies. It is also shown that for given system composition and structure, this numerical methodology is in essence a model built on sound physics principles with *prior* validity, without resorting to ad hoc empirical treatment.

ACKNOWLEDGMENTS

The author sincerely appreciates guidance and comments from Professor N. Pan and helpful discussions from Prof. S.Y. Chen, Dr. J. K. Wang, Prof. R. Zimmerman, and other colleagues. This work is financially supported by the NSFC grant (No. 51176089), the Key Basic Scientific Research Program (2013CB228301), and the Specialized Research Fund for the Doctoral Program of Higher Education of China (No. 20130002110077).

REFERENCES

1. A. Griffith, *Philosophical Transactions of the Royal Society* 1920, A221, 163–198.
2. F. T. Peirce, *Journal of Textile Institute* 1926, 17, T355–T368.
3. S. L. Bryant; K. E. Thompson, *Current Opinion in Colloid & Interface Science* 2001, 6(3), 217–222.
4. C. M. Bishop; M. Tang; R. M. Cannon; W. C. Carter, *Materials Science and Engineering a-Structural Materials Properties Microstructure and Processing* 2006, 422(1–2), 102–114.
5. H. Y. Sun; N. Pan, *Composite Structures* 2006, 74(1), 25–29.
6. H. K. Lee; S. H. Pyo, *Composites Science and Technology* 2008, 68(2), 387–397.
7. A. R. Sepaskhah; L. Boersma, *Soil Science Society of America Journal* 1979, 43(3), 439–444.
8. M. R. Wang; J. K. Wang; N. Pan; S. Y. Chen, *Physical Review E* 2007, 75(3), 036702.
9. Z. Y. Fan, *Philosophical Magazine A—Physics of Condensed Matter Structure Defects and Mechanical Properties* 1996, 73(6), 1663–1684.
10. A. A. Gusev, *Advanced Engineering Materials* 2007, 9(1–2), 117–120.
11. M. Wang; N. Pan, *Materials Science and Engineering: R: Reports* 2008, 63(1), 1–30.
12. A. Alharthi; J. Lange, *Water Resources Research* 1987, 23(4), 591–595.
13. A. R. Dexter, *Journal of Soil Science* 1976, 27(3), 267–278.
14. S. P. Friedman, *Computers and Electronics in Agriculture* 2005, 46(1–3), 45–70.
15. A. Bouguerra, *Journal of Physics D—Applied Physics* 1999, 32(21), 2797–2803.
16. J. F. V. Vincent, *Current Opinion in Solid State & Materials Science* 1998, 3(3), 228–231.
17. J. K. Carson, *International Journal of Refrigeration—Revue Internationale Du Froid* 2006, 29(6), 958–967.
18. J. K. Carson; S. J. Lovatt; D. J. Tanner; A. C. Cleland, *Journal of Food Engineering* 2004, 63(1), 87–95.
19. T. Renaud; P. Briery; J. Andrieu; M. Laurent, *Journal of Food Engineering* 1992, 15(2), 83–97.
20. J. F. VelezRuiz; G. V. B. Canovas, *Critical Reviews in Food Science and Nutrition* 1997, 37(4), 311–359.
21. N. Pan, *Physics of Fibrous Soft Matters*. Higher Education Publishing, Inc.: Beijing, China, 2005.
22. N. Djilali, *Energy* 2007, 32(4), 269–280.
23. J. G. Pharoah; K. Karan; W. Sun, *Journal of Power Sources* 2006, 161(1), 214–224.
24. S. U. S. Choi; Z. G. Zhang; W. Yu; F. E. Lockwood; E. A. Grulke, *Applied Physics Letters* 2001, 79(14), 2252–2254.
25. M. J. Biercuk; M. C. Llaguno; M. Radosavljevic; J. K. Hyun; A. T. Johnson; J. E. Fischer, *Applied Physics Letters* 2002, 80(15), 2767–2769.

26. Y. M. Chen; J. M. Ting, *Carbon* 2002, 40(3), 359–362.
27. F. Frusteri; V. Leonardi; S. Vasta; G. Restuccia, *Applied Thermal Engineering* 2005, 25(11–12), 1623–1633.
28. F. Frusteri; V. Leonardi; G. Maggio, *Applied Thermal Engineering* 2006, 26(16), 1883–1892.
29. V. V. Calmidi. *Transport Phenomena in High Porosity Metal Foams*. University of Colorado: Boulder, CO, 1998.
30. J. W. Wu; W. F. Sung; H. S. Chu, *International Journal of Heat and Mass Transfer* 1999, 42(12), 2211–2217.
31. A. Bhattacharya; V. V. Calmidi; R. L. Mahajan, *International Journal of Heat and Mass Transfer* 2002, 45(5), 1017–1031.
32. E. N. Schmierer; A. Razani, *Journal of Heat Transfer—Transactions of the ASME* 2006, 128(11), 1194–1203.
33. D. M. Wood; N. W. Ashcroft, *Philosophical Magazine* 1977, 35(2), 269–280.
34. J. E. Lugo; J. A. del Rio; J. Taguena-Martinez, *Solar Energy Materials and Solar Cells* 1998, 52(3–4), 239–249.
35. A. G. Marinopoulos; V. Vitek; J. L. Bassani, *Physica Status Solidi A—Applied Research* 1998, 166(1), 453–473.
36. R. Masson; M. Bornert; P. Suquet; A. Zaoui, *Journal of the Mechanics and Physics of Solids* 2000, 48(6–7), 1203–1227.
37. V. A. Buryachenko; N. J. Pagano, *Mathematics and Mechanics of Solids* 2003, 8(4), 403–433.
38. Z. H. Li; C. Wang; C. Y. Chen, *Computational Materials Science* 2003, 27(3), 381–392.
39. Y. J. Liu; X. L. Chen, *Mechanics of Materials* 2003, 35(1–2), 69–81.
40. M. G. Forest; X. Y. Zheng; R. H. Zhou; Q. Wang; R. Lipton, *Advanced Functional Materials* 2005, 15(12), 2029–2035.
41. A. Borbely; P. Kenesei; H. Biermann, *Acta Materialia* 2006, 54(10), 2735–2744.
42. H. Le Quang; Q. C. He, *Journal of the Mechanics and Physics of Solids* 2007, 55(9), 1899–1931.
43. S. R. Annapragada; D. Sun; S. V. Garimella, *Computational Materials Science* 2007, 40(2), 255–266.
44. G. Bonnet, *Journal of the Mechanics and Physics of Solids* 2007, 55(5), 881–899.
45. K. Honjo, *Carbon* 2007, 45(4), 865–872.
46. G. I. Giannopoulos; P. A. Kakavas; N. K. Anifantis, *Computational Materials Science* 2008, 41(4), 561–569.
47. M. Spies, *Materialprufung* 2000, 42(11–12), 445–449.
48. D. L. S. McElwain; A. P. Roberts; A. H. Wilkins, *Acta Materialia* 2006, 54(8), 1995–2002.
49. R. M. Delvecchio, *IEEE Transactions on Magnetics* 1980, 16(5), 809–811.
50. M. Jackson; C. Stern, *Journal of Microwave Power and Electromagnetic Energy* 1992, 27(2), 103–111.
51. R. Kouddane; N. Zouhal; A. Molinari; G. R. Canova, *Materials Science and Engineering A—Structural Materials Properties Microstructure and Processing* 1994, 175(1–2), 31–36.
52. J. Paul; C. Christopoulos; D. W. P. Thomas, *Electromagnetics* 1999, 19(6), 527–546.
53. S. Iwata; N. Shichijo; T. Ashino, *Materials & Design* 2001, 22(1), 77–79.
54. C. P. E. Varsamis, *Applied Spectroscopy* 2002, 56(8), 1107–1113.
55. R. M. Walser, *Introduction to Complex Mediums for Electromagnetics and Optics*. SPIE Press: Bellingham, WA, 2003.
56. K. C. Daoulas; M. Muller; M. P. Stoykovich; Y. J. Papakonstantopoulos; J. J. De Pablo; P. F. Nealey; S. M. Park; H. H. Solak, *Journal of Polymer Science Part B—Polymer Physics* 2006, 44(18), 2589–2604.
57. P. Trovalusci, *International Journal for Multiscale Computational Engineering* 2007, 5(2), VII–IX.
58. W. Y. Ching; P. Rulis, *Physical Review B* 2008, 77(3), 035125.
59. A. C. Balazs; C. Singh; E. Zhulina; Y. Lyatskaya, *Accounts of Chemical Research* 1999, 32(8), 651–657.
60. Z. M. Huang; Y. Z. Zhang; M. Kotaki; S. Ramakrishna, *Composites Science and Technology* 2003, 63(15), 2223–2253.
61. V. A. Buryachenko; A. Roy; K. Lafdi; K. L. Anderson; S. Chellapilla, *Composites Science and Technology* 2005, 65(15–16), 2435–2465.
62. E. T. Thostenson; C. Y. Li; T. W. Chou, *Composites Science and Technology* 2005, 65(3–4), 491–516.
63. F. Hussain; M. Hojjati; M. Okamoto; R. E. Gorga, *Journal of Composite Materials* 2006, 40(17), 1511–1575.
64. Q. H. Zeng; A. B. Yu; G. Q. Lu, *Progress in Polymer Science* 2008, 33(2), 191–269.
65. J. C. Maxwell, *A Treatise on Electricity and Magnetism*. Clarendon Press: Oxford, U.K., 1873.
66. C. J. F. Bottcher, *Theory of Electric Polarization*. Elsevier, 1952.
67. R. W. Zimmerman, *Journal of Petroleum Science and Engineering* 1989, 3, 219–227.

68. W. Kreher; W. Pompe, *Internal Stresses in Heterogeneous Solids*. Akademie-Verlag: Berlin, Germany, 1989.
69. C. P. Wong; R. S. Bollampally, *Journal of Applied Polymer Science* 1999, 74(14), 3396–3403.
70. M. Orrhede; R. Tolani; K. Salama, *Research in Nondestructive Evaluation* 1996, 8(1), 23–37.
71. R. Landauer, *Journal of Applied Physics* 1952, 23(7), 779–784.
72. D. A. G. Bruggeman, *Annalen Der Physik* 1935, 24(7), 636–664.
73. D. A. G. Bruggeman, *Annalen Der Physik* 1935, 24(8), 665–679.
74. L. Gao; J. Z. Gu, *Journal of Physics D—Applied Physics* 2002, 35(3), 267–271.
75. Y. Rao; J. M. Qu; T. Marinis; C. P. Wong, *IEEE Transactions on Components and Packaging Technologies* 2000, 23(4), 680–683.
76. P. N. Sen, *Geophysics* 1981, 46(12), 1714–1720.
77. K. A. Snyder; E. J. Garboczi; A. R. Day, *Journal of Applied Physics* 1992, 72(12), 5948–5955.
78. J. C. Maxwell, *A Treatise on Electricity and Magnetism*, 2nd edn. Oxford University Press: Cambridge, U.K., 1904.
79. A. Eucken, *Forschung Gabiete Ingenieur* 1940, 11(1), 6–20.
80. R. C. Landauer, 1978, Electrical transport and optical properties of inhomogeneous media, *AIP Conference Proceedings*, J. C. Garland; D. B. Tanner, (Eds.), New York.
81. D. S. McLachlan, *Journal of Physics C—Solid State Physics* 1987, 20(7), 865–877.
82. S. B. Jones; S. P. Friedman, *Water Resources Research* 2000, 36(10), 2821–2833.
83. R. Olives; S. Mauran, *Transport in Porous Media* 2001, 43(2), 377–394.
84. Y. M. Poon; F. G. Shin, *Journal of Materials Science* 2004, 39(4), 1277–1281.
85. D. A. Robinson; S. P. Friedman, *Water Resources Research* 2001, 37(1), 33–40.
86. B. Sareni; L. Krahenbuhl; A. Beroual; C. Brosseau, *Journal of Applied Physics* 1996, 80(8), 4560–4565.
87. B. Sareni; L. Krahenbuhl; C. Brosseau, *Journal of Applied Physics* 1996, 80(3), 1688–1696.
88. R. L. Hamilton; O. K. Crosser, *Industrial & Engineering Chemistry Fundamentals* 1962, 1(3), 187.
89. J. A. del Rio; R. W. Zimmerman; R. A. Dawe, *Solid State Communications* 1998, 106(4), 183–186.
90. J. B. Keller, *Journal of Mathematical Physics* 1964, 5(4), 548.
91. K. S. Mendelson, *Journal of Applied Physics* 1975, 46(11), 4740–4741.
92. C. W. Nan; R. Birringer; D. R. Clarke; H. Gleiter, *Journal of Applied Physics* 1997, 81(10), 6692–6699.
93. C. W. Nan; Z. Shi; Y. Lin, *Chemical Physics Letters* 2003, 375(5–6), 666–669.
94. M. Sahimi; G. R. Gavalas; T. T. Tsotsis, *Chemical Engineering Science* 1990, 45(6), 1443–1502.
95. K. J. Singh; R. Singh; D. R. Chaudhary, *Journal of Physics D—Applied Physics* 1998, 31(14), 1681–1687.
96. M. R. J. Wyllie; A. R. Gregory, *Petroleum Transactions AIME* 1953, 198, 103–110.
97. O. Krischer, *Die wissenschaftlichen Grundlagen der Trocknungstechnik (The Scientific Fundamentals of Drying Technology)*. Springer-Verlag: Berlin, Germany, 1963.
98. D. R. Chaudhary; R. C. Bhandari, *Journal of Physics D (British Journal of Applied Physics)* 1968, 1, 815–817.
99. J. K. Carson; S. J. Lovatt; D. J. Tanner; A. C. Cleland, *International Journal of Heat and Mass Transfer* 2005, 48(11), 2150–2158.
100. J. F. Wang; J. K. Carson; M. F. North; D. J. Cleland, *International Journal of Heat and Mass Transfer* 2006, 49(17–18), 3075–3083.
101. Y. Agari; T. Uno, *Journal of Applied Polymer Science* 1986, 32, 5705–5712.
102. A. Bouguerra, *Journal of Physics D—Applied Physics* 1999, 32(12), 1407–1414.
103. P. Lehmann; M. Stahli; A. Papritz; A. Gygi; H. Fluhler, *Transport in Porous Media* 2003, 52(3), 313–332.
104. J. E. J. Staggs, *Fire Safety Journal* 2002, 37(1), 107–119.
105. R. de Borst, *Computational Materials Science* 2008, 43(1), 1–15.
106. D. Raabe, *Modelling and Simulation in Materials Science and Engineering* 2004, 12(6), R13–R46.
107. N. Pan, *Journal of Composite Materials* 1994, 28(16), 1500–1531.
108. I. M. Young; J. W. Crawford; C. Rappoldt, *Soil & Tillage Research* 2001, 61(1–2), 33–45.
109. S. Wolfram., *A New Kind of Science*. Wolfram Media: Champaign, IL, 2002.
110. C. S. Du; D. Heldbrant; N. Pan, *Materials Letters* 2002, 57(2), 434–438.
111. C. S. Du; J. Yeh; N. Pan, *Journal of Materials Chemistry* 2005, 15(5), 548–550.
112. S. Torquato; I. C. Kim; D. Cule, *Journal of Applied Physics* 1999, 85(3), 1560–1571.
113. H. F. Zhang; X. S. Ge; H. Ye, *Journal of Physics D—Applied Physics* 2006, 39(1), 220–226.
114. L. Tacher; P. Perrochet; A. Parriaux, *Transport in Porous Media* 1997, 26(1), 99–107.
115. M. Pilotti, *Transport in Porous Media* 1998, 33(3), 257–278.
116. A. Yang; C. T. Miller; L. D. Turcoliver, *Physical Review E* 1996, 53(2), 1516–1524.
117. Y. S. Li; E. J. LeBoeuf; P. K. Basu; S. Mahadevan, *Advances in Water Resources* 2005, 28, 835–844.

118. Y. Mori; J. W. Hopmans; A. P. Mortensen; G. J. Kluitenberg, *Soil Science Society of America Journal* 2005, 69(3), 599–606.
119. A. P. Mortensen; J. W. Hopmans; Y. Mori; J. Simunek, *Advances in Water Resources* 2006, 29(2), 250–267.
120. D. S. Li; G. Saheli; M. Khaleel; H. Garmestani, *Computational Materials Science* 2006, 38(1), 45–50.
121. K. Makrodimitris; G. K. Papadopoulos; C. Philippopoulos; D. N. Theodorou, *Journal of Chemical Physics* 2002, 117(12), 5876–5884.
122. N. Losic; J. F. Thovert; P. M. Adler, *Journal of Colloid and Interface Science* 1997, 186(2), 420–433.
123. S. Torquato, *International Journal of Solids and Structures* 2000, 37(1–2), 411–422.
124. K. J. Wu; N. Nunan; J. W. Crawford; I. M. Young; K. Ritz, *Soil Science Society of America Journal* 2004, 68(2), 346–351.
125. S. Torquato, *Annual Review of Materials Research* 2002, 32, 77–111.
126. P. M. Adler, *Porous Media: Geometry and Transports*. Butterworth/Heinemann: Stoneham, MA, 1992.
127. S. Torquato, *Random Heterogeneous Materials: Microstructure and Macroscopic Properties*. Springer: New York, 2002.
128. N. Pan; P. Gibson, *Thermal and Moisture Transport in Fibrous Material*. Woodhead Publishing Ltd.: Cambridge, U.K., 2006.
129. P. Meakin, *Fractals, Scaling and Growth Far from Equilibrium*. Cambridge University Press: Cambridge, U.K., 1998.
130. M. R. Wang; N. Pan; J. K. Wang; S. Y. Chen, *Journal of Colloid and Interface Science* 2007, 311, (2), 562–570.
131. M. R. Wang; J. H. He; J. Y. Yu; N. Pan, *International Journal of Thermal Sciences* 2007, 46, 848–855.
132. M. Wang; N. Pan, *International Journal of Heat and Mass Transfer* 2008, 51(5–6), 1325–1331.
133. X. Y. He; L. S. Luo, *Physical Review E* 1997, 55(6), R6333–R6336.
134. M. Wang; S. Chen, *Journal of Colloid and Interface Science* 2007, 314(1), 264–273.
135. S. J. Eichhorn; W. W. Sampson, *Journal of the Royal Society Interface* 2005, 2(4), 309–318.
136. M. Wang; Q. Kang; N. Pan, *Applied Thermal Engineering* 2009, 29(2–3), 418–421.
137. V. V. Calmidi; R. L. Mahajan, *Journal of Heat Transfer-Transactions of the ASME* 1999, 121(2), 466–471.
138. K. Boomsma; D. Poulikakos, *International Journal of Heat and Mass Transfer* 2001, 44(4), 827–836.
139. J. F. Thovert; F. Wary; P. M. Adler, *Journal of Applied Physics* 1990, 68(8), 3872–3883.
140. D. Coelho; J. F. Thovert; P. M. Adler, *Physical Review E* 1997, 55(2), 1959–1978.
141. K. Bakker, *International Journal of Heat and Mass Transfer* 1997, 40(15), 3503–3511.
142. A. G. Fedorov; R. Viskanta, *International Journal of Heat and Mass Transfer* 2000, 43(3), 399–415.
143. A. Horvat; I. Catton, *International Journal of Heat and Mass Transfer* 2003, 46(12), 2155–2168.
144. A. Sutradhar; G. H. Paulino, *Computer Methods in Applied Mechanics and Engineering* 2004, 193(42–44), 4511–4539.
145. H. F. Zhang; X. S. Ge; H. Ye, *Modelling and Simulation in Materials Science and Engineering* 2005, 13(3), 401–412.
146. Z. F. Liu; X. H. Wang, *Journal of Computational Physics* 2013, 235, 286–301.
147. K. Karkkainen; A. Sihvola; K. Nikoskinen, *IEEE Transactions on Geoscience and Remote Sensing* 2001, 39(5), 1013–1018.
148. K. Asami, *Journal of Colloid and Interface Science* 2005, 292(1), 228–235.
149. K. Asami, *Journal of Physics D—Applied Physics* 2006, 39(3), 492–499.
150. E. Tuncer; S. M. Gubanski; B. Nettelblad, *Journal of Applied Physics* 2001, 89(12), 8092–8100.
151. I. Krakovsky; V. Myroshnychenko, *Journal of Applied Physics* 2002, 92(11), 6743–6748.
152. A. Mejdoubi; C. Brosseau, *Journal of Applied Physics* 2006, 100(9), 094103.
153. K. Sekine; C. Kuroda; N. Torii, *Colloid and Polymer Science* 2002, 280(1), 71–77.
154. K. Sekine; Y. Watanabe; S. Hara; K. Asami, *Biochimica et Biophysica Acta-General Subjects* 2005, 1721(1–3), 130–138.
155. J. P. Calame, *Journal of Applied Physics* 2006, 99(8), 2188032.
156. V. Myroshnychenko; C. Brosseau, *Physical Review E* 2005, 71(1), 016701.
157. D. X. Zhang, *Stochastic Method for Flow in Porous Media*. Academic Press: London, U.K., 2002.
158. D. Kulasiri; W. Verwoerd, *Stochastic Dynamics Modeling Solute Transport in Porous Media*. Elsevier: New York, 2002.
159. Y. Shoshany; D. Prialnik; M. Podolak, *Icarus* 2002, 157(1), 219–227.
160. S. Barta; P. Dieska, *Kovove Materialy—Metallic Materials* 2002, 40(2), 99–112.
161. W. Z. Yue; G. Tao; K. Q. Zhu, *Chinese Journal of Geophysics—Chinese Edition* 2004, 47(5), 905–910.
162. W. Z. Yue; G. Tao; K. Q. Zhu, *Chinese Journal of Geophysics—Chinese Edition* 2005, 48(1), 189–195.

163. E. K. Muhammed; H. A. Ahmet; M. Eyad, *Computers and Geotechnics* 2006, 33(8), 381–395.
164. S. Chen; G. D. Doolen, *Annual Review of Fluid Mechanics* 1998, 30, 329–364.
165. S. Succi, *The Lattice Boltzmann Equation for Fluid Dynamics and Beyond*. Oxford Science Press: London, U.K., 2001.
166. J. K. Wang. Lattice Boltzmann simulation on heat transfer and electro-osmotic flow in micro channel. PhD thesis, Tsinghua University, Beijing, China, 2006.
167. J. Wang; M. Wang; Z. Li, *Communications in Nonlinear Science and Numerical Simulation* 2008, 13(3), 575–583.
168. X. Y. He; S. Y. Chen; R. Y. Zhang, *Journal of Computational Physics* 1999, 152(2), 642–663.
169. Y. Peng; C. Shu; Y. T. Chew, *Physical Review E* 2003, 68(2), 026701.
170. J. K. Wang; M. Wang; Z. X. Li, *International Journal of Thermal Sciences* 2007, 46, 228–234.
171. X. Y. He; N. Li, *Computer Physics Communications* 2000, 129(1–3), 158–166.
172. M. Wang, *Journal of Heat Transfer—Transactions of the ASME* 2012, 134(5), 051020.
173. M. Wang; Q. Kang, *Analytical Chemistry* 2009, 81(8), 2953–2961.
174. M. Wang; Q. Kang; H. Viswanathan; B. A. Robinson, *Journal of Geophysical Research—Solid Earth* 2010, 115, B10205.
175. C. Y. Chan; R. J. Knight, *Water Resources Research* 2001, 37(4), 1099–1105.
176. X. Chen; P. Han, *International Journal of Heat and Fluid Flow* 2000, 21(4), 463–467.
177. V. Myroshnychenko; C. Brosseau, *Journal of Applied Physics* 2005, 97(4), 044101.
178. J. Y. Qian; Q. Li; K. Yu; Y. M. Xuan, *Science in China Series E—Technological Sciences* 2004, 47, 716–724.
179. C. R. Wylie; L. C. Barrett, *Advanced Engineering Mathematics*. McGraw-Hill Book Company: New York, 1982.
180. E. J. Garboczi; A. R. Day, *Journal of the Mechanics and Physics of Solids* 1995, 43(9), 1349–1362.
181. M. Wang; N. Pan, *Journal of Computational Physics* 2009, 228(16), 5978–5988.
182. M. Wang; J. K. Wang; S. Y. Chen; N. Pan, *Journal of Colloid and Interface Science* 2006, 304(1), 246–253.
183. M. Wang; N. Pan; J. K. Wang; S. Y. Chen, *Communications in Computational Physics* 2007, 2, 1055–1070.
184. G. D. Doolen, *Lattice Gas Methods for Partial Differential Equations*. Addison Wesley: New York, 1990.
185. Y. H. Qian; D. Dhumieres; P. Lallemand, *Europhysics Letters* 1992, 17(6BIS), 479–484.
186. A. D'Orazio; S. Succi, *Computational Science—ICCS 2003, Pt I, Proceedings* 2003, 2657, 977–986.
187. Q. S. Zou; X. Y. He, *Physics of Fluids* 1997, 9(6), 1591–1598.
188. H. J. Lee; R. E. Taylor, *Journal of Applied Physics* 1976, 47(1), 148–151.
189. A. K. Singh; R. Singh; D. R. Chaudhary, *Journal of Physics D—Applied Physics* 1990, 23(6), 698–702.
190. S. Fukusako, *International Journal of Thermophysics* 1990, 11(2), 353–372.
191. R. Prasher; W. Evans; P. Meakin; J. Fish; P. Phelan; P. Keblinski, *Applied Physics Letters* 2006, 89(14).
192. J. Eapen; J. Li; S. Yip, *Physical Review Letters* 2007, 98(2), 028302.
193. T. Y. Chen; G. J. Weng; W. C. Liu, *Journal of Applied Physics* 2005, 97(10), 1896094.
194. R. Singh; H. S. Kasana, *Applied Thermal Engineering* 2004, 24(13), 1841–1849.
195. W. H. Tao; H. C. Hsu; C. C. Chang; C. L. Hsu; Y. S. Lin, *Journal of Cellular Plastics* 2001, 37(4), 310–332.
196. A. J. Sanchez-Herencia; R. Moreno; J. R. Jurado, *Journal of the European Ceramic Society* 2000, 20(10), 1611–1620.
197. H. M. Yin; G. H. Paulino; W. G. Buttlar; L. Z. Sun, *Journal of Applied Physics* 2005, 98(6), 2039998.
198. P. N. Sen; C. Scala; M. H. Cohen, *Geophysics* 1981, 46(5), 781–795.
199. M. T. Tilbrook; R. Moon; M. Hoffman, *Materials Science and Engineering A—Structural Materials Properties Microstructure and Processing* 2005, 393(1–2), 170–178.
200. G. N. Dulnev; D. P. Volkov; A. B. Utkin, *Journal of Engineering Physics and Thermophysics* 1987, 52(2), 213–217.
201. V. V. Polyakov; M. A. Utemesov; A. V. Egorov, *Journal of Engineering Physics and Thermophysics* 1995, 68(5), 580–583.
202. K. Midttomme; E. Roaldset, *Petroleum Geoscience* 1998, 4(2), 165–172.
203. J. Z. Liang; F. H. Li, *Polymer Testing* 2006, 25(4), 527–531.
204. M. Wang; X. Wang; J. Wang; N. Pan, *Journal of Porous Media* 2013, 16(11), 1043–1048.
205. S. P. Friedman; S. B. Jones, *Water Resources Research* 2001, 37(12), 2929–2942.
206. H. S. Tekce; D. Kumlutas; I. H. Tavman, *Journal of Reinforced Plastics and Composites* 2007, 26, 113–121.

10 Effective Transport through Porous Media under Nonequilibrium Relaxation Conditions

*Faruk Civan**

CONTENTS

10.1 Introduction 392
10.2 Separation of Dissolved Gas from Oil and Water 393
10.2.1 Formulation 393
10.2.2 Summary 397
10.3 Displacement of Immiscible Fluid Phases in Porous Media 397
10.3.1 Relaxation Time 398
10.3.2 Correlation of Relaxation Time 405
10.3.3 Effective Saturation 407
10.3.4 Simulation of Immiscible Fluid Displacement under Relaxation Effect 409
10.3.5 Summary 411
10.4 Transport of Dispersed Wetting/Nonwetting Phases through Porous Media 412
10.4.1 Basic Processes 412
10.4.2 Simulation of Dispersed Particle Transport during Immiscible Fluid Displacement under Relaxation Effect 414
10.4.3 Summary 417
10.5 Permeability Impairment in Porous Media by Precipitate Deposition 417
10.5.1 Formulation 418
10.5.2 Simulation of Particulate Depositions under Nonequilibrium Relaxation Effects 424
10.5.3 Summary 426
10.6 Nonequilibrium Modification of the Gradient Transport Laws 428
10.6.1 Unsteady Darcy's Equation for Accelerating Flow through Porous Media 429
10.6.2 Nonequilibrium Transport in Nonhomogeneous Media Expressed by a Damped-Wave Equation 430
10.6.3 Summary 431
Nomenclature 431
References 435

* Correspondence to Faruk Civan, Mewbourne School of Petroleum and Geological Engineering, The University of Oklahoma, 100 East Boyd, SEC Room 1210, Norman, Oklahoma 73019, USA. Telephone: (405) 325-6778; FAX: (405) 325-7477; E-mail: fcivan@ou.edu.

10.1 INTRODUCTION

Although the assumption of instantaneous equilibrium conditions is often made in modeling of phenomenological processes of porous media, many natural processes nevertheless undergo a gradual change owing to the requirement of a finite time for reorganization of the fluid system and species in porous media from one equilibrium state to another. For example, the freezing and thawing of moist soil is a gradual process occurring over a temperature range (Civan and Sliepcevich, 1985; Civan, 2000a) although many previous works casually assumed instantaneous freezing and melting of water at a constant temperature, such as 0°C at 1 atm. In reality, the equilibrium conditions can never be attained during the porous media transport processes when the magnitude of the relaxation time is larger than the governing process time. Einstein (1920) formulated the kinetics of nonequilibrium relaxation processes by a simple linear kinetics relationship, referred to as a constitutive equation. However, more rigorous constitutive relationships may be required for particular processes as described in this chapter.

Multiphase fluid and suspended-particulate transport through heterogeneous porous media may be affected significantly by the nonequilibrium relaxation processes of various orders of magnitudes depending on the prevailing conditions of fluids and porous media. When the prevailing conditions do not allow the establishment of local equilibrium conditions in porous media instantaneously, the conventional formulation of porous media transport requires an accommodation for various process delays in attaining equilibrium and their effects on the overall transport processes. For example, the redistribution of a multiphase fluid system in porous media may require a certain amount of characteristic time for rearrangement of the multiphase system to respond to local variations in flow conditions (Aryana and Kovscek, 2013). As another example, solid particles separated from a solution of a solute flowing through porous media may not be able to deposit over the pore surface immediately following the formation of the particulate matter such as the paraffin crystals separated from waxy oil (Ekweribe et al., 2009, Ekweribe and Civan, 2009, Michel and Civan, 2009a,b).

This chapter provides an overview of the available approaches, some new critical modifications made by the author himself, and their applications of practical importance with examples taken from the chemical, environmental, and petroleum engineering fields. Specifically, the following topics are reviewed, formulated, and illustrated:

- Separation of dissolved gas from oil and water
- Displacement of immiscible fluid phases in porous media
- Transport of dispersed wetting/nonwetting phases through porous media
- Permeability impairment in porous media by precipitate deposition
- Nonequilibrium modification of the gradient transport laws

Delays in degasification of the liquid phases are shown to yield less free gas than predicted under the equilibrium assumption. The redistribution of fluids in porous media is shown to affect the immiscible displacement processes significantly. The dispersions of gas bubbles in liquid phases and liquid droplets in gas phase or in another immiscible liquid phase are shown to cause delays in attaining equilibrium because of the time required for pore surface deposition and mobilization and pressure pulsations caused by dispersed particles passing through the narrow pore throats and subsequent jetting, deformation, and breakage of these particles. The permeability reduction is influenced by delays in the deposition of the particulates separated from a solution of solute. It is emphasized that the ever popular Darcy's law of flow through porous media requires a correction for delays caused in the transmission of the effect of fluid viscosity from the pore surface to the body of the pore fluid during fluid motion under unsteady-state conditions.

The treatise presented in this chapter provides valuable insights into the nature and formulation of gas separation, immiscible fluid displacement, and deposition, mobilization, and transport

of dispersed fluids and particulates in porous media under nonequilibrium relaxation conditions. In addition to a comprehensive review of the previous approaches, the author also presents some improved approaches that perform better than previous approaches as demonstrated with several numerical examples.

10.2 SEPARATION OF DISSOLVED GAS FROM OIL AND WATER

The gas, oil, and water present in the porous rock formations of the petroleum reservoirs are at considerably elevated pressure and temperature conditions. Therefore, a significant portion of the gas is dissolved in the oil and water phases, while some free gas may exist if the local pressure is below the bubble-point pressure of oil and water. When the reservoir is produced by means of wells completed in the reservoir, the pressure of this three-phase fluid system is reduced when the occupied pore space for a given phase is being depleted. Consequently, some of the dissolved gas separates from the oil and water phases due to pressure decline, a process referred to as degasification, until a new equilibrium state is established. However, the flowing fluid conditions may not allow the full separation of gas necessary to reach a new equilibrium within the time involved in the flow process.

Although most modeling efforts consider instantaneously attainable equilibrium conditions for convenience and simplicity, several studies have proven that gas separation from the liquid phases across the gas/liquid interface is a gradual nonequilibrium process (Civan and Rasmussen, 2003; Civan, 2006; Michel and Civan, 2008). For gas to be transferred from the liquid phases to the gas phase through the gas/liquid interface, it first needs to diffuse toward the interface from the liquid phases, which is usually a rather slow process compared to the rate of fluid transfer through porous media. The transport of the three-phase fluid system through porous media occurs dominantly by bulk flow (convection), which is much faster than diffusive gas transfer occurring in the liquid phases. Thus, the actual gas saturation (fractional pore volume occupied by the gas phase) under the prevailing fluid conditions is usually lower than the equilibrium gas saturation. This section presents a formulation for description of a three-phase fluid system under these flowing conditions by extending the formulation presented by Civan (2006).

10.2.1 Formulation

Consider a three-phase fluid system present in a pore space of porous media as illustrated schematically in Figure 10.1. The subscripts *g*, *o*, and *w* indicate the gas, oil, and oil-field-water (brine) phases, respectively, present in porous media under the actual prevailing fluid conditions. S_g, S_o, and S_w indicate the fractional pore volumes or the saturations of the gas, oil, and water phases, respectively, occupying the pore space. For convenience, sufficiently low-pressure conditions (e.g., 1 atmosphere pressure and 25°C temperature) are considered as the standard reference conditions in the following formulation, indicated by the superscript *s*, such that all the dissolved gas are considered fully separated as the free gas from the liquid phases so that the remaining oil and water phases are referred to as the dead oil and dead water at the reference conditions, meaning they can no longer release dissolved gas. The superscripts of *stat* and *dyn* indicate the static (equilibrium) gas, oil, and water phases and the dynamic (metastable) gas, oil, and water phases, respectively. The oil-field water, indicated by subscript w, is not pure water but contains high concentrations of dissolved salts, including sodium chloride; it is referred to as the brine. The pure water, considered as a reference liquid in the definition of liquid gravity, is indicated by subscript *w**. The dry air, considered as a reference gas in the definition of gas gravity, is indicated by subscript a. In the following formulation, the vaporization of the water and oil phases into the free-gas phase is neglected to avoid further complications.

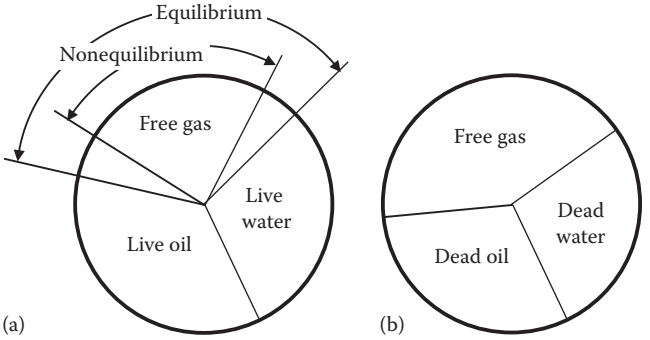

FIGURE 10.1 Partitioning of the gas, oil, and water phases in a pore space: (a) under equilibrium and nonequilibrium conditions and (b) under standard reference conditions. The free-gas phase volume is greater at equilibrium than at nonequilibrium and highest at the standard conditions. (Modified after Civan, F., *SPE Prod. Oper. J.*, 21, 98, 2006.)

The gravity of the gas, oil, and water (brine), indicated by G_g^s, G_o^s, and G_w^s, are defined as their relative density under the standard condition, given, respectively, by

$$G_g^s = \frac{\rho_g^s}{\rho_a^s} \tag{10.1}$$

$$G_o^s = \frac{\rho_o^s}{\rho_{w^*}^s} \tag{10.2}$$

$$G_w^s = \frac{\rho_w^s}{\rho_{w*}^s} \tag{10.3}$$

where $\rho_g^s, \rho_a^s, \rho_o^s, \rho_{w*}^s, \rho_w^s$ indicate the density of gas, air, oil, pure water, and oil-field water (brine) at standard conditions.

The conversion factors between the standard and the actual density for the gas, oil, and brine, indicated by B_g, B_o, and B_w and usually referred to as the formation volume factors in petroleum engineering, are given, respectively, by

$$B_g = \frac{\rho_g^s}{\rho_g} \tag{10.4}$$

$$B_o = \frac{\rho_o^s}{\rho_o} \tag{10.5}$$

$$B_w = \frac{\rho_w^s}{\rho_w} \tag{10.6}$$

where ρ_g, ρ_o, and ρ_w are the density of gas, oil, and water (brine), respectively, at actual conditions.

Further, the volumetric flow rates of the free gas, dead oil, and dead water through porous media at standard conditions are indicated, respectively, by $q_g^s, q_o^s,$ and q_w^s. Thus, the flowing

free-gas to dead-oil and dead-water (brine) to dead-oil ratios at standard conditions are given, respectively, by

$$R_{Pg/o} = \frac{q_g^s}{q_o^s} \tag{10.7}$$

$$R_{Pw/o} = \frac{q_w^s}{q_o^s} \tag{10.8}$$

Let $R_{Sg/o}^{stat}$ and $R_{Sg/w}^{stat}$ indicate the equilibrium amounts of dissolved gas, referred to as the solubility of gas, in the oil and water phases that are given in the units of the standard dissolved free-gas volume per the standard dead-liquid volume. The values of the gas solubility at any condition are obtained from empirical correlations or charts of measured data available in various references. Similarly, consider $R_{Sg/o}^{dyn}$ and $R_{Sg/w}^{dyn}$ indicate the nonequilibrium amounts of dissolved gas in the oil and water phases under the actual metastable conditions, given in the units of the standard dissolved free-gas volume per the standard dead-liquid volume.

The total density of the multiphase fluid system ρ at the actual conditions is defined as

$$\rho = \frac{m}{V} \tag{10.9}$$

The mass and the dynamic (instantaneous) and static (equilibrium) volumes of the three-phase fluid system are given on the basis of per standard unit dead-oil volume, respectively, by

$$m = \rho_a^s G_g^s R_{Pg/o} + \rho_w^s G_o^s + \rho_{w*}^s G_w^s R_{Pw/o} \tag{10.10}$$

$$V = \left(R_{Pg/o} - R_{Sg/o}^{dyn} - R_{Pw/o} R_{Sg/w}^{dyn}\right) B_g + B_o + R_{Pw/o} B_w \tag{10.11}$$

$$V_S = \left(R_{Pg/o} - R_{Sg/o}^{stat} - R_{Pw/o} R_{Sg/w}^{stat}\right) B_g + B_o + R_{Pw/o} B_w \tag{10.12}$$

The following relationship can be written for the volume fraction ε of the mobile gas phase in the multiphase fluid system filling the pore volume:

$$\varepsilon \equiv S_g - S_{gr} = \frac{x\rho}{\rho_g} = \frac{x\rho B_g}{\rho_g^s} = \frac{x\rho B_g}{\rho_a^s G_g^s} \tag{10.13}$$

where

x denotes the mass fraction of the mobile gas phase in the multiphase fluid system

S_{gr} denotes the trapped gas and/or gas adsorbed over the pore surface, which is immobilized in porous media

The mobile gas mass fraction of the three-phase fluid system under the nonequilibrium metastable conditions is given as

$$x = \frac{\rho_a^s G_g^s \left(R_{Pg/o} - R_{Sg/o}^{dyn} - R_{Pw/o} R_{Sg/w}^{dyn}\right)}{M} \tag{10.14}$$

Similarly, the mobile gas mass fraction of the three-phase fluid system under the equilibrium conditions is given as

$$x_S = \frac{\rho_a^s G_g^s \left(R_{Pg/o} - R_{Sg/o}^{stat} - R_{Pw/o} R_{Sg/w}^{stat} \right)}{M} \tag{10.15}$$

The actual total volumetric flow rate q of the three-phase fluid through porous media can be expressed by

$$q = q_o^s V \tag{10.16}$$

The total volumetric flux u of the multiphase fluid system moving through porous media is given as

$$u = \frac{q}{A} \tag{10.17}$$

where A denotes the bulk surface area of porous media normal to the flow direction.

The mass balance equation of gas phase is given as (Bilicki and Kestin, 1990, Downar-Zapolski et al., 1996)

$$\frac{\partial x}{\partial t} + u \frac{\partial x}{\partial l} = \frac{\Gamma_G}{\rho} \tag{10.18}$$

Following Einstein (1920), the rate of gas transfer from the liquid phases Γ_G into the gas phase is given by a first-order relaxation equation (Bilicki and Kestin, 1990, Downar-Zapolski et al., 1996):

$$\frac{\Gamma_G}{\rho} = -\frac{x - x_S}{\tau} \tag{10.19}$$

where τ indicates the relaxation time determined by the local condition of porous media.

Thus, for example, the transition of the nonequilibrium to equilibrium from an initial mobile gas mass fraction x^o can be expressed as the following by solving the equation resulting from the substitution of Equation 10.19 into Equation 10.18 under static conditions ($u = 0$) (Bilicki and Kestin, 1990, Downar-Zapolski et al., 1996):

$$x = x_S - \left(x_S - x^o \right) \exp\left(\frac{-t}{\tau} \right) \tag{10.20}$$

Consequently, substituting Equations 10.14 and 10.15 into Equation 10.20 yields

$$\begin{aligned} R_{Sg/o}^{dyn} + R_{Pw/o} R_{Sg/w}^{dyn} &= R_{Sg/o}^{stat} + R_{Pw/o} R_{Sg/w}^{stat} \\ &\quad - \left[\left(R_{Sg/o}^{stat} + R_{Pw/o} R_{Sg/w}^{stat} \right) - \left(R_{Sg/o}^{stat} + R_{Pw/o} R_{Sg/w}^{stat} \right)^o \right] \exp\left(\frac{-t}{\tau} \right) \end{aligned} \tag{10.21}$$

The superscript o indicates the initial conditions. This can be separated into two nonequilibrium decay equations of the oil and water phases to equilibrium, respectively, as

$$R_{Sg/o}^{dyn} = R_{Sg/o}^{stat} - \left(R_{Sg/o}^{stat} - R_{Sg/o}{}^o \right) \exp\left(\frac{-t}{\tau_{g/o}} \right) \tag{10.22}$$

and

$$R_{Sg/w}^{dyn} = R_{Sg/w}^{stat} - \left(R_{Sg/w}^{stat} - R_{Sg/w}{}^{o}\right)\exp\left(\frac{-t}{\tau_{g/w}}\right) \tag{10.23}$$

A substitution of Equations 10.22 and 10.23 into Equation 10.21 yields the value of the total relaxation time τ in terms of the individual relaxation times $\tau_{g/o}$ and $\tau_{g/w}$:

$$\exp\left(\frac{-t}{\tau}\right) = \frac{\left(R_{Sg/o}^{stat} - R_{Sg/o}{}^{o}\right)\exp(-t/\tau_{g/o}) + R_{Pw/o}\left(R_{Sg/w}^{stat} - R_{Sg/w}{}^{o}\right)\exp(-t/\tau_{g/w})}{\left(R_{Sg/o}^{stat} - R_{Sg/o}{}^{o}\right) + R_{Pw/o}\left(R_{Sg/w}^{stat} - R_{Sg/w}{}^{o}\right)} \tag{10.24}$$

Although the aforementioned formulations are straightforward, the prediction of the local relaxation time τ is a challenging issue. Nevertheless, Equation 10.24 allows for the determination of the relaxation time when experimental data are available. Then, for convenience, the retardation time can be correlated empirically by a power-law equation based on the appropriately selected local fluid conditions, such as the free-gas volume fraction (Civan, 2006):

$$\tau = \tau_o \varepsilon^{k_2} \tag{10.25}$$

where

τ_o is an empirical coefficient
k_2 is an empirical exponent

The same can be done separately for the individual relaxation times of the oil and water phases.

10.2.2 Summary

The multiphase system of gas and liquids present in porous media is at equilibrium with each other only under static (no flow) conditions. Under the flowing conditions, however, there may not be sufficient time to maintain the equilibrium conditions when the fluids flow faster than the time required to attain local pore-scale equilibrium. The degasification process is delayed because the separation of the dissolved gas molecules from the liquid phases is a diffusion-controlled process, which is much slower than the fluid transport through porous media. This causes a partial degasification of the liquid phases. Hence, less gas is liberated than the equilibrium amount. Theoretical formulation of the relevant processes can allow for estimation of the relaxation time when experimental data are available.

10.3 DISPLACEMENT OF IMMISCIBLE FLUID PHASES IN POROUS MEDIA

The redistribution of immiscible phases in porous media can be viewed from the perspectives of the pore scale or the core/formation scale. The conventional approaches such as by Buckley and Leverett (1942) assume that the redistribution of the fluid phases during displacement of immiscible fluid phases in porous media occurs instantaneously at the pore scale to maintain the local equilibrium states at all times. However, numerous studies including those mentioned in this section indicate that the redistribution of various phases in porous media requires a finite amount of time during multiphase flow through porous media. The outstanding efforts made in the literature for derivation of the constitutive relationships of nonequilibrium relaxation and various applications are reviewed here first, and then the author presents new approaches and their illustration by various examples.

10.3.1 Relaxation Time

The capillary pressure is defined as the difference between the individual pressures of the nonwetting and wetting fluid phases denoted by subscripts *nw* and *w*, respectively, as

$$p_c\left(S_w\right) = p_{nw} - p_w \tag{10.26}$$

The static capillary pressure effect occurs because of the surface tension forces applied with a contact angle θ around the perimeter of a meniscus located between the wetting (*w*) and nonwetting (*nw*) fluids in a capillary flow path. The static or equilibrium capillary pressure p_c^{stat} in a given porous media is essentially only a function of fluid saturation, for example, the wetting fluid saturation S_w considered here. The dynamic or nonequilibrium capillary pressure p_c^{dyn} in the same porous media, however, deviates from the static capillary pressure p_c^{stat} because of additional pressure drop caused by the viscous forces depending on the flow rate. Hence, Kalaydjian (1992) derived that the capillary pressure variation for a nonwetting fluid displacing a wetting fluid that is assumed incompressible for simplification purposes is given as

$$\Delta p_c \equiv p_c^{dyn} - p_c^{stat} = \tau \frac{\partial\left(\phi S_{nw}\right)}{\partial t} \tag{10.27}$$

where ϕ is the porosity and τ ($ML^{-1}T^{-1}$) is a relaxation parameter (also named as material coefficient, capillary-damping coefficient, and dynamic coefficient in the literature) that has the units of viscosity (e.g., Pa·s in the SI units). The static capillary pressure is given as

$$p_c^{stat} = \sigma C \tag{10.28}$$

where

σ denotes the interfacial surface tension

C is the curvature of the meniscus of radius *R* given as

$$C = \frac{2\cos\theta}{R} \tag{10.29}$$

The equation of mass balance of an incompressible nonwetting fluid phase without the sink/source term is given as

$$\frac{\partial\left(\phi S_{nw}\right)}{\partial t} + \nabla \cdot u_{nw} = \frac{\partial\left(\phi S_{nw}\right)}{\partial t} + \nabla \cdot \left(u f_{nw}\right) = 0 \tag{10.30}$$

where f_{nw} is the fractional nonwetting fluid function. Inferred by the aforementioned formulation, Equation 10.27 indicates $\underset{u_{nw}\to 0}{\text{Limit}}\, p_c^{dyn} = p_c^{stat}$ in view of Equation 10.30 considering the fact that a fluid phase cannot displace another fluid phase unless it has some velocity.

Kalaydjian (1992) considered a bundle of capillary tube model of the porous media flow paths formed in a constant-porosity porous media $\phi \neq \phi(t)$ (Figure 10.2). Initially, all the tubes are assumed saturated with nonwetting fluid. When wetting fluid is injected into porous media, the different diameter capillary tubes are saturated with the wetting fluid one after another depending on their entry pressures, and those saturated fully with the wetting fluid can no longer participate in change of fluid saturation in porous media. Thus, Kalaydjian (1992) expressed the mean flow q_i through a capillary flow path as being proportional to the pressure drop, which is equal to the

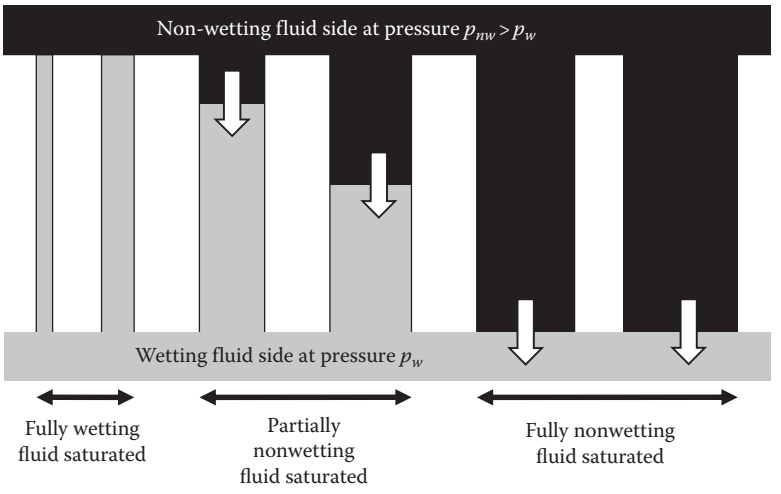

FIGURE 10.2 Schematic distribution of fluid saturations in increasing diameter tubes during drainage in a bundle of capillary tube model of wetting porous media. (Modified after Dahle, H.K. et al., *Transp. Porous Media*, 58, 5, 2005.)

dynamic capillary pressure, and inversely proportional to the fluid viscosity μ (assumed to be the same for both phases in his formulation) as $q_i \sim \left(p_c^{dyn}/\mu\right)$. Let n denote the number of capillary tubes being saturated partially and therefore still participating in the variation of fluid saturation in porous media. Then the total flow through the bundle of n participating capillary tubes can be expressed by $Q = nq_i$, which is causing saturation variation and is proportional to the variation of fluid saturation with time $Q \sim \dfrac{\partial S_w}{\partial t}$. Consequently, Kalaydjian (1992) expressed the material coefficient τ by

$$\tau \sim \frac{\mu}{p_c^{dyn}} \frac{\partial p_c^{dyn}}{\partial S_w} \sim \frac{1}{Q} \frac{\partial p_c^{dyn}}{\partial S_w} \tag{10.31}$$

Hence, Kalaydjian (1992) obtained the following expression by substituting Equations 10.31 into 10.27 modified here for a constant-porosity porous media $\phi \neq \phi(t)$:

$$\begin{aligned} \Delta p_c \equiv p_c^{dyn} - p_c^{stat} &= \tau \frac{\partial \left(\phi S_{nw}\right)}{\partial t} = \frac{1}{Q} \frac{\partial p_c^{dyn}}{\partial S_w} \frac{\partial \left(\phi S_{nw}\right)}{\partial t} \\ &= \frac{-1}{Q} \frac{\partial p_c^{dyn}}{\partial S_{nw}} \frac{\partial \left(\phi S_{nw}\right)}{\partial t} = \frac{-1}{Q} \phi \frac{\partial p_c^{dyn}}{\partial t} \end{aligned} \tag{10.32}$$

Note that S_w indicates the wetting fluid saturation, and therefore, $S_{nw} = 1 - S_w$ is the nonwetting fluid saturation:

$$S_w + S_{nw} = 1, \quad \partial S_w + \partial S_{nw} = 0 \tag{10.33}$$

Then Equation 10.32 can be rearranged in a form of a differential equation that can be solved for the dynamic capillary pressure:

$$\frac{1}{Q} \frac{\partial p_c^{dyn}}{\partial S_{nw}} \frac{\partial \left(\phi S_{nw}\right)}{\partial t} + p_c^{dyn} - p_c^{stat} = \frac{1}{Q} \phi \frac{\partial p_c^{dyn}}{\partial t} + p_c^{dyn} - p_c^{stat} = 0 \tag{10.34}$$

Therefore, Kalaydjian (1992) suggests determining the dynamic capillary pressure by solving Equation 10.34 using the change of saturation with time in dynamic experimental tests and the static capillary pressure measured separately by static tests.

Hassanizadeh and Gray (1993) generalized Equation 10.27 as the following:

$$\Delta p_c \equiv p_c^{dyn} - p_c^{stat} = \tau \frac{D^s\left(\phi S_{nw}\right)}{Dt} \tag{10.35}$$

The substantial or material derivative D^s/Dt is defined as

$$\frac{D^s}{Dt} = \frac{\partial}{\partial t} + \nabla \cdot \tag{10.36}$$

Nevertheless, Hassanizadeh and Gray (1993) and Hassanizadeh et al. (2002) also neglected the spatial derivative in their applications as well as the other researchers, including Barenblatt et al. (2003) and Aryana and Kovscek (2013).

Based on their analyses of experimental data, Dahle et al. (2005), Manthey et al. (2005), and Zhou et al. (2013) modified Equation 10.27 artificially by including an ordinate intercept τ_1 as

$$\Delta p_c \equiv p_c^{dyn} - p_c^{stat} = \tau_1 + \tau \frac{\partial\left(\phi S_{nw}\right)}{\partial t} \tag{10.37}$$

These authors essentially fitted an empirical straight line to the experimental data although theoretically $p_c^{dyn} = p_c^{stat}$ under static conditions when $\frac{\partial\left(\phi S_{nw}\right)}{\partial t} = 0$, and hence, the ordinate intercept τ_1 is theoretically zero.

Tsakiroglou et al. (2003) expressed Equation 10.27 in a dimensionless form as

$$\Delta p_c \equiv p_c^{dyn} - p_c^{stat} = \left(\frac{Ca\sigma}{L\mu_{nw}}\right)\lambda \frac{\partial\left(\phi S_{nw}\right)}{\partial t} \tag{10.38}$$

where

u is the total volumetric flux

μ_{nw} is the nonwetting phase viscosity

The capillary number is given as

$$Ca = \frac{u\mu_{nw}}{\sigma} \tag{10.39}$$

Nieber et al. (2005) proposed that there should be a general nonequilibrium relationship between the saturation and pressure of the wetting phase, which can be expressed in general functionality as

$$F\left(S_w, p_w, \frac{\partial S_w}{\partial t}, \frac{\partial p_w}{\partial t}, \ldots\right) = 0 \tag{10.40}$$

They assumed that the kinetic rheological relationship for the nonequilibrium capillary pressure–saturation relation as a special form of this equation can be expressed as

$$\Delta p_c \equiv p_c^{dyn} - p_c^{stat} = \tau\left(S_w, p_w\right)\frac{\partial\left(\phi S_{nw}\right)}{\partial t} \tag{10.41}$$

They factorized the relaxation parameter as

$$\tau\left(S_w, p_w\right) = \tau_o \tau_S\left(S_w\right)\tau_p\left(p_w\right) \tag{10.42}$$

where τ_o is a constant, and proposed the following empirical expressions:

$$\tau_S\left(S_w\right) = {S_w}^{\gamma}\left(1 - S_w\right)^{\delta} \quad \text{and} \quad \tau_p\left(p_w\right) = \left(p_* - p_w\right)^{\eta} \tag{10.43}$$

where γ, δ, and η are empirical constants, $\eta > 0$.

The deviation of capillary pressure $\Delta p_c\left(x,t\right) \equiv \left(p_c^{dyn} - p_c^{stat}\right)\left(x,t\right)$ is a field function that will be expressed here in terms of a well-defined function, referred to as a constitutive relationship based on the method of dimensional analysis. Its value at a given location should be at least a function of the volume or saturation of wetting fluid phase S_w instantaneously available inside the pore space and its volumetric rate of change $\partial S_w/\partial t$. However, other variables can also affect the absolute or intrinsic permeability of porous media K, the effective viscosity μ, the total volume flux u (= $u_w + u_{nw}$) of the two-phase fluid system, and a characteristic length L of porous media. The general functionality between these variables can be expressed by

$$f_1\left(\Delta p_c, K, L, \mu, u, S_w, \tau, \frac{\partial S_w}{\partial t}\right) = 0 \tag{10.44}$$

Applying the method of dimensional analysis (Civan, 2011), Equation 10.44 can be written in terms of the relevant dimensionless groups of variables as

$$f_2\left(\frac{K\Delta p_c}{\mu u L}, S_w, \tau\frac{\partial S_w}{\partial t}\right) = 0 \tag{10.45}$$

Applying the method of separation of variables, Equation 10.45 can be written as

$$\frac{K\Delta p_c}{\mu u L} = f_3\left(S_w\right) f_4\left(\tau\frac{\partial S_w}{\partial t}\right) \tag{10.46}$$

Now, rearrange and assume that the second function on the right can be approximated by a power-law empirical relationship as confirmed later by analyses of several experimental data so that

$$\Delta p_c = \frac{\mu u L}{K} f\left(S_w\right)\left(-\tau\frac{\partial S_w}{\partial t}\right)^n = \frac{\mu u L}{K} f\left(S_w\right)\tau^n\left(-\frac{\partial S_w}{\partial t}\right)^n = \tau^*\left(-\frac{\partial S_w}{\partial t}\right)^n \tag{10.47}$$

where

$$\tau^* = \frac{\mu u L}{K} f\left(S_w\right)\tau^n \tag{10.48}$$

Equation 10.46 can be manipulated as

$$\left(-\frac{\partial S_w}{\partial t}\right)^n = \frac{1}{\tau^*}\Delta p_c = \frac{1}{\frac{\mu u L}{K} f\left(S_w\right)\tau^n}\Delta p_c = \frac{\frac{K}{uLf\left(S_w\right)\tau^n}}{\mu}\Delta p_c = \frac{k}{\mu}\Delta p_c \tag{10.49}$$

where the new parameters are defined as

$$\tau^* = \frac{\mu}{k}, \quad k = \frac{K}{uLf\left(S_w\right)\tau^n} \tag{10.50}$$

Here the parameter k can be viewed as a rate coefficient and μ as an effective viscosity of the two-phase fluid system.

As emphasized earlier, theoretically $p_c^{dyn} = p_c^{stat}$ under static conditions when $\frac{\partial\left(\phi S_{nw}\right)}{\partial t} = 0$. Thus, the author analyzed the data of Zhou et al. (2013) according to the following equation based on Equation 10.47 derived in this chapter:

$$\Delta p_c = \tau^*\left(-\frac{\partial S_w}{\partial t}\right)^n \tag{10.51}$$

As can be seen in Figure 10.3, Equation 10.49 satisfactorily represents the data of Zhou et al. (2013), proving that there is no basis for artificial fixing according to Dahle et al. (2005), Manthey et al. (2005), and Zhou et al. (2013), which resulted in an ordinate intercept τ_1 considered in Equation 10.37 as shown in Figure 10.4. Table 10.1 presents the best estimate values of the parameter values. The fact that Equation 10.51 describes the data accurately as demonstrated in Figure 10.3 also implies that the relaxation time τ (Pa · s) depends on the fluid saturation where τ^* (Pa · s^n) relates to the relaxation time τ (Pa · s) through Equation 10.48. Note that the values of τ^* and τ reported in the first column of Table 10.1 vary significantly with water saturation. Therefore, assumption of constant relaxation time considered in many studies such as by Aryana and Kovscek (2013) is not valid.

The effective mobility of the two-phase system λ and the mobility of the wetting and nonwetting fluids λ_w and λ_{nw} are expressed, respectively, by

$$\lambda = \frac{K}{\mu}, \quad \lambda_w = \frac{Kk_{rw}}{\mu_w}, \quad \text{and} \quad \lambda_{nw} = \frac{Kk_{rnw}}{\mu_{nw}} \tag{10.52}$$

where

k_{rw} and k_{rnw} denote the relative permeability

μ_w and μ_{nw} denote the viscosity of the wetting and nonwetting fluid phases, respectively

TABLE 10.1
Parameters and Coefficients of Regressions of the Linear and Power-Law Correlations for Different Wetting Phase Saturations

Linear-Law Parameters			
S_w (Fraction)	τ (Pa·s)	τ_1 (Pa)	R^2
0.40	0.94	0.05	0.97
0.60	2.20	0.09	0.99
0.76	6.16	0.12	0.99
0.87	1.72	0.12	0.98
Power-Law Parameters			
S_w (Fraction)	τ^* (Pa·s^n)	n	R^2
0.40	0.91	1.27	0.99
0.60	2.44	1.33	1.00
0.76	10.60	1.45	0.98
0.87	1.60	1.38	1.00

Source: Data from Zhou, Y. et al., *SPE J.*, 18, 634, 2013.

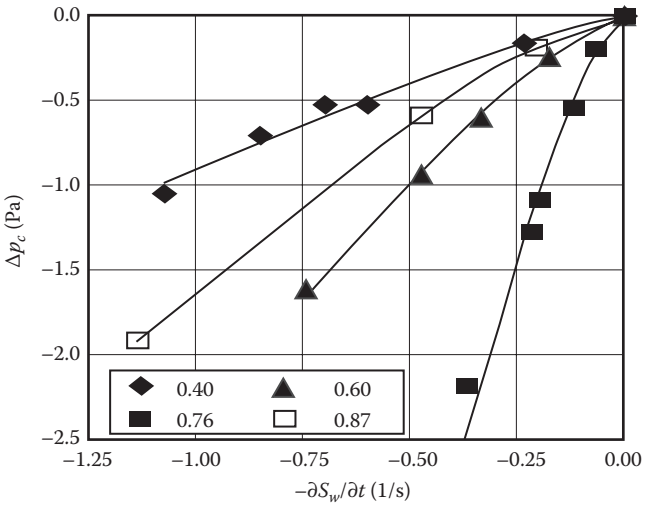

FIGURE 10.3 Power-law correlations of the data of Zhou et al. (2013) for different wetting phase saturations yield adequate regression over the whole region. (Data from Zhou, Y. et al., *SPE J.*, 18, 634, 2013.)

Inferred by Civan (2012), the effective viscosity μ of the two-phase fluid system will be formulated by means of the harmonic average mobility of the wetting and nonwetting fluids, yielding the effective mobility of the two-phase system as

$$\frac{1}{\lambda} = \frac{S_{Dw}}{\lambda_w} + \frac{S_{Dnw}}{\lambda_{nw}} \tag{10.53}$$

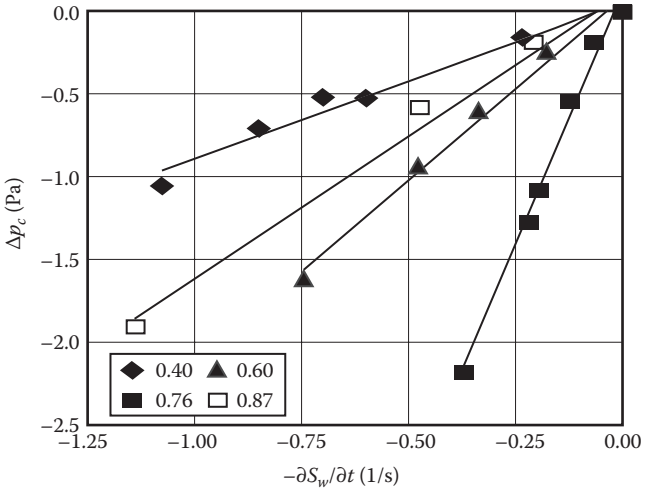

FIGURE 10.4 Linear correlations of the data of Zhou et al. (2013) for different wetting phase saturations do not provide adequate regression over the whole region. (Data from Zhou, Y. et al., *SPE J.*, 18, 634, 2013.)

which simplifies as $S_{Dw} + S_{Dnw} = 1$ as required when $\lambda = \lambda_w = \lambda_{nw}$. S_{Dw} and S_{Dnw} denote the normalized saturations of the mobile wetting and nonwetting fluids present in porous media given, respectively, by

$$S_{Dw} = \frac{S_w - S_{wi}}{1 - S_{nwi} - S_{wi}} \quad \text{and} \quad S_{Dnw} = 1 - S_{Dw} \tag{10.54}$$

where the immobile saturations of the wetting and nonwetting fluid phases are indicated by S_{wi} and S_{nwi}, respectively. Finally, Equation 10.53 can be expressed as the following by invoking Equation 10.52:

$$\mu = \frac{S_{Dw}\mu_w}{k_{rw}} + \frac{\left(1 - S_{Dw}\right)\mu_{nw}}{k_{rnw}} \tag{10.55}$$

For example, the relative permeability can be correlated empirically as a function of the normalized mobile fluid saturation using the power-law form (Brooks and Corey, 1966):

$$k_{rw} = k_{rw}^o \left(S_{Dw}\right)^n \text{ and } k_{rnw} = k_{rnw}^o \left(S_{Dnw}\right)^{m_1} = k_{rnw}^o \left(1 - S_{Dw}\right)^{m_1} \text{ or simply } k_{rnw} = k_{rnw}^o \left(S_{Dw}\right)^m \tag{10.56}$$

where the parameters k_{rw}^o, k_{rnw}^o , n, m_1, and m are determined empirically. Invoking Equations 10.56 into 10.55 results in the following expression for the effective viscosity of the two-phase fluid system:

$$\mu = \frac{S_{Dw}\mu_w}{k_{rw}^o \left(S_{Dw}\right)^n} + \frac{\left(1 - S_{Dw}\right)\mu_{nw}}{k_{rnw}^o \left(1 - S_{Dw}\right)^m} = \frac{\mu_w}{k_{rw}^o \left(S_{Dw}\right)^{n-1}} + \frac{\mu_{nw}}{k_{rnw}^o \left(1 - S_{Dw}\right)^{m-1}} \tag{10.57}$$

Consequently, a substitution of Equations 10.57 into 10.49 yields

$$\tau^* = \frac{\tau_w}{\left(S_{Dw}\right)^{n-1}} + \frac{\tau_{nw}}{\left(1 - S_{Dw}\right)^{m-1}}, \quad n > 0, \quad m > 0 \tag{10.58}$$

τ_w and τ_{nw} are the new parameters, given as

$$\tau_w = \frac{\mu_w}{k_{rw}^o k}, \quad \tau_{nw} = \frac{\mu_{nw}}{k_{rnw}^o k} \tag{10.59}$$

An empirical power-law function of the normalized wetting phase saturation as follows can be assumed for the rate coefficient defined by Equation 10.50:

$$k = k^o \left(S_{Dw}\right)^{p_1} \tag{10.60}$$

where k^o and p_1 are empirical constants. Then substituting Equations 10.59 and 10.54 into Equation 10.58 yields

$$\tau^* = \frac{\tau_w^*}{\left(S_{Dw}\right)^{n-1-p_1}} + \frac{\tau_{nw}^* \left(S_{Dw}\right)^c}{\left(1-S_{Dw}\right)^{m-1}} = \frac{\tau_w^*}{\left(S_{Dw}\right)^a} + \frac{\tau_{nw}^* \left(S_{Dw}\right)^c}{\left(1-S_{Dw}\right)^b} \tag{10.61}$$

where $a = n - 1 - p_1$ and $b = m - 1$. The new parameters are given as

$$\tau_w^* = \frac{\mu_w}{k_{rw}^o k^o}, \quad \tau_{nw}^* = \frac{\mu_{nw}}{k_{rnw}^o k^o} \tag{10.62}$$

10.3.2 Correlation of Relaxation Time

Various physically measured data (Kalaydjian, 1992, Tsakiroglou et al., 2003, Goel and O'Carroll, 2011) and simulated data (Hanspal and Das, 2012) are reported on the dynamic coefficient of various applications in the literature.

Applying the method of dimensional analysis, Das et al. (2007) correlated the relaxation time as

$$\frac{\tau\sqrt{g}}{p_e V^{1/6}} = f\left(S_w, \frac{\mu_w/\rho_w}{\mu_{nw}/\rho_{nw}}, \frac{\phi}{\lambda}, \frac{K}{V^{2/3}}\right) \tag{10.63}$$

where

g [L/T^2] is the gravitational acceleration
p_e [$ML^{-1}T^{-2}$] is the porous medium entry pressure
S_w [1] is the wetting fluid saturation
ρ_w and ρ_{nw}[ML^{-3}] are the density of the wetting and nonwetting fluids
μ_w and μ_{nw}[$ML^{-1}T^{-1}$] are the viscosity of the wetting and nonwetting fluids
ϕ [1] is porosity
λ [1] is pore-size distribution index
K [L^2] is permeability
V [L^3] is the bulk volume of porous media

However, they have not developed an empirical correlation based on Equation 10.63. Examples of empirical correlations are given in the following.

Civan (2012) demonstrated the application of Equation 10.58 for oil/water by correlating the dynamic coefficient data of Goel and O'Carroll (2011) and perchloroethylene/water over the 20°C–80°C temperatures in coarse and fine sands by correlating the dynamic coefficient data of

Hanspal and Das (2012). Civan (2012) correlated the dynamic coefficient τ (Pa·s) data of Hanspal and Das (2012) for perchloroethylene/water in coarse sand adequately in the 20°C–80°C temperature range after simplifying Equation 10.58 by invoking Equation 10.54, $\tau_{nw} = 0$, and $n-1 \equiv a_1 > 0$, $b_1 \equiv \ln\left[\tau_w \left(1 - S_{nwi} - S_{wi}\right)^{a_1}\right]$, considering τ^* (Pa·s^n) relates to the relaxation time τ (Pa·s) through Equation 10.48, and assuming that the dependence of the relaxation time τ (Pa·s) on the fluid saturation can be absorbed by these parameters in correlation of experimental data:

$$\tau = \frac{e^{b_1}}{\left(S_w - S_{wi}\right)^{a_1}} \tag{10.64}$$

Civan (2012) further correlated the parameters a_1, b_1 and the irreducible (immobile) wetting phase saturation S_{wi} of Equation 10.64 as functions of the scaled temperature $x = -\left(\frac{T - T_r}{T - T_c}\right)$, where T_c and T_r are referred to as the asymptote and reference temperatures, respectively. S_{nwi} of Equation 10.64 has a zero value. For example, the correlation of the simulated data of the dynamic coefficients of the coarse sands for the perchloroethylene/water system at various temperatures using Equation 10.64 is shown in Figure 10.5 and the best estimates of the power-law parameters are given in Table 10.2. The plot shown in Figure 10.5 is exponent and monotonic because the second term in Equation 10.58 was omitted.

As another example, the correlation of the dynamic coefficient data of Kalaydjian (1992) for an oil/water system for injection of water at 15 cc/h (4.2×10^{-9} m^3/s) into an oil-saturated limestone core using Equation 10.61 yields $\tau_w^* = 0.739$ mbar·h (2.7×10^5 Pa·s), $\tau_{nw}^* = 20.2$ mbar·h (7.3×10^6 Pa·s), $a = 0.747$, $b = 0$, and $c = 5.55$ as illustrated in Figure 10.6 as a function of the normalized wetting fluid saturation. The initial and residual oil saturations are $S_{oi} = 0.38$ and $S_{or} = 0.18$, respectively. The plot shown in Figure 10.6 is U-shaped because both terms of Equation 10.58 were included over the large saturation range.

An important point of caution is that the measurements of experimental data should be evaluated carefully. Hou et al. (2012) draw attention to the fact that the measurements of the dynamic capillary effects in porous media may need critical corrections concerning the effects of the response

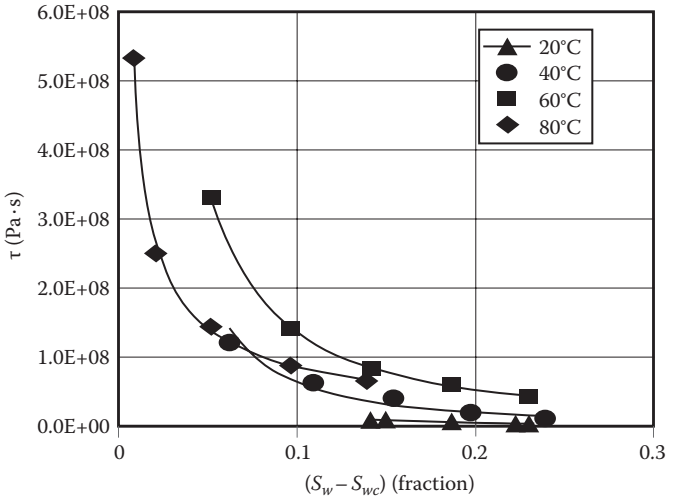

FIGURE 10.5 Power-law correlations of the data of Hanspal and Das (2012) for different wetting phase. (Data from Hanspal, N.S. and Das, D.B., *AICHE J.*, 58(6), 1951, 2012.)

TABLE 10.2
Parameters and Coefficients of Regressions of the Power-Law Correlation for Different Temperatures

T (°C)	a_1	b_1	S_{wi} (Fraction)	R^2
20	3.6E+05	1.68	0.05	0.99
40	1.3E+06	1.68	0.16	0.95
60	5.9E+06	1.36	0.20	1.00
80	1.6E+07	0.72	0.33	1.00

Source: Data from Hanspal, N.S. and Das, D.B., *AICHE J*., 58(6), 1951, 2012.

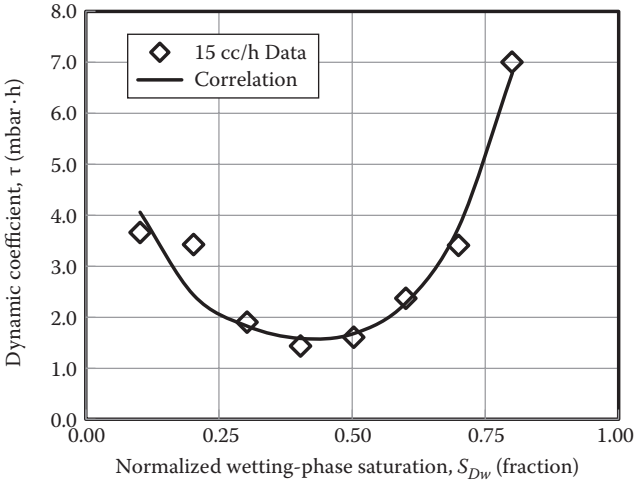

FIGURE 10.6 Correlation of the dynamic coefficient data of Kalaydjian (1992) for the oil/water system in limestone. (Data from Kalaydjian, F.J.M., Dynamic capillary pressure curve for water/oil displacement in porous media: Theory vs. experiment, Paper SPE 24813-MS, *SPE Annual Technical Conference and Exhibition*, Washington, DC, October 4–7, 1992.)

characteristics of the sensors used in these measurements. In other words, what the measurement instrument shows is not necessarily the same as the actual value.

10.3.3 Effective Saturation

Effective saturation is defined as the representative saturation that will be attained at a later time from the present time (Barenblatt et al., 2003). It is required for the evaluation of the relative permeability and capillary pressure functions to be used in the evaluation of the fractional flow function and the fluid flux function as illustrated later in this chapter. It should be emphasized that the effective saturation is not the equilibrium or static saturation. It is simply a proper value necessary to approximate the fluid flux with reasonable accuracy. However, characterization of the effective saturation is a subtle issue. As a simplistic approach, the effective saturation at a later time can be estimated by extrapolation by means of a truncated Taylor series expansion near the present time saturation value using

$$S_w^e\left(t^e\right) = S_w\left(t+\tau\right) = S_w\left(t\right) + \tau\frac{\partial S_w\left(t\right)}{\partial t} + \frac{\tau^2}{2}\frac{\partial^2 S_w\left(t\right)}{\partial t^2} + \frac{\tau^3}{3!}\frac{\partial^3 S_w\left(t\right)}{\partial t^3} + \cdots \tag{10.65}$$

Barenblatt et al. (2003) suggest that the relative permeability $k_{rw}(S_w^e)$, $k_{rnw}(S_w^e)$ and capillary pressure p_c or the dimensionless capillary pressure $J(S_w^e)$ defined by the equation

$$p_c^{stat}\left(S_w^e\right) \equiv p_{nw} - p_w = \sigma\sqrt{\frac{\phi}{K}}J\left(S_w^e\right) \tag{10.66}$$

where

σ is the surface tension

K is the permeability, should be evaluated at an effective wetting fluid saturation S_w^e, the deviation of which from the actual wetting fluid saturation can be expressed by a dimensionless function as

$$S_w^e - S_w = f\left(S_w, \tau, \frac{\partial S_w}{\partial t}\right) \tag{10.67}$$

where τ is interpreted as a redistribution time required to move from one steady state to another. This is the time elapsed during the capillary displacement of the immiscible fluid phases through porous media (Mikhailov and Nikolaevskii, 2000). Applying the dimensional analysis method, the last two terms in the argument list of Equation 10.67 can be combined as a dimensionless group as

$$S_w^e - S_w = f\left(S_w, \tau\frac{\partial S_w}{\partial t}\right) \tag{10.68}$$

Next, they consider a characteristic time of the process denoted by T and define the following dimensionless time θ_τ and redistribution time ε_τ, respectively:

$$\theta_\tau = \frac{t}{T}, \quad \varepsilon_\tau = \frac{\tau}{T} \tag{10.69}$$

Hence, expanding Equation 10.68 in terms of the significantly small parameter $\varepsilon_\tau \ll 1$ yields

$$S_w^e - S_w = f\left(S_w, \tau\frac{\partial S_w}{\partial t}\right) = f\left(S_w, \varepsilon_\tau\frac{\partial S_w}{\partial \theta_\tau}\right) \cong g\left(S_w\right)\varepsilon_\tau\frac{\partial S_w}{\partial \theta_\tau} = g\left(S_w\right)\tau\frac{\partial S_w}{\partial t} \tag{10.70}$$

Here, a new redistribution time is defined as $\tau^*(S_w) = g(S_w)\tau$, and therefore, Equation 10.70 can be written as

$$S_w^e - S_w = \tau^*\left(S_w\right)\frac{\partial S_w}{\partial t} \tag{10.71}$$

The high-order model of Aryana and Kovscek (2013) defines the effective saturation by locally moving time-averaged saturation and evaluates the integral using the Gauss–Legendre quadrature as

$$S_w^e = \frac{1}{2\tau}\int_{t-\tau}^{t+\tau} S_w(\zeta)d\zeta \cong \frac{1}{2}\left[\frac{5}{9}S_w\left(t - \sqrt{\frac{3}{5}}\tau\right) + \frac{8}{9}S_w\left(t\right) + \frac{5}{9}S_w\left(t + \sqrt{\frac{3}{5}}\tau\right)\right] \tag{10.72}$$

They obtained the following high-order model forming a new constitutive relationship upon expansion of the first and third terms on the right into the Taylor series and then truncating after the second-order term:

$$S_w^e \cong S_w\left(t\right) + \frac{\tau^2}{6}\frac{\partial^2 S_w\left(t\right)}{\partial t^2} + \frac{\tau^4}{120}\frac{\partial^4 S_w\left(t\right)}{\partial t^4} + \cdots \tag{10.73}$$

10.3.4 Simulation of Immiscible Fluid Displacement under Relaxation Effect

Aryana and Kovscek (2013) developed a formulation of unsteady-state two-phase flow through porous media by considering the nonequilibrium fluid redistribution effect. The redistribution time of the two-phase system was defined as the characteristic time of rearrangement required for the system to respond to variations in flow conditions. For this purpose, they incorporated the nonequilibrium saturation equation of Barenblatt et al. (2003) into the classical Buckley and Leverett (1942) equation for incompressible fluid displacement in a core and tested their numerical simulation approach with experimental data. Neglecting the capillary and gravity effects, the fractional water flow function f_w is given as

$$f_w\left(S_{Dw}\right) = \frac{\lambda_{nw}}{\lambda_w + \lambda_{nw}} \tag{10.74}$$

where the mobility of the wetting and nonwetting phases are given, respectively, by

$$\lambda_w = \frac{Kk_{rw}\left(S_{Dw}\right)}{\mu_w} \quad \text{and} \quad \lambda_{nw} = \frac{Kk_{rnw}\left(S_{Dw}\right)}{\mu_{nw}} \tag{10.75}$$

The Buckley and Leverett (1942) equation for the central-constant model for 1D horizontal incompressible fluid displacement is given as

$$\frac{\partial S_w}{\partial t} + \frac{u_t}{\phi}\frac{\partial f_w\left(S_w^e\right)}{\partial x} = 0 \tag{10.76}$$

where the fractional water function f_w is evaluated at the effective saturation S_w^e and not the instantaneous saturation S_w. As discussed previously, Barenblatt et al. (2003) expressed the deviation of the effective saturation at a later time from the present actual saturation for the forward-constant model as

$$S_w^e - S_w = \tau\frac{\partial S_w}{\partial t} \tag{10.77}$$

whereas truncated after the second-order term, the Aryana and Kovscek (2013) high-order model given by Equation 10.73 yields a constitutive relationship as

$$S_w^e \cong S_w\left(t\right) + \frac{\tau^2}{6}\frac{\partial^2 S_w\left(t\right)}{\partial t^2} \tag{10.78}$$

where the effective saturation S_w^e is a local time-averaged saturation value.

The Buckley and Leverett (1942) model is referred to as the central-constant model by Aryana and Kovscek (2013) where the flux depends on the present solution, the Barenblatt et al. (2003) model as the forward-constant model by Aryana and Kovscek (2013) where the flux depends on the future solution, and the Aryana and Kovscek (2013) model as the high-order model where the flux depends on both the past, present, and future solutions. Aryana and Kovscek (2013) discretized the nonlinear Equations 10.76 and 10.77 referred to as the forward-constant model and Equations 10.76 and 10.78 of the high-order model numerically using an implicit finite-difference method and solved the resulting set of nonlinear algebraic equation by Newton's method.

The data of one of their drainage tests conducted at $T = 20°C$ considered for numerical simulation can be summarized as follows: The number of grid blocks $N = 1000$; time increments $\Delta t = 5.26 \times 10^{-4}$ PVI (pore volumes injected referring to the number of porous media pore-volume equivalence of the cumulative volume of fluid injected into the sample); core length $L = 60$ cm (0.6 m); core diameter $D = 5.08$ cm (0.0508 m); porosity $\phi = 0.19$; permeability $K = 254$ md (2.54×10^{-7} m^2); total volumetric flux $u_t = u_w + u_{nw} = 0.0061$ PVI/min where u_w and u_{nw} denote the wetting and nonwetting phase volumetric fluxes, respectively; the parameters of the Corey-type relative permeabilities (Equation 10.56) $n = m_1 = 2$, $k^o_{rnw} = 0.85$, $k^o_{rw} = 0.25$; viscosity $\mu_{nw} = 0.92$ cp (9.2×10^{-4} Pa·s), $\mu_w = 1.05$ cp (1.05×10^{-3} Pa·s); and the residual saturations $S_{rnw} = 0.3$, $S_{rw} = 0.25$. The core is initially saturated with the wetting fluid, and the nonwetting fluid is injected at a rate of $q = 1.41$ cc/min (2.35×10^{-8} m^3/s), which leads to a total volumetric flux of $u_t = 1$ m/day (1.16×10^{-5} m/s).

Their numerical solutions obtained using the aforementioned data with both the forward-constant model and the high-order model show that the front disperses more as the value of the redistribution time increases although its effect is reduced in the high-order model. The front sharpens as the value of the redistribution time decreases and approaches to a shock front as the redistribution time approaches to zero, which represents the solution of the original Buckley and Leverett (1942) model. This behavior of solution is illustrated in Figure 10.7, which shows the effect of the redistribution time on the nonwetting fluid phase distribution profiles for 0.03 PVI pore volumes of nonwetting phase injected into the wetting fluid saturated porous media based on the forward-constant model, for example.

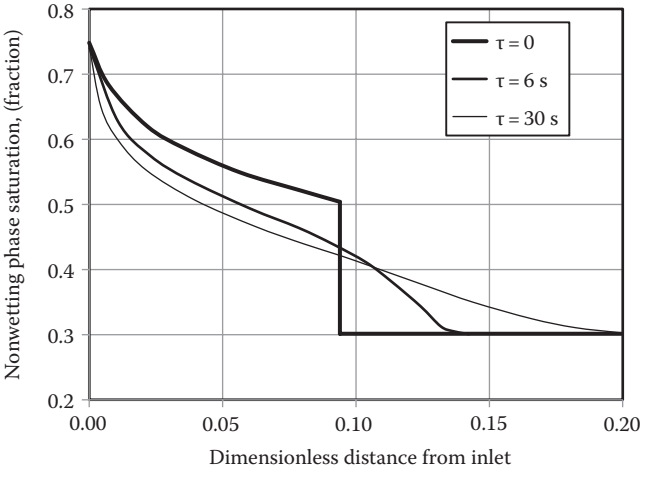

FIGURE 10.7 Effect of the redistribution time on the nonwetting fluid phase distribution profiles for 0.03 PVI pore volumes of nonwetting phase injected into the wetting fluid saturated porous media based on the forward-constant model. (Replotted with modifications of their Fig. 3 after Aryana, S.A. and Kovscek, A.R., *Transp. Porous Media*, 97, 373, 2013.)

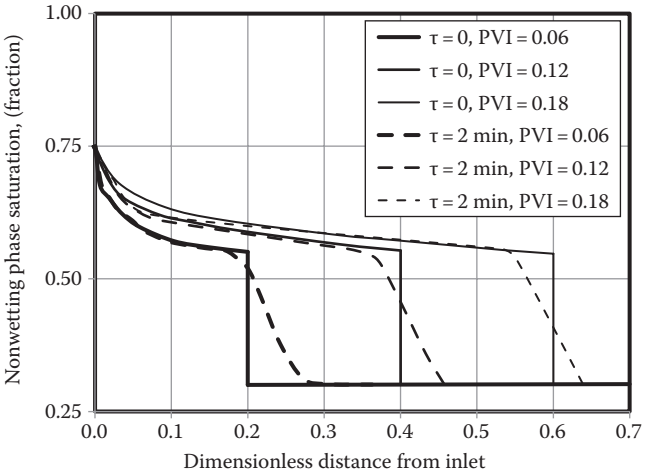

FIGURE 10.8 Effect of the redistribution time τ on the nonwetting fluid phase distribution profiles for 0.06, 0.12, and 0.18 PVI pore volumes of nonwetting phase injected into the wetting fluid saturated porous media based on the high-order model. (Replotted with modifications of their Fig. 10b after Aryana, S.A. and Kovscek, A.R., *Transp. Porous Media*, 97, 373, 2013.)

The comparison of their simulation results by experimental data reveals that the high-order model represents the experimental data more accurately. The value of the redistribution time remained almost constant in their experimental tests around $\tau = 2$ min for the high-order model as determined from the experimental data to be the half of the time required for the saturation front to move through a point along the core sample. However, the value of the redistribution time used for the forward-constant model was determined as $\tau = 0.5$ min in an effort to match the simulation results to the experimental data. Nevertheless, their results indicate that the forward-constant model is unsatisfactory, but the high-order model is capable of describing the experimental data satisfactorily. Figure 10.8 shows the effect of the redistribution time τ on the nonwetting fluid phase distribution profiles for 0.06, 0.12, and 0.18 PVI pore volumes of nonwetting phase injected into the wetting fluid saturated porous media based on the high-order model. Their calculations assumed constant values for the redistribution time. Future studies should consider the variable redistribution times determined from the functional relationships similar to Equation 10.61.

10.3.5 Summary

The redistribution of multiphase fluid systems at the pore scale may take a longer time than the time of fluid transport through porous media under unsteady conditions. Attaining pore-scale local equilibrium requires a sufficiently long time referred to as the relaxation or delay time. This time for multiphase fluid systems is commonly estimated by a relationship of the difference between the dynamic and static capillary pressures. However, determination of the delay time is still a subtle issue. Presently, it is estimated by means of a constitutive equation inferred by various theoretical arguments. Under static or equilibrium conditions, the fluid saturation does not vary with time, and therefore, the dynamic pressure approaches the static pressure. Thus, the author expressed the deviation between the dynamic and static capillary pressures as an empirical power-law function of the fluid saturation change with time where the power-law coefficient represents the relaxation time. It is shown that the relaxation time depends on the fluid saturation and temperature although most previous studies assumed constant values. Next, it was pointed out that the flux term of the immiscible fluid transport equation should be evaluated at an effective saturation and not at the present time dynamic saturation. The effective saturation is defined as

a proper saturation value required for accurate calculation of a representative value for the flux term. The best available method relies upon the locally moving time-average saturation value for the effective saturation. Comparison of numerical predictions with limited experimental data appears to support this approach and indicates an approximately constant relaxation time value. However, other data reported in the literature and analyzed by the author reveal the dependency of the relaxation time to fluid saturation and temperature. Therefore, further research is needed to clarify this issue.

10.4 TRANSPORT OF DISPERSED WETTING/NONWETTING PHASES THROUGH POROUS MEDIA

Mikhailov and Nikolaevskii (2000) suggested that the redistribution times would be different for gas bubbles in liquid and liquid droplets in gas when a phase is dispersed in another during transport through porous media. Thus, jetting of dispersed particles such as deforming gas bubbles and transport of deforming liquid droplets through the pore throats cause pressure oscillations and create a velocity variation due to frequent convective acceleration/deceleration (Blick and Civan, 1988). This is similar to the transport of suspensions of elastic gel particles through pore throats, which causes a change in permeability and therefore pressure drop (Al-Ibadi and Civan, 2013). In the following, first, the conditions for formation and mobilization of the dispersed phases are determined by means of several dimensionless numbers, and then the relevant transport processes are formulated under the relaxation effect (Civan, 2014a).

10.4.1 Basic Processes

The wetting fluid covers the pore surface as a thin stationary immobile layer and the nonwetting fluid fills the rest of the space available in pore volume. When the nonwetting phase is trapped inside the wetting phase as a discontinuous phase, like dispersion of particles such as the gas bubbles in oil and water phases, and water droplets in gas or oil phases, the dispersed particles cannot be mobilized until they can be connected to form a continuous phase. An effective measure of the relative tendency of flow of a dispersed fluid particle present in another continuous fluid phase can be expressed by its apparent mobility as the following (Civan, 2014a):

$$\lambda = \frac{\text{Effective permeability}}{\text{Fluid viscosity}} = \frac{K_e}{\mu} = \frac{Kk_r}{\mu} \tag{10.79}$$

where K_e and k_r are the effective and relative permeabilities of the fluid phase.

Dispersion of one fluid in another may occur, for example, during injection of a surfactant dissolved in water into an oil reservoir (Islam and Ali, 1994). Pore and pore-throat size distributions, capillary forces, and pressure gradient are the important factors affecting this phenomenon. As the gas bubbles dispersed in a liquid phase or the liquid droplets of one phase in an immiscible another liquid phase pass through narrow pore throats, they can deform and/or break and thus induce pressure pulsation and oscillation (Mikhailov and Nikolaevskii, 2000). The Weber number, given in the following, characterizes the conditions favorable for the dispersed particles to break into smaller particles of diameter d by the ratio of the carrier fluid-phase dynamic pressure (ρu^2) at a volumetric flux of u to the surface tension σ to being greater than the unity (Mikhailov and Nikolaevskii, 2000):

$$We = \frac{\rho u^2 d}{\sigma} \tag{10.80}$$

The following mobility criterion determines whether the dispersed phase particles can possibly pass through the pore throats (Mikhailov and Nikolaevskii, 2000):

$$M = \frac{\text{Retaining capillary forces}}{\text{Gravity force + Hydrodynamic buoyancy force + Acoustic dynamic pressure}} = \frac{\sigma\rho\cos\theta}{\left(\gamma_{sp}\sin\alpha + \frac{\partial p}{\partial x} + A_p\rho\omega^2\right) rl\Delta\rho} \tag{10.81}$$

where

- σ is the surface tension
- ρ is the density of the dispersed particle
- θ is the wetting phase contact angle
- γ_{sp} is the specific weight
- α is the angle of inclination of flow direction
- r and l are the characteristic dimensions of an ellipsoidal shape-approximated dispersed particle that vary by deformation of dispersed phases as they pass through the pore throats so that $d = (rl)^{1/2}$ is the average particle diameter
- $\Delta\rho = |\rho_w - \rho_{nw}|$ denotes the absolute value of the difference between the dispersed particle density and the carrier fluid phase density
- ω and A_p are the frequency and the amplitude, respectively, of the pressure oscillations

When $M = 1$, the retaining capillary force equals to the sum of the hydrostatic, hydrodynamic buoyancy, and acoustic—dynamic—pressure forces (or vibration forces, $A_p\rho\omega^2$), Equation 10.81, and therefore (Civan, 2014a),

$$\sigma\rho\cos\theta = \left(\gamma_{sp}\sin\alpha + \frac{\partial p}{\partial x} + A_p\rho\omega^2\right) rl\Delta\rho \tag{10.82}$$

However, the critical value of mobility has been determined to be $M \leq 0.3$ for the vibration forces to be important (Mikhailov and Nikolaevskii, 2000).

Interactions of various immiscible fluid phases with each other as well as with the pore wall during fluid displacement in heterogeneous porous media can cause significant metastability and hysteresis effects (Anton and Hilfer, 1999). The formation of wetting fluid blockage in porous media affects the kinetics of wetting fluid mobilization and alteration of the relative permeability and capillary pressure functions (Bazin et al., 2010). The nonwetting fluid phase entrapment occurring during wetting fluid invasion (imbibition) causes a capillary pressure and relative permeability hysteresis (Civan, 2014a). The drainage of the wetting fluid out of the porous media can take a long time when the mobility of the nonwetting fluid phase ($\lambda_{nw} = Kk_{rnw}/\mu_{nw}$) is unfavorably less than the mobility of the wetting fluid phase ($\lambda_w = Kk_{rw}/\mu_w$) (Civan, 2014a). Thus, the transport of the nonwetting fluid phase can occur only when the applied drawdown pressure can overcome the capillary end effect (Bazin et al., 2010). The capillary end effect is the discontinuity that occurs in the fluid saturations as the multiphase fluids pass across the discontinuity surface located between two different permeability media under the condition of the capillary pressure continuity because the pressures of the individual fluid phases must be the same on both sides of the discontinuity surface (Bear, 1988).

Considering a core-scale representation by means of averaging over an ensemble of pore, the microscopic capillary number Ca_{vc} is the ration of the viscous forces (pressure gradients) and interfacial tension forces affecting the mobilization of dispersed phases (Craft et al., 1991):

$$Ca_{vc} = (\text{A constant})\frac{v\mu_w}{\sigma_{nw}} = (\text{A constant})\frac{K}{\sigma_{nw}\phi}\left(-\frac{\partial p}{\partial x}\right) \tag{10.83}$$

where

v is the fluid velocity (volumetric flux u divided by porosity ϕ)
K is the permeability
p is the fluid pressure
μ is the viscosity
σ is the interfacial tension

However, as emphasized by Anton and Hilfer (1999), only the macroscopic capillary numbers given as $\bar{C}a_w = \mu_w q/\left(p_b Kl\right)$ for the wetting phase and as $\bar{C}a_{nw} = \mu_{nw} q/\left(p_b Kl\right)$ for the nonwetting phase can adequately express the macroscopic balance between the viscous and capillary forces and therefore yield a breakpoint for continuous displacement at $Ca = 1.0$. The symbol q denotes the volumetric flow rate; $P_b = P_c[(S_{wi} - S_{nwi} + 1)/2]$, the capillary pressure at the midsaturation value; $P_c(S)$, the equilibrium capillary pressure function, $l = (L_x L_y L_z)^{1/3}$, the geometric average length of porous media where L_x, L_y, and L_z are the dimensions of porous media in the x-, y-, and z-Cartesian directions, respectively; $K = (K_x K_y K_z)^{1/3}$, the geometric average permeability where K_x, K_y, and K_z are the permeability of anisotropic porous media in the x-, y-, and z-Cartesian directions, respectively; and S_{wi} and S_{nwi}, the irreducible wetting phase and residual nonwetting phase saturations, respectively.

The residual (immobile) nonwetting phase saturation S_{nwi} decreases with increasing macroscopic capillary number (Anton and Hilfer, 1999). Civan (2014a) correlated the nonwetting phase trapped saturation versus porosity data of Iglauer et al. (2011) with a coefficient of regression of $R^2 = 0.86$ by

$$S_{nwi} = A\log\left(\frac{C}{\phi} - 1\right) + B \tag{10.84}$$

where the best estimate parameter values are given as $A = 0.616$, $B = -0.182$, and $C = 1.7$. Note that the dependence of the residual saturation on the capillary number can be shown readily although this equation is expressed in porosity. This is apparent as the macroscopic capillary number given previously for the nonwetting phase by Anton and Hilfer (1999) can be expressed as a function of the porosity ϕ by means of the relationship of the permeability K to the porosity ϕ, for example, by applying Equation 10.137, given later.

10.4.2 Simulation of Dispersed Particle Transport during Immiscible Fluid Displacement under Relaxation Effect

Mikhailov and Nikolaevskii (2000) formulated the transport of a nonwetting/wetting fluid system through porous media where the deposition and mobilization of dispersed particles of one fluid phase in another (e.g., gas bubbles in water and water droplets in gas) over the pore surface creates nonequilibrium relaxation conditions. Further, pressure drop fluctuations occur when deformable dispersed phases are forced to pass through the pore throats, creating pulsating flow conditions. The particles (gas bubbles and oil or water droplets) of the dispersed fluid phase can deposit over the pore surface and be mobilized subsequently during flow through porous media. The capillary displacement of a fluid phase through porous media including the time for deposition and mobilization of dispersed particles occurs with a finite relaxation time. The relaxation time is taken as $\tau_i = d_i/u_i$ for each i-phase

as the ratio of the effective size of the dispersed fluid phase particles (gas bubbles or liquid droplets) to the volumetric flux of the fluid phase u_i. This means that the deposition of the stationary (immobile) portion of i-phase depends on the volumetric flux of this phase through porous media.

In the following formulation, the symbol S denotes the instantaneous saturation value of the displacing phase. S^* is the value of the dynamic threshold phase saturation that represents the stationary phase saturations (immobile-phase saturations like the adsorbed and/or trapped gas, residual oil, or bound water) of the dispersed phase deposited in porous media. This amount obviously varies with time as the dispersed phase is continuously deposited and mobilized during flow through porous media. S^+ is the value of the equilibrium threshold phase saturation that represents the constant value of the stationary phase saturations attained under equilibrium conditions. The change in the dynamic threshold saturation S^* represents the portion of the residual or bound fluids that is the net removal from the pore surface during the deposition and mobilization of the dispersed fluid particles. Consequently, considering the time elapsed for deposition and mobilization of the dispersed fluid particles, the kinetics equation (nonequilibrium) of the dynamic threshold phase saturation variation by net deposition of the dispersed fluid particles is given as (Mikhailov and Nikolaevskii, 2000), written according to Civan (2014a)

$$\frac{\partial S_i^*}{\partial t} = \frac{S_i^+ - S_i^*}{\tau_i}; \quad i = 1 \text{ (nonwetting) or } 2 \text{ (wetting)} \tag{10.85}$$

Next, consider the permeability of the various phases represented by empirical equations. The dispersed fluid particles gain higher mobility relative to their carrier phases, and therefore, their relative permeability curve becomes convex, while the pure fluid phase relative permeability curve is concave as pointed out by Mikhailov and Nikolaevskii (2000). Dynamic phase relative permeability depends on the deposition and mobilization of the stationary dispersed phase. The permeability of the fluid phases varies as a result of the deposition and mobilization of the dispersed phases to form a stationary (immobile) phase over the pore surface, approximated by empirical power-law expressions for the nonwetting phase as

$$k_{r1}\left(S_1, S_1^*\right) = 0, \quad 0 \le S_1 \le S_1^* \tag{10.86}$$

But

$$k_{r1}\left(S_1, S_1^*\right) = \left[\frac{S_1 - S_1^*}{1 - S_1^+}\right]^N, \quad S_1^* \le S_1 \le 1 \tag{10.87}$$

where N is an empirical exponent. Similarly, for the wetting phase,

$$k_{r2}\left(S_2, S_2^*\right) = \left[\frac{\left(1 - S_2^*\right) - S_2}{1 - S_2^+}\right]^N, \quad 0 \le S_2 \le \left(1 - S_2^*\right) \tag{10.88}$$

But

$$k_{r2}\left(S_2, S_2^*\right) = 0, \quad \left(1 - S_2^*\right) \le S_2 \le 1 \tag{10.89}$$

The sum of the saturations of the nonwetting and wetting phases equals to one:

$$S_n + S_w = 1.0 \tag{10.90}$$

The modified Darcy's law is given as

$$u_i = -\frac{K}{\mu_i} k_{ri}\left(S_i, S_i^*\right)\frac{\partial p_i}{\partial x} \tag{10.91}$$

The fractional flow function of the wetting phase is given as

$$f_1\left(S_1, S_1^*, S_2^*\right) = \frac{k_{r1}\left(S_1, S_1^*\right)}{k_{r1}\left(S_1, S_1^*\right) + \dfrac{\mu_1}{\mu_2} k_{r2}\left(S_1, S_1^*\right)} \tag{10.92}$$

The additional relationships are

$$u_1 = u_t f_1\left(S_1, S_1^*, S_2^*\right)$$

$$u_2 = u_t f_2\left(S_1, S_1^*, S_2^*\right)$$

$$u_1 + u_2 = u_t$$

$$f_2\left(S_1, S_1^*, S_2^*\right) = 1 - f_1\left(S_1, S_1^*, S_2^*\right) \tag{10.93}$$

Then the 1D horizontal incompressible fluid displacement is given by the following modified Buckley and Leverett (1942) equation:

$$\frac{\partial S_1}{\partial t} + \frac{u_t}{\phi}\frac{\partial f_1\left(S_1, S_1^*, S_2^*\right)}{\partial x} = 0 \tag{10.94}$$

Mikhailov and Nikolaevskii (2000) demonstrated the application of the aforementioned formulation for gas injection into a trapped gas containing water-saturated porous formation using the following data. The relative permeability exponent is $N = 3.5$, the total volumetric flux is $u_t = 1.0 \times 10^{-5}$ m/s, the porosity is $\phi = 0.2$, the viscosity ration is $\frac{\mu_1}{\mu_2} = 0.01$, and the dispersed particle diameter is $d_i = 1.0$ mm. The initial threshold phase saturation conditions are

$$S_1^* = 0.3, \quad S_2^* = 0.4, \quad 0 \le x \le L, \quad t = 0 \tag{10.95}$$

The injection and outlet boundary conditions are

$$S_1 = 0.7, \quad x = 0, \quad t > 0 \tag{10.96}$$

$$S_1 = 0.1, \quad x = L, \quad t > 0 \tag{10.97}$$

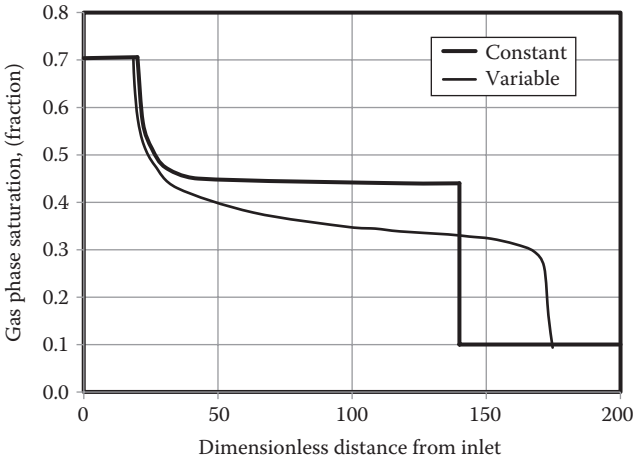

FIGURE 10.9 Effect of the constant and variable phase threshold saturations on the gas distribution profiles during gas injection into water-saturated porous media. (Replotted with modifications of their Fig. 2 after Mikhailov, D. and Nikolaevskii, V., *Fluid Dyn*., 35, 715, 2000.)

Figure 10.9 shows the effect of the constant and variable phase threshold saturations on the gas distribution profiles during gas injection into water-saturated porous media. A shock-front formation occurs when the phase threshold saturations are kept constant.

10.4.3 Summary

Although the majority of the conventional formulations assumed the continuity of each phase, there is a possibility that a fluid phase may disperse in another phase as a discontinuous phase during multiphase transport through porous media under proper conditions determined by the mobility condition and Weber number criteria. The dispersed fluid particles such as gas bubbles in a liquid phase or liquid droplets in a gas or liquid phase can experience particle breaking, pressure pulsation, vibration, and acceleration/deceleration effects. In addition, the continuous deposition and mobilization of dispersed particles over the pore surface can cause some delay in transport of fluids and vary the amount of trapped immobile fluid phases in porous media with time. The immobile fluid saturations are considered constant in conventional modeling and can be correlated against the porosity or the macroscopic capillary number. The porosity can be introduced into the capillary number through the relationship of permeability and porosity. However, during unsteady transport of dispersed fluid particles, the immobile fluid saturations vary depending on the deposition and mobilization rates of the dispersed particles over the pore surface. These processes can cause some delays in transport. This causes the progressing saturation front to disperse in contrast to the shock-front formation observed when the immobile fluid saturations remain constant.

10.5 PERMEABILITY IMPAIRMENT IN POROUS MEDIA BY PRECIPITATE DEPOSITION

The materials presented in this section have been reproduced from the author's previous work (Civan, 2007e). Briefly, a model and its applications are presented for prediction of the permeability impairment in porous media due to deposition of organic and inorganic substances in radial flow occurring within the near-wellbore region under nonequilibrium deposition conditions, described by the relaxation phenomenon. Redistribution of the local conditions during transient-state flow

requires a finite amount of sufficient time to attain equilibrium in porous media. Consequently, there is less precipitate deposition and permeability impairment and slower flow decline than predicted by the equilibrium models. In the following, a nonequilibrium precipitate deposition and permeability impairment model is formulated and solved numerically under the same conditions of the previous equilibrium models. Comparisons indicate that the equilibrium model proposed by Roberts (1997) underestimates the flow rates in porous media because the equilibrium assumption allows for more precipitation than it can actually occur under nonequilibrium conditions. It is demonstrated that the deposition under the nonequilibrium flow conditions is less than that of the equilibrium flow conditions. However, the difference between the two diminishes at later times.

10.5.1 Formulation

The formulation of the nonequilibrium near-wellbore particulate deposition and the consequent porosity and permeability reduction is presented by extending the formulations given by Roberts (1997) for equilibrium deposition and subsequently by Civan (2001a,b, 2007a–e, 2011, 2012) for nonequilibrium deposition conditions. Here, precipitation refers to the separation of precipitate from a supersaturated solution, such as the wax crystals separated from waxy oil, and deposition refers to the actual detainment or capture of the particulates suspended in the solution in the porous formation.

The volumetric flux u for radial flow of a fluid approaching to a well from a reservoir is given by Darcy's law as, noting that the flow direction is opposite to the radial direction measured from the well centerline,

$$u = \frac{qB}{2\pi hr} = \frac{K}{\mu}\frac{\partial p}{\partial r} \tag{10.98}$$

where

q denotes the volumetric flow rate
B is the reservoir fluid formation volume factor (a conversion factor between the standard and the actual density of fluid)
h is the formation thickness, r is the radial distance
K is the absolute permeability
μ and p are the fluid viscosity and pressure, respectively

Thus, according to Equation 10.98, the flow rate is given as

$$q = \frac{2\pi hK}{\mu B} r \frac{\partial p}{\partial r}, \quad r_a \le r \le r_e, \quad t > 0 \tag{10.99}$$

Considering the near-wellbore porous formation damage by particle deposition and the resulting skin effect due to precipitate deposition, the apparent wellbore radius r_a is given as (Hawkins, 1956)

$$r_a = r_w e^{-s} \tag{10.100}$$

where

r_w represents the actual wellbore radius
s is a skin factor used to simulate the effect of permeability impairment and pressure loss as a conceptually based effective shrinkage of the wellbore customarily in petroleum engineering

The range of influence of the well is represented by an external radius of r_e where the boundary of the reservoir domain is located and the pressure of the fluid is p_e. The pressure at the wellbore is p_w. The well is producing at a rate of q from the wellbore into the well.

The productivity index and the productivity index ratio are defined, respectively, as the following, indicating the loss of well performance owing to precipitate deposition in the near-wellbore region:

$$PI(t) = \frac{q_w(t)}{p_e - p_w(t)} \tag{10.101}$$

$$\alpha(t) = \frac{PI(t)}{PI_o} \tag{10.102}$$

The carrier fluid containing a dissolved solute can become saturated because of change in the temperature or pressure conditions. The precipitate particulates separated from the supersaturated solution remain suspended in the liquid phase until deposition in porous media. The total flowing precipitate particulate suspension mass balance equation is given as

$$\frac{\partial(\phi\rho)}{\partial t} + \frac{1}{r}\frac{\partial(r\rho u)}{\partial r} = \dot{m} \tag{10.103}$$

where

$\dot{m}$ denotes the net mass rate of precipitate particulate added to the flowing suspension expressed per unit bulk volume of the porous reservoir formation
ρ is the precipitate suspension density, u is the fluid volumetric flux
ϕ is the porosity

The density of the precipitate suspension is given as a volumetrically weighted average by

$$\rho = \rho_o(1 - \sigma_s) + \rho_s\sigma_s \tag{10.104}$$

where

ρ_o and ρ_s denote the density of the carrier fluid that contains dissolved solute and the material density of the precipitates, respectively
σ_s denotes the volume fraction of the precipitating suspended particulates separated from and migrating with the reservoir fluid

Substituting Equations 10.98 into 10.103 yields

$$\frac{\partial(\phi\rho)}{\partial t} + \frac{1}{r}\frac{\partial}{\partial r}\left(\frac{\rho qB}{2\pi h}\right) =$$

$$\frac{\partial(\phi\rho)}{\partial t} + \frac{1}{r}\frac{\partial}{\partial r}\left(\frac{\rho K}{\mu} r\frac{\partial p}{\partial r}\right) = \dot{m} \tag{10.105}$$

To obtain a reasonably approximate numerical solution, assume that the carrier fluid is almost incompressible because it contains a small or negligible amount of dissolved solute whose relative

magnitude is negligible. This assumption is made only for the equation of continuity (total mass balance) for simplification purposes. When $\sigma_s \cong 0$, ρ = const.; hence, Equation 10.105 simplifies as

$$\frac{\partial \phi}{\partial t} + \frac{1}{r}\frac{\partial}{\partial r}\left(\frac{qB}{2\pi h}\right) =$$

$$\frac{\partial \phi}{\partial t} + \frac{1}{r}\frac{\partial}{\partial r}\left(\frac{K}{\mu} r \frac{\partial p}{\partial r}\right) = \frac{\dot{m}}{\rho} \tag{10.106}$$

The initial and boundary conditions for the producing zone are given as

$$p = p_i, \quad r_w \le r \le r_e, \quad t = 0 \tag{10.107}$$

$$p = p_w(t) \quad \text{and} \quad q_w(t) = \frac{2\pi r_a K h}{\mu B}\left(\frac{\partial p}{\partial r}\right)_a, \quad r = r_a, t > 0 \tag{10.108}$$

and

$$p = p_e, q_e(t) = f_e q_w(t) = \frac{2\pi r_e K h}{\mu B}\left(\frac{\partial p}{\partial r}\right)_e, \quad r = r_e, t > 0 \tag{10.109}$$

The leaky boundary drive strength factor f_e (dimensionless) at the external reservoir boundary is given as (Kumar, 1977), according to the leaky tank model of the domain of influence of the well in a reservoir (Civan, 2000b),

$$f_e = 0, \text{closed boundary, unsteady state} \tag{10.110}$$

$$0 < f_e < 1.0, \text{partial water influx} \tag{10.111}$$

$$f_e = 1.0, \text{full water influx, steady state} \tag{10.112}$$

$$f_e > 1.0, \text{excess fluid invasion} \tag{10.113}$$

Ignoring the dispersive transport effect, the migrating suspended precipitate particle mass balance equation is given as

$$\frac{\partial(\phi\rho\sigma_s)}{\partial t} + \frac{1}{r}\frac{\partial(r\rho u\sigma_s)}{\partial r} = \dot{m} \tag{10.114}$$

Equation 10.114 can be simplified by means of Equation 10.103 as the following:

$$\frac{\partial \sigma_s}{\partial t} + \frac{u}{\phi}\frac{\partial \sigma_s}{\partial r} = \frac{\dot{m}}{\rho}\left(\frac{1-\sigma_s}{\phi}\right) \tag{10.115}$$

Note that Equation 10.115 is applicable regardless of whether the flowing particulate suspension density ρ is constant or variable. The net mass rate of precipitate added to the flowing suspension $\dot{m}$

is given as the difference between the rate of precipitate generation (precipitation from solution plus mobilization from pore surface) and the rate of precipitate deposition in porous formation:

$$\dot{m} = \rho_s \left(\dot{\varepsilon}_p + \dot{\varepsilon}_e - \dot{\varepsilon}_d \right) \tag{10.116}$$

where $\dot{\varepsilon}_p$ and $\dot{\varepsilon}_d$ denote the volumetric rate of separation of dissolved solute as a precipitate and rate of deposition of the particulate precipitate, respectively.

The symbol ε_d denotes the fractional volume occupied by the particulate deposits in the reservoir formation, given as

$$\varepsilon_d = \phi_o - \phi \tag{10.117}$$

Therefore,

$$\dot{\varepsilon}_d \equiv \frac{\partial \varepsilon_d}{\partial t} = -\frac{\partial \phi}{\partial t} \tag{10.118}$$

where ϕ_o and ϕ denote the initial and instantaneous effective porosities, excluding the volume occupied by the immobile or stationary carrier fluid present over the pore space. The effective porosity vanishes when the pore space is completely filled with the deposits, so that

$$\phi = 0, \quad \varepsilon_d = \phi_o \tag{10.119}$$

The rate of precipitation from the reservoir fluid is given as

$$\dot{\varepsilon}_p \equiv \frac{\partial \varepsilon_p}{\partial t} = \left(\frac{qB}{2\pi r h} \right) \left(\frac{d\sigma_s}{dp} \right)_T \frac{\partial p}{\partial r} \tag{10.120}$$

where $\left(\frac{d\sigma_s}{dp} \right)_T$ represents the separation of the precipitate owing to supersaturation caused by pressure reduction in the near-wellbore region. For example, it can be predicted using the ideal solution theory, yielding a simple thermodynamic equation as (Chrastil, 1982)

$$c = \rho_o^{k_c} \exp\left(\frac{A}{T} + B \right) \tag{10.121}$$

where

- c represents the concentration of the precipitate dissolved in the fluid expressed as mass per volume
- ρ_o is the density of the carrier fluid containing dissolved solute
- T is the fluid temperature
- k_c, A, and B are empirical parameters

Thus, the volume fraction of the precipitate in the suspension is given as

$$\sigma_s = \frac{c}{\rho_o} \quad \text{and} \quad \left(\frac{d\sigma_s}{dp} \right)_T = \frac{d}{dp} \left(\frac{c}{\rho_o} \right)_T \tag{10.122}$$

The density is given by the general form as

$$\rho_o = \rho_o\left(p,T,c\right) \tag{10.123}$$

where p is the pressure. Substituting Equations 10.98 into 10.120 yields

$$\dot{\varepsilon}_p \equiv \frac{\partial \varepsilon_p}{\partial t} = \frac{\mu}{K}\left(\frac{d\sigma_s}{dp}\right)_T \left(\frac{qB}{2\pi rh}\right)^2$$

$$= \frac{K}{\mu}\left(\frac{d\sigma_s}{dp}\right)_T \left(\frac{\partial p}{\partial r}\right)^2, \quad r_a \le r \le r_e, \quad t > 0 \tag{10.124}$$

$$\varepsilon_p = 0, \quad r_a \le r \le r_e, \quad t = 0 \tag{10.125}$$

The rate of deposition of the precipitate is given as

$$\frac{\partial \varepsilon_d}{\partial t} = k_d\left(1 + b\varepsilon_d\right)u\sigma \tag{10.126}$$

$$\varepsilon_d = 0, \quad r_a \le r \le r_e, \quad t = 0 \tag{10.127}$$

where
k_d is the deposition rate coefficient
b is a filtration coefficient

The rate of mobilization of the precipitate by erosion is given as

$$\frac{\partial \varepsilon_e}{\partial t} = k_e\varepsilon_d\left(v_f - v_c\right), \quad v_f \ge v_c \tag{10.128}$$

$$\frac{\partial \varepsilon_e}{\partial t} = 0, \quad v_f < v_c \tag{10.129}$$

$$\varepsilon_e = 0, \quad r_a \le r \le r_e, \quad t = 0 \tag{10.130}$$

where
k_e is the erosion rate coefficient
v_f and v_c denote the actual interstitial fluid velocity and the critical interstitial fluid velocity required for precipitate mobilization from the pore surface

Consider now the interstitial fluid velocity in a tortuous flow path in porous media given by Dupuit (1863):

$$v_f = \frac{\tau_f u_f}{\phi} \tag{10.131}$$

where
v_f and u_f are the interstitial and superficial fluid velocities
ϕ is the porosity

The tortuosity τ_f of porous media is defined as the ratio of the flow tube length L_f and porous media length L as

$$\tau_f = \frac{L_f}{L} \tag{10.132}$$

Thus, applying for two different length tortuous flow paths referred to by the subscripts 1 and 2, respectively, for a prescribed superficial velocity (or volumetric flux) and porosity yields

$$\frac{u_f}{\phi} = \frac{v_{f1}}{\tau_{f1}} = \frac{v_{f2}}{\tau_{f2}} \quad \text{or} \quad \frac{v_{f2}}{v_{f1}} = \frac{\tau_{f2}}{\tau_{f1}} \tag{10.133}$$

This equation indicates that $\frac{v_{f2}}{v_{f1}} \geq 1$ when $\frac{\tau_{f2}}{\tau_{f1}} \geq 1$ as pointed out previously by Civan (2007b). Because the fluid moves faster in longer tortuous flow paths in porous media, it is more likely to mobilize a precipitate present at the pore walls of a higher tortuosity media (Civan, 2007b,f, 2010a).

The *effective permeability* denotes the permeability measured under equilibrium conditions. The measurements of permeability for different amounts of precipitate deposition are accomplished usually by interrupting the core flow tests at certain times (Iscan et al., 2009). Thus, when the permeability is measured, the deposit amount is considered to be equivalent to the equilibrium amount. Let $\tilde{\varepsilon}_d$ denote the effective or equilibrium deposit fraction. This amount is greater than the actual or nonequilibrium deposit fraction ε_d of the precipitate separating from the saturated solution because of pressure reduction. At equilibrium, all the precipitate formed in the saturated carrier fluid deposits in porous media. However, in reality, the precipitate deposition in porous media is delayed. Therefore, the constitutive equation for the nonequilibrium rate of interface (pore surface) mass transfer from the suspension to the pore surface, referred to as the deposition phenomenon, can be expressed using a simple linear relaxation relationship, inferred by Einstein (1920):

$$\frac{\partial \varepsilon_d}{\partial t} = -\frac{\varepsilon_d - \tilde{\varepsilon}_d}{\tau} \tag{10.134}$$

where τ denotes the local relaxation time. Equation 10.134 can be written as

$$\tilde{\varepsilon}_d = \varepsilon_d + \tau \frac{\partial \varepsilon_d}{\partial t} \tag{10.135}$$

The initial condition for this ordinary differential equation is given as

$$\varepsilon_d = 0, \quad t = 0 \tag{10.136}$$

Based on a bundle of leaky tube model of porous media, having its parameters represented by the fractal equation, the effective permeability versus effective porosity $\tilde{\phi}$ is assumed to obey the power-law equation (Civan, 2001a, 2002a, 2005):

$$\sqrt{\frac{K}{\tilde{\phi}}} = \Gamma \left(\frac{\tilde{\phi}}{\alpha - \tilde{\phi}} \right)^{\beta} \tag{10.137}$$

where Γ, α, and β, respectively, are the pore connectivity function that expresses the cross-flow effects, a parameter equal to one minus the porosity occupied by cementing materials and clay

minerals that occupies the pore space, and the power-law exponent that expresses the deviations of the natural porous structure from the common assumption of cylindrical-shaped nonleaky flow tubes (Civan, 2014b). The general parametric relationships are given by the following functions:

$$\frac{\beta_{\max}^{-1}-\beta^{-1}}{\beta_{\max}^{-1}-\beta_{\min}^{-1}}=\left[\frac{\Gamma_{\max}-\Gamma}{\Gamma_{\max}-\Gamma_{\min}}\right]^{C/A}=\left[\frac{\phi_{\min}^{\upsilon}-\phi^{\upsilon}}{\phi_{\min}^{\upsilon}-\phi_{\max}^{\upsilon}}\right]^{C/A};\quad \upsilon<0 \tag{10.138}$$

Here, the subscripts *min* and *max* represent the minimum and maximum values. The empirical parameters of Equation 10.138 are υ, *C*/*A*, $\phi_{\min}$, $\phi_{\max}$, $\beta_{\min}$, $\beta_{\max}$, $\Gamma_{\min}$, and $\Gamma_{\max}$. The effective porosity is given as

$$\tilde{\phi}=\phi_o-\tilde{\varepsilon}_d \tag{10.139}$$

Assuming $\alpha = 1.0$, $\beta \cong ct$, $\min \Gamma \cong$ const. in Equation 10.137, the permeability reduction by precipitate deposition is given as

$$\frac{K}{K_o}=\left(\frac{\phi_o-\tilde{\varepsilon}_d}{\phi_o}\right)^{(1+2\beta)}\left(\frac{1-\phi_o}{1-\phi_o+\tilde{\varepsilon}_d}\right)^{2\beta} \tag{10.140}$$

10.5.2 Simulation of Particulate Depositions under Nonequilibrium Relaxation Effects

For illustration purposes, consider the synthetic oil reservoir data given in Table 10.3. The oil is assumed incompressible and the reservoir is at isothermal conditions. For simplification, assume there is no precipitate mobilization by erosion, that is, $\dot{\varepsilon}_e = 0$, because the interstitial fluid velocity remains below that of its critical value necessary for precipitate mobilization, and the precipitate deposition occurs completely, that is, $\dot{\varepsilon}_p = \dot{\varepsilon}_d$. Further, a constant rate production is considered, that is, q = const. Consequently, the following equations can be used to describe the consequences of the

TABLE 10.3
Data Used in Simulation

Parameter	Value
β (dimensionless)	1.0
ϕ_o (fraction)	0.10
K_o (m^2)	5.0×10^{-14}
r_w (m)	0.075
r_e (m)	1500
h (m)	20
s (dimensionless)	0.0
q (m^3/s)	8.0×10^{-3}
p_e (Pa)	2.07×10^7
B (m^3/standard m^3)	1.0
μ (Pa·s)	1.0×10^{-3}
p_o (Pa)	1.0×10^8
τ (days)	115

precipitate deposition under nonequilibrium conditions. The same can be applied under equilibrium conditions when the relaxation time is set equal to zero.

The amount of particulate separation depends on the local saturation conditions. The amount of particulates suspended in the carrier fluid is the net sum of the particulates generated by separation and lost by deposition in porous media plus the particulates migrating through porous media. Therefore, one can have a storage of precipitate in the carrier fluid, while this deposition waits for the chance to occur. From Equation 10.124,

$$\frac{\partial \varepsilon_p}{\partial t} = \frac{\mu}{K}\left(\frac{d\sigma_s}{dp}\right)_T \left(\frac{q}{2\pi r h}\right)^2, \quad r_a \le r \le r_e, \quad t > 0 \tag{10.141}$$

where

$$\left(\frac{d\sigma_s}{dp}\right)_T = \frac{p_o}{p^2} \tag{10.142}$$

Here, p_o is an empirical constant:

$$\varepsilon_p = 0, \quad r_w \le r \le r_e, \quad t = 0 \tag{10.143}$$

$$r_a = r_w e^{-s} \tag{10.144}$$

The change in the amount of particulate deposition in porous media causes the same change in the amount of the particulate contained in the flowing particulate suspension regardless of how slow the deposition occurs, and in fact, this is true with or without any delays, although a delay is considered in the present case. Thus, the following equation can be written by considering the fact that a gain in one is a loss in the other:

$$-\frac{\partial \varepsilon_p}{\partial t} = \frac{\partial \varepsilon_d}{\partial t} \tag{10.145}$$

From Equation 10.135,

$$\tilde{\varepsilon}_d = \varepsilon_d + \tau \frac{\partial \varepsilon_d}{\partial t} \tag{10.146}$$

From Equation 10.140,

$$\frac{K}{K_o} = \left(\frac{\phi_o - \tilde{\varepsilon}_d}{\phi_o}\right)^{(1+2\beta)} \left(\frac{1-\phi_o}{1-\phi_o+\tilde{\varepsilon}_d}\right)^{2\beta} \tag{10.147}$$

Equations 10.106, 10.118, and 10.124 can be combined to obtain

$$\frac{\partial q}{\partial r} = \frac{\mu}{2\pi h}\left(\frac{d\sigma_s}{dp}\right)_T \frac{q}{Kr}^2, \quad r_a < r \le r_e, \quad t > 0 \tag{10.148}$$

$$q = q_w, \quad r = r_a \tag{10.149}$$

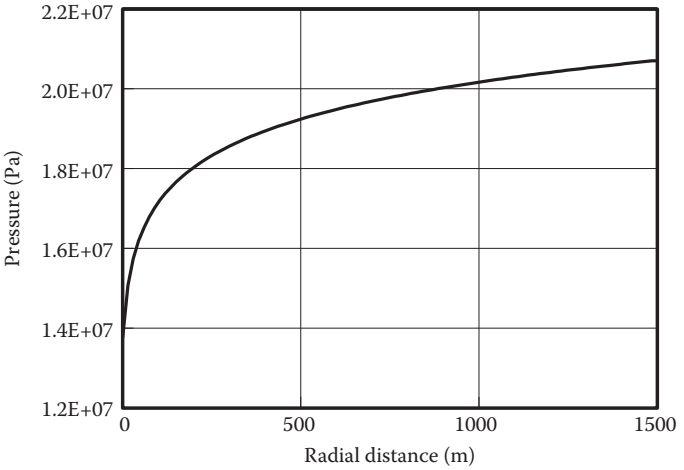

FIGURE 10.10 Nonequilibrium pressure profile after 1 day.

From Equation 10.98,

$$\frac{\partial p}{\partial r} = \frac{q\mu}{2\pi hKr} \tag{10.150}$$

$$p = p_e, \quad r = r_e, \quad t \geq 0 \tag{10.151}$$

From Equations 10.101 and 10.102,

$$PI(t) = \frac{q}{p_e - p_w(t)} \tag{10.152}$$

$$\alpha(t) = \frac{PI(t)}{PI_o} \tag{10.153}$$

The differential equations derived in this section are solved numerically using an implicit second-order accurate finite-difference method. Figure 10.10 shows the pressure profile after 1 day of production. Figures 10.11 through 10.15 show the comparison of the equilibrium and nonequilibrium deposit volume fractions versus the radial distance at various times. The nonequilibrium and equilibrium deposition effects differ initially more and the differences become gradually smaller at later times. It can be observed that the equilibrium deposit fractions are greater than the nonequilibrium deposition as expected.

10.5.3 Summary

The flowing fluid media become a suspension of particulates when particulates are generated by separation of dissolved solute from a solution flowing through porous media. This can occur in the near-wellbore regions in petroleum reservoirs due to the decline of the fluid pressure by depletion and creates conditions favorable for precipitation of particulates. The concentration of the particles in the flowing suspension varies depending on the rates of particulate generation, migration, and

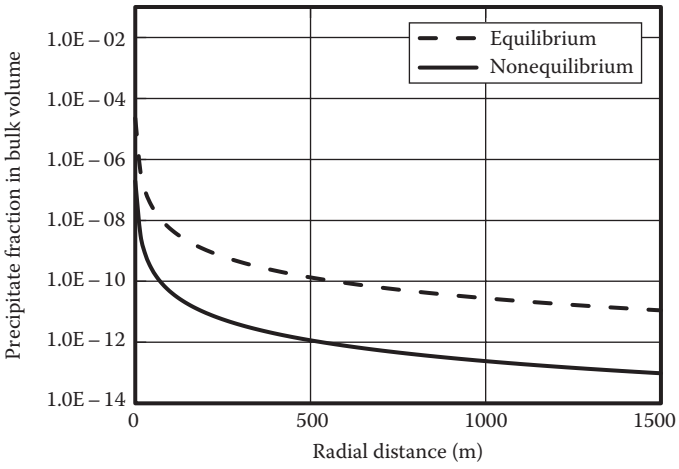

FIGURE 10.11 Equilibrium and nonequilibrium precipitate amounts after 1 day.

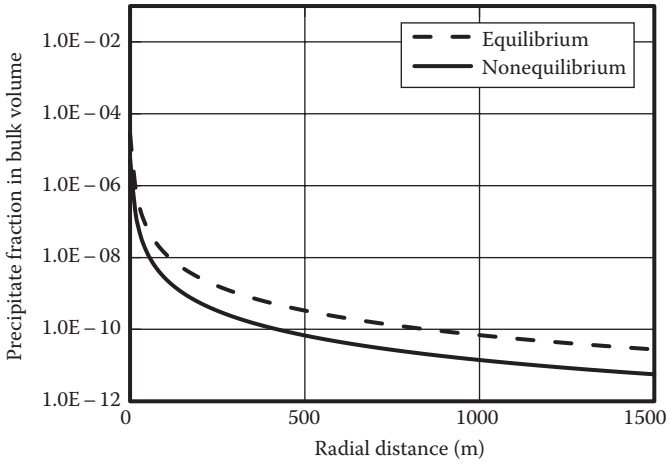

FIGURE 10.12 Equilibrium and nonequilibrium precipitate amounts after 30 days.

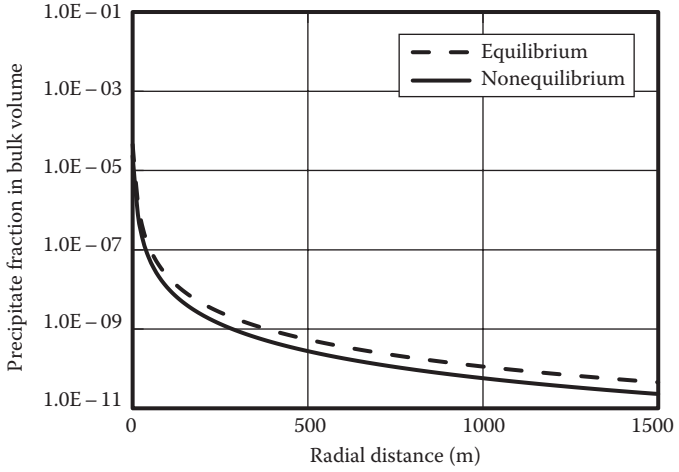

FIGURE 10.13 Equilibrium and nonequilibrium precipitate amounts after 120 days.

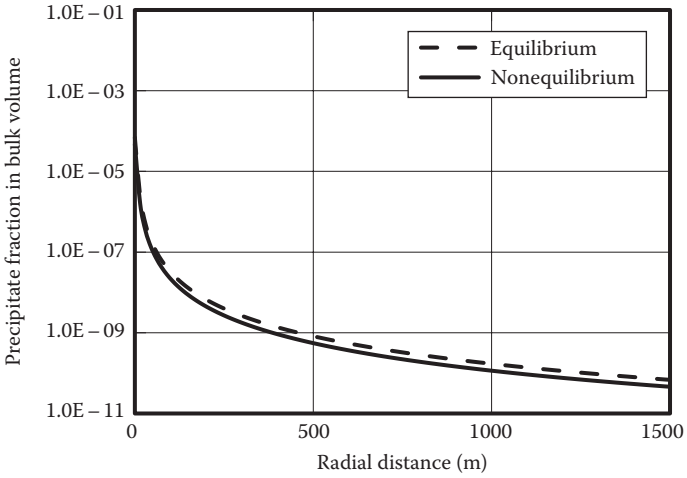

FIGURE 10.14 Equilibrium and nonequilibrium precipitate amounts after 240 days.

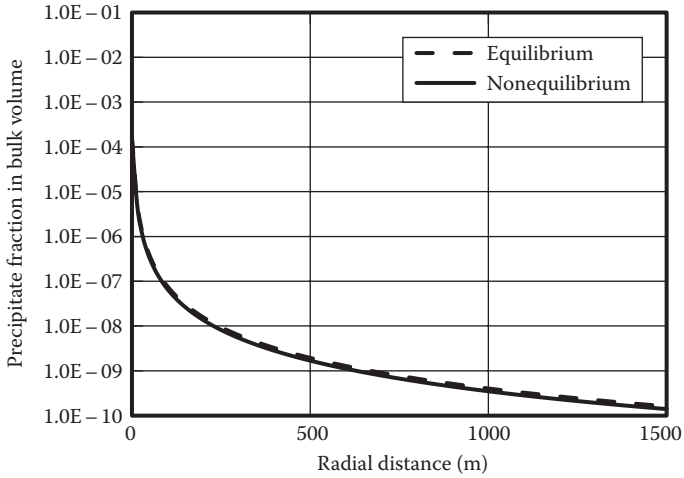

FIGURE 10.15 Equilibrium and nonequilibrium precipitate amounts after 2 years.

deposition, in porous media. Commonly the particle deposition is assumed to occur at an equilibrium amount, whereas some delays may happen under unsteady flow conditions. Therefore, the reduction of porosity and permeability may be slower at the actual conditions than the equilibrium conditions as demonstrated by numerical simulation.

10.6 NONEQUILIBRIUM MODIFICATION OF THE GRADIENT TRANSPORT LAWS

Numerous experimental and theoretical studies have demonstrated that local equilibrium conditions cannot be reached instantaneously during heat and mass transfer in nonhomogeneous materials because of interference of their complex internal features with the transport processes, and therefore, not only the classical Darcy's law but also the classical Fourier and Fickian types of gradient laws require a correction for delay in reaching toward local equilibrium (Civan and Rasmussen,

2003, Reverberi et al., 2008). Such problems can be formulated as a damped-wave equation as demonstrated in this section for convenience in obtaining analytical and numerical solutions.

10.6.1 Unsteady Darcy's Equation for Accelerating Flow through Porous Media

Many attempts have been made for derivation of the porous media macroscopic equation of motion (Blick and Civan, 1988, Civan and Evans, 1998, Civan, 2002b, 2008, 2010b, 2011, 2013, 2014c). The macroscopic porous media equation of fluid motion can be obtained based on the volume-averaged Navier–Stokes equation (Whitaker, 1999), whereas, commonly, Darcy's equation is used in porous media fluid transport problems, given in the following in a simplified form for homogeneous porous media without including the gravity term for illustration purposes:

$$\langle \mathbf{u} \rangle = -\frac{K_D}{\mu} \nabla \langle p \rangle^f \tag{10.154}$$

where

$\langle \mathbf{u} \rangle$ and $\langle p \rangle^f$ denote the bulk-volume average fluid flux and the pore fluid volume average pressure, respectively

K_D is referred to as Darcy's permeability

Zhu et al. (2014) emphasize that K_D is a constant value when determined by applying Equation 10.154 by measurements conducted under steady-state conditions, for example, using core plugs. However, numerous studies reported that the Darcy's equation needs correction as the following for unsteady flow conditions (Sollitt and Cross, 1972, Burcharth and Anderson, 1995, Kuznetsov and Nield, 2006, Rajagopal, 2007):

$$\tau \frac{\partial \langle \mathbf{u} \rangle}{\partial t} + \langle \mathbf{u} \rangle = -\frac{K}{\mu} \nabla \langle p \rangle^f \tag{10.155}$$

Zhu et al. (2014) elaborate by theoretical arguments and numerical studies that, under unsteady flow conditions, the permeability K and delay timescale τ appearing in this equation should vary with time and therefore assuming constant values for these coefficients is not generally valid. This is because the transmission of the effect of fluid viscosity on fluid motion from the pore surface to the pore fluid during acceleration of flow requires a certain amount of time, referred to as the viscous timescale $\tau_{visc} = D^2/\nu$, depending on the kinematic viscosity $\nu = \mu/\rho$ (dynamic viscosity to mass density ration) and the characteristic grain or pore size of porous media D (Zhu et al., 2014). Self-similar velocity profiles cannot be formed during flow acceleration caused by a pressure gradient unless the viscous timescale τ_{visc} is sufficiently less than the flow acceleration timescale $\tau_{vans} = \dfrac{K_D}{\nu\phi}$. Consequently, the coefficients of the unsteady Darcy's equation are dependent upon time, and therefore, the assumption of constant coefficient values made in various studies is invalid (Zhu et al., 2014).

Zhu et al. (2014) review and compare the various approaches taken for derivation of the unsteady Darcy's equation. The first is based on the volume-averaged Navier–Stokes equation (Whitaker, 1999), and the second is based on the volume-averaged kinetic energy equation (Zhu et al., 2014) assuming relatively low Reynolds number flow, uniform bulk flow, and periodic boundary conditions in the representative elementary volume (REV) of a homogeneous porous media. Their results and assumptions/considerations are summarized in Table 10.4 and indicate that the coefficients of the unsteady Darcy's equation in the cases considered are independent of time. In view of the aforementioned discussion, however, Zhu et al. (2014) caution that this requires the velocity

TABLE 10.4
Comparison of the Delay Timescales and Permeability Obtained by Different Approaches

Method	Delay Timescale (τ)	Permeability (K)	Assumptions/Considerations
Volume-averaged Navier–Stokes equation	$\frac{K_D}{\nu\phi}$	K_D	Steady-state closure approximation for pore surface drag force according to Forchheimer.
Volume-averaged Navier–Stokes equation	$\frac{K_D}{\nu\phi}\left[1+\left(\frac{1-\phi}{\phi}\right)C_{vm}\right]$, where C_{vm} is an empirical virtual mass coefficient	K_D	Neglect the Forchheimer inertial flow term and correct the time constant according to the virtual mass compensation for acceleration of volume of fluid across pore constrictions with an empirical virtual mass coefficient $0.5 \le C_{vm} \le 2.0$ (Lowe et al., 2008).
Volume-averaged kinetic energy equation	$\frac{K_D}{\nu}\frac{\langle \mathbf{u}\cdot\mathbf{u}\rangle}{\langle \mathbf{u}\rangle\cdot\langle \mathbf{u}\rangle} = \frac{K_D}{\nu\phi}\frac{\langle \mathbf{u}\cdot\mathbf{u}\rangle^f}{\langle \mathbf{u}\rangle^f\cdot\langle \mathbf{u}\rangle^f}$, where $\langle \mathbf{u}\rangle^f$ denotes the pore fluid velocity	K_D	Correct the time constant by a factor depending on flow and pore structure and assume permeability K remains close to its steady-state value K_D.

Source: After Zhu, T. et al., *Transp. Porous Media*, 2014.

profiles of the accelerating flow to remain self-similar at all times, which does not happen in reality, and the accuracy diminishes with increase in deviation from steady state. Nevertheless, Zhu et al. (2014) suggest that the unsteady Darcy's equation having constant coefficients but derived based on the volume-averaged kinetic energy equation can still produce adequate results inferred by their direct numerical simulation results obtained for incompressible Newtonian fluids. Further research is required for extension to generalized fluid and flow conditions.

10.6.2 Nonequilibrium Transport in Nonhomogeneous Media Expressed by a Damped-Wave Equation

Considering an incompressible medium and the convective and diffusive transfers, the equation of conservation without the source/sink terms is given as

$$\frac{\partial q}{\partial t} + \nabla\cdot\left(q\mathbf{u}\right) + \nabla\cdot\mathbf{J} = 0 \tag{10.156}$$

where
q denotes a transported quantity of a system
$\mathbf{J}$ denotes the diffusive transport vector

The fluid flux vector $\mathbf{u}$ is either prescribed or calculated using Equation 10.155, given in the previous section. The time-delayed diffusive flux equation is given as

$$\tau\frac{\partial \mathbf{J}}{\partial t} + \mathbf{J} = -\mathbf{D}\cdot\nabla q \tag{10.157}$$

where
τ denotes the delay time
$\mathbf{D}$ denotes the diffusive transport coefficient tensor

Derivative of Equation 10.156 with respect to time gives

$$\frac{\partial^2 q}{\partial t^2} + \frac{\partial}{\partial t}\nabla\cdot\left(q\mathbf{u}\right) + \frac{\partial}{\partial t}\nabla\cdot\mathbf{J} = 0 \tag{10.158}$$

Divergence of Equation 10.157 gives

$$\tau\nabla\cdot\frac{\partial\mathbf{J}}{\partial t} + \nabla\cdot\mathbf{J} = -\nabla\cdot\left(\mathbf{D}\cdot\nabla q\right) \tag{10.159}$$

Hence, substituting $\nabla\cdot\mathbf{J} = -\dfrac{\partial q}{\partial t} - \nabla\cdot\left(q\mathbf{u}\right)$ from Equation 10.156 and $\dfrac{\partial}{\partial t}\nabla\cdot\mathbf{J} = -\dfrac{\partial^2 q}{\partial t^2} - \dfrac{\partial}{\partial t}\nabla\cdot\left(q\mathbf{u}\right)$ from Equation 10.158 into Equation 10.159 yields

$$\tau\frac{\partial^2 q}{\partial t^2} + \frac{\partial q}{\partial t} + \tau\frac{\partial}{\partial t}\nabla\cdot\left(q\mathbf{u}\right) + \nabla\cdot\left(q\mathbf{u}\right) = \nabla\cdot\left(\mathbf{D}\cdot\nabla q\right) \tag{10.160}$$

When the bulk flow term is set equal to zero, Equation 10.160 yields a damped-wave equation as

$$\tau\frac{\partial^2 q}{\partial t^2} + \frac{\partial q}{\partial t} = \nabla\cdot\left(\mathbf{D}\cdot\nabla q\right) \tag{10.161}$$

In the heat conduction problem considered by Reverberi et al. (2008), $q = \phi\rho C_p T$ and $\mathbf{D} = \dfrac{\phi\mathbf{k}}{\rho C_p}$ is the thermal diffusivity, where $\mathbf{k}$ denotes the thermal conductivity tensor, ρ is the density, and C_p is the specific heat capacity under constant pressure conditions, leading to the Maxwell–Cattaneo equation. In the problem of gas diffusion in nonhomogeneous media considered by Civan and Rasmussen (2003) and Rasmussen and Civan (2015), $q = c$ is the dissolving gas concentration and $\mathbf{D}$ is the mass diffusivity in the nonhomogeneous media. The solution of Equation 10.161 results in traveling discontinuities similar to the shock-front saturations of the Buckley and Leverett (1942) model. The solution profiles involve the shock fronts progressing with time similar to those shown in Figure 10.8.

10.6.3 Summary

The well-known gradient transport laws of Darcy, Fourier, and Fick are only valid under local pore-scale equilibrium conditions. However, under unsteady conditions, there may not be sufficient time to attain pore-scale equilibrium conditions. The fluid flowing through porous media under accelerating/decelerating flow conditions may involve a delay in transmission of the effect of viscosity from the pore surface to the bulk of the fluid. The conductive heat transfer and diffusive mass transfer processes may be delayed because of interactions in nonhomogeneous porous media owing to their complex internal features. Therefore, the classical gradient laws require modification for the nonequilibrium effects created under unsteady conditions by considering a delay time. However, estimation of the delay time remains a challenging issue for future research.

NOMENCLATURE

a, a_1	Parameters
A	Bulk surface area of porous media or parameter
A_p	Amplitude of pressure oscillations

b	Filtration coefficient or parameter
b_1	Parameter
B	Formation volume factor
B_g	Gas formation volume factor
B_o	Oil formation volume factor
B_w	Water formation volume factor
c	Solubility of precipitate-forming substance, substance M/solution
C	Curvature or parameter or parameter
C_a	Capillary number
Ca_{vc}	Microscopic capillary number
$\bar{C}a_w$	Macroscopic capillary numbers
d	Particle diameter
D	Core diameter or characteristic grain or pore size
$\mathbf{D}$	Mass diffusivity
f_1, f_2, f_3, F	General functions
f_e	Leaky boundary drive strength factor (dimensionless)
f_w	Fractional water flow function
g	Gravitational acceleration
G	Specific gravity
G_g^s, G_o^s, and G_w^s	Gravity of the gas, oil, and water (brine) at standard condition
h	Formation thickness
$J(S_w^e)$	Dimensionless capillary pressure
$\mathbf{J}$	Diffusive transport vector
K	Permeability
K_D	Darcy's permeability
K_x, K_y, and K_z	Permeability of anisotropic porous media in the x-, y-, and z-Cartesian directions
k_c	Empirical parameters
k_r	Relative permeability, dimensionless
k_2	Empirical exponent
k_{rw} and k_{rnw}	Relative permeability of the wetting and nonwetting fluid phases
k_{rw}^o, k_{rnw}^o	Empirical constants
k^o	Empirical constant
l	Distance or characteristic dimensions of an ellipsoidal shape-approximated dispersed particle
L	Characteristic length of porous media
L_x, L_y, and L_z	Dimensions of porous media in the x-, y-, and z-Cartesian directions
m	Mass of multiphase fluid system or empirical constant
m_1	Empirical constant
$\dot{m}$	Rate of precipitate deposition in porous formation
M	Mobility criterion
n	Bundle of participating capillary tubes or a constant
N	Empirical exponent
p	Pressure
p_c	Capillary pressure
p_e	Porous medium entry pressure
p_1	Empirical constant
p_c^{stat}	Static or equilibrium capillary pressure
p_c^{dyn}	Dynamic or nonequilibrium capillary pressure
$\langle p \rangle^f$	Pore fluid volume average pressure
q	A transported quantity of a system or volumetric flow rate

q_g^s, q_o^s, and q_w^s	Volumetric flow rates of the free gas, dead oil, and dead water at standard conditions
q_i	Mean flow through a capillary flow path
Q	Total flow through the bundle of participating capillary tubes
r	Radial distance or characteristic dimensions of an ellipsoidal shape-approximated dispersed particle
R	Meniscus of radius
R^2	Coefficient of regression
R_S	Solubility ratio
$R_{Pg/o}$	Flowing gas-to-oil ratio
$R_{Pw/o}$	Flowing water-to-oil ratio
$R_{Sg/o}^{dyn}$ and $R_{Sg/w}^{dyn}$	Nonequilibrium dissolved gas in the oil and water phases under actual metastable conditions
$R_{Sg/o}^{stat}$ and $R_{Sg/w}^{stat}$	Equilibrium dissolved gas, referred to as the solubility of gas, in the oil and water phases
s	Skin factor, dimensionless
S	Phase saturation, volume fraction
S_w^e	Effective wetting fluid saturation
S_{gr}	Trapped gas and/or gas adsorbed over the pore surface
S_w	Wetting fluid saturation
S_{nw}	Nonwetting fluid saturation
S_{Dn} and S_{Dwn}	Normalized saturations of the mobile wetting and nonwetting fluids
S_{wi} and S_{nwi}	Immobile saturations of the wetting and nonwetting fluid phases
S^*	Dynamic threshold phase saturation
S^+	Equilibrium threshold phase saturation
t	Time
T	Temperature
T_c and T_r	Asymptote and reference temperatures
u	Volumetric flux
u_l	Volumetric flux of fluid phase
u_w and u_{nw}	Wetting and nonwetting phase volumetric fluxes
u	Total volume flux
$\mathbf{u}$	Fluid flux vector
$\langle \mathbf{u} \rangle$	Bulk-volume average fluid flux
v_1	Velocity of fluid phase
v_r	Velocity of the reference fluid phase
v_f and v_c	Actual interstitial fluid velocity and the critical interstitial fluid velocity
V	Volume
x	Mass fraction of the mobile gas phase in the multiphase fluid system, dimensionless, or x-Cartesian direction
x^o	Initial mobile gas mass fraction
x_S	Mobile gas mass fraction of the three-phase fluid system under the equilibrium conditions
We	Weber number

Greek

γ, δ, and η	Empirical constants
σ	Interfacial surface tension
σ_s	Volume fraction of the precipitating suspended particulates
ϕ	Porosity

ϕ_o	Initial porosity
$\tilde{\phi}$	Effective porosity
τ	Relaxation time
τ_f	Tortuosity of porous media
τ_o	Empirical coefficient
τ_o	A constant
τ_1	Ordinate intercept
$\tau_S(S_w)$ and $\tau_p(p_w)$	Empirical expressions
τ_w and τ_{nw}	New parameters
$\tau^*(S_w)$	New redistribution time
μ	Viscosity
μ_{nw}	Nonwetting phase viscosity
μ_w and μ_{nw}	Viscosity of the wetting and nonwetting fluid phases
ρ	Density
ρ_g,ρ_o, and ρ_w	Density of gas, oil, and water (brine) at actual conditions
ρ_a^s	Density of air at standard conditions (reference gas)
ρ_w^s	Density of pure water at standard conditions (reference liquid)
$\rho_g^s, \rho_a^s, \rho_o^s, \rho_{w*}^s, \rho_w^s$	Density of gas, air, oil, pure water, and oil-field water (brine) at standard conditions
ρ_o and ρ_s	Density of the carrier fluid that contains dissolved solute and the material density of the precipitates
ε	Volume fraction of the mobile gas phase in the multiphase fluid system
ε_d	Fractional volume occupied by the particulate deposits in the reservoir formation
ε_τ	Dimensionless redistribution time
$\dot{\varepsilon}_p$ and $\dot{\varepsilon}_d$	Volumetric rate of separation of dissolved solute as a precipitate and rate of deposition of the particulate precipitate
α	Angle of inclination of flow direction, degree
γ_{sp}	Specific weight
Γ	Interface mass transfer rate
Γ_G	Rate of gas transfer from the liquid phases into the gas phase
θ	Contact angle between the wetting (w) and nonwetting (nw) fluids
θ_τ	Dimensionless time
Δp_c	Deviation of capillary pressure
$\Delta\rho = \lvert\rho_w - \rho_{nw}\rvert$	Absolute value of the difference between the dispersed particle density and the carrier fluid phase density
λ	Effective mobility of the two-phase system or pore-size distribution index
λ_w and λ_{nw}	Mobility of the wetting and nonwetting fluids
T	Characteristic time of the process
ω	Frequency of the pressure oscillations.
υ, C/A, ϕ_{min}, ϕ_{max}, β_{min}, β_{max}, Γ_{min}, and Γ_{max}	Empirical parameters

Subscripts

D	Dimensionless
e	External reservoir boundary
g	Gas phase
nw	Nonwetting fluid
o	Oil phase or initial state
s	Damaged region, suspended particulate, or saturation condition

S	Saturation condition
w	Wetting fluid or water
*w**	Brine

Superscripts

dyn	Dynamic
o	Initial condition
s	Standard conditions
stat	Static (equilibrium)

REFERENCES

Al-Ibadi, A. and Civan, F., Experimental investigation and correlation of treatment in weak and high-permeability formations by gel particles, Paper SPE-153557-PA, *SPE Production & Operations*, 28(4) (2013): 387–401.

Anton, L. and Hilfer, R., Trapping and mobilization of residual fluid during capillary desaturation in porous media, *Physical Review E, Statistical Physics, Plasmas, Fluids, and Related Interdisciplinary Topics*, 59(6) (1999): 6819–6823.

Aryana, S.A. and Kovscek, A.R., Nonequilibrium effects and multiphase flow in porous media, *Transport in Porous Media*, 97(3) (2013): 373–394.

Barenblatt, G.I., Patzek, T.W., and Silin, D.B., The mathematical model of nonequilibrium effects in water-oil displacement, Paper SPE-87329-PA, *SPE Journal*, 8(4) (2003): 409–416.

Bazin, B., Bekri, S., Vizika, O., Herzhaft, B., and Aubry, E., Fracturing in tight gas reservoirs: Application of special-core-analysis methods to investigate formation-damage mechanisms, Paper SPE 112460-PA, *SPE Journal*, 15(4) (2010): 969–976.

Bear, J., *Dynamics of Fluids in Porous Media*. Dover, New York (1988).

Bilicki, Z. and Kestin, J., Physical aspects of the relaxation model in two-phase flow, *Proceedings of the Royal Society of London*: *Series A, Mathematical and Physical Sciences*, 428(1875) (1990): 379–397.

Blick, E.F. and Civan, F., Porous media momentum equation for highly accelerated flow, *SPE Reservoir Engineering*, 3(3) (1988): 1048–1052.

Brooks, R.H. and Corey, A.T. Properties of porous media affecting fluid flow, *Journal of Irrigation and Drainage Division: Proceedings of the American Society of Civil Engineers*, 92(IR 2) (1966): 61–88.

Buckley, S.E. and Leverett, M.C., Mechanism of fluid displacement in sands, *Transactions of AIME*, 146 (1942): 107–116.

Burcharth, H.F. and Andersen, O.H., On the one-dimensional steady and unsteady porous flow equations, *Coastal Engineering*, 24 (1995): 233–257.

Chrastil, J., Solubility of solids and liquids in supercritical gases, *Journal of Physical Chemistry*, 86 (1982): 3016.

Civan, F., Unfrozen water content in freezing and thawing soils-kinetics and correlation, *Journal of Cold Regions Engineering*, 14(3) (2000a): 146–156.

Civan, F., Leaky-tank reservoir model including the non-Darcy effect, *Journal of Petroleum Science and Engineering*, 28(3) (2000b): 87–93.

Civan, F., Scale effect on porosity and permeability-kinetics, model, and correlation, *AIChE Journal*, 47(2) (2001a): 271–287.

Civan, F., Modeling well performance under non-equilibrium deposition conditions, Paper SPE 67234, *SPE Mid-Continent Operations Symposium*, Oklahoma City, OK (March 2001b).

Civan, F., Relating permeability to pore connectivity using a power-law flow unit equation, *Petrophysics Journal*, 43(6) (2002a): 457–476.

Civan, F., Implications of alternative macroscopic descriptions illustrated by general balance and continuity equations, *Journal of Porous Media*, 5(4) (2002b): 271–282.

Civan, F., Improved permeability equation from the bundle-of-leaky-capillary-tubes model, SPE Paper 94271, *The Production Operations Symposium*, Oklahoma City, OK (April 17–19, 2005).

Civan, F., Including non-equilibrium relaxation in models for rapid multiphase flow in wells, *SPE Production & Operations Journal*, 21(1) (2006): 98–106.

Civan, F., *Reservoir Formation Damage-Fundamentals, Modeling, Assessment, and Mitigation*, 2nd edn. Gulf Professional Publishing/Elsevier, Burlington, MA, 1114pp. (2007a).

Civan, F., Temperature effect on power for precipitate detachment from pore wall described by an Arrhenius-type equation, *Transport in Porous Media*, 67(2) (2007b): 329–334.

Civan, F., Optimal scheduling of well treatment in commingled formations undergoing a near wellbore damage, Paper SPE-107856-PP, *Seventh SPE European Formation Damage Conference*, Scheveningen, the Netherlands (May 30–June 1, 2007c).

Civan, F., Formation damage mechanisms and their phenomenological modeling-An overview, Paper SPE-107857-PP, *Seventh SPE European Formation Damage Conference*, Scheveningen, the Netherlands (May 30–June 1, 2007d).

Civan, F., Permeability impairment and flow reduction in porous media under non-equilibrium particle deposition conditions, *Second International Conference on Porous Media and Its Applications in Science, Engineering, and Industry*, Kauai, HI (June 17–21, 2007e).

Civan, F., Temperature effect on power for particle detachment from pore wall described by an Arrhenius-type equation, *Transport in Porous Media*, 67(2) (2007f): 329–334.

Civan, F., Generalized Darcy's law by control volume analysis including capillary and orifice effects, *Journal of Canadian Petroleum Technology*, 47(10) (2008): 1–7.

Civan, F., Modeling transport in porous media by control volume analysis, *Journal of Porous Media*, 13(10) (2010a): 855–873.

Civan F., Non-isothermal permeability impairment by fines migration and deposition in porous media including dispersive transport, *Transport in Porous Media*, 85(1) (2010b): 233–258.

Civan, F., *Porous Media Transport Phenomena*. John Wiley & Sons, Hoboken, NJ, (2011).

Civan, F., Temperature dependency of dynamic coefficient for nonequilibrium capillary pressure-saturation relationship, R&D note, *AIChE Journal*, 58(7) (2012): 2282–2285.

Civan, F., Comparison of control volume analysis and porous media averaging for formulation of porous media transport (Chapter 2). In *Modelling and Simulation in Fluid Dynamics in Porous Media*, Proceedings in Mathematics & Statistics, Vol. 28, Ferreira, J.A., Barbeiro, S., Pena, G., Wheeler, M.F. (Eds.), Springer, New York, XV, pp. 27–53 (2013).

Civan, F., Analyses of processes, mechanisms, and preventive measures of shale-gas reservoir fluid, completion, and formation damage control # 14FD-P-108-SPE, SPE-168164-MS, for presentation as a Knowledge Sharing Poster at the *2014 SPE International Symposium & Exhibition on Formation Damage Control*, Lafayette, LA (February 26–28, 2014a).

Civan, F., Volume-averaging issues illustrated for porous-media thermo-fluid transport, *Special Topics & Reviews in Porous Media—An International Journal*, 5(1) (2014b): 83–94.

Civan, F., Improved permeability prediction for heterogeneous porous media by bundle-of-leaky-tubes with cross-flow model, *Proceedings (CD) of the Fifth International Conference on Porous Media and Its Applications in Science, Engineering and Industry (ICPMV)*, Vafai, K. (Ed.), Kona, HI (June 22–27, 2014c).

Civan, F. and Evans, R.D., Determining the parameters of the Forchheimer equation from pressure-squared vs. pseudopressure formulations, *SPE Reservoir Evaluation & Engineering*, 1(1) (1998): 43–46.

Civan, F. and Rasmussen, M. L., Analysis and interpretation of gas diffusion in quiescent reservoir, drilling, and completion fluids: Equilibrium vs. non-equilibrium models, Paper SPE 84072, *SPE Annual Technical Conference and Exhibition*, Denver, CO (October 5–8, 2003).

Civan, F. and Sliepcevich, C.M., Comparison of the thermal regimes for freezing & thawing of moist soils, *Water Resources Research*, 21(3) (1985): 407–410.

Craft, B.C., Hawkins, M., and Terry, R.E., *Applied Petroleum Reservoir Engineering*, 2nd edn. Prentice Hall, Upper Saddle River, NJ (1991).

Dahle, H.K., Celia, M.A., and Hassanizadeh, S.M., Bundle-of-tubes model for calculating dynamic effects in the capillary-pressure-saturation relationship, *Transport in Porous Media*, 58(1–2) (2005): 5–22.

Das, D.B., Gauldie, R., and Mirzaei, M., Dynamic effects for two-phase flow in porous media: Fluid property effects, *AICHE Journal*, 53(10) (2007): 2505–2520.

Downar-Zapolski, P., Bilicki, Z., Bolle, L., and Franco, J., The non-equilibrium relaxation model for one-dimensional flashing liquid flow, *International Journal of Multiphase Flow*, 22(3) (1996): 473–483.

Dupuit, J., *Etudes Théoriques et Pratiques sur le Mouvement des Eaux dans les Canaux Découverts et a Travers les Terrains Perméables*, 2nd edn. Dunod, Paris, France (1863).

Einstein, A., *Schallausbreitung in Teilweise Dissoziierten Gasen*. Verlag der Akademie der Wissenschaften, in Kommission bei der W. de Gruyter, Berlin, Germany, pp. 380–385 (1920). Detached from the Sitzungsberichte der Preussischen Akademie der Wissenschaften, Physikalisch-Mathematischen Klasse, XVIII (1920).

Ekweribe, C. and Civan, F., Transient wax deposition model for shut-in subsea pipelines, Paper Number: OMAE2009-80046, presented at the *28th International Conference on Ocean, Offshore and Arctic Engineering*, Honolulu, HI (May 31–June 5, 2009).

Ekweribe, C., Civan, F., Lee, H.S., and Singh, P., Interim report on pressure effect on waxy-crude pipeline-restart conditions investigated by a model system, Paper 115672-PA DOI, SPE Projects, *Facilities & Construction Journal*, 4(3) (2009): 61–74.

Goel, G. and O'Carroll, D.M., Experimental investigation of nonequilibrium capillarity effects: Fluid viscosity effects, *Water Resources Research*, 47(W09507) (2011): 1–15.

Hanspal, N.S. and Das, D.B. Dynamic effects on capillary pressure-saturation relationships for two-phase porous flow: Implications of temperature. *AIChE Journal,* 58(6) (2012): 1951–1965.

Hassanizadeh, S.M., Celia, M.A., and Dahle, H.K., Dynamic effect in the capillary pressure-saturation relationship and its impacts on unsaturated flow, *Vadose Zone Journal*, 1(1) (2002): 38–57.

Hassanizadeh, S.M. and Gray, W.G., Thermodynamic of capillary pressure in porous media, *Water Resources Research*, 29 (1993): 3389–3405.

Hawkins, Jr., M.F., A note on the skin effect, *Transactions of the AIME*, 207 (1956): 356–357.

Hou, L., Chen, L., and Kibbey, T.C.G., Dynamic capillary effects in a small-volume unsaturated porous medium: Implications of sensor response and gas pressure gradients for understanding system dependencies, *Water Resources Research*, 48 (2012): W11522.

Iglauer, S., Wülling, W., Pentland, C.H., Al-Mansoori, S.K., and Blunt, M.J., Capillary-trapping capacity of sandstones and sandpacks, Paper SPE 120960-PA, *SPE Journal*, 16(4) (2011): 778–783.

Iscan, A.G., Kok, M.V., and Civan, F., Investigation of porosity and permeability impairment in sandstones by x-ray analysis and simulation, *Energy Sources: Part A*, 31(5) (2009): 387–395.

Islam, M.R. and Ali, S.M.F., Numerical simulation of emulsion flow through porous media, *Journal of Canadian Petroleum Technology*, 33(3) (1994): 59–63.

Kalaydjian, F.J.-M., Dynamic capillary pressure curve for water/oil displacement in porous media: Theory vs. experiment, Paper SPE 24813-MS, *SPE Annual Technical Conference and Exhibition*, Washington, DC (October 4–7, 1992).

Kumar, A., Steady flow equations for wells in partial water-drive reservoirs, Paper SPE 5964-PA, *Journal of Petroleum Technology*, 29(12) (1977): 1654–1656.

Kuznetsov, A.V. and Nield, D.A., Forced convection with laminar pulsating flow in a saturated porous channel or tube, *Transport in Porous Media*, 65 (2006): 505–523.

Lowe, R.L., Shavit, U., Falter, J.L., Koseff, J.R., and Monismith, S.G., Modeling flow in coral communities with and without waves: A synthesis of porous media and canopy/low approaches, *Limnology and Oceanography*, 53(6) (2008): 2668–2680.

Manthey, S., Hassanizadeh, S.M., and Helmig, R., Macro-scale dynamic effects in homogeneous and heterogeneous porous media, *Transport in Porous Media*, 58(1–2) (2005): 121–145.

Michel, G. and Civan, F., Modeling nonisothermal rapid multiphase flow in wells under nonequilibrium conditions, Paper SPE-102231, *SPE Production & Operations*, 23(2) (2008): 125–134.

Michel, G. and Civan, F., Modeling multiphase wax deposition in submarine pipelines after shut-in, Paper SPE-124725-PP, *the 2009 SPE Annual Technical Conference and Exhibition*, New Orleans, LA (2009a).

Michel, G. and Civan, F., Accurate well-bore hydraulics simulation considering non-isothermal and liquid slippage phenomena for multiphase flow in oil and gas wells, Paper Number: OMAE2009-80068, presented at *the 28th International Conference on Ocean, Offshore and Arctic Engineering*, Honolulu, HI (May 31–June 5, 2009b).

Mikhailov, D. and Nikolaevskii, V., Dynamics of flow through porous media with unsteady phase permeabilities, *Fluid Dynamics*, 35(5) (2000): 715–724.

Nieber, J.L., Dautov, R.Z., Egorov, A.G. et al., Dynamic capillary pressure mechanism for instability in gravity-driven flows: Review and extension to very dry conditions, *Transport in Porous Media*, 58(1–2) (2005): 147–172.

Rajagopal, K.R., On a hierarchy of approximate models for flows of incompressible fluids through porous solids, *Mathematical Models and Methods in Applied Science*, 17(2) (2007): 215–252.

Rasmussen, M.L. and Civan, F., Analytical modeling of non-Fickian wave-diffusion of gas in heterogeneous media, *Applied Mathematical Modelling*, 39(2), January (2015): 862–880.

Reverberi, A.P., Bagnerini, P., Maga, L., and Bruzzone, A.G., On the non-linear Maxwell-Cattaneo equation with non-constant diffusivity: Shock and discontinuity waves, *International Journal of Heat and Mass Transfer*, 51 (2008): 5327–5332.

Roberts, B.E., The effect of sulfur deposition on gas well inflow performance, *SPE Reservoir Engineering* (1997): 118–123.

Sollitt, C.K. and Cross, R.H., Wave transmission through permeable breakwaters, In *Proceedings of 13th Coastal Engineering*, Reston, Virginia: American Society of Civil Engineers, *ASCE*, Vol. 3, Edge, W. (ed.), pp. 1827–1846 (1972).

Tsakiroglou, C.D., Theodoropoulou, M.A., and Karoutsos, V., Nonequilibrium capillary pressure and relative permeability curves of porous media, *AICHE Journal*, 49(10) (2003): 2472–2486.
Zhou, Y., Helland, J.O., and Jettestuen, E., Dynamic capillary pressure curves from pore-scale modeling in mixed-wet-rock images, Paper SPE-154474-PA, *SPE Journal*, 18(4) (2013): 634–645.
Zhu, T., Waluga, C., Wohlmuth, B., and Manhart, M., A study of the time constant in unsteady porous media flow using direct numerical simulation, *Transport in Porous Media*, 104(1) (2014): 161–179.
Whitaker, S., *The Method of Volume Averaging*. Kluwer Academic Publishers, Boston, MA (1999).

11 Modeling Approach for Gradient-Based Motion of Microorganisms in Porous Media and Applications in Biosystems

Zineddine Alloui and Tri Nguyen-Quang

CONTENTS

11.1 Introduction 439
11.2 Mathematical Formulation 441
11.2.1 Dimensional Governing Equations 441
11.2.2 Dimensionalization 443
11.3 Thermotaxis Patterns via Linear Stability Analysis 444
11.3.1 Linearized Equations 444
11.3.2 Numerical Procedure for the Stability Analysis Equations 445
11.4 Results and Discussion 445
11.4.1 Thresholds of Thermotaxis Patterns 445
11.4.2 Effects of the Thermotaxis Speed 445
11.4.3 Effects of the Double Diffusion 446
11.4.4 Discussion on the Case of $Ra_T = 0$ 449
11.5 Applications and Research Perspectives 450
11.6 Summary 452
List of Symbols 452
Acknowledgments 453
References 453

11.1 INTRODUCTION

One of the adaptive behavioral responses of living organisms in their environment is *thermotaxis*, by which they migrate toward a preferred temperature or away from the uncomfortable heat sources. Thermotaxis or motion in the field of temperature gradient is a very common phenomenon and can be found in many events in nature, from biological ones such as the motion of *Dictyostelium* slugs (Maree et al. 1999), self-organized thermoregulation of honeybees (Watmough and Camazine 1995), *Caenorhabditis elegans* behaviors (Matsuoka et al. 2008), human and animal sperm (Bahat and Eisenbach 2006, Bahat et al. 2012) to the migration of colloidal particles (Golestanian 2012).

Various papers have revealed the characteristics of thermotaxis in the life sciences and in engineering. Different models were suggested to mathematically describe this phenomenon. Watmough and Camazine (1995) suggested a thermotaxis diffusion model for thermoregulating bees. These living organisms respond to decreases in their immediate or local temperature with a combination of increased metabolic activity and with movements toward their neighbors. This is modeled by coupling a thermotaxis diffusion equation for the cluster density to a heat equation with a temperature- and density-dependent source. The authors assumed that the heat transfer within the cluster is dominated by conduction. Maree et al. (1999) modeled the motion of the *Dictyostelium discoideum* slugs in the absence and in the presence of a thermal gradient. Their model is an extension of the hybrid cellular automata/partial differential equation model, as formulated by Savill and Hogeweg (1997). Experiments realized by Maree et al. (1999) showed that the modeled slugs maintain their shape and crawl, with a velocity depending on slug size. The authors also showed thermotactic behavior independent on initial orientation.

Many authors tried to suggest different models on nematodes, *C. elegans*, one of the well-known microorganisms with thermotactic behavior, and researchers expected that they could withdraw many interesting conclusions from this particular species for applications into neurobiology, developmental biology, and various other fields. Matsuoka et al. (2008) suggested a simple model with Monte Carlo simulation for *C. elegans* behavior. One important feature of this model is that the authors incorporated isothermal tracking, based on the investigation of Luo et al. (2006), the cryophilic tendencies and thermal adaptation (Ito et al. 2006, Matsuoka et al. 2008).

Their simple model could reproduce several properties of the population-level thermotaxis observed by Ito et al. (2006) related to the thermophilic and cryophilic tendencies of worms. They found that when thermal gradients are present, the distribution of worms, *C. elegans*, spreads faster toward the direction of falling temperature than toward the direction of rising temperature. However, they were unable to deal with states of the worms that depend on both the temperature and the direction of the worm movement. Their model actually could provide a viewpoint on the analyses of the population-level thermal response of real worms (Matsuoka et al. 2008).

Nakazato and Mochizuki (2009) built a simple biased random walk model of the *C. elegans* population behavior, which reflects the results of individual movement assays. Their results assert the importance of the steepness of the thermal gradient that may change the migration behavior drastically in experiments on thermotaxis.

Golestanian (2012) constructed a stochastic formulation to describe the collective behavior of a number of thermally active colloids. For extended time intervals and large length scale limits, as well as for dilute solutions, the formulation simplifies to a set of two nonlinear coupled differential equations for the density and temperature profiles. He found that when the Soret coefficient is positive, the system could be described in a stationary state by the nonlinear Poisson–Boltzmann equation and could adopt density profiles with significant depletion in the middle region when confined. For colloids with negative Soret coefficient, the system can be described as a dissipative equivalent of a gravitational system. The author also showed that in this case, the thermally active colloidal solution could undergo instability at critical laser intensity.

However, none of the models has mentioned the feedback convection that can be generated by the collective behavior of thermotactic microorganisms. In this chapter, we investigated this aspect in porous media. The mathematical model we suggested is a coupled system of partial differential equations wherein the thermotaxis is described under the form of temperature gradient–following term. The linear stability analysis will help us to define the onset of the thermotactic patterns that can get involved in many phenomena in nature.

Related to the pioneering investigation of bioconvection in porous medium, specifically gravitaxis and gyrotaxis, we should refer to the research of Kuznetsov and collaborators (Kuznetsov and Jiang 2001, 2003, Kuznetsov and Avramenko 2002, 2003a,b, 2005, Kuznetsov et al. 2004). Three previous chapters by Kuznetsov (2005, 2008) and Nguyen-Quang et al. (2010) summarized most of works on different aspects (stability analysis and numerical simulation) of bioconvection in porous medium.

The results in this current chapter highlight the first study of critical thresholds for *thermotactic bioconvection patterning* in porous medium and provide insight into several fundamental processes and give direction for our future research involving thermotaxis, chemotaxis, and prey-taxis behavior of microorganism populations. The results are also relevant to a number of biological and environmental problems including the thermo-osmosis in porous medium (Medved and Cerny 2013).

11.2 MATHEMATICAL FORMULATION

11.2.1 Dimensional Governing Equations

For the conceptual model of bioconvection in a porous medium, the governing equations for unsteady flow in a porous medium are obtained by volume averaging the equations of Pedley et al. (1992) according to the theory of Whitaker (1999). The replacement of the Laplacian viscous terms with the Darcian terms describing viscous resistance in a porous medium is the basic concept of this approach (Nguyen-Quang et al. 2005, 2008, 2010). The validity of Darcy's law in the porous medium bioconvection model is therefore assumed similar to that in a natural convection model in a layer being heated from below. We consider a 2D horizontal porous layer of thickness H' containing an initially uniform concentration N' of thermotactic microorganisms. The upper and lower boundaries of the layer are impermeable and subjected to constant temperatures. The porous medium is assumed isotropic with a permeability K as shown in Figure 11.1.

The following hypotheses are also assumed in order to ensure that the thermotactic behavior is not disturbed: (1) The porous matrix does not absorb microorganisms. (2) The pore sizes are significantly larger than the microbial cell sizes and the microorganism suspension is dilute; therefore, the change of permeability of the porous matrix due to cell deposition is negligible. (3) The possible local vorticity generated by flow through the pores does not affect the ability of microorganisms to reorient themselves. (4) The mortality and the multiplication of microorganism cells are neglected; in other words, the cells are assumed not to die or grow; the number of cells is therefore constant. We assume that all physical properties of the fluid are constant except the density in the buoyancy term of the Boussinesq's approximation. It is also assumed that the suspension of microorganisms is incompressible.

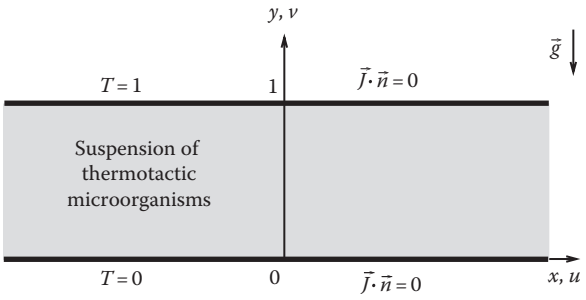

FIGURE 11.1 Physical description of the problem.

The governing equations are therefore

$$\nabla' \cdot \vec{V}' = 0 \tag{11.1}$$

$$\frac{\mu}{K}\vec{V}' = -\nabla' P' + \rho\vec{g} \tag{11.2}$$

$$(\rho C)_p \frac{\partial T'}{\partial t'} + (\rho C)_f \nabla' \cdot (T'\vec{V}') = \nabla' \cdot (k_p \nabla' T') \tag{11.3}$$

$$\varepsilon \frac{\partial N'}{\partial t'} + \nabla' \cdot (N'\vec{V}') = -\nabla' \cdot (N'\vec{V}_c' - D_c \nabla' N') \tag{11.4}$$

where

$\vec{V}'(u',v')$ is the fluid velocity
P' is the pressure
$\vec{V}_c'$ is the average cell swimming velocity due to thermotaxis
$\vec{g}$ is the acceleration of gravity

The thermotaxis velocity is defined as follows:

$$\vec{V}_c' = W_0' \vec{\nabla} T' \tag{11.5}$$

where W_0' is a constant standing for the capacity of thermotactic motion of microorganisms (with the dimension $m^2 \cdot s^{-1} \cdot K^{-1}$), which actually is the diffusivity of microorganisms per 1 temperature degree (this parameter seems equivalent to the *thermo-osmotic permeability* in a thermo-osmosis, fluid flow driven by a temperature gradient discussed by Gonçalvès and Tremosa (2010) and Tremosa et al. (2010)). $\vec{\nabla} T'$ is the thermal gradient exerted on the considered system (K/m).

If we introduce the dimensionless velocity of thermotactic microorganisms *Pe* (Peclet number), we will have

$$Pe = \frac{H'}{D_c} W_0 = \frac{1}{D_c} W_0' \Delta T' \tag{11.6}$$

We can notice that the system of governing equations is quite similar to the one of gravitactic bioconvection with double diffusion treated by Nguyen-Quang et al. (2008) except for the swimming velocity term *Pe*. This would be a base of discussion of our results in the next part.

We would remind herein the swimming velocity of microorganisms in the case of gravitaxis, which is $\vec{V}_c' = (0, V_c)$ with V_c as the upward gravitactic swimming speed (m/s) (Nguyen-Quang et al. 2008).

In the thermotactic behavior, this swimming velocity would be assumed as $\vec{V}_c' = W_0' \vec{\nabla} T'$ with an amplitude (swimming speed) defined as follows:

$$W_0 = \frac{W_0'}{H'} \Delta T' \text{ m/s} \tag{11.7}$$

In the aforementioned equations, $(\rho C)_f$ and $(\rho C)_p$ are, respectively, the heat capacity of fluid and of saturated porous medium. Also, ε is the porosity of the porous medium and K the permeability of

the porous medium. The fluid containing microorganisms is assumed to satisfy the Boussinesq's approximation. The density variation with temperature and concentration is described by the state equation

$$\rho = \rho_f \left[1 - \beta_T (T' - T_0') + \beta_N (N' - N_0')\right] \tag{11.8}$$

where

ρ_f is the fluid density at temperature $T' = T_0'$ and concentration $N' = N_0'$
β_T and β_N are the thermal and concentration expansion coefficients, respectively

The boundary conditions applied on the walls of the layer are

$$v' = T' - T_0' = \vec{J}' \cdot \vec{n} = 0 \quad \text{at } y' = 0 \tag{11.9a}$$

$$v' = T' - T_0' - \Delta T' = \vec{J}' \cdot \vec{n} = 0 \quad \text{at } y' = H' \tag{11.9b}$$

where

$$\vec{J}' = N'(\vec{V}' + \vec{V}_c') - D_c \nabla' N' \tag{11.9c}$$

11.2.2 Dimensionalization

The system of governing equations is dimensionalized by using scaling length by H', velocity by D_c/H', and time by $(\rho C)_p H'^2/[(\rho C)_f D_c]$. Also, we introduce the reduced temperature $T = (T' - T_0')/\Delta T'$ and the reduced concentration $N = (N' - N_0')/\Delta N'$. Using these scales, Equations 11.1 through 11.4 can be transformed in terms of the stream function Ψ to the following dimensionless form:

$$\nabla^2 \Psi = Ra_N \frac{\partial N}{\partial x} - Le\, Ra_T \frac{\partial T}{\partial x} \tag{11.10a}$$

$$\frac{\partial T}{\partial t} + \frac{\partial \Psi}{\partial y}\frac{\partial T}{\partial x} - \frac{\partial \Psi}{\partial x}\frac{\partial T}{\partial y} = Le\, \nabla^2 T \tag{11.10b}$$

$$\phi \frac{\partial N}{\partial t} + \left(\frac{\partial \Psi}{\partial y} + Pe \frac{\partial T}{\partial x}\right)\frac{\partial N}{\partial x} + \left(-\frac{\partial \Psi}{\partial x} + Pe \frac{\partial T}{\partial y}\right)\frac{\partial N}{\partial y} = \nabla^2 N - PeN\nabla^2 T \tag{11.10c}$$

where, in order to satisfy the continuity equation, the stream function Ψ is defined such that $u = \partial\Psi/\partial y$, $v = -\partial\Psi/\partial x$. $Pe = W_0 \Delta T'/D_c$ is the Peclet number, $Ra_N = g\beta_N \Delta N' H' K/\nu D_c$ is the bioconvection Rayleigh number, $Ra_T = g\beta_T \Delta T' H' K/\nu\alpha_p$ is the thermal Rayleigh number, $Le = \alpha_p/D_c$ is the Lewis number, and $\phi = \varepsilon(\rho C)_f/(\rho C)_p$ is the normalized porosity.

The corresponding boundary conditions are

$$\Psi = T = \frac{\partial N}{\partial y} - PeN - \frac{Pe}{e^{Pe} - 1}\frac{\partial T}{\partial y} = 0 \quad \text{at } y = 0 \tag{11.10d}$$

$$\Psi = T - 1 = \frac{\partial N}{\partial y} - PeN - \frac{Pe}{e^{Pe} - 1}\frac{\partial T}{\partial y} = 0 \quad \text{at } y = 1 \tag{11.10e}$$

When the fluid is motionless ($\Psi_B = 0$), the system of equations with boundary conditions (11.10a–e) yields the following temperature and concentration profiles:

$$T_B = y \text{ (linear profile)} \tag{11.11a}$$

and

$$N_B = \frac{e^{Pe\, y}}{e^{Pe} - 1} \text{ (exponential profile)} \tag{11.11b}$$

11.3 THERMOTAXIS PATTERNS VIA LINEAR STABILITY ANALYSIS

11.3.1 Linearized Equations

In this section, the onset of thermotactic patterning is investigated on the basis of the linear stability theory. We perform the linear stability analysis to study the onset of diffusion convection caused by thermotactic microorganisms and by thermal effects. The results are presented as stability diagrams showing the critical Rayleigh number Ra_N vary versus wave number k and as a function of thermal critical Rayleigh number Ra_T. These critical Rayleigh numbers represent for the onset of spatiotemporal pattern predicted by linear stability, focusing on the predicted impacts of thermal stratification on microorganism hydrodynamic processes. Hydrodynamic processes, or flow regimes, are represented by the streamlines traced from the stream function. This dimensionless stream function denotes the path of a fluid particle. In our analysis, streamlines reveal the path of thermotactic cells or/and temperature trajectories in a flow field where temperature and microorganisms interact. The intensity of stream function reflects the importance of hydrodynamic processes (the stronger the value of ψ, the higher the hydrodynamic effect).

The stability to small perturbations from the quiescent state (Ψ_B, T_B, N_B) is introduced by rewriting the governing equations using $\psi = \Psi - \Psi_B$, $\theta = T - T_B$, and $\eta = N - N_B$. As usual, the disturbance solution is assumed to have the following functional form:

$$\left.\begin{aligned} \psi(t,x,y) &= \tilde{\psi}(y) e^{pt+ikx} \\ \theta(t,x,y) &= \tilde{\theta}(y) e^{pt+ikx} \\ \eta(t,x,y) &= \tilde{\eta}(y) e^{pt+ikx} \end{aligned}\right\} \tag{11.12}$$

where

$\tilde{\psi}(y)$, $\tilde{\theta}(y)$, and $\tilde{\eta}(y)$ describe the vertical perturbation profiles
$p = p_r + i\omega$ is the complex growth rate of the perturbation, where p_r is the growth rate of instability and ω is the frequency of instability
$k = \pi/\lambda$ is the real wave number, where λ is the wavelength

Introducing (11.12) into (11.10a–c) and neglecting second higher-order nonlinear terms yield the following linear system:

$$(D^2 - k^2)\,\tilde{\psi} + ik\, Le\, Ra_T\, \tilde{\theta} - ik\, Ra_N\, \tilde{\eta} = 0 \tag{11.13a}$$

$$Le\,(D^2 - k^2)\,\tilde{\theta} + ik\, DT_B\, \tilde{\psi} = p\, \tilde{\theta} \tag{11.13b}$$

$$(D^2 - k^2)\,\tilde{\eta} - Pe\, DT_B\, D\tilde{\eta} - Pe\, N_B (D^2 - k^2)\,\tilde{\theta} - Pe\, DN_B\, D\tilde{\theta} + ik\, DN_B\, \tilde{\psi} = p\, \phi\, \tilde{\eta} \tag{11.13c}$$

The boundary conditions, corresponding to Equations 11.10d and e, are

$$\tilde{\psi} = \tilde{\theta} = D\tilde{\eta} - Pe\ \tilde{\eta} - \frac{Pe}{e^{Pe} - 1} D\tilde{\theta} = 0 \quad \text{at } y = 0,1 \tag{11.14}$$

where $D = d/dy$.

The perturbed state equations (11.13a–c) with the boundary conditions (11.14) may be written in a compact matrix form as

$$M_A(k)\mathbf{Y} = pM_B(k)\mathbf{Y} \tag{11.15}$$

where

$\mathbf{Y} = [\tilde{\psi}, \tilde{\theta}, \tilde{\eta}]$ is a two-component vector of the perturbation

$M_A(k)$ and $M_B(k)$ are two linear differential operators that depend on the control parameters Ra_N, Ra_T, Le, Pe, and ϕ.

11.3.2 Numerical Procedure for the Stability Analysis Equations

For the linear stability analysis, the set of equations (11.15) is solved using a discretization scheme by finite differences, which is one of the straightforward ways to deal with this kind of problem. The system is discretized by using fourth- and second-order central difference schemes in the domain between $y = 0$ and $y = 1$. For n discretized points, the resulting discrete system has $3n$ eigenvalues that can be found by using a standard subroutine for eigenvalues such as EIGENC or QZ. The value of Ra_N for which the maximal growth rate p_r cancels is iteratively determined by Newton's method, holding wave number k, Ra_T, Le, Pe, and ϕ constant. The time needed for computational process to achieve a convergence remains quite reasonable however. The numerical procedure needs hence a discretization number n greater than 100.

11.4 RESULTS AND DISCUSSION

11.4.1 Thresholds of Thermotaxis Patterns

In Figure 11.2, we show a family of stability curves obtained with various Ra_N versus k when $Le = 1$ and $Pe = 0.5$. It divides the parameter space (Ra_N, k) into two regions: the region above the stability curve is unstable, while the one below is stable. For each value of Pe, we get one stability curve with a minimum at $Ra_N = Ra_c$, $k = kC$. This is referred to as the critical point for the onset of bioconvection caused by thermotaxis. Figure 11.3 shows the onset of the bioconvection patterning via isolines of stream function, concentration, and temperature for the case of $Pe = 0.5$, $Le = 1$ when Ra_T adopted three different values 0, −5, and 5.

11.4.2 Effects of the Thermotaxis Speed

Figure 11.4 shows the curves of Ra_N versus k in functions of Pe, for the case of $Ra_T = 0$ (i.e., no double-diffusion effects), $Le = 1$. We can see that when Pe varies, influences of mobility on the pattern are very significant. Precisely, when $Pe \to 0$, the threshold of thermotactic bioconvection Ra_{NC} tends to the value of $4\pi^2$, while the critical wave number k_C tends to π. It is very interesting to observe that these thresholds correspond exactly to the thresholds of a porous layer heated from below with a constant temperature (Nield and Bejan 2012). To understand this important discovery, we have to recall that for the case of $Pe \to 0$ in pure gravitactic bioconvection published in Nguyen-Quang et al. (2005), the obtained thresholds are equivalent to a porous layer heated from below by a constant flux ($Ra_{NC} \to 12$, $k_C \to 0$).

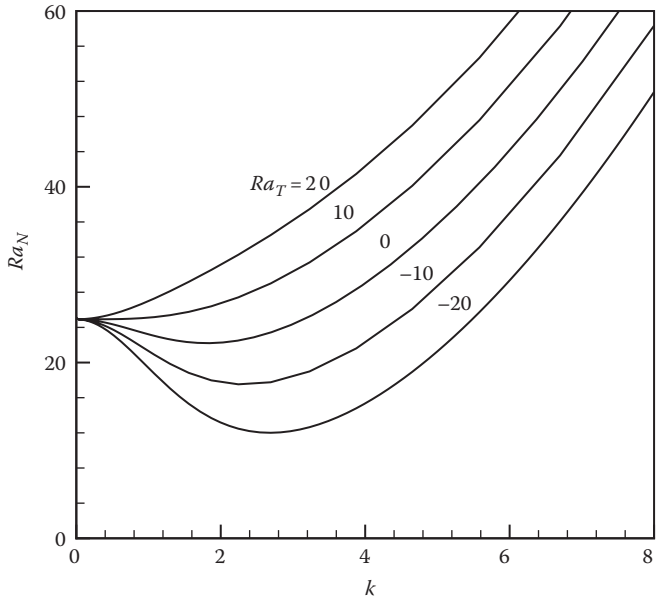

FIGURE 11.2 Stability curves Ra_N versus k for different values of Ra_T when $Pe = 0.5$, $Le = 1$.

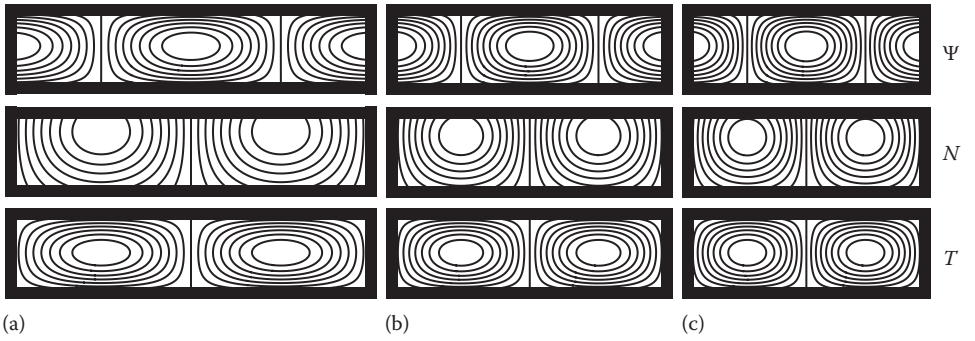

FIGURE 11.3 Isolines of stream function (left), concentration (middle), and temperature (right) for the case of $Pe = 0.5$, $Le = 1$ when (a) $Ra_T = 5$, (b) $Ra_T = 0$, (c) $Ra_T = -5$.

From Figure 11.5, we also observed that there exists a critical value of Pe for the minimal value of Ra_{NC}. That critical Pe value is around 5.9 (where Ra_{NC} reached the minimum value shown in Figure 11.5). The equivalent wave number k_C is not however the equivalent minimum value, and we notice that k_C gets its minimum value when Pe is approaching closer to 1.03. In other words, the critical values of Ra_{NC} and of wavelength k_C do not happen in the same moment.

11.4.3 Effects of the Double Diffusion

Figure 11.6 illustrates the curve Ra_{NC} versus Ra_T for the case of $Le = 1$ at different values of swimming speeds Pe (it is reminded that $Le = \alpha_p/D_c$ is the ratio between thermal diffusivity and cell diffusivity). We notice that negative values of Ra_T (i.e., heating from below according to our temperature gradient context assumed in Figure 11.1) destabilize the system, because the system becomes exactly the classical thermoconvection configuration heated from below by a constant temperature (Nield and Bejan 2012). From Figure 11.6, it is observed that $Ra_{NC} = 0$ when $Ra_T = -4\pi^2$ (i.e., at the

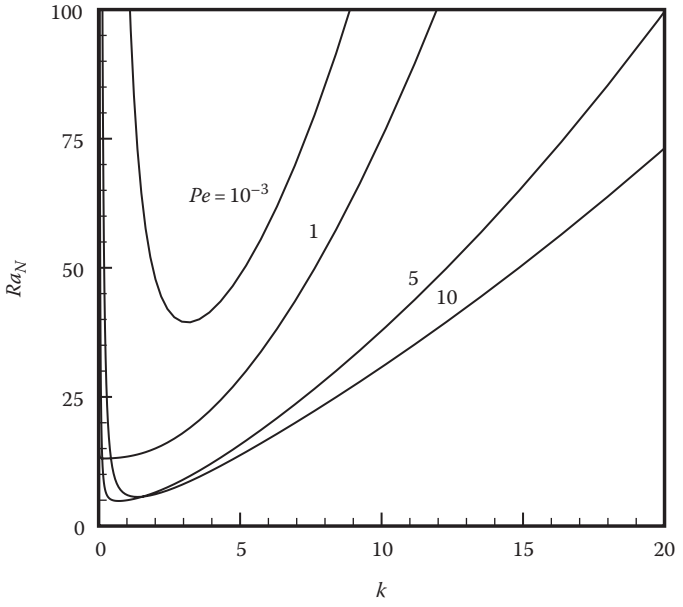

FIGURE 11.4 Ra_N versus k in functions of Pe for the case $Ra_T = 0$ and $Le = 1$.

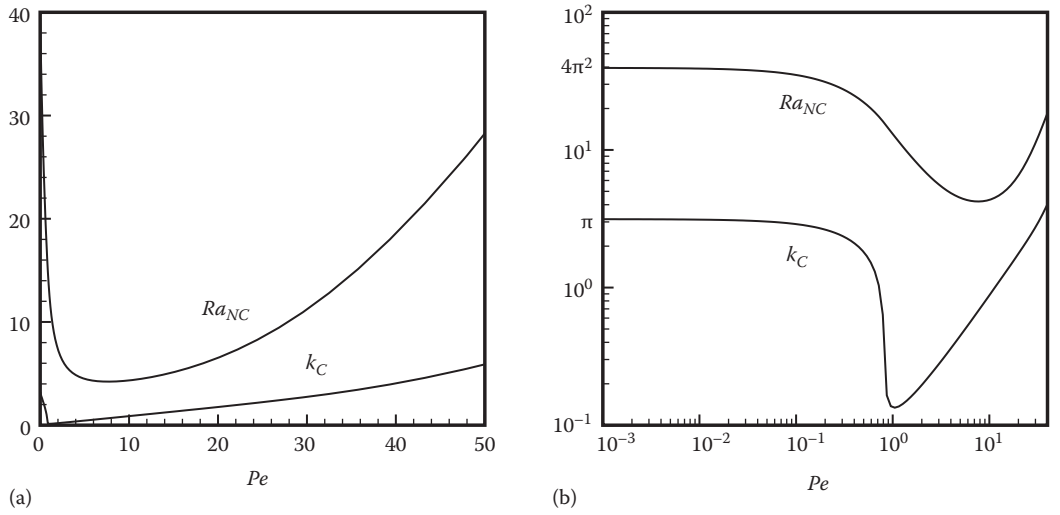

FIGURE 11.5 Ra_{NC} and k_C versus Pe for the case $Ra_T = 0$ and $Le = 1$ (a, normal scale; b, log-scale).

exact value of thermal threshold to decline the thermoconvection) with any value of Pe. In this case, convection patterning may happen and be governed by thermal effects.

When Lewis number Le varies, we obtain the curve of Ra_{NC} versus k_C for $Ra_T = 0$ and $Pe = 10$ (Figure 11.7). We recognized that contrary to the gravitactic thermobioconvection (Nguyen-Quang et al. 2008) where the Lewis number Le did not have any effect when $Ra_T = 0$, here, this ratio plays a very significant role in the quantification of Ra_{NC}. From Figure 11.7, we can see that when $Ra_T = 0$, the larger the Le, the higher the Ra_{NC} and vice versa. However, the critical wave number k_C changes only slightly with this ratio Le.

It is extremely interesting to underline that the thermotaxis linear stability analysis can lead to the case of *overstability* when $Le = 0.1$ (i.e., the cell diffusivity is 10 times greater than thermal

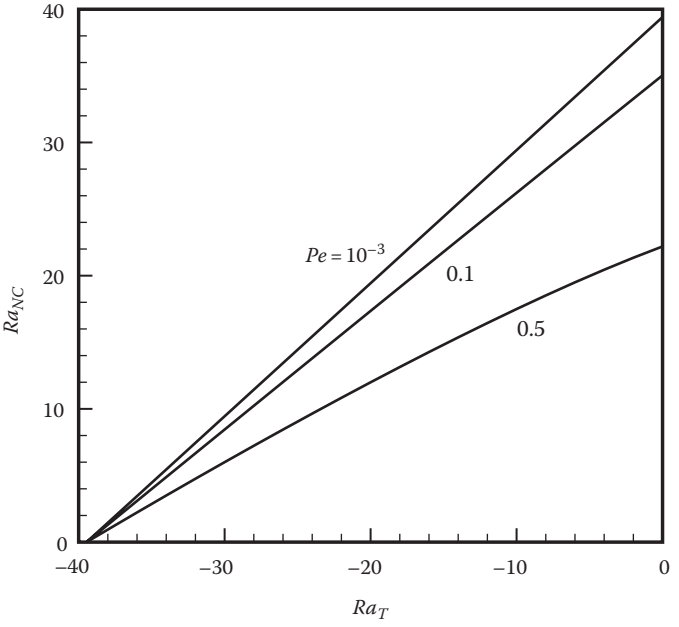

FIGURE 11.6 Ra_{NC} versus Ra_T for $Le = 1$ at various Pe.

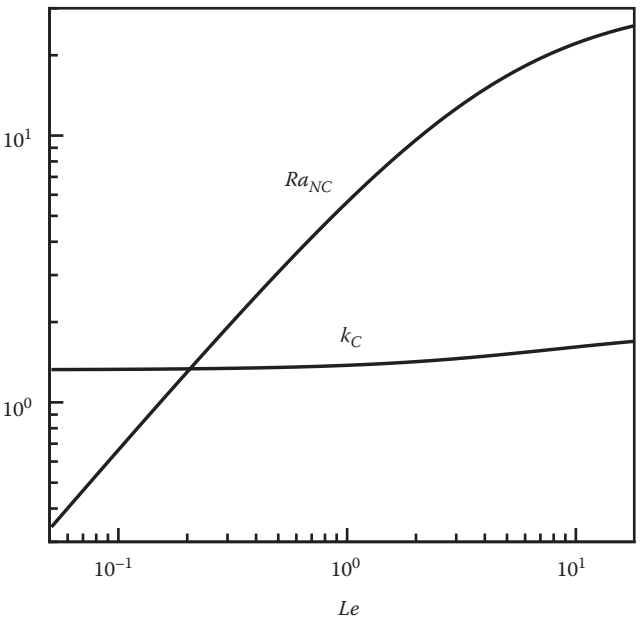

FIGURE 11.7 Ra_{NC} and k_C versus Lewis number for $Ra_T = 0$ and $Pe = 10$.

diffusivity). Figure 11.8a gives us two critical thresholds of Ra_N versus the wave number with three different cases of Ra_T. This phenomenon can be explained by the fact that from Equation 11.12, $p = p_r + i\omega$ was assumed as the complex growth rate of disturbances where p_r and ω stand for the growth rate and the frequency of instability, respectively.

By the theory of linear stability for natural convection, we knew that if p is real, the amplitude of the velocity is a monotonic function of time, and when the growth rate p is a complex quantity,

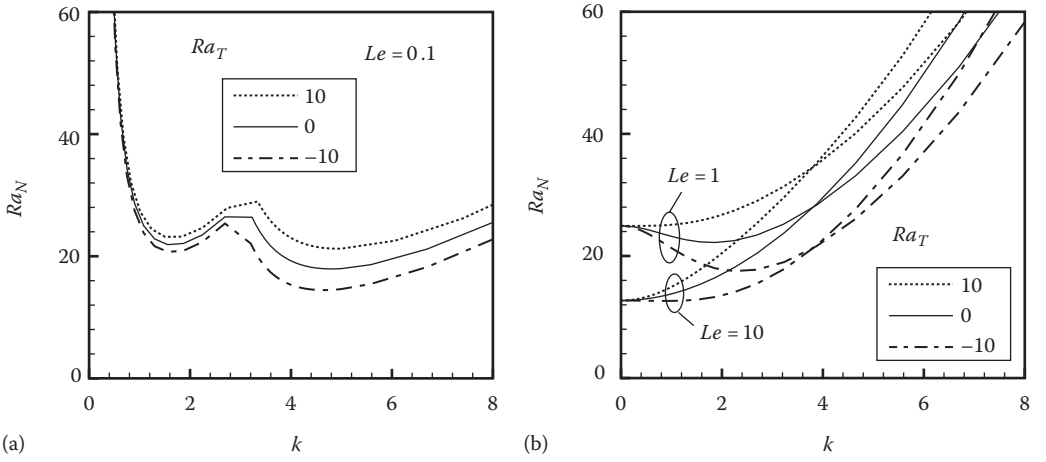

FIGURE 11.8 Ra_N versus k in function of Ra_T, case of $Pe = 0.5$, with $Le = 0.1$ (a, overstability) and $Le = 1$ and 10 (b).

TABLE 11.1
Variation of ω versus *k* in the Case of *Pe* = 0.5, $Ra_T = 0$, and *Le* = 0.1

k	Ra_N	ω
1.56	21.90	3.56
2.69	26.45	3.46
3.23	26.38	0
4.80	17.92	0

the system will become overstable, equivalent to the exponential increase with time of velocity amplitude, but this increase varies periodically (Kosmeider 1993). The results we obtained herein showed that calculated values of ω are nonzero (Table 11.1), meaning clearly that our growth rate p is a complex quantity; hence, the overstability occurs (Figure 11.8a). When the cell diffusivity is equal or less than the thermal diffusivity (Le = 1 or 10, Figure 11.8b), we will not have the overstability anymore.

11.4.4 Discussion on the Case of $Ra_T = 0$

If we replace the expression (11.6) $Pe = \dfrac{H'}{D_c} W_0 = \dfrac{1}{D_c} W_0' \Delta T'$ in the formula $Ra_T = \dfrac{g\beta_T \Delta T' H' K'}{\nu\alpha}$, we will get the thermal Rayleigh number in function of Peclet number Pe as follows:

$$Ra_T = \frac{g\beta_T H' K' D_c Pe}{\nu\alpha W_0'} \tag{11.16}$$

Based on (11.16), we can discuss the following different cases:

1. If $\Delta T' = 0$, it means that there is no thermal gradient, $Ra_T = 0$, then $Pe = 0$ (from (11.6)), and we will have no pattern nor thermotactic behaviors occurring. In this case, the system could be understood as having no thermal effects and hence no thermotactic patterns happening.

2. However, because we have already applied the Dirichlet condition for $T' = 1$ at the top and $T' = 0$ at the bottom, that is, $\Delta T'$ cannot cancel out, there exists always a temperature gradient in the system. We also assumed previously that the capacity of thermotactic motion of microorganisms is W_o (Equation 11.7). Therefore, Pe can tend to 0 when W_o tends to 0 in the case of microorganism cells having a very weak thermotactic motion capacity or not having it anymore due to age or stress. This case of $Pe \to 0$ was previously discussed.

When $Pe \neq 0$ and $\Delta T' \neq 0$, $Ra_T = 0$ could be understood as the following scenarios in the system according to Equation 11.16:

1. $Ra_T = 0$ when $D_c \to 0$: The diffusion coefficient of microorganisms is very small. Depending on the species and taxis velocity, this coefficient varies very much. Le becomes much higher when $D_c \to 0$ ($Le = \alpha_p/D_c$), and Ra_N can be much stronger. In this case, the pattern can be generated by Ra_N and Lewis effects.
2. $Ra_T = 0$ when $K \to 0$: When the porous medium permeability is so low such as in a rock structure (but the porous matrix is large enough for the movement of microorganisms passing through), the Ra_T can tend to 0. Bioconvection patterns may happen due to a temperature gradient and thermotactic motion capacity of cells existing in the system.
3. $Ra_T = 0$ when $\beta_T \to 0$: This case can happen when the coefficient of thermal expansion of the considered porous medium is zero. Because this coefficient describes how the size of the medium changes with a change in temperature, it would imply that the volume of isotropic porous medium does not change significantly under the temperature effects. The thermotactic patterns would happen under Ra_N effects.

When $\Delta T \neq 0$ and $Ra_T \neq 0$, we will have definitely the case of thermotactic or thermophilic patterns. If we simulate the system of governing equations for the supercritical cases, we would observe a very interesting phenomenon: microorganisms will have a preferable place to move forward and to accumulate. This means that the highest concentration zone of cells is not at the top (where $T' = 1$) but somewhere in the lower level because microorganisms would show their behavior to a comfortable and preferable temperature to be growing up. Some very first step simulations (not presented here) of the system of equations and equivalent boundary conditions (11.10) can show that obtained results seem to fit with many experiences on the thermotactic behaviors of microorganisms. The profound simulations with high precision and accuracy are part of our future research.

11.5 APPLICATIONS AND RESEARCH PERSPECTIVES

The direct application of thermotaxis behavior could be firstly linked to the thermo-osmosis. A range of thermo-osmotic permeability (k_T), between 6×10^{-12} and 2×10^{-10} $m^2 \cdot K^{-1} \cdot s^{-2}$, was established by Tremosa et al. (2010) and Goncalves and Tremosa (2010) for argillaceous materials and suggests an effect of pore size on the thermo-osmotic permeability of a clay rock. These works indicate that thermo-osmosis will have an influence on water flow in the presence of a temperature gradient, and this process is to consider in water flow studies in clay rocks (Goncalves and Tremosa 2010, Tremosa et al. 2010).

In many biological systems, the movement of organisms (individually or collectively) occurs in response to transported signals. Several experiments have demonstrated that besides the mechanical driving force, cell migration may also be influenced by chemical, thermal, and/or electrical cues. The effects of chemotaxis, thermotaxis, and electrotaxis to the initial mechanotaxis model of cell migration contribute very significantly to biological and medical events to deal with diseases.

Cell migration constitutes a fundamental phenomenon involved in many biological processes such as wound healing, cancer development, and tissue regeneration (Mousavi et al. 2013).

Actually, the advection terms are denoted by the velocity of the cell motion and the medium velocity. The cell motion suggested in our model herein is the gradient-based velocity or gradient-following velocity. This term therefore seems to be one of the most general cases that can represent for other kinds of taxis we have mentioned in different works (Nguyen-Quang et al. 2010) including prey-taxis (Sapoukhina et al. 2003). We can say that the gradient-based behavior is a common behavior of living organisms and the gradient-following motion model suggested herein for thermotaxis can be generalized in many fields.

Many authors underlined the strong link between the chemotaxis by gradient term with stimuli and bacteria in both soils and water media that must constantly adjust their metabolism and behavior in order to survive and grow under changing environmental conditions (Englert et al. 2009, Xue and Othmer 2009, Ahmed et al. 2010, Marcos et al. 2012, Stocker 2012). Nutrients such as amino acids, sugars, and organic acids, terminal electron acceptors, light, and temperature can affect metabolism, and they may all act as signals. Sensing of specific cues is dependent on the presence of dedicated receptors, which are characterized by specificity and sensitivity for the signal detected. These scenarios can be found in many applications such as in biological processes ranging from tissue development to malignant diseases (Dalton et al. 2001, Suresh 2007, Behesti and Marino 2009, Pompe et al. 2009, Zhao 2009).

In vivo, thermotaxis may be complementary to chemotaxis, with each mechanism working in regions where the other is ineffective (Bahat and Eisenbach 2006). It is remarkable that in all the experimentally thermotactic observations of the cell motility, the cell migrates toward warmer sites (Higazi et al. 1996, Bahat and Eisenbach 2006).

At the scale of animals, thermotaxis is also one of their adaptive behaviors in their environment, by which they migrate toward a preferred temperature. This sensorimotor integration is accomplished by choosing one of two behaviors depending on the surrounding temperature, namely, thermophilic or cryophilic movement. The nematode worm *C. elegans* exhibits thermotaxis, and its migration behavior has been analyzed experimentally at both the population and individual levels. *C. elegans* is an excellent model system for studying neuroscience systems to explain how the structure of neural circuits could lead to changes in behavior (White et al. 1986, Appleby 2012).

Thermotaxis in animal behavior is important as a source of inspiration for all work involving autonomous robots. Animals are able to function perfectly in their environment and to adapt to changes in it. Models of animal behavior, both low-level models involving individual neurons and high-level phenomenological models, can serve as an inspiration for the development of the corresponding behavior in robots. Furthermore, animals are generally experts in allocating time in an optimal or near-optimal fashion to the many activities (such as eating, sleeping, drinking) that they must carry out in various circumstances, and lessons concerning behavior selection in animals can give important clues to the solution of similar problems in robotics.

It should be noted that in the behavior-based approach to robotics, researchers nowadays have the tendency to use a more generous definition of intelligent behavior than in classical artificial intelligence (Wahde 2003). Consequently, the simple behaviors in animals, such as gradient-following or gradient-based taxis play a very important role in the new concepts and models.

The application of the thermotaxis model can be also applied on the scale of humans such as using the thermal information for the characterizing spaces in architecture and building design by presenting thermal information (Narumi et al. 2009).

Finally, one of the significant applications of our model is regarding the prey-taxis model (Arditi et al. 2001, Sapoukhina et al. 2003, Chakraborty et al. 2007). In the prey-taxis model, there are the reaction term showing the predation concentration and the advection term denoting the mobility of predators toward their preys.

11.6 SUMMARY

In this chapter, the linear stability analysis has been realized to predict the onset of thermotaxis patterns in porous media. This kind of taxis, as we mentioned in our last work (Nguyen-Quang et al. 2010), takes part in the various families of directional motions that are not exhaustively studied, especially on the facet of stability analysis and development of convection regimes beyond critical thresholds.

It seems that the gradient-based taxis are the most common behavior of living organisms. The model we suggested in this chapter includes the term of directional motion under the gradient-stimuli-following velocity. This term may mathematically generalize a majority of gradient-based taxis including *chemotaxis*, *phototaxis*, and *prey-taxis*.

Results obtained by linear stability analysis show that thermotactic behaviors may be analogous to the thermal convection heated from below by constant temperature when the Peclet number (capacity of thermotactic motion) is very weak (approaching 0) and there exists an important over-stability state when the cell diffusivity is much greater than the thermal diffusivity.

Actually, the equation of prey-taxis system (Arditi et al. 2001, Sapoukhina et al. 2003, Chakraborty et al. 2007) is exactly our equation of transport for cells herein plus the predation term standing for the function response. The equation prey-taxis including the gradient-following term is therefore under the form of reaction–diffusion–advection. Consequently, our future study will deal with the prey-taxis behavior of mobile microorganisms in porous medium, which is a promising horizon for the bioconvection research.

In the system where temperature and cell motility by thermotaxis can both result in hydrodynamic patterns, we found strong interactions between thermal gradients and cell population via the spatial distribution of cells. Although this pioneering work still has to be developed and tested in natural systems, laboratory experiments with thermophilic species such as *Tetrahymena thermophila* (Shiurba et al. 2006) or *C. elegans* would confirm the results of our model.

The results reported here reveal a biophysical coupling that results from the scale of individual behavior. They also suggest its importance to define the spatiotemporal pattern over larger ecological scales of porous medium. Further investigation will elucidate the robustness of this gradient-based taxis model and its importance in natural ecological systems.

LIST OF SYMBOLS

D_c	Mass diffusivity of microorganisms
g	Gravitational acceleration
H'	Height of porous layer
k	Wave number
k_p	Thermal conductivity of the porous medium
K	Permeability of the porous medium
Le	Lewis number, (α_p/D_c)
N	Reduced concentration of microorganisms, $(N' - N_0')/\Delta N'$
p	Complex growth rate of the perturbation
p_r	Real growth rate of instability
P'	Pressure
Pe	Peclet number, $(W_0 \Delta T'/D_c)$
Ra_N	Bioconvection Rayleigh number, $g\beta_N \Delta N' H' K/\nu D_c$
Ra_T	Thermal Rayleigh number, $g\beta_T \Delta T' H' K/\nu\alpha_p$
t	Dimensionless time, $t'(\rho C)_f D_c / [(\rho C)_p H'^2]$
T	Dimensionless temperature, $(T' - T_0') / \Delta T'$
u	Dimensionless velocity in x direction, $(u'H'/D_c)$
v	Dimensionless velocity in y direction, $(v'H'/D_c)$

$\vec{V}_c'$ Average cell swimming velocity due to thermotaxis
W_0' Constant standing capacity of thermotactic motion of microorganisms
x Dimensionless coordinate axis, (x'/H')
y Dimensionless coordinate axis, (y'/H')

Greek Symbols

α_p Thermal diffusivity
β_N Concentration expansion coefficient
β_T Thermal expansion coefficient
μ Dynamic viscosity of fluid
ν Kinematic viscosity of fluid
ε Porosity of the porous medium
ϕ Normalized porosity, $\varepsilon\ (\rho C)_f/(\rho C)_p$
λ Wavelength
ρ Density of fluid, kg/m^3
ω Frequency of instability
Ψ Dimensionless stream function, Ψ'/α

Subscript

0 Reference state

Superscript

$'$ Referring to dimensional variable

ACKNOWLEDGMENTS

The authors would like to thank Prof. The Hung Nguyen (Ecole Polytechnique de Montreal, Canada) for the first idea of conception related to the *thermotaxis* behavior. TNQ acknowledges Prof. Nick Hill (University of Leeds) and Prof. Kessler (University of Arizona) for some e-mail exchanges from many years ago related to microorganism population conceptions. He also acknowledges support from the NSERC Discovery Grant No. RGPIN 03796.

REFERENCES

Ahmed, T., T.S. Shimizu, and R. Stocker. 2010. Bacterial chemotaxis in linear and nonlinear steady microfluidic gradients. *Nano Letters* 10: 3379–3385.

Ainsebaa, B.E., M. Bendahmaneb, and A. Noussairc. 2008. A reaction–diffusion system modeling predator–prey with prey-taxis. *Nonlinear Analysis: Real World Applications* 9: 2086–2105.

Appleby, P.A. 2012. A model of chemotaxis and associative learning in *C. elegans. Biological Cybernetics* 106: 373–387.

Arditi, R., Y. Tyutyunov, A. Morgulis, V. Govorukhin, and I. Senina. 2001. Directed movement of predators and the emergence of density-dependence in predator-prey models. *Theoretical Population Biology* 59: 207–221.

Bahat, A., S.R. Caplan, and M. Eisenbach. 2012. Thermotaxis of human sperm cells in extraordinarily shallow temperature gradients over a wide range. *PLoS One* 7(7): e41915.

Bahat, A. and M. Eisenbach. 2006. Sperm thermotaxis. *Molecular and Cellular Endocrinology* 252(1–2): 115–119.

Behesti, H. and S. Marino. 2009. Cerebellar granule cells: Insights into proliferation, differentiation, and role in medulloblastoma pathogenesis. *The International Journal of Biochemistry & Cell Biology* 41(3): 435–445.

Chakraborty, A., M. Singh, D. Lucy, and P. Ridland. 2007. Predator-prey model with prey-taxis and diffusion. *Mathematical and Computer Modelling* 46: 482–498.

Dalton, B.A., X.F. Walboomers, M. Dziegielewski, M.D. Evans, S. Taylor, J.A. Jansen, and J.G. Steele. 2001. Modulation of epithelial tissue and cell migration by microgrooves. *Journal of Biomedical Materials Research* 56(2): 195–207.

Englert, D.L., M.D. Manson, and A. Jayaraman. 2009. Flow-based microfluidic device for quantifying bacterial chemotaxis in stable, competing gradients. *Applied and Environmental Microbiology* 75(13): 4557–4564.

Golestanian, R. 2012. Collective behavior of thermally active colloids. *Physical Review Letters* 108(3): 038303-1–038303-5.

Gonçalvès, J. and J. Trémosa. 2010. Estimating thermo-osmotic coefficients in clay-rocks: I. Theoretical insights. *Journal of Colloidal Interface Science* 342(1): 166–174.

Higazi, A.A.R., D. Kniss, J. Manuppello, E.S. Barnathan, and D.B. Cines. 1996. Thermotaxis of human trophoblastic cells. *Placenta* 17: 683–687.

Ito, H., H. Inada, and I. Mori. 2006. Quantitative analysis of thermotaxis in the nematode *Caenorhabditis elegans*. *Journal of Neuroscience Methods* 154: 45–52.

Kimura, S., M. Vynnycky, and F. Alavyoon. 1995. Unicellular natural circulation in a shallow horizontal porous layer heated from below by a constant flux. *Journal of Fluid Mechanics* 294: 231–257.

Koschmieder, E.L. 1993. *Bénard Cells and Taylor Vorticities*. Cambridge University Press, Cambridge, U.K.

Kuznetsov, A.V. 2005. Modeling bioconvection in porous media, in *Handbook of Porous Media*, 2nd edn., K. Vafai (Ed.), Taylor & Francis, New York, pp. 645–686.

Kuznetsov, A.V. 2008. New developments in bioconvection in porous media: Bioconvection plumes, bio–thermal convection, and effects of vertical vibration, in *Emerging Topics in Heat and Mass Transfer in Porous Media—From Bioengineering and Microelectronics to Nanotechnology*, Theory and Applications of Transport in Porous Media, Vol. 22, P. Vadasz (Ed.), Springer, Dordrecht, the Netherlands, pp. 181–217.

Kuznetsov, A.V. and Avramenko, A.A. 2002. A 2D analysis of stability of bioconvection in a fluid saturated porous medium—Estimation of the critical permeability value. *International Communications in Heat and Mass Transfer* 29(2): 175–184.

Kuznetsov, A.V. and Avramenko, A.A. 2003a. Analysis of stability of bioconvection of motile oxytactic bacteria in a horizontal fluid saturated porous layer. *International Communications in Heat and Mass Transfer* 30(5): 593–602.

Kuznetsov, A.V. and Avramenko, A.A. 2003b. Stability analysis of bioconvection of gyrotactic motile microorganisms in a fluid saturated porous medium. *Transport in Porous Media* 53(1): 95–104.

Kuznetsov, A.V. and Avramenko, A.A. 2005. Effect of fouling on stability of bioconvection of gyrotactic microorganisms in a porous medium. *Journal of Porous Media* 8(1): 45–53.

Kuznetsov, A.V., A.A. Avramenko, and Geng, P. 2004. Analytical investigation of a falling plume caused by bioconvection of oxytactic bacteria in a fluid saturated porous medium. *International Journal of Engineering Science* 42(5–6): 557–569.

Kuznetsov, A.V. and Jiang, N. 2001. Numerical investigation of bioconvection of gravitactic microorganisms in an isotropic porous medium. *International Communications in Heat and Mass Transfer* 28(7): 877–886.

Kuznetsov, A.V. and Jiang, N. 2003. Bioconvection of negatively geotactic microorganisms in a porous medium: The effect of cell deposition and declogging. *International Journal of Numerical Methods for Heat and Fluid Flow* 13(2–3): 341–364.

Luo, L., D.A. Clark, D., Biron, L. Mahadevan, and A.D.T. Samuel. 2006. Sensorimotor control during isothermal tracking in *Caenorhabditis elegans*. *Journal of Experimental Biology* 209: 4652–4662.

Marcos, H., H.C. Fu, T.R. Powers, and R. Stocker. 2012. Bacterial rheotaxis. *Proceedings of the National Academic of Science USA* 109: e4780–e4785.

Maree, A.F.M., A.V. Panfilov, and P. Hogeweg. 1999. Migration and thermotaxis of *Dictyostelium discoideum* slugs, a model study. *Journal of Theoretical Biology* 199: 297–309.

Matsuoka, T., S. Gomi, and R. Shingai. 2008. Simulation of *C. elegans* thermotactic behavior in a linear thermal gradient using a simple phenomenological motility model. *Journal of Theoretical Biology* 250: 230–243.

Medved, I. and R. Černý. 2013. Osmosis in porous media: A review of recent studies. *Microporous and Mesoporous Materials* 170: 299–317.

Mousavi, S.J., M.H. Doweidar, and M. Doblaré. 2013. 3D computational modelling of cell migration: A mechano-chemo-thermo-electrotaxis approach. *Journal of Theoretical Biology* 329: 64–73.

Nakazato, K. and A. Mochizuki. 2009. Steepness of thermal gradient is essential to obtain a unified view of thermotaxis in *C. elegans*. *Journal of Theoretical Biology* 260: 56–65.

Narumi, T., T. Akagawa, Y.A. Seong, and M. Hirose. 2009. Thermotaxis. *SIGGRAPH 09*, 1-1.

Nield, D.A. and A. Bejan. 2013. *Convection in Porous Media,* 4th edn., Springer-Verlag, New York, 778pp.

Nguyen-Quang, T., A. Bahloul, and T.H. Nguyen. 2005. Stability of gravitactic micro-organisms in a fluid-saturated porous medium. *International Communication Journal in Heat and Mass Transfer* 32(1–2): 54–63.

Nguyen-Quang, T., T.H. Nguyen, and F. Guichard. 2010. Spatial pattern formation of gravitactic microorganisms: From bioconvection to population dynamics, in *Porous Media: Applications in Biological Systems and Biotechnology* (*PMABSB*), K. Vafai (Ed.), Taylor & Francis Group/CRC Press, Boca Raton, FL, pp. 535–567.

Nguyen-Quang, T., T.H. Nguyen, and G. LePalec. 2008. Gravitactic bioconvection in a fluid-saturated porous medium with double diffusion. *Journal of Porous Media* 11(8): 751–764.

Pedley, T.J. and J.O. Kessler. 1992. Hydrodynamic phenomena in suspensions of swimming micro-organisms. *Annual Review of Fluid Mechanics* 24: 313–358.

Pompe, T., S. Glorius, T. Bischoff, I. Uhlmann, M. Kaufmann, S. Brenner, and C. Werner. 2009. Dissecting the impact of matrix anchorage and elasticity in cell adhesion. *Biophysical Journal* 97(8): 2154–2163.

Sapoukhina, N., Y. Tyutyunov, and R. Arditi. 2003. The role of prey-taxis in biological control. *American Naturalist* 162: 61–76.

Savill, N.J and P. Hogeweg. 1997. Modeling morphogenesis: From single cells to crawling slugs. *Journal of Theoretical Biology* 184: 229–235.

Shiurba, R., T. Hirabayashi, M. Masuda et al. 2006. Cellular responses of the ciliate, *Tetrahymena thermophila*, to far infrared irradiation. *Photochemical Photobiological Science* 5: 799–807.

Stocker, R. 2012. Marine microbes see a Sea of gradients. *Science* 338: 628–633.

Suresh, S. 2007. Biomechanics and biophysics of cancer cells. *Acta Biomaterialia* 3(4): 413–438.

Tremosa, J., J. Gonçalvès, J.M. Matray, and S. Violette. 2010. Estimating thermo-osmotic coefficients in clay-rocks: II. In situ experimental approach. *Journal of Colloidal Interface Science* 342(1): 175–184.

Wahde, M. 2003. A method for behavioural organization for autonomous robots based on evolutionary optimization of utility functions. *Journal of Systems and Control Engineering* 217: 249–258.

Watmough, J. and S. Camazine. 1995. Self-organized thermoregulation of honeybee clusters. *Journal of Theoretical Biology* 176: 391–402.

Whitaker, S. 1999. *The Method of Volume Averaging*. Kluwer Academic, Dordrecht, the Netherlands.

White J., E. Southgate, J. Thomson, and S. Brenner.1986. The structure of the nervous system of the nematode *C. elegans*. *Philosophical Transactions of the Royal Society London B* 314: 1–340.

Xue, C. and H.G. Othmer. 2009. Multiscale models of taxis-driven patterning in bacterial populations. *SIAM Journal of Applied Mathematics* 70(1): 133–169.

Zhao, M. 2009. Electrical fields in wound healing—An overriding signal that directs cell migration. *Seminars in Cell and Developmental Biology* 20(6): 674–682.

Section III

Turbulence in Porous Media

12 Feedback Control for Promoting or Suppressing the Transition to Weak Turbulence in Porous Media Convection

Peter Vadasz

CONTENTS

12.1 Introduction 459
12.2 Problem Formulation for Lorenz Equations with Feedback Control 460
12.3 Linear Stability Analysis 461
12.4 Analytical and Numerical Solutions 462
12.5 Results and Discussion 467
12.6 Conclusions 469
References 469

12.1 INTRODUCTION

Vadasz and Olek (1999a,b, 2000a,b) and Vadasz (1999a,b, 2001a–d, 2002, 2010a) demonstrated theoretically that the transition from steady to chaotic (weak-turbulent) convection in saturated porous media yields a system that is equivalent to Lorenz equations (Lorenz, 1963). Vadasz (1999c, 2006) presented similar results for the corresponding problem of convection in pure fluids and Vadasz and Olek (1998) for centrifugally induced convection in a rotating porous layer (see also Vadasz, 1998; Straughan, 2001).

The linear stability analysis of the Lorenz equations around the nontrivial stationary points provides a critical value of the controlling parameter, the scaled Rayleigh number, $R_o = Ra_o/Ra_{cr}$, representing the transition from steady solutions to chaos, where Ra_{cr} represents the other critical Rayleigh number for the transition from a motionless solution (trivial stationary point) to a steady convection (nontrivial stationary point). A distinction is made here between numerical solutions of the reduced set of equations, such as the Runge–Kutta method, and computational solutions meant to represent basically analytical solutions that are then computed, such as the Adomian decomposition method. Numerical, computational (Vadasz, 1999a–c, 2001a–d, 2002, 2006, 2010b; Vadasz and Olek, 1999a,b, 2000a,b), and experimental results (Wang et al., 1992; Yuen and Bau, 1996) show that the former transition occurs at subcritical values of the Rayleigh number, that is, at $R \leq R_o$. Sparrow (1982) shows that for the Lorenz system analyzed around the origin, the transition to chaos is via a homoclinic explosion and that the homoclinic orbit, which exists just at the point where the solution orbiting around one nontrivial steady solution turns toward the other nontrivial steady solution, belongs to the subcritical Hopf bifurcation obtained at $Ra = Ra_o$.

Mahmud and Hashim (2010) suggested a feedback control system (Bau, 1999) to be applied to the porous media convection based on the porous media feedback control presented by Tang and Bau (1993) and Zhao and Bau (2006). Magyari (2010) demonstrated that the structure of the feedback

control system proposed by Mahmud and Hashim (2010) does not change the original uncontrolled system and the only effect that the feedback control has is in altering the initial conditions of the system. As it is experimentally impossible in practice to know precisely, let alone control, the initial conditions especially when they are treated as small perturbations around the basic stationary convection state, the feedback control system suggested by Mahmud and Hashim (2010) can be used to provide an equivalent means of control of the initial conditions as indicated by Magyari (2010). Such a control can then be applied to promote or suppress chaos within some specified domain of the scaled Rayleigh number. Testing analytically and numerically the feasibility of the latter was undertaken by Vadasz (2010b).

12.2 PROBLEM FORMULATION FOR LORENZ EQUATIONS WITH FEEDBACK CONTROL

The following set of dimensionless equations represents the temporal dynamics of the amplitudes $\tilde{X}$, $\tilde{Y}$, $\tilde{Z}$, corresponding to the lower-order convection modes (Vadasz, 1999a; Vadasz and Olek, 1999a, 2000a), which in addition include feedback control as proposed by Mahmud and Hashim (2010):

$$\dot{\tilde{X}} = \alpha\left[\left(K+1\right)\tilde{Y} - \tilde{X}\right] \tag{12.1}$$

$$\dot{\tilde{Y}} = \frac{R}{\left(K+1\right)}\tilde{X} - \tilde{Y} - \left(R-1\right)\tilde{X}\tilde{Z} \tag{12.2}$$

$$\dot{\tilde{Z}} = 4\gamma\left(\tilde{X}\tilde{Y} - \tilde{Z}\right) \tag{12.3}$$

where the dots ($\dot{}$) denote time derivatives $d(\ )/dt$ and the scaled Rayleigh number was introduced as follows:

$$R = \frac{Ra}{Ra_{cr}} \tag{12.4}$$

with Ra_{cr} representing the critical Rayleigh number for the transition from a motionless solution (trivial stationary point) to a steady convection (nontrivial stationary point), where γ is related to the critical wave number of convection and α is related to the Prandtl number. A value of $\gamma = 0.5$ is consistent with porous media convection. The symbol K represents the scalar gain controller introduced by Mahmud and Hashim (2010). With the porous medium value of $\gamma = 0.5$, the definitions of R and α are explicitly expressed in the form $R = Ra/4\pi^2$ and $\alpha = \eta/2\pi^2$, where $\eta = \phi Pr/Da$ is a dimensionless group including the porosity, Prandtl, and Darcy numbers that Straughan (2001) named the Vadasz number, or the Vadasz coefficient (2008) (see also Sheu, 2006). A value of $\alpha = 5$ corresponds to $\eta \cong 98.7$.

Equations 12.1 through 12.3 are the scaled Lorenz equations (Lorenz, 1963; Sparrow, 1982) subject to feedback control, and their solution is subject to the initial conditions $\tilde{X}_o$, $\tilde{Y}_o$ and $\tilde{Z}_o$ at $t = 0$.

Equations 12.1 through 12.3 can be presented in the vector form $\dot{\tilde{\boldsymbol{x}}} = \tilde{\boldsymbol{f}}(\tilde{\boldsymbol{x}})$, where the vector $\tilde{\mathbf{x}}$ is defined by $\tilde{\boldsymbol{x}} = \left[\tilde{X}, \tilde{Y}, \tilde{Z}\right]^{\mathrm{T}}$ and $\tilde{\boldsymbol{f}}(\tilde{\boldsymbol{x}})$, representing the right-hand side of the equations, has the form $\tilde{\boldsymbol{f}}(\tilde{\boldsymbol{x}}) = \left[\tilde{f}_{\tilde{X}}, \tilde{f}_{\tilde{Y}}, \tilde{f}_{\tilde{Z}}\right]^{\mathrm{T}}$, where $\tilde{f}_{\tilde{X}} = \alpha\left[(K+1)\tilde{Y} - \tilde{X}\right]$, $\tilde{f}_{\tilde{Y}} = \left[R/(K+1)\right]\tilde{X} - \tilde{Y} - (R-1)\tilde{X}\tilde{Z}$, $\tilde{f}_{\tilde{Z}} = 4\gamma(\tilde{X}\tilde{Y} - \tilde{Z})$. The fixed points of the system (12.1 through 12.3) are obtained by setting the time derivative to be zero $\dot{\tilde{\boldsymbol{x}}} = 0$, leading to $\tilde{\boldsymbol{f}}(\tilde{\boldsymbol{x}}) = 0$ and producing the trivial fixed point $\tilde{X}_S = \tilde{Y}_S = \tilde{Z}_S = 0$ and the

nontrivial fixed points $\tilde{X}_S = \pm 1$, $\tilde{Y}_S = \pm 1/(K+1)$, and $\tilde{Z}_S = 1/(K+1)$. The former represents the motionless conduction solution, while the latter represent steady-state solutions consisting of convection cells moving clockwise or counterclockwise.

The Jacobian matrix associated with this system is defined by $\tilde{\boldsymbol{J}} = \left[\partial \tilde{f}_i / \partial \tilde{x}_j\right]_{\substack{i=(\tilde{X},\tilde{Y},\tilde{Z}),\\ j=(\tilde{X},\tilde{Y},\tilde{Z})}}$, and evaluating it at any one of the fixed points yields the original system linearized around the selected fixed point, that is, $\dot{\tilde{\boldsymbol{x}}} = \left[\tilde{\boldsymbol{J}}\right]_{\tilde{x}_S} \tilde{\boldsymbol{x}} + \text{higher-order terms}$, needed for evaluating the eigenvalues of the linear system around any selected fixed point.

12.3 LINEAR STABILITY ANALYSIS

By deriving the determinant of the Jacobian matrix evaluated around any fixed point yields an equation for the eigenvalues of the original system of ordinary differential equations linearized around the selected fixed point. Evaluating the determinant of the Jacobian matrix for the system (12.1 through 12.3) around the trivial fixed point $\tilde{X}_S = \tilde{Y}_S = \tilde{Z}_S = 0$ produces the following algebraic equation for the eigenvalues:

$$\left(\lambda + 4\gamma\right)\left[\left(\lambda + \alpha\right)\left(\lambda + 1\right) - \alpha R\right] = 0 \tag{12.5}$$

It may be observed that despite the fact that the gain controller K appeared explicitly in the Jacobian matrix, its effect disappeared (cancelled out) from its determinant and is not reflected in the eigenvalues equation. Equation 12.5 has three real roots (for $\gamma > 0$, $\alpha > 0$, and $R > 0$):

$$\lambda_3 = -4\gamma < 0; \quad \lambda_2 = -\frac{\left(\alpha+1\right)}{2}\left[1 + \sqrt{1 + \frac{4\alpha\left(R-1\right)}{\left(\alpha+1\right)^2}}\right] < 0; \quad \lambda_1 = -\frac{\left(\alpha+1\right)}{2}\left[1 - \sqrt{1 + \frac{4\alpha\left(R-1\right)}{\left(\alpha+1\right)^2}}\right] \tag{12.6}$$

The first two roots are always negative because $\gamma > 0$, $\alpha > 0$, $R > 0$. The third root, λ_1, provides the stability condition for the motionless solution (trivial fixed points) in the form

$$\lambda_1 < 0 \Leftrightarrow R < 1 \tag{12.7}$$

Evaluating the determinant of the Jacobian matrix around the convection (nontrivial) fixed points $\tilde{X}_S = \pm 1, \tilde{Y}_S = \pm 1/\left(K+1\right)$ and $\tilde{Z}_S = 1/\left(K+1\right)$ yields the eigenvalues' equation in the form

$$\lambda^3 + \left(\alpha + 4\gamma + 1\right)\lambda^2 + 4\gamma\left(\alpha + R\right)\lambda + 8\alpha\gamma\left(R-1\right) = 0 \tag{12.8}$$

It may be observed again that despite the fact that the gain controller K appeared explicitly in the Jacobian matrix, its effect disappeared (cancelled out) from its determinant and is not reflected in the eigenvalues' equation. Furthermore, Equation 12.8 is identical to the one obtained for the uncontrolled Lorenz system (corresponding to $K = 0$) as presented by Vadasz and Olek (1999b, 2000b). The eigenvalues are therefore identical to the ones obtained from the uncontrolled system. Equation 12.8 yields three eigenvalues. Substituting the general form of an eigenvalue as $\lambda = \lambda_r \pm i\lambda_i$, where λ_r and λ_i are the real and imaginary components, respectively, into Equation 12.8 and separating real and imaginary parts yields two equations for the real and imaginary components of the eigenvalues in the form

$$\lambda_r^3 - 3\lambda_r\lambda_i^2 + \left(\alpha + 4\gamma + 1\right)\left(\lambda_r^2 - \lambda_i^2\right) + 4\gamma\left(\alpha + R\right)\lambda_r + 8\alpha\gamma\left(R-1\right) = 0 \tag{12.9}$$

$$\lambda_i\left[\lambda_i^2 - 3\lambda_r^2 - 2\left(\alpha + 4\gamma + 1\right)\lambda_r - 4\gamma\left(\alpha + R\right)\right] = 0 \tag{12.10}$$

The smallest eigenvalue λ_3 is always real and negative over the whole range of parameters' values. The other two are real and negative at slightly supercritical values of R; therefore, the convection fixed points are stable, that is, simple nodes. As the value of R increases, these two roots move on the real axis toward the origin (where $\lambda_r = 0$), the smallest of the two chasing the other one and reducing the distance between them. For $\alpha = 5$ and $\gamma = 0.5$, these roots become equal at $R \cong 1.28$. From this point, these two roots become a pair of complex conjugate eigenvalues $\lambda_{1,2} = \lambda_r \pm i\lambda_i$, where λ_r and λ_i are their real and imaginary components, respectively. However, they still have negative real parts; therefore, the convection fixed points are still stable, that is, spiral nodes. As the value of R increases further, both the imaginary and real parts of these complex conjugate eigenvalues increase. On the complex plane, they cross the imaginary axis (where $\lambda_r = 0$), that is, their real part becomes non-negative at a value of R that is obtained by substituting the λ corresponding to $\lambda_r = 0$, that is, $\lambda = i\lambda_i$, into Equations 12.9 and 12.10 to yield the following two equations:

$$\left(\alpha + 4\gamma + 1\right)\lambda_{io}^2 + 8\alpha\gamma\left(R_o - 1\right) = 0 \tag{12.11}$$

$$\lambda_{io}^2 - 4\gamma\left(\alpha + R_o\right) = 0 \tag{12.12}$$

where the subscript o in R_o and λ_{io} stands to indicate that these are values associated with $\lambda_r = 0$. Solving these equations for R_o and λ_{io} yields

$$R_o = \frac{\alpha\left(\alpha + 4\gamma + 3\right)}{\left(\alpha - 4\gamma - 1\right)}; \quad \lambda_{io}^2 = \frac{8\alpha\gamma\left(\alpha + 1\right)}{\left(\alpha - 4\gamma - 1\right)} \tag{12.13}$$

Therefore, the convective fixed points lose stability in the linear sense at a value of $R = R_o$ and the basic frequency of the oscillations at marginal stability is λ_{io}. Their values are presented in Equation 12.13. For $R < R_o$ the convective fixed points are stable and the solution will produce steady convection. For $R > R_o$ the fixed points are not stable and the other type of solution (chaotic) is anticipated. Note that in order to obtain finite positive values for R_o and λ_{io}^2 from (12.13), their denominator must be positive, implying $\alpha > 4\gamma + 1$. For porous media convection consistent with $\gamma = 0.5$, this condition is $\alpha > 3$.

12.4 ANALYTICAL AND NUMERICAL SOLUTIONS

Magyari (2010) showed that the controlled system (12.1 through 12.3) can be converted into the uncontrolled one via the simple transformation:

$$X = \tilde{X}; \quad Y = \left(K + 1\right)\tilde{Y}; \quad Z = \left(K + 1\right)\tilde{Z} \tag{12.14}$$

Substituting Magyari's transformation (12.14) into Equations 12.1 through 12.3 yields

$$\dot{X} = \alpha\left(Y - X\right) \tag{12.15}$$

$$\dot{Y} = RX - Y - \left(R - 1\right)XZ \tag{12.16}$$

$$\dot{Z} = 4\gamma\left(XY - Z\right) \tag{12.17}$$

which is the uncontrolled Lorenz system. Therefore, as Magyari (2010) concluded, the main effect that the feedback control suggested by Mahmud and Hashim (2010) has is in altering the initial conditions of the system in the form provided by Magyari's transformation (12.14), that is,

$$X_o = \tilde{X}_o; \quad Y_o = \left(K+1\right)\tilde{Y}_o; \quad Z_o = \left(K+1\right)\tilde{Z}_o \tag{12.18}$$

where X_o, Y_o, Z_o and $\tilde{X}_o, \tilde{Y}_o, \tilde{Z}_o$ are the initial conditions in the uncontrolled and controlled Lorenz systems, respectively.

The analytical solution to the problem (12.15 through 12.17) was evaluated via a weak nonlinear analysis by using an expansion around the point where the nontrivial stationary solutions lose stability in the linear sense, that is, around $R = R_o$ ($R_o = 25$ for $\alpha = 5$). The stationary (fixed) points of the system (12.15 through 12.17) are the convection (nontrivial) solutions $X_S = Y_S = \pm 1$, $Z_S = 1$ and the trivial solution $X_S = Y_S = Z_S = 0$. The expansion around the trivial stationary solution yields the familiar results of a pitchfork bifurcation from a motionless state to convection at $R = 1$. We expand the dependent variables around the nontrivial stationary points in the form

$$\left[X,Y,Z\right] = \left[X_S,Y_S,Z_S\right] + \varepsilon\left[X_1,Y_1,Z_1\right] + \varepsilon^2\left[X_2,Y_2,Z_2\right] + \varepsilon^3\left[X_3,Y_3,Z_3\right] + \cdots + \tag{12.19}$$

We also expand R in a finite series of the form $R = R_o(1 + \varepsilon^2)$, which now defines the small expansion parameter as $\varepsilon^2 = (R - R_o)/R_o$, where R_o is the value of R where the stationary nontrivial solutions lose their stability in the linear sense (see Vadasz and Olek, 1999a, 2000a; Vadasz, 2002). Therefore, the present weak nonlinear analysis is expected to be restricted to initial conditions sufficiently close to anyone but only one of the nontrivial fixed points. Introducing a long time scale $\tau = \varepsilon^2 t$ and replacing the time derivatives in Equations 12.15 through 12.17 with $\mathrm{d}/\mathrm{d}t \to \mathrm{d}/\mathrm{d}t + \varepsilon^2\mathrm{d}/\mathrm{d}\tau$ yields a hierarchy of ordinary differential equations at the different orders. The values of R_o and basic frequency λ_{io} were derived via the linear stability analysis and are presented in Equation 12.13. The argument of the decaying term of the solution at order $O(\varepsilon)$, λ_3, corresponding to $\lambda_r = 0$, is $\lambda_3 = -(\alpha + 4\gamma + 1)$. Based on the linear stability analysis, the loss of stability of the nontrivial stationary points occurs at a value of $R = R_o$. For $R < R_o$ the linear stability predicts a solution that converges to one of the stationary points, while for $R > R_o$ a posttransient chaotic solution is anticipated. In reality, computational, numerical, and experimental results show that the transition from the steady solution to chaos occurs at a value of $R = R_t \leq R_o$.

The solutions to order $O(\varepsilon)$ have the form

$$X_1 = a_1 \mathrm{e}^{\lambda_r + i\lambda_{io}t} + a_1^* \mathrm{e}^{\lambda_r - i\lambda_{io}t} + a_{13}\mathrm{e}^{\lambda_3 t} \tag{12.20}$$

$$Y_1 = b_1 \mathrm{e}^{\lambda_r + i\lambda_{io}t} + b_1^* \mathrm{e}^{\lambda_r - i\lambda_{io}t} + b_{13}\mathrm{e}^{\lambda_3 t} \tag{12.21}$$

$$Z_1 = c_1 \mathrm{e}^{\lambda_r + i\lambda_{io}t} + c_1^* \mathrm{e}^{\lambda_r - i\lambda_{io}t} + c_{13}\mathrm{e}^{\lambda_3 t} \tag{12.22}$$

where $\lambda_1 = \lambda_r - i\lambda_{io}$, $\lambda_2 = \lambda_r + i\lambda_{io}$, and λ_3 are the three eigenvalues of the system (12.15 through 12.17) linearized around R_o. At marginal stability, that is, at $R = R_o$, the real part of the complex eigenvalues is zero. Therefore, at order $O(\varepsilon)$, one can set the argument of the exponents in Equations 12.20 through 12.22 to $\lambda_1 = -i\lambda_{io}$ and $\lambda_2 = i\lambda_{io}$, by substituting $\lambda_r = 0$. What typically follows when using the weak nonlinear method of solution is the neglect of the decaying term $a_{13}e^{\lambda_3 t}$ from the solution. Clearly, this term does not bring any contribution to the posttransient solution. However, while indeed this term vanishes at the posttransient state, its inclusion in the solution becomes essential in order to provide a relationship between the initial conditions in the present analytical solution and the numerical one. The coefficients $a_1(\tau), a_1^*(\tau), b_1(\tau), b_1^*(\tau), c_1(\tau)$, and $c_1^*(\tau)$ are allowed to vary over the long time scale τ. By substituting solutions (12.20) through (12.22) into the linearized form

of Equations 12.15 through 12.17, which apply at order $O(\varepsilon)$ (see Vadasz [1999a] for details), one obtains the following relationships between these coefficients:

$$b_1 = \frac{\left(\alpha + i\lambda_{io}\right)}{\alpha} a_1; \quad b_1^* = \frac{\left(\alpha - i\lambda_{io}\right)}{\alpha} a_1^*; \quad b_{13} = \frac{\left(\lambda_3 + \alpha\right)}{\alpha} a_{13} \tag{12.23}$$

$$c_1 = \frac{\lambda_{io}\left[\lambda_{io} - i\left(\alpha+1\right)\right]}{\alpha\left(R_o - 1\right)} a_1; \quad c_1^* = \frac{\lambda_{io}\left[\lambda_{io} + i\left(\alpha+1\right)\right]}{\alpha\left(R_o - 1\right)} a_1^*; \quad c_{13} = \frac{-\lambda_3\left[\lambda_3 + \alpha + 1\right]}{\alpha\left(R_o - 1\right)} a_{13} \tag{12.24}$$

A solvability condition is obtained at order $O(\varepsilon^3)$ producing an equation for the complex amplitudes $a_1(\tau)$ and $a_1^*(\tau)$. The polar coordinates' representation of this equation is obtained by presenting the $O(\varepsilon)$ complex amplitude in the form

$$a = \varepsilon a_1 = re^{i\theta} \cdot a^* = \varepsilon a_1^* = re^{-i\theta} \tag{12.25}$$

The amplitude r and the frequency correction $\dot{\theta}$ of the solution at order $O(\varepsilon)$ are then obtained from the $O(\varepsilon^3)$ solvability condition, transforming the amplitude equation in the form

$$\frac{dr}{dt} = \chi\left[\frac{\varepsilon^2}{\varphi} - r^2\right] r \tag{12.26}$$

$$\frac{d\theta}{dt} = m_{21}\varepsilon^2 - m_{31}r^2 \tag{12.27}$$

where $\chi = \varphi/\beta$ and

$$\frac{\varepsilon^2}{\varphi} = \frac{\left(R - R_o\right)}{R_o\varphi} \tag{12.28}$$

with φ, β, m_{21}, and m_{31} as parameters that depend on the values of α and γ. For $\alpha = 5$, corresponding to $\eta \cong 98.7$, and $\gamma = 0.5$, values consistent with the present study $\varphi = -2.4$, $\beta = 0.403226$, $m_{21} = 3.64394$, $m_{31} = 9.84487$, and the following critical values apply $R_o = 25$ and $\lambda_{io} = \sqrt{60}$. Clearly, $\chi < 0$ over all the cases considered, while $\varepsilon^2/\varphi > 0$ for $R < R_o$ (subcritical conditions), $\varepsilon^2/\varphi < 0$ for $R > R_o$ (supercritical conditions), and $\varepsilon^2/\varphi = 0$ for $R = R_o$ (critical conditions). The post-transient solution to Equation 12.26 yields $r = \pm\sqrt{\varepsilon^2/\varphi}$, which produces a real value of r only for $R < R_o$ (because $\varphi < 0$ as indicated earlier). The Hopf bifurcation at $R = R_o = 25$ is therefore subcritical, and in order to investigate the breakdown of the periodic solution at $R = R_o = 25$, the derivation of the transient solution to Equation 12.29 is undertaken. This transient solution is obtained by direct integration in the form

$$r^2 = \frac{\varepsilon^2}{\varphi\left[1 - \left(1 - \frac{\varepsilon^2}{\varphi r_o^2}\right)\exp\left(-\frac{2\varepsilon^2\chi t}{\varphi}\right)\right]} \tag{12.29}$$

where the following initial condition applies: $r = r_o$ at $t = 0$. The solution (12.29) is valid at $t = 0$ leading to $r^2 = r_o^2$, which can be recovered by substituting $t = 0$ in Equation 12.26. Vadasz (1999a)

has shown that the solution (12.29) becomes singular, that is, its denominator vanishes at a critical value of t expressed by the equation

$$t_{cr} = \frac{\varepsilon^2}{2\chi\varphi}\ln\left[1-\frac{\varepsilon^2}{\varphi r_o^2}\right] \tag{12.30}$$

The existence of this critical time is linked to a condition that the argument of the ln(•) function in this equation is positive and greater or smaller than 1, depending on whether ε^2/φ is negative or positive, respectively. The latter requirement comes to impose a positive value of t_{cr}; otherwise, no physical significance can be associated with this critical time. This condition exists only for subcritical values of R, that is, for $\varepsilon^2/\varphi > 0$ ($R < R_o$), and is presented in the form $\varepsilon^2/\left(\varphi r_o^2\right) < 1$, while for supercritical values of R, that is, for $\varepsilon^2/\varphi < 0$ ($R > R_o$), the critical time exists unconditionally, that is, no condition needs to be satisfied for this critical time to exist, as it emerged for subcritical values of R. Transforming the condition for this transition to occur, from $r_o^2 > \varepsilon^2/\varphi$, to the original physical parameters of the system by substituting the definition of $\varepsilon^2/\varphi = (R-R_o)/R_o\varphi$ leads to a value of $R \le R_o$, say R_t, beyond which the transition occurs, which can be expressed in the form

$$R_t = R_o\left(1-|\varphi| r_o^2\right) \tag{12.31}$$

where the minus sign and the absolute value of φ appear in order to show explicitly that $\varphi < 0$. If $R < R_t$ the solution decays, spiraling toward the corresponding fixed point, and at $R = R_t$ we expect the limit cycle solution. Beyond this transitional value of R, that is, $R > R_t$, the solution moves away from this fixed point. Therefore, at the value of R_t we expect to obtain a limit cycle solution and beyond it a chaotic solution.

Since we attempt to solve the controlled system (12.1 through 12.3) originally subject to constant initial conditions for the controlled system variables $\tilde{X}$, $\tilde{Y}$, $\tilde{Z}$ while varying only the value of the gain controller K, we need to transform the results obtained for the uncontrolled system (12.15 through 12.17) and express them in terms of $\tilde{X}$, $\tilde{Y}$, $\tilde{Z}$. First, there are relationships linking the initial conditions expressed in terms of the analytical solution amplitudes r, θ, and $a_3 = \varepsilon a_{13}$ to the initial conditions in terms of X, Y, Z (Vadasz, 2001d) in the form (the subscript o applied to X, Y, Z or $\tilde{X}$, $\tilde{Y}$, $\tilde{Z}$ and to r, θ, a_3 specifies the initial conditions for these variables)

$$X_o = 1 + 2r_o\cos\left(\theta_o\right) + a_{30} + O\left(\varepsilon^2\right) \tag{12.32}$$

$$Y_o = 1 + \frac{2r_o}{\alpha}\left[\alpha\cos\left(\theta_o\right) - \lambda_{io}\sin\left(\theta_o\right)\right] + \frac{\left(\lambda_3+\alpha\right)}{\alpha}a_{30} + O\left(\varepsilon^2\right) \tag{12.33}$$

$$Z_o = 1 + \frac{2r_o}{\alpha\left(R_o-1\right)}\left[\lambda_{io}^2\cos\left(\theta_o\right) - \lambda_{io}\left(\alpha+1\right)\sin\left(\theta_o\right)\right] - \frac{\lambda_3\left(\lambda_3+\alpha+1\right)}{\alpha\left(R_o-1\right)}a_{30} + O\left(\varepsilon^2\right) \tag{12.34}$$

and the inverse relationships are

$$\tan\left(\theta_o\right) = \frac{\left[\lambda_{io}^2+\lambda_3(\lambda_3+\alpha+1)\right]\left[(\lambda_3+\alpha)X_{o1}-\alpha Y_{o1}\right]-\lambda_3\left[\lambda_3(\lambda_3+\alpha+1)X_{o1}+\alpha(R_o-1)Z_{o1}\right]}{\lambda_{io}\left\{\left[\lambda_3(\lambda_3+\alpha+1)X_{o1}+\alpha(R_o-1)Z_{o1}\right]-(\alpha+1)\left[(\lambda_3+\alpha)X_{o1}-\alpha Y_{o1}\right]\right\}} \tag{12.35}$$

where

$X_{o1} = X_o - 1$
$Y_{o1} = Y_o - 1$
$Z_{o1} = Z_o - 1$

Once the value of θ_o is established from Equation 12.35, one can evaluate the value of r_o by substitution in the form

$$r_o = \frac{\left(\lambda_3 + \alpha\right) X_{o1} - \alpha Y_{o1}}{2\left[\lambda_3 \cos\left(\theta_o\right) + \lambda_{io} \sin\left(\theta_o\right)\right]} \tag{12.36}$$

Substituting Equation 12.35 and the expression for r_o from Equation 12.36 into Equation 12.32 allows expressing a_{30} in the form

$$a_{30} = X_{o1} - \frac{\left[\lambda_3 X_{o1} + \alpha\left(X_{o1} - Y_{o1}\right)\right]}{\left[\lambda_3 + \lambda_{io} \tan\left(\theta_o\right)\right]} \tag{12.37}$$

Equations 12.35 through 12.37 represent the inverse compatibility relationships between the analytical weak nonlinear solution and any numerical solutions, the latter being naturally expressed in terms of $[X_o, Y_o, Z_o]$, while the former expressed in terms of $[r_o, \theta_o, a_{30}]$.

By introducing now Magyari's transformation (Magyari, 2010) from Equation 12.18 into Equations 12.32 through 12.34 yields the relationship between $\left[\tilde{X}_o, \tilde{Y}_o, \tilde{Z}_o\right]$ and $[r_o, \theta_o, a_{30}]$ in the form

$$\tilde{X}_o = 1 + 2r_o \cos\left(\theta_o\right) + a_{30} \tag{12.38}$$

$$\tilde{Y}_o = \frac{1}{\left(K+1\right)} + \frac{2r_o}{\alpha\left(K+1\right)}\left[\alpha \cos\left(\theta_o\right) - \lambda_{io} \sin\left(\theta_o\right)\right] + \frac{\left(\lambda_3 + \alpha\right)}{\alpha\left(K+1\right)} a_{30} \tag{12.39}$$

$$\tilde{Z}_o = \frac{1}{(K+1)} + \frac{2r_o}{\alpha(R_o - 1)(K+1)}\left[\lambda_{io}^2 \cos(\theta_o) - \lambda_{io}(\alpha+1)\sin(\theta_o)\right] - \frac{\lambda_3(\lambda_3 + \alpha + 1)}{\alpha(R_o - 1)(K+1)} a_{30} \tag{12.40}$$

and a corresponding inverse relationship by using $X_{o1} = \tilde{X}_o - 1, Y_{o1} = (K+1)\tilde{Y}_o - 1$ and $Z_{o1} = (K+1)\tilde{Z}_o - 1$, in Equations 12.35 through 12.37. For constant initial conditions, $\left[\tilde{X}_o, \tilde{Y}_o, \tilde{Z}_o\right]$ = constant, and the values to be substituted into (12.35) through (12.37) depend on K only, which is what we aimed, that is, to observe the effect of the gain controller K alone on the solution and its ability to mimic the alteration of the initial conditions in terms of rendering the transition point forward or backward. As for constant initial conditions $\left[\tilde{X}_o, \tilde{Y}_o, \tilde{Z}_o\right]$ = constant, r_o depends on K only, and we can evaluate this dependence and substitute the resulting $r_o(K)$ into Equation 12.31 to produce the analytical curve of the transition point to chaos $R_t(K)$.

A special case when $\theta_o = a_{30} = 0$ is also considered although the latter does not produce constant initial conditions in terms of $\left[\tilde{X}_o, \tilde{Y}_o, \tilde{Z}_o\right]$. When $\theta_o = a_{30} = 0$, the relationships between the initial conditions are

$$\tilde{X}_o = 1 + 2r_o \tag{12.41}$$

$$\tilde{Y}_o = \frac{1}{\left(K+1\right)} + \frac{2r_o}{\left(K+1\right)} \tag{12.42}$$

$$\tilde{Z}_o = \frac{1}{(K+1)} + \frac{2r_o\lambda_{io}^2}{\alpha(R_o-1)(K+1)} \tag{12.43}$$

For any choice of

$$\tilde{Z}_o = C_Z = \text{constant} \tag{12.44}$$

we obtain

$$\tilde{Y}_o = \frac{1}{(K+1)} + \frac{\alpha(R_o-1)\left[(K+1)C_Z-1\right]}{(K+1)\lambda_{io}^2} \tag{12.45}$$

$$\tilde{X}_o = 1 + \frac{\alpha(R_o-1)\left[(K+1)C_Z-1\right]}{\lambda_{io}^2} \tag{12.46}$$

and

$$r_o = \frac{1}{2}\left(\tilde{X}_o - 1\right) = \frac{\alpha(R_o-1)\left[(K+1)C_Z-1\right]}{2\lambda_{io}^2} \tag{12.47}$$

Substituting (12.47) into (12.31) yields the transition point to chaos for this special case of $\theta_o = a_{30} = 0$ in the form

$$R_t = R_o\left[1-|\varphi|\frac{\alpha^2(R_o-1)^2\left[(K+1)C_Z-1\right]^2}{4\lambda_{io}^4}\right] = R_o\left[1-|\varphi|\frac{(\alpha+4\gamma+1)^2\left[(K+1)C_Z-1\right]^2}{256\gamma^2}\right] \tag{12.48}$$

For $\tilde{Z}_o = C_Z = 1$, this produces a simple quadratic function of K in the form

$$R_t = R_o\left[1-|\varphi|\frac{(\alpha+4\gamma+1)^2}{256\gamma^2}K^2\right] \tag{12.49}$$

To validate the results of the analytical solution, which are accurate only in the neighborhood of a fixed point, we solved the system (12.1 through 12.3) to double precision by using the fifth- and sixth-order Runge–Kutta–Verner method from the IMSL Library (DIVPRK) (IMSL, 1991) up to a desired tolerance for error control specified by the parameter *tol*. The accuracy of the analytical solution being only in the neighborhood of a fixed point implies in the present case small values of K.

12.5 RESULTS AND DISCUSSION

For constant initial conditions, we used the values corresponding to the uncontrolled system's convective fixed point $\tilde{X}_o = \tilde{Y}_o = \tilde{Z}_o = 1$. As long as the value of K is not zero, the controlled fixed point does not overlap with $\tilde{X}_o = \tilde{Y}_o = \tilde{Z}_o = 1$. The results for the analytical prediction of the transition

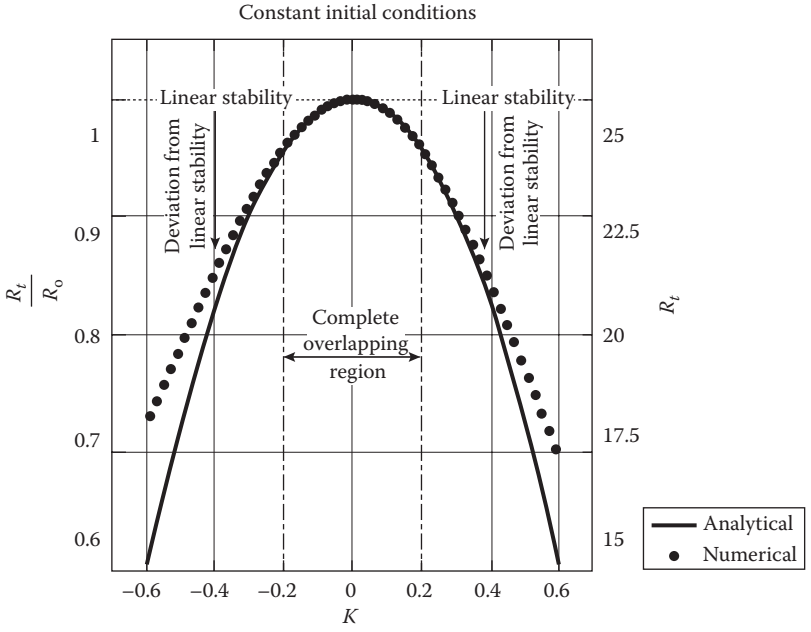

FIGURE 12.1 Transitional subcritical values of the scaled Rayleigh number R_t as a function of the feedback gain controller parameter K corresponding to constant initial conditions of $\tilde{X}_o = \tilde{Y}_o = \tilde{Z}_o = 1 = \text{constant}$. (From Vadasz, P., *Transp. Porous Media*, 85, 287, 2010b. With permission.)

point to chaos are compared with the corresponding transition in the numerical solutions for different values of the gain controller K and are presented in Figure 12.1.

From the figure, it can be observed that the analytical and numerical results overlap for $K < |0.2|$, which reinforces the anticipation that the analytical results are accurate for small values of $|K|$. As the value of $|K|$ increases, the deviation between the analytical and numerical results is evident with a maximum deviation of about 18% at $K = -0.6$. However, the most important outcome that is evident in this figure is that it is possible to use the gain controller K to apparently alter the initial conditions or actually to promote or suppress the transition to chaos (within a certain range of values of $R_{hom} < R < R_o$, where R_{hom} is the value of R associated with the appearance of the homoclinic orbit).

For the special case when $\theta_o = a_{30} = 0$, the initial conditions are not constant anymore but follow Equations 12.44 through 12.46. We used here $\tilde{Z}_o = C_Z = 1$ and Equation 12.49 to evaluate the analytical curve and compare it to the numerical results providing the transition point as presented in Figure 12.2.

From the figure it is evident again that there is a wide region of overlap between the analytical prediction and the numerical one. Again, the results show that it is possible to control the transition to chaos via the feedback control system proposed by Mahmud and Hashim (2010) and modified by Magyari (2010). This implies that by varying the gain controller K, chaos can be either promoted or suppressed within a certain range of values of $R_{hom} < R < R_o$, where R_{hom} is the value of R associated with the appearance of the homoclinic orbit.

In both cases, the deviation between the analytical and numerical results is not symmetrical with respect to $K = 0$, a result that is quite anticipated. In the second case, the analytical result expressed by Equation 12.49 is symmetrical around $K = 0$, as the orbit representing the limit cycle at the transition point is an ellipse when using the analytical solution; however, the numerical solution shows that the ellipse is a good approximation in the neighborhood of the fixed point, but as the orbit moves away from the fixed point and closer to the homoclinic orbit, its shape is by far different from an ellipse.

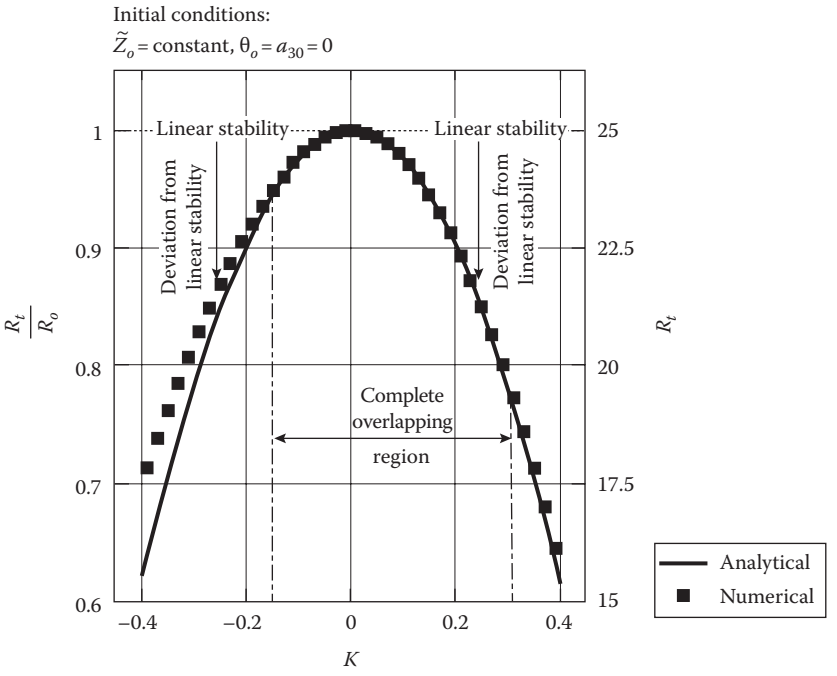

FIGURE 12.2 Transitional subcritical values of the scaled Rayleigh number R_t as a function of the feedback gain controller parameter K corresponding to initial conditions of $\tilde{Z}_o = 1 = \text{constant}; \theta_o = a_{30} = 0$. (From Vadasz, P., *Transp. Porous Media*, 85, 287, 2010b. With permission.)

12.6 CONCLUSIONS

A review of the topic of feedback control in porous media natural convection was presented. The anticipation raised by Magyari's transformation (Magyari, 2010) to the feedback control problem suggested by Mahmud and Hashim (2010) that it might be possible to control chaos in porous media convection was shown to be correct. One may use the gain controller K to promote or suppress chaos in porous media convection. The gain controller acts as an apparent alteration of the initial conditions, the latter being unpredictable and difficult to measure with the accuracy needed to control chaos directly. Therefore, the method presented is an elegant practical way to overcome the latter difficulty.

REFERENCES

Bau, H.H. 1999. Control of Marangoni-Bénard convection. *International Journal of Heat and Mass Transfer* **42**: 1327–1341.

IMSL Library. 1991. *Fortran Subroutines for Mathematical Applications*. Version 2. IMSL, Houston, TX.

Lorenz, E.N. 1963. Deterministic non-periodic flows. *Journal of the Atmospheric Sciences* **20**: 130–141.

Magyari, E. 2010. The "butterfly effect" in a porous slab. *Transport in Porous Media* **84**: 711–715

Mahmud, M.N. and Hashim, I. 2010. Small and moderate Prandtl number chaotic convection in porous media in the presence of feedback control. *Transport in Porous Media* **84**: 421–440.

Sheu, L.-J. 2006. An autonomous system for chaotic convection in a porous medium using a thermal nonequilibrium model. *Chaos, Solitons & Fractals* **30**: 672–689.

Sparrow, C. 1982. *The Lorenz Equations: Bifurcations, Chaos, and Strange Attractors*. Springer-Verlag, New York.

Straughan, B. 2001. A sharp nonlinear stability threshold in rotating porous convection. *Proceedings of the Royal Society of London A* **457**: 87–93.

Straughan, B. 2008. *Stability and Wave Motion in Porous Media* (Applied mathematical sciences series). Springer, New York.

Tang, J. and Bau, H.H. 1993. Feedback control stabilization of the no motion state of a fluid confined in a horizontal porous layer heated from below. *Journal of Fluid Mechanics* **257**: 485–505.

Vadasz, P. 1998. Coriolis effect on gravity driven convection in a rotating porous layer heated from below. *Journal of Fluid Mechanics* **376**: 351–375.

Vadasz, P. 1999a. Local and global transitions to chaos and hysteresis in a porous layer heated from below. *Transport in Porous Media* **37**: 213–245.

Vadasz, P. 1999b. A note and discussion on J.-L. Auriault's letter: Comments on the paper—Local and global transitions to chaos and hysteresis in a porous layer heated from below. *Transport in Porous Media* **37**: 251–254.

Vadasz, P. 1999c. Subcritical transitions to chaos and hysteresis in a fluid layer heated from below. *International Journal of Heat and Mass Transfer* **43**: 705–724.

Vadasz, P. 2001a. Heat transfer regimes and hysteresis in porous media convection. *ASME Journal of Heat Transfer* **123**: 145–156.

Vadasz, P. 2001b. The effect of thermal expansion on porous media convection—Part 1: Thermal expansion solution. *Transport in Porous Media* **44**: 421–443.

Vadasz, P. 2001c. The effect of thermal expansion on porous media convection—Part 2: Thermal convection solution. *Transport in Porous Media* **44**: 445–463.

Vadasz, P. 2001d. Equivalent initial conditions for compatibility between analytical and computational solutions of convection in porous media. *International Journal of Non-Linear Mechanics* **36**: 197–208.

Vadasz, P. 2002. Hysteresis and chaos in porous media convection. *Trends in Heat, Mass & Momentum Transfer, Research Trends* **8**: 59–102.

Vadasz, P. 2006. Chaotic dynamics and hysteresis in thermal convection. *Proceedings of the IMechE (Part C)—Journal of Mechanical Engineering Science* **220**: 309–323.

Vadasz, P. 2010a. Analytical prediction of the transition to chaos in lorenz equations. *Applied Mathematics Letters* **23**: 503–507.

Vadasz, P. 2010b. Controlling chaos in porous media convection by using feedback control. *Transport in Porous Media* **85**: 287–298.

Vadasz, P. and Olek, S. 1998. Transitions and chaos for free convection in a rotating porous layer. *International Journal of Heat & Mass Transfer* **41**: 1417–1435.

Vadasz, P. and Olek, S. 1999a. Weak turbulence and chaos for low prandtl number gravity driven convection in porous media. *Transport in Porous Media* **37**: 69–91.

Vadasz, P. and Olek, S. 1999b. Computational recovery of the homoclinic orbit in porous media convection. *International Journal of Non-Linear Mechanics* **34**: 89–93.

Vadasz, P. and Olek, S. 2000a. Route to chaos for moderate prandtl number convection in a porous layer heated from below. *Transport in Porous Media* **41**: 211–239.

Vadasz, P. and Olek, S. 2000b. Convergence and accuracy of adomian's decomposition method for the solution of Lorenz equations. *International Journal of Heat and Mass Transfer* **43**: 1715–1734.

Wang, Y., Singer, J., and Bau, H.H. 1992. Controlling chaos in a thermal convection loop. *Journal of Fluid Mechanics* **237**: 479–498.

Yuen, P. and Bau, H.H. 1996. Rendering a subcritical Hopf bifurcation supercritical. *Journal of Fluid Mechanics* **317**: 91–109.

Zhao, H. and Bau, H.H. 2006. Limitations of linear control of thermal convection in a porous medium. *Physics of Fluids* **18**: 074109.

13 Advances in Modeling Turbulence Phenomena in Heterogeneous Media
Reactive Systems

Marcelo J.S. de Lemos

CONTENTS

13.1 Introduction 471
13.2 Porous Burners 472
13.3 Macroscopic Flow 472
13.3.1 Macroscopic Continuity Equation 473
13.3.2 Macroscopic Momentum Equation 473
13.3.3 Turbulence Modeling 473
13.4 Macroscopic Heat Transfer 474
13.4.1 LTNE Model 474
13.4.2 LTE Model 476
13.5 Simplified Combustion Modeling 476
13.5.1 Macroscopic Mass Transport for Fuel 476
13.5.2 Simple Chemistry 477
13.6 Heat Release 478
13.6.1 Double Decomposition of Variables 478
13.6.2 Macroscopic Fuel Consumption 479
13.7 Preliminary Simulations 482
13.7.1 Two-Temperature Model, LTNE: 1D Flow 482
13.7.2 One-Temperature Model, LTE: 2D Flow 486
13.8 Summary 489
References 489

13.1 INTRODUCTION

Modeling of flows in inert porous media has attracted the attention of scientists and engineers worldwide, and in the last decade, a number of outstanding books, handbooks, and edited books have been written on the subject (Pop and Ingham 2001, Ingham and Pop 2005, Vafai 2005, Vadasz 2008, Nield and Bejan 2013).

In addition to thermomechanical models, including new research work aimed at biological applications (Vafai 2010), flows with chemical reactions in inert porous media have been also investigated extensively due to their many engineering applications and the demand for high-efficiency power-producing devices. The growing use of efficient radiant burners can be

encountered in the power and process industries, and as such, proper mathematical models of flow, heat, and mass transfer in porous media under combustion can benefit from the development of such engineering equipment.

In this chapter, an overview of recent development in modeling and simulating reactive flow in porous material is presented.

13.2 POROUS BURNERS

The advantages of having a combustion process inside an inert porous matrix are today well documented in the literature (Babkin 1993, Mohamad et al. 1994b, Howell et al. 1996, Bouma and Goey 1999, Henneke and Ellzey 1999, Oliveira and Kaviany 2001, Lammers and Goey 2003, Leonardi et al. 2003), including recent reviews about combustion of gases (Wood and Harries 2008) and liquids (Abdul et al. 2009) in such burners. Hsu et al. (1993) point out some of its benefits, including higher burning speed and volumetric energy release rates, greater combustion stability, and the ability to burn gases with low energy content. Driven by this motivation, the effects on porous ceramic inserts have been investigated in Peard et al. (1993), among others.

Turbulence modeling of combustion within inert porous media has been conducted by Lim and Matthews (1993) on the basis of an extension of the standard $k - \varepsilon$ model of Jones and Launder (1972). Work on direct simulation of turbulence in premixed flames, in cases when the porous dimension is of the order of the flame thickness, also has been reported in Sahraoui and Kaviany (1995).

Further, nonreactive turbulent flow in porous media has been the subject of several studies (Pedras and de Lemos 2001, 2003, de Lemos 2005a), including many applications such as flow through porous baffles (Santos and de Lemos 2006), channels with porous inserts (Assato et al. 2005), and buoyant flows (Braga and de Lemos 2004). In such work, intrapore turbulence is accounted for in all transport equations, but only nonreactive flows have been investigated. Other important contributions in modeling inert flows in porous media can be found in the high-impact and outstanding competing model of turbulence developed by Kuznetsov et al. (2002) and Kuznetsov (2004).

Motivated by the foregoing, this chapter extends previous work on turbulence modeling in porous media to include new predictions of combusting flows. Computations are carried out for inert porous material considering 1D and 2D turbulent flows with one- and two-temperature approaches. In addition, four different thermomechanical models are compared here, namely, laminar flow, laminar flow with radiation transport, turbulent flow, and turbulent flow with radiation transport. As such, this contribution compares the effects of radiation and turbulence in smoothing temperature distributions within porous burners. The material in this chapter reviews the work in de Lemos (2009, 2010) and Coutinho and de Lemos (2012) in a consolidated fashion, in addition to presenting additional information in regard to this topic.

13.3 MACROSCOPIC FLOW

The thermomechanical model employed here is based on the *double-decomposition* concept detailed in de Lemos (2005b) and Saito and de Lemos (2005, 2006). Transport equations are volume averaged according to the volume-averaging theorem (Slattery 1967, Whitaker 1969, Gray and Lee 1977) in addition to using time decomposition of flow variables followed by standard time-averaging procedure for treating turbulence. As the entire equation set is already fully available in the open literature, these equations will be reproduced here, and details about their derivations can be obtained in the aforementioned references. Essentially, in all the aforementioned studies, the flow variables are decomposed in a volume mean and a deviation (classical porous media analysis) in addition to being decomposed in a time mean and a fluctuation (classical turbulent flow treatment).

13.3.1 Macroscopic Continuity Equation

As previously stated, most of the equations to be shown in this chapter are fully detailed in existing open literature, so only their final modeled forms will be repeated.

The continuity of fluid mass reads

$$\nabla \cdot \rho_f \bar{\mathbf{u}}_D = 0 \tag{13.1}$$

Equation 13.1 represents the macroscopic continuity equation for the flowing gas, and its density, ρ_f, is allowed to vary as temperate rises.

13.3.2 Macroscopic Momentum Equation

The momentum equation for macroscopic turbulent flow reads as follows (de Lemos 2005b):

$$\nabla \cdot \left(\rho_f \frac{\bar{\mathbf{u}}_D \bar{\mathbf{u}}_D}{\phi} \right) = -\nabla \left(\phi \langle \bar{p} \rangle^i \right) + \mu \nabla^2 \bar{\mathbf{u}}_D + \nabla \cdot \left(-\rho_f \phi \langle \overline{\mathbf{u}'\mathbf{u}'} \rangle^i \right) - \left[\frac{\mu \phi}{K} \bar{\mathbf{u}}_D + \frac{c_F \phi \rho_f \, | \bar{\mathbf{u}}_D | \, \bar{\mathbf{u}}_D}{\sqrt{K}} \right] \tag{13.2}$$

where the last two terms in Equation 13.2 represent the Darcy and Forchheimer contributions, respectively. The symbol K is the porous medium permeability, $c_F = 0.55$ is the form drag coefficient, $\langle p \rangle^i$ is the intrinsic (fluid phase averaged) pressure, μ is the fluid viscosity, and ϕ is the porosity of the porous medium.

13.3.3 Turbulence Modeling

Turbulence is handled via a macroscopic $k - \varepsilon$ model, given by

$$\nabla \cdot \left(\rho_f \bar{\mathbf{u}}_D \langle k \rangle^i \right) = \nabla \cdot \left[\left(\mu + \frac{\mu_{t_\phi}}{\sigma_k} \right) \nabla \left(\phi \langle k \rangle^i \right) \right] - \rho_f \left\langle \overline{\mathbf{u}'\mathbf{u}'} \right\rangle^i : \nabla \bar{\mathbf{u}}_D + c_k \rho_f \frac{\phi \langle k \rangle^i | \bar{\mathbf{u}}_D |}{\sqrt{K}} - \rho_f \, \phi \langle \varepsilon \rangle^i \tag{13.3}$$

$$\nabla \cdot \left(\rho_f \, \bar{\mathbf{u}}_D \langle \varepsilon \rangle^i \right) = \nabla \cdot \left[\left(\mu + \frac{\mu_{t_\phi}}{\sigma_\varepsilon} \right) \nabla \left(\phi \langle \varepsilon \rangle^i \right) \right] + c_1 \left(-\rho \langle \overline{\mathbf{u}'\mathbf{u}'} \rangle^i : \nabla \bar{\mathbf{u}}_D \right) \frac{\langle \varepsilon \rangle^i}{\langle k \rangle^i} + c_2 c_k \rho_f \frac{\phi \langle \varepsilon \rangle^i | \bar{\mathbf{u}}_D |}{\sqrt{K}} - c_2 \rho \phi \frac{\langle \varepsilon \rangle^{i\,2}}{\langle k \rangle^i} \tag{13.4}$$

Assuming that a model for the macroscopic Reynolds stresses $-\rho_f \phi \langle \overline{\mathbf{u}'\mathbf{u}'} \rangle^i$ can be given by

$$-\rho_f \phi \langle \overline{\mathbf{u}'\mathbf{u}'} \rangle^i = \mu_\phi 2 \langle \bar{\mathbf{D}} \rangle^{\mathbf{v}} - \frac{2}{3} \phi \rho_f \langle k \rangle^i \mathbf{I} \tag{13.5}$$

with

$$\langle \bar{\mathbf{D}} \rangle^v = \frac{1}{2} \left[\nabla \left(\phi \langle \bar{\mathbf{u}} \rangle^i \right) + \left[\nabla \left(\phi \langle \bar{\mathbf{u}} \rangle^i \right) \right]^T \right] \tag{13.6}$$

the momentum Equation 13.2 finally reads (de Lemos 2005b)

$$\nabla\cdot\left(\rho_f\frac{\overline{\mathbf{u}}_D\overline{\mathbf{u}}_D}{\phi}\right)-\nabla\cdot\left\{\left(\mu+\mu_{t_\phi}\right)\left[\nabla\overline{\mathbf{u}}_D+\left(\nabla\overline{\mathbf{u}}_D\right)^T\right]\right\}$$
$$=-\nabla\left(\phi\langle\overline{p}\rangle^i\right)-\left[\frac{\mu\phi}{K}\overline{\mathbf{u}}_D+\frac{c_F\phi\rho_f\,|\,\overline{\mathbf{u}}_D|\,\overline{\mathbf{u}}_D}{\sqrt{K}}\right] \tag{13.7}$$

where

$$\mu_{t\phi}=\rho_f c_\mu\frac{\langle k\rangle^{i2}}{\langle\varepsilon\rangle^i} \tag{13.8}$$

Note that in Equation 13.7, a modified pressure is used, which includes the last term in Equation 13.5. Dealing with combustion processes, it is important to emphasize that the fluid density ρ_f is allowed to vary within the computational domain, as mentioned earlier.

13.4 MACROSCOPIC HEAT TRANSFER

There are two possibilities to handle energy transport across the porous burner. In the simplified model, also named *one-temperature model*, we assume the so-called local thermal equilibrium (LTE) hypothesis, in which the solid temperature is numerically equal to that of the flowing gas. When the solid and the gas temperatures differ by a considerable amount, the *two-temperature model* based on the local thermal nonequilibrium (LTNE) hypothesis applies. In the latter case, distinct energy balances are set for each phase. Transport equations for both models are discussed in the following sections.

13.4.1 LTNE Model

In cases where average temperatures in distinct phases are substantially different, macroscopic energy equations are obtained for both the fluid and solid phases by also applying time- and volume-averaging operators to the instantaneous local equations (Saito and de Lemos 2006). As in the flow case, volume integration is performed over a representative elementary volume or REV. After including the heat released due to the combustion reaction, one gets the following:

$$\text{Gas phase: } \nabla\cdot(\rho_f\,c_{pf}\,\overline{\mathbf{u}}_D\langle\overline{T_f}\rangle^i)=\nabla\cdot\left\{\mathbf{K}_{eff,f}\cdot\nabla\langle\overline{T}_f\rangle^i\right\}$$
$$+h_i a_i\left(\langle\overline{T_p}\rangle^i-\langle\overline{T_f}\rangle^i\right)+\phi\Delta HS_{fu} \tag{13.9}$$

$$\text{Solid phase: } 0=\nabla\cdot\left\{\mathbf{K}_{eff,p}\cdot\nabla\langle\overline{T_p}\rangle^i\right\}-h_i a_i\left(\langle\overline{T_p}\rangle^i-\langle\overline{T_f}\rangle^i\right) \tag{13.10}$$

where

$\langle\overline{T_f}\rangle^i$ and $\langle\overline{T_p}\rangle^i$ are the gas and solid temperatures, respectively
$a_i = A_i/\Delta V$ is the interfacial area per unit volume
h_i is the film coefficient for interfacial transport
ΔH is the heat of combustion (J/kg)
S_{fu} is the rate of fuel consumption (kg/m^2 s, discussed later in this chapter)

Tensors $\mathbf{K}_{eff,f}$ and $\mathbf{K}_{eff,p}$ are the effective conductivity tensors for the fluid and solid phases, respectively, given by

$$\mathbf{K}_{eff,f} = \left\{ \overbrace{\phi\lambda_f}^{conduction} \right\}\mathbf{I} + \underbrace{\mathbf{K}_{f,p}}_{local\,conduction} + \underbrace{\mathbf{K}_{disp}}_{dispersion} + \underbrace{\mathbf{K}_t + \mathbf{K}_{disp,t}}_{turbulence} \tag{13.11}$$

$$\mathbf{K}_{eff,s} = \left\{ \left[\overbrace{(1-\varphi)\lambda_p}^{conduction} + \frac{\overbrace{16\sigma(\langle \overline{T}_p \rangle^i)^3}^{radiation}}{3\beta_r} \right] \right\}\mathbf{I} + \underbrace{\mathbf{K}_{p,f}}_{local\ conduction} \tag{13.12}$$

where

λ is the thermal conductivity for either phase
β_r is the extinction coefficient (1/m)
σ is the Stefan–Boltzmann constant
$\mathbf{I}$ is the unit tensor

All mechanisms contributing to heat transfer within the medium, together with turbulence and radiation, are included here to compare their effect on temperature distribution. Further, such distinct contributions of various mechanisms are the outcome of the application of gradient-type diffusion models in the following forms (see Saito and de Lemos 2006 for more details):

$$\text{Turbulent heat flux: } -\left(\rho c_p\right)_f \left(\phi \overline{\langle \mathbf{u}' \rangle^i \langle T_f' \rangle^i}\right) = \mathbf{K}_t \cdot \nabla \langle \overline{T}_f \rangle^i \tag{13.13}$$

$$\text{Thermal dispersion: } -\left(\rho c_p\right)_f \left(\phi \langle {}^i\overline{\mathbf{u}}^{\,i} \overline{T_f} \rangle^i\right) = \mathbf{K}_{disp} \cdot \nabla \langle \overline{T}_f \rangle^i \tag{13.14}$$

$$\text{Turbulent thermal dispersion: } -\left(\rho c_p\right)_f \left(\phi \left\langle \overline{{}^i\mathbf{u}'\,{}^i T_f'} \right\rangle^i\right) = \mathbf{K}_{disp,t} \cdot \nabla \left\langle \overline{T}_f \right\rangle^i \tag{13.15}$$

$$\text{Local conduction: } \begin{cases} \dfrac{1}{\Delta V}\displaystyle\int_{A_i} \mathbf{n}_i k_f \overline{T_f} dA = \mathbf{K}_{f,p} \cdot \nabla \left\langle \overline{T}_f \right\rangle^i \\ -\dfrac{1}{\Delta V}\displaystyle\int_{A_i} \mathbf{n}_i k_p \overline{T_p} dA = \mathbf{K}_{p,f} \cdot \nabla \left\langle \overline{T}_p \right\rangle^i \end{cases} \tag{13.16}$$

In Equations 13.9 and 13.10, the heat transferred between the two phases was modeled by means of a interfacial convective heat transfer coefficient h_i, as presented earlier. A numerical correlation for it was proposed by Kuwahara et al. (2001) for laminar flow as

$$\frac{h_i D}{\lambda_f} = \left(1 + \frac{4(1-\phi)}{\phi}\right) + \frac{1}{2}(1-\phi)^{1/2}\,\mathrm{Re}_D\,\mathrm{Pr}^{1/3} \quad \text{valid for } 0.2 < \phi < 0.9 \tag{13.17}$$

For turbulent flow, the following expression was proposed in Saito and de Lemos (2006):

$$\frac{h_i D}{\lambda_f} = 0.08\left(\frac{\mathrm{Re}_D}{\phi}\right)^{0.8} \mathrm{Pr}^{1/3}; \quad \text{for } 1.0\times10^4 < \frac{\mathrm{Re}_D}{\phi} < 2.0\times10^7, \quad \text{valid for } 0.2 < \phi < 0.9, \tag{13.18}$$

13.4.2 LTE Model

Although the LTE hypothesis is known to be inappropriate to handle large temperature differences between the solid matrix and the burning gas, for investigating the role of the mechanisms of turbulence and radiation, this simple mathematical framework may provide some initial insight for interpreting more advanced and sophisticated simulation tools. Examples of applications of the one-energy equation model in combustion in porous media are given by Mohamad et al. (1994b) and de Neef et al. (1999).

The governing equation for energy transport in this case is given by

$$\left\{(\rho c_p)_f \phi + (\rho c_p)_p (1-\phi)\right\} \frac{\partial \langle \overline{T} \rangle^i}{\partial t} + (\rho c_p)_f \nabla \cdot \left(\overline{\mathbf{u}}_D \langle \overline{T} \rangle^i \right) = \nabla \cdot \left\{ \mathbf{K}_{eff} \cdot \nabla \langle \overline{T} \rangle^i \right\} + \Delta H S_{fu} \tag{13.19}$$

where $\langle T \rangle^i$ is the average temperature for both the solid and the liquid, $\mathbf{K}_{eff}$, given by

$$\mathbf{K}_{eff} = \left\{ \overbrace{\phi \lambda_f + (1-\phi)[\lambda_p}^{conduction} + \frac{\overbrace{16\sigma \left(\langle \overline{T} \rangle^i \right)^3}^{radiation}}{3\beta_r}] \right\} \mathbf{I} + \underbrace{\mathbf{K}_{tor}}_{tortuosity} + \underbrace{\mathbf{K}_{disp}}_{dispersion} + \underbrace{\mathbf{K}_t + \mathbf{K}_{disp,t}}_{turbulence} \tag{13.20}$$

is the effective conductivity tensor. As in the case of the LTNE model, in Equation 13.20, all mechanisms contributing to heat transfer within the medium, together with turbulence and radiation, are included. Further, the sum of the two terms in Equation 13.16 gives rise to the tortuosity tensor shown in Equation 13.20.

A steady-state form of (13.19) reads

$$\left(\rho c_p\right)_f \nabla \cdot \left(\overline{\mathbf{u}}_D \langle \overline{T} \rangle^i \right) = \nabla \cdot \left\{ \mathbf{K}_{eff} \cdot \nabla \langle \overline{T} \rangle^i \right\} + \Delta H S_{fu} \tag{13.21}$$

where all additional mechanisms of transfer, as previously mentioned, are included in $\mathbf{K}_{eff}$.

13.5 SIMPLIFIED COMBUSTION MODELING

In this work, the gas phase is assumed to be composed by a premixture of air and gaseous fuel that undergoes combustion while flowing through the solid. For analyzing such a system, the equation set (13.1) through (13.18) is complemented with a transport equation for the fuel and a kinetics model for the burning process (de Lemos 2009).

13.5.1 Macroscopic Mass Transport for Fuel

Transport equation for the fuel is

$$\nabla \cdot \left(\rho_f \overline{\mathbf{u}}_D \langle \overline{m}_{fu} \rangle^i \right) = \nabla \cdot \rho_f \mathbf{D}_{eff} \cdot \nabla \left(\phi \langle \overline{m}_{fu} \rangle^i \right) - \phi S_{fu} \tag{13.22}$$

where $\langle \overline{m}_{fu} \rangle^i$ is the mass fraction for the fuel. The effective mass transport tensor, $\mathbf{D}_{eff}$, is defined as

$$\mathbf{D}_{eff} = \underbrace{\mathbf{D}_{disp}}_{dispersion} + \overbrace{\mathbf{D}_{diff}}^{diffusion} + \underbrace{\mathbf{D}_t + \mathbf{D}_{disp,t}}_{turbulence} = \mathbf{D}_{disp} + \frac{1}{\rho_f} \left(\frac{\mu_\phi}{Sc_\ell} + \frac{\mu_{t\phi}}{Sc_{\ell,t}} \right) \mathbf{I} = \mathbf{D}_{disp} + \frac{1}{\rho_f} \left(\frac{\mu_{\phi,eff}}{Sc_{\ell,eff}} \right) \mathbf{I} \tag{13.23}$$

where Sc_ℓ and $Sc_{\ell,t}$ are the laminar and turbulent Schmidt numbers for species ℓ, respectively, and *eff* denotes an effective value. The dispersion tensor is defined such that

$$-\rho_f \phi \left\langle {}^i\bar{\mathbf{u}}\, {}^i\bar{m}_{fu} \right\rangle^i = \rho_f \mathbf{D}_{disp} \cdot \nabla \left(\phi \langle \bar{m}_{fu} \rangle^i \right) \tag{13.24}$$

13.5.2 Simple Chemistry

The chemical exothermic reaction is assumed to be instantaneous and to occur in a single, kinetic-controlled step, which, for combustion of a mixture of air and methane, is given by the following chemical reaction (Mohamad et al. 1994b, Malico and Pereira 1999):

$$CH_4 + 2(1+\Psi)(O_2 + 3.76\,N_2) \rightarrow CO_2 + 2\,H_2O + 2\Psi\,O_2 + 7.52(1+\Psi)\,N_2 \tag{13.25}$$

For *N*-heptane, a similar equation reads as follows (Mohamad et al. 1994a):

$$C_7H_{16} + 11(1+\Psi)(O_2 + 3.76\,N_2) \rightarrow 7\,CO_2 + 8\,H_2O + 11\Psi\,O_2 + 41.36(1+\Psi)\,N_2 \tag{13.26}$$

And for octane, we get

$$C_8H_{18} + 12.5(1+\Psi)(O_2 + 3.76\,N_2) \rightarrow 8C\,O_2 + 9\,H_2O + 12.5\Psi\,O_2 + 47(1+\Psi)\,N_2 \tag{13.27}$$

where Ψ is the excess air in the reactant stream at the inlet of the porous foam. For the stoichiometric ratio, $\Psi = 0$. In all of these equations, the reaction is then assumed to be kinetically controlled and occurring infinitely fast. A general expression for them can be derived as

$$\begin{aligned} &C_nH_{2m} + \left(n + \frac{m}{2}\right)\left(1+\Psi\right)\left(O_2 + 3.76N_2\right) \rightarrow \\ &nCO_2 + mH_2O + \left(n + \frac{m}{2}\right)\Psi O_2 + \left(n + \frac{m}{2}\right)3.76\left(1+\Psi\right)N_2 \end{aligned} \tag{13.28}$$

where the coefficients *n* and *m* can be found in Table 13.1. Here, Equation 13.28 is assumed to hold for the particular examples given in Table 13.1.

TABLE 13.1
Coefficients in the General Combustion Equation 13.28

Gas	*n*	*m*	(*n* + *m*/2)	(*n* + *m*/2) × 3.76
Methane	1	2	2	7.52
N-heptane	7	8	11	41.36
Octane	8	9	12.5	47

The local instantaneous rate of fuel consumption over the total volume (fluid plus solid) was determined by one-step Arrhenius reaction (Kuo 1986, Turns 1996) given by

$$S_{fu} = \rho_f^a A \langle m_{fu}^b \rangle^i \langle m_{ox}^c \rangle^i e^{-E/R\langle \bar{T}_f \rangle^i} \tag{13.29}$$

where

m_{fu} and m_{ox} are the local instantaneous mass fractions for the fuel and oxidant, respectively, the coefficients a, b, c depend on the particular reaction (Kuo 1986)

A is the preexponential factor

E is the activation energy, where numerical values for these parameters depend on the fuel considered (Turns 1996)

For simplicity, in presenting the ideas in this chapter, we assume here that $a = 2$, $b = c = 1$, which corresponds to the burning of a mixture of methane and air (Mohamad et al. 1994b, Malico and Pereira 1999, de Lemos 2009).

Density ρ_f in these equations is determined from the perfect gas equation for a mixture of perfect gases:

$$\rho_f = \frac{P_o}{RT_f \sum_1^{\ell} \frac{m_\ell}{M_\ell}} \tag{13.30}$$

where

P_o is the absolute pressure

R is the universal gas constant (8.134 J/(mol · K))

M_ℓ is the molecular weight of species ℓ

13.6 HEAT RELEASE

13.6.1 Double Decomposition of Variables

Macroscopic transport equations for turbulent flow in a porous medium are obtained through the simultaneous application of time- and volume-averaging operators over a generic fluid property φ. Such concepts are defined as follows (Slattery 1967, Whitaker 1969, Gray and Lee 1977):

$$\langle \varphi \rangle^i = \frac{1}{\Delta V_f} \int_{\Delta V_f} \varphi dV; \quad \langle \varphi \rangle^v = \phi \langle \varphi \rangle^i; \quad \phi = \frac{\Delta V_f}{\Delta V}, \quad \text{with } \varphi = \langle \varphi \rangle^i + {}^i\varphi \tag{13.31}$$

$$\overline{\varphi} = \frac{1}{\Delta t} \int_t^{t+\Delta t} \varphi dt, \quad \text{with } \varphi = \overline{\varphi} + \varphi' \tag{13.32}$$

where ΔV_f is the volume of the fluid contained in a REV ΔV and intrinsic average and volume average are represented, respectively, by $\langle\ \rangle^i$ and $\langle\ \rangle^v$. Also, due to the definition of average, we get

$$\overline{\varphi'} = 0 \tag{13.33}$$

and

$$\langle {}^i\phi \rangle^i = 0 \tag{13.34}$$

The double-decomposition idea, fully described in de Lemos (2005b), combines Equations 13.31 and 13.32 and can be summarized as

$$\overline{\langle\varphi\rangle^i} = \langle\overline{\varphi}\rangle^i; \quad {}^i\overline{\varphi} = \overline{{}^i\varphi}; \quad \langle\varphi'\rangle^i = \langle\varphi\rangle^{i'} \tag{13.35}$$

and

$$\left.\begin{aligned} \varphi' &= \langle\varphi'\rangle^i + {}^i\varphi' \\ {}^i\varphi &= \overline{{}^i\varphi} + {}^i\varphi' \end{aligned}\right\} \quad \text{where } {}^i\varphi' = \varphi' - \langle\varphi'\rangle^i = {}^i\varphi - \overline{{}^i\varphi} \tag{13.36}$$

Therefore, the quantity φ can be expressed by either

$$\varphi = \overline{\langle\varphi\rangle^i} + \langle\varphi\rangle^{i'} + \overline{{}^i\varphi} + {}^i\varphi' \tag{13.37}$$

or

$$\varphi = \langle\overline{\varphi}\rangle^i + {}^i\overline{\varphi} + \langle\overline{\varphi}\rangle^i + {}^i\overline{\varphi}. \tag{13.38}$$

The term ${}^i\varphi'$ can be viewed as either *the temporal fluctuation of the spatial deviation* or the *spatial deviation of the temporal fluctuation* of the quantity φ.

13.6.2 Macroscopic Fuel Consumption

To derive macroscopic equations for the simple combustion model presented earlier, we can take Equation 13.29 with $a = 2$, $b = c = 1$ and note that the rate of fuel consumption is dictated by the product of two local instantaneous values, m_{fu} and m_{ox}, which represent local instantaneous mass fractions for the fuel and oxygen, respectively. Now, if we apply to each one of them the decomposition (13.37), or its equivalent (13.38), we get

$$m_{fu} = \langle\overline{m}_{fu}\rangle^i + {}^i\overline{m}_{fu} + \langle m'_{fu}\rangle^i + {}^i m'_{fu} \tag{13.39}$$

$$m_{ox} = \langle\overline{m}_{ox}\rangle^i + {}^i\overline{m}_{ox} + \langle m'_{ox}\rangle^i + {}^i m'_{ox} \tag{13.40}$$

For the sake of simplicity and manipulation, looking at only the product of the mass fractions ($m_{fu}m_{ox}$) in Equation 13.29 and applying the decompositions (Equations 13.39 and 13.40), we get

$$\begin{aligned} m_{fu}\,m_{ox} = {} & \langle\overline{m}_{fu}\rangle^i\langle\overline{m}_{ox}\rangle^i + {}^i\overline{m}_{fu}\langle\overline{m}_{ox}\rangle^i + \langle m'_{fu}\rangle^i\langle\overline{m}_{ox}\rangle^i + {}^i m'_{fu}\langle\overline{m}_{ox}\rangle^i \\ & + \langle\overline{m}_{fu}\rangle^i\,{}^i\overline{m}_{ox} + {}^i\overline{m}_{fu}\,{}^i\overline{m}_{ox} + \langle m'_{fu}\rangle^i\,{}^i\overline{m}_{ox} + {}^i m'_{fu}\,{}^i\overline{m}_{ox} \\ & + \langle\overline{m}_{fu}\rangle^i\langle m'_{ox}\rangle^i + {}^i\overline{m}_{fu}\langle m'_{ox}\rangle^i + \langle m'_{fu}\rangle^i\langle m'_{ox}\rangle^i + {}^i m'_{fu}\langle m'_{ox}\rangle^i \\ & + \langle\overline{m}_{fu}\rangle^i\,{}^i m'_{ox} + {}^i\overline{m}_{fu}\,{}^i m'_{ox} + \langle m'_{fu}\rangle^i\,{}^i m'_{ox} + {}^i m'_{fu}\,{}^i m'_{ox} \end{aligned} \tag{13.41}$$

Applying the volume-averaging operator (Equation 13.31) to the instantaneous local product (Equation 13.41), we get

$$\begin{aligned}\langle m_{fu}\, m_{ox}\rangle^i = {} & \langle\langle \bar{m}_{fu}\rangle^i\langle \bar{m}_{ox}\rangle^i\rangle^i + \langle {}^i\bar{m}_{fu}\langle \bar{m}_{ox}\rangle^i\rangle^i + \langle\langle m'_{fu}\rangle^i\langle \bar{m}_{ox}\rangle^i\rangle^i + \langle {}^i m'_{fu}\langle \bar{m}_{ox}\rangle^i\rangle^i \\ & + \langle\langle \bar{m}_{fu}\rangle^{i\,i}\bar{m}_{ox}\rangle^i + \langle {}^i\bar{m}_{fu}\,{}^i\bar{m}_{ox}\rangle^i + \langle\langle m'_{fu}\rangle^{i\,i}\bar{m}_{ox}\rangle^i + \langle {}^i m'_{fu}\,{}^i\bar{m}_{ox}\rangle^i \\ & + \langle\langle \bar{m}_{fu}\rangle^i\langle m'_{ox}\rangle^i\rangle^i + \langle {}^i\bar{m}_{fu}\langle m'_{ox}\rangle^i\rangle^i + \langle\langle m'_{fu}\rangle^i\langle m'_{ox}\rangle^i\rangle^i + \langle {}^i m'_{fu}\langle m'_{ox}\rangle^i\rangle^i \\ & + \langle\langle \bar{m}_{fu}\rangle^{i\,i}m'_{ox}\rangle^i + \langle {}^i\bar{m}_{fu}\,{}^i m'_{ox}\rangle^i + \langle\langle m'_{fu}\rangle^{i\,i}m'_{ox}\rangle^i + \langle {}^i m'_{fu}\,{}^i m'_{ox}\rangle^i \end{aligned} \tag{13.42}$$

Now, looking back at Equation 13.34, all terms containing only one deviation factor in Equation 13.42 will vanish, such that

$$\begin{aligned}\langle m_{fu}\, m_{ox}\rangle^i = {} & \left\langle\left\langle \bar{m}_{fu}\right\rangle^i\left\langle \bar{m}_{ox}\right\rangle^i\right\rangle^i + \left\langle {}^i\bar{m}_{fu}\left\langle \bar{m}_{ox}\right\rangle^i\right\rangle^i + \left\langle\left\langle m'_{fu}\right\rangle^i\left\langle \bar{m}_{ox}\right\rangle^i\right\rangle^i + \left\langle {}^i m'_{fu}\left\langle \bar{m}_{ox}\right\rangle^i\right\rangle^i \\ & + \left\langle\left\langle \bar{m}_{fu}\right\rangle^{i\,i}\bar{m}_{ox}\right\rangle^i + \left\langle {}^i\bar{m}_{fu}\,{}^i\bar{m}_{ox}\right\rangle^i + \left\langle\left\langle m'_{fu}\right\rangle^{i\,i}\bar{m}_{ox}\right\rangle^i + \left\langle {}^i m'_{fu}\,{}^i\bar{m}_{ox}\right\rangle^i \\ & + \left\langle\left\langle \bar{m}_{fu}\right\rangle^i\left\langle m'_{ox}\right\rangle^i\right\rangle^i + \left\langle {}^i\bar{m}_{fu}\left\langle m'_{ox}\right\rangle^i\right\rangle^i + \left\langle\left\langle m'_{fu}\right\rangle^i\left\langle m'_{ox}\right\rangle^i\right\rangle^i + \left\langle {}^i m'_{fu}\left\langle m'_{ox}\right\rangle^i\right\rangle^i \\ & + \left\langle\left\langle \bar{m}_{fu}\right\rangle^{i\,i}m'_{ox}\right\rangle^i + \left\langle {}^i\bar{m}_{fu}\,{}^i m'_{ox}\right\rangle^i + \left\langle\left\langle m'_{fu}\right\rangle^{i\,i}m'_{ox}\right\rangle^i + \left\langle {}^i m'_{fu}\,{}^i m'_{ox}\right\rangle^i \end{aligned} \tag{13.43}$$

The following equation is left as

$$\begin{aligned}\langle m_{fu}\, m_{ox}\rangle^i = {} & \langle \bar{m}_{fu}\rangle^i\langle \bar{m}_{ox}\rangle^i + \langle m'_{fu}\rangle^i\langle \bar{m}_{ox}\rangle^i + \langle {}^i\bar{m}_{fu}\,{}^i\bar{m}_{ox}\rangle^i + \langle {}^i m'_{fu}\,{}^i\bar{m}_{ox}\rangle^i \\ & + \langle \bar{m}_{fu}\rangle^i\langle m'_{ox}\rangle^i + \langle m'_{fu}\rangle^i\langle m'_{ox}\rangle^i + \langle {}^i\bar{m}_{fu}\,{}^i m'_{ox}\rangle^i + \langle {}^i m'_{fu}\,{}^i m'_{ox}\rangle^i \end{aligned} \tag{13.44}$$

Another way to write Equation 13.44, using the equivalences shown in Equation 13.35, is

$$\begin{aligned}\left\langle m_{fu}\, m_{ox}\right\rangle^i = {} & \overline{\left\langle m_{fu}\right\rangle^i}\overline{\left\langle m_{ox}\right\rangle^i} + \left\langle m_{fu}\right\rangle^{i'}\overline{\left\langle m_{ox}\right\rangle^i} + \left\langle \overline{{}^i m_{fu}}\;\overline{{}^i m_{ox}}\right\rangle^i + \left\langle {}^i m'_{fu}\;\overline{{}^i m_{ox}}\right\rangle^i \\ & + \overline{\left\langle m_{fu}\right\rangle^i}\left\langle m_{ox}\right\rangle^{i'} + \left\langle m_{fu}\right\rangle^{i'}\left\langle m_{ox}\right\rangle^{i'} + \left\langle \overline{{}^i m_{fu}}\;{}^i m'_{ox}\right\rangle^i + \left\langle {}^i m'_{fu}\;{}^i m'_{ox}\right\rangle^i \end{aligned} \tag{13.45}$$

If we now apply the time-averaging operator over Equation 13.45 and note that, due to Equation 13.33, all terms containing only one time fluctuation factor vanish, such that

$$\begin{aligned}\overline{\langle m_{fu}\, m_{ox}\rangle^i} = {} & \overline{\overline{\langle m_{fu}\rangle^i}\overline{\langle m_{ox}\rangle^i}} + \overline{\langle m_{fu}\rangle^{i'}\overline{\langle m_{ox}\rangle^i}} + \overline{\langle \overline{{}^i m_{fu}}\;\overline{{}^i m_{ox}}\rangle^i} + \overline{\langle {}^i m'_{fu}\;\overline{{}^i m_{ox}}\rangle^i} \\ & + \overline{\overline{\langle m_{fu}\rangle^i}\langle m_{ox}\rangle^{i'}} + \overline{\langle m_{fu}\rangle^{i'}\langle m_{ox}\rangle^{i'}} + \overline{\langle \overline{{}^i m_{fu}}\;{}^i m'_{ox}\rangle^i} + \overline{\langle {}^i m'_{fu}\;{}^i m'_{ox}\rangle^i} \end{aligned} \tag{13.46}$$

we get the following time- and volume-averaged expression after dropping all null values

$$\overline{\left\langle m_{fu}\, m_{ox}\right\rangle^i} = \overline{\left\langle m_{fu}\right\rangle^i}\overline{\left\langle m_{ox}\right\rangle^i} + \left\langle \overline{{}^i m_{fu}}\;\overline{{}^i m_{ox}}\right\rangle^i + \overline{\left\langle m_{fu}\right\rangle^{i'}\left\langle m_{ox}\right\rangle^{i'}} + \overline{\left\langle {}^i m'_{fu}\;{}^i m'_{ox}\right\rangle^i} \tag{13.47}$$

Again, we can make use of an alternative representation for the same terms in Equation 13.47 when looking at equivalences (13.35). We then get

$$\overline{\langle m_{fu}\, m_{ox}\rangle}^{i} = \langle \bar{m}_{fu}\rangle^{i}\langle \bar{m}_{ox}\rangle^{i} + \langle {}^{i}\bar{m}_{fu}\, {}^{i}\bar{m}_{ox}\rangle^{i} + \overline{\langle m'_{fu}\rangle^{i}\langle m'_{ox}\rangle^{i}} + \overline{\langle {}^{i}m'_{fu}\, {}^{i}m'_{ox}\rangle}^{i} \tag{13.48}$$

Including the full decomposition Equation 13.48 back into the expression for S_{fu} (Equation 13.29), we get

$$\begin{aligned}\overline{\langle S_{fu}\rangle}^{i} &= \rho_f^2 A \overline{\langle m_{fu}\, m_{ox}\rangle}^{i} e^{-E/R\langle \bar{T}\rangle^{i}} \\ &= \rho_f^2 A \left(\underbrace{\langle \bar{m}_{fu}\rangle^{i}\langle \bar{m}_{ox}\rangle^{i}}_{\text{I}} + \underbrace{\langle {}^{i}\bar{m}_{fu}\, {}^{i}\bar{m}_{ox}\rangle^{i}}_{\text{II}} + \underbrace{\overline{\langle m'_{fu}\rangle^{i}\langle m'_{ox}\rangle^{i}}}_{\text{III}} + \underbrace{\overline{\langle {}^{i}m'_{fu}\, {}^{i}m'_{ox}\rangle}^{i}}_{\text{IV}} \right) e^{-E/R\langle \bar{T}\rangle^{i}}\end{aligned} \tag{13.49}$$

The four terms on the rhs of Equation 13.49, multiplied by the parameter $\rho_f^2 A e^{-E/R\langle \bar{T}\rangle^{i}}$, can be interpreted physically as follows:

I. *Reaction rate* due to volume- and time-averaged values of fuel and oxidant mass fractions. This is the standard rate of reaction commonly employed in the literature (Mohamad et al. 1994a,b, Malico and Pereira 1999).
II. *Dispersive reaction rate* due to deviation of mean time–mean fuel and oxidant mass fractions. This rate occurs even if the flow is in laminar and is due to fact that both mass fractions present a deviation value about their volume-averaged values.
III. *Turbulent reaction rate* due to time fluctuation of volume-averaged values of fuel and oxidant mass flow rates and represents additional fuel consumption rate because, inside an REV, the volume-averaged mass fractions of both oxygen and fuel fluctuate with time, giving rise to a nonnull time correlation.
IV. *Turbulent dispersive reaction rate* due to simultaneous time fluctuations and volume deviations of both values of fuel and oxidant mass flow rates.

In light of Equation 13.36, terms III and IV in Equation 13.49 can be recombined to form

$$\overline{\langle m'_{fu}\rangle^{i}\langle m'_{ox}\rangle^{i}} + \langle \overline{{}^{i}m'_{fu}\, {}^{i}m'_{ox}}\rangle^{i} = \langle \overline{m'_{fu}\, m'_{ox}}\rangle^{i} \tag{13.50}$$

giving

$$S^{t}_{fu,\phi} = \rho_f^2 A \overline{\langle m'_{fu}\, m'_{ox}\rangle}^{i} e^{-E/R\langle \bar{T}\rangle^{i}} \tag{13.51}$$

which can be seen as the overall effect of turbulence on the fuel consumption rate. Likewise, the dispersive component reads

$$S^{disp}_{fu,\phi} = \rho_f^2 A \langle {}^{i}\bar{m}_{fu}\, {}^{i}\bar{m}_{ox}\rangle^{i} e^{-E/R\langle \bar{T}\rangle^{i}} \tag{13.52}$$

and for the first term in Equation 13.49,

$$S_{fu,\phi} = \rho_f^2 A \langle \bar{m}_{fu} \rangle^i \langle \bar{m}_{ox} \rangle^i e^{-E/R\langle \bar{T} \rangle^i} \tag{13.53}$$

finally giving

$$\overline{\langle S_{fu} \rangle}^i = S_{fu,\phi} + S_{fu,\phi}^{disp} + S_{fu,\phi}^{t} \tag{13.54}$$

The models for Equations 13.51 and 13.52 and evaluation of their relative values when compared to Equation 13.49 remain an open question and shall be the subject of further investigation. They might be related to physically controlled mechanisms associated with the full reaction rate given by Equation 13.49.

13.7 PRELIMINARY SIMULATIONS

For 1D cases, the two-temperature model given in Section 13.4.1 was applied, whereas for the LTE model, detailed in Section 13.4.2, a 2D combustor was considered. Figure 13.1 illustrates both cases here analyzed. In both 1D and 2D cases, the finite-volume technique was employed to discretize the transport equations. The resulting algebraic equation set was relaxed using the well-known segregated method SIMPLE (Patankar 1980). Further, the flame front position was the sole outcome of the solution process, and no artificial numerical setup was implemented for holding the flame at some particular location.

For simulations using the geometry in Figure 13.1a, the parameters and boundary conditions here used are those of the burner developed by Pereira (2002). In Figure 13.1b, the mixture enters through the clearance of the burner on the left and expands as it flows to the exit where a zero diffusion flux is considered.

For 1D cases and the LTNE model (Figure 13.1a), simulations assumed given temperatures (solid and gas) and fuel mass fraction at inlet ($x = 0$ cm). At exit ($x = 8$ cm), for the solid temperature, a balance between the energy conducted to the exit of the burner and the radiation leaving the porous material to the environment was applied. Further, an initial length of 2 cm was considered to be made of a material that prevents flashback of the flame, which is commonly referred to in the literature as *flame trap* (Trimis and Durst 1996). If flow conditions are such that ignition occurs, then the flame front is positioned after $x = 2$ cm.

13.7.1 Two-Temperature Model, LTNE: 1D Flow

For 1D flow using the LTNE model, the computational grid was generated with a concentration of points close to the beginning of the combustion section ($x = 2$ cm), where steep temperature and species gradients were expected to appear.

Figure 13.2 shows results for temperature of both the burning gas and solid porous matrix. Results can correctly predict the increase of the gas temperature when the excess ratio is reduced or the inlet mass flow rate is enhanced.

Figure 13.3a also shows the effect of excess air Ψ on the gas temperature, T_f, and solid temperature, T_p. Temperature levels for the stoichiometric case and for $\Psi = 0.8$ gave numerical values close to those from Kuo (1986). Likewise, mass fraction behavior of species CH_4 and CO_2 (Figure 13.3b) and H_2O and O_2 (Figure 13.3c) follow closely those reported by Kuo (1986), for the one-equation simple combustion model here presented. Excess air reduces the final mass fraction of CO_2 and water and raises the amount of oxygen not participating in the combustion reaction. These results are

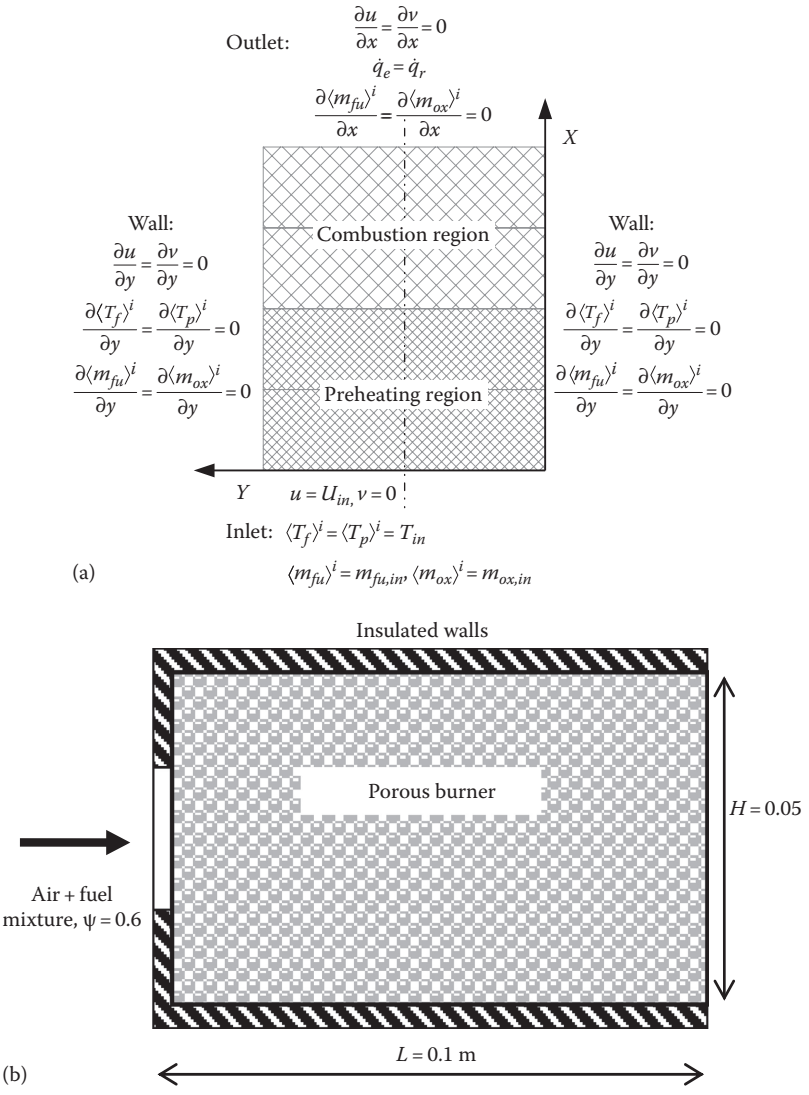

FIGURE 13.1 Cases investigated: (a) 1D combustor model, LTNE model, and (b) 2D combustor model, LTE model.

the outcome of the single-step reaction (Section 13.5.2) that links the consumption and production rates of individual constituents of the mixture.

Figure 13.4 shows the dependence of temperature levels on inlet velocities U_{in}. As axial flow is increased, one can note a slight reduction of peak values of temperatures, followed by the movement of the flame toward the exit of the burner.

Although the movement of the flame front is in accordance with simulations by Trimis and Durst (1996), here, a reduction on the maximum values of temperatures was calculated, which disagrees with that study's findings, where the temperature rises as the inlet mass flow rate is increased. One possible explanation for this contrary behavior is that there are a number of distinct parameters and assumptions in both calculations sets, here and in Trimis and Durst (1996), spanning from mathematical to numerical modeling hypotheses, which might affect the final results.

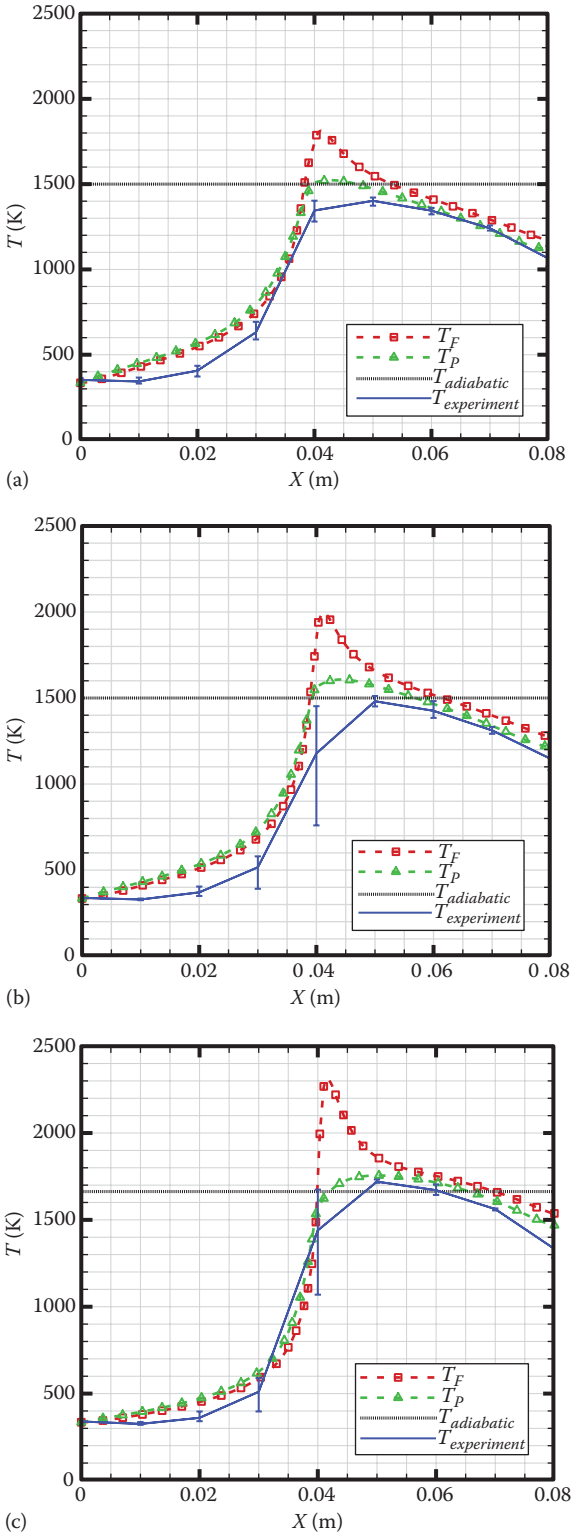

FIGURE 13.2 Code validation, experiments by Pereira (2002): (a) Case 01 ($\psi = 1.0$, $U_{in} = 15$), (b) Case 02 ($\psi = 0.67$, $U_{in} = 0.21$), and (c) Case 03 ($\psi = 0.67$, $U_{in} = 0.40$).

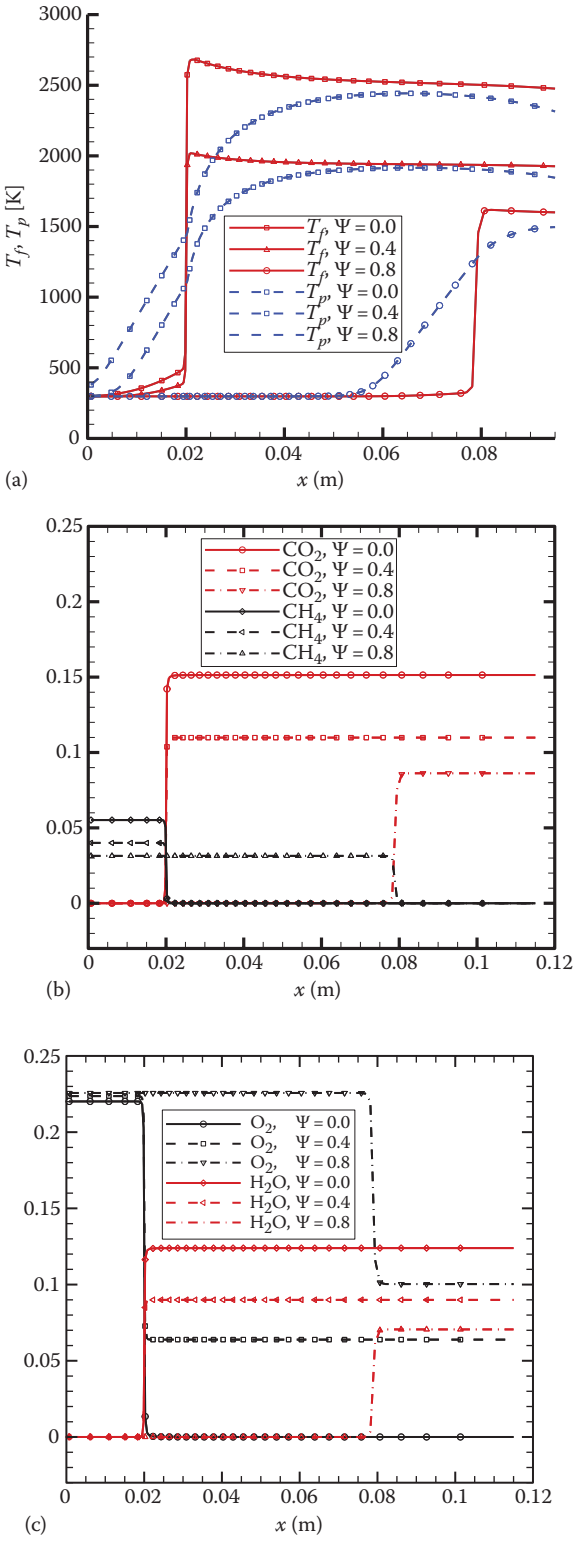

FIGURE 13.3 Effect of excess air Ψ for U_{in} = 0.1 m/s and zero thermal radiation flux at exit, x = 12 cm: (a) temperature fields, (b) fuel and carbon dioxide, and (c) water and oxygen.

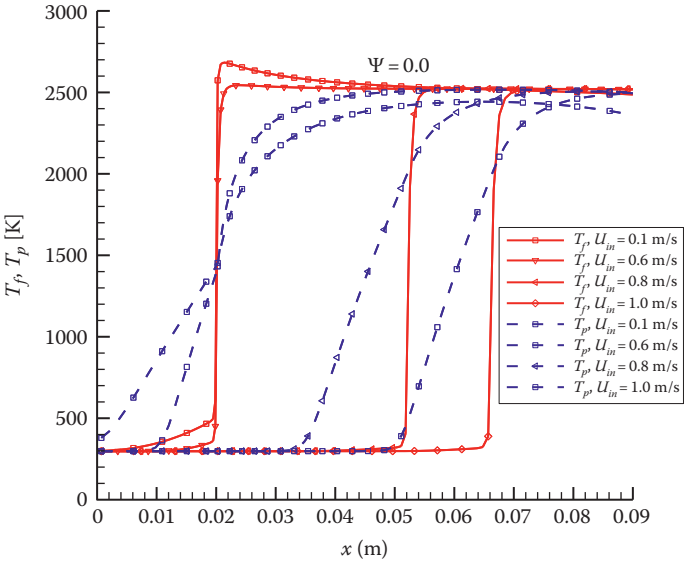

FIGURE 13.4 Effect of inlet gas velocity on temperature fields.

Four different thermomechanical models are compared now, namely, laminar, laminar with radiation transport, turbulent, and turbulent with radiation transport. The radiation model is included by considering the radiation transport term in the T_p (Equation 13.12). Turbulence modeling is handled by resolving the $k - \varepsilon$ model (Equations 13.3 and 13.4) in addition to solving for the macroscopic turbulent eddy viscosity $\mu_{t\phi}$ (Equation 13.8). In all models, combustion is simulated via a unique simple closure, which is presented by Equations 13.25 and 13.29.

Numerical simulations obtained with different models are presented in Figure 13.5 for two values of U_{in}. Figure 13.5a shows that for a low value of U_{in}, the flame (shown by solid lines) stabilizes close to the beginning of the burning section (x = 2 cm), independent of the mathematical model applied. Solid temperatures are influenced by radiation transport, which tends to smooth out temperature differences within the solid matrix, enhancing, as such, the regenerative advantage of porous burners (shown by dashed lines). Regeneration is achieved by preheating the gas prior to the combustion zone. In fact, the use of a turbulence model in conjunction with radiation transport gives the higher-temperature peak of the gas temperature at the flame position. Increasing the inlet mass flow rate (Figure 13.5b), the flame is pushed toward the burner's exit, regardless of the model used. Here also, radiation transport substantially affects the solid temperature distribution, but definitive conclusions on the appropriateness of each model can be reached only after careful comparison to experimental measurements. This shall be the subject of future research efforts.

13.7.2 One-Temperature Model, LTE: 2D Flow

In the thermal equilibrium hypotheses, for the first set of results, the problem considered consists of having a porous media confined in a channel, through which a mixture of fuel and air enters from the left, as shown in Figure 13.1b. The fuel/air mixture is injected through an inlet clearance of size less than the burner height, so that flow expansion occurs past the chamber entrance.

Figure 13.6a shows the effect of inlet velocity U_{in} on the flame front, whose location is here assumed to be related with the heat release rate computed by Equation 13.29.

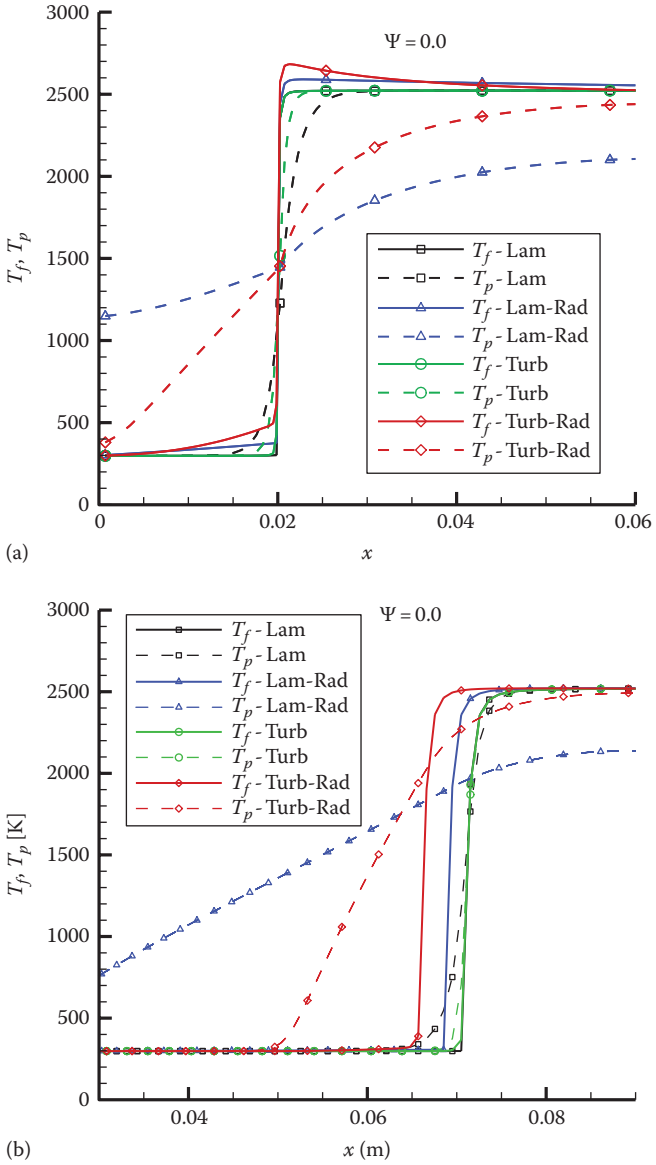

FIGURE 13.5 Comparison of different model solutions: (a) U_{in} = 0.1 m/s and (b) U_{in} = 1.0 m/s.

Figure 13.6b repeats the same simulation of Figure 13.6a, using a higher air-to-fuel ratio, Ψ = 0.8. Combustion of a lean mixture reveals that the flame front is more sensitive to the incoming mass flow rate and that the flame front is pushed toward the exit, leading eventually to the opening of the combustion front for higher velocities. As such, unburned gas leaves the chamber for higher mass flow rates.

Finally, Figure 13.6c presents the effect of air-to-fuel ratio while keeping the total mass flow rate constant through the combustor. As the mixture becomes leaner, the flame front is pushed toward the right, and the effect seen earlier, the opening of the combustion front, is observed. Consequently, unburned fuel leaves the chamber. This effect is more pronounced as Ψ increases, a result that is coherent when comparing Figure 13.6a and b.

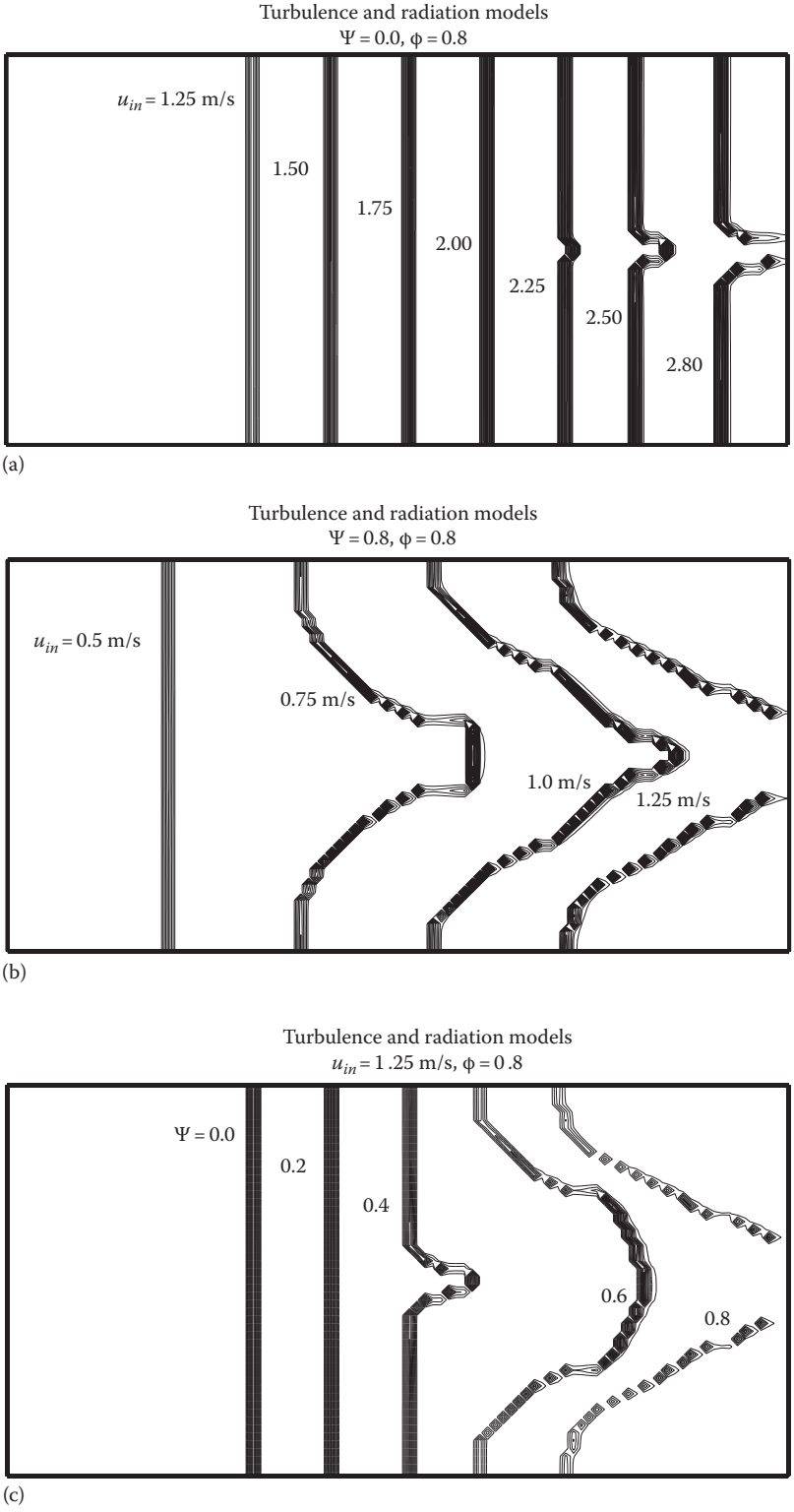

FIGURE 13.6 Flame front location for turbulence and radiation models, ϕ = 0.8: (a) effect of inlet velocity, Ψ = 0.0; (b) effect of inlet velocity, Ψ = 0.8; and (c) effect of excess air Ψ, U_{in} = 1.25 m/s.

13.8 SUMMARY

This chapter presented 1D and 2D simulations for a mixture of air and methane burning in a porous material. Both LTE and LTNE models were applied. Four different thermomechanical models were compared along with a unique simple closure for combustion. The results indicate that a substantially different temperature distribution pattern is obtained depending on the model used. For high excess air or gas velocity, the flame front moves toward the exit of the burner. Results herein motivate further research work on the subject of reactive turbulent flow in porous burners and should be seen as a preliminary step toward reliable simulation of real porous combustors.

REFERENCES

Abdul Mujeebu, M., Abdullah, M.Z., Abu Bakar, M.Z., Mohamad, A.A., and Abdullaha, M.K. 2009. A review of investigations on liquid fuel combustion in porous inert media, *Prog. Energy Combust*., 35(2009): 216–230.

Assato, M., Pedras, M.H.J., and de Lemos, M.J.S. 2005. Numerical solution of turbulent channel flow past a backward-facing step with a porous insert using linear and nonlinear k-models, *J. Porous Media*, 8(1): 13–29.

Babkin, V.S. February 1993. Filtration combustion of gases: Present state of affairs and prospects, *Pure Appl. Chem*., 65(2): 335–344.

Bouma, P.H. and De Goey, L.P.H. October 1999. Premixed combustion on ceramic foam burners, combust, *Flame*, 119(1–2): 133–143.

Braga, E.J. and de Lemos, M.J.S. 2004. Turbulent natural convection in a porous square cavity computed with a macroscopic *k*-ε model, *Int. J. Heat Mass Transfer*, 47(26): 5639–5650.

Coutinho, J.E.A. and de Lemos, M.J.S. 2012. Laminar flow with combustion in inert porous media, *Int. Commun. Heat Mass Transfer*, 39: 896–903.

de Lemos, M.J.S., 2005a. Turbulent kinetic energy distribution across the interface between a porous medium and a clear region, *Int. Commun. Heat Mass Transfer*, 32(1–2): 107–115.

de Lemos, M.J.S. 2005b. Fundamentals of the double—Decomposition concept for turbulent transport in permeable media, *Materialwissenschaft und Werkstofftechnik*, 36(10): 586.

de Lemos, M.J.S. 2009. Numerical simulation of turbulent combustion in porous materials, *Int. Commun. Heat Mass Transfer*, 36: 996–1001.

de Lemos, M.J.S. 2010. Analysis of turbulent combustion in inert porous media, *Int. Commun. Heat Mass Transfer*, 37(4): 331–336.

de Neef, M., Knabner, P., and Summ, G. 2008. Numerical bifurcation analysis of premixed combustion in porous inert media, *High Performance Scientific and Engineering Computing*, Lecture Notes in Computational Science and Engineering, Vol. 8, 1999, Springer-Verlag, Berlin, pp. 39–50.

Gray, W.G. and Lee, P.C.Y. 1977. On the theorems for local volume averaging of multiphase system, *Int. J. Multiphase Flow*, 3: 333–340.

Henneke, M.R. and Ellzey, J.L. 1999. Modeling of filtration combustion in a packed bed, *Combust. Flame*, 117(4): 832–840.

Howell, J.R., Hall, M.J., and Ellzey, J.L. 1996. Combustion of hydrocarbon fuels within porous inert media, *Prog. Energy Combust*., 22(2): 121–145.

Hsu, P.F., Howell, J.R., and Matthews, R.D. 1993. A numerical investigation of premixed combustion within porous inert media, *J. Heat Transfer*, 115: 744–750.

Ingham, D.B. and Pop, I. (Eds.). 2005. *Transport Phenomena in Porous Media*, Vol. III. Elsevier: Oxford, U.K.

Jones, W.P. and Launder, B.E. 1972. The prediction of laminarization with two-equation model of turbulence, *Int. J. Heat Mass Transfer*, 15: 301–314.

Kuo, K.K. 1986. *Principles of Combustion*. John Wiley & Sons: New York.

Kuwahara, F., Shirota, M., and Nakayama, A., 2001. A numerical study of interfacial convective heat transfer coefficient in two-energy equation model for convection in porous media, *Int. J. Heat Mass Transfer*, 44: 1153–1159.

Kuznetsov, A.V. 2004. Numerical modeling of turbulent flow in a composite porous/fluid duct utilizing a two layer k-epsilon model to account for interface roughness, *Int. J. Therm. Sci*., 43: 1047–1056.

Kuznetsov, A.V., Cheng, L., and Xiong, M. 2002. Effects of thermal dispersion and turbulence in forced convection in a composite parallel-plate channel: Investigation of constant wall heat flux and constant wall temperature cases, *Num. Heat Transfer Part A Appl.*, 42: 365–383.

Lammers F.A. and De Goey, L.P.H. 2003. A numerical study of flash back of laminar premixed flames in ceramic-foam surface burners, *Combust. Flame*, 133(1–2): 47–61.

Leonardi, S.A., Viskanta, R., and Gore, J.P. February 2003. Analytical and experimental study of combustion and heat transfer in submerged flame metal fiber burners/heaters, *J. Heat Transfer*, 125(1): 118–125.

Lim, I.G. and Matthews, R.D. 1998. Development of a model for turbulent combustion within porous inert media, *International Journal of Fluid Mechanics Research*, 25: N1–3.

Malico, I. and Pereira, J.C.F. 1999. Numerical predictions of porous burners with integrated heat exchanger for household applications, *J. Porous Media*, 2(2): 1532–1562.

Mohamad, A.A., Ramadhyani, S., and Viskanta, R. 1994b. Modeling of combustion and heat-transfer in a packed-bed with embedded coolant tubes, *Int. J. Heat Mass Transfer*, 37(8): 1181–1191.

Mohamad, A.A., Viskanta, R., and Ramadhyani, S. 1994a. Numerical prediction of combustion and heat transfer in a packed bed with embedded coolant tubes, *Combust. Sci. Technol*., 96: 387–407.

Nield, D.A. and Bejan, A. 2013. *Convection in Porous Media*, 4th edn. Springer: New York.

Oliveira, A.A.M. and Kaviany, M. 2001. Non equilibrium in the transport of heat and reactants in combustion in porous media, *Prog. Energy Combust*., 27(5): 523–545.

Patankar, S.V. 1980. *Numerical Heat Transfer and Fluid Flow*. Hemisphere: Washington, DC.

Peard, T.E., Peters, J.E., Brewster, M.Q., and Buckius, R.O. 1993. Radiative heat transfer augmentation in gas-fired radiant tube burner by porous inserts: Effect on insert geometry, *Exp. Heat Transfer*, 6: 273–286.

Pedras, M.H.J. and de Lemos, M.J.S. 2001. Simulation of turbulent flow in porous media using a spatially periodic array and a low Re two-equation closure, *Num. Heat Transfer Part A Appl.*, 39: 35–59.

Pedras, M.H.J. and de Lemos, M.J.S. 2003. Computation of turbulent flow in porous media using a low Reynolds k-model and an infinite array of transversally-displaced elliptic rods, *Num. Heat Transfer Part A Appl.*, 43(6): 585–602.

Pereira, F.M. 2002. Medição de Características Térmicas e Estudo do Mecanismo de Estabilização de chama em Queimadores Porosos Radiantes, Master's thesis, Universidade Federal de Santa Catarina (*in Portuguese*), Florianópolis, Brazil.

Pop, I. and Ingham, D.B. 2001. *Convective Heat Transfer: Mathematical and Computational Modeling of Viscous Fluids and Porous Media*. Pergamon: Oxford, U.K.

Sahraoui, M. and Kaviany, M. 1995. Direct simulation vs time-averaged treatment of adiabatic, premixed flame in a porous medium, *Int. J. Heat Mass Transfer*, 18: 2817–2834.

Saito, M. and de Lemos, M.J.S. 2005. Interfacial heat transfer coefficient for non-equilibrium convective transport in porous media, *Int. Commun. Heat Mass*, 32(5): 667–677.

Saito, M. and de Lemos, M.J.S. 2006. A correlation for interfacial heat transfer coefficient for turbulent flow over an array of square rods, *J. Heat Transfer*, 128(5): 444–452.

Santos, N.B. and de Lemos, M.J.S. 2006. Flow and heat transfer in a parallel plate channel with porous and solid baffles, *Num. Heat Transfer Part A*, 49(5): 471–494.

Slattery, J.C. 1967. Flow of viscoelastic fluids through porous media, *AICHE J*., 13: 1066–1071.

Trimis, D. and Durst, F. 1996. Combustion in a porous medium—Advances and applications, *Combust. Sci. Technol*., 121: 153–168.

Turns, S.R. 1996. *An Introduction to Combustion: Concepts and Applications*. McGraw-Hill: New York.

Vadasz, P. 2008. *Emerging Topics in Heat and Mass Transfer in Porous Media*. Springer: New York.

Vafai, K. (Ed.). 2005. *Handbook of Porous Media*, 2nd edn. CRC Press: Boca Raton, FL.

Vafai, K. 2010. *Porous Media: Applications in Biological Systems and Biotechnology*. CRC Press: Boca Raton, FL.

Whitaker, S. 1969. Advances in theory of fluid motion in porous media, *Ind. Eng. Chem*., 61: 14–28.

Wood, S. and Harries, A.T. 2008. Porous burners for lean-burn applications, *Prog. Energy Combust*., 34: 667–684.

Section IV

Heat Transfer of Nanofluids in Porous Media

14 Effects of Nanofluids on Convection in Porous Media

D.A. Nield and A.V. Kuznetsov

CONTENTS

14.1 Introduction 493
14.2 Property Variations of Suspensions 494
14.3 Processes Associated with the Smallness of Nanoparticles 495
14.3.1 Buongiorno Model 495
14.3.2 Conservation Equations for a Nanofluid 495
14.3.3 Conservation Equations for a Porous Medium Saturated by a Nanofluid 497
14.4 Forced Convection 499
14.5 Natural Convection 500
14.5.1 Internal Natural Convection 500
14.5.2 External Natural Convection 501
14.6 Mixed Convection 503
14.7 Conclusions 504
References 504

14.1 INTRODUCTION

The term *nanofluid* (as it is commonly used today) was first suggested by Choi (1995) in his paper presented at the *ASME Winter Annual Meeting*. It refers to a liquid containing a dispersion of submicronic solid particles (nanoparticles) whose characteristic dimension is of the order of tens or hundreds of nanometers. The fluid can be water or an organic solvent. The particles are commonly metallic oxides. One obvious effect is that due to the fact that the nanoparticles usually have high thermal conductivity relative to that of the base fluid, although that effect is somewhat offset by the increased viscosity due to the presence of the particles. The first Science Citation Index journal article on nanofluids (Lee et al., 1999) was published by Choi's group in 1999. One of the most interesting features of nanofluids is the enhancement of thermal diffusivity that according to some data may exceed the limits predicted by conventional macroscopic theories of suspensions (Choi, 2009; Choi et al., 2001, 2004; Das et al., 2008; Eastman et al., 2001). The enhancement of effective thermal conductivity was confirmed by experiments conducted by many researchers, including Masuda et al. (1993), although the level of enhancement is still a subject of a debate (Rea et al., 2009). The unique properties of nanofluids suggest the possibility of using nanofluids in a variety of engineering systems, from advanced nuclear systems (Buongiorno and Hu, 2005; Buongiorno et al., 2008; Kim et al., 2009) to drug delivery (Kleinstreuer et al., 2008). It has been shown (Alizad et al., 2012; Shafahi et al., 2010a,b) that a nanofluid can substantially improve the performance of a heat pipe.

Nanofluids can flow through permeable media, and thus they can aid oil recovery. Reviews of studies on nanofluids include those by Chandrasekhar and Suresh (2009), Chandrasekhar et al. (2012), Dalkilic et al. (2012), Das et al. (2006), Daungthongsuk and Wongwises (2007), Haddad et al. (2012), Kakac and Pramuanjaroenkij (2009), Kleinstreuer and Feng (2011), Michaelides (2013), Ozerinc et al. (2010), Sarkar (2011), Sparreboom et al. (2010), and Terekhov (2010a,b). Of these studies, the review of natural convective heat transfer by Haddad et al. (2012) is pertinent here.

In this chapter, we first discuss property variations that are the consequence of the fact that nanofluids are suspensions and then processes that occur due to the smallness of the nanoparticles. (We mention that other explanations have been proposed for the increase of thermal conductivity that has been observed in nanofluids. For example, Vadász [2006, 2008] has proposed that thermal lagging between the particles and the fluid could cause such an effect.)

We then discuss applications to forced convection, natural convection, and mixed convection in various geometries.

14.2 PROPERTY VARIATIONS OF SUSPENSIONS

A common approach is to examine the effect of the variation of thermal conductivity and viscosity with nanofluid particle fraction, utilizing expressions obtained using the theory of mixtures, namely,

$$\frac{\mu_{eff}}{\mu_f} = \frac{1}{\left(1-\phi\right)^{2.5}}, \tag{14.1}$$

$$\frac{k_{eff}}{k_f} = \frac{(k_p + 2k_f) - \phi(k_f - k_p)}{(k_p + 2k_f) + \phi(k_f - k_p)}. \tag{14.2a}$$

where

f denotes the nanoparticle fraction

μ and k denote the viscosity and thermal conductivity, respectively

the suffixes f, p, and eff denote the fluid, the particles, and an effective quantity, respectively

Equation 14.1 was obtained by Brinkman (1952) using ideas due to Einstein, and Equation 14.2a is the Maxwell–Garnett formula for a suspension of spherical particles that dates back to Maxwell (1881), who considered an electrical conductivity analogue to thermal conductivity. An alternative formula for k_{eff}, one based on effective medium theory, was obtained by Bruggeman (1935). This is obtained by solving for k_{eff} the balance equation:

$$\phi\frac{\left(k_p - k_{eff}\right)}{\left(k_p + k_{eff}\right)} + (1-\phi)\frac{\left(k_f - k_{eff}\right)}{\left(k_f + k_{eff}\right)} = 0. \tag{14.2b}$$

Equation 14.2b applies for particles of general shape, and it can be readily generalized to the case of more than one type of particles. It yields slightly smaller values of k_{eff} than those given by Equation 14.2a.

For a convection problem, the specific heat c is important, and it is common practice to employ the weighted volumetric average value:

$$c_{eff} = (1-\phi)c_f + \phi c_p. \tag{14.3a}$$

Alternatively, one can consider a weighted volumetric average of the heat capacity:

$$(\rho c)_{eff} = (1-\phi)(\rho c)_f + \phi(\rho c)_p. \tag{14.3b}$$

More precise models have been proposed, but in any case, variation of specific heat or heat capacity is normally insignificant in comparison with variation of viscosity and thermal conductivity. For these, Khanafer and Vafai (2011) presented a synthesis of results, and further discussion was presented in Nield and Kuznetsov (2013a).

14.3 PROCESSES ASSOCIATED WITH THE SMALLNESS OF NANOPARTICLES

14.3.1 Buongiorno Model

An important study of convective transport in nanofluids was made by Buongiorno (2006). He focused on the heat transfer enhancement observed in convective situations. Buongiorno concluded that turbulence is not affected by the presence of the nanoparticles, so this cannot explain the observed enhancement. Particle rotation has also been proposed as a cause of heat transfer enhancement, but Buongiorno calculated that this effect is too small to explain the observed results. With dispersion, turbulence and particle rotation ruled out as significant agencies for heat transfer enhancement, Buongiorno proposed a new model based on the mechanics of the nanoparticle/base-fluid relative velocity. This we now describe.

Buongiorno (2006) noted that the nanoparticle absolute velocity can be viewed as the sum of the base-fluid velocity and a relative velocity (that he called the slip velocity). He considered in turn seven slip mechanisms: inertia, Brownian diffusion, thermophoresis, diffusiophoresis, Magnus effect, fluid drainage, and gravity settling. He concluded that in the absence of turbulent effects, it is the Brownian diffusion and the thermophoresis that will be important. Buongiorno proceeded to write down conservation equations based on these two effects.

14.3.2 Conservation Equations for a Nanofluid

First, we outline the derivation of conservation equations applicable to a nanofluid in the absence of a solid matrix. Later, we modify these equations to the case of a porous medium saturated by the nanofluid.

The Buongiorno model treats the nanofluid as a two-component mixture (base fluid plus nanoparticles) with the following assumptions:

1. Incompressible flow
2. No chemical reactions
3. Negligible external forces
4. Dilute mixture
5. Negligible viscous dissipation
6. Negligible radiative heat transfer
7. Nanoparticles and base fluid locally in thermal equilibrium

The continuity equation for the nanofluid is

$$\nabla \cdot \mathbf{v} = 0 \tag{14.4}$$

where $\mathbf{v}$ is the nanofluid velocity.

The conservation equation for the nanoparticles in the absence of chemical reactions is

$$\frac{\partial \phi}{\partial t} + \mathbf{v} \cdot \nabla \phi = -\frac{1}{\rho_p} \nabla \cdot \mathbf{j}_p, \tag{14.5}$$

where

ϕ is nanoparticle volume fraction
ρ_p is the nanoparticle mass density
$\mathbf{j}_p$ is the diffusion mass flux for the nanoparticles, given as the sum of two diffusion terms (Brownian diffusion and thermophoresis) by

$$\mathbf{j}_p = \mathbf{j}_{p,B} + \mathbf{j}_{p,T} = -\rho_p D_B \nabla \phi - \rho_p D_T \frac{\nabla T}{T}. \tag{14.6}$$

(Thermophoresis is the *particle* equivalent of the Soret effect in gaseous or liquid mixtures.)

Here, D_B is the Brownian diffusion coefficient given by the Einstein–Stokes equation

$$D_B = \frac{k_B T}{3\pi \mu d_p}, \tag{14.7}$$

where

k_B is the Boltzmann's constant
μ is the viscosity of the fluid
d_p is the nanoparticle diameter

Use has been made of the expression

$$\mathbf{V}_T = -\tilde{\beta} \frac{\mu}{\rho} \frac{\nabla T}{T} \tag{14.8}$$

for the thermophoretic velocity $\mathbf{V}_T$. Here, ρ is the fluid density, and the proportionality factor $\tilde{\beta}$ is given by

$$\tilde{\beta} = 0.26 \frac{k}{2k + k_p}, \tag{14.9}$$

where k and k_p are the thermal conductivities of the fluid and the particle material. Hence, the thermophoretic diffusion flux is given by

$$\mathbf{j}_{p,T} = \rho_p \phi \mathbf{V}_T = -\rho_p D_T \frac{\nabla T}{T}, \tag{14.10}$$

where the thermophoretic diffusion coefficient is given by

$$D_T = \tilde{\beta} \frac{\mu}{\rho} \phi. \tag{14.11}$$

Equations 14.5 and 14.6 then produce the conservation equation in the form

$$\frac{\partial \phi}{\partial t} + \mathbf{v} \cdot \nabla \phi = \nabla \cdot \left[D_B \nabla \phi + D_T \frac{\nabla T}{T} \right]. \tag{14.12}$$

The momentum equation for a nanofluid takes the same form as for a pure fluid, but it should be remembered that μ is a strong function of ϕ. If one introduces a buoyancy force and adopts the Boussinesq approximation, then the momentum equation can be written as

$$\rho\left(\frac{\partial \mathbf{v}}{\partial t} + \mathbf{v}\cdot\nabla\mathbf{v}\right) = -\nabla p + \mu\nabla^2\mathbf{v} + \rho\mathbf{g}, \tag{14.13}$$

where

$$\rho = \phi\rho_p + (1-\phi)\rho_f. \tag{14.14}$$

The nanofluid density ρ can be approximated by the base-fluid density ρ_f when ϕ is small. Then, when the Boussinesq approximation is adopted, the buoyancy term is approximated by

$$\rho\mathbf{g} \cong \left[\phi\rho_p + (1-\phi)\left\{\rho(1-\beta(T-T_0))\right\}\right]\mathbf{g}. \tag{14.15}$$

The thermal energy equation for a nanofluid can be written as

$$\rho c\left[\frac{\partial T}{\partial t} + \mathbf{v}\cdot\nabla T\right] = -\nabla\cdot\mathbf{q} + h_p\nabla\cdot\mathbf{j}_p, \tag{14.16}$$

where

c is the nanofluid specific heat
T is the nanofluid temperature
h_p is the specific enthalpy of the nanoparticle material
$\mathbf{q}$ is the energy flux, relative to a frame moving with the nanofluid velocity $\mathbf{v}$, given by

$$\mathbf{q} = -k\nabla T + h_p\mathbf{j}_p, \tag{14.17}$$

where k is the nanofluid thermal conductivity. Substituting Equation 14.17 in Equation 14.16 yields

$$\rho c\left[\frac{\partial T}{\partial t} + \mathbf{v}\cdot\nabla T\right] = \nabla\cdot(k\nabla T) - c_p\mathbf{j}_p\cdot\nabla T. \tag{14.18}$$

In deriving this equation, use has been made of a vector identity and the fact that $\nabla h_p = c_p\nabla T$, where c_p is the nanoparticle specific heat of the material constituting the nanoparticles, while c is the specific heat (at constant pressure) of the fluid. Then, substitution of Equation 14.6 in Equation 14.18 gives the final form

$$\rho c\left[\frac{\partial T}{\partial t} + \mathbf{v}\cdot\nabla T\right] = \nabla\cdot(k\nabla T) + \rho_p c_p\left[D_B\nabla\phi\cdot\nabla T + D_T\frac{\nabla T\cdot\nabla T}{T}\right]. \tag{14.19}$$

Equations 14.12 and 14.19 constitute a coupled pair of equations for T and ϕ. One observes that the nanofluid terms are similar to the Soret and Dufour cross-diffusion terms that arise in the case of double diffusion in a binary fluid.

14.3.3 Conservation Equations for a Porous Medium Saturated by a Nanofluid

We consider a porous medium whose porosity is denoted by ε and permeability by K. A subscript s will now be used to denote properties of the solid matrix. The Darcy velocity is denoted by $\mathbf{v}_D$.

This is related to $\mathbf{v}$ by $\mathbf{v}_D = \varepsilon\mathbf{v}$. We now have to deal with the following four field equations (corresponding to Equations 14.4, 14.12, 14.13, 14.19, for total mass, momentum, thermal energy, and nanoparticles, respectively)

$$\nabla \cdot \mathbf{v}_D = 0, \tag{14.20}$$

$$\rho\left(\frac{1}{\varepsilon}\frac{\partial \mathbf{v}_D}{\partial t} + \frac{1}{\varepsilon^2}\mathbf{v}_D \cdot \nabla \mathbf{v}_D\right) = -\nabla p + \tilde{\mu}\nabla^2 \mathbf{v}_D - \frac{\mu}{K}\mathbf{v}_D + \left[\phi\rho_p + (1-\phi)\left\{\rho(1-\beta(T-\boldsymbol{T}_0))\right\}\right]\mathbf{g}, \tag{14.21}$$

$$(\rho c)_m \frac{\partial T}{\partial t} + (\rho c)_f \mathbf{v}_D \cdot \nabla T = \nabla \cdot (k_m \nabla T) + \varepsilon(\rho c)_p \left[D_B \nabla\phi \cdot \nabla T + D_T \frac{\nabla T \cdot \nabla T}{T}\right], \tag{14.22}$$

$$\frac{\partial \phi}{\partial t} + \frac{1}{\varepsilon}\mathbf{v}_D \cdot \nabla\phi = \nabla \cdot \left[D_B \nabla\phi + D_T \frac{\nabla T}{T}\right]. \tag{14.23}$$

Here, we have introduced the effective viscosity $\tilde{\mu}$, the effective heat capacity $(\rho c)_m$, and the effective thermal conductivity k_m of the porous medium. We regard the effective viscosity as a semiempirical quantity. The matter is discussed in Section 1.5.3 of Nield and Bejan (2013).

We now draw attention to a subtlety that previously has been overlooked. Equations 14.12 and 14.19 are in the form of that was presented by Buongiorno (2006). As they stand, they are adequate for application to natural convection problems. However, in the case of forced convection and mixed convection problems, an additional contribution to the particle flux (a convective term) must be taken into account. Equation 14.12 needs no change, because a convective term is already properly included in that equation. However, in Equation 14.19, only the convection of heat is already incorporated, and an additional thermophoresis term needs to be inserted. An externally applied pressure gradient leads to a throughflow of the base fluid, and it is the particle flux that results from this that is involved. We propose that Equation 14.19 should then be modified to read

$$\rho c\left[\frac{\partial T}{\partial t} + \mathbf{v} \cdot \nabla T\right] = \nabla \cdot (k \nabla T) + \rho_p c_p \left[D_B \nabla\phi \cdot \nabla T + D_T \frac{\nabla T \cdot \nabla T}{T} - \phi_0 \mathbf{v}_0 \cdot \nabla T\right], \tag{14.24}$$

where

ϕ_0 is the mean particle fraction

$\mathbf{v}_0$ is the mean velocity

It is being assumed here that the nanofluid is dilute and so ϕ_0 is small compared with unity. If the velocity is small, then the new term (the last term in the square brackets) is small in comparison with the other terms within the square brackets on the right-hand side of Equation 14.24. The effect of the new term is to reduce the change in temperature in the direction of the velocity.

In deriving Equations 14.20 through 14.23, we have assumed that the Brownian motion and thermophoresis processes remain coherent, while volume averages over a representative elementary volume are taken. This assumption can be questioned. In the context of modeling transport in porous media, Equations 14.17 and 14.18 are standard. Equation 14.20 involves just intrinsic quantities in the sense that the average is being taken over the nanofluid only, and the solid matrix is not involved. The question thus reduces to whether the terms within the square brackets on the right-hand side of Equation 14.19 need modification. We recall that in nanofluids the particles are so small that for practical purposes they remain in suspension in a uniform manner. We emphasize our assumption

that the nanoparticles are suspended in a nanofluid using either surfactant or surface charge technology, something that prevents particles from agglomeration and deposition on the porous matrix. We suggest that then it is reasonable to assume as a first approximation that no modification to Equation 14.19 is necessary.

Further, we are assuming that we have a regular porous medium, one for which the pore length scale is large compared with the length scale of the nanoparticles. In these circumstances, we do not expect that the solid matrix will to a significant extent act as a filter for the nanoparticles.

We also note in a comprehensive treatment it is desirable that variations in the dynamic viscosity (due to the significant dependence on the temperature and the local concentration) should be taken into account. This means that the viscosity that appears in Equations 14.13 and 14.21 should be regarded as a variable quantity in future studies.

In this chapter, we have simplified matters by neglecting several things such as (1) chemical interaction between the porous matrix and the nanofluid and the particles, (2) mass transfer between the porous matrix and the nanofluid, and (3) radiation effects between the porous matrix and the nanoparticles.

14.4 FORCED CONVECTION

Nanofluid-cooled microchannel heat sinks were studied by Ghazvini and Shokoumand (2009) and Ghazvini et al. (2009) using fin and porous media approaches, but we are aware of just half a dozen papers on forced convection in a porous medium with a nanofluid. Thermally developing forced convection of a nanofluid in a parallel-plate channel was studied numerically by Maghrebi et al. (2012), who employed the Buongiorno model with thermophoresis and Brownian motion. They found that the local Nusselt number is decreased when the Lewis number Le is increased and when the Schmidt number Sc is increased, these parameters being defined by

$$\mathrm{Le} = \frac{\alpha_m}{\phi_0 D_B}, \quad \mathrm{Sc} = \frac{\mu}{\rho D_B}, \tag{14.25}$$

where

α_m is the effective thermal diffusivity
D_B is the Brownian diffusion coefficient
ϕ_0 is the particle fraction at the channel inlet
μ is the nanofluid viscosity
ρ is the nanofluid density

Armaghani et al. (2014b) extended this study to include the effect of local thermal nonequilibrium (LTNE). Further numerical work with LTNE, first taking into account of particle migration and then using a model in which the heat flux in each of the phases is considered, was carried out by Armaghani et al. (2014a,b).

On the other hand, in his analytical study of flow in microchannels, Hung (2010) considered just the variation of thermal conductivity, viscosity, and heat capacity. A more general analytical study using the Buongiorno model was made by Nield and Kuznetsov (2014b). They examined flow in a Darcy porous medium occupying a parallel-plate channel with uniform heat flux on the boundaries. They found that the combined effect of Brownian motion and thermophoresis is to reduce the Nusselt number. The reduction increases as $N_A N_B/\varepsilon$ increases, where N_A and N_B are defined by

$$N_A = \frac{D_T}{D_B T^*_w}, \quad N_B = \frac{\varepsilon(\rho c)_p \phi^*_0}{(\rho c)_f}, \tag{14.26}$$

and so

$$\frac{N_A N_B}{\varepsilon} = \frac{D_T}{D_B}\frac{(\rho c)_p \phi^*_0}{(\rho c)_f T^*_w}, \tag{14.27}$$

that is the product of a diffusivity ratio and a heat capacity ratio. Nield and Kuznetsov (2014b) noted that this reduction in heat transfer due to a modification of the temperature profile by Brownian motion and thermophoresis would oppose any increase due to the thermal conductivity of the nanofluid being higher than that of a regular fluid. This result applies only to the case where the Péclet number based on the thermophoresis diffusivity is small compared with unity. It was pointed out by Nield and Kuznetsov (2014c) that net throughflow produces an extra contribution to the nanoparticle flux and hence an additional term into the thermal energy equation.

Matin and Pop (2013) studied heat and mass transfer with a chemical reaction on the walls. Nasrin et al. (2102), Nasrin and Alim (2013), and Nasrin et al. (2013a,b) have considered a problem with an open cavity. The effect of a magnetic field has been studied by Servati et al. (2014). Forced convection of a non-Newtonian fluid in an annulus was examined by Ellahi et al. (2013).

In contrast, natural convection has been extensively studied.

14.5 NATURAL CONVECTION

14.5.1 Internal Natural Convection

The paradigmatic problem for natural convection is the Rayleigh–Bénard problem, the onset of instability in a horizontal layer of fluid uniformly heated from below. In the case of a porous medium, this is commonly called the Horton–Rogers–Lapwood problem. This problem was treated using a Darcy model by Nield and Kuznetsov (2009b). They considered a problem analogous to the double-diffusion problem studied by Nield (1968), and accordingly, they treated the case of impermeable boundaries held at constant temperatures and constant particle fraction. They recognized that it would be more realistic physically to impose zero particle flux on the boundaries (setting to zero the normal component of the vector $\mathbf{j}_p$ that appears on the left-hand side of Equation 14.6), but in order to make analytical progress, they found it necessary to freeze the basic profile of the particle fraction.

The analysis of Nield and Kuznetsov (2009b) has been extended in several ways. Kuznetsov and Nield (2010a, 2011) included the effect of LTNE. Kuznetsov and Nield (2010b) employed the Brinkman model. Kuznetsov and Nield (2010c) studied double diffusion. Nield and Kuznetsov (2011b) examined the effect of vertical throughflow. Sheu (2011) treated the case of a viscoelastic fluid. Bhadauria and Agarwal (2011a,b) and Bhadauria et al. (2011) presented results for nonlinear instability, first with rotation and then with nonequilibrium. Agarwal et al. (2011) included the effect of rotation and anisotropy. Agarwal and Bhadauria (2011) introduced both rotation and thermal nonequilibrium. Agarwal et al. (2012) considered nonlinear transport. In these papers, the significant effects were those of Brownian motion and thermophoresis. An alternative model, incorporating the effects of conductivity and viscosity variation and with cross-diffusion also included, was examined by Nield and Kuznetsov (2012). The effect of rotation was also studied by Chand and Rana (2012c). The problem of bioconvection in nanofluids was introduced by Kuznetsov's group; bioconvection in nanofluids with either gyrotactic or oxytactic microorganisms or both was investigated by Kuznetsov (2012a,b) and Kuznetsov and Bubnovich (2012) and also by Shaw et al. (2014). Boundary and internal source effects were treated by Yadav et al. (2012). The problem of double diffusion combined with variation of thermal conductivity and viscosity was examined by Yadav et al. (2013). The singular case of a non-Newtonian power-law fluid was discussed by Nield (2011a,b). The case of a magnetic nanofluid was studied by Shivakumara et al. (2010). The effect of thermal modulation was added by Umavathi (2013). The aforementioned studies involved bottom heating.

The case of uniform volumetric heating was investigated by Nield and Kuznetsov (2013b). In this paper, zero particle-flux boundary conditions were employed. Double diffusion and cross-diffusion have also been studied by Umavathi and Mohite (2014a,b). The case of a non-Newtonian fluid with rotation was considered by Yadav et al. (2014).

The Horton–Rogers–Lapwood problem has been revisited by Nield and Kuznetsov (2014a). This time, they treated the case of zero particle-flux boundary conditions. They showed that in this case oscillatory instability was ruled out. They obtained an approximate expression for the nonoscillatory instability boundary in the form

$$\mathrm{Ra} = 40 - \left(N_A + \frac{\mathrm{Le}}{\varepsilon} \right) \mathrm{Rn}, \tag{14.28}$$

this boundary being attained with a dimensionless wave number $\alpha = 3.16$. Here, ε is the porosity, Ra is the usual Rayleigh–Darcy number, Rn is a nanofluid Rayleigh number, Le is a Lewis number, and N_A is a modified diffusivity ratio now defined by

$$\mathrm{Ra} = \frac{\rho g \beta K H (T_h^* - T_c^*)}{\mu \alpha_m}, \tag{14.29}$$

$$\mathrm{Rn} = \frac{(\rho_p - \rho)\phi_0^* \, gKH}{\mu \alpha_m}, \tag{14.30}$$

$$\mathrm{Le} = \frac{\alpha_m}{D_B}, \tag{14.31}$$

$$N_A = \frac{D_T (T_h^* - T_c^*)}{D_B T_c^* \, \phi_0^*}, \tag{14.32}$$

where

T_h^* and T_c^* are the temperatures at the bottom and top boundaries, respectively

ϕ_0^* is a reference nanoparticle volume fraction

Oscillatory convection was investigated by Chand and Rana (2012a), while the case of a viscoelastic fluid was studied by Chand and Rana (2012b). Magnetic nanofluids were treated by Mahajan and Sharma (2014).

The case of a vertical channel partly filled with a porous medium was studied by Hajipour and Dehkordi (2012). A triangular cavity with a flush-mounted heater on a wall was treated numerically by Sun and Pop (2011, 2014) and Ahmed et al. (2013). A similar study, with a square cavity heated along a segment of the bottom wall, was made by Bourantas et al. (2014). Conjugate problems, with a cavity heated by a plane or triangular thick wall, were investigated by Chamkha and Ishmael (2013, 2014). Double-diffusive convection with thermodiffusion in a square cavity subject to various heating conditions was studied numerically by Ahadi et al. (2013). Convection in an H-shaped enclosure with mounted heaters on the vertical walls was examined by Mansour et al. (2014).

14.5.2 External Natural Convection

The Cheng–Minkowycz problem of boundary layer flow over a vertical plate at constant temperature was studied by Nield and Kuznetsov (2009a, 2011a) and (with a revised model, employing zero

TABLE 14.1
Summary of Linear Regression Coefficients and Error Bound for the Reduced Nusselt Number, Applicable to Equation 14.33

Le/ε	C_r	C_b	C_t	ε
5	−0.003	0.004	−0.090	0.030
10	−0.001	0.000	−0.105	0.009
20	−0.001	−0.001	−0.120	0.003
50	−0.002	−0.002	−0.135	0.004
100	−0.002	−0.003	−0.143	0.005
200	−0.003	−0.003	−0.150	0.006
500	−0.003	−0.003	−0.155	0.006
1000	−0.003	−0.003	−0.158	0.007

Note: Here, ε is the maximum relative error defined by $\varepsilon = |(\mathrm{Nu}_{est} - \mathrm{Nu})/\mathrm{Nu}|$, applicable for Nr, Nb, and Nt each in [0, 0.5].

particle-flux boundary conditions) by Kuznetsov and Nield (2013), who obtained a linear regression correlation formula for a Nusselt number of the form

$$\frac{\mathrm{Nu}_{est}}{\mathrm{Ra}_x^{1/2}} = 0.444 + C_r\mathrm{Nr} + C_b\mathrm{Nb} + C_t\mathrm{Nt}, \tag{14.33}$$

where the coefficients are functions of Le/ε, shown in Table 14.1. Here, Le is the Lewis number defined by Equation 14.31, and the local Rayleigh number Ra_x and the parameters Nr, Nb, and Nt are defined by

$$\mathrm{Ra}_x = \frac{(1-\phi_\infty)\rho_{f\infty}\beta g K x}{\mu\alpha_m}, \tag{14.34}$$

$$\mathrm{Nr} = \frac{(\rho_p - \rho_{f\infty})\phi_\infty}{\rho_{f\infty}\beta(T_w - T_\infty)(1-\phi_\infty)}, \tag{14.35}$$

$$\mathrm{Nb} = \frac{\varepsilon(\rho c)_p D_B \phi_\infty}{(\rho c)_f \alpha_m}, \tag{14.36}$$

$$\mathrm{Nt} = \frac{\varepsilon(\rho c)_p D_T (T_w - T_\infty)}{(\rho c)_f \alpha_m T_\infty}. \tag{14.37}$$

It can be seen that the Brownian motion parameter Nb has very little effect on the Nusselt number and coefficient of the buoyancy ratio Nr is also small. The Nusselt number is reduced as the thermophoresis parameter Nt is increased.

The extension to a nonisothermal plate was treated by Gorla and Chamkha (2011a) and to a prescribed surface heat flux by Noghrehabadi et al. (2013a) and by Ghalambaz and Noghrehabadi (2014). Also for a vertical plate, a non-Darcy medium was studied by Tavakoli et al. (2013). Double-diffusion effects with prescribed fluxes were examined by Khan and Aziz (2011), while flow of a non-Newtonian fluid past a vertical plate was investigated by Hady et al. (2011b,c) and by Gorla

and Chamkha (2013). A nanofluid containing gyrotactic microorganisms was studied by Aziz et al. (2012). A non-Newtonian fluid containing gyrotactic microorganisms was studied by Khan et al. (2013a) and Uddin et al. (2013a,b). The case of stratification was treated by RamReddy et al. (2014) and Srinivasacharya and Surenda (2014) (double stratification). The effects of variable viscosity and thermal conductivity were studied by Noghrehabadi et al. (2014). A magnetic effect with a thermally stratified fluid under a convective boundary condition was investigated by Murthy et al. (2013a) and with thermal radiation and rotation by Satya Narayana et al. (2014). Other studies with a magnetic field were made by RamReddy et al. (2013a) and Chamkha et al. (2014). A stretching surface was treated by Ferdows et al. (2012), Khan and Pop (2012), Rosmila et al. (2012), Sheikholeslami et al. (2014), and Khidir and Sibanda (2014). Stagnation-point flow on a heated permeable stretching surface with heat generation/absorption was studied by Hamad and Pop (2011). This paper was discussed by Magyari (2011a,b) and Pop (2011). An MHD problem was studied by Yazdi et al. (2014). An investigation of a non-Newtonian fluid with internal heating was made by Uddin et al. (2013c). A wavy vertical wall was treated by Mahdy and Ahmed (2012). An unsteady flow was examined by Uddin and Harmand (2013).

The case of a heated upward-facing horizontal flat plate was considered by Khan and Pop (2011), Gorla and Chamkha (2011b,c), Uddin et al. (2012a,b), and (for triple diffusion) Khan et al. (2013b). An inclined plate was investigated by Murthy et al. (2013b) for the case of double diffusion.

Convection over a vertical cone was examined by Chamkha and Rashad (2012), Hady et al. (2011a) (with a non-Newtonian fluid), Noghrehabadi et al. (2013b), Cheng (2013) (with double diffusion), Behserest et al. (2014), Chamkha et al. (2013), and Gorla et al. (2014). The case of a vertical truncated cone was treated by Cheng (2012b) and (with a non-Newtonian fluid) by Cheng (2012c). Further work with a cone was reported by Rashad et al. (2011) and Rasekh et al. (2013) (for a non-Newtonian fluid) and by Noghrehabadi and Behseresht (2013). Convection about a sphere was studied by Chamkha et al. (2011a,b). Flow over a wedge was studied by Chamkha et al. (2011c) and Kandasamy et al. (2012, 2013, 2014). Flow over a vertical cylinder was treated by El-Kabeir et al. (2014). Flow over a horizontal cylinder of elliptical cross section was investigated by Cheng (2012a). The effect of LTNE on flow over a vertical wavy surface was examined by Ahmed and Abd El-Aziz (2013). A vertical cylinder embedded in a thermally stratified porous medium was studied by Rashad et al. (2014).

14.6 MIXED CONVECTION

Mixed convection boundary layer flow over a vertical plate was studied by Ahmad and Pop (2010), Syakila and Pop (2010), and (with thermal stratification) Yasin et al. (2013). Rashad et al. (2012) studied a non-Newtonian fluid. Beg et al. (2013) extended the work to a nanofluid containing oxytactic microorganisms. Yasin et al. (2012) studied a problem with internal heat generation. Rashad et al. (2014) included the effect of viscous dissipation.

Flow past a horizontal plate was investigated by Arifin et al. (2012). Mixed convection from a horizontal plate with Forchheimer drag, but considering only the effect of the nanoparticle volume fraction parameter, was investigated by Rosca et al. (2012). Flow over an inclined plate was studied by Rana et al. (2012), Aly and Ebaid (2013), and Rasekh and Ganji (2013). The corresponding flow over a horizontal cylinder was examined by Nazar et al. (2011) and Tham et al. (2013c). The case of a vertical cylinder was treated by Chamkha et al. (2012), Gorla and Abdel-Gaied (2012), Gorla and Khan (2012), Gorla and Hossan (2013), and Rohni et al. (2013). Double-diffusive mixed convection including the Soret effect, but also considering only the effect of the nanoparticle volume fraction parameter, was treated by RamReddy et al. (2013b). Convection over a sphere or a horizontal circular cylinder with a nanofluid containing gyrotactic microorganisms was studied by Tham and Nazar (2012) and Tham et al. (2013a,b). A horizontal cylinder with a convective boundary condition was investigated by Rashad et al. (2013). Convection past a vertical cone with radiation was treated by Chamkha et al. (2013). Mixed convection with viscous heating in a vertical channel was studied

by Memari et al. (2011). An experimental and numerical study of convection in a vertical channel partly occupied by a metallic foam was undertaken by Hajipour and Dehkordi (2014). Flow in the entrance region of a vertical channel was studied by Hajipour et al. (2014). Further work with a vertical channel was undertaken by Matin and Ghanbari (2014). An inclined channel was studied by Cimpean and Pop (2012). Convection in a lid-driven cavity was simulated numerically by Mittal et al. (2013a,b). A problem with various heat source shapes with constant flux in a rectangular horizontal channel was treated numerically by Mahdi et al. (2014).

14.7 CONCLUSIONS

In this chapter, we surveyed current theoretical studies of convection in nanofluid-saturated porous media. We separately considered applications of nanofluid theory to forced, natural and mixed convection. While there are an extensive number of publications on natural convection in nanofluid-saturated porous media and an increasing number of publications on mixed convection, very little has been done on forced convection of nanofluids in porous systems. We envision that several paradigmatic forced convection problems can be extended to the case of nanofluids. This includes forced convection in composite porous/fluid domains. This will be a useful exercise since we anticipate that in many engineering applications of nanofluids, the flow will be driven by a pump. In particular, an investigation of the interaction of nanoparticles and possible turbulence in porous media would be of interest. The importance of experimental validation of the developed nanofluid theories cannot be overemphasized.

The case of LTNE needs further study. A comprehensive treatment would need a three-temperature model, involving the temperature of the base fluid, the temperature of the nanoparticles, and the temperature of the solid matrix. However, we expect that, because of the relatively large specific area of the nanoparticles, the additional effect would generally be small. Further, it is not clear whether the permeability is affected, to some small extent, by the presence of the nanoparticles.

A reviewer has pointed out that Equation 14.9, which was proposed by Lister (1980) and later by Müller-Steinhagen (1999) for microscale particles in water and in n-hexane, is unsatisfactory and a new relation for nanoparticles and for different base fluids is highly desirable.

REFERENCES

Agarwal, S. and Bhadauria, B. S., Natural convection in a nanofluid saturated rotating porous layer with thermal non-equilibrium model. *Transp. Porous Media* **90**¸ 627–654, 2011.

Agarwal, S., Bhadauria, B. S., and Siddheshwar, P. G.,Thermal instability of a nanofluid saturating a rotating anisotropic porous medium *Spec. Top. Rev. Porous Media* **2**, 53–64, 2011.

Agarwal, S., Saceti, N. M., Chanran, P., Bhadauria, B. S., and Singh, A. K., Nonlinear convective transport in a binary nanofluid saturated porous layer. *Transp. Porous Media* **93**, 29–49, 2012.

Ahadi, A., Yousefi, T., and Saghir, M. Z., Double diffusive convection and thermodiffusion of fullerene-toluene nanofluid in a porous cavity. *Can. J. Chem. Eng*. **91**, 1918–1927, 2013.

Ahmad, S. and Pop, I., Mixed convection boundary layer flow from a vertical plate embedded in a porous medium filled with nanofluids. *Int. Commun. Heat Mass Transfer* **37**, 987–991, 2010.

Ahmed, S. E. and Abd El-Aziz, M. M., Effect of local thermal non-equilibrium on unsteady heat transfer by natural convection of a nanofluid over a vertical wavy surface. *Meccanica* **48**, 33–43, 2013.

Ahmed, S. E., Rashad, A. M., and Gorla, R. S. R., Natural convection in triangular enclosures filled with nanofluid saturated porous media. *J. Thermophys. Heat Transfer* **27**, 700–706, 2013.

Alizad, K., Vafai, K., Shafahi, M., Thermal performance and operational attributes of the startup characteristics of flat-shaped heat pipes using nanofluids. *Int. J. Heat Mass Transfer* **55**, 140–155, 2012.

Aly, E. H. and Ebaid, A. New analytical and numerical solutions for mixed convection boundary-layer nanofluid flow along an inclined plate embedded in a porous medium. *J. Appl. Math.* **2013**, 219486, 2013.

Arifin, N. M., Nazar, R., and Pop, I., Free- and mixed-convection flow past a horizontal surface in a nanofluid. *J. Thermophys. Heat Transfer* **26**, 376–382, 2012.

Armaghani, T., Chamkha, A. J, Maghrebi, M. J., and Nazari, M., Numerical analysis of a nanofluid forced convection in a porous channel: A new heat flux model in 'LTNE' condition. *J. Porous Media*, 17, 637–646, 2014b.

Armaghani, T., Maghrebi, M. J., Chamkha, A. J., and Nazari, M., Effects of particle migration on nanofluid forced convection heat transfer in a local thermal non-equilibrium porous channel. *J. Nanofluids* **3**, 51–59, 2014a.

Aziz, A., Khan, W. A., and Pop, I., Free convection boundary layer flow past a horizontal plate embedded in porous medium filled by nanofluid containing gyrotactic microorganisms. *Int. J. Therm. Sci*. **56**, 48–57, 2012.

Beg, O. A., Prasad, V. R., and Vasu, B., Numerical study of mixed bioconvection in porous media saturated with nanofluid containing oxytactic microorganisms. *J. Mech. Med. Biol*. **13**, UNSP 135067, 2013.

Behserest, A., Noghrehabadi, A., and Ghalambaz, M., Natural-convection heat and mass transfer from a vertical cone in porous media filled with nanofluids using practical ranges of nanofluids thermo-physical properties. *Chem. Eng. Res. Des*. **92**, 447–452, 2014.

Bhadauria, B. S. and Agarwal, S., Natural convection in a nanofluid saturated rotating porous layer: A nonlinear study. *Transp. Porous Media* **87**, 585–602, 2011a.

Bhadauria, B. S. and Agarwal, S., Convective transport in a nanofluid saturated porous layer with thermal non-equilibrium model. *Transp. Porous Media* **88**, 107–131, 2011b.

Bhadauria, B. S., Agarwal, S., and Kumar, A., Nonlinear two-dimensional convection in a nanofluid saturated porous medium. *Transp. Porous Media* **90**, 605–625, 2011.

Bourantas, G. C., Skouras, E. D., Lokopoulos, V. C., and Burganos, V. N., Heat transfer and natural convection of nanofluids in porous media. *Eur. J. Mech. B* **43**, 45–56, 2014.

Brinkman, H. C., The viscosity of concentrated suspensions and solutions. *J. Chem. Phys*. **20**, 571–581, 1952.

Bruggeman, D. A. G., Berechnung verschiedener physikalischer konstanten von heterogenen substanzen I. Dielektrizitätskonstahnten und leitfähigkeiten der mischkörper aus isotropen substanzen. (Calculation of different physical constants of heterogeneous substances. I. Dielectric constants and conductivities of mixtures from isotropic substances.) *Ann. Phys. Lpz*. **24**, 636–679, 1935.

Buongiorno, J., Convective heat transfer in nanofluids. *ASME J. Heat Transfer* **128**, 240–250, 2006.

Buongiorno, J., Hu, L., Kim, S. J., Hannink, R., Truong, B., and Forrest, E., Nanofluids for enhanced economics and safety of nuclear reactors: An evaluation of the potential features, issues, and research gaps. *Nucl. Technol*. **162**, 80–91, 2008.

Buongiorno, J. and Hu, W., Nanofluid coolants for advanced nuclear power plants, Paper no. 5705, *Proceedings of ICAPP'05*, Seoul, South Korea, May 15–19, 2005.

Chamkha, A. J., Abbasbandy, S., and Rashad, A. M., Radiation effects on mixed convection over a wedge embedded in a porous medium filled with a nanofluid. *Transp. Porous Media* **91**, 261–279, 2012.

Chamkha, A. J., Abbasbandy, S., Rashad, A. M., and Vajravelu, K., Radiation effects on mixed convection about a cone embedded in a porous medium filled with a nanofluid. *Meccanica* **48**, 275–285, 2013a.

Chamkha, A. J., Gorla, R. S. R., and K. Ghodeswar, K., Non-similar solution for natural convective boundary layer flow over a sphere embedded in a non-Darcy porous medium saturated with a nanofluid. *Int. J. Microscale Nanoscale Therm. Fluid Transp. Phenom*. **2**, 135–158, 2011a.

Chamkha, A. J., Gorla, R. S. R., and Ghodeswar, K., Non-similar solution for natural convective boundary layer flow over a sphere embedded in a porous medium saturated with a nanofluid. *Transp. Porous Media* **86**, 13–22, 2011b.

Chamkha, A. J. and Ismael, M. A., Natural convection in differentially heated partially porous layered cavities filled with a nanofluid. *Num. Heat Transfer A* **65**, 1089–1113, 2013.

Chamkha, A. J. and Ismael, M. A., Conjugate heat transfer in a porous cavity filled with nanofluids and heated by a triangular thick wall. *Num. Heat Transfer A* **67**, 1089–1113, 2014.

Chamkha, A. J. and Rashad, A. M., Natural convection from a vertical cone in a nanofluid saturated porous media for uniform heat and nanoparticles volume fraction fluxes. *Int. J. Numer. Meth. Heat Fluid Flow* **22**, 1073–1085, 2012.

Chamkha, A. J., Rashad, A. M., and Aly, A., Non-Darcy natural convection of a nanofluid about a permeable vertical cone embedded in a porous medium. *Int. J. Microscale Nanoscale Therm. Fluid Transp. Phenom*. **4**, 99–114, 2013.

Chamkha, A. J., Rashad, A. M., El-Hakiem, M. A. and Abdou, M. M., Non-similar solutions for mixed convective boundary layer flow of a non-Newtonian fluid over a wedge embedded in a porous medium filled with a nanofluid. *Int. J. Microscale Nanoscale Therm. Fluid Transp. Phenom*. **2**, 323–341, 2011c.

Chamkha, A. J., Rashad, A. M., RamReddy, C., and Murthy, P. V. S. N., Viscous dissipation and magnetic field effects in a non-Darcy porous medium saturated with a nanofluid under convective boundary conditions. *Spec. Topics Rev. Porous Media*. **5**, 27–39, 2014.

Chand, R. and Rana, G. C. Oscillating convection of nanofluid in porous medium. *Transp. Porous Media* **95**, 269–284, 2012a.

Chand, R. and Rana, G. C., Thermal instability of Rivlin-Ericksen elastic-viscous nanofluid saturated by a porous medium. *ASME J. Fluids Eng*. **134**, 121203, 2012b.

Chand, R. and Rana, G. C., On the onset of thermal convection in rotating nanofluid layer saturating a Darcy-Brinkman porous medium. *Int. J. Heat Mass Transfer* **55**, 5417–5424, 2012c.

Chandrasekhar, M. and Suresh, S., A review on the mechanisms of heat transport in nanofluids. *Heat Transfer Eng*. **30**, 1136–1150, 2009.

Chandrasekhar, M., Suresh, S., and Das, D. K., Mechanisms proposed through experimental investigations on thermophysical properties and forced convective heat transfer characteristics of various nanofluid—A review. *Renew. Sust. Energ. Syst*. **16**, 3917–3938, 2012.

Cheng, C. Y., Free convection boundary layer flow over a horizontal cylinder of elliptic cross section in porous media saturated by a nanofluid. *Int. Commun. Heat Mass Transfer* **39**, 931–936, 2012a.

Cheng, C. Y., Natural convection boundary layer flow over a truncated cone in a porous medium saturated by a nanofluid. *Int. Commun. Heat Mass Transfer* **39**, 231–235, 2012b.

Cheng, C. Y., Free convection of non-Newtonian nanofluids about a vertical truncated cone in a porous medium. *Int. Commun. Heat Mass Transfer* **39**, 1348–1353, 2012c.

Cheng, C. Y., Double-diffusive natural convection from a vertical cone in a porous medium saturated with a nanofluid. *J. Chin. Soc. Mech. Eng*. **34**, 401–409, 2013.

Choi, S., Enhancing thermal conductivity of fluids with nanoparticle. In: *Developments and Applications of Non-Newtonian Flows*, D. A. Siginer and H. P. Wang, eds., ASME, New York, FED-Vol. 231/MD-Vol. 66, pp. 99–105, 1995.

Choi, S. U. S., Nanofluids: From vision to reality through research. *ASME J. Heat Transfer* **131**, 033106, 2009.

Choi, S. U. S., Zhang, Z., and Keblinski, P., Nanofluids. In: *Encyclopedia of Nanoscience and Nanotechnology*, H. Nalwa, ed., American Scientific Publishers, New York, pp. 757–773, 2004.

Choi, S. U. S., Zhang, Z. G., Yu, W., Lockwood, F. E., and Grulke, E. A., Anomalous thermal conductivity enhancement in nanotube suspensions. *Appl. Phys. Lett*. **79**, 2252–2254, 2001.

Cimpean, D. S. and Pop, I., Fully developed mixed convection flow of a nanofluid through an inclined channel filled with a porous medium. *Int. J. Heat Mass Transfer* **55**, 907–914, 2012.

Dalkilic, A. S., Kayaci, N., Celen, A., Tabatabaei, M., Yildiz, O., Daungthongsuk, W. and Wongwises, S., Forced convection heat transfer of nanofluids. *Curr. Nanosci*. **8**, 949–969, 2012.

Das, S., Choi, S. U. S., Yu, W., and Pradeep, T., *Nanofluids Science and Technology*, Wiley, Hoboken, NJ, 2008.

Das, S. K., Choi, S. U. S., and Patel, H. E., Heat transfer in nanofluids—A review. *Heat Transfer Eng*. **27**, 3–19, 2006.

Daungthongsuk, W. and Wongwises, S., A critical review of convective heat transfer of nanofluids. *Renew. Sust. Energ. Syst*. **11**, 797–817, 2007.

Eastman, J. A., Choi, S. U. S., Li, S., Yu, W., and Thompson, L. J., Anomalously increased effective thermal conductivities of ethylene glycol-based nanofluids containing copper nanoparticles. *Appl. Phys. Lett*. **78**, 718–720, 2001.

El-Kabeir, S. M. M., Chamkha, A. J., and Rashad, A. M., Effect of thermal radiation on non-Darcy natural convection from a vertical cylinder embedded in a nanofluid porous media. *J. Porous Media* **17**, 209–278, 2014.

Ellahi, R., Aziz, S., and Zeeshan, A., Non-Newtonian nanofluid flow through a porous medium between two co-axial cylinders with heat transfer and variable viscosity. *J. Porous Media* **16**, 205–216, 2013.

Ferdows, M., Khan, M. S., Alam, M. M., and Sun, S. Y., MHD convective boundary layer flow of a nanofluid through a porous medium due to an exponentially stretching sheet. *Math. Probl. Eng*. **2012**, 408528, 2012.

Ghalambaz, A. and Noghrehabadi, A., Effects of heat generation/absorption on natural convection of nanofluids over the vertical plate embedded in a porous medium using drift-flux model, *J. Comput. Appl. Res. Mech. Eng*. **3**(2), 113–123, 2014.

Ghazvini, M., Akhavan-Behabadi, M. A., and Esmaeili, M., The effect of viscous dissipation on laminar nanofluid flow in a microchannel heat sink. *IME J. Mech. Eng. Sci*. **263**, 2697–2706, 2009.

Ghazvini, M. and Shokouhmand, H., Investigation of nanofluid-cooled microchannel heat sink using fin and porous media approaches. *Energ. Convers. Manag*. **50**, 2373–2380, 2009.

Gorla, R. S. R and Abdel-Gaied, S. M., Mixed convection in a porous medium saturated with a nanofluid: Entire regime. *J. Thermophys. Heat Transfer* **26**, 386–390, 2011.

Gorla, R. S. R. and Chamkha, A., Natural convective boundary layer flow over a non-isothermal vertical plate embedded in a porous medium saturated with a nanofluid. *Nanoscale Microscale Thermophys. Eng*. **15**, 81–94, 2011a.

Gorla, R. S. R. and Chamkha, A. J., Natural convective boundary layer flow over a horizontal plate embedded in a porous medium saturated with a nanofluid. *J. Modern Phys*. **2**, 62–71, 2011b.

Gorla, R. S. R. and Chamkha, A. J., Natural convective boundary layer flow over a horizontal plate embedded in a porous medium saturated with a non-Newtonian nanofluid. *Int. J. Microscale Nanoscale Therm. Fluid Transp. Phenom*. **2**, 211–227, 2011c.

Gorla, R. S. R. and Chamkha, A. J., Free convection past a vertical plate embedded in a porous medium saturated with a saturated porous media. *J. Porous Media* **17**, 269–278, 2014.

Gorla, R. S. R., Chamkha, A. J., and Ghodeswar, K., Natural convective boundary layer flow over a vertical cone embedded in a porous medium saturated with a nanofluid. *J. Nanofluids* **3**, 65–71, 2014.

Gorla, R. S. R., Chamkha, A. J. and Rashad, A. M., Mixed convective boundary layer flow past a vertical cylinder in a nanofluid: Natural convection dominated regime. *Nanoscale Res. Lett*. **6**, 207, 2011.

Gorla, R. S. R. and Hossan, A., Mixed convective boundary layer flow over a vertical cylinder embedded in a porous medium saturated with a nanofluid. *Int. J. Num. Meth. Heat Fluid Flow* **23**, 1393–1405, 2013.

Gorla, R. S. R. and Khan, W., Natural convective boundary-layer flow over a vertical cylinder embedded in a porous medium saturated with a nanofluid. *J. Nanotech. Engng. Med*. **3**, 034501, 2012.

Haddad, Z., Oztop, H. F., Abu-Nada, B., and Mataoui, A. A review on natural convective heat transfer of nanofluids. *Renew. Sust. Energ. Rev*. **16**, 5363–5378, 2012.

Hady, F. M., Ibrahim, F. S., Abdel-Gaied, S. M., and Eid, M. R., Effect of heat generation/absorption on natural convective boundary-layer flow from a vertical cone embedded in a porous medium filled with a non-Newtonian nanofluid. *Int. Commun. Heat Mass Transfer* **38**, 1414–1420, 2011a.

Hady, F. M., Ibrahim, F. S., Abdel-Gaied, S. M. and Eid, M. R., Boundary-layer non-Newtonian flow over vertical plate in porous medium saturated with nanofluid. *Appl. Math. Mech. Engl. Ed*. **32**, 1577–1588, 2011b.

Hady, F. M., Ibrahim, F. S., Abdel-Gaied, S. M., and Eid, M. R., Influence of yield stress on free convective boundary layer flow of a non-Newtonian nanofluid past a vertical plate in a porous medium. *J. Mech. Sci. Tech*. **25**, 2043–2050, 2011c.

Hajipour, M. and Dehkordi, A. M., Analysis of nanofluid heat transfer in parallel-plate vertical channels partially filled with porous medium. *Int. J. Therm. Sci*. **55**, 103–113, 2012.

Hajipour, M. and Dehkordi, A. M., Mixed convection flow of Al_2O_3-H_2O nanofluid in a channel partially filled with porous metal foam. *Exp. Therm. Fluid Sci*. 53, 49–56, 2014.

Hajipour, M., Dehkordi, A. M., and Jamshidi, S., Numerical investigation of nanofluid mixed-convection flow in the entrance region of a vertical channel partially filled with porous medium. *Heat Transfer Asian Res*. **43**, 607–627, 2014.

Hamad, M. A. A. and Pop, I., Scaling transformations for boundary layer flow near the stagnation point on a heated permeable stretching surface in a porous medium saturated with a nanofluid and heat generation/absorption effects. *Transp. Porous Media* **87**, 25–39, 2011.

Hung, Y. M., Analytical study on forced convection of nanofluids with viscous dissipation in microchannels. *Heat Transfer Eng*. **31**, 1184–1192, 2010.

Kakac, S. and Pramuanjaroenkij, A., Review of convective heat transfer enhancement with nanofluids. *Int. J. Heat Mass Transfer* **52**, 5339–5347, 2009.

Kandasamy, R., Muhaimin, I., Khamis, A. B., and Bin Roslan, R., Unsteady Hiemenz flow of Cu-nanofluid over a porous wedge in the presence of thermal stratification due to solar energy radiation: Lie group transformation. *Int. J. Therm. Sci*. **65**, 196–205, 2013.

Kandasamy, R., Muhaimin, I., Ram, N. S., and Prabhu, K. K. S., Thermal stratification effects on Hiemenz flow of nanofluid over a porous wedge sheet in the presence of suction/injection due to solar energy: Lie group transformation. *Transp. Porous Media* **94**, 399–416, 2012.

Kandasamy, R., Muhaimin, I., and Rosmila, A. K., The performance evaluation of unsteady MHD non-Darcy nanofluid flow over a porous wedge due to renewable (solar) energy. *Renew. Energ*. **64**, 1–9, 2014.

Khan, W. A. and Aziz, A., Double-diffusive natural convective boundary layer flow in a porous medium saturated with a nanofluid over a vertical plate: Prescribed surface heat, solute and nanoparticle fluxes. *Int. J. Therm. Sci*. **50**, 2154–2160, 2011.

Khan, W. A. and Pop, I., Free convection boundary layer flow past a horizontal flat plate embedded in a porous medium filled with a nanofluid. *ASME J. Heat Transfer* **133**, 094501, 2011.

Khan, W. A. and Pop, I., Boundary-layer stagnation—Point flow toward a stretching surface in a porous nanofluid- filled medium. *J. Thermophys. Heat Transfer* **26**, 147–153, 2012a.

Khan, W. A. and Pop, I. M., Boundary layer flow past a stretching surface in a porous medium saturated by a nanofluid: Brinkman-Forchheimer model. *PLOS ONE* **7**, e47031, 2012b.

Khan, W. A., Uddin, M. J., and Ishmail, A. I. M., Free convection of non-Newtonian nanofluids in porous media with gyrotactic microorganisms. *Transp. Porous Media* **97**, 241–252, 2013a.

Khan, Z. H., Khan, W. A., and Pop, I., Triple diffusive free convection along a horizontal plate in porous media saturated by a nanofluid with convective boundary condition. *Int. J. Heat Mass Transfer* **66**, 603–612, 2013b.

Khanafer, K. and Vafai, K., A critical analysis of thermophysical characteristics of nanofluids. *Int. J. Heat Mass Transfer* **54**, 4410–4428, 2011.

Khidir, A. A. and Sibanda, P., Nanofluid flow over a nonlinear stretching sheet in porous media with MHD and viscous dissipation effects. *J. Porous Media* **17**, 391–403, 2014.

Kim, S. J., McKrell, T., Buongiorno, J., and Hu, L., Enhancement of flow boiling critical heat flux (CHF) in alumina/water nanofluids. *Adv. Sci. Lett*. **2**, 100–102, 2009.

Kleinstreuer, C. and Feng, Y. Experimental and theoretical studies of nanofluid enhancement: A review. *Nanoscale Res. Lett*. **6**, art. 229, 2011 (Correction: art #439).

Kleinstreuer, C., Li, J., and Koo, J., Microfluidics of nano-drug delivery. *Int. J. Heat Mass Transfer* **51**, 5590–5597, 2008.

Kuznetsov, A. V., Nanofluid bioconvection in a horizontal fluid saturated porous layer. *J. Porous Media* **15**, 11–27, 2012a.

Kuznetsov, A. V., Nanofluid bioconvection in porous media: Oxytactic microorganisms. *J. Porous Media* **15**, 233–248, 2012b.

Kuznetsov, A. V. and Bubnovich, V., Investigation of simultaneous gyrotactic and oxytactic microorganisms on nanofluid bio-thermal convection in porous media. *J. Porous Media* **15**, 617–631, 2012.

Kuznetsov, A. V. and Nield, D. A., Effect of thermal non-equilibrium on the onset of convection in a porous medium layer saturated by a nanofluid. *Transp. Porous Media* **83**, 425–436, 2010a.

Kuznetsov, A. V. and Nield, D. A., The onset of double-diffusive nanofluid convection in a layer of a saturated porous medium. *Transp. Porous Media* **85**, 941–951, 2010b.

Kuznetsov, A. V. and Nield, D. A., Thermal instability in a porous medium layer saturated by a nanofluid: Brinkman model. *Transp. Porous Media* **81**, 409–422, 2010c.

Kuznetsov, A. V. and Nield, D. A., The effect of local thermal nonequilibrium on the onset of convection in a porous medium layer saturated by a nanofluid: Brinkman model. *J. Porous Media* **14**, 285–293, 2011.

Kuznetsov, A. V. and Nield, D. A., The Cheng-Minkowycz problem for natural convective boundary layer flow in a porous medium saturated by a nanofluid: A revised model. *Int. J. Heat Mass Transfer* **65**, 682–685, 2013.

Lee, S., Choi, S. U. S., Li, S., and Eastman, J. A., Measuring thermal conductivity of fluids containing oxide nanoparticles. *ASME J. Heat Transfer* **121**, 280–289, 1999.

Lister, D. H. G., *Corrosion Products in Power Generating Systems*, AECL-6877, Chalk River Nuclear Laboratories, Chalk River, Ontario, 1980.

Maghrebi, M. J., Nazari, M., and Armaghansi, T., Forced convection heat transfer of nanofluids in a porous channel. *Transp. Porous Media* **93**, 401–413, 2012.

Magyari, E., Note on the "Scaling transformations for boundary layer flow near the stagnation point on a heated permeable stretching surface in a porous medium saturated with a nanofluid and heat generation/absorption effects." *Transp. Porous Media* **87**, 41–48, 2011a.

Magyari, E., Reply on the reply on the Note: "Scaling transformations for boundary layer flow near the stagnation point on a heated permeable stretching surface in a porous medium saturated with a nanofluid and heat generation/absorption effects." *Transp. Porous Media* **87**, 53–56, 2011b.

Mahajan, A. and Sharma, M. K., Convection in magnetic nanofluids in porous media. *J. Porous Media* **17**, 439–455, 2014.

Mahdi, R. A., Mohammed, H. A., Munisamy, K. M., and Saied, N. H., Influence of various geometrical shapes on mixed convection through open-cell aluminium foam filled with nanofluid. *J. Comput. Theor. Nanosci*. **11**, 1275–1289, 2014.

Mahdy, A. and Ahmed, S. E., Laminar free convection over a vertical wavy surface embedded in a porous medium filled with a nanofluid. *Transp. Porous Media* **91**, 423–435, 2012.

Mansour, M. A., Ahmed, S. E., and Bakier, M. Y. A., Free convection in H-shaped enclosures filled with a porous medium saturated with nanofluids with mounted heater on the vertical walls. *Special Topics Rev. Porous Media* **4**, 287–297, 2014.

Masuda, H., Ebata, A., Teramae, K., and Hishinuma, N., Alteration of thermal conductivity and viscosity of liquid by dispersing ultra-fine particles, *Netsu Bussei* **7**, 227–233, 1993.

Matin, M. H. and Ghanbari, B., Effects of Brownian motion and thermophoresis on the mixed convection of nanofluid in a porous channel including flow reversal. *Transp. Porous Media*, **101**, 115–136, 2014.

Matin, M. H. and Pop, I., Forced convection heat and mass transfer flow of a nanofluid through a porous channel with a first order chemical reaction on the wall. *Int. Commun. Heat Mass Transfer* **46**, 134–141, 2013.

Maxwell, J. C., *A Treatise on Electricity and Magnetism*, 2nd edn., Clarendon Press, Oxford, U.K., 1881.

Memari, M., Golmakani, A., and Dehkordi, A. M., Mixed convection flow of nanofluids and regular fluids in vertical porous media with viscous heating. *Ind. Eng. Chem. Res*. **50**, 9403–9414, 2011.

Michaelides, E. E. Transport properties of nanofluids. A critical review. *J. Non-Equilib. Thermodyn*. **38**, 1–79, 2013.

Mittal, N., Manoj, V., Kumar, D. S., and Satheesh, A., Numerical simulation of mixed convection in a porous medium filled with water/Al2O3 nanofluid. *Heat Transfer Asian Res*. **42**, 46–59, 2013a.

Mittal, N., Satheesh, A., and Santhos Kumar, Numerical simulation of mixed convection in a lid-driven porous cavity using different nanofluids. *Heat Transfer Asian Res*. **43**, 1–16, 2013b.

Müller-Steinhagen, H., Cooling-water fouling in heat exchangers. *Adv. Heat Transfer* **33**, 415–496, 1999.

Murthy, P. V. S. N., RamReddy, C., Chamkha, A. J., and Rashad, A. M., Magnetic effect on thermally stratified nanofluid saturated non-Darcy porous medium under convective boundary condition. *Int. Commun. Heat Mass Transfer* **47**, 41–48, 2013a.

Murthy, P. V. S. N., Sutradhar, A., and RamReddy, C. Double diffusive free convection flow past an inclined plate embedded in a non-Darcy porous medium saturated with a nanofluid. *Transp. Porous Media* **98**, 553–564, 2013b.

Nasrin, R. and Alim, M. A., Non-Darcy assisted flow along a channel with an open cavity filled with water TiO_2 nanofluid. *Heat Transfer Asian Res*. **42**, 300–318, 2013.

Nasrin, R., Alim, M. A., and Chamkha, A. J., Numerical simulation of non-Darcy forced convection through a channel with nonuniform heat flux in an open cavity using nanofluid. *Numer. Heat Transfer A* **64**, 820–840, 2013a.

Nasrin, R., Alim, M. A., and Chamkha, A. J., Effect of heating wall position on forced convection along two-sided open enclosure with porous medium using nanofluid. *Int. J. Energy Tech*. **5**, Paper 9, 1–13, 2013b.

Nasrin, R., Parvin, S., Alim, M. A., and Chamkha, A. J., Non-Darcy forced convection through a wavy porous channel using CuO nanofluid. *Int. J. Energ. Tech*. **4**, Paper 8, 1–8, 2012.

Nazar, R., Tham, L., Pop, I., and Ingham, D. B., Mixed convection boundary layer flow from a horizontal circular cylinder embedded in a porous medium filled with a nanofluid. *Transp. Porous Media* **86**, 517–536, 2011.

Nield, D. A., Onset of thermohaline convection in a porous medium. *Water Resour. Res*. **4**, 553–560, 1968.

Nield, D. A., A note on the onset of convection in a layer of a porous medium saturated by a non-Newtonian nanofluid of power-law type. *Transp. Porous Media* **87**, 121–123, 2011a.

Nield, D. A., A further note on the onset of convection in a layer of a porous medium saturated by a non-Newtonian nanofluid of power-law type. *Transp. Porous Media* **88**, 187–191, 2011b.

Nield, D. A. and Bejan, A., *Convection in Porous Media*, 4th edn., Springer, New York, 2013.

Nield, D. A. and Kuznetsov, A. V., The Cheng-Minkowycz problem for natural convective boundary layer flow in a porous medium saturated by a nanofluid. *Int. J. Heat Mass Transfer* **52**, 5792–5795, 2009a.

Nield, D. A. and Kuznetsov, A. V., Thermal instability in a porous medium layer saturated by a nanofluid. *Int. J. Heat Mass Transfer* **52**, 5796–5801, 2009b.

Nield, D. A. and Kuznetsov, A. V., The Cheng-Minkowycz problem for the double-diffusive natural convection boundary layer flow in a porous medium saturated by a nanofluid. *Int. J. Heat Mass Transfer* **54**, 374–378, 2011a.

Nield, D. A. and Kuznetsov, A. V., Effect of vertical throughflow on thermal instability in a porous medium layer saturated by a nanofluid. *Transp. Porous Media* **87**, 765–775, 2011b.

Nield, D. A. and Kuznetsov, A. V., The onset of convection in a layer of a porous medium saturated by a nanofluid: Effects of conductivity and viscosity variation and cross-diffusion. *Transp. Porous Media* **92**, 837–846, 2012.

Nield, D. A. and Kuznetsov, A. V., A note on the variation of nanofluid viscosity with temperature, *Int. Commun. Heat Mass Transfer* **41**, 17–18, 2013a.

Nield, D. A. and Kuznetsov, A. V., Onset of convection with internal heating in a porous medium saturated by a nanofluid. *Transp. in Porous Media* **99**, 73–83, 2013b.

Nield, D. A. and Kuznetsov, A. V., Thermal instability in a porous medium layer saturated by a nanofluid: A revised model. *Int. J. Heat Mass Transfer* **68**, 211–214, 2014a.

Nield, D. A. and Kuznetsov, A. V., Forced convection in a parallel-plate channel occupied by a nanofluid or a porous medium saturated by a nanofluid. *Int. J. Heat Mass Transfer* **70**, 430–433, 2014b.

Nield, D. A. and Kuznetsov, A. V., Corrigendum to 'Forced convection in a parallel-plate channel occupied by a nanofluid or a porous medium saturated by a nanofluid'. *Int. J. Heat Mass Transfer* **70**, 430–433, *Int. J. Heat Mass Transfer* **76**, 534–534, 2014c.

Noghrehabadi, A. and Behseresht, A., Flow and heat transfer affected by variable properties of nanofluids in natural-convection over a vertical cone in porous media. *Comput. Fluids* **88**, 313–325, 2013.

Noghrehabadi, A., Behseresht, A., and Ghalambaz, M., Natural convection of nanofluid over vertical plate embedded in porous medium: Prescribed surface heat flux. *Appl. Math. Mech. Engl. Ed*. **34**, 669–686, 2013a.

Noghrehabadi, A., Behseresht, A., Ghalambaz, M., and Behseresht, J., Natural convection flow of nanofluids over vertical cone embedded in non-Darcy porous media. *J. Thermophys. Heat Transfer* **27**, 334–341, 2013b.

Noghrehabadi, A., Ghakambaz, M., and Ghanbarzedeh, A, Effects of variable viscosity and thermal conductivity on natural convection past a vertical plate in porous media. *J. Mech*. **30**, 265–275, 2014.

Ozerinc, S., Kakac, S., and Yazicioglu, A. G., Enhanced thermal conductivity of nanofluids: A state-of-the-art review. *Microfluidics Nanofluidics* **8**, 145–170, 2010.

Pop, I., Reply to the Paper TIPM1512: Note on the "Scaling transformations for boundary layer flow near the stagnation point on a heated permeable stretching surface in a porous medium saturated with a nanofluid and heat generation/absorption effects" by E. Magyari, *Transp. Porous Media* **87**, 49–51, 2011.

RamReddy, C., Murthy, P. V., Chamkha, A. J., and Rashad, A. M., Influence of viscous dissipation on convection in a non-Darcy porous medium saturated with nanofluid in the presence of magnetic field. *Open Transp. Phenom. J*. **5**, 20–29, 2013a.

RamReddy, C., Murthy, P. V. S. N., Chamkha, A. J., and Rashad, A., Soret effect on mixed convection flow in a nanofluid under convective boundary condition. *Int. J. Heat Mass Transfer* **64**, 384–392, 2013b.

RamReddy, C., Murthy, P. V., Chamkha, A. J., and Rashad, A. M., Numerical study of thermally stratified nanofluid flow in a saturated non-Darcy porous medium. *Eur. Phys. J. Plus* **129**, 1–11, 2014.

Rana, P., Bhargavi, R., and Beg, O. A., Numerical solution for mixed convection boundary layer flow of a nanofluid along an inclined plate embedded in a porous medium. *Comput. Math. Appl*. **64**, 2816–2832, 2012.

Rasekh, A. and Ganji, D. D., Analytical approximate solutions of mixed convection about an inclined flat plate embedded in a porous medium filled with nanofluids. *Int. J. Comput. Meth. Eng. Sci. Mech*. **14**, 440–445, 2013.

Rasekh, A., Ganji, D. D., and Tavakoli, S., Analytical solution for natural convection heat transfer about a vertical cone in porous media filled with a non-Newtonian Al2O3-water nanofluid. *Comput. Therm. Sci*. **5**, 73–82, 2013.

Rashad, A. M., Abbasbandy, S., and Chamkha, A. J., Non-Darcy natural convection from a vertical cylinder embedded in a thermally stratified and nanofluid-saturated porous media. *ASME J. Heat Transfer* **136**, 022503, 2014.

Rashad, A. M., Chamkha, A. J., and Abdou, M. M. M., Mixed convection flow of non-Newtonian fluid from vertical surface saturated in porous medium filled with a nanofluid. *J. Appl. Fluid Mech*. **6**, 301–309, 2012.

Rahsad, A. M., Chamkha, A. J., and Modather, M., Mixed convection boundary-layer flow of a nanofluid from a horizontal circular cylinder embedded in a porous medium under convective boundary condition. *Comput. Fluids* **86**, 380–386, 2013.

Rashad, A. M., Chamkha, A. J., Ramreddy, C., and Murthy, P. V. S. N., Influence of viscous dissipation on mixed convection in a non-Darcy porous medium saturated with a nanofluid. *Heat Transfer Asian Res*. **43**, 397–411, 2014.

Rashad, A. M., El-Hakiem, M. A., and Abdou, M. M. M., Natural convective boundary layer of a non-Newtonian fluid about a permeable vertical cone embedded in a porous medium saturated with a nanofluid. *Comput. Math. Appl*. **62**, 3140–3151, 2011.

Rea, U., McKrell, T., Hu, L., and Buongiorno, J., Laminar convective heat transfer and viscous pressure loss of alumina-water and zirconia-water nanofluids. *Int. J. Heat Mass Transfer* **52**, 2042–2048, 2009.

Rohni, A. M., Ahmad, S., Merkin, J. H., and Pop, I., Mixed convection boundary-layer flow along a vertical cylinder embedded in a porous medium filled by a nanofluid. *Transp. Porous Media* **96**, 237–253, 2013.

Rosca, A. V., Rosca, N. C., Grosan, T., and Pop, I., Non-Darcy mixed convection from a horizontal plate embedded in a nanofluid saturated porous medium. *Int. Comm. Heat Mass Transfer* **39**, 1080–1085, 2012.

Rosmila, A. B., Kandasamy, R., and Muhaimin, I., Lie symmetry group transformation for MHD natural convection flow of nanofluid over linearly porous stretching sheet in presence of thermal stratification. *Appl. Math. Mech. Engl. Ed*. **33**, 593–604, 2012.

Sarkar, J., A critical review on convection heat transfer correlations of nanofluids. *Renew. Sust. Energ. Rev*. **15**, 3271–3277, 2011.

Satya Narayana, P. V., Venkateswarlu, B., and Venkataramana, S., Thermal radiation and heat source effects on a MHD nanofluid past a vertical plate in a rotating system with porous medium. *Heat Transfer Asian Res*. **44**, 1–19, 2014.

Servati V. A. A., Javaherdeh, K., and Ashorynejad,H. R. Magnetic field effects on force convection flow of a nanofluid in a channel partially filled with porous media using Lattice Boltzmann Method. *Adv. Powder Tech*. **25**, 666–675, 2014.

Shafahi, M., Bianco, V., Vafai, K., and Manca, O., An investigation of the thermal performance of cylindrical heat pipes using nanofluids. *Int. J. Heat Mass Transfer* **53**, 376–383, 2010a.

Shafahi, M., Bianco, V., Vafai, K., and Manca, O., Thermal performance of flat-shaped heat pipes using nanofluids. *Int. J. Heat Mass Transfer* **53**, 1438–1445, 2010b.

Shaw, S., Kameswaren, P. K., Narayana, M., and Sibanda, P. Bioconvection in a non-Darcy porous medium saturated with a nanofluid and oxytactic micro-organisms. *Int. J. Biomath*. **7**, 1450005, 2014.

Sheikholeslami, H., Eliahi, R., Ashorgnejad, H. R., Domairry, G., and Hayat, T., Effects of heat transfer in flow of nanofluids over a stretching wall in a porous medium. *J. Comput. Theor. Nanosci*. **11**, 486–496, 2014.

Sheu, L. J., Thermal instability in a porous medium layer saturated with a viscoelastic nanofluid. *Transp. Porous Media* **88**, 461–477, 2011.

Shivakumara, I. S., Nanjundappa, C. E., and Ravisha, M., Thermomagnetic convection in a magnetic nanofluid saturated porous medium. *Int. J. Appl. Math. Engl. Sci*. **2**, 157–170, 2010.

Sparreboom, W., van den Berg, A., and Eijkel, J. C. T., Transport in nanofluidic systems: A review of theory and applications. *New J. Phys*. **12**, 015004, 2010.

Srinivasacharya, D. and Surenda, O., Non-similar solution for natural convective boundary layer flow of a nanofluid past a vertical plate embedded in a doubly stratified porous medium. *Int. J. Heat Mass Transfer* **71**, 431–438, 2014.

Sun, Q. and Pop, I., Free convection in a triangle cavity filled with a porous medium saturated with nanofluids with flush mounted heater on wall. *Int. J. Therm. Sci*. **50**, 2141–2153, 2011.

Sun, Q. and Pop, I., Free convection in a tilted triangle porous cavity filled with Cu-water nanofluid with flush mounted heater on the wall. *Int. J. Num. Meth. Heat Fluid Flow* **24**, 17102893, 2–20, 2014.

Syakila, A. and Pop, I., Mixed convection boundary layer flow from a vertical flat plate embedded in a porous medium with nanofluids. *Int. Commun. Heat Mass Transfer* **37**, 987–991, 2010.

Tavakoli, S., Ganji, D. D., Rasekh, A., Haghighi, B., and Jahani, H., Natural convection from a vertical wall embedded in a non-Darcy porous medium filled with nanofluids. *Int. J. Num. Meth. Heat Fluid Flow* **23**, 1304–1319, 2013.

Terekhov, V. I., Kalina, S. V., and Lemanov, V. V., The mechanism of heat transfer in nanofluids: State of the art (review). Part 1. Synthesis and properties of nanofluids. *Thermophys. Aeromech*. **17**, 1–14, 2010a.

Terekhov, V. I., Kalina, S. V., and Lemanov, V. V., The mechanism of heat transfer in nanofluids: State of the art (review). Part 2. Convective heat transfer. *Thermophys. Aeromech*. **17**, 157–171, 2010b.

Tham, L. and Nazar, R., Mixed convection flow about a solid sphere embedded in a porous medium filled with a nanofluid. *Sains Malaysiana* **41**, 1643–1649, 2012.

Tham, L., Nazar, R., and Pop, I., Mixed convection boundary layer flow past a horizontal circular cylinder embedded in a porous medium saturated by a nanofluid: Brinkman model. *J. Porous Media* **16**, 445–457, 2013c.

Tham, L., Nazar, R., and Pop, I., Mixed convection flow over a solid sphere embedded in a porous medium filled by a nanofluid containing gyrotactic microorganisms. *Int. J. Heat Mass Transfer* **62**, 647–660, 2013a.

Tham, L., Nazar, R., and Pop, I. Steady mixed convection flow on a horizontal circular cylinder embedded in a porous medium filled by a nanofluid containing gyrotactic micro-organisms. *ASME J. Heat Transfer* **135**, 102601, 2013b.

Uddin, M. J., Khan, W. A., and Ishmail, A. I. M., Free convection boundary layer flow from a heated upward facing horizontal flat plate embedded in a porous medium filled by a nanofluid with convective boundary condition. *Transp. Porous Media* **92**, 867–881, 2012a.

Uddin, M. J., Khan, W. A., and Ismail, A. I. M., Lie group analysis of natural convective flow from a convectively heated upward facing radiating permeable horizontal plate in porous media filled with nanofluid. *J. Appl. Math*. **2012**, 648675, 2012b.

Uddin, M. J., Khan, W. A., and Ismail, A. I. M., Free convective flow of non-Newtonian nanofluids in porous media with gyrotactic microorganisms. *J. Thermophys. Heat Transfer* **27**, 326–333, 2013a.

Uddin, M. J., Khan, W. A., and Ismail, A. I., Effect of dissipation on free convective flow of a non-Newtonian nanofluid in a porous medium with gyrotactic microorganisms. *IME J. Nanoeng. Nanosys*. **227**, 11–18, 2013b.

Uddin, M. J., Yusoff, N. H. M., Beg, O. A., and Ismail, A. I., Lie group analysis and numerical solutions for non-Newtonian nanofluid flow in a porous medium with internal heat generation. *Phys. Scr*. **87**, 025401, 2013c.

Uddin, Z. and Harmand, S., Nanoscale convection heat transfer of nanofluids along a vertical plate embedded in porous medium. *Nanoscale Res. Lett*. **8**, 64, 2013.

Umavathi, J. C., Effect of thermal modulation on the onset of convection in a porous medium layer saturated by a nanofluid. *Transp. Porous Media* **98**, 59–79, 2013.

Umavathi, J. C. and Mohite, M. B., The onset of convection in a nanofluid saturated porous layer using Darcy model with cross diffusion. *Meccanica* **49**, 1159–1175, 2014a.

Umavathi, J. C. and Mohite, M. B., Double-diffusive convective transport in a nanofluid-saturated porous layer with cross diffusion and variation of viscosity and conductivity. *Heat Transfer Asian Res*. **43**, 628–652, 2014b.

Vadász, P., Heat conduction in nanofluid suspensions. *ASME J. Heat Transfer* **128**, 465–477, 2006.

Vadász, P, Nanofluids suspensions and bi-composite media as derivatives of interface heat transfer modeling in porous media. In: *Emerging Topics in Heat and Mass Transfer in Porous Media*, P. Vadasz, ed., Springer, New York, pp. 283–326, 2008.

Yadav, D., Agrawal, G. S., and Bhargava, R., Onset of double-diffusive nanofluid convection in a layer of saturated porous medium with thermal conductivity and viscosity variation. *J. Porous Media* **16**, 105–121, 2013.

Yadav, D., Bhargava, R., and Agrawal, G. S., Boundary and internal source effects on the onset of Darcy-Brinkman convection in a porous layer saturated by nanofluid. *Int. J. Therm. Sci*. **60**, 244–254, 2012.

Yadav, D., Bhargava, R., Agrawal, G. S., Yadav, N., Lee, J., and Kim, M. C., Thermal instability in a rotating porous layer saturated by a non-Newtonian nanofluid with thermal conductivity and viscosity variation. *Microfluidics Nanofluidics* **16**, 425–440, 2014.

Yasin, M. H. M., Arifin, M. N., Nazar, R., Ishmail, F., and Pop, I., Mixed convection boundary layer with internal heat generation in a porous medium filled with a nanofluid. *Adv. Sci. Lett*. **13**, 833–835, 2012.

Yasin, M. H. M., Arifin, N. M., Nazar, R., Ismail, F., and Pop, I., Mixed convection boundary layer flow embedded in a thermally stratified porous medium saturated by nanofluid. *Adv. Mech. Eng*. **2013**, 121943, 2013.

Yazdi, M. E., Moradi, A., and Dinavand, S., MHD mixed convection stagnation point flow over a stretching vertical plate in porous medium filled with a nanofluid in the presence of thermal radiation. *Arabian J. Sci. Eng*. **39**, 2251–2261, 2014.

15 Analyzing Nanofluids Suspension Using the Porous Media Interface Heat Transfer Model

Peter Vadasz

CONTENTS

15.1 Introduction 513
15.2 Problem Formulation 514
15.3 Two Methods of Solution 516
15.4 Correction of the THW Results 525
15.5 Results and Discussion 527
15.6 Conclusions 531
References 531

15.1 INTRODUCTION

The impressive heat transfer enhancement revealed experimentally in nanofluid suspensions by Eastman et al. (2001), Lee et al. (1999), and Choi et al. (2001) conflicts apparently with Maxwell's (1891) classical theory of estimating the effective thermal conductivity of suspensions, including higher-order corrections and other spherical particle geometries developed by Hamilton and Crosser (1962), Jeffrey (1973), Davis (1986), Lu and Lin (1996), and Bonnecaze and Brady (1990, 1991). Further attempts for independent confirmation of the experimental results showed conflicting outcomes with some experiments such as Das et al. (2003) and Li and Peterson (2006) confirming at least partially the results presented by Eastman et al. (2001), Lee et al. (1999), and Choi et al. (2001), while others such as Buongiorno and Venerus (2010) and Buongiorno et al. (2009) show in contrast results that are in agreement with Maxwell's (1891) effective medium theory. All these experiments were performed by using the transient hot wire (THW) experimental method. On the other hand, most experimental results that used optical methods, such as the *optical beam deflection* (Putnam et al., 2006), *all-optical thermal-lensing method* (Rusconi et al., 2006), and *forced Rayleigh scattering* (Venerus et al., 2006), did not reveal any thermal conductivity enhancement beyond what is predicted by the effective medium theory. A variety of possible reasons for the excessive values of the effective thermal conductivity obtained in some experiments have been investigated, but only few succeeded to show a viable explanation. Jang and Choi (2004) and Prasher et al. (2005) show that convection due to Brownian motion may explain the enhancement of the effective thermal conductivity. However, if indeed this is the case, it is difficult to explain why this enhancement of the effective thermal conductivity is selective and is not obtained in all nanofluid experiments. Alternatively, Vadasz et al. (2005) showed that hyperbolic heat conduction also provides a viable explanation for the latter, although their further research and comparison to later published experimental data presented by Vadasz and Govender (2010) lead them to discard this possibility.

Vadasz (2006) derived theoretically a model for the heat conduction mechanisms of nanofluid suspensions including the effect of the surface area-to-volume ratio of the suspended nanoparticles/nanotubes on the heat transfer. The theoretical model was shown to provide a viable explanation for the excessive values of the effective thermal conductivity obtained experimentally by Eastman et al. (2001), Lee et al. (1999), and Choi et al. (2001). The explanation is based on the fact that the THW experimental method used in all nanofluid suspensions experiments listed in the previous text needs a major correction factor when applied to nonhomogeneous systems. This time-dependent correction factor is of the same order of magnitude as the claimed enhancement of the effective thermal conductivity. However, no direct comparison to experiments was possible because the authors Eastman et al. (2001), Lee et al. (1999), and Choi et al. (2001) did not report so far their temperature readings as a function of time, which is the base upon which the effective thermal conductivity is being evaluated. Nevertheless, in a paper by Liu et al. (2006), the authors reveal three important new results that allow the comparison of Vadasz's (2006) theoretical model with experiments. The first important new result presented by Liu et al. (2006) is reflected in the fact that the value of *effective thermal conductivity* revealed experimentally by using the THW method is time dependent. The second new result is that the authors present graphically their time-dependent *effective thermal conductivity* for three specimens and therefore allow the comparison of their results with theoretical predictions of Vadasz (2011) showing a very good fit. The third new result is that their time-dependent *effective thermal conductivity* converges at steady state to values that according to our calculations confirm the validity of the classical Maxwell's theory (1891) and its extensions Hamilton and Crosser (1962), Jeffrey (1973), Davis (1986), Lu and Lin (1996), and Bonnecaze and Brady (1990, 1991).

The objective of this chapter is to review the controversial results and provide an explanation that settles the conflict between the apparent enhancement of the effective thermal conductivity in some experiments and the lack of enhancement in other experiments. Vadasz (2011) demonstrated that the transient heat conduction process in nanofluid suspensions produces results that fit well the experimental data (Liu et al., 2006) and validates Maxwell's (1891) method of estimating the effective thermal conductivity of suspensions. The theoretical results presented by Vadasz (2011) are combined with experimental data (Liu et al., 2006) to conclude that, while there is no improvement in the effective thermal conductivity of nanofluids beyond the Maxwell's (1891) effective medium theory, there is nevertheless substantial heat transfer augmentation via nanofins. The latter are formed as attachments on the hot wire surface by a mechanism that could be related to electrophoresis and/or thermophoresis, and therefore such attachments depend on the electrical current passing through the wire and varies therefore between different experiments. Also, since the effective thermal conductivity does not increase beyond the Maxwell's (1891) effective medium theory, the experiments using optical methods such as Putnam et al. (2006), Rusconi et al. (2006), and Venerus et al. (2006) are also consistent with this conclusion.

In the present chapter, a *contextual notation* is introduced to distinguish between dimensional and dimensionless variables and parameters. The *contextual notation* implies that an asterisk subscript is used to identify dimensional variables and parameters only when ambiguity may arise when the asterisk subscript is not used. For example, t_* is the dimensional time, while t is its corresponding dimensionless counterpart. However, k_f is the effective fluid phase thermal conductivity, a dimensional parameter that appears without an asterisk subscript without causing ambiguity.

15.2 PROBLEM FORMULATION

The theoretical model derived by Vadasz (2006) to investigate the transient heat conduction in a fluid containing suspended solid particles by considering phase-averaged equations will be presented only briefly without including the details. The phased-averaged equations are

$$\gamma_s \frac{\partial T_s}{\partial t_*} = h\left(T_f - T_s\right) \tag{15.1}$$

$$\gamma_f \frac{\partial T_f}{\partial t_*} = k_f \nabla_*^2 T_f - h\left(T_f - T_s\right) \tag{15.2}$$

where

t_* is time

$T_f(\boldsymbol{r}_*, t_*)$, $T_s(\boldsymbol{r}_*, t_*)$ are temperature values for the fluid and solid phases, respectively, averaged over a representative elementary volume (REV) that is large enough to be statistically valid but sufficiently small compared to the size of the domain

$\boldsymbol{r}_*$ are the coordinates of the centroid of the REV

In Equations 15.1 and 15.2, $\gamma_s = \varepsilon\rho_s c_s$ and $\gamma_f = \left(1-\varepsilon\right)\rho_f c_p$ represent the effective heat capacity of the solid and fluid phases, respectively, with ρ_s and ρ_f being the density of the solid and fluid phases, respectively; c_s and c_p being the specific heat of the solid and fluid phases, respectively; and ε being the volumetric solid fraction of the suspension. Similarly, k_f is the effective thermal conductivity of the fluid that may be defined in the form $k_f = f\left(\varepsilon, \kappa\right)\tilde{k}_f$, where $\tilde{k}_f$ is the thermal conductivity of the fluid, $\kappa = \tilde{k}_s / \tilde{k}_f$ is the thermal conductivity ratio, and ε is the solid fraction of suspended particles in the suspension. In Equations 15.1 and 15.2, the parameter h, carrying units of $\mathrm{W}\cdot\mathrm{m}^{-3}\cdot\mathrm{K}^{-1}$, represents an integral heat transfer coefficient for the contribution of the heat conduction at the solid–fluid interface as a volumetric heat source/sink within an REV. It is assumed to be independent of time, and its general relationship to the surface-area-to-volume ratio (specific area) was derived in Vadasz (2006). Note that $T_s(\boldsymbol{r}_*, t_*)$ is a function of the space variables represented by the position vector $\boldsymbol{r}_* = r_*\hat{\boldsymbol{e}}_r + \phi_*\hat{\boldsymbol{e}}_\phi + z_*\hat{\boldsymbol{e}}_z$, in addition to its dependence on time, because $T_s(\boldsymbol{r}_*, t_*)$ depends on $T_f(\boldsymbol{r}_*, t_*)$ as explicitly stated in Equation 15.1, although no spatial derivatives appear in Equation 15.1. The reason for the lack of macroscopic level conduction mechanism in Equation 15.1 representing the heat transfer within the solid phase is the fact that the solid particles represent the dispersed phase in the fluid suspension, and therefore the solid particles can conduct heat between themselves only via the neighboring fluid. When steady state is accomplished, $\partial T_s/\partial t_* = \partial T_f/\partial t_* = 0$ leading to local thermal equilibrium between the solid and fluid phases, that is, $T_s(\boldsymbol{r}) = T_f(\boldsymbol{r})$.

For the case of a thin hot wire embedded in a cylindrical container insulated on its top and bottom, one can assume that the heat is transferred in the radial direction only, r_*, rendering Equation 15.2 into

$$\gamma_f \frac{\partial T_f}{\partial t_*} = k_f \frac{1}{r_*}\frac{\partial}{\partial r_*}\left(r_* \frac{\partial T_f}{\partial r_*}\right) - h\left(T_f - T_s\right) \tag{15.3}$$

In a homogeneous medium without solid suspended particles, Equation 15.1 is not relevant and the last term in Equation 15.3 can also be omitted. The boundary and initial conditions applicable are an initial ambient constant temperature, T_C, within the whole domain; an ambient constant temperature, T_C, at the outer radius of the container; and a constant heat flux, q_o, over the fluid-wire interface that is related to the Joule heating of the wire in the form $q_o = iV/(\pi d_{w*} l_*)$, where d_{w*} and l_* are the diameter and the length of the wire, respectively, i is the electric current, and V is the voltage drop across the wire. Vadasz (2006) showed that the problem formulated by Equations 15.1 and 15.3 subject to appropriate initial and boundary conditions represents a particular case of dual-phase-lagging heat conduction (see also Wang, 2000, Wang et al., 2001, Wang and Xu, 2002, Xu and Wang, 2002).

An essential component in the application of the THW method for estimating experimentally the effective thermal conductivity of the nanofluid suspension is the assumption that the nanofluid suspension behaves basically like a homogeneous material following Fourier law for the bulk. The THW method is well established as the most accurate, reliable, and robust technique (Hammerschmidt

and Sabuga, 2000) for evaluating the thermal conductivity of fluids. A very thin (5–80 μm in diameter) platinum (or alternatively tantalum) wire is embedded vertically in the selected fluid and serves as a heat source as well as a thermometer (see Vadasz, 2006 for details). Because of the very small diameter and high thermal conductivity of the platinum wire, it can be regarded as a line heat source in an otherwise infinite cylindrical medium. The rate of heat generated per unit length (l_*) of platinum wire due to a step change in voltage is therefore $\dot{q}_{l*} = iV/l_*$ W · m^{-1}. Solving for the radial heat conduction due to this line heat source leads to an approximated temperature solution in the wire's neighborhood in the form

$$T\left(r_*,t_*\right) \approx \frac{\dot{q}_{l*}}{4\pi k}\left[-\gamma_o + \ln\left(\frac{4\alpha t_*}{r_*^2}\right)\right] \tag{15.4}$$

provided that a validity condition for the approximation is enforced, that is, $t_* \gg t_{o*} = r_{w*}^2/4\alpha$, where r_{w*} is the radius of the platinum wire, $\alpha = \tilde{k}_f/\rho_f c_p$ is the fluid's thermal diffusivity, and $\gamma_o = 0.5772156649$ is Euler's constant. Equation 15.4 reveals a linear relationship, on a logarithmic time scale, between the temperature and time. Therefore, one way of evaluating the thermal conductivity is from the slope of this relationship evaluated at $r_* = r_{w*}$. For any two readings of temperature T_1 and T_2 recorded at times t_{1*} and t_{2*}, respectively, the thermal conductivity can be approximated by using Equation 15.4 in the form

$$k \approx \frac{iV}{4\pi\left(T_2 - T_1\right)l_*}\left[\ln\left(\frac{t_{2*}}{t_{1*}}\right)\right]. \tag{15.5}$$

Equation 15.5 is a very accurate way of estimating the thermal conductivity as long as the validity condition is fulfilled. The validity condition implies the application of Equation 15.5 for long times only. However, when evaluating this condition to data used in the nanofluid suspension experiments, one obtains that $t_{o*} \sim 6$ ms, and the time beyond which the solution (15.5) can be used reliably is therefore of the order of hundreds of milliseconds, not so long in the actual practical sense.

15.3 TWO METHODS OF SOLUTION

While the THW method is well established for homogeneous fluids, its applicability to two-phase systems such as fluid suspensions is still under development and no reliable validity conditions for the latter exist so far (see Vadasz [2010] for a discussion and initial work on the latter). As a result one needs to refer to the two equations model presented by Equations 15.1 and 15.3 instead of the one Fourier type equation that is applicable to homogeneous media.

Two methods of solution are in principle available to solve the system of Equations 15.1 and 15.3. The first is the elimination method, while the second is the eigenvectors method. By using the elimination method, one may eliminate T_f from Equation 15.1 in the form

$$T_f = \frac{\gamma_s}{h}\frac{\partial T_s}{\partial t_*} + T_s \tag{15.6}$$

and substitute it into Equation 15.3 hence rendering the two Equations 15.1 and 15.3 that each depends on both T_s and T_f into separate equations for T_s and T_f, respectively, in the form

$$\tau_q \frac{\partial^2 T_i}{\partial t_*^2} + \frac{\partial T_i}{\partial t_*} = \alpha_e\left[\frac{1}{r_*}\frac{\partial}{\partial r_*}\left(r_*\frac{\partial T_i}{\partial r_*}\right) + \frac{\tau_T}{r_*}\frac{\partial}{\partial r_*}\left(r_*\frac{\partial^2 T_i}{\partial r_* \partial t_*}\right)\right] \quad \text{for } i = s, f, \tag{15.7}$$

where the index i takes the values $i = s$ for the solid phase and $i = f$ for the fluid phase, and the following notation was used

$$\tau_q = \frac{\gamma_s \gamma_f}{h\left(\gamma_s + \gamma_f\right)}; \quad \alpha_e = \frac{k_f}{\left(\gamma_s + \gamma_f\right)}; \quad \tau_T = \frac{\gamma_s k_f}{h\left(\gamma_s + \gamma_f\right)\alpha_e} = \frac{\gamma_s}{h}. \tag{15.8}$$

In Equation 15.8, τ_q and τ_T are the heat flux and temperature related time lags linked to dual-phase lagging (Tzou, 1997, Wang, 2000, Wang et al., 2001, Wang and Xu, 2002, Xu and Wang, 2002, Vadasz, 2006), while α_e is the effective thermal diffusivity of the suspension. The resulting Equation 15.7 is identical for both fluid and solid phases. Vadasz (2006) used this equation in providing the solution. The initial conditions applicable to the problem at hand are identical for both phases, that is, both phase temperatures are set to be equal to the ambient temperature T_C

$$t_* = 0 : T_i = T_C = \text{constant}, \quad \text{for } i = s, f \tag{15.9}$$

The boundary conditions are

$$r_* = r_{o*} : T_f = T_C \tag{15.10}$$

$$r_* = r_{w*} : \left(\frac{\partial T_f}{\partial r_*}\right)_{r_* = r_{w*}} = -\frac{q_o}{k_f} \tag{15.11}$$

where r_{o*} is the radius of the cylindrical container. Equation 15.7 is second order in time and second order in space. The initial conditions (15.9) provide one such condition for each phase, while the second order Equation 15.7 requires two such conditions. To obtain the additional initial conditions, one may use Equations 15.1 and 15.3 in combination with (15.9). From (15.9), it is evident that both phase initial temperatures at $t_* = 0$ are identical and constant. Therefore, $\left(T_f\right)_{t_*=0} = \left(T_s\right)_{t_*=0} = T_C = \text{constant}$, leading to $\left(T_f - T_s\right)_{t_*=0} = 0$ and $\left[\partial/\partial r_* \left(r_* \, \partial T_f / \partial r_*\right)\right]_{t_*=0} = 0$ to be substituted in (15.1) and (15.3) leading to the following additional initial conditions for each phase

$$t_* = 0 : \left(\frac{\partial T_i}{\partial t_*}\right)_{t_*=0} = 0 \quad \text{for } i = s, f \tag{15.12}$$

The two boundary conditions (15.10) and (15.11) are sufficient to uniquely define the problem for the fluid phase; however, there are no boundary conditions set for the solid phase as the original Equation 15.1 for the solid phase had no spatial derivatives and did not require boundary conditions. To obtain the corresponding boundary conditions for the solid phase, which are required for the solution of Equation 15.7 corresponding to $i = s$, one may use first the fact that at $r_* = r_{o*}$ both phases are exposed to the ambient temperature, and therefore one may set

$$r_* = r_{o*} : T_s = T_C \tag{15.13}$$

Second, one may use Equation 15.6 and taking its derivative with respect to r_* yields

$$\frac{\gamma_s}{h} \frac{\partial}{\partial t_*}\left(\frac{\partial T_s}{\partial r_*}\right) + \frac{\partial T_s}{\partial r_*} = \frac{\partial T_f}{\partial r_*} \tag{15.14}$$

In Equation 15.14, the spatial variable r_* plays no active role; it may therefore be regarded as a parameter. As a result, one may present Equation 15.14 for any specified value of r_*. Choosing

$r_* = r_{w*}$ where we know the value of $\left(\partial T_f / \partial r_*\right)_{t_{w*}}$ from the boundary condition (15.11) yields from (15.14) the following ordinary differential equation:

$$\frac{\gamma_s}{h}\frac{\mathrm{d}\dddot{\dddot{}}}{\mathrm{d}t_*}\left(\frac{\partial T_s}{\partial r_*}\right)_{r_{w*}} + \left(\frac{\partial T_s}{\partial r_*}\right)_{r_{w*}} = -\frac{q_o}{k_f} \tag{15.15}$$

At steady state, Equation 15.15 produces the solution

$$\left(\frac{\partial T_{s,st}}{\partial r_*}\right)_{r_{w*}} = -\frac{q_o}{k_f} \tag{15.16}$$

where $T_{s,st}$ is the steady-state solution. The transient solution $T_{s,tr} = T_s - T_{s,st}$ satisfies then the equation

$$\frac{\gamma_s}{h}\frac{\mathrm{d}\dddot{\dddot{}}}{\mathrm{d}t_*}\left(\frac{\partial T_{s,tr}}{\partial r_*}\right)_{r_{w*}} + \left(\frac{\partial T_{s,tr}}{\partial r_*}\right)_{r_{w*}} = 0 \tag{15.17}$$

subject to the initial condition

$$\left[\left(\frac{\partial T_{s,tr}}{\partial r_*}\right)_{r_{w*}}\right]_{t_*=0} = \left[\left(\frac{\partial T_s}{\partial r_*}\right)_{r_{w*}}\right]_{t_*=0} = 0 \tag{15.18}$$

because $\left[\partial T_s / \partial r_*\right]_{t_*=0} = 0$ for all values of $r_* \in [r_{w*}, r_{o*}]$ given that according to (15.9) at $t_* = 0$: $\left(T_s\right)_{t_*=0} = \left(T_f\right)_{t_*=0} = T_C = \text{constant}$. Equation 15.17 can be integrated to yield

$$\left(\frac{\partial T_{s,tr}}{\partial r_*}\right)_{r_{w*}} = A\exp\left(-\frac{h}{\gamma_s}t\right) \tag{15.19}$$

which combined with the initial condition (15.18) produces the value of the integration constant $A = 0$, and therefore the transient solution becomes

$$\left(\frac{\partial T_{s,tr}}{\partial r_*}\right)_{r_{w*}} = 0 \tag{15.20}$$

The complete solution for the solid temperature gradient at the wire is therefore obtained by combining (15.20) with (15.16) leading to

$$\left(\frac{\partial T_s}{\partial r_*}\right)_{r_{w*}} = -\frac{q_o}{k_f} \tag{15.21}$$

producing the second boundary condition for the solid phase, which is identical to the corresponding boundary condition for the fluid phase. One may therefore conclude that the solution to the problem formulated in terms of Equation 15.7 that is identical to both phases, subject to initial conditions (15.9) and (15.12) that are identical to both phases and boundary conditions (15.10), (15.11) and (15.13), (15.21) that are also identical to both phases, should be also identical to both phases,

that is, $T_s(t_*, r_*) = T_f(t_*, r_*)$. This, however, may not happen because then $T_f - T_s = 0$ leading to conflicting results when substituted into (15.1) and (15.3). The result obtained here is identical to Vadasz (2007) who demonstrated that a paradox revealed by Vadasz (2005) can be avoided only by refraining from using this method of solution. While the paradox is revealed in the corresponding problem of a porous medium subject to a combination of Dirichlet and insulation boundary conditions, the latter may be applicable to fluid suspensions by setting the effective thermal conductivity of the solid phase to be zero. The fact that in the present case the boundary conditions differ, that is, a constant heat flux is applied on one of the boundaries (such a boundary condition would have eliminated the paradox in porous media), does not eliminate the paradox in fluid suspensions mainly because in the latter case, the steady-state solution is identical for both phases. In the porous media problem, the constant heat flux boundary condition leads to different solutions at steady state, and therefore the solutions for each phase even during the transient differ.

The elimination method yields the same identical equation with identical boundary and initial conditions for both phases apparently leading to the wrong conclusion that the temperature of both phases should therefore be the same. A closer inspection shows that the discontinuity occurring on the boundaries' temperatures at $t = 0$ when a *ramp type* of boundary condition is used is the reason behind the occurring problem and the apparent paradox. The question that still remains is what phase temperature corresponds to the solution presented by Vadasz (2006): the fluid or the solid phase temperature?

By applying the eigenvectors method as presented by Vadasz (2007), one may avoid the paradoxical solution and obtain both phases temperatures. The analytical solution to the problem using the eigenvectors method is obtained following the transformation of the equations into a dimensionless form by introducing the following dimensionless variables:

$$\boldsymbol{q} = \frac{\boldsymbol{q}_*}{q_o}, \quad \theta_i = \frac{\left(T_i - T_C\right)k_f}{q_o r_{o*}}, \quad r = \frac{r_*}{r_{o*}}, \quad t = \frac{\alpha_e t_*}{r_{o*}^2} \tag{15.22}$$

where the following two dimensionless groups emerged:

$$Fo_q = \frac{\alpha_e \tau_q}{r_{o*}^2}; \quad Fo_T = \frac{\alpha_e \tau_T}{r_{o*}^2} \tag{15.23}$$

representing a heat flux Fourier number and a temperature Fourier number, respectively. The ratio between them is identical to the ratio between the time lags, that is,

$$\beta = \frac{Fo_T}{Fo_q} = \frac{\tau_T}{\tau_q} = \frac{\gamma_s + \gamma_f}{\gamma_f} \tag{15.24}$$

Equations 15.1 and 15.3 expressed in a dimensionless form using the transformation listed earlier are

$$Fh_s \frac{\partial \theta_s}{\partial t} = \left(\theta_f - \theta_s\right) \tag{15.25}$$

$$Fh_f \frac{\partial \theta_f}{\partial t} = \frac{1}{Ni_f} \frac{1}{r} \frac{\partial}{\partial r}\left(r \frac{\partial \theta_f}{\partial r}\right) - \left(\theta_f - \theta_s\right) \tag{15.26}$$

where the following additional dimensionless groups emerged:

$$Fh_s = \frac{\alpha_e \gamma_s}{hr_{o*}^2} = Fo_T = \frac{\gamma_s + \gamma_f}{\gamma_f} Fo_q = \beta Fo_q \tag{15.27}$$

$$Fh_f = \frac{\gamma_s + \gamma_f}{\gamma_s} Fo_q = \frac{\alpha_e \gamma_f}{hr_{o*}^2} = \frac{Fo_T}{(\beta - 1)} = \frac{\beta}{(\beta - 1)} Fo_q \tag{15.28}$$

$$Ni_f = \frac{hr_{o*}^2}{k_f} = \frac{(\beta - 1)}{\beta^2 Fo_q} \tag{15.29}$$

where Ni_f is the fluid phase Nield number. The solutions to Equations 15.25 and 15.26 are subject to the following initial and boundary conditions obtained from (15.9), (15.10), and (15.11) transformed in a dimensionless form:

$$t = 0 : \theta_i = 0 \quad \text{for } i = s, f \tag{15.30}$$

The boundary conditions are

$$r = 1 : \theta_f = 0 \tag{15.31}$$

$$r = r_w : \left(\frac{\partial \theta_f}{\partial r} \right)_{r = r_w} = -1 \tag{15.32}$$

No boundary conditions are required for θ_s. The solution to the system of Equations 15.25 and 15.26 is obtained by a superposition of steady and transient solutions $\theta_{i,st}(r)$ and $\theta_{i,tr}(t, r)$, respectively, in the form

$$\theta_i(t, r) = \theta_{i,st}(r) + \theta_{i,tr}(t, r) \quad \text{for } i = s, f \tag{15.33}$$

Substituting (15.33) into (15.25) and (15.26) produces to the following equations for the steady state:

$$(\theta_{f,st} - \theta_{s,st}) = 0 \tag{15.34}$$

$$\frac{1}{Ni_f} \frac{1}{r} \frac{\mathrm{d}\dagger}{\mathrm{d}r} \left(r \frac{\mathrm{d}\theta_{f,st}}{\mathrm{d}r} \right) - (\theta_{f,st} - \theta_{s,st}) = 0 \tag{15.35}$$

leading to the following steady solutions, which satisfy the boundary conditions (15.31) and (15.32):

$$\theta_{f,st}(r) = \theta_{s,st}(r) = -r_w \ln r \tag{15.36}$$

The transient part of the solutions $\theta_{i,tr}(t, r)$ can be obtained by using separation of variables leading to the following form of the complete solution:

$$\theta_i = -r_w \ln r + \sum_{n=1}^{\infty} S_{in}(t) R_{on}(r) \quad \text{for } i = s, f \tag{15.37}$$

Substituting (15.37) into (15.25) and (15.26) produces due to the separation of variables the following equation for the unknown functions $R_{on}(r)$:

$$\frac{1}{r}\frac{\mathrm{d}}{\mathrm{d}r}\left(r\frac{\mathrm{d}R_{on}}{\mathrm{d}r}\right) + \kappa_n^2 R_{on} = 0 \tag{15.38}$$

subject to the boundary conditions

$$r = 1: \; R_{on} = 0 \tag{15.39}$$

$$r = r_w : \left(\frac{\mathrm{d}R_{on}}{\mathrm{d}r}\right)_{r=r_w} = 0 \tag{15.40}$$

and the following system of equations for the unknown functions $S_{in}(t)$, $(i = s, f)$, that is,

$$\begin{cases} \dfrac{\mathrm{d}S_{sn}}{\mathrm{d}t} = aS_{sn} - aS_{fn} \\ \dfrac{\mathrm{d}S_{fn}}{\mathrm{d}t} = cS_{sn} + d_n S_{fn} \end{cases} \tag{15.41}$$

where

$$a = -Fh_s^{-1} = -\frac{1}{\beta\, Fo_q}; \quad c = Fh_f^{-1} = \frac{(\beta - 1)}{\beta\, Fo_q}; \quad d_n = -\frac{\left(\kappa_n^2 + Ni_f\right)}{Ni_f Fh_f} = -\beta\kappa_n^2 - \frac{(\beta - 1)}{\beta\, Fo_q} \tag{15.42}$$

and where the separation constant κ_n^2 represents the eigenvalues in space.

Equation 15.38 is the Bessel equation of order 0 producing solutions in the form of Bessel functions

$$R_{on}(\kappa_n, r) = Y_o(\kappa_n) J_o(\kappa_n r) - J_o(\kappa_n) Y_o(\kappa_n r) \tag{15.43}$$

where $J_o(\kappa_n r)$ and $Y_o(\kappa_n r)$ are the order 0 Bessel functions of the first and second kind, respectively. The solution (15.43) satisfies the boundary condition (15.39) as can be easily observed by substituting $r = 1$ in (15.43). Imposing the second boundary condition (15.40) yields a transcendental equation for the eigenvalues κ_n in the form

$$J_o(\kappa_n) Y_1(\kappa_n r_w) - Y_o(\kappa_n) J_1(\kappa_n r_w) = 0 \tag{15.44}$$

where $J_1(\kappa_n r_w)$ and $Y_1(\kappa_n r_w)$ are the order 1 Bessel functions of the first and second kind, respectively, evaluated at $r = r_w$. The complete solution is obtained by substituting (15.43) into (15.37) and imposing the initial conditions (15.30) in the form

$$\left(\theta_i\right)_{t=0} = -r_w \ln r + \sum_{n=1}^{\infty} S_{in}\left(0\right) R_{on}\left(r\right) \neq 0 \quad \text{for } i = s, f \tag{15.45}$$

At $t = 0$, both phases temperatures are the same leading to the conclusion that

$$S_{sn}\left(0\right) = S_{fn}\left(0\right) = S_{no} \tag{15.46}$$

Multiplying (15.45) by the orthogonal eigenfunction $R_{om}(\kappa_m, r)$ with respect to the weight function r and integrating the result over the domain $[r_w, 1]$, that is, $\int_{r_w}^{1} \left(\bullet\right) R_{om}\left(\kappa_m, r\right) r \, \mathrm{d}r$, yields

$$r_w \int_{r_w}^{1} r \ln r R_{om}\left(\kappa_m, r\right) \mathrm{d}r = \sum_{n=1}^{\infty} S_{no} \int_{r_w}^{1} r R_{on}\left(\kappa_n, r\right) R_{om}\left(\kappa_m, r\right) \mathrm{d}r \tag{15.47}$$

The integral on the right-hand side of (15.47) produces the following result due to the orthogonality conditions for Bessel functions:

$$\int_{r_w}^{1} r R_{on}\left(\kappa_n, r\right) R_{om}\left(\kappa_m, r\right) \mathrm{d}r = \begin{cases} 0 & \text{for } n \neq m \\ N\left(\kappa_n\right) & \text{for } n = m \end{cases} \tag{15.48}$$

where the norm $N(\kappa_n)$ is evaluated in the form

$$N\left(\kappa_n\right) = \int_{r_w}^{1} r R_{on}^2\left(\kappa_n, r\right) \mathrm{d}r = \frac{2}{\pi^2} \frac{\left[J_1^2\left(\kappa_n r_w\right) - J_o^2\left(\kappa_n\right)\right]}{\kappa_n^2 J_1^2\left(\kappa_n r_w\right)} \tag{15.49}$$

The integral on the left-hand side of (15.47) can be evaluated by using integration by parts and the equation for the eigenvalues (15.44) to yield

$$\int_{r_w}^{1} r \ln r R_{on}\left(\kappa_n, r\right) \mathrm{d}r = \frac{1}{\kappa_n^2}\left[J_o\left(\kappa_n\right) Y_o\left(\kappa_n r_w\right) - Y_o\left(\kappa_n\right) J_o\left(\kappa_n r_w\right)\right] \tag{15.50}$$

Substituting (15.48) and (15.50) into (15.47) yields the values of S_{in} at $t = 0$, that is, $S_{no} = S_{sn}(0) = S_{fn}(0)$

$$\frac{r_w}{\kappa_n^2}\left[J_o\left(\kappa_n\right) Y_o\left(\kappa_n r_w\right) - Y_o\left(\kappa_n\right) J_o\left(\kappa_n r_w\right)\right] = S_{no} N\left(\kappa_n\right)$$

that need to be used as initial conditions for the solution of system (15.41)

$$S_{no} = \frac{\pi^2 r_w J_1^2\left(\kappa_n r_w\right)\left[J_o\left(\kappa_n\right) Y_o\left(\kappa_n r_w\right) - Y_o\left(\kappa_n\right) J_o\left(\kappa_n r_w\right)\right]}{2\left[J_1^2\left(\kappa_n r_w\right) - J_o^2\left(\kappa_n\right)\right]} \tag{15.51}$$

to produce the explicit solutions in time. With the initial conditions for S_{in} evaluated ($i = s, f$), one may turn to solving system (15.41) that can be presented in the following vector form:

$$\frac{\mathrm{d}\boldsymbol{S_n}}{\mathrm{d}t} = A\boldsymbol{S_n} \tag{15.52}$$

where the matrix A is explicitly defined by

$$A = \begin{bmatrix} a & -a \\ c & d_n \end{bmatrix} \tag{15.53}$$

with the values of a, c, and d_n given by Equation 15.42 and the vector $\boldsymbol{S}_n$ defined in the form $\boldsymbol{S}_n = [S_{sn}, S_{fn}]^T$. The eigenvalues λ_n corresponding to (15.52) are obtained as the roots of the following quadratic algebraic equation:

$$\lambda_n^2 - \left(a + d_n\right)\lambda_n + a\left(d_n + c\right) = 0 \tag{15.54}$$

leading to

$$\lambda_{1n} = \frac{a + d_n}{2} + \frac{1}{2}\sqrt{\left(a - d_n\right)^2 - 4ac} \quad \text{and} \quad \lambda_{2n} = \frac{a + d_n}{2} - \frac{1}{2}\sqrt{\left(a - d_n\right)^2 - 4ac}$$

which upon substituting a, c, and d_n from Equation 15.42 produces

$$\lambda_{1n} = -\frac{\left(1 + \beta Fo_q \kappa_n^2\right)}{2Fo_q}\left[1 + \sqrt{1 - \frac{4Fo_q\kappa_n^2}{\left(1 + \beta Fo_q\kappa_n^2\right)^2}}\right] \tag{15.55}$$

$$\lambda_{2n} = -\frac{\left(1 + \beta Fo_q \kappa_n^2\right)}{2Fo_q}\left[1 - \sqrt{1 - \frac{4Fo_q\kappa_n^2}{\left(1 + \beta Fo_q\kappa_n^2\right)^2}}\right] \tag{15.56}$$

The following useful relationship is obtained from (15.55) and (15.56):

$$\lambda_{1n}\lambda_{2n} = \frac{\kappa_n^2}{Fo_q} \tag{15.57}$$

The corresponding eigenvectors υ_{1n} and υ_{2n} are evaluated in the form

$$\upsilon_{1n} = \begin{bmatrix} 1 \\ \dfrac{\left(-\lambda_{1n} + a\right)}{a} \end{bmatrix}; \quad \upsilon_{2n} = \begin{bmatrix} 1 \\ \dfrac{\left(-\lambda_{2n} + a\right)}{a} \end{bmatrix} \tag{15.58}$$

leading to the following solution:

$$\boldsymbol{S}_n = \upsilon_{1n} C_{1n} e^{\lambda_{1n} t} + \upsilon_{2n} C_{2n} e^{\lambda_{2n} t} \tag{15.59}$$

and explicitly following the substitution of (15.58) and the initial conditions S_{in} ($i = s, f$), at $t = 0$, that is, $S_{sn}(0) = S_{fn}(0) = S_{no}$, with the values of S_{no} given by Equation 15.51

$$S_{sn} = \frac{S_{no}}{\left(\lambda_{2n} - \lambda_{1n}\right)}\left[\lambda_{2n} e^{\lambda_{1n} t} - \lambda_{1n} e^{\lambda_{2n} t}\right] \tag{15.60}$$

$$S_{fn} = \frac{S_{no}}{\left(\lambda_{2n} - \lambda_{1n}\right)}\left[\lambda_{2n}\left(1 + \beta Fo_q \lambda_{1n}\right) e^{\lambda_{1n} t} - \lambda_{1n}\left(1 + \beta Fo_q \lambda_{2n}\right) e^{\lambda_{2n} t}\right] \tag{15.61}$$

Substituting (15.57) into (15.60) and (15.61) and the latter into the complete solution (15.37) yields

$$\theta_s = -r_w \ln r + \sum_{n=1}^{\infty} B_n \left[\lambda_{2n} e^{\lambda_{1n} t} - \lambda_{1n} e^{\lambda_{2n} t}\right] R_{on}\left(r\right) \tag{15.62}$$

$$\theta_f = -r_w \ln r + \sum_{n=1}^{\infty} B_n \left[\left(\lambda_{2n} + \beta\kappa_n^2\right) e^{\lambda_{1n} t} - \left(\lambda_{1n} + \beta\kappa_n^2\right) e^{\lambda_{2n} t}\right] R_{on}\left(r\right) \tag{15.63}$$

where B_n is

$$B_n = \frac{S_{no}}{\left(\lambda_{2n} - \lambda_{1n}\right)} = \frac{\pi^2 r_w J_1^2\left(\kappa_n r_w\right)\left[J_o\left(\kappa_n\right) Y_o\left(\kappa_n r_w\right) - Y_o\left(\kappa_n\right) J_o\left(\kappa_n r_w\right)\right]}{2\left(\lambda_{2n} - \lambda_{1n}\right)\left[J_1^2\left(\kappa_n r_w\right) - J_o^2\left(\kappa_n\right)\right]} \tag{15.64}$$

Comparing the solutions obtained by Vadasz (2011) and presented here with the solution obtained by Vadasz (2006) via the elimination method, one may conclude that the latter corresponds to the solid phase temperature θ_s.

The Fourier solution is presented now in order to compare the solution obtained from the dual-phase-lagging model to the former. The Fourier solution is the result obtained by solving the thermal diffusion equation

$$\frac{1}{\beta}\frac{\partial \theta}{\partial t} = \frac{1}{r}\frac{\partial}{\partial r}\left(r\frac{\partial \theta}{\partial r}\right) \tag{15.65}$$

subject to the boundary and initial conditions

$$t = 0: \theta = 0 \tag{15.66}$$

$$r = 1: \theta = 0 \tag{15.67}$$

$$r = r_w : \left(\frac{\partial \theta}{\partial r}\right)_{r = r_w} = -1 \tag{15.68}$$

where the same scaling as in Equation 15.22 was applied in transforming the equation into its dimensionless form, hence the reason for the coefficient 1/β in the equation. The Fourier solution for this problem has then the form (Özisik, 1993)

$$\theta = -r_w \ln r + \sum_{n=1}^{\infty} C_n e^{-\beta\kappa_n^2 t} R_{on}\left(r\right) \tag{15.69}$$

where

$$C_n = \frac{\pi^2 r_w J_1^2\left(\kappa_n r_w\right)\left[J_o\left(\kappa_n\right)Y_o\left(\kappa_n r_w\right) - Y_o\left(\kappa_n\right)J_o\left(\kappa_n r_w\right)\right]}{2\left[J_1^2\left(\kappa_n r_w\right) - J_o^2\left(\kappa_n\right)\right]} = S_{no} \tag{15.70}$$

and the eigenvalues κ_n are the solution of the same transcendental Equation 15.44 and the eigenfunctions $R_{on}(r)$ are also identical to the ones presented in Equation 15.43. The relationship between the Fourier coefficient C_n and the dual-phase-lagging model's coefficient B_n is

$$C_n = \left(\lambda_{2n} - \lambda_{1n}\right)B_n \tag{15.71}$$

15.4 CORRECTION OF THE THW RESULTS

When evaluating the thermal conductivity by applying the THW method and using the Fourier law, one obtains for the effective thermal conductivity the following relationship (Vadasz, 2006):

$$k_{f,app} = \frac{q_o r_{o*}}{\left[T_w\left(t\right) - T_C\right]}\left[-r_w \ln\left(r_w\right) + f\left(t\right)\right] \tag{15.72}$$

where the temperature difference $\left[T_w\left(t\right) - T_C\right]$ is represented by the recorded experimental data and the value of the heat flux at the fluid–platinum–wire interface q_o is evaluated from the Joule heating of the hot wire. In Equation 15.72, $f\left(t\right) = \sum_{n=1}^{\infty} C_n R_{on}\left(r_w\right)\exp\left(-\kappa_n^2 t\right)$, where the coefficient C_n is defined by (15.70) and the eigenvalues κ_n are defined by Equation 15.44. Note that the definition of C_n here is different than in Vadasz (2006). The results obtained from the application of Equation 15.72 fit extremely well the approximation used by the THW method via Equation 15.5 within the validity limits of the approximation (15.5). Therefore, the THW method is extremely accurate for homogeneous materials.

On the other hand, for nonhomogeneous materials, by using the solutions (15.62) and (15.63) applicable to fluid suspensions evaluated at $r = r_{w,}$ one obtains

$$\left[T_{sw} - T_C\right] = \frac{q_{o*} r_{o*}}{k_{f,act}}\left[-r_w \ln\left(r_w\right) + g_s\left(t\right)\right] \tag{15.73}$$

$$\left[T_{fw}-T_C\right]=\frac{q_{o*}r_{o*}}{k_{f,act}}\left[-r_w\ln\left(r_w\right)+g_f\left(t\right)\right] \tag{15.74}$$

where

$k_{f,act}$ is the actual effective thermal conductivity

$T_{sw}(t)$ and $T_{fw}(t)$ are the solid and fluid phases temperatures "felt" by the wire at the points of contact with each phase, respectively, and the functions $g_s(t)$ and $g_f(t)$ obtained from the solutions (15.62) and (15.63) evaluated at $r = r_w$ take the form

$$g_s\left(t\right)=\sum_{n=1}^{\infty}B_nR_{on}\left(r_w\right)\left[\lambda_{n2}\exp\left(\lambda_{n1}t\right)-\lambda_{n1}\exp\left(\lambda_{n2}t\right)\right] \tag{15.75}$$

$$g_f\left(t\right)=\sum_{n=1}^{\infty}B_nR_{on}\left(r_w\right)\left[\left(\lambda_{n2}+\beta\kappa_n^2\right)\exp\left(\lambda_{n1}t\right)-\left(\lambda_{n1}+\beta\kappa_n^2\right)\exp\left(\lambda_{n2}t\right)\right] \tag{15.76}$$

When the wire is exposed partly to the fluid phase and partly to the solid phase, there is no justification in assuming that the wire temperature is uniform; on the contrary, the wire temperature will vary between the regions exposed to the fluid and solid phases. Assuming that some solid nanoparticles are in contact with the wire in a way that they form approximately *solid rings* around the wire, then the *effective* wire temperature can be evaluated as electrical resistances in series. By defining the relative wire area covered by the solid nanoparticles as $a_s = A_s/A_{tot} = A_s/2\pi r_{w*}\,l_*$ its corresponding wire area covered by the fluid is $a_f = A_f/A_{tot} = 1-a_s$, then from the relationship between the electrical resistance and temperature accounting for electrical resistances connected in series, one obtains an expression for the effective wire temperature (i.e., the temperature that is evaluated using the wire's lumped electrical resistance in the THW Wheatstone bridge) T_w in the form

$$\left[T_w-T_C\right]=a_s\left(T_{sw}-T_C\right)+\left(1-a_s\right)\left(T_{fw}-T_C\right) \tag{15.77}$$

Substituting (15.73) and (15.74) into (15.77) yields

$$\left[T_w-T_C\right]=\frac{q_{o*}r_{o*}}{k_{f,act}}\left[-r_w\ln\left(r_w\right)+a_sg_s\left(t\right)+\left(1-a_s\right)g_f\left(t\right)\right] \tag{15.78}$$

One may then use (15.78) to evaluate the actual nanofluid's effective thermal conductivity $k_{f,act}$ from (15.78) in the form

$$k_{f,act}=\frac{q_{o*}r_{o*}}{\left(T_w-T_C\right)}\left[-r_w\ln\left(r_w\right)+a_sg_s\left(t\right)+\left(1-a_s\right)g_f\left(t\right)\right] \tag{15.79}$$

When using the single-phase Fourier solution (15.72) applicable for homogeneous materials to evaluate the effective thermal conductivity of nonhomogeneous materials like nanofluid suspensions instead of using Equation 15.79, one obtains a value that differs from the actual one by a factor of

$$\sigma=\frac{k_{f,app}}{k_{f,act}}=\frac{\left[-r_w\ln\left(r_w\right)+f\left(t\right)\right]}{\left[-r_w\ln\left(r_w\right)+a_sg_s\left(t\right)+\left(1-a_s\right)g_f\left(t\right)\right]} \tag{15.80}$$

where $k_{f,app}$ is the apparent effective thermal conductivity obtained from the single-phase Fourier conduction solution, while $k_{f,act}$ is the actual effective thermal conductivity that corresponds to data

that follow a dual-phase-lagging conduction according to the derivations presented here. The ratio between the two provides a correction factor for the deviation of the apparent effective thermal conductivity from the actual one. This correction factor when multiplied by the ratio $k_{f,act}/\tilde{k}_f$ produces the results for $\sigma\left(k_{f,act}/\tilde{k}_f\right) = k_{f,app}/\tilde{k}_f$, where $\tilde{k}_f$ is the thermal conductivity of the base fluid without the suspended particles and $k_{f,act}$ is the effective thermal conductivity evaluated by using Maxwell's (1891) theory, which for spherical particles can be expressed in the form

$$\frac{k_{f,act}}{\tilde{k}_f} = 1 + \frac{3\varepsilon(\kappa - 1)}{(\kappa + 2) - \varepsilon(\kappa - 1)} \tag{15.81}$$

where

$k_{f,act}$ is Maxwell's effective thermal conductivity

$\kappa = \tilde{k}_s/\tilde{k}_f$ is the ratio between the thermal conductivity of the solid phase and the thermal conductivity of the base fluid

ε is the volumetric solid fraction of the suspension

Then, these results of $k_{f,app}/\tilde{k}_f$ can be compared with the experimental results presented by Liu et al. (2006).

15.5 RESULTS AND DISCUSSION

The results for the solid and fluid phases' temperature at $r = r_w$ as a function of time obtained from the solutions (15.62) and (15.63) are presented in Figures 15.1 through 15.3 in comparison with the single-phase Fourier solution (15.69) for three different combinations of values of Fo_q and a_s and plotted on a logarithmic time scale. While the quantitative results differ between the three figures, there are some similar qualitative features that are important to mention. First, it is evident from these figures that the fluid phase temperature is almost the same as the temperature obtained from the single-phase Fourier solution. Second, it is also evident that the solid phase temperature lags

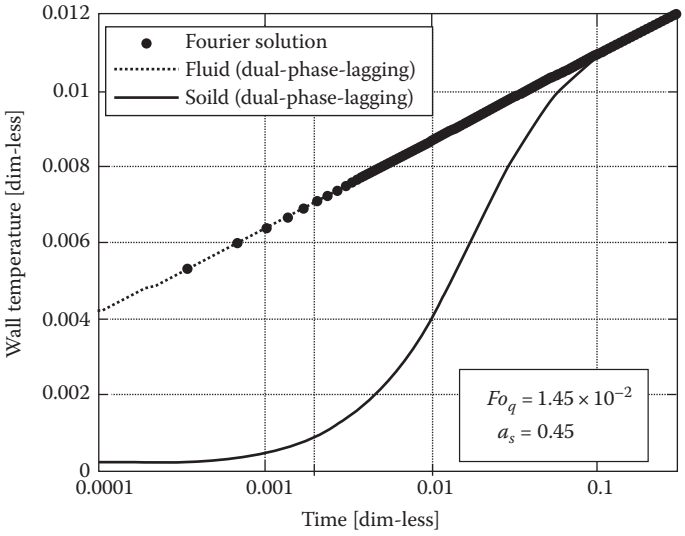

FIGURE 15.1 Dimensionless wire temperature. Comparison between the Fourier and dual-phase-lagging solutions for the following dimensionless parameters values $Fo_q = 1.45 \times 10^{-2}$ and $a_s = 0.45$. (From Vadasz, P., *Nanoscale Res. Lett*., 6, 154, 2011.)

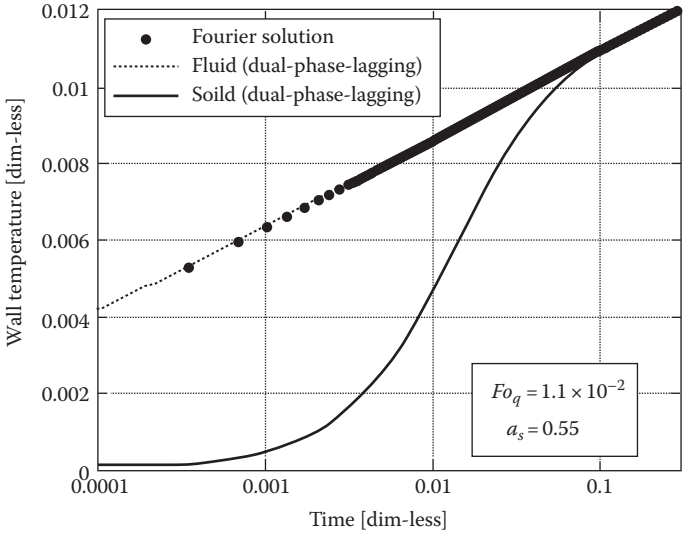

FIGURE 15.2 Dimensionless wire temperature. Comparison between the Fourier and dual-phase-lagging solutions for the following dimensionless parameters values $Fo_q = 1.1 \times 10^{-2}$ and $a_s = 0.55$. (From Vadasz, P., *Nanoscale Res. Lett*., 6, 154, 2011.)

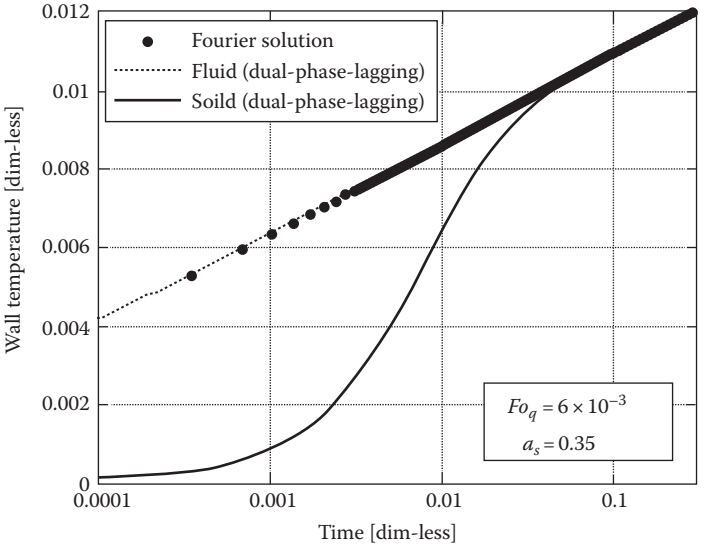

FIGURE 15.3 Dimensionless wire temperature. Comparison between the Fourier and dual-phase-lagging solutions for the following dimensionless parameters values $Fo_q = 6 \times 10^{-3}$ and $a_s = 0.35$. (From Vadasz, P., *Nanoscale Res. Lett*., 6, 154, 2011.)

behind the fluid phase temperature by a substantial difference. They become closer as steady-state conditions approach. It is therefore imperative to conclude that the only way an excessively higher effective thermal conductivity of the nanofluid suspension as obtained by Eastman et al. (2001), Lee et al. (1999), and Choi et al. (2001) could have been obtained even in an apparent form is if the wire was excessively exposed to the solid phase temperature. The latter could have occurred if the electric current passing through the wire created electric fields that activated a possible mechanism of electrophoresis and/or thermophoresis that attracted the suspended nanoparticles toward the wire.

Note that such a mechanism does not cause agglomeration in the usual sense of the word, because as soon as the electric field ceases, the agglomeration does not have to persist, and the particles can move freely from the wire's surface. Therefore, testing the wire's surface after such an experiment for evidence of agglomeration on the wire's surface may not necessarily produce the required evidence for the latter.

Liu et al. (2006) used a very similar THW experimental method as the one used by Eastman et al. (2001), Lee et al. (1999), and Choi et al. (2001) with the major distinction being in the method of producing the nanoparticles and a cylindrical container of different dimensions. They used water as the base fluid and Cu nanoparticles as the suspended elements at volumetric solid fractions of 0.1% and 0.2%. Their data that are relevant to our present discussion were digitized from their Figure 15.3 (Liu et al., 2006) and used in the following presentation to compare our theoretical results. Three specimen data are presented in Figure 15.3 (Liu et al., 2006) resulting in extensive overlap of the various curves and therefore in some digitizing error, which is difficult to estimate when using only this figure to capture the data.

The comparison between the theoretical results presented here with the experimental data (Liu et al., 2006) is presented in Figures 15.4 through 15.6. The separation of these results into three different figures aims to better distinguish between the different curves and avoid overlapping as well as presenting the results on their appropriate scales. Figure 15.4 presents the results that are applicable to specimen No. 4 in Liu et al. (2006) and corresponding to a value of $Fo_q = 1.45 \cdot 10^{-2}$ and $a_s = 0.45$ in the theoretical model. Evaluating Maxwell's (1891) effective thermal conductivity for specimen No. 4 leads to a value of 0.6018 W/m · K, which is by 0.3% higher than that of the base fluid (water), that is, $k_{f,act}/\tilde{k}_f = 1.003$. From the figure, it is evident that the theoretical results match very well the digitized experimental data. Furthermore, the steady-state result for the ratio between the effective thermal conductivity and that of the base fluid was estimated from the digitized data to be $k_{f,act}/\tilde{k}_f = 1.003 \pm 0.001$ clearly validating Maxwell's (1891) predicted value. The results applicable to specimen No. 5 in Liu et al. (2006) and corresponding to values of $Fo_q = 1.1 \cdot 10^{-2}$ and $a_s = 0.55$ in the theoretical model are presented in Figure 15.5. The very good match between the theory and the digitized experimental data is again evident. In addition, the ratio between the

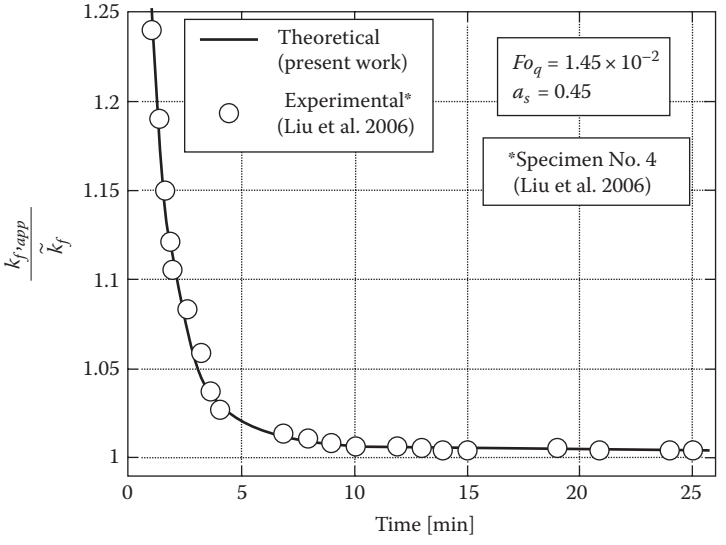

FIGURE 15.4 Comparison of the present theory with experimental data of Liu et al. (2006) (here redrawn from published data) of the effective thermal conductivity ratio for conditions compatible with specimen No. 4, leading to a Fourier number of $Fo_q = 1.45 \times 10^{-2}$ and a solid particles to total wire area ratio of $a_s = 0.45$. (From Vadasz, P., *Nanoscale Res. Lett*., 6, 154, 2011.)

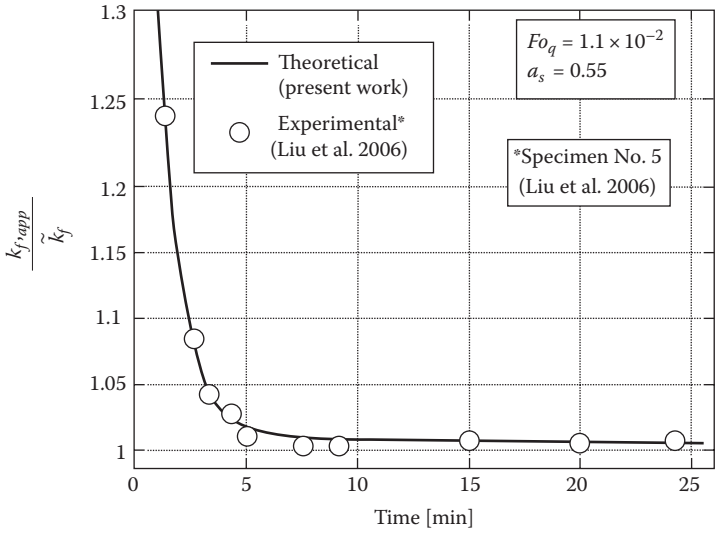

FIGURE 15.5 Comparison of the present theory with experimental data of Liu et al. (2006) (here redrawn from published data) of the effective thermal conductivity ratio for conditions compatible with specimen No. 5, leading to a Fourier number of $Fo_q = 1.1 \times 10^{-2}$ and a solid particles to total wire area ratio of $a_s = 0.55$. (From Vadasz, P., *Nanoscale Res. Lett*., 6, 154, 2011.)

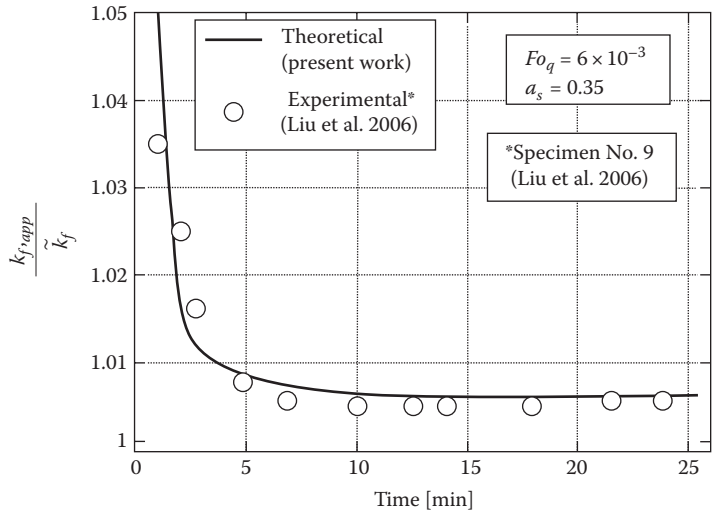

FIGURE 15.6 Comparison of the present theory with experimental data of Liu et al. (2006) (here redrawn from published data) of the effective thermal conductivity ratio for conditions compatible with specimen No. 9, leading to a Fourier number of $Fo_q = 6 \times 10^{-3}$ and a solid particles to total wire area ratio of $a_s = 0.35$. (From Vadasz, P., *Nanoscale Res. Lett*., 6, 154, 2011.)

effective thermal conductivity and that of the base fluid was estimated from the digitized data to be $k_{f,act}/\tilde{k}_f = 1.004 \pm 0.001$ again validating Maxwell's (1891) predicted value of $k_{f,act}/\tilde{k}_f = 1.003$. The last result is presented in Figure 15.6, which corresponds to specimen No. 9 in Liu et al. (2006) and to values of $Fo_q = 6 \cdot 10^{-3}$ and $a_s = 0.35$ in the theoretical model. The results are presented on an appropriately scaled vertical axis and show again a very good match between the theory presented here and the experimental data as digitized from Liu et al. (2006). Since the volumetric

solid fraction for this specimen was 0.2%, its corresponding Maxwell's (1891) effective thermal conductivity for this specimen leads to a value of 0.6036 W/m·K, which is by 0.6% higher than that of the base fluid (water), that is, $k_{f,act}/\tilde{k}_f = 1.006$. The steady-state result for the ratio between the effective thermal conductivity and that of the base fluid was estimated from the digitized data to be $k_{f,act}/\tilde{k}_f = 1.0059 \pm 0.002$ validating again Maxwell's (1891) predicted value.

It should be mentioned that Liu et al. (2006) explain their time-dependent effective thermal conductivity by claiming that it was caused by nanoparticle agglomeration, a conclusion that is consistent with Vadasz (2011) theoretical results.

15.6 CONCLUSIONS

The theoretical results reviewed in this chapter combined with experimental data (Liu et al., 2006) lead to the conclusion that, while there is no improvement in the effective thermal conductivity of nanofluids beyond the Maxwell's (1891) effective medium theory, there is nevertheless the possibility of substantial heat transfer augmentation via nanofins. Nanoparticles attaching to the hot wire by a mechanism that could be related to electrophoresis depending on the strength of the electrical current passing through the wire suggests that such attachments can be deliberately designed and produced on any heat transfer surface to yield an agglomeration of nanofins that exchange heat effectively because of the extremely high heat transfer area as well as the flexibility of such nanofins to bend in the fluid's direction when fluid motion is present hence extending its applicability to include a new and what appears to be a very effective type of heat convection. A quantitative estimate of the effectiveness of nanofins requires however an extension of the model presented in this chapter to include heat conduction within the nanofins.

REFERENCES

Bonnecaze, R.T. and J.F. Brady. 1990. A method for determining the effective conductivity of dispersions of particles. *Proc. R. Soc. Lond. A* **430**: 285–313.

Bonnecaze, R.T. and J.F. Brady. 1991.The effective conductivity of random suspensions of spherical particle. *Proc. R. Soc. Lond. A* **432**: 445–465.

Buongiorno, J. and D.C. Venerus. 2010. Letter to the editor. *Int. J. Heat Mass Transfer* **53**: 2939–2940.

Buongiorno, J., D.C. Venerus, N. Prabhat, T. McKrell, J. Townsend, R. Christianson, Y.V. Tolmachev et al. 2009. A benchmark study on the thermal conductivity of nanofluids. *J. Appl. Phys*. **106**: 094312.

Cheng, L., M. Xu, and L. Wang. 2008. From Boltzmann transport equation to single-phase-lagging heat conduction. *Int. J. Heat Mass Transfer* **51**: 6018–6023.

Choi, S.U.S., Z.G. Zhang, W. Yu, F.E. Lockwood and E.A. Grulke. 2001. Anomalous thermal conductivity enhancement in nanotube suspensions. *Appl. Phys. Lett*. **79**: 2252–2254.

Das, K.S., Putra, N., P. Thiesen, and W. Roetzel. 2003. Temperature dependence of thermal conductivity enhancement for nanofluids. *J. Heat Transfer* **125**: 567.

Davis, R.H. 1986. The effective thermal conductivity of a composite material with spherical inclusions. *Int. J. Thermophys*. **7**: 609–620.

Eastman, J.A., S.U.S. Choi, S. Li,, W. Yu, and L.J. Thompson. 2001. Anomalously increased effective thermal conductivities of ethylene glycol-based nanofluids containing copper nanoparticles. *Appl. Phys. Lett*. **78**: 718–720.

Hamilton, R.L. and O.K. Crosser. 1962. Thermal conductivity of heterogeneous two-component Systems. *I&EC Fundamentals* **1**: 187–191.

Hammerschmidt, U. and W. Sabuga. 2000. Transient hot wire (THW) method: Uncertainty assessment. *Int. J. Thermophys*. **21**: 1255–1278.

Jang, S.P. and S.U.-S. Choi. 2004. Role of Brownian motion in the enhanced thermal conductivity of nanofluids. *Appl. Phys. Lett*. **84**: 4316–4318.

Jeffrey, D.J. 1973. Conduction through a random suspension of spheres. *Proc. R. Soc. Lond. A* **335**: 355–367.

Lee, S., S.U.-S. Choi, S. Li, and J.A. Eastman. 1999. Measuring thermal conductivity of fluids containing oxide nanoparticles. *J. Heat Transfer* **121**: 280–289.

Li, C.H. and G.P. Peterson. 2006. Experimental investigation of temperature and volume fraction variations on the effective thermal conductivity of nanoparticle suspensions (nanofluids). *J. Appl. Phys*. **99**: 084314.

Liu, M.S., M.C.C. Lin, C.Y. Tsai, and C.C. Wang. 2006. Enhancement of thermal conductivity with Cu for nanofluids using chemical reduction method. *Int. J. Heat Mass Transfer* **49**: 3028–3033.

Lu, S. and H. Lin. 1996. Effective conductivity of composites containing aligned spheroidal inclusions of finite conductivity. *J. Appl. Phys*. **79**: 6761–6769.

Maxwell, J.C. 1891. *A Treatise on Electricity and Magnetism*, 3rd edn. Clarendon Press, Oxford. (1954 reprint, Dover, New York). pp. 435–441.

Özisik, M.N. 1993. *Heat Conduction*, 2nd edn. John Wiley & Sons, Inc, New York, Chichester, Brisbane, Toronto, Singapore.

Prasher, R., P. Bhattacharya, and P.E. Phelan. 2005. Thermal conductivity of nanoscale colloidal solutions (Nanofluids). *Phys. Rev. Lett*. **94**: 025901.

Putnam, S.A., D.G. Cahill, P.V. Braun, Z. Ge, and R.G. Shimmin. 2006. Thermal conductivity of nanoparticle suspensions. *J. Appl. Phys*. **99**: 084308.

Rusconi, R., E. Rodari, and R. Piazza. 2006. Optical measurements of the thermal properties of nanofluids. *Appl. Phys. Lett*. **89**: 261916.

Tzou, D.Y. 1997. *Macro-to-Microscale Heat Transfer: The Lagging Behavior*. Taylor & Francis, Washington, D.C.

Vadasz, J.J. and S. Govender. 2010. Thermal wave effects on heat transfer enhancement in nanofluids suspensions. *Int. J. Therm. Sci*. **49**: 235–242.

Vadasz, J.J., S. Govender, and P. Vadasz. 2005. Heat transfer enhancement in nanofluids suspensions: possible mechanisms and explanations. *Int. J. Heat Mass Transfer* **48**: 2673–2683.

Vadasz, P. 2005. Explicit conditions for local thermal equilibrium in porous media heat conduction. *Transport Porous Media* **59**: 341–355.

Vadasz, P. 2006. Heat conduction in nanofluid suspensions. *J. Heat Transfer* **128**: 465–477.

Vadasz, P. 2007. On the paradox of heat conduction in porous media subject to lack of local thermal equilibrium. *Int. J. Heat Mass Transfer* **50**: 4131–4140.

Vadasz, P. 2010. Rendering the transient hot wire experimental method for thermal conductivity estimation to two-phase systems—Theoretical leading order results. *J. Heat Transfer* **132**: 081601.

Vadasz, P. 2011. Heat transfer augmentation in nanofluids via nanofins. *Nanoscale Res. Lett*. **6**: 154.

Venerus, D.C., M.S. Kabadi, S. Lee, and V. Perez-Luna. 2006. Study of thermal transport in nanoparticle suspensions using forced Rayleigh scattering. *J. Appl. Phys*. **100**: 094310.

Wang, L. 2000. Solution structure of hyperbolic heat-conduction equation. *Int. J. Heat Mass Transfer* **43**: 365–373.

Wang, L. and M. Xu. 2002. Well-posedness of dual-phase-lagging heat conduction equation: higher dimensions. *Int. J. Heat Mass Transfer* **45**: 1065–1071.

Wang, L., M. Xu, and X. Zhou. 2001. Well-posedness and solution structure of dual-phase-lagging heat conduction. *Int. J. Heat Mass Transfer* **44**: 1659–1669.

Xu, M. and L. Wang. 2002. Thermal oscillation and resonance in dual-phase-lagging heat conduction. *Int. J. Heat Mass Transfer* **45**: 1055–1061.

Section V

Thermal Transport in Porous Media

16 Thermal Transport in Highly Porous Cellular Materials

Raymond Viskanta

CONTENTS

16.1 Introduction 535
16.2 Overview of Transport in Porous Materials 536
16.3 Local Thermal Equilibrium Model 537
16.3.1 Fluid Mechanical Characteristics 538
16.3.1.1 Permeability and Inertial Coefficient 538
16.3.1.2 Thermal Dispersion 539
16.3.2 Effective Thermal Conductivity 539
16.3.3 Radiative Transfer 540
16.3.4 Total (Equivalent) Conductivity 543
16.3.5 Applications 544
16.3.5.1 Foams as Thermal Insulants 544
16.3.5.2 Metallic and Ceramic Foams as Components 544
16.4 Local Thermal Nonequilibrium Model 545
16.4.1 Effective Thermal Conductivity 546
16.4.2 Radiative Transfer 547
16.4.3 Total (Equivalent) Conductivity 548
16.4.4 Volumetric Heat Transfer Coefficient 548
16.4.5 Applications 549
16.4.5.1 Compact Heat Exchangers 550
16.4.5.2 Gas Enthalpy–Radiation Converters 550
16.4.5.3 Solar to Thermal Energy Converters 551
16.4.5.4 Thermal Protection Systems 553
16.5 Concluding Remarks 553
Nomenclature 554
References 555

16.1 INTRODUCTION

Highly porous cellular materials and foams have many interesting combinations of physical, mechanical, electrical, and thermal properties such as high stiffness, thermal and electrical conductivity, and flow permeability along with low specific weight. The development of plastic, metallic, and ceramic highly porous materials [1–3] has enabled and improved the performance of aerospace, chemical, energy, industrial, thermal, and other technologies. Of primary interest in this discussion are cellular materials (foams) of high porosity($\phi > 0.8$) that are finding increased uses in thermal management applications such as thermal insulations [4], heat exchangers [5–7], solar energy collection and storage [8,9], hydrogen storage [10], wicks for heat pipes [11], energy conservation/waste heat recovery [12], burners for combustion enhancement [13,14], cooling systems [15], thermal control of electronics [16,17], thermal protection systems (TPS) [18], and many others. Foams have

high porosity, large surface area per unit volume, large heat transfer coefficient, and large radiation extinction coefficient and offer low-pressure drop for flow.

Cellular materials of interest here are primarily of two types: (1) closed-cell and (2) open-cell foams. Among the most common closed-cell foams are the expanded polystyrene (EPS) and polyurethane foams. The expanded foams consist only of walls, whereas extruded polystyrene (XPS) and polyurethane foams are formed by walls and struts. Open-cell carbon, metallic, and ceramic foams have a reticular structure. The bulk material is entirely concentrated on the cell sides shaping the struts. The solid matrix is made of struts oriented in different directions in space. The strut thickness is always much smaller than the cell diameter. Both closed-cell and open-cell foams have a wide range of uses [1–3], but this account is primarily concerned with thermal management applications.

Thermal design and operation of components and devices for modern technology that use cellular materials require both qualitative and quantitative knowledge of flow and heat transfer in such materials. The aim of the present overview is twofold: first, to briefly discuss the predictive models for describing the flow, thermal, and radiative processes in cellular porous materials and second, to apply the models for predicting heat transfer in different physical situations. The scope of this overview does not permit detailed discussion; hence, the main focus is to identify for the interested reader up-to-date references dealing with flow and heat transfer in closed-cell and open-cell foams from low to high temperatures. The discussion to follow is restricted to porous materials with random and not with regular structures and with submillimeter and/or larger mean pore (cell) diameters. The solid is inert, and there are no chemical reactions in the fluid; while phase change (i.e., boiling, condensation, solidification, and melting) of the fluid may be of interest for some applications [19], it is not considered in this account.

16.2 OVERVIEW OF TRANSPORT IN POROUS MATERIALS

For design analysis and optimization of transport phenomena in complex chemical, energy, and thermal technologies utilizing highly porous cellular materials, increasingly sophisticated computational modeling capabilities have been developed during the last few decades [20]. The complex phenomena include the transport of mass, momentum, and energy due diffusive and advective motion of the fluid, which are combined with conduction and radiation transport in the confining and embedded solids. The modeling of the relevant transport processes is accomplished on different levels of sophistication. In the analysis of flow through porous media, the model equations are fully derived from more rigorous formulations such as the Navier–Stokes equations by local volume averaging, homogenization, and/or simply from empirical observations. The pseudo-homogeneous approach requires that mean flow quantities be defined on a reasonably sized representative elementary volume [20–22]. The models may be applied if the scales of the system under consideration are significantly larger than the pore size of the porous media.

Transport processes in porous materials may be modeled using two major classes of approaches: (1) a macroscopic approach, where volume-averaged semiempirical equations are used to describe flow and transport characteristics, and (2) a microscopic approach, where small-scale flow and transport details are simulated by considering the specific geometry of the porous medium. In general, heat transfer in a porous material occurs by conduction, convection, and radiation, and the interactions of flow and the three modes of energy transport are illustrated schematically in Figure 16.1. If the cells of the porous material are closed, there will be no throughflow of the fluid, and if the cells are small in diameter, natural convection in the fluid contained in the cells can also be neglected.

Three different types of models have been proposed and are being used to analyze transport in porous materials. They include the following: (1) local thermal equilibrium (LTE) with a homogeneous single fluid and solid temperature (i.e., one-energy equation) model, (2) local thermal nonequilibrium model with separate fluid and solid temperatures (i.e., two-energy equation model), and (3) lattice Boltzmann model. The Boltzmann method is a powerful and sophisticated technique for the computational modeling of complex fluid flow problems, including single and multiphase flow in porous

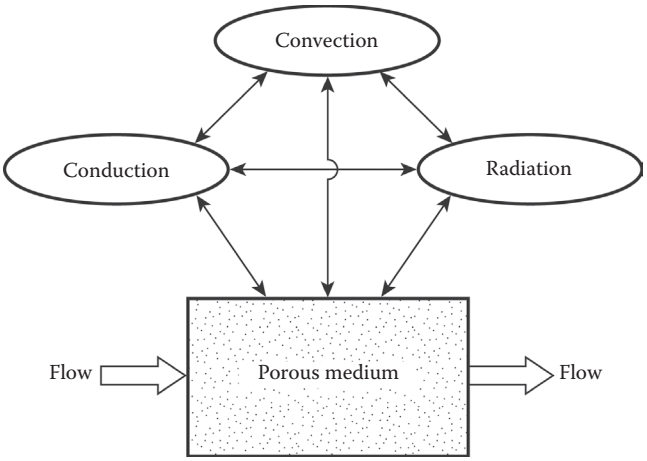

FIGURE 16.1 Interaction of flow and heat transfer in a porous medium.

materials of complex geometries. It is a discrete computational method based on the Boltzmann equation. The method has gained recently popularity in computational fluid dynamics [23,24], but it has also been recognized that the method is both computationally intensive and computer memory demanding.

The conservation equations of mass, momentum, and energy (fluid and solid phases) for porous media can be derived using a local volume–averaging technique [20], but the resulting equations contain a number of parameters that are difficult to calculate. Hence, in order to provide closure, these parameters must be determined experimentally or more recently computationally. For this reason, semiempirical (phenomenological) equations are used to describe flow and transport processes in porous media [20–22,25]. Numerous examples of applications are provided in the references cited.

16.3 LOCAL THERMAL EQUILIBRIUM MODEL

The LTE treatment (single-energy equation) model is the simplest volume-averaged approach used to describe flow and thermal characteristics in porous media. The small-scale flow details are ignored and the information so lost is represented in the governing equations using an engineering (phenomenological) model. If the fluid (gas or liquid) and the solid matrix are in local thermodynamic equilibrium, the one-energy equation (one-temperature) model for an isotropic porous medium becomes [20,21,25]:

Mass

$$\nabla \cdot \mathrm{v} = 0 \tag{16.1}$$

Momentum

$$\rho_f \left[\frac{\partial \mathbf{v}}{\partial t} + \left\{ \nabla \cdot \mathbf{v} \right\} / \phi \right] = -\nabla \rho + \mu_f \nabla^2 \mathbf{v} - \phi \left(\frac{\mu_f}{K} + \frac{\rho_f F}{\sqrt{K}} |\mathbf{v}| \right) \mathbf{v} \tag{16.2}$$

Energy

$$\rho c \frac{\partial T}{\partial t} + \left(\rho c_p \right)_f \mathbf{v} \cdot \nabla T = \nabla \cdot \left[\left(\underline{\underline{K}}_e + \underline{\underline{K}}_d \right) \nabla T) \right] - \nabla \cdot F \tag{16.3}$$

where

$$\rho c = \phi (\rho c_p)_f + (1 - \phi)(\rho c)_s. \tag{16.4}$$

In Equation 16.2, K is the permeability of the porous medium, and F is the Forchheimer (inertial) coefficient. In Equation 16.3, $\underline{\underline{K}}_e$ is the effective thermal conductivity (both due to conduction in the solid and fluid phases) tensor of the porous material, and $\underline{\underline{K}}_d$ is the thermal dispersion tensor. The second term on the right-hand side accounts for radiative transfer in the foam, with F being the radiative flux vector. The thermophysical characteristics of porous materials and the approximations for radiative transfer are discussed in the subsections to follow.

In physical situations where heat transfer between the fluid and solid phases is very effective (i.e., the temperature difference between the fluid and solid matrix is very small), the one-energy equation model is quite adequate, but when the temperature difference is significant, the model cannot describe accurately the temperature structure in porous media. Reference is made to the analytical study of Lee and Vafai [26] and citations therein for the assessment of the volume—averaged LTE model based on the solid and fluid temperature difference obtained from an non local thermal equilibrium (NLTE) model.

16.3.1 Fluid Mechanical Characteristics

For an anisotropic porous medium, the momentum equation, Equation 16.2, contains two parameters that must be determined experimentally or theoretically. The permeability is a second-order tensor with nine components [21], and F is the Forchheimer factor (inertial coefficient). If the foam is assumed to be isotropic, the permeability accounts for the interstitial surface area, the fluid particle path as it follows through the foam and other hydrodynamic characteristics of the material. The inertial coefficient describes the effects of the local aspects of the pore space morphology on momentum transport in the porous media.

Heat transport in porous media through which fluid is flowing consists of both advective and diffusive effects and is generally referred to as thermal dispersion. Thermal dispersion is the spreading of heat as a result of the simultaneous existence of temperature and velocity gradients within the pores. Due to the value averaging over the pore space, this contribution is not included in the Darcian convection. Owing to its dependence on the gradient of temperature fluctuation, this effect is accounted for in the energy equation, Equation 16.3, through the thermal dispersion conductivity tensor $\underline{\underline{K}}_d$ [21] included with the effective thermal conductivity $\underline{\underline{K}}_e$ (first term on the right-hand side of the equation).

16.3.1.1 Permeability and Inertial Coefficient

In the past, for open-cell foams, the permeability K has been determined experimentally [27], but more recently there have been some computational attempts [28]. Predicted permeability and friction factors have been compared with experimental data, and good agreement has been obtained using the nominal cell diameter as the characteristic length [29]. An extensive discussion of the past literature on the permeability and inertial coefficient of open-cell foams is available [29]. The experimental permeability and inertial coefficient data have been correlated using one of two characteristic lengths, namely, (1) the nominal cell diameter [27] or (2) the equivalent strut diameter of a cylinder [30]. A simple microstructure–based model for the permeability of open-pore microcellular materials has been proposed [31].

A comprehensive analytical and experimental investigation of permeability (K) and inertial coefficient (F) of high porosity metallic foams has been carried out [29]. A wide range of porosities and pore diameters have been investigated. The experimental results reveal that the permeability increases with the porosity and the cell (pore) diameter of the porous medium, while the inertial coefficient depends only on the porosity. Simple empirical correlations have been developed for both the permeability and the inertial coefficient and were shown to be in reasonable agreement with measured data. More recently, Kamiuto [30] compared available experimental data of several investigators for both K and F and developed simple empirical correlations in terms of the porosity

and the equivalent strut diameter. Additional research attention is needed to determine if the cell diameter or the equivalent strut diameter are more meaningful physically as correlating parameters for the permeability.

16.3.1.2 Thermal Dispersion

The tortuous flow path through a porous material promotes lateral and axial mixing when a fluid flows from one cell to the neighboring cells through the openings between cells. In the presence of temperature gradients in a porous material, the flow causes net energy transport called thermal dispersion. The available experimental results indicate that axial dispersion can be about three orders of magnitude greater than the lateral (radial) dispersion [30]. The dispersion cannot be separated from that of turbulence, and the experimentally determined dispersion coefficients involve both contributions. Thermal dispersion contributes (adds) to thermal conduction in the solid and fluid and thus generates what is called an effective thermal conductivity.

For open-cell porous materials, the thermal dispersion conductivity tensor becomes a second-rank tensor with zero off-diagonal elements and can be written as [30]

$$\underline{\underline{K}}_d = \mathbf{nn}k_{dl} + (\underline{\underline{I}} - \mathbf{nn})k_{da} \tag{16.5}$$

where

k_{dl} and k_{da} represent, respectively, the lateral and axial components of the diagonal term of $\underline{\underline{K}}_d$
n is the unit vector perpendicular to the flow direction

Kamiuto [30] has reviewed the state of knowledge of thermal dispersion in cellular and porous materials and concluded that the axial dispersion is about 1200 times greater than the lateral. He suggested the following empirical expression for the axial dispersion conductivity,

$$\frac{k_{da}}{k_f} = \gamma_{da}\,\mathrm{Pr}\left(\frac{u\sqrt{K}}{\nu_f}\right) = \gamma_{da}\,\mathrm{Pr}\,\mathrm{Re} \tag{16.6}$$

where γ_{da} is the axial dispersion coefficient and is given by

$$\gamma_{da} = 9.269 + 2{,}005.4(\phi - 0.8) - 16{,}330(\phi - 0.8)^2. \tag{16.7}$$

It should also be noted that the effects of turbulence cannot be separated from thermal dispersion in the experimentally measured thermal dispersion conductivities. As pointed out by Kamiuto and Yee [32], the experimentally determined dispersion coefficients for highly porous cellular materials include both contributions. Thermal dispersion has received limited attention [33,34], and the mechanisms of dispersion in highly porous foams are not fully understood and require future research.

16.3.2 Effective Thermal Conductivity

The effective thermal conductivity of an equivalent homogeneous closed-cell and open-cell porous medium can be expressed as a superposition of the contributions due to the fluid (gas) and solid conduction. Effective thermal conductivity models for plastic [4,35–38], metallic [36,39], and ceramic [36,39] cellular materials have been reviewed, and simple expressions that have been proposed are discussed. Effective thermal conductivity results of fluid-saturated foams have been reported for cubic, dodecahedral, and tetrakaidecahedral unit cell geometries illustrated in Figure 16.2.

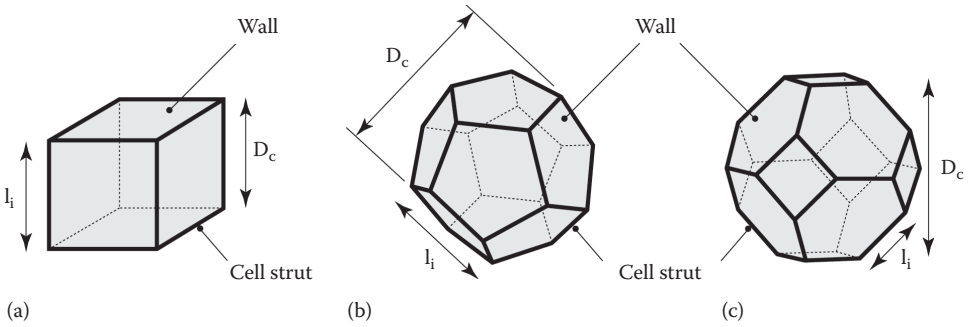

FIGURE 16.2 Models of cellular structure: (a) cube, (b) pentagon dodecahedron, and (c) tetrakaidecahedron.

The effective thermal conductivity of isotropic and anisotropic polymeric (polystyrene and polyurethane) foams has been discussed in detail by Glicksman [4]. Expressions for the combined struts and cell walls as well as for overall solid and gas conduction have been suggested. For high porosity foams ($\phi > 0.95$), a simple expression is recommended,

$$\frac{k_e}{k_f}\phi + (1-\phi)\left[\frac{(2-f_s)}{3}\right]\left(\frac{k_s}{k_f}\right) \tag{16.8}$$

where

f_s represents the fraction of the solid phase in the struts

k_s is the thermal conductivity of walls and strut

When the entire polymer is present in the struts, we have $f_s = 1$, while $f_s = 0$ when the entire polymer is in the walls.

The effective thermal conductivity (due to both fluid and solid) for low-density polymeric foams with anisotropic walls has also been determined and can be represented by [4]

$$\frac{k_e}{k_f} = \phi + \frac{1}{3}(1-\phi)\left[f_s\left(\frac{a}{b}\right)^{1/2} + 2(1-f_s)\left(\frac{a}{b}\right)^{1/4}\right]\left(\frac{k_s}{k_f}\right) \tag{16.9}$$

where a and b are the cell major and minor axis dimensions, respectively. According to the available results, the spheroidal and the elongated cube show a modest conductivity increase with a/b.

Probably the most detailed numerical investigation of conductive heat transfer in cellular (open-cell and closed-cell) materials has been carried out recently by Coquard and Baillis [37]. They reviewed a large number of empirical and semiempirical models that have been proposed to evaluate the effective thermal conductivity for different cellular morphologies. In order to estimate the reliability of these models, a finite volume method for numerical computation of the effective thermal conductivity has been developed. The conductivities computed numerically are noticeably different as none of the models predict faithfully the effect of the lumps of matter shown by the numerical model. The existing models do not seem to be reliable for open-cell materials.

16.3.3 Radiative Transfer

The importance of radiative transfer in porous materials particularly at elevated temperatures has been recognized [38,39], and different approaches for modeling radiation heat transfer in cellular materials has been developed. Suffice it to mention that a number of different approaches have been

suggested [40–42], and the needed radiation characteristics have been recently discussed [38,39,43]. Since porous cellular materials are sufficiently dense optically, here only the simplest treatment, that is, the Rosseland diffusion approximation, is briefly discussed.

For radiatively participating (absorbing and scattering) media such as porous materials that are relatively strong absorbers and scatterers and possess relatively high opacities, the Rosseland diffusion approximation is appropriate. Radiative transfer is treated as a diffusion process, analogous to heat conduction. In such case, the radiative flux (say, in the x direction) can be expressed as [40–42]

$$F_x = -k\frac{\partial T}{\partial x} = -\frac{16n^2\sigma T^3}{3\beta_R}\frac{\partial T}{\partial x} \tag{16.10}$$

where

n is the effective index of refraction (i.e., close to unity) for a highly porous medium

β_R is the Rosseland mean extinction coefficient defined as

$$\frac{1}{\beta_R} = \frac{1}{4\sigma T^3}\int_0^\infty \frac{1}{\beta_\lambda}\frac{\partial I_{b,\lambda}(T)}{\partial T}d\lambda \tag{16.11}$$

with β_λ being the spectral extinction (absorption plus scattering) coefficient, and $I_{b,\lambda}(T)$ is the Planck's function of black body radiation.

The early studies on the radiation characteristics of polymeric foams needed to evaluate the Rosseland mean extinction coefficient β_R have been reviewed by Glicksman [4]. For example, he has determined the extinction coefficient β_R of closed-cell polymeric foam to be given by

$$\beta_R = 4.10\left(\frac{f_s\rho_f}{\rho_s}\right)^{1/2}/D_c + \left[(1-f_S)\frac{\rho_f}{\rho_s}\right]\beta_s \tag{16.12}$$

where

D_c is the cell diameter

β_s is the extinction coefficient of the cell wall material

Note that β_R of a foam depends on multiple factors as well as the aging process. Thus, without the measurement of these physical parameters, thermophysical and radiation properties, it is difficult to compare the theoretical model predictions with experimental measurements.

The more recent experimental and theoretical studies on radiation properties of closed-cell polymeric foams have been discussed by Baillis et al. [43]. They compared the radiative conductivity of several XPS foams from Equations 16.10 and 16.11 computed by taking into account the radiation characteristics of struts and walls with the values computed from Equation 16.10 using Glicksman's Equation 16.12 for the Rosseland mean extinction coefficient. The results are shown in Figure 16.3, and significant differences are noted particularly at small cell diameters. For each cell diameter D_c, different strut volume fractions f_s (between 0% and 40%) were considered. According to the Rosseland diffusion approximation, the minimum radiative conductivity occurs for a cell diameter of about 140 μm.

A comparison of experimental data for the radiative conductivity of FeCrAlY metal foam based on the Rosseland diffusion approximation and the radiosity models has been made [44,45]. The radiosity model considers the metal foam to be an array of idealized representative

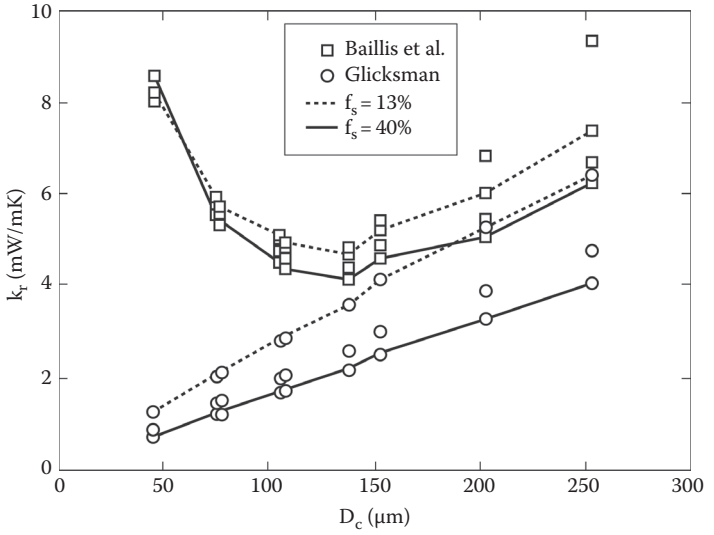

FIGURE 16.3 Comparison of radiative conductivities predicted by Baillis et al. [43] and Glicksman [4] using the Rosseland diffusion approximation for extruded polystyrene foams. (After Baillis, D. et al., *Spec. Top. Rev. Porous Media-An Int. J.*, 4, 111, 2013.)

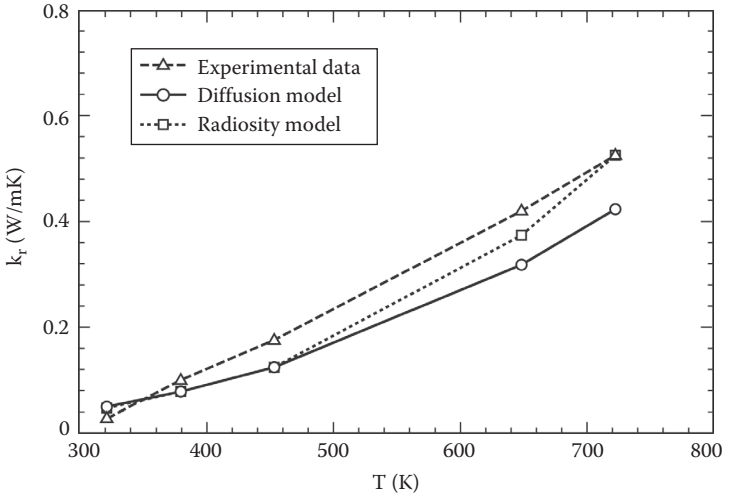

FIGURE 16.4 Comparison of model prediction with experimental data for metal (FeCrAlY) foam: 30 PPI (12.8 PPcm) with a 5% relative density.

cells, and the standard radiosity formulation [41,42] is employed to predict radiation heat transfer in a cell and adjacent cells in series. The walls of the cells are assumed to be opaque, diffuse, and gray. Figure 16.4 shows that the Rosseland diffusion and radiosity models are in good agreement with each other, but the radiation conductivity is somewhat under predicted for temperatures above 375 K. The discrepancy between the experimental data and the diffusion model predictions increases with an increase in temperature and becomes greater for 60 pores per inch (PPI) (not shown).

For metallic and ceramic foams, Coquard et al. [39] have deduced a simple expression for the radiative conductivity based on the Rosseland diffusion approximation that results in errors of less than 4% for a range of foams they studied. The effects of the structural parameters such as the cell diameter (D_c), porosity (ϕ), solid fraction ($1 - \phi$) of the solid phase, and the specularity parameter (sp) for reflection have been investigated and are presented for tetrakaidecahedron and dodecahedron cell models with and without struts junctures. The radiant conductivity based on the Rosseland diffusion approximation was found to be in excellent agreement with the values obtained by solving the radiative transfer equation using the discrete ordinates method [41,42].

16.3.4 Total (Equivalent) Conductivity

If it is postulated that there is no interaction between conduction and radiation, then taking each heat transfer mechanism separately, we can express the total apparent (equivalent, overall) thermal conductivity (k_t) due to solid and fluid conduction (k_e), thermal dispersion (k_d), and radiation (k_r) as

$$k_t = k_e + k_d + k_r \tag{16.13}$$

The total conductivity of a plastic foam depends on multiple factors such as ρ_f, ρ_s, D_c, f_s, ϕ, and a/b as indicated by Equation 16.9 as well as the aging process. The total conductivities with air and CFC-11-filled polymeric foams as a function of density have been reported [4]. The effect of gas and solid conduction and of radiation has been examined, and a simple semiempirical equation has been suggested. It was found that the contribution of radiation decreases as the density of gas filling the voids increases. Also, the total conductivities versus temperature of all air-filling voids were found to be higher than all CFC-11 filling the voids, because the thermal conductivity of air is higher than that of CFC-11.

Probably the most detailed study of combined heat transfer by conduction and radiation in closed-cell foams has been conducted by Coquard and Baillis [35]. They investigated heat transfer in low-density EPS foams by solving numerically the energy equation and took into account full coupling between conduction and radiation. They modeled structural characteristics of EPS foams such as foam density and cell diameter. The spectral radiation characteristics were modeled, and the radiative transfer equation [40–42] was solved using the discrete ordinates method. Detailed results showing the effects of foam density, mean cell diameter, mean bead diameter, and interbead porosity are reported for cubic and dodecahedral cell models. The evolution of the total thermal conductivity with the cell diameter (from about 100 to 300 μm) was found to decrease with the increase in the cell diameter for the two cell shapes considered (Figure 16.5). The effect of the mean cell diameter on the conductivity, with the density of the foam as a parameter, for both cubic and dodecahedral cells shows that the conductivity decreases with an increase in the mean cell diameter, and the optimum value depends on the foam density [35]. The results also show that foams with small cell diameters tend to enhance radiative heat transfer. The total (equivalent) thermal conductivities predicted were compared with available experimental data, and reasonably good correspondence has been obtained between the two theoretical models and the data.

Kamiuto [46] compared their theoretical model predictions for combined conduction and radiation heat transfer in cordierite and zirconia porous plates with experimental data. He found that the total (equivalent) thermal conductivities based on the exact formulation for radiative transfer and those based on the spherical harmonics P_1-approximation were in excellent agreement with each other.

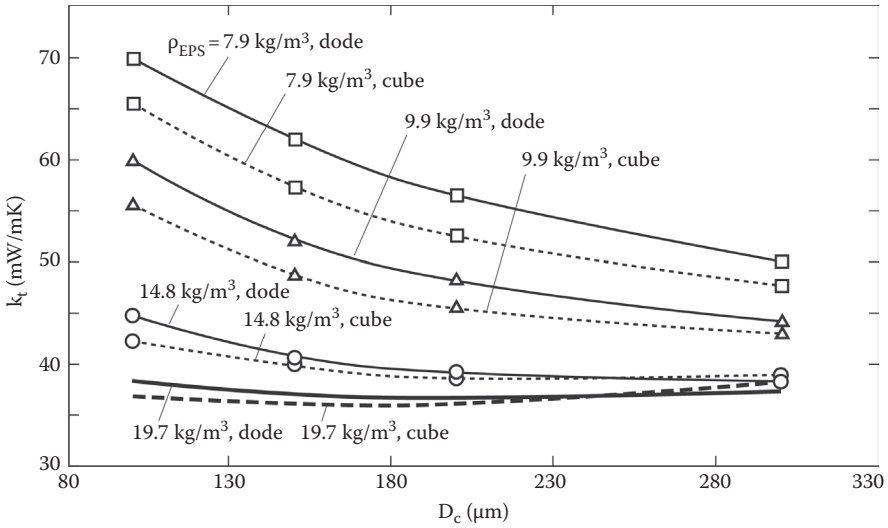

FIGURE 16.5 Evolution of the equivalent thermal conductivity of low-density EPS foams with the mean cell diameter for different densities. (After Coquard, R. and Baillis, D., *J. Heat Transfer*, 128, 538, 2006.)

16.3.5 Applications

16.3.5.1 Foams as Thermal Insulants

Rigid closed-cell polyurethane, EPS, and other foams are widely used as thermal insulants in buildings and industry due to their low-apparent thermal conductivity. They have been recognized all over the world as one of the most efficient insulation materials commercially available since their introduction. The foams are convenient to manipulate due to their mechanical properties (lightness and stiffness) and are relatively cheap and have good thermal performance.

Even at relatively low temperatures ($T < 300$ K), radiation heat transfer needs to be accounted for, and comprehensive discussions are available [4,35–39]. Reference is made to recent published accounts [18,19,31,35,36] for applications of highly porous cellular materials to the solution of numerous technological problems.

16.3.5.2 Metallic and Ceramic Foams as Components

Metallic, ceramic, and carbon foams exhibit thermal, mechanical, and heat transfer characteristics that make them potential candidates for many applications. For example, owing to their ability to integrate multiple functions, open-cell foams are very attractive as thermal management materials. Applications include heat exchangers [1,2,6] and heat sinks for cooling of electronics [16,17], for TPS [18], for solar energy absorbers/receivers [8,9], for supporting combustion of fossil fuels [14,15], and for many others.

Closed-cell metallic foams are being used for fire walls [47], and open-cell silicon carbide foams are being considered for high-temperature protection systems [48,49]. Even though the SiC foams are open-celled, Tseng et al. [48,49] ignored fluid flow and neglected convective heat transfer between the solid and fluid phases. They studied the effect of radiation on heat transfer in SiC foams at high temperature (up to 2000 K) and examined the effects of foam physical properties (density), number of PPI, carbon mass fraction, as well as other effects using the spherical harmonics P_1—approximation for radiative transfer [40–42]. Reasonably good correspondence has been found between the model predictions and reported test data as well as with their own measurements. As an illustration, the effect of temperature of the foam, with PPI as a parameter, is shown in Figure 16.6. Note that for the 20 PPI foam radiation starts to dominate the total (equivalent) thermal conductivity at about 800 K.

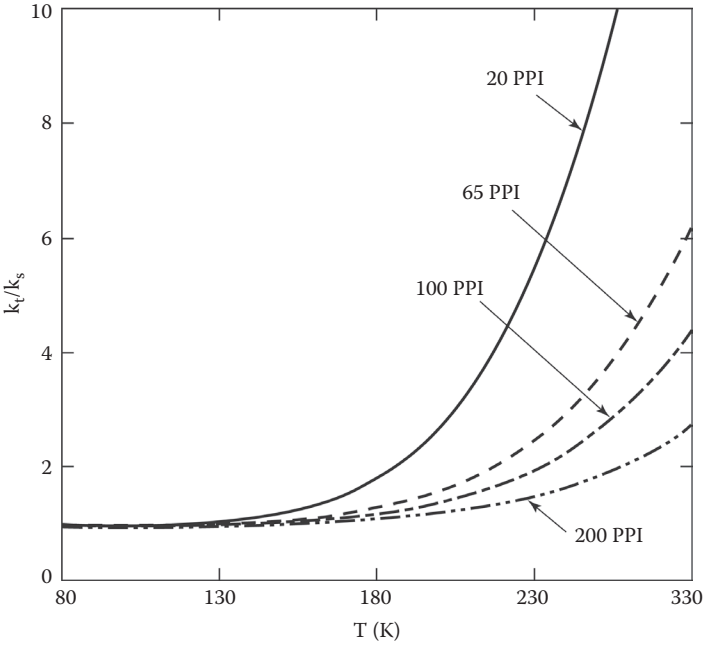

FIGURE 16.6 Effect of PPI on the dependence of the total (equivalent) thermal conductivity on temperature for 7.5% dense SiC foam. (After Tseng, C.C. et al., *High Temp. High Pressure*, 42, 387, 2013.)

16.4 LOCAL THERMAL NONEQUILIBRIUM MODEL

For the local thermal nonequilibrium treatment (two-energy equation) transport model in porous media, the mass and momentum conservation equations are the same as for the single-energy equation model. To correctly capture interface heat transfer between the fluid and solid, the control-volume-averaged energy equations are derived separately for the fluid and solid phases. The two equations are coupled through the volumetric heat transfer coefficient as a phenomenological parameter.

With forced flow in a uniform porosity medium, the effects of buoyancy, viscous heat dissipation, thermal expansion, and hydrodynamic dispersion are neglected. The volume-averaged conservation equations of mass, momentum, and energy can be written as [20,21,50]

Mass

$$\nabla \cdot \mathrm{v} = 0 \tag{16.14}$$

Momentum

$$\rho_f \left[\frac{\partial \mathrm{v}}{\partial t} + \left\{ \nabla \cdot \left(\mathbf{v} \right) \right\} / \phi \right] = -\nabla \rho + \mu_f \nabla^2 \mathbf{v} - \phi \left(\frac{\mu_f}{K} + \frac{\rho_f F}{\sqrt{K}} |\mathbf{v}| \right) \mathbf{v} \tag{16.15}$$

Fluid energy

$$\phi \left(\rho c_p \right)_f \frac{\partial T_f}{\partial t} + \left(\rho c_p \right)_f \mathbf{v} \cdot \nabla T_f = \nabla \cdot \left[\left(\underline{\underline{K}}_{cf} + \underline{\underline{K}}_{d} \right) \cdot \nabla T_f \right] - h_v \left(T_f - T_s \right) \tag{16.16}$$

Solid energy

$$(1-\phi)(\rho c)_s \frac{\partial T_s}{\partial t} = \nabla \cdot \left[\left(\underline{\underline{K}}_{cs} + \underline{\underline{K}}_d \right) \cdot \nabla T_s \right] - h_v (T_s - T_f) + \nabla \cdot F \tag{16.17}$$

The subscripts f and s refer to the fluid and solid phases, respectively. The thermophysical characteristics of the porous medium such as density, specific heat, and the effective thermal conductivity tensors $\underline{\underline{K}}_{cf}$ and $\underline{\underline{K}}_{cs}$ represent the effective thermal conductivity tensors for the fluid and solid phases, respectively. They refer to local volume-averaged quantities. In Equations 16.16 and 16.17, h_v is the volumetric heat transfer coefficient. This is the key parameter that couples the energy equation for the fluid to that of the solid and differentiates the single-energy equation model from the two-equation model. For mathematical closure, the boundary and initial conditions must also be specified.

The model equations, Equations 16.14 through 16.17, reveal a need as input a large number of empirical and/or semiempirical model parameters and include flow characteristics such as permeability K and Forchheimer factor F; effective thermal conductivity tensors $\underline{\underline{K}}_t$, $\underline{\underline{K}}_{cf}$, and $\underline{\underline{K}}_{cs}$ including thermal dispersion conductivity tensor $\underline{\underline{K}}_t$; and the volumetric heat transfer coefficient h_v. The radiation characteristics (extinction, absorption, and scattering) coefficients are needed to model radiative transfer. These parameters must be determined experimentally or predicted from theoretical models for different cellular porous materials and their geometrical structures. With the exception of the volumetric heat transfer coefficient h_v, these model parameters have already been discussed in the preceding section. In the past, this parameter has been determined experimentally, but more recently it has been calculated theoretically [28,51].

An extensive list references on flow and thermal characteristics in foams has been provided [7,19]. Some of the input data needed in the model and not yet discussed are highlighted in the following subsections. Probably the most comprehensive discussion of thermal transport and radiation characteristics of highly porous cellular materials has been reported by Kamiuto [30] who reviewed the past experimental and theoretical work and suggested correlations for all the model input parameters.

For open-cell foams, the experimental fluid flow data have been correlated using either one of two characteristic lengths: (1) the nominal cell diameter D_c [26,30] or (2) the equivalent strut diameter of cylinder D_s [31,32]. A brief discussion of the past literature of fluid mechanical characteristics of open-cell foams has been provided in Section 16.3.1. Suffice it to mention that semiempirical expressions for the permeability K and the Forchheimer (inertial) factor F have been compared with their own experimental data. More recently, Kamiuto [30] has developed empirical correlations for both K and F and obtained reasonably good agreement between the correlations and the experimental results with his own data as well as those of others.

16.4.1 Effective Thermal Conductivity

For anisotropic porous media, the effective thermal conductivities are second-rank tensors, but for isotropic porous materials such as open-cell foams, the effective thermal conductivities can be represented in terms of the scalar quantities (i.e., the thermal conductivities of the fluid, solid, and porous medium) and a unit tensor. Extensive reviews of the effective thermal conductivity models for open-cell metallic, carbon, and ceramic foams are available [36,38,39,51]. The models of Coquard et al. [39] reveal that open-cell foams in which the large part of the solid phase is concentrated in the cell vortices of cells exhibit the lowest effective conductivities. They proposed a simple but accurate analytical model, in which the only parameters are the fraction of the solid phase, its distribution between struts and lumps, the shape of the lumps, and the thermal

conductivities of the fluid and solid phases. The effective thermal conductivity was well fitted by the equation of the form

$$\frac{k_e}{k_s} = \frac{k_f}{k_s} + \alpha_{D/d}(1-\phi) + \chi_{D/d}(1-\phi)^2 \tag{16.18}$$

where $\chi_{D/d}$ and $\alpha_{D/d}$ are correlation coefficients that depend on the ratio of D/d only or on D/d and k_s/k_f [39]. They applied the effective thermal conductivity model, Equation 16.18, to different foams that have been studied experimentally by previous researchers. Specifically, they predicted the effective thermal conductivity for Al foams with $\phi > 0.85$ under vacuum, air at atmospheric pressure, and water at ambient temperature. They also obtained good agreement between the model predictions and their own experimental data for NiCrAl, FeCrAl, ZrO_2, and mullite at temperatures up to 673 K.

16.4.2 Radiative Transfer

It is beyond the scope of this brief account to discuss radiative transfer and/or the radiation characteristics needed for analyzing thermal radiative transfer in porous media. Reference is made to Baillis and coworkers [36–39,43] for recent comprehensive discussions of the theoretical and experimental approaches and results for the radiation characteristics of foams. The continuum approach is discussed here briefly because it is consistent with the approach for treating the flow and heat transfer in porous media (see Equations 16.14 through 16.17). The spectral absorption and scattering coefficients as well as the single scattering albedo are required as input in the solution of the radiative transfer or the radiant energy conservation equations. Such detailed data are typically not available for porous materials [36–38,43,52–58] and usually mean (spectrum averaged) values are used in the calculations [52]. The spectral absorption and extinction coefficient data for metallic and ceramic foams are rather limited and analyses are typically performed on a gray basis.

A number of attempts have been made to model the radiation characteristics of complex open-cellular structures by assuming the cell geometry [36,43]. Probably, the simplest semiempirical model for the radiation characteristics of open-cell porous materials is due to Hsu and Howell [57]. According to the model, the absorption (κ), scattering (σ), and extinction (β) coefficients are given by very simple algebraic equations in terms of the cell diameter(D_c), the emissivity of the solid phase (ε), (assumed to be opaque to radiation), and the porosity (ϕ). Comparison of experimental data with predictions based on the geometrical optics theory reveals that the theory under predicts the extinction coefficient.

Kamiuto [58] has developed analytical expressions for the radiation characteristics of open-cell porous media by decomposing a unit cell into two cylindrical struts and one strut juncture. He applied geometrical optics and diffraction theories to these scatters by assuming that they are randomly oriented in space. Extinction coefficients predicted by the model agree with experimental results to within accuracy of ±25% [30]. Comparisons of theoretical predictions for the spectral single scattering albedo ($\omega_\lambda = \sigma_\lambda/\beta_\lambda$) with corresponding experimental data reveal that the theoretical model under predicts the data. This may be due to the fact that the model does not take into account of the surface condition of the material such as the roughness and/or composition.

The radiative conductivities for open-cell foams for both decahedron and tetrakaidecahedron cell models have been computed and negligible difference was found between results for metal and ceramic foams based on the Rosseland diffusion approximation and discrete ordinates method for solving the radiative transfer equation [39]. Based on the computational results obtained, empirical expressions have been deduced for the radiative conductivity, $k_r(\phi, D_c, \rho, T, sp)$, where ρ is the reflectivity and sp is the specularity factor. When strut junctures are present, the radiative conductivity k_r

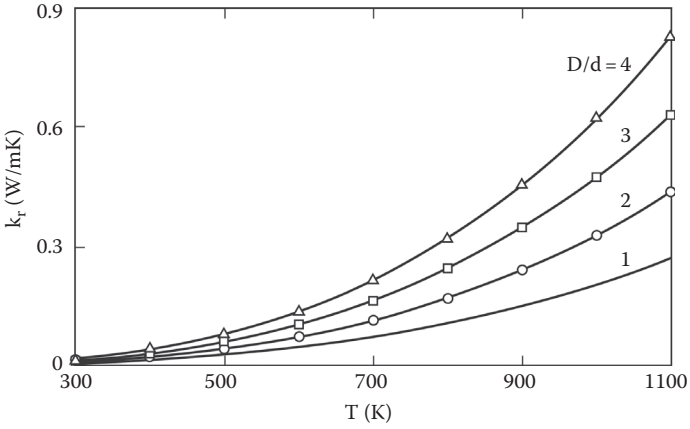

FIGURE 16.7 Influence of the temperature on the radiative conductivity of a foam: tetrakaidecahedron cell model with $\phi = 0.9$, $D_c = 1$ mm, $\rho = 1.0$ and sp = 0. (After Coquard, R. et al., *Spec. Issue Fire Technol. Mater. Fire*, 699, 2012.)

becomes also a function of the structural parameter, D/d, that is, the ratio of the characteristic size of the lumps D and the thickness (diameter) of the cell struts d. When struts junctures are present, no direct relations between k_r and the parameters listed earlier could be obtained. Observe that the magnitude of radiation heat transfer increases almost linearly with the ratio D/d (Figure 16.7). Note also that k_r is strongly dependent on the temperature of the foam.

16.4.3 Total (Equivalent) Conductivity

Coupled conduction and radiation heat transfer in open-cell metallic ceramic foams has been studied experimentally [59], and measured total conductivities of steel alloy FrCrAl foams in the temperature range between 300 and 800 K have been reported at both vacuum and atmospheric conditions. They found that the total conductivity can be three times higher at 800 K than at room temperature.

More recently, Coquard et al. [60] studied combined conduction and radiation heat transfer in metallic and ceramic foams at temperatures between 293 and 673 K. The results for several NiCrAl, FeCrAl, PsZ, and mullite foams showed that for metallic foams, the conduction contribution increases with temperature due to the increase of the thermal conductivity, but it remains practically unchanged for ceramic foams. The results also show that for low-density metal foams with large cell diameters, the relative contribution of radiation heat transfer can vary from 10% at ambient temperature to more than 60% at 673 K. As expected, comparison of the results show that larger cell size enhances radiation heat transfer and larger solid fraction increases conduction. The cell size has no influence on conduction, and the solid fraction has no influence on radiation. These findings are consistent with the results of Zhao et al. [59] and the theoretical models of Coquard et al. [39,60].

If the foam can be treated as isotropic and the interaction of, say, conduction and radiation can be neglected, then the total (equivalent) conductivity of open-cell foams can be expressed as a simple sum of conductive (k_e), thermal dispersive (k_d), and radiative (k_r) contributions as in Equation 16.13.

16.4.4 Volumetric Heat Transfer Coefficient

The volumetric heat transfer coefficient h_v couples the energy equation for the fluid, Equation 16.16, to the energy equation for the solid matrix, Equation 16.17. The available data have been discussed [30,61]. The past studies have been primarily experimental; however, some theoretical studies have been recently published presenting methods for calculating the volumetric heat transfer

coefficient [28,51]. The intricate geometry of the porous structure is accounted for, and flow and heat transfer through the structure is computed. The approach is computationally expensive if the entire physical domain were to be simulated. However, the computational time can be reduced by exploiting periodicity where periodicity can be justified.

Examination of experimental data reveals that there is no unique characteristic length for scaling the relevant dimensionless parameters [61–65]. For example, Younis and Viskanta [63] correlated their experimental data for ceramic foams in terms of the mean cell diameter and the thickness of the specimen tested, while Hamaguchi et al. [65] adopted the strut diameter as characteristic length for the relevant dimensionless parameters (Reynolds and Nusselt numbers). Kamiuto and Yee [66] examined the various characteristic lengths for correlating the experimental data and recommended use of the equivalent strut diameter $D_s (= 2D_c w/\sqrt{\pi})$, with D_c being the average diameter of the cell and w, the dimensionless width of the strut. Fu et al. [64] correlated their experimental heat transfer coefficient data for four different ceramic foams by the empirical equation,

$$\mathrm{Nu}_v = \frac{h_v D_c^2}{k_f} = \left[0.06 + 1.74\left(\frac{D_c}{L}\right)\right] \mathrm{Re}_{D_c}\,\mathrm{Pr} \tag{16.19}$$

The correlation is valid for $L/D_c = 5.55 - 22.2$ and $\mathrm{Re}_{D_c}\,\mathrm{Pr} = 1.42 - 591$. The experimental data are within ±20% bands for $\mathrm{Re}_{D_c}\,\mathrm{Pr} > 35$ [64]. There is a reasonably good correspondence between the results of Kamiuto and Yee [66] and Equation 16.19 for specific values of the experimental parameters, but there is a lack of agreement between the correlations developed [64,66] for the choice of the characteristic length in defining the Nusselt number. This suggests a need for more fundamental research attention to establish interfacial heat transfer coefficient correlations, particularly the choice of proper characteristics length(s) for generalizing the experimental data.

More recently, Nakayama et al. [62] reviewed available experimental data on interstitial heat transfer of low-density foams. The results revealed that the volumetric Nusselt number Nu_v is sensitive to the porosity but is fairly insensitive to other factors. They developed a correlation that covers a wide range of available experimental data,

$$\mathrm{Nu}_v = \frac{h_v D_c^2}{k_f} = 0.07\left(\frac{\phi}{1-\phi}\right)^{2/3}\left(\frac{u_m D_c}{\nu}\right)\mathrm{Pr}, \tag{16.20}$$

for the range of parameters: $0.7 < \phi < 0.95$, $3 < u_m D_c/\nu < 1000$. The Nu_v values calculated from Equation 16.20 are very close to those of Fu et al. [64] obtained from empirical equations for mullite ($\phi = 0.916$) and cordierite ($\phi = 0.742$) ceramic foams. Note, however, that Equation 16.20 does not account for the relative thickness L/D_c of the foam as is indicated in Equation 16.19. Note also that Equations 16.19 and 16.20 as well as others reported in the literature cited have neglected to account for interaction between convection and radiation as they are based on low-temperature experimental data when radiation heat transfer is negligible in comparison to convection.

16.4.5 Applications

Ceramic, metallic, silicon carbide, and other open-cell foams are lightweight porous materials that are used for structural, thermal, acoustic, and other engineering applications. Here, we specifically focus on the use of foams for thermal purposes. Open-cell porous materials consisting of continuous solid and gas phases are being widely used for fire barriers [39,47], porous radiant barriers [13,14,40], gas enthalpy–radiation converters [12], TPS for hypersonic vehicles [18], transpiration cooling [31], compact heat exchangers [6,7], heat sinks for power electronics and electronics cooling [7,17,67], heat pipes [7,19], and many others. For example, metallic foams have found application

in compact heat exchangers, matrix for absorption and desorption, catalytic reactors for biodiesel or steam reformers for fuel cells, wicks for heat pipes and vapor chambers, and others [7,19]. A few specific applications are discussed in greater detail in the next few subsections.

16.4.5.1 Compact Heat Exchangers

Open-cell metallic foams are lightweight, offer large surface area per unit volume, and make attractive heat compact heat exchangers for applications where high efficiency in heat dissipation is demanded, that is, heat sinks for high-power electronic devices and many others. Different types of metal foam heat exchangers have been discussed, and an array of applications have been identified [7,19]. The applications range from fuel cells, high heat load removal systems, metal heat sinks for electronics cooling, solar energy absorbers/heaters, heat pipes, air-cooled condenser towers and cooling systems, and metal foam tube channel heat exchangers. Microstructure-based correlations for flow and heat transfer in metal foam heat exchangers have been assessed, and performance factors for tube and channel heat exchangers have been compared [5,68,69]. The results indicate considerable improvement in heat transfer performance by inserting the metal foam with a rather modest increase in pressure drop.

In the basic studies and applications reported in the literature, the interaction between convection and radiation has been neglected, and convection heat transfer at, say, a channel wall, has been calculated by assuming that the two transport processes are independent of each other. A theoretical study of forced convection and radiation heat transfer in a channel occupied by a saturated cellular porous medium has been studied [70]. In the analysis conduction, conduction and radiation heat transfer has been accounted for, and the Rosseland diffusion approximation has been used for radiative transfer. Analytical closed-form and numerical solutions are reported for the Nusselt number when the channel wall is either heated or cooled. The Nusselt numbers based on the total (combined convection and radiation) wall heat flux show that the interaction between convection and radiation can significantly affect the wall Nusselt number.

Metal foams with high thermal conductivity, large surface area-to-volume ratio, and tortuous coolant flow path are preferred in the design of compact, high-performance heat exchangers and heat sinks. Use of metal foams in heat exchangers for thermal management requires not only good heat transfer performance but also reduction of the pumping power. For the two parameters, heat transfer performance and pressure drop, one has to optimize the conditions in terms of geometry and flow conditions to obtain the best performance.

16.4.5.2 Gas Enthalpy–Radiation Converters

In many high-temperature technologies, it is often desirable to recover as much as possible of the residual energy in the exhaust gases. In order to achieve this goal, Echigo [12,71] has proposed an innovative idea of placing high-porosity media normal to the flow direction to recapture some of the energy in a form of directed thermal radiation that could be used in processing/heating of materials. In the scheme, the hot waste gas stream and the radiation incident on the porous medium are partially absorbed and converted to raise the temperature of the solid matrix, which in turn radiates energy in both upstream and downstream directions. Through this process, the gas temperature downstream of the porous material becomes lower than in the incoming stream. The converter concept and processes are indicated schematically in Figure 16.8.

The fundamental heat transfer processes occurring in the converter have received and continue to receive considerable theoretical [72] and experimental [73] research attention. Both Ni–Cr [74,75] and Ni–Cr–Al [74] open-cell porous plates have been used in the experiments, and both single [74,75] and multiple (two and three) [75,76] layers were employed. Radiative transfer in the cellular material was treated using the spherical harmonics P_1-approximation. Good agreement has been reported between the model predictions and experimental data, thus establishing the idea. The enthalpy–radiation conversion concept has been successfully applied for improving energy efficiency of reformers, metallurgical furnaces, and ceramic radiant tubes for lean combustion

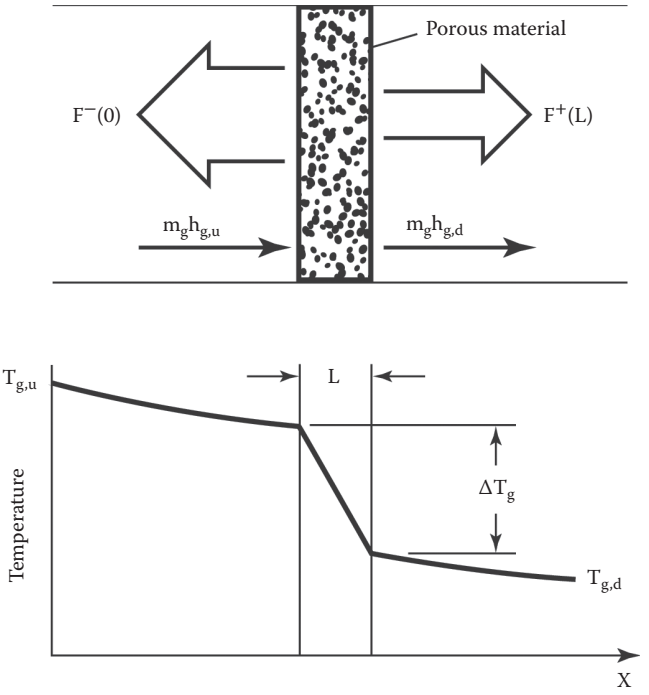

FIGURE 16.8 Schematic diagram of the gas enthalpy-to-radiation converter. ($T_{g,u}$ and $T_{g,u}$ are the upstream and downstream gas temperatures, respectively, m_g is the gas flow rate, and $h_{g,n}$ and $h_{g,d}$ are the upstream and downstream enthalpies, respectively.)

enhancement [12]. However, design hints on effective use of the converter have not yet been fully elucidated due to the lack of more complete understanding and of predictive model for enthalpy–radiation converter utilizing ceramic and metallic highly porous materials.

16.4.5.3 Solar to Thermal Energy Converters

A description of the various solar energy converters is available [77], and suggestions for future research on solar energy conversion systems and applications have been made [78]. Basically, there are two methods for capturing and converting solar energy to thermal energy of a working fluid: (1) direct and (2) indirect (i.e., through an intermediary absorber). In the direct approach, solar energy is absorbed in the working fluid such as a liquid with chromosphere combinations, gas-containing particles, and molten salts.

In the indirect conversion scheme, solar radiation is first absorbed by a solid and converted to heat that is then transferred to the working fluid [77]. Porous materials have been proposed for use as volumetric absorbers of solar radiation [8,9,79,80]. This approach is indicated schematically in Figure 16.9 and shows a solar radiation flux F_s incident on an open-cell foam through which a fluid (say, air) is transpired in the opposite direction. Figure 16.10 illustrates the effect of the Reynolds number (based on the cell diameter) and reveals that a 1 cm thick foam layer is not sufficiently opaque to absorb the incident solar radiation. Silicon carbide is more effective than cordierite or metal for converting solar radiation to thermal energy of an air stream. This is owing primarily to the radiation characteristics of the foams. The results indicate that a thicker metal foam would be needed to increase the conversion efficiency and would result in a greater pressure drop across the foam.

Fend et al. [8] have carried out an experimental study employing a double layer of foam materials of different cell density for converting solar-to-thermal energy. The experimental results showed that the performance of the double layer silicon carbide metal foam was better compared to a single

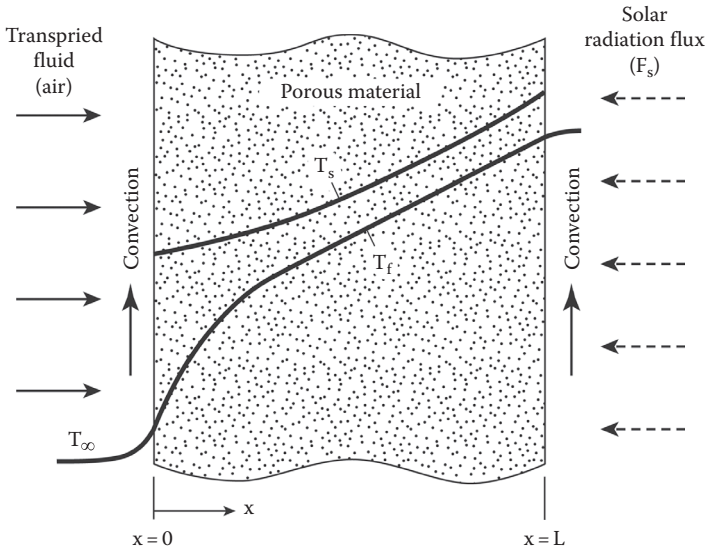

FIGURE 16.9 Schematic of a physical system for solar energy-to-thermal energy conversion using a porous cellular material.

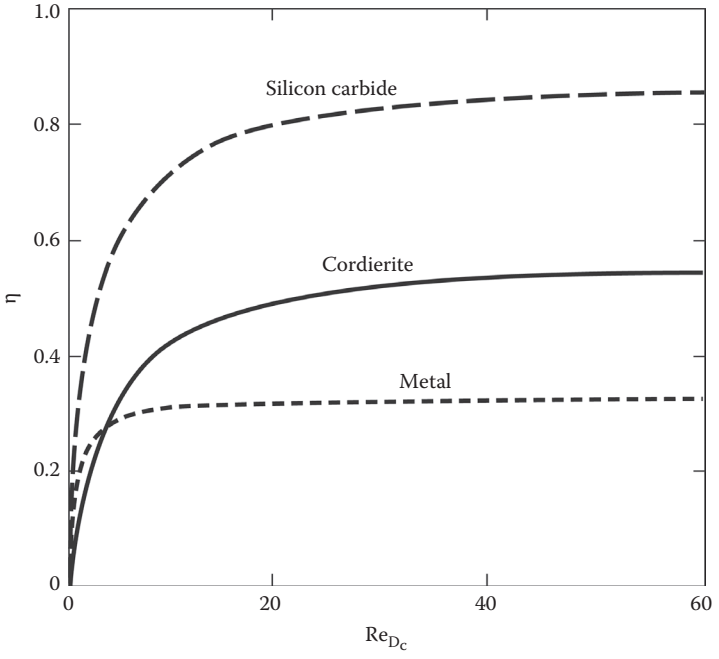

FIGURE 16.10 Comparison of solar-to-thermal conversion efficiencies for metal, cordierite, and silicon foam layers: L = 1.0 cm, 5.5 pores/cm and F_s = 10 kW/m^2.

layered material. Albanakis et al. [9] used a variety of foams as receivers of concentrated solar radiation, but they presented pressure drop and heat transfer results only for Inconel and nickel having porosities of 93% and 92%, respectively.

A theoretical study of combined conduction, convection, and radiation in Ni–Cr and cordierite–alumina plates heated by an external thermal radiation source has been carried out by Kamiuto [30].

He used the spherical harmonics P_1-approximation to model radiative transfer. The model predictions for different PPI foams were compared with available experimental data and found that the Ni–Cr plates resulted in a higher radiation-to-thermal-energy conversion efficiency (~80%) than for the cordierite–aluminum (~60%) plates. This was attributed to the lower effective reflectance of the former plates.

16.4.5.4 Thermal Protection Systems

Different passive and active cooling technologies for protecting critical engineering components (i.e., gas turbine blades), hypersonic aircraft during flight, spacecraft reentering the atmosphere, and others from high convective and/or radiative heat loads are by now over 50 years old. Many different TPS have been developed, are under development, or are being considered. Often in many of the integrated TPS, porous materials are included as components of such systems designs because cellular materials have low thermal conductivity and low density [18,48,49,81–85]. Reference is made to the cited literature for details and a variety of applications. Here, we only discuss a single combined theoretical and experimental study concerned with transpiration cooling of cellular materials.

A fundamental experimental and theoretical study of heat transfer in irradiated (nickel–chromium and cordierite–alumina) plates and transpiration cooled has been carried out by Kamiuto et al. [86]. In the experimental setup, the highly porous ($\phi > 0.89$) plates were irradiated from high-temperature infrared lamps, and incident radiation fluxes were varied from 5.25 to 22.2 kW/m^2. Radiative transfer analysis in the highly porous cellular materials was carried out using the spherical harmonics P_1-approximation. The measured air (fluid) and the irradiated porous materials surface temperatures were measured and compared with the theoretical predictions. The results show that an optical thickness of about five (5) or greater is needed to effectively absorb the incident radiation and shield an open-cell ceramic plate from external radiation.

16.5 CONCLUDING REMARKS

During the last few decades, technology has been developed to produce plastic, metallic, and ceramic materials that have highly porous cellular random structures. Cellular materials comprise a wide range of different arrangements and forms of the structures. The combination of specific mechanical and physical properties makes cellular materials particularly suitable for potential multifunctional applications in the future.

Assessment of the LTE (one-energy equation) model for transport in cellular porous media has shown that it is quite adequate for engineering applications when the volumetric convective heat transfer between the fluid and the solid phases is effective (i.e., the temperature difference between the two phases is small). But, thermal dispersion needs to be accounted for since it is generally recognized that axial dispersion depends on the Reynolds (Peclet) number. To the best knowledge of the author, models for thermal dispersion for flow (including turbulence) and heat transfer in cellular porous materials have not been developed.

The LNTE (two-energy equation) model is attractive for simulating thermal energy transport in highly porous cellular materials. The model requires introduction of time and length scale constraints that are based on physical microstructural parameters (i.e., pore geometry, cell size, porosity) that control flow and heat transfer processes in the inert porous medium. In spite of the fact that some of the model parameters are not well established, significant progress has been made in simulating heat transfer in cellular materials at both low and high temperatures and is amply documented in the published literature. A number of important issues needing research attention have been identified in the body of this chapter.

Porous cellular materials of technological interest have typically large enough opacities such that the Rosseland diffusion or the spherical harmonics P_1-approximation is sufficiently accurate for predicting radiative transfer, particularly when taking into account the uncertainty of the physical and radiation characteristics of the foams.

The solid matrix limits access to optical and mechanical probes for experimental measurements of flow and temperature in porous materials. This presents a great challenge and identifies the need for experimental and theoretical research of transport phenomena for determination of thermophysical, transport, and radiation characteristics of cellular porous media. The lack of reliable characteristics leads to discrepancies between model predictions and experimental data that need to be overcome in the future.

NOMENCLATURE

c	Specific heat
c_p	Specific heat at constant pressure
D_c	Cell diameter (see Figure 16.2)
d	Diameter of pore or of particle
F	Forchheimer (inercial) factor
$\mathscr{I}_x$	Radiative flux in the x-direction
$\mathscr{I}$	Radiation flux vector
f	Fraction
h	Enthalpy or convective heat transfer coefficient
h_v	Volumetric heat transfer coefficient
K	Permeability of porous medium
$\underline{\underline{K}}$	Thermal conductivity tensor
k	Thermal conductivity
L	Thickness
Nu	Nusselt number
p	Pressure
Pr	Prandtl number
Re	Reynolds number
T	Temperature
u	Velocity in the x-direction
v	Velocity vector

Greek Symbols

β	Extinction coefficient (-k+)
ε	Emissivity
κ	Absorption coefficient
μ	Dynamic viscosity
ν	Kinematic viscosity
ρ	Density
σ	Scattering coefficient or Stefan-Boltzmann constant
ϕ	Porosity

Subscripts

cf	Refers to fluid conduction
cs	Refers to conduction solid conduction
d	Refers to dispersion
e	Refers to effective
f	Refers to fluid
r	Refers to radiation
s	Refers to solid or strut
t	Refers to total (equivalent)

REFERENCES

1. L. Gibson and M.J. Ashby. *Cellular Solids*. Cambridge, U.K.: Cambridge University Press, 1999.
2. M. Scheffler and P. Colombo (Eds.). *Cellular Ceramics*. Weinheim, Germany: Wiley-VCH Verlag GmbH, 2005.
3. A. Öchsner, G.E. Murch, and M.J.S. de Lemos (Eds.). *Cellular and Porous Materials: Thermal Properties Simulation and Prediction.* Weinheim, Germany: Wiley-VCH Verlag GmbH, 2008.
4. L.R. Glicksman. Heat transfer in foams. In: N.C. Hilyard and A. Cunningham (Eds.), *Low Density Cellular Plastics, Physical Basis of Behavior.* London, U.K.: Chapman & Hall, 1994, pp. 104–150.
5. S.Y. Kim, J.W. Paek, and B.H. Kang. Flow and heat transfer correlations for porous fin in a plate-fin heat exchangers. *J. Heat Transfer* 122:572–578, 2000.
6. K. Boomsma, D. Poulikakos, and F. Zwick. Metal foams as compact high performance heat exchangers. *Mech. Mater*. 35:1161–1176, 2003.
7. S. Mahjoob and K. Vafai. A synthesis of fluid and thermal transport models for metal foam heat exchangers. *Int. J. Heat Mass Transfer* 51:3701–3711, 2008.
8. T. Fend, B. Hoffschmidt, R. Pitz-Paul, O. Reutter, and R. Rietbrock. Porous materials as open volumetric solar receivers: Experimental determination of thermophysical and heat transfer properties. *Energy* 29:823–833, 2004.
9. C. Albanakis, D. Missiris, N. Michailidis, K. Yakintos, A. Goulas, H. Omar, D. Tsipos, and B. Granier. Experimental analysis of the pressure drop and heat transfer through metal foams used as volumetric receivers under concentrated solar radiation. *Exp. Therm. Fluid Sci*. 33:246–252, 2009.
10. S. Mellouli, H. Dhaou, F. Askri, A. Jemni, and S. Ben Nasrallah. Hydrogen storage in metal hydride tanks equipped with metal foam heat exchanger. *Int. J. Hydrogen Energ.* 34:9393–9401, 2009.
11. P.D. Dunn and D.A. Reay. The heat pipe. *Phys. Technol*. 4:187–201, 1973.
12. R. Echigo. Sophisticated applications of radiation heat transfer. In: W.-J. Wang and Y. Mori (Eds.), *Heat Transfer in High, Temperature Technology and Power Engineering*. Washington, DC: Hemisphere Publishing, 1987, pp. 503–514.
13. S. Wood and A.T. Harris. Porous burners for lean-burn applications. *Prog. Energ. Combust. Sci*. 34:667–684, 2008.
14. R. Viskanta. Modeling of combustion in porous inert media. *Spec. Top. Rev. Porous Media Int. J.* 2:181–204, 2011.
15. S. Ebara, S. Toda, and H. Hashizume. Application of porous matrix to high heat load removal system. *Heat Mass Transfer* 36:273–276, 2000.
16. R. Rachedie and S. Chikh. Enhancement of electronic cooling by insertion of foam materials. *Heat Mass Transfer* 37:371–378, 2001.
17. A. Bhattacharya and R.L. Mahajan. Finned metal foam heat sinks for electronics cooling in forced convection. *J. Elect. Packag*. 124:155–163, 2002.
18. D.E. Glass. Ceramic matrix composite (CMC) thermal protection systems (TPS) and hot structures for hypersonic vehicles. Paper AIAA-1008-2682, Washington, DC: AIAA, 2008.
19. C.Y. Zhao. Review of thermal transport in high porosity cellular metal foams with open cells. *Int. J. Heat Mass Transfer* 55:3618–3632, 2012.
20. S. Whitaker. *The Method of Volume Averaging*. Dordrecht, the Netherlands: Kluwer, 1999.
21. M. Kaviany. *Principles of Heat Transfer in Porous Media*, 2nd edn. Berlin, Germany: Springer Verlag, 1999.
22. K. Vafai (Ed.). *Handbook of Porous Media*, 2nd edn. New York: Taylor & Francis, 2004.
23. S. Chen and G.D. Doolen. Lattice Boltzmann method for fluid flows. *Ann. Rev. Fluid Mech*. 30:329–364, 1998.
24. S. Succi. *The Lattice Boltzmann Equation for Fluid Dynamics and Beyond*. New York: Oxford University Press, 2001.
25. C.L. Tien and K. Vafai. Convective and radiative heat transfer in porous media. In: J.W. Hutchinson and T.Y. Wu (Eds.), *Advances in Applied Mechanics*. San Diego, CA: Academic Press, 1990, Vol. 27, pp. 225–281.
26. D.Y. Lee and K.Vafai. Analytical characterization and conceptual assessment of solid and fluid temperature differentials in porous media. *Int. J. Heat Mass Transfer* 42:423–435, 1999.
27. J.P. DuPlesis, A. Montilet, J. Comiti, and J. Legrand. Pressure drop prediction for flow through high porosity metallic foams. *Chem. Eng. Sci*. 17:3545–3553, 1994.
28. S.R. Annaprogada, J. Murthy, and S. Garimella. Permeability and transport in compressed open-celled foams. *Num. Heat Transfer Fundamentals* 54:1–22, 2008.

29. A. Bhattacharya, V.V. Calmidi, and R.L. Mahajan. Thermophysical properties of high porosity foams. *Int. J. Heat Mass Transfer* 45:1017–1031, 2002.
30. K. Kamiuto. Modeling of Composite heat transfer in open-cellular materials at high temperatures. In: A. Öchsner, G.E. Murch, and M.J.S. de Lemos (Eds.), *Cellular and Porous Materials: Thermal Properties Simulation and Prediction*. Weinheim, Germany: Wiley-VCH Verlag, 2008, pp.165–198.
31. J.-F. Despois and A. Mortensen. Permeability of open-pore microcellular materials. *Acta Mater*. 53:1381–1388, 2005.
32. K. Kamiuto and S.S. Yee. Axial thermal dispersion conductivity of open-cellular porous materials. *J. Thermophys. Heat Transfer* 16:478–480, 2002.
33. T. Metzger, S. Didierjean, and D. Maillet. Optimal dispersion estimation of thermal dispersion coefficients in porous media. *Int. J. Heat Mass Transfer* 47:3341–3353, 2004.
34. S. Liu and J.H. Masliyah. Dispersion in porous media. In: K. Vafai (Ed.), *Handbook of Porous Media*, 2nd edn. Boca Raton, FL: CRC Press, 2005, pp. 81–140.
35. R. Coquard and D. Baillis. Modeling of heat transfer in low-density EPS foams. *J. Heat Transfer* 128:538–549, 2006.
36. D. Baillis and R. Coquard. Radiative and conductive thermal properties of foams. In: A. Öchsner, G.E. Murch, and J.J.S. de Lemos (Eds.), *Cellular and Porous Materials: Thermal Properties Simulation and Prediction*. Weinheim, Germany: Wiley-VCH Verlag GmbH, 2008, pp. 343–384.
37. R. Coquard and D. Baillis. Numerical investigation of conductive heat transfer in high-porosity foams. *Acta Mater*. 57:5466–5479, 2009.
38. L.A. Dombrovsky and D. Baillis. *Thermal Radiation in Disperse Systems: An Engineering Approach.* Redding, CA: Begell House Inc., 2010.
39. R. Coquard, D. Rochais, and D. Baillis. Conductive and radiative heat transfer in ceramic and metallic foams at fire temperature. *Spec. Issue Fire Technol. Mater. Fire* 699–732, 2012.
40. R. Viskanta. *Radiative Transfer in Combustion Systems: Fundamentals and Applications*. New York: Begell House, 2005.
41. J.R. Howell, R. Siegel, and M.P. Mengüç. *Thermal Radiation Heat Transfer*, 5th edn. Boca Roton, FL: CRC Press, 2010.
42. M.F. Modest. *Radiative Heat Transfer*, 5th edn. New York: Academic Press, 2013.
43. D. Baillis, R. Coquard, J. Randrianalisoa, L. Dombrovsky, and R. Viskanta. Thermal radiation properties of highly porous cellular foams. *Spec. Top. Rev. Porous Media Int. J.* 4:111–136, 2013.
44. C.Y. Zhao, T.J. Lu, and H.P. Hodson. Thermal radiation in ultralight metal foams with open cells. *Int. J. Heat Mass Transfer* 47:2927–2939, 2004.
45. C.Y. Zhao, S.A. Tassou, and T.J Lu. Analytical consideration of thermal radiation in cellular metal foams with open cells. *Int. J. Heat Mass Transfer* 51:920–940, 2008.
46. K. Kamiuto. Combined conductive and radiative heat transfer through open-cellular porous plates. *JSME Int. J. Ser. B* 43:273–278, 2000.
47. T.J. Lu and C. Chen. Thermal transport and fire retardance properties of cellular aluminum alloys. *Acta Mater*. 47:1469–1485, 1999.
48. C.C. Tseng, R.L. Sikorski, R. Viskanta, and M.Y. Chen. Effect of foam properties on heat transfer in high temperature open-cell foams. *J. Am. Ceramic Soc*. 96:2015–2021, 2012.
49. C.C. Tseng, T.A. Parthasarathy, R.L. Sikorski, R. Viskanta, and M.Y.Chen. Effect of thermal radiation on the effective thermal conductivity of open-cell SiC foams. *High Temp. High Pressure* 42:387–403, 2013.
50. R. Viskanta. Modeling of transport phenomena in porous media using a two-energy equation model. In: L.S. Flectcher and T. Aihara (Eds.), *Proceedings of the ASME/JSME Thermal Engineering Joint Conference*. New York: ASME, 1995, Vol. 3, pp. 11–22
51. S. Krishnan, S.V. Garimella, and J.Y. Murthy. Thermal characterization of open-celled metal foams by direct simulation. In: A. Öchsner, G.E. Murch, and M.J.S. de Lemos (Eds.), *Cellular and Porous Materials: Thermal Properties Simulation and Prediction*. Weinheim, Germany: Wiley-VCH Verlag GmbH, 2008, pp. 267–289.
52. J.R. Howell. Radiative transfer in porous media. In: K. Vafai (Ed.), *Handbook of Porous Media*. New York: Marcell Dekker, 2000, pp. 663–698.
53. J.T. Hendricks and J.R. Howell. Absorption/scattering coefficients and scattering phase functions in reticulated porous ceramics. *J. Heat Transfer* 118:79–87, 1996.
54. D. Doermann and J.F. Sacadura. Heat transfer in open cell foam insulation. *J. Heat Transfer* 118:88–93, 1996.
55. D. Baillis, M. Raynaud, and J.F. Sacadura. Spectral radiative properties of open-cell foam insulation. *J. Thermophys. Heat Transfer* 13:292–299, 1999.

56. D. Baillis, M. Raynaud, and J.F. Sacadura. Determination of spectral radiative properties of open cell foam: Model validation. *J. Thermophys. Heat Transfer* 14:137–143, 2000.
57. F.F. Hsu and J.R. Howell. Measurements of thermal conductivity and optical properties of partially stabilized zirconia. *Exp. Heat Transfer* 5:293–313, 1992.
58. K. Kamiuto. Study of Dulnev's model for the thermal and radiative properties of open-cellular materials. *JSME Int. J. Ser. B* 40:577–582, 1997.
59. C.Y.Zhao, T.J. Ju, H.P. Hodson, and J.B. Jackson. The temperature dependence of effective thermal conductivity of open-cell steel alloy foams. *Mater. Sci. Eng. A* 367:123–131, 2004
60. R. Coquard, D. Rochais, and D. Baillis. Experimental investigations of the coupled conductive and radiative heat transfer in metallic/ceramic foams. *Int. J. Heat Mass Transfer* 52:4907–4916, 2009.
61. K. Kamiuto, S.S. Yee, and K. Matsuda. Experimental determination of the heat transfer and fluid flow characteristics for open-cellular porous materials. *Proceedings of the 12th International Heat Transfer Conference.* Paris, France: Elsevier, 2002, pp. 815–820.
62. A. Nakayama, K. Ando, C. Yang, Y. Sano, F. Kuwahara, and J. Liu. A study on interstitial heat transfer in consolidated and unconsolidated porous media. *Heat Mass Transfer* 45:1365–1372, 2009.
63. L.B. Younis and R. Viskanta. Experimental determination of the volumetric heat transfer coefficient between a stream of air and ceramic flam. *Int. J. Heat Mass Transfer* 36:1425–1434, 1993.
64. X. Fu, R. Viskanta, and J.P. Gore. Measurement and correlation of volumetric heat transfer coefficients of cellular ceramics. *Exp. Therm. Fluid Sci*. 17:285–293, 1998.
65. K. Hamaguchi, S. Takahashi, and T. Miyabe. Friction loss and heat transfer performance of regenerator matrix (in the case of formed metal). *Trans. JSME Ser. B* 49:1991–1999, 1983.
66. K. Kamiuto and S.S. Yee. Heat transfer correlations for open-cellular porous materials. *Int. Commun. Heat Mass Transfer* 32:947–953, 2005.
67. C.J.M. Lasance. Advances in high-performance cooling for electronics. *Elect. Cooling* 11(4), 2005.
68. W. Lu, C.Y. Zhao, and S.A. Tassou. Thermal analysis of metal-foam filled heat exchangers. Part I: Metal foam filled pipes. *Int. J. Heat Mass Transfer* 49:2751–2761,2006.
69. I. Ghosh. How good is open-cell metal foam as heat transfer surface? *J. Heat Transfer* 131:101004–1, 2009.
70. D.A. Nield and A.V. Kuznetsov. Forced convection in cellular porous materials: Effect of temperature-dependent conductivity arising from radiative transfer. *Int. J. Heat Mass Transfer* 53:2680–2684, 2010.
71. R. Echigo. *Effective Energy Conversion Method between Gas Enthalpy and Thermal Radiation and Applications to Industrial Furnaces: Heat Transfer*. Washington, DC: Hemisphere Publishing, Vol. 6, pp. 361–366, 1982.
72. K.Y. Wang and C.L. Tien. Thermal insulation in flow systems: Combined radiation and convection through a porous segment. *J. Heat Transfer* 106:453–459, 1984.
73. P. Khantikomal and K. Kamiuto. Design considerations of porous gas enthalpy-radiation converters for exhaust-heat recovery systems. *J. Thermal Sci. Technol*. 3:319–329, 2008.
74. P. Khantikomol, S. Saito, K. Kamiuto, and T. Yakomine. Study on single layer flow insulation utilizing NiCr open-cellular porous plate. *Int. Commun. Heat Mass Transfer* 37:1015–1024, 2010.
75. P. Khautikomol, S. Saito, and T. Yokimine. Enhancement of gas-enthalpy-radiation conversion by utilizing multilayer open cellular porous materials. *Proceedings of the 14th International Heat Transfer Conference*. Washington, DC: ASME, Paper No. IHTC14-22179, 2010.
76. M. Sajedi, S.A. Gandjalikhan Nassab, and E. Jahanshahi Javaran. Thermal analysis of a three-layered radiant porous heat exchanger including fluid flow simulation. *Proc. Inst. Mech. Eng. J. Mech. Eng. Sci*. 228(8):1375–1390, 2014.
77. S.A. Kalogirou. Solar thermal collectors and applications. *Prog. Energ. Combust. Sci*. 30:231–245, 2004.
78. Z. Ssen. Solar energy in progress and future research trends. *Prog. Energ. Combust. Sci*. 30:267–416, 2004.
79. L.K. Matthews, R. Viskanta, and F.P. Incropera. Combined conduction and radiation heat transfer in porous material heated by intense solar radiation. *J. Solar Energ. Eng*. 107:29–34,1985.
80. C.C. Tseng and R. Viskanta. Solar-to thermal energy conversion via porous materials. In: P. Coelho, D. Lemonier, P. Lyabeth and N. Selcuk (Eds.), *Proceedings of Eurotherm 83-Computational Thermal Radiation in Participating Media III* 2009. Lisbon, Portugal: IST Press, 2009.
81. S. Maruyama, R. Viskanta, and T. Aiahara. Analysis of an active high-temperature thermal insulation system. *Int. J. Heat Fluid Flow* 11:196–203, 1990.
82. C. Gogu, S.K. Bapanapalli, R.T. Hafka, and B.V. Sankar. Comparison of materials for an integrated protection system for spacecraft reentry. *J. Spacecraft Rockets* 46:501–513, 2009.
83. S. Liu and B. Zhang. Experimental study of a transpiration cooling thermal protection system. *Sci. China Technol. Sci*. 53:2765–2771, 2010.

84. H.Bőhrk, O. Piol, and M. Kuhn. Heat balance of a transpiration-cooled heat sink. *J. Thermophys. Heat Transfer* 24:581–588, 2010.
85. S. Liu and B. Zhang. Effects of active cooling on metal thermal protection systems. *Aerospace. Sci. Technol*. 15:226–533, 2011.
86. K. Kamiuto, K. Unoki, and J. Andou. Thermal characteristics of transpiration cooling system using open-cellular porous materials in a radiative environment. *Int. J. Trans. Phenomena* 7:85–96, 2005.

17 Convection of a Bingham Fluid in a Porous Medium

D. Andrew S. Rees

CONTENTS

17.1 Introduction 559
17.2 Yield-Stress Fluids and Their Modeling 560
17.2.1 Bingham Fluids 560
17.2.2 Flows of Bingham Fluids in Porous Media 563
17.3 Isothermal Flows of a Bingham Fluid in a Porous Medium 565
17.3.1 Plane Buckingham–Reiner Model 565
17.3.2 Modifications for Multiple Channels 567
17.3.3 Distributions of Channels 568
17.3.4 Flow through a Network: Yield-Stress-Induced Anisotropy 569
17.4 Network Modeling of the Convection of a Bingham Fluid in a Porous Medium 572
17.4.1 Convection in a Sidewall-Heated Vertical Layer Formed of Channels 572
17.4.2 Convection in a Sidewall-Heated Square Cavity 574
17.5 Convection of a Bingham Fluid in a Sidewall-Heated Cavity 578
17.5.1 The Double Glazing Problem 578
17.5.2 Unit Cavity: Isotropic Model 579
17.5.3 Unit Cavity: Anisotropic Model 583
17.6 Darcy–Bénard Convection 586
17.7 Convective Boundary-Layer Flows of a Bingham Fluid 588
17.7.1 Unsteady Boundary-Layer Flow 588
17.7.1.1 Infinite Domain 589
17.7.1.2 Tall Cavity 590
17.7.2 Comment on Steady Boundary-Layer Flows 592
References 594

17.1 INTRODUCTION

The chief purpose of this chapter is to consider convective flows of a Bingham fluid when it saturates a porous medium. My interest in this topic arose after seeing the work of Turan et al. (2012) at the *Advances in Computational Heat Transfer Symposium*, which was held at the University of Bath. In that paper, the authors considered the convection of a Bingham fluid in a square cavity heated from a vertical sidewall and cooled by the other. Plots of streamlines show unyielded regions where the local shear stress is less than the yield stress. I immediately wondered what the equivalent would be for a porous medium, and I started searching for papers on the topic. I was assisted in this work by a final year undergraduate who also worked on some network modeling aspects (Nash 2013). Of course, the presence of the solid matrix means that flow in a porous medium will happen only when the yield stress is exceeded locally. If one were, in the first instance, to think of a porous medium as a bundle of tubes or a collection of channels or even a network of channels, then

simple considerations of Poiseuille flow or Hagen–Poiseuille flow in these tubes or channels lead one immediately to realize that *unyielded* in the porous medium context actually means *no flow*. This is not necessarily the case for the so-called clear fluid flows, such as Poiseuille flow, where one may have flow within a channel, but the unyielded central portion still moves. Therefore, I have used the opportunity to provide this chapter as one where I would have an extra impetus to study the general topic of Bingham fluids and how they convect in a porous medium.

It has become apparent, at one and the same time, that (1) there is a huge literature associated with yield-stress fluids in general, one that I had no idea existed, and (2) there are very few papers indeed that deal with the convection of a yield-stress fluid in a porous medium even though there is much interest in isothermal flows in porous media. This juxtaposition of glut and famine has therefore guided how I have approached the task of writing. So this chapter begins with a brief, possibly too brief, introduction first to the concept of a yield-stress fluid in general, and second to the modeling of isothermal flows in porous media. There are some controversies that the reader, new to this topic, will, I hope, find useful to know. There are varieties of constituent models and even the questioning of whether there is indeed such a thing as a yield stress. My aim here is not to provide a definitive set of textbook information, but merely to indicate some of the issues that may usefully be pursued.

After a long time spent searching the published literature, I was successful in finding only about a dozen papers on the convection of a yield-stress fluid in a porous medium, and I was surprised to find that all of these are devoted to boundary-layer flows. There was nothing at all on convection in channels, on convection in cavities, or on the analog to the Darcy–Bénard problem. Therefore, much of this chapter concentrates on the new work on these topics and gives a flavor of what to expect in more detailed studies.

After introducing more fully the concept of a yield-stress fluid and of how it is modeled when flowing through a porous medium, the chapter continues with further new studies of isothermal flows in distributions of channels and in square networks. The latter allows the definition of a new type of Darcy–Bingham law for flow in such a structured medium and demonstrates that flow is anisotropic in periodic media. After that, we consider the flow which is induced in a sidewall-heated vertical channel, and it is possible to derive analytical solutions for this case. Nonlinear convection in sidewall-heated cavities are also computed, as are flows of Darcy–Bénard type; in both cases, certain qualitative features that are present for fluids without yield stresses are changed. An unsteady boundary-layer flow is also considered in some detail. Finally, the steady boundary-layer flows mentioned earlier are considered. In this case, we make an argument that there are some difficulties with the classical type of boundary-layer analysis where the subsequent consideration is not made of the flow that occurs in the outer external region. We show that, when the yield criterion lies within the boundary layer itself, then entrainment into the boundary, something that must happen (1) to provide fluid to replace that which is convected upward and (2) to prove a mechanism for restricting the conduction of heat perpendicularly away from the surface, cannot happen because it is too weak to overcome the yield criterion. Thus, this chapter provides a great deal of new information on new topics. It is not comprehensive but provides a foundation for more detailed studies, which I intend to pursue in the next few years.

17.2 YIELD-STRESS FLUIDS AND THEIR MODELING

In this section, we take a brief look at various models of Bingham fluids and how one might then define macroscopic laws for the flow of such fluids in porous media.

17.2.1 Bingham Fluids

A Bingham fluid is essentially a Newtonian fluid but one with a yield stress. Thus, the fluid flows only when a sufficiently large stress is imposed, but thereafter, it flows with a constant

viscosity. This is seen most easily for unidirectional flow where u is the velocity in the x-direction but is one that is a function of y. A one-dimensional Newtonian flow obeys the following stress/strain relationship:

$$\tau = \mu\dot{\gamma} = \mu\frac{du}{dy}, \tag{17.1}$$

where

τ is the shear stress

$\dot{\gamma}$ is the rate of strain

In terms of these quantities, the x-momentum equation for one-dimensional flow without buoyancy may be rewritten in the form

$$0 = -\frac{dp}{dx} + \frac{d\tau}{dy}. \tag{17.2}$$

A Bingham fluid has a yield stress which we notate as τ_0. The equivalent of (17.1) is

$$\begin{aligned} \tau > \tau_0 \quad &\Rightarrow \quad \mu\frac{du}{dy} = \tau - \tau_0, \\ -\tau_0 < \tau < \tau_0 \quad &\Rightarrow \quad \frac{du}{dy} = 0, \\ \tau < -\tau_0 \quad &\Rightarrow \quad \mu\frac{du}{dy} = \tau + \tau_0. \end{aligned} \tag{17.3}$$

It is the second equation in (17.3) that gives u = constant when the fluid is in its unyielded state. In such equations, the quantity, μ, is sometimes called the plastic viscosity (Denn and Bonn 2011).

It is worth mentioning that two of the many other commonly used models for yield-stress fluids are those describing Casson and Herschel–Bulkley fluids. If we were to summarize the Bingham properties given in (17.3) by

$$\tau = \tau_0 + \mu\dot{\gamma}, \tag{17.4}$$

where it is assumed that $\tau > \tau_0$, then a Casson fluid is given by

$$\sqrt{\tau} = \sqrt{\tau_0} + \sqrt{\mu\dot{\gamma}}, \tag{17.5}$$

or equivalently by

$$\tau = \tau_0 + \mu\dot{\gamma} + 2\sqrt{\tau_0\mu\dot{\gamma}}, \tag{17.6}$$

while a Herschel–Bulkley fluid is given by

$$\tau = \tau_0 + \mu\dot{\gamma}^n, \tag{17.7}$$

when n is a power-law exponent. Thus, the Herschel–Bulkley fluid is a power-law fluid with a yield stress. Of course, care needs to be taken over applying these formulae when $\dot{\gamma}$ is negative.

With regard to applications, much interest in the flow of Bingham fluids lies in the oil industry. Such fluids include heavy oils, foams, polymer solutions, and viscoelastic surfactants (Sochi and

Blunt 2008). Bingham's original list of yield-stress fluids, quoted in Barnes (1999), includes clay, oil paint, toothpaste, drilling mud, molten chocolate, molten rubbers, and printing inks. To these, Barnes adds ceramic pastes, electro-viscous fluids, thixotropic paints, heavy-duty washing fluids, mayonnaise, yoghurts, purées, liquid pesticides, biomass broths, blood, water–coal mixtures, plastic explosives, and foams. Shenoy (1991) provides the following: certain asphalts and bitumin, fly ash, water suspensions of clay, and sewage sludges. Recent work has considered the modeling of marine sediments (Jeong 2013) and the convection of magma (Maßmeyer 2013). It almost seems that all of life is represented by these examples of yield-stress fluids, notable exceptions being air, water, wine, and beer!

Use of the Bingham law as given by (17.3) is complicated by the fact that the yield surface needs to be found as part of the calculation. For simple flows like Poiseuille flow, Hagen–Poiseuille flow, or the *double glazing* problem (Bayazitoglu et al. 2007), the whole analysis proceeds analytically. But more generally, the yield surface presents very great numerical difficulties. Therefore, authors have modified (termed *regularized*) the law to one which is more amenable to computation. In one dimension, the regularization of Papanastasiou (1987) is given by

$$\tau = \left[\frac{\tau_0}{|\dot{\gamma}|}\left(1 - e^{-m|\dot{\gamma}|}\right) + \mu\right]\dot{\gamma}. \tag{17.8}$$

A schematic of how this law compares with the strict Bingham law is shown in Figure 17.1. From this, we see that at small rates of strain, the effective viscosity is $\mu + m\tau_0$. The approach to the Bingham law then corresponds to $m \to \infty$. The high-viscosity regime inhibits flow but renders the equations much less difficult to solve numerically. A second common approximation is the bilinear law; this too is sketched in Figure 17.1.

Although the computation of Bingham fluid flows is more difficult than for their Newtonian counterparts, some authors have questioned various aspects of the strict Bingham law. Barnes and Walters (1985), for example, have questioned whether there is such a concept as a yield stress. If one views the stress/strain relationship given in Equation 17.3 in terms of an effective viscosity being the

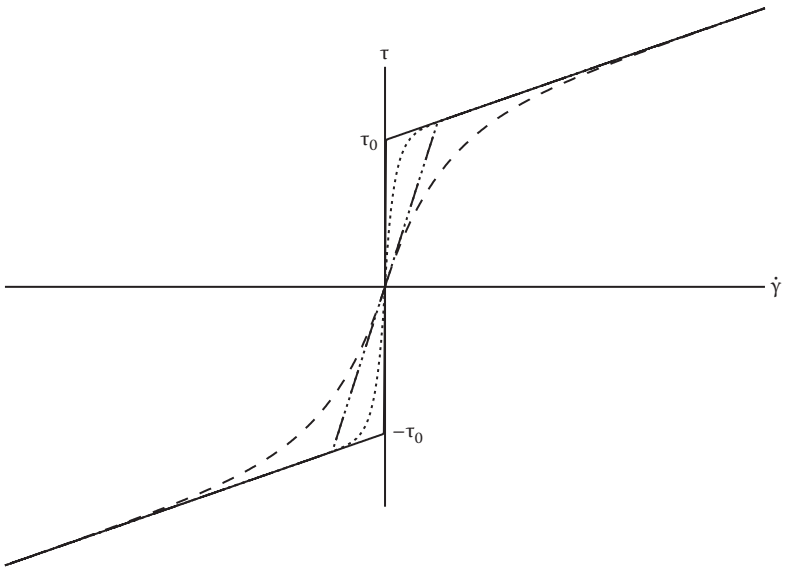

FIGURE 17.1 Displaying the Bingham law (continuous line), Papanastasiou's (1987) regularization with small m (dashes) and large m (dotted), and the bilinear law (dash-dotted).

gradient of the graph shown in Figure 17.1, then at the yield stress, the viscosity suddenly becomes infinite. But Barnes and Walters cite evidence that some fluids possess three different regimes. At high shear rates, the viscosity is constant and therefore Newtonian. At very low shear rates, the fluid is also Newtonian, but the viscosity is very high indeed. Near to what would normally be termed the yield stress, the viscosity changes very rapidly between the two neighboring constant values. In many ways, this is similar to Papanastasiou's regularization.

Cheng (1986) discusses the transient response of fluids with structure. Such fluids may exhibit responses to changing conditions over more than one timescale. There may, for example, be a transient creep response to an imposed shear stress, and this will eventually relax either to no flow or to flow. Thus, the determination of an accurate yield stress depends on when measurements take place, and the accurate computation of flows under changing circumstances may also depend on the relative durations of the creeping response and the externally imposed timescales.

The paper by Liu et al. (2012) discusses the properties of heavy oils. The main message from their work is that the yield stress may, under some circumstances, be temperature dependent. In the case of heavy oils, there exists a temperature, the *converting temperature*, above which the flow is Newtonian. At lower temperatures, there is a yield stress, and its value is proportional to $\ln(T/T_{\text{conv}})$, where T_{conv} is the converting temperature.

Finally, Steffe (1992) sounds a warning note that "an absolute yield stress is an elusive property." By this, it is meant that the yield stress obtained using one experimental technique will often be different from that found by another technique. Such techniques include initiation of movement on an inclined plane, the stress to initiate flow, and backward extrapolation from the flowing regime.

The present author recommends the long paper by Barnes (1999) as a very good first paper to read on the yield stress, and it contains an excellent historical account of the topic.

17.2.2 Flows of Bingham Fluids in Porous Media

In this section, we discuss in some detail the modeling of the flow of a Bingham fluid in a porous medium. The purpose of this subsection is simply to present the various models that have appeared in the literature.

One of the earliest papers to consider such flows is that of Pascal (1981). Citing experimental considerations, a threshold gradient model was chosen, which is the simplest possible model that may be used. Using the notation of this chapter, the one-dimensional form of the threshold model is

$$u = \begin{cases} -\dfrac{K}{\mu}\left[1 - \dfrac{G}{|p_x|}\right] p_x & \text{when } |p_x| > G, \\ 0 & \text{otherwise,} \end{cases} \tag{17.9}$$

where we use G to denote the threshold gradient. A more complicated relationship is given by the Buckingham–Reiner (or BR) model. In the present context, we may write this as

$$u = \begin{cases} -\dfrac{K}{u}\left[1 - \dfrac{4}{3}\left(\dfrac{G}{|p_x|}\right) + \dfrac{1}{3}\left(\dfrac{G}{|p_x|}\right)^4\right] p_x & \text{when } |p_x| > G, \\ 0 & \text{otherwise,} \end{cases} \tag{17.10}$$

although a very wide range of notations may be found in the literature. This model is derived by assuming that the porous medium consists of a bundle of identical circular cross-sectioned tubes for which an exact solution of the polar coordinate form of Equations 17.2 and 17.3 may be found. Thus, we have Hagen–Poiseuille flow. The mean flow is then averaged and finally expressed in a form where K denotes the overall permeability of the same configuration when saturated with a Newtonian fluid.

A similar procedure will be used in Section 17.3 for plane channels. This model has been adopted by many authors including Balhoff and Thompson (2004) and Mendes et al. (2002).

The corresponding form for plane channels in which Poiseuille flow exists is what we shall term the plane Buckingham–Reiner (or BR2D) model; it is,

$$u = \begin{cases} -\dfrac{K}{\mu}\left[1 - \dfrac{3}{2}\left(\dfrac{G}{|p_x|}\right) + \dfrac{1}{2}\left(\dfrac{G}{|p_x|}\right)^3\right] p_x & \text{when } |p_x| > G, \\ 0 & \text{otherwise.} \end{cases} \tag{17.11}$$

Both the standard and the plane Buckingham–Reiner models are shown in Figure 17.2, together with the threshold model for comparison. It may be seen that there is a gradual rise in the velocity as the driving pressure gradient passes the threshold value. If one were to allow the pressure gradient to be just above the threshold value, that is, $-p_x = G(1 + \epsilon)$, where ϵ is small and positive, then the standard and plane Buckingham–Reiner models yield

$$u \simeq -\frac{K}{\mu}\left[2\epsilon^2 + \cdots\right] p_x, \quad \text{and} \quad u \simeq -\frac{K}{\mu}\left[\frac{3}{2}\epsilon^2 + \cdots\right] p_x, \tag{17.12}$$

respectively, and therefore the linear rise of the threshold model immediately post yield is replaced by a quadratic rise. One may also consider the reciprocal of the slopes of the curves given in Figure 17.2 as being the effective viscosities for the three models.

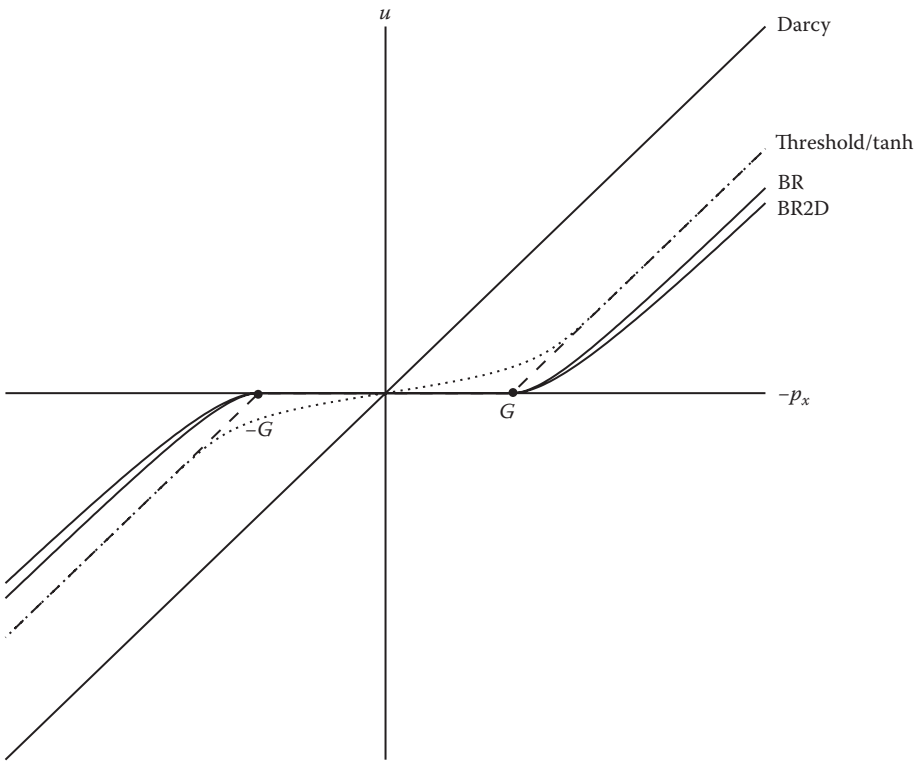

FIGURE 17.2 Displaying Darcy's law, the threshold law (dashed line), the tanh law (dotted line), and the two Buckingham–Reiner laws.

The final model takes the form of a regularization similar in intent to that of Papanastasiou (1987) mentioned earlier. We will name it the tanh model, and it takes the form

$$\left[1 + G\frac{K}{\mu}\frac{\tanh(cu)}{u}\right]u = -\frac{K}{\mu}p_x. \tag{17.13}$$

This fourth model is shown in Figure 17.2 as the dotted line, and the presence of the tanh function causes the effective viscosity to become large under small pressure gradients. More precisely, the effective viscosity rises from its large pressure gradient value of μ to the value, $\mu + GKc$, as the pressure gradient decreases toward zero. This model holds very distinct advantages over the other three when numerical computations are required. The threshold model is difficult to implement because of the need to determine the yield surface. The two BR models have the same difficulty, but u is also a nonlinear function of the pressure gradient in the yielded regime. Thus, if one wished to solve a two-dimensional convection problem using the streamfunction, then (1) one would need to apply the appropriate Cardan solution for a cubic (for the BR2D model) or the appropriate Ferrari solution for a quartic (for the BR model) in order to find p_x in terms of u, and (2) the yield surface still needs to be found. On the other hand, the tanh model suffers from none of these defects. As we will see later, the equation for the streamfunction in the tanh model becomes nonlinear, but the numerical difficulties associated with that aspect are relatively small.

We note, finally, that all four models have to take suitably modified forms when considering flows in two and three dimensions. These will be introduced as necessary later.

17.3 ISOTHERMAL FLOWS OF A BINGHAM FLUID IN A POROUS MEDIUM

We will consider plane Poiseuille flow in channels. From this, we will derive the BR2D model mentioned earlier, extend it first to cases where the bundle of channels consists of channels of different width, and second to a continuous distribution of channels. Finally, a square network of channels of identical widths will be considered, and this is used to demonstrate a natural anisotropy that arises because of the presence of the yield stress but which is absent when the fluid is Newtonian. It is important to note that much of this section is taken from Nash (2013).

17.3.1 Plane Buckingham–Reiner Model

We consider the motion of a Bingham fluid in a uniform channel of width h under the action of the pressure gradient, $-p_x$. For mathematical convenience, the channel has boundaries at $y = \pm h/2$, and for presentational convenience, we will set $G = -p_x > 0$ to be the pressure gradient. We may solve Equation 17.2 easily and apply the appropriate symmetry to show that

$$\tau = -Gy. \tag{17.14}$$

Therefore, it is clear that $-Gh/2 \leq \tau \leq Gh/2$ in the channel. If $Gh/2 < \tau_0$ is satisfied, then there will be no flow. If there is flow, then the yield surfaces will lie where $Gy = \pm\tau_0$. Let this be at $y = \pm\epsilon h/2$, where ϵ denotes the fraction of the channel that is unyielded. Thus, we find that

$$\epsilon = \frac{2\tau_0}{Gh}. \tag{17.15}$$

The solution is shown in Figure 17.3 together with the solutions in the various yielded and unyielded portions of the channel.

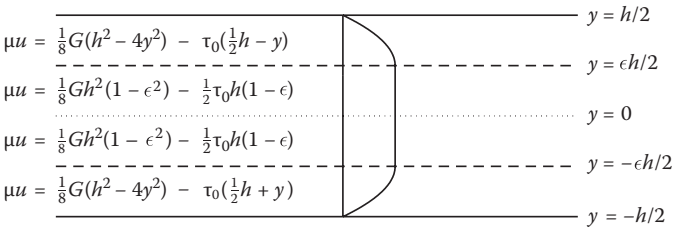

FIGURE 17.3 Displaying the velocity profile for the Poiseuille flow of a Bingham fluid in a channel.

The total volumetric flux, Q, is given by

$$\mu Q = \int_{-h/2}^{h/2} u\,dy = \begin{cases} \dfrac{Gh^3}{12}\left[1 - \dfrac{3\epsilon}{2} + \dfrac{\epsilon^3}{2}\right] & \text{when } G > \dfrac{2\tau_0}{h}, \\ 0 & \text{when } 0 \le G \le \dfrac{2\tau_0}{h}, \end{cases} \tag{17.16}$$

and thus

$$G = \frac{2\tau_0}{h} \tag{17.17}$$

is the yield pressure gradient. Equation 17.16 may now be written in terms of a scaled pressure gradient, σ, where

$$\sigma = \frac{1}{\epsilon} = \frac{Gh}{2\tau_0}. \tag{17.18}$$

Hence we have,

$$\mu Q = \frac{Gh^3}{12} f(\sigma), \tag{17.19}$$

where

$$f(\sigma) = \begin{cases} 1 - \dfrac{3}{2|\sigma|} + \dfrac{1}{2|\sigma|^3} & \text{when } |\sigma| \ge 1, \\ 0 & \text{when } |\sigma| \le 1. \end{cases} \tag{17.20}$$

Equation 17.19 is the BR2D law, which was introduced earlier, though now in nondimensional form using the function, $f(\sigma)$. It is also in a form in which Equation 17.19 applies for either possible sign for G.

If we consider a porous medium to consist of a periodic array of channels of width h and with period H, then the Darcy velocity of the Bingham fluid through that medium is

$$u_{DB} = \frac{1}{H}\int_{-H/2}^{H/2} u\,dy = \frac{\phi G h^2}{12\mu} h^2 f(\sigma), \tag{17.21}$$

where $\phi = h/H$ is the porosity. The corresponding Darcy velocity of a Newtonian fluid is $u_D = \phi G h^2/12\mu$, and therefore $f(\sigma)$ is the ratio of the two velocities.

17.3.2 Modifications for Multiple Channels

If one now considers that the periodic bundle of channels contains one channel of width h and a second one of width γh per period where $\gamma < 1$, then we may simply add the appropriate forms of Equation 17.19:

$$\mu Q = \begin{cases} 0 & \sigma\gamma < \sigma < 1, \\ \dfrac{Gh^3}{12} f(\sigma) & \sigma\gamma < 1 < \sigma, \\ \dfrac{Gh^3}{12}\left[f(\sigma) + \gamma^3 f(\sigma\gamma) \right] & 1 < \gamma\sigma < \sigma. \end{cases} \tag{17.22}$$

The porosity is now $\phi = h(1 + \gamma)/H$, and therefore the Darcy–Bingham velocity is

$$u_{\mathrm{DB}} = \begin{cases} 0 & \sigma\gamma < \sigma < 1, \\ \dfrac{\phi G h^2}{12\mu} \dfrac{f(\sigma)}{1+\gamma} & \sigma\gamma < 1 < \sigma, \\ \dfrac{\phi G h^2}{12\mu} \dfrac{f(\sigma) + \gamma^3 f(\sigma\gamma)}{1+\gamma} & 1 < \gamma\sigma < \sigma. \end{cases} \tag{17.23}$$

In these formulae, three different forms of expression have been used purely to differentiate between the three different regimes: (1) no flow, (2) flow in the wider channel, and (3) flow in both channels. Given the definition of $f(\sigma)$ in Equation 17.20, noting specifically that it takes zero values when $\sigma < 1$, then we may formally use the third expression in Equation 17.23 in all cases.

These expressions may be generalized further by taking N channels per period, where the channel widths are taken to be $\gamma_i h$, $i = 1, \ldots, N$, and where

$$1 = \gamma_1 \geq \gamma_2 \geq \gamma_3 \geq \cdots \geq \gamma_N. \tag{17.24}$$

This definition allows for multiple instances of any chosen width. For this system, the Darcy velocity is now

$$u_{\mathrm{DB}} = \frac{\phi G h^2}{12\mu} \left[\frac{\sum_{i=1}^{N} \gamma_i^3 f(\sigma\gamma_i)}{\sum_{i=1}^{N} \gamma_i} \right]. \tag{17.25}$$

Some representative cases are shown in Figure 17.4 in the form of a scaled Darcy velocity, that is, the figure shows the velocity relative to that of a Newtonian fluid.

The single channel is the uppermost curve, and this represents the variation of $f(\sigma)$. At first, it may seem surprising that the addition of narrower channels appears to reduce the Darcy velocity for a given σ, but this is due to the redefinition of the porosity, ϕ. We may say, therefore, that for a given porosity, ψ, the *scaled* Darcy velocity (which is what is shown in Figure 17.4) will decrease whenever extra channels are introduced because the velocity flux of the Bingham fluid then decreases relative to that of the corresponding Newtonian fluid.

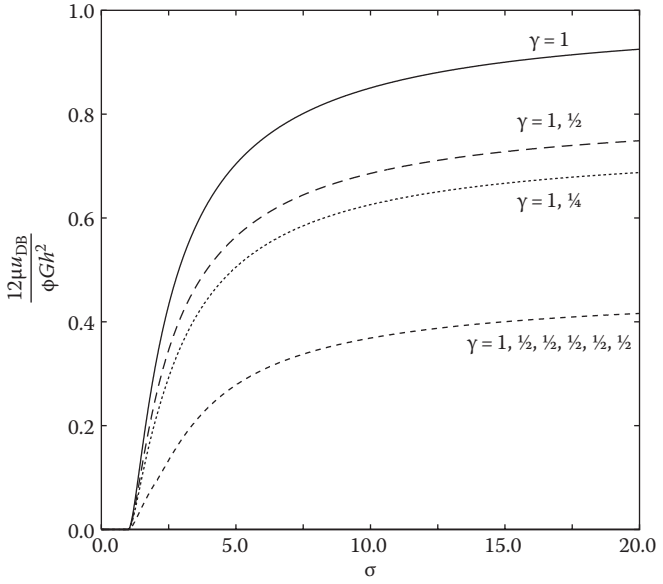

FIGURE 17.4 Displaying the Darcy velocity for different sets of channel bundles.

17.3.3 Distributions of Channels

In practice, a porous medium is most likely to be formed from channels that have randomly distributed widths. If this distribution is taken to be uniform, for example, then a uniform distribution of channels in the range, $a \le \gamma \le 1$, yields the following:

$$u_{DB} = \frac{\phi G h^2}{12\mu}\left[\frac{\int_a^1 \gamma^3 f(\sigma\gamma)\mathcal{H}(\sigma\gamma - 1)d\gamma}{\int_a^1 \gamma d\gamma}\right], \tag{17.26}$$

where $\mathcal{H}$ is the Heaviside or unit step function; this has been included to ensure that due care is taken with the integral and simply represents the fact that $f(\sigma\gamma) = 0$ when $\sigma\gamma < 1$. Hence,

$$\frac{12\mu u_{DB}}{\phi G h^2} = \begin{cases} 0 & \sigma < 1, \\ \dfrac{(\sigma-1)^3(\sigma+1)}{2\sigma^4(1-a^2)} & 1 < \sigma < \dfrac{1}{a}, \\ \dfrac{1+a^2}{2} - \dfrac{1+a+a^2}{(1+a)\sigma} + \dfrac{1}{\sigma^3(1+a)} & \dfrac{1}{a} < \sigma. \end{cases} \tag{17.27}$$

The behavior of this function for three different values of a may be found in Figure 17.5. We note that when σ is just above 1, then the Darcy velocity rises initially as a cubic, rather than as a quadratic as happens for a single channel, given the factor $(\sigma - 1)^3$ in the second line of Equation 17.27.

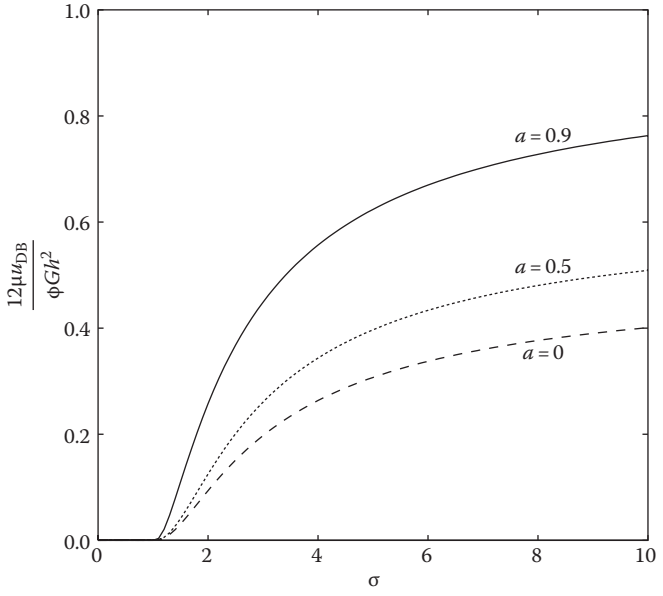

FIGURE 17.5 Displaying the Darcy velocity for uniformly distributed channels.

It is also interesting to note that we are able to recover the BR2D formula given by Equation 17.21 from Equation 17.27 by taking the limit $a \to 1$. In this limit, the intermediate regime, namely, $1 < \sigma < 1/a$, disappears, while the $\sigma > 1/a$ regime reproduces the BR2D formula.

17.3.4 Flow through a Network: Yield-Stress-Induced Anisotropy

Although we have not exhausted the possibilities for one-dimensional flow—one may also consider different types of discrete and continuous distributions of both channels and tubes—we turn now to a simple square network of uniform channels. These channels are aligned in the x- and y-directions, and are of width h again where each channel is separated from its nearest parallel neighbor by a distance, H. Thus, the analysis of Section 17.3.1 applies. We also note the assumption that $h \ll H$ so that the interactions at intersections may be neglected at leading order.

A sketch of the square network of channels is given in Figure 17.6. A pressure gradient of magnitude G is applied to this network at an angle, θ_G, to the horizontal (x) direction. This pressure gradient may be resolved into its two horizontal and vertical components, and the analysis of Section 17.3.1 applied to each direction separately by means of the appropriate modifications of Equation 17.21. Therefore, we obtain

$$\frac{12\mu u_{DB}}{\phi G h^2} = f(\sigma_x)\cos\theta_G, \qquad \sigma_x = \frac{Gh\cos\theta_G}{2\tau_0}, \tag{17.28}$$

$$\frac{12\mu v_{DB}}{\phi G h^2} = f(\sigma_y)\sin\theta_G, \qquad \sigma_y = \frac{Gh\sin\theta_G}{2\tau_0}. \tag{17.29}$$

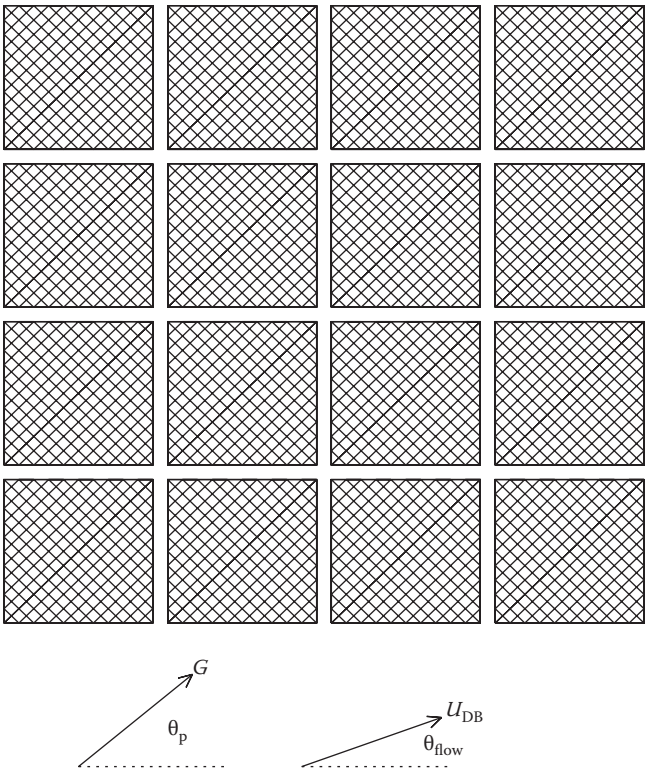

FIGURE 17.6 Showing a square network of channels.

From these expressions, we may determine the total velocity which has been induced and its direction:

$$\frac{12\mu\,|\,\underline{u}\,|_{\mathrm{DB}}}{\phi G h^2} = \sqrt{\left[f(\sigma_x)\cos\theta_G\right]^2 + \left[f(\sigma_y)\sin\theta_G\right]^2} \quad \text{and} \quad \tan\theta_{\mathrm{flow}} = \frac{f(\sigma_y)\sin\theta_G}{f(\sigma_x)\cos\theta_G}. \tag{17.30}$$

The variation of the magnitude of the induced flow and its direction with both G and the orientation of the applied pressure gradient, θ_G, are shown in Figure 17.7. Here, we see that the magnitude of the velocity varies with θ_G, and when $\sigma < \sqrt{2}$, there are directions centered on 45° where the pressure gradient is insufficient to drive a flow. The maximum velocity for a given G is always attained when the pressure gradient is in the direction of the channels, while the minimum always corresponds to it being at an orientation of 45°.

We also see that when σ takes relatively small values, the flow will often be either in the horizontal or in the vertical direction. This is because the component of the pressure gradient in the direction orthogonal to the flow is insufficient to cause yield. Thus, we see a rapid change in the direction of the induced flow near to $\theta_G = 45°$ as θ_G varies from 0° to 90°. But as G increases, we find that variations in velocity tend to vanish and $\theta_f \to \theta_G$. Thus, the large-G limit, the Newtonian limit, yields an isotropic system where the underlying grid of channels is not evident in the response of the fluid to the pressure gradient. Therefore, for a Bingham fluid, we have a strong anisotropy in the response to an applied pressure gradient, one that is caused by the presence of the yield stress, and which is entirely absent when the fluid is Newtonian.

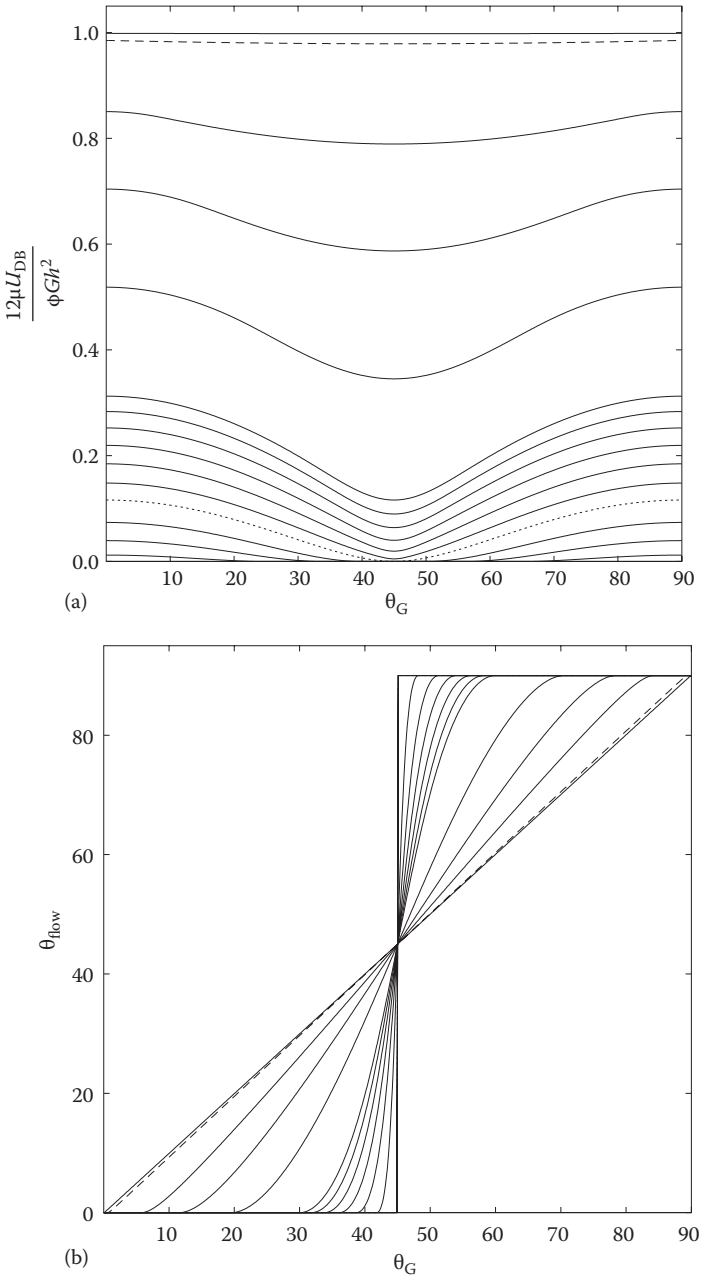

FIGURE 17.7 Displaying (a) the Darcy velocity and (b) the direction of flow for $\sigma = 1.1, 1.2, 1.3, \sqrt{2}$ (dotted), 1.5, 1.6, 1.7, 1.8, 1.9, 2, 3, 5, 10, 100 (dashed), and 1000. Angles are in degrees.

17.4 NETWORK MODELING OF THE CONVECTION OF A BINGHAM FLUID IN A POROUS MEDIUM

We may apply the same network modeling ideas to problems involving convection. Thus far, we have been interested in isothermal flows, and therefore we need to adapt some of our earlier analyses to allow for buoyancy as a body force.

17.4.1 Convection in a Sidewall-Heated Vertical Layer Formed of Channels

We will consider a porous medium that consists of $N + 1$ identical narrow vertical channels through which a Bingham fluid may flow. These channels are separated by N identical solid regions. The channels have width h, and the overall vertical layer is of width H where $h \gg H$. The layer is depicted in Figure 17.8, and we see that there is a temperature drop of magnitude ΔT across the layer. We have no need to consider the effect of having different conductivities of the fluid and the solid because the buoyancy force will depend on the magnitude of the departure of the fluid temperature from the reference value, rather than the temperature drop across the fluid channel. This scenario will change only when the fluid-to-solid thermal conductivity ratio is of the same order of magnitude as h/H.

We intend to work from this point forward in nondimensional terms, and therefore our earlier work needs to be reformulated. For channels of dimensional width, h, under the action of a pressure gradient, $-G$, the volumetric flux along one channel may be written in the form $Q = (h^3/12\mu)Gf(\sigma)$, where $\sigma = Gh/2\tau_0$. This form allows for pressure gradients of either sign. After averaging in the usual way, the overall (Newtonian) permeability of the layer shown in Figure 17.8 is, therefore, $K = (N + 1)h^3/12H$ or $\phi h^2/12$, where ϕ is the porosity. Therefore, we may write

$$Q = \frac{K}{(N+1)\mu} Gf(\sigma) \tag{17.31}$$

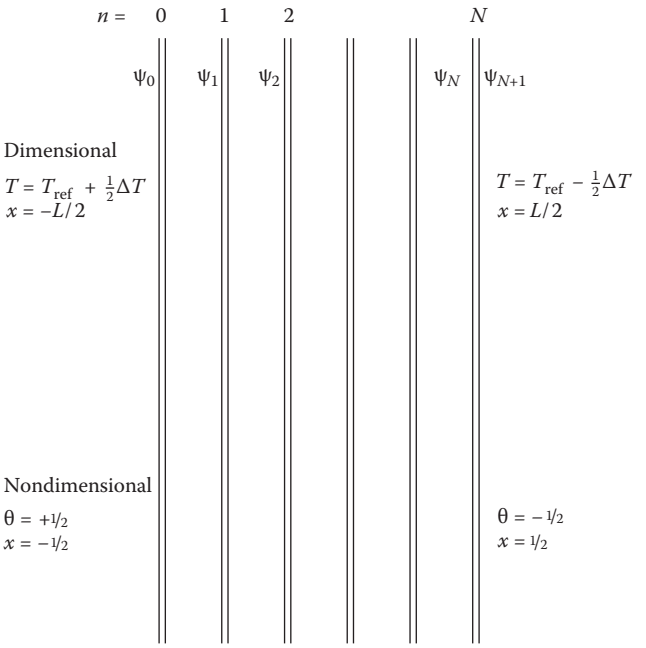

FIGURE 17.8 Displaying a vertical layer with thin vertical channels subject to sidewall heating and cooling. Both the dimensional and nondimensional boundary conditions are shown.

for the volumetric flux in *one* channel. Previously, we had $G = -p_x$, which denoted a pressure gradient in the x-direction. Now we replace the pressure gradient by the buoyancy force, and therefore we set $G = \rho g\beta(T - T_{\text{ref}})$, where ρ is the density of the fluid at the reference temperature, T_{ref} (which is at the center of the layer), g is the gravity, and β is the volumetric expansion coefficient. Additionally, the Boussinesq approximation has been assumed. Therefore, Equation 17.31 becomes

$$Q = \frac{K}{(N+1)\mu}\rho g\beta(T - T_{\text{ref}})f(\sigma), \tag{17.32}$$

where

$$\sigma = \rho g\beta(T - T_{\text{ref}})\frac{h}{2\tau_0}. \tag{17.33}$$

Now we will rescale according to

$$Q_{\text{dim}} = \frac{\alpha}{L(N+1)}Q_{\text{nondim}}, \quad T = T_{\text{ref}} + \Delta T\theta. \tag{17.34}$$

This has the effect of changing Equations 17.32 and 17.33 to the nondimensional forms

$$Q = \text{Ra}\,\theta f(\sigma) \quad \text{where } \sigma = \text{Ra}\,\theta/\text{Rb}, \tag{17.35}$$

where the Darcy–Rayleigh number and a dimensionless yield stress are defined as

$$\text{Ra} = \frac{\rho g\beta\Delta TKL}{\mu\alpha} \quad \text{and} \quad \text{Rb} = \frac{2\tau_0}{h}\frac{KL}{\mu\alpha}. \tag{17.36}$$

In the rest of this chapter, these two numbers will be referred to as the Rayleigh and Rees–Bingham numbers, respectively, although we need to note that a Bingham number defined by $\text{Bn} = \tau_0 L/\mu V$, where V is a velocity, is already well known in other contexts and represents the ratio of yield stresses (τ_0) and viscous stresses ($\mu V/L$). We also note that the earlier expression for the Rees–Bingham number contains the group, $2\tau_0/h$, which is the yield pressure gradient (or body force) for flow in a one-dimensional system of channels of width, h, as described in the previous section. More generally, therefore, we may write the Rees–Bingham number as

$$\text{Rb} = \frac{GKL}{\mu\alpha}, \tag{17.37}$$

where $|G|$ is the magnitude of the pressure gradient above which the fluid flows.

Finally, we note that the value, Q, may also be interpreted as the difference between the nondimensional streamfunction values on the two sides of the narrow channels, and Figure 17.8 denotes how we label the different values of the streamfunction. The nondimensional boundary conditions are as shown in Figure 17.8, and therefore the temperature field is simply, $\theta = -x$. From this, we see that the maximum buoyancy force corresponds to the two outer channels (i.e., numbers 0 and N) for which $x = \pm 1/2$. Therefore, as the Rayleigh number increases, flow will arise first in those channels. Using Equation 17.35 and setting $\sigma = \pm 1$, we find that the condition for this happening is that

$$\text{Ra} > 2\text{Rb}. \tag{17.38}$$

The neighboring channels, $n = 1$ and $n = N - 1$, correspond to $x = \pm(N - 2)/2N$, and therefore fluid begins to flow in these channels when

$$\mathrm{Ra} > 2\mathrm{Rb}\frac{N}{N-2}. \tag{17.39}$$

In a similar fashion, the next two channels, $n = 2$ and $n = N - 2$, which are located at $x = \pm(N - 4)/2N$, begin to admit flow when

$$\mathrm{Ra} > 2\mathrm{Rb}\frac{N}{N-4}, \tag{17.40}$$

with the obvious extension to further channels.

We see that convective *onset* happens at discrete values of Ra with increasing numbers of channels admitting flow as the Rayleigh number increases.

17.4.2 Convection in a Sidewall-Heated Square Cavity

We now consider convection in a square cavity of the type depicted in Figure 17.6, but the detailed analysis begins with one block as shown in Figure 17.9.

Within the horizontal channels, we have $\tau_z = -p_x$, and in the vertical channels, $\tau_x = -p_z + \mathrm{Ra}\,\theta$. The subscript notation on the G–values in Figure 17.9 denotes the compass directions. Convection is assumed to be weak in the sense that it is not strong enough to modify the temperature field from $\theta = -x$. The streamfunction is set to be zero on the outer boundary.

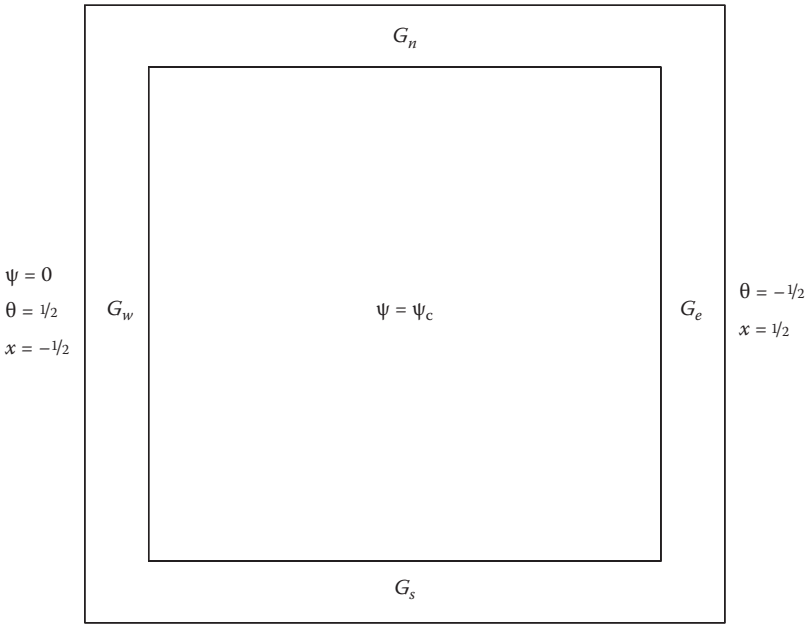

FIGURE 17.9 Displaying the single-block case of a network of channels showing the streamfunction values and the notation for the body force terms.

The following network analysis follows the method outlined in Jamalud-Din et al. (2010). On applying the general theory derived earlier and which is represented by Equation 17.35, we obtain the following equations for each of the four channels surrounding the central block:

$$\begin{aligned}
&\text{West:} && \psi_c = G_w f(\sigma_w) && G_w = -\left.\frac{\partial p}{\partial z}\right|_w + \frac{1}{2}\mathrm{Ra}, && \sigma_w = \frac{G_w}{\mathrm{Rb}},\\
&\text{East:} && -\psi_c = G_e f(\sigma_e) && G_e = -\left.\frac{\partial p}{\partial z}\right|_e - \frac{1}{2}\mathrm{Ra}, && \sigma_e = \frac{G_e}{\mathrm{Rb}},\\
&\text{South:} && -\psi_c = G_s f(\sigma_s) && G_s = -\left.\frac{\partial p}{\partial x}\right|_s, && \sigma_s = \frac{G_s}{\mathrm{Rb}},\\
&\text{North:} && \psi_c = G_n f(\sigma_n) && G_n = -\left.\frac{\partial p}{\partial x}\right|_n, && \sigma_n = \frac{G_n}{\mathrm{Rb}}.
\end{aligned} \tag{17.41}$$

To these equations, we must add the condition that the pressure difference between the bottom left corner and the top right corner is independent of the direction of travel:

$$\left.\frac{\partial p}{\partial z}\right|_w + \left.\frac{\partial p}{\partial x}\right|_n = \left.\frac{\partial p}{\partial z}\right|_e + \left.\frac{\partial p}{\partial x}\right|_s. \tag{17.42}$$

The solution of this system of five equations is

$$\sigma_w = \sigma_n = -\sigma_e = -\sigma_s = \frac{\mathrm{Ra}}{4\mathrm{Rb}}, \quad \psi_c = \frac{\mathrm{Ra}}{4} f(\sigma) \quad \text{where } \sigma = \frac{\mathrm{Ra}}{4\mathrm{Rb}}. \tag{17.43}$$

Given that flow takes place in the channels only when $\sigma > 1$, we conclude that convection begins when Ra = 4Rb. This is double the value that was found for the vertical layer in Section 17.4.1. This may be justified by appealing to the fact that, for a unit vertical distance, the buoyancy forces need to move the fluid through twice the distance in the cavity than they do in the vertical layer.

We may now extend this analysis to larger systems of blocks within the square cavity. A definition sketch of a 3 × 3 system is shown in Figure 17.10, where, for convenience, a new notation for the body force in the horizontal (H_{ij}) and vertical (V_{ij}) channels is introduced.

Here, $H_{ij} = -p_x$ and $V_{ij} = -p_z + \mathrm{Ra}\, x_i$ denote the horizontal and vertical body forces, respectively, while $x_1 = -1/2$, $x_2 = -1/6$, $x_3 = -1/6$, and $x_4 = 1/2$. On applying the same method as for the single-block case, we obtain the following set of 33 equations for 33 unknowns:

$$\begin{aligned}
\psi_{11} &= V_{11} f(V_{11}/\mathrm{Rb}) & \psi_{11} &= -H_{11} f(H_{11}/\mathrm{Rb}) & V_{11} + H_{12} &= H_{11} + V_{21} + \mathrm{Ra}/3\\
\psi_{12} &= V_{12} f(V_{12}/\mathrm{Rb}) & \psi_{21} &= -H_{21} f(H_{21}/\mathrm{Rb}) & V_{21} + H_{22} &= H_{21} + V_{31} + \mathrm{Ra}/3\\
\psi_{13} &= V_{13} f(V_{13}/\mathrm{Rb}) & \psi_{31} &= -H_{31} f(H_{31}/\mathrm{Rb}) & V_{31} + H_{32} &= H_{31} + V_{41} + \mathrm{Ra}/3\\
\psi_{21} - \psi_{11} &= V_{21} f(V_{21}/\mathrm{Rb}) & \psi_{12} - \psi_{11} &= -H_{12} f(H_{12}/\mathrm{Rb}) & V_{12} + H_{13} &= H_{12} + V_{22} + \mathrm{Ra}/3\\
\psi_{22} - \psi_{21} &= V_{22} f(V_{22}/\mathrm{Rb}) & \psi_{22} - \psi_{21} &= -H_{22} f(H_{22}/\mathrm{Rb}) & V_{22} + H_{23} &= H_{22} + V_{32} + \mathrm{Ra}/3\\
\psi_{23} - \psi_{13} &= V_{23} f(V_{23}/\mathrm{Rb}) & \psi_{32} - \psi_{31} &= -H_{32} f(H_{32}/\mathrm{Rb}) & V_{32} + H_{33} &= H_{32} + V_{42} + \mathrm{Ra}/3\\
\psi_{31} - \psi_{21} &= V_{31} f(V_{31}/\mathrm{Rb}) & \psi_{13} - \psi_{12} &= -H_{13} f(H_{13}/\mathrm{Rb}) & V_{13} + H_{14} &= H_{13} + V_{23} + \mathrm{Ra}/3\\
\psi_{32} - \psi_{22} &= V_{32} f(V_{32}/\mathrm{Rb}) & \psi_{23} - \psi_{22} &= -H_{23} f(H_{23}/\mathrm{Rb}) & V_{23} + H_{24} &= H_{23} + V_{33} + \mathrm{Ra}/3\\
\psi_{33} - \psi_{23} &= V_{23} f(V_{23}/\mathrm{Rb}) & \psi_{33} - \psi_{32} &= -H_{33} f(H_{33}/\mathrm{Rb}) & V_{33} + H_{34} &= H_{33} + V_{43} + \mathrm{Ra}/3\\
-\psi_{31} &= V_{41} f(V_{41}/\mathrm{Rb}) & -\psi_{13} &= -H_{14} f(H_{14}/\mathrm{Rb})\\
-\psi_{32} &= V_{42} f(V_{42}/\mathrm{Rb}) & -\psi_{23} &= -H_{24} f(H_{24}/\mathrm{Rb})\\
-\psi_{33} &= V_{43} f(V_{43}/\mathrm{Rb}) & -\psi_{33} &= -H_{34} f(H_{34}/\mathrm{Rb})
\end{aligned} \tag{17.44}$$

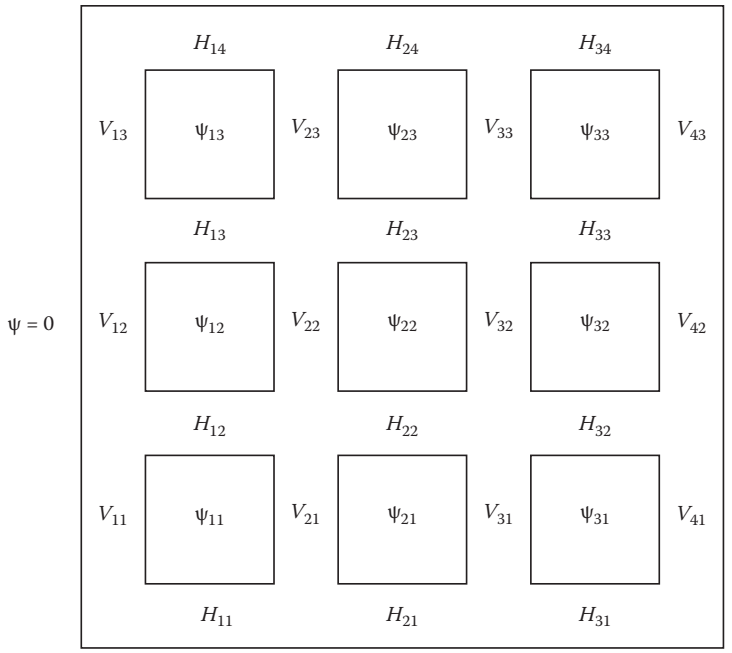

FIGURE 17.10 Displaying the 3 × 3 system of identical blocks within a square cavity.

These equations were solved using a general-purpose user-written Newton–Raphson program using numerical differentiation to obtain the Jacobian matrix. However, the Jacobian matrix is singular whenever the fluid is unyielded in any channel, and therefore, we have adopted the following regularization-like modification to the definition of $f(\sigma)$:

$$f(\sigma) = \begin{cases} \left(1 - \dfrac{3}{2|\sigma|} + \dfrac{1}{|\sigma|^3}\right) + \epsilon|\sigma| & |\sigma| > 1, \\ \epsilon|\sigma| & 0 < |\sigma| < 1, \end{cases} \tag{17.45}$$

where we took $\epsilon = 10^{-5}$, which is small enough to affect the resulting solutions minimally, but large enough to allow solutions to be obtained robustly.

Figure 17.11 shows how the streamfunction values vary with the Rayleigh number for this 3 × 3 system of blocks and for a 9 × 9 system. The abscissae in this figure are both Ra/4Rb because curves for different values of Rb collapse down to a unique curve when this is done. In fact, one may rescale the variables in Equation 17.44 so that the dependence on Ra/Rb becomes explicit.

As with the vertical channel, we see successive bifurcations within these two cases as increasing numbers of channels begin to flow as Ra increases. A detailed examination of the numerical solutions indicate that the first bifurcation to flow arises when Ra = 4Rb, as for the single-block case. This indicates that only the outermost circuit flows when Ra is slightly above this value. Successive bifurcations, which are indicated by black disks in the figure, then correspond to new square circuits being released to flow.

For the 3 × 3 system, the bifurcations arise when Ra/4Rb = 1 and 3, while for the 9 × 9 system, they arise at Ra/4Rb = 1, 9/7, 9/5, 3, and 9. Indeed, for odd values of N, successive bifurcations happen when Ra/4Rb = N/j where $j = N, N-2, N-4, \ldots, 1$. For even values, the same sequence happens

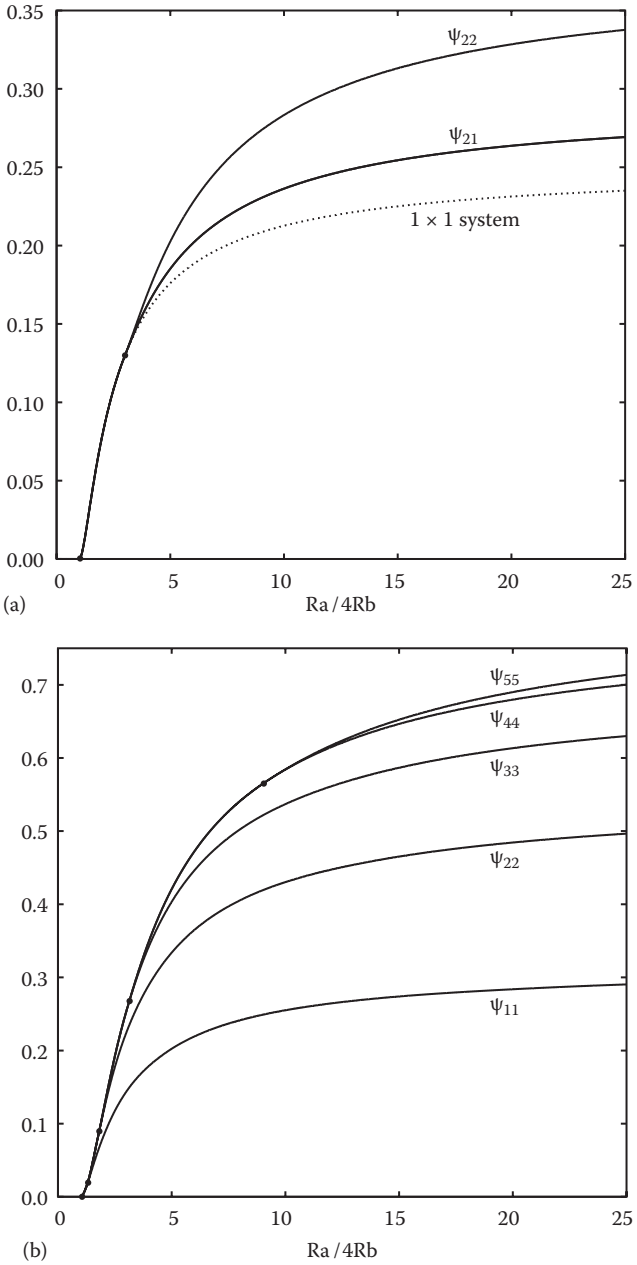

FIGURE 17.11 The variation of ψ with Rayleigh number for a (a) 3 × 3 and a (b) 9 × 9 system of blocks. The dotted line indicates the variation of ψ for the single-block system.

but ends with $j = 2$, in which case the central 2 × 2 system has no flow between its blocks, and these four act as a single block of double the linear dimension.

These observations may be explained by appealing to the temperature drop across each of these successively smaller square circuits; the value of Ra/4Rb is then the reciprocal of the width of that circuit compared with that of the square cavity.

No doubt a different network morphology will yield quite different results from those presented here, and it is intended to pursue this aspect in the immediate future.

17.5 CONVECTION OF A BINGHAM FLUID IN A SIDEWALL-HEATED CAVITY

This section is devoted to analyzing convection, which is caused by heating a sidewall in a vertical channel or cavity. The major difference between this section and Section 17.4 is that we will now be employing macroscopic laws for the momentum equations, ones that are motivated by our previous results. Thus, our aim is to consider strongly nonlinear convection and to determine how the different types of Darcy–Bingham law that arise will affect the flow pattern and the strength of convection.

We will consider two different systems briefly. The first is the so-called double glazing problem where the porous medium is confined between two vertical impermeable vertical surfaces that are held at temperatures that are steady and uniform but that are different. The second is a square cavity with the same sidewall heating and cooling, but where the upper and lower surfaces are insulating. This is a classic test case for numerical computation for porous cavities, but especially for clear fluids with high Rayleigh numbers. This second system is divided into three cases that are distinguished by the type of Darcy–Bingham law which is used. In the first case, we consider an isotropic threshold gradient law as modified/regularized for computational reasons by a tanh profile. The second is an anisotropic form that is equivalent to the square grid pattern used in the network modeling of Section 17.4.1. Here there are preferential flow directions for the Bingham fluid, and these are in the x- and z-directions. Then, the third case allows for these preferential directions to be rotated by an angle, α.

17.5.1 The Double Glazing Problem

The configuration we study is identical to that shown in Figure 17.8 except that we now adopt a macroscopic law to replace the channels that were considered in Section 17.4.1.

The channel is presumed to have infinite height, and therefore the flow, whenever it arises, will be in the vertical direction, z, and will be a function of x only. The nondimensional macroscopic equation for the vertical velocity is

$$w = f(\sigma_z)\left[-\frac{\partial p}{\partial z} + \mathrm{Ra}\theta\right], \tag{17.46}$$

where

$$\sigma_z = \frac{1}{\mathrm{Rb}}\left[-\frac{\partial p}{\partial z} + \mathrm{Ra}\theta\right], \quad \text{and} \quad \theta = -x. \tag{17.47}$$

This one-dimensional equation is the natural upscaled version of Equation 17.35, which describes Darcy–Bingham flow based on the BR2D model for microscopic flows in channels.

We now set $\partial p/\partial z = 0$ in order to maintain a zero overall fluid flux up the layer, and therefore we obtain $w = -\mathrm{Ra}\, x\, f(-\mathrm{Ra}\, x/\mathrm{Rb})$. This velocity profile may therefore be written in the form

$$w = \begin{cases} -\mathrm{Ra}\, x\left[1 - \dfrac{3\mathrm{Rb}}{2\mathrm{Ra}\,|x|} + \dfrac{\mathrm{Rb}^3}{\mathrm{Ra}^3\,|x|^3}\right] & \text{when} \quad \left|\dfrac{\mathrm{Ra}\, x}{\mathrm{Rb}}\right| > 1. \\ 0 & \text{when} \quad \left|\dfrac{\mathrm{Ra}\, x}{\mathrm{Rb}}\right| < 1. \end{cases} \tag{17.48}$$

Clearly, convection begins when $\mathrm{Ra} = 2\mathrm{Rb}$, as with the earlier discretely layered vertical channel, and immediately post-onset convection is confined to those regions near the external walls.

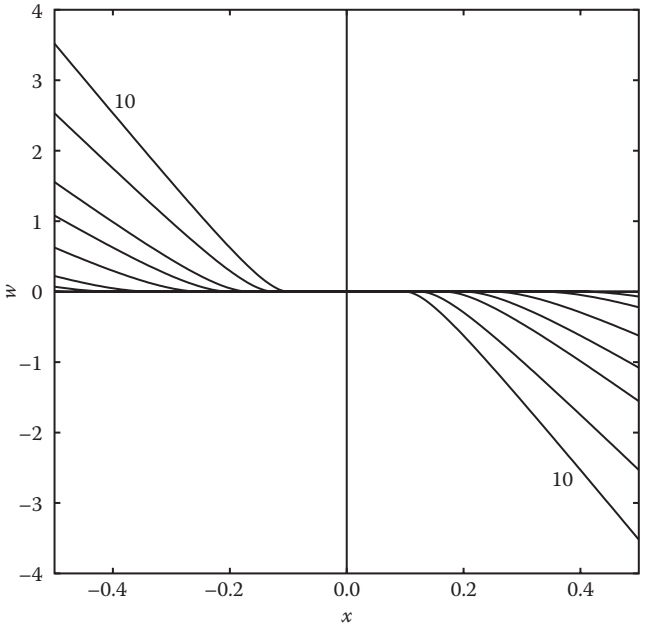

FIGURE 17.12 Velocity profiles for Ra/Rb = 2.5, 3, 4, 5, 6, 8, and 10.

Figure 17.12, which presents velocity profiles for different values of Ra/Rb, shows this clearly. As Ra/Rb increases, more and more of the channel begins to flow, and once Ra/Rb is sufficiently large, the velocity profile eventually becomes linear, which is equivalent to that for a Newtonian fluid.

17.5.2 Unit Cavity: Isotropic Model

We now begin to consider nonlinear two-dimensional convection. In this pioneering work, we will adopt the threshold model for flow, rather than the BR2D model, but in the interests of computational ease, this will be regularized using the tanh model, which was discussed earlier. Therefore, the x-momentum equation

$$u = \begin{cases} -\dfrac{K}{\mu}\left[1 - \dfrac{G}{|p_x|}\right] p_x & \text{when } |p_x| > G \\ 0 & \text{otherwise} \end{cases} \tag{17.49}$$

will be replaced by

$$\left[1 + G\frac{K}{\mu}\frac{\tanh(cu)}{u}\right] u = -\frac{K}{\mu} p_x. \tag{17.50}$$

These two equations appeared earlier as Equations 17.9 and 17.13, but are quoted here so that this section is self-contained. We also note that for porous media consisting of channels of width h, the yield pressure gradient is given by Equation 17.17 and is $G = 2\tau_0/h$.

For fully nonlinear convection, the appropriate frame-invariant momentum equations now take the form

$$\left[1 + G\frac{K}{\mu}\frac{\tanh(cq)}{q}\right] u = -\frac{K}{\mu} p_x, \tag{17.51}$$

$$\left[1+G\frac{K}{\mu}\frac{\tanh(cq)}{q}\right]w=-\frac{K}{\mu}\left[p_z-\rho g\beta(T-T_{\text{ref}})\right], \tag{17.52}$$

where $q^2 = u^2 + w^2$. These two equations are supplemented by the equations of continuity and heat transfer:

$$u_x + w_z = 0, \tag{17.53}$$

$$\chi T_t + uT_x + wT_z = \alpha\left(T_{xx} + T_{zz}\right). \tag{17.54}$$

Now we nondimensionalize using the following scalings:

$$(x,z)\to L(x,z),\ \ (u,w)\to\frac{\alpha}{L}(u,w),\ \ \ p\to\frac{\alpha\mu}{K}p,\ \ T\to T_{\text{ref}}+\Delta T\,\theta,\ \ \ c\to\frac{L}{\alpha}c,\ \ \ t\to\chi\frac{L^2}{\alpha}t. \tag{17.55}$$

In this equation, χ is the ratio of the specific heats of the porous medium and the fluid, while L is the height of the cavity. The full set of nondimensional equations that govern the two-dimensional convection of a Bingham fluid in a porous medium is, therefore,

$$u_x + w_z = 0, \tag{17.56}$$

$$\left[1+\text{Rb}\frac{\tanh(cq)}{q}\right]u=-p_x, \tag{17.57}$$

$$\left[1+\text{Rb}\frac{\tanh(cq)}{q}\right]w=-p_z+\text{Ra}\,\theta, \tag{17.58}$$

$$\theta_t + u\theta_x + w\theta_z = \theta_{xx} + \theta_{zz}. \tag{17.59}$$

These four equations may be reduced to two by the introduction of the streamfunction, ψ, defined according to $u = -\psi_z$ and $w = \psi_x$. The equation of continuity is satisfied, while the momentum and heat transport equations reduce to the following forms:

$$\nabla^2\psi+\frac{\text{Rb}\tanh(cq)}{q^3}\left[\psi_z^2\psi_{xx}-2\psi_x\psi_z\psi_{xz}+\psi_x^2\psi_{zz}\right]$$
$$+\frac{\text{Rb}\,c\,\text{sech}^2(cq)}{q^2}\left[\psi_x^2\psi_{xx}+2\psi_x\psi_z\psi_{xz}+\psi_z^2\psi_{zz}\right]=\text{Ra}\theta_x, \tag{17.60}$$

$$\theta_t + \psi_x\theta_z - \psi_z\theta_x = \nabla^2\theta, \tag{17.61}$$

where

$$q=\sqrt{\psi_x^2+\psi_z^2}. \tag{17.62}$$

The cavity is a unit square which lies between −1/2 and 1/2 in the x-direction. The streamfunction is zero on all four boundaries. We set $\theta = \pm\frac{1}{2}$ on $x = \pm\frac{1}{2}$, while $\theta_z = 0$ on both $z = 0$ and $z = 1$. Thus, the upper and lower surfaces are insulated.

We have adopted a very straightforward and quite standard method of discretization where three-point central differences were used to approximate each spatial derivative in Equations 17.60 through 17.62. The Neumann conditions for θ on the upper and lower surfaces use the fictitious point approach described well in Roache (1976) and used frequently by the present author. Steady-state solutions were undertaken using Gauss–Seidel iteration as this was quicker than using an explicit time-stepping method. The author is aware that faster methods exist, and these will be adopted for a more wide-ranging survey of the effects of yield stress on convection. We used 48 equally spaced intervals in each direction—this was a compromise between accuracy and speed of computation. Again, future work with faster methods will also use finer grids and also allow the investigation of cavities with aspect ratios other than unity. In the present computations, we have used $c = 3$ in the tanh profile.

Figure 17.13 shows the streamlines (continuous) and isotherms (dashed) for six cases where Ra = 100. The values of Rb are 0, 5, 10, 15, 20, and 25. The value, Rb = 0, corresponds to a Newtonian fluid without a yield stress. At this value of Ra, boundary layers on the vertical walls are only just beginning to become distinct. Flow is quite rapid near the base of the hot wall, as is inferred by the closeness of the streamlines and also near the top of the cold wall. At this value of Ra, there is quite a strong deformation of the isotherms from the vertical orientation that they have when Ra = 0 and which corresponds to a conduction solution.

As Rb increases, first to 5 and then to 10, we see an increasingly large central region that, if one were using a threshold gradient model, would correspond to a stagnant region. Here there is

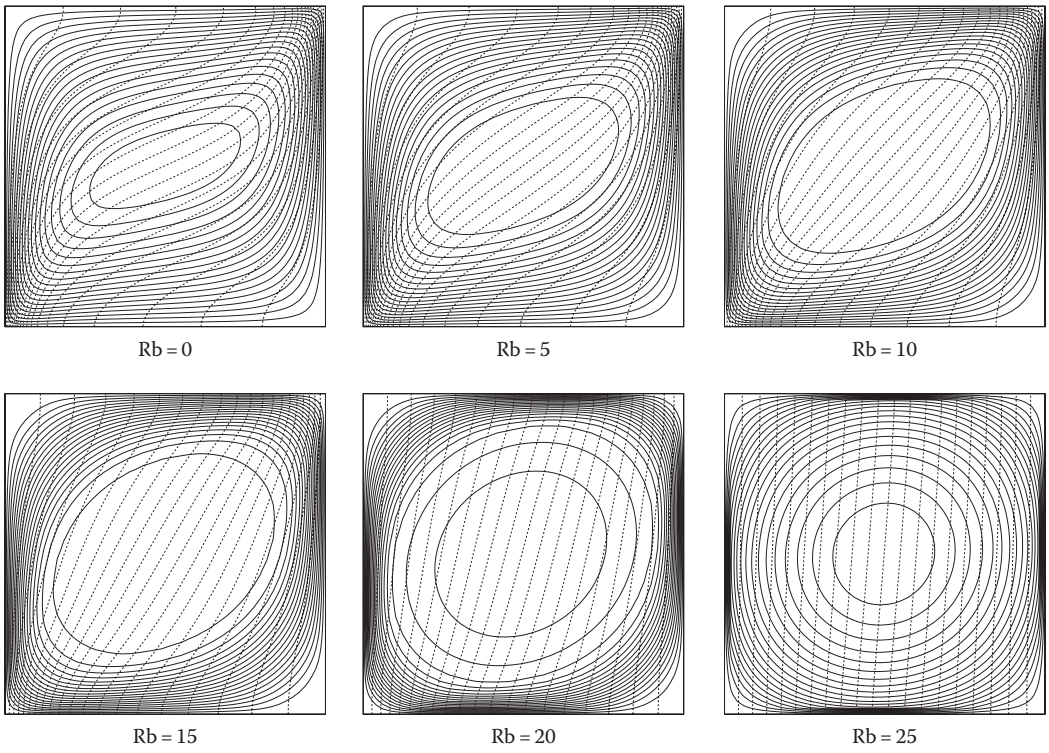

FIGURE 17.13 Streamlines (continuous) and isotherms (dashed) for $c = 3$ and Ra = 100 using an isotropic model.

very slow flow. Although the boundary layers near the vertical wall appear more distinctly, the overall circulation of fluid has decreased as Rb has increased, and this may also be inferred by the decreasing deformation of the isotherms. At still higher values of Rb, flow tends to be confined to a racetrack-like circuit mainly near the four straight boundaries, which is reminiscent of the network analysis in Section 17.4. As Rb increases, the width of the racetrack decreases. When Rb = 25, the overall flow is quite weak, and the isotherms are almost vertical. In this case, the racetrack is very narrow indeed, and a further slight increase in Rb would cause the flow to stop. The concentric streamlines that appear here reflect the fact that $c = 3$; fewer streamlines will appear in the central region when c takes larger values.

We summarize a more extensive set of computations in Figure 17.14. This figure shows the variation of both $|\psi|_{\max}$ and the Nusselt number with Ra for various values of Rb. Here we define the Nusselt number as

$$\mathrm{Nu} = -\int_0^1 \frac{\partial \theta}{\partial x}\, dy, \tag{17.63}$$

at either $x = 0$ or $x = 1$. Although the derivative is evaluated using a one-sided finite difference approximation, the value obtained may be shown to be of second-order accuracy, and the integral is performed using the trapezium rule. When Ra = 0, the conduction solution prevails, and Nu = 1.

When Rb = 0, we see both $|\psi|_{\max}$ and Nu increasing with Ra. When Rb takes nonzero values, both these quantities rise very slowly as Ra increases from zero due to the high apparent viscosity for such small buoyancy forces; see Equation 17.58. This rise becomes even more sedate as c increases. A more rapid rise then ensues once the yield threshold has been passed, and once more, it is necessary to point out that larger values of c will show the transition from slow growth to a rapid ascent increasingly clearly. The effect of increasing values of Rb is seen quite clearly in this figure, and one

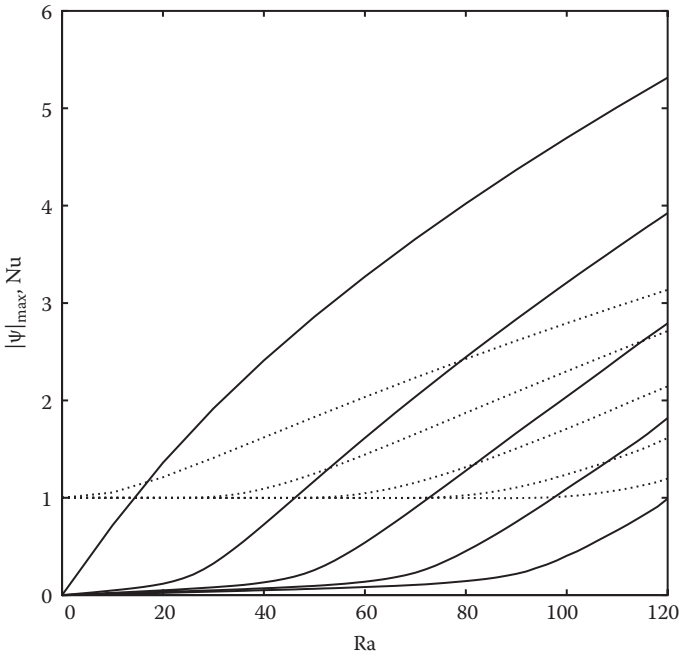

FIGURE 17.14 Variation of $|\psi|_{\max}$ (continuous) and Nu (dashed) with Ra for Rb = 0, 5, 10, 15, and 20. The value $c = 3$ was used.

may extrapolate easily to higher values of both Rb and Ra, at least in a qualitative sense. Finally, we note that the variations in $|\psi|_{\max}$ and Nu are consistent with the earlier network analysis, which gives Ra = 4Rb as being the value above which flow begins to ensue.

17.5.3 Unit Cavity: Anisotropic Model

We now consider a Darcy–Bingham model which displays the characteristics that were found in the network analysis of Section 17.4. If the porous medium is composed solely of equally spaced vertical and horizontal channels, then it is clear that flow in, say, the z-direction at one point will not affect the flow in the x-direction. Therefore, we may replace Equations 17.57 and 17.58 by

$$\left[1 + \mathrm{Rb}\,\frac{\tanh(cu)}{u}\right] u = -p_x, \tag{17.64}$$

$$\left[1 + \mathrm{Rb}\,\frac{\tanh(cw)}{w}\right] w = -p_z + \mathrm{Ra}\,\theta. \tag{17.65}$$

These may be simplified to the forms

$$u + \mathrm{Rb}\tanh(cu) = -p_x, \tag{17.66}$$

$$w + \mathrm{Rb}\tanh(cw) = -p_z + \mathrm{Ra}\,\theta. \tag{17.67}$$

Introduction of the streamfunction as before yields the following momentum equation:

$$\left[1 + \mathrm{Rb}\,c\,\mathrm{sech}^2(c\psi_x)\right]\psi_{xx} + \left[1 + \mathrm{Rb}\,c\,\mathrm{sech}^2(c\psi_z)\right]\psi_{zz} = \mathrm{Ra}\,\theta_x, \tag{17.68}$$

while the heat transport equation is unchanged. This new system of equations was solved in an identical manner to those in the previous subsection.

Figure 17.15 shows how the streamlines and isotherms vary as Rb increases where $c = 3$ and Ra = 100 have been taken. Superficially, these contour plots look very much like those for the isotropic model, but there is a difference. At intermediate values of Rb, such as the range from 10 to 20 for the present value of the Rayleigh number, the racetrack path of the streamlines is now confined to regions very close to the bounding surfaces where the flow is essentially either vertical or horizontal, the flow turns close to the corners, and the region in which flow takes place is narrower. There is little change in the isotherms.

For the sake of brevity, we do not include a figure that corresponds to Figure 17.14, as it takes an identical qualitative form, and the quantitative data are very similar.

Now we turn to the case of a porous medium where the network of channels is aligned at an angle α to the coordinate directions. Equations 17.66 and 17.67 correspond to $\alpha = 0$, and their modified form to account for an oblique network is

$$u + \mathrm{Rb}\left[\cos\alpha\tanh c(u\cos\alpha + w\sin\alpha) - \sin\alpha\tanh c(w\cos\alpha - u\sin\alpha)\right] = -p_x, \tag{17.69}$$

$$w + \mathrm{Rb}\left[\sin\alpha\tanh c(u\cos\alpha + w\sin\alpha) + \cos\alpha\tanh c(w\cos\alpha - u\sin\alpha)\right] = -p_z + \mathrm{Ra}\,\theta. \tag{17.70}$$

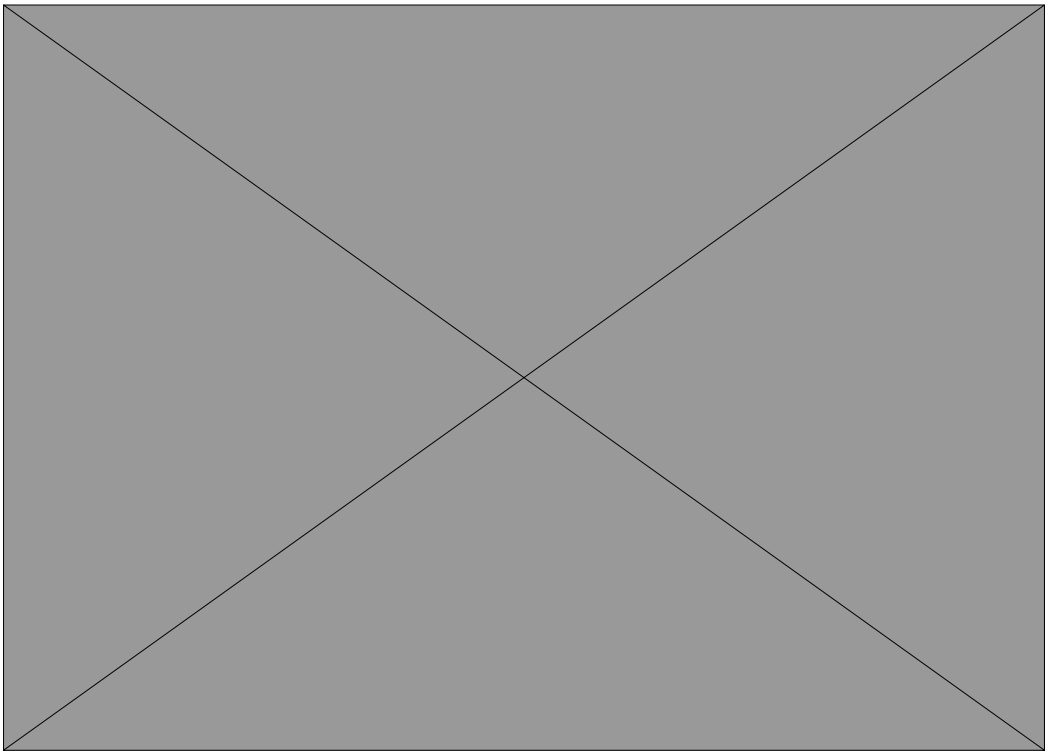

FIGURE 17.15 Streamlines (continuous) and isotherms (dashed) for $c = 3$ and Ra = 100 using a square-network-based anisotropic model.

In terms of the streamfunction, this more complicated pair of equations becomes

$$\nabla^2\psi + \mathrm{Rb}\, c\left[\psi_{xx}\sin^2\alpha - 2\psi_{xz}\sin\alpha\cos\alpha + \psi_{zz}\cos^2\alpha\right]\mathrm{sech}^2 c(\psi_x\sin\alpha - \psi_z\cos\alpha)$$
$$+\mathrm{Rb}\, c\left[\psi_{xx}\cos^2\alpha + 2\psi_{xz}\sin\alpha\cos\alpha + \psi_{zz}\sin^2\alpha\right]\mathrm{sech}^2 c(\psi_x\cos\alpha + \psi_z\sin\alpha) = \mathrm{Ra}\,\theta_x, \tag{17.71}$$

where the heat transport equation is again unchanged.

Figure 17.16 shows six sets of streamlines and isotherms for different values of Rb when Ra = 100, $c = 3$, and $\alpha = 45°$. We see that, even when Rb is as small as 5, the orientation of the microchannels is very evident in the pattern of the streamlines. There are now quite pronounced dead zones in the top left and bottom right corners, where it is very difficult for the fluid to penetrate because of the microstructure. As Rb increases, the racetrack pattern evolves once more, taking its clearest form when Rb = 15. The flow has become very weak when Rb = 20 with only a hint of strong flow near the central portions of each of the four walls. Convection is almost nonexistent when Rb = 25, and the case lies well within the high-viscosity zone of the tanh model. At this point, the isotherms have deformed only slightly from the vertical.

Figure 17.17 shows the effect of varying α on the flow pattern for the case $c = 3$, Rb = 10, and Ra = 100. For these values of Rb and Ra, the flow is quite strong, and there is a large, essentially unyielded, zone in the center of the cavity. The orientation of the underlying network is very evident indeed in the computed streamlines. As α increases from zero, the natural path for the flow near the hot left surface becomes increasingly misaligned with the direction of the buoyancy force, and

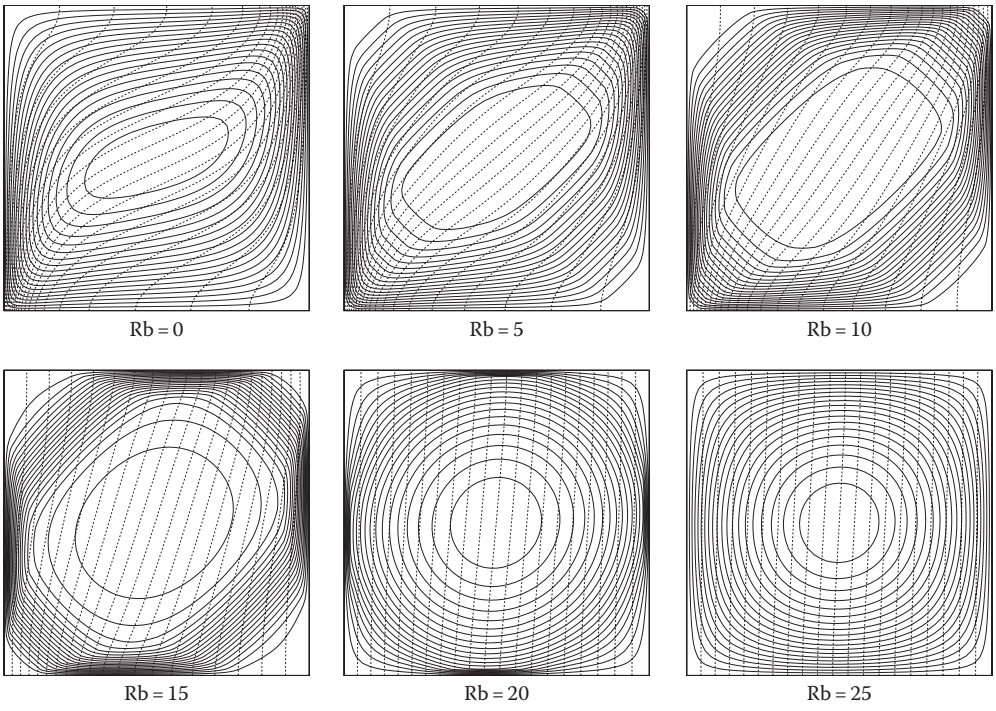

FIGURE 17.16 Streamlines (continuous) and isotherms (dashed) for $c = 3$ and Ra = 100 using a square-network-based anisotropic model with $\alpha = 45°$.

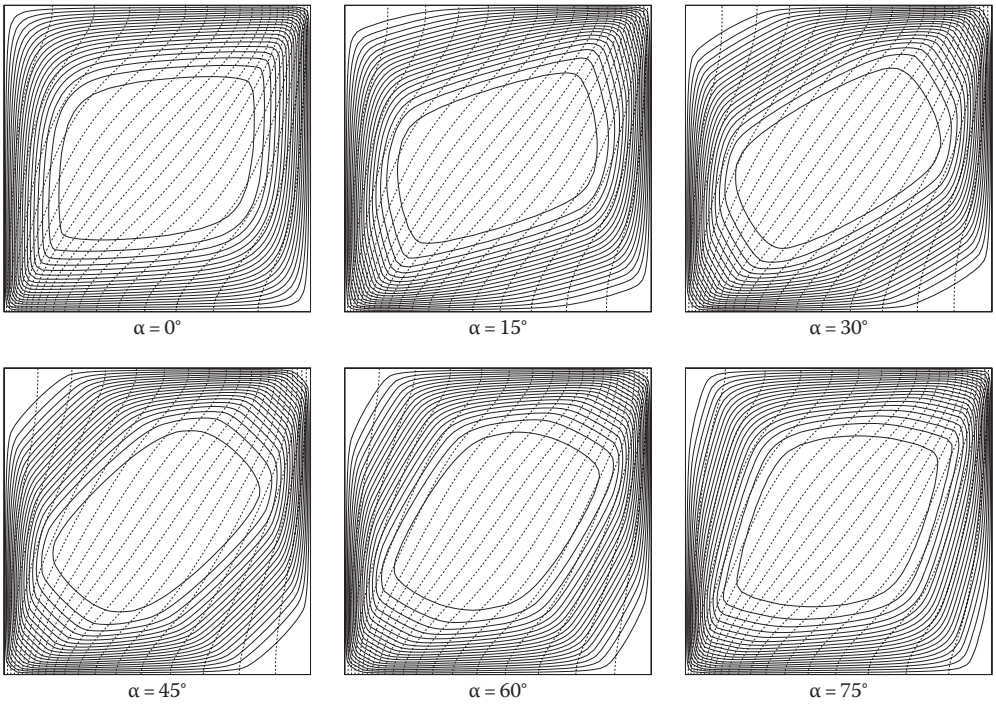

FIGURE 17.17 Streamlines (continuous) and isotherms (dashed) for Rb = 10, $c = 3$, and Ra = 100 using a square-network-based anisotropic model with different values of α.

therefore buoyancy becomes less effective to move the fluid. Therefore, there is a weakening of the flow and a reduction in the heat transfer across the layer. That this is so may be seen by the movement of the top of the leftmost isotherm as α increases from zero. When α approaches 90°, a case that is identical to $\alpha = 0°$, then the flow strengthens once more.

Finally, it is worth saying that the double glazing problem in porous media is one where, for a Newtonian fluid without a yield stress, all that happens as Ra increases is that the flow gets stronger and the rate of heat transfer across the layer increases. There is no instability that will occur, and the thermal boundary layers on the sidewalls become thinner. Indeed, even for a vertical channel, the studies of Gill (1969) and Lewis et al. (1995) have shown that instability does not happen when the flow is governed by Darcy's law. We suspect strongly that this property will also be shared by a convecting Bingham fluid.

17.6 DARCY–BÉNARD CONVECTION

We now consider the convection of a Bingham fluid in a horizontal porous layer which is heated from below. This is, in effect, the double glazing problem rotated through 90° with the hot surface located below the cold one. This generic problem is known by a variety of names: the Darcy–Bénard problem, the porous Bénard problem, the Lapwood problem, and the Horton and Rogers problem, with occasional merging between names, such as the HRL or Horton–Rogers–Lapwood problem. The various names that appear here were the pioneers, and the papers by Horton and Rogers (1945) and Lapwood (1948) are considered to be the founding works. It is these authors who determined that, for a Newtonian fluid, convection arises first when the Rayleigh number reaches $4\pi^2$ and the wavenumber is equal to π. Thus, the convection cells which appear first as Ra increases have a precisely square cross section. In this section, we present some very preliminary computations for what we shall call the Darcy–Bingham–Bénard problem. In view of the fact that the first cell to appear as Ra increases has unit aspect ratio, we will confine our studies for now to the same unit square that was the subject of the previous section. Our primary interest is to see how the presence of a yield stress alters the classical onset behavior, namely, a supercritical bifurcation to strongly convecting flow. Our numerical simulations were undertaken in an identical way and with the same precautions as were used for the sidewall-heated cavity. The only difference was that the Gauss–Seidel iterations were initiated using a strongly perturbed temperature field.

Figure 17.18 shows a comparison between the various types of Darcy–Bingham models for the case Ra = 200, with $c = 10$, and Rb = 12. In Figure 17.18, we compare the flow of a Newtonian fluid with the isotropic Darcy–Bingham model and the anisotropic models with $\alpha = 0°$ and $\alpha = 45°$. We have chosen to use the parameter values, Ra = 200, $c = 10$, and Rb = 12, in order to show clearly the essential differences in the resulting flow pattern between these models; other parameter sets tend not to be so clear.

For the Newtonian fluid, Ra = 200 is well into the nonlinear regime and represents a value which is very close to five times the critical value. This steady flow is very strong, and the isotherms have been deformed into a very clear S-shape by the power of the flow. It is very noticeable that the three Darcy–Bingham models have isotherms that are less deformed than for the Newtonian fluid due to the flow being weaker as it had to overcome the yield threshold.

The nature of each of the Darcy–Bingham models is particularly evident when looking at the streamlines. The isotropic model has streamlines which follow a racetrack pattern that is quite round, and the flow tends to avoid the downstream corners on the vertical surfaces. On the other hand, the anisotropic model yields streamline patterns which follow quite closely the imposed direction of the underlying network with relatively sharp "corners" when the fluid has to turn.

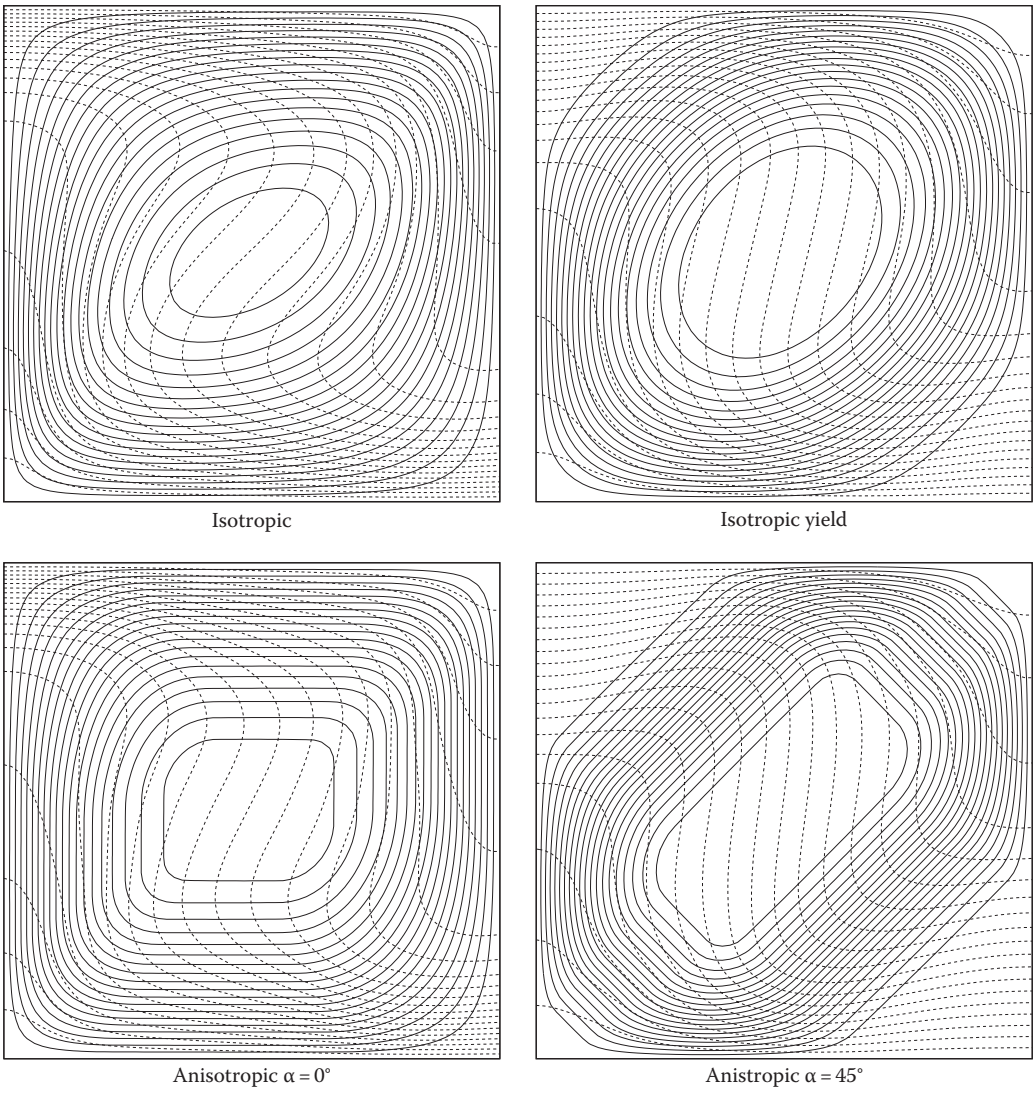

FIGURE 17.18 Comparing four Darcy–Bingham models for Ra = 200, Rb = 12, and $c = 10$.

The usual first step when considering a flow with convective instability is to undertake a linear stability analysis. This involves perturbing the quiescent basic state with a disturbance of small amplitude. For Darcy–Bingham flows, such a disturbance will not overcome the yield threshold, and therefore such a configuration is stable to all small-amplitude disturbances. If, however, one considers the tanh model regularization of the Darcy–Bingham law, then given that the effective viscosity is $(1 + \mathrm{Rb}\, c)$ times the true viscosity when the flow is slow, a linear stability analysis will yield a value of $4\pi^2(1 + \mathrm{Rb}\, c)$ for onset. For the isotropic yield case considered earlier, this means that the critical Rayleigh number is $484\pi^2$, which is well above the value of 200 which was used. So at this juncture, it would seem logical to assume that the point of linear instability represents a subcritical bifurcation given that we have already computed flows at a much lower value of Ra; this facet is presently being studied in detail.

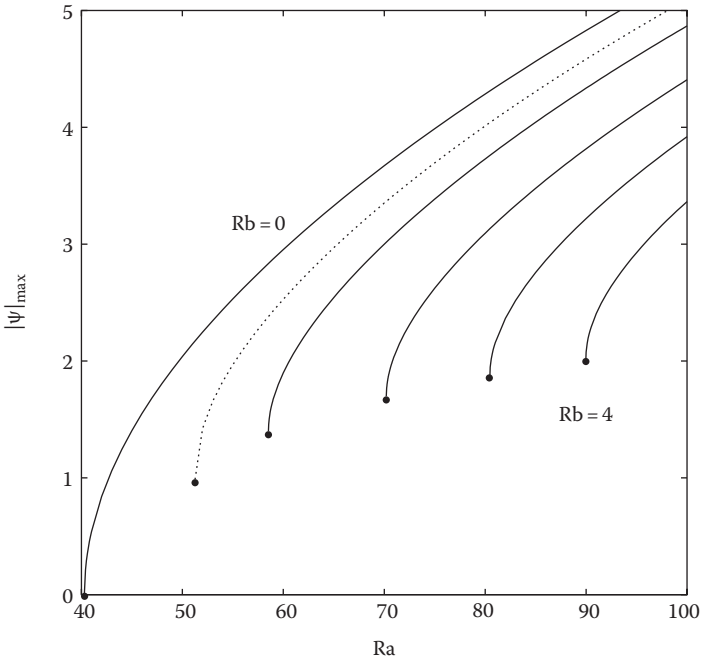

FIGURE 17.19 Variation of $|\psi|_{max}$ with Ra for $c = 3$ and for Rb = 0, 0.5 (dashed), 1, 2, 3, and 4. Turning points, which represent the nonlinear onset of convection, are shown as black disks.

In Figure 17.19, we show the variation of $|\psi|_{max}$ with Ra when $c = 3$ and for selected values of Rb. Apart from when Rb = 0, which represents a Newtonian fluid, all these solution curves have a turning point at a nonzero value of $|\psi|_{max.}$ A different type of solver to the one used here would be necessary to compute beyond the turning point since this branch of solutions is expected to join up with the point of linear instability due to the present adoption of the tanh model for the computations. But for now, we may at least conclude that we are able to find steady convecting solutions for the Darcy–Bingham–Bénard convection although it was necessary to introduce a large perturbation in order to be able to compute them. As will be expected, the solution curves tend toward that of the Newtonian fluid as Rb → 0.

17.7 CONVECTIVE BOUNDARY-LAYER FLOWS OF A BINGHAM FLUID

In this final section, we will consider an unsteady boundary-layer flow and comment on certain aspects of steady boundary-layer flows in an infinite domain.

17.7.1 Unsteady Boundary-Layer Flow

The problem that we will solve in detail here is the consequence of suddenly raising the temperature of a vertical surface which bounds a porous medium to a new constant value. It is well known that the temperature field conducts inward with a complementary error function profile and that buoyancy forces then cause a unidirectional flow. Therefore, no entrainment into the boundary layer occurs because the induced flow is parallel to the heated surface. This will be considered for two different cases: (1) where the flow domain is infinite in extent and (2) where there is a second cold boundary that is parallel to the hot one. We note that the coordinate directions are defined in the traditional way for boundary layers, namely, that x represents the streamwise direction, which is vertical here. The coordinate z represents the cross-stream direction, that is, the horizontal direction.

17.7.1.1 Infinite Domain

We will adopt momentum equations which are the appropriate modification of the threshold model given in Equation 17.9, which account for buoyancy. These will be in nondimensional form, and we will adopt the standard convention for boundary-layer flows that the heated surface is always in the x-direction. The full governing equations are, therefore,

$$\bar{u}_{\bar{x}} + \bar{w}_{\bar{z}} = 0, \tag{17.72}$$

$$\bar{u} = \begin{cases} \left[1 - \dfrac{\mathrm{Rb}}{\sqrt{(\mathrm{Ra}\,\theta - \bar{p}_{\bar{x}})^2 + \bar{p}_{\bar{z}}^2}}\right]\left(\mathrm{Ra}\,\theta - \bar{p}_{\bar{x}}\right) & \text{when } \sqrt{(\mathrm{Ra}\,\theta - \bar{p}_{\bar{x}})^2 + \bar{p}_{\bar{z}}^2} > \mathrm{Rb}, \\ 0 & \text{otherwise}, \end{cases} \tag{17.73}$$

$$\bar{w} = \begin{cases} -\left[1 - \dfrac{\mathrm{Rb}}{\sqrt{(\mathrm{Ra}\,\theta - \bar{p}_{\bar{x}})^2 + \bar{p}_{\bar{z}}^2}}\right]\bar{p}_{\bar{z}} & \text{when } \sqrt{(\mathrm{Ra}\,\theta - \bar{p}_{\bar{x}})^2 + \bar{p}_{\bar{z}}^2} > \mathrm{Rb}, \\ 0 & \text{otherwise}, \end{cases} \tag{17.74}$$

and

$$\theta_{\bar{t}} + \bar{u}\theta_{\bar{x}} + \bar{w}\theta_{\bar{z}} = \theta_{\bar{x}\bar{x}} + \theta_{\bar{z}\bar{z}}, \tag{17.75}$$

where Rb is the yield threshold. The initial condition is that $\theta = 0$ everywhere, but that $\theta = 1$ on the vertical boundary at $\bar{z} = 0$. The domain is doubly infinite in the x-direction, and therefore there is no x-dependence. We may therefore set $\bar{w} = 0$ and $\bar{p}_{\bar{z}} = 0$, and let both $\bar{u}$ and θ be functions of $\bar{z}$ and t. The equation of continuity is satisfied, and therefore only the $\bar{x}$-momentum and heat transport equations need to be solved.

A rescaling is introduced:

$$\bar{u} = \mathrm{Ra}\,u, \quad \bar{x} = x, \quad \bar{z} = z, \quad \bar{t} = t, \quad \bar{p} = p, \quad \mathrm{Rb} = \mathrm{Ra}\,B, \tag{17.76}$$

and therefore we need to solve

$$u = \begin{cases} \theta - p_x - B & \text{when } B < \theta - p_x \\ 0 & \text{when } -B < \theta - p_x < B \\ \theta - p_x + B & \text{when } \theta - p_x < -B, \end{cases} \tag{17.77}$$

and

$$\theta_t = \theta_{zz}. \tag{17.78}$$

The solution for θ is

$$\theta = \mathrm{erfc}\,\eta = \frac{2}{\sqrt{\pi}}\int_{\eta}^{\infty} e^{-\xi^2}\,d\xi, \tag{17.79}$$

where $\eta = z/2\sqrt{t}$.

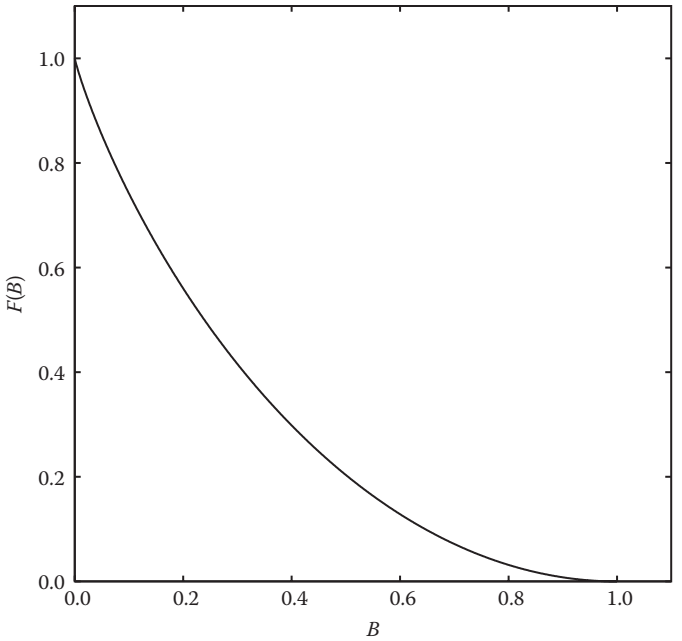

FIGURE 17.20 The function $F(B)$ as given by Equation 17.81.

In this infinite domain, we expect the suddenly heated surface to provide only upward movement of the fluid, and therefore we may set $p_x = 0$. This means that the hydrostatic component of the vertical pressure gradient is precisely that for the ambient fluid at $\theta = 0$. Equation 17.77 simplifies to

$$u = \begin{cases} \theta - B & \text{when } 0 < B < \theta \\ 0 & \text{when } 0 < \theta < B. \end{cases} \tag{17.80}$$

Thus, flow is induced only when $B < 1$ and when B takes larger values then buoyancy provides insufficient body force to cause the fluid to yield.

The total velocity flux may now be found as a function of time and B when $0 < B < 1$. If we define η_B to be where the yield surface is, that is, where erfc $\eta_B = B$, then the velocity flux is

$$Q = \int_0^\infty u\,dz = 2\sqrt{t}\int_0^{\eta_B} (\operatorname{erfc}\xi - B)\,d\xi = \frac{2\sqrt{t}}{\sqrt{\pi}}(1 - e^{-\eta_B^2}) \equiv \frac{2\sqrt{t}}{\sqrt{\pi}}F(B). \tag{17.81}$$

The variation of $F(B)$ is given in Figure 17.20, for reference, and we see how this scaled velocity flux decreases toward zero as $B \to 1$. Therefore, we conclude that free convective boundary-layer flow is possible for the suddenly heated problem in an infinite domain provided that $B < 1$ or equivalently that Rb < Ra.

17.7.1.2 Tall Cavity

We now consider a tall cavity or, equivalently, a cavity of finite width that is very tall. For this finite but tall cavity, the flow field well away from the upper and lower ends will be unidirectional and therefore independent of x, but the presence of the upper and lower surfaces means that there will necessarily be an overall zero mass flux up the layer, in contrast to the infinite domain case just considered.

Equation 17.78 will be solved subject to $\theta = 1$ at $z = 0$ and $\theta = 0$ at $z = 1$ with $\theta = 0$ at $t = 0$. Using Laplace Transforms, we find that

$$\theta = \sum_{n=0}^{\infty} \left[\operatorname{erfc}\left(\eta + \frac{n}{\sqrt{t}} \right) - \operatorname{erfc}\left(\frac{n+1}{\sqrt{t}} - \eta \right) \right]. \tag{17.82}$$

The temperature field now evolves at least initially according to the complementary error function solution given in Equation 17.79. Subsequently, this growing profile is modified when it encounters the cold boundary at $z = 1$, and it eventually attains the steady linear profile given by $\theta = 1 - z$.

As the temperature field evolves, we cannot allow p_x in Equation 17.77 to remain zero. It has to change in time until it takes the value 1/2 as $t \to \infty$; this latter value means that there is no net fluid flux up the layer. At intermediate times, we need to find the value of p_x to ensure an overall zero flux. We also note that there will be an unyielded section in the middle of the evolving temperature field, and if these are located at $\eta = \eta_1$ and $\eta = \eta_2$, where $\eta_1 < \eta_2$, then we have

$$\theta(\eta_1, t) = p_x + B \tag{17.83}$$

and

$$\theta(\eta_2, t) = p_x - B. \tag{17.84}$$

Now the zero flux condition is equivalent to

$$I = \int_0^{\eta_3} u \, d\eta = \int_0^{\eta_1} \left[\theta - p_x - B \right] d\eta + \int_{\eta_2}^{\eta_3} \left[\theta - p_x + B \right] d\eta. \tag{17.85}$$

It is possible to proceed analytically with this, and we obtain

$$\begin{aligned}
I = {} & p_x(-\eta_1 + \eta_2 - \eta_3) + B(-\eta_1 - \eta_2 + \eta_3) \\
& + \frac{1}{\sqrt{\pi}} \sum_{n=0}^{\infty} \left[e^{-[\eta_0 + n/\sqrt{t}]^2} + e^{-[(n+1)/\sqrt{t} - \eta_0]^2} - e^{-[\eta_1 + n/\sqrt{t}]^2} + e^{-[(n+1)/\sqrt{t} - \eta_1]^2} \right] \\
& + \frac{1}{\sqrt{\pi}} \sum_{n=0}^{\infty} \left[e^{-[\eta_2 + n/\sqrt{t}]^2} + e^{-[(n+1)/\sqrt{t} - \eta_2]^2} - e^{-[\eta_3 + n/\sqrt{t}]^2} + e^{-[(n+1)/\sqrt{t} - \eta_3]^2} \right] \\
& - \sum_{n=0}^{\infty} \left[\left(\eta_0 + n/\sqrt{t} \right) \operatorname{erfc}\left(\eta_0 + n/\sqrt{t} \right) + \left((n+1)/\sqrt{t} - \eta_0 \right) \operatorname{erfc}\left((n+1)/\sqrt{t} - \eta_0 \right) \right] \\
& + \sum_{n=0}^{\infty} \left[\left(\eta_1 + n/\sqrt{t} \right) \operatorname{erfc}\left(\eta_1 + n/\sqrt{t} \right) + \left((n+1)/\sqrt{t} - \eta_1 \right) \operatorname{erfc}\left((n+1)/\sqrt{t} - \eta_1 \right) \right] \\
& - \sum_{n=0}^{\infty} \left[\left(\eta_2 + n/\sqrt{t} \right) \operatorname{erfc}\left(\eta_2 + n/\sqrt{t} \right) + \left((n+1)/\sqrt{t} - \eta_2 \right) \operatorname{erfc}\left((n+1)/\sqrt{t} - \eta_2 \right) \right] \\
& + \sum_{n=0}^{\infty} \left[\left(\eta_3 + n/\sqrt{t} \right) \operatorname{erfc}\left(\eta_3 + n/\sqrt{t} \right) + \left((n+1)/\sqrt{t} - \eta_3 \right) \operatorname{erfc}\left((n+1)/\sqrt{t} - \eta_3 \right) \right]
\end{aligned} \tag{17.86}$$

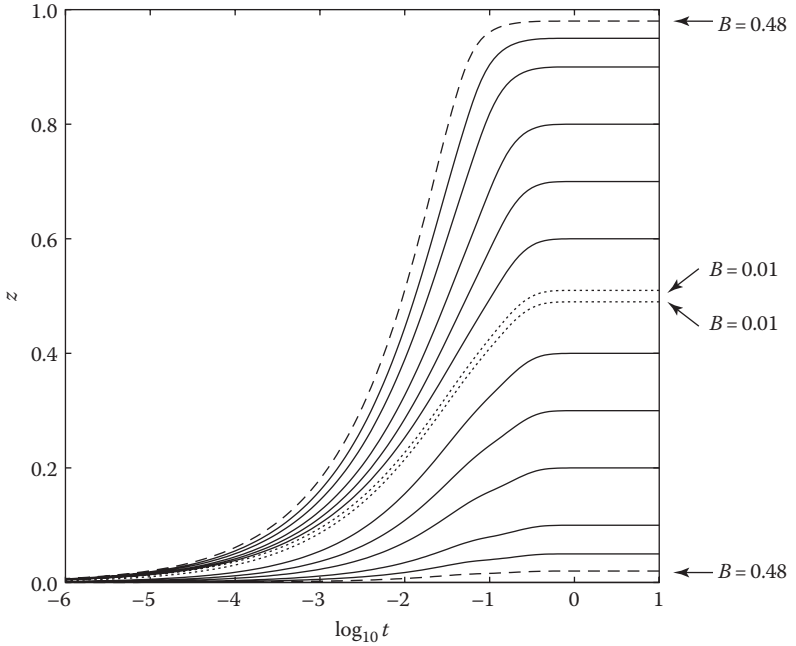

FIGURE 17.21 Displaying where the yield surfaces are used as a function of time for $B = 0.01$ (dotted lines) 0.1, 0.2, 0.3, 0.4, 0.45, and 0.48 (dashed lines). Each value of B has two yield surfaces, and the fluid is stationary between these surfaces.

where $I = 0$. Here we have used $\eta_0 = 0$ and $\eta_3 = 1/2\sqrt{t}$ (i.e., $y = 1$) to make the above formula more easily readable. Therefore, we have three equations to solve for η_1, η_2, and p_x. A straightforward multidimensional Newton–Raphson scheme was used to find these values.

Figure 17.21 shows where the two yield surfaces are as a function of time. At early times, the thermal boundary layer is thin, and therefore the yield surfaces are also close to the heated surface. But as the boundary layer thickens, the yield surfaces move away from the hot surface and eventually become located at equal distances either side of $y = ½$. We also note that the width of the unyielded zone remains small when B is small, but it eventually fills the whole channel as $B \to ½$. This represents the maximum value of B for which flow will arise and should be contrasted with $B = 1$ for the infinite domain.

Figure 17.22 shows how p_x evolves with time. At large times, the temperature field has reached a steady state, and we have already noted that an overall zero fluid flux corresponds to $p_x = ½$. This value of p_x is equivalent to changing the reference temperature from zero, the cold boundary temperature, to ½, which is the mean temperature of the two walls. At early times, p_x is very slightly above the value of B; given the form of Equation 17.77 (third case), this allows for a very small but negative velocity in almost the whole cavity, and this balances a relatively strong upward flow in the very thin thermal boundary layer near $y = 0$. Then, as time progresses, p_x adjusts toward the value ½.

17.7.2 Comment on Steady Boundary-Layer Flows

The reader will have noticed that while there have been references to many papers in the chapter so far, almost none has been to papers on the effect of a yield stress on convective flows. However, there are 13 papers on boundary-layer flows. Apart from Pascal (1981) and Wang and Tu (1989), these tend to be quite complicated because of the inclusion of many different effects. Thus, Cheng

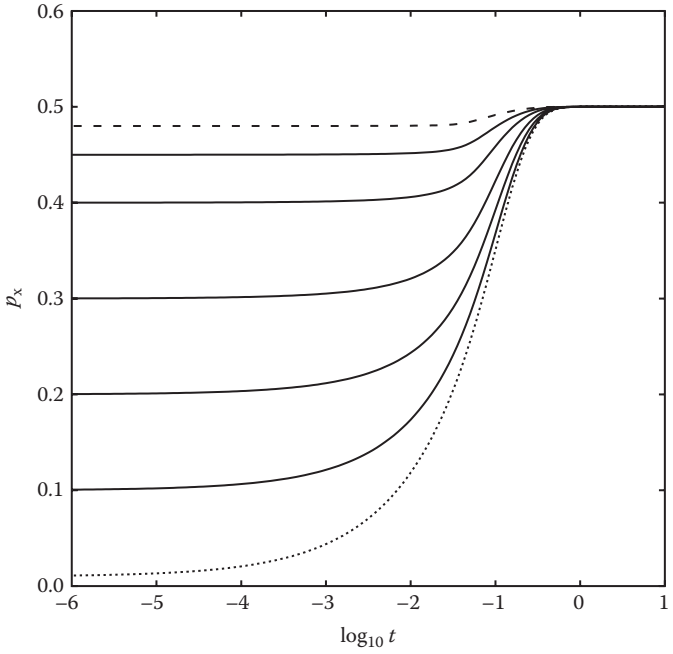

FIGURE 17.22 Displaying the variation with time of the value of p_x, for $B = 0.01$ (dotted line) 0.1, 0.2, 0.3, 0.4, 0.45, and 0.48 (dashed line).

(2006) considers the effect of a variable wall temperature, while Cheng (2011) also includes mass flux. Others who have studied double-diffusive effects are Jumah and Mujumdar (2000, 2001) and Lakshmi Narayana et al. (2009). Ibrahim et al. (2010) consider chemical reactions, while Hady et al. (2011) study nanofluids with a yield stress. Pascal and Pascal (1997) analyze the effect of a lateral mass flux, and Abdel-Gaied and Eid (2011), Wang et al. (2002), and Yang and Wang (1996) all consider boundary layers on axisymmetric bodies.

However, a recent paper by Rees (2015) has sounded a warning note about the general principle of such boundary-layer flows. A common feature of the earlier-quoted papers is that the yield surface lies within the thermal boundary layer. This has a serious consequence when the boundary layer has been formed in a domain of infinite extent. A formal asymptotic theory will involve the limit $\mathrm{Ra} \to \infty$, and for a Newtonian fluid, it is always the case that the induced flow along the heated surface has an asymptotically larger magnitude than the inflow velocity, which is caused by entrainment. Entrainment from the region outside of the boundary layer must happen in order to replenish the upward-moving fluid and to bring cold fluid toward the hot surface in order to inhibit heat conduction into the external domain. For a Bingham fluid with a yield surface within the thermal boundary layer, this entrainment cannot happen, and therefore the computed boundary layer cannot exist.

Rees (2015) also considers in detail what happens when a strict yield threshold is replaced by the tanh law as characterized by the parameter, c, seen earlier. In this case, it is possible to find the induced external circulation, but when the yield threshold model is approached by letting $c \to \infty$, the external pressure gradient also becomes infinite. This confirms the order-of-magnitude argument given in the previous paragraph.

Thus, we need to be very careful when considering thermal boundary-layer flows because the effect on the external environment must also be considered. It is important to mention that certain types of mixed convection problem are exempt from these restrictions. The lateral flux problem considered by Pascal and Pascal (1997) is such that the surface suction at the heated surface will

have already caused the yield threshold to be exceeded, and therefore the upward free convection component merely pushes the overall body force further from the threshold. The same argument will also apply to mixed convection where there is an aiding external flow.

REFERENCES

Abdel-Gaied, S.M., Eid, M.R.: Natural convection of non-Newtonian power-law fluid over axisymmetric and two-dimensional bodies of arbitrary shape in fluid-saturated porous media. *Applied Mathematics and Mechanics*—English Edition **32** (2), 179–188 (2011).

Balhoff, M.T., Thompson, K.E.: Modeling the steady flow of yield-stress fluids in packed beds. *American Institute of Chemical Engineers Journal* **50**, 3034–3048 (2004).

Barnes, H.A.: The yield stress—A review or 'παντα ρει'—Everything flows? *Journal of Non-Newtonian Fluid Mechanics* **81**, 133–178 (1999).

Barnes, H.A., Walters, K.: The yield stress myth. *Rheologica Acta* **24**, 323–326 (1985).

Bayazitoglu, Y., Paslay, P.R., Cernocky, P.: Laminar Bingham fluid flow between vertical parallel plates. *International Journal of Thermal Sciences* **46**, 349–357 (2007).

Cheng, C.-Y.: Natural convection heat and mass transfer of non-Newtonian power law fluids with yield stress in porous media from a vertical plate with variable wall heat and mass fluxes. *International Communications in Heat and Mass Transfer* **33** (9), 1156–1164 (2006).

Cheng, C.-Y.: Soret and Dufour effects on free convection boundary layers of non-Newtonian power law fluids with yield stress in porous media over a vertical plate with variable wall heat and mass fluxes. *International Communications in Heat and Mass Transfer* **38** (5), 615–619 (2011).

Cheng, D.C.-H.: Yield stress: A time-dependent property and how to measure it. *Rheologica Acta* **25**, 542–554 (1986).

Denn, M.M., Bonn, D.: Issues in the flow of yield-stress fluids. *Rheologica Acta* **50**, 307–315 (2011).

Gill, A.E.: A proof that convection in a porous vertical slab is stable. *Journal of Fluid Mechanics* **35**, 545–547 (1969).

Hady, F.M., Ibrahim, F.S., Abdel-Gaied, S.M., Eid, M.R.: Influence of yield stress on free convective boundary-layer flow of a non-Newtonian nanofluid past a vertical plate in a porous medium. *Journal of Mechanical Science and Technology* **25** (8), 2043–2050 (2011).

Horton, C.W., Rogers, F.T. Jr.: Convection currents in a porous medium. *Journal of Applied Physics* **16**, 367–370 (1945).

Ibrahim, F.S., Hady, F.M., Abdel-Gaied, S.M., Eid, M.R.: Influence of chemical reaction on heat and mass transfer of non-Newtonian fluid with yield stress by free convection from vertical surface in porous medium considering Soret effect. *Applied Mathematics and Mechanics*—English Edition **31** (6), 675–684 (2010).

Jamalud-Din, S.-D., Rees, D.A.S., Reddy, B.V.K., Narasimhan, A.: Prediction of natural convection flow using a network model and numerical simulations inside an enclosure with distributed solid blocks. *Heat and Mass Transfer* **46**, 333–343 (2010).

Jeong, S.W.: Determining the viscosity and yield surface of marine sediments using modified Bingham models. *Geosciences Journal* **17** (3), 241–247 (2013).

Jumah, R.Y., Mujumdar, A.S.: Free convection heat and mass transfer of non-Newtonian power law fluids with yield stress from a vertical flat plate in saturated porous media. *International Communications in Heat and Mass Transfer* **27** (4), 485–494 (2000).

Jumah, R.Y., Mujumdar, A.S.: Natural convection heat and mass transfer from a vertical flat plate with variable wall temperature and concentration to power-law fluids with yield stress in a porous medium. *Chemical Engineering Communications* **185**, 165–182 (2001).

Lakshmi Narayana, P.A., Murthy, P.V.S.N., Postelnicu, A.: Soret and Dufour effects on free convection of non-Newtonian power law fluids with yield stress from a vertical flat plate in saturated porous media. *Journal of Porous Media* **12** (10), 967–981 (2009).

Lapwood, E.R.: Convection of a fluid in a porous medium. *Proceedings of the Cambridge Philosophical Society* **44**, 508–521 (1948).

Lewis, S., Bassom, A.P., Rees, D.A.S.: The stability of vertical thermal boundary layer flow in a porous medium. *European Journal of Mechanics B: Fluids* **14**, 395–408 (1995).

Liu, H., Wang, J., Xie, Y., Ma, D., Shi, X.: Flow characteristics of heavy oil through porous media. *Energy Sources Part A—Recovery Utilization and Environmental Effects* **34** (1–4), 347–359 (2012).

Maßmeyer, A.: Thermal instabilities in a yield-stress fluid: From the laboratory to the planetary scale. PhD thesis. Université Paris Sud, Orsay, France (2013).

Mendes, P.R.S., Naccache, M.F., Braga, C.V.M., Nieckele, A.O., Ribeiro, F.S.: Flows of Bingham materials through ideal porous media: An experimental and theoretical study. *Journal of the Brazilian Society of Mechanical Engineers* **24** (1), 40–45 (2002).

Nash, S.: Investigating the flow behaviours of Bingham fluids in porous media. Final year MEng project report supervised by Dr. D.A.S.Rees, Department of Mechanical Engineering, University of Bath, Bath, U.K. (2013).

Papanastasiou, T.C.: Flow of materials with yield. *Journal of Rheology* **31**, 385–404 (1987).

Pascal, H.: Nonsteady flow through porous media in the presence of a threshold gradient. *Acta Mechanica* **39**, 207–224 (1981).

Pascal, J.P., Pascal, H.: Free convection in a non-Newtonian fluid saturated porous medium with lateral mass flux. *International Journal of Non-linear Mechanics* **32** (3), 471–482 (1997).

Rees, D.A.S.: On convective boundary layer flows of a Bingham fluid in a porous medium. *International Journal of Heat and Mass Transfer* **82**, 206–217 (2015).

Roache, P.J.: *Computational Fluid Dynamics*. Hermosa, Albuquerque, NM (1976).

Shenoy, A.V.: Non-Newtonian fluid heat transfer. *Advances in Heat Transfer* **24**, 102–190 (1991).

Sochi, T., Blunt, M.J.: Pore-scale network modeling of Ellis and Herschel-Bulkley fluids. *Journal of Petroleum Science and Engineering* **60**, 105–124 (2008).

Steffe, J.F.: *Rheological Methods on Food Process Engineering*. Freeman Press, East Lansing, MI (1992).

Turan, O., Poole, R.J., Chakraborty, N.: Boundary condition effects on natural convection of Bingham fluids in a square enclosure with differentially heated horizontal walls. Paper NC-05. *Proceedings of CHT-12, the Fifth ICHMT Symposium on Advances in Computational Heat Transfer*, University of Bath, Bath, U.K. (July 1–6, 2012).

Wang, C.Y., Tu, C.J.: Boundary-layer flow and heat-transfer of non-Newtonian fluids in porous-media. *International Journal of Heat and Fluid Flow* **10** (2), 160–165 (1989).

Wang, S.C., Chen, C.K., Yang, Y.T.: Natural convection of non-Newtonian fluids through permeable axisymmetric and two-dimensional bodies in a porous medium. *International Journal of Heat and Mass Transfer* **45** (2), 393–408 (2002).

Yang, Y.T., Wang, S.J.: Free convection heat transfer of non-Newtonian fluids over axisymmetric and two-dimensional bodies of arbitrary shape embedded in a fluid-saturated porous medium. *International Journal of Heat and Mass Transfer* **39** (1), 203–210 (1996).

18 High-Heat-Flux Distributed Capillary Artery Evaporators

Gisuk Hwang, Chanwoo Park, and Massoud Kaviany

CONTENTS

18.1 Introduction 598
18.1.1 Motivation and Background 598
18.1.2 Boiling and Film Evaporation 598
18.1.3 Various Thermal–Hydraulic Limits 600
18.1.3.1 Hydrodynamic Limit 600
18.1.3.2 Capillary–Viscous Limit 601
18.1.3.3 Kinetic Limit 602
18.1.3.4 Boiling Limit 602
18.1.3.5 Other Limits 602
18.1.4 Figure of Merit 602
18.1.5 Capillary Evaporator Wick Designs 603
18.2 Pool Boiling (Design A to C, Hydrodynamic Limit) 604
18.2.1 Plain Surface (Design A) 604
18.2.2 Uniform Wick Thickness (Design B) 605
18.2.2.1 Monoporous Wick 605
18.2.2.2 Biporous Wick 607
18.2.3 Liquid-Artery Wick (Design C) 608
18.2.4 Other Surface/Fluid Modifications 609
18.2.5 Summary 610
18.3 Film Evaporation (Design D to E, Capillary–Viscous Limit) 611
18.3.1 Uniform Thickness Wick (Design D) 611
18.3.1.1 Monoporous Wick 612
18.3.1.2 Biporous Wick 612
18.3.1.3 Nanostructures 614
18.3.2 Liquid-Artery Wick 615
18.3.2.1 Vertical (Design E) 615
18.3.2.2 Lateral (Design F) 619
18.3.3 Summary 623
18.4 Flow Boiling (Design G) 623
18.5 Concluding Remarks and Outlooks 624
Nomenclature 625
References 625

18.1 INTRODUCTION

18.1.1 Motivation and Background

High-heat-flux thermal management systems are in demand for enhancing cooling performances and minimizing degradation for many practical applications such as electronics, nuclear power plants, energy, automotive, and aerospace systems. The phase-change (liquid–vapor, releasing or absorbing heat of evaporation) thermal management systems such as pool boiling and film evaporation systems (single pipe, loop heat pipes [LHPs], vapor chambers, etc.) offer high performances and reliabilities, with no external power consumption and minimal temperature difference. These systems generally consist of three components, namely, an evaporator, liquid–vapor conduits, and a condenser, and transport bottlenecks are liquid, vapor, and heat transport in them. The heat is absorbed at the evaporator, and transported through the vapor conduit, and released at the condenser. The condensate returns the evaporator via gravity (pool boiling) and/or capillarity (heat pipes and vapor chambers). Concentrated heat sources make the evaporator to be the most critical bottleneck, since the condenser surface area is generally sufficiently large.

The optimal design requires continuous liquid (coolant) supply to the evaporator, avoiding dryout, while minimizing evaporator thermal resistance. It generally employs porous structures, such as grooves and sintered metallic particles, to enhance the capillary pumping capability and minimize the thermal resistance across high thermal conducting metals.

There have been significant advances in the capillary evaporator wick designs to enhance the performance utilizing grooves and uniform and nonuniform-thickness sintered particle wicks (O'Neill et al. 1972; Chi 1976; Polezhaev and Kovalev 1990; Peterson 1994; Faghri 1995; Chang and You 1997a,b; Liter and Kaviany 2001; Hwang et al. 2007, 2010, 2011; Mori and Okuyama 2009). In this chapter, the fundamentals of the liquid and vapor transport in the capillary evaporators are briefly reviewed, and the evolution of the capillary evaporator wick design is discussed regarding the pool boiling (Section 18.2) and film evaporation (Section 18.3) systems. Future capillary evaporator wick design in flow boiling is discussed (Section 18.4), followed by the outlook and conclusions (Section 18.5).

18.1.2 Boiling and Film Evaporation

Here, boiling and film evaporation mechanisms are briefly reviewed before discussing various wick designs for the enhanced boiling and film evaporation performance. The first part primarily focuses on the liquid–vapor transport above the wick in pool boiling, and the second part discusses about the microscale heat and liquid transport near the thin wick. More detailed background and discussion can be found in the literature (Chi 1976; Collier and Thome 1994; Peterson 1994; Webb and Kim 1994; Faghri 1995; Johnson 1998; Kandlikar 1999, 2001; Kaviany 2002).

Pool boiling employs liquid (coolant) pool to remove heat from the surface of a substrate via phase change (boiling). When the substrate is at a temperature higher than a saturation temperature, the liquid can begin boiling at the solid–liquid interface, and without forced liquid flow, this is called pool boiling. The heat flux q across the interface is released to the heat transfer coefficient through the temperature difference between the solid surface T_s and saturation temperature T_{lg} (superheat, $T_s - T_{lg}$, °C). The generated vapor begins to form bubbles at the surface, which escapes from the solid surface by the phase buoyancy force when those are sufficiently large. As the heat flux (or superheat) increases, the vapor morphology and dynamics evolve, and these are illustrated in Figure 18.1.

As the superheat increases, the nucleate boiling regimes are reached, corresponding to a sharp heat flux increase. At low surface superheats, isolated bubbles are formed at active nucleation sites (isolated-bubbles regime), and at higher superheat, the frequency of the bubble departure increases, and the number of active sites also increases. This is referred to as the combined isolated-bubbles and jets subregime. Next, these neighboring jets coalesce and the vapor-mushroom

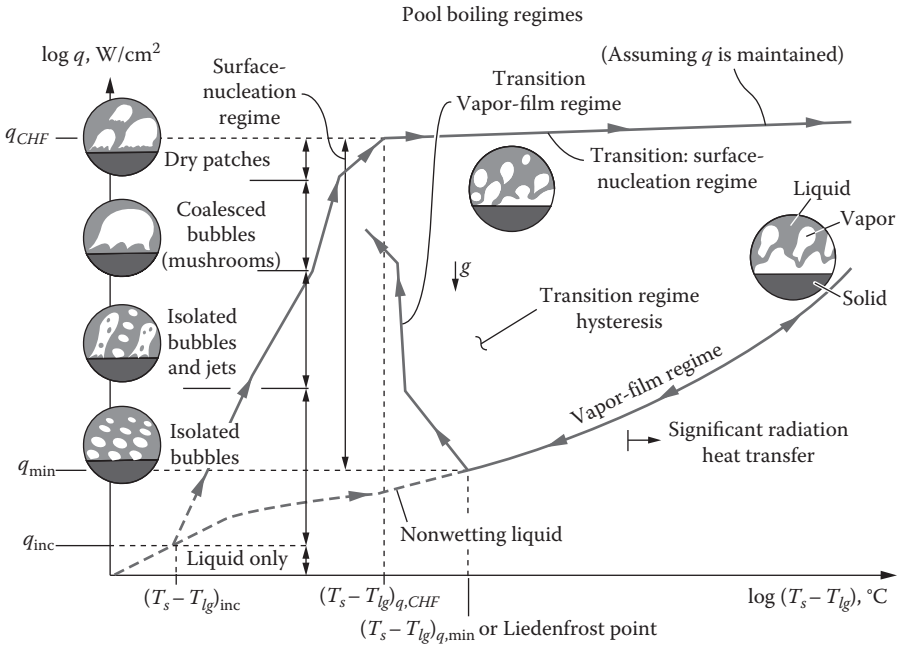

FIGURE 18.1 Bubble morphology and regimes in pool boiling presented as variations of heat flux with respect to the surface superheat. (From Kaviany, M., *Principles of Heat Transfer*, Wiley, New York, 2002; Lienhard, J.H., *A Heat Transfer Textbook*, 2nd edn., Prentice-Hall, Englewood Cliffs, NJ, 1987; Kaviany, M., *Essentials of Heat Transfer: Principles, Materials, and Applications*, Cambridge University Press, Cambridge, U.K., 2011.)

regime is found. As the heat flux further increases, the dry-patches subregime appears, and with a further increase in the surface superheat, the maximum in the heat flux is found, which is called the critical heat flux (CHF), designated by q_{CHF}, and the corresponding approaching superheat is designated by ΔT_{CHF}. Beyond this point, the surface dries out, caused by the liquid chocking from the hydrodynamic instability (Zuber 1959). In this regime, the film evaporation is dominant. This maximum heat transfer rate limits the cooling performance. While the hydrodynamics stability limits the heat flux for plain surfaces, for wick-coated surfaces, there are other limiting mechanisms (usually higher than the hydrodynamic limit), which will be discussed next.

For high flux thermal management (heat pipes and vapor chambers), the film evaporation is designed while removing the liquid pool and supplying the liquid through the liquid-permeable wick and capillary pumping to the evaporator. The dominant film evaporation generally occurs at the solid–vapor–liquid interfaces through the thin liquid film as shown in Figure 18.2, while the liquid is continuously supplied via capillary pressure (Hanlon and Ma 2003; Li and Peterson 2006). The thin liquid film region is called extended meniscus (from Greek meaning crescent), undergoing a drastic change in the liquid film thickness from nano- to micro- to macroscales. The extended meniscus is divided into three regions: (1) nonevaporating region (adsorbed layer governed by intermolecular-bonding forces between liquid and solid molecules of thickness ~10 nm), (2) evaporating film region (disjoining-pressure-dominant region of thickness ≥ ~100 nm, where evaporation dominantly occurs due to small thermal resistance of thin liquid film), and (3) meniscus film region (capillary-pressure-dominant region of thickness > ~100 μm) (Wang et al. 2007; Carey 2008; Ranjan et al. 2011; Zhao et al. 2011; Kunkelmann et al. 2012; Maroo and Chung 2013). The evaporating film region has been extensively studied since this dominantly determines the performance, that is, CHF and superheat. Under an assumption that the dominant thermal resistance is caused by the heat transfer through the thin liquid film, the disjoining pressure difference derives

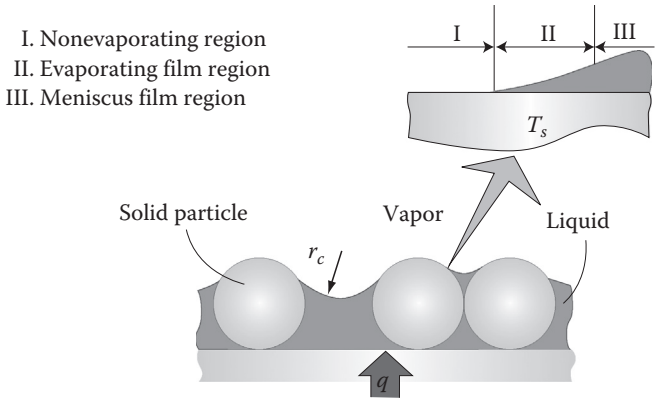

FIGURE 18.2 Thin film evaporation in liquid-soaked sintered particles, including the three nonevaporating/evaporating regions, is also shown. (From Hanlon, M.A. and Ma, H.B., *J. Heat Transfer*, 125(4), 644, 2003.)

the liquid film flow, and it develops the Nusselt and nondimensional numbers to predict the heat transfer coefficient (Xu and Carey 1990), while the effects of the various liquid thin film morphologies on the thermal resistances are discussed in details (Stephan and Busse 1992; Wayner 1994; Khrustalev and Faghri 1995; Kobayashi et al. 1996; Ranjan et al. 2011). Using a realistic, nonuniform temperature distribution treatment on the liquid film due to the surface-interaction-driven pressure variations, the authors found that the thermal resistance was lower than a homogeneous treatment (Ma and Peterson 1997). They suggested that the more detailed model needs to articulate the underlying physics.

When the wick thickness becomes the same order of the capillary meniscus, the capillary meniscus recess becomes dominant for the thermal resistance. At high flux, the effective liquid thickness becomes nearly half due to capillary meniscus recess compared to the fully liquid-filled wick. This has been studied using pore-level model (Ranjan et al. 2011; Ju et al. 2013) and using homogeneous treatment with the effective thickness (Hwang et al. 2010, 2011).

18.1.3 Various Thermal–Hydraulic Limits

To enhance the liquid-coolant supply (hydrodynamic limit and capillary) as well as to increase the number of the nucleation sites, the porous coatings have been often employed. In this case, there are three main processes for the liquid delivery to the evaporation sites, that is, (1) the liquid delivery by gravity from the condenser, (2) permeation of liquid into the wick structure by capillary suction, and (3) evaporation at the phase-change kinetics rate. They are controlled by the hydrodynamic, capillary–viscous, and kinetic limits, respectively, as indicated in Figure 18.3.

18.1.3.1 Hydrodynamic Limit

Hydrodynamic limit was elaborated by Zuber, employing the fundamental thermal-hydrodynamic instability (Zuber 1959). He postulated that a hydrodynamic liquid choking limit is mechanistically related to hydrodynamic instabilities associated with the flow-critical length scales, based on the idealized hydrodynamics of a liquid–vapor interface system above the heated surface. Idealizing the vapor flow, he equated the boiling heat flux q to the rate of heat escape by buoyant flow of the vapor through the liquid; then the maximum heat transfer q_{CHF} is calculated when the vapor enthalpy approached the heat of evaporation. He hypothesized the vapor escaped through the idealized cylindrical vapor channels. As the heat flux increases, the vapor velocity increases until the liquid–vapor interface of the vapor channel boundary becomes unstable,

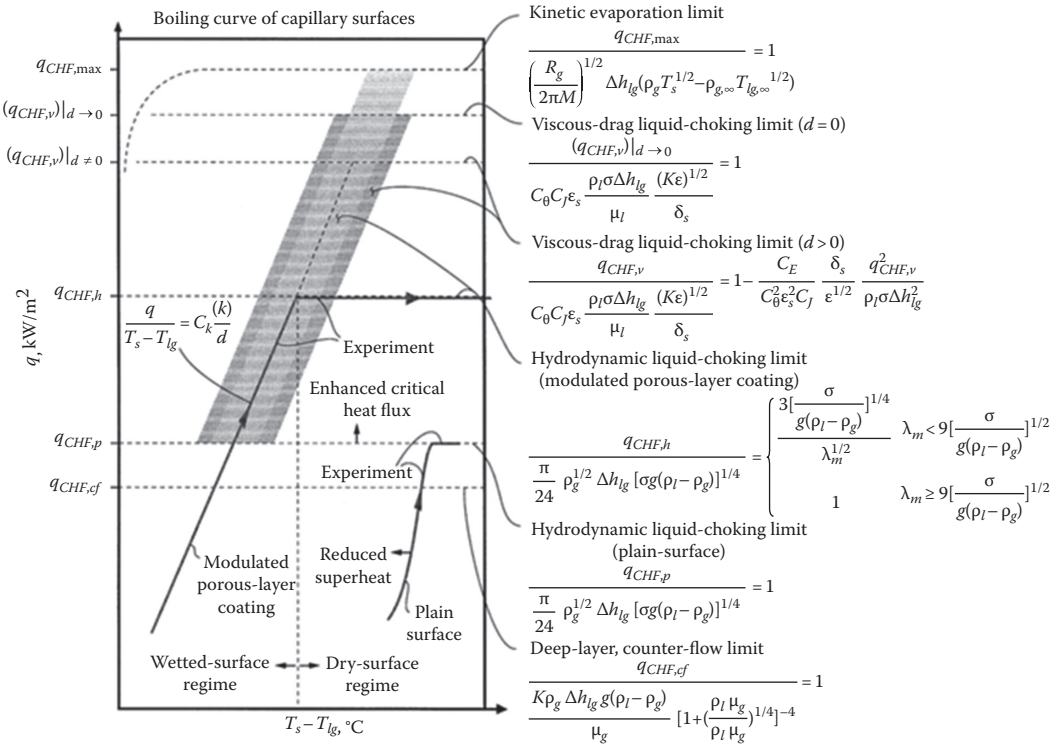

FIGURE 18.3 Various regimes and the upper heat flux limits, in pool boiling with modulated porous-layer coating. The hydrodynamic limit is reached first, followed by the capillary–viscous regime. The kinetic limit is the highest of the limits. (From Liter, S.G. and Kaviany, M., *Int. J. Heat Mass Transfer*, 44(22), 4287, 2001.)

which is associated with the Kelvin–Helmholtz and Rayleigh stability wavelengths. The resulting relation for CHF is given as (Zuber 1959)

$$\frac{q_{CHF,p}}{(\pi/24)\rho_g^{1/2}\Delta h_{lg}[\sigma g(\rho_l-\rho_g)]^{1/4}}=1 \tag{18.1}$$

This idealized model not only predicts the CHF reasonably but also provides insights into optimal designs of the high-heat-flux cooling systems.

18.1.3.2 Capillary–Viscous Limit

Another liquid transport limit is related to the liquid flow within the capillary evaporator wick, which is generally higher than the hydrodynamic limit. The capillarity drives the liquid flow through permeable porous wick and toward the active evaporation sites, while the liquid loses pressure through the Darcy law both in the pool boiling (Liter and Kaviany 2001) and film evaporation (Chi 1976). For the pool boiling, the CHF is given as

$$\frac{q_{CHF}}{\varepsilon_s C_J(\rho_l\sigma\Delta h_{lg}/\mu_l)[(K\epsilon)^{1/2}/\delta_s]}=1-\frac{C_E}{C_J}\frac{\delta_s}{\epsilon_s^{1/2}\epsilon^{1/2}}\frac{q_{CHF}^2}{\rho_l\sigma\Delta h_{lg}^2} \tag{18.2}$$

For the film evaporation, the viscous–capillary limit is given as

$$p_{c,\max} = 2\sigma\left(\frac{1}{r_{c,e}} - \frac{1}{r_{c,c}}\right) \quad \text{and} \quad \Delta p_l + \Delta p_v + \Delta p_g \le p_{c,\max} \tag{18.3}$$

Generally, the liquid pressure drop via the viscosity (as compared to inertia) is dominant, and the capillary–viscous limit occurs when the liquid pressure drop reaches the maximum capillary pumping capability.

18.1.3.3 Kinetic Limit

Another transport limit is related to the phase-change kinetic limit, which is associated with the kinetics from the vapor molecular flux at the interface, designated as the q_{CHF}. This theoretical maximum, described by Gambill and Lienhard, is the kinetic limit for evaporation given as (Gambill and Lienhard 1989)

$$\frac{q_{CHF,\max}}{(R_g/2\pi M)^{1/2}\Delta h_{lg}(\rho_g T_{lg}^{1/2} - \rho_{g,\infty} T_{lg,\infty}^{1/2})} = 1 \tag{18.4}$$

where

ρ_g, T_{lg}, and Δh_{lg} are the functions of the saturation pressure p_g
$T_{lg,\infty}$ and $p_{g,\infty}$ are the far-field temperature and pressure

The interface p_g is larger than $p_{g,\infty}$. So far, the passive enhanced q_{CHF} is two orders of magnitude smaller than the kinetic limit, and this shows that there is much room for enhancement.

18.1.3.4 Boiling Limit

At high superheats, boiling occurs within the capillary evaporator wick (Chi 1976; Peterson 1994; Faghri 1995). The bubbles often trap within the porous coating, and this in turn results in a significant thermal resistance across the wick and a poor liquid supply to the evaporation sites. This ultimately limits the heat transfer rate (CHF).

18.1.3.5 Other Limits

There are other limits controlling the maximum heat transfer, primarily related to the vapor flow or vapor–liquid interfaces, such as vapor pressure drop and entrainment, which in general occur at much higher heat fluxes than the liquid flow dominant limit (Faghri 1995). Here, we focus on the limits primarily associated with the liquid- or liquid–vapor-related hydrodynamics including capillary–viscous flow, generally occurring within the capillary evaporator wicks.

18.1.4 Figure of Merit

For the capillary–viscous-limit-dominated operation, an optimum working fluid should have high liquid density ρ_l, high surface tension σ, high heat of evaporation Δh_{lg}, and a low liquid dynamic viscosity μ_l. These properties were combined into a parameter referred to as a figure of merit, N, given as (Chi 1976)

$$N = \frac{\rho_l \sigma \Delta h_{lg}}{\mu_l} \tag{18.5}$$

which can be used to evaluate the effectiveness of various working fluids at specific operating temperatures. However, this does not include the wick properties, which are crucial in the liquid viscous–capillary limit, as well as the wick superheat. These properties include the cross-sectional

area, active evaporation area, and conduction length, which are given in the extrinsic figure of merit. Thus, we have (Hwang et al. 2007)

$$\frac{Q^*_{CHF}}{R^*_k} = \left(1 + \frac{A_{w,s}}{A_{w,u}}\right)\frac{\ln(1-R^{*-1})^{-1}}{\ln(1-R^{*-1}\delta'^*)^{-1}} \quad \text{for cylindrical heat pipe}$$
$$\frac{Q^*_{CHF}}{R^*_k} = \delta'^{*-1}\left(1 + \frac{A_{w,s,f}}{A_{w,u,f}}\right) \quad \text{for flat heat pipe} \tag{18.6}$$

where

$A_{w,u}$ and $A_{w,s}$ are the cross-sectional areas of the uniform wick and modulated wick for the cylindrical heat pipe, respectively

R^* is the dimensionless inner radius of the heat pipe

δ'^* is the dimensionless equivalent wick thickness ($\delta'^* = 1$ for the uniform wick thickness)

$A_{w,u,f}$ and $A_{w,s,f}$ are the cross-sectional areas of the uniform wick and modulated wick for the flat heat pipe

The figure of merit for the flat heat pipe establishes the maximum performance for the cylindrical heat pipe. The extrinsic figure of merit indicates the overall performance including both the hydrodynamic and thermal perspectives, which maximizes at the thin wick with the capillary liquid arteries below.

An optimal evaporator wick design requires a minimal thermal resistance using a thin (monolayer) evaporation wick, while supplying sufficient liquid to the evaporation sites through a thick liquid-artery wick. One design employs a distributed wick, which allows for liquid arteries and thin wicks at the evaporator. Since the thin wick spreads the liquid to the evaporator, the capillary–viscous limit through the monolayer wick is the bottleneck of the system. Details will be discussed in the following sections.

18.1.5 Capillary Evaporator Wick Designs

To enhance the CHF and/or reduce the superheat, various wick designs have been developed both in the pool boiling and film evaporation as shown in Figure 18.4. This also illustrates the CHF enhancement by surface structure modifications in pool boiling and film evaporation. The first

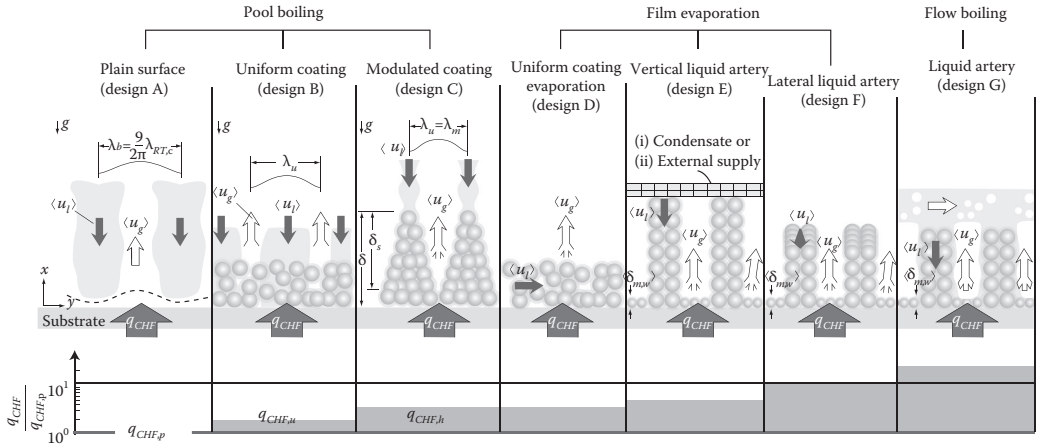

FIGURE 18.4 Enhancement of the CHF using the distributed capillary wick in pool boiling (designs A to C), film evaporation (designs D to F), and flow boiling (design G).

group (designs A to C) is related to the microstructure modifying the pool boiling (hydrodynamic limit), while the second group (designs D to F) shows the CHF enhancement of the film evaporation (capillary–viscous limit). The CHF has been significantly improved using these designs (up to an order of magnitude compared to pool boiling on plain surface, from design A to F). Design G is suggested for the flow boiling enhancement (enhancement is future goal).

18.2 POOL BOILING (DESIGN A TO C, HYDRODYNAMIC LIMIT)

The study on the pool boiling process began to be examined as early as the eighteenth century. A detailed study on the effect of the large superheat was first performed by Nukiyama (1934, 1966), and Farber and Scorah (1948) further elaborated the pool boiling processes with respect to the superheat. Since then, numerous studies on the pool boiling have been performed on its various aspects, particularly on the thermal–hydraulic behaviors near the interface where the dominant transport phenomena occur (Tong and Tang 1997). One significant challenge is the small CHF and its associated high superheat. There are numerous studies on understanding the fundamental mechanisms and the engineering approaches to improve them, and here, we particularly emphasize on the distributed capillary wick design.

18.2.1 Plain Surface (Design A)

The CHF phenomenon has drawn significant attention since it is related to the compelling scientific and engineering challenge in the thermal–hydraulic field. There are numerous experimental and theoretical studies as summarized in Table 18.1. As mentioned earlier, Zuber model significantly contributed to the fundamental understandings of the CHF, employing the hydrodynamic instability to the infinite surface (Zuber 1959), and his correlation is one of the reasonably accepted models to predict and analyze the CHF and is often used as the reference to compare the performance enhancement with the porous coatings. There are also other models for the CHF. Lienhard and Dhir argued that the Rayleigh–Taylor instability wavelength is the dominating flow-critical length scale along the surface from experimental observations (Lienhard and Dhir 1973). For infinite surfaces, these waves would continue into the vapor channels, thus effecting the destabilization of the channel boundary before the Rayleigh waves. They suggested a different choice for the critical wavelength, which results in 1.14 times larger than that of the Zuber (Equation 18.1). Lienhard et al. also suggest

TABLE 18.1
Summary of the Previous Studies on CHF and Superheat in Pool Boiling on Plain Surfaces (Design A)

Authors	Wick Structure	CHF, q_{CHF} (W/cm^2)	ΔT_{CHF} (°C)	Working Fluid	Heater Size (cm^2)
Zuber (1959)	Plain surface (model, infinite)	110.8	—	Water (1 atm)	—
Moissis and Berenson (1963)	Plain surface (model, infinite)	152.4	—	Water (1 atm)	—
Lienhard and Dhir (1973)	Plain surface (model, finite)	126.9	—	Water (1 atm)	—
Chang and You (1996)	Plain surface (copper)	13.4	30	FC-72	1 × 1 cm^2
Auracher et al. (2001)	Plain surface (copper with thin nickel coating)	139.0	40	Water (1 atm)	2.6 cm^2 (circular)
Liter and Kaviany (2001)	Plain surface (copper)	24.5	34	*n*-Pentane (1 atm)	4 cm^2 (circular)
Li and Peterson (2006)	Plain surface (copper)	149.7	26	Water (1 atm)	0.8 × 0.8 cm^2
Mori and Okuyama (2009)	Plain surface (copper)	101	32	Water (1 atm)	2 cm^2 (circular)
Li and Peterson (2010)	Plain surface (copper)	141.3	20	Water (1 atm)	0.5 cm^2 (circular)

that the CHF relation should be modified based on the perturbed wavelength for the finite heated surface (Lienhard et al. 1973). However, here, we adopt the Zuber model as the reference, which is q_{CHF} = 111, 24.5, and 13.4 W/cm^2 for water, *n*-pentane, and FC-72 at 1 atm, respectively (Zuber 1959; Chang and You 1996; Liter and Kaviany 2001). There is no universally accepted model for the superheat at the CHF, and we chose the values from the available experimental results, that is, $\Delta T_{sh,CHF}$ = 26°C, 34°C, and 30°C for water for water, *n*-pentane, and FC-72 at 1 atm, respectively (Chang and You 1996; Liter and Kaviany 2001; Li and Peterson 2006). These values are used to normalize the CHF and superheat, that is, q^*_{CHF} and ΔT^*_{CHF}.

18.2.2 Uniform Wick Thickness (Design B)

To increase the CHF and reduce the superheat, various surface structures, for example, meshes, grooves, pin fins, sintered particles, have been employed. These surface structures have resulted in reducing the thermal–hydraulic instability wavelength and enhancing CHF. The microstructure using high thermal conductivity metals in turn has reduced the superheat (O'Neill et al. 1972; Nakayama et al. 1982; Nishikawa et al. 1983; Polezhaev and Kovalev 1990; Webb and Kim 1994; Liter and Kaviany 2001; Honda and Wei 2004; Pioro et al. 2004; Hwang and Kaviany 2006; Patil and Kandlikar 2013, 2014).

The surface modifications include simple surface indentations or microgrooves. Corty and Foust (1955) and Berensen (1962) extensively studied the effect of the simple microstructures (lapping or sanding) on the nucleate boiling performance. They observed that the increased surface roughness resulted in decreasing the superheat in experiments with *n*-pentane. However, the enhancement lasted for a short time, and the performance degraded after long operation. To overcome this, stable, micro surface structures were developed to improve the thermal–hydraulic behaviors near the surface and enhance the performance employing porous metallic coatings by Milton (1968). Webb also proposed three types of surface structures, attached nucleation promoters, metal or nonmetal coating, and nucleation sites formed by mechanical working or chemical etching of the base surface (Webb 1981). Since then, porous metallic coating has been considered as an enhancement technique. Here, we primarily focus on the porous metallic coatings for the CHF enhancement and superheat reduction. The details of the performance and experimental approaches are listed in Table 18.2. The detailed performance and approaches will be discussed in the following section.

18.2.2.1 Monoporous Wick

Various geometric parameters of the porous metallic coatings for CHF enhancement and superheat reduction have been examined, for example, particle size, particle shape, coating thickness, and porosity. Webb thoroughly reviewed the various geometrical parameters and their evolution of the surface structure on the pool boiling both in the experimental and theoretical approaches in early days (Webb 1981). He also extensively studied the boiling performance of the porous coated surface and concluded that the particle size has little effect on the performance, whereas the preferred coating thickness is in the range of three to four particle diameters (Webb 1983). Thome also reviewed the enhanced performance from the porous coatings (Thome 1990), and his major conclusion was that the coating thickness should be less than 1.5–3 mm to avoid additional thermal resistance by the particles and entrapment of vapor, for the particle sizes ranging from 12 to 1000 μm. He suggested that the enhancement due to the porous coatings was through improved effective boiling surface area from the porous layer, where the active evaporation area is the vapor–liquid contact surface area near the pore necks. Nakayama et al. studied the boiling phenomena on the porous coating with the pore diameter of 50, 100, and 150 μm using R-11 (Nakayama et al. 1982). They observed that the intense bubble formation from the porous coating does not necessarily yield high heat transfer performance and concluded that capillary liquid suction and evaporation within the pores are available boiling mechanisms at the small superheat. Bergles and Chyu (1982) observed that the porous metallic coatings enhanced the

TABLE 18.2
Summary of Studies on CHF and Superheat for Uniform Wicks in Pool Boiling (Design B)

Authors	Wick Structure	CHF, q_{CHF} (W/cm^2)	ΔT_{CHF} (°C)	Working Fluid	Heater Size (cm^2)
Afgan et al. (1985)	Dendrite and spherical, Cr–Ni sintered particle d_p, 63–100 μm δ, 450–2200 μm ε, 0.3–0.7	~180–250 (water) ~60 (Freon-133) ~100–150 (ethanol) q^*_{CHF}, 1.6–2.3 (water) (Best, 180@70)	~70–400 (water) ~140–180 (Freon-133) ~200–220 (ethanol) ΔT^*_{CHF}, 2.69–15.38 (water)	Water, ethanol, Freon-113 (1 atm)	Wire diameter (4–18 mm)
Malyshenko (1991)	Sintered nichrome coating d_p, 130–400 μm δ, 1.5 mm ε, 0.4–0.5	~50 q^*_{CHF}, 0.45 —	~10 ΔT^*_{CHF}, 0.38	Water (1 atm)	—
Chang and You (1997b)	Aluminum (1–20 μm) Copper (1–50 μm) Diamond (8–12 μm) Silver (3–10 μm)	23.9–33.5 q^*_{CHF}, 1.7–2.5 (Best, 33.5@15)	~10–25 ΔT^*_{CHF}, 0.33–0.83	FC-72 (1 atm)	1 × 1 cm^2
Chang and You (1997a)	Uniform diamond coating d_p, 2–70 μm δ, 30–250 μm ε, 0.4–0.48	23–28 q^*_{CHF}, 1.7–2.1	— —	FC-72 (1 atm)	1 × 1 cm^2
Liter and Kaviany (2001)	Uniform sintered copper particles d_p, 200 μm δ, 600 μm ε, 0.4	480 q^*_{CHF}, 1.96	9 ΔT^*_{CHF}, 0.26	*n*-Pentane (1 atm)	4 cm^2 (circular)
Hwang and Kaviany (2006)	Uniform sintered copper particles d_p, 40–80 μm δ, 120–400 μm ε, 0.4	398–467 q^*_{CHF}, 1.62–1.9 (Best, 454@2.2)	2.2–5.7 ΔT^*_{CHF} = 0.065–0.17	*n*-Pentane (1 atm)	4 cm^2 (circular)
Li and Peterson (2010)	Uniform sintered Cu particle wick d_p, 250 μm δ, 0.55–1.2 mm ε, 0.274	227–290 q^*_{CHF}, 2.04–2.6 (Best, 227@23) (Best, 290@48) —	23–48 ΔT^*_{CHF}, 0.88–1.84	Water (1 atm)	0.5 cm^2 (circular)
Mori and Okuyama (2009)	Biporous honeycomb (commercial CaO/Al_2O_3–SiO_2–TiO_2) w_s, 0.4 mm w_p, 1.3 μm δ, 1.2–10 mm Porous honeycomb d_p, 37 nm ε, 0.248	~50–251 q^*_{CHF}, 0.45–2.26 (Best, 251@50)	17–50 ΔT^*_{CHF}, 0.65–1.92	Water (1 atm)	7.06 cm^2 (circular)

For normalized CHF and superheat, q^*_{CHF} and ΔT^*_{CHF}, q_{CHF} = 110.8, 24.5, and 13.4 W/cm^2 for water, *n*-pentane, and FC-72 at 1 atm, respectively [Zuber 1959, Liter and Kaviany 2001, and Chang and You 1996]. ΔT_{CHF} = 26°C, 34°C, and 30°C for water, *n*-pentane, and FC-72 at 1 atm, respectively [Li et al, 2006, Liter and Kaviany 2001, and Chang and You 1996].

nucleate boiling heat transfer using wire and water or R-113 (Bergles and Chyu 1982). Afgan et al. (1985) utilized Ni–Cr porous coated wires for the pool boiling in water, ethanol, and Freon-113 at atmospheric pressure condition (Afgan et al. 1985). This coating showed approximately one-time CHF enhancement compared to the plain surface, and the authors concluded that the coatings reduced the hydrodynamic wavelength. In the 1980s, there were a series of studies about the detailed boiling mechanisms of the uniform coatings (non–thermally conducting material) (Malyshenko 1991), and the authors articulated the boiling mechanisms including the transition from the nucleate to film boiling, employing the Al_2O_3- and nichrome-sprayed and sintered particles. These primarily showed significant reduction on the superheat. Chang and You (1997b) designed microstructures using aluminum, copper, diamond, and silver particles with 1–50 μm particle sizes with the different porosity for the pool boiling performance (Chang and You 1997b). The CHF were q_{CHF} = 23.9 to 33.5 W/cm^2 with maximum superheats of $\Delta T_{sh,CHF}$ ~ 12°C–22°C using FC-72, where the CHF doubles the plain surface. It was observed that the incipient boiling point decreases in the presence of the microporous structure and the heat transfer coefficient increases. Chang and You (1997a) observed doubling the CHF enhancement using uniform diamond porous coating, 2–70 μm thick, using FC-72 (Chang and You 1997a). The authors concluded that the enhancement is due to increased active evaporation sites on the porous coatings. Liter and Kaviany employed sintered copper particles and observed $q^*_{CHF} = 1.96$ and $\Delta T^*_{CHF} = 0.26$ (Liter and Kaviany 2001), concluding that the origin of the CHF enhancement is related to the reduced hydrodynamic instability wavelength and the reduction of the superheat is related to the significant effective thermal conductivity of the sintered copper particles. Similar CHF enhancement was found using various porous, surface-treated particle coatings, while it resulted in significant superheat reduction, $\Delta T^*_{CHF} = 0.065$–0.17 (Hwang and Kaviany 2006). Li and Peterson (2010) also tested the sintered copper particles using water; the CHF enhanced nearly 1–1.6 times over the plan surface at the 0.88–1.84 superheat compared to the plan surface.

The CHF enhancement is related to the critical hydrodynamic changes in the presence of the sintered particle coating; the empirical/theoretical correlations were developed and given as (Polezhaev and Kovalev 1990; Liter and Kaviany 2001)

$$\frac{q_{CHF,p}}{(\pi/24)\rho_g^{1/2}\Delta h_{lg}\left[\sigma g\left(\rho_l-\rho_g\right)\right]^{1/4}} = \frac{3\left[\sigma/\left(g\left(\rho_l-\rho_g\right)\right)\right]^{1/4}}{\lambda_u^{1/2}}, \quad \text{where } \lambda_u = (\pi/5.88\epsilon^{2.28})^2 d \tag{18.7}$$

The origin of the enhancement is postulated to be related to vapor morphologies, thus controlling the instability (Liter and Kaviany 2001; Hwang and Kaviany 2006). The smaller particle size resulted in the small superheat, since it reduced the thermal conduction path (Hwang and Kaviany 2006).

18.2.2.2 Biporous Wick

Biporous sintered wick is heterogeneous porous structure using the two distinctive particle sizes as shown in Figure 18.5. The biporous sintered wick has been used in pool boiling to increase the CHF and to reduce the superheat, expecting that the larger pores would allow for vapor escape, whereas the smaller pores are primarily for the capillary suction (Wang and Catton 2001; Mori and Okuyama 2009). Mori and Okumaya utilized the commercially available porous honeycomb thin disk (CaO–/Al_2O_3–SiO_2–TiO_2-based nanoporous material) with thickness of 1.2–10 mm (Mori and Okuyama 2009). They observed that dryout occurred primarily due to the capillary–viscous limit through the nanoporous structure (which was lower than the hydrodynamic limit due to the low permeability of the nanoporous). In this case, the maximum CHF was observed with the thinnest porous honeycomb, where the capillary–viscous limit is relatively high. Note that the capillary–viscous limit is inversely proportional to the height (or liquid flow path).

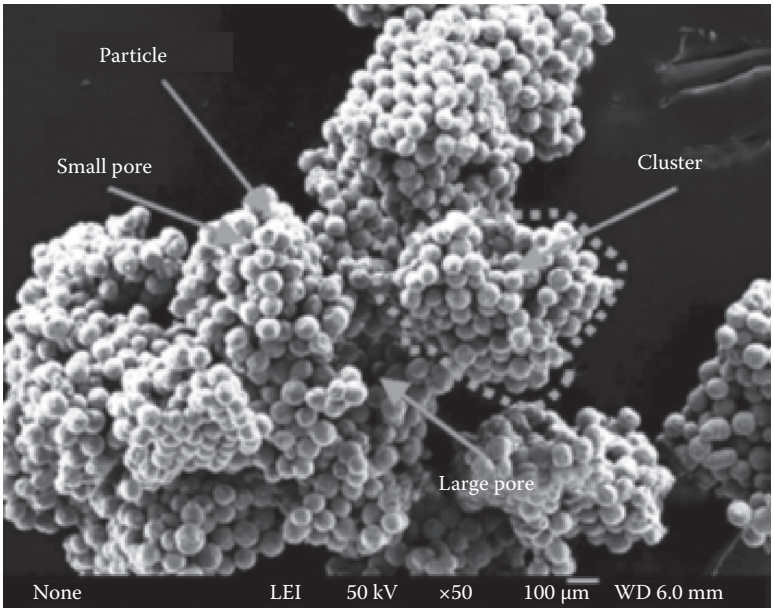

FIGURE 18.5 SEM image of a biporous wick, including the primary and secondary pore structures. (From Semenic, T. and Catton, I., *Int. J. Heat Mass Transfer*, 52(21–22), 5113, 2009.)

18.2.3 Liquid-Artery Wick (Design C)

The hydrodynamic limit of the CHF was further controlled using modulated, sintered porous particle wick (nonuniform wick thickness) (Liter and Kaviany 2001) as shown in Figure 18.4 (design C) and Figure 18.6b. The thick wick provides liquid supply pathway, while the thin wick maximizes the vapor escape and minimizes the thermal resistance (reducing superheat). The pitch of the modulated wick (conical shape, 3-D modulation) was designed to reduce the critical hydrodynamic wavelength,

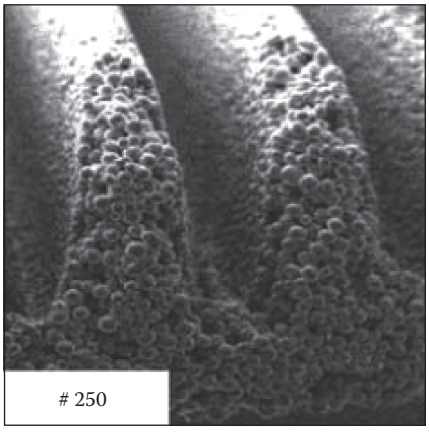

(a)

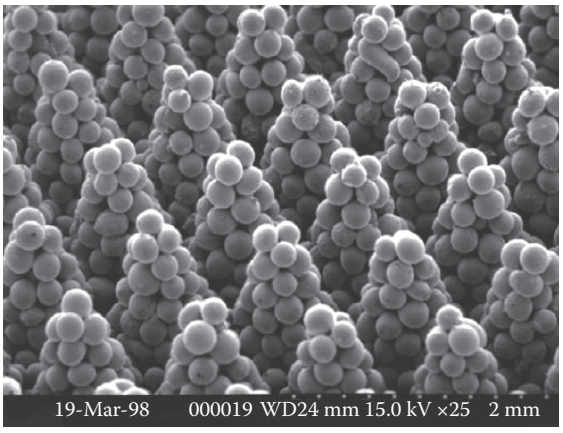

(b)

FIGURE 18.6 SEM micrographs of (a) 2-D (From Min, D.H. et al., *Int. J. Heat Mass Transfer*, 52(11–12), 2607, 2009b.) and (b) 3-D modulated, sintered particle wicks. (From Liter, S.G. and Kaviany, M., *Int. J. Heat Mass Transfer*, 44(22), 4287, 2001.)

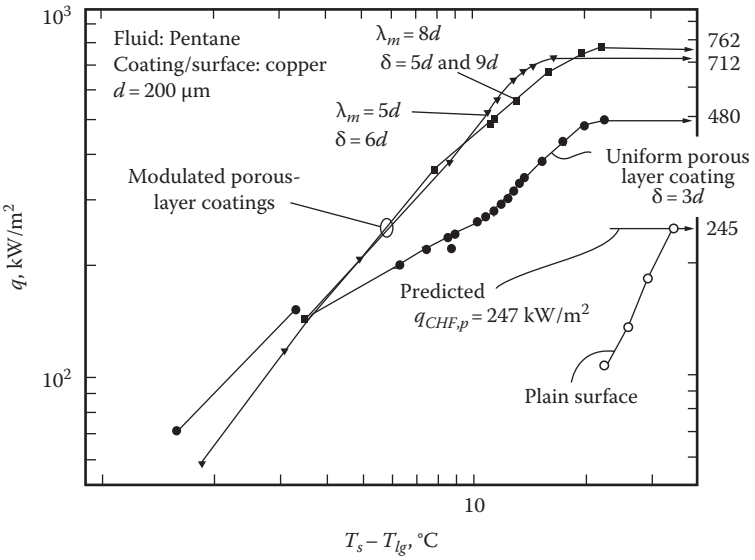

FIGURE 18.7 Measured pool boiling heat flux from plain, uniformly coated, and modulated (liquid artery) coated surfaces using *n-pentane* at 1 atm. (From Liter, S.G. and Kaviany, M., *Int. J. Heat Mass Transfer*, 44(22), 4287, 2001.)

which in turn resulted in enhancing the CHF by two times over the plain surface. For the modulated wick, they modified the Zuber correlation (Equation 18.1) as (Liter and Kaviany 2001)

$$\frac{q_{CHF,h}}{(\pi/24)\rho_g^{1/2}\Delta h_{lg}[\sigma g(\rho_l-\rho_g)]^{1/4}} = \frac{3[\sigma/(g(\rho_l-\rho_g))]^{1/4}}{\lambda_m^{1/2}}$$

where λ_m is the modulated wick pitch.

The modulated wick structures also succeeded in controlling the hydrodynamic wavelength using 2-D modulation (long stripe, 2-D modulation) (Min et al. 2009b). The detailed structure is shown in Figure 18.6a. The authors also found that the height of the modulated wick needs to be sufficiently large to influence the hydrodynamic instability (Min et al. 2009). The aforementioned work provided insights into the optimal wick design for the film evaporation, which in turn leads to effective liquid supply and vapor escape, with very small thermal resistance.

A typical pool boiling performance is measured by the heat flux with respect to the superheat as shown in Figure 18.7. As discussed earlier, the evaporator wick not only enhances the CHF via the reduced hydrodynamic instability wavelength but also reduces the superheat due to the increased effective thermal conductivity, that is, high effective thermal conductivity metallic wick, in the pre-CHF regime and at CHF. The improvements are more pronounced with use of the modulated wick, with enhanced liquid supply in the liquid-artery wick segment and the reduced thermal resistance of the thin evaporation wick. Here, we primarily focus on the CHF enhancement and the associated reduction in the superheat at CHF. The same principles are successfully demonstrated in film evaporation coatings (Section 18.3) (Table 18.3).

18.2.4 Other Surface/Fluid Modifications

Surface/fluid modifications have been suggested for enhancing the CHF and/or reducing the superheat. One is to improve the surface wetting using various coating techniques and/or nanostructures (Kandlikar 2001; Li et al. 2008; Chen et al. 2009; Betz et al. 2010, 2013; Feng et al. 2012; Dai et al. 2013b). Also, pool boiling using the nanoliquid (suspended nanoparticles in Brownian motion)

TABLE 18.3
Summary of Studies on Modulated Capillary Evaporator Wicks in Pool Boiling (Design C)

Authors	Wick Structure	CHF, q_{CHF} (W/cm²)	ΔT_{CHF} (°C)	Working Fluid	Heater Size (cm²)
Liter and Kaviany (2001)	Modulated sintered Cu particle wick (3-D modulation) d_p, 200 μm λ_m, 1 or 1.6 mm δ, 1–1.8 mm ε, 0.4	71.2 (single height) 76.2 (dual height) q^*_{CHF}, 2.91–3.11	16 (single height) 22 (dual height) $\Delta T^*_{CHF}s$, 0.47–0.65	*n*-Pentane (1 atm)	4 cm² (circular)
Min et al. (2009b)	Modulated sintered Cu particle wick (2-D modulation) d_p, 45–200 μm λ_m, 0.83 or 1.9 mm δ, 1–1.8 mm ε, 0.4	61.1–81.5 (2-D) 37.5–48.2 (3-D) q^*_{CHF}, 2.5–3.3 (2-D) q^*_{CHF}, 1.53–1.97 (3-D) (Best, 81.5@17.4, 2-D) (Best, 70.9@12.6, 2-D)	12.6–31.7 (2-D) 5.85–6.96 (3-D) ΔT^*, 0.37–0.93 (2-D) ΔT^*, 0.17–0.2 (3-D)	*n*-Pentane (1 atm)	4 cm² (circular)
Li and Peterson (2010)	Modulated sintered Cu particle wick d_p, 250 μm λ_m, ~2 mm δ_u, 0.55 mm δ_m, 3.6 mm ε, 0.274	435 q^*_{CHF}, 3.92	25 ΔT^*, 0.96	Water (1 atm)	0.5 cm² (circular)

For normalized CHF and superheat, q^*_{CHF} and ΔT^*_{CHF}, q_{CHF} = 110.8 and 24.5 W/cm² (Zuber 1959; Liter and Kaviany 2001) and ΔT_{CHF} = 26°C and 34°C (Liter and Kaviany 2001; Li and Peterson 2006) for water and *n*-pentane at 1 atm, respectively.

results in the CHF enhancement. The origin of the enhancement is still under discussions; one explanation is enhanced effective liquid thermal conductivity, and the other is the nanoparticle coating to the heated surface. This surface modification results in increased wettability or changes the hydrodynamic instability wavelength (Park et al. 2010; Park and Bang 2014). Generally, the enhancements are not as significant as those from the capillary wick evaporators; thus, here, we limit our discussions to the hydrodynamically controlled CHF.

18.2.5 Summary

The uniform and distributed (liquid artery) capillary evaporator wicks on the pool boiling not only enhance the CHF but also decrease the superheat. The normalized CHF and superheat (at CHF) by those of the plain surface are summarized in Figure 18.8. The uniform capillary wicks enable increasing the CHF generally up to one time over the plain surface, with large variations in the superheat depending of the geometry and surface treatment. Note that the maximum increase reported is up to nearly three times, but it was demonstrated on small heated area, so there are size effects with very large superheat. The challenge with the uniform capillary wick evaporators is limited capability to separate the liquid pathway from the vapor escape path and to minimize the thermal resistance across the wick. This challenge is overcome with the distributed (liquid artery) capillary evaporator wick; the thick wick assists the liquid supply and reduces the hydrodynamic instability wavelength thus enhancing the CHF, while the thin wick significantly reduces the thermal resistance, resulting in the reduced superheat. Similar approach is used in the film evaporation design, which will be discussed in the following section.

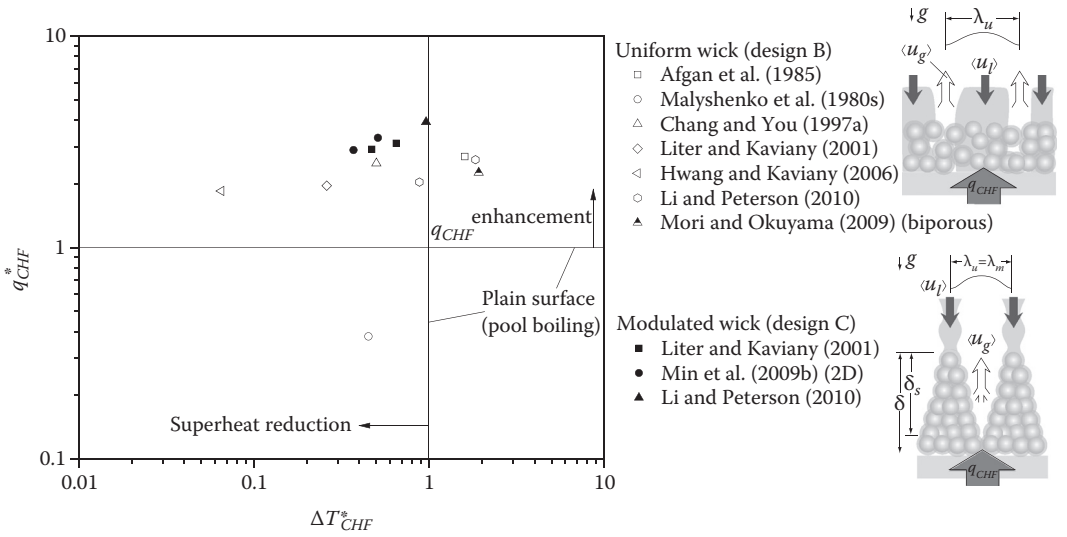

FIGURE 18.8 Enhancement of the CHF and reduction of superheat with uniform and distributed capillary wick evaporator in pool boiling (designs B and C). The specifications are listed in Tables 18.2 and 18.3.

18.3 FILM EVAPORATION (DESIGN D TO E, CAPILLARY–VISCOUS LIMIT)

High-heat-flux cooling system is in great demand, especially when the heat source becomes small (i.e., small electronic device). The heat flux is often much higher than the cooling capability (i.e., pre-CHF) in the pool boiling (designs A to C, Figure 18.4), and there is a strong need to further improve the CHF. Generally, the film evaporation enables to deliver larger heat through the thin, liquid-filled evaporator wicks, that is, heat pipe and vapor chamber. A key to this system is to continuous liquid supply to the evaporator wick for the CHF (Equation 18.3) and small thermal resistance across it. The liquid supply system requires capillary pumping capability as well as liquid-permeable structures, which are competing mechanisms; thus, an optimal design needs to be examined. There have been tremendous efforts into developing/optimizing the wick structure utilizing uniform wicks (mesh, groove, and sintered particles) and distributed, nonuniform (capillary artery) wicks.

One fundamental challenge of the uniform thickness wick (design D) is, however, limited capability to simultaneously achieve both high CHF (thick wick) and low superheat (thin wick). To overcome this challenge, distributed (liquid artery) wick structure is developed (Mughal and Plumb 1996; Hwang et al. 2007, 2010, 2011; Ju et al. 2013). The liquid-artery wick assists the liquid supply from condensation or external supply to the evaporator, while the thin wick provides the dominant heat flow (low resistance). The liquid-artery wick can be either vertical (normal to the heat flow, design E) or lateral (perpendicular to the heat flow, design F). The performance enhancements using the liquid-artery wick have been successfully demonstrated in the practical applications such as heat pipe (Hwang et al. 2007) and vapor chamber (Min et al. 2009a; Hwang et al. 2010, 2011; Ju et al. 2013; Weibel and Garimella 2013). Here, the recent advance is discussed based on the design structures, particularly emphasizing the capillary artery wick.

18.3.1 Uniform Thickness Wick (Design D)

A simple wick design is a porous structure with uniform thickness, typically sintered copper particles, mesh screens, and grooves. The wick could be characterized by one or two length scales of geometrical features such as hydraulic diameter and particle size. A monoporous wick is characterized

by one length scale such as the diameter of particle or mesh wire, while a biporous wick has two length scales, that is, the diameters of particle and particle cluster for desired liquid–vapor transport aiming at high CHF and low superheat.

18.3.1.1 Monoporous Wick

Mesh screens and grooves are popular as wick structures because of their well-defined geometries and dimensions for further analysis. Thus, there are numerous studies using them, but the performance is generally poor since the capillary pumping capability is limited. The details of the experimental approaches are summarized in Table 18.4. Plesch et al. (1991) employed two types of microgrooves in the heat pipe, which were tested both in vertical and horizontal configurations using water (Plesch et al. 1991). The maximum heat transfer was obtained at 120 W/cm^2 (vertical) and 60 W/cm^2 (horizontal). Similarly, Hopkins et al. (1999) used a water-filled microgroove and showed the maximum heat transfer performance of 37 W/cm^2 for horizontal configuration and 113.2 W/cm^2 for vertical configuration (Hopkins et al. 1999). Liao and Zhao (1999) utilized the spherical glass particles for the uniform wick and observed the maximum heat flux of 26.89 W/cm^2 (Liao and Zhao 1999). Brautsch and Kew (2002) used stainless steel mesh screen as the uniform thickness wick, with the diameter of the mesh wire ranging from 40 to 190 μm with 0.313–0.469 porosity and one to five layer thickness (Brautsch and Kew 2002). The maximum heat flux of 8.24–21.39 W/cm^2 with superheats of 18°C–40°C at the vertical heat source placement using water was reported. Hanlon and Ma (2003) demonstrated the maximum heat flux of 55 W/cm^2 using the sintered copper particle wick (Hanlon and Ma 2003). The monoporous sintered copper wick having the particle size of 635 μm with 0.43 porosity and 1.9–5.7 mm wick thickness was used. In the horizontal heat source placement, the maximum heat flux of 32–55 W/cm^2 with the superheat of 80°C–100°C was obtained. Li et al. (2006) utilized the sintered copper mesh screen, with the ranges of wire diameter of 56 μm, porosity of 0.693–0737, and wick thickness of 210–820 μm (Li and Peterson 2006). The CHF was significantly enhanced up to 367.9 W/cm^2 at a moderate superheat ΔT_{sh} ~ 22°C using water. They observed that the increased mesh thickness enhanced the CHF. Li and Peterson also examined the effects of the mesh size and porosity in the rage of wire diameter of 56–191 μm and the porosity of 0.409–0.698 at the thickness of 740 μm (Li and Peterson 2006). They enhanced the CHF up to ~350 W/cm^2 at the superheat ΔT_{sh} ~ 28°C. They also found that the optimal porosity was nearly 0.6 and the small capillary meniscus formed between the mesh wire and solid wall was essential to the enhanced CHF.

Semenic et al. employed the sintered copper particles with the porosity of 0.318–0.371 and particle sizes of 53–710 μm and the thickness of 1 mm. The CHF reached up to 223 W/cm^2 at the superheat of 37°C using water. This indicates the CHF enhanced one time over that of the pool boiling on the plain surface. Weibel et al. tested the sintered copper wick with the particle size of 60–302.5 μm and 0.6–1.2 mm wick thickness (Weibel et al. 2010). The maximum heat flux q_{CHF} was 596.5 W/cm^2 with the superheat of 25 K, that is, thermal resistance $R_{k,w}$ ~ 0.04 K/(W/cm^2), where the wick performance was tested with an evaporator of 0.5 × 0.5 cm^2 using the vertical placement and water. This study also visualized the bubble generation/evolution within the wick to articulate the boiling mechanisms. The similar test was performed using monoporous wick structure in the vertical heater placement (Oshman et al. 2011; Weibel 2012; Famouri et al. 2014).

18.3.1.2 Biporous Wick

To effectively separate the liquid flow from the vapor, biporous wick was developed, aiming at the enhanced CHF. The vapor escapes from the large pores, while the liquid flows through the small pores (Figure 18.5). North et al. developed a biporous wick using sintered nickel or copper particles, having the particle size of 66–89 μm, the cluster size of 250–710 μm, and the wick thickness of 640 μm (North et al. 1995). The maximum heat flux was obtained at q_{CHF} = 27–70 W/cm^2 with the superheat of 10°C–12°C using water. Semenic et al. also significantly improved the CHF using the biporous wick, showing that the maximum heat transfer rate was 150–494 W/cm^2

TABLE 18.4
Summary of the Uniform Thickness, Capillary Evaporator Wick in Film Evaporation (Design D)

Authors	Wick Structure	CHF, q_{CHF} (W/cm²)	ΔT_{CHF} (°C)	Working Fluid	Heat Source Area (cm²)
Plesch et al. (1991)	Microgrooves w_g, 30–120 μm	120 (vertical), 60 (horizontal) q^*_{CHF}, 0.54–1.08 (Best, 60@68)	45 (vertical), 68 (horizontal) ΔT^*_{CHF}, 1.7–2.6 —	Water (1 atm)	0.5 × 2 cm²
Hopkins et al. (1999)	Microgrooves w_g, 200–450 μm	37 (horizontal), 113.2 (vertical) q^*_{CHF}, 0.33–1.02 (Best, 37@4)	20 (vertical), 4 (horizontal) ΔT^*_{CHF}, 0.16–0.76	Water (T_{lg} ~60°C–95°C)	—
Liao and Zhao (1999)	Spherical glass particles d_p, 550–2560 μm δ, 80 mm	12–26.89 q^*_{CHF}, 0.11–0.24	68–100 ΔT^*_{CHF}, 2.62–3.85	Water (T_{lg} ~ 80°C)	2.8 × 9.9 cm² (four groove channels)
Brautsch and Kew (2002)	Stainless steel (304L) mesh ε, 0.313–0.469 d, 40–190 μm δ, 1–5 layers	8.24–21.39 q^*_{CHF}, 0.07–0.19	18–40 ΔT^*_{CHF}, 0.7–1.5	Water (1 atm)	—
Hanlon and Ma (2003)	Sintered copper particles ε, 0.43 d, 635 μm δ, 1.9–5.7 mm	~32–55 q^*_{CHF}, 0.3–0.5 —	80–100 ΔT^*_{CHF}, 3.07–3.84	Water (1 atm)	1 × 2 cm²
Li and Peterson (2006)	Copper mesh ε, 0.693–0.737 d, 56 μm δ, 210–820 μm	190–367.9 q^*_{CHF}, 1.7–3.3 (Best, 367.9@22)	10–22 ΔT^*_{CHF}, 0.38–0.84 —	Water (1 atm)	0.8 × 0.8 cm²
Li and Peterson (2006)	Copper mesh ε, 0.409–0.698 d, 56–191 μm δ, 740 μm	220–350 q^*_{CHF}, 1.98–3.16 (Best, 350@28)	10–28 ΔT^*_{CHF}, 0.38–1.08 —	Water (1 atm)	0.8 × 0.8 cm²
Semenic et al. (2008)	Monoporous sintered copper particles ε, 0.318–0.371 d, 53–710 μm δ, 1000 μm	209.5–223 q^*_{CHF}, 1.89–2.0 (Best, 223@37)	18–73 ΔT^*_{CHF}, 0.69–2.8	Water (0.1 atm)	0.709 cm² (Circular)
Weibel et al. (2010)	Monoporous sintered copper particles ε, 0.635–0.657 d, 60–302.5 μm δ, 600–1200 μm	500–596.5 q^*_{CHF}, 4.5–5.38	17–33.5 ΔT^*_{CHF}, 0.65–1.29	Water (1 atm)	0.5 × 0.5 cm²
North et al. (1995)	Biporous sintered copper particles ε, ~0.7 d_p, 66–89 μm[f] d_c, 250–710 μm[g] δ, 640 μm	27–70 q^*_{CHF}, 0.24–0.63	10–12 ΔT^*_{CHF}, 0.38–0.46	Water (T_{lg} = 20°C)	3 × 0.8 cm²

(*Continued*)

TABLE 18.4 (*Continued*)
Summary of the Uniform Thickness, Capillary Evaporator Wick in Film Evaporation (Design D)

Authors	Wick Structure	CHF, q_{CHF} (W/cm²)	ΔT_{CHF} (°C)	Working Fluid	Heat Source Area (cm²)
Semenic et al. (2008)	Biporous sintered copper particles ε, 0.597–0.631 d_p, 29–63 μm[f] d_c, 250–710 μm[g] δ, 1000–4000 μm	150–494 q^*_{CHF}, 1.35–4.45	18–128 ΔT^*_{CHF}, 0.69–4.92	Water (0.1 atm)	0.709 cm² (Circular)
Semenic and Catton (2009)	Biporous sintered copper particles ε, 0.51–0.68 d_p, 41–83 μm[a] d_c, 302–892 μm[b] δ, 800–3000 μm	400–990 q^*_{CHF}, 3.6–8.1 (Best thin, 520@50) (Best thick, 990@147)	50–147 ΔT^*_{CHF}, 1.92–5.65	Water (T_{lg} = 36°C–46°C)	0.322 cm² (Circular)
Nam et al. (2011)	Copper oxide nanostructured microposts ε, 0.54–0.73 d, 50 μm L_p, 70–100 μm δ, 100 μm	800–930 (0.2 × 0.2 cm²) 125–180 (0.5 × 0.5 cm²) q^*_{CHF}, 1.13–8.39	~80 ~60–70 ΔT^*_{CHF}, 2.3–3.1 —	Water (T_{lg} = 44°C)	0.2 × 0.2 cm² 0.5 × 0.5 cm²
Kousalya et al. (2013)	Copper functionalized CNT-coated sintered copper powder ε, 0.5 d, 100 μm d_{CNT}, ~85–275 nm δ, 200 μm δ_{CNT}, 250–750 nm	350–450 q^*_{CHF}, 3.15–4.06 (Best, 450@14)	14–23 ΔT^*_{CHF}, 0.54–0.88 —	Water (1 atm)	0.5 × 0.5 cm²

For normalized CHF and superheat, q^*_{CHF} and ΔT^*_{CHF}, q_{CHF} = 110.8 W/cm² (Zuber 1959) and ΔT_{CHF} = 26°C (Li et al. 2006) for water at 1 atm.

[a] Particle diameter.

[b] Cluster diameter.

(Semenic et al. 2008), and also further enhanced CHF up to 990 W/cm² using a relatively small heated region, ~0.3 cm² (Semenic and Catton 2009). However, these enhancements were achieved at the expense of the large superheat (up to 7.1 times larger than the plan surface), and overall the biporous wick has capability to delay the complete dryout.

18.3.1.3 Nanostructures

Nanostructured wicks are generally employed for large evaporation surface areas and increased capillary pressure (small capillary meniscus). However, the nanoscale pore size significantly decreases the permeability, where the liquid supply suffers, and the overall CHF is expected to be similar to the microstructure. Nam et al. used the copper oxide (CuO) microposts with the nanostructures on thin silicon substrates (Nam et al. 2011). Liquid was primarily supplied through a fixed micropost diameter of 50 μm, with varying interpost spacing (porosity of 0.54 and 0.73). It was observed that the smaller interpost spacing resulted in the reduced superheat due to larger evaporation surface

area. For a heater of 0.2 × 0.2 cm^2, the CHF was 800–930 W/cm^2 with the superheat ΔT ~ 80°C, and while using a 0.5 × 0.5 cm^2 heater, the CHF was 128–180 W/cm^2 with the superheat ΔT ~ 60°C–70°C. Note that the smaller heater size resulted in significant CHF enhancement, where possible heater size effect. Kousalya et al. also fabricate the copper functionalized carbon nanotube (CNT) on the copper particle and observed four times higher CHF than the plain surface (pool boiling) with a reduced superheat (Kousalya et al. 2013). Dai et al. recently fabricated SiO_2 coating on copper mesh and found reduced superheat with modest CHF improvement (Dai et al. 2013a).

18.3.2 Liquid-Artery Wick

To effectively separate the liquid and vapor flows to/from the evaporator, distributed (liquid artery) wick is designed (similarly done in pool boiling, design C). This design is shown in Figure 18.4 (design F). The liquid artery increases the liquid supply to the evaporator, which in turn allows for a very thin (monolayer) wick to minimize the thermal resistance. The liquid-artery wick can be vertical or lateral depending on the design constraints, that is, location of the condenser. Also, the source of the condensate can be condensation (heat pipe and vapor chamber) or external liquid supply (LHP or hybrid two-phase loop).

18.3.2.1 Vertical (Design E)

18.3.2.1.1 Vapor Chamber

The vertical liquid-artery wick is desirable to the system, where the evaporator is in line with the condenser and the aspect ratio is large. Since the liquid-artery wick is placed normal to the evaporator, an enlargement of the evaporator can be simply extended by having the large number of the liquid-artery wick. The previous work of the vertical liquid-artery wick is found in Table 18.5.

Hwang et al. (2010) designed the thin (monolayer) wick with the vertical liquid-artery wick evaporator and condenser on top, as shown in Figure 18.9 (Hwang et al. 2010).

Evaporation dominantly occurred in the thin monolayer evaporator wick, and vapor readily escaped out of the evaporation sites through the vapor space between the vertical capillary arteries,

TABLE 18.5
Summary of the Vertical Liquid-Artery Wick in Film Evaporation (Design E)

Authors	Wick Structure	CHF, q_{CHF} (W/cm^2)	ΔT_{CHF} (°C)	Working Fluid	Heat Source Area (cm^2)
Hwang et al. (2010)	Monolayer of sintered copper particles with vertical liquid artery ε, ~0.4 d_p, 60 μm L_p, 3.25 mm δ, 60 μm	387 q^*_{CHF}, 3.47	20 ΔT^*_{CHF}, 0.77	Water (T_{lg} ~ 40°C–70°C)	1 × 1 cm^2 —
Crepinsek and Park (2011)	Uniform layer with vertical liquid artery made of sintered copper particles ε, ~ 0.3 d_p, 75 μm δ, 1 mm	102 (*pre-CHF*) q^*, 0.92	12.2 (*pre-CHF*) ΔT^*, 0.5	Water ($T_{lg} \leq$ 70°C)	2.41 × 2.41 cm^2

For normalized CHF and superheat, q^*_{CHF} and ΔT^*_{CHF}, q_{CHF} = 110.8 W/cm^2 (Zuber 1959) and ΔT_{CHF} = 26°C (Li et al. 2006) for water at 1 atm.

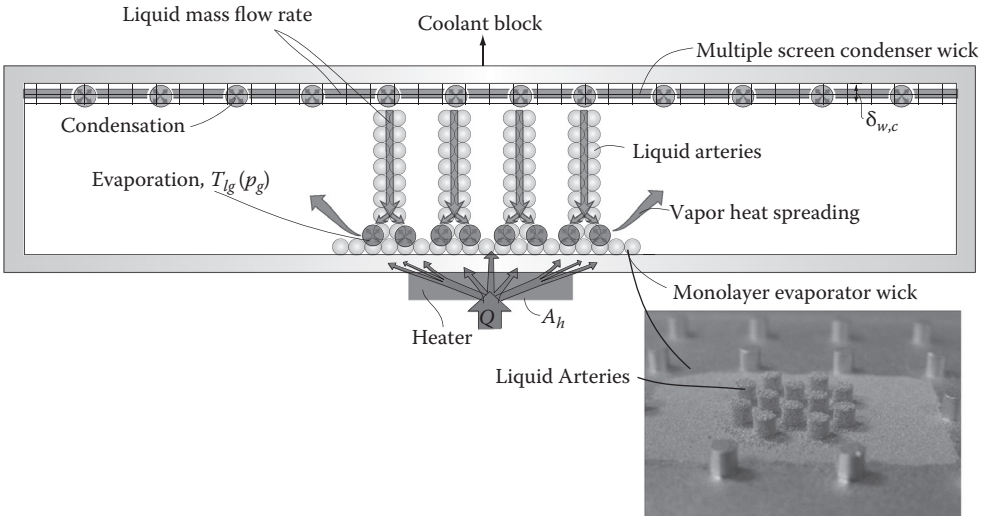

FIGURE 18.9 A schematic of vertical liquid artery with the thin monolayer wicks. Phase change, heat, liquid and vapor flow paths, and evaporator wick image are also shown. (From Hwang, G.S. et al., *Int. J. Heat Mass Transfer*, 53(13–14), 2662, 2010.)

while the liquid coolant from the multilayer screen condenser supplied liquid flow rate significantly. However, due to the significant pressure drop through the monolayer, at very high heat flux, sudden and total dryout occurred at q_{CHF} ~ 380 W/cm^2 with a moderate superheat ΔT = 20°C and a small thermal wick resistance (equivalently, $R_{k,w}$ = 0.05 K/(W/cm^2)).

18.3.2.1.2 Capillary-Pumped Loops and Loop Heat Pipes

The pump heads of capillary heat pipes are set by the pore size of the capillary wicks in the evaporator (Reay et al. 2013). To increase the cooling performance, the total liquid–vapor pressure drop (flow circulation) needs to be minimized. To minimize the liquid and vapor flow interactions and therefore the pressure drop, a closed loop design have been used, that is, capillary-pumped loop (CPL) and LHP. The CPL was first introduced by Stenger in the United States in 1965 (Stenger 1965), while the first LHP was developed by Gerasimov and Maydanik in 1975 (Gerasimov et al. 1975). The innovative designs not only reduce the pressure drop due to the single-phase flows in the open loop but also eliminate the entrainment limit of the conventional heat pipes due to the interaction between the fast vapor flow originated from the evaporator and the condensate flow returning to evaporator. Thanks to the noncapillary loop design, the loops can be as long as 2 m. But an additional flow control is required to prime the evaporator during start-up using a cold-biased liquid reservoir integral to the evaporator in LHP or separate from the evaporator in CPL.

The evaporator for the CPLs and LHPs employs a liquid artery to feed the liquid into a cylindrical evaporator wick as shown in Figure 18.10. As a result, the liquid transport path in the evaporator wick of small pore radii (r = 0.7 ~ 10 μm) is only a few millimeters long. Since the liquid flow through the vertical wick is in an opposing direction to the heat input, the liquid subcooling in the liquid artery can be maintained relatively well. The fluid in vapor and liquid phases in the loop is driven by the capillary pressure head of the evaporator wick, which matches the pressure drops of the fluid flows and their gravitational head changes, if any.

The flat evaporator design has been reported (Hopkins et al. 1999), which provides a direct installation of the evaporator on common flat heat sources without using a saddle interfacing between the cylindrical envelope of the conventional LHP evaporators and flat heat source. The saddle is responsible for an extra thermal resistance and nonuniform heat input in the circumferential direction causing local dryout.

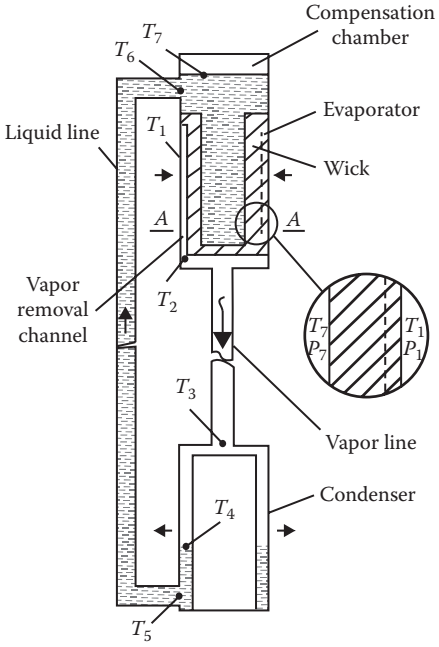

FIGURE 18.10 Schematic of loop heat pipe. (From Maydanik, Y.F., *Appl. Therm. Eng.*, 25(5–6), 635, 2005.)

18.3.2.1.3 Active/Passive Two-Phase Cooling Loop

Active two-phase cooling systems such as microchannels (Hetsroni et al. 2005; Qu and Mudawar 2005; Rojas and deAndrés 2006; Lee and Yao 2010) and evaporative spray (Glassman et al. 2004; Lin et al. 2006; Silk et al. 2008; Mudawar et al. 2009) have been used for high-heat-flux cooling and robust operation. The active cooling systems, however, requires complex fluid handling/conditioning to control the boiling condition in evaporator. To address this challenge, pump-assisted and capillary-driven (hybrid) two-phase cooling loops have been developed (Park et al. 2005, 2006, 2007, 2009; Crepinsek and Park 2011). A key to a successful two-phase cooling loop is to employ a good phase separator in the evaporator for continuous liquid supply and vapor escape as shown in Figure 18.11a. A main component is a porous membrane to separate evaporation region with a liquid artery, boiling surface, and vapor space from an external liquid supply region, while the liquid seamlessly flows through the porous structure (columns or posts) driven by capillary pressure. The overall liquid flow is also important to continuously supply liquid to the porous membrane. In Figure 18.11b, a subcooled liquid is mechanically fed into the liquid artery from the liquid reservoir, where it enhances the capillary liquid supply to the evaporator, while the excess liquid returns to the reservoir.

In such a design, the cooling performance is determined by the capillary–viscous limit through the liquid artery and porous membrane and posts (similar to the vapor chamber). The capillary–viscous limit can be further increased by shortening the post height (~3 mm), whereas the conventional heat pipes tend to use longer flow passages. Figure 18.12 shows the photos of the evaporator parts being assembled, that is, (a) porous membrane, (b) evaporator heater block with porous-layer coating and circular pin fins, (c) assembled pieces, and (d) finished evaporator after brazed to the evaporator enclosure.

In this system using the hybrid liquid pumping, an optimal operation condition is important, where the vapor pressure in the evaporator is maintained higher than the liquid pressure in the liquid artery, to avoid the flooding (or to maintain a thin film evaporation) in the evaporator. An active flow control based on the heat input is proven to be very effective to promote the thin film

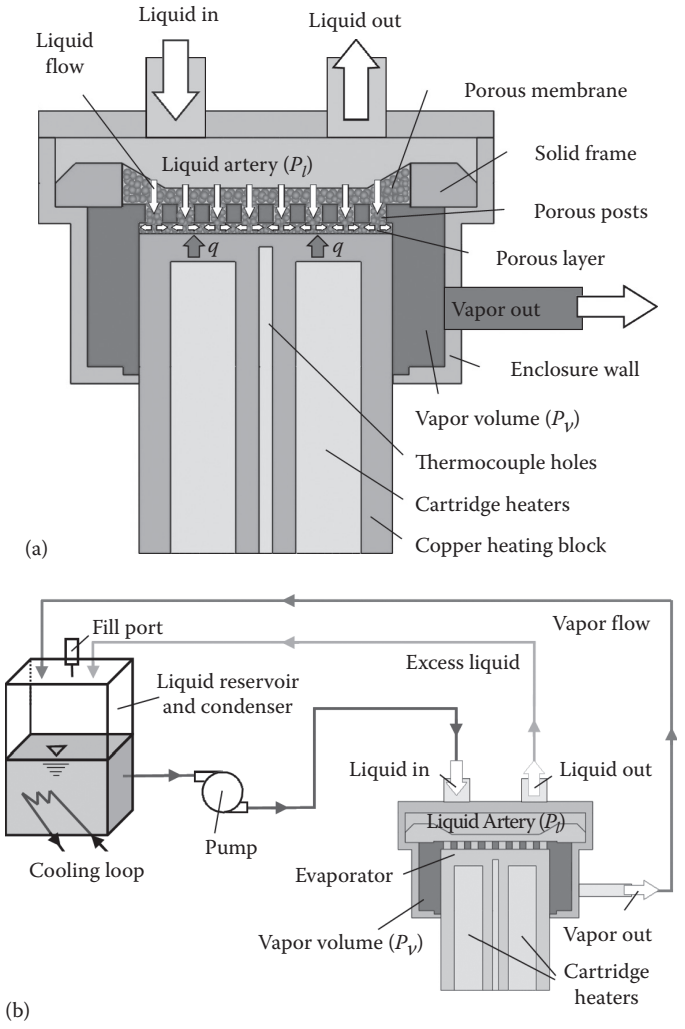

FIGURE 18.11 (a) Cross-sectional view of the evaporator for hybrid two-phase loop. (b) Schematic of single-evaporator configuration of hybrid two-phase loop. (From Park, C. and Crepinsek, M., *J. Thermophys. Heat Transfer*, 25(4), 572, 2011; Crepinsek, M. and Park, C., *Appl. Therm. Eng.*, 38(0), 133, 2012.)

evaporation of small thermal resistances, which significantly lowers the liquid pumping power as compared with constant flow cases (Bejarano and Park 2014).

In addition, the effects of various operation variables such as dynamic and stepwise heat inputs, system pressure, liquid flow rate, and heat sink temperature on the cooling performance of the hybrid two-phase loop were experimentally investigated (Park et al. 2005, 2006, 2007, 2009; Crepinsek and Park 2011). The hybrid two-phase loop has also a good design flexibility to handle multiple discrete heat sources such as a single-evaporator setup (Park et al. 2005, 2006, 2007, 2009; Crepinsek and Park 2011) and dual-evaporator setup in parallel and series (Crepinsek and Park 2012). The wick thermal resistance of the evaporator was measured to be $R_{k,w}$ = 0.12 K-cm^2/W at the heat flux of 102 W/cm^2, which was limited by the heater capacity. Otherwise, a higher maximum heat flux could be achieved.

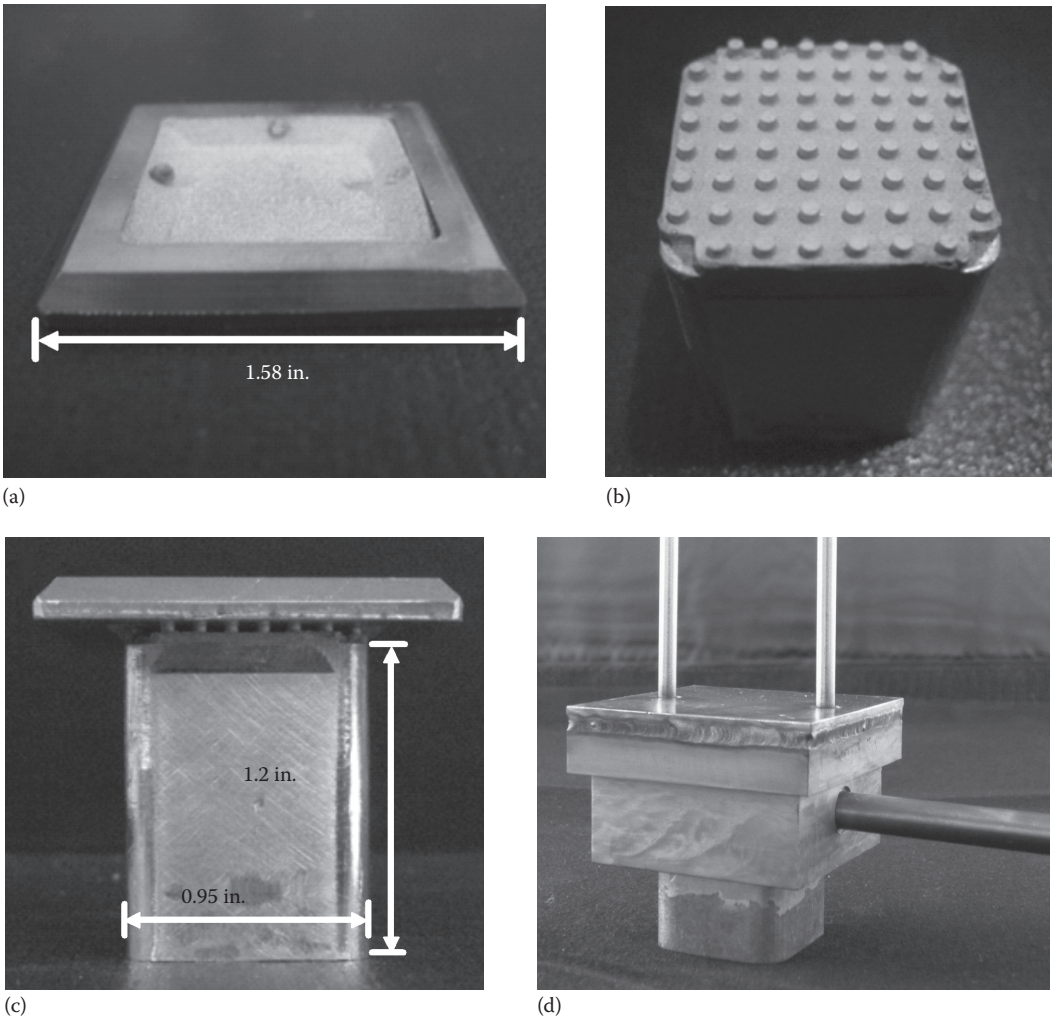

FIGURE 18.12 Photos of (a) porous membrane, (b) evaporator heater block with porous-layer coating and circular pin fins, (c) assembled pieces before brazed to the evaporator enclosure, and (d) finished evaporator. (From Park, C. and Crepinsek, M., *J. Thermophys. Heat Transfer*, 25(4), 572, 2011; Crepinsek, M. and Park, C., *Appl. Therm. Eng.*, 38(0), 133, 2012.)

18.3.2.2 Lateral (Design F)

The lateral liquid artery has been employed when the heat and liquid flow are perpendicular. The liquid supplies through the grooves or capillary body (liquid artery) in the lateral direction. This provides a design flexibility where the condenser is placed at the sides of the heated area as shown in Figure 18.13a and b.

Similar to the vertical artery, the later liquid-artery wick provides liquid to the thin wick to enhance the CHF and to reduce the superheat. The previous studies are summarized in Table 18.6. Mughal and Plumb (1996) used grooved wick structure as lateral capillary artery to minimize the thermal resistance and simultaneously to enhance the liquid-coolant supply (Mughal and Plumb 1996). Using the microgrooved copper metal foam with R11 as working fluid, the CHF was enhanced by double with 4.5 times reduced superheat, compared to those without the groove structures.

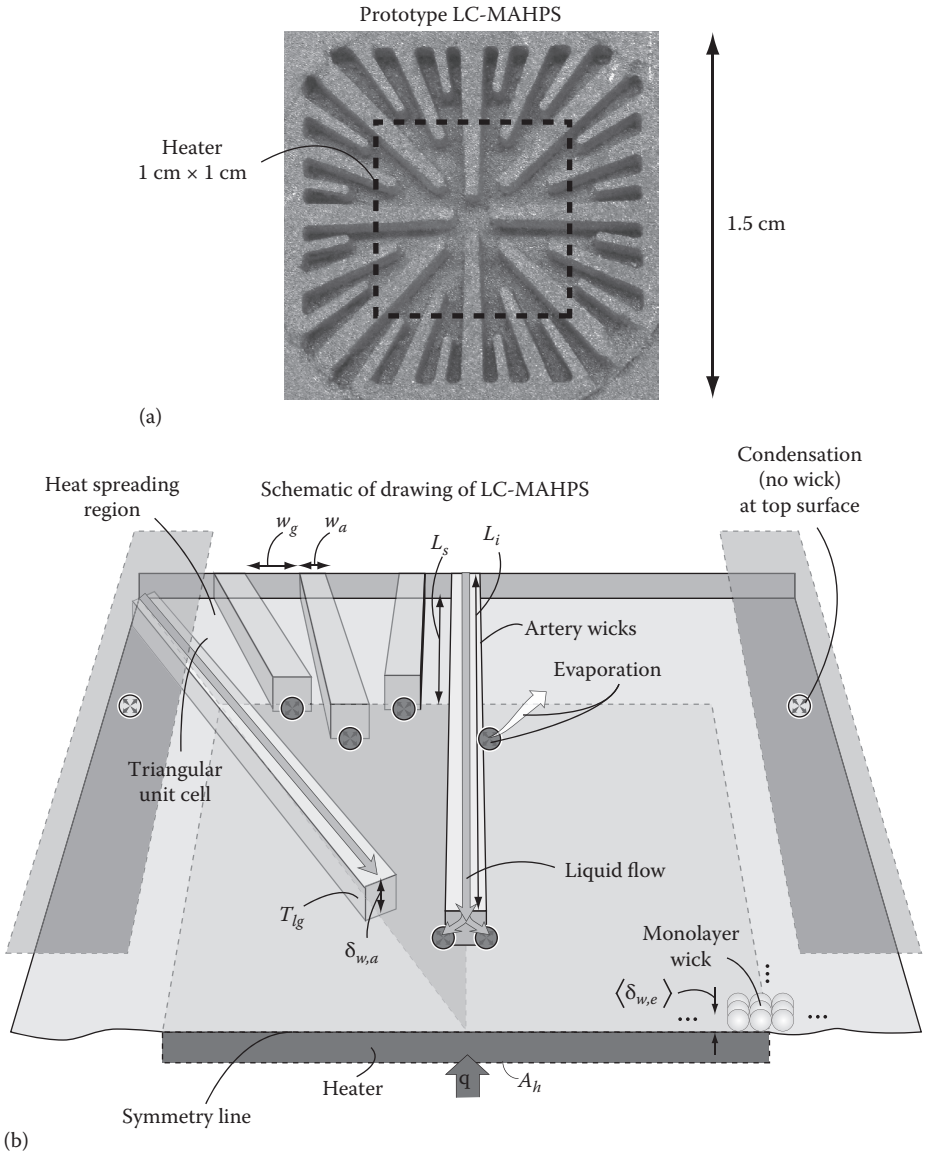

FIGURE 18.13 (a) An image of a lateral liquid-artery wick. (b) A schematic drawing showing the thin evaporator monolayer wick and a set of lateral-converging liquid arteries. Phase change, heat, liquid and vapor flow paths, and key dimensions are illustrated. (From Hwang, G.S. et al., *Int. J. Heat Mass Transfer*, 54(11–12), 2334, 2011.)

Zhao and Chen (2006) utilized the sintered copper particles with microgrooves and observed the doubled CHF enhancement over that of the plain surface pool boiling at the moderate superheat at 0.5 × 0.5 cm^2 (Zhao and Chen 2006). To solve the competing effects, the pillars and stripes of the CNT array (forest) with the microgrooves, where the CNT forest is dominantly used for the evaporation area and the microgrooves are used for the efficient liquid flow channels (Cai and Chen 2010, 2011; Cai and Bhunia 2012). Cai and Chen (2010) used the 0.2 × 0.2 cm^2 heated area and observed the heat flux rate up to q_{CHF} ~ 600 W/cm^2 with the superheat of 25°C–45°C without dryout (Cai and Chen 2010). In other work, using 1 × 1 cm^2 heated area, the CHF was observed at q_{CHF} ~ 130–195 W/cm^2 with the superheat of 29–150 K, while, in the smaller heated area of 0.2 × 0.2 cm^2, the CHF

TABLE 18.6
Summary of the Lateral Liquid-Artery Wick in Film Evaporation (Design F)

Authors	Wick Structure	CHF, q_{CHF} (W/cm²)	ΔT_{CHF} (°C)	Working Fluid	Heat Source Area (cm²)
Mughal and Plumb (1996)	Copper metal foam with channels ε, 0.94–0.95 d, 460 μm N_c, 0–15 δ, 3.175–4.762 mm	0.16 (no channel) 0.32 (7 channels) 0.35 (15 channels)	70 (no channel) 32 (7 channels) 16 (15 channels)	R11 (1 atm)	6.35 × 7.6 cm²
Zhao and Chen (2006)	Sintered copper particles with microgrooves d_p, 50 μm w_g, 150–500 μm w_b, 250–500 μm δ, 2000 μm	350 q^*_{CHF}, 3.15	23 ΔT^*_{CHF}, 0.88	Water (1 atm)	0.5 × 0.5 cm²
Hwang et al. (2011)	Monolayer of sintered copper particles with lateral liquid artery ε, ~0.4 d_p, 60 μm L_p, 2.6 mm δ, 60 μm	580 q^*_{CHF}, 5.23	72 ΔT^*_{CHF}, 2.77	Water (T_{lg} ~ 40°C–110°C)	1 × 1 cm²
Ju et al. (2013)	Monolayer of sintered copper particles with lateral liquid artery ε, ~0.62–0.65 d, 29–71 μm L_p, 2.6 mm δ, 29–71 μm	350–400 q^*_{CHF}, 3.15–3.61 (Best, 400@22)	22–48 ΔT^*_{CHF}, 0.85–1.85 —	Water (T_{lg} ~ 40°C–70°C)	1 × 1 cm²
Cai and Chen (2010)	CNT forest (pillar and stripe) microgroove l_p, ~2–20 nm w_p, 50–180 nm L_g, 50 μm W_p, 100 μm δ, 250 μm	600 (pre-CHF) q^*, 5.41	25–45 (pre-CHF) ΔT^*, 0.96–1.73	Water (T_{lg} = 50°C–95°C)	0.2 × 0.2 cm²
Cai and Chen (2011)	CNT forest with microgroove L_g, 50 μm W_p, 100–150 μm δ, 210–300 μm	195 (on 1 × 1 cm²) 938 (on 0.2 × 0.2 cm²) q^*_{CHF}, 1.75–8.46	150 (on 1 × 1 cm²) 135 (on 0.2 × 0.2 cm²) ΔT^*_{CHF}, 5.76–5.19	Water (T_{lg} ~ 40°C–100°C)	0.2 × 0.2 and 1 × 1 cm²
Cai and Bhunia (2012)	CNT forest (pillar and stripe) microgroove l_p, ~2–20 nm w_p, 50–180 nm L_g, 50 μm W_p, 100 μm δ, 250 μm	130 (on 1 × 1 cm²) 770 (on 0.2 × 0.2 cm²) q^*_{CHF}, 1.17–6.94	29 (on 1 × 1 cm²) 38 (on 0.2 × 0.2 cm²) ΔT^*_{CHF}, 1.12–1.46	Water (1 atm)	0.2 × 0.2 and 1 × 1 cm²

(*Continued*)

TABLE 18.6 (*Continued*)
Summary of the Lateral Liquid-Artery Wick in Film Evaporation (Design F)

Authors	Wick Structure	CHF, q_{CHF} (W/cm²)	ΔT_{CHF} (°C)	Working Fluid	Heat Source Area (cm²)
Weibel and Garimella (2012)	Functionalized Cu- or CNT-coated, multilayered, sintered copper particles with lateral liquid artery ε, 0.5 d_p, 100 μm L_p, 0.5 mm δ, 1000 μm	437–558 q^*_{CHF}, 3.94–5.04 (Best, 558@36)	36–46 ΔT^*_{CHF}, 1.38–1.77 —	Water (1 atm)	0.5 × 0.5 cm²
Ćoso et al. (2012)	Biporous silicon pin fins with microgrooves l_p, 100 μm w_p, 4.9–28 μm L_g, 30–61 μm W_p, 144–288 μm Δ, 56–243 μm	73.6 (1 × 1 cm²) 733.1 (0.24 × 0.26 cm²) q^*_{CHF}, 0.66–6.62	7 (1 × 1 cm²) 18 (0.24 × 0.26 cm²) ΔT^*_{CHF}, 0.27–0.70	Water (1 atm)	0.24 × 0.26 and 1 × 1 cm²

For normalized CHF and superheat, q^*_{CHF} and ΔT^*_{CHF}, q_{CHF} = 110.8 W/cm² (Zuber 1959) and ΔT_{CHF} = 26°C (Li et al. 2006) for water at 1 atm.

was found at 733.1–938 W/cm² with the maximum superheat of 38–135 K, which shows the heater size effect (Cai and Chen 2011; Cai and Bhunia 2012). Hwang et al. (2011) also designed the lateral capillary artery with the thin (monolayer) wick as an evaporator wick (Hwang et al. 2011). This design reaches the CHF up to 580 W/cm² without the total dryout at a given superheat ΔT = 72°C. This superheat is relatively larger compared to the vertical liquid artery at given higher CHF, where it allows for the partial dryout at high heat flux. Ju et al. (2013) further studied the effects on the liquid artery and monolayer using the different number of arteries and the different particle diameters (Ju et al. 2013). Also, they tested larger heater surface area, 2 × 2 cm², to show that the lateral liquid artery with the monolayer wick design does not have significant heater size effect compared to 1 × 1 cm². Weibel and Garimella (2012) also designed the liquid-artery wick using multilayered, sintered copper particles of 100 μm in diameter and CNT-coated wicks with 0.5 mm pitch distance (Weibel and Garimella 2012). This design resulted in high CHFs, q_{CHF} = 437~558 W/cm² with the moderate superheat ΔT = 36°C~46°C. This study articulated the boiling mechanism near the corners of the liquid-artery and multilayered wick structures. Ćoso et al. (2012) fabricated the micropatterned (biporous), pin fins using silicon for the capillary evaporator (Ćoso et al. 2012). The individual pin sizes were 3.1–29 μm, having an array size of 156–288 μm with microgroove of 30–60 μm, where the individual pin fins were designed for the dominant evaporation surface and the microgrooves for the primary liquid flow channels. With 1 × 1 cm² heated area, the CHF was observed at q_{CHF} ~ 280 W/cm² with the maximum superheat of 18°C, while, in the smaller heated area, 6.25 × 10^{-2} cm², the CHF was found at 733.1 W/cm² with the maximum superheat of ~12°C, showing the heater size effect. Dai et al. employed hybrid structures using the microchannels as a main liquid supply pathway and obtained nearly similar CHF to that of the pool boiling (Dai et al. 2013c). Also, Oshman et al. and Famouri et al. implemented this hybrid wick in microscale flat heat pipes (Oshman et al. 2011; Famouri et al. 2014).

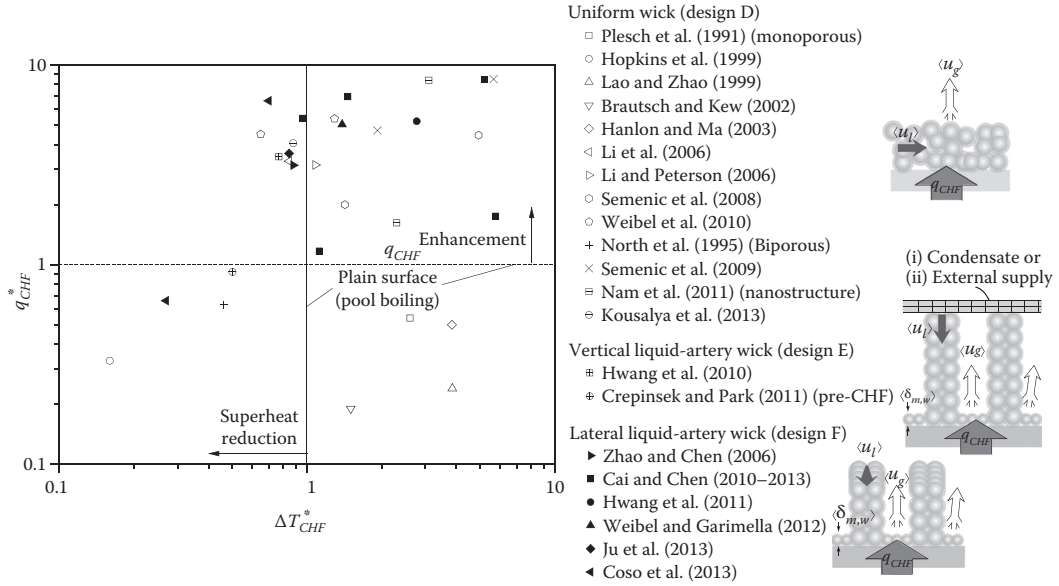

FIGURE 18.14 Enhancement of the CHF and reduction of superheat with uniform and distributed capillary wick evaporator in film evaporation (designs E and F). The specifications are listed in Tables 18.4 through 18.6.

18.3.3 Summary

Some uniform capillary wicks increase the CHF and reduce the superheat compared to that of the plain pool boiling, and this increased limit is related to the capillary–viscous limit within the wicks. The distributed (liquid artery) wicks with the thin wicks further enhance the CHF and decrease the superheat. The normalized CHF and superheat (at CHF) by those of the plain surface are summarized in Figure 18.14.

Although the performance of the uniform capillary wicks scatters, some designs enable to increase the CHF generally up to two times over the plain surface. Similar to the pool boiling, the challenge of the uniform capillary wick evaporators is limited liquid supply to the evaporator through the thin wick or large superheat from the thick wick. This challenge is overcome with the distributed (liquid artery) capillary evaporator wick; the thick wick enhances the liquid supply (increasing capillary–viscous limit), thus enhancing the CHF, while the thin wick significantly reduces the thermal resistance, resulting in the reduced superheat. Similar approach could be used for high CHF and small superheat in flow boiling, which will be discussed in the following section.

18.4 FLOW BOILING (DESIGN G)

The flow boiling heat transfer in micro-/millichannels has a similar challenge, especially under a high vapor quality, where the limited liquid supply to the evaporation sites occurs, that is, CHF (Peng and Wang 1993; Kandlikar 2001, 2004, 2010; Palm 2001). At the downstream, the vapor quality becomes large, and excessive bubbles hinder the liquid supply to the evaporator as well as reduce the effective thermal resistance near the surface. Optimal surface design should provide the good liquid supply, especially at high vapor quality, while it maintains low thermal resistance.

There are numerous studies using wick or wetting structures to enhance the CHF and reduce the superheat. Rainey et al. reported the CHF enhancement in flow boiling using porous coatings, where they found a low resistance of 0.5 K/(W/cm^2) or conductance (heat transfer coefficient) of

2 W/cm^2-K, for subcooled, low vapor quality regime (Rainey et al. 2001). The coating is a mixture of aluminum and ceramic particle with a binder, having 0.1–1 μm pores and a thickness of 50 μm. Krishnamurthy and Peles employed 100 μm circular pin fins in 250 μm height microchannels, observing a resistance of 0.133 K/(W/cm^2) or conductance of 7.5 W/cm^2-K (Krishnamurthy and Peles 2008). Qu and Siu-Ho utilized 200 μm square pin fins in 670 μm height microchannels with water and observed a maximum heat flux of 248.5 W/cm^2 at a mass flux of 417 kg/m^2-s. The largest heat transfer coefficient obtained was 0.08 K/(W/cm^2) or 12.5 W/cm^2-K at low quality. Xue et al. used 30 μm square pin fins in 60 μm high silicon microchannels and observed a CHF of ~65 W/cm^2 with FC-72 (Xue et al. 2011). Yang et al. employed superhydrophilic silicon nanowires (20 nm in diameter and 5 μm long) grown in the five parallel channels, 10 mm long, 200 mm wide, and 250 mm deep five parallel channels. This nanostructure led to an annular flow (thin film evaporation) and favorable bubble departure diameters, resulting in heat transfer enhancement. They observed a CHF up to ~450 W/cm^2 (three times compared to a plain surface) with a reduced superheat using a subcooled liquid with flow rates of 113–389 kg/m^2-s (Yang et al. 2013). Similar work was performed in the subsequent work, showing nearly three times CHF compared to the plain surface (Yang et al. 2014a,b). A relatively smaller enhancement was found using copper nanowires (~56% increase in CHF) (Morshed et al. 2012) and using Si nanowires (Li et al. 2012).

Perhaps, the performance could be further enhanced using the capillary artery wick as successfully demonstrated in the pool boiling and film evaporation. At the high vapor quality, the capillary artery wick design could further assist the liquid supply to the evaporator, which in turn results in increasing CHF.

18.5 CONCLUDING REMARKS AND OUTLOOKS

High, in particular localized, heat flux removal has been demonstrated by evaporation employing various capillary wick evaporators in the pool boiling and film evaporation. Especially, the distributed capillary arteries show a significant improvement on liquid supply and vapor removal, which in turn results in enhancing CHF. Capillary bodies actively separate the liquid and vapor phase, thus avoiding the pressure penalty associated with two-phase flow, which in turn improves liquid flow rate to the evaporator. The separated vapor would only require limited space to travel to the condenser, thus allowing for a compact, robust, passive heat exchange devices. This review is a partial survey of the designs, materials, and performance of such evaporators and shows that the very low thermal resistance as low as 0.05 K/(W/cm^2) (small surface superheat) at the very high CHF as large as 500 W/cm^2 has been achieved, using nonuniform capillary liquid-artery wicks for significant liquid supply improvement. Achieving low thermal resistance is a balance between thin porous coating where the meniscus recedes with increasing heat flux, yet having sufficient thickness to spread the liquid through the capillary pressure. The optimal wick design (generally sintered particles) requires large effective thermal conductivity as well as large capillary pressure with low liquid permeability. The 2-D structures (e.g., pin, wicks, and mesh) do allow for large effective thermal conductivity, but their capillary pressure is not as large as the spherical particles. The nanostructure also provides high capillary pressures, at the expense of the significant liquid permeability reduction, limiting the liquid supply. The spherical particles offer more versatility for a 3-D, convoluted meniscus to form over the randomly arranged spheres, where the versatility lends to favorable liquid-phase permeability, and this generally shows good performance and considers as an optimal and promising design.

The future trends would continue to design the capillary body around the heat source geometry. This also includes the optimal wick design in flow boiling where similar challenges need to be overcome, that is, limited liquid supply to the evaporator, resulting in reducing CHF in the large vapor quality region. The search for the optimal wick design, possessing large effective thermal conductivity, capillary pressure, and liquid permeability, will continue.

NOMENCLATURE

A	Area, m^2
d	Particle or wire diameter, m
g	Gravitational acceleration, m/s^2
K	Permeability, m^2
L	Length, m
l	Length or width, m
M	Molecular weight, kg/kmol
N	Number or figure of merit
p	Pressure, Pa
q	Heat flux, W/m^2
R	Universal gas constant
T	Temperature, K
w	Width, m

Greek Symbol

Δh_{lg}	Enthalpy of vaporization, J/kg
δ	Wick thickness, m
ε	Porosity
λ	Wavelength, m
μ	Dynamic viscosity, Pa-s
σ	Surface tension, N-m

Subscript

b	Bank
CHF	Critical heat flux
c	Cluster or critical
g	Gas or vapor or groove
J	Leverett coefficient, $C_J = 0.53$.
k	Thermal conduction
l	Liquid
lg	Liquid–vapor or saturation
m	Modulated
p	Pore or particle or pitch or pin or plain
RT	Rayleigh–Taylor
s	Solid
sh	Superheat
t	Tube
u	Uniform porous-layer coating
w	Water
Z	Zuber
∞	Far field

REFERENCES

Afgan, N. H., L. A. Jovic, S. A. Kovalev, and V. A. Lenykov. 1985. Boiling heat transfer from surfaces with porous layers. *International Journal of Heat and Mass Transfer* 28 (2):415–422.

Auracher, H., W. Marquardt, M. Buchholz, R. Hohl, T. Luttich, and J. Blum. 2001. New experimental results on steady-state and transient pool boiling heat transfer. *Thermal Science and Engineering* 9 (5):29–39.

Bejarano, R. and C. Park. 2014. Active flow control for cold-start performance enhancement of a pump-assisted, capillary-driven, two-phase cooling loop. *International Journal of Heat and Mass Transfer* 78:408–415.

Berenson, P. J. 1962. Experiments on pool-boiling heat transfer. *International Journal of Heat and Mass Transfer* 5 (10):985–999.

Bergles, A. E. and M. C. Chyu. 1982. Characteristics of nucleate pool boiling from porous metallic coatings. *Journal of Heat Transfer* 104 (2):279–285.

Betz, A. R., J. Jenkins, C.-J. "Cj" Kim, and D. Attinger. 2013. Boiling heat transfer on superhydrophilic, superhydrophobic, and superbiphilic surfaces. *International Journal of Heat and Mass Transfer* 57 (2):733–741.

Betz, A. R., J. Xu, H. Qiu, and D. Attinger. 2010. Do surfaces with mixed hydrophilic and hydrophobic areas enhance pool boiling? *Applied Physics Letters* 97 (14):141909–141909–3.

Brautsch, A. and P. A. Kew. 2002. Examination and visualisation of heat transfer processes during evaporation in capillary porous structures. *Applied Thermal Engineering* 22 (7):815–824.

Cai, Q. and A. Bhunia. 2012. High heat flux phase change on porous carbon nanotube structures. *International Journal of Heat and Mass Transfer* 55 (21–22):5544–5551.

Cai, Q. and C.-L. Chen. 2010. Design and test of carbon nanotube biwick structure for high-heat-flux phase change heat transfer. *Journal of Heat Transfer* 132 (5):052403.

Cai, Q. and Y.-C. Chen. 2011. Investigations of biporous wick structure dryout. *Journal of Heat Transfer* 134 (2):021503.

Carey, V. P. 2008. *Liquid-Vapor Phase-Change Phenomena*, 2nd edn. New York: Taylor & Francis Group.

Chang, J. Y. and S. M. You. 1996. Heater orientation effects on pool boiling of micro-porous-enhanced surfaces in saturated FC-72. *Journal of Heat Transfer* 118 (4):937–943.

Chang, J. Y. and S. M. You. 1997a. Boiling heat transfer phenomena from microporous and porous surfaces in saturated FC-72. *International Journal of Heat and Mass Transfer* 40 (18):4437–4447.

Chang, J. Y. and S. M. You. 1997b. Enhanced boiling heat transfer from microporous surfaces: Effects of a coating composition and method. *International Journal of Heat and Mass Transfer* 40 (18):4449–4460.

Chen, R., M.-C. Lu, V. Srinivasan, Z. Wang, H. H. Cho, and A. Majumdar. 2009. Nanowires for enhanced boiling heat transfer. *Nano Letters* 9 (2):548–553.

Chi, S. W. 1976. *Heat Pipe Theory and Practice: A Sourcebook*. New York: McGraw Hill.

Collier, J. G. and J. R. Thome. 1994. *Convective Boiling and Condensation*. Gloucestershire, England: Clarendon Press.

Corty, C. and A. S. Foust. 1955. Surface variables in nucleate boiling. *Chemical Engineering Progress Symposium Series* 51 (17):1–12.

Ćoso, D., M.-C. Lu, J.-Y. Chang, A. Majumdar, and V. Srinivasan. 2012. Enhanced heat transfer in biporous wicks in the thin liquid film evaporation and boiling regimes. *Journal of Heat Transfer* 134 (10):101501.

Crepinsek, M. and C. Park. 2011. Effect of operational conditions on cooling performance of pump-assisted capillary-driven two-phase loop. *Journal of Thermophysics and Heat Transfer* 25 (4):572–580.

Crepinsek, M. and C. Park. 2012. Experimental analysis of pump-assisted and capillary-driven dual-evaporators two-phase cooling loop. *Applied Thermal Engineering* 38 (0):133–142.

Dai, X., M. Famouri, A. I. Abdulagatov, R. Yang, Y.-C. Lee, S. M. George, and C. Li. 2013a. Capillary evaporation on micromembrane-enhanced microchannel wicks with atomic layer deposited silica. *Applied Physics Letters* 103 (15):151602–151602–5.

Dai, X., X. Huang, F. Yang, X. Li, J. Sightler, Y. Yang, and C. Li. 2013b. Enhanced nucleate boiling on horizontal hydrophobic-hydrophilic carbon nanotube coatings. *Applied Physics Letters* 102 (16):161605–161605–5.

Dai, X., F. Yang, R. Yang, Y.-C. Lee, and C. Li. 2013c. Micromembrane-enhanced capillary evaporation. *International Journal of Heat and Mass Transfer* 64 (0):1101–1108.

Faghri, A. 1995. *Heat Pipe Science and Technology*. Washington, DC: Taylor & Francis.

Famouri, M., G. Carbajal, and C. Li. 2014. Transient analysis of heat transfer and fluid flow in a polymer-based micro flat heat pipe with hybrid wicks. *International Journal of Heat and Mass Transfer* 70:545–555.

Farber, E. A. and R. L. Scorah. 1948. Heat transfer to water boiling under pressure. Paper read at *Transactions of the ASME* 70:369–384.

Feng, B., K. Weaver, and G. P. Peterson. 2012. Enhancement of critical heat flux in pool boiling using atomic layer deposition of alumina. *Applied Physics Letters* 100 (5):053120–053120–3.

Gambill, W. R. and J. H. Lienhard. 1989. An upper bound for the critical boiling heat flux. *Journal of Heat Transfer* 111 (3):815–818.

Gerasimov, Y. F., Y. F. Maidanik, G. T. Shchegolev, G. A. Filippov, L. G. Starikov, V. M. Kiseev, and Y. E. Dolgirev. 1975. Low-temperature heat pipes with separate channels for vapor and liquid. *Journal of Engineering Physics* 28 (6):683–685.

Glassman, B., S. Kuravi, J. Du, Y. Lin, G. Zhao, and L. Chow. 2004. A fluid management system for a multiple nozzle array spray cooler. *Proceedings of 37th AIAA Thermophysics Conference*, AIAA-2004–2574.

Hanlon, M. A. and H. B. Ma. 2003. Evaporation heat transfer in sintered porous media. *Journal of Heat Transfer* 125 (4):644–652.

Hetsroni, G., A. Mosyak, E. Pogrebnyak, and Z. Segal. 2005. Explosive boiling of water in parallel micro-channels. *International Journal of Multiphase Flow* 31 (4):371–392.

Honda, H. and J. J. Wei. 2004. Enhanced boiling heat transfer from electronic components by use of surface microstructures. *Experimental Thermal and Fluid Science* 28 (2):159–169.

Hopkins, R., A. Faghri, and D. Khrustalev. 1999. Flat miniature heat pipes with micro capillary grooves. *Journal of Heat Transfer* 121 (1):102–109.

Hwang, G. S., E. Fleming, B. Carne, S. Sharratt, Y. Nam, P. Dussinger, Y. S. Ju, and M. Kaviany. 2011. Multi-artery heat-pipe spreader: Lateral liquid supply. *International Journal of Heat and Mass Transfer* 54 (11–12):2334–2340.

Hwang, G. S. and M. Kaviany. 2006. Critical heat flux in thin, uniform particle coatings. *International Journal of Heat and Mass Transfer* 49 (5):844–849.

Hwang, G. S., M. Kaviany, W. G. Anderson, and J. Zuo. 2007. Modulated wick heat pipe. *International Journal of Heat and Mass Transfer* 50 (7):1420–1434.

Hwang, G. S., Y. Nam, E. Fleming, P. Dussinger, Y. S. Ju, and M. Kaviany. 2010. Multi-artery heat pipe spreader: Experiment. *International Journal of Heat and Mass Transfer* 53 (13–14):2662–2669.

Johnson, R. W. 1998. *Handbook of Fluid Dynamics*. Boca Raton, FL: Taylor & Francis Group.

Ju, Y. S., M. Kaviany, Y. Nam, S. Sharratt, G. S. Hwang, I. Catton, E. Fleming, and P. Dussinger. 2013. Planar vapor chamber with hybrid evaporator wicks for the thermal management of high-heat-flux and high-power optoelectronic devices. *International Journal of Heat and Mass Transfer* 60:163–169.

Kandlikar, S. G. 1999. *Handbook of Phase Change: Boiling and Condensation*. Boca Raton, FL: Taylor & Francis Group.

Kandlikar, S. G. 2001. A theoretical model to predict pool boiling CHF incorporating effects of contact angle and orientation. *Journal of Heat Transfer* 123 (6):1071.

Kandlikar, S. G. 2004. Heat transfer mechanisms during flow boiling in microchannels. *Journal of Heat Transfer* 126 (1):8–16.

Kandlikar, S. G. 2010. Similarities and differences between flow boiling in microchannels and pool boiling. *Heat Transfer Engineering* 31 (3):159–167.

Kaviany, M. 2002. *Principles of Heat Transfer*. New York: Wiley.

Kaviany, M. 2011. *Essentials of Heat Transfer: Principles, Materials, and Applications*. Cambridge, U.K.: Cambridge University Press.

Khrustalev, D. and A. Faghri. 1995. Heat transfer during evaporation on capillary-grooved structures of heat pipes. *Journal of Heat Transfer* 117 (3):740–747.

Kobayashi, Y., S. Ikeda, and M. Iwasa. 1996. Evaporative heat transfer at the evaporative section of a grooved heat pipe. *Journal of Thermophysics and Heat Transfer* 10 (1):83–89.

Kousalya, A. S., J. A. Weibel, S. V. Garimella, and T. S. Fisher. 2013. Metal functionalization of carbon nanotubes for enhanced sintered powder wicks. *International Journal of Heat and Mass Transfer* 59 (0):372–383.

Krishnamurthy, S. and Y. Peles. 2008. Flow boiling of water in a circular staggered micro-pin fin heat sink. *International Journal of Heat and Mass Transfer* 51 (5–6):1349–1364.

Kunkelmann, C., K. Ibrahem, N. Schweizer, S. Herbert, P. Stephan, and T. Gambaryan-Roisman. 2012. The effect of three-phase contact line speed on local evaporative heat transfer: Experimental and numerical investigations. *International Journal of Heat and Mass Transfer* 55 (7–8):1896–1904.

Lee, H. J. and S. C. Yao. 2010. System instability of evaporative micro-channels. *International Journal of Heat and Mass Transfer* 53 (9–10):1731–1739.

Li, C. and G. Peterson. 2010. Experimental study of enhanced nucleate boiling heat transfer on uniform and modulated porous structures. *Frontiers in Heat and Mass Transfer (FHMT)* 1 (2):023007.

Li, C. and G. P. Peterson. 2006. Evaporation/boiling in thin capillary wicks (II)—Effects of volumetric porosity and mesh size. *Journal of Heat Transfer* 128 (12):1320–1328.

Li, C., G. P. Peterson, and Y. Wang. 2006. Evaporation/boiling in thin capillary wicks (l)—Wick thickness effects. *Journal of Heat Transfer* 128 (12):1312–1319.

Li, C., Z. Wang, P.- I. Wang, Y. Peles, N. Koratkar, and G. P. Peterson. 2008. Nanostructured copper interfaces for enhanced boiling. *Small* 4 (8):1084–1088.

Li, D., G. S. Wu, W. Wang, Y. D. Wang, D. Liu, D. C. Zhang, Y. F. Chen, G. P. Peterson, and R. Yang. 2012. Enhancing flow boiling heat transfer in microchannels for thermal management with monolithically-integrated silicon nanowires. *Nano Letters* 12 (7):3385–3390.

Liao, Q. and T. S. Zhao. 1999. Evaporative heat transfer in a capillary structure heated by a grooved block. *Journal of Thermophysics and Heat Transfer* 13 (1):126–133.
Lienhard, J. H. 1987. *A Heat Transfer Textbook*, 2nd edn. Englewood Cliffs, NJ: Prentice-Hall.
Lienhard, J. H. and V. K. Dhir. 1973. Hydrodynamic prediction of peak pool-boiling heat fluxes from finite bodies. *Journal of Heat Transfer* 95 (2):152–158.
Lienhard, J. H., V. K. Dhir, and D. M. Riherd. 1973. Peak pool boiling heat-flux measurements on finite horizontal flat plates. *Journal of Heat Transfer* 95 (4):477–482.
Lin, L. C., R. Ponnappan, and K. Yerkes. 2006. Actively pumped two-phase loop for spray cooling. *Journal of Thermophysics and Heat Transfer* 20 (1):107–110.
Liter, S. G. and M. Kaviany. 2001. Pool-boiling CHF enhancement by modulated porous-layer coating: Theory and experiment. *International Journal of Heat and Mass Transfer* 44 (22):4287–4311.
Ma, H. B. and G. P. Peterson. 1997. Temperature variation and heat transfer in triangular grooves with an evaporating film. *Journal of Thermophysics and Heat Transfer* 11 (1):90–97.
Malyshenko, S. P. 1991. Features of heat transfer with boiling on surfaces with porous coatings. *Thermal Engineering* 38 (2):81–88.
Maroo, S. C. and J. N. Chung. 2013. A possible role of nanostructured ridges on boiling heat transfer enhancement. *Journal of Heat Transfer* 135 (4):041501.
Maydanik, Y. F. 2005. Loop heat pipes. *Applied Thermal Engineering* 25 (5–6):635–657.
Milton, R. M. 1968. Heat exchange system. US 3384154 A.
Min, D. H., G. S. Hwang, and M. Kaviany. 2009a. Multi-artery, heat-pipe spreader. *International Journal of Heat and Mass Transfer* 52 (3):629–635.
Min, D. H., G. S. Hwang, Y. Usta, O. N. Cora, M. Koc, and M. Kaviany. 2009b. 2-D and 3-D modulated porous coatings for enhanced pool boiling. *International Journal of Heat and Mass Transfer* 52 (11–12):2607–2613.
Moissis, R. and P. J. Berenson. 1963. On the hydrodynamic transitions in nucleate boiling. *Journal of Heat Transfer* 85 (3):221–226.
Mori, S. and K. Okuyama. 2009. Enhancement of the critical heat flux in saturated pool boiling using honeycomb porous media. *International Journal of Multiphase Flow* 35 (10):946–951.
Morshed, A. K. M. M., F. Yang, M. Yakut Ali, J. A. Khan, and C. Li. 2012. Enhanced flow boiling in a microchannel with integration of nanowires. *Applied Thermal Engineering* 32 (0):68–75.
Mudawar, I., D. Bharathan, K. Kelly, and S. Narumanchi. 2009. Two-phase spray cooling of hybrid vehicle electronics. *IEEE Transactions on Components and Packaging Technologies* 32 (2):501–512.
Mughal, M. P. and O. A. Plumb. 1996. An experimental study of boiling on a wicked surface. *International Journal of Heat and Mass Transfer* 39 (4):771–777.
Nakayama, W., T. Daikoku, and T. Nakajima. 1982. Effects of pore diameters and system pressure on saturated pool nucleate boiling heat transfer from porous surfaces. *Journal of Heat Transfer* 104 (2):286–291.
Nam, Y., S. Sharratt, G. Cha, and Y. Sungtaek Ju. 2011. Characterization and modeling of the heat transfer performance of nanostructured Cu micropost wicks. *Journal of Heat Transfer* 133 (10):101502.
Nishikawa, K., T. Ito, and K. Tanaka. Augmented heat transfer by nucleate boiling at prepared surfaces. *Proceedings ASME/JSME Thermal Engineering Conference* 1:387–393.
North, M. T., J. H. Rosenfeld, and R. M. Shaubach. 1995. Liquid film evaporation from bidisperse capillary wicks in heat pipe evaporators. Paper read at *Proceedings on the 9th International Heat Pipe Conference*, May 1–5, 1995, Albuquerque, NM.
Nukiyama, S. 1934. The maximum and minimum values of the heat Q transmitted from metal to boiling water under atmospheric pressure. *Journal of the Japan Society of Mechanical Engineers* 37 (206):367–374.
Nukiyama, S. 1966. The maximum and minimum values of the heat Q transmitted from metal to boiling water under atmospheric pressure. *International Journal of Heat and Mass Transfer* 9 (12):1419–1433.
O'Neill, P. S., C. F. Gottzmann, and J. W. Terbot. 1972. *Novel Heat Exchanger Increases Cascade Cycle Efficiency for Natural Gas Liquefaction*. Berlin, Germany: Springer.
Oshman, C., S. Bo, L. Chen, R. Yang, Y. C. Lee, G. P. Peterson, and V. M. Bright. 2011. The development of polymer-based flat heat pipes. *Journal of Microelectromechanical Systems* 20 (2):410–417.
Palm, B. 2001. Heat transfer in microchannels. *Microscale Thermophysical Engineering* 5 (3):155–175.
Park, C. and M. Crepinsek. 2011. Effect of operational conditions on cooling performance of pump-assisted and capillary-driven two-phase loop. *Journal of Thermophysics and Heat Transfer* 25 (4):572–580.
Park, C., A. Vallury, and J. Perez. 2006. Advanced hybrid cooling loop technology for high performance thermal management. *Proceedings of Fourth International Energy Conversion Engineering Conference*, San Diego, CA, AIAA2006-4059.

Park, C., A. Vallury, and J. Zuo. 2009. Performance evaluation of pump-assisted capillary-driven two-phase loop. *ASME Journal of Thermal Science and Engineering Applications* 1 (2):0220041–8.

Park, C., A. Vallury, J. Zuo, J. Perez, and P. Rogers. 2007. Electronics thermal management using advanced hybrid two-phase loop technology. *Proceedings of ASME-JSME Thermal Engineering Summer Heat Transfer Conference*, Vancouver, British Columbia, Canada, HT2007-321962.

Park, C., J. Zuo, and J. Perez. 2005. Advanced hybrid loop technology for high heat flux laser cooling. *Proceedings of Third International Energy Conversion Engineering Conference*, San Francisco, CA, AIAA2005-5696.

Park, S. D. and I. C. Bang. 2014. Experimental study of a universal CHF enhancement mechanism in nanofluids using hydrodynamic instability. *International Journal of Heat and Mass Transfer* 70 (0):844–850.

Park, S. D., S. W. Lee, S. Kang, I. C. Bang, J. H. Kim, H. S. Shin, D. W. Lee, and D. W. Lee. 2010. Effects of nanofluids containing graphene/graphene-oxide nanosheets on critical heat flux. *Applied Physics Letters* 97 (2):023103–023103–3.

Patil, C. M. and S. G. Kandlikar. 2013. Review of the manufacturing techniques for porous surfaces used in enhanced pool boiling. *Heat Transfer Engineering* 35 (10):887–902.

Patil, C. M. and S. G. Kandlikar. 2014. Review of the manufacturing techniques for porous surfaces used in enhanced pool boiling. *Heat Transfer Engineering* 35 (10):887–902.

Peng, X. F. and B. X. Wang. 1993. Forced convection and flow boiling heat transfer for liquid flowing through microchannels. *International Journal of Heat and Mass Transfer* 36 (14):3421–3427.

Peterson, G. P. 1994. *An Introduction to Heat Pipes: Modeling, Testing, and Applications*, Wiley Series in Thermal Management of Microelectronic and Electronic Systems. New York: Wiley.

Pioro, I. L., W. Rohsenow, and S. S. Doerffer. 2004. Nucleate pool-boiling heat transfer. I: Review of parametric effects of boiling surface. *International Journal of Heat and Mass Transfer* 47 (23):5033–5044.

Plesch, D., W. Bier, D. Seidel, and K. Schubert. 1991. Miniature heat pipes for heat removal from microelectronic circuits. *Micromechanical Sensors, Actuators, and Systems* 32:303–313.

Polezhaev, Y. V. and S. A. Kovalev. 1990. Modelling heat transfer with boiling on porous structures. *Thermal Engineering* 37 (12):617–621.

Qu, W. L. and I. Mudawar. 2005. A systematic methodology for optimal design of two-phase micro-channel heat sinks. *Journal of Electronic Packaging* 127 (4):381–390.

Rainey, K. N., S. M. You, and G. Li. 2001. Flow boiling heat transfer from plain and microporous coated surfaces in subcooled FC-72. *Journal of Heat Transfer* 123 (5):918–925.

Ranjan, R., J. Y. Murthy, and S. V. Garimella. 2011. A microscale model for thin-film evaporation in capillary wick structures. *International Journal of Heat and Mass Transfer* 54 (1):169–179.

Reay, D., R. McGlen, and P. Kew. 2013. *Heat Pipes*, 6th edn. Oxford, U.K.: Butterworth-Heinemann.

Rojas, M. E. and M. C. de Andrés. 2006. Theoretical and experimental study of two-phase flow in microchannels grooved into horizontal pipes. *International Journal of Multiphase Flow* 32 (4):517–526.

Semenic, T. and I. Catton. 2009. Experimental study of biporous wicks for high heat flux applications. *International Journal of Heat and Mass Transfer* 52 (21–22):5113–5121.

Semenic, T., Y. Y. Lin, I. Catton, and D. B. Sarraf. 2008. Use of biporous wicks to remove high heat fluxes. *Applied Thermal Engineering* 28 (4):278–283.

Silk, E. A., E. L. Golliher, and R. P. Selvam. 2008. Spray cooling heat transfer: Technology overview and assessment of future challenges for micro-gravity application. *Energy Conversion and Management* 49 (3):453–468.

Stenger, F. J. 1965. Closed fluid system without moving parts controls temperature, O. NASA Lewis Research Center, ed., Cleveland, OH.

Stephan, P. C. and C. A. Busse. 1992. Analysis of the heat transfer coefficient of grooved heat pipe evaporator walls. *International Journal of Heat and Mass Transfer* 35 (2):383–391.

Thome, J. R. 1990. *Enhanced Boiling Heat Transfer*. Washington, DC: Hemisphere Publishing Corporation.

Tong, L. S. and Y. S. Tang. 1997. *Boiling Heat Transfer and Two-Phase Flow*, Series in Chemical and Mechanical Engineering. Boca Raton, FL: Taylor & Francis Group.

Wang, H., S. V. Garimella, and J. Y. Murthy. 2007. Characteristics of an evaporating thin film in a microchannel. *International Journal of Heat and Mass Transfer* 50 (19–20):3933–3942.

Wang, J. and I. Catton. 2001. Evaporation heat transfer in thin biporous media. *Heat and Mass Transfer* 37 (2–3):275–281.

Wayner, P. C. 1994. Thermal and mechanical effects in the spreading of a liquid film due to a change in the apparent finite contact angle. *Journal of Heat Transfer* 116 (4):938–945.

Webb, R. L. 1981. The evolution of enhanced surface geometries for nucleate boiling. *Heat Transfer Engineering* 2 (3–4):46–69.

Webb, R. L. 1983. Nucleate boiling on porous coated surfaces. *Heat Transfer Engineering* 4 (3–4):71–82.

Webb, R. L. and N.-H. Kim. 1994. *Principle of Enhanced Heat Transfer*. New York: John Wiley & Sons.

Weibel, J. A. 2012. Characterization of fluid-thermal transport and boiling in micro/nano-engineered porous structures. PhD thesis, Purdue University, West Lafayette, IN.

Weibel, J. A. and S. V. Garimella. 2012. Visualization of vapor formation regimes during capillary-fed boiling in sintered-powder heat pipe wicks. *International Journal of Heat and Mass Transfer* 55 (13–14):3498–3510.

Weibel, J. A. and S. V. Garimella. 2013. Recent advances in vapor chamber transport characterization for high-heat-flux applications. In *Advances in Heat Transfer*, Y. I. C. J. P. A. Ephraim M. Sparrow and M. G. John, eds., Chapter 4. Amsterdam, the Netherlands: Elsevier.

Weibel, J. A., S. V. Garimella, and M. T. North. 2010. Characterization of evaporation and boiling from sintered powder wicks fed by capillary action. *International Journal of Heat and Mass Transfer* 53 (19):4204–4215.

Xu, X. and V. P. Carey. 1990. Film evaporation from a micro-grooved surface-An approximate heat transfer model and its comparison with experimental data. *Journal of Thermophysics and Heat Transfer* 4 (4):512–520.

Xue, Y., M. Yuan, A. Ma, and J. Wei. 2011. Enhanced boiling heat transfer by using micro-pin-finned surface in three different test systems. *Heat Transfer Engineering* 32 (11–12):1062–1068.

Yang, F., X. Dai, Y. Peles, P. Cheng, J. Khan, and C. Li. 2014a. Flow boiling phenomena in a single annular flow regime in microchannels (I): Characterization of flow boiling heat transfer. *International Journal of Heat and Mass Transfer* 68 (0):703–715.

Yang, F., X. Dai, Y. Peles, P. Cheng, J. Khan, and C. Li. 2014b. Flow boiling phenomena in a single annular flow regime in microchannels (II): Reduced pressure drop and enhanced critical heat flux. *International Journal of Heat and Mass Transfer* 68 (0):716–724.

Yang, F., X. Dai, Y. Peles, P. Cheng, and C. Li. 2013. Can multiple flow boiling regimes be reduced into a single one in microchannels? *Applied Physics Letters* 103 (4):043122–043122–5.

Zhao, J.-J., Y.-Y. Duan, X.-D. Wang, and B.-X. Wang. 2011. Effects of superheat and temperature-dependent thermophysical properties on evaporating thin liquid films in microchannels. *International Journal of Heat and Mass Transfer* 54 (5–6):1259–1267.

Zhao, Y. and C.-L. Chen. 2006. An investigation of evaporation heat transfer in sintered copper wicks with microgrooves. Paper read at *ASME International Mechanical Engineering Congress and Exposition*, November 5–10, 2006, Chicago, IL.

Zuber, N. 1959. Hydrodynamic aspects of boiling heat transfer. PhD thesis, University of California, Los Angeles, CA.

19 Impinging Jets in Porous Media

Bernardo Buonomo, Oronzio Manca, and Sergio Nardini

CONTENTS

19.1 Introduction 631
19.2 Basic Assumptions and Governing Equations 639
19.3 Physical Geometry for a Two-Dimensional Confined Slot Jet 644
19.4 Methods of Solution and Numerical Procedure 646
19.5 Comparison and Discussion of Results for Different Parameter Values 649
19.6 Conclusions 657
Nomenclature 658
References 659

19.1 INTRODUCTION

Heat transfer enhancement technologies play an important role, and they have been widely adopted, in several applications such as in refrigeration, automotive, aerospace, process industry, and solar energy heaters. The targets in terms of technical advantages and cost savings could be achieved by the employing suitable techniques. Jet impingement of a cold fluid is an efficient cooling method of a heated surface. This method is one of the techniques employed in heat transfer enhancement technologies. An intensive research activity has been developed on impinging jets as reported in the reviews given in Arganbright and Resch (1971), Martin (1977), Polat et al. (1989), Jambunathan et al. (1992), Viskanta (1993), Webb and Ma (1995), Han and Goldstein (2001), Sarkar et al. (2004), Zuckerman and Lior (2006), Ebadian and Lin (2011), Dewan et al. (2012), Harmand et al. (2013), Lindeman and Shedd (2013), and Molana and Banooni (2013).

The characteristics of jet impingement cooling through porous medium are becoming important in many engineering applications, for example, turbine blade internal cooling, electronic cooling systems, and solar collectors. Furthermore, new applications of high-permeability porous media are being developed to enhance heat transfer. This is the case of porous heat sink in electronic cooling and the use of porous inserts in injection molding. As indicated in literature, jets employed together with porous media with high porosity and thermal conductibility, such as aluminum foams, allow improvement in the heat removal from a heated surface. Moreover, it has been observed that several parameters have effects on the fluid and thermal behaviors and they should be investigated to evaluate optimal configurations in order to enhance the heat transfer. But also some fundamental studies are needed to understand and characterize the thermal and fluid dynamic behaviors of this system. The different investigations have been developed for system partially and totally filled by porous medium between the outlet section of the jet and the opposite solid surface, in Figure 19.1. The systems can be unconfined or confined as reported in Figure 19.1.

One of the first studies on impinging jets in porous medium was carried out by Fu and Huang (1997). A numerical investigation on the effects of a laminar jet on the heat transfer performance of porous blocks mounted on a heated plate was accomplished. In the study, three different shapes of porous blocks were examined, rectangle, convex, and concave, and only forced convection analysis

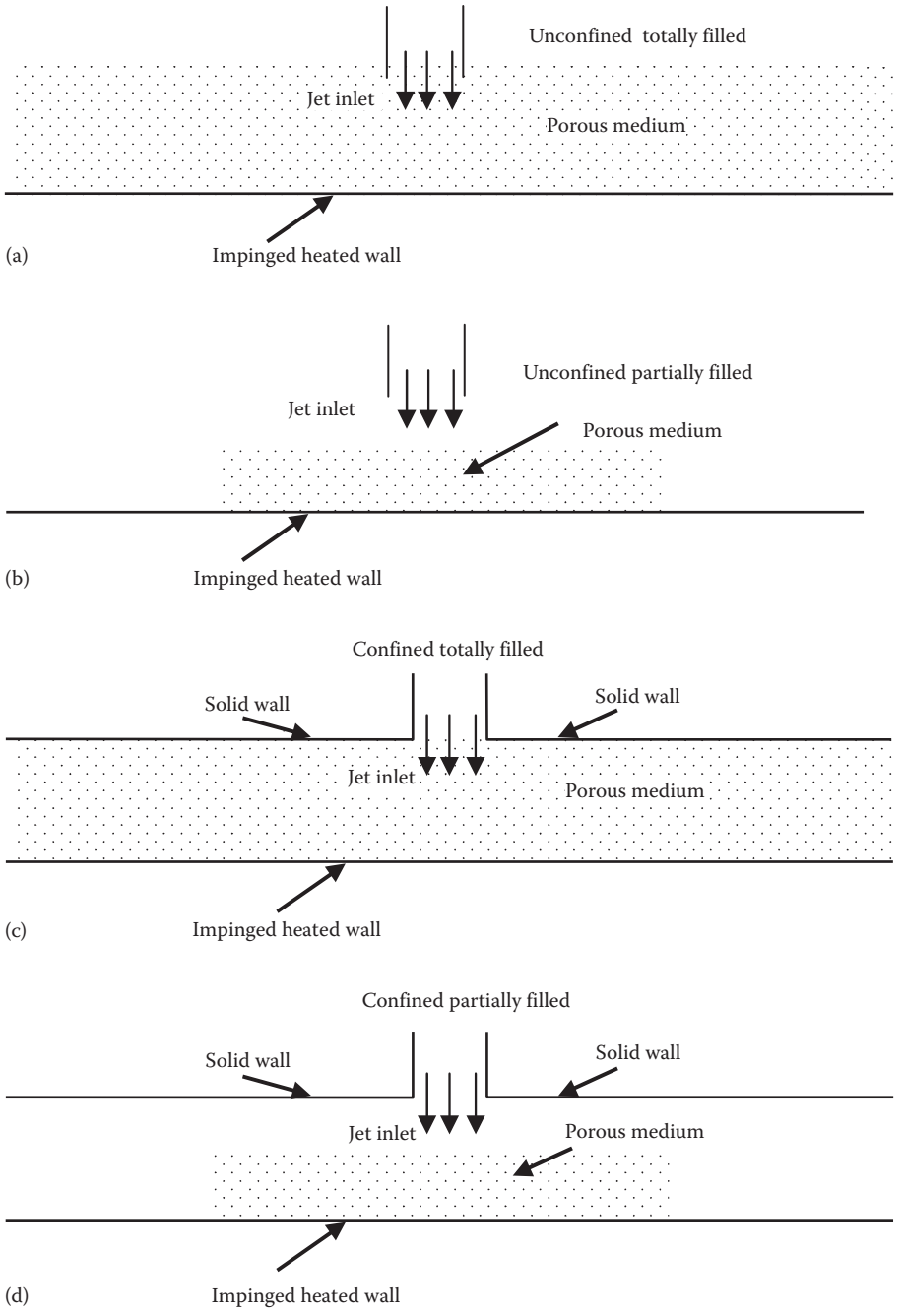

FIGURE 19.1 Sketch of impinging jet configurations.

was considered neglecting buoyancy effects. Results show that the heat transfer is mainly affected by a fluid flowing near the heated region. Moreover, for a lower porous block, the three types of porous blocks enhance the heat transfer, whereas for a higher porous block, the concave porous block only enhances heat transfer. The effects of the porosity distributed casually inside a porous block mounted on a heated region with a laminar slot impinging jet on flow and thermal fields were investigated numerically by Fu and Huang (1999). A one-equation thermal model with van Driest's wall function

was adopted and the non-Darcian effects including the solid boundary and inertial effects were considered. Three different porosity models of constant, variable, and random were examined.

Fluid dynamic behaviors of turbulent flow without heat transfer on a porous layer were investigated by means of experimental and numerical flow visualization by Prakash et al. (2001a,b). A confined round impinging jet in a partially filled system was considered. The effect of the parameters such as the jet Reynolds number, the permeability of the porous foam, the thickness of the porous foam, and the height of the overlying fluid layer were studied. A confined impinging slot jet in an aluminum-foam heat sink was studied numerically by Kim et al. (2001). The effect of anisotropy and effective thermal conductivity in the foam, with the bottom plate at uniform heat flux, was investigated. The results indicate that the anisotropy in permeability and effective thermal conductivity yields a significant change in the heat transfer rate. An experimental investigation to evaluate high potential of a porous surface for heat transfer enhancement with impinging jets is carried out by Paek et al. (2001). The study was accomplished for aluminum foam attached to an isolated heat source and it was found, at the given porosity, that the porous surface with small pores is inefficient for the heat transfer enhancement due to the large flow friction. The heat transfer enhancement is strongly dependent on the jet Reynolds number and shows the maximum value at a moderate Reynolds number. A pin-fin heat sink in a horizontal channel was modeled as an anisotropic porous medium by Kim and Kuznetsov (2003). The system was similar to a confined impinging jet partially filled by a porous medium. The bottom of the heat sink was assumed at uniform heat flux. Cool air was supplied from the top opening of the channel and exhausts to the channel outlet. The governing Navier–Stokes and energy equations using the Brinkman–Forchheimer extended Darcy model and the local thermal nonequilibrium (LTNE) porous model for the region occupied by the heat sink were employed.

Impinging slot jet in a confined porous medium with a heated solid wall was numerically studied by Jeng and Tzeng (2005) in the forced convection mode. The bottom solid surface was isothermal and the upper one was assumed adiabatic and the fluid was air. Their results show that the aluminum-foam heat sink could enhance the heat transfer from the heated horizontal source by impinging cooling. Moreover, the heat transfer performance of impinging cooling with the aluminum-foam heat sink is two to three times larger than that without it. A numerical investigation on impinging confined slot jet in a fluid saturated porous media in the mixed convection regime was carried out by Saeid and Mohamad (2006). The horizontal bottom surface presented the heated portion at uniform temperature. They limited the investigation at Darcy model in local thermal equilibrium (LTE). Results showed, for high values of Péclet number that increasing either Rayleigh number or jet width lead to increase in the average Nusselt number. Decreasing the distance between the jet and the heated solid surface could increase the average Nusselt number. An experimental investigation on the heat transfer characteristics of aluminum-foam heat sinks with restricted flow outlets under round impinging jet flow conditions was accomplished by Shih et al. (2007). The effects of porosity, pore density and length of sample, air velocity, and flow outlet height on the heat transfer characteristics of aluminum-foam heat sinks were investigated. It was found that the effect of the flow outlet height is stronger than that of the pore density, porosity, or height of the aluminum heat sinks. The jet impingement cooling of heated portion, at assigned temperature, of a horizontal surface immersed in a porous layer with the presence of a crossflow was studied numerically by Saeid (2007). The analysis was carried out for a confined slot jet at steady, 2D laminar flow based on Darcy model and two-energy equation for fluid and solid phases (LTNE assumption). The heated portion of the bottom surface was at uniform temperature. The results were presented to show the effect of crossflow and the thermal nonequilibrium parameters. Moreover, it was shown that the average Nusselt number calculated from the thermal equilibrium model are the maximum possible values.

The convective heat transfer and pressure drop in the metallic porous block with a confined slot air jet was investigated experimentally by Jeng and Tzeng (2007). The results indicated that Nusselt number with the aluminum-foam block was three to five times larger than that without it, qualitatively, in agreement with their numerical results given by Jeng and Tzeng (2005). The same authors performed a numerical investigation on the heat transfer of a sintered porous block under a

confined slot air jet impinging on a partially heated surface at uniform heat flux (Jeng and Tzeng, 2008). A 2D laminar and steady flow with the Brinkman–Forchheimer–extended Darcy model and LTNE assumption was considered. Results indicated that the cooling performance with the sintered porous block was better than that with an aluminum-foam block and was at least 5.8 times as large as that without it. Laminar impinging slot jets on surfaces covered with a layer of a porous material were studied numerically by Graminho and De Lemos (2008). The analysis was carried out for a 2D laminar and steady flow with the Brinkman–Forchheimer–extended Darcy model. Results for clear and porous domains showed that the influence of porosity on the flow pattern was very low in comparison to the effects caused by varying permeability, fluid-layer height, and porous layer thickness. Non-Darcian effects on the mixed convection heat transfer in a metallic porous block with a confined slot jet were numerically studied by Marafie et al. (2008). The analysis was accomplished in 2D laminar steady state, and the Forchheimer–Brinkman–extended Darcy model was used in representing the fluid motion inside the porous layer in LTE condition. The heated part of the impinging surface is assumed at uniform temperature. The governing equations were solved using the finite element formulation based on the Galerkin method of weighted residuals. Results revealed that the heat transfer performance of the slot jet was 2.4 times as large as that without the presence of a porous block. In addition, the average Nusselt number was found to increase with a decrease in porosity and an increase in the thermal conductivity ratio. A numerical investigation on confined slot jets impinging against a heated surface covered with a layer of a porous material was accomplished by De Lemos and Fischer (2008). The bottom heated flat plate was at uniform temperature and the analysis was carried out for a 2D laminar and steady flow with the Brinkman–Forchheimer–extended Darcy model in LTE. Results showed that the presence of a porous layer decreases the peak in Nu avoiding excessive heating or cooling at the stagnation point. Moreover, the average wall heat flux is enhanced for certain range of values of layer thickness, porosity, and thermal conductivity ratio.

A turbulent impinging round jet into a cylindrical enclosure with and without a porous layer at the bottom was studied numerically by Graminho and de Lemos (2009). Turbulence was treated with a macroscopic $k - \varepsilon$ model and the same set of equations for both the fluid layer and the porous matrix was employed. Results denoted that the flow pattern depended on the permeability of the porous layer and the height of the fluid layer. A numerical investigation on the fluid flow and heat transfer of an air-cooled metal foam heat exchanger under a laminar slot jet confined by two parallel walls was presented by Ejlali et al. (2009). The effects of LTNE, thermal dispersion, porosity, and pore density on the heat transfer augmentation were analyzed for different Reynolds numbers. Results indicate that the heat removal rate can be greatly improved at almost no excess cost.

A numerical study on the non-Darcian effects for the jet impingement cooling of a heated surface immersed in a confined porous channel was investigated by Wong and Saeid (2009a). The bottom wall was partially heated at uniform temperature. The governing equations for steady-state mixed convection with Brinkman–Forchheimer–extended Darcy model in LTE assumption were solved. Results showed that a minimum average Nusselt number was found in the mixed convection regime. A numerical investigation of jet impingement cooling of a heated surface immersed in a confined porous channel was performed by Wong and Saeid (2009b) under mixed convection conditions with Brinkman–extended Darcy model in LTE assumption. In the analysis, the heated part of the bottom impinging surface was at uniform temperature and the Darcian and non-Darcian effects were evaluated. The results were presented in the mixed convection regime with wide ranges of Rayleigh number, Péclet number jet width, and Darcy number in Darcy regime and non-Darcy regime. It was shown that mixed convection mode can cause minimum Nu unfavorably due to counteraction of jet flow against buoyancy-driven flow. It was observed that minimum Nusselt number occurs more at higher Rayleigh number. They underlined that, as a consequence, mixed convection conditions should be carefully considered when designing a system of jet impingement cooling through porous medium. A numerical study on the opposing mixed convection arises from jet impingement cooling of a heated bottom surface, at uniform temperature, of an open cavity in a horizontal channel filled

with porous medium was carried out by Wong and Saeid (2009c). Two-dimensional laminar steady-state flow with Brinkman–extended Darcy model with Boussinesq approximation and LTNE was considered. The opposing mixed convection caused a deterioration in average Nusselt number for fluid at certain Péclet number. The average Nusselt number for fluid was found to increase with the increase in Rayleigh number, but the effect of Rayleigh number becomes insignificant at Péclet number higher than 500. Mixed convection arises from jet impingement cooling of a partially heated surface, at uniform temperature, immersed in a confined porous channel under LTNE conditions was numerically performed by Wong and Saeid (2009d). The same assumptions given by Wong and Saeid (2009c) were employed in the mathematical model. The results presented as average Nusselt numbers against Péclet number allowed to determine that minimum Nusselt numbers were found at some values of Péclet number in the mixed convection regime. Moreover, the total average Nusselt number could be enhanced by increasing the value of porosity. Wong and Saeid (2009e) extended their work given by Wong and Saeid (2009c) to mixed convection–conduction problem of impingement cooling of a finite thickness solid wall conjugated with a porous medium. The cavity was filled with a solid material and the bottom surface in the open cavity was at uniform temperature. The same assumptions given by Wong and Saeid (2009c,d) were used to provide the governing equations. Results demonstrated that opposing mixed convection occurs except for low solid wall thermal conductivity and the increase in thickness of the solid wall decreases the average Nusselt numbers.

Flow visualization and numerical simulations of a slot jet in a horizontal channel partially filled with FeCrAlY foam were studied by Wong et al. (2009). The heated part of the bottom wall was at uniform temperature and the investigation allowed to observe the flow structure under buoyancy effect. The governing equations in the porous medium for steady-state mixed convection with Brinkman–Forchheimer–extended Darcy model in LTE assumption were considered. The flow patterns obtained from simulations were similar to the experimental results. Buoyancy-driven roll was detected near the edge of the metal foam, and jet-driven roll was observed above the metal foam. Numerical study of a confined slot jet impingement cooling of a fluid-superposed porous medium heated from below at uniform temperature was performed by Wong and Saeid (2009f) to investigate the oscillatory mixed convection. The governing equations for mixed convection were considered for 2D steady and transient regimes and in the porous medium the Brinkman–Forchheimer–extended Darcy model in LTE were assumed. The results showed that the average Nusselt number increases with the increase in Darcy number or Rayleigh number. It was demonstrated that as the Darcy number decreases, the fluid is pushed to flow in the overlying fluid layer above the porous medium. It was found that for some combination of Rayleigh numbers and Péclet numbers, the oscillatory convection occurs. The oscillation of average Nusselt number was also investigated for different porous medium height and porous medium-to-fluid heat capacity ratio. An experimental investigation to explore the convective heat transfer enhancement in an impinging unconfined air round jet on a layers of graphitic foam to a heated metal substrate was presented by Sultan et al. (2009). The effects of foam protrusion, foam thickness, and foam properties were considered. The results showed that surfaces with a layer of foam protruding upward with open edges had the highest convective enhancement over that of the bare substrate under the same conditions. The highest enhancements were observed for foam specimens with the most open, interconnected void structure.

The fluid flow and heat transfer characteristics of the vertical oncoming airflow onto the brass-beads packed bed was experimentally investigated by Jeng et al. (2010). The brass-beads packed bed was fully filled in a rectangular horizontal channel. The permeability of the brass-beads packed bed drops was compared with high-porosity aluminum foam (>0.9). Some correlations of experimental results were presented. An experimental investigation on jet impingement heat transfer on a target plate covered with a thick porous layer with or without a cylindrical center cavity was accomplished by Wu et al. (2010). Experimental results showed that the attachment of the porous layer with a center cavity can either hamper or effectively enhance the jet impingement heat transfer

over a flat plate. It was detected that the addition of the thick porous layer without a center cavity gave rise to severe adverse effect on jet impingement heat transfer. An experimental study on heat transfer and pressure loss characteristics of a high aspect ratio duct, which are measured under both jet impingement and channel flow conditions, respectively, was carried out by Rallabandi et al. (2010). The results showed that the porous foam presents a more significant increase in heat transfer coefficient for both channel flow and impingement cases. Moreover, the pressure loss for porous foam in the channel flow configuration was much larger than corresponding ribbed cases. However, the porous foam under jet impingement cooling did not incur a higher pressure loss compared to axial ribs.

Sivasamy et al. (2010a,b) accomplished a numerical investigation of jet impingement cooling of a constant heat flux horizontal surface immersed in a confined porous channel under mixed convection conditions. Unsteady stream function–vorticity formulation to solve the governing equations and LTE was assumed to employ one-energy equation. Results showed that for high values of Péclet number, increasing either the Rayleigh number or jet width increases the average Nusselt number. Narrowing the distance between the jet and the heated portion could increase the average Nusselt number. Moreover, Sivasamy et al. (2010b) show that average Nusselt number decreases with the increase in *Da* for the non-Darcy regime when Reynolds number, *Re*, is low ($Re < 23$). For high *Re* values, the average Nusselt number increases with the increase in *Da* for the non-Darcy regime. Variation of *Da* in Darcy regime has negligible effect on the heat transfer performance.

Fisher and De Lemos (2010) extended to the turbulent flows the numerical investigation given by De Lemos and Fischer (2008). Results delineated that inclusion of a porous layer decreases the peak in Nu avoiding excessive heating or cooling at the stagnation point. Moreover, the integral heat flux from the wall is enhanced for certain ranges of values of porosity, layer thickness, and thermal conductivity ratio. Yakkatelli et al. (2010) presented an experimental investigation on unconfined single impinging round jet on a foamed aluminum heat sink. The effects of permeability of the porous medium, jet-to-surface spacing, and Reynolds number on flow structures were examined. A numerical investigation on 2D slot jet impingement cooling of an isothermal horizontal surface immersed in an unconfined porous medium to gain insight into thermal characteristics under mixed convection conditions with the limitation of the Darcy model was accomplished by Sivasamy et al. (2011). The governing equations were obtained assuming the Boussinesq approximation and the LTE. The results were provided in the mixed convection regime with wide ranges of the governing parameters: Péclet number, Rayleigh number, half jet width, and the distance between the jet and the heated surface.

A numerical simulation of an impinging jet on a flat plate at uniform temperature covered with a layer of a porous material was performed by Dórea and de Lemos (2010). Two macroscopic models were employed for analyzing energy transport based on the LTE and the LTNE assumptions. Parameters such as porosity, porous layer thickness, material permeability, and thermal conductivity ratio were varied to analyze their effects on fluid and thermal behaviors. Results indicate that for low porosities, low permeabilities, thin porous layers, and high thermal conductivity ratios, a different distribution of local Nusselt number at the wall was detected depending on the energy model applied. The use of the LNTE model indicates that it is advantageous to use a layer of highly conducting and highly porous material attached to the hot wall. Numerical results for a turbulent confined slot jet impinging against a flat plane covered with a layer of permeable and thermally conducting material was presented by De Lemos and Dórea (2011). They extended the model given by Dórea and de Lemos (2010) to turbulent flows. Results indicated that inclusion of a porous layer eliminates the peak in Nu at the stagnation region. Further, an enhancement in heat transfer is noted for highly porous and highly permeable material.

The enhancement of impingement heat transfer on a flat plate covered with a thick layer of porous medium with or without a center hole was numerically investigated by Wu et al. (2011).

The renormalization group $k - \varepsilon$ turbulence model was selected for the fluid region, while Forchheimer extended Darcy's model was used for porous region. The results showed that an attached porous medium with a center hole can enhance jet impingement heat transfer, while an attached thick porous layer without a center hole has detrimental effect.

Jeng et al. (2012) numerically investigated the thermal characteristics of the aluminum-foam block under the confined impinging confined air jet flow with straightening or nonstraightening jet flow models. In the porous zone, the momentum equations were formulated by the Darcy–Brinkman–Forchheimer model and the LTNE assumption was adopted for the energy equation. Different velocity profiles were detected mainly in nonstraightening case. The analysis in terms of two porosity values, different geometrical ratios, and Reynolds numbers allowed to have several indications on heat transfer results. Correlations of geometrical optimal conditions having the maximum Nu and the corresponding parametric ranges were provided. A numerical investigation on a single slot jet impinging in a porous parallel-plate channel containing an air-saturated high-permeability porous medium was accomplished by Buonomo et al. (2012). The opposite wall to the slot jet is partially heated at uniform heat flux and the buoyancy effect was taken into account. The governing equations were formulated in 2D, laminar, and steady-state conditions, and the Brinkman–Forchheimer–extended Darcy model in LTNE hypothesis was adopted. Results demonstrated that for high Biot numbers (1000), the diffusion has significant effect at high Péclet numbers (1000), whereas for lower Péclet numbers ($\leq$10), temperature differences, between solid and fluid phases, were negligible. This suggests that the LTE can be employed in these cases. The presence of porous medium allowed to have a more significant heat transfer close to the end of the heated part of the plate. The fluid flow and heat transfer characteristics of a confined laminar impinging slot jet on a plate covered with porous layer were studied by Zhang and Zou (2012). The channel was partially filled with the porous medium. The governing equations in the porous medium were formulated adopting the Darcy–Brinkman–Forchheimer model and LTNE assumption. The effects of Reynolds number, porosity, Darcy number, thermal conductivity ratio, Biot number, and porous layer thickness on the flow pattern and local heat transfer performance were investigated. Results showed that the Reynolds number and porosity do not have a strong effect on the flow pattern of porous channel. Heat transfer is significantly influenced by the parameters considered. A thermal analysis on a FeCrAlY foam subjected to jet impingement cooling in a horizontal channel was carried out by Wong (2012) both experimentally and numerically. The heated part of the bottom wall was at uniform temperature. The temperature contours of the metal foam obtained numerically were similar to the thermographic images. A 3D steady-state numerical model of fluid flow and heat transfer characteristics in the metallic porous block subjected to a confined turbulent slot jet was presented by Hwang and Yang (2012). The governing equations in the porous medium were formulated adopting the Darcy–Brinkman–Forchheimer model and LTE assumption. Results showed that the flow field can be adjusted and the thickness of the boundary layer can be decreased by the inserted porous block and, consequently, the heat transfer can be enhanced in the channel. An experimental work by Jeng et al. (2013) investigated the heat transfer of a rotating porous cylinder under an impinging round air jet at the confined/unconfined conditions. Several parameters were considered in the investigation including the rotational Reynolds number, the jet Reynolds number, and the relative impinging height. The experiments were carried out for two porosity values (0.90 and 0.93). Results indicated that the fluid flow and heat transfer have different behaviors, and several conclusions were provided in terms of different flow conditions and geometrical parameters. Moreover, an empirical correlation for average Nusselt number was proposed for the applications of the confined/unconfined systems at the pure rotating, pure jet flow, and combined conditions.

The main contributions on the impinging jet in a porous medium are summarized in Table 19.1 with some information on jet geometry, thermal conditions on target plate, flow regime, LTE, and LTNE.

TABLE 19.1
Studies on Impinging Jet in Porous Media with Some Information on Jet Geometry, Thermal Conditions on Target Plate, Flow Regime, Local Thermal Equilibrium (LTE), and Local Thermal Nonequilibrium (LTNE)

Reference	Slot Jet (SJ) / Round Jet (RJ)	Unconfined Jet (UCJ) / Confined Jet (CJ)	Partially Filled (PF) / Totally Filled (TF)	Wall Temperature (WT) / Wall Heat Flux (WHF)	Steady (s) / Transient (t)	Experimental (E) / Numerical (N)	LTE / LTNE
Fu and Huang (1997)	SJ	UCJ	PF	WT	s	N	LTE
Fu and Huang (1999)	SJ	UCJ	PF	WT	s	N	LTE
Prakash et al. (2001a)	RJ	CJ	PF	—	s	E and N	—
Prakash et al. (2001b)	RJ	CJ	PF	—	s	E and N	—
Kim et al. (2001)	SJ	CJ	PF	WHT	s	N	LTE
Paek et al. (2001)	RJ	CJ	PF		s	E	—
Kim and Kuznetsov (2003)	SJ	CJ	PF	WHT	s	N	LTNE
Jeng and Tzeng (2005)	SJ	CJ	TF	WT	s	N	LTNE
Saeid and Mohamad (2006)	SJ	CJ	TF	WT	s	N	LTE
Shih et al. (2007)	RJ	CJ	TF	WT	s	E	—
Saeid (2007)	SJ	CJ	TF	WT	s	N	LTNE
Jeng and Tzeng (2007)	SJ	CJ	PF	WHT	s	E	—
Jeng and Tzeng (2008)	SJ	CJ	PF	WHT	s	N	LTNE
Graminho and De Lemos (2008)	SJ	CJ	PF	—	s	N	—
Marafie et al. (2008)	SJ	CJ	PF	WT	s	N	LTE
de Lemos and Fischer (2008)	SJ	CJ	PF	WT	s	N	LTE
Graminho and De Lemos (2009)	RJ	CJ	PF	—	s	N	—
Ejlali et al. (2009)	SJ	CJ	PF	WHT	s	N	LTNE
Wong and Saeid (2009a)	SJ	CJ	TF	WT	s	N	LTE
Wong and Saeid (2009b)	SJ	CJ	TF	WT	s	N	LTE
Wong and Saeid (2009c)	SJ	CJ	TF	WT	s	N	LTNE
Wong and Saeid (2009d)	SJ	CJ	TF	WT	s	N	LTNE
Wong and Saeid (2009e)	SJ	CJ	TF	WT	s	N	LTNE
Wong et al. (2009)	SJ	CJ	PF	WT	s	E and N	LTE
Wong and Saeid (2009f)	SJ	CJ	PF	WT	s and t	N	LTE
Sultan et al. (2009)	RJ	UCJ	PF	WT	s	E	—
Jeng et al. (2010)	SJ	CJ	TF	WT	s	E	—
Wu et al. (2010)	RJ	CJ	PF	WT	s	E	—

(*Continued*)

TABLE 19.1 (*Continued*)
Studies on Impinging Jet in Porous Media with Some Information on Jet Geometry, Thermal Conditions on Target Plate, Flow Regime, Local Thermal Equilibrium (LTE), and Local Thermal Nonequilibrium (LTNE)

Reference	Slot Jet (SJ) Round Jet (RJ)	Unconfined Jet (UCJ) Confined Jet (CJ)	Partially Filled (PF) Totally Filled (TF)	Wall Temperature (WT) Wall Heat Flux (WHF)	Steady (s) Transient (t)	Experimental (E) Numerical (N)	LTE LTNE
Rallabandi et al. (2010)	RJ	CJ	PF	WHF	s	E	—
Sivasamy et al. (2010a)	SJ	CJ	TF	WHF	s	N	LTE
Sivasamy et al. (2010b)	SJ	CJ	TF	WHF	t	N	LTE
Fischer and de Lemos (2010)	SJ	CJ	PF	WT	s	N	LTE
Yakkatelli et al. (2010)	RJ	UCJ	PF	—	s	E	—
Dórea and de Lemos (2010)	SJ	CJ	PF	WT	s	N	LTNE
Sivasamy et al. (2011)	SJ	UCJ	PF	WT	s	N	LTE
de Lemos and Dórea (2011)	SJ	CJ	PF	WT	s	N	LTNE
Wu et al. (2011)	RJ	UCJ	PF	WHF	s	N	LTE
Jeng et al. (2012)	SJ	CJ	PF	WHF	s	N	LTNE
Buonomo et al. (2012)	SJ	CJ	TF	WHF	s	N	LTNE
Zhang and Zou (2012)	SJ	CJ	PF	WT	s	N	LTNE
Wong (2012)	SJ	CJ	PF	WT	s	E and N	LTE
Hwang and Yang (2012)	SJ	CJ	PF	WHF	s	N	LTE
Jeng et al. (2013)	RJ	CJ and UCJ	PF	WT	s	E	—

19.2 BASIC ASSUMPTIONS AND GOVERNING EQUATIONS

The macroscopic governing equations for the transport of momentum and energy in porous media are obtained applying the volume averaging process at the microscopic flow equations as indicated by Nield and Bejan (2006). In the volume averaging process, a representative elementary volume (REV) V occupied by fluid and porous matrix is considered. In Figure 19.2, an elementary volume is shown.

The generic scalar or vector quantity ψ_k in the phase k (solid or fluid) is associated with the following average values, as proposed by Whitaker (1999):

- Total volume average

$$\langle \psi_k \rangle = \frac{1}{V}\int_V \psi_k dV \tag{19.1}$$

- Intrinsic volume average

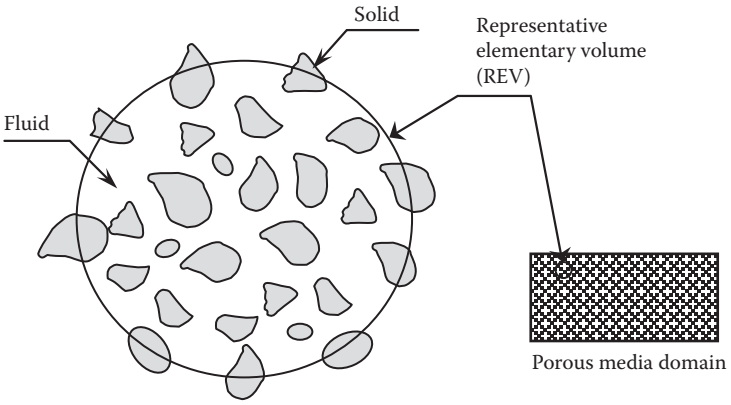

FIGURE 19.2 The REV.

Table 19.1 shows studies on impinging jet in porous media with some information on jet geometry, thermal conditions on target plate, flow regime, LTE, and LTNE:

$$\left\langle \psi_k \right\rangle^k = \frac{1}{V_k}\int_{V_k} \psi_k dV \tag{19.2}$$

The total volume average and intrinsic volume average are related by the following equation:

$$\left\langle \psi_k \right\rangle = \varphi \left\langle \psi_k \right\rangle^k \tag{19.3}$$

where $\varphi = V_k/V$ is the volume fraction or porosity of the k-phase.

The following assumptions are considered:

- Transient flow.
- Laminar and incompressible flow.
- Uniform properties and porosity of porous media.
- The Darcy–Forchheimer for drag model.
- The effect of buoyancy is taken into account.
- The LTNE model for two phases.
- The viscous dissipation and the work done by the pressure forces are neglected.

Under these hypotheses, the volume-averaged equations of continuity, momentum, and energy for fluid and solid phase (Amiri and Vafai, 1994; Whitaker, 1999) are as follows:

- Continuity equation

$$\nabla \cdot \left\langle \mathbf{u}_f \right\rangle = 0 \tag{19.4}$$

- Momentum equation

$$\rho_f \left(\frac{1}{\varphi}\frac{\partial \left\langle \mathbf{u}_f \right\rangle}{\partial t} + \frac{1}{\varphi^2}\left\langle \mathbf{u}_f \right\rangle \cdot \nabla \left\langle \mathbf{u}_f \right\rangle \right) = -\nabla \left\langle p \right\rangle^f + \rho_f \, \mathbf{g} + \frac{\mu_f}{\varphi}\nabla^2 \left\langle \mathbf{u}_f \right\rangle +$$

$$-\frac{\mu}{K}\left\langle \mathbf{u}_f \right\rangle - \frac{C_F}{K^{1/2}}\rho_f \left|\left\langle \mathbf{u}_f \right\rangle\right| \left\langle \mathbf{u}_f \right\rangle \tag{19.5}$$

- Energy equation for the fluid phase

$$\varphi\rho_f c_{p,f}\frac{\partial\langle T_f\rangle^f}{\partial t}+\rho_f c_{p,f}\langle\mathbf{u}_f\rangle\cdot\nabla\langle T_f\rangle^f=\varphi k_f\nabla^2\langle T_f\rangle^f+h_{sf}a_{sf}\left(\langle T_s\rangle^s-\langle T_f\rangle^f\right) \tag{19.6}$$

- Energy equation for the solid phase

$$(1-\varphi)\rho_s c\frac{\partial\langle T_s\rangle^s}{\partial t}=(1-\varphi)k_s\nabla^2\langle T_s\rangle^s-h_{sf}a_{sf}\left(\langle T_s\rangle^s-\langle T_f\rangle^s\right) \tag{19.7}$$

where K and C_F are the permeability and inertia coefficients, respectively. In the energy equations, the thermal dispersion and thermal tortuosity are not taken into account. The presence of the last term in both energy equations is due to the LTNE assumption, which accounts for the convective heat exchange between fluid and solid phases.

A single-energy equation can be derived for the thermal equilibrium assumption, $\langle T_f\rangle^f=\langle T_s\rangle^s=\langle T\rangle$, by adding Equations (19.6 and 19.7). It is obtained

$$(\rho c)_m\left(\frac{\partial\langle T\rangle}{\partial t}+\langle\mathbf{u}_f\rangle\cdot\nabla\langle T\rangle\right)=k_m\nabla^2\langle T\rangle \tag{19.8}$$

where

$$(\rho c)_m=(1-\varphi)\rho_s c_s+\varphi\rho_f c_{p,f} \tag{19.9a}$$

$$k_m=(1-\varphi)k_s+\varphi k_f \tag{19.9b}$$

are, respectively, the heat capacity per unit volume and effective thermal conductivity of the porous medium.

In the following, the volume average symbol < > is dropped for convenience.

The governing equations for 2D impinging slot jet are presented, in Cartesian coordinates, as follows:

- Continuity equation

$$\frac{\partial u}{\partial x}+\frac{\partial v}{\partial y}=0 \tag{19.10}$$

- x-momentum equation

$$\rho_f\left(\frac{1}{\varphi}\frac{\partial u}{\partial t}+\frac{u}{\varphi^2}\frac{\partial u}{\partial x}+\frac{v}{\varphi^2}\frac{\partial u}{\partial y}\right)=-\frac{\partial p}{\partial x}+\frac{\mu_f}{\varphi}\left(\frac{\partial^2 u}{\partial x^2}+\frac{\partial^2 u}{\partial y^2}\right)-\frac{\mu u}{K}$$
$$-\frac{C_F}{K^{1/2}}\rho_f\sqrt{u^2+v^2}\,u+\rho_f\, g\,\beta_f\left(T_f-T_\infty\right) \tag{19.11}$$

- y-momentum equation

$$\rho_f\left(\frac{1}{\varphi}\frac{\partial v}{\partial t}+\frac{u}{\varphi^2}\frac{\partial v}{\partial x}+\frac{v}{\varphi^2}\frac{\partial v}{\partial y}\right)=-\frac{\partial p}{\partial y}+\frac{\mu_f}{\varphi}\left(\frac{\partial^2 v}{\partial x^2}+\frac{\partial^2 v}{\partial y^2}\right)-\frac{\mu}{K}v-\frac{C_F}{K^{1/2}}\rho_f\sqrt{u^2+v^2}\,v \tag{19.12}$$

- Energy equation for fluid phase

$$\varphi\rho_f c_{p,f}\frac{\partial T_f}{\partial t}+\rho_f c_{p,f}\left(u\frac{\partial T_f}{\partial x}+v\frac{\partial T_f}{\partial y}\right)=\varphi k_f\left(\frac{\partial^2 T_f}{\partial x^2}+\frac{\partial^2 T_f}{\partial y^2}\right)+h_{sf}a_{sf}\left(T_s-T_f\right) \quad (19.13)$$

- Energy equation for solid phase

$$\left(1-\varphi\right)\rho_s c\frac{\partial T_s}{\partial t}=\left(1-\varphi\right)k_s\left(\frac{\partial^2 T_s}{\partial x^2}+\frac{\partial^2 T_s}{\partial y^2}\right)-h_{sf}a_{sf}\left(T_s-T_f\right) \quad (19.14)$$

where u and v are the velocity components in (x, y) Cartesian coordinates.

The governing equations for symmetric impinging jet are presented, in cylindrical coordinates, as follows:

- Continuity equation

$$\frac{\partial u}{\partial x}+\frac{1}{r}\frac{\partial v}{\partial r}=0 \quad (19.15)$$

- x-momentum equation

$$\rho_f\left(\frac{1}{\varphi}\frac{\partial u}{\partial t}+\frac{u}{\varphi^2}\frac{\partial u}{\partial x}+\frac{v}{\varphi^2}\frac{\partial u}{\partial r}\right)=-\frac{\partial p}{\partial x}+\frac{\mu_f}{\varphi}\left(\frac{\partial^2 u}{\partial x^2}+\frac{1}{r}\frac{\partial}{\partial r}\left(r\frac{\partial u}{\partial r}\right)\right)-\frac{\mu u}{K}$$
$$-\frac{C_F}{K^{1/2}}\rho_f\sqrt{u^2+v^2}u+\rho_f\, g\,\beta_f\left(T_f-T_\infty\right) \quad (19.16)$$

- r-momentum equation

$$\rho_f\left(\frac{1}{\varphi}\frac{\partial v}{\partial t}+\frac{u}{\varphi^2}\frac{\partial v}{\partial x}+\frac{v}{\varphi^2}\frac{\partial v}{\partial r}\right)=-\frac{\partial p}{\partial r}+\frac{\mu_f}{\varphi}\left(\frac{\partial^2 v}{\partial x^2}+\frac{1}{r}\frac{\partial}{\partial r}\left(r\frac{\partial v}{\partial r}\right)-\frac{v}{r^2}\right)-\frac{\mu}{K}v$$
$$-\frac{C_F}{K^{1/2}}\rho_f\sqrt{u^2+v^2}v \quad (19.17)$$

- Energy equation for fluid phase

$$\varphi\rho_f c_{p,f}\frac{\partial T_f}{\partial t}+\rho_f c_{p,f}\left(u\frac{\partial T_f}{\partial x}+v\frac{\partial T_f}{\partial r}\right)=\varphi k_f\left(\frac{\partial^2 T_f}{\partial x^2}+\frac{1}{r}\frac{\partial}{\partial r}\left(r\frac{\partial T_f}{\partial r}\right)\right)+h_{sf}a_{sf}\left(T_s-T_f\right) \quad (19.18)$$

- Energy equation for solid phase

$$\left(1-\varphi\right)\rho_s c\frac{\partial T_s}{\partial t}=\left(1-\varphi\right)k_s\left(\frac{\partial^2 T_s}{\partial x^2}+\frac{1}{r}\frac{\partial}{\partial r}\left(r\frac{\partial T_s}{\partial r}\right)\right)-h_{sf}a_{sf}\left(T_s-T_f\right) \quad (19.19)$$

where u and v are the velocity components in (x, r) cylindrical coordinates.

The continuity Equation 19.4 and momentum Equations 19.5 and 19.6 for 2D incompressible flow in the porous medium are written in terms of *primitive* variables, that is, in terms of velocity components and pressure. An alternative formulation of the governing Equations 19.4 through 19.6 is obtained by defining the stream function, ψ, and vorticity, ω, as follows:

$$u = \frac{\partial \psi}{\partial y}; \quad v = -\frac{\partial \psi}{\partial x}; \quad \omega = \frac{\partial v}{\partial x} - \frac{\partial u}{\partial y} \tag{19.20}$$

The stream function, defined by Equation 19.20, enforces automatically the continuity Equation 19.4.

The dimensional momentum equations, in terms of stream function and vorticity, are written as follows:

$$\frac{\partial^2 \psi}{\partial x^2} + \frac{\partial^2 \psi}{\partial y^2} = -\omega \tag{19.21}$$

$$\frac{1}{\varphi}\frac{\partial \omega}{\partial t} + \frac{1}{\varphi^2}\frac{\partial (u\omega)}{\partial x} + \frac{1}{\varphi^2}\frac{\partial (v\omega)}{\partial y} = \frac{\nu}{\varphi}\left(\frac{\partial^2 \omega}{\partial x^2} + \frac{\partial^2 \omega}{\partial y^2}\right) - \nu\left(\frac{1}{K} + \frac{C_F |V|}{\sqrt{K}}\right)$$
$$\omega - \frac{C_F}{\sqrt{K}}\left(v\frac{\partial |V|}{\partial x} - u\frac{\partial |V|}{\partial y}\right) - g\,\beta_f \frac{\partial T_f}{\partial y} \tag{19.22}$$

where

$\nu = \mu/\rho$ is kinematic viscosity

$|V| = \left(u^2 + v^2\right)^{1/2}$ is velocity magnitude

The dimensionless forms of momentum and energy equations for 2D thermal nonequilibrium model are, in terms of stream function and vorticity,

$$\frac{\partial^2 \Psi}{\partial X^2} + \frac{\partial^2 \Psi}{\partial Y^2} = -\Omega \tag{19.23}$$

$$\frac{1}{\varphi}\frac{\partial \Omega}{\partial t} + \frac{1}{\varphi^2}\frac{\partial (U\Omega)}{\partial X} + \frac{1}{\varphi^2}\frac{\partial (V\Omega)}{\partial Y} = \frac{Pr}{\varphi Pe}\left(\frac{\partial^2 \Omega}{\partial X^2} + \frac{\partial^2 \Omega}{\partial Y^2}\right) - \left(\frac{1}{Da} + \frac{C_F |V|}{\sqrt{Da}}\right)$$
$$\Omega - \frac{C_F}{\sqrt{Da}}\left(V\frac{\partial |V|}{\partial X} - U\frac{\partial |V|}{\partial Y}\right) - \frac{PrRa}{Pe^2}\frac{\partial \theta_f}{\partial Y} \tag{19.24}$$

where

$$\frac{\partial \Psi}{\partial Y} = U; \quad \frac{\partial \Psi}{\partial X} = -V; \quad \Omega = \frac{\partial V}{\partial X} - \frac{\partial U}{\partial Y} \tag{19.25}$$

The energy equations are, for fluid phase,

$$\varphi\frac{\partial \theta_f}{\partial \tau} + \left(U\frac{\partial \theta_f}{\partial X} + V\frac{\partial \theta_f}{\partial Y}\right) = \frac{\varphi}{Pe}\left(\frac{\partial^2 \theta_f}{\partial X^2} + \frac{\partial^2 \theta_f}{\partial Y^2}\right) + \frac{Bi_f}{Pe}\left(\theta_s - \theta_f\right)\frac{n!}{r!(n-r)!} \tag{19.26}$$

and for solid phase,

$$\Gamma \frac{\partial \theta_s}{\partial \tau} = \left(\frac{\partial^2 \theta_s}{\partial X^2} + \frac{\partial^2 \theta_s}{\partial Y^2} \right) + Bi_f \gamma \left(\theta_f - \theta_s \right) \tag{19.27}$$

The employed dimensionless variables are defined as follows:

$$X = \frac{x}{L_r}; \quad Y = \frac{y}{L_r}; \quad U = \frac{uL_r}{V_r}; \quad V = \frac{vL_r}{V_r}; \quad \tau = \frac{V_r t}{L_r};$$
$$|V| = \sqrt{U^2 + V^2}; \quad \theta_f = \frac{\left(T_f - T_{jet}\right)}{\Delta T_r}; \quad \theta_s = \frac{\left(T_s - T_{jet}\right)}{\Delta T_r} \tag{19.28a}$$

$$Re = \frac{V_r L_r}{\nu_f}; \quad Pr = \frac{\nu_f}{\alpha_f}; \quad Pe = \frac{V_r L_r}{\alpha_f} = PrRe; \quad Ra = \frac{g\beta \Delta T_r K L_r}{\nu \alpha_f};$$
$$\kappa = \frac{k_{f,eff}}{k_{s,eff}}; \quad \gamma = \frac{\kappa}{\varphi}; \quad Bi_f = \frac{h_{sf} a_{sf} L_r^2}{k_f}; \quad Da = \frac{K}{L_r^2}; \quad \Gamma = \frac{\alpha_f}{\alpha_s} Pe \tag{19.28b}$$

with

$$\alpha_f = \frac{k_f}{\left(\rho c_p\right)_f}; \quad \alpha_s = \frac{k_s}{\left(\rho c_p\right)_s}; \quad k_{f,eff} = \varphi k_f; \quad k_{s,eff} = \left(1 - \varphi\right) k_s \tag{19.29}$$

where

k_f and k_s are the fluid and solid thermal diffusivities

L_r, V_r, ΔT_r are the reference length, velocity, and temperature difference, respectively.

19.3 PHYSICAL GEOMETRY FOR A TWO-DIMENSIONAL CONFINED SLOT JET

In the following, a confined impinging slot jet on a heated surface in a porous foam will be analyzed in detail. The physical problem and geometry are shown in Figure 19.3. The lower impinging surface is partially heated at uniform heat flux, q_w, and the upper surface is adiabatic. The flow is 2D, unsteady, laminar, and incompressible. The slot jet, wide $2D$, impinges through a saturated porous medium on a horizontal surface with a heat source, $2L_h$ long. The inlet slot jet velocity and temperature are V_j and T_j, respectively. The distance between the upper confining surface and the lower partially heated surface is H. The length of the lower plate is $2L$ and the unheated symmetrical zone of the lower surface is assumed adiabatic. Fully developed fluid dynamic and thermal flow is assumed at the outlet sections and the fluid is air, $Pr = 0.71$. The buoyancy effect is taken into account. The porous material is considered as homogeneous and isotropic.

All the thermophysical properties of the fluid and the solid matrix of the porous medium are assumed constant except for the variation in density with temperature (Boussinesq approximation) giving rise to the buoyancy forces. In the porous medium, the Brinkman–Forchheimer–extended Darcy model is used in the momentum equations to enable the study of Darcian and non-Darcian effects. The LTNE is used in the energy equations for solid and fluid phases, whereas the dissipation effect is assumed negligible.

Under these hypotheses, the conservation equations for mass, momentum, and energy for the 2D thermal nonequilibrium model are, in terms of stream function and vorticity and dimensionless

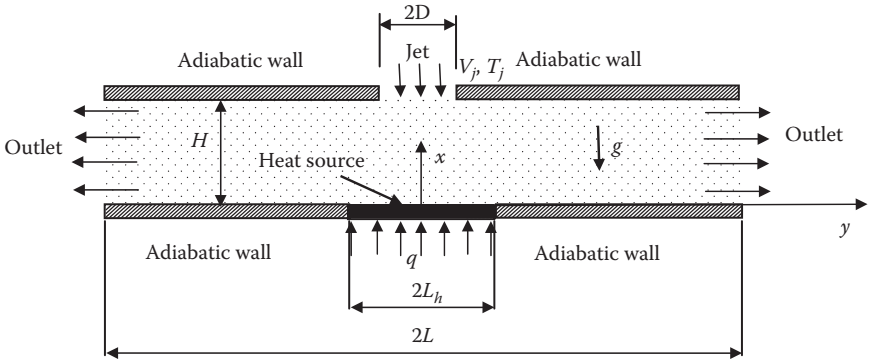

FIGURE 19.3 Sketch of geometrical and physical model with coordinate system.

form, the equations from 19.23 through 19.27 with the dimensionless variables defined in Equations 19.28a and b. The reference variables are assumed as in the following:

$$L_r = H; \quad V_r = V_j; \quad T_r = T_j; \quad \Delta T_r = \frac{q_w H}{k_f} \tag{19.30}$$

The initial conditions assumed on all variable are

$$\Omega = 0; \quad \Psi = 0; \quad \theta_f = \theta_s = 0 \tag{19.31}$$

The boundary conditions are reported in the following:

- At $Y = 0$ and $0 \leq X \leq 1$ and when the symmetry conditions are imposed,

$$\Omega = 0; \quad \Psi = 0; \quad \frac{\partial \theta_f}{\partial Y} = \frac{\partial \theta_s}{\partial Y} = 0 \tag{19.32}$$

- For $X = 0$ at the heated surface (Lee and Vafai, 1999),

$$\Psi = 0; \quad \Omega = -\frac{\partial^2 \Psi}{\partial X^2}; \quad \varphi \frac{\partial \theta_f}{\partial X} + (1-\varphi)\frac{k_s}{k_f}\frac{\partial \theta_s}{\partial X} = -1 \quad \text{and} \quad \theta_f = \theta_s = \theta_w \tag{19.33}$$

- For $X = 0$ and $X = 1$ at the insulated surfaces,

$$\Psi = 0; \quad \Omega = -\frac{\partial^2 \Psi}{\partial X^2} \quad \text{and} \quad \frac{\partial \theta_f}{\partial X} = \frac{\partial \theta_s}{\partial X} = 0 \tag{19.34}$$

- For $X = 1$ at the inlet flow surface,

$$\Psi = X; \quad \Omega = 0 \quad \text{and} \quad \theta_f = \theta_s = 0 \tag{19.35}$$

- For $Y = L/H$ at the outlet flow surface with a dimensionless length such as the flow is fully developed,

$$\frac{\partial \Psi}{\partial Y} = \frac{\partial \Omega}{\partial Y} = 0 \quad \text{and} \quad \frac{\partial \theta_f}{\partial X} = \frac{\partial \theta_s}{\partial X} = 0 \tag{19.36}$$

Local and average Nusselt numbers and total local and average Nusselt numbers, along the heated surface, for the fluid and solid phases are defined as follows:

$$Nu_f(Y) = \frac{q_f H}{k_f \Delta T_r} = \varphi\left(\frac{1}{\theta_w}\frac{\partial \theta_f}{\partial X}\right); \quad Nu_s(Y) = \frac{q_s H}{k_f \Delta T_r} = \frac{(1-\varphi)}{\kappa}\left(\frac{1}{\theta_w}\frac{\partial \theta_s}{\partial X}\right);$$

$$Nu_t(Y) = Nu_f(Y) + Nu_s(Y) = \frac{1}{\theta_w}$$

$$\overline{Nu_t} = \frac{H}{L_h}\int_0^{L_h/H} Nu_t(Y)\,dY \tag{19.37}$$

19.4 METHODS OF SOLUTION AND NUMERICAL PROCEDURE

A numerical procedure has been developed to solve the governing Equations 19.23 through 19.27 subjected to the assigned initial and boundary conditions, Equations 19.31 through 19.36. The numerical computation is carried out by means of the finite volume method (Patankar, 1980), using rectangular cells with constant mesh spacing along the dimensionless coordinate directions, *X* and *Y*. The vorticity and energy equations for fluid and solid phases, Equations 19.24, 19.26 and 19.27, are solved by means of the alternating direction implicit (ADI) method (Roache, 1998). The second-order upwind scheme (Torrance, 1985; Jaluria and Torrance, 2001) is employed to discretize the convective derivatives, while the diffusive derivatives are discretized by the classical central three-point scheme. The convective terms are linearized following the iterative procedure suggested by Roache (1998). The stream function equation, Equation 19.2, is solved by the successive line overrelaxation (SLOR) method (Roache, 1998), using a relaxation factor *r* of about 1.2.

With regard to the numerical implementation of the boundary conditions for the vorticity, it must give attention to the conditions on the solid walls. The conditions on the vorticity are not explicitly assigned, but the condition of no slip is imposed for the velocity. On a solid wall, with reference to Figure 19.4, developing the stream function in Taylor series along the direction of the normal, *n*, to the wall and taking as initial point *w* on the wall:

$$\Psi_w = \Psi_{w+1} + \left(\frac{\partial \Psi}{\partial n}\right)\Delta n + \left(\frac{\partial^2 \Psi}{\partial n^2}\right)\frac{\Delta n^2}{2!}O\left(\Delta n^3\right) \tag{19.38}$$

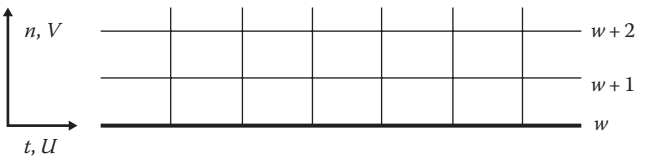

FIGURE 19.4 Coordinates on the solid boundary and discretization on the wall. (Reprinted from *Int. J. Therm. Sci*., 48, Wong, K.-C. and Saeid, N.H., Numerical study of mixed convection on jet impingement cooling in a horizontal porous layer under local thermal non-equilibrium conditions, 860–870, Copyright (2009d), with permission of Elsevier.)

Applying the following *no-permeability* and *no-slip* conditions on the solid wall,

$$U_w = \left(\frac{\partial \Psi}{\partial n}\right)_w = 0, \quad V_w = \left(\frac{\partial \Psi}{\partial t}\right)_w = 0 \tag{19.39}$$

and taking into account the equation

$$\Omega_w = \left(\frac{\partial V}{\partial t}\right)_w - \left(\frac{\partial U}{\partial n}\right)_w = -\left(\frac{\partial U}{\partial n}\right)_w = -\left(\frac{\partial^2 \Psi}{\partial n^2}\right)_w \tag{19.40}$$

it is obtained

$$\Psi_w = \Psi_{w+1} - \Omega_w \frac{\Delta n^2}{2!} + O\left(\Delta n^3\right) \tag{19.41}$$

Hence,

$$\Omega_w = \frac{2\left(\Psi_{w+1} - \Psi_w\right)}{\Delta n^2} + O\left(\Delta n\right) \tag{19.42}$$

which is known as Thom's formula (see Roache, 1998) and is accurate to the first order. A formula of the same type but accurate to the second order, due to Briley (1970), is

$$\Omega_w = \frac{-7\Psi_w + 8\Psi_{w+1} - \Psi_{w+2}}{2\Delta n^2} + O\left(\Delta n^2\right) \tag{19.43}$$

In the developed procedure, Thom's formula has been employed that, although accurate to the first order, provides results similar to those obtained with formulas of higher order, and in some cases, even better (Roache, 1998).

Once the equations of vorticity, stream function, and energy are solved until the steady state is reached. The steady-state solution is attained when the vorticity and thermal fields variations are less than a prescribed accuracy equal to 10^{-6}.

A preliminary analysis is accomplished to evaluate the computational domain extension, the results dependence on mesh, and the validation analysis for the steady-state regime. The first and second analysis was carried out for $C_F = 0.1$, $Da = 10^{-3}$, $Ra = 100$, $Bi = 1.0$, $\varphi = 0.87$, $\kappa = 1.0$, and $Pe = 1$ and 1000, monitoring average wall temperature and varying L/L_h from 1 to 6. It is found that the value L/L_h equal to 4 leads to a percentage difference, with respect to the value at $L/L_h = 6$, less than 0.5% for all considered Pe values. Then, the computational domain for the simulations is chosen with $L/L_h = 5$. The grid analysis is performed for five meshes ($N_X \times N_Y$) 15×71, 31×151, 61×301, 121×601, and 241×1201. For $Pe = 1.0$, a percentage error, with respect to the Richardson extrapolation value, of less than 1%, is found for the grid 31×151, whereas for $Pe = 1000$, this accuracy is found for a grid with 61×301 nodes. In the simulations, the first grid, 31×51, is employed for $1 \leq Pe \leq 100$ and the 61×301 grid is used for $Pe > 100$.

The validation test is accomplished by comparing the present model adapted to the study given by Wong and Saeid (2009d) for heated plate at assigned temperature. The results of this comparison

are depicted in Figure 19.5 for $Pe = 1$ and 1000 in terms of stream function and temperature fields; the agreement between the two data sets is very satisfying.

A comparison among the average wall temperature profiles, as a function of time, for three different time steps was carried out. For $Pe = 1.0$, the employed time steps are $\Delta\tau = 10^{-4}$, 10^{-3}, and 10^{-2}, whereas for $Pe = 1000$, $\Delta\tau = 10^{-3}$, 10^{-2}, and 10^{-1} are employed. The temperature profiles showed a maximum differences at $\tau = 0.43$, for $Pe = 1$, and at $\tau = 456$, for $Pe = 1000$. The maximum percent difference for both the Pe values was about 0.5%. The value was estimated between $\Delta\tau = 10^{-3}$ and 10^{-2} and $\Delta\tau = 10^{-2}$ and 10^{-1} for $Pe = 1$ and 1000, respectively. Thus, the time step in the transient calculations was fixed at $\Delta\tau = 10^{-3}$ from $Pe = 1$ to $Pe = 10$ and at $\Delta\tau = 10^{-2}$ from $Pe = 100$ to $Pe = 1000$.

The validation test is accomplished by comparing the present model adapted to the study given by Wong and Saeid (2009d) for heated plate at assigned temperature and in LTNE assumption. The results of this comparison are carried out for $Pe = 1$ and 1000 in terms of stream function and temperature fields and reported in Figure 19.5a and b, respectively. The figures show that the agreement between the two data sets is satisfying.

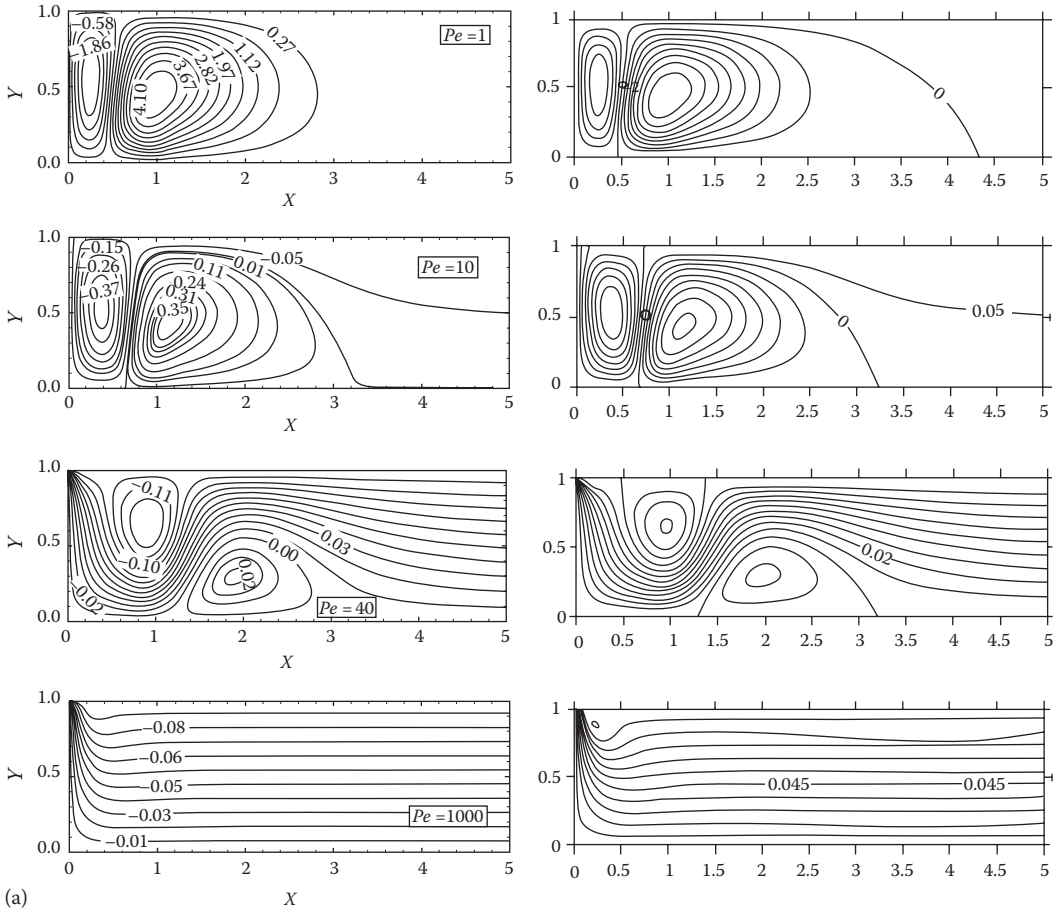

FIGURE 19.5 (a) Comparison of the streamlines for different values of Pe, with $D/H = 0.1$, $\varphi = 0.87$, $C_F = 0.1$, $Ra = 100$, $Da = 10^{-3}$, and $Bi = 1$ and $\varphi k_f/(1-\varphi)k_s = 1$. (Right—present data; left—Reprinted from *Int. J. Therm. Sci*., Wong, K.-C. and Saeid, N.H., Numerical study of mixed convection on jet impingement cooling in a horizontal porous layer under local thermal non-equilibrium conditions, 48, 860–870, Copyright (2009d), with permission of Elsevier.) (*Continued*)

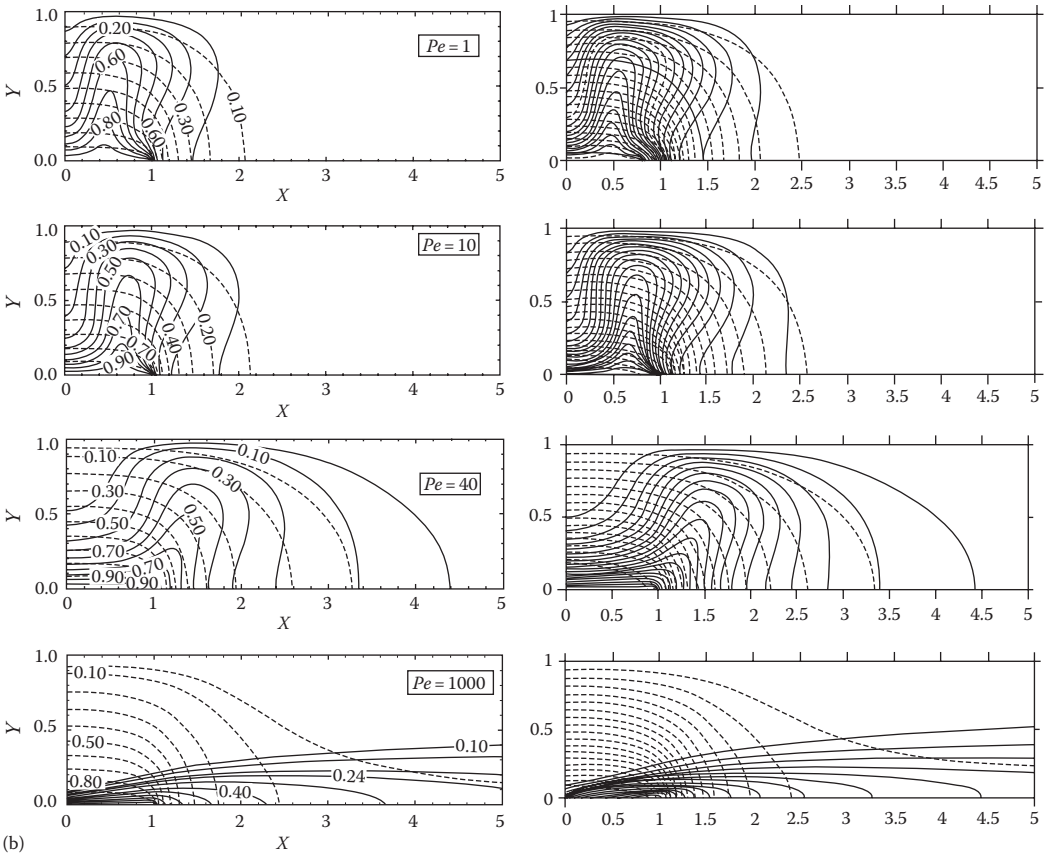

FIGURE 19.5 (*Continued*) (b) Comparison of the temperature fields for (——— θ_f, ----- θ_s) different values of *Pe*, with $D/H = 0.1$, $\varphi = 0.87$, $C_F = 0.1$, $Ra = 100$, $Da = 10^{-3}$, and $Bi = 1$ and $\varphi k_f/(1-\varphi)k_s = 1$. (Right—present data; left—Reprinted from *Int. J. Therm. Sci*., Wong, K.-C. and Saeid, N.H., Numerical study of mixed convection on jet impingement cooling in a horizontal porous layer under local thermal non-equilibrium conditions, 48, 860–870, Copyright (2009d), with permission of Elsevier.)

19.5 COMPARISON AND DISCUSSION OF RESULTS FOR DIFFERENT PARAMETER VALUES

Results are carried out for characteristic dimensionless parameters: Prandtl number, *Pr*, equal to 071 (air); Péclet number, *Pe*, in the range 1–5000; Rayleigh number, *Ra*, equal to 10 and 100; Darcy number, *Da*, between 10^{-6} and 10^{-2}; and Biot number, *Bi*, from 0.1 to 1000. It is worth noting that the maximum *Pe* value, equal to 5000, corresponds to Re_j equal to about 700, which guarantees a laminar flow inside the domain. The geometric dimensionless parameters, here considered with reference to Figure 19.3, are the ratio *D*/*H* between the half slot jet width, *D*, and the distance between the jet exit section and the heated plate, *H*, the ratio H/L_h between the distance *H* and the heated part half width of the partially heated plate, L_h, and their values are in the range 0.1–1. The porosity, ϕ, is varied from 0.7 to 0.98. Moreover, the dimensionless physical properties parameters κ ($= k_{f,eff}/k_{s,eff}$) is in the range 10^{-3} and 1, whereas the thermal diffusivity ratio is equal to 1 and the inertial coefficient is assumed equal to 0.1.

In Figure 19.6, dimensionless average temperature profiles are reported as functions of dimensionless time for $Ra = 100$, $Da = 10^{-6}$, $Bi = 10$, $\varphi = 0.80$, $\alpha_f/\alpha_s = 1.0$, $\kappa = 0.001$, and different

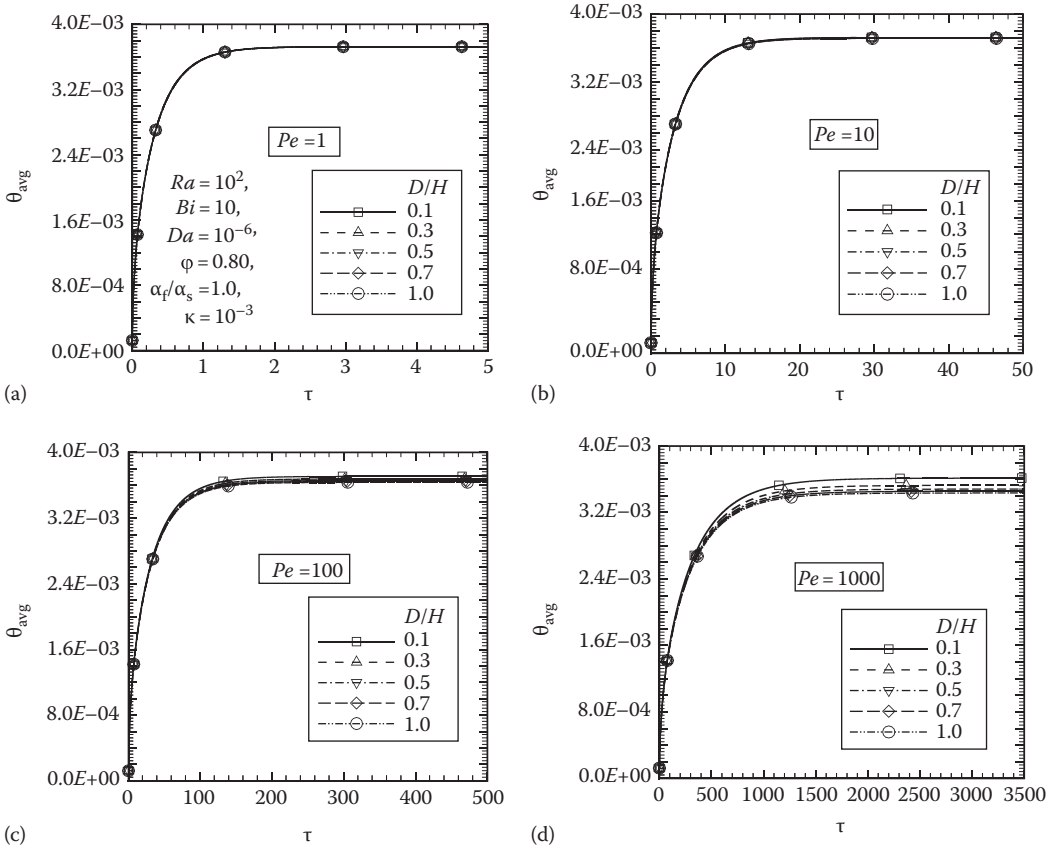

FIGURE 19.6 Dimensionless average wall temperature versus dimensionless time for $Ra = 100$, $Da = 10^{-6}$, $Bi = 10$, $\varphi = 0.80$, $\alpha_f/\alpha_s = 1.0$, $\kappa = 10^{-3}$, for different jet diameters and Péclet number: (a) $Pe = 1$, (b) $Pe = 10$, (c) $Pe = 100$, and (d) $Pe = 1000$.

dimensionless jet radius values D/H. For low Péclet number values, Pe lower than 10, Figure 19.6a and b, dimensionless average temperature is almost independent of the jet diameter because the solid phase is much more conductive than the fluid one due to the low value of the Péclet number. When Péclet number increases, Figure 19.6c and d, the effect of jet diameter is stronger and heat removal increases as diameter increases.

For $\kappa = 1$, Figure 19.7, temperature profiles depend on jet diameter after a maximum value is reached. In particular, as jet diameter increases, nondimensional temperature value is higher. For Pe lower than 10, Figure 19.7a and b, and for each jet diameter value, the temperature profile presents a relative maximum and minimum values. In the first instants, buoyancy effect is negligible and, therefore, the regime is only conductive. When temperature reaches a value so to activate natural convection, the temperature profile has a maximum (overshoot), and then temperature decreases till a minimum value. Dimensionless average temperature profiles for $Pe = 100$ and 1000, Figure 19.7c and d, do not show the presence of the overshoot for each jet diameter value.

In Figure 19.8, stream line fields are reported at different times for $Ra = 100$, $Da = 10^{-6}$, $Bi = 10$, $\varphi = 0.80$, $\alpha_f/\alpha_s = 1.0$, $D/H = 0.1$, $\kappa = k_{f,eff.}/k_{s,eff.} = 1$, and Péclet numbers. For $Pe = 1$, Figure 19.8a, vortex cell configuration is mainly due to natural convection effect. On the contrary, for high Péclet numbers, Figure 19.8b, the effect of forced convection due to the jet is stronger than natural convection effect. As a matter of fact, the vortex cell is not present even in the first instants.

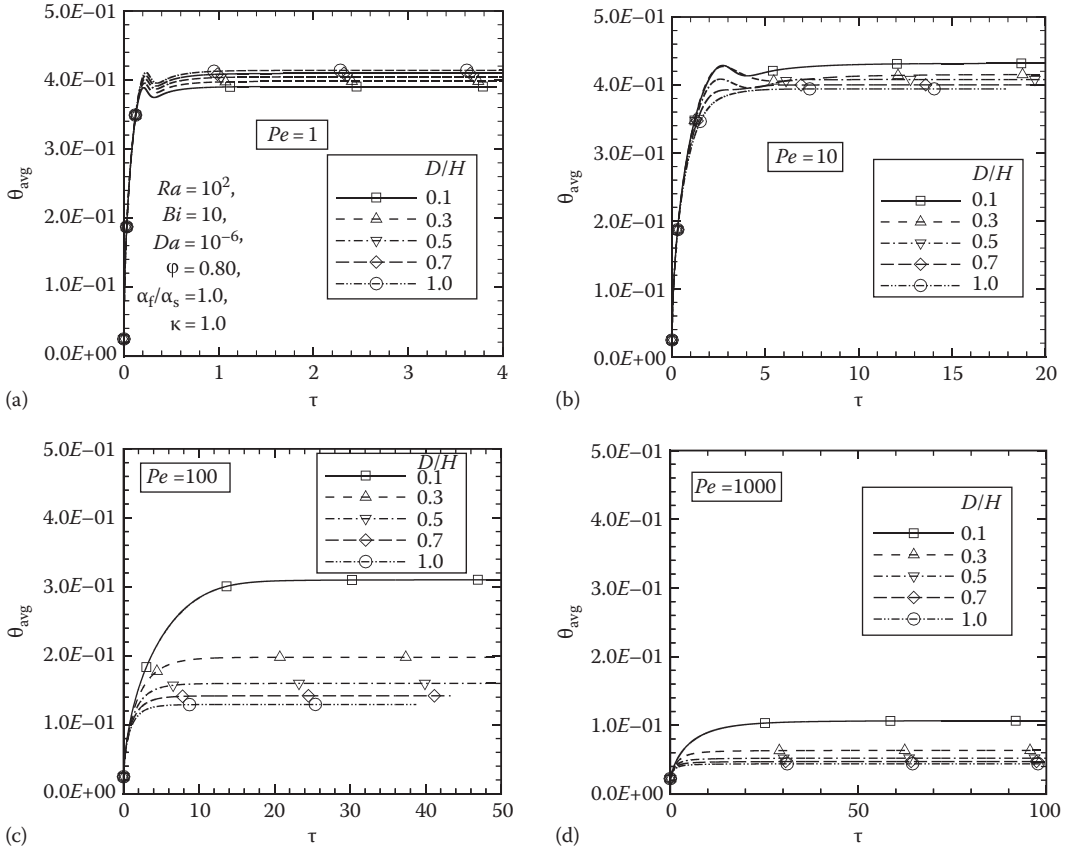

FIGURE 19.7 Dimensionless average wall temperature versus dimensionless time for $Ra = 100$, $Da = 10^{-6}$, $Bi = 10$, $\varphi = 0.80$, $\alpha_f/\alpha_s = 1.0$, $\kappa = 1$ and for different jet diameters: (a) $Pe = 1$, (b) $Pe = 10$, (c) $Pe = 100$, and (d) $Pe = 1000$.

Temperature fields in fluid and solid phases are reported in Figure 19.9a and b, respectively, for $Ra = 100$, $Da = 10^{-6}$, $Bi = 10$, $\varphi = 0.80$, $\alpha_f/\alpha_s = 1.0$, $D/H = 0.1$, $\kappa = 1$, $Pe = 1$ at the steady state ($\tau = \tau_{ss} = 1.0$). When the Péclet number is low as in this case, $Pe = 1$, temperature fields are mainly conductive and therefore they are affected by heat conductivity of the medium. If fluid and solid phases have the same conductivity values as in the case reported in Figure 19.9 temperature fields are very similar.

For high Péclet number values, the effect of forced convection is stronger and temperature fields are different for the fluid and solid phases even when heat conductivity are the same, as shown in Figure 19.10 for $Pe = 1000$. In particular, isotherms for the two media extend farther from the impinging zone and, at a fixed location, temperature value of the fluid phase is higher than that of the solid phase.

The effect of different effective thermal conductivity ratio values between the fluid and solid phases is reported in Figures 19.11 and 19.12 at different times for $Ra = 100$, $Da = 10^{-6}$, $Bi = 10$, $\varphi = 0.80$, $\alpha_f/\alpha_s = 1.0$, $D/H = 0.1$, $\kappa = k_{f,eff.}/k_{s,eff.} = 0.001$, and for $Pe = 1$ and 1000, respectively. It is worth noting that when Péclet number value is low, $Pe = 1$, temperature fields are very similar even if heat conductivity of fluid phase is much lower than that of the solid phase, Figure 19.11. On the contrary when the effect of forced convection is stronger, $Pe = 1000$, temperature field for the fluid phase extends much further from impinging zone with respect to the one for the solid phase. At the steady state, temperature field for solid phase is nearly independent on Péclet number value because thermal diffusion in the solid phase is weakly affected by flow motion.

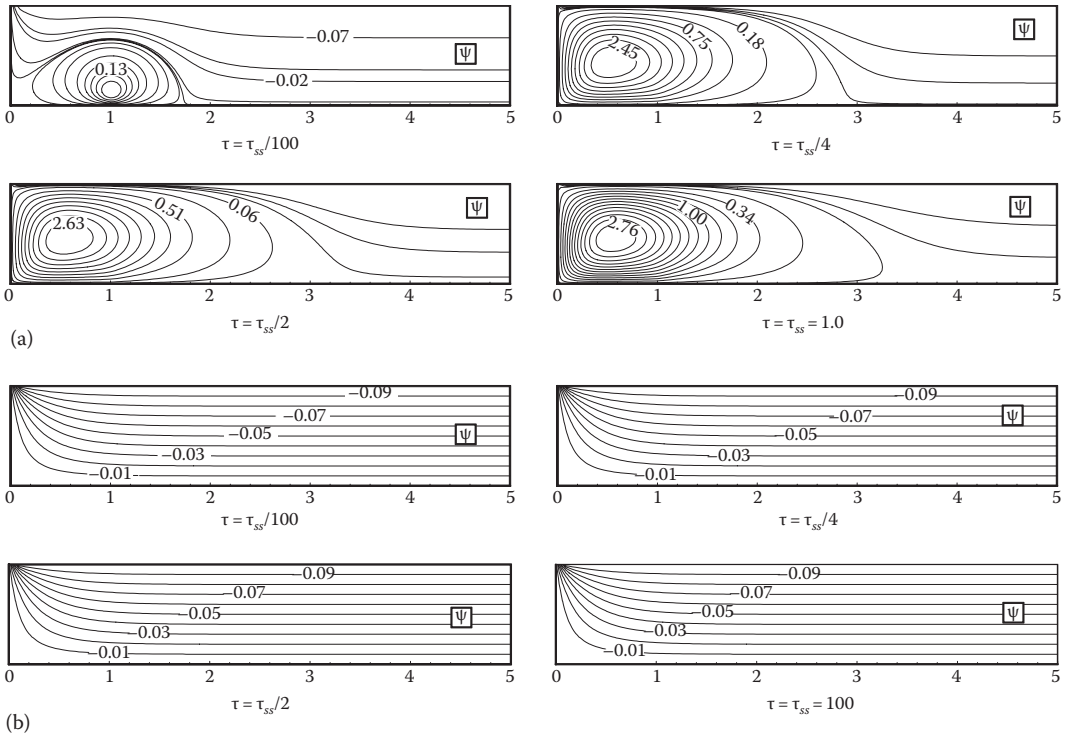

FIGURE 19.8 Stream function for $Ra = 100$, $Da = 10^{-6}$, $Bi = 10$, $\varphi = 0.80$, $\alpha_f/\alpha_s = 1.0$, $D/H = 0.1$, $\kappa = 1$, and (a) $Pe = 1$ and (b) $Pe = 1000$.

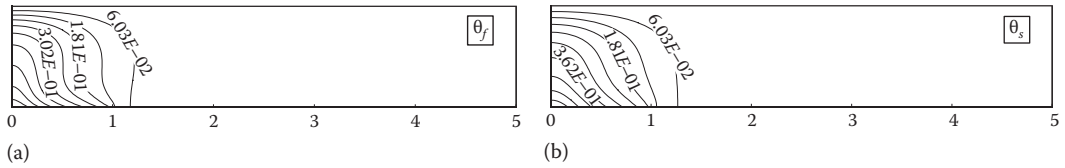

FIGURE 19.9 Dimensionless temperature fields for $Ra = 100$, $Da = 10^{-6}$, $Bi = 10$, $\varphi = 0.80$, $\alpha_f/\alpha_s = 1.0$, $D/H = 0.1$, $\kappa = 1$, $Pe = 1$ at the steady state ($\tau = \tau_{ss} = 1.0$): (a) fluid and (b) solid.

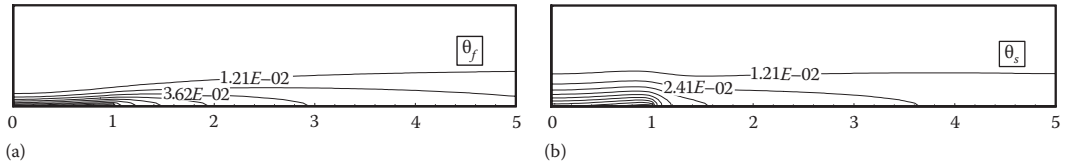

FIGURE 19.10 Dimensionless temperature fields for $Ra = 100$, $Da = 10^{-6}$, $Bi = 10$, $\varphi = 0.80$, $\alpha_f/\alpha_s = 1.0$, $D/H = 0.1$, $\kappa = 1$, $Pe = 1000$ at the steady state ($\tau = \tau_{ss} = 100$): (a) fluid and (b) solid.

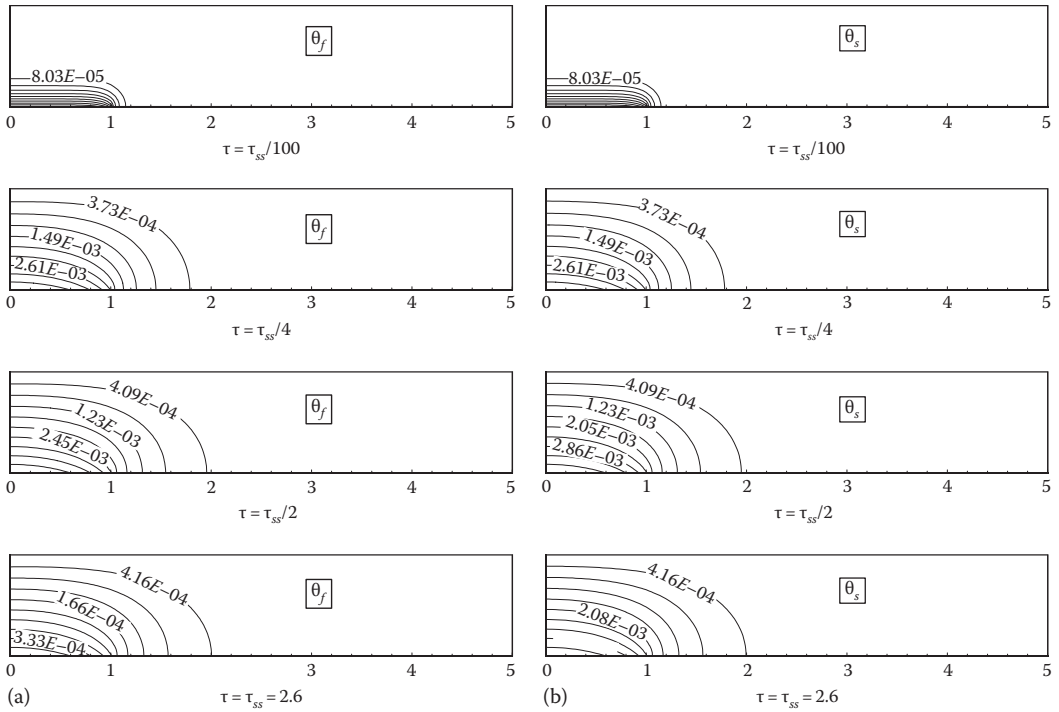

FIGURE 19.11 Dimensionless temperature fields for $Ra = 100$, $Da = 10^{-6}$, $Bi = 10$, $\varphi = 0.80$, $\alpha_f/\alpha_s = 1.0$, $D/H = 0.1$, $\kappa = 10^{-3}$, $Pe = 1$ at different instants: (a) fluid and (b) solid.

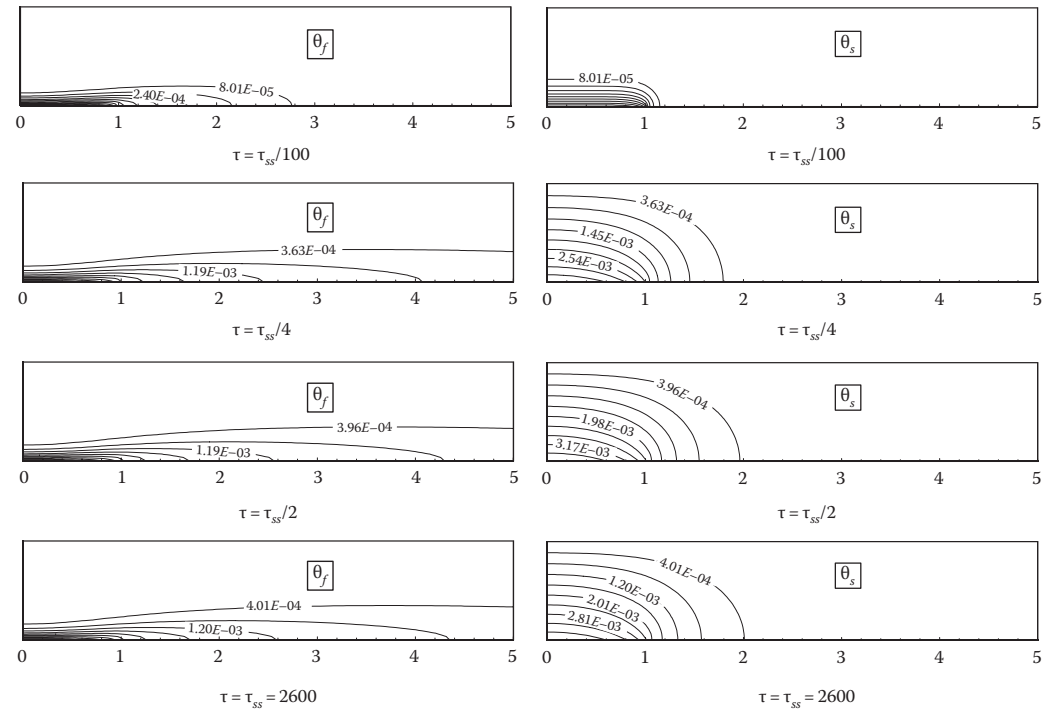

FIGURE 19.12 Dimensionless temperature fields for $Ra = 100$, $Da = 10^{-6}$, $Bi = 10$, $\varphi = 0.80$, $\alpha_f/\alpha_s = 1.0$, $D/H = 0.1$, $\kappa = 10^{-3}$, $Pe = 1000$ at different times: (a) fluid and (b) solid.

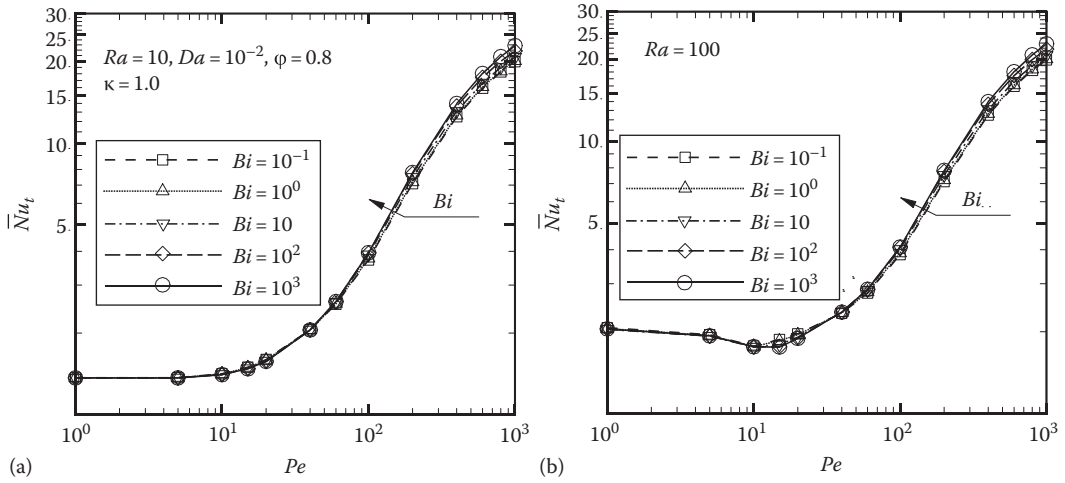

FIGURE 19.13 Average total Nusselt number as a function of Péclet number for different Biot numbers and Darcy number equal to10^{-2} and (a) $Ra = 10$ and (b) $Ra = 100$.

Total average Nusselt number value as a function of Péclet number is given in Figures 19.13 and 19.14 at steady state for $Da = 10^{-2}$ and 10^{-6}, respectively. The values are given for a porosity $\varphi = 0.8$, $H/L_h = 1$, $D/H = 0.1$, and an effective thermal conductivity ratio equal to 1.

Nusselt number values for $Da = 10^{-2}$ and $Ra = 10$, in Figure 19.13a, increase as Pe increases but the increase is lower for low Pe value, whereas for $Pe > 20$, the increase is significant. For low Pe (<1), the buoyancy effect are comparable with the forced convection effect due to the impinging flow and, because they have an opposite direction, there is a mutual contrast between them. The opposing effect due to the buoyancy becomes weak for higher Pe values due to the dominance of the forced flow on the opposite natural convective flow. For higher Ra values, the buoyancy effect increases, as showed in Figure 19.13b for $Ra = 100$. The Nu_t is higher than the previous one for $Ra = 10$ for $Pe = 1$ but increasing Pe values Nu_t decreases up to about $Pe = 15$ where a minimum Nu_t value is attained. For Pe equal to about 21, Nu_t value presents the same value reached at

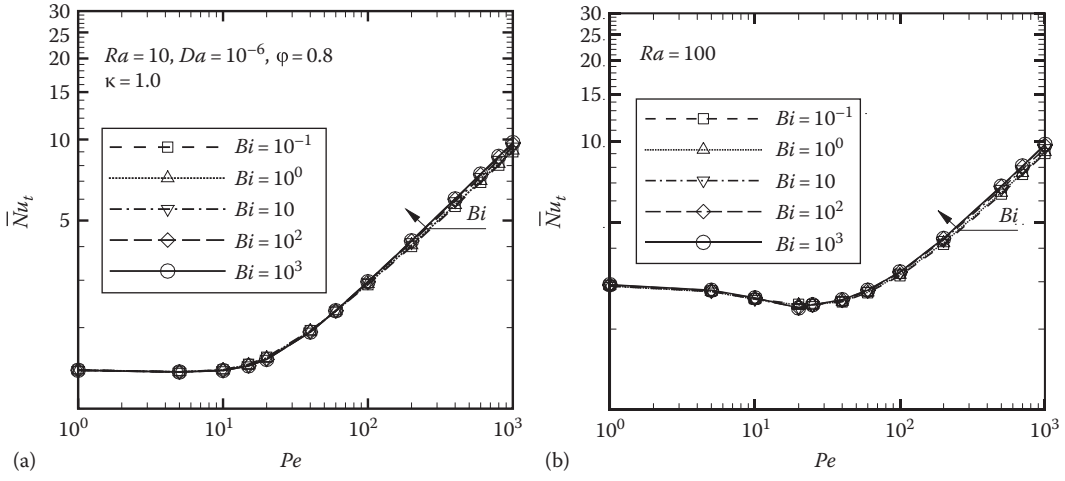

FIGURE 19.14 Average total Nusselt number as a function of Péclet number for different Biot numbers and Darcy number equal to10^{-6} and (a) $Ra = 10$ and (b) $Ra = 100$.

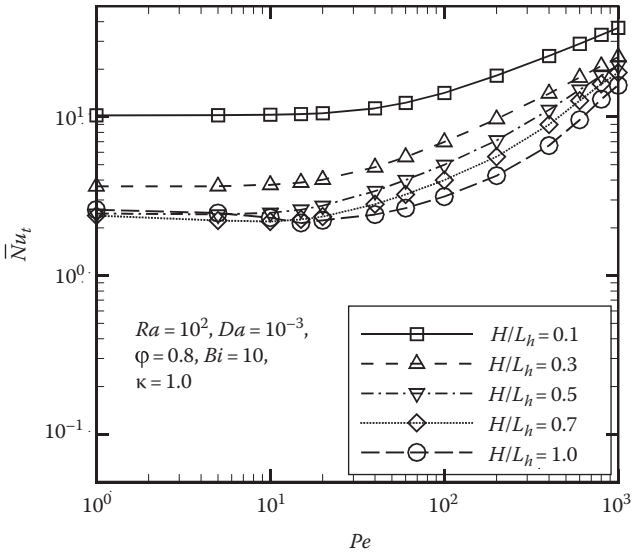

FIGURE 19.15 Average total Nusselt number as a function of Péclet number for different dimensionless distance between the slot jet outlet section, H/L_h, and heated wall and $Da = 10^{-3}$.

$Pe = 1$ and increases with Pe. It should be underlined that the Pe value at which the buoyancy effect becomes negligible with respect to the forced flow increases as the Ra value increases. The previous observations are in agreement with the results given by Wong and Saeid (2009d) for assigned wall temperature on the target. In Figure 19.13, it is also noted that the Nu_t values depend weakly on Biot number values and the dependence is weak as Pe is low.

At lower Darcy number value, $Da = 10^{-6}$, in Figure 19.14, for Pe values lower than 1, Nu_t is higher than the one at $Da = 10^{-2}$. The difference is negligible for $Ra = 10$, in Figures 19.13a and 19.14a, whereas it increases for $Ra = 100$. The increase is due to the lower velocity close to the heated wall of the forced flow in the porous medium with a lower Darcy and then with a lower permeability. This determines that the convective heat transfer due to the buoyancy effect is slightly stronger for lower Da value. The effect is lower as lower as Ra value. At increasing of Pe value, the forced flow effect becomes stronger and the buoyancy effect decreases with respect to the forced flow. For higher Pe values, Nu_t values are higher for the lower Da values and an inversion is detected; this is also in agreement with the results reported in Wong and Saeid (2009d). For $Ra = 10$, the inversion happens for Pe value close to 1, in Figures 19.13a and 19.14a, whereas for $Ra = 100$, in Figures 19.13b and 19.14b, the inversion is detected at about $Pe = 75$. It is interesting to observe that for $Pe = 1000$, Nu_t values for $Da = 10^{-6}$, in Figure 19.14, are less than half of the corresponding values for $Da = 10^{-2}$, in Figure 19.13.

The effect of distance between the outlet section of slot jet and heated wall, H/L_h, in terms of total average Nusselt number is reported in Figure 19.15. Nu_t values are given as functions of Péclet number, and as observed in the previous results in Figures 19.13 and 19.14, it is noted that for lower Pe values, different trends are detected, whereas for $Pe > 50$, Nu_t is a crescent function. For lower H/L_h (<0.3), the effect of forced flow is significantly prevalent also at lower Pe values (<10) though the opposing buoyancy force determines a low increase in the heat transfer coefficient values up to $Pe = 30$. For $Pe > 100$, at the same Pe value, the slopes increase with the dimensionless distance H/L_h and the trends seem to present a unique oblique asymptote. For $H/L_h \geq 0.5$, a decrease in Nu_t is noted due to the opposing direction of buoyancy and forced flow. A minimum value is detected for all three considered H/L_h values and it is attained at lower Pe value as lower H/L_h value.

Total average Nusselt number as a function of Péclet number for different effective thermal conductivity ratio, $\kappa = \varphi k_f/(1 - \varphi)k_s$, is showed in Figure 19.16 for $Ra = 10$, in Figure 19.16a,

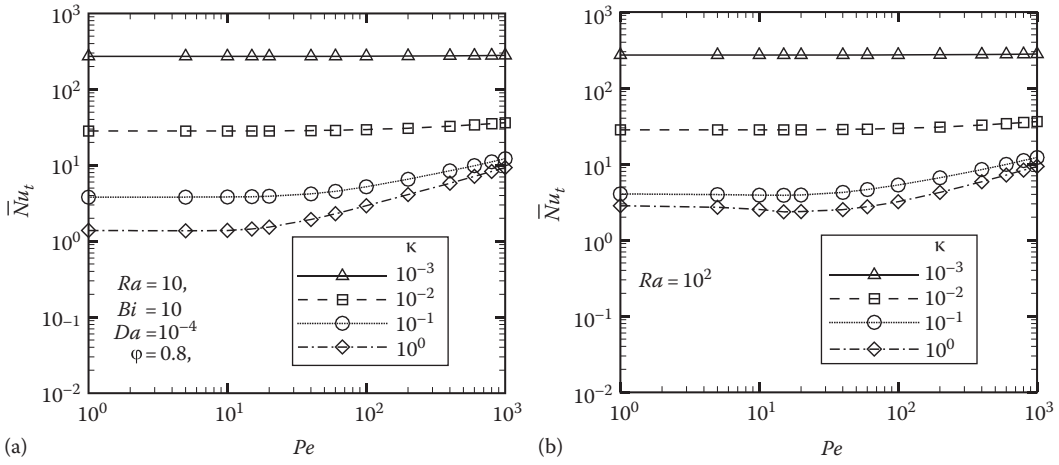

FIGURE 19.16 Average total Nusselt number as a function of Péclet number for different thermal conductivity ratio and Darcy number equal to 10^{-4} and (a) $Ra = 10$ and (b) $Ra = 100$.

and $Ra = 100$, in Figure 19.16b, respectively. The other parameters are $Ra = 10$, $Da = 10^{-4}$, $\varphi = 0.8$, and $Bi = 10$.

For the lower effective thermal conductivity ratio, κ, ($\leq 10^{-2}$), Nu_t is almost constant. For $\kappa = 10^{-2}$, a slight increase starts at about $Pe = 100$ for both $Ra = 10$ and 100. The Nu_t value is higher as lower κ. For lower κ values, the main contribution to the heat transfer is due to the solid matrix that has a significantly higher heat transfer value compared to the fluid also for high Péclet number values. In fact, for $\kappa = 10^{-3}$, Nu_t is almost constant for $Pe \leq 1000$ where for $\kappa = 10^{-2}$, Nu_t is constant up to $Pe = 100$. For higher κ values, for $Ra = 10$ in Figure 19.16a, the Nu_t increases for $Pe > 20$ and $Pe > 12$ for $\kappa = 0.1$ and 1, respectively. For this Ra value, in Figure 19.16a, the buoyancy effects are negligible with respect to the forced flow also for lower Pe values. For $Ra = 100$, in Figure 19.16b, the buoyancy effect are more evident for lower Pe value (<10) and the Nu_t decreases up to Pe about 12, for $\kappa = 0.1$, and Pe about 20, for $\kappa = 1$, where the minimum Nu_t value is reached.

The dependence on the Darcy number, Da, of average total Nusselt number is reported in Figure 19.17. Nu_t is given for some Pe values, $Ra = 100$, $Bi = 100$, and $\kappa = 10^{-2}$ and 1 in Figure 19.17a

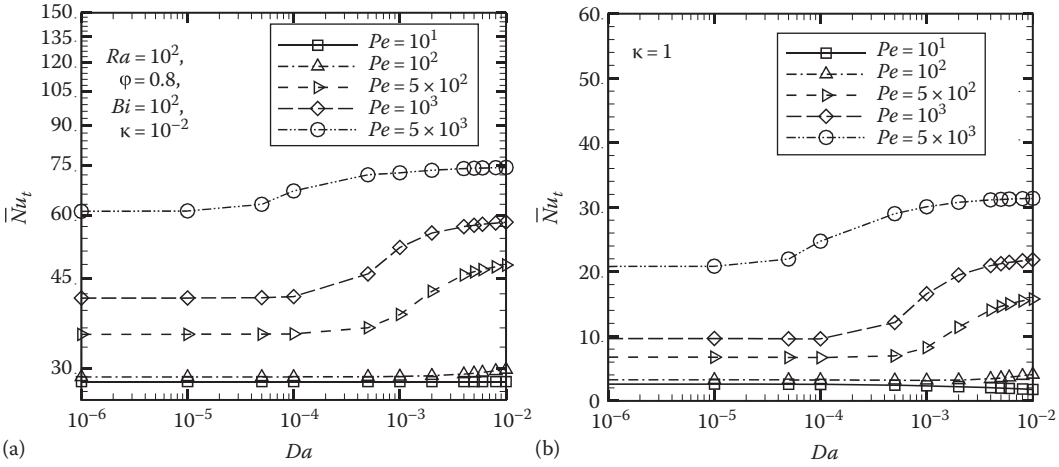

FIGURE 19.17 Average total Nusselt number as a function of Darcy number for different Péclet number values and (a) $\kappa = 10^{-2}$ and (b) $\kappa = 1$.

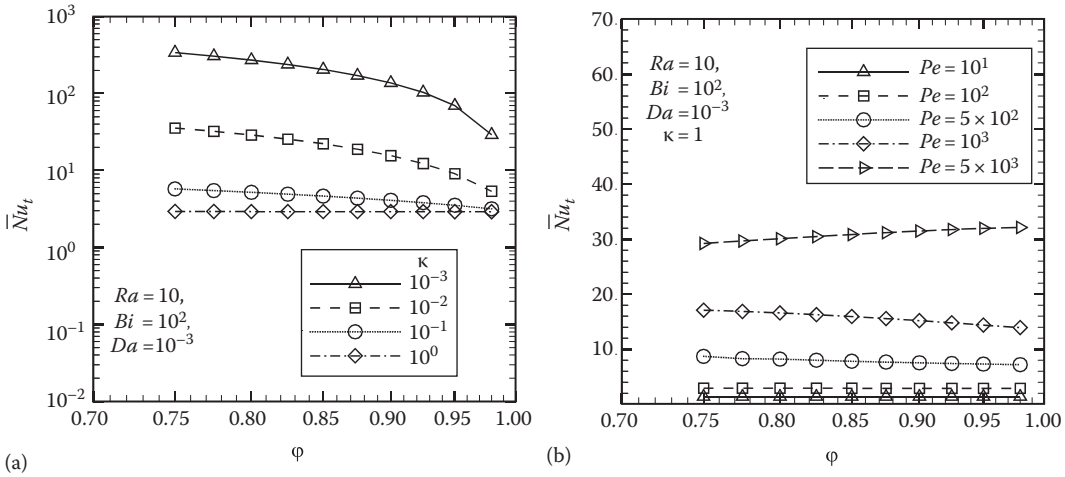

FIGURE 19.18 Average total Nusselt number as a function porosity for (a) different effective thermal conductivity ratio values, κ, and (b) Péclet number values, *Pe*.

and b, respectively. It is noted that Nu_t values are almost constant for $Pe = 10$ and 100. The forced flow is weak and, for these *Pe* values, it is significantly affected by the opposing buoyancy flow. By increasing *Pe* value, it is observed that the Nu_t increases and the increase begins at the lower *Da* values at low *Pe* values. This is due to the permeability increase as the Darcy number increases, which determines, at the same *Pe* value, a higher velocity inside the porous medium and a higher heat transfer coefficient on the heated wall. However, an asymptotic value is attained for an assigned *Pe* value for high *Da* values. The effect could be as a thermal saturation of the forced flow with respect to the increase in the permeability, for assigned porosity. For higher κ values, the increase begins for slightly higher *Da* values and a slight decrease is observed for $\kappa = 1$ and $Pe = 10^5$. The latter could be due to the presence of a vortex cell close to the jet and the heated wall that determines a preheating of the forced flow and a lower heat transfer between the impinging fluid and the heated wall.

The porosity effect on the average total Nusselt number is shown in Figure 19.18. For different thermal conductivity ratios, in Figure 19.18a, Nu_t decreases with the increase in porosity at lower κ value. For $\kappa = 1$, the Nu_t is practically constant. It is interesting to observe, for $\kappa = 10^{-3}$ and 10^{-2}, that the decreasing is higher at higher porosity. It can be explained by Equation 19.37 where the term related to the solid decreases as the porosity increases. The results suggest that for high solid thermal conductivity values to employ a porous medium with high porosity could not be convenient. The porosity effect on Nu_t is negligible for assigned *Pe* value, as shown in Figure 19.18b. For the considered porosity range, for $Pe \leq 100$, the Nu_t is almost constant, whereas for $Pe = 500$ and 1000, the Nu_t presents a decrease increasing the porosity. The trend is opposite for $Pe = 5000$.

19.6 CONCLUSIONS

A numerical model to simulate slot jet impinging on a partially heated target at assigned heat flux has been proposed to evaluate the heat transfer behaviors in terms of the main dimensionless characteristic parameters. The model is developed assuming the LTNE and in 2D transient regime and solved by means of the finite volume method. Some indications are given to explain the numerical procedure developed to carry out results. The simulation allows to determine thermal behaviors in terms of the main dimensionless parameters such as the Péclet, Rayleigh, Darcy, and Biot numbers for air as working fluid with a Prandtl number equal to 0.71, dimensionless geometric parameters,

and physical properties. Results are presented in both transient and steady-state regimes, and they are given mainly in terms of temperature profiles as a function of time and average total Nusselt number for different values of the various dimensionless parameters.

Dimensionless average heated wall temperature profiles as a function of time presented for different values of distance ratio, H/L_h, small differences among the curves for low effective thermal conductivity ratios, κ, and the differences among the profiles were significant for high κ values and they became greater for higher Péclet numbers. Further, for low Péclet number values, ≤10, and κ = 1, overshoots were detected, and for high *Pe* and κ = 1, the overshoot disappears and wall temperatures decrease significantly. For the highest *Ra* values considered, equal to 100, the buoyancy force determined vortex cells close to the heated part for low *Pe* values, whereas for high *Pe*, the cells were not present and the flow was about parallel after the impingement zone. It is interesting to observe that steady state was reached before for the lower *Pe* values.

At steady state, results given in terms of total average Nusselt numbers, Nu_t, allowed to observe significant different behaviors for *Ra* = 10 and 100 due to the different buoyancy effect. Forced flow and buoyancy have an opposite direction and the consequence for low *Pe* values a decrease in Nu_t was detected, whereas for high *Pe* values, the buoyancy effect was very weak and Nu_t increased. For the considered parameters, a weak dependence of Nu_t on *Bi* was noted, whereas the effect of dimensionless distance between the jet outlet section and heated plate, H/L_h, and effective thermal conductivity ration, κ, is significant. The dependence on *Da* is significant for higher *Pe* values ($Pe \geq 500$) for the parameters values here considered. For lower assigned κ values, it seems that the heat transfer decreases increasing the porosity, whereas for assigned Péclet numbers, the increase in porosity value has a slight effect on the heat transfer variation.

NOMENCLATURE

a_{sf}	Specific surface area	$m^2\ m^{-3}$
Bi	Biot number	Equation 19.28b
C_F	Inertia coefficient	Equation 19.5
D	Half of the jet width	m
Da	Darcy number	Equation 19.28b
g	Gravitational acceleration	$m\ s^{-2}$
H	Width of the channel	m
h_{sf}	Interstitial heat transfer coefficient	$W\ m^{-2}\ K^{-1}$
k	Thermal conductivity	$W\ m^{-1}\ K^{-1}$
K	Permeability	m^2
L	Half of the channel length	m
L_h	Half of the heat source length	m
p	Pressure	Pa
Ra	Rayleigh number	Equation 19.28b
Nu(*X*)	Local Nusselt number	Equation 19.37
Nu_t	Total average Nusselt number	Equation 19.38
Pr	Prandtl number	Equation 19.28b
q	Heat flux	$W\ m^{-2}$
Pe	Péclet number	Equation 19.28b
t	Time or tangential	s
T	Temperature	K
u, *v*	Velocity components	$m\ s^{-1}$
U, V	Dimensionless velocity components	Equation 19.28a
x, y, r	Coordinate distance	m
X, Y	Dimensionless coordinate	Equation 19.28a

Greek Symbols

α	Thermal diffusivity	$m^2\ s^{-1}$
β	Volumetric expansion coefficient	K^{-1}
γ	Modified conductivity ratio	Equation 19.28b
θ	Dimensionless temperature	Equation 19.28a
μ	Dynamic viscosity	$kg\ m^{-1}s^{-1}$
ν	Kinematic viscosity	$m^2\ s^{-1}$
τ	Dimensionless time	
ϕ	Porosity coefficient	Equation 19.3
ψ	Stream function	Equation 19.20
Ψ	Dimensionless stream function	Equation 19.25
ω	Vorticity	Equation 19.20
Ω	Dimensionless vorticity	Equation 19.25
ρ	Density	$kg\ m^{-3}$

Subscripts

e	Effective
f	Fluid
s	Solid
w	Wall
< >	Average
eff	Effective

REFERENCES

Amiri, A. and K. Vafai. 1994. Analysis of dispersion effects and non-thermal equilibrium, non-Darcian, variable porosity incompressible flow through porous media. *Int. J. Heat Mass Transfer* 37 (6): 939–954.

Arganbright, D.G. and H. Resch. 1971. A review of basic aspects of heat transfer under impinging air jets. *Wood Sci. Technol.* 5 (2): 73–94.

Briley, W.R. 1970. A numerical study of laminar separation bubbles using the Navier-Stokes equations. Report J110614-1. East Hartford, CT: United Aircraft Research Laboratories.

Buonomo, B., Manca, O., and S. Nardini. 2012. Laminar slot-jet impinging on confined porous medium in local thermal non-equilibrium conditions with bottom surface at uniform heat flux. *Proceedings of the Fourth International Conference on Porous Media and Its Applications in Science and Engineering, ICPM4*, Potsdam, Germany, June 17–22, 2012.

De Lemos, M.J.S. and C. Fischer. 2008. Thermal analysis of an impinging jet on a plate with and without a porous layer. *Numer. Heat Transfer, A Appl.* 54 (11): 1022–1041.

De Lemos, M.J.S. and F.T. Dórea. 2011. Simulation of a turbulent impinging jet into a layer of porous material using a two-energy equation model. *Numer. Heat Transfer, A Appl.* 59 (10): 769–798.

Dewan, A., Dutta, R., and B. Srinivasan. 2012. Recent trends in computation of turbulent jet impingement heat transfer. *Heat Transfer Eng.* 33 (4–5): 447–460.

Dórea, F. T. and M. J.S. de Lemos. 2010. Simulation of laminar impinging jet on a porous medium with a thermal non-equilibrium model. *Int. J. Heat Mass Transfer* 53: 5089–5101.

Ebadian, M.A. and C.X. Lin. 2011. A review of high-heat-flux heat removal technologies. *ASME J. Heat Transfer* 133 (11): 110801.

Ejlali, A., Ejlali, A., Hooman, K., and H. Gurgenci. 2009. Application of high porosity metal foams as air-cooled heat exchangers to high heat load removal systems. *Int. Commun. Heat Mass Transfer* 36 (7): 674–679.

Fischer, C. and M.J.S. de Lemos. 2010. A turbulent impinging jet on a plate covered with a porous layer. *Numer. Heat Transfer, A Appl.* 58 (6): 429–456.

Fu, W.S. and H.C. Huang. 1997. Thermal performances of different shape porous blocks under an impinging jet. *Int. J. Heat Mass Transfer* 40: 2261–2272.

Fu, W.-S. and H.-C. Huang. 1999. Effects of a random porosity model on heat transfer performance of porous media. *Int. J. Heat Mass Transfer* 42 (1): 13–25.

Graminho, D.R. and M.J.S. De Lemos. 2008. Laminar confined impinging jet into a porous layer. *Numer. Heat Transfer, A Appl.* 54 (2): 151–177.

Graminho, D.R. and M.J.S. de Lemos. 2009. Simulation of turbulent impinging jet into a cylindrical chamber with and without a porous layer at the bottom. *Int. J. Heat Mass Transfer* 52 (3–4): 680–693.

Han, B. and R.J. Goldstein. 2001. Jet-impingement heat transfer in gas turbine systems. *Ann. N. Y. Acad. Sci.* 934: 147–161.

Harmand, S., Pellé, J., Poncet, S., and I.V. Shevchuk. 2013. Review of fluid flow and convective heat transfer within rotating disk cavities with impinging jet. *Int. J. Therm. Sci.* 67: 1–30.

Hwang, M.-L. and Y.-T. Yang. 2012. Numerical simulation of turbulent fluid flow and heat transfer characteristics in metallic porous block subjected to a confined slot jet. *Int. J. Therm. Sci.* 55: 31–39.

Jaluria, Y. and Torrance, K. E., 2001. *Computational Heat Transfer*, 2nd edn. Washington, DC: Taylor & Francis.

Jambunathan, K., Lai, E., Moss, M.A., and B.L. Button. 1992. A review of heat transfer data for single circular jet impingement. *Int. J. Heat Fluid Flow* 13 (2): 106–115.

Jeng, T.-M. and S.-C. Tzeng. 2005. Numerical study of confined slot jet impinging on porous metallic foam heat sink. *Int. J. Heat Mass Transfer* 48: 4685–4694.

Jeng, T.-M. and S.-C. Tzeng. 2007. Experimental study of forced convection in metallic porous block subject to a confined slot jet. *Int. J. Therm. Sci.* 46 (12): 1242–1250.

Jeng, T.-M. and S.-C. Tzeng. 2008. Height effect on heat transfer characteristics of sintered porous blocks with a confined slot jet. *Int. Commun. Heat Mass Transfer* 35: 30–38.

Jeng, T.-M., Tzeng, S.-C., and C.-W. Chang. 2010. Forced convection of the brass-beads packed bed situated in a vertical oncoming flow. *Int. J. Therm. Sci.* 49 (5): 829–837.

Jeng, T.-M., Tzeng, S.-C., and X.-Y. Huang. 2012. Numerical study of impinging cooling of a porous block under a straightening or non-straightening jet flow. *Numer. Heat Transfer, A Appl.* 61 (7): 502–526.

Jeng, T.-M., Tzeng, S.-C., Su, H.-M., Hsiao, C.-S., and Y.-C. Wei. 2013. Heat transfer characteristics of a rotating Al-foam cylinder under the confined/unconfined impinging jet. *Int. J. Therm. Sci.* 66: 71–81.

Kim, S.Y., Koo, J.-M., and A.V. Kuznetsov. 2001. Effect of anisotropy in permeability and effective thermal conductivity on thermal performance of an aluminum foam heat sink. *Numer. Heat Transfer, A Appl.* 40 (1): 21–36.

Kim, S.Y. and A.V. Kuznetsov. 2003. Optimization of pin-fin heat sinks using anisotropic local thermal non-equilibrium porous model in a jet impinging channel. *Numer. Heat Transfer, A Appl.* 44 (8): 771–787.

Lee, D.Y. and K. Vafai. 1999. Analytical characterization and conceptual assessment of solid and fluid temperature differentials in porous media. *Int. J. Heat Mass Transfer* 42: 423–435.

Lindeman, B.A. and T.A. Shedd. 2013. Comparison of empirical correlations and a two-equation predictive model for heat transfer to arbitrary arrays of single-phase impinging jets. *Int. J. Heat Mass Transfer* 66: 772–780.

Marafie, A., Khanafer, K., Al-Azmi, B., and K. Vafai. 2008. Non-Darcian effects on the mixed convection heat transfer in a metallic porous block with a confined slot jet. *Numer. Heat Transfer, A Appl.* 54 (7): 665–685.

Martin, H. 1977. Heat and mass transfer between impinging gas jets and solid surfaces. *Adv. Heat Transfer* 13 (C): 1–60.

Molana, M. and S. Banooni. 2013. Investigation of heat transfer processes involved liquid impingement jets: A review. *Braz. J. Chem. Eng.* 30 (3): 413–435.

Nield, D. A. and A. Bejan. 2006. *Convection in Porous Media*, 3rd edn. New York: Springer Science.

Paek, J.W., Kim, S.Y., and B.H. Kang. 2001. Heat transfer enhancement by impinging air jet on porous surfaces. *Proc. Natl. Heat Transfer Conf.* 2: 1227–1233.

Patankar, S.V. 1980. *Numerical Heat Transfer and Fluid Flow*. New York: McGraw-Hill.

Polat, S., Huang, B., Majumdar, A.S., and W.J.M. Douglas. 1989. Numerical flow and heat transfer under impinging jets: A review. *Annu. Rev. Heat Transfer* 2: 157–197.

Prakash, M., Turan, O.F., Li, Y., Mahoney, J., and G.R. Thorpe. 2001a. Impinging round jet studies in a cylindrical enclosure with and without a porous layer: Part I—Flow visualizations and simulations. *Chem. Eng. Sci.* 56: 3855–3878.

Prakash, M., Turan, O.F., Li, Y., Mahoney, J., and G.R. Thorpe. 2001b. Impinging round jet studies in a cylindrical enclosure with and without a porous layer: Part II—LDV measurements and simulations. *Chem. Eng. Sci.* 56: 3879–3892.

Rallabandi, A.P., Rhee, D.-H., Gao, Z., and J.-C. Han. 2010. Heat transfer enhancement in rectangular channels with axial ribs or porous foam under through flow and impinging jet conditions. *Int. J. Heat Mass Transfer* 53 (21–22): 4663–4671.

Roache, J.P. 1998. *Fundamentals of Computational Fluid Dynamics*. Albuquerque, NM: Hermosa.

Saeid, N.H. 2007. Jet impingement interaction with cross flow in horizontal porous layer under thermal non-equilibrium conditions. *Int. J. Heat Mass Transfer* 50: 4265–4274.

Saeid, N.H. and A.A. Mohamad. 2006. Jet impingement cooling of a horizontal surface in a confined porous medium: Mixed convection regime. *Int. J. Heat Mass Transfer* 49: 3906–3913.

Sarkar, A., Nitin, N., Karwe, M.V., and R.P. Singh. 2004. Fluid flow and heat transfer in air jet impingement in food processing. *J. Food Sci.* 69 (4): CRH113–CRH122.

Shih, W.H., Chou, F.C., and W.H. Hsieh. 2007. Experimental investigation of the heat transfer characteristics of aluminum-foam heat sinks with restricted flow outlet. *ASME J. Heat Transfer* 129: 1554–1563.

Sivasamy, A., Rajesh Kanna, P., and V. Selladurai. 2011. Jet impingement cooling of a horizontal surface in an unconfined porous medium: Mixed convection regime. *Int. J. Heat Mass Transfer* 54: 4127–4134.

Sivasamy, A., Selladurai, V., and P. Rajesh Kanna. 2010a. Jet impingement cooling of a constant heat flux horizontal surface in a confined porous medium: Mixed convection regime. *Int. J. Heat Mass Transfer* 53: 5847–5855.

Sivasamy, A., Selladurai, V., and P. Rajesh Kanna. 2010b. Mixed convection on jet impingement cooling of a constant heat flux horizontal porous layer. *Int. J. Therm. Sci.* 49: 1238–1246.

Sultan, K., DeGroot, C.T., Straatman, A.G., Gallego, N.C., and H. Hangan. 2009. Thermal characterization of porous graphitic foam—Convection in impinging flow. *Int. J. Heat Mass Transfer* 52: 4296–4301.

Torrance, K.E. 1985. Numerical methods in heat transfer. In *Handbook of Heat Transfer-Fundamentals*, eds. W.H. Rohsenow, J.P. Hartnett, and E.N. Ganic, New York: McGraw-Hill.

Viskanta, R. 1993. Heat transfer to impinging isothermal gas and flame jets. *Exp. Therm. Fluid Sci.* 6 (2): 111–134.

Webb, B.W. and C.-F. Ma. 1995. Single-phase liquid jet impingement heat transfer. *Adv. Heat Transfer* 26 (C): 105–217.

Whitaker, S. 1999. *The Method of Volumetric Averaging*. Dordrecht, the Netherlands: Kluwer Academic Publishers.

Wong, K.C. 2012. Thermal analysis of a metal foam subject to jet impingement. *Int. Commun. Heat Mass Transfer* 39: 960–965.

Wong, K.-C. and N.H. Saeid. 2009a. Numerical study of non-Darcian effects on jet impingement cooling in a horizontal porous layer in the mixed convection regime. *Int. Commun. Heat Mass Transfer* 36 (1): 45–50.

Wong, K.-C. and N.H. Saeid. 2009b. Numerical study of mixed convection on jet impingement cooling in a horizontal porous layer-using Brinkman-extended Darcy model. *Int. J. Therm. Sci.* 48: 96–104.

Wong, K.-C. and N.H. Saeid. 2009c. Numerical study of mixed convection on jet impingement cooling in an open cavity filled with porous medium. *Int. Commun. Heat Mass Transfer* 36: 155–160.

Wong, K.-C. and N.H. Saeid. 2009d. Numerical study of mixed convection on jet impingement cooling in a horizontal porous layer under local thermal non-equilibrium conditions. *Int. J. Therm. Sci.* 48: 860–870.

Wong, K.-C. and N.H. Saeid. 2009e. Jet impingement cooling of a finite thickness solid layer conjugated with porous medium. *Numer. Heat Transfer A, Appl.* 55 (7): 706–720.

Wong, K.-C. and N.H. Saeid. 2009f. Unsteady mixed convection of a confined jet in a fluid-superposed high porosity medium. *Numer. Heat Transfer A, Appl.* 56 (10): 827–845.

Wong, K.-C., Saeid, N.H., and C.S. Tan. 2009. Visualization of mixed convective rolls of a slot jet in a fluid-superposed metallic porous foam heated from below. *Numer. Heat Transfer A, Appl.* 56 (1): 20–41.

Wu, P.-S., Hsieh, C.-Y., and S.-T. Tsai. 2010. Heat transfer enhancement of jet impingement on a flat plate attached by a porous medium with a center cavity. *Defect Diffus. Forum* 297–301: 427–432.

Wu, P.S., Lo, Y.W., and F.C. Cheng. 2011. Numerical investigation of impingement heat transfer enhancement on a flat plate with an attached porous medium. *Defect Diffus. Forum* 312–315: 477–482.

Yakkatelli, R., Wu, Q., and A.S. Fleischer. 2010. A visualization study of the flow dynamics of a single round jet impinging on porous media. *Exp. Therm. Fluid Sci.* 34 (8): 1008–1015.

Zhang, H.J. and Z.P. Zou. 2012. Investigation of a confined laminar impinging jet on a plate with a porous layer using the preconditioned density-based algorithm. *Numer. Heat Transfer A, Appl.* 61 (4): 241–267.

Zuckerman, N. and N. Lior. 2006. Jet impingement heat transfer: Physics, correlations, and numerical modeling. *Adv. Heat Transfer* 39 (C): 565–631.

20 Thermohydromechanical Behavior of Poroelastic Media

A. P. S. Selvadurai

CONTENTS

20.1 Introduction 663
20.2 Thermohydromechanical Modeling and Governing Equations 665
20.3 One-Dimensional Problems in Thermoporoelasticity 671
20.3.1 Axial Loading and Boundary Heating of the 1D Element 671
20.3.2 Thermomechanical Problem: Formulation 673
20.3.3 Hydromechanical Problem 675
20.3.4 Hydromechanical Problem: The Effect of Solid Phase and Fluid Compressibility 677
20.3.5 Thermohydromechanical Problem: Formulation 679
20.3.6 Thermohydromechanical Problem: The Effects of Solid Phase and Fluid Phase Compressibility 684
20.3.7 Thermohydromechanical Problem: Numerical Results 686
20.3.8 Thermohydromechanical Problem: Computational Estimates 688
20.4 Spherically Symmetric Problems in Thermoporoelasticity 694
20.4.1 Boundary Heating of a Poroelastic Sphere 695
20.4.2 Computational Results for the Boundary Heating of a Poroelastic Sphere 697
20.5 Concluding Remarks 703
Nomenclature 703
Disclaimer 705
Acknowledgments 705
References 705

20.1 INTRODUCTION

The classical problem in geomechanics dealing with the stress-induced isothermal flow of a fluid through a deformable porous medium, usually referred to as the process of soil consolidation, is a cornerstone in the development of the subject of *soil mechanics* and is generally regarded as the start of multiphasic treatment of the mechanics of porous media. Although the development of the theory of 1D soil consolidation is generally attributed to Terzaghi [1], the important contributions of others, Fillunger [2] in particular, are now being recognized [3,4]. The 1D theory certainly provides an explanation of the processes involved in soil consolidation but does not constitute a formal theory. The formal theory of isothermal soil consolidation presented by Biot [5] is a generalization of the 1D theory to three dimensions. This is a complete theory, which is rigorous in the sense of a continuum formulation applicable to a medium with voids. It is also an elegantly simple theory that continues to flourish after seven decades. The theory employs linear elasticity to characterize the mechanical behavior of the porous skeleton, and Darcy's law governs fluid flow through the accessible porous space. Extensive expositions of both the fundamental aspects of Biot's theory of isothermal poroelasticity and its applications to the analytical solution of problems in geomechanics are documented by Mandel [6], de Josselin de Jong [7], McNamee and Gibson [8],

Cryer [9], de Wiest [10], Agbezuge and Deresiewicz [11], Gaszynski and Szefer [12], Chiarella and Booker [13], Rice and Cleary [14], Booker and Small [15,16], Booker and Randolph [17], Bear and Corapcioglu [18], Whitaker [19–21], Kassir and Xu [22], Ehlers [23], de Boer and Ehlers [24], Atkinson and Craster [25], Detournay and Cheng [26], Selvadurai and Yue [27], Yue and Selvadurai [28,29], Lan and Selvadurai [30], Oyen [31], and Galli and Oyen [32]. The volumes by Coussy [33], Selvadurai [34], Cheng et al. [35], Thimus et al. [36], Lewis and Schrefler [37], Drew and Passman [38], Wang [39], de Boer [3], and Verruijt [40] also give recent advances in the applications of Biot's theory. These references, along with the review articles by Scheidegger [41], Paria [42], Schiffman [43], Selvadurai [44], and Cowin [45], inter alia, contain a significant number of references to further work concerning the application of Biot's classical theory of 3D poroelasticity, via both analytical and computational modeling, to a wide range of problems in environmental geosciences, geomechanics, biomechanics, materials science, and materials engineering. The classical theory of isothermal poroelasticity is now firmly established in terms of the formulation of the governing equations and the availability of relevant existence and uniqueness theorems [46]. An alternative to Biot's approach to the formulation of the governing equations uses developments based on the continuum theory of mixtures; examples of these are given by Bowen [47,48], Green and Naghdi [49], Green and Steel [50], Crochet and Naghdi [51], Crochet [52], Mills and Steel [53], Atkin and Craine [54], Bedford and Drumheller [55,56], Drumheller [57], Bennethum and Cushman [58], Coussy [33], Murad et al. [59], Gajo [60], Rajagopal and Tao [61], and Dell'Isola and Romano [62]. While the mixture theory approaches are certainly elegant and complete from the point of view of continuum formulations, there appears to be no significant advantages offered, at least from the point of view *of linearized theories of poromechanics* and their applications to the solution of initial boundary value problems in the area. The mixture theory–based formulations have advantages when dealing with nonlinear theories of material behavior, where the porous skeleton can experience large strains or large strain nonlinear viscoelastic and viscoplastic phenomena that have corresponding influences on the fluid transport problem, which is of interest to modeling living biological tissues.

The extension of Biot's classical theory of isothermal poromechanics to include nonisothermal effects has been prompted by applications to a number of areas of particular interest to energy and environmental geomechanics. The inclusion of thermal effects when considering poromechanical behavior of fluid-saturated media, particularly in the context of geomechanics, becomes important to areas such as deep geologic disposal of heat-emitting nuclear fuel wastes (Holister et al. [63], Gnirk [64], Selvadurai [65,66], Selvadurai and Nguyen [67,68], Nguyen and Selvadurai [69,70], Rutqvist et al. [71], Stephansson et al. [72], Nguyen et al. [73], Alonso et al. [74], Chijimatsu et al. [75]), frictional heating during earthquake slip along fault zones (Lachenburch [76], Mase and Smith [77,78], Aagaard et al. [79], Sulem et al. [80], Rice [81]), geothermal and ground source energy extraction and seafloor hydrothermal systems (Dickson and Fanelli [82], Duffield and Sass [83], Jupp and Schultz [84), Knellwolf et al. [85]), mechanics of freezing action in soils (Selvadurai et al. [86,87], Michałowski and Zhu [88], Gens [89]), response of rock masses containing deep geologic repositories to glaciation loadings (Selvadurai and Nguyen [90], Chan et al. [91]), and geomechanical modeling of the geologic sequestration of greenhouse gases (Rutqvist et al. [92], Selvadurai [93,94]. Vargas et al [95]). In these subject areas, the coupled processes associated with mechanical deformations of the porous skeleton, fluid movement through the accessible pore space under thermal, hydraulic, and mechanical effects, and conductive heat transfer through the saturated porous medium are necessary to examine the problem areas of practical importance. Further related studies are given by Smith and Booker [96], Jiang and Rajapakse [97], Seneviratne et al. [98], Bai and Roegiers [99], Wang and Papamichos [100], Bai and Abousleiman [101], Giraud et al. [102], Zhou et al. [103], Selvadurai [104], Wu et al. [105], and Belotserkovets and Prevost [106].

An early development in the extension of Biot's classical theory of poroelasticity to include thermal effects is due to Schiffman [107] who presented a thermoelastic theory of soil consolidation, with applications in geoenvironmental and geophysical heat transfer. The work of Brownell et al. [108] dealt with applications relevant to geothermal reservoirs and the work of Morland [109] examined the

flow of a viscous fluid through a heated porous matrix. Derski and Kowalski [110] presented the development of equations governing the linear problem of thermal consolidation. Bear and Corapcioglu [111] examined the problem of thermoelastic effects in aquifers due to injection of hot water into aquifers. The studies by Delaney [112,113] deal with the problem of heating a fluid-saturated half-space and the influence of thermohydraulic coupling on the intrusion of magma into wet rock. A mixture approach to the formulation and solution of the linearized equations governing thermoporoelasticity is given by Palciauskas and Domenico [114], and similar developments are given by McTigue [115].

20.2 THERMOHYDROMECHANICAL MODELING AND GOVERNING EQUATIONS

We consider a poroelastic material consisting of a linear elastic porous skeleton where the accessible pore space is saturated by a nonviscous liquid. The solid phase and liquid are assumed to be compressible. The porosity of the porous elastic material (i.e., the ratio of volume of the pores to the total volume) is denoted by n. Typical examples of such a porous medium are soil and rock saturated with water. For poroelastic materials, the linear elastic stress–strain relation can be expressed in terms of elastic constants of the drained skeleton or the porous skeleton without any pore fluid. Under drained conditions, the fluid is allowed to flow in and out of the accessible pore space, but in the fully drained state, the pressure remains independent of time (Rice and Cleary [14]). For example, the drained conditions can be reached when the pore fluid pressure dissipates with time and eventually becomes zero. The effective mechanical properties and effective thermal expansion coefficient of such a *drained* poroelastic medium will be equivalent to those of the porous skeleton with empty or unoccupied pores. (Note, however, that even when pressure is zero, the liquid is technically present in the pore space of the medium since the medium remains fully saturated.)

For the fully saturated isotropic, homogeneous thermoelastic poroelastic medium, under general and not necessarily drained conditions, the macroscopic stress–strain temperature relation can be written as (Rice and Cleary [14]; Savvidou and Booker [116]; Selvadurai and Nguyen, [90])

$$\sigma_{ij} = 2G_D\varepsilon_{ij} + \left(K_D - \frac{2G_D}{3}\right)\varepsilon_V\delta_{ij} - 3K_D\alpha_s T\delta_{ij} - \left(1 - \frac{K_D}{K_s}\right)p\delta_{ij} \tag{20.1}$$

where

σ_{ij} is the total Cauchy stress tensor in the porous medium referred to the Cartesian coordinate system $\mathbf{x} = (x_1, x_2, x_3)$ and Einstein's summation convention over the full range is adopted for repeated indices

ε_{ij} is the infinitesimal strain tensor of the porous skeleton, which is related to the displacement components u_i by the usual relationship (Timoshenko and Goodier [117], Davis and Selvadurai [118], Selvadurai [119])

$$\varepsilon_{ij} = \frac{1}{2}\left(u_{i,j} + u_{j,i}\right) \tag{20.2}$$

In Equation 20.1,

$\varepsilon_V = \varepsilon_{kk} = u_{i,i}$ is the volumetric strain

p is the pore fluid pressure

K_D and G_D are, respectively, the linear elastic bulk modulus and the linear elastic shear modulus of the porous skeleton under drained conditions

K_s is the bulk modulus of the solid material phase

α_s is the coefficient of linear thermal expansion of the solid phase

T is the temperature change

Notice that the absence of the thermal expansion coefficient of the fluid α_f in (20.1) does not imply that it was set to zero. All the field quantities (stresses, strains, pressure, and temperature) in Equation 20.1 are, in general, functions of coordinates x and time t. (In the analysis of specific problems, however, we shall use the simplified designations, $x_1 = x$, $x_2 = y$, and $x_3 = z$.) The last term in Equation 20.1 represents the contribution of the fluid pressure to the total stress. The multiplier in front of the pore pressure term in Equation 20.1 is referred to as the *Biot parameter*:

$$\alpha = 1 - \frac{K_D}{K_s} \tag{20.3}$$

If the solid phase is locally incompressible, $K_D \ll K_s$ and the Biot parameter $\alpha = 1 - K_D/K_s \approx 1$. However, this assumption may not be valid if the porosity n is small, even if the solid phase compressibility is small. It can be shown that the Biot parameter must lie within the bounds $n \leq \alpha \leq 1$ (Lydzba and Shao [120]). These bounds can be obtained from the bounds on the effective bulk modulus K_D. Usually, the value of porosity in a geomaterial does not exceed 0.20–0.25.

The total stress in Equation 20.1 can be considered as the sum of the effective Cauchy stress term $\tilde{\sigma}_{ij}$ and a second term that accounts for the fluid pressure. The effective stress is the stress supported by the porous skeleton, and it is defined as

$$\tilde{\sigma}_{ij} = 2G_D\varepsilon_{ij} + \left(K_D - \frac{2G_D}{3}\right)\varepsilon_V\delta_{ij} - 3K_D\alpha_s T\delta_{ij} \tag{20.4}$$

To obtain the first governing equation, the equations of equilibrium and the strain-displacement relations must be used. In the absence of body forces and inertia effects, the equation of equilibrium is

$$\sigma_{ij,j} = 0 \tag{20.5}$$

where the comma denotes the partial derivative with respect to the spatial variable.

Substitution of Equation 20.1 into the equilibrium equation (Equation 20.5) and the use of Equation 20.2 leads to the governing equation

$$\left(K_D + \frac{G_D}{3}\right)u_{k,ki} + G_D u_{i,kk} - K_D 3\alpha_s T_{,i} - \left(1 - \frac{K_D}{K_s}\right)p_{,i} = 0 \tag{20.6}$$

The unknown variables here are the displacement components u_i, the pore fluid pressure p, and the temperature T.

The second governing equation can be derived from Darcy's law and the void occupancy equation. The latter can be written as

$$-n\frac{\Delta m_f}{m_f} + \left(1 - \frac{K_D}{K_s}\right)\varepsilon_V + n\frac{p}{K_f} + \left(1 - \frac{K_D}{K_s} - n\right)\frac{p}{K_s} = n3\alpha_f T + \left(1 - \frac{K_D}{K_s} - n\right)3\alpha_s T \tag{20.7}$$

where

K_f, K_s are the bulk moduli of the fluid and solid phases, respectively
α_f, α_s are the linear thermal expansion coefficients of the fluid and solid phase
n is the porosity
Δm_f is the change in the fluid mass m_f in a small volume

The relation between the change in the fluid mass and the fluid velocity is

$$\frac{\Delta m_f}{m_f} = -\int_0^t v_{k,k}\, dt \tag{20.8}$$

where v_l is the component of the fluid velocity vector. By differentiating Equation 20.8 and multiplying the expression by the porosity, we obtain

$$n\frac{\partial}{\partial t}\left(\frac{\Delta m_f}{m_f}\right) = -nv_{k,k}$$

Thus, differentiation of the void occupancy equation (Equation 20.7) with respect to time gives

$$-nv_{k,k} = \left(1-\frac{K_D}{K_s}\right)\frac{d\varepsilon_V}{dt} + \frac{n}{K_f}\frac{\partial p}{\partial t} + \left(1-\frac{K_D}{K_s}-n\right)\frac{1}{K_s}\frac{\partial p}{\partial t} - n3\alpha_f\frac{\partial T}{\partial t} - \left(1-\frac{K_D}{K_s}-n\right)3\alpha_s\frac{\partial T}{\partial t} \tag{20.9}$$

In this chapter, attention is restricted to porous media that are also hydraulically isotropic, and thus Darcy's law for an isotropic porous medium can be used (Verruijt [121], Bear [122], Whitaker [19], Philips [123], Ichikawa and Selvadurai [124]), although the discussions can be extended to accommodate hydraulically transversely isotropic media (Selvadurai [125–127]) and heterogeneous media (Selvadurai and Selvadurai [128]). We have

$$nv_l = -\frac{k}{\gamma}p_{,l} \tag{20.10}$$

where

k is the permeability
$\gamma = \rho g$ is the specific weight of the fluid
v_l is the component of the fluid velocity vector

Using Darcy's law (Equation 20.10), we can derive from Equation 20.9 the second governing equation applicable to fluid flow in the porous medium as

$$\begin{aligned} &-\frac{k}{\gamma}p_{,kk} + \left(1-\frac{K_D}{K_s}\right)\frac{\partial \varepsilon_V}{\partial t} \\ &+\frac{n}{K_f}\frac{\partial p}{\partial t} + \left(1-\frac{K_D}{K_s}-n\right)\frac{1}{K_s}\frac{\partial p}{\partial t} = n3\alpha_f\frac{\partial T}{\partial t} + \left(1-\frac{K_D}{K_s}-n\right)3\alpha_s\frac{\partial T}{\partial t} \end{aligned} \tag{20.11}$$

Finally, we assume that the fluid flow velocity in the pore space and the rates of deformation of the porous skeleton generate negligible heat. Also, considering the low values of permeability associated with porous media, the mode of heat transfer is mainly by conduction, and convective heat transfer effects can be neglected. Therefore, heat transfer in the porous medium can be described by Fourier's law of heat conduction:

$$h_i = -k_c^* T_{,i} \tag{20.12}$$

where

k_c^* is the effective thermal conductivity of the porous medium
h_i is the component of the heat flux vector

Finally, the heat conduction equation constitutes the third governing equation that can be solved for the temperature change T:

$$c_p^* \frac{\partial T}{\partial t} - k_c^* T_{,kk} = 0 \tag{20.13}$$

where c_p^* is the effective specific heat of the porous medium. More complicated models for heat transfer and flow in porous media can also be incorporated (Koh et al. [129], Slattery [130], Vafai and Tien [131], Vafai [132], Vasco [133]), but these aspects are not considered in the present study.

The constitutive equations can be also written in terms of the properties of the undrained porous medium. In the undrained deformation of the porous medium, the fluid is constrained from flowing in and out, but changes in the pressure p can be induced.

Following the general form of the stress–strain relationship for the isotropic homogeneous solid body subjected to the action of volumetric eigenstrains (e.g., the eigenstrains induced by temperature change), we can express the total stress in the porous medium as

$$\sigma_{ij} = 2G_u \varepsilon_{ij} + \left(K_u - \frac{2G_u}{3} \right) \varepsilon_V \delta_{ij} - K_u 3\alpha_u^* T \delta_{ij} - Q\alpha n \frac{\Delta m_f}{m_f} \delta_{ij} \tag{20.14}$$

where

K_u and G_u are the effective bulk and shear modulus of the undrained porous medium
α_u^* is the effective thermal expansion coefficient of the undrained porous medium
$3\alpha_u^* T$ represents the effective thermal eigenstrain applied to the undrained porous medium
$\Delta m_f / m_f$ is the volumetric eigenstrain associated with a loss or gain of liquid mass Δm_f
Q is a certain factor yet unknown having a dimension of stress

To obtain the effective elastic properties of the undrained porous medium and the parameter Q appearing in Equation 20.14, we make use of the void occupancy relation given by Equation 20.7. Expressing the fluid pressure from Equation 20.7 and substituting it into the constitutive equation (Equation 20.1), we can derive the stress–strain relation

$$\sigma_{ij} = 2G_u \varepsilon_{ij} + \left(K_u - \frac{2G_u}{3} \right) \varepsilon_V \delta_{ij} - (K_u - Q\alpha n) 3\alpha_s T \delta_{ij} - Q\alpha n 3\alpha_f T \delta_{ij} - Q\alpha n \frac{\Delta m_f}{m_f} \delta_{ij} \tag{20.15}$$

and relate the bulk modulus of the undrained medium K_u to the bulk modulus under drained conditions K_D:

$$K_u = K_D + \frac{\alpha^2}{\dfrac{n}{K_f} + \dfrac{\alpha - n}{K_s}} = K_D + \alpha^2 Q \tag{20.16a}$$

$$Q = \frac{1}{\dfrac{n}{K_f} + \dfrac{\alpha - n}{K_s}} = \frac{K_f}{n + (\alpha - n)(1 - \alpha) K_f / K_D} \tag{20.16b}$$

where

K_s and K_f denote the bulk modulus of the solid phase and liquid, respectively
the parameter Q defined by (20.16b) is referred to as the Biot modulus

The shear modulus of the undrained geomaterial is equal to that of the drained porous medium, that is, $G_u = G_D$. Equation 20.16a is called Biot–Gassmann equation.

By comparing Equations 20.14 and 20.15, the effective thermal expansion coefficient of the geomaterial can be defined as

$$\alpha_u^* = K_u^{-1}[(K_u - Q\alpha n)\alpha_s + Q\alpha n\alpha_f] \tag{20.17}$$

It can be confirmed that this expression is equivalent to the alternative expression

$$\alpha_u^* = (n\alpha_f + (1-n)\alpha_s) + \left[\frac{1}{K_u} - n\frac{1}{K_f} - (1-n)\frac{1}{K_s}\right](\alpha_f - \alpha_s)/\left(\frac{1}{K_f} - \frac{1}{K_s}\right) \tag{20.18}$$

derived, for example, by Christensen [134] for a composite material consisting of two isotropic phases.

To verify Equation 20.17 or Equation 20.18, we can see that, when the porosity is equal to zero, $n = 0$, $\alpha_u^* = \alpha_s$, which is the expected result. Also, when the thermal expansion coefficients of the phases are equal, that is, $\alpha_s = \alpha_f$, then regardless of elastic moduli of the phases, the effective thermal expansion coefficient $\alpha_u^* = \alpha_s = \alpha_f$. It is worth noting that the effective thermal expansion coefficient of the porous medium under drained conditions α_D^* (i.e., when the stiffness of the pores is zero) is simply equal to α_s. This result can be obtained from Equation 20.18 by replacing the bulk modulus of the undrained material K_u with the bulk modulus of the drained porous material K_D (not even necessary) and letting the fluid bulk modulus $K_f \to 0$.

The effective specific heat appearing in the heat conduction Equation 20.13 can be obtained in the form

$$c_{eq}^* = \left[n\rho_f c_f + (1-n)\rho_s c_s\right] + 9T_0\left(\frac{1}{K_u} - \frac{n}{K_f} - \frac{1-n}{K_s}\right)\frac{(\alpha_f - \alpha_s)^2}{\left(\frac{1}{K_f} - \frac{1}{K_s}\right)^2} \tag{20.19}$$

where

c_f and c_s are the specific heat of the fluid phase and the solid phase
ρ_f and ρ_s are their densities
T_0 is the base temperature in Kelvin

Usually, however, an average of the phase-specific heats, that is, the first bracketed term on the right of Equation 20.19, is a very good approximation to the effective specific heat c_{eq}^*.

The partial differential equations governing thermohydromechanical (THM) phenomena in the fluid-saturated porous medium are Equations 20.6, 20.11, and 20.13 for the displacement components $u_i(\mathbf{x}, t)$, the pore fluid pressure $p(\mathbf{x}, t)$, and the temperature $T(\mathbf{x}, t)$ (Biot [5], Savvidou and Booker [116], Detournay and Cheng [26], Selvadurai and Nguyen [90], Selvadurai [135], Dell'Isola et al. [136], Verruijt [40]). These equations are weakly coupled in the sense that the temperature field in the porous medium can be solved independent of the displacement components and pressure field, once the initial value problem for the temperature is formulated. Also, Equation 20.6 reduces to the Navier equations for deformations of a purely elastic material when the influences of temperature and pressure are ignored. Similarly, Equation 20.11 reduces to the pressure diffusion or piezoconduction equation when the effects of deformability of the porous skeleton and temperature are ignored. Also, when the permeating fluid is incompressible and in the absence of deformability and thermal effects of the porous medium, the piezoconduction equation reduces to

the well-known Laplace equation. For the solution of the governing partial differential equations, appropriate boundary and initial conditions must be prescribed. For the deformations of the porous medium, traction and displacement boundary conditions can be prescribed on respective regions S_d^M and S_t^M of the body B, with surface $S = S_d^M \cup S_t^M$, that is,

$$u_i(\mathbf{x}, t) = u_i^0; \quad \mathbf{x} \in S_d^M \tag{20.20}$$

$$\sigma'_{ij}(\mathbf{x}, t) n_j = t_i^0; \quad \mathbf{x} \in S_t \tag{20.21}$$

where u_i^0 and t_i^0 are generally specified as functions of position and time. Also in the absence of moving boundaries in the prescription of the mechanical and kinematic conditions, $S_d^M \cap S_t^M = 0$; since we shall focus attention on purely quasi-static problems governing THM phenomena, the initial conditions for the displacement field should correspond to $u_i(\mathbf{x}, t = 0) = u_i^0(\mathbf{x})$, where $u_i^0(\mathbf{x})$ can be identified with solutions applicable to the undrained thermoelastic problem.

The boundary conditions governing the pressure field are prescribed in relation to either Dirichlet boundary conditions applied on surface S_D^p or Neumann (or Robin) boundary conditions prescribed on S_N^p:

$$p(\mathbf{x}, t) = f_D^0(\mathbf{x}, t); \quad \mathbf{x} \in S_D^p \tag{20.22}$$

$$\frac{\partial p(\mathbf{x}, t)}{\partial n} = f_N^0(\mathbf{x}, t); \quad \mathbf{x} \in S_N^p \tag{20.23}$$

where $f_D^0(\mathbf{x}, t)$ and $f_N^0(\mathbf{x}, t)$ are prescribed functions of position and time, $\partial/\partial n$ denotes the derivative in the direction of the outward normal vector to the appropriate surface (Selvadurai [137]).

The surfaces on which the Dirichlet and Neumann pore fluid pressure boundary conditions are prescribed satisfy $S = S_D^p \cup S_N^p$. In the absence of moving boundaries in the pore pressure field, $S_D^p \cap S_N^p = 0$. The initial condition governing the pore pressure field can be specified as

$$p(\mathbf{x}, 0) = p^0(\mathbf{x}) \tag{20.24}$$

where $p^0(\mathbf{x})$ is a specified initial pore pressure field. The boundary conditions governing the temperature field can be prescribed in a similar manner. Either Dirichlet or Neumann (or Robin) boundary conditions are prescribed on S_D^T and S_N^T, respectively, that is,

$$T(\mathbf{x}, t) = g_D^0(\mathbf{x}, t); \quad \mathbf{x} \in S_D^T \tag{20.25}$$

$$\frac{\partial T(\mathbf{x}, t)}{\partial n} = g_N^0(\mathbf{x}, t); \quad \mathbf{x} \in S_N^T \tag{20.26}$$

where $g_D^0(\mathbf{x}, t)$ and $g_N^0(\mathbf{x}, t)$ are prescribed functions of position and time.

The surfaces on which the Dirichlet and Neumann temperature boundary conditions are prescribed satisfy $S = S_D^T \cup S_N^T$. In the absence of moving boundaries in the temperature field, $S_D^T \cap S_N^T = 0$. The initial condition governing the temperature field can be specified as

$$T(\mathbf{x},0) = T^0(\mathbf{x}) \tag{20.27}$$

where $T^0(\mathbf{x})$ is a prescribed initial temperature field.

20.3 ONE-DIMENSIONAL PROBLEMS IN THERMOPOROELASTICITY

It is instructive to develop solutions to 1D problems relevant to the THM problems; these are used as the first-stage benchmarks for the validation of computational schemes that can be applied for the solution of more complex initial boundary value problems of practical interest, which cannot be directly solved using analytical approaches. While the 1D solution can be developed to accommodate full THM modeling, it is instructive and convenient to consider separate situations where the 1D element is subjected to a combination of external stresses, temperatures, and pore fluid pressures. For the purposes of developing the 1D solution, we consider a state of deformation that is independent of the spatial coordinates x_1 and x_3, and we also assume that this *column* is allowed to deform only in the vertical direction, along the axis x_1 or x where $x \in (0, L)$, but laterally constrained in the x_2 (or y) and x_3 (or z) directions, that is,

$$u_y(x) = u_z(x) = 0 \quad x \in (0,L) \tag{20.28}$$

20.3.1 Axial Loading and Boundary Heating of the 1D Element

We consider the problem of a 1D poroelastic material that is restrained from movement at the location $x = L$, as shown in Figure 20.1, and subjected to an axial stress and boundary heating at the location $x = 0$. One boundary of the element is hydraulically impervious and the other boundary is free draining. Similarly, the boundary $x = L$ is thermally insulated and the boundary $x = 0$ is subjected to heating. The boundary conditions applicable to the problem are as follows:

$$u_x(L,t) = 0 \tag{20.29}$$

$$\sigma_{xz}(0,t) = \sigma_{xy}(0,t) = 0 \tag{20.30}$$

$$\sigma_{xx}(0,t) = \sigma_0 \tag{20.31}$$

$$p(0,t) = 0 \tag{20.32}$$

$$\left(\frac{k}{\gamma}\frac{\partial p}{\partial x}\right)_{x=L} = 0 \tag{20.33}$$

$$\left(k_{eq}^{*}\frac{\partial T}{\partial x}\right)_{x=L} = 0 \tag{20.34}$$

$$T(0,t) = \bar{T}_0 \tag{20.35}$$

where σ_0 and $\bar{T}_0$ are prescribed values of the constant normal stress and the constant temperature on the upper surface ($x = 0$) of the 1D element (Figure 20.1).

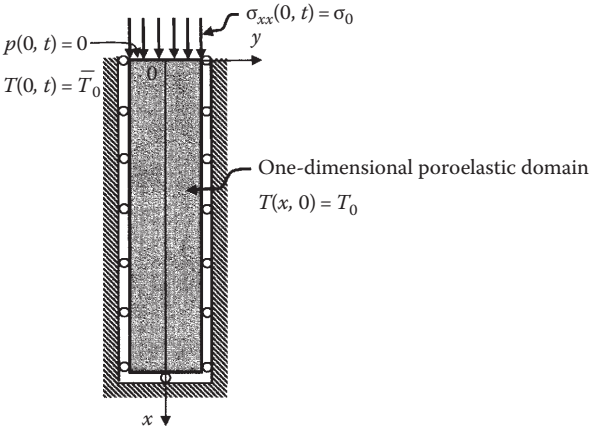

FIGURE 20.1 One-dimensional element of the poroelastic material subjected to temperature rise and surface tractions.

The initial conditions applicable to the problem are

$$p(x,0) = p_0 \tag{20.36}$$

$$T(x,0) = T_0 \tag{20.37}$$

where

p_0 is the initial pressure

T_0 is the prescribed initial temperature within the column

The analytical solution can be easily found for this type of problem (see, e.g., Selvadurai [137]), as shown in the following. The initial conditions given in Equations 20.36 and 20.37 are not unrealistic; the uniform temperature change and pressure inside the poroelastic medium can be reached in the long term in the 1D column subjected to the following auxiliary boundary and initial conditions:

$$u_x(L,0) = 0 \tag{20.29a}$$

$$\sigma_{xz}(0,t) = \sigma_{xy}(0,t) = 0 \tag{20.30a}$$

$$\sigma_{xx}(0,t) = 0 \tag{20.31a}$$

$$\left(\frac{k}{\gamma}\frac{\partial p}{\partial x}\right)_{x=0} = 0 \tag{20.32a}$$

$$\left(\frac{k}{\gamma}\frac{\partial p}{\partial x}\right)_{x=L} = 0 \tag{20.33a}$$

$$\left(k^*_{eq}\frac{\partial T}{\partial x}\right)_{x=L} = 0 \tag{20.34a}$$

$$T(0,t) = T_0 \tag{20.35a}$$

$$p(x,0) = 0 \tag{20.36a}$$

$$T(x,0) = 0 \tag{20.37a}$$

Here, the initial pressure and temperature change are zero. In Equation 20.35a, the temperature change at the upper surface is prescribed as equal to T_0. In the long term, the temperature becomes equal to T_0 everywhere within the 1D element, which is consistent with the initial condition Equation 20.37. The velocities of the fluid at both the upper and lower surfaces are taken equal to zero so that the nonzero value of the fluid pressure p could be reached in the long term as a result of heating. The axial stress in the auxiliary problems has been set to zero. Once the steady state of the auxiliary problem Equations 20.29a through 20.37a has been reached, one can modify the boundary conditions and prescribe zero pressure (Equation 20.32), temperature change (Equation 20.35), and the stress σ_0 (Equation 20.31) at the upper surface.

20.3.2 Thermomechanical Problem: Formulation

We first examine a thermomechanical (TM) problem in which the effect of fluid pressure on the constitutive equations is ignored. Thus, the constitutive relation Equation 20.1 can be written as

$$\sigma_{ij} = 2G_D\varepsilon_{ij} + \left(K_D - \frac{2G_D}{3}\right)\varepsilon_V\delta_{ij} - 3K_D\alpha_s T\delta_{ij} \tag{20.38}$$

Consequently, the governing equations are

$$\left(K_D + \frac{G_D}{3}\right)u_{k,ki} + G_D u_{i,kk} - K_D 3\alpha_s T_{,i} = 0 \tag{20.39}$$

$$c_p^* \frac{\partial T}{\partial t} - k_c^* T_{,kk} = 0 \tag{20.40}$$

Since the problem is 1D, Equations 20.38 through 20.40 can be reduced to

$$\sigma_{xx} = \left(K_D + \frac{4G_D}{3}\right)u_{x,x} - 3K_D\alpha_s T \tag{20.41}$$

$$\left(K_D + \frac{4G_D}{3}\right)u_{x,xx} - K_D 3\alpha_s T_{,x} = 0 \tag{20.42}$$

$$c_p^* \frac{\partial T}{\partial t} - k_c^* T_{,xx} = 0 \tag{20.43}$$

We assume that the temperature change on the upper surface is zero:

$$T(0,t) = \bar{T}_0 = 0$$

(Note that the equations designated [...] have been defined previously, but are listed here for clarity and completeness and for the convenience of the reader.) The initial temperature within the thermoelastic region is T_0, that is,

$$T(x,0) = T_0$$

The temperature field satisfying the equation for heat conduction given by Equation 20.43, and the boundary conditions (Equations 20.34 and 20.35), and the initial condition (Equation 20.37) is given by

$$T(x,t) = T_0 \sum_{m=1,3,5} \frac{4}{m\pi} \sin\left(\frac{m\pi}{2L}x\right) \exp(-\kappa_m^2 t); \quad \kappa_m^2 = \frac{m^2\pi^2}{4L^2}\frac{k_c^*}{c_p^*} \tag{20.44}$$

If the upper surface is stress-free,

$$\sigma_{xx}(0,t) = 0$$

From Equations 20.41 and 20.42, it follows that $\sigma_{xx,x} = 0$, and hence, the stress σ_{xx} is zero in the entire column. Then, from Equation 20.41, the strain is

$$u_{x,x} = \varepsilon_{xx} = \varepsilon_V = \frac{K_D 3\alpha_s T}{K_D + \frac{4}{3}G_D} \tag{20.45}$$

The axial displacement is given by

$$u_x = \int \frac{K_D 3\alpha_s T}{K_D + 4G_D/3}\,dx + U \tag{20.46}$$

and the constant of integration U can be found from the boundary condition

$$u_x(L,t) = 0$$

After substituting the temperature field given by Equation 20.44 into Equation 20.46, the vertical displacement can be obtained in the form

$$u_x(x,t) = \frac{1}{K_D + 4G_D/3}\left[-K_D 3\alpha_s T_0 \sum_{m=1,3,5\ldots} \frac{8L}{m^2\pi^2}\cos\left(\frac{m\pi}{2L}x\right)\exp(-\kappa_m^2 t)\right] \tag{20.47}$$

Since

$$\sum_{m=1,3,5,} \frac{8L}{m^2\pi^2} = L$$

the initial displacement in the 1D element is given by

$$u_x(x,0) = \frac{L}{K_D + 4G_D/3}\left(1 - \frac{x}{L}\right)[-K_D 3\alpha_s T_0] \tag{20.48}$$

20.3.3 Hydromechanical Problem

We consider the poroelasticity problem that accounts for only hydromechanical (HM) coupling and neglects the influence of the temperature field (i.e., $T(x, t) \equiv 0$). Thus, the constitutive relationship given by Equation 20.1 can be written as

$$\sigma_{ij} = 2G_D\varepsilon_{ij} + \left(K_D - \frac{2G_D}{3}\right)\varepsilon_V\delta_{ij} - \left(1 - \frac{K_D}{K_s}\right)p\delta_{ij} \tag{20.49}$$

The governing equations are

$$\left(K_D + \frac{G_D}{3}\right)u_{k,ki} + G_D u_{i,kk} - \left(1 - \frac{K_D}{K_s}\right)p_{,i} = 0 \tag{20.50}$$

$$-\frac{k}{\gamma}p_{,kk} + \left(1 - \frac{K_D}{K_s}\right)\frac{\partial\varepsilon_V}{\partial t} + \frac{n}{K_f}\frac{\partial p}{\partial t} + \left(1 - \frac{K_D}{K_s} - n\right)\frac{1}{K_s}\frac{\partial p}{\partial t} = 0 \tag{20.51}$$

Due to the 1D nature of the problem, Equations 20.45 through 20.47 can be reduced to

$$\sigma_{xx} = \left(K_D + \frac{4G_D}{3}\right)u_{x,x} - \left(1 - \frac{K_D}{K_s}\right)p \tag{20.52}$$

$$\left(K_D + \frac{4G_D}{3}\right)u_{x,xx} - \left(1 - \frac{K_D}{K_s}\right)p_{,x} = 0 \tag{20.53}$$

$$-\frac{k}{\gamma}p_{,xx} + \left(1 - \frac{K_D}{K_s}\right)\frac{\partial u_{x,x}}{\partial t} + \frac{n}{K_f}\frac{\partial p}{\partial t} + \left(1 - \frac{K_D}{K_s} - n\right)\frac{1}{K_s}\frac{\partial p}{\partial t} = 0 \tag{20.54}$$

Assume that the tractions applied on the upper surface of the 1D element are equivalent to a constant stress σ_0:

$$\sigma_{xx}(0, t) = \sigma_0$$

From Equations 20.52 and 20.53, it follows that $\sigma_{22,2} = 0$, and hence the total stress σ_{22} is uniform and equal to σ_0 for all points within the 1D element.

Considering Equation 20.48, the strain within the 1D element is

$$\varepsilon_{xx}(x, t) = u_{x,x} = \frac{1}{K_D + \frac{4}{3}G_D}\left[\sigma_0 + \left(1 - \frac{K_D}{K_s}\right)p\right] \tag{20.55}$$

Substitution of this strain into the governing Equation 20.48 leads to the partial differential equation for the pressure

$$-\frac{k}{\gamma}p_{,xx} + \left[\frac{n}{K_f} + (\alpha - n)\frac{1}{K_s} + \frac{\alpha^2}{K_D + \frac{4}{3}G_D}\right]\frac{\partial p}{\partial t} = 0 \tag{20.56}$$

The fluid can flow freely in and out through the upper surface, and thus the pressure on the upper surface $x = 0$ is taken as equal to zero, that is,

$$p(0, t) = 0$$

The fluid velocity is set equal to zero at the lower surface of the element $x_2 = L$, that is,

$$\left(\frac{k}{\gamma}\frac{\partial p}{\partial x}\right)_{x=L} = 0$$

The solution of Equation 20.56 that satisfies these boundary conditions is given in standard texts on diffusion problems and partial differential equations (see, e.g., Sneddon [138,139], Carslaw and Jaeger [140], Selvadurai [137]) and takes the form

$$\begin{aligned} p(x,t) &= \sum_{m=1,3,5} C_m \sin\left(\frac{m\pi}{2L}x\right)\exp(-\omega_m^2 t); \\ \omega_m^2 &= \frac{k}{\gamma}\frac{m^2\pi^2}{4L^2}\frac{K_D + \dfrac{4}{3}G_D}{\left(\dfrac{n}{K_f} + (\alpha - n)\dfrac{1}{K_s}\right)\left(K_D + \dfrac{4}{3}G_D\right) + \alpha^2} \end{aligned} \tag{20.57}$$

The unknown constants C_m are obtained using the initial the condition

$$p(x,0) = p_0$$

where p_0 is an as yet unknown initial pressure. Since

$$\sum_{m=1,3,5} \frac{4}{m\pi}\sin\left(\frac{m\pi}{2}\right) = 1 \tag{20.58}$$

it follows that

$$C_m = p_0\frac{4}{m\pi} \tag{20.59}$$

and therefore,

$$p(x,t) = p_0\sum_{m=1,3,5}\frac{4}{m\pi}\sin\left(\frac{m\pi}{2L}x\right)\exp(-\omega_m^2 t) \tag{20.60}$$

To determine the constant p_0, we make use of the constitutive relationship given by Equation 20.1 (or Equation 20.6) and the constitutive relationship given by Equation 20.15 for the isothermal case. Recall that the constitutive Equation 20.1 is expressed in terms of the elastic moduli of the poroelastic material under drained conditions, whereas Equation 20.15 is expressed in terms of the

elastic moduli of the undrained medium. Equating the normal stresses σ_{22} obtained from these two relationships, we obtain

$$\left(K_u + \frac{4}{3}G_u\right)\varepsilon_V - Q\alpha n\frac{\Delta m_f}{m_f} = \left(K_D + \frac{4}{3}G_D\right)\varepsilon_V - \alpha p_0 = \sigma_0 \tag{20.61}$$

By setting the initial change in the fluid mass to zero $\Delta m_f(t=0) = 0$, we obtain, from Equation 20.55, the initial pressure

$$p_0 = -\frac{\alpha\sigma_0}{\alpha^2 + \left(\dfrac{n}{K_f} + \dfrac{\alpha - n}{K_s}\right)\left(K_D + \dfrac{4}{3}G_D\right)} \tag{20.62}$$

In deriving Equation 20.62, we expressed the bulk modulus of the undrained porous medium K_u in terms of the bulk modulus of the fluid K_f and the bulk modulus of the solid phase K_s as given by Equation 20.16a. Also, $G_u = G_D$.

The vertical displacement can be found by integrating the normal strain given by Equation 20.55:

$$u_x = \int \frac{\sigma_0 + \alpha p}{K_D + 4G_D/3}\,dx + U \tag{20.63}$$

where U is a constant of integration, which can be found from the boundary condition at the lower surface

$$u_x(L,0) = 0$$

Using the pressure field from Equation 20.60 in Equation 20.63, we obtain the vertical displacement

$$u_x(x,t) = \frac{1}{K_D + 4G_D/3}\left[-\alpha p_0 \sum_{m=1,3,5,\ldots} \frac{8L}{m^2\pi^2}\cos\left(\frac{m\pi}{2L}x\right)\exp(-\omega_m^2 t) + \sigma_0(x - L)\right] \tag{20.64}$$

where the initial pressure is given by Equation 20.62 and the coefficient ω_m is given in Equation 20.57. Note that the initial displacement is

$$u_x(x,0) = \frac{L}{K_D + 4G_D/3}\left(1 - \frac{x}{L}\right)[-\alpha p_0 - \sigma_0] \tag{20.65}$$

20.3.4 Hydromechanical Problem: The Effect of Solid Phase and Fluid Compressibility

Consider first the effect of the fluid compressibility on the value of the fluid pressure. *We will first establish that the fluid pressure is smaller in absolute value for a porous medium with a compressible fluid.*

From Equation 20.60, it is evident that it is sufficient to just examine the initial pressure. The initial pressure Equation 20.62 can be expressed using the definition of the Biot parameter given by Equation 20.3 as

$$p_0 = -\frac{\sigma_0 K_f}{\alpha K_f + \left[\dfrac{n}{\alpha} + \dfrac{K_f}{K_D}\left(1 - \dfrac{n}{\alpha}\right)(1-\alpha)\right]\left(K_D + \dfrac{4}{3}G_D\right)} \tag{20.66}$$

For an incompressible pore fluid, the initial pressure given by Equation 20.66 becomes

$$p_0 = -\frac{\sigma_0}{\alpha + \frac{1}{K_D}\left(1-\frac{n}{\alpha}\right)(1-\alpha)\left(K_D + \frac{4}{3}G_D\right)} \tag{20.67}$$

The absolute value of the pressure given by Equation 20.67 appears to be larger than the absolute value of Equation 20.66 since the denominators satisfy the inequality

$$\alpha + \left[\frac{n}{\alpha K_f} + \frac{1}{K_D}\left(1-\frac{n}{\alpha}\right)(1-\alpha)\right]\left(K_D + \frac{4}{3}G_D\right) > \alpha + \frac{1}{K_D}\left(1-\frac{n}{\alpha}\right)(1-\alpha)\left(K_D + \frac{4}{3}G_D\right)$$

The difference depends on the value of the fluid bulk modulus—for very small K_f, the difference becomes more significant since the term $(K_D + 4G_D/3)/K_f$ on the left dominates over $(K_D + 4G_D/3)/K_D$. Thus, the pressure is reduced for porous media saturated with compressible fluids.

Consider now the influence of the solid phase compressibility on the value of the pressure. We consider only the case of a compressible fluid. When the solid phase is incompressible, that is, $K_s \to \infty$, $\alpha = 1$, the initial pressure given by Equation 20.66 is

$$p_0 = -\frac{\sigma_0 K_f}{K_f + n\left(K_D + \frac{4}{3}G_D\right)} \tag{20.68}$$

We assume that the pressure in the porous medium with an incompressible solid phase is larger than the pressure in the geomaterial with a compressible solid phase, that is,

$$-\frac{\sigma_0 K_f}{K_f + n\left(K_D + \frac{4}{3}G_D\right)} > -\frac{\sigma_0 K_f}{\alpha K_f + \left[\frac{n}{\alpha} + \frac{K_f}{K_D}\left(1-\frac{n}{\alpha}\right)(1-\alpha)\right]\left(K_D + \frac{4}{3}G_D\right)} \tag{20.69}$$

To verify this, it is sufficient to evaluate the ratio between the pressures given by Equations 20.66 and 20.68 and to show that

$$\frac{K_f + n\left(K_D + \frac{4}{3}G_D\right)}{\alpha K_f + \left[\frac{n}{\alpha} + \frac{K_f}{K_D}\left(1-\frac{n}{\alpha}\right)(1-\alpha)\right]\left(K_D + \frac{4}{3}G_D\right)} < 1 \tag{20.70}$$

Multiplying both the numerator and denominator of this inequality by α/n gives

$$\frac{\frac{\alpha}{n}K_f + \alpha\left(K_D + \frac{4}{3}G_D\right)}{\alpha\frac{\alpha}{n}K_f + \left(K_D + \frac{4}{3}G_D\right) + \frac{K_f}{K_D}\left(\frac{\alpha}{n}-1\right)(1-\alpha)\left(K_D + \frac{4}{3}G_D\right)} < 1 \tag{20.71}$$

Since usually $K_f \ll K_D$, this inequality is satisfied because it is approximately reduced to the inequality $\alpha < 1$. Thus, the fluid pressure generated in a fluid-saturated porous medium with a compressible

solid phase is smaller than the fluid pressure generated in a fluid-saturated porous medium with an incompressible solid phase; the ratio between these pressures is approximately equal to α, the Biot parameter of the porous medium with the compressible solid phase. To prove the aforementioned inequality of Equation 20.71 more rigorously, we can rewrite it as

$$\alpha\frac{\alpha}{n}K_f+\left(K_D+\frac{4}{3}G_D\right)+\frac{K_f}{K_D}\left(\frac{\alpha}{n}-1\right)(1-\alpha)\left(K_D+\frac{4}{3}G_D\right)-\frac{\alpha}{n}K_f-\alpha\left(K_D+\frac{4}{3}G_D\right)>0 \qquad (20.72)$$

Dividing Equation 20.72 by $\left(K_D+\frac{4}{3}G_D\right)$, we obtain

$$1+\left[\frac{K_f}{K_D}-\frac{K_f}{K_D+\frac{4}{3}G_D}\right](1-\alpha)\frac{\alpha}{n}>\frac{K_f}{K_D}(1-\alpha)+\alpha \qquad (20.73)$$

It is evident that $K_f/K_D > K_f/(K_D + 4G_D/3)$. Thus, the left side of the inequality is always larger than 1. On the other hand, the right side of the inequality does not exceed one, because for most poromechanics applications, $K_f \ll K_D$ (even in the worst case scenario, when $K_f \approx K_D$, the right side of the inequality is strictly equal to 1). Thus, the inequality in Equation 20.69 is proven.

It is evident that by assuming the solid phase to be incompressible, we overestimate the absolute value of the initial pressure, by roughly a factor 1/α, compared to the case where the liquid phase is compressible. (Here, α is the Biot parameter of the porous medium with a compressible solid phase.)

When the pore fluid is incompressible, it is more difficult to establish the relationship between the pore fluid pressures for the medium with either a compressible or an incompressible solid phase; however, in this case, it is more feasible to assume that the solid phase is also incompressible because usually, in terms of applications in the geosciences, the bulk modulus of the skeletal material of the porous medium is larger than the bulk modulus of the fluid.

20.3.5 Thermohydromechanical Problem: Formulation

We now consider the fully coupled THM problem where the constitutive equation is

$$\sigma_{ij}=2G_D\varepsilon_{ij}+\left(K_D-\frac{2G_D}{3}\right)\varepsilon_V\delta_{ij}-3K_D\alpha_sT\delta_{ij}-\left(1-\frac{K_D}{K_s}\right)p\delta_{ij}$$

and the governing equations are

$$\left(K_D+\frac{G_D}{3}\right)u_{k,ki}+G_Du_{i,kk}-K_D3\alpha_sT_{,i}-\left(1-\frac{K_D}{K_s}\right)p_{,i}=0$$

$$-\frac{k}{\gamma}p_{,kk}+\left(1-\frac{K_D}{K_s}\right)\frac{d\varepsilon_V}{dt}$$

$$+\frac{n}{K_f}\frac{dp}{dt}+\left(1-\frac{K_D}{K_s}-n\right)\frac{1}{K_s}\frac{dp}{dt}=n3\alpha_f\frac{dT}{dt}+\left(1-\frac{K_D}{K_s}-n\right)3\alpha_s\frac{dT}{dt}$$

$$c_p^*\frac{\partial T}{\partial t}-k_c^*T_{,kk}=0$$

Due to the 1D nature of the problem, one can reduce Equations 20.6, 20.11, and 20.13 to

$$\sigma_{xx} = \left(K_D + \frac{4G_D}{3}\right)u_{x,x} - 3K_D\alpha_s T - \left(1 - \frac{K_D}{K_s}\right)p \tag{20.74}$$

$$\left(K_D + \frac{4G_D}{3}\right)u_{x,xx} - K_D 3\alpha_s T_{,x} - \left(1 - \frac{K_D}{K_s}\right)p_{,x} = 0 \tag{20.75}$$

$$-\frac{k}{\gamma}p_{,xx} + \left(1 - \frac{K_D}{K_s}\right)\frac{\partial u_{x,x}}{\partial t} + \frac{n}{K_f}\frac{\partial p}{\partial t} + \left(1 - \frac{K_D}{K_s} - n\right)\frac{1}{K_s}\frac{\partial p}{\partial t} = n3\alpha_f\frac{\partial T}{\partial t} + \left(1 - \frac{K_D}{K_s} - n\right)3\alpha_s\frac{\partial T}{\partial t} \tag{20.76}$$

$$c_p^*\frac{\partial T}{\partial t} - k_c^* T_{,xx} = 0 \tag{20.77}$$

Consider the case where the initial temperature within the 1D region is T_0; the temperature change on the upper surface is kept equal to zero, that is, $\overline{T}_0 = 0$:

$$T(x,0) = T_0$$

$$T(0,t) = \overline{T}_0 = 0$$

The temperature field satisfying the heat conduction (Equation 20.77), the boundary conditions (Equations 20.34 and 20.35), and the initial condition (Equation 20.37) is given, as before, by

$$T(x,t) = T_0\sum_{m=1,3,5}\frac{4}{m\pi}\sin\left(\frac{m\pi}{2L}x\right)\exp(-\kappa_m^2 t); \quad \kappa_m^2 = \frac{m^2\pi^2}{4L^2}\frac{k_c^*}{c_p^*} \tag{20.78}$$

Consider the constant tractions σ_0 that are applied on the upper surface of the 1D region, that is,

$$\sigma_{xx}(0,t) = \sigma_0$$

From Equations 20.74 and 20.75, it is clear that $\sigma_{xx,x} = 0$, and hence, the total stress σ_{22} is uniform and equal to σ_0 at all points within the 1D region. Therefore, from Equation 20.74, the strain within the column can be obtained as

$$\varepsilon_{xx}(x) = u_{x,x} = \frac{1}{K_D + \frac{4}{3}G_D}\left(\sigma_0 + \left(1 - \frac{K_D}{K_s}\right)p + 3K_D\alpha_s T\right) \tag{20.79}$$

Substituting this strain into the governing equation (Equation 20.76) gives the differential equation for the pressure:

$$-\frac{k}{\gamma}p_{,xx}+\left[\frac{n}{K_f}+(\alpha-n)\frac{1}{K_s}+\frac{\alpha^2}{K_D+\frac{4}{3}G_D}\right]\frac{\partial p}{\partial t}=n(3\alpha_f)\frac{\partial T}{\partial t}+\left(\alpha-n-\alpha\frac{K_D}{K_D+\frac{4}{3}G_D}\right)(3\alpha_s)\frac{\partial T}{\partial t} \tag{20.80}$$

The pore fluid can flow freely in and out through the upper surface, and thus the pore fluid pressure on the upper surface $x = 0$ is taken as equal to zero:

$$p(0,t)=0$$

The lower end of the 1D column $x = L$ is considered to be impervious, giving a zero velocity at the base, that is,

$$\left(\frac{k}{\gamma}\frac{\partial p}{\partial x}\right)_{x=L}=0$$

We assume that both the general solution of the homogeneous version of Equation 20.80 and a particular solution of Equation 20.80 will satisfy the boundary conditions given by Equations 20.32 and 20.33. Solution of the homogeneous equation is taken in the form

$$\begin{aligned}p^H(x,t)&=\sum_{m=1,3,5}C_m\sin\left(\frac{m\pi}{2L}x\right)\exp(-\omega_m^2t)\\ \omega_m^2&=\frac{k}{\gamma}\frac{m^2\pi^2}{4L^2}\frac{K_D+\frac{4}{3}G_D}{\left(\frac{n}{K_f}+(\alpha-n)\frac{1}{K_s}\right)\left(K_D+\frac{4}{3}G_D\right)+\alpha^2}\end{aligned} \tag{20.81}$$

where C_m are constants to be determined.

The particular solution of Equation 20.80 that also satisfies the boundary conditions presented in Equations 20.32 and 20.33 can be taken as

$$p^P(x,t)=\sum_{m=1,3,5}A_m\frac{4}{m\pi}\sin\left(\frac{m\pi}{2L}x\right)\exp(-\kappa_m^2t);\quad \kappa_m^2=\frac{m^2\pi^2}{4L^2}\frac{k_c^*}{c_p^*} \tag{20.82}$$

where A_m are unknown constants. The solution of Equation 20.80 is the sum $p = p^H + p^P$. The constants A_m can be found by substitution of $p^P(x, t)$ given by Equation 20.82 and the temperature field given by Equation 20.78 into the equation for the pressure (Equation 20.80), which gives

$$A_m=-T_0\frac{(n3\alpha_f+(\alpha-n)3\alpha_s-\frac{\alpha K_D}{K_D+4G_D/3}3\alpha_s)}{\frac{k}{\gamma}\frac{c_p^*}{k_c^*}-\left(\frac{n}{K_f}+(\alpha-n)\frac{1}{K_s}+\frac{\alpha^2}{K_D+4G_D/3}\right)} \tag{20.83}$$

It is evident that $A_m = A$ is independent of m. It is now necessary to obtain the unknown constants C_m; these constants can be found from the initial condition on the pressure field

$$p(x,0) = p_0$$

where p_0 is an as yet unknown initial pressure.

Since

$$\sum_{m=1,3,5} \frac{4}{m\pi} \sin\left(\frac{m\pi}{2}\right) = 1$$

and since $p = p^H + p^P$, we establish that

$$p_0 \frac{4}{m\pi} = C_m + A_m \frac{4}{m\pi} \tag{20.84}$$

where p_0 is the initial pressure. Equation 20.84 allows us to obtain the constants C_m.

Therefore, the solution of Equation 20.79 is

$$p(x,t) = p_0 \sum_{m=1,3,5} \frac{4}{m\pi} \sin\left(\frac{m\pi}{2L} x\right) \exp(-\omega_m^2 t) - \sum_{m=1,3,5} A_m \frac{4}{m\pi} \sin\left(\frac{m\pi}{2L} x\right) \exp(-\omega_m^2 t)$$

$$+ \sum_{m=1,3,5} A_m \frac{4}{m\pi} \sin\left(\frac{m\pi}{2L} x\right) \exp(-\kappa_m^2 t) \tag{20.85}$$

To determine the constant p_0, we make use of the constitutive relationship given by Equation 20.1 (or Equation 20.4) and the constitutive relationship given by Equation 20.15. Recall that Equation 20.1 is expressed in terms of the elastic moduli of the porous medium under drained conditions, whereas Equation 20.15 is expressed in terms of the elastic moduli of the undrained material. Equating the normal stresses σ_{22} given by these two relationships, we obtain

$$\left(K_u + \frac{4}{3} G_u\right) \varepsilon_V - (K_u - Q\alpha n) 3\alpha_s T - Q\alpha n 3\alpha_f T - Q\alpha n \frac{\Delta m_f}{m_f}$$

$$= \left(K_D + \frac{4}{3} G_D\right) \varepsilon_V - K_D 3\alpha_s T - \alpha p = \sigma_0 \tag{20.86}$$

where, as before,

K_u is the bulk modulus of the undrained material

Q is the parameter, having the dimension of stress, given by Equation 20.14

σ_0 is the applied stress

By setting the initial change in the fluid mass to zero $\left(\Delta m_f\right)_{t=0} = 0$, we can obtain, from Equation 20.86, the initial pressure:

$$p_0 = -\frac{\alpha\sigma_0}{\alpha^2 + \left(\frac{n}{K_f} + \frac{\alpha - n}{K_s}\right)\left(K_D + \frac{4}{3}G_D\right)} + \frac{\left(K_D + \frac{4}{3}G_D\right)[(\alpha - n)3\alpha_s T_0 + n3\alpha_f T_0] - K_D 3\alpha_s T_0 \alpha}{\alpha^2 + \left(\frac{n}{K_f} + \frac{\alpha - n}{K_s}\right)\left(K_D + \frac{4}{3}G_D\right)} \tag{20.87}$$

In deriving Equation 20.87, we have expressed the bulk modulus of the undrained material K_u in terms of the bulk modulus of the fluid K_f and the solid phase K_s as given by Equation 20.14. Also, $G_u = G_D$. This formula will be simplified if the solid phase is incompressible, that is, $K_s \to \infty$, $\alpha = 1$. In this case, the initial pressure becomes

$$p_0 = -\frac{\sigma_0}{1 + \frac{n}{K_f}\left(K_D + \frac{4}{3}G_D\right)} + \frac{\left(K_D + \frac{4}{3}G_D\right)[(1 - n)3\alpha_s T_0 + n3\alpha_f T_0] - K_D 3\alpha_s T_0}{1 + \frac{n}{K_f}\left(K_D + \frac{4}{3}G_D\right)} \tag{20.88}$$

The vertical displacement can be found by integrating the expression for the axial strain (Equation 20.79), which gives

$$u_x(x,0) = \int \frac{\sigma_0 + \alpha p + 3K_D\alpha_s T}{K_D + 4G_D/3}\,dx + U \tag{20.89}$$

where U is a constant of integration, which can be found from the boundary condition at the base of the 1D element

$$u_x(L,0) = 0$$

Substituting the expressions for the pressure field given by Equation 20.85 and the temperature field given by Equation 20.78 into Equation 20.89, we obtain the expression for the vertical displacement:

$$u_x(x,t) = \frac{1}{K_D + 4G_D/3} - \left\{ \begin{array}{l} K_D 3\alpha_s T_0 \sum_{m=1,3,5,\ldots} \frac{8L}{m^2\pi^2} \cos\left(\frac{m\pi}{2L}x\right) \exp(-\kappa_m^2 t) \\ -\alpha p_0 \sum_{m=1,3,5,\ldots} \frac{8L}{m^2\pi^2} \cos\left(\frac{m\pi}{2L}x\right) \exp(-\omega_m^2 t) \\ +\alpha \sum_{m=1,3,5,\ldots} A_m \frac{8L}{m^2\pi^2} \cos\left(\frac{m\pi}{2L}x\right) \exp(-\omega_m^2 t) \\ -\alpha \sum_{m=1,3,5,\ldots} A_m \frac{8L}{m^2\pi^2} \cos\left(\frac{m\pi}{2L}x\right) \exp(-\kappa_m^2 t) + \square_0(x - L) \end{array} \right\} \tag{20.90}$$

where the initial pressure is given by Equation 20.87, the coefficient ω_m by Equation 20.81, the coefficient κ_m by Equation 20.78, and the coefficient A_m by Equation 20.83.

Note that the initial displacement is given by

$$u_x(x,0) = \frac{L}{K_D + 4G_D/3}\left(1 - \frac{x}{L}\right)[-K_D 3\alpha_s T_0 - \alpha p_0 - \sigma_0] \tag{20.91}$$

since

$$\sum_{m=1,3,5,} \frac{8L}{m^2\pi^2} = L$$

20.3.6 Thermohydromechanical Problem: The Effects of Solid Phase and Fluid Phase Compressibility

We first consider the effect of fluid compressibility on the fluid pressure and assume that the initial temperature change within the 1D region is $T_0(\neq 0)$, but the axial stress on the upper surface of the 1D element is set to zero (i.e., $\sigma_0 \equiv 0$). *We will show first that for the THM problem, the pore fluid pressure is smaller, in absolute value, for a porous medium with a compressible fluid.*

If the fluid phase is compressible, the initial pressure is given by

$$p_0 = \frac{1}{\alpha}\left\{\frac{\left(K_D + \frac{4}{3}G_D\right)[(\alpha - n)3\alpha_s T_0 + n3\alpha_f T_0] - \alpha K_D 3\alpha_s T_0}{\alpha + \left(\frac{n}{\alpha K_f} + K_D^{-1}\left(1 - \frac{n}{\alpha}\right)(1-\alpha)\right)\left(K_D + \frac{4}{3}G_D\right)}\right\} \tag{20.92}$$

We have used the definition of the Biot parameter defined by Equation 20.3 to obtain Equation 20.92. Alternatively, when the saturating fluid is incompressible, $K_f \to \infty$, and the initial pressure becomes

$$p_0 = \frac{1}{\alpha}\left\{\frac{\left(K_D + \frac{4}{3}G_D\right)[(\alpha - n)3\alpha_s T_0 + n3\alpha_f T_0] - K_D 3\alpha_s T_0 \alpha}{\alpha + \left(K_D^{-1}\left(1 - \frac{n}{\alpha}\right)(1-\alpha)\right)\left(K_D + \frac{4}{3}G_D\right)}\right\} \tag{20.93}$$

Usually, $\alpha_f \gg \alpha_s$ (i.e., the thermal expansion of the fluid is much larger than that of the solid phase). In this case, the expression for the fluid pressure given by Equation 20.92 is simplified to

$$p_0 = \frac{1}{\alpha}\left\{\frac{\left(K_D + \frac{4}{3}G_D\right)n3\alpha_f T_0}{\alpha + \left(\frac{n}{\alpha K_f} + K_D^{-1}\left(1 - \frac{n}{\alpha}\right)(1-\alpha)\right)\left(K_D + \frac{4}{3}G_D\right)}\right\} \tag{20.94}$$

For a porous medium with an incompressible fluid phase, Equation 20.93 reduces to

$$p_0 = \frac{1}{\alpha}\left\{\frac{(K_D + \frac{4}{3}G_D)n\,3\alpha_f T_0}{\alpha + \left(K_D^{-1}(1 - \frac{n}{\alpha})(1-\alpha)\right)(K_D + \frac{4}{3}G_D)}\right\} \tag{20.95}$$

It would appear that the fluid pressure in a porous medium with a compressible fluid phase is smaller than that in the porous medium with an incompressible liquid since

$$\alpha + \left(\frac{n}{\alpha K_f} + K_D^{-1} \left(1 - \frac{n}{\alpha} \right) (1 - \alpha) \right) \left(K_D + \frac{4}{3} G_D \right) > \alpha + \left(K_D^{-1} \left(1 - \frac{n}{\alpha} \right) (1 - \alpha) \right) \left(K_D + \frac{4}{3} G_D \right) \tag{20.96}$$

The difference depends on the value of the fluid bulk modulus: for very small K_f, the difference becomes more significant since the term $(K_D + 4G_D/3)/K_f$ on the left dominates over $(K_D + 4G_D/3)/K_D$.

We now consider the influence of the solid phase compressibility on the value of the initial pore fluid pressure. We examine only the case where the pore fluid is compressible. Consider first the situation where the thermal expansion of the pore fluid is much greater than that of the solid phase, $\alpha_f \gg \alpha_s$. The approximate value of the initial pressure in this case is given by Equation 20.94, which can also be written as

$$p_0 = \frac{\left(K_D + \frac{4}{3} G_D \right) K_f n}{\left(K_D + \frac{4}{3} G_D \right) \left[n + \frac{K_f}{K_D} (\alpha - n)(1 - \alpha) \right] + \alpha^2 K_f} 3\alpha_f T \tag{20.97}$$

When the solid phase is incompressible $K_s \to \infty$, $\alpha = 1$, the initial pressure given by Equation 20.97 becomes

$$p_0 = \frac{\left(K_D + \frac{4}{3} G_D \right) K_f n}{\left(K_D + \frac{4}{3} G_D \right) n + K_f} 3\alpha_f T \tag{20.98}$$

Evaluating the ratio between the pressures for the porous medium with a compressible and an incompressible solid skeletal material gives

$$\frac{\left(K_D + \frac{4}{3} G_D \right) n + K_f}{\left(K_D + \frac{4}{3} G_D \right) \left[n + \frac{K_f}{K_D} (\alpha - n)(1 - \alpha) \right] + \alpha^2 K_f} = \frac{p_0(\alpha < 1)}{p_0(\alpha = 1)} \tag{20.99}$$

Since usually $K_f \ll K_D$, the ratio between the pressures is approximately equal to 1.

Consider now a special case when the thermal expansion coefficients of the fluid and the solid phase are equal, that is, $\alpha_f = \alpha_s$. Then the pressure (obtained in Equation 20.92) becomes

$$p_0 = \frac{\frac{4}{3} K_f G_D 3\alpha_s T}{\left(K_D + \frac{4}{3} G_D \right) \left[\frac{n}{\alpha} + \frac{K_f}{K_D} (1 - \frac{n}{\alpha})(1 - \alpha) \right] + \alpha K_f} \tag{20.100}$$

For an incompressible solid phase, $\alpha = 1$, the initial pressure obtained from Equation 20.100 becomes

$$p_0 = \frac{\frac{4}{3} K_f G_D 3\alpha_s T}{\left(K_D + \frac{4}{3} G_D \right) n + K_f} \tag{20.101}$$

A comparison between these two values of the initial pressure can be performed in a similar manner to the case of loading only by surface tractions σ_0 (the denominators in Equations 20.100 and 20.101 are identical to those in Equations 20.62 and 20.66). It can be concluded that if $\alpha_f = \alpha_s$, the absolute value of pressure for the porous medium with compressible solid grains is smaller than that for a porous medium with an incompressible solid phase; the ratio between the two pressures is approximately equal to α, the Biot parameter for the poroelastic material with the compressible solid phase. Numerical tests also show that when $\alpha_f < \alpha_s$ (an unlikely situation), the difference between the initial fluid pressures can be even more pronounced.

20.3.7 Thermohydromechanical Problem: Numerical Results

In the ensuing, we evaluate the initial pressure given by Equation 20.87 for the geomaterial with given poroelastic properties subjected to a surface traction σ_0 and the initial temperature change T_0. The initial pressure is

$$p_0 = -\frac{\alpha\sigma_0}{\alpha^2 + \left(\frac{n}{K_f} + \frac{\alpha - n}{K_s}\right)\left(K_D + \frac{4}{3}G_D\right)} + \frac{\left(K_D + \frac{4}{3}G_D\right)[(\alpha - n)3\alpha_s T_0 + n3\alpha_f T_0] - K_D 3\alpha_s T_0 \alpha}{\alpha^2 + \left(\frac{n}{K_f} + \frac{\alpha - n}{K_s}\right)\left(K_D + \frac{4}{3}G_D\right)}$$

Typical material parameters used for numerical simulations are estimated from published literature available for competent fluid-saturated rocks (see, e.g., Hart and Wang [141], Selvadurai and Najari [142], Najari and Selvadurai [143], Nasseri et al. [144]). Table 20.1 gives the value of the initial pressure in the 1D column resulting from the application of an external surface traction σ_0 only.

The results demonstrate the relative influences of the fluid compressibility on the value of the initial pressure. The fluid compressibility has a greater influence on the pore fluid pressure generated in the column than the solid phase compressibility. The results, however, should not imply that the compressibility of the porous skeleton should be ignored; the ratio between the pore fluid pressures generated in the porous medium with compressible and incompressible solid phases is approximately equal to the Biot parameter 0.75, that is, $0.0982/0.0754 \approx 0.75$.

Consider now the influence of the initial temperature change T_0 on the value of the initial pore water pressure. First, assume that $\alpha_f/\alpha_s \gg 1$ (most probable condition); Table 20.2 presents

TABLE 20.1
Initial Pressure in the Poroelastic Column due to the Application of an External Compressive Stress σ_0 at the Upper Surface, Depending on Fluid Compressibility and the Value of the Biot Parameter

Variable or Parameter	Case I	Case II	Case III	Case IV
$\left(K_D + \frac{4}{3}G_D\right)\Big/K_D$	1.6154	1.6154	1.6154	1.6154
$\left(K_D + \frac{4}{3}G_D\right)\Big/K_f$	36.7133	18.356	0.0	36.7133
Biot parameter α	0.75	0.75	0.75	1
Porosity n	0.25	0.25	0.25	0.25
Initial pore fluid pressure	$-0.0754\sigma_0$	$-0.1401\sigma_0$	$-0.9811\sigma_0$	$-0.0982\sigma_0$

TABLE 20.2
Initial Pore Fluid Pressure in the 1D Column of the Poroelastic Material, Subjected to an Initial Uniform Temperature Change T_0

Variable or Parameter	Case I	Case II	Case III	Case IV
$\left(K_D + \frac{4}{3}G_D\right)\Big/K_D$	1.6154	1.1654	1.6154	1.6154
$\left(K_D + \frac{4}{3}G_D\right)\Big/K_f$	36.7133	18.356	0.0	36.7133
Biot parameter α	0.75	0.75	0.75	1
Porosity n	0.25	0.25	0.25	0.25
α_f/α_s	8.3133	8.3133	8.3133	8.3133
Initial pore fluid pressure	$0.3435K_D3\alpha_sT_0$	$0.6379K_D3\alpha_sT_0$	$4.4674K_D3\alpha_sT_0$	$0.3506K_D3\alpha_sT_0$

the influence of the fluid compressibility, the value of the Biot parameter and the ratio between thermal expansion coefficients of the solid phase and the fluid on the pore fluid pressures in the 1D column subjected to a uniform temperature change, T_0. Again, these results indicate that the effect of fluid compressibility on the magnitude of the initial pressure is very significant. We also note that if the thermal expansion coefficient of the fluid is much larger than the thermal expansion coefficient of the solid phase, the ratio between the generated pore fluid pressures for a poroelastic medium with compressible and incompressible solid phases is approximately equal to unity, that is, $0.3506/0.3435 \approx 1$.

Now consider the case when $\alpha_f/\alpha_s = 1$, that is, the thermal expansion coefficient of the fluid is equal to the thermal expansion coefficient of the solid phase. The results given in Table 20.3 are analogous to Table 20.2 but for the case when $\alpha_f/\alpha_s = 1$. From Tables 20.2 and 20.3, it is clear that, as the thermal expansion coefficient for the fluid decreases, the pore fluid pressure generated, due to the temperature effects of thermal loading, is reduced. We also note that if the thermal expansion coefficient of the fluid is equal to the thermal expansion coefficient of the solid phase, the ratio between the pressures for the porous medium with compressible and incompressible solid phases is approximately equal to α, the Biot parameter, that is, $0.0605/0.0464 \approx 0.75$.

TABLE 20.3
Role of the Fluid Compressibility on the Initial Pore Fluid Pressure in a 1D Column of a Poroelastic Material Subjected to an Initial Uniform Temperature Change T_0

Variable or Parameter	Case I	Case II	Case III	Case IV
$\frac{(3K_D + 4G_D)}{3K_D}$	1.6154	1.1654	1.6154	1.6154
$\frac{(3K_D + 4G_D)}{3K_f}$	36.7133	18.356	0.0	36.7133
Biot parameter α	0.75	0.75	0.75	1
Porosity n	0.25	0.25	0.25	0.25
α_f/α_s	1	1	1	1
Initial pore fluid pressure	$0.0464K_D3\alpha_sT_0$	$0.0862K_D3\alpha_sT_0$	$0.6038K_D3\alpha_sT_0$	$0.0605K_D3\alpha_sT_0$

20.3.8 Thermohydromechanical Problem: Computational Estimates

Computational procedures, notably the application of finite element techniques for obtaining solutions to initial boundary value problems related to the weakly coupled set of partial differential equations described by Equations 20.6, 20.7, and 20.13, have been presented by a number of investigators and described in the articles by Aboustit et al. [145], Schrefler and Simoni [146], Lewis et al. [147], Modaressi et al. [148], Seneviratne et al. [98], Selvadurai and Nguyen [90], Nguyen and Selvadurai [69], Nguyen et al. [73], Ehlers and Bluhm [149], Hudson et al. [150], Rutqvist et al. [151,152], Tong et al. [153], Selvadurai and Suvorov [154,155], and Selvadurai et al. [156].

When the problem governing the THM processes is well posed in terms of a system of governing partial differential equations and a consistent set of boundary conditions and initial conditions, it is convenient to take advantage of the Galerkin-type weighted residual technique to formulate the computational scheme. Comprehensive expositions of the basic procedures are given in a number of advanced texts on finite element modeling, and the reader is referred, in particular, to the texts by Huyakorn and Pinder [157], Lewis and Schrefler [37], and Zienkiewicz and Taylor [158] and the articles cited previously. Considering standard finite element procedures, the domain is discretized into N^e elements. When modeling the poroelastic region with isoparametric elements, the displacements within the element are interpolated as functions of displacements of all nodes, whereas the pore fluid pressure and temperature are interpolated as functions of the values at the corner nodes. Details of the rationale for the procedure are well documented (Lewis and Schrefler [37]). The Galerkin procedure, when applied to the partial differential equations given by Equations 20.6, 20.7, and 20.13, gives rise to matrix equations of the general forms

$$\begin{bmatrix} [\mathbf{K}] & \alpha[\mathbf{CP}] \\ \alpha[\mathbf{CP}]^T & -\theta(\Delta t)[\mathbf{KP}] - \xi_1[\mathbf{CM}] \end{bmatrix} \begin{Bmatrix} \{\mathbf{d}\}^{(n+1)} \\ \{\mathbf{p}\}^{(n+1)} \end{Bmatrix}$$

$$= \begin{bmatrix} \left(\frac{\theta-1}{\theta}\right)[\mathbf{K}] & \alpha\left(\frac{\theta-1}{\theta}\right)[\mathbf{CP}] \\ \alpha[\mathbf{CP}]^T & (1-\theta)(\Delta t)[\mathbf{KP}] - \xi_2[\mathbf{CM}] \end{bmatrix} \begin{Bmatrix} \{\mathbf{d}\}^{(n)} \\ \{\mathbf{p}\}^{(n)} \end{Bmatrix}$$

$$+ \begin{bmatrix} \frac{\xi_\square}{\theta}[\mathbf{K}] & [\square] \\ [\square] & \xi_\square[\mathbf{CM}] \end{bmatrix} \begin{Bmatrix} (1-\theta)\{\square\}^{(n)} + \theta\{\square\}^{(n+1)} \\ \{\square\}^{(n+1)} - \{\square\}^{(n)} \end{Bmatrix} \tag{20.102}$$

and

$$\left[\theta[\mathbf{KH}] + \left(\frac{\xi_5}{\Delta t}\right)[\mathbf{CM}]\right]\{\mathbf{T}\}^{(n+1)} = \{\mathbf{FH}\} + \left[(1-\theta)[\mathbf{KH}] + \left(\frac{\xi_6}{\Delta t}\right)[\mathbf{CM}]\right]\{\mathbf{T}\}^{(n)} \tag{20.103}$$

where the unknowns are the nodal displacements $\{\mathbf{d}\}^{(n+1)}$, the nodal temperatures $\{\mathbf{T}\}^{(n+1)}$, and the nodal pore pressure values $\{\mathbf{p}\}^{(n+1)}$ at the current time step $\{\}^{(n+1)}$; the superscripts $\{\}^{(n)}$ refer to the values of the corresponding variables at the preceding step. The parameters $\xi_i (i = 1, 2,..., 6)$ depend on the parameters describing the THM process. Also $\{\mathbf{FH}\}$ is the heat flux vector, Δt is a time increment, and θ is a time-integration parameter. This time-integration parameter can vary between 0 and 1. It is found that by setting $\theta = 0.75$, a reliable stable solution is achieved. All other matrices, [**K**], [**CP**], etc., are assembled from element matrices, which

are dependent on the thermal, mechanical, and hydraulic properties of the individual elements and the interpolation functions used. An early development in this area is the FRACON 3D code, which validated the code against isothermal analytical solutions for both 1D and axisymmetric problems. This is documented by Nguyen [159], Nguyen and Selvadurai [69], Nguyen et al. [73], Selvadurai et al. [156], and Thomas et al. [160]. The computational treatment of the coupled THM problem is now a routine feature in many general purpose finite element codes and finite element approaches developed for examining multiphysics problems in the engineering sciences. The accuracy of these codes is generally left unproven unless an intercode validation exercise is conducted that also involves comparisons with analytical solutions (see, e.g., Selvadurai and Nguyen [90], Nguyen and Selvadurai [69], Nguyen et al. [73], Rutqvist et al. [151,152], Tong et al. [153], Selvadurai and Suvorov [154,155]).

In this section, we use the analytical solutions developed in previous sections to validate the computational solutions achieved using the multiphysics finite element code COMSOL™. The accuracy of the computational modeling has been verified by comparison with analytical solutions obtained for the 1D TH, HM, and THM behavior of a finite column of a fluid-saturated porous medium that was subjected, where appropriate, to surface tractions and/or a temperature rise in the form of Heaviside step functions. In the computational modeling, the 1D behavior is simulated by considering a 3D prismatic region, the surfaces of which are subjected to appropriate temperature, fluid pressure, displacement, and traction boundary conditions consistent with the 1D behavior. The relationships between the properties of the poroelastic column and their specific uses are shown in Table 20.4. The values for the height of the poroelastic column, the bulk modulus under drained conditions, the applied normal stress, and the temperature change are shown in Table 20.5. It should be noted that the specification of a temperature change of 100°C is purely for the purpose of the computational simulations. No phase transformations are allowed to occur in the pore water.

Figure 20.2 illustrates the time-dependent distribution of temperature within the 1D poroelastic column, where the entire region is at 100°C and, at $t = 0$, the temperature at the upper surface of the 1D column is reduced to zero, maintaining the boundary at $x = 10$ min an insulated condition. The analytical results are shown as a solid line, and the computational results are indicated by points.

TABLE 20.4
Properties of the 1D Poroelastic Material Used in the Computational Modeling of TM, HM, and THM Processes

Name of Variable or Parameter	Value	Use of Parameter
$\left(K_D + \frac{4}{3}G_D\right)\Big/K_D$	1.6154	
$\left(K_D + \frac{4}{3}G_D\right)\Big/K_f$	36.7133	
Biot parameter α	0.75	
Porosity n	0.25	
α_f/α_s	1	
$\frac{k_c^*}{c_p^*}\frac{1}{L^2}$	1.6227E−8 [1/s]	To specify κ_m^2 in the expression for temperature
$\frac{k}{\gamma}\frac{(K+4G/3)}{L^2}$	2.4231E−7 [1/s]	To specify ω_m^2 in the expression for pressure
$\frac{L}{(K+4G/3)}$	1.2381E−10 [m³/N]	To specify displacement
Initial pressure	$0.0464K_D 3\alpha_s T_0 - 0.0754\sigma_0$	

TABLE 20.5
Specific Values for the Geometric, Physical, and Mechanical Parameters of the Poroelastic Region Used in the Computational Modeling

Name of Variable or Parameter	Value
L	10 m
K_D	50 GPa
$\alpha_s = \alpha_f$	8.3E−6 1/C
σ_0	−10 MPa
T_0	100°C

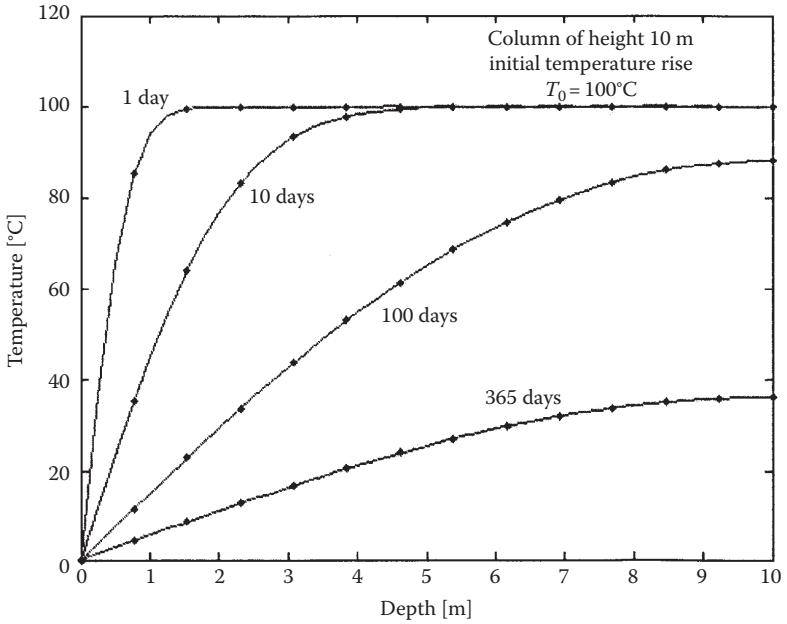

FIGURE 20.2 Temperature distribution within a 1D poroelastic column subjected to an initial temperature change 100°C and the subsequent reduction of the surface temperature to zero.

Figure 20.3 illustrates the time-dependent reduction of the temperature at the insulated end of the 1D column. Given sufficient time, the temperature at the insulated end will reduce to zero. Figure 20.4 illustrates the distribution of pore fluid pressure within the 1D column that is at 100°C at $t = 0$, and the boundary temperature is then reduced to zero. The pore water pressure at the surface is maintained at zero, and the base of the column is assumed to be impervious. The initial pore pressure distribution is compressive and the values of the pore water pressure can become tensile as the temperature within the column experiences the decay illustrated in Figure 20.2. Given sufficient time, the pore fluid pressures will reduce to zero everywhere within the column. This effect is demonstrated in Figure 20.5. The axial displacement of the 1D poroelastic column is shown in Figure 20.6. Before the surface temperature of the poroelastic column is reduced to zero, the axial displacement in the poroelastic column is linear, and a negative displacement is indicative of the thermal expansion of the column. As the temperature decays according to the typical variations shown in Figure 20.2, the

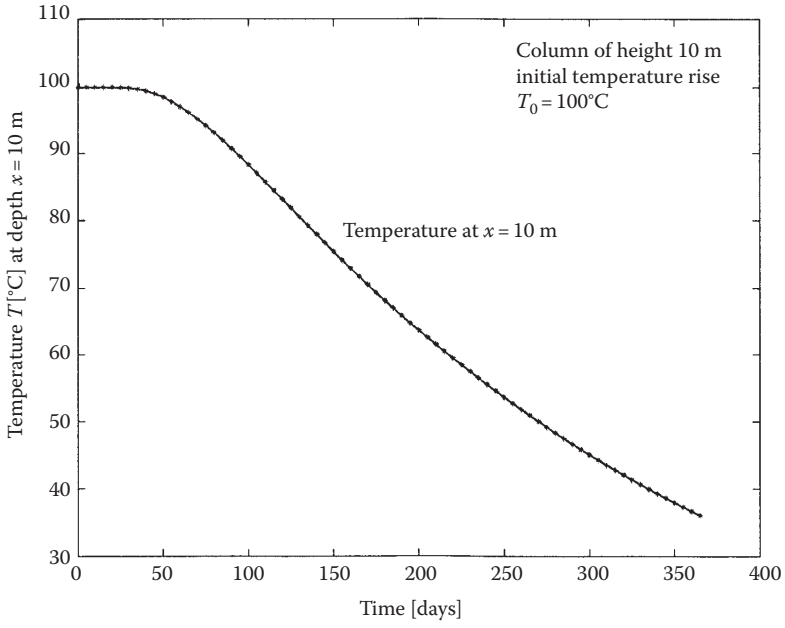

FIGURE 20.3 Evolution of temperature with time at the bottom surface of 1D column subjected to an initial temperature change of 100°C and subsequent heat dissipation.

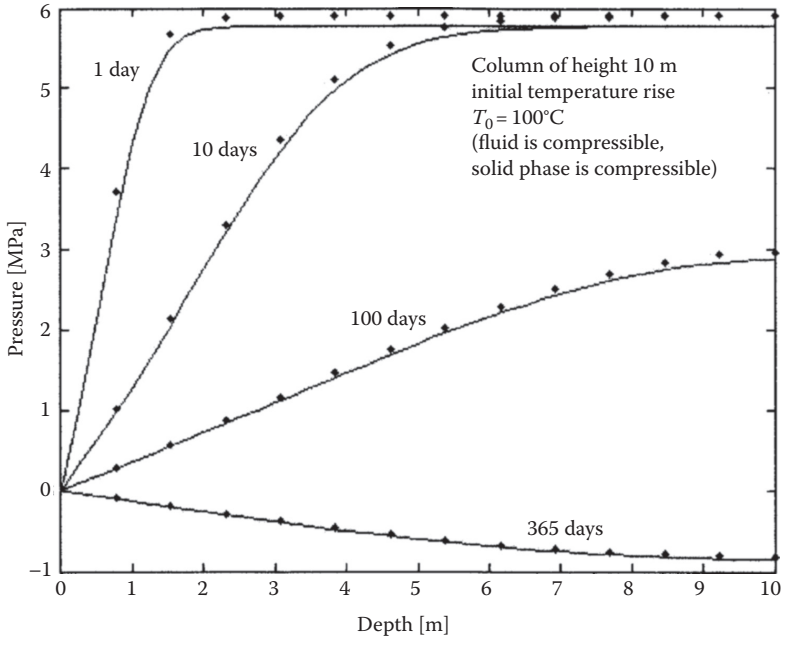

FIGURE 20.4 Pore fluid pressure distribution in a 1D poroelastic column subjected to the temperature change shown in Figure 20.2. Pressure at the upper surface is maintained at zero, and the base of the poroelastic column is impervious.

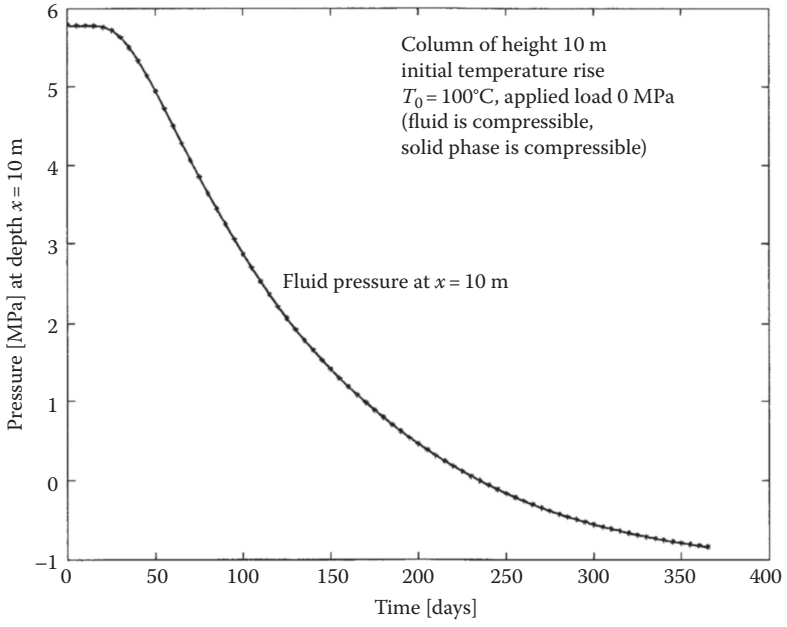

FIGURE 20.5 Pore fluid pressure evolution at a 10 m depth in a 1D column subjected to the temperature change shown in Figure 20.2.

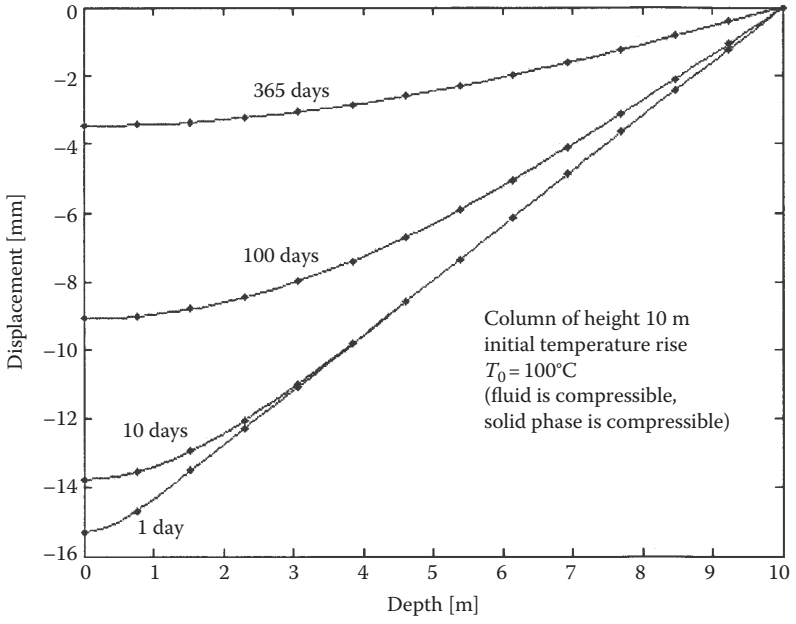

FIGURE 20.6 Time-dependent variation in the axial displacement of the 1D poroelastic column subjected to the temperature change shown in Figure 20.2. Displacement is zero at the base of the column. Negative displacements signify expansion of the column.

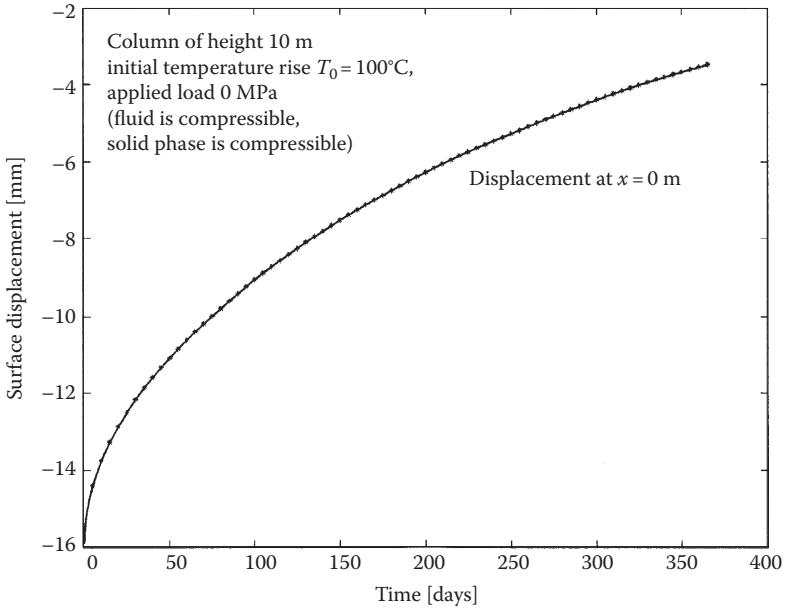

FIGURE 20.7 Surface displacement of a 1D poroelastic column subjected to the temperature change shown in Figure 20.2.

poroelastic column contracts, and ultimately, the axial displacements reduce to zero. This variation is demonstrated in Figure 20.7 for the surface of the 1D poroelastic column.

We now present results for case where the 1D poroelastic domain is subjected to a surface stress of 10 MPa. Figure 20.8 illustrates the time-dependent variation of pore water pressure at the sealed base of the 1D poroelastic column, and Figure 20.9 illustrates the variation in the displacement at the surface of the region. The computational results are consistent with the trends

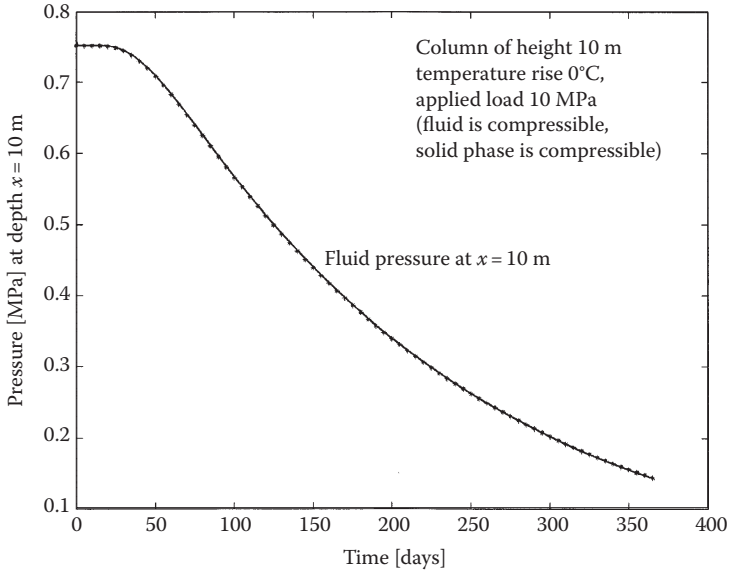

FIGURE 20.8 Pore fluid pressure distribution at a 10 m depth in the 1D poroelastic column subjected to a compressive load of 10 MPa at the upper surface.

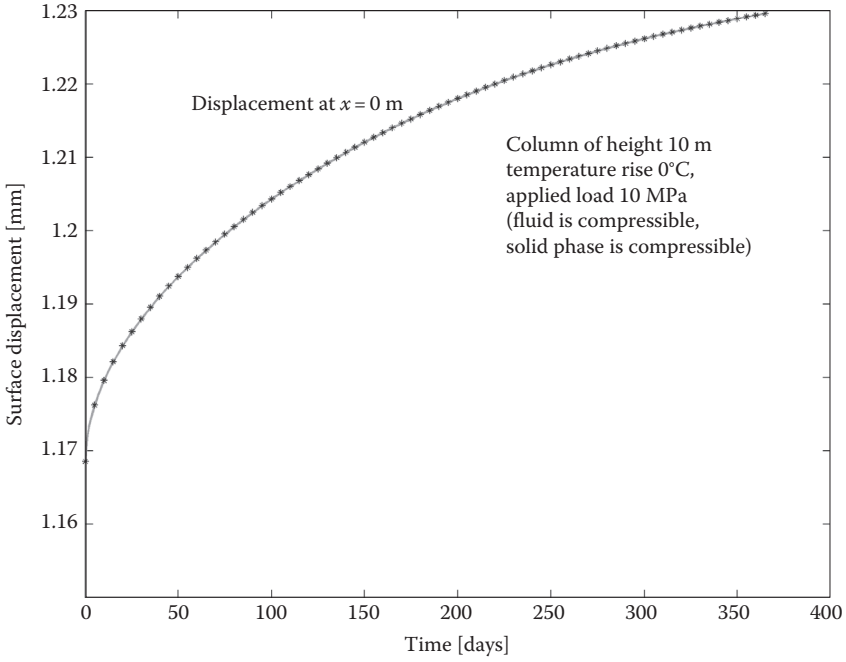

FIGURE 20.9 Time-dependent variation of surface displacement of a 1D poroelastic column subjected to a compressive load of 10 MPa at the surface.

predicted by the analytical results. In general, there is very good agreement between the analytical solutions and the computational results. A small discrepancy is observed in the computational estimates for the pore fluid pressure distribution within the poroelastic column; the general trends are, however, consistent.

20.4 SPHERICALLY SYMMETRIC PROBLEMS IN THERMOPOROELASTICITY

The 1D problems discussed in the previous section yield canonical solutions to the linearized thermoporoelasticity problems applicable to a finite domain. Its extension to semi-infinite domains needs to be treated with caution since in the limiting case where there is only the fluid flow problem, a steady-state condition for Laplace's equation is not attainable. Many standard mathematical techniques for solving partial differential equations in applied mathematics can be used to obtain a range of results to examine elemental experimental configurations and to test the accuracy of computational techniques. A limitation of the 1D formulation also stems from the fact that manifestations of effects that are particular to poroelasticity cannot be observed unless 3D effects are incorporated. Such an example is the Mandel–Cryer effect of amplification of the pore fluid pressure in a 3D poroelastic analysis, which was identified by Mandel [6] and Cryer [9] and observed by Gibson et al. [161] during radial loading of a saturated clay sphere. Of related interest are the studies by de Josselin de Jong [162] that observed similar manifestations in the pore pressure response of piezometers installed in low permeability soils such as clay. References to further studies are also given by Selvadurai and Shirazi [163]. The thermoporoelastic problem for a hollow sphere subjected to a sudden rise in temperature and pressure on its inner wall was studied by Kodashima and Kurashige [164]. In their work, the heat transport equation included a nonlinear convective term; the analytical solution of the problem was obtained for the steady-state case, and the transient solution was obtained numerically. Rehbinder [165] considered problems with cylindrical and spherical symmetries, and the stationary solutions for the nonlinear thermoporoelastic problem were obtained using a

perturbation technique. Belotserkovets and Prevost [106] studied the transient response of a thermoporoelastic sphere subjected to an applied radial stress. The goal of their studies was to characterize the influence of the applied stress on the change in temperature within the sphere. The poroelastic framework can also be extended to accommodate poroelastic solids that experience brittle damage that can lead to micromechanical damage as opposed to failure; the poroelastic behavior is maintained but albeit with altered mechanical and fluid transport properties (Selvadurai [166], Selvadurai and Mahyari [167], Mahyari and Selvadurai [168], Selvadurai and Shirazi [169,170], Shirazi and Selvadurai [171], Massart and Selvadurai [172]).

20.4.1 Boundary Heating of a Poroelastic Sphere

We consider the problem of a fluid-saturated poroelastic sphere that is subjected to heating at the boundary. The equations governing the thermoporoelastic problem are exactly the same as those described by Equations 20.6, 20.11, and 20.13, except that the coordinate system chosen should correspond to the state of spherical symmetry that will allow the formulation of the problem more conveniently. A fluid-saturated poroelastic sphere of radius R_0 is subjected to boundary heating, that is, a prescribed temperature change at the boundary. Since the problem of uniform heating of the sphere exhibits spherical symmetry, the only nonzero primary dependent variables are the radial displacement $u(R, t)$, the pore fluid pressure $p(R, t)$, and the temperature $T(R, t)$, where R is the spatial variable corresponding to a state of spherical symmetry. The solution of the problem of a sphere subjected to the temperature change at the boundary allows us to derive solutions for other, related problems such as a sphere subjected to radial stress at the boundary and also to a uniform temperature change applied to the entire sphere.

The equilibrium equation (Equation 20.6) in the spherical coordinate system takes the form

$$(K_D + 4/3G_D)\frac{\partial^2 u}{\partial R^2} + 2(K_D + 4/3G_D)\frac{1}{R}\frac{\partial u}{\partial R} - 2(K_D + 4/3G_D)\frac{u}{R^2} - 3K_D\alpha_s\frac{\partial T}{\partial R} - \alpha\frac{\partial p}{\partial R} = 0 \tag{20.104}$$

Equation 20.104 can also be written in terms of the volumetric strain $e = (\partial u/\partial R) + (2u/R)$ as

$$(K_D + 4/3G_D)\nabla e - 3K_D\alpha_s\nabla T - \alpha\nabla p = 0 \tag{20.105}$$

From Equation 20.105, the pressure can be expressed as

$$\alpha p(R,t) = (K_D + 4/3G_D)e - 3K_D\alpha_s T + f(t) \tag{20.106}$$

where $f(t)$ is an arbitrary function of time.

Equation 20.11 for fluid flow is given by

$$-\frac{K}{\eta}\left(\frac{\partial^2 p}{\partial R^2} + \frac{2}{R}\frac{\partial p}{\partial R}\right) + \alpha\left(\frac{\partial \dot{u}}{\partial R} + \frac{2\dot{u}}{R}\right) + \frac{1}{M_B}\frac{\partial p}{\partial t} = -\frac{K}{\eta}\nabla^2 p + \alpha\dot{e} + \frac{1}{M_B}\dot{p} = 3\phi\alpha_f\dot{T} + 3(\alpha - \phi)\alpha_s\dot{T} \tag{20.107}$$

where $M_B = \left(\frac{\phi}{K_f} + \frac{\alpha - \phi}{K_s}\right)^{-1}$ is the Biot modulus.

Now assume that the fluid and solid phases are incompressible. By taking the divergence of the equilibrium equation (Equation 20.105) and substituting $\nabla^2 p$ into the expression for fluid

flow given by Equation 20.107, we can obtain the following result for the governing equation for the volumetric strain:

$$\dot{e} = \frac{K}{\eta}(K_D + 4/3G_D)\nabla^2 e - \frac{K}{\eta}3K_D\alpha_s\nabla^2 T + 3\phi\alpha_f\dot{T} + 3(1-\phi)\alpha_s\dot{T} \tag{20.108}$$

In the case of compressible phases, Equation 20.108 will be coupled with the fluid pressure Belotserkovets and Prevost [106].

The temperature satisfies the heat conduction equation given by

$$\left(\frac{\partial^2 T}{\partial R^2} + \frac{2}{R}\frac{\partial T}{\partial R}\right) = \frac{\rho c_p}{k_c}\frac{\partial T}{\partial t} \tag{20.109}$$

A solution to the governing equations (Equations 20.108 and 20.109, respectively), for the volumetric strain and temperature, should satisfy the boundary and initial conditions applicable to a problem.

When the boundary of the sphere is subjected to a temperature change T_0 and the fluid pressure and radial stress at the boundary are maintained at zero values, we require

$$T(R_0,t) = T_0; \quad p(R_0,t) = 0; \quad \sigma_{RR}(R_0,t) = 0; \quad t \geq 0 \tag{20.110}$$

It was shown by Mason et al. [173] that the stress boundary condition can be written in terms of the volumetric strain as

$$\sigma_{RR}(R_0,t) = \left(K_D + \frac{4}{3}G_D\right)e(R_0,t) - \frac{4G_D}{R_0^3}\int_0^{R_0} R^2 e(R,t)dR - 3K_D\alpha_S T(R_0,t) - \alpha p(R_0,t) = 0 \tag{20.111}$$

At time $t = 0$, all the dependent variables within the sphere are assumed to be zero; this corresponds to the initial conditions

$$u(R,0) = p(R,0) = T(R,0) = 0; \quad 0 \leq R \leq R_0 \tag{20.112}$$

The solution of the heat conduction equation given by Equation 20.109 can be obtained by using a Laplace transform technique; the Laplace transform of the temperature field can be found as

$$\bar{T}(R,s) = \frac{T_0}{s}\frac{R_0}{R}\frac{\sinh(R/R_0\sqrt{s\kappa})}{\sinh(\sqrt{s\kappa})} \quad \kappa = \frac{R_0^2\rho c_p}{k_c} \tag{20.113}$$

where s is the Laplace transform parameter (Sneddon [138,139], Selvadurai [137], Carslaw and Jaeger[140]). By using the Cauchy residue theorem, Equation 20.113 for $\bar{T}(R,s)$ can be inverted, and the temperature field can be obtained in the form

$$T(R,t) = T_0 - 2T_0\left[\sum_{n=1}^{\infty}(-1)^{n+1}e^{-n^2\pi^2\tau}\frac{\sin(n\pi R/R_0)}{n\pi R/R_0}\right] \quad \tau = \frac{k_c}{\rho c_p}\frac{t}{R_0^2} = \frac{t}{\kappa} \tag{20.114}$$

In the limit as $R \to 0$, $\dfrac{\sin(n\pi R/R_0)}{n\pi R/R_0} = 1$.

We can use procedures similar to those prescribed previously and obtain an expression for $\bar{e}(R,s)$, which can be inverted to determine the time-dependent variation in the volumetric strain. The details of the procedures are described in Selvadurai and Suvorov [154]. It is sufficient to record here only the time-dependent variation in the volumetric strain:

$$
\begin{aligned}
e(R,t) = {} & \frac{1}{(\kappa/\omega - 1)} C_\alpha T_0 + 3\alpha_s T_0 + C_\alpha \frac{1}{1-\kappa/\omega} \left\{ T_0 - 2T_0 \left[\sum_{n=1}^{\infty} (-1)^{n+1} \exp(-n^2\pi^2 t/\kappa) \frac{\sin(n\pi R/R_0)}{n\pi R/R_0} \right] \right\} \\
& + 8G_D \frac{\omega/\kappa}{(1-\kappa/\omega)} C_\alpha T_0 \sum_{n=1}^{\infty} \frac{1}{Q_n} \frac{R_0}{R} \sin\left(n\pi\sqrt{\omega/\kappa}\, \frac{R}{R_0} \right) \exp(-n^2\pi^2 t/\kappa) \\
& + \frac{\omega/\kappa}{(1-\kappa/\omega)} C_\alpha T_0 \sum_{n=1}^{\infty} \frac{1}{x_n \sin(\sqrt{x_n \kappa/\omega})} \frac{T_n}{H_n} \frac{R_0}{R} \sin\left(\sqrt{x_n}\, \frac{R}{R_0} \right) \exp(-x_n t/\omega) \\
& + 3K_D \alpha_s T_0 \sum_{n=1}^{\infty} \frac{1}{H_n} \frac{R_0}{R} \sin\left[\sqrt{x_n} R/R_0 \right] \exp(-x_n t/\omega)
\end{aligned}
\tag{20.115}
$$

where

$$
\begin{aligned}
Q_n &= (K_D + 4/3G_D)(-n^2\pi^2\omega/\kappa)\sin(n\pi\sqrt{\omega/\kappa}) - 4G_D n\pi\sqrt{\omega/\kappa}\cos(n\pi\sqrt{\omega/\kappa}) \\
&\quad + 4G_D \sin(n\pi\sqrt{\omega/\kappa}) \\
H_n &= (K_D - 2/3G_D)\sin(\sqrt{x_n}) + (K_D + 4/3G_D)\sqrt{x_n}\cos(\sqrt{x_n})/2 \\
T_n &= (K_D + 4/3G_D)(-x_n\kappa/\omega)\sin(\sqrt{x_n\kappa/\omega}) - 4G_D\sqrt{x_n\kappa/\omega}\cos(\sqrt{x_n\kappa/\omega}) \\
&\quad + 4G_D \sin(\sqrt{x_n\kappa/\omega}), \quad n = 1,2,\ldots
\end{aligned}
\tag{20.116}
$$

The result given by Equation 20.115 can be integrated to determine the time-dependent radial displacement of the sphere and the time-dependent pore fluid pressure distribution within the poroelastic sphere. For example, the radial displacement can be found by integrating the result for the volumetric strain, that is,

$$
u = \frac{1}{R^2} \int_0^R R^2 e(R,t)\, dR \tag{20.117}
$$

Other results and limiting cases of interest are presented in the article by Selvadurai and Suvorov [154].

20.4.2 Computational Results for the Boundary Heating of a Poroelastic Sphere

The analytical solution for the thermoporoelastic sphere presented in Section 20.4.1 was used to examine the computational results for the boundary heating of a thermoporoelastic sphere of radius $R_0 = 10$ m. The sphere is subjected to a temperature rise of 100°C on the external surface. (As indicated previously, we implicitly assume that although the temperature of the fluid is set to 100°C, we do not account for any phase transformations during heating.) The initial temperature in the sphere is assumed to be zero. The outer boundary of the sphere is assumed to be free draining, the radial skeletal tractions are prescribed to be zero, and the surface of the sphere is subjected to a constant temperature. The boundary conditions associated with the heating of the poroelastic sphere are given in Equation 20.110, and the initial conditions governing the thermoporoelasticity problem are given by Equation 20.112.

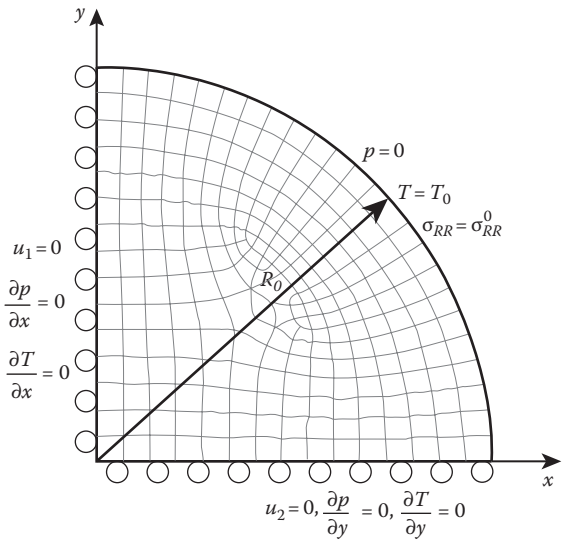

FIGURE 20.10 The 2D finite element discretizations used in COMSOL (241 elements).

The results were evaluated analytically, using the closed-form analytical expressions for the volumetric strain (e), the pore fluid pressure (p), the hoop stress ($\sigma_{\Phi\Phi}$), and the surface displacement (u_R) given by Selvadurai and Suvorov [154] and numerically using the finite element program COMSOL. The computational modeling can be performed using a 2D axisymmetric formulation. Figure 20.10 shows the projection of the sphere onto the x-y plane of the Cartesian coordinate system and the finite element mesh generated by COMSOL. Appropriate zero boundary conditions were imposed on the displacements, fluid velocity, tractions, and thermal gradients at the relevant boundaries of the domain to ensure symmetry.

The mechanical and physical parameters of the thermoporoelastic problem are specified as follows: Young's modulus of the drained skeleton, $E = 60 \times 10^9$ Pa; Poisson's ratio, $\nu = 0.30$; viscosity of the pore fluid, $\eta = 0.001$ Pa s; permeability, $K = 3 \times 10^{-19}$ m^2 or 3×10^{-20} m^2; thermal conductivity, $k_c = 3.15$ W/m°C; specific heat of the solid material, $c_s = 700$ J/kg/°C; density of the solid material, $\rho_s = 2700$ kg/m^3; specific heat of the fluid, $c_w = 4190$ J/kg/°C; density of the fluid, $\rho_w = 1000$ kg/m^3; coefficient of linear thermal expansion of dry skeleton, $\alpha_s = 8.3 \times 10^{-6}(°C)^{-1}$; coefficient of linear thermal expansion of fluid, $\alpha_f = 69 \times 10^{-6}(°C)^{-1}$ (°C)$^{-1}$; and porosity, $\phi = 0.25$. Both the solid material composing the porous skeleton and the fluid are assumed to be incompressible. The time-dependent evolution of the temperature in the sphere can be obtained using Equation 20.114. The temperature is initially equal to zero at all points except at the external surface, where it is prescribed equal to $T_0 = 100$°C, and it then gradually increases reaching the maximum value of 100°C. The time-dependent evolution of volumetric strain at the center, the midradius, and the external surface of the poroelastic sphere subjected to boundary heating is shown in Figure 20.11, for the case where the permeability of the sphere is set to $K = 3E{-}19$ m^2. The initial value of the volumetric strain is zero at all points within the sphere except at the boundary, where it is equal to $3\alpha_S T_0 K_D/(K_D + 4/3G_D) = 0.0015$. The long-term value of the volumetric strain is equal to the thermoelastic expansion of the drained skeleton of the elastic sphere, that is, $3\alpha_S T_0 = 0.0025$, applicable to all locations. Figure 20.12 shows the volumetric strain at the boundary of thermoporoelastic sphere for two values of permeability, $K = 3E{-}19$ m^2 and $K = 3E{-}20$ m^2. If the permeability is $K = 3E{-}19$ m^2, the volumetric strain monotonically increases as a function of time. If the permeability is an order of magnitude lower (i.e., $K = 3E{-}20$ m^2), the evolution of the volumetric strain is not monotonic, and the transient value of the strain exceeds its steady-state value, that is, $3\alpha_S T_0 = 0.0025$. This behavior does not occur in the thermoelastic

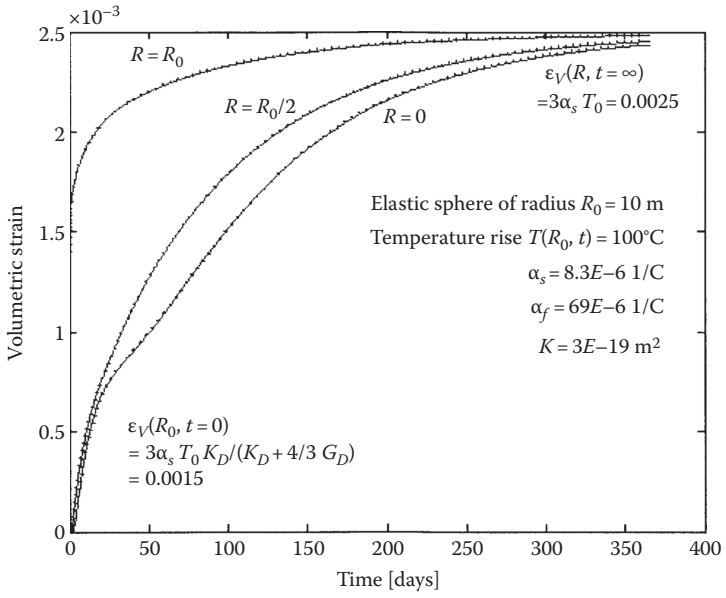

FIGURE 20.11 Volumetric strain for the poroelastic sphere of radius 10 m subjected to a sudden temperature rise of 100°C at the boundary. The permeability is $K = 3E{-}19$ m^2. (The points indicate the solution derived using the COMSOL code, and the solid line indicates the analytical solution.)

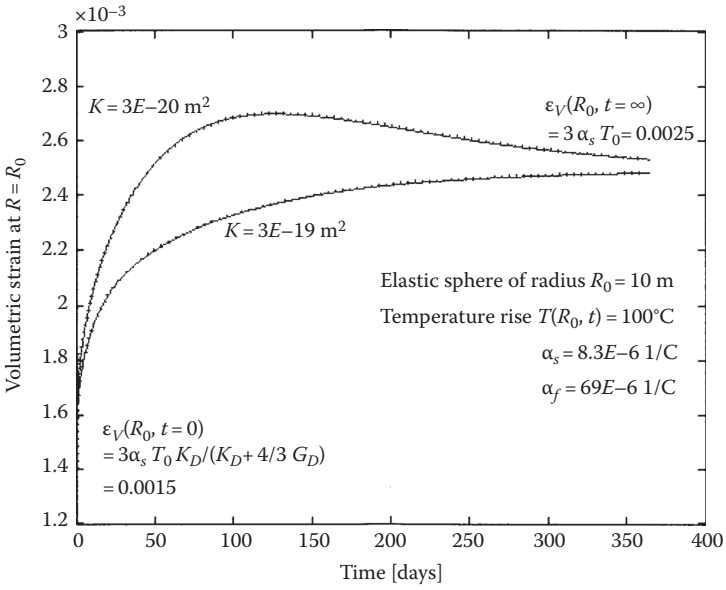

FIGURE 20.12 Volumetric strain at the boundary of the poroelastic sphere for two values of permeability, $K = 3E{-}19$ m^2 and $K = 3E{-}20$ m^2. The sphere is subjected to a sudden temperature rise of 100°C at the boundary. (Dotted line indicates the solution derived using the COMSOL code, and the solid line indicates the analytical solution.)

sphere, and this effect is a consequence of the thermal expansion of the fluid that flows out of the sphere very slowly because of the low permeability.

Figure 20.13 illustrates the time-dependent evolution of the hoop stress $\sigma_{\phi\phi}$ at the boundary of the thermoporoelastic sphere. As before, two values of permeability are used, $K = 3E{-}19$ m^2 and $K = 3E{-}20$ m^2. From the results given by Selvadurai and Suvorov [154], the initial value of the hoop stress is given by $-6\alpha_S T_0 K_D G_D/(K_D + 4/3G_D) = -71.14$ MPa. The hoop stress is a monotonic function of time and entirely compressive if the permeability is $K = 3E{-}19$ m^2. However, if the permeability is $K = 3E{-}20$ m^2, the hoop stress is not a monotonic function and can become tensile for some period of time during the deformation. This phenomenon can be explained by the thermal expansion of the fluid and cannot be captured by the thermoelastic model. The steady-state value of the stress is zero.

The time-dependent evolution of the surface displacement of the poroelastic sphere is illustrated in Figure 20.14, for two values of the permeability: $K = 3E{-}19$ m^2 and $K = 3E{-}20$ m^2. The initial displacement is zero, and the final displacement is equal to that of the displacement due to the thermal expansion of the elastic sphere, $\alpha_S T_0 R_0 = 0.0083$ m. If the permeability of the sphere is small, the surface displacement is not a monotonic function of time and exceeds its steady-state value for some period of time.

A striking feature of the poroelastic solution is the presence of the fluid pressure as a dependent variable. Figure 20.15 shows the fluid pressure at the center of the poroelastic sphere for the two different values of permeability, $K = 3E{-}19$ m^2 and $K = 3E{-}20$ m^2. The fluid pressure is shown to be smaller in the sphere with the larger permeability. The fluid pressure is a nonmonotonic function of time for both values of the permeability. The initial and the final values of the fluid pressure are zero, and the result is consistent with the diffusive character of the pore pressure variation.

Figure 20.16 illustrates the influence of the thermal expansion coefficient of the solid and fluid phases on the fluid pressure at the center of the poroelastic sphere. The thermal expansion of the solid phase is $\alpha_s = 0$ or $\alpha_s = 8.3E{-}61$/C, and the thermal expansion of the fluid phase is $\alpha_f = 6.9E{-}51$/C. The permeability is set to $K = 3E{-}20$ m^2. By comparing the two graphs, it is apparent that the thermal expansion of the solid phase gives rise to negative fluid pressure, while the thermal expansion of the fluid phase leads to positive pressure. Figure 20.17 illustrates the fluid pressure evolution at

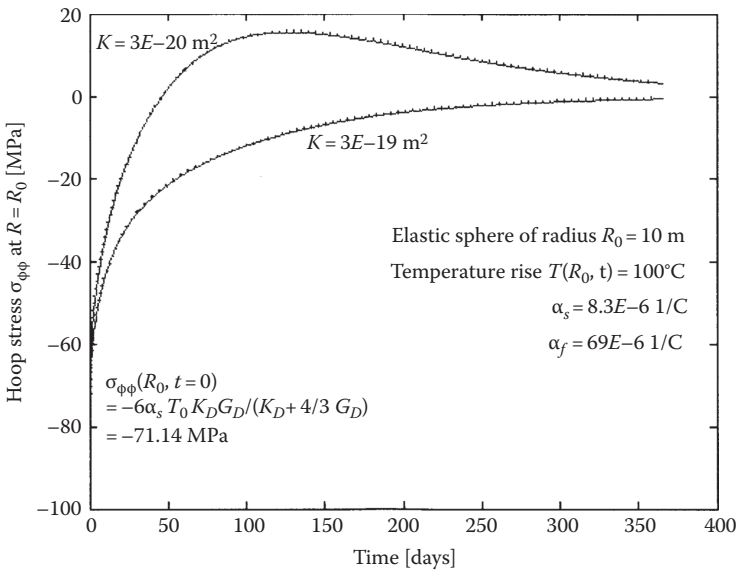

FIGURE 20.13 Hoop stress at the boundary of the poroelastic sphere for two values of permeability, $K = 3E{-}19$ m^2 and $K = 3E{-}20$ m^2. The sphere is subjected to a sudden temperature rise of 100°C at the boundary. (Dotted line indicates the solution derived using the COMSOL code, and the solid line indicates the analytical solution.)

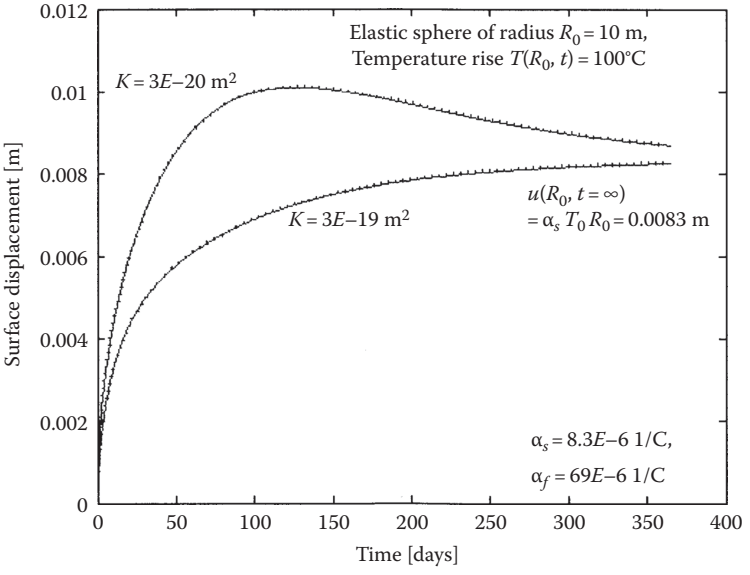

FIGURE 20.14 Displacement of the boundary surface of the poroelastic sphere for two values of permeability, $K = 3E{-}19$ m^2 and $K = 3E{-}20$ m^2. The sphere is subjected to a sudden temperature rise of 100°C at the boundary. (Dotted line indicates the solution derived using the COMSOL code, and the solid line indicates the analytical solution.)

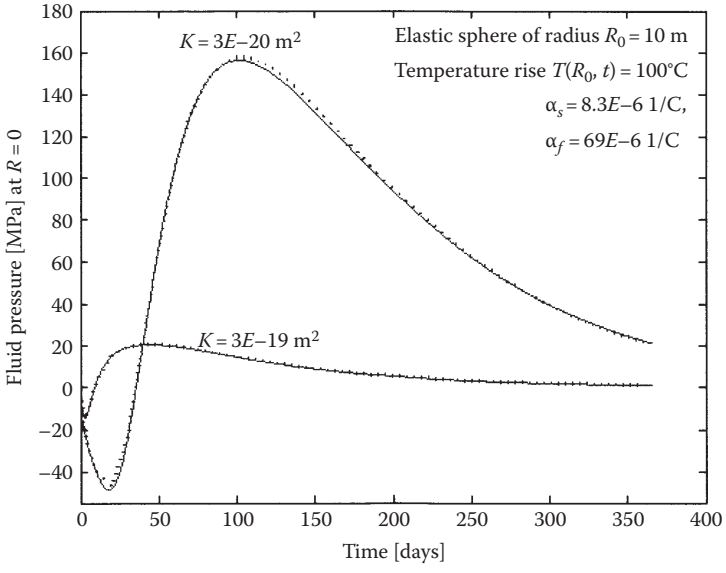

FIGURE 20.15 Fluid pressure at the center of the poroelastic sphere for two values of permeability, $K = 3E{-}19$ m^2 and $K = 3E{-}20$ m^2. The sphere is subjected to a sudden temperature rise of 100°C at the boundary. (Dotted line indicates the solution derived using the COMSOL code, and the solid line indicates the analytical solution.)

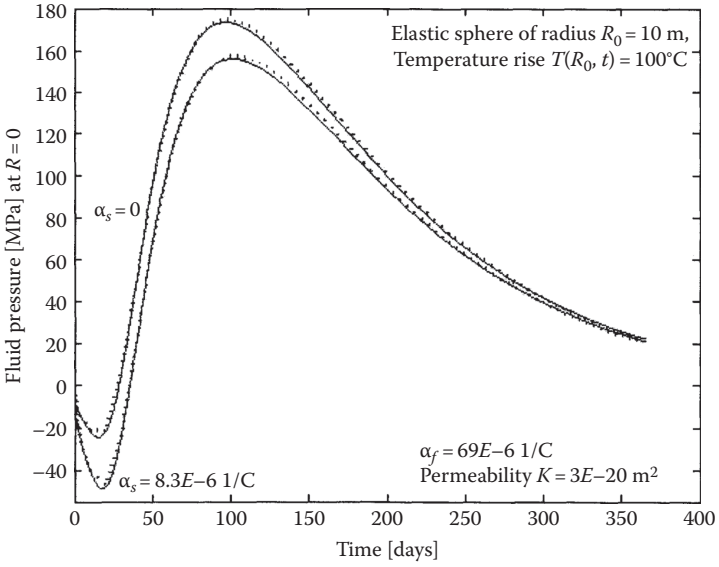

FIGURE 20.16 Fluid pressure at the center of the poroelastic sphere for two values of the thermal expansion of the solid phase equal to 0 and 8.3*E*−61/°C. The thermal expansion of the fluid is 6.9*E*−51/°C, and the permeability is set to K = 3*E*−20 m². The sphere is subjected to a sudden temperature rise of 100°C at the boundary. (Dotted line indicates the solution derived using the COMSOL code, and the solid line indicates the analytical solution.)

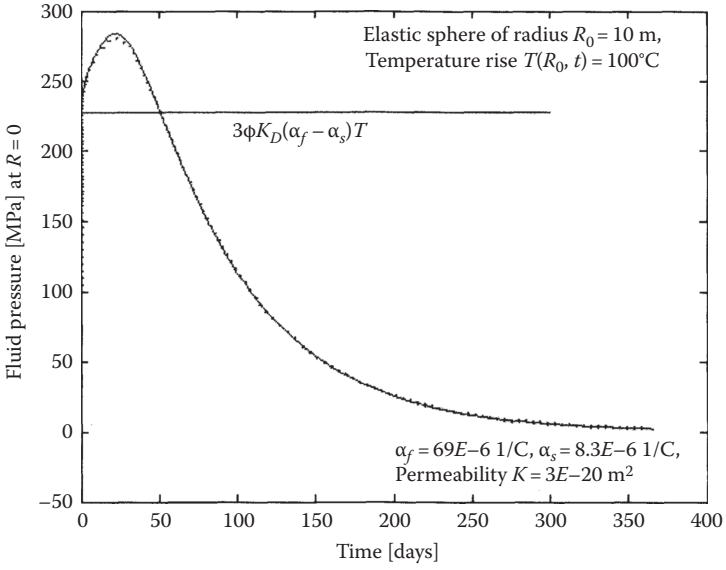

FIGURE 20.17 Fluid pressure at the center of two poroelastic spheres subjected to a uniform and constant temperature rise of 100°C inside the domain. The two poroelastic spheres have either zero pressure or zero flux prescribed at the boundary. (Dotted line indicates the solution derived using the COMSOL code, and the solid line indicates the analytical solution.)

the center of two poroelastic spheres subjected to a *uniform* temperature change $T(R, t) = 100°C$ for all R and t. It is assumed that this temperature change is applied instantaneously as a Heaviside step function of time. In one case, the fluid pressure at the boundary is maintained at zero (drained sphere), and in the second case, the velocity at the boundary is set to zero (undrained sphere). For the case of the poroelastic sphere with an undrained boundary, the pressure remains constant with time and equal to $3\phi K_D(\alpha_f - \alpha_s)T = 227$ MPa, if the porosity is $\phi = 0.25$. In the case of the poroelastic sphere with a fully drained boundary, in the short term, the pore fluid pressure at the center of the poroelastic sphere experiences the thermoporoelastic Mandel–Cryer effect (Mason et al. [173]). Further discussions of these effects are given in the articles by Selvadurai and Suvorov [154,155].

20.5 CONCLUDING REMARKS

The topic of coupled processes resulting from THM effects in porous media with an elastic skeleton is the canonical extension of the classical theory of poroelasticity first proposed by Biot. The degree of coupling between the deformations of the porous skeleton, the pore fluid pressures, and the temperature fields can take various forms, and the simplest approach is to consider the range of mechanical and fluid flow problems that will not contribute to the heat transport in the poroelastic medium. This will result in a heat transport mechanism that involves heat conduction as an uncoupled heat conduction equation. This approximation is not expected to be universally applicable to all porous media but can have wider applicability to porous media, such as geomaterials, including rocks, concrete, and other cementitious materials with relatively low permeability values. The temperature field can influence the deformation of the fluid-saturated poroelastic medium and thermally generated fluid velocities. The decoupling of the contributions of the fluid flow and the mechanical deformations to the heat transfer process results in a weakly coupled system, where the temperature fields can be computed independent of the mechanical and fluid flow processes. This is a convenient strategy for developing analytical and computational solutions for problems associated with THM processes in porous media. The chapter presents analytical results for the 1D problem, and these results are used to calibrate a computational approach for solving the identical problem. There is a good comparison between the computational results and the analytical solutions. The discussion is also extended to the development of analytical solutions to the problem of a fluid-saturated sphere that is subjected to boundary heating. These solutions are also used to calibrate the accuracy of computational results. The comparisons are good and both approaches are able to predict the thermally induced Mandel–Cryer effects in the fluid-saturated porous medium.

The scope of this chapter is restricted to presenting thermoporoelastic effects in fluid-saturated porous media. This naturally excludes discussion of some aspects of THM responses including unsaturated flow, nonlinear mechanical behavior of the porous skeleton that can include plasticity, viscoplasticity, and viscoelasticity effects, and dynamic effects in the poroelastic medium that can be initiated by the sudden application of mechanical loads and heating. The literature review is therefore narrow in scope and not intended to cover informative developments in the aforementioned topics.

NOMENCLATURE

x	Coordinate vector
x_1, x_2, x_3	Cartesian coordinates
x, y, z	Cartesian coordinates
R	Radial coordinate for spherical symmetry
R_0	Radius of sphere
t	Time
δ_{ij}	Kronecker's delta function
$u_i(\mathbf{x}, t)$	Displacement components
$v_i(\mathbf{x}, t)$	Fluid velocity components

$\varepsilon_{ij}(\mathbf{x}, t)$	Strain tensor
$\varepsilon_V = \varepsilon_{kk}$	Volumetric strain
α	Biot parameter
M_B	Biot modulus
G_D	Linear elastic shear modulus for the porous skeleton
G_u	Effective shear modulus of the undrained material
K_D	Linear elastic bulk modulus for the porous skeleton
K_u	Effective bulk modulus of the undrained porous medium
K_s	Bulk modulus of the solid material composing the skeleton
K_f	Bulk modulus of the fluid
n	Porosity
T	Temperature
p	Pore fluid pressure
α_s	Coefficient of linear expansion of the solid phase
α_f	Coefficient of linear expansion of the fluid phase
α_u^*	Effective thermal expansion coefficient
T_0	Reference temperature in degree Kelvin
$\sigma_{ij}(\mathbf{x}, t)$	Total Cauchy stress tensor
$\tilde{\sigma}_{ij}(\mathbf{x}, t)$	Effective Cauchy stress tensor
m_f	Fluid mass
Δm_f	Change in the fluid mass
k	Permeability
$h_i(\mathbf{x}, t)$	Heat flux vector
k_c^*	Effective thermal conductivity of the porous medium
c_f	Specific heat of the fluid phase
c_s	Specific heat of the solid phase
c_p^*	Effective specific heat of the porous medium
S	Surface of control volume
S_d^M, S_t^M	Surfaces on which displacement and tractions are prescribed
S_D^p, S_N^p	Surfaces on which Dirichlet and Neumann pressure boundary conditions are prescribed
S_D^T, S_N^T	Surfaces on which Dirichlet and Neumann temperature boundary conditions are prescribed
$u_i^0(\mathbf{x}), t_i^0(\mathbf{x})$	Initial values of displacements and tractions
$p^0(\mathbf{x})$, $T^0(\mathbf{x})$	Initial values of pressure and temperature
L	Length of 1D element
p_0, T_0	Initial values of pressure and temperature
$\{\mathbf{d}\}^{(n+1)}$	Nodal displacements
$\{\mathbf{T}\}^{(n+1)}$	The nodal temperatures
$\{\mathbf{p}\}^{(n+1)}$	Nodal pore pressures
$\{\}^{(n+1)}$	Values at the current time step
$\{\}^{(n)}$	Values at the preceding step
$\{\mathbf{FH}\}$	Heat flux vector
Δt	Time increment
θ	Time-integration parameter
$[\mathbf{K}]$, $[\mathbf{CP}]$	Assembled from element matrices
s	Laplace transform parameter
σ_{RR}, $\sigma_{\Phi\Phi}$	Stresses in spherical coordinates
κ	Thermal diffusivity parameter
τ	Nondimensional time
ω_m^2, κ_m^2	Parameters in summation of series

DISCLAIMER

The use of the COMSOL Multiphysics code is purely for demonstration purposes only. The author and the research sponsors do not advocate or recommend the use of this code without conducting suitable validation procedures that test the computational accuracy of the code in a rigorous fashion.

ACKNOWLEDGMENTS

The work presented in this chapter was supported by the James McGill Research Chairs program at McGill University and through research grants awarded by the Natural Sciences and Engineering Research Council of Canada and the Nuclear Waste Management Organization of Ontario. The work was completed during a visit to the Departamento de Engenharia Civil, Pontifícia Universidade Católica do Rio de Janeiro, Brazil, through a research fellowship awarded by CAPES Special Visiting Researcher Program. The author is grateful to Professor Ney A. Dumont for research discussions and the department for its kind hospitality. The author acknowledges the contributions of his former doctoral students, Quentin Yue, Son Nguyen, Jun Hu, Ali Shirazi, Qifeng Yu, Wenjun Dong, Hani Ghiabi, and Meysam Najari, and postdoctoral fellows and research associates, Gilles Armand Alex Suvorov and Paul Selvadurai, for their contributions to the research effort in environmental geomechanics in the Department of Civil Engineering and Applied Mechanics, McGill University. Thanks also to Sally Selvadurai for her editorial assistance.

REFERENCES

1. Terzaghi, K. *Erdbaumechanik auf Bodenphysikalischer Grundlage*, Vienna, Austria, Franz Deuticke, 1925.
2. Fillunger, P. *Erdbaumechanik*?, Wien, Germany: Selbstverlag des Verfassers, 1936.
3. De Boer, R., Ed. *Porous Media: Theory and Experiments*, Dordrecht, the Netherlands, Kluwer Academic Publishers, 2000.
4. Lade, P.V. and De Boer, R. The concept of effective stress for soil, concrete and rock, *Géotechnique* 47: 61–78, 1997.
5. Biot, M.A. General theory of three-dimensional consolidation, *J. Appl. Phys*. 12: 155–164, 1941.
6. Mandel, J. Etude mathematique de la consolidation des sols, Actes du colloque International de mecanique, *Poitiers* 4: 9–19, 1950.
7. de Josselin de Jong, G. Application of stress functions to consolidation problems, *Proceedings of the Fourth International Conference on Soil Mechanics and Foundation Engineering*, London, U.K., Vol. 1, pp. 320–323, 1957.
8. McNamee, J. and Gibson, R.E. Plane strain and axially symmetric problems of the consolidation of a semi-infinite clay stratum, *Q. J. Mech. Appl. Math*. 13: 210–227, 1960.
9. Cryer, C.W. A comparison of the three-dimensional consolidation theories of Biot and Terzaghi, *Q. J. Mech. Appl. Math*. 16: 401–412, 1963.
10. de Wiest, R.J.M. *Flow through Porous Media*, New York, Academic Press, 1969.
11. Agbezuge, L.K. and Deresiewicz, H. The consolidation of a circular footing, *Isr. J. Technol*. 13: 264–269, 1975.
12. Gaszynski, J. and Szefer, G. Axisymmetric problem of the punch for the consolidating semi-space with mixed boundary permeability conditions, *Arch. Mech*. 30: 17–26, 1978.
13. Chiarella, C. and Booker, J.R. The time-settlement behaviour of a rigid die resting on a deep clay layer, *Q. J. Mech. Appl. Math*. 28: 317–328, 1975.
14. Rice, J.R. and Cleary, M.P. Some basic stress diffusion solutions for fluid-saturated elastic porous media with compressible constituents, *Rev. Geophys. Space Phys*. 14: 227–241, 1976.
15. Booker, J.R. and Small, J.C. Finite layer analysis of soil consolidation I, *Int. J. Numer. Analyt. Methods Geomech*. 6: 151–171, 1982.
16. Booker, J.R. and Small, J.C. Finite layer analysis of soil consolidation II, *Int. J. Numer. Analyt. Methods Geomech*. 6: 173–194, 1982.
17. Booker, J.R. and Randolph, M.F. Consolidation of a cross-anisotropic soil medium, *Q. J. Mech. Appl. Math*. 37: 479–495, 1984.

18. Bear, J. and Corapcioglu, M.Y. (Eds.) *Fundamentals of Transport Phenomena in Porous Media*, Dordrecht, the Netherlands, Nijhoff, 1985.
19. Whitaker, S. Flow in porous media. I. A theoretical derivation of Darcy's law, *Transp. Porous Media* 1: 3–25, 1986.
20. Whitaker, S. Flow in porous media II. The governing equations for immiscible, two phase flow, *Transp. Porous Media* 1: 105–125, 1986.
21. Whitaker, S. Flow in porous media III. Deformable media, *Transp. Porous Media* 1: 127–154, 1986.
22. Kassir, M.K. and Xu, J. Interaction functions of a rigid strip bonded to saturated elastic halfspace, *Int. J. Solids Struct*. 24: 915–936, 1988.
23. Ehlers, W. Toward finite theories of liquid-saturated elasto-plastic porous media, *Int. J. Plast*. 7: 433–475, 1991.
24. de Boer, R. and Ehlers, W. Uplift, friction and capillarity: Three fundamental effects for liquid-saturated porous solids, *Int. J. Solids. Struct*. 26: 43–57, 1990.
25. Atkinson, C. and Craster, R.V. Plane strain fracture in poroelastic media, *Proc. R. Soc. Math. Phys. Ser. A* 434: 605–663, 1991.
26. Detournay, E. and Cheng, A.H.-D. Fundamentals of poroelasticity. In *Comprehensive Rock Engineering* (J. Hudson, Ed.), Oxford, U.K., Pergamon Press, Vol. 2, 1993, pp.113–171.
27. Selvadurai, A.P.S. and Yue, Z.Q. On the indentation of a poroelastic layer, *Int. J. Numer. Analyt. Methods Geomech*. 18: 161–175, 1994.
28. Yue, Z.Q. and Selvadurai, A.P.S. On the mechanics of a rigid disc inclusion embedded in a fluid saturated poroelastic medium, *Int. J. Eng. Sci*. 33: 1633–1662, 1995.
29. Yue, Z.Q. and Selvadurai, A.P.S. Contact problems for saturated poroelastic solid, *J. Eng. Mech. Div. ASCE* 121: 502–512, 1995.
30. Lan, Q. and Selvadurai, A.P.S. Interacting indenters on a poroelastic halfspace, *J. Appl. Math. Phys.* (*ZAMP*) 47: 695–716, 1996.
31. Oyen, M.L. Poroelastic nanoindentation responses of hydrated bone, *J. Math. Res*. 23: 1307–1314, 2008.
32. Galli, M. and Oyen, M.L. Fast identification of poroelastic parameters from indentation tests, *Comp. Model. Eng. Sci*. 48: 241–268, 2009.
33. Coussy, O. *Mechanics of Porous Media*, New York, John Wiley, 1995.
34. Selvadurai, A.P.S. (Ed.). *Mechanics of Porous Media*, Dordrecht, the Netherlands, Kluwer Academic, 1996.
35. Cheng, A.H.-D., Detournay, E., and Abousleiman, Y. (Eds.). Poroelasticity, *Maurice A. Biot Memorial Issue, Int. J. Solids Struct*. 35: 4513–5031, 1998.
36. Thimus, J.-F., Abousleiman, Y., Cheng, A.H.-D., Coussy, O., and Detournay, E. (Eds.). *Poromechanics: A Tribute to Maurice A. Biot, Proc. Biot Conf. Poromech., Louvain-la-Neuve, Belgium*, Rotterdam, the Netherlands, A.A. Balkema, 1998.
37. Lewis, R.W. and Schrefler, B.A. *The Finite Element Method in the Static and Dynamics Deformation and Consolidation of Porous Media*, New York, John Wiley, 1998.
38. Drew, D.A. and Passman, S.L. *Theory of Multicomponent Fluids*, Berlin, Germany, Springer-Verlag, 1998.
39. Wang, H.F. *Theory of Linear Poroelasticity with Applications to Geomechanics and Hydrogeology*, Princeton, NJ, Princeton University Press, 2000.
40. Verruijt, A. *Theory and Problems of Poroelasticity*, Delft, the Netherlands, Delft University of Technology, 2014.
41. Scheidegger, A.E. Flow through porous media, *Appl. Mech. Rev*. 13: 313–318, 1960.
42. Paria, G. Flow of fluids through porous deformable solids, *Appl. Mech. Rev*. 16: 901–907, 1963.
43. Schiffman, R.L. A bibliography on soil consolidation in fundamentals of transport. In *Porous Media* (J. Bear and M.Y. Corapcioglu, Eds.), Dordrecht, the Netherlands, Martinus Nijhoff Publishers, 1984, pp. 617–669.
44. Selvadurai, A.P.S. The analytical method in geomechanics, *Appl. Mech. Rev*. 60: 87–106, 2007.
45. Cowin, S.C. (Ed.) *Bone Mechanics Handbook*, New York, Taylor & Francis, 2001.
46. Altay, G. and Dokmeçi, M.C. A uniqueness theorem in Biot's poroelasticity theory. *J. Appl. Math. Phys*. (*ZAMP*) 49: 838–846, 1998.
47. Bowen, R.M. Theory of mixtures. In *Continuum Physics*, Vol. III (A.C. Eringen, Ed.), New York, Academic Press, 1976.
48. Bowen, R.M. Incompressible porous media models by use of the theory of mixtures, *Int. J. Eng. Sci*. 18: 1129–1148, 1980.
49. Green, A.E. and Naghdi, P.M. The flow of fluid through an elastic solid, *Acta Mech*. 9: 329–340, 1970.

50. Green, A.E. and Steel, T.R. Constitutive equations for interacting continua, *Int. J. Eng. Sci*. 4: 483–500, 1966.
51. Crochet, M.J. and Naghdi, P.M. On constitutive equations for flow of fluid through an elastic solid, *Int. J. Eng. Sci*. 4: 383–401, 1966.
52. Crochet, M.J. A mixture of two simple materials, *Acta Mech*. 12: 189–208, 1971.
53. Mills, N. and Steel, T.R. Non-linear deformations of a mixture of two isotropic elastic solids, *Acta Mech*. 9: 229–244, 1970.
54. Atkin, R.J. and Craine, R.E. Continuum theories of mixtures: Basic theory and historical development, *Q. J. Mech. Appl. Math*. 29: 209–244, 1976.
55. Bedford, A. and Drumheller, D.S. A variational theory of immiscible mixtures, *Arch. Rat. Mech. Anal*. 68: 37–51, 1978.
56. Bedford, A. and Drumheller, D.S. Theories of immiscible and structured mixtures, *Int. J. Eng. Sci*. 8: 863–960, 1983.
57. Drumheller, D.S. On theories of reacting immiscible mixtures, *Int. J. Eng. Sci*. 38: 347–382, 2000.
58. Bennethum, L.S. and Cushman, J.H. Multiscale, hybrid mixture theory for swelling systems, Part II: Constitutive theory, *Int. J. Eng. Sci*. 34: 147–169, 1996.
59. Murad, M.A., Bennethum, L.S., and Cushman, J.H. A multiscale theory of swelling porous media: Application to one-dimensional consolidation. *Transp. Porous Media* 19: 93–122, 1995.
60. Gajo, A. A general approach to the isothermal hyperelastic modelling of saturated porous media at finite strains with compressible solid constituents, *Proc. R. Soc. A. Math. Phys*., 2010.
61. Rajagopal, K.R. and Tao, L. *Mechanics of Mixtures*, Singapore, World Scientific Publishing, 1995.
62. Dell'Isola, F. and Romano, A. On the derivation of thermomechanical balance equations for continuous systems with a nonmaterial interface, *Int. J. Eng. Sci*. 25: 1459–1468, 1987.
63. Holister, C.D., Anderson, D.R., and Heath, G.R. Seabed disposal of nuclear wastes, *Science* 213: 1321–1326, 1981.
64. Gnirk, P. *OECD/NEA International Stripa Project Overview. Natural Barriers*, Stockholm, Sweden, SKB, 1993.
65. Selvadurai, A.P.S. Heat-induced moisture movement in a clay barrier I. Experimental modelling of borehole emplacement, *Eng. Geol*. 41: 239–256, 1996.
66. Selvadurai, A.P.S. Heat-induced moisture movement in a clay barrier II. Computational modelling and comparison with experimental results, *Eng. Geol*. 41: 219–238, 1996.
67. Selvadurai, A.P.S. and Nguyen, T.S. Scoping analyses of the coupled thermal-hydrological-mechanical behaviour of the rock mass around a nuclear fuel waste repository, *Eng. Geol*. 47: 379–400, 1996.
68. Selvadurai, A.P.S. and Nguyen, T.S. Mechanics and fluid transport in a degradable discontinuity, *Eng. Geol*. 53: 243–249, 1999.
69. Nguyen, T.S. and Selvadurai, A.P.S. Coupled thermal-mechanical-hydrological behaviour of sparsely fractured rock: Implications for nuclear fuel waste disposal, *Int. J. Rock Mech. Min. Sci. Geomech. Abstr*. 32: 465–479, 1995.
70. Nguyen, T.S. and Selvadurai, A.P.S. A model for coupled mechanical and hydraulic behaviour of a rock joint, *Int. J. Numer. Analyt. Meth. Geomech*. 22: 29–48, 1998.
71. Rutqvist, J., Borgesson, L., Chijimatsu, M., Nguyen, T.S., Jing, L., Noorishad, J., and Tsang, C.-F. Coupled thermo-hydro-mechanical analysis of heater test in fractured rock and bentonite at Kamaishi Mine—Comparison of field results to predictions of four finite element codes, *Int. J. Rock Mech. Min. Sci*. 38: 129–142, 2001.
72. Stephansson, O., Jing, L., and Tsang, C.-F. (Eds.). *Coupled Thermo-Hydro-Mechanical Processes of Fractured Media: Mathematical and Experimental Studies, Developments in Geotechnical Engineering*, Amsterdam, the Netherlands, Elsevier Science Publishing Co., 1996, p. 79.
73. Nguyen, T.S., Selvadurai, A.P.S., and Armand, G. Modelling of the FEBEX THM experiment using a state surface approach, *Int. J. Rock Mech. Min. Sci*. 42: 639–651, 2005.
74. Alonso, E.E. and Selvadurai, A.P.S. The FEBEX benchmark test: Case definition and comparison of modelling approaches, *Int. J. Rock Mech. Min. Sci*. 42: 611–638, 2005.
75. Chijimatsu, M., Giraud, A., Jing, L., Millard, A., Nguyen, T.S., Rejeb, A., Rutqvist, J., Souley, M., Sugita, Y., and Thoraval, A. Building confidence in the mathematical models by calibration with a T-H-M Experiment, Geoproc, SKB, 2003.
76. Lachenburch A. Friction heating, fluid pressure and the resistance to fault motion, *J. Geophys. Res*. 85: 6097–6112, 1980.
77. Mase, C.W. and Smith, L. Pore-fluid pressures and frictional heating on a fault surface, *Pure Appl. Geophys*. 122: 583–607, 1985.

78. Mase, C.W. and Smith, L. The role of pore fluids in tectonic processes, *Rev. Geophys*. 25: 1348–1358, 1987.
79. Aagaard, B.T., Heaton, T.H., and Hall, J.F. Dynamic earthquake ruptures in the presence of lithostatic normal stresses: Implications for friction models and heat production, *Bull. Seismol. Soc. Am*. 91: 1765–1796, 2001.
80. Sulem, J., Vardoulakis, I., Ouffroukh, H., Boulon, M.J., and Hans, J. Experimental characterization of the thermo-poro-mechanical properties of the Aegion Fault gouge, *C.R. Sci*. (*Geoscience*), 2004.
81. Rice, J.R. Heating and weakening of faults during earthquake slip, *J. Geophys. Res*. 111: 1–29, 2006.
82. Dickson, M.H. and Fanelli, M. (Eds.). *Geothermal Energy*, New York, John Wiley, 1995.
83. Duffield, W.A. and Sass, J.H. Geothermal energy-clean power from the earth's heat, Tech. Rep. Report C1249, U. S. Geological Survey, Reston, VA, 2003.
84. Jupp, T.E. and Schultz, A. A poroelastic model for the tidal modulation of seafloor hydrothermal systems, *J. Geophys. Res*. 109: B03105, 2004.
85. Knellwolf, C., Peron, H., and Laloui, L. Geotechnical analysis of heat exchanger piles, *J. Geotech. Geoenviron. Eng*., 2011.
86. Selvadurai, A.P.S., Hu, J., and Konuk, I. Computational modelling of frost heave induced soil-pipeline interaction. I. Modelling of frost heave, *Cold Reg. Sci. Tech*. 29: 215–228, 1999.
87. Selvadurai, A.P.S., Hu, J., and Konuk, I. Computational modelling of frost heave induced soil-pipeline interaction. II. Modelling of experiments at the caen test facility, *Cold Reg. Sci. Tech*. 29: 229–257, 1999.
88. Michałowski, R.L. and Zhu, M. Modelling of freezing in frost-susceptible soils, *Comp. Assist. Mech. Eng. Sci*. 13: 613–625, 2006.
89. Gens, A. Soil-environment interaction in geotechnical engineering, *Géotechnique* 60: 3–74, 2010.
90. Selvadurai, A.P.S. and Nguyen, T.S. Computational modelling of isothermal consolidation of fractured media, *Comp. Geotech*. 17: 39–73, 1995.
91. Chan, T., Christiansson, R., Boulton, G.S., Ericsson, L.O., Hartikainen, J., Jensen, M.R., Mas Ivars, D., Stanchcell, F.W., Vistrand, P., and Wallroth, T. DECOVALEX III BMT 3/BENCHPAR WP4: The thermo-hydro-mechanical responses to a glacial cycle and their potential implications for deep geological disposal of nuclear fuel waste in a fractured crystalline rock mass, *Int. J. Rock Mech. Min. Sci*. 42: 805–827, 2005.
92. Rutqvist, J., Vasco D., and Meyer, L. Coupled reservoir-geomechanical analysis of CO2 injection and ground deformations at In Salah, Algeria, *Int. J. Greenhouse Gas Control* 4: 225–230, 2010.
93. Selvadurai, A.P.S. Heave of a surficial rock layer due to pressures generated by injected fluids, *Geophys. Res. Lett*. 36: L14302, 2009.
94. Selvadurai, A.P.S. Caprock breach: A potential threat to secure geologic sequestration of CO_2. In *Geomechanics in CO_2 Storage Facilities* (G. Pijaudier-Cabot, J.-M. Pereira, Eds.), Hoboken, NJ, John Wiley & Sons, Inc., 2013, pp.75–93.
95. Vargas Jr., E.A., Velloso, R.Q., Ribeiro, W.N., Muller, A.L., and Vaz, L.E. Considerations on the numerical modelling of injection processes of CO_2 in geologic formations with emphasis on carboniferous formations and abandoned coal mines. In *CO_2 Storage in Carboniferous Formations and Abandoned Coal Mines* (M. He, Ribero e Sousa, L., Elsworth, D. Vargas, Jr., E.A. Eds.), Boca Raton, FL, CRC Press, 2012, pp. 107–123.
96. Smith, D.W. and Booker, J.R. Boundary element analysis of linear thermoelastic consolidation, *Int. J. Numer. Analyt. Meth. Geomech*. 20: 457–488, 1996.
97. Jiang, Q. and Rajapakse, R.K.N.D. On coupled heat-moisture transfer in deformable porous media, *Q. J. Mech. Appl. Math*. 47: 53–68, 1994.
98. Seneviratne, H.N., Carter, J.P., and Booker, J.R. Analysis of fully coupled thermomechanical behaviour around a rigid cylindrical heat source buried in clay, *Int. J. Numer. Analyt. Meth. Geomech*. 18: 177–203, 1994.
99. Bai, M. and Roegiers, J.-C. Fluid flow and heat flow in deformable fractured porous media, *Int. J. Eng. Sci*. 32: 1615–1633, 1994.
100. Wang, Y. and Papamichos, E. Thermal effects on fluid flow and hydraulic fracturing from wellbores and cavities in low permeability formations, *Int. J. Numer. Analyt. Methods Geomech*. 23: 1819–1834, 1999.
101. Bai, M. and Abousleiman, Y. Thermoporoelastic coupling with application to consolidation, *Int. J. Numer. Analyt. Methods Geomech*. 21: 21–132, 1997.
102. Giraud, A., Homand, F., and Rousset, G. Thermoelastic and thermoplastic response of a double-layer porous space containing a decaying heat source, *Int. J. Numer. Analyt. Methods Geomech*. 22: 133–139, 1998.
103. Zhou, Y., Rajapakse, R.K.N.D., and Graham, J. Coupled consolidation of a porous medium with a cylindrical or a spherical cavity, *Int. J. Numer. Analyt. Methods Geomech*. 22: 449–275, 1998.

104. Selvadurai, A.P.S. Weakly coupled problems in environmental geomechanics: Computational aspects and analytical constraints, *Proceedings of the Fourth GRACM Congress on Computational Mechanics*, Patras, Greece, pp.1–12, 2002.
105. Wu, B., Zhang X., and Jeffrey, R.G. A semi-analytical solution of a wellbore in a non-isothermal low-permeability porous medium under non-hydrostatic stresses, *Int. J. Solids Struct*. 49: 1472–1484, 2012.
106. Belotserkovets, A. and Prevost, J.H. Thermoporoelastic response of a fluid-saturated porous sphere: An analytical solution, *Int. J. Eng. Sci*. 49: 1415–1423, 2011.
107. Schiffman, R.L. A thermoelastic theory of consolidation. In *Environmental and Geophysical Heat Transfer*, C.J. Cremers, F. Kreith and J.A. Clark (Eds.) New York, ASME, 1971, pp. 78–84.
108. Brownell, D.H., Jr., Garg, S.K., and Pritchett, J.W. Governing equations for geothermal reservoirs, *Water Resour. Res*. 13: 929–934, 1977.
109. Morland, L.W. A theory of slow fluid flow through a porous thermoelastic matrix, *Geophys J. R. Astron. Soc*. 55: 393–410, 1978.
110. Derski, W. and Kowalski, S.J. Equations of linear thermo-consolidation, *Arch. Mech*. 31: 303–316, 1979.
111. Bear, J. and Corapcioglu, M.Y. A mathematical model for consolidation in a thermoelastic aquifer due to hot water injection or pumping, *Water Resour. Res*. 17: 723–736, 1981.
112. Delaney, P. Rapid intrusion of magma into wet rock: Groundwater flow due to pore pressure increases, *J. Geophys. Res*. 87: 7739–7756, 1982.
113. Delaney, P. Heating of a fully saturated Darcian halfspace: Pressure generation, fluid expulsion and phase change, *Int. J. Heat Mass Transfer* 27: 1327–1355, 1984.
114. Palciauskas, V.V. and Domenico, P.A. Characterization of drained and undrained response of thermally loaded repository rocks, *Water Resour. Res*. 18: 281–290, 1982.
115. McTigue, D.F. Thermoelastic response of fluid-saturated porous rock, *J. Geophys. Res*. 91: 9533–9542, 1986.
116. Savvidou, C. and Booker, J.R. Consolidation around a heat source buried in a deep porous thermoelastic medium with anisotropic flow properties, *Int. J. Numer. Analyt. Methods Geomech*. 13: 75–90, 1989.
117. Timoshenko, S.P. and Goodier, J.N. *Theory of Elasticity*, New York, McGraw-Hill, 1970.
118. Davis, R.O. and Selvadurai, A.P.S. *Elasticity and Geomechanics*, Cambridge, U.K., Cambridge University Press, 1996.
119. Selvadurai, A.P.S. *Partial Differential Equations in Mechanics Vol. 2: The Biharmonic Equation, Poisson's Equation*, Berlin, Germany, Springer-Verlag, 2000.
120. Lydzba, D. and Shao, J.F. Study of poroelasticity material coefficients as response of microstructure, *Mech. Cohes. Frict. Mat*. 5: 149–171, 2000.
121. Verruijt, A. *Theory of Groundwater Flow*, New York, Macmillan, 1970.
122. Bear, J. *Dynamics of Fluids in Porous Media*, Toronto, Ontario, Canada, Dover Publications, 1972.
123. Philips, O.M. *Flow and Reactions in Permeable Rocks*, Cambridge, U.K., Cambridge University Press, 1991.
124. Ichikawa, Y. and Selvadurai, A.P.S. *Transport Phenomena in Porous Media: Aspects of Micro/Macro Behaviour*, Berlin, Germany, Springer-Verlag, 2012.
125. Selvadurai, A.P.S. On intake shape factors for entry points in porous media with transversely isotropic hydraulic conductivity, *Int. J. Geomech*. 3: 152–159, 2003
126. Selvadurai, A.P.S. Fluid intake cavities in stratified porous media*, J. Porous Med*. 7: 165–181, 2004.
127. Selvadurai, A.P.S. On the hydraulic intake shape factor for a circular opening located at an impervious boundary: Influence of inclined stratification, *Int. J. Numer. Analyt. Methods Geomech*. 35: 639–651, 2010.
128. Selvadurai, A.P.S. and Selvadurai, P.A. Surface permeability tests: Experiments and modelling for estimating effective permeability, *Proc. R. Soc. Math. Phys. Sci. Ser. A* 466: 2819–2846, 2010.
129. Koh, J.C., Dutton, J.C., Benson, B.A., and Fortini, A. Friction factor for isothermal and non-isothermal flow through porous media, *J. Heat Transfer* 99C: 367–373, 1977.
130. Slattery, J.C. *Advanced Transport Phenomena*, Cambridge, U.K., Cambridge University Press, 1999.
131. Vafai, K. and Tien, C.L. Boundary and inertia effects on flow and heat transfer in porous media, *Int. J. Heat Mass Transfer* 24: 195–203, 1981.
132. Vafai, K. (Ed.). *Handbook of Porous Media*, Boca Raton, FL, CRC Press, 2000.
133. Vasco, D.W. On fluid flow in a heterogeneous medium under nonisothermal conditions, *Water Resour. Res*. 46: W12513, 2010.
134. Christensen, R.M. *Mechanics of Composite Materials*, New York, John Wiley, 1979.
135. Selvadurai, A.P.S. Interface porosity and the Dirichlet/Neumann pore pressure boundary condition in poroelasticity, *Transp. Porous Media* 64, 2007.

136. Dell'Isola, F., Madeo, A., and Seppecher, P. Boundary conditions at fluid-permeable interfaces in porous media, *Int. J. Eng. Sci*. 46: 3150–3164, 2009.
137. Selvadurai, A.P.S. *Partial Differential Equations in Mechanics Vol. 1: Fundamentals, Laplace's Equation, the Diffusion Equation, the Wave Equation*, Berlin, Germany, Springer-Verlag, 2000.
138. Sneddon, I.N. *Fourier Transforms*, New York, McGraw-Hill, 1950.
139. Sneddon, I.N. *The Applications of Integral Transforms*, New York, McGraw-Hill, 1972.
140. Carslaw, H.S. and Jaeger, J.C. *Conduction of Heat in Solids*, Oxford, U.K., Oxford University Press, 1959.
141. Hart, D.J. and Wang, H.F. Poroelastic effects during a laboratory transient pore pressure test. In *Poromechanics* (Thimus JF, Abousleiman Y, Cheng AHD, Coussy O, Detournay E, Eds.), Rotterdam, the Netherlands, Balkema, pp. 579–582, 1998.
142. Selvadurai, A.P.S. and Najari, M. On the interpretation of hydraulic pulse tests on rock specimens, *Adv. Water Resour*. 53: 139–149, 2013.
143. Najari, M. and Selvadurai, A.P.S. Thermo-hydro-mechanical response of granite to temperature changes, *Env. Earth Sci*., 2014.
144. Nasseri, M.H.B., Goodfellow, S.D., Wanne, T. and Young, R.P. Thermo-hydro-mechanical properties of Cobourg limestone, *Int. J. Rock Mech. Min. Sci*. 61: 212–222, 2013.
145. Aboustit, B.L., Advani, S.H., and Lee, J.K. Variational principles and finite element simulations for thermo-elastic consolidation, *Int. J. Numer. Analyt. Methods Geomech*. 9: 49–69, 1985.
146. Schrefler, B.A. and Simoni, L. Non-isothermal consolidation of unbounded porous media using mapped infinite elements, *Commun. Appl. Numer. Methods* 3: 445–452, 1987.
147. Lewis, R.W., Roberts, P.J., and Schrefler, B.A. Finite element modelling of two-phase heat and fluid flow in deforming porous media, *Trans. Porous Med*. 4: 319–334, 1989.
148. Modaressi, H., Foerster, E., and Laloui, L. Stability analysis of coupled thermo-hydro-mechanical schemes for deformable porous media. In *Numerical Methods in Thermal Problems, VII Part 2* (Lewis, R.W., Chin, J.H., and Homsy, G.M., Eds.), *Proceedings of the Seventh International Conference*, Stanford, CA, pp. 1073–1083, 1991.
149. Ehlers, W. and Bluhm, J. (Eds.). *Porous Media: Theory, Experiments and Numerical Applications*, Berlin, Germany, Springer-Verlag, 2002.
150. Hudson, J.A., Stephansson, O., and Andersson, J. Guidance on numerical modelling of thermo-hydro-mechanical coupled processes for performance assessment of radioactive waste repositories, *Int. J. Rock Mech. Min. Sci*. 42: 850–870, 2005.
151. Rutqvist, J., Noorishad, J., Stephansson, O., and Tsang, T.-F. Theoretical and field studies of coupled hydromechanical behaviour of fractured rocks-2, Field experiment and modelling, *Int. J. Rock Mech. Min. Sci*. 29: 411–419, 1992.
152. Rutqvist, J., Barr, D., Datta, R., Gens, A., Millard, A., Olivella, S., Tsang, C.-F., and Tsang, Y. Coupled thermal-hydrological-mechanical analyses of the Yucca Mountain Drift Scale Test—Comparison of field predictions of four different numerical models, *Int. J. Rock Mech Min. Sci*. 42: 680–697, 2005.
153. Tong, F., Jing, L., and Zimmermann, R.W. A fully coupled thermo-hydro-mechanical model for simulating multiphase flow, deformation and heat transfer in buffer material and rock masses, *Int. J. Rock Mech. Min. Sci*. 47: 205–217, 2010.
154. Selvadurai, A.P.S. and Suvorov, A.P. Boundary heating of poroelastic and poro-elastoplastic spheres, *Proc. R. Soc. A Math. Phys. Sci. Ser. A*, 2012.
155. Selvadurai, A.P.S. and Suvorov, A.P. Thermo-poromechanics of a fluid-filled cavity in a fluid-saturated porous geomaterial, *Proc. R. Soc. A Math. Phys. Sci. Ser. A* 470: 20130634, 2014.
156. Selvadurai, A.P.S., Suvorov, A.P., and Selvadurai, P.A. Thermo-hydro-mechanical processes in a fractured rock formation during glacial advance, *Geoscientific Model Development (Discussions)*, 7: 1–44, 2014.
157. Huyakorn, P.S. and Pinder, G.F. *Computational Methods in Subsurface Flows*, New York, Academic Press, 1983.
158. Zienkiewicz, O.C. and Taylor, R.L. *The Finite Element Method Set*, Oxford, U.K., Butterworth-Heinemann, 2005.
159. Nguyen, TS. Description of the computer code FRACON. In *Coupled Thermo-Hydro-Mechanical Processes of Fractured Media* (Stephansson, O., Jing, L., and Tsang C.-F., Eds.), Amsterdam, the Netherlands, Elsevier, 1996, pp. 539–544.
160. Thomas, H.R., He, Y., Sansom, M.R., and Li, C.L.W. On the development of the thermo-mechanical-hydraulic behaviour of unsaturated soil, *Eng. Geol*. 41: 197–218, 1996.
161. Gibson, R.E., Knight, K., and Taylor, P.W. A critical experiment to examine theories of three-dimensional consolidation, *Proceedings of the European Conference of Soil Mechanics and Foundation Engineering*, Weisbaden, Germany, 1963, pp. 69–76.

162. de Josselin de Jong G. Consolidation around pore pressure meters, *J. Appl. Phys*. 24: 922–928, 1953.
163. Selvadurai, A.P.S. and Shirazi, A. Mandel-Cryer effects in fluid inclusions in damage susceptible poroelastic media, *Comp. Geotech*. 37: 285–300, 2004.
164. Kodashima, T. and Kurashige, M. Thermal stresses in a fluid-saturated poroelastic hollow sphere, *J. Therm. Stress* 19: 139–151, 1996.
165. Rehbinder, G. Analytical solutions of stationary coupled thermo-hydro-mechanical problems, *Int. J. Rock Mech. Min. Sci*. 32: 453–463, 1995.
166. Selvadurai, A.P.S. Stationary damage modelling of poroelastic contact, *Int. J. Solids Struct*. 41: 2043–2064, 2004.
167. Selvadurai, A.P.S. and Mahyari, A.T. Computational modelling of steady crack extension in poroelastic media, *Int. J. Solids Struct*. 35: 4869–4885, 1998.
168. Mahyari, A.T. and Selvadurai, A.P.S. Enhanced consolidation in brittle geomaterials susceptible to damage, *Mech. Cohes. Frict. Mat*. 3, 291–303, 1998.
169. Selvadurai, A.P.S. and Shirazi, A. An elliptical disc anchor in a damage-susceptible poroelastic medium, *Int. J. Numer. Methods Eng*. 16: 2017–2039, 2005.
170. Selvadurai, A.P.S. and Shirazi, A. Fluid-filled spherical cavity in a damage susceptible poroelastic solid, *Int. J. Damage Mech*. 13: 347–370, 2004.
171. Shirazi, A. and Selvadurai, A.P.S. Lateral loading of a rock socket embedded in a damage-susceptible poroelastic solid, *Int. J. Geomech*. 5: 276–295, 2005.
172. Massart, T.J. and Selvadurai, A.P.S**.** Stress-induced permeability evolution in quasi-brittle geomaterials, *J. Geophys. Res*. (*Solid Earth*), 117, B07207, 2012.
173. Mason, D.P., Solomon, A., and Nicolaysen, L.O. Evolution of stress and strain during the consolidation of a fluid-saturated porous elastic sphere, *J. Appl. Phys*. 70: 4724–4740, 1991.

21 Thermogravitational Diffusion in a Porous Medium Saturated by a Binary Fluid

Abdelkader Mojtabi, Marie Catherine Charrier-Mojtabi, Bilal ElHajjar, and Yazdan Pedram Razi

CONTENTS

21.1 Introduction 714
21.1.1 Thermodiffusion 715
21.1.2 Thermogravitational Diffusion in a Binary Fluid 716
21.1.3 Thermodiffusion in a Multicomponent System 718
21.1.4 Measurements of Soret Coefficients 719
21.2 Mathematical Formulation 720
21.2.1 Governing Equations Describing the Conservation Laws 720
21.2.1.1 Momentum Equation 720
21.2.1.2 Continuity Equation 721
21.2.1.3 Energy Equation 721
21.2.1.4 Mass Transfer Equation 722
21.2.1.5 Combined Heat and Mass Transfer 722
21.2.2 Model and Basic Equations (Darcy Model) 722
21.2.2.1 Governing Equations Describing the Conservation Laws 722
21.3 Analytical and Numerical Solution 724
21.3.1 Inclined Porous Cell Maintained at Constant and Different Temperatures 724
21.3.1.1 Dimensionless Boundary Conditions 724
21.3.1.2 Analytical Solution 724
21.3.1.3 Numerical Results 726
21.3.1.4 Linear Stability Analysis of the Unicellular Flow in an Infinite Cell Heated from Below 730
21.3.1.5 Experiments 732
21.3.2 Horizontal Cell Submitted to a Vertical Heat Flux 733
21.3.2.1 Separation 734
21.3.2.2 Comparison between the Separations Obtained in a Thermogravitational Column and in a Horizontal Layer Submitted to a Constant Heat Flux 735
21.3.2.3 Numerical Simulations 736
21.4 Soret-Driven Convection in a Horizontal Porous Layer: The Effect of Conducting Bounding Plates 738
21.4.1 Mathematical Formulation 738
21.4.2 Linear Stability of the Equilibrium Solution 739
21.4.2.1 Linear Stability of the Equilibrium Solution in an Infinite Horizontal Cell 739

21.5 Vibration and Thermogravitational Diffusion in a Porous Medium 748
21.5.1 Influence of Horizontal Vibrations on the Separation of Binary Mixture in a Vertical Porous Layer 748
21.5.1.1 Mathematical Formulation 749
21.5.1.2 Results 752
21.5.2 Influence of Vertical Vibrations on the Separation of a Binary Mixture in a Horizontal Porous Layer Heated from Below 752
21.5.2.1 Mathematical Formulation 753
21.5.2.2 Linear Stability of the Equilibrium Solution in an Infinite Horizontal Porous Layer 753
21.5.2.3 Analytical Solution of the Unicellular Flow 755
21.5.2.4 Linear Stability of the Unicellular Flow 755
21.5.2.5 Numerical Simulations 757
21.6 Conclusions and Outlook 760
Nomenclature 761
References 762

21.1 INTRODUCTION

Double-diffusive convection in a saturated porous medium due to temperature and concentration gradients has been widely studied because of its numerous fundamental and industrial applications. Reviews of recent development and publications in this field are given in the books of Nield and Bejan (2012), Ingham and Pop (2000, 2002, 2005), and Vafai (2005).

The linear stability analysis of the flow in a porous medium saturated by a fluid mixture, in the presence of a temperature gradient and taking into account the Soret effect, was investigated by Ouarzazi and Bois (1994). The temperature gradient was assumed to vary periodically with respect to time. The two-dimensional (2D) instability thresholds, for both oscillatory and stationary instabilities, were predicted by these authors. The onset of Soret-driven convection in an infinite horizontal porous layer heated isothermally from below or from above has been considered by Sovran et al. (1996) using a linear stability analysis and nonlinear perturbation theories. A linear stability analysis was used to predict the onset of motion in terms of the buoyancy ratio, the Lewis number, and the normalized porosity. Depending on the value of the separation ratio, it was found analytically and numerically that the motionless solution lost its stability via stationary or Hopf bifurcations. Knobloch (1986), Platten and Legros (1984) studied the onset and development of convection in horizontal rectangular cavity. The two vertical walls of the cavity are impermeable and adiabatic, while the impermeable horizontal walls are maintained at constant and different temperatures. For a given Lewis number, Le, they obtained the stability diagram in which the critical Rayleigh number is given as a function of the separation ratio ψ. Bahloul et al. (2003) studied the onset of Soret-driven convection in a shallow porous horizontal layer submitted to a vertical heat flux on the two horizontal walls. The thresholds for finite amplitude, oscillatory, and monotonic convection instabilities are determined in terms of the governing parameters of the problem. For their study, the authors used a closed-form analytical solution based on the parallel flow approximation. However, they were not interested in the separation of the binary mixture components.

This work was extended by Bourich et al. (2004) not only for a shallow horizontal porous cavity but also for a shallow enclosure with a binary fluid. The critical Rayleigh numbers for the onset of oscillatory and stationary convection were determined explicitly as functions of the governing parameters for infinite layers and bounded boxes. At the onset of instability, they found that the wave number was equal to zero, and they also showed the dependency of critical parameters on the normalized porosity. Three-dimensional numerical modeling of Soret-driven convection in a cubic

cell filled with a binary mixture of water (90%) and isopropanol (10%) was performed by Shevtsova et al. (2006). Batiste et al. (2006) noted that the convections identified in binary mixture convection are located below the onset of absolute instability and hence in a parameter regime, where the instability of the conduction state is only advective. Alonso et al. (2007) presented results for direct numerical simulations of convection in binary fluids in large-aspect-ratio containers. They focused on binary mixtures with negative values of the separation ratio, for which the primary bifurcation is of subcritical and oscillatory nature, and with weak Soret coupling.

During the last 10 years, many works were devoted to the improvement of the experimental device in order to increase separation. Platten et al. (2003) used a tilted cavity heated from the top. ElHajjar et al. (2008) studied the unicellular flow appearing at the onset of convection in a binary fluid saturating a horizontal porous cavity heated from below. If the separation ratio ψ is positive and greater than a certain value of $\psi_{uni,}$ it was shown that it is possible to separate the species of the binary fluid mixture between the two ends of the cell. Moreover, the optimal Rayleigh number in the case of a horizontal cell is larger than in the case of a vertical one (thermogravitational column, TGC). This allows performing separation in a larger cell. Bennacer et al. (2009) suggested splitting a column filled with a porous medium saturated by a binary fluid into three sub-domains. In all the works aforementioned, two walls of the thermogravitational cell are maintained at constant and different temperatures, while the two other walls are considered adiabatic. It should be noted that all the walls are considered impermeable. Bennacer et al. (2003) studied both numerically and analytically the natural convection with Soret effect in a binary fluid saturating a shallow horizontal porous layer. The vertical walls of the enclosure are heated and cooled by uniform heat fluxes, and a solutal gradient is imposed vertically.

In the present chapter, the previous study with a focus on the species separation in a porous cell filled with a binary mixture for different inclinations from the vertical is reconsidered. Two configurations are studied: the porous cell heated from the top and from the bottom. Some experiments are also presented. An analytical solution is presented in the case of a shallow cavity (aspect ratio $A \gg 1$), and the species separation is expressed in terms of thermal Rayleigh number, Lewis number, separation ratio, and aspect ratio of the cell. The value of the Rayleigh number leading to the maximum separation is obtained analytically. The analytical results are corroborated by direct nonlinear numerical simulations performed using a finite element method. Then, a comparison between the separation obtained in this new configuration with the one obtained in TGC column is performed. The influence of the thickness and physical proprieties of the walls on the species separation are also analyzed. There are very few papers that consider the effect of the presence of horizontal bounding plates on the onset of thermal convection (Riahi 1983, Mojtabi and Rees 2011). The chief objective is to determine the effect of conducting bounding plates on the stability properties of a horizontal porous layer saturated by a binary fluid. As such, this provides a better approximation of how experiments are set up in the laboratory compared to the usual fixed temperature or heat flux boundary conditions. Recently, mechanical vibrations were also used to control thermoconvective or thermosolutal flows in incompressible fluids in order to optimize the heat and mass transfer (Ahadi and Saghir 2013). Generally speaking, vibrations can, in some cases depending on the relative orientation of vibration and temperature/concentration gradients, lead to an increase or to a decrease in heat and mass transfer. Also, it can delay or accelerate the onset of convection and allow us to select the flow structure. We have found that the vibration in the direction of temperature gradient enhances the species separation between the bottom and the top of the column.

21.1.1 Thermodiffusion

Thermodiffusion is a physical process occurring when a thermal gradient is applied to a pure multicomponent mixture or porous cavity saturated by multicomponent fluids. The concentration

gradient is created by the temperature field when pressure diffusion is negligible; the mass flux for binary mixture is given by

$$\boldsymbol{J_m} = -\rho D \nabla C - \rho F\left(C\right) D_T \nabla T \tag{21.1}$$

where

$D > 0$ and is the mass diffusion coefficient
D_T is the thermal diffusion coefficient
ρ is the density
C is the mass fraction of the considered component (we always take the denser component as the reference, but the opposite choice could equally well be used)

$F(C)$ is a particular function of C satisfying $F(C = 0) = 0$ and $F(C = 1) = 0$, so most of the authors use $F(C) = C(1 - C)$. The function $F(C) = \sin(\pi C)/4$ satisfying the same conditions, for $C = 0$ and $C = 1$, could also be used and leads to a similar result. Generally, the function $C(1 - C)$ is replaced by $C_0(1 - C_0)$ for small values of the initial mass fraction C_0 and small variation of mass fraction C. ∇C is the gradient of mass fraction induced by the temperature gradient ∇T. Under steady-state conditions $\boldsymbol{J_m} = 0$, we have

$$\nabla C = -\frac{D_T}{D} C_0(1 - C_0) \nabla T \tag{21.2}$$

The ratio $(D_T/D) = S_T$ is called the Soret coefficient. When $(D_T/D) = S_T > 0$, ∇C is of opposite sign to ∇T. In other words, C decreases approaching the hot wall of the container: the denser component migrates to the cold wall, and the lighter to the hot wall. The absolute value of S_T remains rather small and usually does not exceed 10^{-2} K^{-1}. Its magnitude and sign, usually in the 10^{-3} –10^{-2} K^{-1} range, may vary to a large extent from one chemical to another and for a given chemical. S_T is a complicated function of the state variables T and C. Therefore, the mass fraction gradient induced by the Soret effect remains small, but it has far-reaching implications in many important processes in nature and technology. A particular example is thermohaline convection in oceans driven by salinity gradients associated with temperature differences and mass transport across membranes. It may be induced by small thermal gradients in living matter where thermal diffusion could assume a sizable magnitude for an ensemble of cells with the dimensions of an organ or a tumor.

This physical phenomenon was initially discovered in the nineteenth century by Ludwig (1856) and by Soret (1880). It is now known as the Ludwig–Soret effect.

Thermal diffusion has various technical applications, such as isotope separation in liquid and gaseous mixtures, characterization and separation of polymers, and surface coating. This phenomenon is supposed to play an important role in the crystal growth too. Soret-driven convective effects cannot be neglected in many industrial processes. Thermal diffusion together with isothermal and pressure diffusion significantly affects the composition of petroleum reservoirs, see Firoozabadi (1999).

21.1.2 Thermogravitational Diffusion in a Binary Fluid

The combination of two phenomena, convection and thermodiffusion, is called thermogravitational diffusion. The coupling of these two phenomena leads to large species separation.

Clusius and Dickel (1938) successfully carried out the separation of gas mixtures in a vertical cavity heated from the side (TGC). In the following years, two fundamental theoretical and experimental works on species separation in binary mixtures by thermogravitation were published. Furry et al. (1939) (FJO theory) developed the theory of thermodiffusion to interpret the

experimental processes of isotope separation. Subsequently, many works appeared, aimed at justifying the assumptions or extending the results of the theory of FJO as, for example, to the case of binary liquids (De Groot 1942).

The fundamental parameter characterizing the influence of thermal diffusion on the convection in a binary mixture is the separation ratio ψ. For the binary mixture, the density is generally a function of the temperature and the mass fraction: $\rho = \rho(T, C)$; it can be deduced that the density gradient is a function of the temperature and the mass fraction gradient:

$$\nabla\rho = \left(\frac{\partial\rho}{\partial T}\right)_C \nabla T + \left(\frac{\partial\rho}{\partial C}\right)_T \nabla C \tag{21.3}$$

For small variation of T and C, the density varies linearly with local temperature and mass fraction:

$$\rho = \rho_0(1 - \beta_T(T - T_0) - \beta_C(C - C_0)) \tag{21.4}$$

where β_T and β_C are the thermal and solutal expansion coefficients defined as

$$\beta_T = -\frac{1}{\rho_0}\left(\frac{\partial\rho}{\partial T}\right)T_0, C_0 \quad \text{and} \quad \beta_C = -\frac{1}{\rho_0}\left(\frac{\partial\rho}{\partial C}\right)T_0, C_0 \tag{21.5}$$

Note that β_C is positive (negative) if C is the mass fraction of the lighter (heavier) component. β_T is generally positive, too. For the steady-state mechanical equilibrium, the gradient of mass fraction ∇C is given by the relation (21.2). Replacing ∇C in the relation (21.3), we obtain

$$\nabla\rho = -\rho_0\beta_T\left(1 - \frac{\beta_C}{\beta_T}\frac{D_T}{D}C_0(1 - C_0)\nabla T = -\rho_0\beta_T(1 + \psi)\right)\nabla T \tag{21.6}$$

The separation ratio can be also expressed in terms of Soret coefficient by

$$\psi = -\frac{\beta_C}{\beta_T}C_0(1 - C_0)\frac{D_T}{D} = -\frac{\beta_C}{\beta_T}C_0(1 - C_0)S_T \tag{21.7}$$

Let us note, from Equation 21.7, that the sign of ψ is independent of the choice of the reference component: indeed, if we skip from the denser to lighter component for reference, D_T as well as β_C will change sign leaving the sign ψ unchanged. ψ represents the mass fraction contribution to the buoyancy force relative to the thermal contribution, independent of any choice of the reference component.

In the presence of gravity, the density gradient can cause convective motion. In this case, the separation ratio characterizes the influence of thermal diffusion on buoyancy force. One may deduce from Equation 21.6 that when $\psi > 0$, the variation of the density is more pronounced when the thermodiffusion is taken into account rather than the variation of ρ caused by thermal expansion alone. For the separation ratio in the range $-1 < \psi < 0$, the variation of the density is smaller. We can affirm that for $\psi > 0$, the linear critical Rayleigh number associated with the onset of convection in the Rayleigh–Bénard or in the Horton–Rogers–Lapwood problem with binary fluid is smaller than the classical one associated with mono-constituent fluid in infinite horizontal cell ($Ra_c = 1707.76$ and $Ra_c = 4\pi^2$) respectively, and bigger for $-1 < \psi < 0$. This dimensionless parameter is widely used in describing convection in binary systems with the Soret effect; see Platten and Legros (1984), Wiegand (2004), and Shevtsova et al. (2006).

Other works related to the improvement of the experimental devices to increase separation may be mentioned. One way to decrease the velocity and to increase the separation is to tilt the cell by a given angle from the vertical. In this situation, the horizontal component of the temperature gradient decreases, which decreases the buoyancy force and the velocity of the flow. The tilted cell has already been used by De Groot (1942) in the case of bulk fluid but for different configuration of the cells. Platten et al. (2003) used an inclined cavity, keeping the hot plate on the top, to increase separation. ElHajjar et al. (2006) used a horizontal cavity heated from above, with temperature gradients imposed on the horizontal walls, to improve the separation process with two control parameters. Lorenz and Emery (1959) proposed the introduction of a porous medium into the cavity.

21.1.3 Thermodiffusion in a Multicomponent System

The liquids appearing in nature and industrial applications are essentially multicomponent. The behavior of multicomponent systems is more complicated in comparison with pure fluids due to a complex interplay between heat and mass transfer processes (Ghorayeb et al. 2003). In mixtures, the diffusive mass transport of a given component is induced not only by its compositional gradient (main or principal diffusion), but also by the compositional gradients of the other components (cross-diffusion) and the temperature gradient.

There are many important processes in nature and technology, where these phenomena play a crucial role. The composition of hydrocarbon reservoirs is significantly affected by diffusion as well as by the Soret effect (due to the presence of geothermal gradient) (ElHajjar et al. 2006). The prediction of mass transfer processes in such systems greatly relies on the knowledge of diffusion and thermodiffusion coefficients, which appear in the equations describing these phenomena.

Kempers (1989, 2001) introduced a new way of calculation for the thermodiffusion factor. His theory was developed for multicomponent mixtures with n different species. He denotes the mass fraction of component i by C_i and obtains the equation giving the mass flux of the constituent i:

$$\boldsymbol{J}_1 = -\rho_0 \sum_{k=1}^{n} D_{ik} \nabla C_k - \rho_0 C_i \left(1 - C_i\right) D_{Ti} \nabla T \tag{21.8}$$

For a ternary mixture, we consider that the two components 1 and 2 are independent, and the third one is chosen as a solvent, then

$$\boldsymbol{C}_1 + \boldsymbol{C}_2 + \boldsymbol{C}_3 = 1$$

and the diffusive fluxes of independent components can be written as

$$\boldsymbol{J}_1 = -\rho_0 D_{11} \nabla C_1 - \rho_0 D_{12} \nabla C_2 - \rho_0 F_1 \left(C_1, C_2\right) D_{T1} \nabla T \tag{21.9}$$

$$\boldsymbol{J}_2 = -\rho_0 D_{21} \nabla C_1 - \rho_0 D_{22} \nabla C_2 - \rho_0 F_2 \left(C_1, C_2\right) D_{T2} \nabla T \tag{21.10}$$

Different formulations, giving the expression of functions $F_1(C_1, C_2)$ and $F_2(C_1, C_2)$, are used. Shevtsova et al. (2011) adapted the equation obtained by Kempers (1989) for multicomponent system for the ternary mixture:

$$F_1(C_1, C_2) = C_1(1 - C_2) \quad \text{and} \quad F_2(C_1, C_2) = C_2(1 - C_1)$$

Ghorayeb and Firoozabadi (2003) employed

$$F_1(C_1, C_2) = C_1(1 - C_1 - C_2) \quad \text{and} \quad F_2(C_1, C_2) = C_2(1 - C_1 - C_2)$$

while Larre et al. (1997) used a new form of phenomenological laws:

$$\boldsymbol{J}_1 = -\rho_0 D_{11}\nabla C_1 - \rho_0 D_{12}\nabla C_2 - \rho_0 \left(C_1 C_2 D_{T12} + C_1 C_3 D_{T13} \right)\nabla T$$

$$\boldsymbol{J}_2 = -\rho_0 D_{21}\nabla C_1 - \rho_0 D_{22}\nabla C_2 - \rho_0 (C_1 C_2 D_{T21} + C_2 C_3 D_{T23}\nabla T$$

where

D_{ij} are the mass-based diffusion coefficients
D_{Ti} are the thermal diffusion coefficients

The transport coefficients are supposed to be constant in a sufficiently small range of temperature and concentration variations and correspond to the mean temperature T_0 and composition $C_0 = C_1^0, C_2^0, C_3^0$. The diffusive flux of J_3 is defined from the condition that the fluxes of all components must sum up to zero (Ryzhkov and Shevtsova 2009).

The coefficients D_{ij} and D_{Ti} can be estimated from theoretical models or measured experimentally. Presently, there is no finished and self-consistent theory for the ternary systems, but there is a hope that such a theory can be formulated using thermodynamic approaches and verified by reliable measurements. Nowadays, there are very few experimental studies in ternary liquid mixtures where the thermodiffusion coefficients are determined. Until now, the values of Soret coefficient were measured only in three hydrocarbon liquid ternary mixtures. The binary contributions of one among the three hydrocarbon mixtures were used as benchmark liquids (Platten et al. 2003b), and it appears that this mixture also plays the role of a benchmark mixture among the ternary ones.

The validity of some empirical additive rule to estimate the thermodiffusion coefficients in a ternary mixture from those in the three corresponding binary mixtures is still under investigation.

21.1.4 Measurements of Soret Coefficients

Measurements of Soret coefficients for various binary mixtures have been undertaken since the discovery of the thermodiffusion phenomenon, but this is not an easy task (and measurements are not usually very accurate) because of the combined effects of the smallness of concentration gradients and the possible undesired convective currents in the liquid bulk, almost all experimental methods being at the stationary state.

The oil industry is particularly interested in multicomponent systems of saturated porous media, but before starting experiments, even in a ternary system, one has to be sure of the correctness of the measured Soret coefficient in binary systems. The direct determination of S_T based on Equation 21.2 could be delicate, given that it implies the absence of convection, which is not always easy under terrestrial conditions (normal gravity), but convection can be avoided in well-conducted experiments (Platten 2006). Alternatively, experiments in microgravity have been proposed and performed (Shevtsova 2011) to alleviate the difficulty that could result from unexpected convective currents.

Several research groups from different universities and research institutes met in Fontainebleau (Platten et al. 2003b) in order to establish a reliable database of Soret, thermodiffusion, and isothermal diffusion coefficients, using different techniques such as thermogravitational cells (vertical TGC using coaxial tubes column or parallel plates column) (Bou-Ali et al. 1998, Blanco et al. 2011) and laser Doppler velocimetry to analyze the influence of the Soret-induced solutal contribution to the buoyancy force and its consequence on velocity amplitudes (Dutrieux et al. 2002), or very precise optical techniques such as thermal diffusion forced Rayleigh scattering. This technique was first suggested by Allain and Lallemand (1977) and was later developed by Köhler (1993). They used binary mixtures of dodecane, isobutylbenzene, and 1,2,3,4-tetrahydronaphthalene (components of interest in the oil industry); the values produced by each group did not differ too much from each other.

Two recent reviews and PhD thesis by Gonzales Bagnoli (2004) have summarized the current experimental approach (Wiegand and Köhler 2002). Roughly, the experimental methods can be divided into two classes: (1) methods that employ the presence of buoyant convection in the measurements, and (2) methods in which buoyant convection plays a deleterious role, and efforts are made to minimize its effect. The major part of the second group is optical methods that rely on the variation of refractive index with composition.

Nowadays, there are two very actively used methods: optical beam deflection (Königer et al. 2010) and optical digital interferometry used onboard of the ISS in addition to ground experiments (Mialdun et al. 2012). The performance of these two techniques as well as TGC have recently discussed and compared for binary mixtures (Mialdun et al. 2013).

The main features of optical methods are nonintrusiveness and sensitivity. A significant advantage of these methods is the absence of mechanically driven parts in contact with the liquid, so measurements do not disturb the experiment. The main disadvantage is that the media under investigation must be transparent. Recent advances in laser and electronic cameras as well as increasing possibilities of computer-aided data processing have enabled considerable progress in the development of new optical measurement techniques along with a revival of traditional techniques. In fact, there is no universal working technique acting satisfactory for every mixture, and each technique has its own limitations.

21.2 MATHEMATICAL FORMULATION

21.2.1 Governing Equations Describing the Conservation Laws

21.2.1.1 Momentum Equation

The basic dynamic equations for the description of the flow in porous media have been the subject of controversial discussion for several decades. Most of the analytical and numerical work presented in the literature is based on the Darcy–Oberbeck–Boussinesq formulation. Darcy's law is valid only when the pore Reynolds number Re is of the order of 1. Lage (1992, 1998) studied the effect of the convective inertia term for Bénard convection in porous media. He concluded that the convective term, included in the general momentum equation, has no significant effect on the calculation of overall heat transfer. Chan et al. (1970) utilized Brinkman's extension to study natural convection in porous media with impermeable boundaries. However, they essentially concluded that non-Darcian effects have very little influence on heat transfer results. For many practical applications, however, Darcy's law is not valid, and boundary and inertial effects need to be accounted for. A fundamental study of boundary and inertial effects can be found in the work of Vafai and Tien (1989) and Hsu and Cheng (1985). A systematic study of the non-Darcian effects in natural convection is presented in the work of Ettefagh et al. (1991). These authors report a formal derivation of a general equation for fluid flow through an isotropic, rigid, and homogeneous porous medium. The general final equation for an incompressible fluid is

$$\rho\left[\frac{\partial \vec{V}'}{\varepsilon \partial t} + \frac{1}{\varepsilon^2}\vec{V}'\cdot\nabla\vec{V}'\right] = -\nabla P' + \rho\vec{g} + \mu_e\nabla^2\vec{V}' - \frac{\mu}{K}\vec{V}' - \frac{b\rho}{K^{1/2}}\left\|\vec{V}'\right\|\vec{V}' \tag{21.11}$$

where ρ, μ, μ_e, K, b, and ε are fluid density, dynamic viscosity, effective viscosity, permeability, form coefficient, and porosity, respectively.

We suppose that the medium is homogeneous and spatially invariant, and the viscosity is taken as a constant. Double-diffusive convection with Soret effect is often studied using the Darcy formulation and Boussinesq approximation, provided the fluid moves slowly so that the inertial effects are

negligible and one can usually drop the time derivative term completely based on the analysis given by Nield and Bejan (2012), as

$$\vec{V}' = \frac{K}{\mu}(-\nabla P' + \rho g\vec{k}) \tag{21.12}$$

where

$\vec{V}'=(u', v', w')$

P' are the seepage (Darcy) velocity and pressure, respectively

$\vec{k} = -\sin(\alpha)\vec{e}_x + \cos(\alpha)\vec{e}_z$ defines the tilt of the cavity

21.2.1.2 Continuity Equation

Conservation of fluid mass, assuming an incompressible fluid and no sources or sinks, can be expressed as

$$\nabla \cdot \vec{V}' = 0 \tag{21.13}$$

21.2.1.3 Energy Equation

The macroscopic description of heat transfer in porous media by a single energy equation implies the assumption of local thermal equilibrium between the moving fluid phase and the solid phase ($T_s' = T_f' = T'$). This hypothesis has been investigated by several authors (Sözen and Vafai 1990, Gobbé and Quintard 1994, Kaviany 1995, Quintard and Whitaker 1996a,b). For situations in which local thermal equilibrium is not valid, models have been proposed based on the concept of two macroscopic continua, one for the fluid phase and the other for the solid phase (see Quintard et al. 1997).

The temperature differences imposed across the boundaries are small, and consequently the Boussinesq approximation is valid. The single-energy equation is

$$\frac{(\rho c)_m}{(\rho c)_f}\frac{\partial T'}{\partial t'} + \vec{V}' \cdot \nabla T' = \alpha_e \nabla^2 T' \tag{21.14}$$

where

c is the specific heat

α_e is the effective thermal conductivity of saturated porous medium divided by the specific heat capacity of the fluid

Subscript f refers to fluid properties, while subscript m refers to the fluid–solid mixture and s to the solid matrix, where

$$(\rho c)_m = \varepsilon(\rho c)_f + (1-\varepsilon)(\rho c)_s \tag{21.15}$$

$$\alpha_e = \varepsilon\frac{k_f}{(\rho c)_f} + (1-\varepsilon)\frac{k_s}{(\rho c)_f} = \varepsilon\alpha_f + (1-\varepsilon)\frac{k_s}{(\rho c)_f} \tag{21.16}$$

which corresponds to the effective thermal conductivity obtained as weighted arithmetic mean of the conductivities k_s and k_f. In general, the effective thermal conductivity depends in a complex fashion on the geometry of the medium. Many other expressions giving k^* do exist like geometric mean $k^* = k_s^{\varepsilon} k_f^{1-\varepsilon}$ and many others listed in the book of Kaviany (1995).

21.2.1.4 Mass Transfer Equation

For a porous solid matrix saturated by a binary mixture, when the Soret effect is taken into account, we have

$$\varepsilon \frac{\partial C'}{\partial t'} + \vec{V}' \cdot \nabla C' = -D\nabla C' - F(C) D_T \nabla T' \tag{21.17}$$

One finds several expressions in the literature (Bear 1972, De Marsily 1986, Nield and Bejan 1992, 1998) for the link between diffusion coefficients in free layers and in porous medium, like $D^* = \varepsilon D$ or $D^* = D/\tau^2$, where ε is the porosity and τ the tortuosity of the porous medium. More complex expressions based on homogenization theory are proposed by Adler (1992), but are not always of practical application.

Regardless of which expression is used, the value of the thermodiffusion coefficient D_T is also affected by the solid matrix. One finds in the literature (Jamet et al. 1992) the statement that the Soret coefficient should have the same value in a porous medium and in a free liquid layer, based on the argument that since both coefficients D_T and D are of the same nature, the corrections should be the same, and therefore their ratio should be unaffected by the porous medium. This argument seems intuitively correct at first sight and could be true, but on the other hand could be incorrect owing to the fact that the thermodiffusion coefficient could also depend on the ratio of the thermal conductivity of the liquid mixture to that of the solid matrix (see Platten and Costesèque 2004).

21.2.1.5 Combined Heat and Mass Transfer

Generally, the transport of heat and mass are not directly coupled, and Equations 21.4 and 21.6 hold without change. In thermosolutal convection, coupling takes place because the density of the binary fluid depends on both temperature T' and mass fraction C'. For small density variations due to temperature and mass fraction changes at constant pressure, the density variations can be expressed as

$$\rho(T', C') = \rho_0 (1 - \beta_T (T' - T_0) - \beta_C (C' - C_0)) \tag{21.18}$$

where T_0 and C_0 are taken as the reference state. Coefficients of volumetric expansion with temperature β_T and with concentration β_C are assumed constant. It is noted that β_T is usually positive, and β_C is negative (if C corresponds to the mass fraction of the denser component).

In some circumstances, there is direct coupling. This occurs when cross-diffusion (Soret and Dufour effects) is not negligible. The Dufour effect refers to the heat flux produced by a concentration gradient. With no heat or mass sources, (21.14) can expressed as

$$\frac{(\rho c)_m}{(\rho c)_f} \frac{\partial T'}{\partial t'} + \vec{V'} \cdot \nabla T' = \alpha_{e\dagger} \left(\nabla^2 T' + \frac{\alpha_m}{\alpha_e} \nabla^2 C' \right) \tag{21.19}$$

where $\alpha_m/\alpha_e = D_f$ is the Dufour dimensional coefficient of the porous medium.

21.2.2 Model and Basic Equations (Darcy Model)

21.2.2.1 Governing Equations Describing the Conservation Laws

We consider a rectangular cell of aspect ratio $A = L/e$ where L is the length of the cell along the axis $\vec{e}_z$ and e is its width along the axis $\vec{e}_x$. The cavity is filled with a porous medium saturated with viscous binary fluid with density ρ and dynamic viscosity μ. The Soret effect is taken into account.

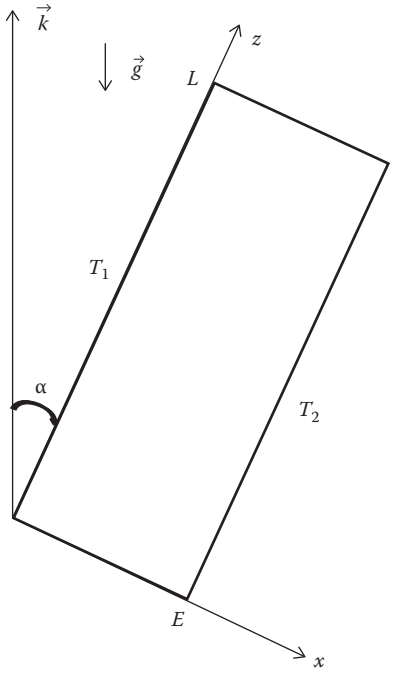

FIGURE 21.1 Geometrical configuration of the inclined cell.

The cavity is inclined by an angle α from the vertical. The gravity vector is $\vec{g} = -g\vec{k}$ where $k = -\sin(\alpha)\vec{e}_x + \cos(\alpha)\vec{e}_z$ (Figure 21.1).

The impermeable walls ($x = 0$, $x = e$) are kept at different and constant temperatures T_1 for $x = 0$ and T_2 for $x = e$, with $T_1 < T_2$. The walls ($z = 0$, $z = L$) are impermeable and insulated. All the boundaries are assumed rigid.

The fluid flow within the porous medium is assumed to be incompressible and governed by Darcy's law. The contribution to the heat flux by Dufour effect is assumed negligible in liquids. The Oberbeck–Boussinesq approximation is applicable in the range of temperatures and concentrations studied. We set all the properties of the binary fluid constant except the density ρ′ in the buoyancy term, which depends linearly on the local temperature and the mass fraction (Equation 21.4). Subject to these constraints, the governing conservation equations for mass, momentum, energy, and chemical species are

$$\begin{cases} \nabla.\vec{\mathbf{V}}' = 0 \\ \nabla P' = \rho'\vec{g} - \dfrac{\mu}{K}\vec{\mathbf{V}}' \\ (\rho c)^* \dfrac{\partial T'}{\partial t'} + (\rho c)_f \vec{\mathbf{V}}' \cdot \nabla T' = \nabla \cdot (\lambda \nabla T') \\ \varepsilon \dfrac{\partial C'}{\partial t} + \vec{\mathbf{V}} \cdot \nabla C' = \vec{\nabla} \cdot \left[D\nabla C' + C'(1 - C')D_T \nabla T \right] \end{cases} \tag{21.20}$$

The variables are made dimensionless with e for the length, a^*/e for the velocity, $(re^2)/a^*$ for the time, $(\mu a^*)/K$ for the pressure (with $r = (\rho c)^*/(\rho c)_f$, where $(\rho c)^*$ is the effective volumic heat capacity of the porous medium, and a^* the effective thermal diffusivity of the porous medium, $\Delta T = T_2 - T_1$ for temperature ($T_{nd} = (T - T_1)/\Delta T$) and $\Delta C = \Delta T C_0(1 - C_0)D_T/D$ for the mass fraction ($C = (C' - C_0)/\Delta C'$), where D_T, D are the thermodiffusion and the mass diffusion coefficients of the denser component of mass fraction C'.

21.2.2.1.1 Dimensionless Equations

The dimensionless governing conservation equations for mass, momentum, energy, and chemical species are

$$\begin{cases} \nabla \cdot \vec{\mathbf{V}} = 0 \\ \vec{\mathbf{V}} = -\nabla P + Ra(T - \psi C)\left[-\sin(\alpha)\vec{e}_x + \cos(\alpha)\vec{e}_z\right] \\ \dfrac{\partial T}{\partial t} + \vec{\mathbf{V}} \cdot \nabla T = \nabla^2 T \\ \varepsilon \dfrac{\partial C}{\partial t} + \vec{\mathbf{V}} \cdot \nabla C = \dfrac{1}{\mathrm{Le}}(\nabla^2 C + \nabla^2 T) \end{cases} \tag{21.21}$$

The problem under consideration depends on five nondimensional parameters: the thermal Rayleigh number $\mathrm{Ra} = Kg\beta_T H\Delta T(\rho c)_f/(\lambda^* \upsilon)$, the separation ratio $\psi = -(\beta_C/\beta_T)(D_T^*/D^*)C_0(1 - C_0)$, the Lewis number $\mathrm{Le} = a^*/D^*$, the normalized porosity $\varepsilon = \varepsilon^*((\rho c)_f/(\rho c)^*)$, and the aspect ratio $A = L/e$.

21.3 ANALYTICAL AND NUMERICAL SOLUTION

21.3.1 Inclined Porous Cell Maintained at Constant and Different Temperatures

21.3.1.1 Dimensionless Boundary Conditions

The associated dimensionless boundary conditions are

$$\begin{cases} T = 0 & \text{for} & x = 0 \\ T = 1 & \text{for} & x = 1 \\ \dfrac{\partial T}{\partial z} = -\dfrac{\partial C}{\partial z} = 0 & \text{for} & z = 0, A \\ \dfrac{\partial T}{\partial x} = -\dfrac{\partial C}{\partial x} & \text{for} & x = 0, 1 \\ \vec{\mathbf{V}} \cdot \vec{\mathbf{n}} = 0 & \text{for} & \forall M \in \partial\Omega \end{cases} \tag{21.22}$$

21.3.1.2 Analytical Solution

In the case of a shallow cavity $A \gg 1$, we considered the parallel flow approximation used by Cormack et al. (1974). The basic flow is given as follows:

$$\vec{\mathbf{V}} = W(x)\vec{e}_z; \quad T = bz + f(x); \quad C = mz + g(x) \tag{21.23}$$

We should have $b = 0$, since constant temperatures are imposed on the walls ($x = 0$, 1).

By replacing $\vec{\mathbf{V}}$, T, and C by their expressions (Equation 21.23), and by eliminating the pressure in the system (21.21), we get the following system:

$$\begin{cases} \dfrac{dW(x)}{dx} = \mathrm{Ra}\left(\dfrac{df(x)}{dx} - \psi\dfrac{dg(x)}{dx}\right)\cos(\alpha) - \mathrm{Ra}\psi\, m\sin(\alpha) \\ \dfrac{d^2 f(x)}{dx^2}\mathrm{Le} = 0 \\ W(x)m = \dfrac{1}{\mathrm{Le}}\dfrac{d^2 g(x)}{dx^2} \end{cases} \tag{21.24}$$

By using the boundary conditions for temperature, we obtain

$$T = x \tag{21.25}$$

By eliminating $g(x)$ between the first and third equations of the system (21.6), we obtain the following equation for the velocity:

$$\frac{d^2 W(x)}{dx^2} = -\mathrm{RaLe}\psi m\cos(\alpha)W(x) \tag{21.26}$$

We restrict our study to the case of positive separation ratio ($\psi > 0$). In this case, the denser species moves toward the cold wall, that is, the wall ($x = 0$), then the unicellular flow advects this species to the bottom wall, that is, the wall ($z = 0$), so we get a higher mass fraction of the denser species at the bottom of the cavity and therefore $m < 0$.

The angle varies from −90°, which corresponds to a horizontal cell heated from above, to +90° corresponding to a horizontal cell heated from below, so cos(α) is always positive.

Therefore, −Ra Le ψm cos(α) is positive; we assume that $\omega^2 = -\mathrm{Ra\ Le}\ \psi m\cos(\alpha)$, so we get

$$\frac{d^2 W(x)}{dx^2} = \omega^2 W(x) \tag{21.27}$$

The solution of Equation 21.27 is given by

$$W(x) = k_1 ch(\omega x) + k_2 sh(\omega x) \tag{21.28}$$

where k_1 and k_2 are constants to be evaluated.

To find these constants, we use the following two conditions:

1. At the stationary state, there is no flow rate through any section perpendicular to the z axis, so $\int_0^1 W(x)dx = 0$
2. The first equation of the system (21.24) is valid on the boundaries, so

$$\left.\frac{dW(x)}{dx}\right|_{x=0} = \left[\mathrm{Ra}\left(\frac{df(x)}{dx} - \psi\frac{dg(x)}{dx}\right)\cos(\alpha) - \mathrm{Ra}\psi\, m\sin(\alpha)\right]_{x=0}$$

but for $x = 0$, we have $\frac{\partial C}{\partial x} = \frac{dg(x)}{dx} = -\frac{\partial T}{\partial x} = -\frac{df(x)}{dx} = -1$, so we obtain the following condition for the velocity:

$$\left.\frac{dW(x)}{dx}\right|_{x=0} = \mathrm{Ra}\left[(1+\psi)\cos(\alpha) - \psi m \sin(\alpha)\right].$$

Using these two conditions, we find the following expression for the velocity:

$$W(x) = \frac{\mathrm{Ra}\left[(1+\psi)\cos(\alpha) - \psi m \sin(\alpha)\right]\left[ch(\omega x) - ch(\omega x - \omega)\right]}{sh(\omega)\omega} \tag{21.29}$$

This solution is not valid for the limiting cases $\alpha = \pm 90°$. The case $\alpha = 90°$ has been studied by Charrier-Mojtabi et al. (2007) and ElHajjar et al. (2008). For the case $\alpha = -90°$, the equilibrium solution is unconditionally stable.

Once the velocity field has been obtained, we determine the function $g(x)$ using the first equation of the system (21.24). In order to find the constants of integration, we use the equation of conservation of the mass of the denser species:

$\int_0^A \left(\int_0^1 C dx\right) dz = 0$ (The integral is equal to zero because the initial dimensionless mass fraction is equal to zero.)

By applying these assumptions, we obtain the following expression of the mass fraction:

$$C = -\frac{W(x)}{\mathrm{Ra}\cos(\alpha)\psi} + \frac{\cos(\alpha) - \psi m \sin(\alpha)}{\cos(\alpha)\psi}\left(x - \frac{1}{2}\right) - \frac{mA}{2} + mz \tag{21.30}$$

We still have to determine m, so we use the fact that the mass flow of the component having the mass fraction C is zero through any cross section at the stationary state:

$$\int_0^1 \left(\vec{V}C - \frac{1}{\mathrm{Le}}\left(\nabla C + \nabla T\right)\right)\vec{e}_z dx = 0 \Rightarrow \int_0^1 \left(W(x)C - \frac{1}{\mathrm{Le}}\frac{\partial C}{\partial z}\right) dx = 0 \tag{21.31}$$

Since $\int_0^1 W(x) mz dx = 0$, we get

$$\int_0^1 \left(W(x)g(x) - \frac{m}{\mathrm{Le}}\right) dx = 0 \tag{21.32}$$

This leads to a transcendental equation permitting the determination of m.

21.3.1.3 Numerical Results

In the case of a finite value of A, this problem has been studied numerically by solving the system (21.21) using a finite element method (using the industrial code COMSOL) and a collocation spectral method. The spatial resolution is 200 × 30 for the industrial code and 150 × 20 for the collocation method. The numerical results are in good agreement with the analytical ones.

The separation S is defined as the difference of the mass fractions of the denser species between the two ends of the cell ($z = 0$) and ($z = A$): $S = mA$.

In the case of a vertical cell ($\alpha = 0°$), and for Le = 100 and $\psi = 0.1$, the maximum separation is obtained for Ra ≈ 0.1 (Figure 21.2).

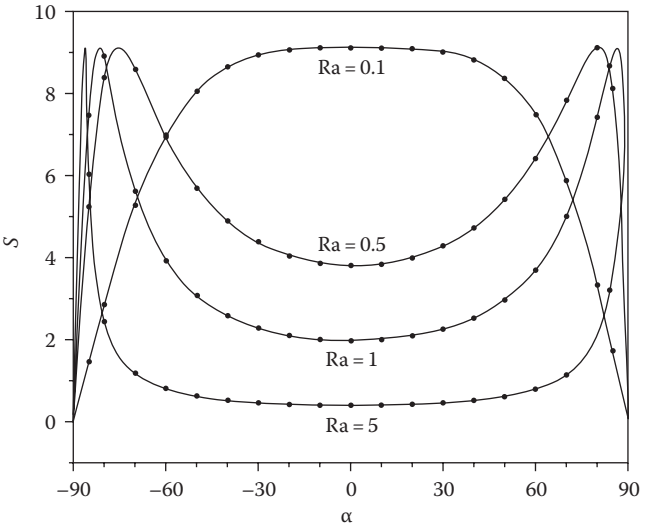

FIGURE 21.2 Variation of the separation with the angle of inclination for Le = 100, $\psi = 0.1$, $A = 20$, and Ra = 0.1, 0.5, 1, 5. Solid curves represent the analytical results and the black dots the numerical results.

For a given binary mixture, it is interesting to choose, for the same value of separation, the cell corresponding to the highest value of the Rayleigh number. Indeed, if we examine Figure 21.2, we note that the separation obtained for $\alpha \approx -84°$ and Ra = 5 is equal to the maximum separation obtained for $\alpha \approx 0°$ and Ra = 0.1. If the temperature difference imposed on the cell is the same in both situations, then the thickness of the cell for Ra = 5 would be 50 times greater than that associated with Ra = 0.1. It follows that for the same degree of separation, the production of species would be greater in the cell of greater thickness.

Figure 21.2 shows the variation of separation with the angle of inclination for different values of the Rayleigh number and for Le = 100 and $\psi = 0.1$. The cell is heated from above if $\alpha \in [-90°, 0°]$ and from below if $\alpha \in [0°, 90°]$. This figure shows the separation for Ra = 0.1 and for Rayleigh numbers relatively high in comparison with the optimal Rayleigh number corresponding to the vertical cell (Ra = 0.5, 1, 5).

For Ra = 0.1, we note that the separation decreases when α varies from 0° to 90° or from 0° to −90°. Indeed for Ra = 0.1 and in the case of a vertical cell, the coupling between thermodiffusion and convection is optimal. If the cell is inclined from the vertical, the temperature gradient in the x direction remains constant so the influence of thermodiffusion does not change; on the other hand, the horizontal temperature gradient decreases so the intensity of convection decreases, and we lose the optimal coupling between thermodiffusion and convection. Also for Ra = 0.1, the maximum separation is obtained for $\alpha = 0°$; when α increases, the separation decreases and is zero for $\alpha = 90°$. In the latter case, we are dealing with a horizontal cell heated from below, and the critical Rayleigh number of the onset of convection is $Ra_c = 12/(Le\psi)$, which gives for ($\psi = 0.1$, and Le = 100) $Ra_c = 12/(100^* 0.1) = 1.2$; this value is greater than 0.1, which means that in this case the equilibrium solution is stable, and therefore there is no separation between the ends of the cell. If the angle of inclination decreases from 0°, the intensity of thermodiffusion does not change, while the intensity of convection decreases, so the separation decreases and is zero for $\alpha = -90°$. For this position, the cell is horizontal and heated from above with a separation factor $\psi > 0$. For this configuration, the equilibrium solution is stable, so there is no flow and then no separation between the two ends of the cell.

For Le = 100, $\psi = 0.1$, the value Ra = 5 of the Rayleigh number is higher than the value of Ra, which gives the maximum separation (this value of Ra will be called the *optimal Rayleigh number*) (0.1) for the vertical cell. This value of the Rayleigh number is associated with a thickness of the cell larger than that used for Ra = 0.1 for fixed value of ΔT; we note in Figure 21.2 that the separation is

much lower for this value of the Rayleigh number in the case of vertical cell. In order to increase the separation, the cell is inclined from the vertical. If the angle of inclination increases, we see that the separation increases to its maximum value for $\alpha = 90°$. This maximum value is slightly lower than that obtained for Ra = 0.1; indeed, by tilting the cell, the velocity decreases but does not reach the velocity giving the optimal coupling between convection and thermodiffusion.

If the angle decreases, the separation increases to a maximum value equal to that obtained in the case Ra = 0.1, then the separation decreases to zero for $\alpha = -90°$.

For Ra = 0.5, 1, the curves of separation have the same form. If the angle increases, the separation increases to reach a maximum and then decreases to 0. For $\alpha = 90°$, the cell is horizontal. The Rayleigh numbers 0.5 and 1 are smaller than the critical Rayleigh number of the onset of convection (1.2); in these conditions, there is no separation since there is no flow.

For Ra = 0.5, 1, when the angle of inclination varies from 0° to −90°, the separation increases to reach a maximum and then decreases to 0. We note that the optimal angles of inclination are closer to −90° and 90° for Ra = 1. In fact, this value of Ra is higher than the value of Ra, which gives the maximum separation for the vertical cell and is higher than 0.5, so the velocity is much higher than that required to obtain maximum separation, so the velocity should be further reduced by tilting the cell to reach the maximum value of the separation.

Figures 21.3 and 21.4 show the variation of separation with the angle of inclination for Le = 100 and $\psi = 0.1,\ 0.4$, for two values of Ra, Ra = 0.2 and Ra = 1. Here also we notice that the value of the maximum of separation is the same in every case.

Figure 21.5 shows the variation of the mass fraction field with the angle of inclination α for a cell of aspect ratio $A = 20$ and for Le = 100, $\psi = 0.1$, and Ra = 0.5. The lines show the isoconcentrations and the colors the intensity of the mass fraction of the denser species.

For $\alpha = 0°$ (vertical cell), the separation is relatively small in comparison with the separations obtained in the case of inclined cells. Indeed, in the case of a vertical cell, the Rayleigh number Ra = 0.5 is higher than the Rayleigh number leading to maximum separation (Ra = 0.1), so the velocity is high and the separation is small. When the cell is titled, the separation increases; indeed, when the cell is inclined, the horizontal component of the thermal gradient decreases, and then the velocity of the flow decreases to reach the velocity giving the maximum separation.

One note, on this figure, is that the separation does not have the same value for the same positive or negative inclination. If $\alpha \in [-90°, 0°]$, the temperature gradient in the x direction has a vertical

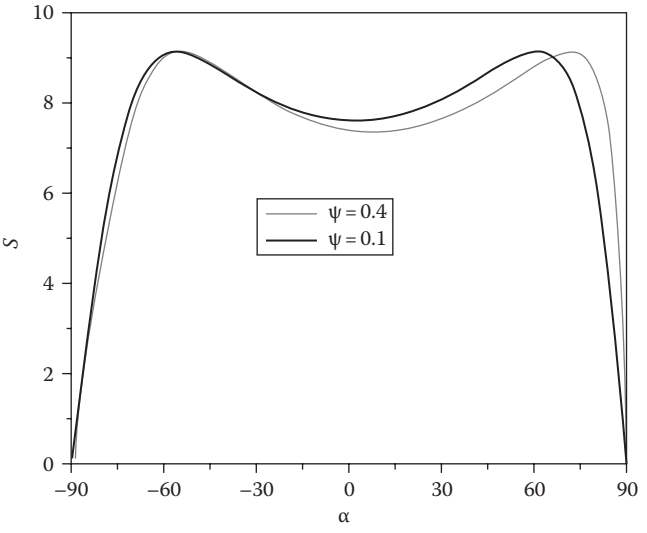

FIGURE 21.3 Variation of the separation with the angle of inclination for Le = 100, Ra = 0.2, $A = 20$, and $\psi = 0.1, 0.4$. Solid curves represent the analytical results and thin line the numerical results.

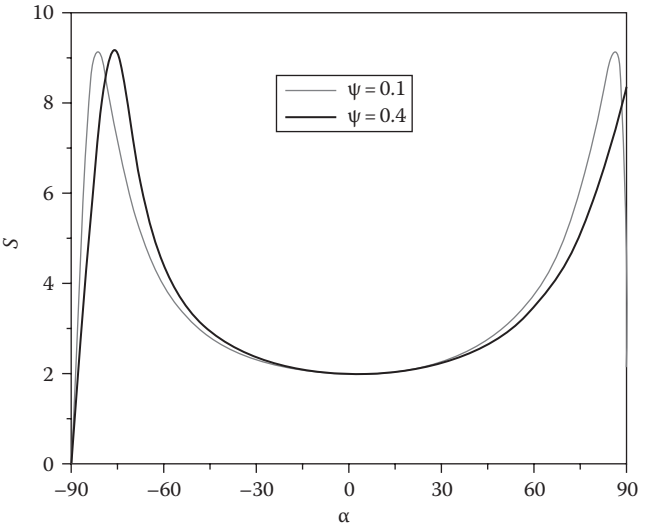

FIGURE 21.4 Variation of the separation with the angle of inclination for Le = 100, Ra = 1, A = 20, and ψ = 0.1, 0.4. Solid curves represent the analytical results and the black dots the numerical results.

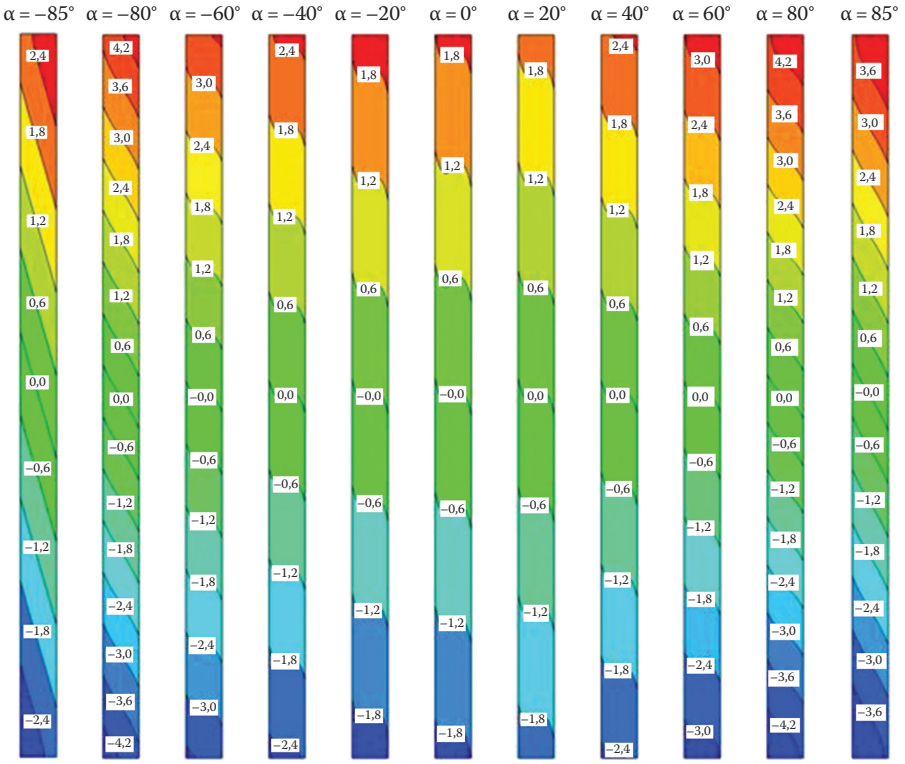

FIGURE 21.5 Variation of the mass fraction field with the angle of inclination for Le = 100, ψ = 0.1, Ra = 0.5, and A = 20.

component and a horizontal one; the horizontal component imposes the magnitude of velocity while the vertical component (cell heated from above) has a stabilizing effect. If $\alpha \in [0°, 90°]$, the temperature gradient in the x direction has a vertical component and a horizontal one; both the horizontal and the vertical components impose the magnitude of the velocity because the cell is heated from below. So in the case of positive inclinations, we should further increase the angle of inclination to obtain lower velocities, which lead to a maximum separation.

21.3.1.4 Linear Stability Analysis of the Unicellular Flow in an Infinite Cell Heated from Below

In the case of a cell heated from below, the unicellular flow may lose stability, and in this case, the inclined cell cannot be used for separation. So we will study the stability of the unicellular flow to see if it remains stable for a Rayleigh number higher than the optimal Rayleigh number leading to a maximum of separation.

Table 21.1 gives the values of the optimal Rayleigh number for different values of the angle of inclination with $\psi = 0.1$ and Le = 100. As we can see from this table, the optimal Rayleigh number increases with the angle of inclination. In fact, when α increases at fixed Ra, the buoyancy forces decrease and the velocity decreases. Thus, in order to maintain the optimal coupling between thermodiffusion and convection, we must increase Ra by increasing ΔT or E.

There are some studies concerning the stability of the unicellular flow in vertical cell (Bou-Ali et al. 1998, Zebib 2007, Ryzhkov et al. 2009) or horizontal cells (Charrier-Mojtabi et al. 2007, ElHajjar et al. 2008). To our knowledge, the linear stability analysis of the unicellular flow obtained in an inclined cell is developed here for the first time. In order to simplify the stability analysis, we have adopted the usual assumption used in the case of the vertical cell. We neglect the term ψC in the momentum transport equation. As it has been shown (Bou-Ali et al. 1998), this assumption is valid for most of the mixtures considered.

By applying this assumption and solving the system (21.21) with the corresponding boundary conditions and the earlier-mentioned assumptions, we obtain the following expressions for velocity, temperature, and mass fraction fields of the unicellular flow:

$$\begin{cases} T_0 = x \\ W_0 = \mathrm{Ra}\cos(\alpha)(x - 1/2) \\ C_0 = mz + m\mathrm{Ra}\cos(\alpha)\mathrm{Le}\left(x^3/6 - x^2/4\right) - x \\ \qquad + \left[m\mathrm{Ra}\cos(\alpha)\mathrm{Le}\right]/24 + 1/2 - (mA)/2 \\ m = -\left(10\mathrm{Le}\cos(\alpha)\mathrm{Ra}\right)/\left(\mathrm{Le}^2\mathrm{Ra}^2\cos^2(\alpha) + 120\right) \end{cases} \tag{21.33}$$

TABLE 21.1
Effect of the Angle of Inclination on the Optimal Rayleigh Number for Le = 100 and $\psi = 0.1$

α	Ra_{opt}
60	0.19
65	0.24
70	0.27
75	0.35
80	0.48
85	0.80

In order to investigate the stability of this unicellular flow, it is convenient to rewrite the governing equations using the perturbations of velocity $\vec{\mathbf{v}}$, temperature θ, pressure p, and mass fraction c:

$$\vec{\mathbf{v}} = \vec{\mathbf{V}} - \vec{\mathbf{V}}_0, \quad \theta = T - T_0, \quad c = C - C_0, \quad p = P - P_0 \tag{21.34}$$

It is assumed that the perturbation quantities are sufficiently small so that the second-order terms may be neglected. We obtain the linear equations where the unknowns are the disturbances.

To take into account more easily the boundary conditions for the temperature and the mass fraction at $x = 0, 1$, we introduce the new variable $\eta = c + \theta$. By developing the disturbances in the form of normal modes $(u, \theta, \eta) = (u(x), \theta(x), \eta(x))e^{ikz + \sigma t}$, we obtain the following system of equations for the perturbations:

$$\begin{cases} (D^2 - k^2)u = -ik\mathrm{Ra}\cos(\alpha)\left[(1+\psi)\dfrac{d\theta}{dx} - \psi\dfrac{d\eta}{dx}\right] + \mathrm{Ra}k^2\sin(\alpha)[(1+\psi)\theta - \psi\eta] \\ (D^2 - k^2)\theta = \sigma\theta + u\dfrac{dT_0}{dx} + ikW_0\theta \\ \dfrac{ik}{\mathrm{Le}}(D^2 - k^2)\eta = \varepsilon\sigma ik(\eta - \theta) + iku\dfrac{\partial C_0}{\partial x} - \dfrac{du}{dx}\dfrac{\partial C_0}{\partial z} - k^2W_0(\eta - \theta) \end{cases} \tag{21.35}$$

where

$D = \partial/\partial x$

k is the horizontal wave number

$\sigma = \sigma_r + i\sigma_i$ is the temporal amplification of the perturbation

$i^2 = -1$

The corresponding boundary conditions are

$$u = 0, \theta = 0, \frac{\partial \eta}{\partial x} = 0 \quad \text{for } x = 0, 1 \tag{21.36}$$

The resulting linear problem is solved by means of a sixth-order Galerkin method, using the following expansions:

$$u = \sum_{i=1}^{N} a_i(x-1)x^i, \quad \theta = \sum_{i=1}^{N} b_i(x-1)x^i, \quad \eta = c_1 + c_2(x^2 - 2x^3/3) + \sum_{i=1}^{N-2} c_{i+2}(x-1)^2x^{i+1},$$

Such a generalized eigenvalue problem is solved with the spectral Tau–Chebyshev collocation method by means of a numerical procedure using the QZ eigenvalue solver of the NAG library. From the thresholds $\mathrm{Ra}_0(\mathrm{Le}, \psi, \alpha, k)$ for which an eigenvalue has a real part equal to zero whereas all the other eigenvalues have negative real parts, the critical Rayleigh Ra_c is obtained after a minimization procedure with respect to the wave number k:

$\mathrm{Ra}_c = \min_k \mathrm{Ra}_0(\mathrm{Le}, \psi, \alpha, k)$. We have also used different methods to determine the critical Rayleigh number: a finite element method is used for the discretization of the generalized eigenvalue problem (21.34 and 21.35) (method 3) and direct numerical simulations (method 4) (ElHajjar et al. 2010).

As we can see from this table, the critical Rayleigh number decreases when α increases through positive values. Indeed, when α increases, the vertical component of the temperature gradient that is responsible of the instability increases, so the critical Rayleigh number decreases.

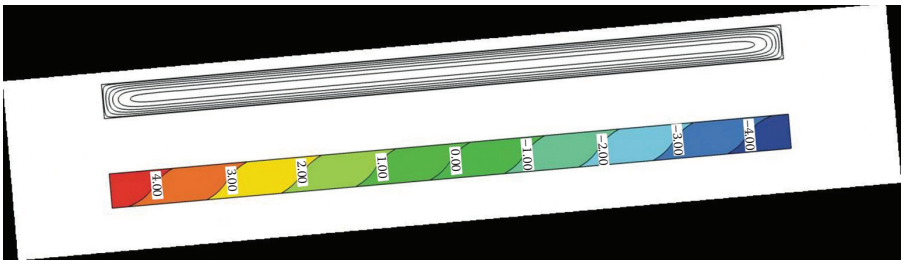

FIGURE 21.6 Streamlines and isoconcentrations for Le = 100, $\psi = 0.1$, $\alpha = 85°$, $A = 20$, and for the corresponding optimal Rayleigh number Ra = 0.8.

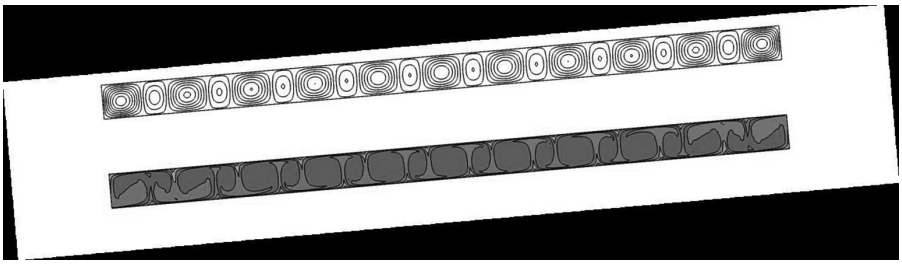

FIGURE 21.7 Streamlines at transition between the unicellular and multicellular flows for Le = 100, $\psi = 0.1$, Ra = 42, $\alpha = 85°$, and $A = 20$.

We can also note from this table that the critical Rayleigh number is much higher than that leading to the maximum separation. We can conclude that we can use the inclined cell to separate the components of a binary mixture without fearing the remixing of the components of the mixture due to instabilities. Figure 21.6 shows the streamlines and the isoconcentrations for $\alpha = 85°$ and for the corresponding optimal Rayleigh number, that is, Ra = 0.8. In this case, a unicellular flow is observed, and we obtain a separation between the top and the bottom of the cell. Figure 21.7 shows the streamlines for Ra = 42 at the transition from unicellular flow to multicellular flow. For this value of Ra, a multicellular flow is obtained, and then the inclined cell cannot be used for separation.

21.3.1.5 Experiments

We used two types of cells, both of them having two stainless-steel plane boundaries (the plates) maintained at different temperatures in order to create a temperature gradient in a parallelepiped working space. The dimensions of the first cell (Cell1) (Figure 21.8) are 38 cm × 8 cm × 1.5 cm ($A = 25.3$) and for the second one (Cell2) are 5.8 cm × 4.4 cm × 0.4 cm ($A = 14.5$). Between the plates, a regular gap e was maintained by a brace made of Plexiglas (thickness $e = 1.5$ cm for Cell1 and $e = 0.4$ cm for Cell2). The temperature at each boundary was kept constant by a regulated water bath. The cells are filled with a porous medium consisting of zircon beads chemically inert (315−400 μm). We did two experiments with the two cells. The first experiment was with (Cell1) using an aqueous solution of $CuSO_4$ whose concentration expressed as mass fraction is 0.0733. This solution has been studied (Costesèque 1982, Costesèque et al. 2004). For the presented experiment, we chose an inclination of 75° from the vertical with the cold wall at 10°C and the hot wall at 30°C.

The experiment lasted 20 days to make sure we reached the steady state. The samples were taken at both ends of the cell. The samples were analyzed with a high-resolution refractometer (0.00001). The calibration curve was performed on solutions prepared at different concentrations.

We found a difference of mass fraction ΔC (separation) = 0.008925 between the two ends of the cell, which corresponds to a relative separation 12%.

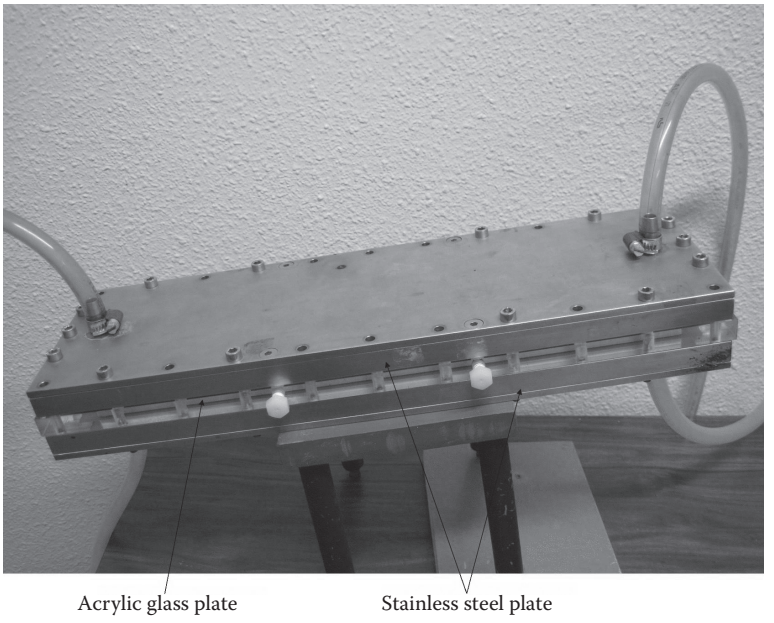

FIGURE 21.8 External view of the thermogravitational cell.

TABLE 21.2
Comparison between the Numerical and Experimental Results Obtained, in the Two Experimental Cells

Experiment	Cell	ΔT	C_0	α	Time of Experience (days)	ΔC_{exp}	ΔC_{num}
1	$Cell_1$	20	0.074	75°	20	0.0089	0.0105
2	$Cell_2$	10	0.0857	−45°	8	0.0453	0.0652

These experimental results have been compared to the results of 2D numerical simulations under the conditions of the experiment. To conduct the numerical simulation, we must know the permeability of the mixture. To determine the permeability of the used porous medium, several measurements were performed. After repeating the measurements several times, we found a permeability value of 9.2×10^{-11} m^2. The conditions and the results for the two experiments are given in Table 21.2. This discrepancy between the experimental and numerical results was reported by most authors who have studied the problem of separation in vertical TGC (Jamet et al. 1992).

21.3.2 Horizontal Cell Submitted to a Vertical Heat Flux

In the case of a shallow cavity $A \gg 1$, we consider the parallel flow approximation used previously (Equation 21.23). The associated boundary conditions are

$$\begin{cases} \dfrac{\partial T}{\partial z} = \dfrac{\partial C}{\partial z} = -1 \quad \text{for } z = 0, 1 \; \forall x \in [0, A] \\ \dfrac{\partial T}{\partial x} = \dfrac{\partial C}{\partial x} = 0 \quad \text{for } x = 0, A \; \forall z \in [0,1] \\ \vec{\mathbf{V}} \cdot \vec{\mathbf{n}} = 0 \quad \text{for } \forall M \in \partial\Omega \end{cases} \tag{21.37}$$

Using the boundary conditions (21.37), we obtain the following expression for the stream function:

$$\psi = \psi_0(1-4y^2) \quad \text{with } \psi_0 = \frac{1}{8}\mathrm{Ra}(b+\varphi m) \tag{21.38}$$

In order to obtain the expression of b and m, respectively, we use the fact that at the steady state, the total heat transfer through any cross section perpendicular to the x axis and the mass flow of the component of mass fraction C are zero, which leads to the expression of b and m:

$$b = \frac{10\psi_0}{8\psi_0^2+15} \quad \text{and} \quad m = -\frac{8\mathrm{Le}\psi_0^2 b - 10\mathrm{Le}\psi_0 - 15b}{8\mathrm{Le}^2\psi_0^2+15} \tag{21.39}$$

By inserting b and m by their expressions in Equation 21.39, we obtain a fifth-order polynomial equation for ψ_0, for which solutions are $\psi_0 = 0$ and

$$\psi_0 = \pm\frac{\sqrt{5}}{8}\frac{1}{\mathrm{Le}}\left(\frac{\mathrm{RaLe}^2 - 12 - 12\mathrm{Le}^2 \pm}{\sqrt{\mathrm{Ra}^2\mathrm{Le}^4 + 24\mathrm{RaLe}^2 - 24\mathrm{RaLe}^4 + 144 - 288\mathrm{Le}^2 + 144\mathrm{Le}^4 + 48\mathrm{Le}^3\mathrm{Ra}\varphi + 48\mathrm{Le}^2\mathrm{Ra}\varphi}}\right)^{1/2} \tag{21.40}$$

In conclusion, the analytical solution in the case $A \gg 1$ is

$$\begin{cases} \psi = \psi_0(1-4y^2) \\ T = bx - \dfrac{4}{3}\psi_0 b y^3 + \psi_0 b y - y \\ C = mx - \dfrac{4}{3}\psi_0 y^3(m\mathrm{Le}+b) + (\psi_0 m\mathrm{Le} + \psi_0 b - 1)y \\ \psi_0 = \pm\dfrac{\sqrt{5}}{8}\dfrac{1}{\mathrm{Le}} \\ \left(\dfrac{\mathrm{RaLe}^2 - 12 - 12\mathrm{Le}^2 \pm}{\sqrt{\mathrm{Ra}^2\mathrm{Le}^4 + 24\mathrm{RaLe}^2 - 24\mathrm{RaLe}^4 + 144 - 288\mathrm{Le}^2 + 144\mathrm{Le}^4 + 48\mathrm{Le}^3\mathrm{Ra}\phi + 48\mathrm{Le}^2\mathrm{Ra}\phi}}\right)^{1/2} \end{cases} \tag{21.41}$$

21.3.2.1 Separation

We study the species separation of the binary mixture between the two vertical ends of the horizontal porous cavity. The separation S is defined as the difference of the mass fraction of the denser species between the two ends of the cell ($x = A/2$) and $x = -A/2$), and its expression is $S = m \cdot A$.

As indicated in Equations 21.11 and 21.12, m and the separation S are a function of the Lewis number Le and $\psi_0 = f(\mathrm{Ra}, \mathrm{Le}, \varphi)$. We choose the set of parameters Le = 2, 50, 100, and $\varphi = 0.4$. The cases Le = 50, 100 correspond to liquid binary mixtures, while the case Le = 2 corresponds to gas binary mixture.

The vertical stratification of the mass fraction field is obtained at low Rayleigh numbers. The maximum separation is obtained for an optimal value of the Rayleigh number Ra_{opt}.

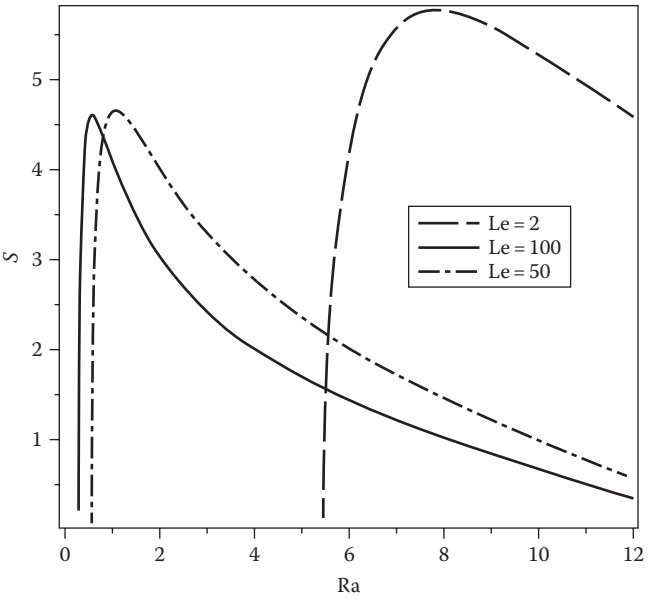

FIGURE 21.9 Separation $S = mA$ versus Rayleigh number for $\psi = 0.4$, Le = 2, 50, 100.

For each value of φ, we can obtain the value of Ra_{opt} with the software Maple. So, for $\varphi = 0.4$ and for Le = 2, $\mathrm{Ra}_{opt} = 7.85$; for Le = 50, $\mathrm{Ra}_{opt} = 1.05$; and for Le = 100, $\mathrm{Ra}_{opt} = 0.56$. In Figure 21.9, the curves $S = f(\mathrm{Ra})$ for $\varphi = 0.4$ and Le = 2, 50, 100 are plotted.

For Ra_{opt}, the coupling between the two phenomena, thermodiffusion and convection, is optimal. If Ra is lower than Ra_{opt}, the convection is weak, and the separation is small, and when Ra is higher than Ra_{opt}, the intensity of convection increases so the separation decreases. One can note that for Le = 50 and Le = 100, the maximum separation is quite the same $S_{\max} \approx 4.6$, while for Le = 2, $S_{\max} \approx 5.7$.

It will be noted that due to the reference scale used for the mass fraction, the separation S may be higher than one. Using the forgotten effect, that is, the term φC in the Darcy's law is neglected, we can obtain an approximate relation that gives the following expression of Ra_{opt}:

$$\mathrm{Ra}_{opt} = \frac{\left(40\mathrm{Le}^4 + 2000\mathrm{Le}^3 - 2400\mathrm{Le}^2 - 400 + 40\sqrt{1816\mathrm{Le}^2 - 220\mathrm{Le} + 121)}\right)^{1/2}}{\mathrm{Le}^2\left(10\mathrm{Le}^2 + 197\mathrm{Le} - 253\right)} \tag{21.42}$$

21.3.2.2 Comparison between the Separations Obtained in a Thermogravitational Column and in a Horizontal Layer Submitted to a Constant Heat Flux

In order to show the advantage the horizontal configuration submitted to heat flux, the separation obtained in this case is compared to the one obtained in TGC.

ElHajjar et al. (2008) studied the thermogravitation in a vertical column of height H and thickness E. The vertical walls of the cell were kept at constant and different temperatures. To obtain an analytical solution in the case $A = H/E \gg 1$, the authors used the same assumptions as that in Section 21.3.1. The term φC in the Darcy's law was neglected (forgotten effect, Fury et al. 1939). Under these assumptions, the separation is $S_v = m_v A$ with

$$m_v = \frac{(10\mathrm{LeRa})}{(\mathrm{Le}^2\mathrm{Ra}^2 + 120)} \tag{21.43}$$

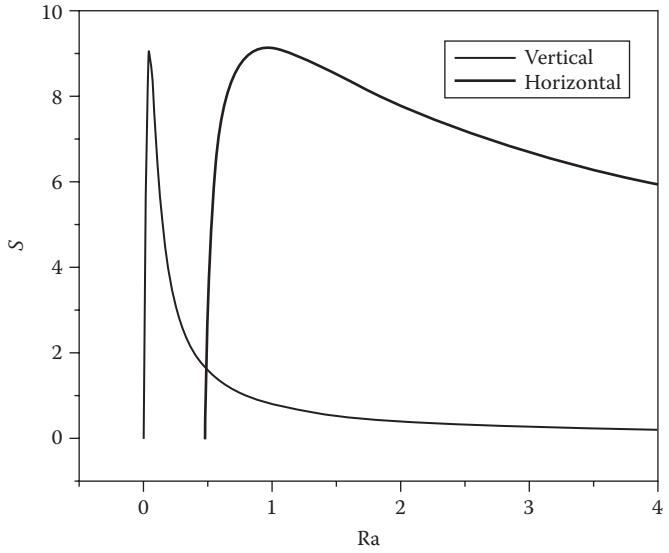

FIGURE 21.10 Separation in horizontal and TGC cells for Le = 100, ψ = 0.1.

Thus, the maximum separation is obtained for an optimum value of the Rayleigh number $\mathrm{Ra}_{optv} = \sqrt{120}/\mathrm{Le}$. For Le = 100 and φ = 0.1 (Figure 21.10), the two curves $S = f(\mathrm{Ra})$ are plotted in the case of the horizontal cell submitted to heat flux and in a TGC column, with the Rayleigh number based on H for the horizontal cavity and the thickness e for the TGC column, so $\dfrac{\mathrm{Ra}_H}{\mathrm{Ra}_v} = \dfrac{(\Delta T_H/\Delta T_v)}{(H/E)}$.

If we now compare the ratio of the optimal Rayleigh numbers in the two configurations, we obtain

$$\begin{cases} r = \dfrac{\mathrm{Ra}_{opth}}{\mathrm{Ra}_{optv}} \\ r = \dfrac{0.091287(40\mathrm{Le}^4 - 2400\mathrm{Le}^2 + 2000\mathrm{Le}^3 - 400\mathrm{Le} + 440 + 40\sqrt{121 - 220\mathrm{Le} + 1816\mathrm{Le}^2})}{\mathrm{Le}(10\mathrm{Le}^2 + 197\mathrm{Le} - 253)} \end{cases}^{\dagger} \quad (21.44)$$

So, for Le = 2, r = 2.52; Le = 50, r = 26.07; and for Le = 100, r = 45, 67.

In Figure 21.10, we note that the maximum separation is quite the same in the two configurations. S_v decreases very quickly with Ra, while the separation in the horizontal cell decreases slowly. Then, the separation in the horizontal cell can occur in a wider range of Ra and allows the use of greater height cells. In conclusion, for the same difference of temperature, in a horizontal cell with a height H much higher than the width E of a TGC column, the separation obtained is largest in the horizontal cell and the amount of separated species is higher. It is also easier to realize these cells experimentally. Indeed, the width of the TGC column at the maximum separation is about a fraction of mm.

21.3.2.3 Numerical Simulations

The system of Equations 21.21 with the boundary conditions (21.22) are solved numerically using a finite element code of second-order accuracy (Comsol industrial code) with a rectangular grid, better suited to the rectangular configuration. For the computations, we consider an aspect ratio A = 10. The spatial resolution is 120 × 20.

TABLE 21.3
Analytical and Numerical Separation for Le = 100 and ψ = 0.4

Ra	*S* Analytical	*S* Numerical	Ra	*S* Analytical	*S* Numerical
0.3	1.6862	1.605	0.75	4.4540	4.454
0.4	4.1492	4.149	1	4.1034	4.103
0.5	4.5651	4.591	1.5	3.4886	3.488
0.56	4.6092	4.640	2	3.0352	3.033
0.6	4.6014	4.601	2.5	2.6903	2.690
0.64	4.5754	4.575	3	2.4162	2.416
0.68	4.5376	4.537	4	1.9989	1.999
0.70	4.5155	4.515	5	1.6855	1.685

In order to eliminate the effects due to the presence of the two vertical ends for calculating the separation, we plot the curve $C = f(x)$ at a given value of y ($y = 0$, for instance), and we calculate the slope of the curve, which is a straight line in the central part of the cell.

In Table 21.3, we present the separations obtained numerically and analytically for Le = 100 and φ = 0.4. The results obtained numerically are in very good agreement with those obtained analytically. The same result is obtained for Le = 2, Le = 50, and φ = 0.4. For Le = 100 and φ = 0.4, Figure 21.11 shows the mass fraction field and the streamlines for Ra = 0.3, $Ra_{opt} = 0.56$, and Ra = 2.5.

We can see in Figure 21.11a through c that for Ra = 0.3, the stratification of the mass fraction field is not vertical and that the assumption of parallel flow is respected only near the center of the cavity. For $Ra = Ra_{opth}$, the maximum separation is obtained: the assumption of parallel flow is respected except near the two vertical walls. As Ra increases from Ra_{opth}, the convection increases as indicated by the deformation of the mass fraction field. Thus, the separation decreases.

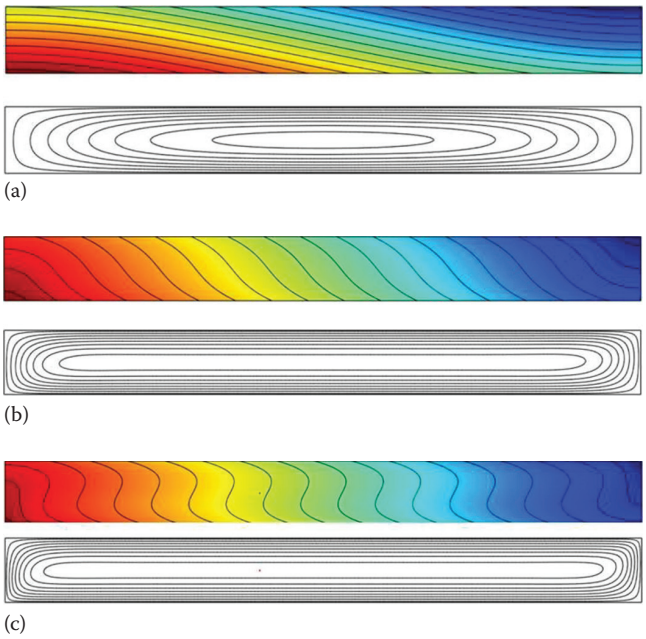

FIGURE 21.11 (a) Isoconcentrations and streamlines for Ra = 0.3, Le = 100, ψ = 0.4. (b) Isoconcentrations and streamlines for $Ra_{opt} = 0.56$, Le = 100, ψ = 0.4. (c) Isoconcentrations and streamlines for Ra = 2.5, Le = 100, ψ = 0.4.

21.4 SORET-DRIVEN CONVECTION IN A HORIZONTAL POROUS LAYER: THE EFFECT OF CONDUCTING BOUNDING PLATES

21.4.1 Mathematical Formulation

We consider a rectangular cavity with high aspect ratio $A = L/H$, where H is the height of the cavity and L is its width (Figure 21.12). The cavity is filled with a porous medium saturated by a binary fluid mixture. This cavity is placed between two metal plates of uniform thickness h. The impermeable horizontal walls ($y = -h$, $y = H + h$) are subjected to a uniform heat flux q'. The vertical walls ($x = 0$, $x = L$) are impermeable and adiabatic. All boundaries are assumed rigid. We consider an isotropic and homogeneous porous medium. We assume that Darcy–Oberbeck–Boussinesq approximation is valid.

The dimensionless mathematical formulation of the problem is given by

$$\begin{cases} \nabla^2\varphi = -\mathrm{Ra}\dfrac{\partial}{\partial x}\left(T_2 + \psi C\right) \\ \dfrac{\partial T_2}{\partial t} + \vec{V}\cdot\nabla T_2 = \nabla^2 T_2 \\ \varepsilon\dfrac{\partial C}{\partial t} + \vec{V}\cdot\nabla C = \dfrac{1}{\mathrm{Le}}\left(\nabla^2 C - \nabla^2 T_2\right) \\ \dfrac{\partial T_1}{\partial t} = \alpha\nabla^2 T \\ \dfrac{\partial T_3}{\partial t} = \alpha\nabla^2 T \end{cases} \tag{21.45}$$

The reference scales are H for the length, a/H for the velocity with $a = \lambda_p/(\rho c)_f$ (a is the effective thermal diffusivity), $\phi H^2/a$ for the time (with $\phi = (\rho c)_p/(\rho c)_f$, the heat capacity ratio), $\Delta T = q'H/\lambda_p$ for the temperature, $\Delta C = -\Delta T C_0(1 - C_0)(D_T^*/D^*)$ for the mass fraction, where D_T^* and D^* are, respectively, the thermodiffusion and mass diffusion coefficient of the denser component. $\vec{V}$ is the Darcy velocity, and φ is the stream function. In the following analysis, the stream function formulation is introduced in the mathematic model. The stream function φ is defined such that $u = \partial\varphi/\partial y$ and $v = -\partial\varphi/\partial x$.

The problem under consideration depends on eight nondimensional parameters: the thermal Rayleigh number, $\mathrm{Ra} = (g\beta_T K\Delta TH)/(a\nu)$ (K is the permeability of the porous medium); the separation ratio, $\psi = -(\beta_C/\beta_T)(D_T^*)C_0(1 - C_0)$; the Lewis number, $\mathrm{Le} = a/D^*$; the normalized porosity, $\varepsilon = \varepsilon^*/\phi$; the thermal diffusivity ratio, $\alpha = a_s/a_p$, where $a_s = \lambda_s/(\rho c)_s$ and $a_p = \lambda_p/(\rho c)_p$ are, respectively,

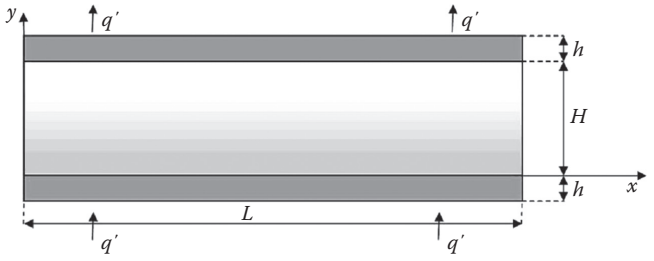

FIGURE 21.12 Saturated porous medium of height H and length L bounded by two horizontal plates of thickness h. The upper and lower surfaces of the system are subject to a uniform heat flux. The vertical sidewalls are assumed to be perfectly insulated.

the thermal diffusivity of metal plates and porous medium; the thermal conductivity ratio, $d = \lambda_s/\lambda_p$; the aspect ratio, $\delta = h/H$, and the aspect ratio of the porous cell, $A = L/H$. In the present study, the intensity of the thermal buoyancy forces is expressed solely in terms of the parameter Ra.

The corresponding dimensionless boundary conditions are

$$\begin{cases} \text{for} \quad y = -\delta, \quad \dfrac{\partial T_1}{\partial y} = -\dfrac{\lambda_p}{\lambda_s} = \dfrac{-1}{d}; \\ \text{for} \quad y = 0, \quad \dfrac{\partial T_1}{\partial y} = \dfrac{1}{d}\dfrac{\partial T_2}{\partial y}, \quad T_1 = T_2, \quad \phi = 0, \quad \dfrac{\partial C}{\partial y} - \dfrac{\partial T_2}{\partial y} = 0; \\ \text{for} \quad y = 1, \quad = \dfrac{1}{d}\dfrac{\partial T_2}{\partial y}, \quad T_2 = T_3, \quad \phi = 0, \quad \dfrac{\partial C}{\partial y} - \dfrac{\partial T_2}{\partial y} = 0; \\ \text{for} \quad y = 1 + \delta, \quad \dfrac{\partial T_3}{\partial y} = \dfrac{-1}{d}. \end{cases} \tag{21.46}$$

21.4.2 Linear Stability of the Equilibrium Solution

21.4.2.1 Linear Stability of the Equilibrium Solution in an Infinite Horizontal Cell

It is straightforward to show that there exists an equilibrium solution characterized by

$$\vec{V} = 0, \quad T_{1,0} = -y/d + T_a, \quad T_{2,0} = T_a - y, \quad T_{3,0} = (1-y)/d + T_a - 1, \quad C_0 = 1/2 - y \tag{21.47}$$

where T_a is an arbitrary constant temperature. In order to analyze the stability of this equilibrium solution, we first introduce the perturbations of stream function, of temperatures, namely, θ_1, θ_2, and θ_3, and of the mass fraction c. We assume that the perturbations (φ, θ_1, θ_2, θ_3, c) are of small amplitude, and for simplicity, we introduce the new function $\eta = c - \theta_2$. The perturbation quantities are chosen as follows:

$$(\varphi, \theta_1, \theta_2, \theta_3, \eta) = (\tilde{\varphi}, \tilde{\theta}_1, \tilde{\theta}_2, \tilde{\theta}_3, \tilde{\eta})(y)\exp(Ikx + \sigma t) + c.c \tag{21.48}$$

where

k is the wave number in the horizontal (x) direction

$i^2 = -1$

σ is the temporal exponential growth rate of perturbation

21.4.2.1.1 Stationary Transition

In the first part, we focus on steady bifurcation. By combining the Darcy and the energy equations, we obtain the following linearized equations:

$$\begin{cases} \left(D^2 - k^2\right)\tilde{\varphi} + ik\mathrm{Ra}\left[\left(1+\Psi\right)\tilde{\theta}_2 + \Psi\tilde{\eta}\right] = 0 \\ \left(D^2 - k^2\right)\tilde{\theta}_2 - ik\tilde{\varphi} = 0 \\ \left(D^2 - k^2\right)\tilde{\eta} - ik\mathrm{Le}\tilde{\varphi} = 0 \\ \left(D^2 - k^2\right)\tilde{\theta}_1 = 0 \\ \left(D^2 - k^2\right)\tilde{\theta}_3 = 0 \end{cases} \tag{21.49}$$

where $D = d/dy$.

Removing $\bar{\varphi}$ from the system (21.49), the following linear system is obtained:

$$\begin{cases} \left(D^2 - k^2\right)^2 \tilde{\theta}_2 - \mathrm{Ra}k^2 \left[1 + \psi + \psi\mathrm{Le}\right]\tilde{\theta}_2 = \mathrm{Ra}k^2\psi \left[A\sinh(ky) + B\cosh(ky)\right] \\ \left(D^2 - k^2\right)\tilde{\theta}_1 = 0 \\ \left(D^2 - k^2\right)\tilde{\theta}_3 = 0 \end{cases} \tag{21.50}$$

where A and B satisfy

$$\begin{cases} \mathrm{Le}\left(\dfrac{d\tilde{\theta}_2}{dy}\right) + kA = 0 \quad \text{for } y = 0; \\ \mathrm{Le}\left(\dfrac{d\tilde{\theta}_2}{dy}\right) + kA\cosh(k) + kB\sinh(k) = 0 \quad \text{for } y = 1 \end{cases} \tag{21.51}$$

with the associated boundary conditions

$$\begin{cases} \text{for} \quad y = -\delta, & \dfrac{\partial\tilde{\theta}_1}{\partial y} = 0; \\ \text{for} \quad y = 0, & \dfrac{\partial\tilde{\theta}_1}{\partial y} = \dfrac{1}{d}\dfrac{\partial\tilde{\theta}_2}{\partial y}, \quad \tilde{\theta}_1 = \tilde{\theta}_2, \quad (D^2 - k^2)\tilde{\theta}_2 = 0; \\ \text{for} \quad y = 1, & \dfrac{\partial\tilde{\theta}_3}{\partial y} = \dfrac{1}{d}\dfrac{\partial\tilde{\theta}_2}{\partial y}, \quad \tilde{\theta}_2 = \tilde{\theta}_3, \quad (D^2 - k^2)\tilde{\theta}_2 = 0; \\ \text{for} \quad y = 1 + \delta, & \dfrac{\partial\tilde{\theta}_3}{\partial y} = 0. \end{cases} \tag{21.52}$$

The general solution of the fourth-order ordinary differential Equation 21.50 is given as a combination of four particular independent functions whose expression depends on the sign of Ra(1 + ψ + ψLe). These considerations permit us to consider four regions of the plane (Ra, ψ). The solution of the first equation of system (21.50) is the sum of the general solution of the homogeneous associated equation $\tilde{\theta}_{2hs}$ and a particular solution $\tilde{\theta}_{2ps}$

$$\tilde{\theta}_{2ps} = \frac{-\psi[A\sinh(ky) + B\cosh(ky)]}{1 + \psi + \psi\mathrm{Le}} \tag{21.53}$$

The solution $\tilde{\theta}_{2hs}$ is sought under e^{ry} form, which leads to the following characteristic equation:

$$(r^2 - k^2)^2 - \mathrm{Ra}k^2(1 + \psi + \psi\mathrm{Le}) = 0$$

It is an algebraic equation of the fourth degree. Real or complex nature of the four roots of this equation depends on the sign of Ra (1 + ψ + ψLe).

21.4.2.1.1.1 Case $\mathrm{Ra}\,(1+\psi+\psi\mathrm{Le})>0$ In this last case, we find, $\tilde{\theta}_{2hs}=C\cosh(R_1y)+D\sinh(R_1y)+E\cos(R_2y)+F\sin(R_2y)$.

The general solution of system (21.51) associated with this case is

$$\tilde{\theta}_2(y)=C\cosh(R_1y)+D\sinh(R_1y)+E\cos(R_2y)+F\sin(R_2y)-\frac{\psi[A\sinh(ky)+B\cosh(ky)]}{(1+\psi+\psi\mathrm{Le})};$$

$$\tilde{\theta}_1(y)=G\cosh(ky)+H\sinh(ky);$$

$$\tilde{\theta}_3(y)=M\cosh(ky)+N\sinh(ky).$$

where

$$R_1=\sqrt{\left(\sqrt{Ra(1+\psi+\psi\mathrm{Le})}+k\right)k}$$

$$R_2=\sqrt{\left(\sqrt{\mathrm{Ra}(1+\psi+\psi\mathrm{Le})}-k\right)k}$$

The solution obtained depends on 10 arbitrary constants A, B, C, D, E, F, G, H, M, and N.

When we assume that this general solution satisfies the 10 boundary conditions given in Equations 21.52 and 21.53, we obtain 10 homogeneous linear algebraic equations and 10 unknowns corresponding to the 10 constants. This system has a nontrivial solution if the associated matrix determinant, $\det(\mathrm{Ra}(k), k, \delta, d, \psi, \mathrm{Le})$, is equal to zero. The expression of this determinant was obtained using the Maple algebra code. Once we have calculated the determinant, we obtain the dispersion relation function of the Rayleigh number, the wave number k, the aspect ratio δ, the thermal conductivity ratio d, the Lewis number Le, and the separation ratio ψ. The expression of the dispersion equation is very long and complicated, so it will be given only later for particular cases.

21.4.2.1.1.2 Case $\mathrm{Ra}\,(1+\psi+\psi\mathrm{Le})<0$ We proceed in the same manner as before. We calculate first the four roots of the characteristic equation, which are complex (the complex part, its conjugate, and their opposites). The general solution of the differential equation of order 4 without a second member is of the form

$$\tilde{\theta}_2(y)=e^{\alpha y}[A\sin(\beta y)+B\cos(\beta y)]+e^{-\alpha y}[C\sin(\beta y)+D\cos(\beta y)] \tag{21.54}$$

$$\text{with } \alpha=\sqrt{\frac{k^2}{2}+\frac{k}{2}\sqrt{\mathrm{Ra}_m^2-k^2}},\ \beta=\sqrt{-\frac{k^2}{2}+\frac{k}{2}\sqrt{\mathrm{Ra}_m^2-k^2}}\ \mathrm{Ra}_m=\sqrt{-\mathrm{Ra}(1+\psi+\mathrm{Le}\psi)}$$

In this case, the determinant is written as

$$\det(\mathrm{Ra}(k),k,\delta,d,\psi,\mathrm{Le})=\frac{k^4}{8}\frac{\sqrt{2k^2+2k\sqrt{\mathrm{Ra}_m^2-k^2}}}{(1+\psi+\psi\mathrm{Le})^2}G(\mathrm{Ra},\delta,d,\psi,\mathrm{Le})$$

From this relation, we directly determine the critical values of Rayleigh and wave number, Ra_c and k_c.

21.4.2.1.1.3 Case $1+\psi+\psi\mathrm{Le}=0$ For the particular case $1+\psi+\psi\mathrm{Le}=0$, the system of Equation 21.50 is solved analytically, using Maple algebra code. We obtain two possible dispersion equations corresponding to the first and second bifurcation

$$\mathrm{Ra}_1=g_1(d,\delta,k)\frac{(\mathrm{Le}+1)}{\mathrm{Le}}\quad\text{and}\quad\mathrm{Ra}_2=g_2(d,\delta,k)\frac{(\mathrm{Le}+1)}{\mathrm{Le}} \tag{21.55}$$

where

$$g_1(d,\delta,k)=\frac{8k^2(1-e^{2k})[(1-d)(e^k+e^{2k\delta})+(1+d)(1+e^{k(1+2\delta)})]}{d(e^{2k\delta}-1)[2k^2e^{2k}-2k^2e^k-2ke^k-2ke^{2k}+e^{3k}+e^{2k}-e^k-1]}$$

$$g_2(d,\delta,k)=\frac{8k^2(1-e^{2k})[(1-d)(e^k-e^{2k\delta})+(1+d)(e^{k(1+2\delta)}-1)]}{d(e^{2k\delta}-1)[2k^2e^{2k}-2k^2e^k-2ke^k-2ke^{2k}+e^{3k}+e^{2k}-e^k-1]}$$

Using the experimental values taken by Platten et al. (2003a), the thermophysical properties of glass spheres and copper (d, δ, Le) = (28.4, 3, 232), we deduce the critical values of Rayleigh and wave number associated with the first and second bifurcations:

$$\mathrm{Ra}_{c1}=-12\frac{(\mathrm{Le}+1)}{\mathrm{Le}},\quad k_{c1}=0$$

$$\mathrm{Ra}_{c2}=-64.30\frac{(\mathrm{Le}+1)}{\mathrm{Le}},\quad k_{c2}=3.40$$

All analytical results found from Equation 21.55 are in very good agreement with those obtained using the spectral Tau method. The disturbances are developed in terms of polynomial functions verifying all the boundary conditions except along the inner plates:

$$\begin{cases}\theta_1(y)=a_1+a_2\left[y+\dfrac{y^2}{2\delta}\right]+\displaystyle\sum_{n=1}^{N}a_{n+2}y^n(y+\delta)^2;\quad \theta_2(y)=\sum_{n=1}^{N}b_ny^{n-1}\\ \theta_3(y)=c_1+c_2\left[y-\dfrac{y^2}{2(1+\delta)}\right]+\displaystyle\sum_{n=1}^{N}c_{n+2}y^n(y-1-\delta)^2\\ \phi(y)=\displaystyle\sum_{n=1}^{N}f_n(1-y)y^n;\quad \eta(y)=d_1+d_2\left(y^2-\frac{2}{3}y^3\right)+\sum_{n=1}^{N}d_{n+2}y^{n+1}(1-y)^2\end{cases}\tag{21.56}$$

Table 21.4 reports the critical values of Ra_c and k_c obtained with the exact solution and spectral Tau method, for the first bifurcation by fixing the values of Le, d, δ, and for different values of ψ. In Figure 21.13a and b, we present the stability diagrams $\mathrm{Ra}_c=f(\psi)$ obtained for (Le, d, δ) = (5, 5, 1) and (Le, d, δ) = (232, 28.4, 3). In Figure 21.14a and b, the stability diagram $k_c=f(\psi)$ for (Le, d, δ) = (5, 5, 1) and (Le, d, δ) = (232, 28.4, 3) clearly shows the variation of the critical wave number versus the separation ratio for stationary bifurcation.

$\mathrm{Ra}_c=\mathrm{Ra}_0$ and $k_c=0$ for $\mathrm{Ra}<0\ \forall\ \psi$ and $\mathrm{Ra}>0$ only for $\psi\geq\psi_{uni}$.

For $\psi\in[\psi_H,\psi_{uni}]$, we have $k_c\neq 0$. The expression of ψ_H, ψ_{uni}, and Ra_0 will be given in Section 21.4.2.1.1.4.

For $\psi>0$, the denser component moves toward the cooler wall. The pure double-diffusive solution is then infinitely linearly stable when the horizontal layer is heated from above, while it loses its stability for the critical Rayleigh numbers smaller than $4\pi^2$, which corresponds to the critical Rayleigh number for the pure thermal problem and for $\mathrm{Ra}>0$.

For $\psi<0$, the denser component moves toward the warmer wall. For $\mathrm{Ra}<0$, the equilibrium solution is not linearly stable, unlike the pure thermal problem, so we can expect that $\mathrm{Ra}_{cs}\to-\infty$ when $\psi\to 0^-$. This result was confirmed by our direct simulations.

TABLE 21.4
Comparison between the Values of Critical Rayleigh Number Ra_{cs} and the Critical Wave Number k_{cs}, Obtained by Exact Solution and the Spectral Tau Method at Order 4

		$d = 5, \delta = 1, Le = 5$		$d = 28.4, \delta = 3, Le = 232$	
		Ra_c	k_c	Ra_c	k_c
$\Psi = -0.1$	Exact	146.83	4.60	∞	—
	Tau	146.78	4.63	∞	—
$\Psi = -0.05$	Exact	61.75	3.49	∞	—
	Tau	61.50	3.49	∞	—
$\Psi = -0.02$	Exact	43.03	3.04	∞	—
	Tau	42.90	3.04	∞	—
$\Psi = 0.00$	Exact	35.17	2.79	38.16	3.070
	Tau	35.17	2.79	38.16	3.070
$\Psi = 0.02$	Exact	29.43	2.56	2.55	0.00
	Tau	29.42	2.57	2.58	0.00
$\Psi = 0.10$	Exact	16.94	1.87	0.52	0.00
	Tau	16.93	1.88	0.52	0.00
$\Psi = 0.15$	Exact	13.06	1.54	0.34	0.00
	Tau	13.06	1.54	0.34	0.00
$\Psi = 0.20$	Exact	10.50	1.23	0.26	0.00
	Tau	10.50	1.24	0.26	0.00

For $Ra > 0$ and $(1 + \psi + \psi Le) > 0$ and $\psi < 0$, the downward migration of the denser component leads to an increase in the critical Rayleigh number ($Ra_{cs} > 4\pi^2$). For $Ra > 0$ and $(1 + \psi + \psi Le) < 0$, we do not obtain the transition to the stationary convective regime.

21.4.2.1.1.4 Limiting Case of Long-Wave Disturbances $k \approx 0$ The case of long-wave disturbances (for which the wave number, k, is close to zero) may be studied analytically using the dispersion relation, by developing a regular perturbation expansion with k as a small parameter. In our case, we expand the function F in the vicinity of $k = 0$ using Maple software, then we obtain

$$\det(\mathrm{Ra}(k), k, \delta, d, \psi, \mathrm{Le}) = \frac{\mathrm{Ra}k^6}{1 + \psi + \psi \mathrm{Le}} F(\mathrm{Ra}, \delta, d, \psi, \mathrm{Le}) \tag{21.57}$$

The singular case $1 + \psi + \psi Le = 0$ will be studied separately. From this dispersion equation, we determine the critical wave number and the critical Rayleigh number. For this purpose, we fix the value of d, δ, and the Lewis number, Le. For every value of ψ fixed, we look for the value of $k = k_c$, which minimizes the Rayleigh number to obtain the associated value Ra_c.

We develop the function F in the vicinity of $k = 0$, which gives

$$F(\mathrm{Ra}, \delta, d, \psi, \mathrm{Le}) = F_1(\mathrm{Ra}, \delta, d, \psi, \mathrm{Le}) + k^2 F_2(\mathrm{Ra}, \delta, d, \psi, \mathrm{Le}) + 0(k^4) \tag{21.58}$$

The function $F_1(\mathrm{Ra}, \delta, d, \psi, \mathrm{Le})$ is equal to zero for

$$\mathrm{Ra}_0 = \frac{12(1 + 2d\delta)}{1 + \psi(2\mathrm{Le}d\delta + \mathrm{Le} + 1)} \tag{21.59}$$

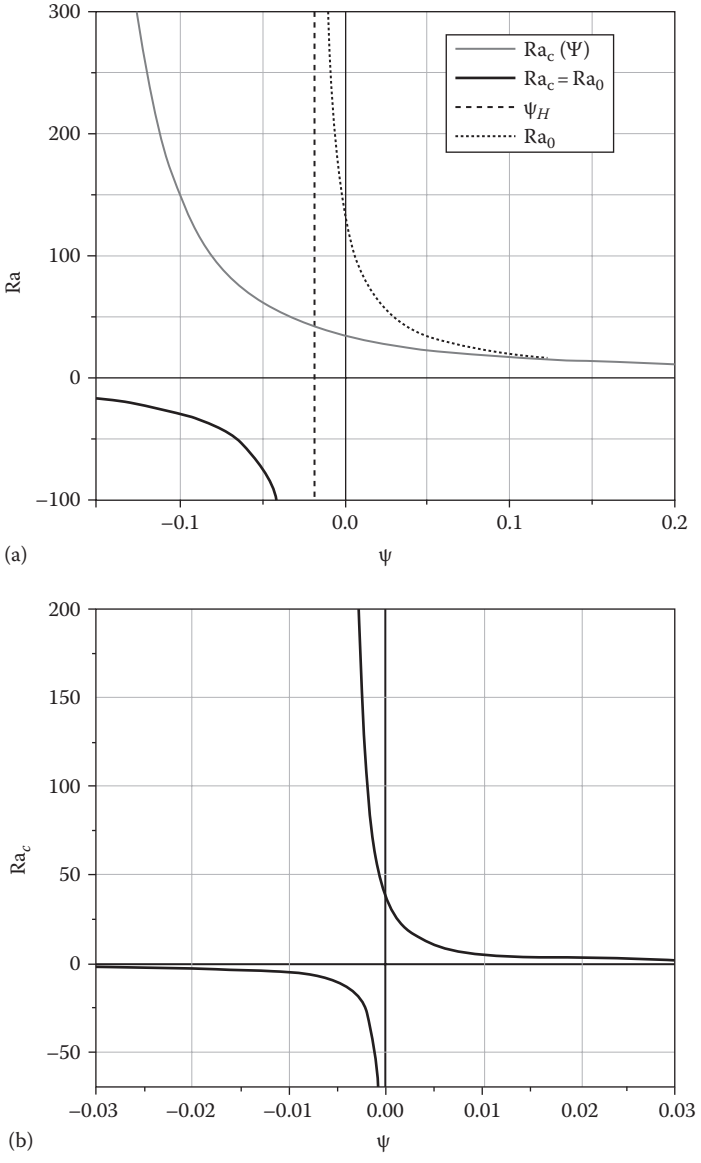

FIGURE 21.13 (a–b) Critical Rayleigh number at the onset of convection versus separation ratio for (a) Le = 5, δ = 1, d = 5, (b) Le = 232, δ = 3, d = 28.4. Dashed lines: $\psi_H = -1/(\mathrm{Le}(1 + 2d\delta) + 1)$ and $\mathrm{Ra}_0 = 12(1 + 2d\delta)/[1 + \psi(2d\delta\mathrm{Le} + \mathrm{Le} + 1)]$.

This value of Ra_0 corresponds to the onset of the unicellular flow associated with $k = 0$. Ra_0 does not necessarily correspond to a critical Rayleigh number of the problem considered, as shown in Figure 21.13a. By replacing Ra by Ra_0 in the expression of F_2, the equation $F_2(\mathrm{Ra}, \delta, d, \psi, \mathrm{Le}) = 0$, after simplification, leads to a relationship linking the various physical parameters (Le, δ, d, ψ), which is written as

$$10(1 + 2d\delta)^2\psi\mathrm{Le} + [10 - d\delta(1 + \psi)(70\delta^3 + 51d\delta - 12)] = 0 \tag{21.60}$$

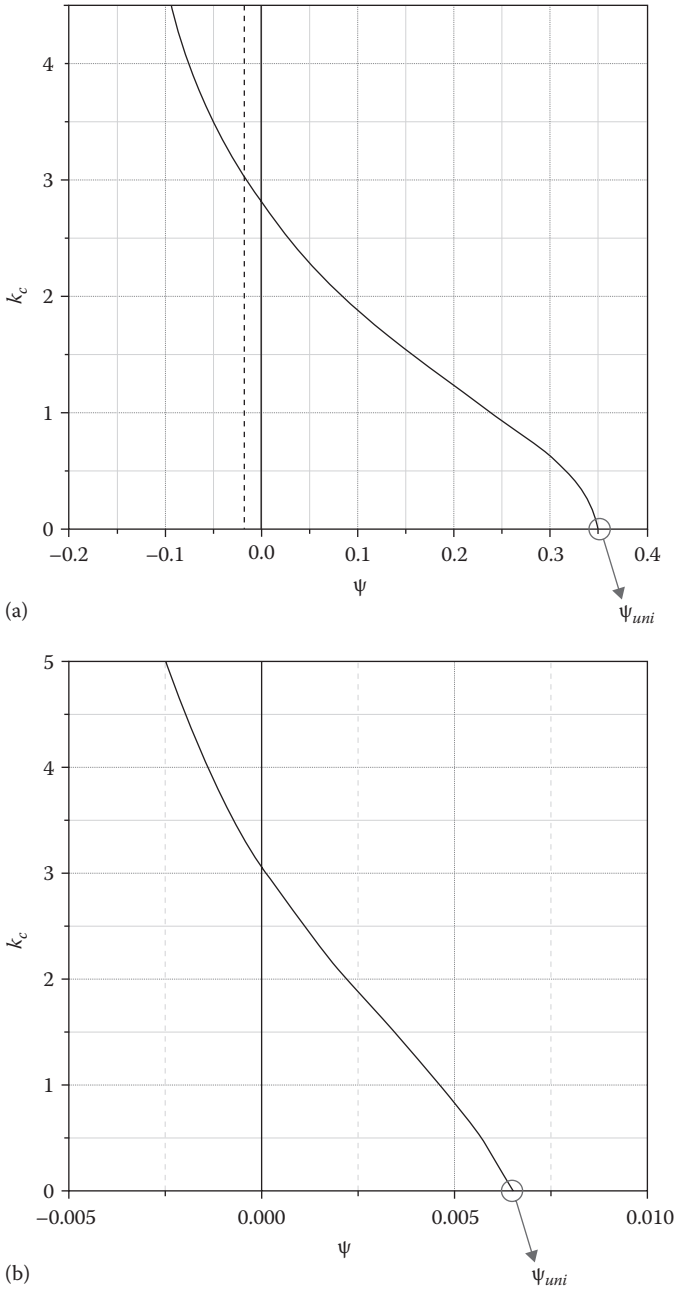

FIGURE 21.14 Critical wave number at the onset of convection versus separation ratio for (a) Le = 5, δ = 1, d = 5, (b) Le = 232, δ = 3, d = 28.4. Dashed line: $\psi_H = -1/(\text{Le}(1 + 2d\delta) + 1)$.

The solution of this Equation 21.60 with regard to ψ leads to

$$\psi_{uni} = \frac{1}{\dfrac{10(1+2d\delta)^2}{51d^2\delta^2 + 70d\delta^3 - 10 - 12d\delta} - 1} \tag{21.61}$$

Let us look at which conditions $k = 0$ and $\mathrm{Ra}_0 = \dfrac{12(1+2d\delta)}{1+\psi(2\mathrm{Le}d\delta + \mathrm{Le} + 1)}$ correspond to the critical parameters $k_c = 0$, $\mathrm{Ra}_c = \mathrm{Ra}_0$. For this purpose, we distinguish two cases, $\mathrm{Ra} > 0$ and $\mathrm{Ra} < 0$.

For $\mathrm{Ra} > 0$, we have to show that $d\mathrm{Ra}/dk^2 \geq 0$, and for $\mathrm{Ra} < 0$, we have to show that $d\mathrm{Ra}/dk^2 \leq 0$ in the neighborhood of $k = 0$.

When k tends toward zero, we verify that

$$\left(\frac{d\mathrm{Ra}}{dk^2}\right)_{k=0} = -F_2(\mathrm{Ra}_0, \delta, d, \psi, \mathrm{Le}) \tag{21.62}$$

and we deduce that

$$\left(\frac{d\mathrm{Ra}}{dk^2}\right)_{k=0} = \frac{4[10(1+2d\delta)^2\psi\mathrm{Le} + (1+\psi)(12d\delta + 10 - 70d\delta^3 - 51d^2\delta^2)]}{35(\psi[\mathrm{Le}(2d\delta+1)+1]+1)^2} \tag{21.63}$$

The sign of $\left(\dfrac{d\mathrm{Ra}}{dk^2}\right)$ is the same as the sign of the numerator, N_{num} of Equation 21.63, and thus $\left(\dfrac{d\mathrm{Ra}}{dk^2}\right)_{k=0} \to \infty$ for $\psi = \psi_H = \dfrac{-1}{1+\mathrm{Le}(1+2d\delta)}$.

We can make three remarks concerning the critical number of Rayleigh found in our study.

Remark 21.1

$\delta \to 0$ means that the thickness of the walls delimiting the porous medium tends to zero. This configuration corresponds to a constant heat flux directly imposed on the porous layer studied previously by Bahloul et al. (2003) for $a = 1$. We find the same result as obtained by these authors when $\delta \to 0$, $\mathrm{Ra}_c = 12/(1 + \psi + \psi\mathrm{Le})$.

Remark 21.2

$d \to \infty$ means that the walls delimiting the porous medium are infinitely more conductive than the porous layer saturated by binary fluid. This configuration is similar to a porous cell maintained at constant temperatures. This configuration was studied by Knobloch (1986) and Charrier-Mojtabi et al. (2007). For $d \to \infty$, the relation giving Ra_c leads to $\mathrm{Ra}_c = 12/\psi\mathrm{Le}$, a result obtained previously by Knobloch (1986) and Charrier-Mojtabi et al. (2007).

Remark 21.3

When we take into account the effect of the walls delimiting the porous medium, and for $\psi = 0$ (natural convection), the relation giving Ra_c leads to $\mathrm{Ra}_c = 12(1 + 2d\delta)$, a result obtained recently by Mojtabi and Rees (2011).

21.4.2.1.2 Oscillatory Instability

In order to study the stability of the equilibrium solution, we introduce and expand the perturbations using Equation 21.41. When we replace the disturbances by their developed form in system (21.53), we find the second-order differential system:

$$\begin{cases} \left(D^2 - k^2\right)\varphi + ik\mathrm{Ra}\left[\left(1+\Psi\right)\theta_2 + \Psi\right] = 0 \\ \left(D^2 - k^2 - i\omega\right)\theta_2 - ik\varphi = 0 \\ \left(D^2 - k^2 - i\mathrm{Le}\omega\varepsilon\right) - i\mathrm{Le}\omega\varepsilon\theta_2 - ik\varphi = 0 \\ \alpha\left(D^2 - k^2\right)\theta_1 - i\omega\theta_1 = 0 \\ \alpha\left(D^2 - k^2\right)\theta_3 - i\omega\theta_3 = 0 \end{cases} \tag{21.64}$$

The corresponding boundary conditions are given by (21.52).

To solve this linear differential system, we use the spectral Tau method and the same disturbances given in Equation 21.56.

Replacing the disturbances, by their developments in system (21.64), leads to a homogeneous linear algebraic system. This system has a nontrivial solution if the associated matrix determinant is equal to zero. In this study, the determinant is a complex:

$$\det(A) = R(\mathrm{Ra}, k, \omega, \varepsilon, \mathrm{Le}, \psi, d, \delta) + IQ(\mathrm{Ra}, k, \omega, \varepsilon, \mathrm{Le}, \psi, d, \delta) = 0$$

where R and Q are real polynomial. To calculate the value of the critical Rayleigh number corresponding to a Hopf bifurcation, we proceed as follows, using the computer algebra code Maple:

We first fix particular values of ψ, ε, d, δ, and Le. We resolve the following algebraic system, with two unknowns (Ra, ω) and a parameter k:

$$\begin{cases} R(\mathrm{Ra}, k, \omega) = 0 \\ Q(\mathrm{Ra}, k, \omega) = 0 \end{cases} \tag{21.65}$$

When we solve this system, we obtain the real roots of indices j: $\mathrm{Ra}_j = f_j(k)$ and $\omega_j = h_j(k)$.

We can then look for the minimum value of Ra according to k and obtain the critical parameters $\mathrm{Ra}_{jc} = f_j(k_c)$ and $\omega_{jc} = h_j(k_c)$.

When we set $\omega = 0$ in the expression of the determinant det (A), we verify that the critical Rayleigh numbers obtained correspond to the stationary transition. When ω is different from 0, we are led to determine the critical Rayleigh numbers corresponding to the oscillatory bifurcation. We were able to determine these critical parameters using the Maple software code.

In the case of a cell heated from below, for $\psi < 0$, the heavier constituent migrates toward the hot wall, and a stabilizing effect occurs.

In Figure 21.15a, we show that, for values of ψ less than $\psi_H = -1/(\mathrm{Le}(1 + 2d\delta) + 1)$, the primary bifurcation is a Hopf bifurcation. Using the Tau spectral method to order 4 with d, δ, Le fixed and for different values of ε and ψ, we determined the critical Rayleigh number, Ra_{co}, the critical Hopf frequency, ω_c, and the associated critical wave number, k_c (Figure 21.15b). The marginal stability curves associated with the Hopf bifurcations are slightly below the curve of marginal stability associated with the stationary bifurcation regardless of the value of the normalized porosity considered.

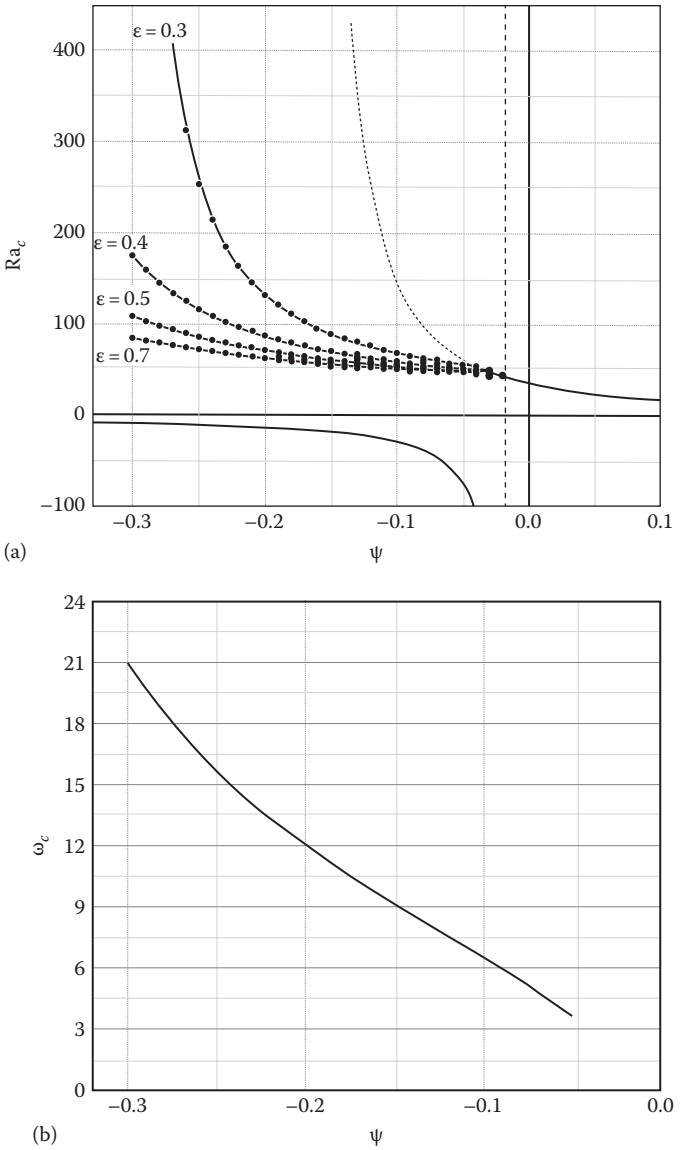

FIGURE 21.15 (a) Stability diagram for different normalized porosity values (ε = 0.3, 0.4, 0.5, 0.7) (the spectral Tau method at order 4) and for Le = 5, δ = 1, d = 5. Doted line: stationary bifurcation; solid line: Hopf bifurcation; dashed line: $\psi_H = -1/(\text{Le}(1 + 2d\delta) + 1)$, (b) critical Hopf frequency number versus separation ratio at order 4 for ε = 0.4, Le = 5, δ = 1, d = 5.

21.5 VIBRATION AND THERMOGRAVITATIONAL DIFFUSION IN A POROUS MEDIUM

21.5.1 Influence of Horizontal Vibrations on the Separation of Binary Mixture in a Vertical Porous Layer

In this section, we propose to study the TGC subject to high-frequency horizontal vibrations with the aim of enhancing the separation.

Thermovibrational convection in an enclosure has been investigated during the last four decades due to its extensive applications in microgravity research. Examples are weightlessness experiments and

crystal growth to name a few (see Polezaev 2006). For applications of thermovibrational convection in the measurement of Soret coefficient, see Ahadi and Saghir (2013) and Costesèque et al. (2011).

The problem of vibrational convective instability for the case of a binary mixture with Soret effect has been investigated by Gershuni et al. (1997). The effect of longitudinal high-frequency vibration on a plane horizontal layer of the mixture with rigid and isothermal boundaries was studied. It was shown that convective instability is caused by both mechanisms of excitation thermogravitational and thermovibrational, which are superimposed. Later, Gershuni et al. (1999) have considered the case where the axis of vibration is vertical, that is, transversal with respect to the layer. This study confirmed that if the axis of vibration is parallel to the temperature gradient, the mechanical equilibrium is stable. In both of these works, the time-averaged formulation has been used. Razi et al. (2004) completed these studies for all directions of vibrations. In addition, they proved several analytical relations showing from which separation ratio unicellular convection can begin. Later, they extended this work to porous media and compared the results in fluid and porous media (Razi et al. 2009).

Several authors have also studied the action of vibration on the onset of convection; it was found that the vibration can be used to delay the onset of the convection in the presence of gravity in a porous layer saturated by a pure fluid Charrier-Mojtabi et al. (2003). For a detailed review of thermovibrational convection in porous media, see Razi et al. (2005).

Cissé et al. (2004) have investigated the thermovibrational convection in a container where the horizontal walls are maintained at constant temperatures. The vertical boundaries are thermally insulated, impermeable, and adiabatic; it should be noted that this study is in fluid media. They have shown that high-frequency vertical oscillations can delay convective instabilities and, in this way, reduce the convective flow.

Elhajjar et al. (2009) have studied the influence of vertical vibrations on the separation of a binary mixture in a horizontal porous layer heated from below (2009).

In this section, we numerically investigate a vertical rectangular enclosure filled with a homogeneous isotropic porous medium saturated by a two-component fluid and subjected to high-frequency horizontal vibrations. The vertical walls of the cavity are maintained at constant temperatures, while the horizontal ones are adiabatic and impermeable.

21.5.1.1 Mathematical Formulation

Let us consider a plane vertical layer of porous medium saturated by a binary mixture. The layer is confined between two rigid isothermal and impermeable planes $x = 0$ and $x = e$ (Figure 21.16). The flow domain is $(x, z) \in \Omega = [0, e] \times [0, H]$. The vertical walls at $x = 0$ and e are kept at constant and uniform temperatures T_H and T_F with $T_H > T_F$, and these walls are impermeable. The top and bottom horizontal walls at $z = H$ and $z = 0$ are insulated. The fluid layer and its boundaries undergo linear harmonic oscillations in the x-axis direction. The binary fluid is assumed to be Newtonian and to satisfy the Boussinesq approximation.

The gravitational field is replaced by the sum of the gravitational and vibrational acceleration in the momentum equation.

The governing conservation equations for mass, momentum, energy, and chemical species when the Soret effect is taken into account can be written as

$$\begin{cases} \nabla \cdot \vec{V} = 0 \\ \dfrac{\rho_0}{\varepsilon^*} \dfrac{\partial \vec{V}}{\partial t} = -\nabla P + \rho_0 \left[\beta_T \left(T - T_0 \right) + \beta_C \left(C - C_0 \right) \right] \left[g - B\omega^{*2} \sin\left(\omega^* t' \right) \right] \vec{e}_z - \dfrac{\mu}{K} \vec{V} \\ \left(\rho c \right)^* \dfrac{\partial T}{\partial t} + \left(\rho c \right)_f \vec{V} \cdot \nabla T = \lambda^* \nabla^2 T \\ \varepsilon^* \dfrac{\partial C}{\partial t} + \vec{V} \cdot \nabla C = D \nabla^2 C + D_T C_0 \left(1 - C_0 \right) \nabla^2 T \end{cases} \tag{21.66}$$

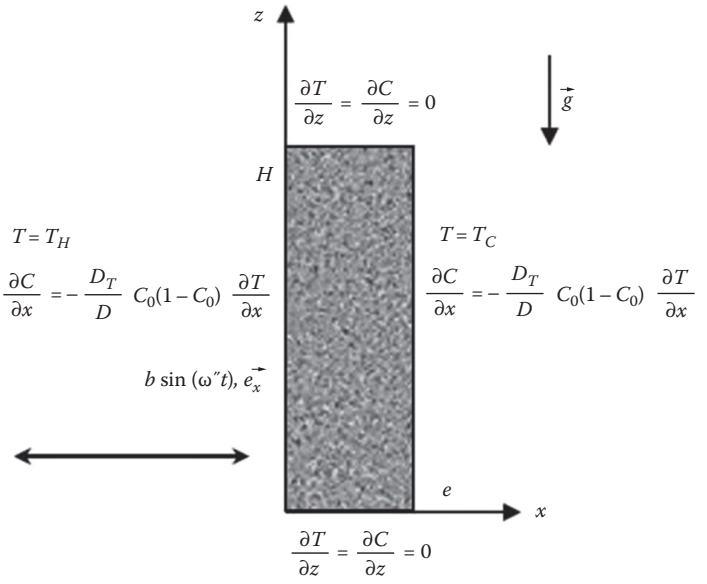

FIGURE 21.16 Geometrical configuration of the cavity.

The boundary conditions are

$$\begin{cases} \vec{V}\cdot\vec{n}=0 \quad \forall M\in\partial\Omega \\ T=T_1,\left(D\nabla C+D_T C_0\left(1-C_0\right)\nabla T\right)\cdot\vec{n}=0 \quad \text{for } x=0,\forall z \\ T=T_2,\left(D\nabla C+D_T C_0\left(1-C_0\right)\nabla T\right)\cdot\vec{n}=0 \quad \text{for } x=e,\forall z \\ \dfrac{\partial T}{\partial z}=\dfrac{\partial C}{\partial z}=0 \quad \text{for } z=0,H,\forall x \end{cases} \tag{21.67}$$

We introduce nondimensional variables with the help of the following scales: H for distance, a^*/H for velocity, $\sigma H^2/a^*$ for time, $(\sigma = (\rho c_p)^*/(\rho c_p)_f)$, $\Delta T = T_H - T_C$ for the temperature, $\Delta C = -D_T/D\cdot C_0 (1 - C_0)\,\Delta T$, and $(\nu a^*\rho_0)/k$ for pressure; we obtain the following system of equations:

$$\begin{cases} \nabla\cdot\vec{\mathrm{V}}=0 \\ B\dfrac{\partial\vec{V}}{\partial t}+\vec{V}=-\nabla P+\mathrm{Ra}(T+\psi C)(1-R\sin(\omega t))\vec{e}_z \\ \dfrac{\partial T}{\partial t}+\vec{V}\cdot\nabla T=\nabla^2 T \\ \varepsilon\dfrac{\partial C}{\partial t}+\vec{V}\cdot\nabla C=\dfrac{1}{\mathrm{Le}}(\nabla^2 C-\nabla^2 T) \end{cases} \tag{21.68}$$

where

$$\mathrm{Ra}=\frac{(kgH\beta_T\Delta T)}{(\nu a^*)},\quad \omega=\frac{\omega^*\sigma H^2}{a^*},\quad R=\frac{(b\omega^{*2})}{g},\quad \psi=\frac{(-\beta_c D_T C_0(1-C_0))}{(\beta_T D)},\quad \frac{\sigma=(\rho c)^*}{(\rho c)_f},\quad \varepsilon^*=\frac{\varepsilon}{\sigma}$$

The high-frequency oscillations correspond to the case where the period of the displacement $\tau = 2\pi/\omega^*$ is very small compared to the characteristic times of thermal, kinematic, and mass diffusion ($\tau \ll \sigma H^2/a^*$, $\tau \ll K/\varepsilon\nu$, $\tau \ll \varepsilon H^2/D$); we can apply the method of time-averaging used by Simonenko (1972) in these conditions, so we may write

$$\begin{cases} \vec{V} = \bar{\vec{V}} + \vec{V}' \\ P = \bar{P} + P' \\ T = \bar{T} + T' \\ C = \bar{C} + C' \end{cases} \tag{21.69}$$

Here

$\bar{\vec{V}}, \bar{P}, \bar{T}$, and $\bar{C}$ are the averaged fields

$\vec{V}', P', T'$, and C' are the quick parts

Using a method for averaging analogous to that employed by Gershuni et al. (1997), we obtain the following closed system of equations for mean fields with the nondimensional variables being used:

$$\begin{cases} \vec{\nabla} \cdot \vec{\nabla} = 0 \\ B\dfrac{\partial \vec{V}}{\partial t} + \vec{V} + \nabla P = \mathrm{Ra}_T (T + \psi C)\vec{e}_z + R_v \left(\vec{W} . \left(\nabla T + \dfrac{\psi}{\varepsilon} \nabla C \right) \right) \vec{e}_x \\ \dfrac{\partial T}{\partial t} + \vec{V} \cdot \nabla T = \nabla^2 T \\ \varepsilon \dfrac{\partial C}{\partial t} + \vec{V} \cdot \nabla C = \dfrac{1}{\mathrm{Le}} \left(\nabla^2 C - \nabla^2 T \right) \\ \nabla \xi + \vec{W} = (T + \psi C)\vec{e}_x \\ \nabla \cdot \vec{W} = 0 \end{cases} \tag{21.70}$$

$$\text{where:} \quad R_v = \frac{((\mathrm{Ra}_T R)^2 B)}{(2(1 + B^2\omega^2))}$$

The corresponding nondimensional forms of the boundary conditions are

$$\begin{cases} \vec{V} \cdot \vec{n} = 0 \quad \text{and} \quad \vec{W} \cdot \vec{n} = 0 \quad \forall M \in \partial\Omega \\ T = 1_1 = 0 \quad \dfrac{\partial C}{\partial x} = \dfrac{\partial T}{\partial x} \quad \text{for } x = 0, \quad \forall z \\ T = 0, \quad \dfrac{\partial C}{\partial x} = \dfrac{\partial T}{\partial \boldsymbol{x}} \quad \text{for } x = 1, \quad \forall z \\ \dfrac{\partial T}{\partial z} = \dfrac{\partial C}{\partial z} = 0 \quad \text{for } z = 0, \quad H, \forall x \end{cases} \tag{21.71}$$

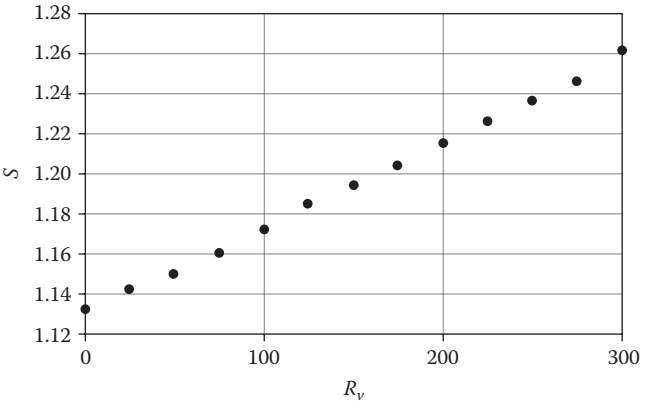

FIGURE 21.17 Variation of separation with R_v.

We have solved this problem numerically with the industrial code Comsol 3.5a. This software solves the partial differential equations using the finite elements method. We have used a uniform quadratic mesh, which is more convenient for our rectangular cell configuration.

Using the phenomenological theory of transport in the columns with porous garnishing, Lorenz and Emery (1959) have showed that in a vertical cell containing a porous medium and saturated by a binary mixture, there is a maximum of separation associated with an optimal Ra value, $\mathrm{Ra}_{opt} = (A\sqrt{30})/\mathrm{Le}$ where A is the aspect ratio of the cell and Le is the Lewis number.

This value corresponds to the optimal coupling between convection and thermal diffusion.

We will work with an Ra larger than Ra_{opt} to separate with a bigger volume, and we will study the influence of the horizontal vibration on separation. In this case, the convection is predominant.

We take the following numerical values: $B = 10^{-6}$, $\psi = 0.4$, $\varepsilon = 0.5$, Le = 100, $\mathrm{Ra}_T = 10$, with several R_v. All the numerical results presented in this investigation were obtained for a cavity with an aspect ratio $A = 100$.

21.5.1.2 Results

Here we showed how stabilizing influence of vibration can be used to optimize separation. The separation S is defined as the difference of mass fraction of the denser component C between the bottom and the top of the cell: $S = C_{bot} - C_{top}$. Figure 21.17 shows the influence of R_v on the dimensionless separation S; it can be noticed that the separation increases with R_v. This can be explained by the fact that the vibration in the direction of the temperature gradient tends to stabilize the movement, that is, to decrease the convection. Since for the chosen Ra the convection is dominant in comparison with thermal diffusion, the use of vertical vibration will approach the optimal coupling between convection and thermal diffusion, then the separation will increase.

21.5.2 Influence of Vertical Vibrations on the Separation of a Binary Mixture in a Horizontal Porous Layer Heated from Below

We study the influence of vertical high-frequency and small-amplitude vibrations on the separation of a binary mixture saturating a shallow horizontal porous layer heated from below.

In this study, we use the same formulation as the one used by Charrier-Mojtabi et al. (2007) for a shallow porous cavity, saturated by a binary mixture and heated from below. We consider the case of high-frequency, small-amplitude vibrations, so that a formulation using time-averaged equations can be used. The results of the linear stability analysis of the mechanical equilibrium and the unicellular flow in an infinite porous layer heated from below, in the case of a separation ratio $\psi > \psi_{uni} > 0$, are corroborated by the direct numerical simulations.

21.5.2.1 Mathematical Formulation

We consider a rectangular cavity with aspect ratio $A = L/H$, where H is the height of the cavity along the vertical axis and L is the width along the horizontal axis. The aspect ratio is assumed infinite in the stability analysis. The cavity is filled with a porous medium saturated by a binary fluid for which the Soret effect is taken into account. The impermeable horizontal walls are kept at different uniform temperatures: T_1 for $z = 0$ and T_2 for $z = H$, with $T_1 > T_2$. The vertical walls ($x = 0$, $x = L$) are impermeable and adiabatic. All the boundaries are assumed rigid. The cavity is subjected to linear harmonic oscillations in the vertical direction (amplitude b and dimensional frequency ω).

21.5.2.2 Linear Stability of the Equilibrium Solution in an Infinite Horizontal Porous Layer

The stability of the equilibrium solution was studied by Charrier-Mojtabi et al. (2004). They restricted their study to the case of Le = 2 for which the fluid considered is in the gaseous state, and so the Dufour effect should be taken into account. We extended this study to the case of high Lewis number, and we focused on the transition from the equilibrium solution to the unicellular flow obtained for binary mixtures with positive separation ratio: $\psi > \psi_{uni} > 0$.

This problem admits a mechanical equilibrium, and its solution is characterized by

$$V_0 = 0, \quad T_0 = 1 - z, \quad C_0 = \frac{1}{2} - z, \quad W_0 = 0 \tag{21.72}$$

In order to analyze the stability of this conductive solution, we introduced the perturbation of the vertical velocity component w, the perturbation of the vertical component of $\vec{W}$, w_2, and the perturbations of temperature θ, and concentration c. We assumed that the perturbations (w, w_2, θ, c) were small.

We introduced a new function $\eta = c - \theta$, in order to more easily take into account the boundary conditions on θ and c for $z = 0$ and 1.

The linear stability equations were solved using the fourth-order Galerkin method.

For $\psi > 0$, the first bifurcation is stationary. The factor B was set to 10^{-6} and $\varepsilon = 0.5$. For Le = 100, we determined the stability diagrams, $\mathrm{Ra}_c = f(\psi)$ and $k_c = f(\psi)$, where Ra_c and k_c are, respectively,

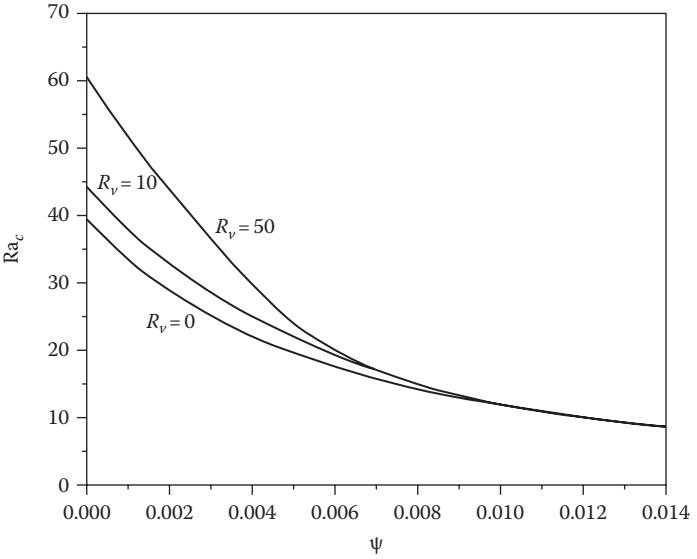

FIGURE 21.18 Critical Rayleigh number at the onset of convection versus separation ratio for Le = 100, $B = 10^{-6}$, and $\varepsilon = 0.5$.

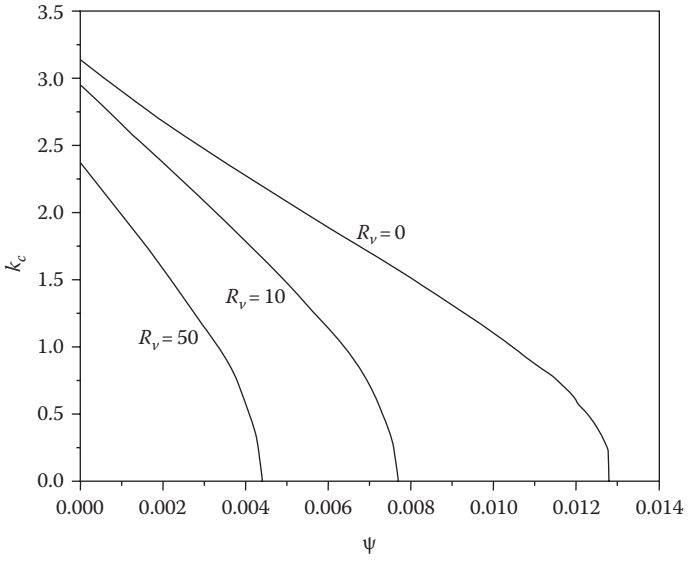

FIGURE 21.19 Critical wave number at the onset of convection versus separation ratio for Le = 100, $B = B = 10^{-6}$, and $\varepsilon = 0.5$.

the critical thermal Rayleigh number and the critical wave number in the infinite horizontal direction. The results are illustrated in Figures 21.18 and 21.19 for the case Le = 100, $\varepsilon = 0.5$, and for $R_v = 0, 10, 50$.

For a layer heated from below, we observe that Ra*c* increases with R_v, whereas k_c decreases with R_v. For $\psi > 0$, when R_v increases, the value ψ_{uni} of the separation ratio beyond which the critical wave number vanishes (i.e., $k_c = 0$) decreases. Table 21.5 shows the influence of vibrations (R_v) on ψ_{uni}. We note that ψ_{uni} decreases and becomes close to 0 when R_v increases. For Le = 100, we obtain $\psi_{uni} = 0.0129$ without vibration and $\psi_{uni} = 0.0033$ for $R_v = 100$. This value of ψ is very small, and most binary fluids have a separation ratio higher than this value. So, by adding vibrations, we can use the horizontal cell to separate most of binary mixtures. Using a regular perturbation method in the case of long wave disturbances (i.e., $k =$), we showed that, for $\psi > \psi_{uni}$, the first primary

TABLE 21.5
Effect of Vibrations on the Value of the Separation Ratio ψ_{uni} beyond Which the Flow at the Onset of Convection Becomes Unicellular for $\varepsilon = 0.5$ and $B = 10^{-6}$

R_v	ψ_{uni} for Le = 100	ψ_{uni} for Le = 30
0	0.0129	0.0444
10	0.0077	0.0257
20	0.0062	0.0205
30	0.0054	0.0177
40	0.0048	0.0159
50	0.0044	0.0146
60	0.0041	0.0136
70	0.0039	0.0128
80	0.0037	0.0121
90	0.0035	0.0115
100	0.0033	0.0110

bifurcation is a stationary one and the critical thermal Rayleigh number is $\mathrm{Ra}_c = 12/(\mathrm{Le}\psi)\ \forall\ R_v$. Furthermore, we noticed that when the vibrational Rayleigh number, R_v, increased, the value of the separation ratio ψ_{uni} beyond which the wave number $k_c = 0$ decreased. To conclude, vertical vibrations have a stabilizing effect on the convective motions whereas they do not modify the value of Ra*c* for the flow associated with the long wave mode (i.e., $k_c = 0$). The same results can be observed in a horizontal binary fluid layer (Gershuni et al. 1999).

21.5.2.3 Analytical Solution of the Unicellular Flow

In the case of a shallow cavity $A \gg 1$, we considered the parallel flow approximation used by Cormack et al. (1974). The basic flow, denoted with a subscript 0, is then given as follows:

$$\overrightarrow{V_0} = U_0(z)\overrightarrow{e_x};\quad T_0 = bx + f(z);\quad C_0 = mx + g(z);\quad \overrightarrow{W_0} = W_{10}(z)\overrightarrow{e_x} \tag{21.73}$$

For the stationary state, when the earlier-mentioned assumptions are made and the corresponding boundary conditions are considered, we obtain the velocity, temperature, and concentration fields:

$$\begin{cases} T_0 = 1 - z \\ U_0 = \mathrm{Ra}m\Psi(1/2 - z) \\ C_0 = mx + [m^2\mathrm{RaLe}\Psi(3z^2 - 2z^3)]/12 - z - (m^2\mathrm{RaLe}\Psi)/24 + (1 - mA)/2 \\ m = \pm\sqrt{(10\mathrm{LeRa}\Psi - 120)}/(\mathrm{LeRa}\Psi) \\ W_{10} = (b + \psi m)(1/2 - z) \end{cases} \tag{21.74}$$

The expressions obtained for the velocity, the temperature, and the mass fraction show that the basic state, corresponding to the unicellular flow, is independent of the high-frequency and small-amplitude vibrations.

The separation, $S = mA$, is defined as the difference in mass fraction of the denser component in the vicinity of the left and the right vertical walls of the cell. Then, the maximum separation is obtained for $\mathrm{Ra} = 24/(\mathrm{Le}\psi)$. This value is denoted as Ra_{opt}.

Figure 21.20 presents the separation value versus RaLeψ obtained analytically and numerically for an arbitrary moderate chosen value of R_v. We verified numerically, solving the averaged Equations 21.70 for $R_v = 50$, that the unicellular flow remains stable and leads to the exact separation value obtained analytically with Equation 21.74. It can be seen that the separation has a maximum corresponding to the optimal coupling between thermodiffusion and convection. For small values of the Rayleigh number, the convection is weak, and the separation is mainly caused by thermodiffusion. For high values of the Rayleigh number, the convection is strong, and the flow increases the mixing of the species leading to a small separation. It can be noted that, due to the reference scale used for the concentration field, the separation *S* may be higher than 1.

21.5.2.4 Linear Stability of the Unicellular Flow

We studied the stability of the unicellular solution in order to confirm that the species separation could occur in a horizontal porous cell heated from below. For this study, we write the governing equations using the perturbations of the velocity $\vec{v}$, , temperature θ, pressure *p*, mass fraction *c*, and solenoidal field $\vec{w}$:

$$\vec{v} = \vec{V} - \overrightarrow{V_0},\dagger\ \ \theta = T - T_0,\dagger\ \ c = C - C_0,\dagger\ \ p = P - P_0,\dagger\ \ \vec{w} = \vec{W} - \overrightarrow{W_0}$$

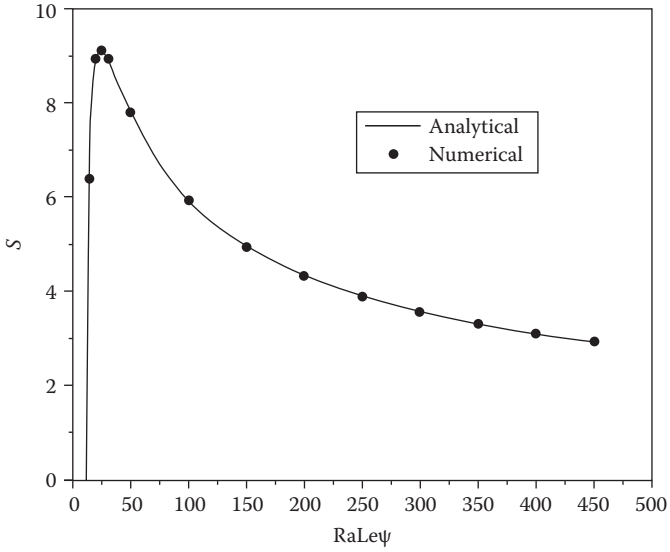

FIGURE 21.20 Separation versus Ra Le ψ for $R_v = 50$ and $(\text{RaLe}\psi)_{opt} = 24$.

The second-order terms are neglected; we obtain the linear equations where the unknown functions are the perturbations.

To take the boundary conditions for temperature and concentration at $z = 0$ and 1 into account more easily, we introduce the new variable $\eta = c - \theta$.

The disturbances are developed in normal modes:

$$(w, \theta, \eta, w_2) = (w(z), \theta(z), \eta(z), w_2(z))e^{(ikx+ \sigma t)}$$

We obtain the following system of equation:

$$\begin{cases} (B\sigma+1)(D^2-k^2)w + \text{Ra}k^2(\theta(1+\psi)+\psi\eta) + R_v\left[ikDw_2 m\left(\frac{\Psi}{\varepsilon}\right)\right. \\ \quad \left. + w_2k^2\left(DT_0 + \frac{\Psi}{\varepsilon}DC_0\right) + ik^3W_{10}\left(\left(1+\frac{\Psi}{\varepsilon}\right)\theta + \eta\frac{\Psi}{\varepsilon}\right)\right] = 0 \\ (D^2-k^2)\theta - \sigma\theta + w - ikU_0\theta = 0 \\ \frac{ik(D^2-k^2)\eta}{\text{Le}} - (\eta+\theta)(\varepsilon\sigma ik - k^2U_0) + mDw - ikwDC_0 = 0 \\ (D^2-k^2)w_2 + k^2((1+\psi)\theta + \psi\eta) = 0 \end{cases} \tag{21.75}$$

where

$D = \partial/\partial z$

k is the horizontal wave number

$\sigma = \sigma_r + i\sigma_i$ is the temporal amplification of the perturbation

$i^2 = -1$

w is the vertical component of the velocity

w_2 is the vertical component of w

The corresponding boundary conditions are

$$w = 0, \quad \theta = 0, \quad w_2 = 0 \quad \text{for } z = 0, 1 \tag{21.76}$$

TABLE 21.6
Effect of Vibrations on the Critical Values of Rayleigh Number Ra_{c2}, Wave Number k_{c2}, and Frequency ω_{c2} Associated with Transition from Unicellular to Multicellular Flow for Le = 30, $\varepsilon = 0.5$, $B = 10^{-6}$ (Order 4 Galerkin Method)

R_v	Ra_{c2}	k_{c2}	ω_{c2}
0	31.48	2.84	2.21
10	36.51	2.63	2.25
20	40.96	2.45	2.25
30	44.98	2.30	2.24
40	48.67	2.18	2.23
50	52.08	2.08	2.21
60	55.28	2.00	2.20
70	58.28	1.92	2.18
80	61.12	1.86	2.17
90	63.83	1.81	2.16
100	66.41	1.76	2.15

The resulting linear problem is solved using the fourth-order Galerkin method. The perturbation quantities are chosen as follows:

$$w(z) = \sum_{i=1}^{N} a_i \sin(i\pi z); \quad \theta(z) = \sum_{i=1}^{N} b_i \sin(i\pi z);$$

$$c(z) = \sum_{i=1}^{N} c_i cos(i\pi z); \quad w_2(z) = \sum_{i=1}^{N} d_i \sin(i\pi z)$$

The critical values of the Rayleigh number and the wave number were obtained for a stationary and a nonstationary bifurcation. For the values of ψ and Le studied, the critical Rayleigh number leading to stationary bifurcation is always higher than the one leading to the Hopf bifurcation. So, in this study, we focus on the values of the critical wave number k_{c2}, the critical Rayleigh number Ra_{c2}, and the critical frequency ω_{c2} related to the Hopf bifurcation. The results of linear stability analysis for Le = 30 and Le = 100 and for $\psi = 0.1$ are presented in Tables 21.6 and 21.7. It can be observed in these two tables that the vibrations have a stabilizing effect and lead to an increase in the critical value of the thermal Rayleigh number. So the vibrations can be used to maintain the unicellular flow and then allow the separation of the binary mixture components over a wide range of thermal Rayleigh number. But it should be noted that the separation value decreases for the high values of Ra. It should be mentioned that vibrations reduce the critical wave number k_{c2} and the Hopf frequency ω_{c2}. This means that vibrations can also be used to decrease the number of convective rolls at the transition from the unicellular flow to the multicellular flow.

21.5.2.5 Numerical Simulations

The averaged Equation 21.70 with the associated boundary conditions were solved using the finite element method and the spectral collocation method. The influence of vibrations on the onset of convection was investigated for a cell of aspect ratio $A = 20$ for Le = 30 and Le = 100, $\varepsilon = 0.5$ (B is fixed to $B = 10^{-6}$).

TABLE 21.7
Effect of Vibrations on the Critical Values of Rayleigh Number Ra_{c2}, Wave Number k_{c2}, and Frequency ω_{c2} Associated with Transition from Unicellular to Multicellular Flow for Le = 100, ε = 0.5, and $B = 10^{-6}$ (Order 4 Galerkin Method)

R_v	Ra_{c2}	k_{c2}	ω_{c2}
0	27.67	3.04	1.44
10	32.29	2.81	1.43
20	36.44	2.61	1.40
30	40.21	2.44	1.37
40	43.67	2.3	1.34
50	46.88	2.18	1.32
60	49.88	2.08	1.30
70	52.70	2.00	1.28
80	55.37	1.92	1.26
90	57.91	1.86	1.25
100	60.33	1.81	1.24

21.5.2.5.1 Stability of the Equilibrium Solution

It was observed that the critical control parameters of the bifurcations differed very little between the case $A = 20$ and the case of a cell of infinite horizontal extension. A structured mesh 150 × 30 was used for the finite element method for $A = 20$ and 120 × 20 collocation points for the spectral method. For the onset of stationary convection, the results for Le = 30 and Le = 100 are presented later. For Le = 30 and $\psi = 0.03$, without vibrations ($R_v = 0$), the critical parameters $Ra_c = 12.92$, $k_c = 1.356$ are obtained from the linear stability analysis. For the same values of Le and ψ but with vibrations ($R_v = 10$), we obtain $Ra_c = 13.36$, $k_c = 0$ from the linear stability analysis, so the critical wave number is zero, which means that the flow at the onset of convection is unicellular. To confirm this result, we used the direct numerical simulation to study the case Le = 30 and $\psi = 0.03$ for a value of Ra_c close to the critical value (Ra = 13.5) first without vibration ($R_v = 0$) and then with vibrations ($R_v = 10$). Figure 21.21a shows the streamlines and isoconcentrations for $R_v = 0$. In this case, the flow is multicellular, and we cannot use the horizontal cell to separate the components of a binary mixture. Figure 21.21b shows the streamlines and isoconcentrations for the same values of all parameters but with vibrations. We observed that vibrations modify the structure of the flow from multicellular to unicellular, leading to the stratification of the concentration field and the separation of the binary mixture components.

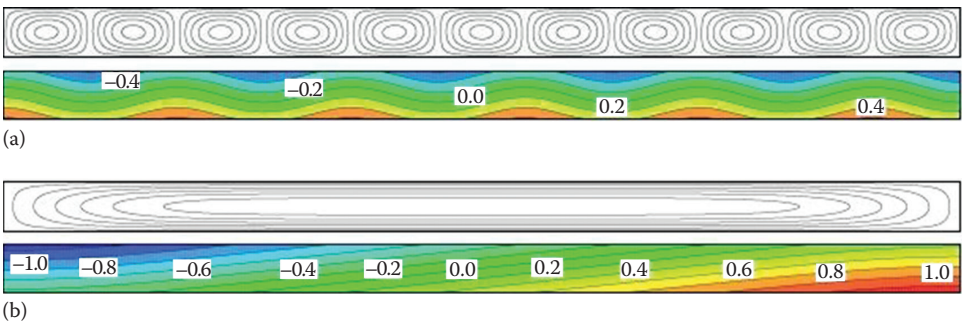

FIGURE 21.21 Streamlines and isoconcentrations for Le = 30, $\psi = 0.03$, Ra = 13.5 (a) $R_v = 0$ (without vibration) (b). $R_v = 10$. A multicellular flow is obtained at the transition from the equilibrium solution for $R_v = 0$, whereas a unicellular flow is obtained for $R_v = 10$.

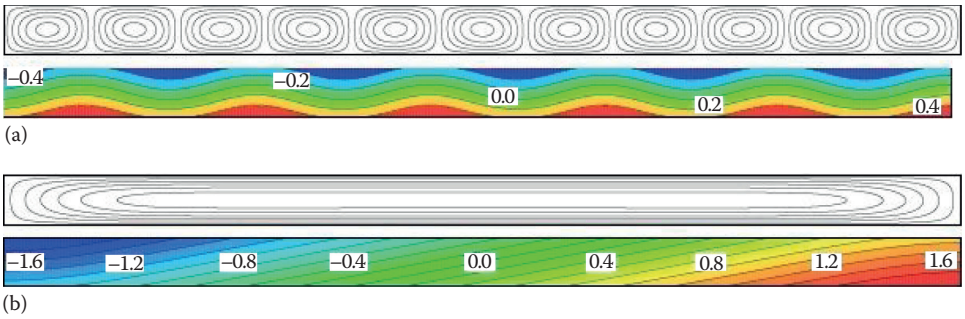

FIGURE 21.22 Streamlines and isoconcentrations for Le = 100, ψ = 0.01, and Ra = 12.5 (a) $R_v = 0$ (without vibration) (b). $R_v = 10$. A multicellular flow is obtained at the transition from the equilibrium solution for $R_v = 0$, whereas a unicellular flow is obtained for $R_v = 10$.

But this separation is not very strong because the value of Ra is close to the stability threshold and is far from $\mathrm{Ra}_{opt} = 24/(\mathrm{Le}\psi)$. Similar results were obtained for Le = 100 and ψ = 0.01 (Figure 21.22).

21.5.2.5.2 Stability of the Unicellular Flow

In the following results presented, the values of B and ε were fixed at $B = 10^{-6}$ and 0.5, respectively. As in the previous part, the results for Le = 30 and 100 are presented.

For Le = 30, we obtain a unicellular flow at the onset of convection for $\psi = \psi_{uni} = 0.044$ if $R_v = 0$ and for $\psi = \psi_{uni} = 0.014$ if $R_v = 50$. We present here some results for a value of ψ higher than these two values; we use $\psi = -0.1$. The stability analysis shows that, without vibrations, the unicellular flow loses its stability, via a Hopf bifurcation, for the critical parameters $\mathrm{Ra}_{c2} = 31.48$ and $\omega_{c2} = 2.84$. For the same mixture ($\psi = -0.1$) under the influence of vibrations characterized by a modified vibrational Rayleigh number $R_v = 50$, the unicellular flow loses its stability for $\mathrm{Ra}_{c2} = 52.08$ and $\omega_{c2} = 2.21$. These results were confirmed by the direct numerical simulations.

Figure 21.23a shows the instantaneous streamlines and isoconcentrations at a given time during the oscillation for Ra = 31.4. This value of Ra corresponds to the transition from unicellular flow to multicellular one without vibrations ($R_v = 0$).

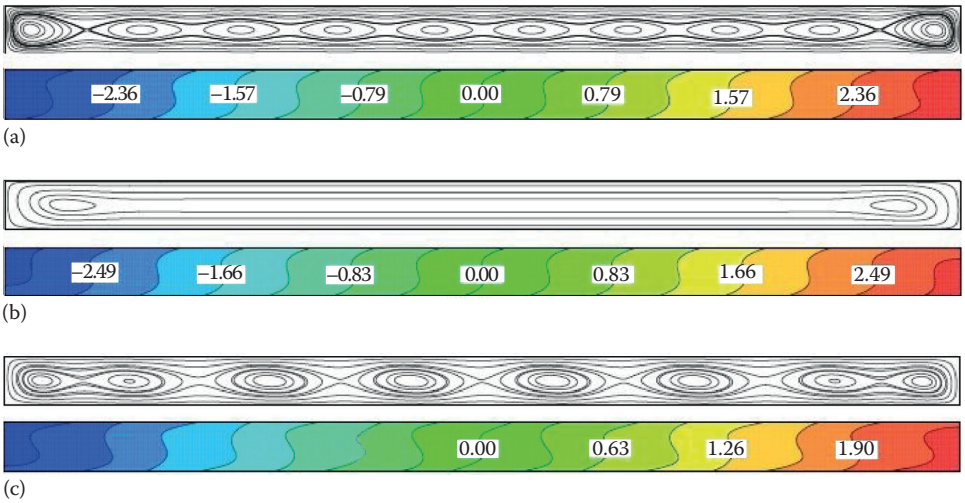

FIGURE 21.23 Le = 30, ψ = 0.1: instantaneous streamline and isoconcentrations at a given time during the oscillation for (a) Ra = 31.4, and $R_v = 0$. (b) Streamline and isoconcentrations for Ra = 31.4, and $R_v = 50$ and (c) Ra = 52.2 and $R_v = 50$. The vibrations maintain the unicellular flow for a higher value of the Rayleigh number (a and b).

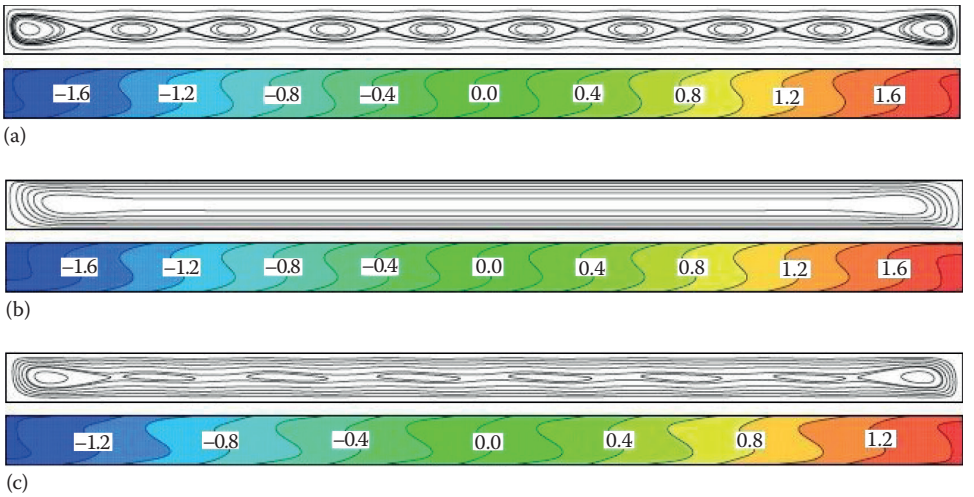

FIGURE 21.24 Le = 100, ψ = 0.1: instantaneous streamline and isoconcentrations at a given time during the oscillation for (a) Ra = 27.3, and R_v = 0. (b) Streamline and isoconcentrations for Ra = 27.3 and R_v = 50 and (c) Ra = 45.3 and R_v = 50.

Figure 21.23b shows the streamlines and the isoconcentrations for the same mixture with the same parameters but with vibrations (R_v = 50). It was noted that, with vibrations, the unicellular flow could be maintained for a higher value of the Rayleigh number leading to the separation of the species between the left and right vertical walls of the horizontal cell. But this separation is not very strong because the value of RaLeψ = 94.2 is far from the optimal value: $(\text{RaLe}\psi)_{opt}$ = 24. This unicellular flow remains stable up to Ra = 52.2. Figure 21.23c shows the instantaneous streamlines and isoconcentrations at a given time during the oscillation at the transition from the unicellular flow to multicellular flow (Ra = 52.2) for R_v = 50. For Le = 100, we observe the same behavior as for the case Le = 30. As shown in Table 21.7, for Le = 100, the following critical parameters are obtained from the linear stability analysis: Ra_{c2} = 27.67 and ω_{c2} = 1.44 for R_v = 0 and Ra_{c2} = 46.88 and ω_{c2} = 1.32 for R_v = 50.

Figure 21.24a shows the instantaneous streamlines and isoconcentrations at a given time during the oscillation for the transition from the unicellular flow to multicellular flow and for R_v = 0. Under certain conditions, the vibrations lead to a change from multicellular to unicellular flow (Figure 21.24b). This unicellular flow remains stable for a Rayleigh number much higher than the one obtained without vibrations. Thus, the vibrations allow separation for high values of the Rayleigh number. When the Rayleigh number is increased slightly, the unicellular flow loses its stability to give a multicellular flow (Figure 21.24c). The numerical results are in good agreement with the analytical results.

The Hopf bifurcation frequency was found numerically for all the cases studied. For example, for Le = 30, ψ = 0.1, Ra = 52.2, and R_v = 50, it was observed that the flow remains oscillatory for all the computing times considered. The value of the critical frequency obtained by the linear stability analysis is ω_{c2} = 2.21. Using the Fourier transform of the horizontal component of the velocity at one point of the domain, we obtained a numerical critical frequency $\omega_{c2\,num}$ = 2.19. For all the studied cases, a good agreement was found between the theoretical and numerical results.

21.6 CONCLUSIONS AND OUTLOOK

Several modern engineering processes can benefit from a better understanding of double-diffusive convection taking into account the Soret effect in saturated porous medium where the flow and mass transport follow complex patterns that depend on the interaction between diffusion coefficients and

buoyancy ratio. The double-diffusive convection phenomena, in the presence of the Soret effect described in this chapter, depend essentially on the gravity field, but they can also be observed in the case of pure weightlessness in a cavity filled with a saturated porous medium subjected to vibrations. Comprehensive predictions are made possible by means of a thermogravitational diffusion model that requires experimental values of the Soret coefficient. For most binary mixtures, and especially ternary mixtures, the Soret coefficient is unknown. To date, quantitative experimental data suitable for model validation are quite scarce, and, thus, coordinated efforts between modeling and experimentation are needed in order to provide an ultimate understanding of double-diffusive convection in porous media**.**

We also studied the influence of vibrations on Soret-driven convection in a large aspect ratio horizontal porous layer, uniformly heated, saturated by a binary fluid. The enclosure is subjected to high-frequency and small-amplitude vibrations, which allows us to use time-averaged formulation. The stability diagrams and different flow structures are presented and discussed. These results may be used to achieve maximum separation.

NOMENCLATURE

Roman letters

A	Aspect ratio of the cell H/L
a	Thermal diffusivity
a^*	Thermal diffusivity of the mixture
C	Mass fraction
C_0	Reference mass fraction = C_0
c	Disturbance concentration
H	Height of the cavity
L	Width of the cavity
Le	Lewis number, Le = a/D
D	Mass diffusivity of the constituent through the fluid mixture
D_T	Thermal diffusion coefficient
g	Intensity of gravity, $\vec{g} = -g\vec{e_y}$
K	Permeability
k	Wavenumber
k_c	Critical wave number
k^*	Effective thermal conductivity of the porous medium
i	$\sqrt{-1}$
N	Order of approximation
Nu	Average Nusselt number
q	Vertical separation
Ra_T	Thermal Rayleigh number based on H, Ra = $[KHg\beta_T\Delta T(\rho c)_f]/(\lambda^* \nu)$
Ra_c	Critical thermal Rayleigh number
S	Separation
S_T	Dimensionless Soret coefficient
Sh	Average Sherwood number
T	Dimensionless temperature
T_r	Reference temperature = T'_0
t	Nondimensional time
u	Dimensionless horizontal component of the velocity
w	Dimensionless vertical component of the velocity

Greek letters

α	The inclination of the cell
α_e	Effective thermal diffusivity of the porous medium
α_f	Thermal diffusivity of the binary fluid
α_s	Thermal diffusivity of the solid porous medium
β_T	Coefficient of volumetric expansion with respect to the temperature
β_c	Coefficient of volumetric expansion with respect to the concentration
ε	Normalized porosity, $\varepsilon = \varepsilon^*(\rho c)_f/(\rho c)^*$
σ	Heat capacity ratio, $\sigma = (\rho c)_f/(\rho c)^*$
ε^*	Porosity of the porous matrix
ν	Kinematic viscosity of fluid
λ	Thermal conductivity
λ^*	Effective thermal conductivity
ρ	Binary fluid density
$(\rho c)_f$	Heat capacity of fluid
$(\rho c)_S$	Heat capacity of solid
$(\rho c)^*$	Heat capacity of saturated porous medium
ρ_0	Reference binary fluid density
θ	Disturbance temperature
Ψ	The separation ration

REFERENCES

Adler, P.M., *Porous Media: Geometry and Transport*, Butterworth-Heinemann, Stoneham, MA, 1992.

Ahadi, A. and Ziad Saghir, M., Experimental study of impacts of forced vibration on thermodiffusion phenomenon in microgravity environment, *App. Thermal Eng*., 60, 348–358, 2013.

Allain, C. and Lallemand, P. Principle of a method to determine thermal-diffusion ratio using forced Rayleigh-scattering, *Comptes rendus Académie des sciences, Série B*, 285(8), 187–190, 1977.

Alonso, A., Batiste, O., Meseguer, A., and Mercader, I., Complex dynamical states in binary mixture convection with weak negative Soret coupling, *Phys. Rev. E*, 75, 026310, 2007.

Bahloul, A., Boutana, N., and Vasseur, P., Double-diffusive and Soret induced convection in a shallow horizontal porous layer, *J. Fluid Mech*., 491, 325–352, 2003.

Batiste, O., Knobloch, E., Alonso, A., and Mercader, I., Spatially localized binary-fluid convection, *J. Fluid. Mech*., 560, 149–158, 2006.

Bear, J., *Dynamics of Fluid in Porous Media*, Elsevier, New York, 1972.

Bennacer, R., Mahidjiba, A., Vasseur, P., Beji, H., and Duval, R., The Soret effect on convection in a horizontal porous domain under cross temperature and concentration gradient, *Int. J. Num. Methods Heat Fluid Flow*, 13(2), 199–215, 2003.

Bennacer, R., Mohamad, A.A., and El Ganaoui, M., Thermodiffusion in porous media: Multi-domain constituent separation, *Int. J. Heat Mass Transfer*, 52, 1725–1733, 2009.

Blanco, P.M., Bou-Ali, M., Platten, J.K., de Mezquia, D.A., Madariaga, J.A., and Santamaría, C., Thermodiffusion coefficients of binary and ternary hydrocarbon mixtures, *J. Chem. Phys*., 132, 114506, 2010.

Bou-Ali, M.M., Ecenarro, O., Madariaga, J.A., Santamaria, C.M., and Valencia, J.J., Thermogravitational measurement of the Soret coefficient of liquid mixtures, *J. Phys.-Conden. Matter*, 10(15), 3321–3331, 1998.

Bourich, M., Hasnaoui, M., Mamou, M., and Amahmid, A., Soret effect inducing subcritical and Hopf bifurcation in shallow enclosure filled with a clear binary fluid or saturated porous medium: A comparative study, *Phys. Fluids*, 16, 551–568, 2004.

Chan, B.K.C., Ivey, C.M., and Arry, J.M., Natural convection in enclosed porous media with rectangular boundaries, *J. Heat Transfer*, 92, 21–27, 1970.

Charrier-Mojtabi, M.C., Elhajjar, B., and Mojtabi, A., Analytical and numerical stability analysis of Soret-driven convection in a horizontal porous layer, *Phys. Fluids*, 19(12), 124104, 1–14, 2007.

Charrier-Mojtabi, M.C., Maliwan, K., Pedramrazi, Y., Bardan, G., and Mojtabi, A., Control of thermoconvective flows by vibration, *Mécanique Ind*., 4, 545–549, 2003.

Cissé, I., Bardan, G., and Mojtabi, A., Rayleigh Bénard convective instability of a fluid under high-frequency vibration, *Int. J. Heat Mass Transfer*, 47, 4101–4112, 2004.

Clusius, K. and Dickel, G., Neues Verfahren zur Gasenmischung und Isotroprennung, *Naturwisse*, 6(1938), 546, 1938.

Cormack, D.E., Leal, V., and Imberger, J., Natural convection in a shallow cavity with differentially heated end walls. Part 1. Asymptotic theory, *J. Fluid Mech. Digital Arch*., 65(02), 209–229, 1974.

Costesèque, P., Sur la migration sélective des isotopes et des éléments par la thermodiffusion dans les solutions. Application de l'effet thermogravitationnel en milieux poreux. Observations Expérimentales et conséquences géochimiques, PhD thesis, Université Paul Sabatier, Toulouse, France, 1982.

Costesèque, P., Mojtabi, A., and Platten, J.K., Thermodiffusion phenomena, *C.R. Mécanique*, 339(2011), 275–279, 2011.

Costesèque, P., Pollak, T., Platten, J.K., and Marcoux, M., Transient-state method for coupled evaluation of Soret and Fick coefficients, and related tortuosity factors, using free and porous packed thermodiffusion cells: Application to CuSO4 aqueous solution (0.25M), *Eur. Phys. J. E Soft Matter*, 15(3), 249–253, 2004.

De Groot, S.R., Théorie phénoménologique du procédé thermogravitationnel de séparation dans un liquide, *Physica*, 9, 801–816, 1942.

De Marsily, G., *Quantitative Hydrogeology, Groundwater Hydrology for Engineers*, Academic Press, Orlando, FL, 1986.

Dutrieux, J.F., Platten, J.K., Chavepeyer, G., and Bou-Ali, M.M., On the measurement of positive soret coefficients, *J. Phys. Chem. B*, 106(23), 6104–6114, 2002.

Elhajjar, B., Charrier-Mojtabi, M.C., and Mojtabi, A., Separation of a binary fluid mixture in a porous horizontal cavity, *Phys. Rev*. *E*, 77(1–6), 026310, 2008.

Elhajjar, B., Mojtabi, A., and Charrier-Mojtabi, M.C., Influence of vertical vibrations on the separation of a binary mixture in a horizontal porous layer heated from below, *Int. J. Heat Mass Transfer*, 52, 165–172, 2009.

Elhajjar, B., Mojtabi, A., Costesèque, P., and Charrier-Mojtabi, M.C., Separation in an inclined porous thermogravitational cell, *Int. J. Heat Mass Transfer*, 53, 4844, 2010.

Elhajjar, B., Mojtabi, A., Marcoux, M., and Charrier-Mojtabi, M.C., Study of thermogravitation in a horizontal fluid layer, *C.R. Mecanique*, 334(10), 621–627, 2006.

Ettefagh, J., Vafai, K., and Kim, S.J., Non-Darcian effects in open-ended cavities filled with a porous medium, *J. Heat Transfer*, 113, 747–756, 1991.

Firoozabadi, A., *Thermodynamics of Hydrocarbon Reservoirs*, Mc Graw Hill, New York, 1999.

Fury, W.H., Jones, R.C., and Onsager, L., On the theory of isotope separation by thermal diffusion, *Phys. Rev*., 55, 1083–1095, 1939.

Gershuni, G.Z., Kolesnikov, A.K., Legros, J.C., and Myznikova, B.I., On the vibrational convective instability of a horizontal binary mixture layer with Soret effect, *J. Fluids Mech*., 330, 251–269, 1997.

Gershuni, G.Z., Kolesnikov, A.K., Legros, J.C., and Myznikova, B.I., On the convective instability of a horizontal binary mixture layer with Soret effect under transversal high frequency vibrations, *Int. J. Heat Mass Transfer*, 42(3), 547–553, 1999.

Ghorayeb, K., Firoozabadi, A., and Anraku, T., Interpretation of the unusual fluid distribution in the Yufutsu gas-condensate field, *SPE J*., 8(2), 114–123, 2003.

Gobbé, C. and Quintard, M., Macroscopic description of unsteady heat transfer in heterogeneous media, *High Temp.-High Pres*., 26, 1–14, 1994.

Gonzalez Bagnoli, M.G., *Modeling the Thermal Diffusion Coefficients*, Technical University of Denmark, Department of Chemical Engineering, Lyngby, Denmark, 2004.

Hsu, C.T. and Cheng, P., The Brinkman model for natural convection about a semi-infinite vertical flat plate in porous medium, *Int. J. Heat Mass Transfer* 28, 683–697, 1985.

Ingham, D.B. and Pop, I., *Transport Phenomena in Porous Media*, Vol. I, Pergamon Press, 2000.

Ingham, D.B. and Pop, I., *Transport Phenomena in Porous Media*, Vol. II, Pergamon Press, Elsevier Science, Oxford, U.K., 2002.

Ingham, D.B. and Pop, I., *Transport Phenomena in Porous Media*, Vol. III, Pergamon Press, Oxford, U.K., 2005.

Jamet, P., Fargue, D., Costesèque, P., de Marsily, G., and Cernes, A., The thermogravitational effect in porous media: A modelling approach, *Transp. Porous Media*, 9, 223–240, 1992.

Kaviany, M., *Principles of Convective Heat Transfer in Porous Media*, 2nd edn., Springer, New York, 1995.

Kempers, L.J.T.M., Thermodynamic theory of the Soret effect in a multicomponent liquid, *J. Chem. Phys*., 90, 6541, 1989.

Kempers, L.J.T.M., A comprehensive thermodynamic theory of the Soret effect in a multi component gas, liquid, or solid, *J. Chem. Phys*., 115, 6330–6341, 2001.

Knobloch, E., Oscillatory convection in binary mixtures, *Phys. Rev. A*, 34, 1538, 1986.

Köhler, W., Thermodiffusion in polymer solutions as observed by forced Rayleigh scattering, *K. Chem. Phys.,* 98, 660, 1993.

Koniger, A., Wunderlich, H., and Köhler, W., Measurement of diffusion and thermal diffusion in ternary fluid mixtures using a two-color optical beam deflection technique, *J. Chem. Phys*., 132, 17, 2010.

Lage, J.L., Effect of the convective inertia term on Bénard convection in a porous medium, *Numer. Heat Transfer, Part A*, 22, 469–485, 1992.

Lage, J.L., The fundamental theory of flow through permeable media from Darcy to turbulence, in: D.B. Ingham and I. Pop (Eds.), *Transport Phenomena in Porous Media*, Pergamon Elsevier Science, Oxford, U.K., 1998, pp. 1–30.

Larre, J.P., Platten, J.K., and Chavepeyer, G., Soret effects in ternary systems heated from below, *Int. J. Heat Mass Transfer*, 40, 545, 1997.

Lorenz, M. and Emery, A.H., The packed thermal diffusion column, *Chem. Eng. Sci*., 11(1), 16–23, 1959.

Ludwig, C., Diffusion zwichen unfleigh erw¨armten orten gleich zusammengesetzlos¨ungen, *Akad. Wiss. Wien, Math Naturwiss*, 20, 539, 1856.

Mialdun, A., Minetti, C., Gaponenko, Y., Shevtsova, V., and Dubois, F., Analysis of the thermal performance of SODI instrument for DCMIX configuration, *Microgravity Sci. Technol*., 25, 83–94, 2013.

Mialdun, A., Yasnou, V., Shevtsova, V., Koeniger, A., Koehler, W., Alonso de Mezquia, D., and Bou-Ali, M.M., A comprehensive study of diffusion, thermodiffusion, and Soret coefficients of water-isopropanol mixtures, *J. Chem. Phys*., 136(24), 244512–244513, 2012.

Mojtabi, A. and Rees, D.A.S., The effect of conducting bounding plates on the onset of Horton-Rogers-Lapwood convection, *Int. J. Heat Mass Transfer*, 54,(1–3, 15), 293–301, 2011.

Nield, D.A. and Bejan, A., *Convection in Porous Medium*, 4th edn., Springer Sciences and Business Media, New York, 2012.

Ouarzazi, M.N. and Bois, P.A., Convection instability of a fluid mixture in a porous medium with time-dependent temperature gradient, *Eur. J. Mech. B Fluid*, 13, 275–278, 1994.

Platten J.K., The Soret effect: A review of recent experimental results, *ASME J. Appl. Mech*. 73, 5–15, 2006.

Platten, J.K., Bou-Ali, M.M., Costeseque, P., Dutrieux, J.F., Kohler, W., Leppla, C., Wiegand, S., and Wittko, G., Benchmark values for the Soret thermal diffusion and diffusion coefficients of three binary organic liquid mixtures, *Phil. Mag*. 83, 1965, 2003a.

Platten, J.K., Bou-Ali, M.M., and Dutrieux, J.F., Enhanced molecular separation in inclined thermogravitational columns, *J. Phys. Chem. B*, 107, 11763–11767, 2003b.

Platten, J.K. and Costeséque, P., The Soret coefficient in porous media, *J. Porous Media*, 7(4), 329–342, 2004.

Platten, J.K. and Legros, J.C., *Convection in Liquids*, Springer, Berlin, Germany, 1984.

Polezhaev, V.I., Convection and heat/mass transfer processes under space flight conditions, *Fluid Dyn*., 41(5), 736–754, 2006.

Quintard, M., Kaviany, M., and Whitaker, S., Two-medium treatment of heat transfer in porous media: Numerical results for effective's properties, *Adv. Water Resour*., 20(2–3), 77–94, 1997.

Quintard, M. and Whitaker S., Transport in chemically and mechanically heterogeneous porous media I: Theoretical development of region averaged equations for slightly compressible single-phase flow, *Adv. Water Resour*., 19, 2779–2796, 1996a.

Quintard, M. and Whitaker, S. Transport in chemically and mechanically heterogeneous porous media II: Theoretical development of region averaged equations for slightly compressible single-phase flow, *Adv. Water Resour*., 19, 49–60, 1996b.

Razi, Y.P., Maliwan, K., Charrier-Mojtabi, M.C., and Mojtabi, A., Importance of direction of vibration on the onset of Soret-driven convection under gravity or weightlessness, *Eur. J. Phys*., E(15), 335–341, 2004.

Razi, Y.P., Maliwan, K., Charrier-Mojtabi, M.C., and Mojtabi, A., Influence of vibrations on the onset of thermo-convection in porous media, in: K. Vafai (Ed.), *Handbook of Porous Media*, 2nd edn., Chapter 8, Marcel Dekker, New York, 2005, pp. 321–370.

Razi, Y.P., Mojtabi, A., and Mojtabi, M.C., A summary of new predictive high frequency thermo-vibrational models in porous media, *Transp. Porous Media*, 77, 207–228, 2009.

Rees, D.A.S. and Mojtabi, A., The effect of conducting boundaries on weakly nonlinear Darcy-Bénard convection, *Transp. Porous Media*, 88, 45–63, 2011.

Riahi, D.N., Nonlinear convection in a porous layer with finite conducting boundaries, *J. Fluid. Mech*., 129, 153–171, 1983.

Ryzhkov, I. and Shevtsova, V., Long-wave instability of a multicomponent fluid layer with the Soret effect, *Phys. Fluids*, 21, 014102, 2009.

Ryzhkov, I. and Shevtsova, V.M., Convective stability of multicomponent fluids in the thermogravitational column, *Phys. Rev. E*, 79, 026308 1–15, 2009.

Shevtsova, V., Sechenyh, V., Nepomnyashchy, A., and Legros, J.C., Feasibility study for application of optical two wavelength techniques to measurement of the Soret coefficients in ternary mixtures, *Philos. Mag*., 91(26), 3498–3518, 2011.

Shevtsova, V.M., Melnikov, D.E., and Legros, J.C., Onset of convection in Soret-driven instability, *Phys. Rev. E*, 73, 047302, 2006.

Simonenko, I.B., A justification of the averaging method for a problem of convection in a field rapidly oscillating forces and other parabolic equations, *Math. Sb*., 2(129), 245–263, 1972.

Soret, C., Influence de la température sur la distribution des sels dans leurs solutions, *Compte-Rendu de l'Académie des Sciences Paris*, 91, 303–384, 1880.

Sovran, O., Charrier-Mojtabi, M.C., and Mojtabi, A., Onset on Soret-driven convection in an infinite porous layer, *C. R. Acad. Sci. Ser. II B Mech*., 329, 287–293, 1996.

Sözen, M. and Vafai, K., Analysis of the non-thermal equilibrium condensing flow of gas through a packed bed, *Int. J. Heat Mass Transfer*, 33, 1247–1261, 1990.

Vafai, K., *Handbook of Porous Media*, 2nd edn., Marcel Dekker, New York, 2005, pp. 269–320.

Vafai, K. and Tien, H.C., Boundary and inertia effects on flow and heat transfer in porous media, *Int. J. Heat Mass Transfer*, 24, 195–1277, 1989.

Wiegand, S., Thermal diffusion in liquid mixtures and polymer solutions, *J. Phys. Condens. Matter*, 16, 357, 2004.

Wiegand, S. and Kohler, W., Measurements of transport coefficients by an optical grating technique, in: W. Kohler, and S. Wiegand (Eds.), *Thermal Nonequilibrium Phenomena in Fluid Mixtures*, vol. LNP 584, Springer Verlag, 2002, pp. 189–210.

Zebib, A., Convective instabilities in thermogravitational columns, *J. Non-Equilibrium Thermodyn*., 32, 211–219, 2007.

Section VI

Geological Applications in Porous Media

22 Digital Petrophysics
Imaging, Modeling, and Experimental Challenges Related to Porous Media in Oil Fields

Peter Tilke

CONTENTS

22.1 Introduction 769
22.2 Porosity and Permeability in the Oil Field 770
22.3 Digital Rocks and Their Interpretation 772
22.3.1 Reconstruction 772
22.3.2 CT Imaging 773
22.3.3 FIB-SEM Imaging 775
22.3.4 Dynamic Imaging 775
22.4 Modeling Digital Rocks 777
22.4.1 Segmenting the Image 777
22.4.2 Building the Model 779
22.4.2.1 Lattice Boltzmann 779
22.4.2.2 Finite Difference 779
22.4.2.3 Finite Element 779
22.4.2.4 Pore Network 780
22.4.2.5 Smooth Particle Hydrodynamics 781
22.4.2.6 Density Functional Hydrodynamics 781
22.5 Structural Analysis 782
22.6 Modeling Transport Properties 782
22.7 Upscaling Digital Rocks 783
22.8 Future Directions 785
Acknowledgments 785
References 785

22.1 INTRODUCTION

The complex interaction of liquids, gases, and solids at the pore scale is of interest in many areas of geoscience including oil and gas production, enhanced oil recovery, hydraulic fracturing, analysis of shale oil and shale gas, and carbon sequestration. This chapter presents the background and an overview of the rapidly evolving field of digital petrophysics: the imaging and modeling of porous media in the oil field along with experimental issues related to their understanding.

Modeling multiphase fluid flow at the pore scale gives us much insight into the physics at nanometer and micrometer scales. However, when interpreting and modeling porous media in the oil

field, one must consider the wide spectrum of scales that must be addressed and the challenges in reconciling the physics and geology at these different scales.

An overview of the digital imaging workflow with an emphasis on x-ray computed tomography (CT) is presented. This is followed by a discussion of the various elements of the digital petrophysics workflow that includes imaging, image processing, and the modeling of transport properties. A review of experimental approaches to imaging dynamic multiphase interactions at the microscopic level during drainage and imbibition follows.

Finally, some of the challenges involved in relating studies conducted at the pore scale to the phenomena observed at the macroscopic reservoir scale are addressed.

22.2 POROSITY AND PERMEABILITY IN THE OIL FIELD

The term oil field can refer to either a geographic area where oil is produced or to the subsurface accumulation of oil trapped in reservoir rock. The latter definition is the one used in this chapter. Oil fields are composed of sedimentary rock composed of mineral grains and interconnected pores. This aspect of porous rock can easily be seen in a geologic precursor such as beach sand; a hole in beach sand rapidly fills with water. When porous sediment such as beach sand is buried and transformed into rock (diagenesis), the connate water in the pores can remain, migrate away, migrate in, or be chemically incorporated into the cement-forming minerals. Many types of sediment contain abundant organic material that, during the diagenetic process caused by increasing temperature and pressure, transform to kerogen and, ultimately, to oil and gas.

The sedimentary rocks in an oil field are generally either clastic or carbonates. Clastic sediments are deposited by wind (e.g., sand dunes), rivers (e.g., point bars and deltas), marine reworking (e.g., beaches), and deep-sea currents (turbidites). The minerals comprising these clastic rocks can represent the weathered remains of ancient mountain ranges and include quartz, feldspar, and clay minerals. Carbonates, on the other hand, are of biological origin and can represent deposition ranging from buildups by living organisms, for example, coral reefs to the gradual accumulation of biogenic calcite. When these sediments are buried and compacted, diagenetic processes cement the grains together forming rock.

During diagenesis, dissolution of original minerals may increase the pore space or precipitation of minerals may decrease the pore space. As a result, the rock is now a complex network of pores connected with pore throats in which the mineral composition of the pores and pore throats can be quite variable.

Whereas porosity represents the capacity of reservoir rocks to store oil, permeability represents the ability of fluids to flow through these rocks. The most direct measurement of permeability is absolute permeability, measured in darcies or millidarcies, which is an intrinsic property of the rock. Relative permeability, on the other hand, results from the complex interaction of multiple immiscible fluid phases in the pore network. It is a dimensionless term that describes the flow of a fluid in the presence of other fluids. Relative permeability is influenced by fluid compositions, relative saturations, wettability, and capillary pressure, which must all be considered when trying to understand the fluid flow in reservoir rocks.

In conventional oil fields, the oil formed in the organic-rich source rock migrates to relatively high-porosity reservoir rock. In the reservoir rock, the oil may be trapped in structural or stratigraphic traps. As oil migrates into the reservoir rock, it displaces some of the original water. Because of the complex wettability and relative permeability relationships, some fraction of the connate water generally remains.

In shale oil fields, the oil is being produced directly from the source rock. In these rocks, the matrix permeability is extremely low, typically in the nanodarcy range. To produce oil from these rocks, fluid must be injected at high pressure from a borehole into the formation to induce fractures or open existing natural fractures. Thus, understanding the interplay of fluid flow between the low-permeability matrix and fracture network is crucial.

The properties of porous rock in the oil field must be considered at scales spanning many orders of magnitude. At the smallest scale, pore throats connecting the pores, which store fluid, will influence the permeability. In shale formations and tight reservoirs, these pore throats can be 10–100 nm in diameter, while in conventional reservoirs, they may be micrometer sized. The interplay of water and oil wettability may be influenced by the mineralogy of rock at the nanometer scale. At the centimeter and meter scales, fine-scale heterogeneities in the rock layering come into play and will affect fluid flow in the vertical direction and are often modeled as a series network. At still larger scales, on the order of tens of meters, lateral heterogeneities are important. A high-porosity river channel deposit may give way laterally to a very low-porosity floodplain deposit. At still larger scales of hundreds of meters to kilometers, heterogeneity due to faults, fracture networks, and folds dictate variation in porous properties. It is clear that all these scales must be considered when an oil field is being developed.

Measuring the static and dynamic properties in situ is the most direct measurement of rock and fluid properties. To do this, a well must be drilled, and logging measurements—measurement of the rock's response to electric, electromagnetic, sonic, and other signals by specialized tools lowered into the hole—are made to infer the mineralogy of the rock, the porosity, and fluid composition. New technologies now allow fluids to be sampled downhole, which gives insight into the current fluid composition. However, to measure the properties under a variety of fluid compositions, a sample of the rock must be obtained, either full-diameter cylinders (cores) of the formation being drilled or as smaller sidewall cores taken from the formation surrounding the borehole and the measurements made in the laboratory. The difficulty with this approach is that while the measurement may be relevant to the sample, the observed heterogeneity in rock properties and fluid composition as already discussed makes it difficult to extrapolate the results to the entire reservoir. For this reason, it is necessary to complement these small-scale measurements with larger-scale and lower-resolution measurements using technologies such as reflection seismology. Seismic data are a measurement of acoustic properties in which the measurement size or *voxel* is at the scale of tens of meters. Modeling of seismic attributes can yield very accurate insights into the rock and fluid properties, albeit at a coarse scale relative to the in situ measurements.

When a core sample is obtained from a well, a standard suite of measurements is generally made in the laboratory. This conventional core analysis includes a description of the lithology and measurements of porosity, grain density, fluid saturations, and absolute permeability parallel to bedding. The lithological description is done on the whole, full-diameter core while the other measurements are done on smaller *plugs* taken from the whole core. The measurements are performed either at standard temperature and pressure (STP), or at reservoir conditions, or both.

Special core analysis (SCAL) is performed when more complex reservoir engineering properties are required. This includes relative permeability, capillary pressure, and wettability under a variety of combinations of two-phase or even three-phase conditions.

Because of the cost, time, and uncertainty in these core analysis measurements, there has recently been great interest in computational approaches. These techniques involve imaging a microscopic sample of the rock using techniques such as confocal microscopy, x-ray CT, scanning electron microscopy (SEM), or focused ion beam (FIB) tomography. These three-dimensional (3D) images are then analyzed to generate models of the mineral, grain, and pore network. Using these geometric models with physical properties, many of the traditional laboratory measurements can now be modeled.

As noted earlier, the microscopic physical properties obtained from the core plug will not necessarily agree with the macroscopic properties and behavior at the reservoir scale. Therefore, it is standard practice to complement core plug measurements with the interpretation of reservoir properties from observed well performance (i.e., its production history). Over the life of a well, the fluid production rate and/or bottom-hole pressure will decline as the reservoir is depleted. These changes in the well performance are interpreted using decline and rate transient analysis techniques to infer the macroscopic reservoir properties.

If many wells have been producing in a reservoir over an extended period, then the model-based interpretation of the well performance is interpreted using a reservoir simulator. This exercise is termed history matching and involves refinement of the reservoir model so that an optimal match is found between the observed historical behavior of the wells and the model of the structure of the reservoir and the distribution of different rock types.

Related to the question of scale and history matching is the reconciliation of the microscopic and macroscopic measurements, physics, and geology. That is, how laboratory measurements made on millimeter-sized core samples relate to the performance over 30 years of hundreds of wells in an oil field. Interpretations and inferences made at one scale must be consistent with the other scale.

22.3 DIGITAL ROCKS AND THEIR INTERPRETATION

Understanding the physics underlying the interaction between fluids, pores, and rock matrix is crucial to explaining the experimental observations and measurements made at the laboratory and field scales. Only by developing good explanations can we make reliable forecasts of the behavior (Deutsch, 2012).

The macroscopic transport properties of porous rocks are the aggregate or emergent properties of phenomena occurring at the pore scale. Therefore, models of the 3D microstructure resulting from the mineral grains and pore network must be constructed to derive the macroscopic properties.

Katz and Thompson (1986) presented an early effort to develop a relationship between pore-network geometry and macroscopic transport properties such as electrical conductivity. Their work suggested a characteristic length for percolation in porous media.

With improving computational tools during the late 1980s, many workers began investigating the idea of generating *digital* or *synthetic* microstructural rock models to better understand the emergent behavior of fine-scale rock–fluid interactions at the larger rock or even reservoir scale.

22.3.1 Reconstruction

In recognition of the need for good microstructural models, there has been much interest in reconstructing 3D microstructural models from lower-dimension (2D) data. Adler et al. (1992) worked with 2D thin section images of Fontainebleau sandstone. The 2D image was binarized and statistically modeled to obtain the porosity and the spatial autocorrelation of the grain and pore space. Assuming spatial isotropy and ergodicity, the sample was then statistically reconstructed in 3D.

Yeong and Torquato (1998) developed a more general approach to reconstructing porous media and also illustrated the procedure with a Fontainebleau sandstone example. They showed that it is necessary to invoke a hybrid model for the morphology, which incorporates the two-point autocorrelation and a lineal path function.

Hazlett (1997), working on Berea sandstone, compared different approaches to reconstruct a 3D model of the pore network. In addition to statistical and visual comparisons of the reconstructions, lattice Boltzmann (Chen and Doolen, 1998) simulations of the permeability performed a further validation. It was found that the purely geometry-based reconstructions were insufficient to model the measured permeability. However, if the image-based reconstructions were supplemented with pore connectivity information obtained from capillary pressure drainage experiments, satisfactory results could be achieved.

This work is further developed by Manwart et al. (2000), who also extend the work of Yeong and Torquato (1998) by considering two-point statistics, lineal path, and pore size distribution. Further refinements to the simulated annealing approach introduced by Yeong and Torquato (1998) are found. In applying this approach to the reconstruction of Berea and Fontainebleau sandstones, it is recognized in agreement with the findings of Hazlett (1997) that the image-derived properties are insufficient to reproduce the transport properties. The authors suggest incorporating local

porosity theory (Hilfer, 1992) to refine the reconstruction by modeling variations in morphological properties such as porosity, specific surface, and connectivity.

Bakke and Øren (1997) developed a process-based reconstruction approach in which sandstone is reconstructed by simulating the processes of deposition, compaction, and diagenesis. Øren and Bakke (2003) further developed this approach by interpreting 2D thin sections of Berea sandstone to identify porosity, grain-size distributions, and mineral phases. The 3D model is then constructed by depositing spherical and ellipsoidal grains honoring the observed grain-size and phase distributions. The rock is then compacted and diagenetically altered. Subsequent modeling of the transport properties using this reconstruction approached yielded results consistent with experiment.

Using multipoint geostatistics, Strebelle and Journel (2001) allow a training image to be defined, which gives a much richer description of the spatial statistics than that can be obtained with two-point and lineal techniques. Okabe and Blunt (2004) applied this approach to reconstruct Berea sandstone and obtained good results when simulating permeability.

22.3.2 CT Imaging

Withjack (1988) introduced CT imaging of porous rock with an emphasis on evaluating potential core damage and characterizing the distribution of fluids during flooding experiments. This early work involved imaging at the millimeter scale. Although there is a trade-off between resolution and sample size, scanner technology has advanced such that, for example, Vega et al. (2013a) report 20 nm resolution images of small 60 μm samples. A typical resolution for conventional porous rock is 3.52 μm voxels with sample dimensions 1024 × 1024 × 1484 (Sheng et al., 2011). Imaging volume has also increased with some vendors reporting 20 μm resolution for a 1.5″ core plug.

Figure 22.1 is an example of the high-quality imagery now available illustrated by a carbonate with image voxel size of 2 μm, while Figure 22.2 is a shale sample imaged at a voxel size of 500 nm.

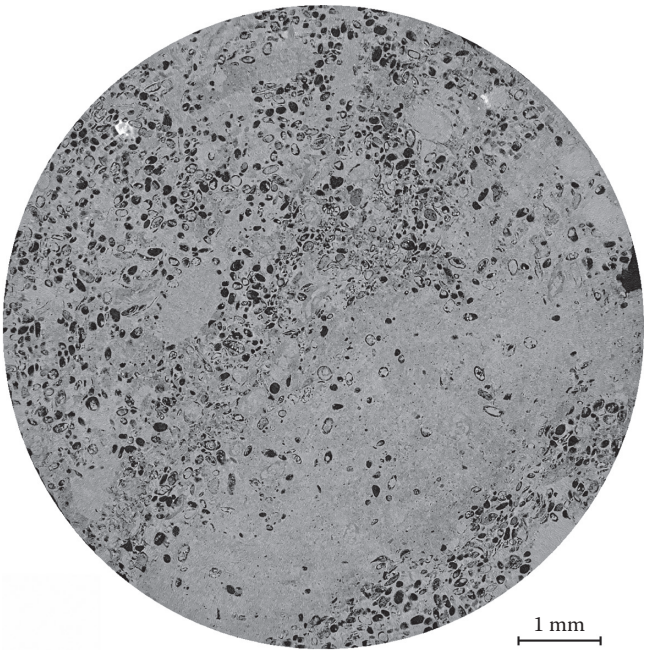

FIGURE 22.1 Grayscale 2D micro-CT cross section of carbonate (voxel size is 2 μm) acquired from 8 mm cylindrical core mini-plug. (Image copyright Schlumberger Technology Corporation, Sugar Land, TX. Used with permission.)

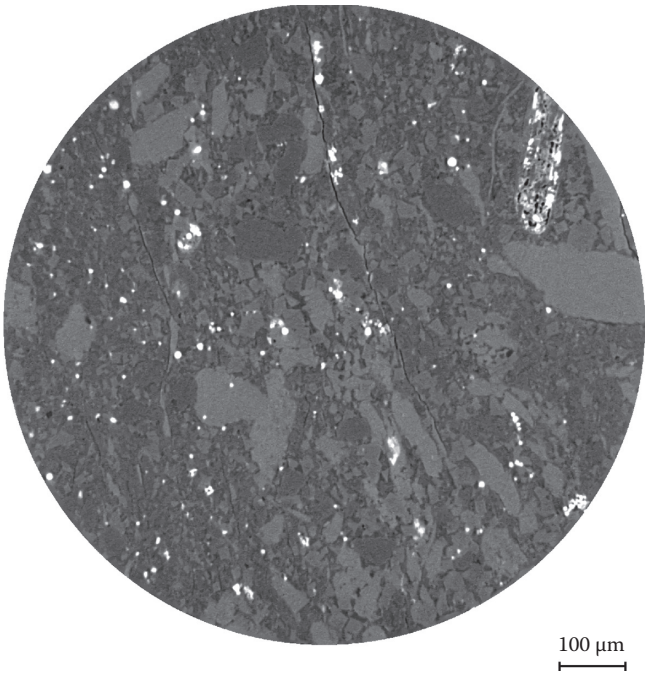

FIGURE 22.2 Grayscale 2D micro-CT cross section of shale (voxel size is 500 nm—resolution) acquired from 8 mm cylindrical core mini-plug. (Image copyright Schlumberger Technology Corporation, Sugar Land, TX. Used with permission.)

CT imaging of the pore structure is possible because the CT number of mineral grains is sufficiently high, where CT number in Hounsfield units (HU) is defined as

$$\mathrm{HU} = \frac{\mu_X - \mu_{water}}{\mu_{water}}$$

μ_X is the average linear attenuation coefficient of the voxel
μ_{water} is the linear attenuation coefficient of water

Akin et al. (2000) list some typical CT numbers.

It is now possible to *zoom in* on a sample so that a high-resolution image can be obtained from a large sample without physically cutting the sample. Figure 22.1 illustrates a 5 μm resolution image of sandstone obtained from a 1.5-in. cylindrical core mini-plug using this capability (Figure 22.3).

Not only has the resolution of CT instruments improved, but the experimental techniques and workflows have advanced so that mineral phases can be distinguished and even fluid types. For example, Zacher et al. (2010) studied numerous limestone samples at 500 nm with impressive resolution of fossiliferous pore structures.

Vega et al. (2013a) studied gas shale samples from the Eagle Ford, Barnett, and Fayetteville fields. Using a relatively low-resolution CT of 200 μm, they were able to study relatively large samples of 2.5 cm diameter. By injecting high-contrast xenon and krypton gas into the sample, the authors imaged the porosity and fracture distributions.

Although CT is proving to be excellent at resolving different mineral phases, it does not provide insight into the chemistry of these phases. Boone et al. (2010) present a workflow for combining CT imagery with x-ray fluorescence elemental maps.

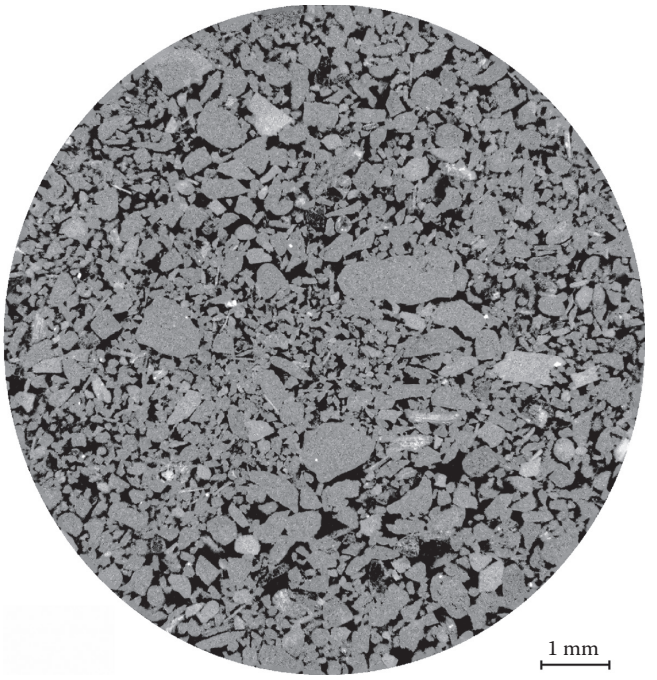

FIGURE 22.3 Grayscale 2D micro-CT cross section of sandstone (voxel size is 5 μm) acquired from 1.5 in. cylindrical core mini-plug using zoom-in option for scanning entire rock volume without physically cutting the sample. (Image copyright Schlumberger Technology Corporation, Sugar Land, TX. Used with permission.)

22.3.3 FIB-SEM Imaging

FIB tomography allows 3D images to be constructed at the resolution of several nm to yield insight into the microporous structures of carbonates and shales. In this approach, the SEM images the sample surface, while an FIB etches away a fresh surface after each scan. Stacking sequential 2D SEM images thus composes the 3D image.

22.3.4 Dynamic Imaging

Many questions in understanding transport properties involve time. Darcy's law for single-phase fluid flow relates fluid flux to absolute permeability:

$$u = -\frac{k}{\mu}\frac{\partial p}{\partial x}$$

where
- u is the velocity of the fluid
- k is the absolute permeability
- μ is the viscosity of the fluid
- $\partial p/\partial x$ is the pressure gradient of the fluid

Multiphase fluid flow involves relative permeability of the interacting phases. Displacement of a non-wetting phase by an immiscible wetting phase is termed imbibition. Complex flow geometry

and wettability cause hysteresis in both capillary pressure and relative permeability. The concept of relative permeability allows Darcy's law to be extended to multiple phases:

$$u_w = -\frac{kk_{rw}}{\mu_w}\frac{\partial p_w}{\partial x}$$

where

u_w is the velocity of the wetting phase
k is the absolute permeability
k_{rw} is the relative permeability of the wetting phase
μ_w is the viscosity of the wetting phase
$\partial p_w/\partial x$ is the pressure gradient of the wetting phase

A variety of laboratory methods exist to measure relative permeability (e.g., Dandekar, 2013) However, novel application of CT imaging has provided a new approach to measuring relative permeability. For example, Akin et al. (2000) and Schembre and Kovscek (2003) present imbibition experiments in which diatomite cores are dried and placed in a water jacket, and a CT image of the dry sample is acquired. Water is then injected from the side of the core sample, and a series of time-lapse CT images is acquired. Water and air have different CT numbers as shown in Akin et al. (2000). Images at different time steps are subtracted from the reference (air only) image. The differences in CT number are transformed to saturation maps using (Akin et al., 2000)

$$S_w = \frac{\mathrm{CT}_{obj} - \mathrm{CT}_{dry}}{\mathrm{CT}_{wet} - \mathrm{CT}_{dry}}$$

where

S_w is the saturation of the wetting phase
CT_{dry} is the CT number of the dry phase
CT_{wet} is the CT number of the wetting phase
CT_{obj} is the CT number of the object

At different time steps during the experiment, saturation profiles are obtained across the core samples (Figure 4 in Schembre and Kovscek, 2003). These experiments were also conducted on oil–water systems in diatomite and Berea sandstone. Schembre and Kovscek (2003) also develop the equations to interpret relative permeability from these experimental observations and obtain consistent results for both the diatomite and Berea sandstone.

Rangel-German and Kovscek (2002) applied a similar time-lapse CT approach to analyzing imbibition when an idealized fracture is present to compare the behavior of different fracture widths. They identified two different flow regimes when comparing flow in the fracture with respect to flow in matrix.

Lee and Karpyn (2010) studied Berea sandstone with a single tensile fracture. They explored different injection rates to understand fracture–matrix transfer mechanisms. This yielded a comprehensive set of data showing fluid recovery and saturation maps (Figures 5 and 6 in Lee and Karpyn, 2010). Alshehri and Kovscek (2012) studied waterflooding of fractured carbonate cores with and without surfactants using this dynamic CT imaging technique. The major flow pathways were successfully imaged in these experiments (Alshehri and Kovscek, 2012, Figure 11).

Dynamic CT imaging has given insight on directly imaging the major fluid flow pathways during imbibition. Pioneering work with dynamic high-resolution confocal microscopy is beginning to yield greater insights into the pore-scale spatial fluctuations of fluid flow through these porous media. Krummel et al. (2013) demonstrate that during imbibition, the wetting phase (water) pinches off threads of the non-wetting phase (oil) in the narrow crevices of the porous medium, forming

disconnected, non-wetting phase ganglia. Some of these ganglia remain trapped within the medium. By fully imaging the fluid distributions in 3D, Krummel et al. (2013) are able to show that the typical ganglion size and the total amount of residual non-wetting (oil) decrease as the capillary number increases. This behavior reflects the competition between the viscous pressure in the wetting phase and the capillary pressure required to force the non-wetting phase through the pore network. Thus, the influence of pore-scale fluid dynamics on multiphase flow at a macroscopic scale is better understood.

22.4 MODELING DIGITAL ROCKS

The advent of imaging techniques such as x-ray CT and confocal microscopy has enabled the routine acquisition of 3D images of porous rock. To apply modeling techniques to these images, they must first be *segmented*. Image segmentation involves classifying the voxels to either grain or void (pore) space. Ideally, the grains may be further classified into their distinct mineral phases.

22.4.1 Segmenting the Image

Image segmentation is widely studied in many fields ranging from character recognition to medical imaging to remote sensing. The challenge in any of the domains is to reduce the misclassification of pixels and voxels that occurs in naive thresholding approaches. Thresholding can often be applied to classify grains and pores when the entire pixel/voxel is occupied by the phase. However, difficulty arises when the pixel/voxel is partially occupied.

Recognizing the unique characteristics of porous rocks, Oh and Lindquist (1999) extended the thresholding technique to incorporate spatial geostatistics. The authors evaluate the spatial covariance in the image and then use indicator kriging to identify grain edges even when pixels/voxels are partially filled.

To efficiently prepare a 3D image for modeling, it is insufficient to simply distinguish grain from pore. Lindquist et al. (2000) and Sok et al. (2002) recognized that other key geometric properties must be extracted from the image, including pore size distribution, throat size distribution, coordination number distribution, and pore channel length. When comparing Fontainebleau sandstone to stochastically generated rocks, Sok et al. (2002) found modeled transport properties to be different from the imaged rocks, even when the noted geometric properties were consistent. They found it necessary to introduce additional properties including pore–pore correlations and local pore–throat correlations.

Thompson et al. (2005) present a grain-based reconstruction algorithm, which, as with the process-based and multipoint geostatistics approaches, extracts a wide range of grain properties from a training image. These properties include grain size, aspect ratios, orientation, and surface area. Each individual grain is labeled (Thompson et al., 2005 Figure 4). The basis of the image is now the set of grains rather than voxels. This allows pores to be identified and their interconnections to be modeled more efficiently (Thompson et al., 2005, Figure 7).

Figure 22.4 is an example illustrating the workflow for CT image processing. Grayscale images from the micro-CT reconstruction pass through the binarization phase of segmentation, followed by rock structure analysis, which identifies individual grains and labels them with colors.

Images acquired with the FIB-SEM approach go through similar processing steps. Figure 22.5 illustrates an example of this workflow applied to shale. Here each phase (pore, organic, minerals with different electron densities) is classified. The result is each pixel in the image being classified to a particular phase.

As tomographic imaging is applied to more complex problems, the segmentation requirements have also increased. Of interest to many workers on porous media in the oil field is the ability to image multiple fluid phases in the pores: water, oil, and gas. Image contrast between these fluid phases is often difficult to resolve, and the signal peaks can have significant overlap. Bhattad et al. (2010) leveraged techniques from medical imaging, such as anisotropic diffusion, to complement the geostatistical indicator kriging approaches discussed earlier.

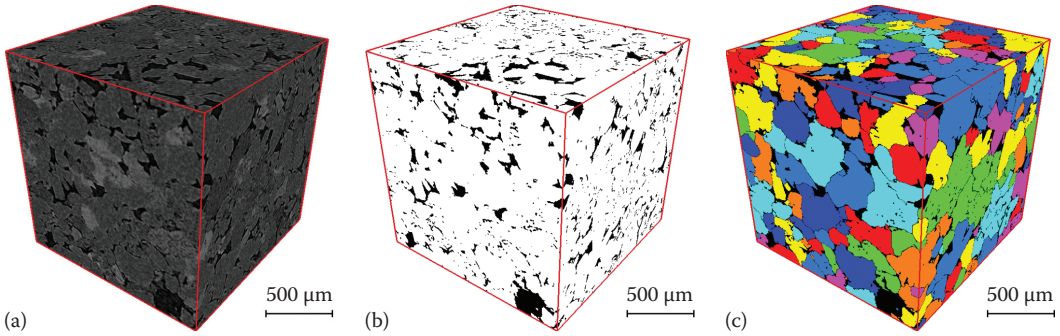

FIGURE 22.4 X-ray micro-CT image processing and analysis workflow. (a) Visualization of 3D cubical stack of grayscale images (cropped from scanned volume, usually cylindrical). (b) Binarized 3D volume created with preserving grain/pore boundaries. (c) Visualization of well-separated grains in sandstone. (Images copyright Schlumberger Technology Corporation, Sugar Land, TX. Used with permission.)

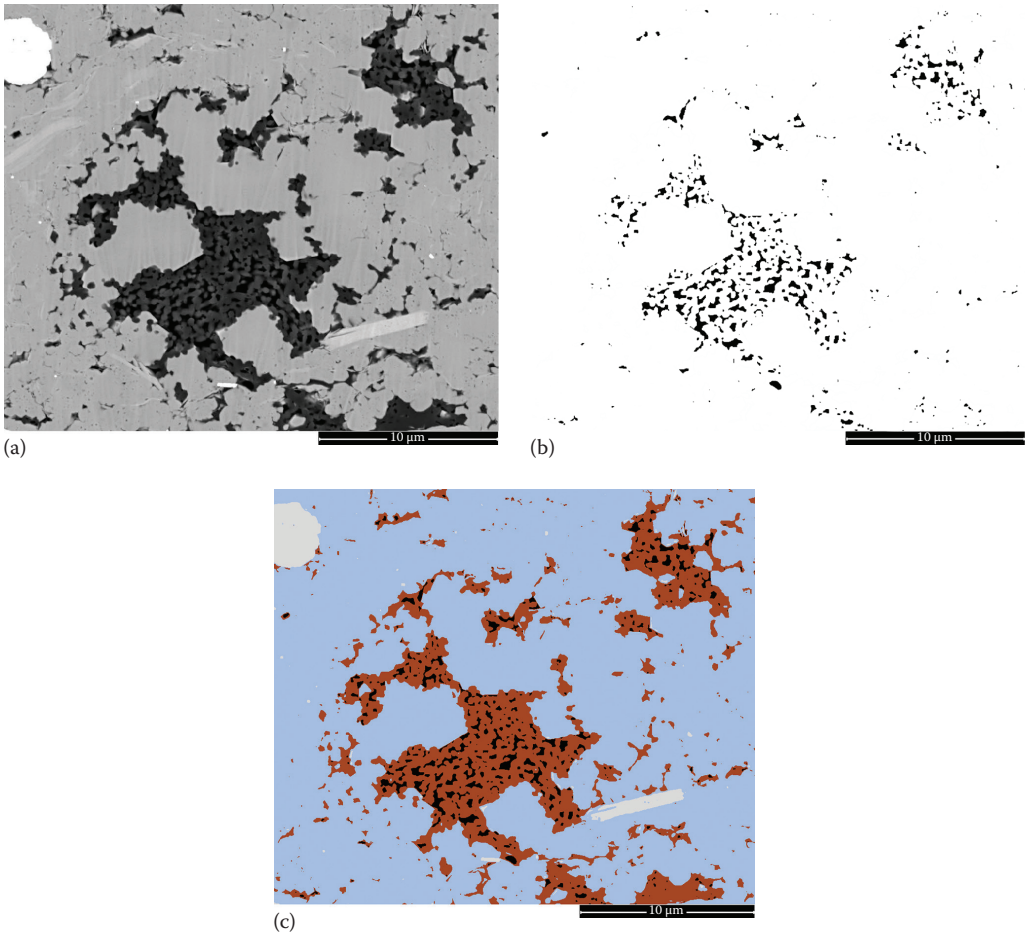

FIGURE 22.5 SEM image processing and analysis workflow. (a) Two-dimensional grayscale image acquired via electron backscattering to achieve high contrast between minerals with different density. (b) Binary images are then generated for each phase of interest. (c) Binary images of each phase are then combined: pores (black), organic (orange), main minerals (blue), and dense minerals (white). (Images copyright Schlumberger Technology Corporation, Sugar Land, TX. Used with permission.)

Software packages now exist (e.g., Cnudde et al., 2010) to routinely segment tomographic images into different phases for the analysis of geometrical and material properties such as porosity, partial porosity, pore size distribution, grain size, grain orientation, and surface determination.

22.4.2 Building the Model

Once the 3D image of the rock has been segmented into different mineral and fluid phases, a decision of how to model the volume for subsequent simulation must be made. The choice of model and simulation tool depends on a number of factors, including the physics being modeled, the scale of the problem, and the computational capabilities. Some of the model classes and simulation approaches are summarized later.

22.4.2.1 Lattice Boltzmann

The lattice Boltzmann simulation method is a simulation technique that solves a discretized Boltzmann equation (Gunstensen et al., 1991; Chen and Doolen, 1998). It can be shown that the macroscopic dynamics of this technique obeys the Navier–Stokes equation. The technique has been successfully applied to a variety of porous media problems (e.g., Ferreol and Rothman, 1995). The fluid is modeled as particles that move on a regular lattice.

Many investigators have found the lattice Boltzmann approach to give satisfactory solutions to the Navier–Stokes equation for transport properties such as absolute permeability (e.g., Manwart et al., 2002; Arns et al., 2004, 2005a, 2008; Okabe and Blunt, 2004; White et al., 2006) The general lattice Boltzmann method has also been extended to support immiscible multiphase fluids (Reis and Phillips, 2007). However, there are still significant limitations in the ability of lattice Boltzmann to model differences in the fluid properties such as viscosity of the different phases.

One major advantage of the lattice Boltzmann method is that a 3D lattice can be simulated directly, rather than implementing a simplified pore-network model. However, the disadvantage is the computationally large model that must be created for lattice Boltzmann. Despite increasing computing capacity, the largest models that can be accommodated with lattice Boltzmann are significantly smaller than what can be modeled with the compressed pore-network models.

22.4.2.2 Finite Difference

The finite difference approach lends itself to simulating many properties of porous rock. Manwart et al. (2002) compared the finite difference and lattice Boltzmann methods to model absolute permeability. Haney et al. (2006) demonstrated finite difference for modeling the acoustic properties of porous media.

A key advantage of finite difference approaches is the wide range of available standard approaches. Another advantage of finite difference is that the voxels of CT images may be used directly as the finite difference cells without the need for the upscaling that must be done for pore-network modeling. On the other hand, the computational resources limit the size of the modeled rock volume.

22.4.2.3 Finite Element

While the finite difference method is suitable for modeling many problems in porous media, it is often necessary and valuable to apply the finite element method to these problems. For example, Könnö (2011) uses the finite element method to model Brinkman flow in porous media, which balances Darcy and Stokes flow in a single model. Another important advantage of finite elements over finite difference is that complex models can be constructed. Figure 22.6 illustrates a finite element mesh model of porous rock at the pore and pore threat scale. Note the wide variation in the size and shape of the individual elements of the model. The fine elements in the pores allow accurate modeling of the multiphase and multicomponent fluids, while the fine elements on either side of the boundary between solid and liquid phases allow surface phenomena to be modeled.

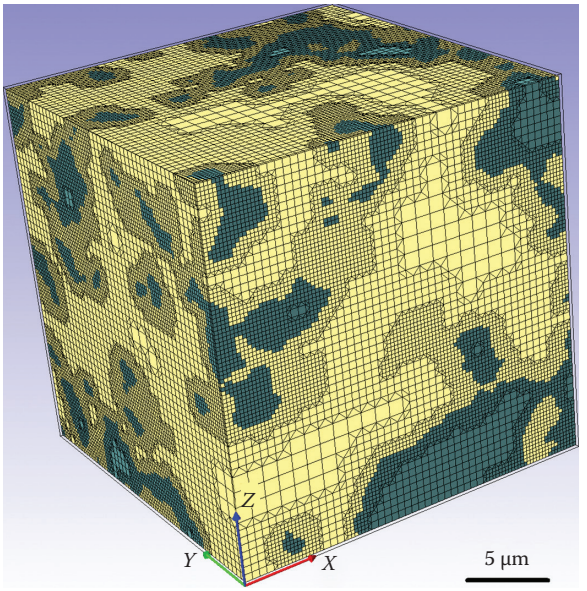

FIGURE 22.6 Visualization of mesh rock model. This type of model can be used by commercial finite element multiphysics simulation software. (Image copyright Schlumberger Technology Corporation, Sugar Land, TX. Used with permission.)

When the porous medium is represented with such a mesh, the physical and chemical properties may be modeled using commercial multiphysics simulation software.

22.4.2.4 Pore Network

Representing the pore space as a graphical network is a powerful model for simulating transport properties. In this pore-network approach, vertices represent pores and the throats connecting pores are represented as edges (Piri and Blunt, 2005, Figure 2). This approach acquired momentum when Blunt (1997b) developed a pore-network model to study the effects of wettability by integrating the pore-level approach introduced by Kovscek et al. (1993).

In this approach, the throats represented by the edges of the graphical network can assume a variety of cross-sectional shapes (Piri and Blunt, 2005, Figure 5). Blunt (1997a) and Blunt (1998) were able to investigate pore-network models with a variety of initial oil saturations and differing contact angles. Modeling of relative permeability and capillary pressure on the model gave insight into the behavior at the pore and throat levels.

Bakke and Øren (1997) and Øren et al. (1998) also demonstrated the value of building large pore-network models to predict a variety of transport properties in good agreement with experimental results on several sandstones. These workers were also able to model multiphase properties such as relative permeability.

Applications of pore-network modeling have become increasingly complex. Hui and Blunt (2000) investigated three-phase flow. An initially water-filled water-wet system is invaded by oil to represent initial oil migration. Water injection followed by gas injection results in many possible different combinations of wettability (Hui and Blunt, 2000, Figure 2). Hughes and Blunt (2000) studied imbibition with varying flow rate and contact angles. Using the pore-network model, they identified five generic types of displacement pattern. Knackstedt et al. (2001) and Arns et al. (2003) demonstrated that pore-network models are consistent with experimental results only if correlated heterogeneity is considered when modeling the pore geometry.

Despite ever-increasing computational power, there continues to be a need to make larger models of the microstructure. Pore-network models are ideally suited for this as they are a highly

compressed representation of the microstructure. The models can now be made large enough to bridge the gap to the larger continuum representations. Sheng and Thompson (2013) take such an approach by embedding large pore networks into grid blocks of a reservoir model. In this approach, the network model can predict transport properties such as relative permeabilities, while the continuum reservoir simulator provides boundary conditions from time step to time step.

An obvious difficulty with the pore-network approach is that the true geometry of individual pores and pore throats is highly simplified. Further, it is difficult to determine a priori what complexities in the pore and throat geometry and properties must be modeled to properly replicate multiphase flow.

22.4.2.5 Smooth Particle Hydrodynamics

Recently, Leonardi et al. (2011) demonstrated a porous media simulator using a 3D smooth particle hydrodynamics approach.

Smooth particle hydrodynamics is a mesh-free Lagrangian particle simulation method first developed for astrophysical problems by Gingold and Monaghan (1977) and Lucy (1977). It is now applied widely to fluid mechanics problems and continuum problems involving large deformation or brittle fracture (e.g., Liu and Liu, 2003; Onate and Owen, 2011) As with other particle methods, a key advantage of particle methods such as smooth particle hydrodynamics is the ability to advect mass with each particle. Thus, phase interfaces do not have to be explicitly tracked during the simulation. There is a computational expense for managing the free particles. However, in many circumstances, the versatility for solving multiphysics problems can be justified.

22.4.2.6 Density Functional Hydrodynamics

Density functional hydrodynamics (DFH) is an application of density functional theory (DFT) in the hydrodynamics of multiphase compositional mixtures (Dinariev, 1995, 1998). DFH is substantiated in both classical and quantum statistical mechanics (Dinariev, 2000). The central idea of DFT is the representation of energy of a heterogeneous system as a functional of densities of chemical components constituting this system. The first consistent results in DFT are related to the Thomas–Fermi model of electron gas developed in 1927. DFT is successfully applied in quantum chemistry, nuclear physics, physics of semiconductors, superconductivity, and diamagnetics. DFH can be considered as a generalization of DFT. Detailed exposition of DFH and its applications is given by Demianov et al. (2011).

DFH is a simulation technique that combines classical thermodynamics and hydrodynamics via constitutive relations. These relations use a particular expression for the density functional that is based on Helmholtz energy or entropy of multiphase multicomponent system. The specific expression for the density functional uses square gradients of molar densities, which enable description of surface tension. The existing realization of the DFH developed by Schlumberger Moscow Research models mass (i.e., chemical components), momentum, and energy balance together with a diffuse interface description. The diffuse interface approach is a consistent and efficient way to model the evolution of the fluid–fluid interfaces in multiphase flow. The thermodynamic state of the mixture is described by means of bulk and surface Helmholtz energies, where the latter enables correct description of liquid–solid interaction, that is, wettability and adsorption.

The method covers various classes of multiphase hydrodynamic problems while taking into account many special phenomena and allowing for complex modeling scenarios including complex compositional fluids with phase transitions: gas–liquid, liquid–liquid, liquid–solid; wettability and adsorption; complex rheologies of phases; presence of surfactants, solvents, and polymers (Figure 22.7). Koroteev et al. (2013a,b) present examples of DFH applications to real problems in the oil and gas industry.

There is a high-performance computing realization of the DFH that allows simulating complex compositional flows using large models consisting of several tens of billions of cells within practical computational times.

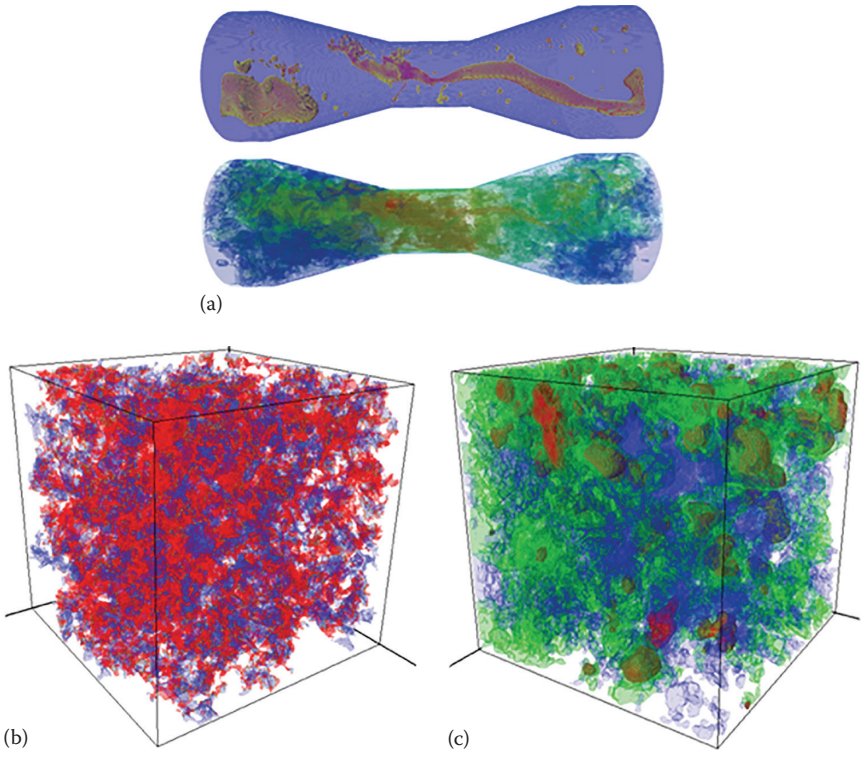

FIGURE 22.7 DFH numerical modeling examples. (a) Two-phase turbulent flow (phases and velocity). (b) Oil primary drainage. (c) Oil recovery by water alternating gas (WAG). (Images copyright Schlumberger Technology Corporation, Sugar Land, TX. Used with permission.)

22.5 STRUCTURAL ANALYSIS

The workflow of segmenting the 3D grayscale image into pore and grain space, identifying individual grains and mineral phases, then building pore-network or finite element meshes gives a very rich representation of the rock. It has been recognized that analyzing these representations alone can yield many insights into the microstructural properties of the rock (e.g., Thompson et al., 2005; Sheppard et al., 2006) This type of analysis yields direct information on grain sizes, aspect ratios, orientations, surface areas, etc.

22.6 MODELING TRANSPORT PROPERTIES

Early efforts to model petrophysical properties such as absolute permeability and electrical conductivity with CT imaging held much promise but generally underestimated predictions with respect to experimental results (e.g., Schwartz et al., 1994; Spanne et al., 1994; Auzerais et al., 1996). Arns et al. (2001) recognized that some of the inaccuracies in simulating transport properties could be minimized by removing three sources of error: finite size effects, discretization errors, and statistical fluctuations. They were able to obtain accurate predictions of electrical conductivity properties on Fontainebleau sandstone.

These studies led to an expansion in the variety of petrophysical and transport properties researchers attempted to simulate from digital imagery of the microstructure. Arns et al. (2004) demonstrated that absolute permeability could be modeled on Fontainebleau sandstone over a wide range of porosities. Fredrich et al. (2006) used lattice Boltzmann simulation to compute absolute permeability on three natural and one synthetic sandstone and again obtained results consistent

with experiment. Note that, at about the same time, Schembre and Kovscek (2003) were using CT dynamic imaging to infer relative permeability.

Recognizing the importance and challenges of carbonate rocks, many workers focused modeling and simulation efforts in this area. By integrating additional data sources such as high-resolution 2D thin sections, Okabe and Blunt (2004) simulated absolute permeability with reasonable results. Recognizing the multiple scales of porosity that characterize carbonates from vuggy macroporosity to intragranular microporosity, several workers (Arns et al., 2005; Lucia, 2007) imaged carbonate samples at multiple resolutions. A variety of pore-scale and petrophysical properties (permeability, drainage capillary pressure, formation factor, and nuclear magnetic resonance (NMR) response) were then computed on the highest resolution samples. Permeability measured on the small subsamples was then upscaled to the larger core sample and was found to be consistent with experimental measurements. Knackstedt et al. (2007b) presented a comprehensive study of six core plugs spanning four different classes of carbonate (oomoldic, vuggy, and bioclastic limestone, and sucrosic dolomite). Comparing modeled transport properties with experiment, they reported good results.

One of the foundational assumptions of NMR imaging of porous rocks is pore connectivity and isolation. Directly imaging the 3D pore network with CT allows this and other assumptions to be tested. Arns et al. (2005b) present an NMR-response simulation tool to model T_1, T_2 relaxation and dephasing based on pore connectivity. They studied 20 sandstone and 2 carbonate samples. Arns and Sheppard (2006), Arns et al. (2006, 2008) further developed the interpretation and modeling of NMR response.

Imaging synthetic rocks of sintered glass beads, Haney et al. (2006) modeled acoustic properties. Using finite difference simulation, they were able to show the rock behaving as an effective medium at low frequencies and strong scattering at higher frequencies.

Archie's equations form the basis of interpreting resistivity logs:

$$F = \frac{R_0}{R_w} = \frac{a}{\Phi^m}$$

and

$$I_R = \frac{R_t}{R_0} = S_w^{-n}$$

where

F is the formation factor, which is the ratio of the brine-saturated rock resistivity R_0 to the resistivity of the brine R_w

The resistivity index I_R is the ratio of the partially brine-saturated rock R_t to R_0

m and n are the cementation and saturation exponents

a is an empirical constant

Variability in m and n as measured in the laboratory is attributed to heterogeneity between the samples. CT imaging affords the opportunity to directly image this heterogeneity and therefore yield insight into the behavior of m and n. Knackstedt et al. (2007a) present a comprehensive study of 12 samples and are able to reconcile Archie's exponents with the observed pore structures.

22.7 UPSCALING DIGITAL ROCKS

Due to the advances in imaging and modeling at the pore scale that we have seen over the past 30 years, our understanding of the phenomena affecting multiphase fluid flow at the pore scale in petroleum reservoirs has increased substantially. However, from a practical standpoint, the

motivation driving this has been to better understand how to optimize production at the scale of the entire petroleum reservoir. Thus, in parallel with advances in our knowledge of pore-scale physics, we have seen advances not only in macroscopic modeling and simulation, but also in efforts to better reconcile the physics modeled at the pore scale with that at the reservoir scale.

It should be emphasized that the range of scales we must consider and reconcile when modeling and interpreting porous media behavior in the oil field rivals that in many other fields of physics. Vega et al. (2013a) report 20 nm (2×10^{-8} m) resolution images of gas shale using transmission electron microscopy; this resolution is routinely obtained to analyze the mineralogical structures within porous rocks. At the other extreme, the Ghawar oil field in Saudi Arabia is 230 km in length. This range in scale represents 13 orders of magnitude.

Given the complexities of porous rock, the concept of effective properties or effective media has gained wide acceptance. The effective property of a rock at a given scale of observation or modeling is that of a simple homogeneous sample at that scale (e.g., Wang and Pan, 2008). However, the mapping of the fine scale to the coarser scale (upscaling) is not unique. This upscaling is highly dependent on the scale in question, the types of rock, the fluid phase composition and distribution, and the physics of interest.

Christie (1996) introduced many in the petroleum engineering world to the needs and challenges of upscaling geological models to reservoir simulation models. At this phase of the modeling workflow, the oil field might be composed of a geological model described by cells 10 m (width) × 10 m (length) × 0.1 m (thickness). An oil reservoir 10 km × 10 km × 100 m would then be built from approximately 10^9 cells. The geological model describes the spatial variation of rock types and properties. The relatively fine vertical scale describes modeled variations in the stratigraphic layering. However, for modeling fluid flow over the life of the field, for example, 30 years, this resolution is too fine from a computational perspective. The number of cells might be reduced by three orders of magnitude for effective simulation (Figure 22.1). Thus, a simulation model represents an effective medium model of the finer-resolution geological model. Christie (1996) outlines some of the approaches for upscaling in this scale range. For contemporary discussions on the issues related to reservoir simulation at this scale, see, for example, Fanchi (2005), Ahmed (2010), or Guo (2011) (Figure 22.8).

As discussed earlier, a typical resolution for CT imaging is 1–5 μm, which still involves upscaling approximately six to seven orders of magnitude. Hurley et al. (2012) present a workflow for upscaling from the CT scale to the reservoir scale (see Hurley et al., 2012, Figure 22.1).

Correctly modeling the rock heterogeneity is key in this upscaling process. Hurley et al. (2012) introduce the concept of representative element volume (REV) as the smallest volume of rock that can represent the rock heterogeneity within specified limits of variance of the underlying property, such as porosity or permeability, at a given scale. Thus, if at a fine scale such as a 1 μm CT image, a variance for the effective medium volume is defined for the upscaled porosity and permeability.

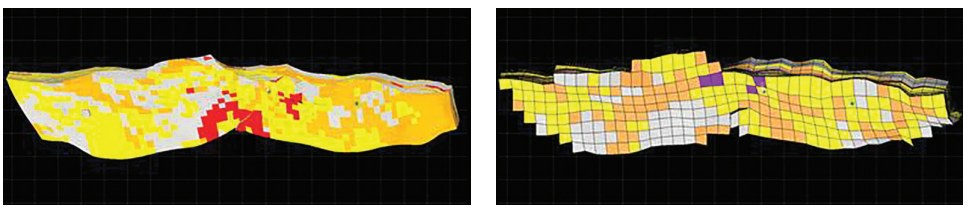

(a) (b)

FIGURE 22.8 Model of the oil reservoir discussed in the text. The colors represent different rock types. (a) The fine-scale geological model and (b) the coarser upscaled simulation model. The differences between the models are partly because visualization is of the top layer and the upscaled model involves averaging over several fine layers.

The determination of REV sizes is practically determined by relating a volume to a subvolume. For example, if a 1 m volume is to be modeled, the REV is the subvolume size that yields the desired variance in a property. Many subvolumes are sampled and their property determined, and the aggregate variance of the subvolume samples computed. Subvolume size is then increased and variance recomputed. The REV is then the largest subvolume size that reflects the desired variance.

Once the REV for a given scale is obtained, it is necessary to upscale from the REV subvolume to the larger volume. This is nontrivial because of spatial autocorrelation and different physics and geological processes operating at different scales (e.g., Hilfer, 2002). A wide range of geostatistical tools and approaches are available for the autocorrelation issues depending on the scale interval of interest. For example, at the reservoir scale, multipoint geostatistics is commonly applied (e.g., Strebelle and Journel 2001). As discussed previously, when upscaling from the CT scale (1–5 μm) to the core plug scale (~10 mm), pore-network models are commonly constructed (Blunt, 1998), although additional measurements must be integrated to reduce nonuniqueness. Ghous et al. (2008) present a workflow for integrating complementary techniques with CT including thin section analysis, mercury injection experiments, and FIB-SEM. White et al. (2006); Balhoff et al. (2007); and Sheng and Thompson (2013) present examples of coupling pore-network models with coarser continuum models.

22.8 FUTURE DIRECTIONS

As CT imaging has become an increasingly common tool in the petroleum industry over the past 20 years, many innovative imaging, interpretation, and modeling techniques have been developed. There is now increasing recognition that robust workflows can and need to be developed that combine CT with other imaging tools (e.g., Kumar et al., 2010; Hurley et al., 2012). Iterative registration of images acquired with these different techniques is desirable so that consistent models at this scale are obtained.

Despite these advances in the digital petrophysics workflow, they cannot and will not replace laboratory core analysis. As such, we can expect to see improved integration of the imaging and modeling techniques described here into the overall core analysis workflow.

ACKNOWLEDGMENTS

I thank Schlumberger for permission to publish this work. I am grateful to Mark Andersen, Austin Boyd, Nikolay Evseev, Denis Klemin, and Alexander Nadeev for helpful discussions, reviewing of the manuscript, and providing imagery from their work.

REFERENCES

Adler, P. M., Jacquin, C. G., and Thovert, J.-F. (1992). The formation factor of reconstructed porous media. *Water Resources Research*, *28*, 1571–1576.

Ahmed, T. (2010). *Reservoir Engineering Handbook*, 4th edn. Burlington, MA: Elsevier.

Akin, S., Schembre, J. M., Bhat, S. K., and Kovscek, A. R. (2000). Spontaneous imbibition characteristics of diatomite. *Journal of Petroleum Science and Engineering*, *25*, 149–165.

Alshehri, A. J. and Kovscek, A. R. (2012). An x-ray CT study of multidimensional imbibition in dual porosity carbonates. Paper presented at the *SPE Annual Technical Conference and Exhibition*, San Antonio, TX.

Arns, C. H., Bauget, F., Limaye, A., Sakellariou, A., Senden, T. J., Sheppard, A. P., Sok, R. M. et al. (2005a). Pore-scale characterization of carbonates using x-ray microtomography. *SPE Journal*, *10*, 475–484.

Arns, C. H., Knackstedt, M. A., and Pinczewski, W. V. (2001). Accurate estimation of transport properties from microtomographic images. *Geophysical Research Letters*, *28*, 3361–3364.

Arns, C. H., Knackstedt, M. A., Pinczewski, W. V., and Martys, N. (2004). Virtual permeametry on microtomographic images. *Petroleum Science and Engineering*, *45*, 41–46.

Arns, C. H., Sheppard, A. P., Saadatfar, M., and Knackstedt, M. A. (2006). Prediction of permeability from NMR response: Surface relaxivity heterogeneity. Paper presented at the *SPWLA 47th Annual Logging Symposium*, Veracruz, Mexico, 498610GG.

Arns, C. H., Sheppard, A. P., and Knackstedt, M. A. (2008). A comparison of pore structure analysis by NMR and Xray-CT techniques. Paper presented at the *SPWLA 49th Annual Logging Symposium*, Edinburgh, Scotland, May 25–28, 2008.

Arns, C. H., Sheppard, A. P., Sok, R. M., and Knackstedt, M. A. (2005b). NMR petrophysical predictions on digitized core images. Paper presented at the *SPWLA 49th Annual Logging Symposium*, New Orleans, LA, May 25–28, 2008.

Arns, C. H., Washburn, K. E., and Callaghan, P. T. (2006). Multidimensional NMR inverse Laplace spectroscopy in petrophysics. Paper presented at the *SPWLA 47th Annual Logging Symposium*, Veracruz, Mexico, June 4–7, 2006.

Arns, J., Arns, C. H., Sheppard, A. P., Sok, R. M., Knackstedt, M. A., and Pinczewski, W. V. (2003). Relative permeability from tomographic images; effect of correlated heterogeneity. *Journal of Petroleum Science and Engineering*, *39*, 247–259.

Auzerais, F. M., Dunsmuir, J., Ferreol, B. B., Martys, N. S., Olson, J., Ramakrishnan, T. S., Rothman, D. H., and Schwartz, L. M. (1996). Transport in sandstone: A study based on three-dimensional microtomography. *Geophysical Research Letters*, *23*, 705–708.

Bakke, S. and Øren, P.-E. (1997). 3-D pore-scale modelling of sandstones and flow simulations in the pore networks. *SPE Journal*, *2*, 136–149.

Balhoff, M. T., Thompson, K. E., and Hjortsø, M. (2007). Coupling pore-scale networks to continuum-scale models of porous media. *Computers and Geosciences*, *33*, 393–410.

Bhattad, P., Willson, C. S., and Thompson, K. E. (2010). Segmentation of low-contrast three-phase x-ray computed tomography images of porous media. In Alshibi, K. A. and Reed, A. H. (Eds.), *Advances in Computed Tomography for Geomaterials* (pp. 254–261). Hoboken, NJ: Wiley.

Blunt, M. J. (1997a). Effects of heterogeneity and wetting on relative permeability using pore level modeling. *SPE Journal*, *2*, 70–87.

Blunt, M. J. (1997b). Pore level modeling of the effects of wettability. *SPE Journal*, *2*, 70–87.

Blunt, M. J. (1998). Physically-based network modeling of multiphase flow in intermediate-wet porous media. *Journal of Petroleum Science and Engineering*, *20*, 117–125.

Boone, M. N., Dewanckele, J., Cnudde, V., Silversmit, G., Van Hoorebeke, L., Vincze, L., and Jacobs, P. (2010). Combination of laboratory micro-CT and micro-XRF on geological objects. In Alshibi, K. A. and Reed, A. H. (Eds.), *Advances in Computed Tomography for Geomaterials* (pp. 205–212). Hoboken, NJ: Wiley.

Chen, S. and Doolen, G. D. (1998). Lattice Boltzmann method for fluid flows. *Annual Reviews in Fluid Mechanics*, *30*, 329–364.

Christie, M. A. (1996). Upscaling for reservoir simulation. *Journal of Petroleum Technology*, *48*, 1004–1007.

Cnudde, V., Vlassenbroeck, J., De Witte, Y., Brabant, L., Boone, M. N., Dewanckele, J., Van Hoorebeke, L., and Jacobs, P. (2010). Latest developments in 3D analysis of geomaterials by Morpho+. In Alshibi, K. A. and Reed, A. H. (Eds.), *Advances in Computed Tomography for Geomaterials* (pp. 84–92). Hoboken, NJ: John Wiley and Sons, Inc.

Dandekar, A. Y. (2013). *Petroleum Reservoir Rock and Fluid Properties*, 2nd edn. Boca Raton, FL: CRC Press.

Demianov, A., Dinariev, O., and Evseev, N. (2011). Density functional modelling in multiphase compositional hydrodynamics. *Canadian Journal of Chemical Engineering*, *89*, 206–226.

Deutsch, D. (2012). *The Beginning of Infinity: Explanations That Transform the World*. New York: Penguin Books.

Dinariev, O. (1995). A hydrodynamic description of a multicomponent multiphase mixture in narrow pores and thin layers. *Journal of Applied Mathematics and Mechanics*, *59*, 745–752.

Dinariev, O. (1998). Thermal effects in the description of a multicomponent mixture using the density functional method. *Journal of Applied Mathematics and Mechanics*, *62*, 397–405.

Dinariev, O. (2000). Substantiation of the method of density functional in classical and quantum statistical mechanics. *Russian Physics Journal*, *43*, 713–717.

Fanchi, J. R. (2005). *Principles of Applied Reservoir Simulation*, 3rd edn. Burlington, MA: Gulf Professional Publishing.

Ferreol, B. B., and Rothman, D. H. (1995). Lattice-Boltzmann simulations of flow through Fontainebleau sandstone. *Transport in Porous Media*, *20*, 3–20.

Fredrich, J. T., Digiovanni, A. A., and Noble, D. R. (2006). Predicting macroscopic transport properties using microscopic image data. *Journal of Geophysical Research*, *111*, 1–14.

Ghous, A., Knackstedt, M. A., Arns, C. H., Sheppard, A. P., Kumar, M., Sok, R. M., and Senden, T. (2008). 3D imaging of reservoir core at multiple scales: Correlations to petrophysical properties and pore scale fluid distributions. Paper presented at the *Proceedings of International Petroleum Technology Conference*, Kuala Lumpur, Malaysia.

Gingold, R. A. and Monaghan, J. J. (1977). Smoothed particle hydrodynamics: Theory and application to non-spherical starts. *Monthly Notices of the Royal Astronomical Society*, *181*, 375–389.

Gunstensen, A. K., Rothman, D. H., Zaleski, S., and Zanetti, G. (1991). Lattice Boltzmann model of immiscible fluids. *Physical Review A*, *43*, 4320–4327.

Guo, B. (2011). *Petroleum Production Engineering, A Computer-Assisted Approach*. Burlington, MA: Gulf Professional Publishing.

Haney, M. M., Fredrich, J. T., Zadler, B. J., Scales, J. A., and Aldridge, D. F. (2006). Numerical simulation of resonances in microtomographic models. Paper presented at the *SEG Technical Program Expanded Abstracts*, New Orleans, LA.

Hazlett, R. D. (1997). Statistical characterization and stochastic modeling of pore networks in relation to fluid flow. *Mathematical Geology*, *29*, 801–822.

Hilfer, R. (1992). Local-porosity theory for flow in porous media. *Physical Review B*, *45*, 7115–7121.

Hilfer, R. (2002). Review on scale dependent characterization of the microstructure of porous media. *Transport in Porous Media*, *46*, 373–390.

Hughes, R. G. and Blunt, M. J. (2000). Pore scale modeling of rate effects in imbibition. *Transport in Porous Media*, *40*, 295–322.

Hui, M.-H. and Blunt, M. J. (2000). Effects of wettability on three-phase flow in porous media. *The Journal of Physical Chemistry B*, *104*, 3833–3845.

Hurley, N. F., Zhao, W., and Zhang, T. (2012). Multiscale workflow for reservoir simulation. Paper presented at the *SPWLA 53rd Annual Logging Symposium*, Cartagena, Colombia, June 16–20, 2012.

Katz, A. J. and Thompson, A. H. (1986). Quantitative prediction of permeability in porous rock. *Physical Review B*, *34*, 8179–8181.

Knackstedt, M. A., Arns, C. H., Sheppard, A. P., Senden, T. J., Sok, R. M., Cinar, Y., Pinczewski, W. V., Ioannidis, M., and Padhy, S. (2007a). Archie's exponents in complex lithologies derived from 3D digital core analysis. Paper presented at the *SPWLA 36th Annual Logging Symposium*, Austin, TX.

Knackstedt, M. A., Arns, C. H., Sok, R. M., and Sheppard, A. P. (2007b). 3D pore scale characterisation of carbonate core: Relating pore types and interconnectivity to petrophysical and multiphase flow properties. Paper presented at the *Proceedings of International Petroleum Technology Conference*, Dubai, United Arab Emirates.

Knackstedt, M. A., Sheppard, A. P., and Sahimi, M. (2001). Pore network modelling of two-phase flow in porous rock: The effect of correlated heterogeneity. *Advances in Water Resources*, *24*, 257–277.

Könnö, J. (2011). *Finite Element Methods for Flow in Porous Media.* Doctoral dissertation, Aalto University, Espoo, Finland.

Koroteev, D., Dinariev, O., Evseev, N., Klemin, D., Nadeev, A., Safonov, S., Gurpinar, O. et al. (2013a). Direct hydrodynamic simulation of multiphase flow in porous rock. Paper presented at the *International Symposium of the Society of Core Analysts*, Napa Valley, CA.

Koroteev, D., Dinariev, O., Evseev, N., Klemin, D., Nadeev, A., Safonov, S., Gurpinar, O. et al. (2013b). Application of digital rock technology for chemical EOR screening. Paper presented at the *SPE Enhanced Oil Recovery Conference*, Kuala Lumpur, Malaysia.

Kovscek, A. R., Wong, H., and Radke, C. J. (1993). A pore-level scenario for the development of mixed wettability in oil reservoirs. *AIChE Journal*, *39*, 1072–1085.

Krummel, A. T., Datta, S. S., and Weitz, D. A. (2013). Visualizing multiphase flow and trapped fluid configurations in a model three-dimensional porous medium. *AIChE Journal*, *59*, 1022–1020.

Kumar, M., Lebedeva, E., Melean, Y., Madadi, M., Sheppard, A. P., Varslot, T. K., Knackstedt, M. A. (2010). Micro-petrophysical experiments via tomography and simulation. In Alshibi, K. A. and Reed, A. H. (Eds.), *Advances in Computed Tomography for Geomaterials* (pp. 238–253). Hoboken, NJ: John Wiley and Sons, Inc.

Lee, C. H. and Karpyn, Z. T. (2010). Experimental investigation of rate effects on two-phase flow through fractured rocks using x-ray computed tomography. In Alshibi, K. A. and Reed, A. H. (Eds.), *Advances in Computed Tomography for Geomaterials* (pp. 230–237). Hoboken, NJ: John Wiley and Sons, Inc.

Leonardi, C. R., Holmes, D. W., Williams, J. R., and Tilke, P. (2011). A multi-core numerical framework for characterizing flow in oil reservoirs. Paper presented at the *SCS Spring Simulation Multi-Conference*, Boston, MA.

Lindquist, W. B., Venkatarangan, A., Dunsmuir, J., and Wong, T.-F. (2000). Pore and throat size distributions measured from synchrotron x-ray tomographic images of Fontainebleau sandstones. *Journal of Geophysical Research*, *105*, 21509–21527.

Liu, G. R. and Liu, M. B. (2003). *Smoothed Particle Hydrodynamics: A Meshfree Particle Method*. London, U.K.: World Scientific Pub Co Inc.

Lucia, F. J. (2007). *Carbonate Reservoir Characterization*, 2nd edn., Springer-Verlag, Berlin, Heidelberg, New York.

Lucy, L. B. (1977). A numerical approach to the testing of the fission hypothesis. *The Astronomical Journal*, *82*, 1013–1024.

Manwart, C., Aaltosalmi, U., Koponen, A., Hilfer, R., and Timonen, J. (2002). Lattice-Boltzmann and finite-difference simulations for the permeability for three-dimensional porous media. *Physical Review E*, *66*, 016702.

Manwart, C., Torquato, S., and Hilfer, R. (2000). Stochastic reconstruction of sandstones. *Physical Review E*, *62*, 893–899.

Oh, W. and Lindquist, W. B. (1999). Image thresholding by indicator kriging. *IEEE Transactions on Pattern Analysis and Machine Intelligence*, *21*, 590–602.

Okabe, H. and Blunt, M. J. (2004). Prediction of permeability for porous media reconstructed using multiple-point statistics. *Physical Review E*, *70*, 1–10.

Onate, E. and Owen, R. (Eds.). (2011). *Particle-Based Methods: Fundamentals and Applications*. Dordrecht, the Netherlands: Springer.

Øren, P.-E. and Bakke, S. (2003). Reconstruction of Berea sandstone and pore-scale modelling of wettability effects. *Journal of Petroleum Science and Engineering*, *39*, 177–199.

Øren, P.-E., Bakke, S., and Arntzen, O. J. (1998). Extending predictive capabilities to network models. *SPE Journal*, *3*, 324–336.

Piri, M. and Blunt, M. J. (2005). Three-dimensional mixed-wet random pore-scale network modeling of two- and three-phase flow in porous media. I. Model description. *Physical Review E*, *71*, 1–30.

Rangel-German, E. R. and Kovscek, A. R. (2002). Experimental and analytical study of multidimensional imbibition in fractured porous media. *Journal of Petroleum Science and Engineering*, *36*, 45–60.

Reis, T. and Phillips, T. N. (2007). Lattice Boltzmann model for simulating immiscible two-phase flows. *Journal of Physics A: Mathematical and Theoretical*, *40*, 4033–4053.

Schembre, J. M. and Kovscek, A. R. (2003). A technique for measuring two-phase relative permeability in porous media via x-ray CT measurements. *Journal of Petroleum Science and Engineering*, *39*, 159–174.

Schwartz, L. M., Auzerais, F., Dunsmuir, J., Martys, N., Bentz, D. P., and Torquato, S. (1994). Transport and diffusion in three-dimensional composite media. *Physica A: Statistical Mechanics and its Applications*, *207*, 28–36.

Sheng, Q. and Thompson, K. E. (2013). Dynamic coupling of pore-scale and reservoir-scale models for multi-phase flow. *Water Resources Research*, *49*, 5973–5988.

Sheng, Q., Thompson, K. E., Fredrich, J. T., and Salino, P. A. (2011). Numerical prediction of relative permeability from MicroCT images: Comparison of steady-state versus displacement methods. Paper presented at the *SPE Annual Technical Conference and Exhibition*, Denver, CO.

Sheppard, A. P., Sok, R. M., Averdunk, H., Robins, V. V., and Ghous, A. (2006). Analysis or rock microstructure using high-resolution x-ray tomography. Paper presented at the *International Symposium of the Society of Core Analysts*, Trondheim, Norway.

Sok, R. M., Knackstedt, M. A., Sheppard, A. P., Pinczewski, W. V., Venkatarangan, A., and Paterson, L. (2002). Direct and stochastic generation of network models from tomographic images; Effect of topology on residual saturations. *Transport in Porous Media*, *46*, 345–372.

Spanne, P., Thovert, J., Jacquin, C., Lindquist, W., Jones, K., and Adler, P. (1994). Synchrotron computed microtomography of porous media: Topology and transports. *Physical Review Letters*, *73*, 2001–2004.

Strebelle, S. and Journel, A. G. (2001). Reservoir modeling using multiple-point statistics. Paper presented at the *SPE Annual Technical Conference and Exhibition*, New Orleans, LA.

Thompson, K. E., Willson, C. S., White, C. D., Nyman, S., Bhattacharyya, J., and Reed, A. H. (2005). Application of a new grain-based reconstruction algorithm to microtomography images for quantitative characterization and flow modeling. Paper presented at the *SPE Annual Technical Conference and Exhibition*, Dallas, TX.

Vega, B., Andrews, J. C., Liu, Y., Gelb, J., and Kovscek, A. R. (2013a). Nanoscale visualization of gas shale pore and textural features. Paper presented at the *Unconventional Resources Technology Conference*, Denver, CO.

Vega, B., Dutta, A., and Kovscek, A. R. (2013b). CT imaging of low-permeability, dual-porosity systems using high x-ray contrast gas. *Transport in Porous Media*, *101*, 81–97.

Wang, M. and Pan, N. (2008). Predictions of effective physical properties of complex multiphase materials. *Materials Science and Engineering: R: Reports*, *63*, 1–30.

White, J. A., Borja, R. I., and Fredrich, J. T. (2006). Calculating the effective permeability of sandstone with multiscale lattice Boltzmann/finite element simulations. *Acta Geotechnica*, *1*, 195–209.

Withjack, E. M. (1988). Computed tomography for rock-property determination and fluid-flow visualization. *SPE Formation Evaluation*, *3*, 696–704.

Yeong, C. and Torquato, S. (1998). Reconstructing random media. *Physical Review E*, *57*, 495–506.

Zacher, G., Santillan, J., Brunke, O., and Mayer, T. (2010). 3D microanalysis of geological samples with high-resolution computed tomography. In Alshibi, K. A. and Reed, A. H. (Eds.), *Advances in Computed Tomography for Geomaterials* (pp. 197–204). Hoboken, NJ: John Wiley and Sons, Inc.

23 Modeling of Subsurface CO_2 Migration at Geological Carbon Sequestration Sites in Deep Saline Aquifers

Sumit Mukhopadhyay

CONTENTS

23.1 Introduction 792
23.2 Physicochemical Processes and CO_2 Trapping Mechanisms 794
23.3 Overview of CO_2 Migration Modeling Approaches 797
23.3.1 Coupled Flow, Geomechanics, and Reactive Transport Models 797
23.3.2 3D Flow-Only Numerical Models 797
23.3.3 Vertical Equilibrium Flow Models 798
23.3.4 Sharp Interface Flow Models 798
23.4 Simulators for CO_2 Migration Modeling 799
23.4.1 Commercial Simulators 799
23.4.2 Research Simulators 799
23.5 Numerical Modeling of CO_2 Migration 800
23.5.1 Governing Equations for Flow and Transport 800
23.5.2 Constitutive Relationships 802
23.5.2.1 Thermophysical Properties of Fluid Phases 803
23.5.2.2 Relative Permeability Measurements 806
23.5.2.3 Capillary Pressure Measurements 806
23.5.2.4 Relative Permeability and Capillary Pressure Relationships 807
23.5.3 Spatial and Temporal Discretization and Numerical Solution 808
23.6 Analytical and Semi-Analytical Solutions 810
23.6.1 CO_2 Plume Extent 810
23.6.1.1 VE with Sharp Interface Solutions 810
23.6.1.2 VE with Capillary Transition Solutions 814
23.6.2 Pressure Buildup 816
23.6.3 Leakage 817
23.6.4 Storage Efficiency 818
23.6.5 Injectivity 819
23.7 Assessment of CO_2 Migration Risk 822
23.7.1 Certification Framework 823
23.7.2 CO_2-Pens 824
23.7.3 Integrated Assessment Models 824
23.8 Model Uncertainties and Model Comparison 825
23.8.1 2004 LBNL Code Comparison Study 826
23.8.2 2009 Stuttgart Benchmark Study 826

23.8.3 2012 Bergen Model Comparison Study 827
23.8.4 2014 Princeton Model Comparison Study with Models of Varying Complexity 828
23.8.5 Sim-SEQ Model Comparison Study 828
23.9 Summary 829
Acknowledgments 829
Nomenclature 830
References 831

23.1 INTRODUCTION

The latest assessment report (Assessment Report 5 or AR5) from Working Group III (WGIII) of the Intergovernmental Panel on Climate Change (IPCC) observes that despite institutional, national, and international policies aimed at mitigating anthropogenic greenhouse gas (GHG) emissions, GHG emissions have actually grown at a rate of 2.2% per year during 2000–2010, which is faster than the rate (1.3% per year) over the entire period 1970–2000 (IPCC, 2014). The WGIII makes the additional observation that GHG emissions, approximately 76% of which are estimated to be carbon dioxide (CO_2), will continue to rise in the coming decades and will have significant impacts on global climate unless effective mitigation strategies are put in place. While no one mitigation strategy on its own is expected to stabilize or reduce GHG levels in the atmosphere, carbon capture and storage (CCS) has been identified as one of the viable technologies for accomplishing this objective (IPCC, 2005).

CCS is a physical process that involves capturing anthropogenic CO_2 from stationary sources (e.g., power plants) and storing it before its release to the atmosphere. An integrated CCS system, as summarized by Folger (2013), would include three main steps (see Figure 23.1): (1) capturing CO_2 and separating it from other gases; (2) purifying, compressing, and transporting the captured CO_2 to the sequestration site; and (3) injecting the CO_2 in subsurface geological formations, where it is expected to remain potentially trapped for hundreds, if not thousands, of years without any negative

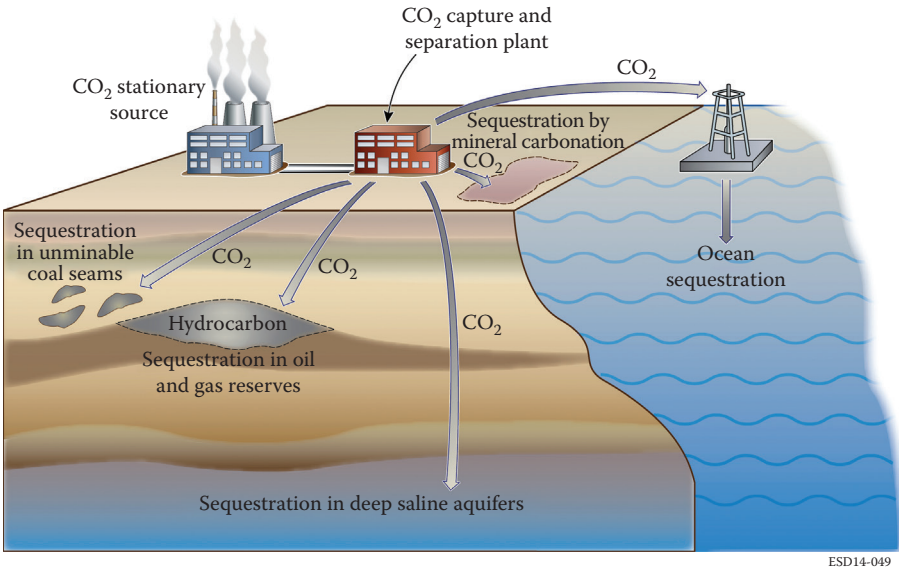

FIGURE 23.1 Schematic drawing illustrating the essential components of an integrated CCS, and available sequestration options, which include sequestration by mineral carbonation, ocean sequestration, and sequestration in unminable coal seams, oil and gas reserves, and DSA. The focus of this chapter is modeling CO_2 migration in DSA.

impact on the terrestrial environment or underground sources of drinking water (USDW). It is this last item that has been commonly termed as "geologic carbon sequestration," or GCS in short (Gale, 2004; Pacala and Socolow, 2004; IPCC, 2005; Bachu, 2008), and is the focus of this chapter.

Before discussing GCS, for the sake of completeness, we mention that, in the context of permanently storing CO_2, mineral carbonation (IPCC, 2005), in which CO_2 is chemically reacted with calcium- and/or magnesium-containing minerals to form stable carbonate materials (see Figure 23.1), has been investigated as a possible option—see Olajire (2013) for a review on mineral carbonation as a sequestration option. Note also that sequestration of CO_2 by directly injecting it into the open ocean, as demonstrated schematically in Figure 23.1, has also been evaluated (Chow, 2014, and references therein); however, environmental concerns have forestalled planned experiments in the open ocean (Folger, 2013). Since these are not the main focus of this chapter, we will not discuss CO_2 storage by mineral carbonation or ocean sequestration any further here.

GCS has been a topic of intense research over the last decade or more, and the literature on GCS has been growing at a rapid pace, such that a comprehensive review is not possible within the scope of this chapter. For an overview of GCS, and also of the broader topic of CCS, we refer the readers to the books by Nordbotten and Celia (2011), Gluyas and Mathias (2013), and Smit et al. (2014). As shown schematically in Figure 23.1, three main geological formations—that is, unminable coal seams, depleted oil and gas reservoirs, and deep saline aquifers (DSAs)—are likely targets for long-term geologic storage of CO_2. Of these three geological formations, unminable coal seams have the smallest potential capacity for storing CO_2 globally compared to the other two target formations (IPCC, 2005). Depleted oil and gas reservoirs have many advantages as potential targets for CO_2 storage (Folger, 2013), including the possibility of enhanced oil recovery (EOR). While it is expected that EOR through stored CO_2 will increase in the future because of economic benefits, the volume of CO_2 that will be needed for such EOR will still be a small fraction of the large volume of CO_2 that will need to be stored, if GCS is to become a viable GHG emission mitigation option.

Given these scenarios, DSAs are probably the best targets for CO_2 storage, not only because they provide the largest potential storage capacity but also because of the larger probability of finding a DSA close to a big stationary CO_2 emission source. Various estimates (e.g., Birkholzer et al., 2009; Dooley, 2011; Szulczewski et al., 2012) are available regarding available storage capacity in DSAs. The latest estimates from the U.S. Department of Energy (USDOE) (National Energy Technology Laboratory, NETL, 2012) show that storage capacity of DSAs in the United States and parts of Canada is anywhere between 1,800 and 20,000 gigatons of CO_2 ($GtCO_2$). The U.S. Geological Survey (USGS), on the other hand, estimates that approximately 3000 $GtCO_2$ can be stored below onshore areas in the United States and underlying state waters (USGS, 2013)—note that the USGS estimate includes not only DSAs but all storage volume available in 36 sedimentary basins across the United States as well. The relatively large range in the estimates of potential storage capacity is an indication of the complexities involved in making a prediction about the fate of CO_2 after it is injected into subsurface geologic formations, or more specifically into DSAs.

As it stands now, understanding and accurately predicting the fate of the injected CO_2, both during injection and many decades after injection ceases, have become one of the key prerequisites of planning and successful implementation of CCS projects (Jiang, 2011). The concerns regarding the fate of the injected CO_2 often center around the questions of how far and how fast a large volume of CO_2 will migrate inside the storage formation (Huppert and Neufeld, 2014), what will be the nature of its interaction with the resident fluid phase (e.g., brine), and whether it will ever be able to escape from its storage location and cause harm (IPCC, 2005). Furthermore, from a GHG emission mitigation perspective, if injected CO_2 does indeed find a leakage pathway back to the surface, it can negate the whole purpose of GCS. While an effective monitoring, verification, and accounting framework (Chadwick et al., 2009; Plasysnski et al., 2011; Monea et al., 2013) may be able to provide answers regarding some of these concerns, reliable and directly observed information about CO_2 migration over extended spatial and temporal scales will continue to remain elusive and expensive. More specifically, such information will simply not be available before designing a GCS

project and, when available, will assist only in validation and iterative improvement of predictive models. Modeling will thus remain an integral and critical component of designing and implementing a GCS project for the foreseeable future.

Consequently, in order to increase stakeholders' confidence in GCS, considerable effort has been and continues to be invested in developing mathematical models and numerical simulators for not only gaining insights into the processes controlling CO_2 migration, but also making reliable and accurate predictions about its fate at GCS sites. While we will discuss the processes controlling CO_2 migration in detail later, it will suffice to state here that these models must account for multiple physicochemical processes involving interactions between the injected CO_2, the formation fluids (either brine or hydrocarbons), and reservoir rocks over multiple spatial and temporal scales (Kang et al., 2010). Depending upon the nature of the fluids already residing in the formation, these processes may include (but are not necessarily limited to) fluid flow under pressure gradients created by the injection process; buoyancy-driven flow caused by density difference between the injected and formation fluids; diffusion, dispersion, and fingering (arising from formation heterogeneities and mobility contrast between the fluids); capillarity (resulting from different wetting characteristics of the fluids concerned); dissolution into the formation fluid, mineralization, and adsorption of CO_2 (IPCC, 2005).

Because of the intense focus on modeling, and also because of the complexities associated with the modeling task, a large number of conceptual models—starting from the simplest analytical solutions to the most complex, fully coupled three-dimensional (3D) numerical simulators—have been developed for understanding and predicting CO_2 migration at GCS sites. Because it is not possible to deal with all the issues involved in modeling CO_2 migration at geologic storage sites within the scope of this chapter, the focus here will be on CO_2 migration modeling in DSAs only. We will also be restricting ourselves to discussing mainly the flow aspects of the modeling challenge, that is, we will not discuss coupled flow, or geomechanical and reactive transport processes, other than making a summary mention in the context of overall process modeling.

We begin by describing, in Section 23.2, the processes controlling the flow of CO_2 after it is injected into a DSA and the mechanisms that are expected to keep it trapped inside the storage formations for a long time. In Section 23.3, an overview of the different modeling approaches associated with CO_2 migration in DSAs is presented. In Section 23.4, some of the leading numerical simulators currently in use for predicting CO_2 flow are discussed. Section 23.5 provides a detailed discussion of the mass and energy conservation equations associated with CO_2 migration, and the constitutive relationships, including thermophysical properties of the fluid phases and rock-fluid characteristic curves, needed to solve the conservation equations, and the numerical solution approach in the context of one selected simulator, namely, TOUGH2. In Section 23.6, we present the analytical and semi-analytical solutions that have been developed over the years for estimating plume migration extent, pressure buildup, leakage, storage efficiency, and injectivity. A number of models have been recently developed for assessing risks associated with GCS in DSAs, a review of which is provided in Section 23.7. Section 23.8 contains a discussion of benchmarking and model comparison studies that have been undertaken to understand and quantify uncertainties associated with CO_2 migration modeling in DSAs. We conclude the chapter by providing a summary in Section 23.9.

23.2 PHYSICOCHEMICAL PROCESSES AND CO_2 TRAPPING MECHANISMS

For long-term storage of CO_2 in DSAs, the target formations must have the requisite pore space to allow storage of a large volume of CO_2; they should have sufficient injectivity to prevent excessive pressure buildup and damage to the formation, and they must possess an effective sealing caprock, such that the injected CO_2 is not able to escape (Bachu, 2000, 2008; IPCC, 2005). To minimize pore space requirements for storage, it is further expected that the storage formations be situated at depths of 800 m or more, so that CO_2 can migrate as a supercritical fluid with a liquid-like density (IPCC, 2005). When supercritical CO_2 ($scCO_2$) is injected into such a DSA, a number of physical

and chemical processes control its migration through the formation and work toward keeping it trapped. In the following, we briefly discuss these physicochemical processes and trapping mechanisms, because they will help us better understand the mathematical formulations presented later in this chapter.

When $scCO_2$ is injected into a DSA, its flow (and also that of the ambient brine) depends on the relative densities and viscosities of the two fluid phases, both of which depend on the temperature and pressure (and hence depth) of the aquifer. According to Nordbotten et al. (2005a), under typical storage conditions, the density ratios of $scCO_2$ and brine are likely to be in the range 0.22–0.75 ($scCO_2$ is the lighter fluid phase, and hence the density ratio is less than 1); however, the viscosity ratios of these two fluid phases are expected to be in the range 0.026–0.22. These differences in density and viscosity have important consequences for the fate of the injected CO_2. For example, the comparatively large density difference between CO_2 and formation brine creates strong buoyancy forces that drive CO_2 upward. However, the rise of the buoyant plume is nonuniform and is controlled by formation heterogeneity, such that sub-horizontal low-permeability layers within the formation retard the upward motion of the buoyant plume and force it to move laterally. This is particularly true once the plume reaches a sealing caprock at the top of the storage formation, after which it cannot rise any further, and continues to spread laterally along this sealing boundary, as is shown in Figure 23.2. Additionally, the large contrast in mobility between the injected $scCO_2$ and the resident brine, resulting from the significantly smaller viscosity of the former, causes it to move ahead of the brine phase, bypassing most of the pore space in its flow path, the degree of which depends on the heterogeneity and anisotropy in formation permeability.

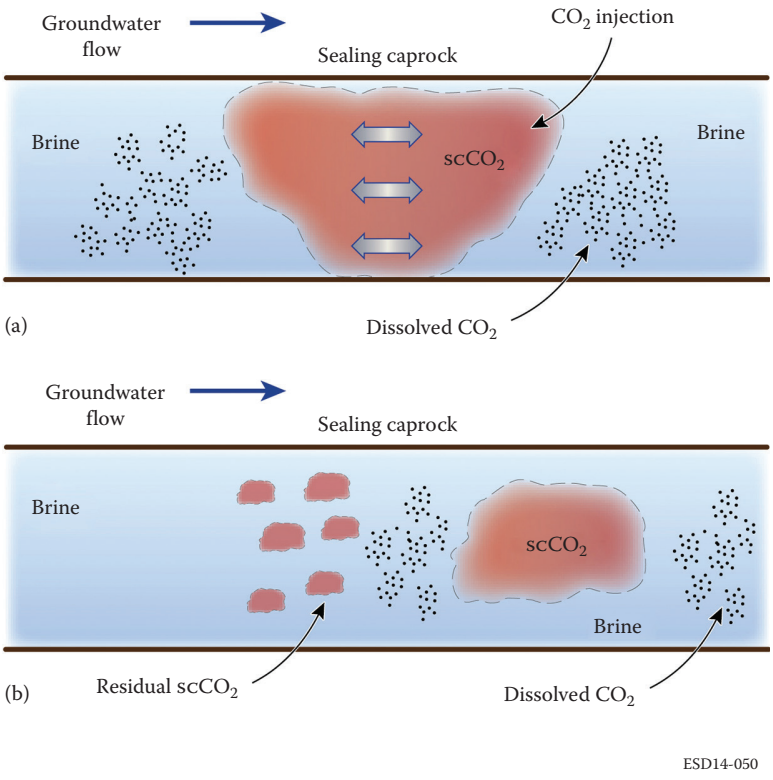

FIGURE 23.2 Schematic representation of physical processes controlling the migration of CO_2 after it is injected into the brine of a deep saline aquifer. (a) CO_2 migration during active injection, and (b) CO_2 migration after injection ceases. Note that geomechanical and geochemical changes arising from CO_2 injection in DSA are not shown in this figure.

As CO_2 migrates through the storage formation, some of it dissolves into the formation brine (see Figure 23.2a), after which the dissolved CO_2 migrates along with regional groundwater flow. DSAs are often characterized by low permeability and high salinity, and have extremely low groundwater flow velocities. As a result, migration rates of dissolved CO_2 are substantially lower than that of gas-phase (or supercritical-phase) CO_2. Furthermore, as CO_2 migrates through the DSA, some of it is retained in the pore space by capillary force, with the potential to immobilize significant amounts of CO_2 (see Figure 23.2b). Over time, much of the CO_2 retained by capillary forces dissolves in the formation water and ceases to exist as a separate gas phase.

Injection of large volumes of CO_2 is also likely to bring about substantial geomechanical changes in the storage formation. In fact, the area over which geomechanical changes may occur is likely to extend far beyond the area of actual pressure changes, which in turn extends far beyond the CO_2 plume (Rutqvist, 2012). Even a small pressure change and straining of the rock (resulting from injection and associated thermal effects) might result in small microseismic events because of rock heterogeneities, including fractures and local stress concentrations that could be released locally. If reservoir pressure becomes sufficiently high, more substantial, irreversible mechanical changes could occur, for example, creating new fractures, straining the well assembly, or reactivating larger faults within the reservoir, in the caprock or overburden. This could possibly open new flow paths through otherwise low-permeability capping formations and thereby enable enhanced, buoyancy-driven, upward migration of the injected CO_2 (Teatini et al., 2011, 2014; Rutqvist, 2012). Moreover, reactivation of a fault could potentially result in a notable seismic event that, if felt, may raise concern in local communities. Readers interested in knowing more about these geomechanical changes associated with GCS and the progress made in modeling these changes are referred to Rutqvist (2012).

In addition to geomechanical processes, geochemical processes (such as salt precipitation resulting from evaporation of water near the injection well) also can lead to significant formation overpressuring, reduction in permeability, and loss of injectivity during CO_2 injection in DSA. During the injection phase, large temperature gradients also exist between the injection well and the storage formation, because the injected CO_2 is considerably cooler than the original formation temperature. This results in significant water–rock interactions involving carbonate minerals, as well as sulfate and evaporate minerals, because their reaction kinetics are fast, and equilibrium is reached almost instantaneously (Gaus, 2010). Over longer terms, dissolved CO_2 in brine and acidification of the brine will generate chemical interactions with the minerals of the reservoir rock. Understanding these longer-term water–rock interactions is important in predicting the capacity of the reservoir to permanently trap CO_2 in a mineral, which is termed mineral trapping. Water–rock interactions can also alter the properties of the sealing caprocks, opening up the possibility of enhanced leakage and contamination of available USDW. Injection of large volumes of CO_2 in DSA also causes large-scale migration of brine, which may contaminate aquifers. An excellent review of the water–rock interactions during CO_2 injection and afterward can be found in Gaus (2010).

Summarizing, it can be stated that the spread of CO_2 in storage formations is restrained by two dominant trapping processes, namely, physical and chemical trapping (IPCC, 2005; Bachu, 2008). Physical trapping includes structural and stratigraphic trapping, wherein the injected $scCO_2$ is stored in closed, physically bound traps or structures, often under low-permeability caprocks. Physical trapping also refers to residual trapping, wherein the DSA may not have a closed trap, but the injected CO_2 is retained by capillary forces. In chemical trapping, CO_2 is trapped through dissolution into brine (i.e., solubility trapping), adsorption onto the rock matrix (i.e., adsorption trapping), and/or reaction with minerals in the rock matrix.

The trapping mechanisms mentioned earlier occur over distinctly different timescales. Initially, injected CO_2 migrates away from the point of injection under the influence of either the applied pressure gradient or the forces of buoyancy. During this time period, when active injection happens, which generally lasts a few decades, the spread of CO_2 is mainly diminished by structural and stratigraphic trapping. This is followed by residual and solubility trapping in the intermediate time

scales spanning from 100 to 1000 years (IPCC, 2005; Zhang and Song, 2014). Mineral trapping, on the other hand, is a much slower process and continues to occur long after injection ceases, often extending into hundreds of thousands of years. Because of these differences in timescales, storage by stratigraphic and structural trapping has been often termed as primary trapping, whereas that by solubility and mineral trapping is called secondary trapping. While secondary trapping does not necessarily increase the storage capacity, it is important for increasing the security of storage.

From the foregoing discussion, it is clear that GCS is an extremely complex process involving multiphase flow and transport in porous media, along with slow chemical reactions. Modeling of long-term geological storage of CO_2 needs to address all the relevant physical and chemical processes that may take place. In addition, CO_2 properties, as well as the properties of the geological media (including their spatial variability), need to be taken into account in the model being developed. Since carbon storage takes place within an extraordinary long timescale, as well as in a large spatial scale involving a variety of mechanisms, it poses a significant challenge to theoretical modeling and numerical simulation (Jiang, 2011).

23.3 OVERVIEW OF CO_2 MIGRATION MODELING APPROACHES

In general, while modeling subsurface fluid migration processes, modelers can follow two end-member modeling philosophies (Celia and Nordbotten, 2011). The first modeling philosophy builds on the idea that "as many processes as possible should be represented, in as much detail as possible." The second modeling philosophy relies on making the predictive models as simple as possible, often making extremely restrictive assumptions. Within these two extreme philosophies, the models for CO_2 migration can be classified in four broad groups (Celia and Nordbotten, 2011). From the most complex to the simplest, these models are (1) full 3D multiphase, multicomponent nonisothermal models with full geomechanical and geochemical coupling, (2) simplified 3D flow-only models, (3) vertically integrated, mostly 2D models, and (4) sharp interface models.

23.3.1 Coupled Flow, Geomechanics, and Reactive Transport Models

The first group of models is clearly the most comprehensive and includes all processes that could possibly be important, including multiphase flow, multicomponent transport with complex phase partitioning, coupled geomechanical and geochemical reactions, energy transport with nonisothermal effects, and coupling among all of the processes and parameters. While these models provide a fairly accurate description for the system, they are fraught with complications, including parameter identification and associated heterogeneities, model couplings, possibly extreme nonlinearities, and severe computational limitations. Readers interested in learning more about these models are referred to Rutqvist (2012) for a review of coupled flow and geomechanical processes. Similarly, the physical and chemical consequences of CO_2 geologic storage, the insights that can be obtained from coupled flow and reactive transport processes, and constraints on such models can be found in Johnson et al. (2004), Gaus et al. (2008), and Xu et al. (2011). Full coupling between thermal, hydrological, mechanical, and chemical processes in the context CO_2 storage has also been investigated, and progress has been made in developing a numerical simulator including these couplings (see, e.g., Zhang, 2013, and references therein).

23.3.2 3D Flow-Only Numerical Models

Given the complexities, uncertainties (arising from lack of scale-specific geological and hydrological data), and computational cost associated with implementing the first group of models, models belonging to the second group have been developed by decoupling the processes. This can be realized, for example, by decoupling the flow equations from the equations of geomechanics based on the assumption that deformations do not alter flow properties significantly. Coupling between flow

and geochemical processes can similarly be ignored, based on the observation that chemical processes occur over timescales that are substantially longer than the timescales associated with flow modeling. The governing mass and energy balance equations can then be simplified and solved using reasonable computational resources, even when the model geometries are complicated and/or the properties are spatially distributed.

23.3.3 Vertical Equilibrium Flow Models

Further simplifications of the flow equations are possible when it is noted that the height of the migrating plume (say, H) from a reference surface (e.g., either the top or bottom of the storage formation) is often considerably smaller than its length (say, L measured from the point of injection), that is, $H/L = 1$. In such circumstances, the fluid velocities in the direction perpendicular to flow (i.e., in the vertical direction) are small compared to those in the horizontal direction (more precisely, along the principal direction of flow), and the pressure within each phase is nearly hydrostatic. These can be expressed mathematically as

$$\frac{\partial p_w}{\partial z} = \rho_w g \tag{23.1}$$

$$\frac{\partial p_{nw}}{\partial z} = \rho_{nw} g \tag{23.2}$$

where

p, ρ, g, and z are pressure, density, acceleration due to gravity, and distance along the vertical direction, respectively

the subscripts "w" and "nw" refer to the wetting (i.e., water or brine) and nonwetting (e.g., $scCO_2$) phases, respectively

Because the capillary pressure between the wetting and nonwetting phases $P_c = P_{nw} - P_w$, Equation 23.1 can be subtracted from Equation 23.2 to yield

$$\frac{\partial P_c}{\partial z} = -(\rho_w - \rho_{nw})g = -\Delta\rho g \tag{23.3}$$

In other words, when $H/L \ll 1$, the forces of gravity approximately balance out the capillary forces. This concept of vertical gravity–capillarity equilibrium, or simply vertical equilibrium (VE), has often been invoked in the study of two-phase flows (e.g., Yortsos, 1995; Lake, 1996; Golding et al., 2011; Wang et al., 2014) and allows the governing 3D flow equations to be integrated in the z-direction, essentially reducing the system to a 2D flow problem. While the VE models have been widely used (see Wang et al., 2014, and references therein) to obtain estimates of plume migration and its shape, it has been demonstrated that their applicability to CO_2 sequestration depends on the timescale of vertical brine drainage within the plume, relative to the timescale of simulation (Court et al., 2012).

23.3.4 Sharp Interface Flow Models

It is possible to further simplify the flow models if, in addition to assuming VE, it is also assumed that the thickness of the capillary transition zone (CTZ) is small or zero. The resultant models have been variably called the sharp interface (e.g., Huppert and Woods, 1995; Nordbotten and

Celia, 2006; Hesse et al., 2007; Celia and Nordbotten, 2009; Juanes et al., 2010) or abrupt interface models (e.g., Dentz and Tartavosky, 2009a). Though some concerns exist about the applicability of sharp or abrupt interface models (Lu et al., 2009), and also about the more general VE models, in predicting the shape of the migrating CO_2 plume, Court et al. (2012) concluded that the validity of the sharp interface assumption depended on the spatial scale of the capillary forces, which controlled the thickness of the CTZ. Court et al. (2012) also found that a finite-CTZ VE numerical model with saturation reconstruction (see Court et al., 2012 for definition) closely matched results from full 3D numerical flow simulations, including capillary pressure, as long as the segregation timescales (i.e., the time needed for complete density-driven segregation of the two fluid phases) were respected. We will discuss these issues in further detail in Section 23.6.

23.4 SIMULATORS FOR CO_2 MIGRATION MODELING

To simulate the migration of CO_2 in storage formations, and more specifically in DSA, a large number of multiphase nonisothermal flow and transport simulators have been developed. Jiang (2011) and Bacon (2013) have compiled an extensive list of contemporary simulators for CO_2 migration modeling. Jiang (2011) and Bacon (2013) discuss the special features of these simulators and provide information regarding their developers (i.e., institutes/commercial entities and persons who have developed these simulators). To avoid repetition, the full list is not presented here. However, for the sake of completeness, the capabilities of a few selected simulators are briefly discussed in the following.

23.4.1 Commercial Simulators

One of the commercial simulators widely used for CO_2 migration modeling is Generalized Equation-of-State Model (GEM), a compositional simulator developed by CMG (Computer Modeling Group), Canada (http://www.cmgl.ca/software/soft-gem). GEM uses an integral finite difference (IFD) scheme and an adaptive implicit scheme for spatial and temporal discretization, respectively. Another commercial simulator, developed by Schlumberger Corporation, is ECLIPSE (http://www.software.slb.com/products/foundation/Pages/eclipse.aspx), which has both black oil and compositional simulator versions. The black oil simulator in ECLIPSE is a general-purpose 3D, three-phase, fully implicit simulator, and the compositional simulator, while retaining those core features, also implements a cubic equation of state.

23.4.2 Research Simulators

Many research simulators are also available. Notable among them are (1) FEHM—a fully coupled heat, mass, and stress balance simulator for 3D, nonisothermal, multiphase fluid flow in porous media from Los Alamos National Laboratory (Zyvoloski et al., 2012); (2) DuMu^x, from the University of Stuttgart, Germany, a free and open-source simulator for flow and transport processes in porous media using continuum mechanical approaches and based on a distributed and unified numerics environment or DUNE (Flemisch et al., 2011); (3) OpenGeoSys, also from the University of Stuttgart, which provides a flexible numerical framework, using primarily the finite element method, for solving multifield problems in porous and fractured media (Kolditz et al., 2012); (4) NUFT, from Lawrence Livermore National Laboratory, which provides a flexible framework for modeling multiphase, multicomponent heat and mass flow in saturated and unsaturated porous media (Hao et al., 2012); (5) STOMP-CO2e from Pacific Northwest National Laboratory (White et al., 2012), which has been developed specifically for simulating the nonisothermal migration of CO_2 in saline reservoirs within the framework of the generalized multiphase flow and transport simulator STOMP; and (6) TOUGH2 (Pruess et al., 2012), developed by Lawrence Berkeley National Laboratory, which simulates the coupled transport of water, vapor, noncondensible gas,

and heat in porous and fractured media. TOUGH2 provides two different modules for simulating CO_2 migration in DSA, which are EOS7C and ECO2N. EOS7C (Oldenburg et al., 2004) is a fluid property module for the TOUGH2 simulator that has been developed for applications involving geologic storage of CO_2 in formations containing water and methane (but cannot accommodate salt). On the other hand, ECO2N (Spycher and Pruess, 2005; Pruess and Spycher, 2007) is designed for modeling CO_2 injection and storage in saline aquifers (but no methane). A newer ECO2M module is also available (Pruess, 2013), which can model scenarios of CO_2 storage and leakage all the way to the land surface, including transitions between super- and subcritical conditions, and phase change between liquid and gaseous CO_2.

Most of these numerical simulators have specialized modules for modeling additional processes coupled with flow, such as reactive geochemical transport or geomechanical impacts of CO_2 storage. For example, to model reactive geochemical transport, extensions such as STOMP-ECKEChem (White and Fang, 2012), NUFT-TRANS (Hao et al., 2012), and TOUGHREACT (Xu et al., 2012) of their original codes STOMP, NUFT, and TOUGH2, respectively, have been developed. Note that other reactive transport simulators such as PFLOTRAN (Hammond et al., 2012) have also been developed for this purpose. For coupled flow and geomechanics simulations, in addition to FEHM, DuMu^x, and OpenGeoSys, all of which incorporate mechanical computations within their general framework, simulators such as CODE-BRIGHT (Olivella et al., 1996) and TOUGH-FLAC (Rutqvist, 2011) have also been developed and used for modeling rock deformations associated with injection of $scCO_2$.

23.5 NUMERICAL MODELING OF CO_2 MIGRATION

23.5.1 Governing Equations for Flow and Transport

While the numerical simulators mentioned in Section 23.4 all have the same objective of accurately modeling CO_2 migration inside storage formations, they differ from one another in terms of how spatial and temporal discretization is implemented, and how the resulting nonlinear algebraic equations are solved. They also differ in terms of how the properties of different fluid phases and the porous media are computed and implemented in the simulators. Having said that, it is, however, also true that all of them share some common features. For example, all of them begin with developing differential conservation equations for component masses (which could include water, CO_2, salt, methane, and/or inert gases) and energy, and writing suitable equations for the fluxes of each of these components in different phases (e.g., liquid, supercritical gas, and salt). To solve the differential conservation equations, they are first converted into nonlinear algebraic equations using a selected discretization option over a specified computational grid and then are closed by using suitable constitutive relationships (e.g., capillary pressure and relative permeability functions, fluid properties as functions of pressure and temperature). Finally, the nonlinear algebraic equations are solved by an efficient iterative solution scheme. In the following, we describe how these steps are implemented in one particular simulator, namely, TOUGH2 (Pruess et al., 2012).

TOUGH2 is a numerical code (Pruess et al., 2012) for simulating coupled flow and transport of water, water vapor, air, and heat in heterogeneous porous and fractured media. TOUGH2 accounts for the movement of gaseous and liquid phases (under pressure, viscous, and gravity forces according to Darcy's law, with interference between the phases represented by relative permeability functions); transport of latent and sensible heat; and phase transition between liquid and vapor, wherever applicable. Mass and energy balance equations are written in integral form for an irregular flow domain in one, two, or three dimensions. Fluid flow is described with a multiphase extension of Darcy's law. Heat occurs by conduction and convection. The description of thermodynamic conditions is based on a local equilibrium model of the three phases (liquid, gas, and solid rock matrix). Note that, even though CO_2 is referred to here as gas, it is actually a supercritical fluid.

The basic mass and energy balance equations solved by TOUGH2 (Pruess et al., 2012) can be written in the general form

$$\frac{d}{dt}\int_{V_n} M^\kappa dV_n = \int_{\Gamma_n} \mathbf{F}^\kappa \cdot \mathbf{n} d\Gamma_n + \int_{V_n} q^\kappa dV_n \tag{23.4}$$

The integration is over an arbitrary subdomain V_n of the flow and transport domain under study, which is bounded by the closed surface Γ_n. The quantity M appearing in the accumulation term of Equation 23.4 represents mass or energy per volume, with $\kappa = 1$, 2, and 3 labeling the mass components water, salt (i.e., NaCl), and carbon dioxide, respectively, and $\kappa = 4$ (the *heat component*). F denotes mass or heat flux (see later), q denotes sinks and sources, and n is a normal vector on surface element $d\Gamma_n$, pointing inward into V_n.

The general form of the mass accumulation term is

$$M^\kappa = \phi \sum_\beta S_\beta \rho_\beta X_\beta^\kappa \tag{23.5}$$

The total mass of component κ is obtained by summing over the phases β (= liquid, gas, or solid salt), with ϕ the porosity, S_β the saturation of phase β (i.e., the fraction of pore volume occupied by phase β), ρ_β the density of phase β, and X_β^κ the mass fraction of component κ in phase β.

Similarly, the heat accumulation term in a multiphase system is

$$M^4 = (1-\phi)\rho_R C_R T + \phi \sum_\beta S_\beta \rho_\beta u_\beta \tag{23.6}$$

where

ρ_R and C_R are, respectively, rock-grain density and specific heat capacity of the rock
T is the temperature
u_β is the specific internal energy in phase β

Advective mass flux is a sum over phases

$$\mathbf{F}^\kappa\Big|_{adv} = \sum_\beta X_\beta^\kappa F_\beta, \tag{23.7}$$

and individual phase fluxes are given by a multiphase version of Darcy's law (continuum representation)

$$\mathbf{F}_\beta = \rho_\beta \mathbf{v}_\beta = -\underline{\mathbf{k}} \frac{k_{rel,\beta}\rho_\beta}{\mu_\beta}(\nabla P_\beta - \rho_\beta \mathbf{g}) \tag{23.8}$$

where

$\mathbf{v}_\beta$ is the Darcy velocity in phase β
$\underline{\mathbf{k}}$ is the permeability tensor
$k_{rel,\beta}$ is the relative permeability of phase β
μ_β is viscosity

$$P_\beta = P + P_{C\beta} \tag{23.9}$$

is the fluid pressure in phase β, which is the sum of the pressure P of a reference phase (gas pressure) and the capillary pressure $P_{C\beta}$ (≤ 0); $\boldsymbol{g}$ is the vector of gravitational acceleration.

Heat flux includes conductive and convective components

$$\mathbf{F}^4 = -\sigma\nabla T + \sum_\beta h_\beta \mathbf{F}_\beta \tag{23.10}$$

where

σ is the thermal conductivity of the rock–fluid mixture
h_β is the specific enthalpy in phase β

Finally, in addition to advective mass fluxes, mass transport can also occur by diffusion and hydrodynamic dispersion, as follows (de Marsily, 1986):

$$\mathbf{F}^\kappa\big|_{dis} = -\sum_\beta \rho_\beta \overline{\mathbf{D}}_\beta^\kappa \nabla X_\beta^\kappa \tag{23.11}$$

The hydrodynamic dispersion tensor ($\overline{\mathbf{D}}_\beta^\kappa$) can be expressed as

$$\overline{\mathbf{D}}_\beta^\kappa = D_{\beta,T}^\kappa \bar{\mathbf{I}} + \frac{\left(D_{\beta,L}^\kappa - D_{\beta,T}^k\right)}{v_\beta^2}\mathbf{v}_\beta\mathbf{v}_\beta \tag{23.12}$$

where

$$D_{\beta,L}^\kappa = \phi\tau_0\tau_\beta d_\beta^\kappa + \alpha_{\beta,L} v_\beta \tag{23.13}$$

$$D_{\beta,T}^\kappa = \phi\tau_0\tau_\beta d_\beta^\kappa + \alpha_{\beta,T} v_\beta \tag{23.14}$$

are longitudinal and transverse dispersion coefficients, respectively. d_β^κ is the molecular diffusion coefficient for component κ in phase β, $\tau_0\tau_\beta$ is the tortuosity that includes a porous medium dependent factor τ_0 and a coefficient that depends on phase saturation, that is, $\tau_\beta = \tau_\beta(S_\beta)$, and α_L, α_T are longitudinal and transverse dispersivities. In Equation 23.12, $\bar{\mathbf{I}}$ is the identity tensor. If hydrodynamic tensor is ignored, when $\alpha_{\beta,L} = \alpha_{\beta,T} = 0$, diffusive flux of component κ in phase β is simply given by

$$\mathbf{f}_\beta^\kappa = -\phi\tau_0\tau_\beta\rho_\beta d_\beta^\kappa \nabla X_\beta^\kappa \tag{23.15}$$

Note that the total mass flux for component κ is the sum of the advective and dispersive fluxes, that is,

$$\mathbf{F}^\kappa = \mathbf{F}^k\big|_{adv} + \mathbf{F}^\kappa\big|_{dis} \tag{23.16}$$

23.5.2 Constitutive Relationships

For predicting CO_2 flow and transport behavior in storage reservoirs, the governing equations in Section 23.5.1 need to be closed with constitutive relationships, which basically involve providing mathematical expressions or tabular data about the thermophysical properties of the fluid phases as functions of pressure and temperature (i.e., the primary system variables), and characteristic rock

properties as functions of phase saturations, which are also primary system variables. In this section, we therefore discuss these constitutive relationships for the CO_2–brine system. We first discuss the phase behavior of CO_2 and the thermophysical properties of CO_2 and brine. We next discuss the current status of measured relative permeability and capillary pressure data, and the mathematical expressions used to represent them in numerical simulators.

23.5.2.1 Thermophysical Properties of Fluid Phases

We first discuss the phase behavior of CO_2, and the thermophysical properties of CO_2 and brine, after which the properties of fluid mixtures are discussed. The discussion also makes specific mention of how the fluid properties (as functions of pressure, temperature, and phase condition) have been incorporated in TOUGH2.

23.5.2.1.1 Phase Behavior and Thermophysical Properties of Pure CO_2

At subsurface depths where CO_2 can be stored permanently, formation temperature and formation pressure are expected to exceed the critical temperature (T_c = 304.1282 K) and critical pressure (P_c = 7.3773 MPa) of CO_2. As a result, under typical storage conditions, CO_2 behaves like a supercritical fluid, where it has a liquid-like density and gas-like viscosity. The critical point of CO_2 is shown in the pressure–temperature (P–T) diagram (Figure 23.3) of CO_2, which also shows the saturation line, the melting line, and the sublimation line of CO_2. The triple point in Figure 23.3 is defined as the pressure (= 0.51795 MPa) and temperature (= 216.592 K) at which all three phases (solid, liquid, and gas) coexist. Note that Figure 23.3 was generated using the correlations given in Span and Wagner (1996).

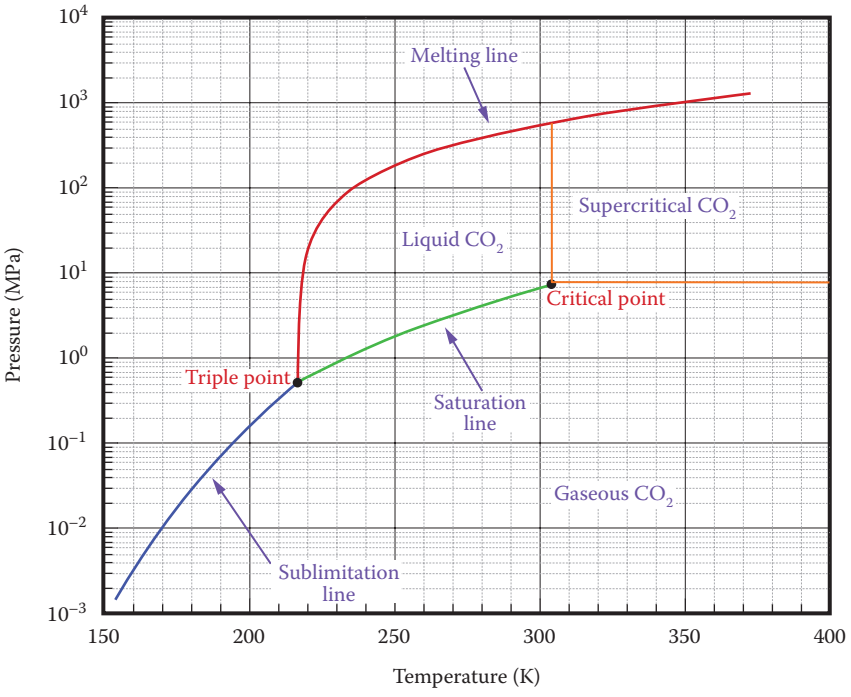

FIGURE 23.3 Phase diagram of CO_2 showing the sublimation, saturation, and melting lines. The phase diagram also shows the triple and critical points of CO_2. It also shows the pressure and temperature conditions at which CO_2 is expected to remain in supercritical phase. The phase diagram was generated using the Span and Wagner (1996) correlations, as available in the *NIST Chemistry Webbook* (Lemmon et al., 2005).

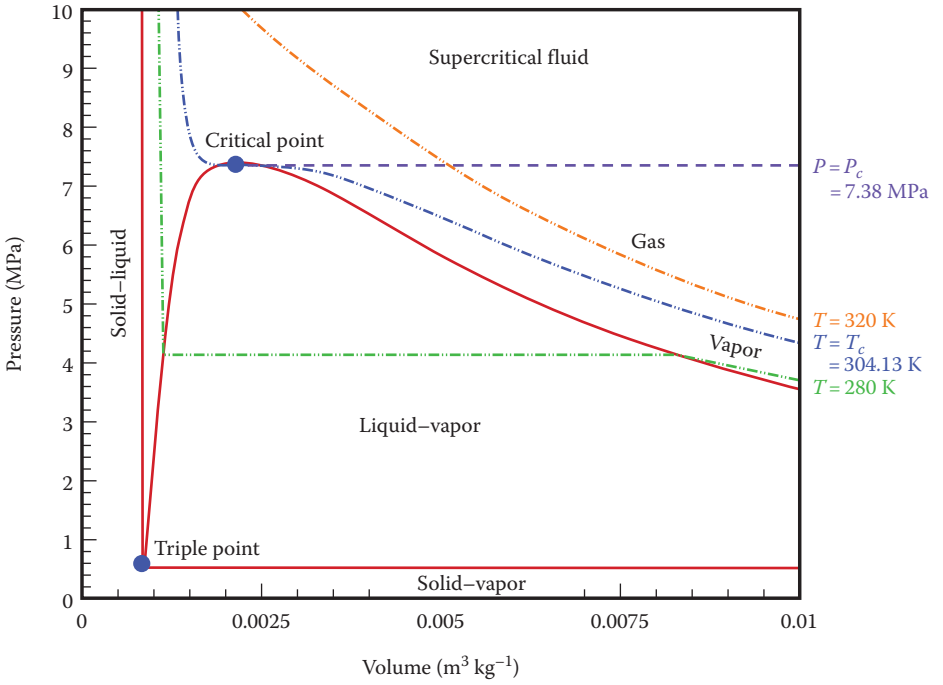

FIGURE 23.4 Pressure–volume diagram for CO_2 at different temperatures. The pressure–volume data were obtained from the *NIST Chemistry Webbook* (Lemmon et al., 2005), which is based on the Span and Wagner (1996) correlations.

Figure 23.4 shows the different phase regions on a pressure versus volume diagram for carbon dioxide, with three isotherms superimposed. Lines for subcritical temperatures (e.g., T_1 = 280 K in Figure 23.4) consist of three segments. The horizontal segment represents all the possible mixtures of liquid and vapor equilibrium. The two end points indicate pure liquid (at the left) and pure vapor (at the right). The locus of these end points defines a bell-shape curve under which the liquid–vapor region lies (e.g., Garcia, 2003). Subcooled liquid and superheated vapor lie to the left and right, respectively. One can generate similar curves at different temperatures to obtain the volume (which is the inverse of density) of CO_2 at any specified pressure and temperature. Note that the pressure–volume curves in Figure 23.4 were plotted based on the thermophysical data of 74 pure fluids (including CO_2) compiled by Lemmon et al. (2005) and as available on the NIST (National Institute of Standards and Technology) Chemistry WebBook (http://webbook.nist.gov). The other thermophysical properties of CO_2 needed for modeling CO_2 geologic storage—including viscosity, specific enthalpy, specific internal energy, entropy, Joule–Thomson coefficients, thermal conductivities, and specific heat capacities—can be similarly obtained using the correlations of Span and Wagner (1996) and as available in the *NIST Chemistry WebBook*.

While the Span and Wagner (1996) correlations for thermophysical properties of pure CO_2 have been widely used and implemented in different numerical simulators, the TOUGH2 simulator uses a different approach. In the ECO2N fluid property module (Pruess and Spycher, 2007), phase behavior of CO_2 and other thermophysical properties are generated from the correlations by Altunin (Altunin, 1975). Garcia (2003) performed a comprehensive review of CO_2 thermophysical properties generated using Altunin's correlations and found them to compare well with experimental data and other correlations (including the Span and Wagner correlations). Note that independent estimates of multicomponent gas mixture properties, including those of pure CO_2, can also be obtained using WebGasEOS (Reagan, 2006), see http://esdtools.lbl.gov/gaseos/home.html.

23.5.2.1.2 Thermophysical Properties of Brine

The thermophysical properties of brine are discussed in the context of how they are implemented in TOUGH2, after acknowledging that other options are available and have been implemented in other numerical simulators. In TOUGH2, thermophysical properties of pure water substance as a function of pressure and temperature are mostly obtained from the steam table formulations (e.g., Meyer et al., 1993). To compute the changes in water properties because of the presence of dissolved salt (i.e., brine), suitable correlations are used in most numerical simulators. For example, starting with pure water density, brine density can be calculated using the correlations of Haas (1976) for vapor-saturated brine and the correlation of Andersen et al. (1992) for brine compressibility. Similarly, brine viscosity can be calculated from pure water viscosity using the correlations of Philips et al. (1981). Finally, it is possible to obtain specific enthalpy and internal energy of brine using the correlations of Michaelides (1981) and Gudmundsson and Thrainsson (1989). Note that these correlations are not accurate below 100°C, when salinities are large. Newer correlations have recently become available that are accurate down to 25°C for saturated NaCl solutions and to lower temperature for less concentrated brines. These newer correlations have been implemented in the ECO2N fluid properties module of the TOUGH2 simulator (Pruess and Spycher, 2007).

23.5.2.1.3 Thermophysical Properties of Fluid Mixtures

Thermophysical properties of different phases (aqueous and/or gaseous) are calculated from the properties of the pure components using some specified rules. For example, in TOUGH2–ECO2N (Pruess and Spycher, 2007), the aqueous-phase density is calculated by assuming additivity of the volumes of brine and dissolved CO_2, that is,

$$\frac{1}{\rho_l} = \frac{1 - X_l^{CO_2}}{\rho_b} + \frac{X_l^{CO_2}}{\rho_{CO_2}} \tag{23.17}$$

where

$X_l^{CO_2}$ is the mass fraction of CO_2 in the aqueous phase

ρ_l, ρ_b, and ρ_{CO_2} are the aqueous-phase, brine, and pure CO_2 densities, respectively

While the impact of dissolved CO_2 on brine viscosity can be ignored because the amount of dissolved CO_2 is generally small (Pruess and Spycher, 2007), and the aqueous-phase viscosity can be assumed to be similar to that of brine, correlations are available (Reid et al., 1987) to account for changes in aqueous viscosity with changes in dissolved CO_2, and these correlations have been implemented in some numerical simulators (White et al., 2012). Enthalpy of the aqueous phase is mostly calculated using the formulations of Battistelli (Battistelli et al., 1997) using the enthalpies of brine and CO_2, heat of solution of CO_2, and the aqueous-phase mass fractions as input.

With knowledge of pure component CO_2 and water vapor properties (e.g., density and enthalpy), the gas-phase properties can be calculated as follows:

$$\rho_g = X_g^{CO_2}\rho_{CO_2} + X_g^{H_2O}\rho_g^{H_2O} \tag{23.18}$$

$$h_g = X_g^{CO_2}h_g^{CO_2} + X_g^{H_2O}h_g^{H_2O} \tag{23.19}$$

where

$X_g^{CO_2}$ and $X_g^{H_2O}$ are the mass fractions of CO_2 and water, respectively, in the gas phase

$\rho_g^{CO_2}$ and $\rho_g^{H_2O}$ are the densities of pure components CO_2 and water, respectively, in the gas phase

$h_g^{CO_2}$ and $h_g^{H_2O}$ are the specific enthalpies of pure CO_2 and water, respectively, in the gas phase

In low-temperature storage formations, particularly if the temperature is below 100°C, mass fraction of water in the gas (i.e., vapor) phase is expected to be low, $X_g^{H_2O} \oplus 0$. Under those conditions, it may be acceptable to not use Equations 23.18 and 23.19, and instead assume that the gas-phase density and specific enthalpy are identical to that of pure CO_2 properties (Pruess and Spycher, 2007). Viscosity of the gas phase is computed from the viscosities of pure CO_2 and water vapor based on the extension proposed by Wilke of the Chapman–Enskog theory for multicomponent gas mixtures (Reid et al., 1987).

Note that the ECO2N module reproduces fluid properties of H_2O–NaCl–CO_2 largely within experimental error for the temperature, pressure, and salinity conditions of interest ($10°C \leq T \leq 110°C$; $P \leq 600$ bar; salinity up to full halite saturation). Flow processes can be modeled isothermally or nonisothermally, and phase conditions represented may include a single (aqueous or CO_2-rich)-phase as well as two-phase mixtures. Fluid phases may appear or disappear in the course of a simulation, and solid salt may precipitate or dissolve. ECO2N can model super- as well as subcritical conditions, but it does not make a distinction between liquid and gaseous CO_2, and hence is not applicable for processes that involve two CO_2-rich phases.

23.5.2.2 Relative Permeability Measurements

One of the key parameters affecting fate and transport of the injected CO_2 in the subsurface is its relative permeability, which is a property of both the rock and the fluid phases involved. Relative permeability is a parameter that quantifies the extent to which the injected CO_2 and the formation fluids (e.g., brine) interfere with each other as they move through the pore space of the rocks. It affects not only the spatial extent of the plume but also the injectivity of a well (see Section 23.6.5), extent of capillary trapping, and leakage through the seal (Benson et al., 2013). In any analytical model or numerical simulator designed to accurately predict the subsurface migration of CO_2, one needs to provide relative permeability data for the fluid phases involved as an input, either as a constitutive relationship or as measured data in a tabulated form. As a result, reliable relative permeability measurements are required.

Despite its obvious importance, no measurements of the relative permeability for CO_2/brine systems were performed until the early 2000s, when capture and storage became an important climate mitigation strategy (Bachu, 2013). To address this gap in knowledge, Bennion and Bachu (2008, 2010) published a relatively large set of relative permeability data for the CO_2/brine system. They performed relative permeability measurements on sandstone and carbonate rock cores from potential sequestration targets in Canada. For a given relative permeability measurement, pressure, temperature, and brine compositions were chosen to match the reservoir conditions from which the core originated, resulting in the generation of relative permeability curves across a wide range of reservoir conditions. Relative permeability data for CO_2/water systems performed on core samples from Berea, Mt. Simon, and Tuscaloosa sandstones in the United States, and Otway and Paaratte sandstones in Australia, are also available in the literature (Perrin and Benson, 2010; Krevor et al., 2012; Zuo et al., 2012; Akbarabadi and Piri, 2013). A library of existing relative permeability curves measured with the CO_2–brine system has recently been created that can be accessed online at https://pangea.stanford.edu/reserach/bensonlab/relperm. Note that a comprehensive analysis of the measured relative permeability data for the CO_2/brine system can be found in Mathias et al. (2013). Additionally, Benson et al. (2013) identify the current gaps and data needs for establishing reliable relative permeability relationships for CO_2 geologic storage.

23.5.2.3 Capillary Pressure Measurements

The dependence of capillary pressure (P_C) on wetting phase (i.e., water or brine) saturation (S_W) under reservoir conditions is a basic constitutive relation needed to predict CO_2 flow and capillary trapping during sequestration. In this context, it is worth noting that knowing only the dependence of relative permeability on S_W is not enough to accurately predict fluid flow or equilibrium saturations in a system involving multiphase flow of different fluids. It is also essential

to include a capillary pressure relationship in the mathematical description of such multiple fluid systems. More specifically, in GCS, where capillary trapping is expected to be one of the key storage mechanisms, a reliable $P_C(S_W)$ constitutive relationship for the water/$scCO_2$ system is needed for reliably predicting the fate of injected CO_2 and estimating the storage potential of a reservoir.

As noted by Tokunaga et al. (2013), introduction of $scCO_2$ into reservoirs may result in geochemical reactions (Kaszuba et al., 2003; Kharaka et al., 2006; Shao et al., 2011), including wettability alterations (Dickson et al., 2006; Chiquet et al., 2007a,b; Bikkina, 2011; Jung and Wan, 2012; Kim et al., 2012). Because of these geochemical and wettability alterations, capillary behavior of water–$scCO_2$ systems cannot be reliably estimated from scaling-based extrapolation of nonreactive immiscible fluids such as air, certain oils, or mercury, even though researchers in the past have routinely employed such approaches in numerical simulations of sequestration systems. The paucity of experimental determinations of capillary pressure relations for water–$scCO_2$ is further complicated by the fact that reservoir conditions span a very broad range of P, T, and chemistry, over which large variations occur in $scCO_2$ density (Span and Wagner, 1996), water–$scCO_2$ interfacial tension (Bachu and Bennion, 2009; Chalbaud et al., 2010; Li et al., 2012), and wettability of mineral surfaces (Chiquet et al., 2007a,b; Bikkina, 2011; Jung and Wan, 2012; Wang et al., 2013).

Tokunaga et al. (2013) provide a comprehensive discussion on the current status of measured capillary pressure data for water–$scCO_2$ systems, and the following is summarized from their work. Capillary pressure during drainage and imbibition for distilled water–CO_2 (gas), distilled water–CO_2 (liquid), and distilled water–$scCO_2$ systems on quartz and sand packs has been reported in Plug and Bruining (2007). Capillary pressure data during drainage for brine–$scCO_2$, brine–decane, and air–mercury on Berea sandstone cores have been reported in Pentland et al. (2011). Pini et al. (2012) measured drainage capillary pressure data for water–$scCO_2$ and air–mercury on Berea and Arqov sandstone cores. Perrin and Benson (2010) coupled multiphase (CO_2–water) flow with x-ray computed tomography for obtaining insights into CO_2 trapping associated with finer-scale heterogeneity. Tokunaga et al. (2013) measured drainage and imbibition processes on quartz sand with brine–$scCO_2$ at pressures of 8.5 and 12.0 MPa (45°C) and air–brine at 21°C and 0.1 MPa.

23.5.2.4 Relative Permeability and Capillary Pressure Relationships

In numerical flow simulations of CO_2 and brine, it is possible to provide the measured relative permeability and capillary pressure data in tabular form. It is, however, more customary to provide these data in the form of functional relationships. In other words, the measured relative permeability and capillary pressure data are fitted to some mathematical functions, and the resulting relationships are included in the numerical simulators as continuous functions of (usually) the wetting-phase saturation, S_w. Of the functional forms available for this purpose, the most widely used ones for capillary pressure are those due to Mualem (1976) and van Genuchten (1980), that is,

$$P_C = -\frac{1}{\alpha}\left[(S_{w,eff})^{-1/m} - 1\right]^{1-m} \tag{23.20}$$

where

$S_{w,eff}$ is effective saturation of the wetting phase

m and $1/\alpha$ are fitting parameters, the latter related to the capillary strength of the medium

The corresponding van Genuchten relationship for wetting-phase relative permeability is

$$k_{rel,w} = (S_{w,eff})^{1/2}\left[1 - \left(1 - (S_{w,eff})^{1/m}\right)^m\right]^2 \tag{23.21}$$

In Equations 23.20 and 23.21, $S_{w,eff}$ is defined as

$$S_{w,eff} = \frac{(S_w - S_{wr})}{(S_{ws} - S_{wr})} \tag{23.22}$$

where S_{wr} and S_{ws} are the residual and satiated saturations, respectively, of the wetting phase. Relative permeability for gas flow is described by the Corey (1954) formulation as follows:

$$k_{rel,nw} = (1 - \hat{S})^2(1 - \hat{S}^2) \tag{23.23}$$

where $\hat{S} = (S_w - S_{wr})/(1 - S_{wr} - S_{nwr})$, and S_{nwr} is the residual saturation of the nonwetting phase. Note that different relative permeability and capillary pressure curves may be necessary for the injection and postinjection periods because of hysteresis (Doughty, 2007).

23.5.3 Spatial and Temporal Discretization and Numerical Solution

In TOUGH2 simulator, once all the flux and accumulation terms have been gathered for each grid block of the model domain, they are discretized in space using the IFD approach (Narasimhan and Witherspoon, 1976), and time is discretized as fully implicit. In IFD, for any grid block having a volume of V_n, the integral on the left-hand side of Equation 23.4 can be expressed as

$$\int_{V_n} M^\kappa dV_n = M_n^\kappa V_n \tag{23.24}$$

where M_n^κ is the average value of M^κ over V_n. Similarly, the surface integrals on the right-hand side can be approximated as discrete sum of averages over surface segments A_{nm} as follows:

$$\int_{\Gamma_n} \mathbf{F}^\kappa \cdot \mathbf{n} d\Gamma_n = \sum_m A_{nm} F_{nm}^\kappa \tag{23.25}$$

where F_{nm}^κ is the average value of the (inward) normal component of $\mathbf{F}^\kappa$ over the surface segment A_{nm} between volume elements V_n and V_m (see Figure 23.5). The discretized flux is expressed in terms

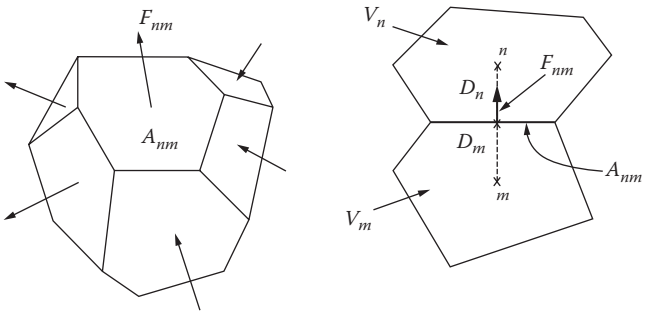

FIGURE 23.5 Schematic representation of spatial discretization implemented in the IFD approach of the TOUGH2 simulator. (The figure is adapted from Pruess, K. et al., *TOUGH2 Users Guide*, Ver. 2.0, LBNL-43134, Lawrence Berkeley National Laboratory, Berkeley, CA, 2012.)

of averages over parameters for elements V_n and V_m. For example, the basic Darcy flux term in Equation 23.8 can be discretized as

$$F_{\beta,nm}^{\kappa} = -k_{nm}\left(\frac{k_{rel,\beta}\rho_{\beta}^{\kappa}}{\mu_{\beta}}\right)_{nm}\left[\frac{P_{\beta,n}-P_{\beta,m}}{D_{nm}} - \rho_{\beta,nm}^{\kappa} g_{nm}\right] \tag{23.26}$$

where the subscripts (nm) denote a suitable averaging at the interface between grid blocks n and m. $D_{nm} = D_n + D_m$ is the distance between the nodal points n and m, and g_{nm} is the component of gravitational acceleration in the direction from m to n (see Figure 23.5). Inserting the discretized accumulation and flux terms in Equations 23.24 and 23.25, respectively, into Equation 23.4, we obtain the following equation:

$$\frac{dM_n^k}{dt} = \frac{1}{V_n}\sum_m A_{nm}F_{nm}^{\kappa} + q_n^{\kappa} \tag{23.27}$$

A fully implicit temporal discretization of Equation 23.27 results in a set of coupled nonlinear algebraic equations, that is,

$$R_n^{\kappa,k+1} = M_n^{\kappa,k+1} - M_n^{\kappa,k} - \frac{\Delta t}{V_n}\left[\sum_m A_{nm}F_{nm}^{\kappa,k+1} + V_n q_n^{\kappa,k+1}\right] \tag{23.28}$$

where we have introduced residuals $R_n^{\kappa,k+1}$, and the objective of the numerical solution scheme is to minimize these residuals. In Equation 23.28, the superscripts k and $k + 1$ refer to discrete time steps such that $t^{k+1} = t^k + \Delta t$, where Δt is the size of time increment between steps k and $k + 1$. In general, each grid block is associated with $N_{EQ} = N_{\kappa} + 1$ equations, where N_{κ} is the number of components present in the system. Note that, in the ECO2N module of TOUGH2, $N_{\kappa} = 3$ (water, NaCl, and CO_2). In a numerical grid containing N_{EL} grid blocks, Equation 23.28 represents a total of $N_{EL} \times N_{EQ}$ coupled, nonlinear algebraic equations. The unknowns are the $N_{EL} \times N_{EQ}$ independent primary variables $\{x_i;\ i = 1,\ldots, N_{EL} \times N_{EQ}\}$, which completely define the state of the flow system at time level t^{k+1}. In the ECO2N module of TOUGH2, the four independent primary variables associated with each grid block are taken to be pressure, mass fraction of NaCl dissolved in water, mass fraction of CO_2 dissolved in water, and temperature, if single-phase conditions persist. However, if two-phase conditions evolve, where CO_2 can exist as an independent supercritical fluid (for simplicity, referred to as the gas phase), these primary variables are pressure, mass fraction of NaCl dissolved in water, gas saturation, and temperature.

The $N_{EL} \times N_{EQ}$-coupled nonlinear equations in Equation 23.28 are solved using the Newton–Raphson technique. In this approach, an iteration index p is introduced, and the residuals $R_n^{\kappa,k+1}$ at iteration step $p + 1$ are expanded in a Taylor series in terms of thus at step p as

$$R_n^{\kappa,k+1}(x_{i,p+1}) = R_n^{\kappa,k+1}(x_{i,p}) + \sum_i \frac{\partial R_n^{\kappa,k+1}}{\partial x_i}\Big|_p (x_{i,p+1} - x_{i,p}) + \cdots \tag{23.29}$$

Retaining only terms up to first order, a set of linear equations are obtained for the increments $(x_{i,p+1} - x_{i,p})$, which are solved iteratively using the preconditioned conjugate gradient method.

Iteration is continued until the residuals are reduced below a preset convergence tolerance limit, that is,

$$\left|\frac{R_{n,p+1}^{\kappa,k+1}}{M_{n,p+1}^{\kappa,k+1}}\right| \leq \varepsilon_1 \tag{23.30}$$

Note that when the accumulation terms $M_{n,p+1}^{\kappa,k+1}$ themselves are smaller than ε_2, an absolute convergence criterion is also imposed, that is,

$$\left|R_{n,p+1}^{\kappa,k+1}\right| \leq \varepsilon_1\varepsilon_2 \tag{23.31}$$

If convergence cannot be attained within a specified number of iterations, the time step size Δt is reduced, and a new iteration process is started.

23.6 ANALYTICAL AND SEMI-ANALYTICAL SOLUTIONS

The attraction of numerical solutions lies in their versatility and ability to handle complex processes and various geologic settings, including complex subsurface geometries (Dentz and Tartakovsky, 2009a). However, there are inherent challenges associated with numerical modeling of CO_2 migration in DSA. For example, to accurately predict the fate of the injected CO_2, it would be, in general, necessary to solve the conservation equations (as described in Section 23.5.1) in the presence of the nonlinear constitutive relationships (as presented in Section 23.5.2) over a 3D, irregular model domain. At scales where geologic carbon storage can make a significant impact on reducing atmospheric CO_2 emissions, it will involve injecting CO_2 at storage sites spanning over two to three decades and then monitoring the plume migration over many more decades after injection ceases. Over this time frame, which includes both the injection and postinjection periods, the injected CO_2 plume, depending on injection rates and properties of the storage formation, may travel many kilometers, even many tens of kilometers. Developing an efficient numerical model over such spatial and temporal scales can be computationally prohibitive, even after ignoring all the coupling between flow, and geomechanical and geochemical processes.

Because of these challenges, a large number of analytical and semi-analytical solutions have been developed for predicting the migration of CO_2 in DSA. Because they do not solve the full set of balance equations in 3D space, instead relying on elegant simplifications, these analytical and semi-analytical solutions are more efficient, less intensive computationally, often serve as effective screening mechanisms (Bacon, 2013), and offer significant insight into the controlling processes and parameters not generally obtainable through numerical simulations (Huppert and Neufeld, 2014). While it will not be possible to include all these simplified modeling approaches, we discuss a few representative ones in this section.

23.6.1 CO_2 Plume Extent

23.6.1.1 VE with Sharp Interface Solutions

Assuming that the VE approximations are valid and that capillary pressure effects can be excluded (i.e., sharp interface models), Nordbotten and Celia (2006) present analytical solutions for transient plume extent and shape when CO_2 is injected into a planar, homogeneous, confined DSA of thickness H. When it is further assumed that all fluid phases are incompressible, have constant properties, are completely immiscible, and thermal effects can be ignored, the set of partial differential equations represented by Equation 23.4 can be reduced to a system of ordinary differential equations in a single similarity variable (Nordbotten and Celia, 2006). Under these conditions, the injected CO_2 forms a radially symmetric invasion front in the (r, z) plane, with its thickness denoted by $h(r, t)$ as shown in

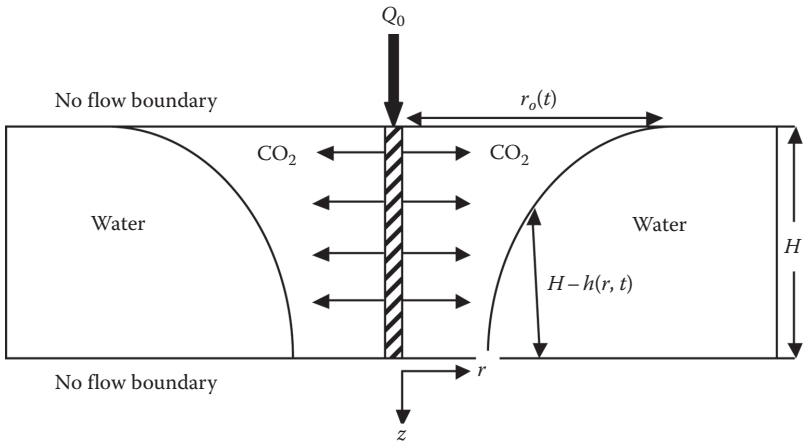

FIGURE 23.6 A schematic diagram showing a 2D vertical cross section of a DSA with radial symmetry, where CO_2 is injected at the center through a vertical well at the volumetric injection rate of Q_0. The radial location of the moving front at time is $r_o(t)$, and its depth (from the top of the formation) is $h(r, t)$. The formation depth is H. This schematic diagram, (Adapted from Nordbotten, J.M. and Celia, M.A., *J. Fluid Mech*., 561, 307, 2006), provides the basis for the conceptual model used by Nordbotten and Celia (2006) in developing their analytical solution for estimating the extent of plume migration at a specified time t.

Figure 23.6, where Q_0 is the volumetric rate of injection of CO_2, assumed to be constant. According to Nordbotten and Celia (2006), the evolution of the invasion front $h(r,t)$ can be described by

$$\frac{\partial \zeta(\xi,\tau)}{\partial \tau} = \frac{1}{\xi}\frac{\partial}{\partial \xi}\left[\frac{\Gamma\lambda\zeta(1-\zeta)\xi}{\lambda\zeta+(1-\zeta)}\frac{\partial \zeta}{\partial \xi}+\frac{1-\zeta}{\lambda\zeta+(1-\zeta)}\right] \tag{23.32}$$

where

$\zeta = h/H$
$\xi = r/\sqrt{k}$
$\tau = Q_0 t/(2\pi\varphi H k(1-S_{wr}))$
$\Gamma = (2\pi\Delta\rho g k\lambda_w H^2)/Q_0$
$\lambda = \lambda_{nw}/\lambda_w$
$\lambda_\beta = k_{rel,\beta}/\mu_\beta$

In this, k is the intrinsic permeability of the confined DSA, $k_{rel,\beta}$ and $\mu_{rel,\beta}$ are the relative permeability and viscosity of phase β (=water, the wetting phase—w, and CO_2, the nonwetting phase—nw), φ is the porosity, and S_{wr} is the residual saturation of the wetting phase.

Nordbotten and Celia (2006) further establish that for negligibly small values of the dimensionless parameter Γ, Equation 23.32 has a solution of the form

$$\begin{aligned}\zeta(\xi,\tau) &= 1, \quad \eta \le \frac{2}{\lambda}\\ &= \frac{1}{\lambda-1}\left[\sqrt{\frac{2\lambda}{\eta}}-1\right], \quad \frac{2}{\lambda} < \eta < 2\lambda\\ &= 0, \quad \eta \ge 2\lambda\end{aligned} \tag{23.33}$$

where $\eta = \xi^2/\tau$ is the similarity variable. Note that the solution in Equation 23.33 is valid for all values of $\lambda \ge 1$ and cannot be used for values of $\lambda < 1$ because it does not capture the physical nature

of the solution, which has an inherent assumption of gravity override (Nordbotten and Celia, 2006). For situations in which Γ is not negligibly small, Equation 23.33 needs to be solved numerically subject to overall mass balance constraints, such as

$$2\pi \int_0^{r_o(t)} \phi(1 - S_{wr})hrdr = Q_0 t \tag{23.34}$$

An iterative scheme will be necessary because $r_o(t)$, which specifies the transient location of the moving CO_2 front, is not known. The solution in Equation 23.33 can be used as an initial guess for this iterative solution. Note that Nordbotten and Celia (2006) further extended their mathematical derivation to include the situation in which the injected CO_2 partitions into the brine phase, and there is mass transfer between these two phases.

Another set of sharp interface solution for the invading CO_2 front in a DSA has been developed by Dentz and Tartakovsky (2009a), though they have called their approach "abrupt interface models." Invoking the Dupuit approximation, Dentz and Tartakovsky (2009a) establish that in 3D porous media with radial symmetry, the location of the CO_2 front can be written as

$$\frac{h(r,t)}{H} = \gamma_{cw} \ln\left[\frac{r}{r_i(t)}\right] \tag{23.35}$$

where

$$\gamma_{cw} = \frac{Q_0}{2\pi k H^2 g}\frac{\Delta\mu}{\Delta\rho}$$

$r_i(t)$ is the inner location of the advancing plume (see Figure 23.7) as a function of time

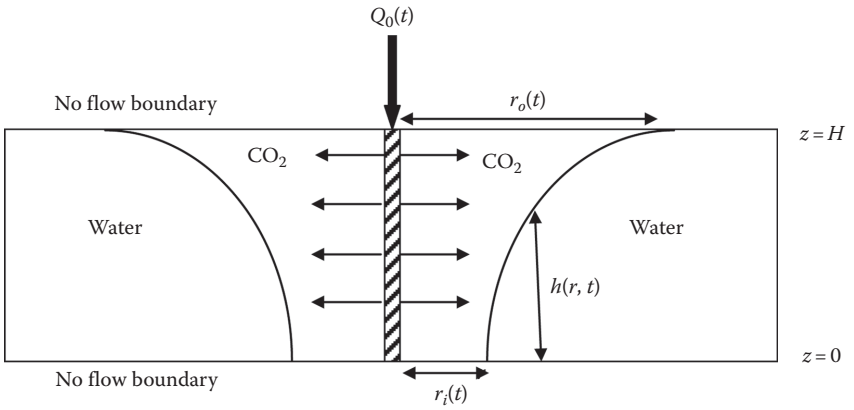

FIGURE 23.7 A schematic diagram showing a 2D vertical cross section of a DSA with radial symmetry, where CO_2 is injected at the center through a vertical well at the volumetric injection rate of Q_o. The radial location of the moving front at time is $r_o(t)$, and its depth (from the bottom of the formation) is $h(r, t)$. The formation depth is H. This schematic diagram, provides the basis for the conceptual model used by Dentz and Tartakovsky (2009) in developing their analytical solution for estimating the extent of plume migration at a specified time t. Note the differences between the conceptual model of Dentz and Tartkovsky (2009) and Nordbotten and Celia (2006), see Section 23.6.1.1 for details. (Adapted from Dentz, M. and Tartakovsky, D.M., *Transp. Porous Media*, 79, 15, 2009.)

Note that $\Delta\mu = \mu_w - \mu_{nw}$ is the difference between viscosities of the water and CO_2 phases, and $\Delta\rho$ is the density difference. Dentz and Tartakovsky (2009a) show that

$$r_i(t) = \sqrt{\frac{2V_0(t)}{\pi\phi H\gamma_{cw}}\left[\exp\left(\frac{2}{\gamma_{cw}}\right)-1\right]^{-1}} \tag{23.36}$$

where $V_0(t)$ is the total volume of CO_2 injected over time t and that the outer location of the plume can be computed from

$$r_o(t) = r_i(t)\exp\left(\frac{1}{\gamma_{cw}}\right) \tag{23.37}$$

If a constant rate of CO_2 injection is maintained, $V_0(t) = Q_0 t$, which implies that the invading plume advances as $\sim\sqrt{t}$, which is similar to the prediction by Nordbotten and Celia (2006). The other critical observation from Dentz and Tartakovsky (2009a) is that the invading plume is characterized by logarithmic interface whose evolution is controlled by a single parameter γ_{cw}, which includes not only the effects of differences in physical properties of the fluids (in terms of their density and viscosity differences) but also the effects of injection rate relative to formation conductivity.

Lu et al. (2009) found that the semi-analytical solutions of Nordbotten and Celia (2006) and those of Dentz and Tartakovsky (2009a) differed from one another, even though both had employed sharp interface limits. This is not surprising, because the two sets of solutions have been developed for two different flow regimes. More specifically, while the semi-analytical solutions of Nordbotten and Celia (2006) are valid for viscosity-dominated flow regimes, the analytical solutions of Dentz and Tartakovsky (2009a) are appropriate for buoyancy-dominated flow regimes. In that sense, these two solutions are complementary to each other (Dentz and Tartakovsky, 2009b). In addition, comparing these semi-analytical and analytical solutions with numerical simulation results, Lu et al. (2009) commented that neither solution could predict the shapes and spreading distances of the displacement front with reasonable accuracy. This is not surprising given that those solutions have been developed under a number of simplifying assumptions.

A sharp interface mathematical model of CO_2 migration in DSA was also developed by Juanes et al. (2010). In addition to the migration mechanisms included in Nordbotten and Celia (2006) and Dentz and Tartakovsky (2009a), the models from Juanes et al. (2010) also accounted for the impacts of natural groundwater flow on plume migration. Their model, which includes many injection wells with uniform spacing in a linear pattern and identical injection rates in each well, presents solutions not only for the injection period but also for the postinjection period. The details of their mathematical derivations, some of which are also presented in Juanes and MacMinn (2008), are not repeated here because of space limitation. Briefly, because the mobility ratio λ defined by

$$\lambda = \frac{k_{rel,w}/\mu_w}{k_{rel,nw}/\mu_{nw}} \tag{23.38}$$

is relatively small (i.e., $\lambda \ll 1$) for CO_2 displacing resident brine in a DSA, Juanes et al. (2010) show that the governing equation for $h(r, t)$ is a hyperbolic partial differential equation, which they solve using the methods of characteristics. They show that there exists a dimensionless time ($\tau'_{\max}$) for complete trapping to occur, given by

$$\tau'_{\max} = \frac{(2-\Omega)\left[1-\lambda(1-\Omega)\right]}{\Omega^2} \tag{23.39a}$$

and a maximum dimensionless migration distance ($x_{D,\max}$)

$$x_{D,\max} = \frac{\tau'_{\max}}{\lambda(1 - S_{wr})} \tag{23.39b}$$

where dimensionless time is defined by $\tau' = 1 + (UH/Q)((t-t_{inj})/t_{inj})$(for postinjection period) and dimensionless distance is given by $x_{D,\max} = x/L$. In the preceding, $L = (Q_0 t_{inj}/\phi H)$, Q is the total volumetric injection rate of CO_2 for all wells, t_{inj} is the duration of the injection period, and Ω is defined as the capillary trapping coefficient, that is, $\Omega = S_{nwr}/(1-S_{wr})$, where S_{nwr} is the residual saturation of the nonwetting phase, and S_{wr} is the irreducible saturation of the wetting phase.

Migration of the CO_2 plume is also affected by the dip of the storage formation. For example, Gunn and Woods (2011) studied the migration of a plume of incompressible buoyant fluid injected into a confined dipping aquifer with an outflow at a single fault that may be up-dip or down-dip from the point of injection. They developed a longtime asymptotic solution for the motion of the injected fluid and established that for the case in which the outflow fault is up-dip from the point of injection, there is a critical injection rate above which the injected fluid floods the full depth of the aquifer. Gunn and Woods further showed that for the case in which the outflow fault is down-dip from the point of injection, there is a critical injection rate below which all injected fluid initially flows up-dip. Their analysis leads to expressions for the lateral extent of the injected fluid as a function of time, and they illustrate the implications of their findings for the dispersal of CO_2 injected into DSA. Their evaluation indicates that the geometry of the system may have a significant effect on (1) the total volume of CO_2 that can be sequestered in a faulted aquifer, and (2) the interpretation of the dispersed position of any injected tracer(s).

23.6.1.2 VE with Capillary Transition Solutions

In subsurface fluid flow problems involving multiple fluids, when the fluids are also of different phases, capillary forces may lead to a significant saturation transition zone, which renders the sharp interface assumption questionable. In the particular case of CO_2–brine systems, the potentially large unstable viscosity contrast could further increase the size of the saturation or capillary transition zone. Furthermore, sharp interface models do not capture the strong reduction in relative permeability experienced by the nonwetting phase current, which could considerably affect predictions for its spreading velocity (Bickle et al. 2007). This provides an important motivation for the systematic development of a two-phase capillary transition model.

In this context, Golding et al. (2011) considered the buoyancy-driven flow of a nonwetting fluid along a horizontal barrier and developed a vertically integrated model for a two-phase gravity current. As the current propagates (see Figure 23.8), the nonwetting phase displaces the wetting phase, which initially fills the pores in a primary drainage process. Fed by a constant flux per unit width q, the gravity current propagates beneath an impermeable upper boundary in an infinite reservoir initially fully saturated with a denser, wetting, fluid. The current height, $h(x, t)$, denotes the depth below which no nonwetting phase is present and where the nonwetting-phase saturation drops to zero, $s = 0$ (see Figure 23.8). The depth of the reservoir is much greater than the height of the current, and so the horizontal pressure gradient and the velocity in the wetting phase are negligible below the current. They additionally assume that the fluids are simply connected, which implies that, to leading order, there are no horizontal pressure gradients driving flow of the wetting phase within the current.

Under VE assumption, Equation 23.3 can be integrated to provide (Golding et al., 2011)

$$P_C = P_e - \Delta\rho g(z - h) \tag{23.40}$$

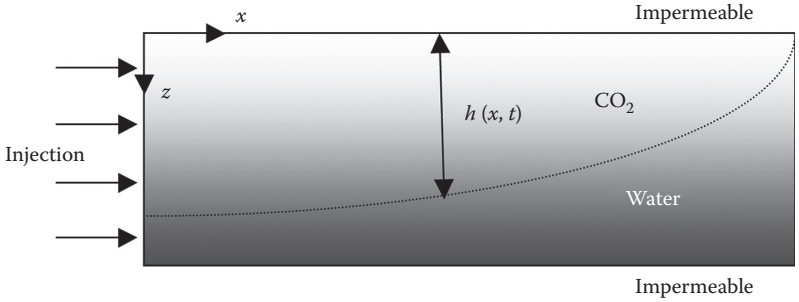

FIGURE 23.8 Schematic diagram of capillary transition zone conceptual model developed by Golding et al. (2011) for estimating plume migration extent—see Section 23.6.1.2 for details.

where P_e can be thought of as a capillary entry pressure. Assuming that capillary pressure–saturation has a power-law relationship of the type

$$P_C(s) = P_{ent}(1-s)^{-1/\Lambda} \tag{23.41}$$

where $s = S_{nw}/(1-S_{wr})$, Golding et al. (2011) show that the evolution of $h(x, t)$ can be described by

$$\phi(1-S_{wr})s_0\left(\frac{h}{h_e}\right)\frac{\partial h}{\partial t} = \frac{\tilde{k}\Delta\rho g}{\mu_{nw}}\frac{\partial}{\partial x}\left[h\frac{\partial h}{\partial x}\Im\left(\frac{h}{h_e}\right)\right] \tag{23.42}$$

where

$h_e = P_e/\Delta\rho g$

$s_0(h/h_e) = 1-(1+(h/h_e))^{-\Lambda}$

$\tilde{k} = kk^0_{rel,nw}$, which results from the assumption that relative permeability of the nonwetting phase changes with its saturation according to $k_{rel,nw} = k^0_{rel,nw}s^{\alpha}$

The function $\Im(h/h_e)$ was provided by Golding et al. (2011) as

$$\Im\left(\frac{h}{h_e}\right) = \frac{h_e}{\Lambda h}\int_0^{s_0} S^{\alpha}(1-S)^{-(1+\Lambda)/\Lambda} \tag{23.43}$$

Golding et al. (2011) were able to perform the integration in Equation 23.43 and obtain analytical expressions for the function $\Im(h/h_e)$ using different values of Λ but for one specific value of $\alpha = 2$. Equation 23.42 cannot be solved analytically and must be solved using a suitable numerical scheme and specific boundary conditions. If, however, instead of assuming that the reservoir is infinite, it is assumed that the reservoir has a characteristic length scale of L such that $h(L) = 0$, it is possible to obtain a steady-state plume depth as a function of x, as given in Golding et al. (2011):

$$\begin{aligned} 2(1-x) &= h^2 + 6\frac{h}{B} + \frac{16}{3B^2}\left[1-(1+hB)^{3/2} + \frac{2}{B^2}(1+hB)\ln(1+hB)\right], \quad \Lambda = 0.5 \\ &= h^2 + 6\frac{h}{B} - \frac{2}{B^2}(3+2hB)\ln(1+hB), \quad \Lambda = 1 \end{aligned} \tag{23.44}$$

where $B = \dfrac{\Delta\rho g H}{P_e}$. Note that in writing Equation 23.44, Golding et al. (2011) used the boundary condition $h\dfrac{dh}{dx}\Im(hB) = -1$. Note also that, as $B \to \infty$, Equation 23.44 predicts that $h \approx \sqrt{2(1-x)}$, which is essentially the steady-state plume depth profile if one uses the sharp interface approximation. Recently, Wang et al. (2014) extended the mathematical development of Golding et al. (2011) to predict the transient plume depth in a dipping DSA with natural groundwater flow assuming VE and observed that there is a critical value of the injection rate below which no CO_2 can flow in the down-dip direction.

23.6.2 Pressure Buildup

In addition to understanding the evolution of the CO_2 plume, it is also necessary to understand evolution of pressure after $scCO_2$ is injected into a storage formation. This is because knowledge of expected pressure evolution resulting from a planned injection process can help decide safe injection limits (i.e., the maximum rate at which CO_2 can be injected without causing formation damage). A priori knowledge of the pressure buildup also helps in determining compression energy needed for injection, density of the injected fluid, and stability of the sealing caprock (Rutqvist et al., 2007; Zhou et al., 2009; Birkholzer et al., 2009; Ferronato et al., 2010, Mukhopadhyay et al., 2012a; Vilarrasa et al., 2013). Because of its importance, a large number of analytical and semi-analytical solutions (e.g., Saripalli and McGrail, 2002; Mathias et al., 2009, 2011; Ehlig-Economides and Economides, 2010; Vilarrasa et al., 2010, 2013; Azizi and Cinar, 2013) have been developed to predict the spatial and temporal evolution of pressure in a storage formation, particularly in DSA.

Saripalli and McGrail (2002) developed semi-analytical solutions for pressure evolution within the two-phase $scCO_2$/brine flow region, based on a conceptual model comprising injection of an immiscible CO_2 phase into a DSA with radial symmetry, its axisymmetric flow around the injection well, and eventual buoyancy-driven flow with simultaneous dissolution into the brine phase. A limitation of these semi-analytical solutions is that they are developed assuming that both the geological formations and the fluids are incompressible. Later, Mathias et al. (2009) used the similarity solution in Nordbotten et al. (2005b) to calculate a vertical average of the fluid pressure in the aquifer. While Mathias et al. (2009) treated the gas phase as compressible, they assumed a gas compressibility independent of pressure and comparable to that of brine. Vilarrasa et al. (2010) illustrated that CO_2 compressibility could be one to two orders of magnitude larger than that of brine and argued that this could have significant impact on pressure buildup in the aquifer. They then proposed a method to account for compressibility effects and viscosity variations, and using the abrupt interface solutions of Dentz and Tartakovsky (2009a), calculated pressure at every point within the aquifer. However, according to Vilarrasa et al. (2010), the slope of CO_2 pressure as a function of the logarithm of distance obtained using their solutions differs significantly from that of numerical solutions. While not specifically for CO_2 injection into DSA, Mukhopadhyay et al. (2012a) presented a semi-analytical solution for pressure buildup in a gas reservoir where CO_2 compressibility was expressed as a function of pressure based on Pitzer's generalized equation of state.

While the approximate analytical solutions of Mathias et al. (2009) were developed for formations with infinite radial extension, these were later (Mathias et al., 2011) extended to radial domains with closed boundaries. However, these latest solutions also have the limitations that the rock and the two fluid phases all have small and fixed (i.e., independent of pressure) compressibilities. Note that analytical solutions have also been obtained for estimating risks of pressure buildup resulting from CO_2 injection (see Oruganti et al., 2011). Finally, Vilarrasa et al. (2013) recently developed a semi-analytical solution for CO_2 plume geometry and fluid-pressure evolution, accounting for CO_2 compressibility and buoyancy effects in the injection well, such that CO_2

was not uniformly injected along the aquifer thickness. They formulated the injection problem in terms of a CO_2 potential that facilitates solution in horizontal layers. Capillary pressure was considered at the interface between the CO_2-rich phase and the brine phase. In this formulation, when a prescribed CO_2 mass flow rate is injected, CO_2 advances initially through the top portion of the DSA. As CO_2 is being injected, the CO_2 plume advances not only laterally, but also vertically downward. However, the CO_2 plume does not necessarily occupy the whole thickness of the aquifer. Vilarrasa et al. (2013) found that even in the cases in which the CO_2 plume reached the bottom of the DSA, most of the injected CO_2 enters the aquifer through the layers at the top. According to Vilarrasa et al. (2013), both CO_2 plume position and fluid-pressure evolution predicted by their model compared well with numerical simulations.

23.6.3 Leakage

Injection of CO_2 into DSA can potentially displace large volumes of the resident brine. The displaced brine may subsequently migrate into other parts of the aquifer via permeable pathways, such as abandoned wells or faults (Birkholzer et al., 2009; Cihan et al., 2011, 2013; Zhou and Birkholzer, 2011). Understanding and predicting the impacts of leakage require modeling/analysis tools of considerable complexity (Celia et al., 2011). For example, pressure changes resulting from injection may extend more than thousands of square kilometers in the horizontal plane (Birkholzer et al., 2009; Zhou et al., 2010), while often comprising multiple layers of high-permeability (aquifer) and low-permeability (aquitard) formations in the vertical direction. In addition, the necessity of evaluating large spatial domains is often accompanied by the need for considering hundreds or even thousands of local features, such as injection or extraction wells as well as potentially leaky wells and faults. As noted by Cihan et al. (2013), numerical simulation of regional-scale flow processes in large multilayered model domains, combined with local flow phenomena in/near multiple wells and/or faults, pose tremendous challenges, often demanding impractical computational resources. Consequently, a number of analytical and semi-analytical solutions have been developed for predicting leakage in the context of GCS. Note again that a second motivating factor for developing these simpler analytical and semi-analytical solutions is that they often provide better insights into the processes. Such insights are not always obtainable from numerical simulations.

Based on their sharp interface solution (Nordbotten and Celia, 2006) for plume migration in DSA (see Section 23.6.1.1), which was developed under the assumption of VE, Nordbotten et al. (2009) developed a computer code ELSA (estimating leakage semi-analytically), which provides quantitative estimates of fluid distribution and leakage rates in systems involving a sedimentary succession of multiple aquifers and aquitards, penetrated by an arbitrary number of abandoned wells. While the various subcomponents of the overall conceptual model are computed analytically or semi-analytically, the large-scale modeling framework is designed such that it results in a grid-free approximation of leakage rates and fluid distribution.

A related approach, which has been termed VESA or vertical equilibrium subgrid analytical (Gasda et al., 2009), also provides an effective modeling strategy. It combines a numerical model and subgrid analytical models to produce an efficient numerical–analytical hybrid model. In VESA, the overall governing equations for flow (obtained using VE and sharp interface assumptions) are solved numerically on a relatively coarse grid, with an analytical model embedded to solve for wellbore flow occurring at the sub–grid block scale. As a result, VESA, while retaining the flexibility of a numerical method, which makes it possible to simulate flow in heterogeneous and geologically complex systems, also maintains the efficiency and accuracy of an analytical method, eliminating the requirement of expensive grid refinement for subscale features. Gasda et al. (2009) applied their VESA approach to benchmark problems used in the model comparison study described in Class et al. (2009). The first of these benchmark problems was a modified version of a two-aquifer system with a single leaky well presented originally in Nordbotten et al. (2005a). Based on the results of the benchmarking exercise, Gasda et al. (2009) concluded that VESA provided a viable alternative

to traditional numerical methods that could capture the essential large- and small-scale features of geological CO_2 sequestration, but at significantly lower computational cost.

While a number of other approaches (e.g., Zeidouni, 2011; Zeidouni and Pooladi-Darvish, 2012; Sun et al., 2013) have been suggested for characterizing and estimating leakage from CO_2 storage sites, we make a specific mention of the analytical models of Cihan et al. (2011). They developed generalized analytical solutions that account for the combined effect of diffuse leakage (i.e., through aquitards) and focused leakage (i.e., through abandoned wells). Their approach involves solving for pressure changes in a system of N aquifers with alternating leaky aquitards in response to fluid injection/extraction with any number, N_I, of injection/pumping (active) wells, and passive leakage/recharge in any number, N_L, of leaky wells. In their formulation, the equations for horizontal groundwater flow in the aquifers are coupled with the vertical flow equations in the aquitards and with the flow continuity equations in the leaky wells. Their solution strategy includes transforming transient flow equations into Laplace transfer space, decoupling the resulting ordinary differential equations via eigenvalue analysis, solving a system of $N_L \times N$ linear algebraic equations for the unknown rates of flow through leakage wells, and superposing the solution of pressure buildup/drawdown in aquifers and aquitards resulting from flow in the N_I active and N_L leaky wells. Cihan et al. (2011) compared their solution methodology with existing analytical solutions for diffuse leakage (e.g., Hemker and Maas, 1987) and for focused leakage (e.g., Avci, 1994; Nordbotten et al., 2004), and against a numerical solution for combined diffuse and focused leakage.

The accuracy of the analytical solution presented in Cihan et al. (2011), which was developed, assuming single-phase flow conditions, for predicting far-field flow processes, was later verified by comparing it with a numerical simulation study that considers the details of two-phase flow (Cihan et al., 2013). Several example applications for a hypothetical CO_2 injection scenario (without consideration of two-phase flow) were presented in Cihan et al. (2013) to demonstrate that the analytical solution in Cihan et al. (2011) is an efficient tool for analyzing regional pressure buildup in a multilayered system, as well as for gaining insights into the leakage processes of flow-through aquitards, leaky wells, and/or leaky faults. Their solution might be particularly useful when a large number of calculations are needed to be performed, that is, for uncertainty quantification, for parameter estimation, or for optimization of pressure-management schemes.

23.6.4 Storage Efficiency

Storage efficiency can be defined as the ratio between the amount of CO_2 stored in an aquifer and the maximum amount of CO_2 that could theoretically be stored in the same aquifer volume (van der Meer, 1995). While large-scale numerical simulations have been performed to estimate CO_2 storage efficiency in DSA (van der Meer, 1995; Obi and Blunt, 2006; Kopp et al., 2009), as has been noted earlier, these simulations are associated with considerable computational cost. Okwen et al. (2010) were one of the first to present simple analytical expressions for estimating CO_2 storage efficiency under the assumptions of a constant-rate injection of CO_2 into a confined, homogeneous, isotropic, saline aquifer. Assuming that the analytical solutions provided in Nordbotten et al. (2005) and Nordbotten and Celia (2006) are good approximations for CO_2 plume evolution in DSA (see Section 23.6.1.1), Okwen et al. (2010) showed that storage efficiency can be estimated from expressions such as

$$\varepsilon \approx \left(1 - S_{wr}\right)\frac{1}{\lambda}, \quad 0 \le \Gamma \le 0.5$$

$$\approx \frac{2\left(1 - S_{wr}\right)}{\left(0.0324\lambda - 0.0952\right)\Gamma + \left(0.1778\lambda + 5.9682\right)\Gamma^{1/2} + 1.6962\lambda - 3.0472}, \quad 0.5 \le \Gamma \le 50 \qquad (23.45)$$

where ε is the storage efficiency, which is defined in Okwen et al. (2010) as

$$\varepsilon = \frac{V_{injected}}{V_{formation}} = \frac{Q_0 t}{\phi \pi H r_{\max}^2} \tag{23.46}$$

In Equation 23.46, $r_{\max}$ is the maximum radial extent of the plume at time t; the other symbols in Equations 23.45 and 23.46 have already been defined in the context of Equation 23.32 (see also Figure 23.6).

Based on Equation 23.45, Okwen et al. (2010) observe that storage efficiency of CO_2 depends on three parameters, namely, (1) the residual saturation of brine (S_{wr}), (2) the mobility ratio (λ) of CO_2 and brine, and (3) the dimensionless group Γ, which quantifies the importance of CO_2 buoyancy relative to CO_2 injection rate, see the following Equation 23.32 for the definition of Γ. Note that Γ has been termed *the gravity factor* in Okwen et al. (2010). Storage efficiency decreases as the gravity factor increases, because increased buoyancy of CO_2 causes it to occupy a thin layer at the top of the confined aquifer, while leaving its lower parts relatively underutilized. Okwen et al. (2010) found that the estimates of storage efficiency from Equation 23.45 compared well with results obtained using extensive numerical simulations and suggested that it could be used as a simple and rapid tool to screen the technical or economic feasibility of a proposed CO_2 injection scenario.

The sharp interface model developed by Juanes et al. (2010) (see Section 23.6.1.1) also permits an estimation of the storage efficiency. Juanes et al. (2010) found that the storage efficiency can be computed from

$$\varepsilon = 2\left(1 - S_{wr}\right)\lambda \frac{\Omega^2}{\Omega^2 + \left(2 - \Omega\right)\left[1 - \lambda\left(1 - \Omega\right)\right]} \tag{23.47}$$

The symbols in Equation 23.47 have been defined in Section 23.6.1.1. Note that the storage efficiency in Equation 23.47 reflects long-term storage through capillary trapping, unlike Okwen et al. (2010), where only short-term storage during active injection is considered.

More recently, Song et al. (2014) published a multilayer supercritical CO_2–brine two-phase displacement model with vertical heterogeneity, which they used to understand the impact of heterogeneity on storage efficiency. They found that a larger heterogeneity coefficient or injection rate would result in lower sweep efficiency and reduce storage efficiency. Their calculations show that the heterogeneity coefficient has more significant effect on storage efficiency than other factors such as injection rate, radial extent, and porosity. Their analytical solutions, which account for vertical heterogeneity, provide an easy and rapid, even if first-order, estimate for storage efficiency.

23.6.5 Injectivity

In earlier sections, we have discussed CO_2 storage capacity (i.e., how much pore volume is theoretically available for storage) and storage efficiency (i.e., how much of the available pore volume is actually used for storage), both of which essentially provide a volumetric measure of storage. For long-term storage of CO_2, it is not sufficient to require only that the target formations have large storage capacities; it is also necessary to require that they have satisfactory injectivity characteristics (IPCC, 2005; Bachu et al., 2007). Injectivity, unlike storage capacity, is a time-dependent quantity and provides a measure of the ability to inject fluid without causing damage to the formation (Azizi and Cinar, 2013). Injectivity is thus closely related to pressure buildup resulting from injection.

It is well accepted by now that formation permeability (k) and thickness (h) exert the maximum control over injectivity. More precisely, a storage formation with a large value of kh is likely to have a better injectivity than one with a smaller value of this product (Burton et al., 2008). In the context of GCS, however, there are other factors and processes that exercise significant controls over injectivity. For example, relative permeabilities of the CO_2 and brine phases (Mathias et al., 2013), their mutual solubilities (Burton et al., 2008), and reservoir heterogeneities can strongly alter the injectivity characteristics of a storage formation. In addition, injection of CO_2 can cause the resident brine to evaporate, resulting in salt precipitation and permeability reduction near the injection well (see Pruess and Müller, 2009 and references therein) significantly impacting injectivity. At injection rates generally associated with GCS, it is also likely that inertial effects and non-Darcy flow effects will influence injectivity (Mijic et al., 2014). In summary, the combination of relative permeability, salt precipitation, gas compressibility, and inertial and thermal effects is likely to control injectivity (Mijic et al., 2014). Note that, in addition to these physicochemical processes, injection rates are often limited by regulations aimed at avoiding the possibility of damaging the formation through fracturing (Environmental Protection Agency, EPA, 2008).

As with estimating the extent of plume migration, pressure buildup, and storage efficiency, numerical simulation remains the preferred method for estimating injectivity. However, analytical solutions (Burton et al., 2008; Azizi and Cinar, 2013; Mijic et al., 2014) have also been developed to investigate the control of different factors, parameters, and processes on injectivity. To understand the evolution of CO_2 injectivity in DSA, it is customary to assume that injection creates three different zones around the well (see Figure 23.9). Closest to the injection well is a *dryout* zone, from

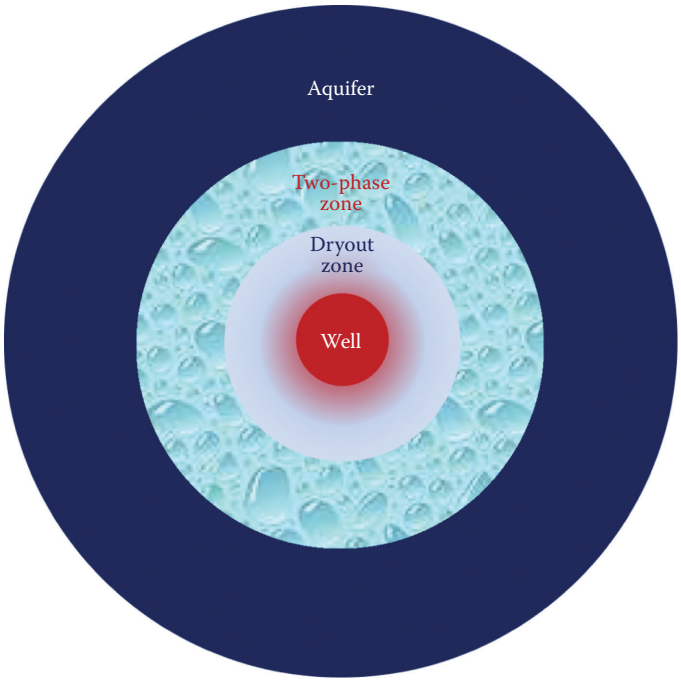

FIGURE 23.9 Schematic diagram showing the existence of different zones around a CO_2 injection well (Burton et al., 2008; Azizi and Cinar, 2013; Mijic et al., 2014). In Burton et al. (2008), the injection well has a radius of r_w and the drainage radius is r_e. The dryout zone extent from the injection well to $r_{dry}(t)$, which is a function of time t, and the two-phase region is situated between radial locations $r_{dry}(t)$ and r_{BL} (t), which also is a function of t. For further details about the conceptual models used for estimating injectivity analytically, see Section 23.6.5.

which brine has been completely removed either through evaporation or by displacement. The outermost region away from the injection well is a saturated brine flow zone, which is yet to be invaded by the injected CO_2. In between these two zones is the two-phase flow region, where both CO_2 and brine remain in mobile conditions. These three regions are separated by two fronts (see Figure 23.9), which move at characteristic speeds (Burton et al., 2008) depending on the rate of injection and other system parameters.

Assuming the fluid phases to be incompressible with constant (i.e., independent of pressure) viscosities, Burton et al. (2008) developed a 1D radial flow model to compute the pressure buildup in each of the earlier three zones and developed the following relationship between the injection rate of CO_2 (q) and overall pressure drop (Δp):

$$\Delta p = \frac{q}{2\pi kH}\left[\frac{\mu_{nw}}{k_{rel,nw}\big|_{S_{nw}=1}}\ln\left(\frac{r_{dry}}{r_w}\right)+\frac{1}{\left(\frac{k_{rel,nw}}{\mu_{nw}}+\frac{k_{rel,w}}{\mu_w}\right)\Big|_{S_{nw,avg}}}\ln\left(\frac{r_{BL}}{r_{dry}}\right)+\mu_w\ln\left(\frac{r_e}{r_{BL}}\right)\right] \tag{23.48}$$

In Equation 23.48, $k_{rel,nw}\big|_{S_{nw}=1}$ is postulated by Burton et al. (2008) as the relative permeability of the nonwetting phase in the dryout zone, which includes the effect of salt precipitation, and is expected to have values in the range of 0.7–0.85. Additionally, in Equation 23.48, r_w, r_{dry}, r_{BL}, and r_e are the radius of the injection well, dryout zone, two-phase region, and drainage boundary, respectively. Based on a modified Buckley–Leverett theory for fractional flow, Burton et al. (2008) provide expressions for r_{dry} and r_{BL}, which are

$$r_{dry} = r_e\sqrt{V_D\nu_{D,dry}} \tag{23.49}$$

$$r_{BL} = r_e\sqrt{V_D\nu_{D,BL}} \tag{23.50}$$

In Equations 23.49 and 23.50, V_D is the dimensionless cumulative injected volume as defined in the following:

$$V_D = \int_0^t \frac{q(t)}{\pi\phi r_e^2 H}\,dt \tag{23.51}$$

and $\nu_{D,m}(m = dry, BL)$ are dimensionless front velocities given by

$$\nu_{D,m} = \frac{r_m^2}{r_e^2 V_D},\dagger \quad m = dry, BL \tag{23.52}$$

Burton et al. (2008) argue that, because the overall pressure drop is known or specified, the instantaneous permissible injection rate can be computed from Equation 23.48, which is a measure of the formation injectivity. Note that in deriving Equation 23.48, it has been assumed that injection happens at constant pressure, the effects of buoyancy can be ignored, and flow is in the Darcy flow regime.

Azizi and Cinar (2013) formulated the problem of injectivity estimation in terms of a maximum allowable injection rate (= $q_{\max}$) such that the pressure at the injection well will not exceed the

fracture pressure (= p_f). Using a conceptual model similar to that of Burton et al. (2008), but also accounting for the pressure dependence of compressibility, they showed that

$$q_{\max} = \frac{2\pi H k \bar{k}_{rel,nw}}{B_g \mu_{nw} \Phi}\left(p_f - p_i\right) \tag{23.53}$$

where

$\bar{k}_{rel,nw}$ is the relative permeability of the nonwetting phase in the dryout zone
B_g is the gas formation volume factor
p_i is the initial reservoir pressure

Azizi and Cinar (2013) developed expressions for the function Φ for different outer boundary conditions, for example, infinite, closed-boundary, and constant-pressure-boundary formation. They show that their bottomhole pressure and injectivity predictions match reasonably well with numerical simulation results. Based on their sensitivity analyses, it is observed that gas compressibility and gas relative permeability in the dryout zone have moderate effects on the evolution of bottomhole pressure and injectivity.

Note that the models of Burton et al. (2008) and Azizi and Cinar (2013) were developed based on the assumptions of applicability of Darcy and incompressible flow conditions. More recently, Mijic et al. (2014) have developed analytical solutions to describe the compositional and compressible CO_2–brine displacement to understand the impact of non-Darcy flow conditions on injectivity. Results obtained with their analytical solutions suggest that non-Darcy flow conditions, which are likely to prevail at high injection rates, lead to a reduction in salt precipitation. Mijic et al. (2014) also argue that conceptual models based on incompressible flow assumptions lead to overestimation of both pressure and frontal advance, depicting a less favorable injectivity scenario. Contrary to this, according to Mijic et al. (2014), compressible flow conditions increase gas saturations in the two-phase region and decreases gas-phase mobility, both of which have a positive impact on injectivity.

23.7 ASSESSMENT OF CO_2 MIGRATION RISK

A review of the progress made in modeling CO_2 migration in DSA is not complete without a discussion on the significant progress that has been made in modeling risks associated with GCS, more so because modeling and numerical simulations are essential tools for estimating risk (NETL, 2013). Duncan et al. (2009) identify four types of risks associated with an integrated CCS project, namely, (1) the operational risks of capturing, compressing, transporting, and injecting CO_2; (2) the risk of blowouts or rapid CO_2 release from wells; (3) the risk that CO_2 put into long-term geologic storage will leak into shallow aquifers and contaminate USDW; and (4) the risk that sequestered CO_2 will leak into the atmosphere, reversing the expected climate change benefits of GCS. In this section, we mainly focus on the modeling risk at GCS site, more specifically on the unplanned or unintended CO_2 migration out of a *storage complex*, which is defined as the storage reservoir or reservoirs and the surrounding rocks that can affect the overall integrity and security of storage (Research into Impacts and Safety in CO_2 Storage, RISCS, 2014).

In the context of unintended migration of CO_2 out of a storage location, the objective of risk analysis and assessment is to provide stakeholders with information for predicting the long-term fate of CO_2—including, but not limited to, the projected amount of long-term CO_2 storage, potential risks and consequences of CO_2 leakage from that area, and probabilistic leakage rates from specific geologic formations where CO_2 is injected. Over time, by comparing measured data to the predicted risk assessment, it may be possible to *history match* the predicted location of the CO_2 and its actual measured location (NETL, 2013). This history match becomes an important part of the process of

ensuring that a project is safely storing CO_2 and can be safely closed once the site has reached a point of verified negligible risk (NETL, 2013).

Since modeling and numerical simulation play a vital role in predicting the fate of the injected CO_2, they also form the backbone of risk assessment and/or risk management strategies for GCS. Modeling and numerical simulations are needed not only to evaluate and quantify risks, but also to optimize monitoring design and facilitate more effective site characterization. Monitoring and site characterization, in turn, are critical for developing improved models and associated risk analysis, and they also play a role in accounting and verification. In other words, an integrated and iterative procedure of predictive modeling, monitoring, and verification design, and risk analysis is needed to develop a defensible storage strategy—see NETL (2013) for a more comprehensive discussion on this iterative and integrated approach for risk assessment based on CO_2 migration modeling and simulation. NETL (2013) also provide a list of risk assessment tools that incorporate GCS risk assessment methodologies. In the following, we discuss three of these risk assessment methodologies, namely, the (1) the certification framework (CF; Oldenburg et al., 2009), (2) CO_2-PENS (Stauffer et al., 2009), and (3) the integrated assessment models (IAMs; Pawar et al., 2013a,b). Readers interested in the other available risk assessment methodologies associated with GCS are referred to NETL (2013) and the references therein.

23.7.1 Certification Framework

Oldenburg et al. (2009) developed a CF for certifying the safety and effectiveness of GCS sites. Oldenburg et al. (2009) argue that safety is achieved if CO_2 and displaced brine have no significant adverse impact on humans, other living things, resources, or the environment, and effectiveness is achieved if the site contains indefinitely the vast majority of the injected CO_2. In CF, storage region is defined as the 3D subsurface volume that is expected to contain the injected CO_2, and leakage is defined as its migration across the boundaries of the storage region. Postulating any vulnerable entity or entities (such as USDW) as compartments, CF defines CO_2 leakage risk as the risk to these compartments because of CO_2 migration. In this context, risk is defined as the product of the probability of an impact occurring and the consequences of that impact, where impact is a consequence to a compartment, with severity evaluated by proxy concentrations or fluxes. Finally, CF is based on the assumption that wells and faults are the only leakage conduits, that is, these are the only flow paths through which CO_2 can migrate into a compartment.

CF is a risk-based approach that uses two likelihoods to estimate the probability of leakage. The first is the likelihood of intersection of the CO_2 source with a conduit. The second is the likelihood of intersection of the conduit and a compartment. The product of these likelihoods is the probability of the given source-to-compartment leakage scenario. The risk associated with that leakage is the product of the likelihood of leakage and the impact of that leakage event. The probabilities of source/conduit and conduit/compartment intersections are site specific (e.g., they depend on the volume of CO_2 injection and the number of wells per unit area). Acceptable risks from CO_2 leakage will be those below a threshold provided by external sources such as regulators.

To simplify the determination of the extent of the injected CO_2 plume, a catalog of 3D reservoir simulations of CO_2 injection and migration was developed using the simulator GEM (see Section 23.4.1) and the Peng–Robinson equation of state for the CO_2–brine system. A large number of cases were simulated with a range of combinations of key reservoir properties, such as thickness, dip, porosity, permeability, permeability anisotropy, injection interval, and injection rate. Oldenburg et al. (2009) demonstrate the applicability of the CF approach on a hypothetical GCS site in a Texas Gulf Coast saline formation. Through its generality and flexibility, according to Oldenburg et al. (2009), CF can contribute to the assessment of the risk of CO_2 and brine leakage as part of the certification process for the licensing and permitting of GCS sites around the world, regardless of the specific regulations in place in any given country.

23.7.2 CO_2-PENS

Developed at LANL, CO_2-PENS (where PENS stands for Predicting Engineered Natural Systems) is a system model linking together process-level modules that describe the entire CO_2 sequestration pathway, starting from capture at a power plant and following the CO_2 through pipelines to the injection site and into the storage reservoir (Stauffer et al., 2009). After injection, simulation of CO_2 migration continues through the subsurface where it may mineralize, dissolve into brine, or react with wellbore casing or grout. CO_2 that may escape from the storage reservoir is followed along pathways that lead back toward the surface, including leaking wellbores and faults. The system level of CO_2-PENS manages global variables (e.g., CO_2 mass balance, CO_2 mass flow rate, and costs) and has been developed using Goldsim (2006).

The system-level model is backed by a number of process-level models such as the injection module or the wellbore-leakage module. These process-level models are created outside of the GoldSim framework to maintain flexibility. Because of the large number of variables involved in system-level calculations, some process-level calculations are abstracted or simplified to reduce simulation times and permit execution of multiple realizations necessary to gather statistical measures of overall system behavior. Both simple and complex process-level calculations are linked via dynamic link libraries (DLLs). These DLLs are used to perform such varied calculations as the development of a 3D CO_2 plume during injection, total flux through a leaking wellbore, fracture flow, mineral formation and dissolution, and atmospheric mixing.

In the initial phases of development in CO_2-PENS, the process models were often based on simple analytical solutions. For example, the extent of plume migration was calculated using the analytical solutions of Nordbotten et al. (2005)—see Equation 23.33. Similarly, injectivity was estimated assuming infinite storage formations as given in standard petroleum engineering literature (Matthews and Russel, 1967). Leakage was estimated based on the ELSA computer code (Nordbotten et al., 2009), which had been discussed in Section 23.6.3. Note that an economic module has also been coupled to the injection module in order to compare costs for different injection cases, based on the number of wells and drilling completion and maintenance costs. Because of its flexible structure, CO_2-PENS has evolved significantly over the years and is currently being used by the National Risk Assessment Partnership (NRAP) in the United States for GCS risk assessment within the framework of IAMs (Pawar et al., 2013a,b). We discuss these IAMs in Section 23.7.3.

23.7.3 Integrated Assessment Models

NRAP is using an IAM approach for implementing a system model for predicting long-term performance and to compute risk profiles at GCS sites. In this approach, a storage site is treated as a system made up of subsystems such as a storage reservoir, overlying seal, wellbores, faults or other transport pathways, and shallow permeable zones, including groundwater systems. The behavior of each of the components is predicted using reduced-order models (ROMs), which are based on detailed process-level simulations (Pawar et al., 2013a). For example, the storage reservoir ROM is used to predict time-dependent changes in reservoir pressure and saturation (at the reservoir–seal interface) resulting from CO_2 injection and is based on detailed simulations of the Kimberlina reservoir in southern San Joaquin basin in California (Wainwright et al., 2012). In all, 300 simulation runs were performed to capture the effect of variability in three parameters (porosity and permeability of the storage reservoir, and permeability of the seal). Sensitivity analysis on these parameters was used to further reduce the 300 runs to 54 representative runs that captured the effect of variability in the reservoir parameters. The time- and space-dependent reservoir pressure and saturation results from these 54 runs were brought into IAM as lookup tables.

Similarly, two wellbore ROMS (one each for open and cemented boreholes) were generated for calculating the CO_2/brine flow rate through wellbores as a function of the wellbore properties and the pressure and saturation at the reservoir–wellbore boundary. While the open borehole ROM is

developed using a lookup table for fluxes into the wellbores, which is based on detailed wellbore flow modeling with the T2Well simulator (Pan and Oldenburg, 2014), the cemented wellbore ROM is based on the FEHM simulator (Zyvoloski et al., 2012). The fault ROM was developed using results of detailed numerical simulations of CO_2/brine flow along a 2D fault connecting a storage reservoir and a shallow aquifer. The simulations were performed using the NUFT simulator (Hao et al., 2012), and ~900 simulation runs were performed by varying pressure and saturation at the intersection of fault with storage reservoir, as well as the physical properties of fault (porosity, permeability, and thickness), caprock (permeability), and shallow aquifer (permeability and porosity). Ultimately, the simulation results and the reduced variable set were used in a Problem Solving environment for Uncertainty Analysis and Design Exploration (PSUADE) package from LLNL (https://computation.llnl.gov/casc/uncertainty_quantification) to develop ROM for leakage through fault.

For the shallow aquifer, two ROMs, one for a confined sandstone aquifer and the other for an unconfined carbonate aquifer, have been developed. For the sandstone aquifer, a numerical simulation model based on the NUFT simulator (Hao et al., 2012) was developed using the data for high plains aquifers in the United States. For the carbonate aquifer, simulations were performed using the FEHM (Zyvoloski et al., 2012) and STOMP (White et al., 2012) simulators, and these simulations were based on data for Edwards's Aquifer in the United States. These numerical models were used to simulate changes in the pH and TDS in the aquifers due to CO_2 and brine leakage in the aquifers. A set of Monte Carlo runs were performed by varying values of multiple uncertain parameters, including aquifer hydraulic properties and geochemical properties. Results of the Monte Carlo simulations were used to develop ROMs for various quantities of interest using the PSUADE package. Note that in the first version of IAM, no ROMs were developed for the seal and atmosphere components.

The process-level models were integrated at the system level using CO_2-PENS (Stauffer et al., 2009), and the resulting IAM has been used to compute risk profiles for impacts due to CO_2 and brine leakage from a storage reservoir through wellbores. It has also been used to address questions such as the effect of wellbore density on CO_2 containment (Pawar et al., 2013a). Note that the ROMs discussed here have been called first-generation ROMs. A second generation of ROMs with increased complexities of the underlying processes is currently under development (e.g., Zhang and Pau, 2012; Houseworth et al., 2013; Zhang and Sahinidis, 2013; Carroll et al., 2014).

23.8 MODEL UNCERTAINTIES AND MODEL COMPARISON

GCS is unlikely to be perfectly effective or completely risk free. This is because there are still considerable uncertainties regarding storage capacity, injectivity, caprock or seal integrity, leakage pathways, impact on reservoir rock and formation fluids, and effectiveness of postinjection monitoring of the injected CO_2 plume (Wilson et al., 2007; Stauffer et al., 2009; Li et al., 2011; Seto and McRae, 2011; Dethlefsen et al., 2012). While convincing scientific research targeted at understanding, quantifying, and reducing these uncertainties is currently in progress to assure policy makers (and the public in general) that GCS is a viable technology and that it can be deployed with adequate safeguards, we focus on a different type of uncertainty in this section, namely, modeling uncertainty.

While modeling and numerical simulations are essential and critical tools for making a defensible case in favor of GCS, the modeling activity itself introduces significant uncertainty in the overall evaluation of the viability of a specific GCS scheme. Given the complexities of the underlying physical and chemical processes (see Section 23.2), building reliable conceptual models for flow and transport of CO_2 in the subsurface is a challenging task. Reiterating what we have discussed in detail in Sections 23.2 and 23.3, modelers must take into consideration a multiplicity of length scales (from pore scale to field scale), a wide range of timescales (e.g., different trapping mechanisms playing dominant roles at different times), the coupling between processes (e.g., fluid flow, heat transfer, geochemistry, and geomechanics), different model components (e.g., fluids and

their properties, caprocks, overburdens, faults and fractures, and wells), and the spatial variability of most model input parameters (and often limited knowledge about them) (Keating et al., 2010; Jahangiri and Zhang, 2011).

Consequently, modelers make different choices regarding the implementation of multiphase behavior of fluids and their equations of state, approaches for coupling of processes, modeling techniques, and selection/interpretation of site characterization and monitoring data. Such model choices often cause a wide range in predictions made by different models, even if each of these models is considering the same injection scenario at the same GCS site. In other words, model building itself is prone to bias associated with selecting a single set of domain-specific interpretations, processes, and mathematical systems. This uncertainty, referred to as model selection uncertainty, forms one of the greatest sources of uncertainty and risk for predictive modeling (Devooght, 1998). To reduce and ultimately eliminate these modeling uncertainties, benchmarking—including code comparison and model comparison exercises—has been undertaken in the context of flow and transport modeling at hypothetical and/or actual CO_2 injection sites. In the following, we discuss some of these benchmarking and model comparison studies with respect to GCS.

23.8.1 2004 LBNL Code Comparison Study

The details of this code comparison study can be found in Pruess et al. (2004). Ten different teams participated in this code comparison study and used their own numerical simulators, which included some of those discussed in Section 23.4—such as TOUGH2/EOS7C and TOUGHREACT, NUFT, STOMP, ECLIPSE, and GEM. Eight simplified test problems were selected that investigated advective and diffusive transport under multiphase flow conditions and partitioning of CO_2 between gas and aqueous phases. In addition, two out of those eight test problems also included solid minerals and oil phases. The test problems were designed to address basic processes in different potential storage formations including DSA. Most problems were for 1D homogeneous media, although a heterogeneous 2D problem was also included.

In this first code comparison study, when most of the numerical simulators for CO_2 storage were in their initial developmental stage, a few bugs were found in the simulators. Apart from that, substantial agreement was found between results predicted by different simulators, but there were also areas with only fair agreement, as well as some significant discrepancies. While most disagreements could be traced to differences in fluid property descriptions, some disagreements were also caused by effects from space and time discretization. Note that, even though the selected test problems were relatively simple, well-defined, and well-constrained, in comparison to flow and transport behavior in an actual storage situation, some uncertainties still existed in results obtained by different teams. The participating teams therefore recommended not only continued code improvement, including inclusion of coupled geochemical and geomechanical processes, but also further code comparison and benchmarking exercises in fully coupled 3D heterogeneous storage formations, constrained by actual field observations.

23.8.2 2009 Stuttgart Benchmark Study

Based on recommendations from Pruess et al. (2004), a group of researchers (Class et al., 2009), under the leadership of the University of Stuttgart, carried out another benchmark study, focusing on 3D geometries and considering the sophistication and improvement of the model concepts that have been achieved since the first code comparison study in 2004. The benchmark study involved 14 research teams and numerical simulators, which had among its mix the previously mentioned numerical simulators (e.g., DUMU^x, FEHM, NUFT, STOMP, TOUGH2, GEM, and ECLIPSE) and also the semi-analytical codes ELSA and VESA. The participating teams considered three benchmark problems, namely, (1) leakage of CO_2 into an overlying formation through a leaky well, (2) enhanced gas recovery through injection of CO_2, and (3) CO_2 plume spreading and dissolution

and storage mechanisms in a large-scale heterogeneous reservoir. For each problem, the extent of model domains, model input parameters, boundary conditions, simulation times, and expected model outputs were formulated and supplied to the participating teams. Note that the problems included in this benchmark study involved physical processes that were highly nonlinear, and the fluid properties and phase-transition behaviors were also nonlinear functions of pressure, temperature, salinity, and composition.

From this benchmark study, it was concluded that available models were capable of accounting for the relevant processes, parameters, and properties reasonably well with only minor quantitative deviations, notwithstanding the differences in the manner by which individual processes were implemented in different simulators. It was further observed that deviating results among different participating teams can be mostly sourced to errors in gridding, simple human oversight in dealing with input parameters, and different interpretations of problem specifications. Class et al. (2009) also opined that the uncertainties arising from the geological input data were likely to be (orders of magnitude) larger than the differences between simulation codes. Thus, according to Class et al. (2009), once gross errors have been eliminated, the contribution to the final uncertainty in simulator predictions from the code itself is likely to be relatively small. However, what is noteworthy from this benchmark study, where team members were given strictly defined problem specifications, is the observation that human oversight and differences in interpretation are the major causes for differences in model predictions, even when the systems being modeled are relatively simple.

23.8.3 2012 Bergen Model Comparison Study

A model comparison study was also carried out under the leadership of University of Bergen (Nordbotten et al., 2012), wherein participating teams were asked to model a hypothetical injection scenario involving 1 km long horizontal well at the bottom of a homogeneous formation with a constant tilt of 1%. The model domain extended 50 km downslope and 150 km upslope from the injection well and was 100 km wide. No-flow boundary conditions were to be applied at the top and bottom surfaces of the injection formation, while the outer boundary conditions were to be assumed hydrostatic. Modelers were asked to include an injection period of 20 years and a postinjection period lasting until all fluid movement had ceased. The modeling of fluid properties and physical processes were left open to the participants. Critical questions to be answered included phase partitioning, together with physical measures of extent such as farthest up-dip plume extent, and mean and variance of the location of the CO_2 phase.

According to Nordbotten et al. (2012), the benchmark problem could not be solved precisely with available computational technology and resources, and simplifications were needed, the extent of which (i.e., simplification) was left to the best scientific judgment of a group of participating researchers with significant numerical modeling expertise. Six research groups participated in this benchmark study, four of which used coupled physical models discretized on 3D numerical grids. The fifth group used vertically upscaled models, while the last group simplified the physics of the problem such that the resulting equations could be approximated using dedicated solvers with reasonable numerical accuracy. After analyzing the predictions from different groups for this simple, idealized injection scenario, Nordbotten et al. (2012) observed that the variability in model results was greater than expected. Nordbotten et al. (2012) identified four major sources for this variability in model predictions. All four sources (e.g., specific physical processes included or excluded, numerical modeling approach, method for upscaling, and interpretation of the problem definition and comparison metrics) are related to choices made by the modelers. This substantiates what we stated at the beginning of this section, that is, the choices made by modelers during conceptualizing a given injection scenario have significant impacts on model predictions, even when modeling a highly simplified system, and these choices are expected to cause significant uncertainties in actual field settings, unless properly constrained by field observation data.

23.8.4 2014 Princeton Model Comparison Study with Models of Varying Complexity

In this study (Huang et al., 2014), a suite of models with varying complexities were compared to determine the ability of each model to predict the pressure response of a very large formation, that is, the Canadian section of the mid-continent Basal Aquifer, covering an area of 811,000 km^2 and involving a total injection rate of 63 Mt per year. The authors considered five modeling approaches, which are, in descending order of complexity, (1) VESA with CTZ (see Sections 23.3.3, 23.3.4, and 23.6.3), (2) VESA with sharp interface (see Sections 23.3.4 and 23.6.3), (3) a single-phase brine injection simulator, (4) ELSA (see Section 23.6.3), and (5) Theis solution (Theis, 1935). Results obtained using these modeling approaches were evaluated both qualitatively and quantitatively—see Huang et al. (2014) for details of this comparison procedure. Huang et al. (2014) observed that the predictions from the three numerical simulators were quite similar to one another, which, according to them, indicated that simple numerical models, such as the single-phase numerical simulator, might be good enough to predict the pressure response over a large aquifer. Huang et al. (2014) also observed that the semi-analytical and analytical solutions did not compare well with the numerical models. They thus concluded that a simple superposition of the semi-analytical or analytical solution was not a sufficiently accurate tool for large DSA with heterogeneous parameters.

23.8.5 Sim-SEQ Model Comparison Study

Sim-SEQ is a model comparison study for GCS, initiated by USDOE, and led and coordinated by LBNL—see Mukhopadhyay et al. (2012b) for a discussion of the objectives and scope of Sim-SEQ. Briefly, Sim-SEQ is unique in that it is not a code comparison or benchmarking effort, and also because it involves an actual CO_2 field injection test. Unlike previous benchmarking efforts, Sim-SEQ engages in model comparison in a broader and comprehensive sense, allowing modelers the choice of interpretation of site characterization data, boundary conditions, rock and fluid properties, etc., in addition to their choice of simulator. In Sim-SEQ, 15 different modeling teams, 9 of which are from outside the United States, are engaged in building their own models for one specific CO_2 injection field test site located in the southwestern part of Mississippi. The complex geology of the site, its location in the water leg of a CO_2-EOR field with a strong water drive, and the presence of methane in the reservoir brine make this a challenging task, requiring the modelers to make a large number of choices about how to model various processes and properties of the system.

In Sim-SEQ, each model team starts with the same characterization data provided to them, but uses its own conceptual models and simulators to come up with model predictions, which can be iteratively refined with the observation data provided to them at later stages. The ultimate objective of Sim-SEQ is to make model-to-model and model-to-data comparisons, allowing us to understand and quantify model uncertainties. Sim-SEQ is an ongoing project, and at the time of writing this chapter, participating teams have developed their initial predictive models, that is, models that have been developed without the knowledge of field observation data, and limited model-to-model comparison has been completed (Mukhopadhyay et al., 2014). A preliminary uncertainty analysis of selected flow models have also been completed (Mukhopadhyay et al., 2013), using a generalized linear model approach and Akaike's (Akaike, 1974) information-criterion-based backward removal approach to identify the most significant parameters. It has been shown that differences in model conceptualization and interpretation of site characterization data cause a significant range in predictions. At present, modeling teams participating in Sim-SEQ are engaged in iteratively refining their conceptual models based on field observation data (e.g., pressure from injection and two observation wells, and CO_2 breakthrough time at the observation wells). It is expected that prediction uncertainties will eventually decrease when the model refinement and calibration (with field data) are complete.

23.9 SUMMARY

GCS in DSA is at present emerging as a viable GHG emission mitigation option. Modeling and numerical simulations, whose ultimate objective is to accurately predict the fate of the injected CO_2, are essential tools for assessing the feasibility of any GCS scheme. In this chapter, we reviewed the recent progress that had been made in modeling the migration of CO_2 in DSA at GCS sites. Beginning with a discussion of the physical and chemical processes controlling the fate of the injected CO_2, we provided an overview of the modeling approaches currently in use for predicting the flow and transport of CO_2. These modeling approaches included, at one extreme, 3D numerical simulators involving coupled flow, geochemical, and geomechanical processes, and, at the other extreme, simplified analytical and semi-analytical solutions, including the VE and sharp interface solutions. We discussed the main commercial and research numerical simulators currently in use for CO_2 flow modeling and briefly mentioned some of the simulators available for coupled reactive transport and geomechanical simulations.

Out of the available choices among research numerical simulators for CO_2 migration modeling in DSA, we selected the TOUGH2 simulator as an example and discussed in detail the mass and energy conservation equations, as well as the spatial and temporal discretization procedures, implemented in that simulator. We discussed the relevant fluid property modules in the TOUGH2 simulator, including the phase behavior of CO_2, and thermophysical properties of pure CO_2 and brine, and those of their mixtures. A critical component of modeling multiphase flow and transport is the constitutive relationships, such as the phase relative permeability and capillary pressure as functions of phase saturations. We provided a comprehensive review of the current status of relative permeability and capillary pressure measurement for the CO_2–brine system. We also discussed how these measured data could be incorporated into a numerical simulator either in the form of a lookup table or in the form of a mathematical equation.

The discussion on numerical simulation techniques and numerical simulators was followed by an extensive review of available analytical and semi-analytical solutions for estimating the extent of CO_2 plume migration, pressure buildup resulting from injection, vertical leakage into overlying shallow aquifers, storage efficiency, and injectivity. This discussion revealed the physical parameters that exerted the strongest influence and control over CO_2 migration in DSA and eventually determined the efficacy of any planned injection scheme. Injection of CO_2 into DSA has many inherent risks associated with it, and significant progress has been recently made in modeling and quantifying these risks, and confirming the safety and effectiveness of any storage scheme. We reviewed some of these risk assessment tools as well, including CF, CO_2-PENS, and IAM, which are system-level models based on many process-level models, developed using ROM.

In addition to the uncertainties associated with fully characterizing a geological site at scales relevant for GCS and over the large temporal scales needed for safe storage, the modeling activity itself is prone to uncertainty. For example, because of the complexities of the underlying processes, modelers often implement model simplifications, which differ from one modeler to another. Furthermore, interpretations of available site characterization and observation data also differ from one modeler to another. These uncertainties, arising from modeling activities and termed *modeling uncertainties* as a whole, constitute a significant risk. In order to reduce these modeling uncertainties, a number of benchmarking and model comparison studies have been undertaken with respect to GCS. We concluded this chapter by reviewing these benchmarking and model comparison studies, which included both hypothetical and actual injection scenarios, and assessing the current status of modeling uncertainties associated with CO_2 migration at GCS sites in DSA.

ACKNOWLEDGMENTS

The author thanks Curtis M. Oldenburg (LBNL) and Dan Hawkes (LBNL) for their constructive reviews of the draft manuscript. The author also thanks three anonymous reviewers for their critical comments on the draft manuscript. Assistance from Diana Swantek in preparing some of

the graphics included in this chapter is gratefully acknowledged. The author gratefully acknowledges partial financial support for writing this book chapter from the U.S. Department of Energy (USDOE). Funds were provided to LBNL through the USDOE Contract No. DE-AC02-05CH11231. The publisher, by accepting this book chapter for publication, acknowledges that the U.S. government retains a nonexclusive, paid-up, irrevocable, worldwide license to publish or reproduce the published form of this book chapter or allow others to do so for U.S. government purposes. The views expressed in this chapter are those of the author and do not necessarily reflect the views or policies of the USDOE or LBNL.

NOMENCLATURE

B_g	Gas formation factor
C_R	Specific heat capacity of the rock
$\mathbf{F}_\beta$	Flux vector for phase β
g	Acceleration due to gravity
H	Height or depth of a storage formation
$h(x, t)$	Vertical location of the migrating CO_2 front at a distance of x from the injection point and at time t
h_β	Specific enthalpy of phase β
k	Formation permeability
$\underline{\mathbf{k}}$	Permeability tensor
$k_{rel,nw}$	Relative permeability of nonwetting phase
$k_{rel,w}$	Relative permeability of wetting phase
$k_{rel,\beta}$	Relative permeability of phase β
L	Length of a storage formation
M^κ	Mass or energy accumulation term for component κ
P_C	Capillary pressure
P_β	Pressure in phase β
p_i	Initial formation pressure
p_f	Fracture pressure
p_{nw}	Pressure in nonwetting phase
p_w	Pressure in wetting phase
Q_0	Volumetric rate of CO_2 injection
$q(t)$	Variable injection rate of CO_2
$q_{\max}$	Maximum allowable injection rate
r	Radial distance
r_{BL}	Radius of the two-phase Buckley–Leverett zone
r_{dry}	Radius of the dryout zone
r_e	Radius of the outer drainage boundary
r_i	Radial location of the inner boundary of the moving CO_2 plume
r_o	Radial location of the outer boundary of the moving CO_2 plume
r_w	Radius of the injection well
S_{nw}	Saturation of nonwetting phase
S_{nwr}	Residual saturation of the nonwetting phase
S_s	Satiated saturation of wetting phase
S_w	Saturation of wetting phase
S_{wr}	Irreducible saturation of the wetting phase
S_β	Saturation of phase β
t	Time
t_{inj}	Duration of CO_2 injection

T	Temperature
U	Groundwater speed
u_β	Specific internal energy of phase β
$V_0(t)$	Total volume of CO_2 injected after time t
$\mathbf{v}_\beta$	Velocity vector for phase β
X_β^κ	Mass fraction of component κ in phase β

Greek Symbols

ε	Storage efficiency
ϕ	Porosity
λ_{nw}	Mobility ratio of nonwetting phase
λ_w	Mobility ratio of wetting phase
λ_β	Mobility ratio of phase β
μ_{nw}	Viscosity of nonwetting phase
μ_w	Viscosity of wetting phase
μ_β	Viscosity of phase β
ρ_{nw}	Density of nonwetting phase
ρ_w	Density of wetting phase
ρ_β	Density of phase β
Σ	Thermal conductivity
T	Dimensionless time
Ω	Capillary trapping coefficient
ξ	Dimensionless radial distance
$\zeta(\xi, \tau)$	Dimensionless location of the moving CO_2 front at radial distance ξ and at dimensionless time τ

REFERENCES

Akaike, H. (1974), New look at statistical-model identification, *IEEE Transactions on Automatic Control*, AC-19, 716–723.

Akbarabadi, M. and Piri, M. (2013), Relative permeability hysteresis and capillary trapping characteristics of supercritical CO2/brine systems: An experimental study at reservoir conditions, *Advances in Water Resources*, 52, 190–206.

Altunin, V.V. (1975), *Thermophysical Properties of Carbon Dioxide*, Publishing House of Standards, Moscow, Russia (in Russian), 551pp.

Andersen, G., Probst, A., Murray, L., and Butler, S. (1992), An accurate PVT model for geothermal fluids as represented by H_2O–NaCl–CO_2 mixtures, in *Proceedings of the 17th Workshop on Geothermal Reservoir Engineering*, Stanford, CA, pp. 239–248.

Avci, C. (1994), Evaluation of flow leakage through abandoned wells and boreholes, *Water Resources Research*, 30, 2565–2578.

Azizi, E. and Cinar, Y. (2013), Approximate analytical solutions for CO_2 injectivity into saline formations, *SPE Reservoir Evaluation and Engineering*, 16, 122–133.

Bachu, S. (2000), Sequestration of carbon dioxide in geological media: Criteria and approach for site selection, *Energy Conservation and Management*, 41, 953–970.

Bachu, S. (2008), CO_2 storage in geological media: Role, means, status and barriers to deployment, *Progress in Energy and Combustion Science*, 34, 254–273.

Bachu, S. (2013), Drainage and imbibition CO_2/brine relative permeability curves at in situ conditions for sandstone formations in western Canada, *Energy Procedia*, 37, 4428–4436.

Bachu, S. and Bennion, D.B. (2009), Interfacial tension between CO_2, freshwater, and brine in the range of pressure from (2 to 27) MPa, temperature from (20 to 125) degrees C, and water salinity from (0 to 334000) mg L^{-1}, *Journal of Chemical Engineering Data*, 54, 765–775.

Bachu, S., Bonijoly, D., Bradshaw, J., Burruss, R., Holloway, S., Christensen, N.P., and Mathiassen, O.M. (2007), CO_2 storage capacity estimation: Methodology and gaps, *International Journal of Greenhouse Gas Control*, 1, 430–443.

Bacon, D.H. (2013), Modeling long-term CO_2 storage, sequestration and cycling, in *Geological Storage of Carbon Dioxide (CO_2): Geosciences, Technologies, Environmental Aspects and Legal Frameworks*, Gluyas, J. and Mathias, S. (eds.), Woodhead Publishing, Philadelphia, PA, pp. 110–146.

Battistelli A., Calore, C., and Pruess, K. (1997), The simulator TOUGH2/EWASG for modeling geothermal reservoirs with brines and non-condensable gas, *Geothermics*, 26, 437–464.

Bennion, D.B. and Bachu, S. (2008), Drainage and imbibition relative permeability relationships for supercritical CO_2/brine and H_2S/brine systems in intergranular sandstone, carbonate, shale and anhydrite rocks. *SPE Reservoir Evaluation and Engineering*, 11, 487–496.

Bennion, D.B. and Bachu, S. (September 19–22, 2010), Drainage and imbibition relative permeability curves at reservoir conditions for carbonate formations, SPE-134028, in *SPE Annual Technical Conference and Exhibition*, Florence, Italy.

Benson, S., Pini, R., Reynolds, C., and Krevor, S.C.M. (2013), Relative permeability analyses to describe multiphase flow in CO_2 storage reservoirs, prepared for the Global CCS Institute, http://www.globalccsinstitute.com/publications/relative-permeability-analysis-describe-multi-phase-flow-co2-storage-reservoirs.

Bickle, M., Chadwick, A., Huppert, H.E., Hallworth, M., and Lyle, S. (2007), Modeling carbon dioxide accumulation at Sleipner: Implications for underground carbon storage, *Earth and Planetary Science Letters*, 255, 164–176.

Bikkina, P.K. (2011), Contact angle measurements of CO_2-water-quartz/calcite systems in the perspective of carbon sequestration, *International Journal of Greenhouse Gas Control*, 5, 1259–1271.

Birkholzer, J.T., Zhou, Q., and Tsang, C.-F. (2009), Large-scale impact of CO_2 storage in deep saline aquifers: A sensitivity study on pressure response in stratified systems, *International Journal of Greenhouse Gas Control*, 3, 181–194.

Burton, M., Kumar, N., and Bryant, S.L. (April 20–23, 2008), Time-dependent injectivity during CO_2 storage in aquifers, SPE-113937, in presented at *SPE/DOE Symposium on Improved Oil Recovery*, Society of Petroleum Engineers, Tulsa, OK.

Carroll, S.A., Mansoor, K., and Sun, Y. (2014), Second-generation reduced-order model for calculating groundwater impacts as a function of pH, total dissolved solids, and trace metal concentration, NRAP-TRS-III-002–2014, NRAP Technical Report Series, U.S. Department of Energy, National Energy Technology Laboratory, Morgantown, WV.

Celia, M.A. and Nordbotten, J.M. (2009), Practical modeling approaches for geological storage of carbon dioxide, *Ground Water* 47, 627–638.

Celia, M.A. and Nordbotten, J.M. (2011), How simple can we make models for CO_2 injection, and leakage? *Energy Procedia*, 4, 3857–3864.

Celia, M.A., Nordbotten, J.M., Court, B., Dobossy, M., and Bachu, S. (2011), Field-scale application of a semi-analytical model for estimation of CO_2 and brine leakage along old wells, *International Journal of Greenhouse Gas Control*, 5, 257–269.

Chadwick, R.A., Arts, R., Bentham, M., Eiken, O., Holloway, S., Kirby, G.A., Pearce, J.M., Williamson, J.P., and Zweigel, P. (2009), Review of monitoring issues and technologies associated with the long-term underground storage of carbon dioxide, in *Underground Gas Storage: Worldwide Experiences and Future Development in the UK and Europe*, D.J. Evans and R.A. Chadwick (eds.), Geological Society Special Publications 313, Geological Society of London, London, U.K., pp. 257–275.

Chalbaud, C., Robin, M., Lombard, J.-M., Bertin, H., and Egermann, P. (2010), Brine/CO_2 interfacial properties and effects on CO_2 storage in deep saline aquifers, *Oil and Gas Science and Technology*, 65, 541–555.

Chiquet, P., Broseta, D., and Thibeau, S. (2007a), Wettability alteration of caprock minerals by carbon dioxide, *Geofluids*, 7, 112–122.

Chiquet, P., Daridon, J.L., Broseta, D., and Thibeau, S. (2007b), CO_2/water interfacial tensions under pressure and temperature conditions of CO_2 geological storage, *Energy Conversion and Management*, 48, 736–744.

Chow, A. (2014), Ocean carbon sequestration by direct injection, in *CO_2 Sequestration and Valorization*, Morgado, C.R.V. and Esteves, V.P.P. (eds.), InTech Europe, Rijeka, Croatia.

Cihan, A., Birkholzer, J.T., and Zhou, Q. (2013), Pressure buildup and brine migration during CO_2 storage in multilayered aquifers, *Groundwater*, 51, 252–267.

Cihan, A., Zhou, Q., and Birkholzer, J.T. (2011), Analytical solutions for pressure perturbation and fluid leakage through aquitards and wells in multilayered aquifer systems, *Water Resources Research*, 47, W10504.

Class, H., Ebigbo, A., Helmig, R., Dahle, H., Nordbotten, J.M., Celia, M.A. et al. (2009), A benchmark study on problems related to CO_2 storage in geologic formations, *Computational Geosciences*, 13, 409–434.

Corey, A.T. (1954), The interrelation between gas and oil relative permeabilities, *Producers Monthly*, 19, 38–41.

Court, B., Bandilla, K.W., Celia, M.A., Janzen, A., Dobossy, M., and Nordbotten, J.M. (2012), Applicability of vertical-equilibrium and sharp-interface assumptions in CO_2 sequestration modeling, *International Journal of Greenhouse Gas Control*, 10, 134–147.

de Marsily, G. (1986), *Quantitative Hydrogeology*, Academic Press, Orlando, FL.

Dentz, M. and Tartakovsky, D.M. (2009a), Abrupt-interface solution for carbon dioxide injection into porous media, *Transport in Porous Media*, 79, 15–27.

Dentz, M. and Tartakovsky, D.M. (2009b), Response to "Comments on abrupt-interface solution for carbon dioxide injection into porous media by Dentz and Tartakovsky (2008)" by Lu et al., *Transport in Porous Media*, 79, 39–41.

Dethlefsen, F., Hasse, C., Ebert, M., and Dahmke, A. (2012), Uncertainties of geochemical modeling during CO_2 sequestration applying batch equilibrium calculations, *Environmental Earth Sciences*, 65, 1105–1117.

Devooght, J. (1998), Model uncertainty and model inaccuracy, *Reliability Engineering and System Safety*, 59, 171–185.

Dickson, J.L., Gupta, G., Horozov, T.S., Binks, B.P., and Johnston, K.P. (2006), Wetting phenomena at the CO_2/water/glass interface, *Langmuir*, 22, 2161–2170.

Dooley, J.J. (2011), Valuing national and basin level geologic CO_2 storage capacity assessments in a broader context, *International Journal of Greenhouse Gas Control*, 5, 177–178.

Doughty, C. (2007), Modeling geologic storage of carbon dioxide: Comparison of non-hysteretic and hysteretic characteristic curves, *Energy Conversion and Management*, 48, 1768–1781.

Duncan, I.J., Nicot, J.-P., and Choi, J.-W. (2009), Risk assessment for future CO_2 sequestration based CO_2 enhanced oil recovery in the US, *Energy Procedia*, 1, 2037–2042.

Ehlig-Economides, C. and Economides, M.J. (2010), Sequestering carbon dioxide in a closed underground volume, *Journal of Petroleum Science and Engineering*, 70, 123–130.

EPA (2008), 40 CFR parts 144 and 146—Federal requirements under the Underground Injection Control (UIC) Program for Carbon Dioxide (CO_2) Geologic Sequestration (GS) Wells; Proposed Rule, *Federal Register*, 73(144), July 25, 43492–43541.

Ferronato, M., Gambolati, G., Janna, C., and Teatini, P. (2010), Geomechanical issues of anthropogenic CO_2 sequestration in exploited gas fields, *Energy Conversion and Management*, 51, 1918–1928.

Flemisch, B., Darcis, M., Erbertseder, K., Faigle, B., Lauser, A., Mosthaf, K. et al. (2011), DUMUX: DUNE for multi-{Phase, Component, Scale, Physics,…} flow and transport in porous media, *Advances in Water Resources*, 34, 1102–1112.

Folger, P. (2013), *Carbon Capture and Sequestration (CCS): A Primer*, R42532, Congressional Research Service, http://www.crs.gov, Washington, DC.

Gale, J. (2004), Geological storage of CO_2: What do we know, where are the gaps, and what more needs to be done? *Energy*, 29, 1329–1338.

Garcia, J.E. (2003), Fluid dynamics of carbon dioxide disposal into saline aquifers, PhD thesis, University of California, Berkeley, CA.

Gasda, S.E., Nordtotten, J.M., and Celia, M.A. (2009), Vertical equilibrium with sub-scale analytical methods for geological CO_2 sequestration, *Computational Geosciences*, 13, 469–481.

Gaus, I. (2010), Role and impact of CO_2–rock interactions during CO_2 storage in sedimentary rocks, *International Journal of Greenhouse Gas Control*, 4, 73–89.

Gaus, I., Audigane, P., André, L., Lions, J., Jacquemet, N., Durst, P., Czernichowski-Lauriol, I., and Azaroual, M. (2008), Geochemical and solute transport modeling for CO_2 storage, what to expect from it? *International Journal of Greenhouse Gas Control*, 2, 605–625.

Gluyas, J. and Mathias, S. (2013), *Geological Storage of Carbon Dioxide (CO_2): Geosciences, Technologies, Environmental Aspects and Legal Frameworks*, Woodhead Publishing, Philadelphia, PA.

Golding, M.J., Neufeld, J.A., Hesse, M.A., and Huppert, H.E. (2011), Two-phase gravity currents in porous media, *Journal of Fluid Mechanics*, 678, 248–270.

Goldsim (2006), *Goldsim User's Guide*, Goldsim Technology Group, Issaquah, WA.

Gudmundsson, J.S. and Thrainsson, H. (1989), Power potential of two-phase geothermal wells, *Geothermics*, 18, 357–366.

Gunn, I. and Woods, A.W. (2011), On the flow of buoyant fluid injected into a confined, inclined aquifer, *Journal of Fluid Mechanics*, 672, 109–129.

Haas Jr., J.L. (1976), *Physical Properties of the Coexisting Phases and Thermochemical Properties of the H_2O Component in Boiling NaCl Solutions*, USGS Bulletin 1421-A, Washington, DC, 73pp.

Hammond, G.E., Lichtner, P.C., Lu, C., and Mills, R.T. (2012), PFLOTRAN: Reactive flow & transport code for use on laptops to leadership-class supercomputers, in *Groundwater Reactive Transport Models*, Zhang, F., Yeh, G.-T., and Parker, J.C. (eds.), Bentham Science Publishers, Oak park, IL, pp. 141–159.

Hao, Y., Sun, Y., and Nitao, J.J. (2012), Overview of NUFT: A versatile numerical model for simulating flow and reactive transport in porous media, in *Groundwater Reactive Transport Models*, Zhang, F., Yeh, G.-T., and Parker, J.C. (eds.), Bentham Science Publishers, Oak park, IL, pp. 212–239.

Hemker, C.J. and Maas, C. (1987), Unsteady flow to wells in a layered and fissured aquifer systems, *Journal of Hydrology*, 90, 231–249.

Hesse, M.A., Tchelepi, H.A., Cantwell, B.J., and Orr Jr., F.M. (2007), Gravity currents in horizontal porous layers: Transition from early to late self-similarity, *Journal of Fluid Mechanics*, 577, 363–383.

Houseworth, J., Wainwright, H., and Birkholzer, J. (2013), Assessment of decoupling wellbore leakage from reservoir flow in reduced-order models, NRAP-TRS-III-001-2013, NRAP Technical Report Series, U.S. Department of Energy, National Energy Technology Laboratory, Morgantown, WV.

Huang, X., Bandilla, K.W., Celia, M.A., and Bachu, S. (2014), Basin-scale modeling of CO_2 storage using models of varying complexity, *International Journal of Greenhouse Gas Control*, 20, 73–86.

Huppert, H.E. and Neufeld, J.A. (2014), The fluid mechanics of carbon dioxide sequestration, *Annual Review of Fluid Mechanics*, 46, 255–272.

Huppert, H.E. and Woods, A.W. (1995), Gravity driven flows in porous layers, *Journal of Fluid Mechanics*, 292, 55–69.

IPCC (2005), *IPCC Special Report on Carbon Dioxide Capture and Storage*, Cambridge University Press, New York.

IPCC (2014), Climate change 2014: Mitigation of climate change, working group III contribution to IPCC 5th assessment report, available at http://ipcc.ch/report/ar5/wg3/. (accessed March 20, 2014).

Jahangiri, H.R. and Zhang, D. (2011), Effect of spatial heterogeneity on plume distribution and dilution during CO_2 sequestration, *International Journal of Greenhouse Gas Control*, 5, 281–293.

Jiang, X. (2011), A review of physical modeling and numerical simulation of long-term geological storage of CO_2, *Applied Energy*, 88, 3557–3566.

Johnson, J.W., Nitao, J.J., and Knauss, K. (2004), Reactive transport modeling of CO_2 storage in saline aquifers to elucidate fundamental processes, trapping mechanisms and sequestration partitioning, *Geological Society, London, Special Publications*, 233, 107–128.

Juanes, R. and MacMinn, C.W. (2008), Upscaling of capillary trapping under gravity override: Application to CO_2 sequestration in aquifers, SPE-113496, in *SPE/DOE Symposium on Improved Oil Recovery*, Tulsa, OK.

Juanes, R., MacMinn, C., and Szulczewski, M. (2010), The footprint of the CO_2 plume during carbon dioxide storage in saline aquifers: Storage efficiency for capillary trapping at the basin scale, *Transport in Porous Media*, 82, 19–30.

Jung, J.-W. and Wan, J. (2012), Supercritical CO_2 and ionic strength effects on wettability of silica surfaces: Equilibrium contact angle measurements, *Energy and Fuels*, 26, 6053–6059.

Kang, Q., Lichtner, P.C., Viswanathan, H.S., and Abdel-Fattah, A.L. (2010), Pore-scale modeling of reactive transport involved in geologic CO_2 sequestration, *Transport in Porous Media*, 82, 197–213.

Kaszuba, J.P., Janecky, D.R., and Snow, M.G. (2003), Carbon dioxide reaction processes in a model brine aquifer at 200 degrees C and 200 bars: Implications for geologic sequestration of carbon, *Applied Geochemistry*, 18, 1065–1080.

Keating, E.H., Fessenden, J., Kanjorski, N., Koning, D.J., and Pawar, R.J. (2010), The impact of CO_2 on shallow groundwater chemistry: Observations at a natural analog site and implications for carbon sequestration, *Environmental Earth Sciences*, 60, 521–536.

Kharaka, Y.K., Cole, D.R., Hovorka, S.D., Gunter, W.D., Knauss, K.G., and Freifeld, B.M. (2006), Gas-water-rock interactions in Frio formation following CO_2 injection: Implications for the storage of greenhouse gases in sedimentary basins, *Geology*, 34, 577–580.

Kim, Y., Wan, J., Kneafsey, T.J., and Tokunaga, T.K. (2012), Dewetting of silica surfaces upon reactions with supercritical CO_2 and brine: Porescale studies in micromodels, *Environmental Science and Technology*, 46, 4228–4235.

Kolditz, O., Bauer, S., Bilke, L., Böttcher, N., Delfs, J.O., Fischer, T. et al. (2012), OpenGeoSys: An open-source initiative for numerical simulation of thermo-hydro-mechanical/chemical (THM/C) processes in porous media, *Environmental Earth Sciences*, 67, 589–599.

Kopp, A., Class, H., and Helmig, R. (2009), Investigations on CO_2 storage capacity in saline aquifers Part 2: Estimation of storage capacity coefficients, *International Journal of Greenhouse Gas Control*, 3, 277–287.

Krevor, S.C.M., Pini, R., Zuo, L., and Benson, S.M. (2012), Relative permeability and trapping of CO2 and water in sandstone rocks at reservoir conditions, *Water Resources Research*, 48, W02532.

Lake, L.W. (1996), *Enhanced Oil Recovery*, Prentice-Hall, Englewood Cliffs, NJ.

Lemmon, E.W., McLinden, M.O., and Friend, D.G. (2005), Thermophysical properties of fluid systems, in *NIST Chemistry WebBook*, Mallard, W.G. and Linstrom, P.J. (eds.), NIST Standard Reference Database Number 69, National Institute of Standards and Technology, Gaithersburg, MD (http://webbook.nist.gov).

Li, S., Zhang, Y., and Zhang, X. (2011), A study of conceptual model uncertainty in large-scale CO_2 storage simulation, *Water Resources Research*, 47, W05534.

Li, X., Boek, E., Maitland, G.C., and Trusler, J.P.M. (2012), Interfacial tension of (brines+CO_2): (0.864 NaCl+0.136 KCl) at temperatures between (298 and 448) K, pressures between (2 and 50) MPa, and total molalities of (1 to 5) mol kg^{-1}, *Journal of Chemical and Engineering Data*, 57, 1078–1088.

Lu, C., Lee, S., Han, W., McPherson, B., and Lichtner, P. (2009), Comments on "Abrupt-Interface Solution for Carbon dioxide Injection into Porous Media" by M. Dentz and D. Tartakovsky, *Transport in Porous Media*, 79, 29–37.

Mathias, S., Gluyas, J., Gonzalez, G., Bryant, S., and Wilson, D. (2013), On relative permeability data uncertainty and CO2 injectivity estimation for brine aquifers, *International Journal of Greenhouse Gas Control*, 12, 200–212, http://dx.

Mathias, S.A., González Martínez de Miguel, G.J., Thatcher, K.E., and Zimmerman, R.W. (2011), Pressure buildup during CO_2 injection into a closed brine aquifer, *Transport in Porous Media*, 89, 383–397.

Mathias, S.A., Hardisty, P.E., Trudell, M.R., and Zimmerman, R.W. (2009), Approximate solutions for pressure buildup during CO_2 injection in brine aquifers, *Transport in Porous Media*, 79, 265–284.

Matthews, C.S. and Russel, D.G. (1967), *Pressure Buildup and Flow Tests in Wells*, Monographs of the Society of Petroleum Engineers, Vol. 1, Society of Petroleum Engineers, New York.

Meyer, C.A., McClintock, R.B., Silvestri, G.J., and Spencer, R.C. (1993), *ASME Steam Tables*, 6th edn., The American Society of Mechanical Engineers, New York.

Michaelides, E.E. (1981), Thermodynamic properties of geothermal fluids, *Geothermal Resources Council Transactions*, 5, 361–364.

Mijic, A., LaForce, T.C., and Muggeridge, A.H. (2014), CO_2 injectivity in saline aquifers: The impact of non-Darcy flow, phase miscibility, and gas compressibility, *Water Resources Research*, 50, 4163–4185.

Monea, M., Knudsen, R., Worth, K., Chalaturnyk, R., White, D., Wilson, M., Plasynski, S., Mcilvried, H.G., and Srivastava, R.D. (2013), Considerations for monitoring, verification, and accounting for geologic storage of CO_2, in *Carbon Sequestration and Its Role in the Global Carbon Cycle*, Mcpherson, B.J. and Sundquist, E.T. (eds.), American Geophysical Union, Washington, DC, pp. 303–316.

Mualem, Y.A. (1976), New model for predicting the hydraulic conductivity of unsaturated porous media, *Water Resources Research*, 12, 513–522.

Mukhopadhyay, S., Birkholzer, J.T., Nicot, J.-P., and Hosseini, S.A. (2012b), A model comparison initiative for a CO_2 injection field test: An introduction to Sim-SEQ, *Environmental Earth Sciences*, 67, 601–611.

Mukhopadhyay, S., Doughty, C.A., Bacon, D.H., Li, J., Wei, L., Yamamoto, H., Gasda, S.E., Hosseini, S.A., Nicot, J.-P., and Birkholzer, J.T. (2015), The Sim-SEQ project: Comparison of selected flow models for the S-3 Site, *Transport in Porous Media*.

Mukhopadhyay, S., Hou, Z., Gosink, L., Bacon, D., Doughty, C., Li, J. et al. (2013), Model comparison and uncertainty quantification for geologic carbon storage: The Sim-SEQ initiative, *Energy Procedia*, 37, 3867–3874.

Mukhopadhyay, S., Yang, S.-Y., and Yeh, H.-D. (2012a), Pressure buildup during supercritical carbon dioxide injection from a partially penetrating borehole into gas reservoirs, *Transport in Porous Media*, 91, 889–911.

Narasimhan, T.N. and Witherspoon, P.A. (1976), An integrated finite difference method for analyzing fluid flow in porous media, *Water Resources Research*, 12, 57–64.

NETL (2012), *The 2012 United States Carbon Storage and Utilization Atlas*, 4th edn. (Atlas IV), US Department of Energy, Washington, DC, http://www.netl.doe.gov/research/coal/carbon-storage/atlasiv.

NETL (2013), Risk analysis and simulation for geologic carbon storage, DOE/NETL-2013/1603, National Energy Technology Laboratory, Morgantown, WV, http://www.netl.doe.gov/File%20Library/Research/Carbon-Storage/Project-Portfolio/BPM_RiskAnalysisSimulation.pdf.

Nordbotten, J.M. and Celia, M.A. (2006), Similarity solutions for fluid injection into confined aquifers, *Journal of Fluid Mechanics*, 561, 307–327.

Nordbotten, J.M. and Celia, M.A. (2011), *Geological Storage of CO_2: Modeling Approaches for Large-Scale Simulations*, John Wiley & Sons, Inc., Hoboken, NJ.

Nordbotten, J.M., Celia, M.A., and Bachu, S. (2004), Analytical solutions for leakage rates through abandoned wells, *Water Resources Research*, 40, W04204.

Nordbotten, J.A., Celia, M.A., Bachu, S., and Dahle, H. (2005a), Semianalytical solution for CO_2 leakage through an abandoned well, *Environmental Science and Technology*, 39, 602–611.

Nordbotten, J.M., Celia, M.A., and Bachu, S. (2005b), Injection and storage of CO_2 in deep saline aquifers: Analytical solution for CO_2 plume evolution during injection, *Transport in Porous Media*, 58, 339–360.

Nordbotten, J.M., Kavetski, D., Celia, M.A., and Bachu, S. (2009), Model for CO_2 leakage including multiple geological layers and multiple leaky wells, *Environmental Science and Technology*, 43, 743–749.

Nordbotten, J.M., Flemisch, B., Gasda, S.E., Nilsen, H.M., Fan, Y., Pickup, G.E. et al. (2012), Uncertainties in practical simulation of CO_2 storage, *International Journal of Greenhouse Gas Control*, 9, 234–242.

Obi, E.-O.I. and Blunt, M.J. (2006), Streamline-based simulation of carbon dioxide storage in a North Sea aquifer, *Water Resources Research*, 42, W03414.

Okwen, R.T., Stewart, M.T., and Cunnigham, J.A. (2010), Analytical solution for estimating storage efficiency of geologic sequestration of CO_2, *International Journal of Greenhouse Gas Control*, 4, 102–107.

Olajire, A.A. (2013), A review of mineral carbonation technology in sequestration of CO_2, *Journal of Petroleum Science and Engineering*, 109, 364–392.

Oldenburg, C.M., Bryant, S.L., and Nicot, J.-P. (2009), Certification framework based on effective trapping for geologic carbon sequestration, *International Journal of Greenhouse Gas Control*, 3, 444–457.

Oldenburg, C.M., Moridis, G.J., Spycher, N., and Pruess, K. (2004), EOS7C version 1.0: TOUGH2 module for carbon dioxide or nitrogen in natural gas (methane) reservoirs, Report LBNL-56589, Lawrence Berkeley National Laboratory, Berkeley, CA.

Olivella, S., Gens, A., Carrera, J., and Alonso, E.E. (1996), Numerical formulation for a simulator (CODE_BRIGHT) for the coupled analysis of saline media, *Engineering Computations*, 13, 87–112.

Oruganti, Y., Gupta, A.K., and Bryant, S.L. (2011), Analytical estimation of risk due to pressure buildup during CO_2 injection in deep saline aquifers, *Energy Procedia*, 4, 4140–4147.

Pacala, S. and Socolow, R. (2004), Stabilization wedges: Solving the climate problem for the next 50 years with current technologies, *Science*, 305, 968–972.

Pan, L. and Oldenburg, C.M. (2014), T2Well—An integrated wellbore-reservoir simulator, *Computers and Geosciences*, 65, 46–55.

Pawar, R., Bromhal, G., Dilmore, R., Foxall, B., Jones, E., Oldenburg, C., Stauffer, P., Unwin, S., and Guthrie, G. (2013a), Quantification of risk profiles for atmospheres and groundwater, NRAP-TRS-III-003-2013, NRAP Technical Report Series, U.S. Department of Energy, National Energy Technology Laboratory, Morgantown, WV.

Pawar, R., Bromhal, G., Dilmore, R., Foxall, B., Jones, E., Oldenburg, C., Stauffer, P., Unwin, S., and Guthrie, G. (2013b), Quantification of risk profiles and impacts of uncertainties as part of US DOE's National Risk Assessment Partnership (NRAP), *Energy Procedia*, 37, 4765–4773.

Pentland, C.H., El-Maghraby, R., Iglauer, S., and Blunt, M.J. (2011), Measurements of the capillary trapping of supercritical carbon dioxide in Berea sandstone, *Geophysical Research Letters*, 38, L06401.

Perrin, J.C. and Benson, S.M. (2010), An experimental study on the influence of sub-core scale heterogeneities on CO_2 distribution in reservoir rocks, *Transport in Porous Media*, 82, 93–109.

Phillips, S.L., Igbene, A., Fair, J.A., Ozbek, H., and Tavana, M. (1981), *A Technical Databook for Geothermal Energy Utilization*, LBL-12810, Lawrence Berkeley National Laboratory, Berkeley, CA.

Pini, R., Krevor, S.C.M., and Benson, S.M. (2012), Capillary pressure and heterogeneity for the CO_2/water system in sandstone rocks at reservoir conditions, *Advances in Water Resources*, 38, 48–59.

Plasynski, S.I., Litynski, J.T., McIlvried, H.G., Vikara, D.M., and Srivastava, R.D. (2011), The critical role of monitoring, verification, and accounting for geologic carbon dioxide storage projects, *Environmental Geosciences*, 18, 19–34.

Plug, W.J. and Bruining, J. (2007), Capillary pressure for the sand-CO_2-water system under various pressure conditions: Application to CO_2 sequestration, *Advances in Water Resources*, 30, 2339–2353.

Pruess, K. (2013), ECO2M: A TOUGH2 fluid property module for mixtures of water, NaCl, and CO_2, including super-and sub-critical conditions, and phase change between liquid and gaseous CO_2, LBNL-4590E, Lawrence Berkeley National Laboratory, Berkeley, CA.

Pruess, K., Garcia, J., Kovscek, T., Oldenburg, C., Rutqvist, J., Steefel, C., and Xu, T. (2004), Code comparison builds confidence in numerical simulation models for geologic disposal of CO_2, *Energy*, 29, 1431–1444.

Pruess, K. and Müller, N. (2009), Formation dry-out from CO_2 injection into saline aquifers: 1. Effects of solids precipitation and their mitigation, *Water Resources Research*, 45, W03402.

Pruess, K., Oldenburg, C.M., and Moridis, G.J. (2012), *TOUGH2 Users Guide*, Version 2.0, LBNL-43134, Lawrence Berkeley National Laboratory, Berkeley, CA.

Pruess, K. and Spycher, N. (2007), ECO2N—A fluid property module for the TOUGH2 code for studies of CO_2 storage in deep saline aquifers, *Energy Conversion and Management*, 48, 1761–1767.

Reagan, M.T., (2006), *WebGasEOS 1.0 User Guide*, LBNL/PUB-3188, Lawrence Berkeley National Laboratory, Berkeley, CA.

Reid, R.C., Prausnitz, J.M., and Poling, B.E. (1987), *The Properties of Gases and Liquids*, McGraw-Hill, New York.

RISCS (2014), Types of leakage, *A Guide to Potential Impacts of Leakage from CO_2 Storage*, Pearce, J.M. (ed.), British Geological Survey, Nottingham, U.K., www.riscs-CO2.eu.

Rutqvist, J. (2011), Status of the TOUGH-FLAC simulator and recent applications related to coupled fluid flow and crustal deformations, *Computers and Geosciences*, 37, 739–750.

Rutqvist, J. (2012), The geomechanics of CO_2 storage in deep sedimentary formations, *Geotechnical and Geological Engineering*, 30, 525–551.

Rutqvist, J., Birkholzer, J.T., Cappa, F., and Tsang, C.-F. (2007), Estimating maximum sustainable injection pressure during geological sequestration of CO_2 using coupled fluid flow and geomechanical fault-slip analysis, *Energy Conversion and Management*, 48, 1798–1807.

Saripalli, P. and McGrail, P. (2002), Semi-analytical approaches to modeling deep well injection of CO_2 for *geological* sequestration, *Energy Conversion and Management*, 43, 185–198.

Seto, C.J. and McRae, G.J. (2011), Reducing risk in basin scale CO_2 sequestration: A framework for integrated monitoring design, *Environmental Science & Technology*, 45, 845–849.

Shao, H., Ray, J.R., and Jun, Y.S. (2011), Effects of salinity and the extent of water on supercritical CO_2-induced phlogopite dissolution and secondary mineral formation, *Environmental Science and Technology*, 45, 1737–1743.

Smit, B., Reimer, J.A., Oldenburg, C.M., and Bourg, I.C. (2014), *Introduction to Carbon Capture and Sequestration*, Imperial College Press, London, U.K.

Song, H., Huang, G., Li, T., Zhang, Y., and Lou, Y. (2014), Analytical model of CO_2 storage efficiency in saline aquifer with vertical heterogeneity, *Journal of Natural Gas Science and Engineering*, 18, 77–89.

Span, R. and Wagner, W. (1996), A new equation of state for carbon dioxide covering the fluid region from the triple-point temperature to 1100 K at pressures up to 800 MPa, *Journal of Physical and Chemical Reference Data*, 25, 1509–1596.

Spycher, N. and Pruess, K. (2005), CO_2-H_2O mixtures in the geological sequestration of CO_2: II Partitioning in chloride brines at 12–100°C and up to 600 bars, *Geochimica and Cosmochimica Acta*, 69, 13, 3309–3320.

Stauffer, P.H.,Viswanathan, H.S., Pawar, R.J., and Guthrie, G.D. (2009), A system model for geologic sequestration of carbon dioxide, *Environmental Science and Technology*, 43, 565–570.

Sun, A.Y., Zeidouni, M., Nicot, J.-P., Lu, Z., and Zhang, D. (2013), Assessing leakage detectability at geologic CO_2 sequestration sites using the probabilistic collocation method, *Advances in Water Resources*, 56, 49–60.

Szulczewski, M.L., McMinn, C.W., Herzog, H.J., and Juanes, R. (2012), Lifetime of carbon capture and storage as a climate-change mitigation technology, *Proceedings of the National Academy of Sciences USA*, 109, 5185–5189.

Teatini, P., Castelleto, N., and Gambolati, G. (2014), 3D geomechanical modeling for CO_2 geological storage in faulted formations: A case study in an offshore northern Adriatic reservoir, Italy, *International Journal of Greenhouse Gas Control*, 22, 63–76.

Teatini P., Gambolati, G., Ferronata, M., Settari, A., and Walters, D. (2011), Land uplift due to subsurface fluid injection, *Journal of Geodynamics*, 51, 1–16.

Theis, C.V. (1935), The relation between lowering of the piezometric surface and the rate and duration of discharge of a well using ground water storage, in *Transactions of American Geophysical Union, 16th Annual Meeting*, Part 2, pp. 519–524.

Tokunaga, T.K., Wan, J., Jung, J.-W., Kim, T.W., Kim, Y., and Dong, W. (2013), Capillary pressure and saturation relations for supercritical CO_2 and brine in sand: High-pressure Pc(Sw) controller/meter measurements and capillary scaling predictions, *Water Resources Research*, 49, 4566–4579.

USGS (2013), *National Assessment of Geologic Carbon Dioxide Storage Resources—Data*, USGS, Reston, VA, http://pubs.usgs.gov/ds/774/.

van der Meer, L.G.H. (1995), CO_2 storage efficiency of aquifers, *Energy Conversion and Management*, 36, 513–518.

van Genuchten, M.Th. (1980), A closed-form equation for predicting the hydraulic conductivity of unsaturated soils, *Soil Science Society of America Journal*, 44(5), 892–898.

Vilarrasa, V., Bolster, D., Dentz, M., Olivella, S., and Carrera, J. (2010), Effects of CO_2 compressibility on CO_2 storage in deep saline aquifers, *Transport in Porous Media*, 85, 619–639.

Vilarrasa, V, Carrera, J., Bolster, D., and Dentz, M. (2013), Semianalytical solution for CO_2 plume shape and pressure evolution during CO_2 injection in deep saline formations, *Transport in Porous Media*, 97, 43–65.

Wainwright, H., Finsterle, S., Zhou, Q., and Birkholzer, J.T. (2012), Modeling the performance of large-scale CO_2 storage systems: A comparison of different sensitivity analysis methods, NRAP-TRS-III-002-2012; NRAP Technical Report Series; U.S. Department of Energy, National Energy Technology Laboratory, Morgantown, WV.

Wang, S., Edwards, I.M., and Clarens, A.F. (2013), Wettability phenomena at the CO_2-brine-mineral interface: Implications for geologic carbon sequestration, *Environmental Science and Technology*, 47, 234–241.

Wang, S., Vafai, K., and Mukhopadhyay, S. (2014), Two-phase CO_2 migration in tilted aquifers in the presence of groundwater flow, *International Journal of Heat and Mass Transfer*, 77, 717–729.

White, M.D., Bacon, D.H., McGrail, B.P., Watson, D.J., White, S.K., and Zhang, Z.F. (2012), *STOMP Subsurface Transport Over Multiple Phases: STOMP-CO2 and STOMP-CO2e Guide: Version 1.0*, Rep. PNNL-21268, Pacific Northwest National Laboratory, Richland, WA.

White, M.D. and Fang, Y. (2012), STOMP-ECKEChem: An engineering perspective on reactive transport in geologic media, in *Groundwater Reactive Transport Models*, Zhang, F., Yeh, G.-T., Parker, J.C. (eds.), Bentham Science Publishers, Oak Park, IL, pp. 112–140.

Wilson, E., Friedmann, S.J., and Pollak, M.F. (2007), Research for deployment: Incorporating risk, regulation, and liability for carbon capture and sequestration, *Environmental Science and Technology*, 41, 5945–5952.

Xu, T., Sonnenthal, E., Spycher, N., Zhang, G., Zheng, L., and Pruess, K. (2012), TOUGHREACT: A simulation program for subsurface reactive chemical transport under non-isothermal multiphase flow conditions, in *Groundwater Reactive Transport Models*, Zhang, F., Yeh, G.-T., Parker, J.C. (eds.), Bentham Science Publishers, Oak Park, IL, pp. 74–95.

Xu, T., Zheng, L., and Tian, H. (2011), Reactive transport modeling for CO_2 geological sequestration, *Journal of Petroleum Science and Engineering*, 78, 765–777.

Yortsos, Y.C. (1995), A theoretical analysis of vertical flow equilibrium, *Transport in Porous Media*, 18, 107–129.

Zeidouni, M. (2011), Analytical and inverse models for leakage characterization of CO_2 storage, PhD thesis, University of Calgary, Calgary, Alberta, Canada.

Zeidouni, M. and Pooladi-Darvish, M. (2012), Leakage characterization through above-zone pressure monitoring: 1—Inversion approach, *Journal of Petroleum Science and Engineering*, 98–99, 95–106.

Zeidouni, M., Pooladi-Darvish, M., and Keith, D.W. (2011), Analytical models for determining pressure change in an overlying aquifer due to leakage, *Energy Procedia*, 4, 3833–3840.

Zhang, D. and Song, J. (2014), Mechanisms for geological carbon sequestration, *Procedia IUTAM*, 10, 319–327.

Zhang, R. (2013), Numerical simulation of thermal-hydrological-mechanical-chemical processes during CO_2 geological sequestration, PhD thesis, Colorado School of Mines, Boulder, CO.

Zhang, Y. and Pau, G. (2012), Reduced-order model development for CO_2 storage in brine reservoirs, NRAP-TRS-III-005-2012, NRAP Technical Report Series, U.S. Department of Energy, National Energy Technology Laboratory, Morgantown, WV.

Zhang, Y. and Sahinidis, N.V. (2013), Developing surrogate models for CO_2 Sequestration using polynomial chaos expansion, NRAP-TRS-III-004–2013; NRAP Technical Report Series, U.S. Department of Energy, National Energy Technology Laboratory, Morgantown, WV.

Zhou, Q. and Birkholzer, J.T. (2011), On scale and magnitude of pressure build-up induced by large-scale geologic storage of CO_2, *Greenhouse Gases: Science and Technology*, 1, 11–20.

Zhou, Q., Birkholzer, J.T., Mehnert, E., Lin, Y.F., and Zhang, K. (2010), Modeling basin- and plume-scale processes of CO_2 storage for full-scale deployment, *Ground Water*, 48, 494–514.

Zhou, Q., Birkholzer, J.T., and Tsang, C.-F. (2009), A semi-analytical solution for large-scale injection induced pressure perturbation and leakage in a laterally bounded aquifer-aquitard system, *Transport in Porous Media*, 78, 127–148.

Zuo, L., Krevor, S., Falta, R.W., and Benson, S.M. (2012), An experimental study of CO_2 exsolution and relative permeability measurements during CO_2 water depressurization, *Transport in Porous Media*, 91, 459–78.

Zyvoloski, G.A., Robinson, B.A., Dash, Z.V., Kelkar, S., Viswanathan, H.S., Pawar, R.J., and Stauffer, P.H. (2012), *Software Users Manual (UM) for the FEHM Application*, Version 3.1–3.x, LA-UR-12-24493, Los Alamos National Laboratory, Los Alamos, NM.

24 Groundwater Flows and Velocity Measurements

Shigeo Kimura

CONTENTS

24.1 Introduction 841
24.2 Groundwater Velocity and Darcy's Law 844
24.2.1 Darcy's Law 844
24.2.2 Hydraulic Conductivity and Permeability 846
24.3 Hydraulic Conductivity and Porosity Measurements 847
24.3.1 Slug and Bail Test 847
24.3.2 Well Test 848
24.3.2.1 Storativity and Transmissivity 848
24.3.2.2 Theoretical Background of Well Test 850
24.3.3 Porosity 855
24.4 Groundwater Velocity Measurements 855
24.4.1 Velocity Defined in Large Scale 855
24.4.2 Velocity Measurements in Small Scale 856
24.4.2.1 Point Dilution Test 857
24.4.2.2 Point Velocity Probe Based on Tracer Transport 858
24.4.2.3 Thermal Method 860
24.5 Conclusion 864
Acknowledgment 865
Nomenclature 865
References 866

24.1 INTRODUCTION

Various data, although relatively unpublicized, exist in support of the quantitative importance of groundwater relative to other components of the hydrologic cycle on the earth. With reference to Table 24.1, excluding the large amount of the earth's water resting in the oceans and seas at high levels of salinity, groundwater accounts for about one-third of the freshwater resources of the world. If we limit our consideration to the liquid-phase freshwater, groundwater will account for almost the total volume available for use. If we consider only the most active groundwater regimes, for example, in subsurface reservoirs of good hydraulic permeability, water quantity will be reduced just to about two-thirds of the total amount. Considering this, the freshwater breakdown comes to 95% of subsurface groundwater; 3.5% of surface water such as lakes, swamps, reservoirs, and river channels; and 1.5% of soil moisture. From the usability point of view, however, this volumetric superiority of subsurface groundwater should be somewhat moderated by the average residence times listed in the right column of the table. River water has a turnover time on

TABLE 24.1
Water Balance on the Earth

Parameter	Volume Percentage (%)	Residence Time
Oceans and seas	97.5	~4,000 years
Lakes and reservoir	<0.01	~10 years
River channels	<0.01	~2 weeks
Groundwater	0.70	2 weeks to 10,000 years
Icecaps and glaciers	1.70	10–1,000 years
Atmospheric water	<0.01	~10 days

Source: Data are taken from Freeze, R.A. and Cherry, J.A., *Groundwater*, Prentice Hall, Upper Saddle River, NJ, 1979; Shiklomanov, I.A. (ed.), *World Water Resources: A New Appraisal and Assessment for the 21st Century*, UNESCO, Paris, France, 1998.

the order of 2 weeks in average. On the other hand, groundwater moves at much slower speeds, with residence times spanning from tens to thousands of years [1–4].

In the field of hydrology, the continuous circulation of water among ocean, atmosphere, and land is known as the *hydrologic cycle*, and groundwater flows play an important role in order to close the cycle as shown in Figure 24.1. Focusing on the land-based portion of the cycle, inflow arrives as *precipitation*, in the form of rainfall or snowmelt. Outflow takes place as runoff and as *evapotranspiration*; the latter is a combination of evaporation from open bodies of water, evaporation from ground surfaces, and transpiration from the subsurface soils by plants. Precipitation delivers water to such streams as *surface runoff* or *overland flow*, and eventually to rivers and channels on the land surface, and by subsurface flow routes, as groundwater *base flow* following *infiltration* into the permeable soil. The figure of the hydrologic cycle makes it clear that a mass balance in a watershed must be considered as a combination of both the surface drainage area and the parcel of subsurface soils and geological formations that underlie it. Therefore, the

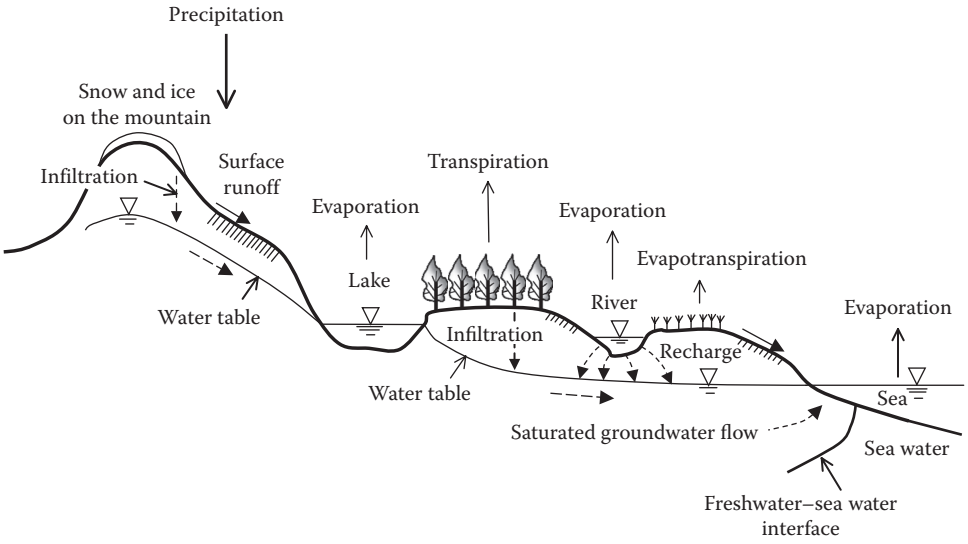

FIGURE 24.1 Hydrologic cycle in land. (Redrawn from Bear, J., *Hydraulics of Groundwater*, McGraw-Hill, New York, 1979.)

amount of temporal and spatial flow rates in rivers and channels can be determined only after evaluating the recharges from and discharges to the subsurface base flows. The interaction between the surface streams and the subsurface base flows is one of the hottest research topics in hydrogeology today [5,6].

There are a variety of concerns regarding groundwater today, and it is worth pointing out that nearly all of them originate from the characteristic nature of groundwater flows, that is, the very slow velocity of the base flow, typically less than 1 m/day in the plains. In the following, we will look into individual problems in some detail and show how vital the information of groundwater velocity is.

Groundwater as a resource: The primary motivation for groundwater study has come from recognition of its importance as a resource. In the United States and Canada, the significant role of groundwater as a component of national water use is evidenced from various sources of statistical surveys [2,7]. According to the reports, groundwater provides about 20%, and the rest is from surface water. It is interesting to note that this 20% groundwater ratio to the total water use is the same as in Japan [8]. The most crucial parameter in respect to the development of the water resources, that is, extracting water from the subsurface water reservoir, which is often called *aquifer*, is the hydraulic conductivity or permeability of the reservoir matrix (soils and rocks). In fact, the estimated amount of water present in the reservoir is not nearly as important as the reservoir permeability for development purposes. The proper amount of water extraction from a particular aquifer can be determined from the mass balance between the water production rate and the recharge rate expected from the outer boundaries of the aquifer when the production is under way.

Groundwater contamination: Landfills, sludge ponds, evaporation ponds, sewage lagoons, and deep-well injection are common ways to dispose of the waste generated by our economic activities. The growth of economic activities in the last half a century, however, has begun to produce quantities of waste that are far greater than what the natural environment can easily absorb by dilution and decomposition. In particular, the mentioned disposals may threaten the subsurface environment and cause possible subsurface-water pollution [9]. In occurrences of pollution, the process that controls the migration of dissolved contaminants in groundwater is very characteristic for its invisibility and slow spreading, in comparison with other processes, such as surface-water pollution, air pollution, and ocean pollution. The very small velocity of groundwater, typically from 0.1 to 1 m/day, is largely responsible for this characteristic property. Therefore, information about groundwater velocity vectors is critical in order to predict the spreading scale and direction of the pollutants. When pollution is detected in the groundwater, environmental remediation is very difficult and often costly [10]. In fact, the most serious problem that the Fukushima nuclear site is currently facing after its calamity is how to control the influx of groundwater to the site, which continuously produces radiation-contaminated water.

Geotechnical problems: It is not uncommon to find very efficient groundwater flow systems penetrating rock formations in geotectonically active areas, such as California, New Zealand, and Japan. Near such a natural groundwater flow system, tunnel constructions are often held up for many months because of the massive unexpected inflows of groundwater through the highly fractured fault zones [11]. Such highly permeable zones may be discovered, however, by measuring the local groundwater flow directions in their vicinity and detecting the particular behavior of the flows. Due to extreme weather conditions, as recently observed, preparedness for unprecedentedly heavy rainfall must take place. In such cases, increased groundwater pressures in hillside slopes can cause

geo-mechanical instability and trigger large-scale landslides that can take many lives [12,13]. Monitoring and detection of sudden increases in groundwater flows can be very helpful in order to estimate the pressure buildup rate.

Groundwater as a heat source: During the last few decades, it has been recognized that the subsurface space, such as water-saturated soils, is a good heat source both for tapping heat in wintertime and for disposing of heat in summertime, since the aquifer temperature does not vary much throughout a year and keeps a constant temperature of around 15°C in middle latitude regions. This is an attractive heat source in the regions where the temperatures drop near 0°C during wintertime and rise beyond 30°C during summertime. Coupled with heat pump systems, the tapped thermal energy can be used for residential heating in winter, and the heat from residential space in summer can be disposed in the aquifer [14–17]. Such a system is called ground-source heat pump (GSHP). Over one million units in the world have been installed, notably in the United States, Canada, European countries, and China. The coefficients of performance (COPs) of the GSHP show significantly improved values, usually 1.3–1.5 times greater than those of atmosphere-based heat pump systems [8]. Again, however, the performance of GSHP is largely dependent on the heat transfer rates from boreholes or ground heat exchangers, where the heat transfer coefficients there increase with the groundwater velocity [18–24]. Therefore, in order that the effect of groundwater be reflected in the design of GSHPs and underground thermal storage systems, it is essential to determine groundwater velocity at the point where the ground heat exchangers are installed.

Permeable reacting barriers: A PRB is a relatively new technology for in situ groundwater remediation, and it has been recognized as being a cost-effective scheme. The first field-scale experiment of PRBs was carried out in Base Borden, Ontario, Canada. In the experiment, the treatment zone was constructed by digging an area isolated by sheet piles and then refilling the space with a permeable reacting material, for example, a mixture of granular iron and sand. The permeable iron-bearing treatment zone was then created by removing the sheet piles. In the experiments, chlorinated ethylene was introduced upstream as contaminants. The results show that fully dechlorinated groundwater is produced downstream [25,26]. The success of this field experiment developed a great deal of interest in this new technology. Especially the schemes using granular iron and other zerovalent metals have been proven very effective [27–30]. In order to analyze and to predict the PRB performance, however, precise information on the groundwater velocity within an extent of a few meters of the water-saturated subsurface space is vital, since groundwater velocities determine residence times in the treatment zone, and these are intimately related to the barrier performance.

24.2 GROUNDWATER VELOCITY AND DARCY'S LAW

24.2.1 Darcy's Law

It is instructive to look at Darcy's law from groundwater hydrological point of view [2,31,32]. In the groundwater hydrology, the gravitational potential and the fluid pressure are considered to be two interchangeable components, and the potential that drives groundwater is expressed as the sum of both gravitational potential measured from an arbitrary vertical position and the pressure that the fluid particle bears at the point. This can be demonstrated by the following imaginary case simulations. Referring to Figure 24.2, we envisage an apparatus consisting of a circular pipe filled with sands, and a situation where steady water flow is set up in the pipe, by introducing water into one end and discharging from the other. The two narrow tubes inserted in the pipe center and vertically positioned are manometers, which bear a different name, *piezometer*,

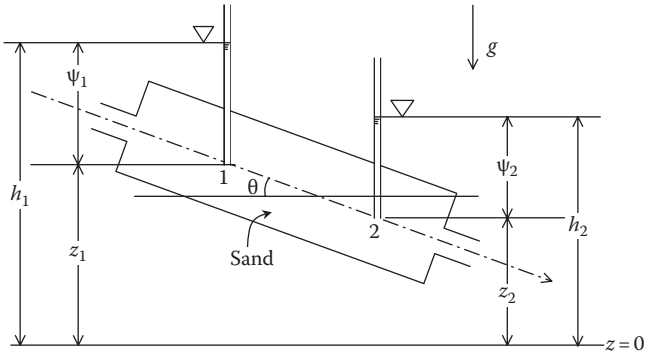

ψ: Pressure or pressure head
z: Gravitational potential or elevation head
h: Hydraulic head

FIGURE 24.2 Darcy apparatus.

when it is used in the field measurements. The apparatus is sometimes called Darcy apparatus, named after Henry Darcy, a French hydraulic engineer. If the Darcy apparatus is set up vertically ($\theta = \pi/2$), flow will certainly occur downward in response to gravity, without introducing any pressure difference between the two positions, denoted as 1 and 2 in the figure. On the other hand, if the cylinder is placed horizontally, the gravity does not drive flow, and one needs to set up some pressure difference between the two positions in order to generate flow. These thought experiments clearly show that the gravitational potential or elevation head, and the water pressure are the two coupled components that cause the groundwater flow. Therefore, Darcy's law in groundwater hydrology is more convenient for being written in terms of *hydraulic head h*, which is defined as a sum of elevation head z and pressure head ψ, as seen in Figure 24.2. Assuming that the flow is mainly horizontal and the vertical component is sufficiently small, Darcy's law in one dimension gives

$$v = -K\frac{\Delta h}{\Delta x} \tag{24.1}$$

or in differential form

$$v = -K\frac{dh}{dx} \tag{24.2}$$

where

v is the Darcy velocity (flow rate per unit area of cross section)
dh/dx is the *hydraulic gradient*
K is a constant proportionality factor

The parameter K is known as the *hydraulic conductivity*, and it has the same dimension as velocity. The K value can be considered as the flow rate per unit area when the hydraulic gradient is a unity, $dh/dx = 1$. The hydraulic conductivity is one of the most important properties that characterize aquifer.

Suppose the hydraulic conductivity of aquifer is known, then, as shown in Figure 24.3a, the groundwater velocity is determined by the water table elevation difference in the unconfined aquifer,

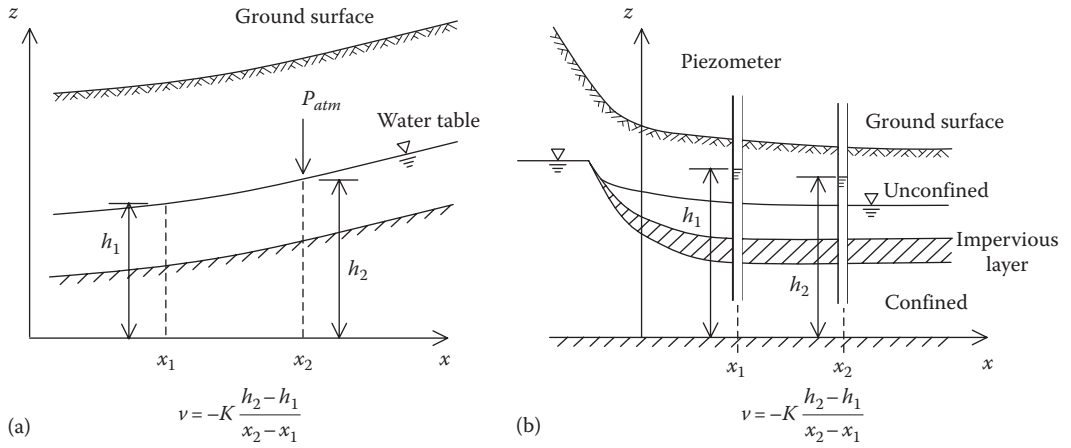

FIGURE 24.3 Velocity calculation based on Darcy's law in (a) unconfined aquifer and (b) confined aquifer.

since the pressure on the water table is the atmospheric pressure, and it is constant over the water table. On the other hand, in the confined aquifer, it is often the pressure variations in the horizontal direction that drive the groundwater, as illustrated in Figure 24.3b. This is typical for confined aquifers in the plains, where the ground slopes are very small.

24.2.2 Hydraulic Conductivity and Permeability

It appears that the proportionality factor is a function not only of porous matrix, but also of the fluid properties. After extensive experiments carried out using an ideal porous media consisting of uniform glass beads of diameter d, and various fluids of density ρ and dynamic viscosity μ, under a constant hydraulic gradient dh/dx, the results are summarized by a new version of Darcy's law [2,32,33]:

$$v = -\frac{Cd^2\rho g}{\mu}\frac{dh}{dx} \tag{24.3}$$

where C is again a proportionality constant. Since the quantity Cd^2 is a function of porous matrix alone, whereas ρ and μ are functions of the fluid, the first component in the right-hand side can be rewritten in order to form a new quantity k:

$$k = Cd^2 \quad \text{and} \quad K = \frac{k\rho g}{\mu} \tag{24.4}$$

The parameter k is known as the *intrinsic permeability*, or simply *permeability*. Now we are in a position to combine Equations 24.3 and 24.4 to form

$$v = -\frac{k}{\mu}\frac{d(\rho g h)}{dx} = -\frac{k}{\mu}\frac{dp}{dx} \tag{24.5}$$

where we used a relation between the hydrodynamic head and the corresponding hydrostatic pressure $p = \rho g h$. This is well-known Darcy's law commonly seen in porous media transport problems. Typical values of hydraulic conductivity and permeability of unconsolidated deposits (soils) and rocks are listed in Table 24.2 [33].

TABLE 24.2
Values of Hydraulic Conductivity and Permeability of Soils and Rocks

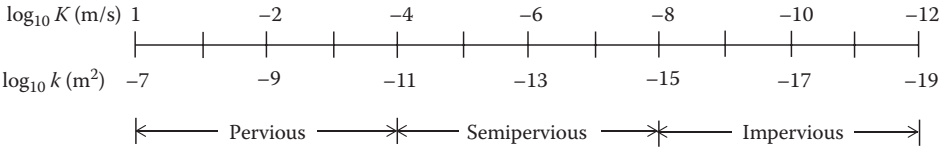

Soil	Clean gravel	Clean sand or Sand and gravel	Very fine sand, silt, Loess, loam, solonetz		
		Peat	Stratified clay	Unweathered clay	
Rocks		Oil rocks	Sandstone	Limestone, dolomite	Breccia, granite

Source: Based on Bear J., *Hydraulics of Groundwater*, McGraw-Hill, New York, 1979.

24.3 HYDRAULIC CONDUCTIVITY AND POROSITY MEASUREMENTS

Hydraulic conductivity is the most important aquifer property, since it determines the groundwater velocity for a given hydraulic gradient. It is worthy to note that the hydraulic conductivity exhibits significant variation through aquifer formation. In the following, we briefly discuss a few widely used field measurements that can evaluate the hydraulic conductivity at a particular site.

24.3.1 Slug and Bail Test

The simplest way to determine in situ hydraulic conductivity values is carried out by means of a single piezometer. According to Dunnicliff [34], the term "piezometer" is defined for such a small-diameter observation well, whose diameter is often less than 5 cm and designed to measure a pressure history in the specific layer with installation of such a device as transducer for continuous monitoring. The test is initiated by causing an instantaneous change in water level in a piezometer by a sudden introduction or removal of a known volume of water. The recovery of water level with time is then observed and recorded. When water is removed, the tests are called *bail tests*, whereas when it is added, they are termed as *slug tests*. It is considered that the test results reflect the hydraulic conductivity adjacent to the piezometer, often within a few meters' range. An extensive review of this method is available in a book by Butler [35].

Referring to Figure 24.4a, the simplest theory of piezometer recovery test relies on the basic assumption that the rate of inflow q at the piezometer tip at any time t is proportional to the hydraulic conductivity K of the soil and to the unrecovered head difference $H - h$, which is the driving force to collect water from the surrounding aquifer formation. This is called the method of Hvorslev [36]. This proposed theory can be transformed into the following differential equation:

$$q(t) = \pi r^2 \frac{dh}{dt} = FK(H - h) \tag{24.6}$$

with F as an empirical factor depending on the shape of the piezometer intake, and r is the piezometer casing pipe radius. Given the initial condition of $h = H_0$ at $t = 0$, the solution for this differential equation is straightforward.

$$\frac{H - h}{H - H_0} = e^{-t/T_0} \quad \text{and} \quad T_0 = \frac{\pi r^2}{FK} \tag{24.7}$$

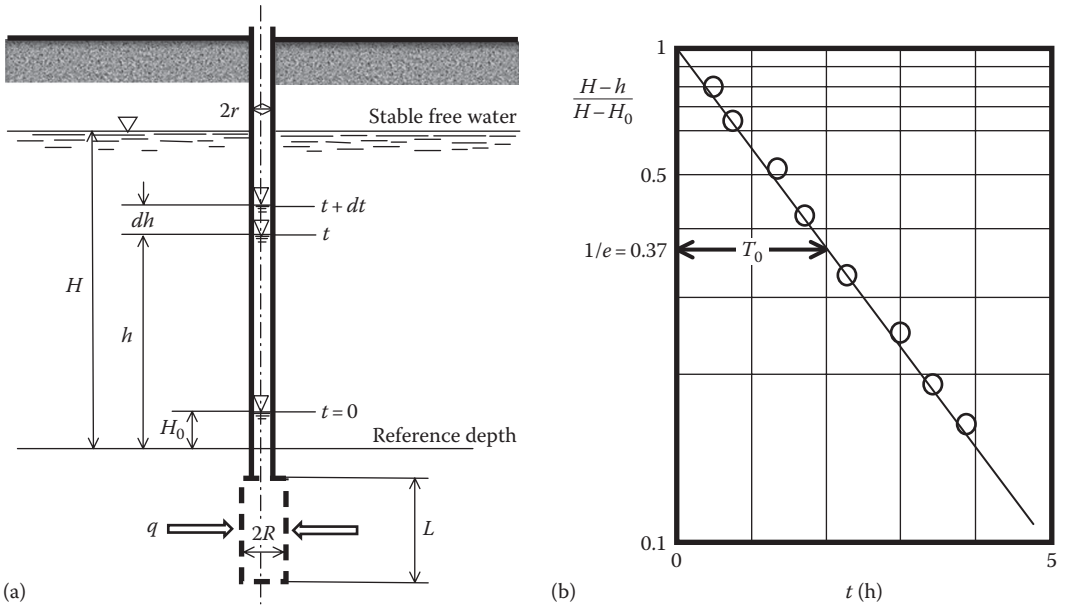

FIGURE 24.4 Slug and bail test to evaluate the hydraulic conductivity of neighboring region. (a) Piezometer recovery test. (b) Semi-log plot of data. (Redrawn from Freeze, R.A. and Cherry, J.A., *Groundwater*, Prentice Hall, Upper Saddle River, NJ, 1979.)

When the recovery level, the left-hand side of this equation, becomes 1/*e*, which is about 37%, the required time is known as the time constant of the solution. By reading the value of time constant T_0 from the observed data in the semi-log plot as shown in Figure 24.4b, the hydraulic conductivity K can be determined, provided that F is known for a particular intake shape of piezometer. If the screen radius R and length L at the bottom of casing pipe are given, the intake factor F is calculated by

$$F = \frac{2L\pi}{\ln(L/R)} \tag{24.8}$$

provided that the aspect ratio of the bottom screen is slender enough, that is, $L/R > 8$ [2,36].

Obviously, there is no solid foundation in justifying the assumption of the linear proportionality between the recovery rate and the unrecovered head difference. But its simplicity is often appreciated in the field test analyses. There are many variations of the earlier theory, taking into account the many different types of aquifer and the associated boundary conditions [37–39].

24.3.2 Well Test

24.3.2.1 Storativity and Transmissivity

Before we describe theoretical background of well tests, it is necessary to prepare two important hydraulic concepts, which are related to aquifer porosity n and hydraulic conductivity K. One of such concepts is *Specific Storage* S_s and is defined as the volume of water that a unit volume of aquifer can release from storage when a unit decline in hydraulic head (equivalent to unit decline in pressure) is made in confined aquifer, as shown in Figure 24.5a. Since the interstitial stress in the confined layer is a sum of effective stress σ_e among soil grains and the pore water pressure, the sum is constant at specific elevation and must balance with the load by the overlying upper layer. The reduction of water pressure, therefore, automatically increases the effective stress σ_e in the aquifer [2,33]. The increase in the effective stress among soil grains causes compactions of aquifer

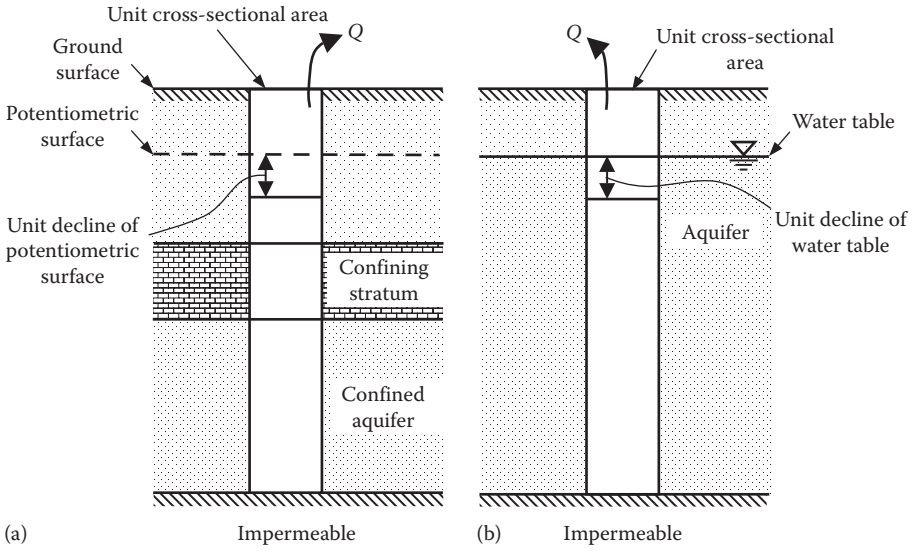

FIGURE 24.5 Storativity definitions in (a) confined aquifer and (b) unconfined aquifer.

pores, and the pore compactions drive the water out of aquifer. The magnitude of pore space reduction can be characterized by the aquifer compressibility α. At the same time, the pressure reduction causes the volume expansion of water itself, which is controlled by the water compressibility β. The water volume expansion produces additional release from a unit volume of aquifer. In concluding the aforementioned discussion, the specific storage S_s can be expressed as the sum of the two effects:

$$S_s = \rho g(\alpha + n\beta) \tag{24.9}$$

If we restrict ourselves to a confined aquifer of thickness b, the *transmissivity* T is defined as

$$T = Kb \tag{24.10}$$

and the *storativity* S is defined as

$$S = S_s b \tag{24.11}$$

The storativity is intuitively understandable as a value defined by $S = \Delta Q/V_T$, in which an amount of water ΔQ must be removed from an initial volume of aquifer V_T vertically cut off by unit horizontal area when a unit drop in piezometer is required. The process is illustrated in Figure 24.6. Typical values of S in confined aquifer are of the order of 10^{-6} –10^{-4}.

Unfortunately, these two concepts or parameters are not well defined, if we consider an unconfined aquifer. This is because the aquifer thickness, now defined by the height of water table b measured from the underlying aquitard (a geologic formation which is of semipervious nature, but transmits water at a very low rate) at the bottom, cannot be constant any more, due to the fact that a drawdown of the water table near the pumping well is unavoidable (see Figure 24.11). Nonetheless, since the drawdown surface is not very steep in the region far from the well, it is possible to analyze the flows to the pumping well with Dupuit approximation [40], which transforms two-dimensional flows with approximate one-dimensional flows, and the same definition for the transmissivity as in Equation 24.10 can be still applicable in the analysis.

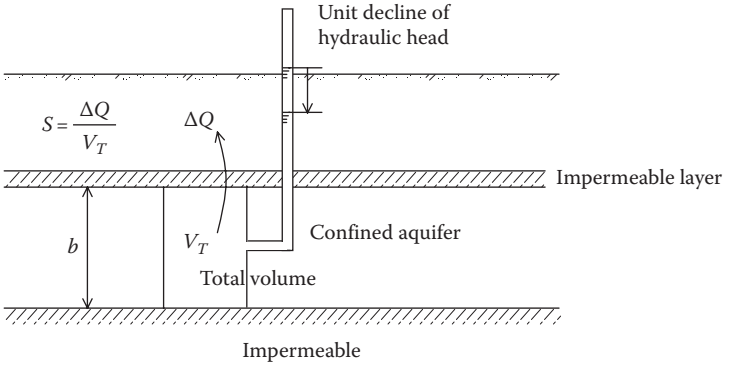

FIGURE 24.6 Intuitive interpretation of storativity in confined aquifer.

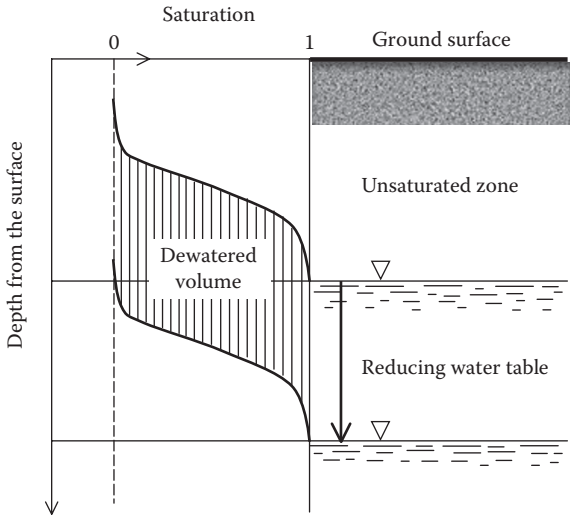

FIGURE 24.7 Dewatering process in unconfined aquifer when the water table is dropped. (Redrawn from Freeze, R.A. and Cherry, J.A., *Groundwater*, Prentice Hall, Upper Saddle River, NJ, 1979.)

The storage term in unconfined aquifer is replaced by the *Specific Yield* S_y. The specific yield is defined as the volume of water released from storage per unit surface area of aquifer per unit decline in the water table (see Figure 24.5b). The specific yields of unconfined aquifers are much higher than the storativities of confined aquifers and usually fall in the range of 0.01–0.30 (see Figure 24.13). The higher values reflect the fact that water release in unconfined aquifer is due to actual dewatering from the soil pores, whereas in the confined aquifer, water release is due to only the secondary effects of pore compactions and water expansion. The effect by reducing the water table elevation is illustrated in Figure 24.7, where the hatched area represents the amount of water produced by dewatering process.

24.3.2.2 Theoretical Background of Well Test

A pumping test to determine hydraulic conductivity requires at least two wells, one for pumping and the other for observation, often called as *piezometer*, in the capture zone, which usually covers a large area extending up to a few kilometers. The results are considered to represent average hydrodynamic properties over the area. Water is pumped at a constant rate from one well, and drawdown in the adjacent piezometer is measured. Theoretical background for the case of *ideal confined aquifer* is relatively simple. Later, we will discuss some of the basic aspects of the well

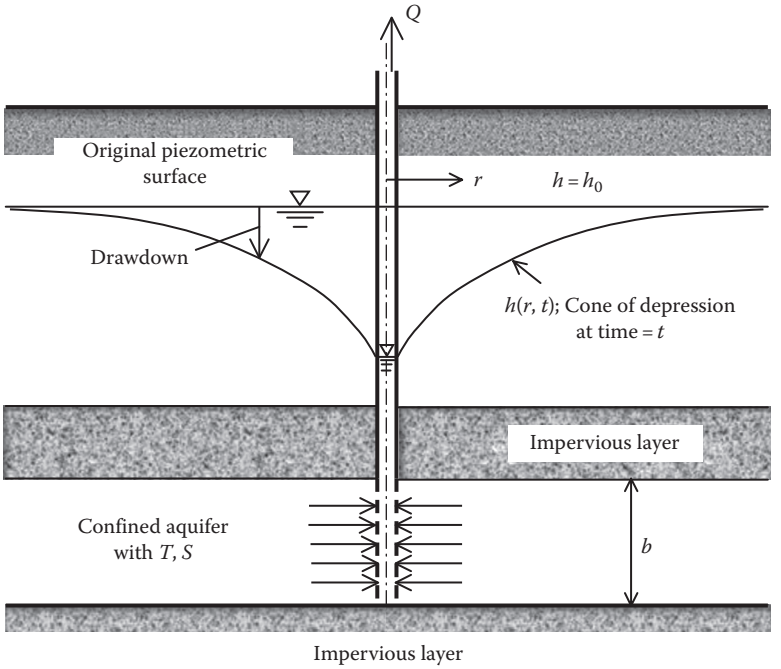

FIGURE 24.8 Radial flow to a production well in a horizontal confined aquifer. (Redrawn from Freeze, R.A. and Cherry, J.A., *Groundwater*, Prentice Hall, Upper Saddle River, NJ, 1979.)

test analysis for this ideally confined case, as seen in Figure 24.8. By an ideal confined aquifer, we mean a horizontally infinite extent of homogeneous, isotropic porous medium with a constant thickness b, which is sandwiched by two parallel impervious layers. For this case, it is possible to develop an analytical solution for the transient drawdown behavior at a given radial position from the pumping well. Applying the mass conservation law and Darcy's law, with further assumptions of the infinitely thin well diameter and the entire well penetration into the aquifer, it is not difficult to show that the transient behavior of hydraulic head $h(r, t)$ can be governed by the following diffusion-type equation [41]:

$$\frac{\partial^2 h}{\partial r^2} + \frac{1}{r}\frac{\partial h}{\partial r} = \frac{S}{T}\frac{\partial h}{\partial t} \tag{24.12}$$

When the constant pumping rate Q (m^3/s) is given at the well, and the aquifer has initially a constant hydraulic head, the following set of initial and boundary conditions can be employed:

$$h(r,0) = h_0 \quad \text{for all } r \tag{24.13}$$

$$\lim_{r\to 0}\left(r\frac{\partial h}{\partial r}\right) = \frac{Q}{2\pi T} \quad \text{for } t > 0, \quad \text{and} \quad h(\infty,t) = h_0 \quad \text{for all } t \tag{24.14}$$

Utilizing an analogy to heat flow, the solution in terms of drawdown head $h_0 - h(r, t)$ can be expressed as

$$h_0 - h(r,t) = \frac{Q}{4\pi T}\int_u^\infty \frac{e^{-u}}{u}\,du \tag{24.15}$$

where

$$u = \frac{r^2 S}{4Tt} \tag{24.16}$$

This is the well-known Theis solution. This solution is often written in terms of the *well function*, $W(u)$. With this notation, Equation 24.15 becomes

$$h_0 - h(r,t) = \frac{Q}{4\pi T} W(u) \tag{24.17}$$

The values of well function are often tabulated or graphically shown as in Figure 24.9, but the following series expression is also useful.

$$W(u) = -0.5772 - \ln u + u - \frac{u^2}{2\times 2!} + \frac{u^3}{3\times 3!} - \frac{u^4}{4\times 4!} + \cdots \tag{24.18}$$

When $1/u > 10$, however, the first two terms become dominant, and the earlier series can be truncated in order to yield a much simpler expression for Equation 24.17 as

$$h_0 - h(r,t) \simeq \frac{Q}{4\pi T} \ln \frac{2.25Tt}{r^2 S} = \frac{2.30Q}{4\pi T} \log \frac{2.25Tt}{r^2 S} \tag{24.19}$$

and the associated errors are 5.3%, 2.2%, 0.4% at $1/u = 10$, 20, 100 respectively.

The graphical representation is used as a type curve for which the observed transient drawdown data plots are superimposed, so that the best matching is obtained between the two. This can be done in the following way. First, taking the logarithm of Equations 24.16 and 24.17,

$$\log(h_0 - h(r,t)) = \log W(u) + \log \frac{Q}{4\pi T} \tag{24.20}$$

$$\log t = \log \frac{1}{u} + \log \frac{r^2 S}{4T} \tag{24.21}$$

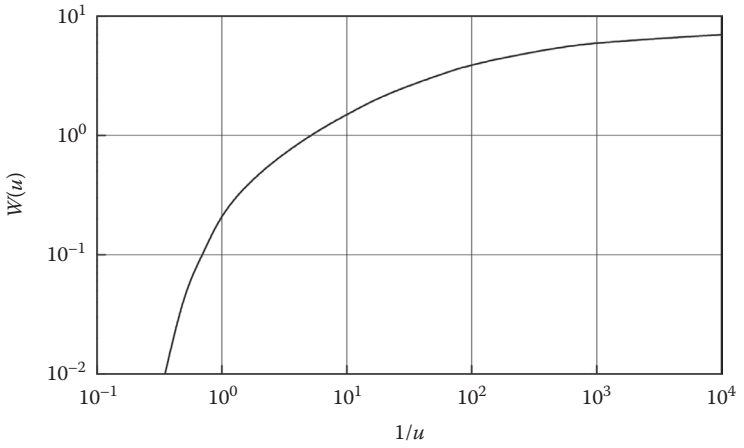

FIGURE 24.9 Well function W versus nondimensional variable $1/u$ in the Theis solution.

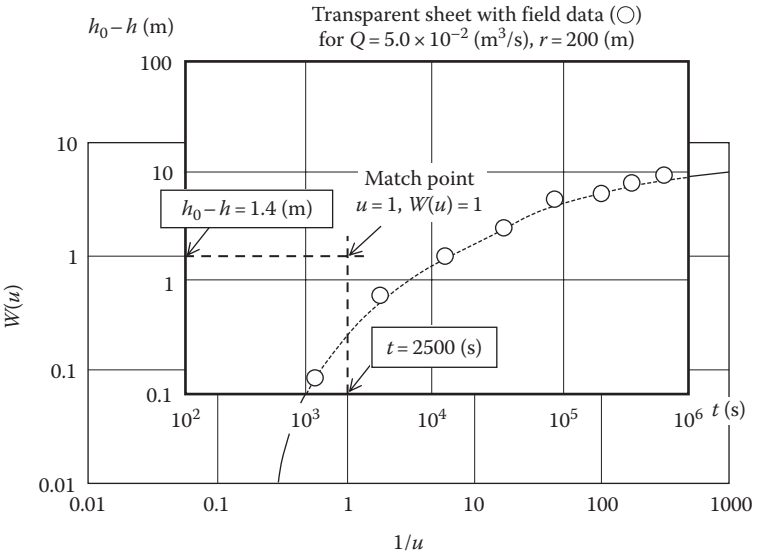

FIGURE 24.10 Illustration to determine T and S for confined aquifer by the type curve matching. (Redrawn from Freeze, R.A. and Cherry, J.A., *Groundwater*, Prentice Hall, Upper Saddle River, NJ, 1979.)

If one plots the observed drawdown data as a function of t in a transparent log–log sheet, it can be easily recognized from equations of (24.20) and (24.21) that the plot is only different from a type curve of $\log(h_0 - h(r, t)) = \log W(u)$ versus $\log 1/u$, by $\log Q/4\pi T$ in the ordinate, and by $\log r^2S/4T$ in the abscissa. Therefore, sliding the plot of $\log(h_0 - h(r, t))$ versus $\log t$ over the type curve until the two curves overlap exactly, one can read off the quantities of $Q/4\pi T$ in the ordinate difference and of $r^2S/4T$ in the abscissa difference. The procedure is illustrated in Figure 24.10. In this example, an arbitrary point (1, 1) on the type curve is chosen as a match point, then the corresponding coordinates on the drawdown data plot can be read as $h_0 - h(r, t) = 1.4$ m and $t = 2500$ s. From these values and the assumption of $r = 200$ m, T and S can be calculated as

$$T = \frac{QW(u)}{4\pi(h_0 - h)} = \frac{(5.0 \times 10^{-2})1.0}{4.0 \times 3.14 \times 1.4} = 0.0028 \text{ m}^2/\text{s}$$

$$S = \frac{4uTt}{r^2} = \frac{4.0 \times 1.0 \times 0.0028 \times 2500}{200^2} = 7.0 \times 10^{-4}$$

Well test analysis for an unconfined aquifer, as illustrated in Figure 24.11, is mathematically much more involved due to the fact that the flows to the pumping well are no longer a function of r and t only, but also a function of the vertical coordinate z. An analysis that is widely used in practice today was advanced by Neuman [42–44]. It is based on a crucial observation of drawdown behavior that can be divided into three stages. At the first stage, which covers only short period of time after the pumping starts, an unconfined aquifer reacts in the same way as does a confined aquifer, that is, water is released instantaneously from the pores by aquifer compactions and volume expansion of water itself. In the second stage, the gravity drainage from soil pores becomes significant due to the fall of water table, which results in a decrease in the slope of the time–drawdown curve. At the third stage, time–drawdown data once again approach to a Theis-type curve. This reflects the fact that a significant fall of water table comes to an end, as the influenced area by pumping becomes

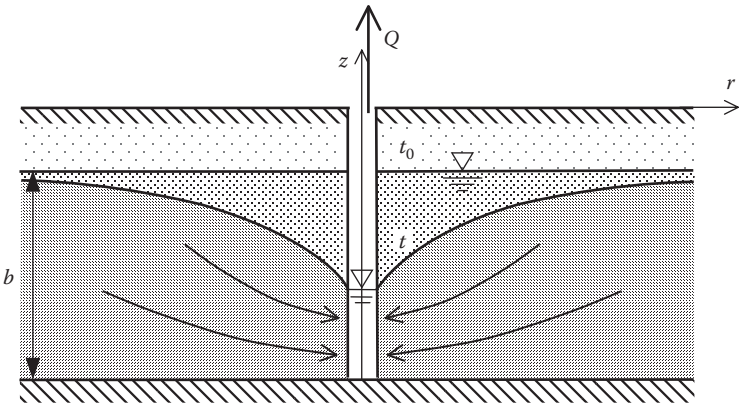

FIGURE 24.11 Well test in an unconfined aquifer.

large enough for a given rate of pumping. The last stage tends to conform to another Theis curve, defined by the specific yield S_y, instead of the storativity S. The drawdown solution can be written formally as

$$h_0 - h(r,t) = \frac{Q}{4\pi T} W(u_A, u_B, \eta) \tag{24.22}$$

where

$u_A = r^2S/4Tt$
$u_B = r^2S_y/4Tt$
$\eta = r^2/b^2$

The solution is also represented graphically as $W(u_A, u_B, \eta)$ versus u_A and u_B with η as a parameter as shown in Figure 24.12. The type curves can be used to determine the transmissivity and other aquifer parameters graphically from the observed drawdown data. The detailed procedure of graphical solution should be referred to Neuman [44]. Well test is still a subject of research for various boundary conditions [45,46].

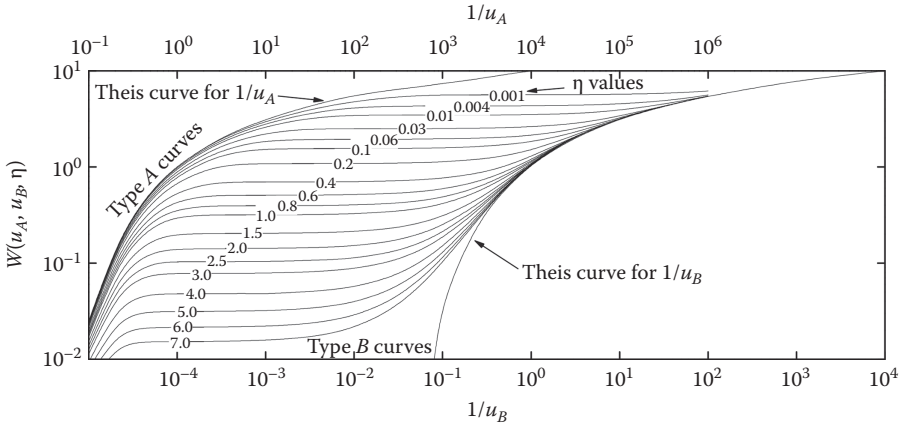

FIGURE 24.12 $W(u_A, u_B, \eta)$ versus $1/u_A$, $1/u_B$ with the parameter $\eta = r^2K_S/b^2K_r$ for unconfined aquifer.

TABLE 24.3
Range of Values of Porosity *n* of Soils and Rocks

		n **(%)**
Unconsolidated	Gravel	25–40
	Sand	25–50
	Silt	35–50
	Clay	40–70
Rocks	Fractured basalt	5–50
	Karst limestone	5–50
	Sandstone	5–30
	Limestone, dolomite	0–20
	Shale	0–10
	Fractured crystalline rock	0–10
	Dense crystalline rock	0–5

Source: Based on Freeze, R.A. and Cherry, J.A., *Groundwater*, Prentice Hall, Upper Saddle River, NJ, 1979.

24.3.3 Porosity

The porosity n is defined by the volume ratio of the voids V_v to the total volume of a soil or rock V_T: $n = V_v/V_T$. The porosity of a soil or a sediment sample can be determined by relating the bulk of mass density of the sample to the particle mass density. The bulk mass density is defined as the oven-dried mass divided by the field volume of the sample (the total volume). The particle mass density is defined as the oven-dried mass divided by the volume of the solid particles, which can be determined by a water displacement test. Then, the value of $(1 - n)$ can be computed by the bulk density divided by the particle density. The porosity of soil or rock is often tightly related to its hydraulic conductivity. But its translation into hydraulic conductivity is not straightforward. Certainly, a large value of porosity is a necessary condition for good hydraulic conductivity, but the connectivity among pores is also important. The hydraulic conductivity of soils, therefore, is a function of these two properties. The porosity is important to relate the Darcy velocity $\overline{v}$ with the actual fluid particle velocity $\overline{v}_p$ as $\overline{v} = \overline{v}_p \cdot n$. The porosities of some representative unconsolidated deposits and rocks are listed in Table 24.3 [2,47].

For the unconsolidated formations, however, the porosities, the specific yields, and the hydraulic conductivities have been generally found correlated with the grain sizes. Therefore, there are many proposed grain size analyses, attempting to determine such hydraulic properties [48–50]. One example of such results is presented graphically in Figure 24.13. Since the errors compared with in situ well tests are often large, the methods are recommended to use only as a first estimation [51].

24.4 GROUNDWATER VELOCITY MEASUREMENTS

24.4.1 Velocity Defined in Large Scale

One of the commonly employed methods to estimate vertically averaged groundwater velocities in large areas uses techniques that rely on the Darcy equation [2,52]. The Darcy-based techniques require information on the hydraulic conductivity K, porosity n, and the distribution of the hydraulic heads in the region in which we want to estimate the velocities. The hydraulic head differences measured by piezometers and the horizontal distances among them give the hydraulic gradients. Given the earlier information, one can calculate average velocities over the horizontal plane according to the Darcy equation in principle. It should be noted, however, that the employed parameters such as K and n have large inherent uncertainties in the field, and so the resulting velocities may be in considerable error.

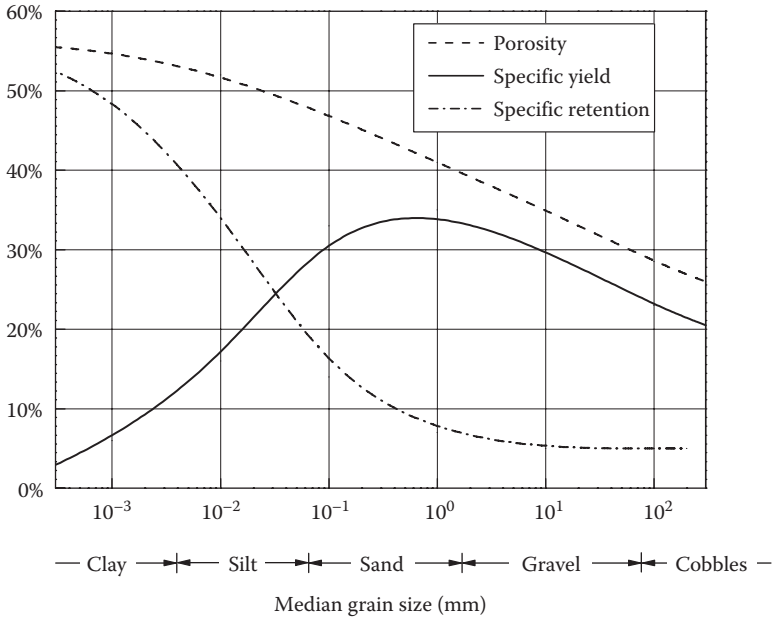

FIGURE 24.13 Porosity, specific yield, and specific retention as a function of soil grain size. (Redrawn from Bear J., *Hydraulics of Groundwater*, McGraw-Hill, New York, 1979.)

A more direct method for velocity measurement relies on introducing an artificial tracer at one well and observing its arrival time and concentration at other wells [2,53]. After some data adjustments for tracer dispersion effect, the velocity can be obtained from dividing the distance by the travel time. There is a variety of tracers tested in the fields. Simple tracers such as NaCl or $CaCl_2$ often work satisfactorily enough, and the tracer arrival can be conveniently monitored by the measurement of electrical conductance. The artificial tracer method, however, has at least two disadvantages. One is caused by the extremely slow movement of the groundwater under natural conditions, which leads to undesirably long periods of time for tracers to travel significant distances. The other is due to the fact that geological heterogeneity may distort the flow paths and that the actual passage may not be straight. Also numerous observation wells are necessary in the downstream in order not to miss the travelling tracer, which is obviously very costly.

Environmental isotopes such as tritium and carbon 14 are used for groundwater age-dating. Since the onset of thermonuclear tests in the atmosphere in 1953, the tritium content in precipitation increased significantly. Therefore, if the sample water has a low content of tritium, it is reasonable to conclude that significant amounts of post-1953 water are not present. Tritium data from groundwater samples of different locations can be used to distinguish and to map different age zones in the area of interest. If tritium concentrations of two adjacent zones are well defined, the mixing process can be monitored to determine average movement of groundwater. The usefulness of tritium monitoring in groundwater studies is strengthened by the fact that it is not significantly affected by chemical reactions with geological materials, other than radioactive decay. There are many other environmental isotopes that can be used as tracers. Exhaustive information on isotope tracers in geological hydrology can be found, for example, in the book edited by Kendall and McDonnell [54].

24.4.2 Velocity Measurements in Small Scale

In the following sections, we describe some representative methods for determining the velocity across a borehole. Since such methods do all the measurements through a single borehole, they

be called *single borehole velocimeter* or *single borehole velocimetry* and deemed to be quite cost effective. Emphasizing a particular device itself that performs velocity measurements, it is also called a *point velocity probe* (PVP). These methods can be employed for monitoring a time history of the groundwater flow at a particular position. In the following, we describe three such methods; the first one is based on well-known classical approach, while the other two are relatively new ones reported in the recent literatures. It should be noted, however, that there is a variety of other proposed methods that also fall in this category, such as the colloidal borescope by Kearl [55], and the laser Doppler velocimeter by Momii et al. [56], and others to name a few.

24.4.2.1 Point Dilution Test

This is a classical method and has been adopted and widely employed mainly due to the simplicity of its theoretical background and the easiness of carrying out the measurement. The idea was originally developed in Russia in the late 1940s: the technique is now called borehole dilution tests or point dilution method [2,53,57]. The measurement instrumentation is illustrated in Figure 24.14a. The concentration time history of a tracer, for example, NaCl, released in a well screen segment, isolated by two inflatable packers, is measured. The introduced tracer is gradually displaced by the lateral fresh flow coming into the concerned volume, while the concentration time history is monitored, which exposes a dilution versus time relation as illustrated in Figure 24.14b.

Although the theoretical background is simple, some care should be taken for the evaluation of the horizontal velocity. As shown in Figure 24.15, the streamlines of the uniform flow in the formation are straight and parallel to each other, but they are deformed in the vicinity of the well due to the significant differences in the flow resistance between the adjacent formation and the open space in the borehole. In general, given a horizontal hydraulic gradient, the lateral flow velocity across the borehole $\overline{v}_b$ is greater than the Darcy velocity in the formation $\overline{v}$. Denoting the vertical cross-sectional area through the center of the isolated segment as A, the volume of the segment W, and the average concentration in the bore space C at an arbitrary time, the decrease in the tracer mass in the segment volume during a time interval dt must be equal to the tracer mass in the displaced water by lateral flow velocity $\overline{v}_b$:

$$-dC \cdot W = A\overline{v}_b dt \cdot C \tag{24.23}$$

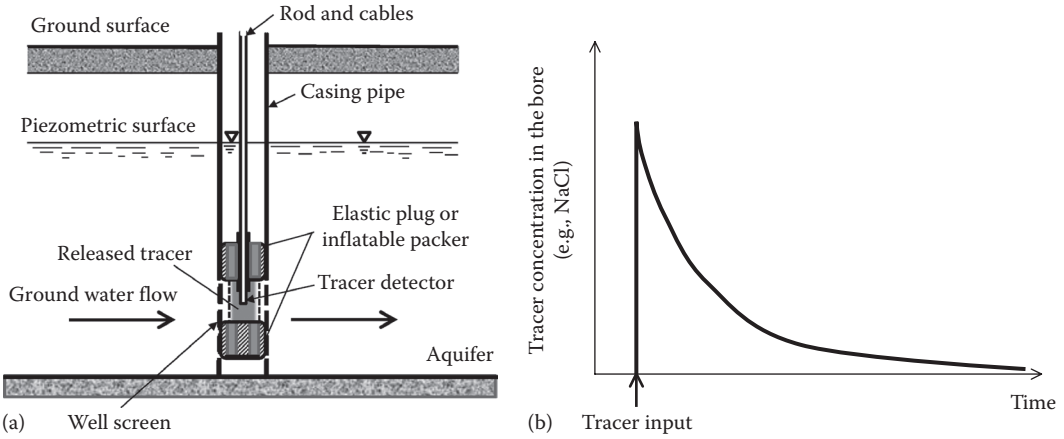

FIGURE 24.14 Schematic of point dilution method to measure groundwater velocity (a) and dilution of tracer with time (b). (Based on Freeze, R.A. and Cherry, J.A., *Groundwater*, Prentice Hall, Upper Saddle River, NJ, 1979.)

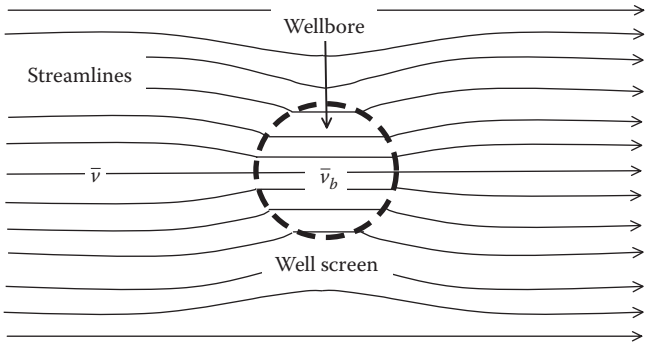

FIGURE 24.15 Illustrating concentration of water flow through borehole. (Redrawn from Freeze, R.A. and Cherry, J.A., *Groundwater*, Prentice Hall, Upper Saddle River, NJ, 1979.)

Rearranging this, the following ordinary differential equation yields:

$$\frac{dC}{dt} = -\frac{A\bar{v}_b C}{W} \tag{24.24}$$

Integrating with the initial condition, $C = C_0$ at $t = 0$, the average borehole velocity can be expressed as

$$\bar{v}_b = -\frac{W}{A \cdot t} \ln\left(\frac{C}{C_0}\right) \tag{24.25}$$

The average Darcy velocity in the aquifer $\bar{v}$ is obtained by

$$\bar{v} = \xi \bar{v}_b \tag{24.26}$$

where ξ is an adjustment factor that depends on the geometry of the well screen and on the hydraulic conductivity of the sand or gravel pack around the screen. The range of ξ in sand or gravel aquifers is reported to be 0.25–2.0 [2,57].

24.4.2.2 Point Velocity Probe Based on Tracer Transport

Labaky et al. [58] recently introduced a PVP consisting of a cylinder outfitted with a tracer release and detection system on its surface. By timing the arrival of tracer between two or more detectors on the cylinder surface, both magnitude and direction of the average velocity vector can be determined. Referring to Figure 24.16, and assuming Darcy's law, and the angle of α between the approaching flow and the injection port, the undisturbed ambient groundwater velocity (particle velocity) $\bar{v}_\infty$ is estimated by

$$\bar{v}_\infty = \frac{v_{app}\gamma}{2(\cos\alpha - \cos(\alpha + \gamma))} \tag{24.27}$$

$$\alpha = \tan^{-1}\left[\frac{v_{app1}\gamma(\cos\gamma_2 - 1) + v_{app2}\gamma_2(1 - \cos\gamma)}{v_{app1}\gamma\sin\gamma_2 - v_{app2}\gamma_2\sin\gamma}\right] \tag{24.28}$$

where

v_{app} is the apparent particle velocity of the tracer measured at a detector on the probe surface
γ is the angle between a detector and the injection port

The subscripts 1 and 2 indicate the different detectors.

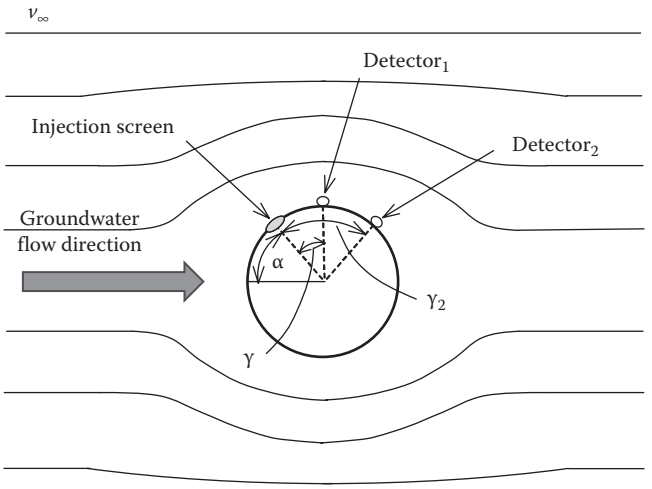

FIGURE 24.16 Concept of PVP measurement. The tracer is released at an injection port and detected at two detectors 1 and 2. (Redrawn from Labaky, W. et al., *Environ. Sci. Technol*., 41, 8453, 2007.)

The PVP instrument was constructed of two half-cylinders of stainless steel, 7.5 cm in length with a 3 cm outside diameters (Figure 24.17), which are put together with machine screws. One of the half-cylinders is hollow and contains the injection and detection ports. The other half-cylinder is solid and contains a groove to stabilize the injection line. The stainless injection line is connected to a plastic syringe filled with tracer solution. The probe was tested by a sand-filled tank, similar to the one shown in Figure 24.20, with velocities ranging from 5 to 90 cm/day. A fairly good agreement was observed between the expected velocities, that is, flow rates divided by the tank cross section and the PVP measured velocities based on Equations 24.27 and 24.28, whose errors are less than 10% in both magnitude and direction of velocity vector. A carefully controlled field experiment was also conducted by the same group of authors [59]. Detailed comparison with other methods in the field tests at a tidally influenced site has been recently reported by Kempf et al. [60].

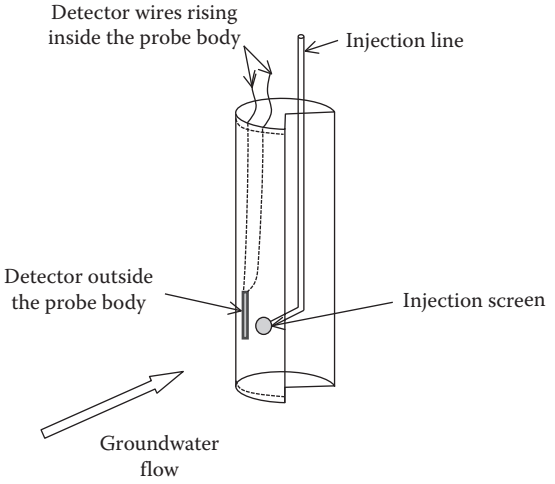

FIGURE 24.17 PVP structure. (Redrawn from Labaky, W. et al., *Environ. Sci. Technol*., 41, 8453, 2007.)

24.4.2.3 Thermal Method

Kimura et al. [61] proposed a single borehole groundwater velocity meter based on steady-state thermal convection from a thin cylindrical heater. The method is unique in the sense that it relies on the steady-state temperature field, which is fundamentally different from the predecessor using thermal energy as a tracer, such as one by Hess and Paillet [62], who use a fluid parcel of temperature anomaly produced by a heat pulse, moving together with the flow. However, due to large diffusivity of heat compared with mass diffusivity, the thermal print in the flow will get blurred very quickly. Note that the Lewis numbers have an order of 100 for most mass diffusion processes in water. Therefore, it was generally believed that the thermal tracer method can be used only for large groundwater velocities. The proposed method, however, overcame this difficulty by detecting the slightest distortions in the steady temperature field around the vertical thin heater, when the lateral groundwater velocity varies. The idea is best illustrated in Figure 24.18, showing the temperature field distortion in the horizontal cross section due to the presence of lateral flow.

Figure 24.19 shows the actual construction of the probe schematically. In the probe center, a vertical heater is installed and 16 thermistors are placed in a circular position in order to detect the temperature distortion. The vacant space in the housing is filled with 0.4 mm glass beads, and the outer casing is fitted with a permeable metal screen. A picture of the developed probe is shown in Figure 24.20; the length is 500 mm and its diameter is 35 mm. The flow detection takes place in a lower part of the probe, whose length is about 80 mm. The thermistors can detect temperature changes as small as 0.01°C.

Extensive three-dimensional numerical simulations were performed in order to investigate the mixed convection around a vertical heated cylinder. The results show that the natural convection does not make a significant impact, unless the permeability in the housing space is extremely high [63]. Therefore, the temperature field is basically governed by forced convection, that is, the lateral flows crossing the sensing part of the probe, and it can be expected that the distortion of the temperature field at circular positions will be correlated with the velocity magnitude. The flow direction can be also determined easily from the detected circumferential temperature variation.

A calibration water tank was constructed in order to simulate groundwater flows. The tank is 2 m long and has a 0.6 m × 0.6 m cross-sectional area. It has two water chambers at its respective ends, where the difference between their pressure heads drives a uniform flow in the sand-filled tank. The apparatus is schematically shown in Figure 24.21. The Darcy velocity in the tank can be varied from 0.0001 to 1 mm/s by carefully controlling the chamber pressures. The average size of the sand filling the tank has an equivalent diameter of 0.4 mm. Water flow rate is measured by a magnetic

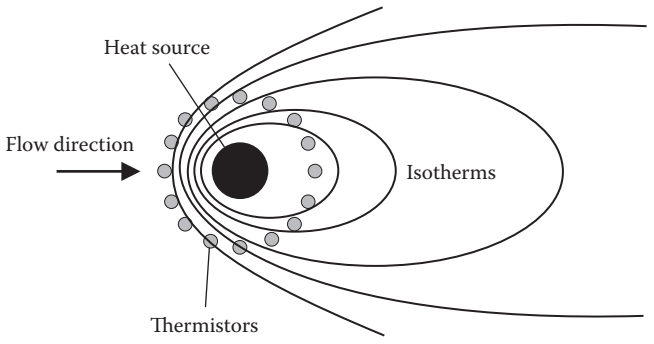

FIGURE 24.18 Measurement concept of steady thermal method. (Redrawn from Kimura, S. et al., Development of groundwater flowmeter: A way to estimate an amount of heat collected by geothermal heat pumps, *Proceedings of the World Geothermal Congress 2005*, Antalya, Turkey, April 24–29, 2005.)

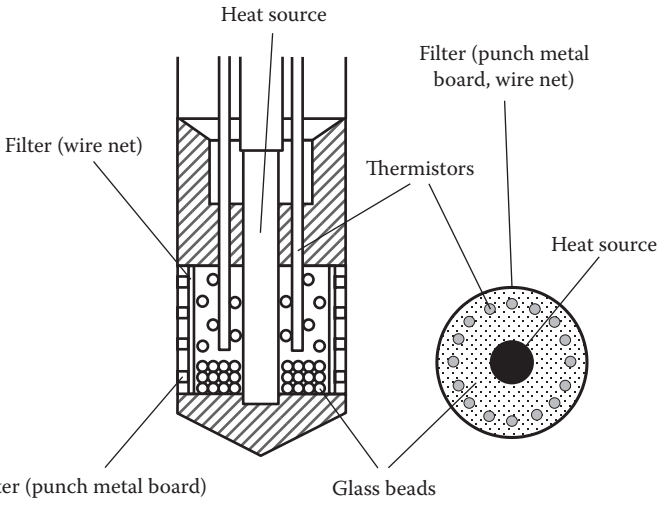

FIGURE 24.19 Probe structure of the steady-state thermal method. (Redrawn from Kimura, S. et al., Development of groundwater flowmeter: A way to estimate an amount of heat collected by geothermal heat pumps, *Proceedings of the World Geothermal Congress 2005*, Antalya, Turkey, April 24–29, 2005.)

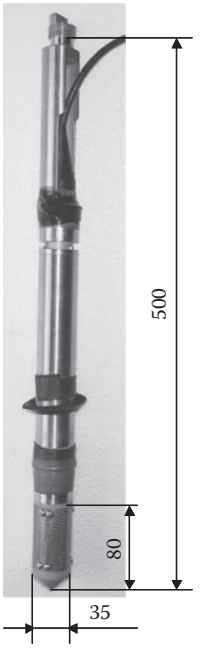

FIGURE 24.20 A constructed probe based on steady-state thermal method. (Reprinted from Takeda, H. et al., *J. Geother. Res. Soc. Jpn*., 31(4), 193, 202, 2009. With permission.)

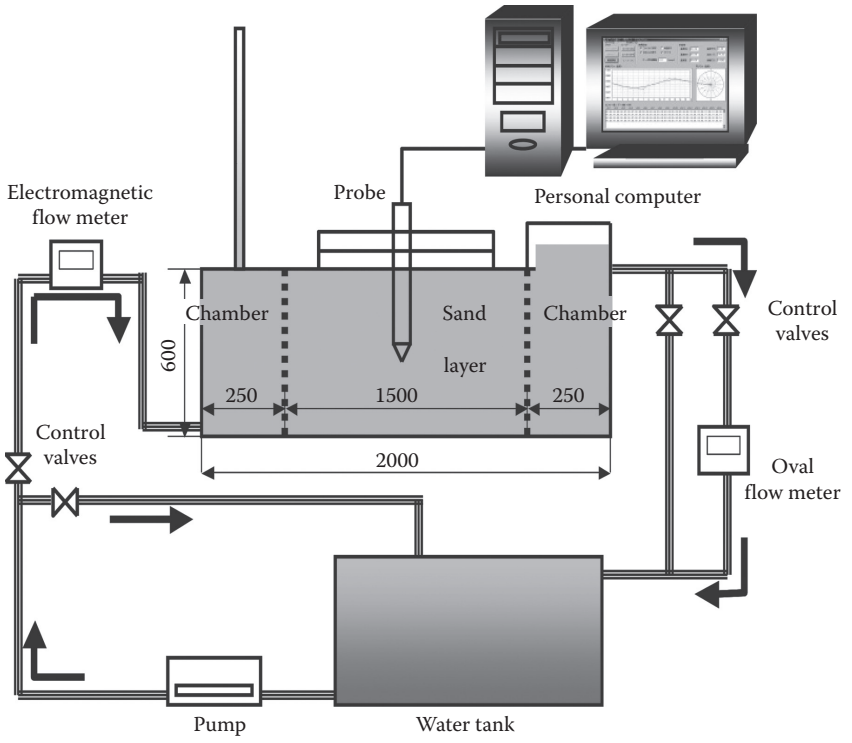

FIGURE 24.21 Calibration tank simulating groundwater flow. (Reprinted from Takeda, H. et al., *J. Geother. Res. Soc. Jpn*., 31(4), 193, 202, 2009. With permission.)

flow meter when the velocity is large, while measurement of the overflow volume of water from the outflow chamber in a specific time interval is used for the small velocities.

In Figure 24.22, the normalized temperature deviations as defined by Equations 24.29 through 24.31 are shown against the Darcy velocity in the calibration tank.

$$T_{dev} = \frac{T_{rms}}{\bar{T}} \tag{24.29}$$

where

$$\bar{T} = \frac{1}{N}\sum_{i=1}^{N} T_i \tag{24.30}$$

and

$$T_{rms} = \sqrt{\frac{\sum_{i=1}^{N}(T_i - \bar{T})^2}{N}} \tag{24.31}$$

In the course of the calibration, the measured Darcy velocities were found to be in the range of 10^{-5} and 10^{-1} cm/s. A steady state of the temperature field is reached within 10–20 min. When the Darcy

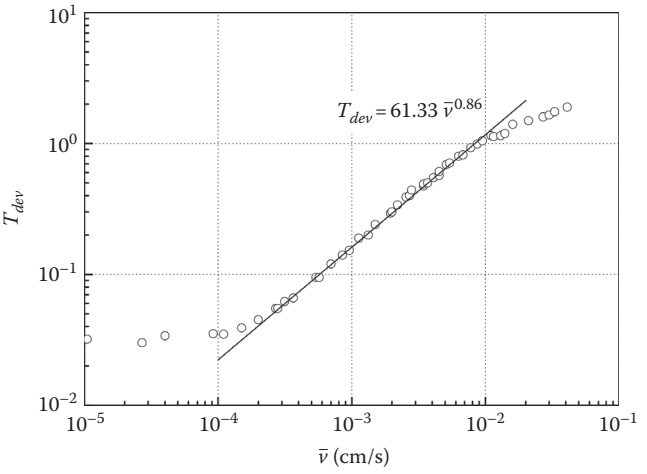

FIGURE 24.22 Temperature deviations detected by the probe as a function of simulated ground water velocity. (Redrawn from Kimura, S. et al., Development of groundwater flowmeter: A way to estimate an amount of heat collected by geothermal heat pumps, *Proceedings of the World Geothermal Congress 2005*, Antalya, Turkey, April 24–29, 2005.)

velocity is within the range of 2×10^{-4} and 10^{-2} cm/s, a strong correlation with a positive slope is observed, which can be well described by

$$T_{dev} = 61.33\bar{v}^{0.86} \tag{24.32}$$

Solving this equation for the unknown velocity U, we derive a formula to determine the horizontal velocity from the measured temperature field within the probe:

$$\bar{v} = \left(\frac{T_{dev}}{61.33}\right)^{1.16} \tag{24.33}$$

Note, however, that the correlation between the temperature deviation and the Darcy velocity becomes weaker, when the velocity exceeds $\bar{v} = 10^{-2}$cm/s.

In order to extend the capabilities of the present method, the average temperature rise measured by the 16 thermistors around the heated cylinder at steady state was examined. The average temperature rises ΔT_m are plotted against the Darcy velocities in Figure 24.23, where another strong correlation becomes evident at the velocities exceeding $\bar{v} = 10^{-2}$cm/s. This occurs because the thermal boundary layer, or the thermally affected region, formed around the heated cylinder becomes thinner for larger lateral velocities. The correlation between the average temperature rise and the Darcy velocity is expressed by

$$\Delta T_m = 0.053\bar{v}^{-0.84} \tag{24.34}$$

Solving this equation for U, we similarly obtain the following expression:

$$\bar{v} = \left(\frac{\Delta T_m}{0.053}\right)^{-1.19} \tag{24.35}$$

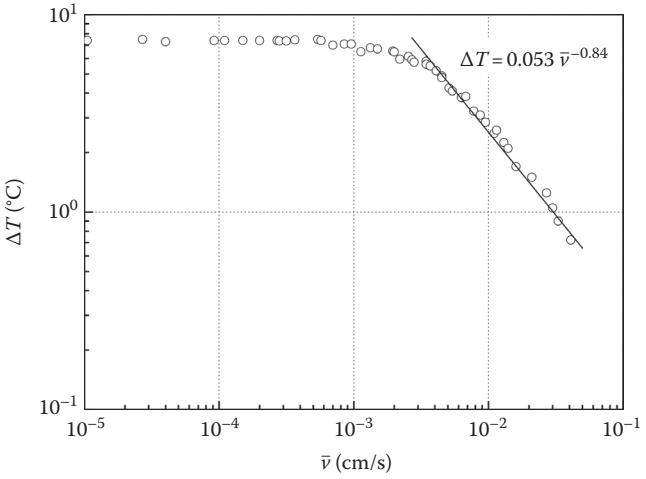

FIGURE 24.23 Average temperature rises detected by the probe as a function of simulated ground water velocity. (Redrawn from Kimura, S. et al., Development of groundwater flowmeter: A way to estimate an amount of heat collected by geothermal heat pumps, *Proceedings of the World Geothermal Congress 2005*, Antalya, Turkey, April 24–29, 2005.)

Before closing this section, it should be mentioned that the groundwater velocity measurements in the field often have to be conducted by positioning the probe in the well segment fitted with permeable screen, for example, slotted pipes. Since the screen pipes may have a lower permeability than the surrounding aquifer formation, the temperature deviation defined by Equation 24.29 may give a smaller value than the calibrated value, that is, Equation 24.32, for a given velocity. Care should be taken also when one places the probe in the slotted casing pipe, where an open space between the probe and the casing pipe is unavoidable. In order to fill the space, the probe should be wrapped with a permeable sponge. In order to ensure more reliable measurements, additional calibrations with more realistic conditions encountered in the field measurements were also carried out [64].

24.5 CONCLUSION

In the introduction, we discussed the important and most characteristic aspects of the groundwater, for example, the huge amounts of water stored in the subsurface space, and the very long turnaround time of such water resources due to the small flow velocities, as well as related geotechnical problems, subsurface pollution and remediation technologies, and groundwater as a thermal depot. Then, Darcy's equation was introduced as a basic law to describe groundwater flows, in terms of hydraulic conductivity and hydraulic gradient. The relation between these hydrodynamic properties in groundwater hydrology and their counterparts, that is, permeability and pressure gradient, which are common terminologies in mechanical and chemical engineering, was delineated.

It turns out that the hydrodynamic behavior of groundwater is governed by the hydraulic conductivity and porosity of aquifer formation. Some of the representative methods to determine the hydraulic conductivity and porosity in the field were described. Theoretical background of slug and bail test, and well tests, was presented for some of the simplest cases.

In the last part, groundwater velocity measurements were described for both large and small scales. For the determination of large-scale groundwater flow, a method based on Darcy's law and the measured data of hydraulic gradient was presented. The principles of artificial and environmental tracer methods were also discussed. Much smaller-scale groundwater velocity measurement techniques using a single borehole, such as a PVP with tracer transport and a thermal method based

on steady-state temperature distortions, were described in more details. The continuing research and development in this area is driven by the strong demand for information on small-scale ground hydrology in such fields as PRB and GSHP.

ACKNOWLEDGMENT

The author acknowledges the support from Mr. Tomohiro Kuratani, technician at Fluid Engineering Laboratory, School of Mechanical Engineering, Kanazawa University, for drawing most of the illustrations and graphs in this chapter.

NOMENCLATURE

A	Cross-sectional area in point dilution test, m^2
b	Aquifer thickness, m
C	Constant, and also concentration in point dilution test
d	Diameter of glass beads, m
F	Empirical factor in slug and bail test
g	Gravitational acceleration, m/s^2
h	Hydraulic head, m
H	Initial hydraulic head in slug and bail test, m
k	Permeability, m^2
K	Hydraulic conductivity, m/s
L	Screen length in slug and bail test, m
n	Porosity
p	Pressure, Pa
q	Inflow rate in slug and bail test, m^3/s
Q	Pumping rate, m^3/s
ΔQ	volume of water taken from aquifer, m^3
r	Radial coordinate and also piezometer casing radius, m
R	Screen radius in slug and bail test, m
S	Storativity, defined by $S = S_s b$
S_s	Specific storativity, m^{-1}
t	Time, s
T	Transmissivity defined by Kb, m^2/s, and also temperature, K
u	Nondimensional variable defined by $r^2S/4Tt$ in the Theis solution
v	Darcy velocity, m/s
V	Volume, m^3
x	Horizontal coordinate, m
z	Vertical coordinate, m

Greek Letters

α	Aquifer compressibility, Pa^{-1}, and initial orientation in Equations 24.27 and 24.28, rad
β	Water compressibility, Pa^{-1}
γ	Angular position of detector, rad
μ	Dynamic viscosity of water, $Pa \cdot s$
ψ	Pressure head, m
ρ	Density, kg/m^3
σ_e	Effective stress among soil grains, Pa
ξ	Adjustment factor
η	Nondimensional parameter defined by r^2/b^2 in Neuman's solution

Subscripts and Superscript

app	Apparent fluid particle velocity, m/s
A, *B*	Referring to two type curves in Neuman's solution
b	Velocity in borehole
dev	Deviation
m	Mean value
o	Initial state
p	Fluid particle velocity
r	Referring to specific yield in unconfined aquifer
rms	Root mean square
T	Referring to total quantity
v	Void
1, 2	Referring to different positions
∞	Referring to far field
¯	Average

REFERENCES

1. V.T. Chow, Hydrology and its development, In *Handbook of Applied Hydrology*, ed. V.T. Chow, New York: McGraw-Hill, pp. 1.1–1.22, 1964.
2. R.A. Freeze and J.A. Cherry, *Groundwater*, Upper Saddle River, NJ: Prentice Hall, 1979.
3. R.E. Nace, ed., *Scientific Framework of World Water Balance, UNESCO Technical Papers Hydrology*, Vol. 7, Paris, France: UNESCO, 1971.
4. I.A. Shiklomanov, ed., *World Water Resources: A New Appraisal and Assessment for the 21st Century*, Paris, France: UNESCO, 1998.
5. W. Brutsaert, *Hydrology: An Introduction*, Cambridge, U.K.: Cambridge University Press, 2005.
6. E. Kalbus, F. Reinstorf, and M. Schirmer, Measuring methods for groundwater-surface water interactions: A review, *Hydrol. Earth Syst. Sci.*, 10: 873–887, 2006.
7. C.R. Murry, Water use, consumption, and outlook in the U.S. in 1970, *J. Am. Water Works Assoc.*, 65: 302–308, 1973.
8. Water Balance Research Group (ed.), *Groundwater Resources and Environment*, 3rd edn., Tokyo, Japan: Kyoritsu Shuppan Co., Ltd., 1995.
9. J.J. Fried, *Groundwater Pollution*, Amsterdam, the Netherlands: Elsevier, 1975.
10. V.K. Dir, Remediation of soils contaminated with hydrocarbons, In *Handbook of Porous Media*, ed. K. Vafai, New York: Mercel Dekker, pp. 787–844, 2000.
11. R.E. Goodman, D.G. Moye, A. van Schalkwyk, and I. Javandel, Groundwater inflows during tunnel driving, *Eng. Geol.*, 2: 39–46, 1965.
12. K. Terzaghi, Mechanics of landslides, In *Berkey Volume: Application of Geology to Engineering Practice*, New York: Geological Society America, pp. 83–123, 1950.
13. A.S. Stipho, The Impact of rising ground water level on the geotechnical behavior of soil in hot climate regions (paper No.8.05), *Proceedings of the Third International Conference on Case Histories in Geotechnical Engineering*, St. Louis, MI, June 1–4, 1993, pp. 1159–1164, 1993.
14. C.R. Aldwell, Heat extraction from Irish groundwaters, In *Hydrogeology in the Service of Man, Memoires of the 18 Congress of IAH*, International Association of Hydrogeologists, Cambridge, pp. 79–94, 1985.
15. H. Hyden, Seasonal heat storage in shallow aquifer, In *Hydrogeology in the Service of Man, Memoires of the 18 Congress of IAH*, International Association of Hydrogeologists, Cambridge, pp. 35–49, 1985.
16. K. Morita and M. Tago, Operational characteristics of the Gaia snow melting system in Ninohe, Iwate, Japan, *World Geothermal Congress 2000*, Beppu-Morioka, Japan, pp. 3511–3516, 2000.
17. G.V. Tomarov and A.A. Shipkov, The World Geothermal Congress WGC-2010, *Therm. Eng.,* 57(11): 989–992, 2010.
18. S. Kimura, Forced convection heat transfer about an elliptic cylinder in a saturated porous medium, *Int. J. Heat Mass Transfer*, 31: 197–199, 1988.
19. N. Diao, L. Qinyun, and F. Zhaohon, Heat transfer in ground heat exchanger with groundwater advection, *Int. J. Therm. Sci.,* 43: 1203–1211, 2004.

20. T. Katsura, K. Nagano, S. Takeda, and K. Shimakura, Heat transfer experiment in the ground with groundwater advection, ed. Stiles, *Proceedings of the 10th Energy Conservation Thermal Energy Storage Conference on Ecostock 2006*, Stockton, NJ, 2006.
21. H.J.L. Witte, Geothermal response tests using controlled multi-power level heating and cooling pulses (MPL-HCP): Quantifying ground water effects on heat transport around a borehole heat exchanger, ed. Stiles, *Proceedings of the 10th Energy Conservation Thermal Energy Storage Conference on Ecostock 2006*, Stockton, NJ, 2006.
22. A.J. van Gelder, H.J.L. Witte, and P. Heaton, A ground source energy plant for the New Assembly for Wales, ed. Stiles, *Proceedings of the 10th Energy Conservation Thermal Energy Storage Conference on Ecostock 2006*, Stockton, NJ, 2006.
23. H.J.L. Witte, A.J. van Gelder, and P. Klep, A very large distributed ground source heat pump project for domestic heating: Schoenmakershoek,Etten-Leur (the Netherlands), ed. Stiles, *Proceedings of the 10th Energy Conservation Thermal Energy Storage Conference on Ecostock 2006*, Stockton, NJ, 2006.
24. R. Bruno, M. Salvatore, F. Tinti, and H.J.L. Witte, Probabilistic approach to TRT analysis: Evaluation of groundwater flow effects and machine-borehole interaction, *European Geothermal Congress 2013*, Pisa, Italy, 2013.
25. R.W. Gillham, J. Vogan, L. Gui, M. Duchene, and J. Son, Iron barrier walls for chlorinated solvent remediation, In *In situ Remediation of Chlorinated Solvent Plumes*, eds. H.F. Stroo and C.H. Ward, New York: Springer, pp. 537–571, 2010.
26. M.M. Scherer, S. Richter, R.L. Valentine and P.J.J. Alvarez, Chemistry and microbiology of permeable reactive barriers for in situ groundwater clean up, *Crit. Rev. Environ. Sci. Technol.,* 30(3): 363–411, 2000.
27. J. Farrell, M. Kason, N. Melitas, and T. Li, Investigation of the long-term performance of zero-valent iron for reductive dechlorination of trichloroethene, *Environ. Sci. Technol*., 34(3): 514–521, 2000.
28. S. Yabusaki, K. Cantrell, B. Sass, and C. Steefel, Multicomponent reactive transport in an in situ zero-valent iron cell, *Environ. Sci. Technol*., 35(7): 1493–1503, 2001.
29. Y. Zhang and R.W. Gillham, Effects of gas generation and precipitates on performance of Fe0 PRBs, *Ground Water*, 43(1): 113–121, 2005.
30. K. Seki, M. Thullner, J. Hanada, and T. Miyazaki, Moderate bioclogging leading to preferential flow paths in biobarriers, *Ground Water Monit. Remed*., 26(3): 68–76, 2006.
31. J. Bear, *Dynamics of Fluids in Porous Media*, New York: Elsevier, 1972.
32. J. Bear, *Hydraulics of Groundwater*, New York: McGraw-Hill, 1979.
33. J. Bear, D. Zaslavsky, and S. Irmay, *Physical Principles of Water Percolation and Seepage*, Paris, France: UNESCO, 1968.
34. J. Dunnicliff, *Geotechnical Instrumentation for Monitoring Field Performance*, New York: Wiley-Interscience, 1993.
35. J.J. Butler, *The Design, Performance, and Analysis of Slug Tests*, Boca Raton, FL: Lewis, 1998.
36. M.J. Hvorslev, Time lag and soil permeability in groundwater observations, *U.S. Army Corps Eng. Waterways Exp. Sta, Bull.,* 36: 1–50, 1951.
37. H.H. Cooper, I.S. Papadopulos, and J.D. Bredehoeft, Response to a finite-diameter well to an instantaneous charge of water, *Water Resour. Res*., 3(1): 263–269, 1967.
38. I.S. Papadopoulos, J.D. Bredehoeft, and H.H. Cooper, On the analysis of slug test data, *Water Resour. Res*., 9(4): 1087–1089, 1973.
39. Z. Hyder, J.J. Butler, C.D. Mcelwee, and W.Z. Liu, Slug tests in partially penetrating wells, *Water Resour. Res*., 30(11): 2945–2957, 1994.
40. D.L. Turcotte and G. Schubert, *Geodynamics: Applications of Continuum Physics to Geological Problems*, New York: John Wiley & Sons, 1982.
41. C.V. Theis, The relation between the lowering the piezometric surface and the rate and duration of discharge of a well using groundwater storage, *Trans. Am. Geophys. Union*, 16: 519–524, 1935.
42. S.P. Neuman, Theory of flow in unconfined aquifers considering delayed response of the water table, *Water Resour. Res.*, 8(4): 1031–1045, 1972.
43. S.P. Neuman, Supplementary comments on theory of flow in unconfined aquifers considering delayed response of the water table, *Water Resour. Res.*, 9(4): 1102–1103, 1973.
44. S.P. Neuman, Analysis of pumping test data from anisotropic unconfined aquifers considering delayed gravity response, *Water Resour. Res.*, 11(2): 329–342, 1975.
45. A.F. Moench, Combining the Neuman and Boulton models for flow to a well in an unconfined aquifer, *Ground Water*, 33(3): 378–384, 1995.

46. S.E. Kelly and L.C. Murdoch, Measuring the hydraulic conductivity of shallow submerged sediments, *Ground Water*, 41(4): 431–439, 2003.
47. S.N. Davis, Porosity and permeability of natural materials, In *Flow through Porous Media*, ed. R.J.M. De Wiest, New York: Academic Press, pp. 54–89, 1969.
48. S.N. Davis and R.J.M. De Wiest, *Hydrogeology*, New York: Wiley, 1966.
49. R.G. Shepherd, Correlations of permeability and grain-size, *Ground Water*, 27(5): 633–638, 1989.
50. M.S. Alyamani and Z. Sen, Determination of hydraulic conductivity from complete grain-size distribution curves, *Ground Water*, 31(4): 551–555, 1993.
51. M.K. Landon, D.L. Rus, and F.E. Harvey, Comparison of instream methods for measuring hydraulic conductivity in sandy streambeds, *Ground Water*, 39(6): 870–885, 2001.
52. C. Baxter, F.R. Hauer, and W.W. Woessner, Measuring the groundwater-stream water exchange: New techniques for installing minipiezometers and estimating hydraulic conductivity, *Trans. Am. Fisher Soc.*, 132(3): 493–502, 2003.
53. D.K. Todd and L.W. Mays, *Groundwater Hydrology*, Hoboken, NJ: Wiley, 2003.
54. C. Kendall and J.J. McDonnell eds., *Isotope Tracers in Catchment Hydrology*, Amsterdam, the Netherlands: Elsevier Science, 1998.
55. P.M. Kearl, Observations of particle movement in a monitoring well using the colloidal borescope, *J. Hydrol*., 200: 323–344, 1997.
56. K. Momii, K. Jinno, and F. Hirano, Laboratory studies on a new laser doppler velocimeter system for horizontal groundwater velocity measurements in a borehole, *Water Resour. Res.*, 29(2): 283–291, 1993.
57. W. Drost, D. Klotz, A. Koch, H. Moser, F. Neumaier, and W. Rauert, Point dilution methods of investigating groundwater flow by means of radioisotopes, *Water Resour. Res.*, 4(1): 125–146, 1968.
58. W. Labaky, J.F. Devlin, and R.W. Gillham, Probe for measuring groundwater velocity at the centimeter scale, *Environ. Sci. Technol*., 41: 8453–8458, 2007.
59. W. Labaky, J.F. Devlin, and R.W. Gillham, Field comparison of the point velocity probe with other groundwater velocity measurement methods, *Water Resour. Res.*, 45: W00D30.
60. A. Kempf, C.E. Divine, G. Leone, S. Holland, and J. Mikac, Field performance of point velocity probe at a tidally influenced site, *Remediation*, 23(1): 37–61.
61. S. Kimura, H. Takeda, M. Nakamura, T. Kiwata, and A. Okajima, Development of groundwater flowmeter: A way to estimate an amount of heat collected by geothermal heat pumps, *Proceedings of the World Geothermal Congress 2005*, Antalya, Turkey, April 24–29, 2005.
62. A.E. Hess and F.L. Paillet, Applications of the thermal pulse flowmeter in the hydraulic characterization of fractured rocks, In *Geophysical Applications for Geotechnical Investigations*, eds. F.L. Paillet and W.R. Saunders, Philadelphia, PA: American Society for Testing and Materials, pp. 99–112, 1990.
63. L. Li and S. Kimura, Numerical simulation of mixed convection in a porous medium heated by a vertical cylinder, *J. Mech. Eng*., 51(7–8): 491–494, 2005.
64. H. Takeda, Y. Igeta, S. Kimura, T. Kiwata, and N. Komatsu, Development of groundwater flow meter using a single borehole, *J. Geother. Res. Soc. Jpn.*, 31(4): 193–202, 2009.

25 Geostatistical Simulation and Reconstruction of Porous Media

Pejman Tahmasebi and Muhammad Sahimi

CONTENTS

25.1 Introduction 869
25.2 Stochastic Simulation and Reconstruction Based on Two-Point Statistics 871
25.2.1 Sequential Gaussian Simulation 871
25.2.2 Random Residual Additions 873
25.2.3 Sequential Indicator Simulation 873
25.3 Multiple-Point Geostatistical Simulation and Reconstruction of Porous Media 874
25.3.1 Iterative Algorithms 875
25.3.1.1 Artificial Neural Networks 875
25.3.1.2 Simulated Annealing 875
25.3.1.3 Genetic Algorithm 876
25.3.1.4 Gibbs Sampler 879
25.3.1.5 Markov Random Fields 879
25.3.2 Sequential Algorithms 879
25.3.2.1 Single Normal Equation Simulation 879
25.3.2.2 Integrated Methods 880
25.3.2.3 Direct Sampling 880
25.3.2.4 Cumulants Approach 880
25.3.2.5 Markov-Mesh Model 881
25.3.3 Pattern-Based Algorithms 881
25.3.3.1 Simulation of Pattern 881
25.3.3.2 Filter-Based Simulation 881
25.3.3.3 GROWTHSIM Algorithm 882
25.3.3.4 Simulation Using Wavelet Transformation 882
25.3.3.5 Distance-Based Pattern Simulation 882
25.3.3.6 Cross-Correlation-Based Simulation 882
25.4 Summary 886
References 887

25.1 INTRODUCTION

An important problem in the modeling of large-scale porous media, such as oil, gas, and geothermal reservoirs, and the simulation of fluid flow therein is the identification of the flow paths that consist of the interwell zones with significant permeabilities. Kriging (Jensen et al., 2000; Sahimi, 2011) has been used for many years for extrapolating the existing data to the interwell regions. But Kriging produces permeability and porosity fields that are excessively

smooth (Journel and Deutsch, 1993; Goovaerts, 1997; Jensen et al., 2000; Sahimi, 2011) with the consequence that the low and high property values are under- and overestimated, respectively. Hence, Kriging estimates are not suitable for representing highly structured systems, such as heterogeneous aquifers and oil and gas reservoirs, and predicting fluid flow through such porous formations. For example, the shortcomings of Kriging become clear when one tries to predict the water breakthrough in an oil reservoir in various flow regimes, because in the Kriging approach, the subsurface connectivity and variability cannot be reproduced with enough resolution to be useful in practice.

Another main shortcoming of Kriging-based geostatistical modeling is its inability for reproducing complex patterns. The main reason is that such methods consider only two-point statistics, hence limiting the order of the complexity that can be reproduced, if higher-order statistical properties are considered, computed, and analyzed, or data for them are available. Over the last two decades, the need for developing methods that can make simultaneous use of many points has been emphasized. Therefore, many alternative methods have been proposed.

Some of such alternatives are based on stochastic or geostatistical simulations, which have been developed to overcome the problems associated with the smoothness problem (Matheron, 1973; Journel, 1974; Journel and Huijbregts, 1978; Jensen et al., 2000; Sahimi, 2011). Stochastic methods generate many realizations of a porous medium that reproduce the broad heterogeneity and spatial uncertainty in the medium's properties (Caers, 2005; Sahimi, 2011). Multiple realizations allow assessing the uncertainty and quantifying it accurately. Due to such a distinct advantage, geostatistical simulations are used frequently in mining, reservoir modeling, and hydrogeology.

Several stochastic methods have been proposed that are based on variograms. They include sequential Gaussian simulation (SGSIM) and sequential indicator simulation, which have been popular and used extensively. Their main difference with Kriging is that stochastic simulations reproduce the spatial heterogeneity that the variograms represent, whereas Kriging aims only at determining a unique estimate by minimizing the error's variance, which is smooth.

In general, geostatistical methods may be grouped into three main classes. In one group, there are object-based simulation methods that consist of marked point process (Kleingeld et al., 1997), and the Boolean method in which a porous medium is represented as a collection of independent stochastic objects whose geometries are based on a specific statistical distribution (Haldorsen and Damsleth, 1990; Deutsch and Wang, 1996; Holden et al., 1998; Skorstad et al., 1999).

Pixel-based methods belong to the second group. They are based on defining an array of points or pixels in a regular grid (Goovaerts, 1997; Deutsch and Journel, 1998; Chiles and Delfiner, 1999), with the pixels representing various properties of a reservoir.

Such methods as conditional simulations via the lower-upper (LU) decomposition of the covariance matrix (Davis, 1987), the SGSIM (Dimitrakopoulos and Luo, 2004), frequency-domain simulation (Borgman et al., 1984; Chu and Journel, 1993), simulated annealing (SA; Deutsch, 1992; Hamzehpour and Sahimi, 2006; Hamzehpour et al., 2007; Sahimi, 2011), and the genetic algorithm (GA; for a discussion, see Sahimi, 2011) are in the last group. The last two methods are optimization techniques that determine the most plausible realization of a porous medium, given some data.

Each of such methods has some advantages, as well as limitations. For example, object-based simulations are accurate in reproducing geological features, but they require intensive computation and encounter difficulty when one tries to condition the model to dense hard (quantitative) data and integrate them with soft (qualitative) data. Pixel-based simulations work on one pixel at a time and, thus, are accurate for data conditioning, but because they use variograms that represent two-point statistics, they cannot capture complex and curvilinear features of porous media and, thus, fail when the models that they generate are used in the simulation of flow and transport problems in large-scale porous media. In addition, they are usually quite slow.

Such shortcomings have led to the development of more accurate methods, based on multiple-point statistics (MPS) (Journel, 1992; Guardiano and Srivastava, 1993; Srivastava, 1994), which

are accurate algorithms for addressing many of the aforementioned problems. The essence of any MPS method is to use useful features of both the variogram-based and object-based algorithms by using a tool—a training image (TI) of the system that is the multiple-point analog of variogram/covariance models in geostatistical models that utilize two-point statistics. In other words, a TI is the conceptual framework that depicts the subsurface heterogeneity and/or a prior numerical geological feature that represents mainly the spatial continuity, patterns, and distribution of the available features in a large-scale porous medium. It is then used for computing multiple-points properties of the system. Therefore, because an MPS method considers more than two points of a system at a time, one may expect the complex facies in a reservoir or large-scale porous media to be reproduced more accurately. In recent years, several MPS methods have been developed to address issues related to the computational intensity and improved representation of the realizations produced.

Geostatistical simulation for the modeling of large-scale porous media belongs to a more general class of problems called *reconstruction* (Sahimi, 2003): given a set of data for a disordered medium that can be quantitative (numerical) or, say, a TI, how can one reconstruct the medium in such a way that it not only honors the data, but also provides accurate predictions for the medium's properties for which there are no data, or if there are, they are not used in the reconstruction. The problem has been studied extensively since the 1970s, and very significant advances have been made. Thus, in this chapter, we use simulation and reconstruction interchangeably, as they both represent the same problem.

The goal of the present chapter is to provide a review of the stochastic simulation and reconstruction methods. We first describe the methods that are based on two-point statistics. We than review and discuss the basic ideas and concepts of the MPS methods, describe the various methods that have been proposed, and explain the advantages and disadvantages associated with each method.

25.2 STOCHASTIC SIMULATION AND RECONSTRUCTION BASED ON TWO-POINT STATISTICS

We consider a set of N random variables $Z(\mathbf{x}_i)$, with $i = 1, \ldots, N$, defined at spatial locations $\mathbf{x}_i$. To remove the smoothness of the Kriging estimates, sequential simulation is often used, which also offers a tool for accurate quantification of the uncertainty. Sequential simulation produces realizations $\{z(\mathbf{x}_i)\}$ with $i = 1, \ldots, N$, conditioned to n available data points and produces a given multivariate distribution function $F[\mathbf{x}_1, \ldots, \mathbf{x}_N; z_1, \ldots, z_N|(n)]$. Using the basic principles of the probability theory, the multivariate distribution F is decomposed into a set of N univariate conditional cumulative distribution functions (CCDFs), such that

$$\begin{aligned} &F[\mathbf{x}_1,\ldots,\mathbf{x}_N; z_1,\ldots,z_N \mid (n)] \\ &\quad = F[\mathbf{x}_1; z_1 \mid (n)]F[\mathbf{x}_2; z_2 \mid (n+1)]\cdots F[\mathbf{x}_{N-1}; z_{N-1} \mid (n+N-2)]F[\mathbf{x}_N; z_N \mid (n+N-1)], \end{aligned} \quad (25.1)$$

where $F[\mathbf{x}_N; z_N|(n + N - 1)] = \text{Prob}\{Z(\mathbf{x}_N) \leq z_N|(n + N - 1)\}$ is the CCDF of $Z(\mathbf{x}_N)$, conditioned to a set of *n original data points* and $(N - 1)$ *previously simulated* (*estimated*) *values*. Let us now discuss the various stochastic simulation methods based on two-point statistics.

25.2.1 Sequential Gaussian Simulation

In the SGSIM, the lower statistical orders, such as histograms and variograms, are used to determine the multivariate distribution F. As its name suggests, the higher-order statistics are expressed by a multivariable Gaussian distribution, which is completely characterized by its mean and covariance matrix, with the two characteristics estimated along a random path using Kriging and its variance. The entire procedure may be summarized as follows (Jensen et al., 2000).

Suppose that we have n data points, $Z(x_i)$ with $i = 1, 2, \ldots, n$, and wish to generate property values for M grid blocks, numbered $j = 1, 2, \ldots, M$, including those at which the data are available. Thus, there are $M - n$ grid blocks that are *unconditioned*, that is, no data for them are available. We also assume that the semivariogram of the data is available, as it can be computed using the n data points. The data are also assumed to be error-free. The property values of the *conditioned* blocks, that is, those for which the data are available, do not change during the SGSIM.

1. The data are first transformed to become Gaussian. Such transformations can be accomplished using normal-score transforms or histogram anamorphosis through Hermite polynomials.
2. The $M - n$ unconditioned grid blocks are assigned property values equal to those of the nearest conditioned blocks.
3. A random walk-through the unconditioned blocks is constructed such that each of such blocks is visited only once.
4. Each time an unconditioned block is visited, the number and locations of the *local* conditioned blocks around it are identified. To do so, one must specify the shape and boundary of the region that constitutes the local neighborhood of the visited unconditioned block. Typically, the local neighborhood is defined in such a way that it has roughly the ellipse range identified by the semivariogram model (recall that most large-scale porous media are typically anisotropic). The local neighborhood may contain the blocks that have already been simulated, that is, a property value has already been assigned to them.
5. Unbiased Kriging (or co-Kriging if needed) is carried out for the local neighborhood, using the data (actual as well as the already simulated, or estimated, which may be in the local neighborhood) as the conditioning points. Once this is done, the mean and variance of the local region are computed. The estimate $\hat{Z}$ has a Gaussian probability distribution function (PDF) with the computed mean and variance. Local Kriging is used in order to avoid solving the large-scale problem. But one may also use a single Kriging for all the unconditioned grid blocks at once, which would include all the trends at all the data points.
6. A random number r, uniformly distributed in [0, 1], is generated and used to pick a property value p from the Gaussian PDF constructed in step 5 by solving the equation

$$r = \int_{p_{\min}}^{p} f(x)dx,$$

   where
   $f(x)$ is the Gaussian PDF
   $p_{\min}$ is the minimum value of the property

   The computed value is attributed to the unconditioned grid block. Thus, the number of the data points (measured as well as already estimated) increases by one.
7. The next step of the random walk to the next unconditioned grid block is taken, and steps 4–6 are repeated.
8. Steps 6–8 are repeated until all the unconditioned grid blocks are visited, and property values are attributed to them. The final result is a realization of the model, conditioned upon the available data.

Clearly, multiple realizations of the model can also be generated using this procedure. Each realization is a plausible representation of the porous medium to be modeled.

25.2.2 Random Residual Additions

The random residual addition method is, in some sense, more realistic than the SGSIM, because it no longer uses the concept of local neighborhood around an unconditioned grid block. What follows is a step-by-step description of the method.

1. An unbiased Kriging is carried out for the entire grid, using the available data as the conditioning points.
2. An unconditioned grid is also generated using the semivariogram. Because it is unconditioned, it does not honor the data at their specified points. But it does have all the required statistical properties, including the same second moment of the PDF of the data, because the semivariogram is used. The unconditioned system is *not* deterministic, but represents a single realization of the ensemble of all the possible realizations with the required statistical properties. The unconditioned grid is generated by any appropriate method.
3. The results of step 2 at the blocks for which the actual data are available are used as the conditioning points, in order to carry out a second unbiased Kriging (or co-Kriging).
4. The unconditioned grid values of step 2 are subtracted from those generated by the second conditioned Kriging (or co-Kriging). Clearly, since the second Kriging is conditioned upon the unconditioned grid, the residuals for the blocks at which actual data are available are zero.
5. The resulting residuals obtained in step 4 are then added to the first Kriging carried out in step 1. Thus, the data are honored at the specified points—zero residuals are attributed to such grid blocks—and the nonzero residuals represent the uncertainty in the property values at the unconditioned grid blocks.

The resulting distribution of the property values in the computational grid has many desirable features: (1) it honors the data exactly at the specified points, (2) it has the correct statistical properties, (3) it is unbiased, and (4) it includes the large-scale heterogeneity that is expected to exist in the geological formation and its model.

25.2.3 Sequential Indicator Simulation

This method classifies each grid block into a facies category. The category is built up using a variety of data, such as seismic-amplitude maps that are calibrated using core and log data and include, for example, channels, overbank deposits, and others.

It is assumed that no two facies can exist in the same grid block. Thus, the method is sometimes regarded as a simulation algorithm for generating the facies. After each grid block is assigned to its facie category, its property value is attributed to it from the PDF of the facie. Thus, the method is also called *sequential indicator simulation-probability distribution function* (SIS-PDF). The overall PDF of the facies represents the pattern of their occurrence at the length scale of the porous medium to be modeled. The PDF is obtained from the usual sources, that is, either log data or a map of the facies. The overall procedure for the SIS-PDF is as follows:

1. As in the SGSIM, a random walk is taken through the computational grid that represents the porous medium, such that the unconditioned blocks are visited once and only once.
2. For each visited unconditioned grid block, the prespecified number of conditioning facies data from the wells and already simulated blocks, as well as any other sources of data, is identified.
3. An *indicator Kriging* is carried out in order to estimate the conditional probability for each facies category. An indicator Kriging uses indicator functions, instead of the process itself, in order to estimate the transition probabilities. It proceeds exactly like the usual Kriging,

except that an *indicator* semivariogram γ_I is used in place of the usual semivariogram, and the data values Z_i are replaced by their respective indicators. To construct γ_I, a threshold value Z_c is introduced that varies between a minimum and a maximum value and, hence, can take on several values Z_{ci}. Then, the indicator variable $I(Z_{ci})$ is defined by

$$I(Z_{c_i}) = \begin{cases} 1 & Z_i \le Z_{c_i}, \\ 0 & Z_i > Z_{c_i}. \end{cases}$$

The cumulative distribution function $\hat{F}(Z_c)$ is then constructed by

$$\hat{F}(Z_c) = \frac{1}{M} \sum_{i=1}^{M} I(Z_{c_i}),$$

where $M < n$, with n being the number of the data points. The indicator semivariogram is constructed based on $I(Z_{ci})$, and the cumulative probability distribution is used for estimating the conditional probabilities.

4. Each facie's probability is then normalized by the sum of the probabilities of all facies. The result is then used to construct a local cumulative probability distribution.
5. A random number r, distributed uniformly in [0, 1], is generated and used together with the local cumulative distribution function in order to determine the simulated facies category in the visited unconditioned grid block.
6. For each unconditioned block in the random path, steps 2–5 are repeated. The final result is the facies distribution.

25.3 MULTIPLE-POINT GEOSTATISTICAL SIMULATION AND RECONSTRUCTION OF POROUS MEDIA

A common feature of all the two-point geostatistical simulation methods is their inability for capturing broadly distributed heterogeneities and complex spatial patterns. In particular, such methods cannot reproduce the long-range connectivity and heterogeneity, when the system considered contains definite patterns or structures. For example, SGSIM maximizes the entropy of the stochastic functions and, therefore, prevents the realizations to be structured (Haldorsen and Damsleth, 1990). To capture such structures and their important properties, including long-range connectivity and heterogeneity, use of many points at a time is necessary; two-point statistics are simply inadequate.

Object-based, or Boolean, methods present an alternative. In such algorithms, the simulation grid is filled with proper-shape objects that honor the hard data (HD; Haldorsen and Damsleth, 1990; Guardiano and Srivastava, 1993; Deutsch and Wang, 1996; Holden et al., 1998; Viseur, 1999; Lantuéoul, 2002). Since the geometrical parameters, such as size and direction, are all spatially distributed, the algorithm for generating them is stochastic. Then, as discussed later, an iterative algorithm is used in order to remove, vary, add, or modify the objects.

The object-based simulation methods are well suited for reproducing the TIs and can be conditioned on a limited amount of data. Generally speaking, the TI is a conceptual model or image that conveys or represents the porous formation's main features and heterogeneity. A TI is not conditioned to any local data, but represents the general features of interest and is able to quantify some qualitative information and integrate it with the available quantitative data, such as well logs and seismic data. If, however, one simulates a grid with dense data, identifying and adjusting the objects can be problematic. On the other hand, pixel-based simulations are better conditioned to HD, but they may fail to reproduce the long-range connectivity and complex patterns in the TIs.

The initial idea for the MPS simulation was developed by Guardiano and Srivastava (1993). The basic idea was to scan the TI with a template in order to develop the replicates within the TI. The main problem with this method is that it must rescan the TI for simulating each location, and therefore, it needs a tremendous amount of computation time. As a result, it is impractical for large systems. Ever since the original work of Guardiano and Srivastava (1993), several other methods have been proposed, which can be classified into three main categories, namely, iterative algorithms, probabilistic methods, and pattern-based simulation techniques. In what follows, we describe the main features of these algorithms and their limitations, as well as advantages.

25.3.1 Iterative Algorithms

Most of such algorithms are based on an optimization method that attempts to determine the global minimum of an *objective function*, which is usually defined as the sum of the square of the differences between the computed values and the data.

25.3.1.1 Artificial Neural Networks

An artificial neural network (ANN) is a computation algorithm that somehow exhibits *intelligence*. In practice, an ANN is simply a computational tool that fits a linear or nonlinear function to a set of data, which can be hydraulic conductivities, porosity data, etc. An early application of the ANNs was proposed by Caers and Journel (1998) in which the MPS was inferred from a TI, and then, an ANN was used to estimate the values conditioned to the statistics. Caers and Ma (2002) used an ANN for data integration. For recent applications of the ANNs, see Tahmasebi and Hezarkhani (2009, 2010, 2011, 2012), Asadisaghandi and Tahmasebi (2011), and Li et al. (2011, 2012, 2014), where many references to the earlier works are also given.

The method is reasonably accurate if, after fitting the data set, the ANN is used for simulating systems or TIs that are more or less similar to the data that were used in the fitting. Otherwise, the ANN may fail to converge to some representative system. Moreover, the ANN methods are computationally very intensive. Tahmasebi and Hezarkhani (2011, 2012) showed that the architecture of an ANN should be optimized in order to prevent the network from becoming trapped in local minima.

25.3.1.2 Simulated Annealing

SA is a powerful stochastic optimization method, developed by Kirkpatrick et al. (1983) that, in theory, is capable of determining the global minimum of an objective function and has been used in a variety of applications. Let us define an *energy E*—the aforementioned objective function—by

$$E = \sum_{j=1}^{n} [f(\mathbf{O}_j) - f(\mathbf{S}_j)]^2, \tag{25.2}$$

where $\mathbf{O}_j$ and $\mathbf{S}_j$ represent the observed (or measured) and the corresponding simulated (calculated) properties of a porous medium, respectively, with n being the number of data points. If there are more than one set of data for *distinct* properties of the medium, the energy E is generalized to

$$E = \sum_{i=1}^{m} w_i E_i, \tag{25.3}$$

where

E_i is the total energy for the data set i

w_i is the corresponding weight, as two distinct set of data for the same porous medium do not necessarily have the same weight or significance

To initiate the simulation in order to generate a realization of the system, one begins with an initial guess for the structure (properties of interest) of the porous formation. Two randomly selected points of the model are then interchanged. The new energy E' of the system and the energy difference, $\Delta E = E' - E$, are then computed. The interchange is then accepted with a probability $p(\Delta E)$. According to the Metropolis algorithm,

$$p(\Delta E) = \begin{cases} 1, & \Delta E \le 0, \\ \exp(-\Delta E/T), & \Delta E > 0, \end{cases} \tag{25.4}$$

where T is a fictitious temperature.

Statistical mechanics of thermal systems provides the theoretical foundation for such an algorithm. We know that if a system is heated up to a high temperature T and then slowly cooled down to absolute zero, the equilibrium state of the system will be its ground state. The cooling, usually called the *annealing schedule*, is selected to be sufficiently slow so as to allow the system to reach its true equilibrium state, rather than getting trapped in a local energy minimum (a metastable state), and attain its true global minimum energy. At each annealing step i, the system is allowed to evolve long enough to *thermalize* at $T(i)$. We then lower T according to a prescribed annealing schedule. The cooling continues until the true ground state of the system is reached within some acceptable error, that is, when E is deemed to be small enough.

Such a procedure was utilized by Yeong and Torquato (1998a,b), Cule and Torquato (1999), Manwart and Hilfer (1999), and Sheehan and Torquato (2001) for simulating and reconstructing various models of random media. Manwart et al. (2000) used the method to reconstruct sandstones, given some data for the porous medium. Talukdar and Torsaeter (2002) and Talukdar et al. (2002a,b) used the SA to reconstruct a variety of porous media, including chalk. The SA method has also been used for simulating and reconstructing models of the large-scale porous media, such as oil reservoirs. Farmer (1990) and Deutsch (1992) used the algorithm to reproduce some MPS properties. Panda and Lake (1993) used the method, together with a parallel computational strategy, in order to simulate and reconstruct a model of an oil reservoir by optimizing its permeability field. Quenes and Saad (1993) also used the method for oil reservoir characterization, utilizing a parallel computational strategy, as did Savioli et al. (1996) and Saccomano et al. (2001). Hamzehpour and Sahimi (2006) and Hamzehpour et al. (2007) showed that the SA in conjunction with static and dynamic data for an oil reservoir produces a highly accurate model of the reservoir, also Fang and Wang (1997) and Peredo and Ortiz (2010).

The main disadvantage of the SA method is that it cannot be used easily in massively parallel computations. Although algorithms have been developed for this purpose (see, e.g., Bevilacqua, 2002; Ye and Lin, 2006), they have yet to be tested for the type of large and complex optimization problems that one must tackle for simulating a large-scale porous medium.

25.3.1.3 Genetic Algorithm

Another well-known and heavily used optimization method is the GA; see, for example, Reeves and Rowe (2003) for a good discussion of its essential concepts. The GA has also been utilized in the simulation and reconstruction of large-scale porous media. For example, Romero et al. (2000) and Romero and Carter (2001) used the GA to develop a model of an oil reservoir by optimizing the performance of a flow simulator that computed the pressures and water flow rates at a number of extraction wells in the reservoir. Sanchez et al. (2007) and Li et al. (2011, 2012, 2014) utilized the GA to reconstruct a model of landfills—large-scale porous media with the additional complexity relative to oil reservoirs that, in addition to flow and transport, biodegradation, and reactions with nonlinear kinetics also occur there.

Let us describe and discuss the essentials of the GA. Any optimization problem that utilizes a GA involves four steps:

1. The *selection* process for generating solutions
2. The *design* of the *genome* to constrain the variables that define a possible solution and to generate the *phenotype* that, in the present problem, is the model of flow and transport
3. The *crossover* and *mutation* operations that are used for generating new solutions and approaching the true optimal one
4. *Eliticism*, which selects those solutions that lead eventually to the global minimum of the energy, or objective function

Each time we carry out all the four sets of operations, we have completed one *generation* of the computations. The various steps that are involved in using the GAs are as follows.

25.3.1.3.1 Selection

In Darwin's theory, species that can adapt to their environment are selected to produce the next generation of the offsprings. In simulating and reconstructing a large-scale porous medium, each species is the set of all the parameters that we wish to determine their optimal values, given some data for one or more properties of the medium, such as the spatial distributions of the permeabilities and porosities. Selection is the method by which the species are chosen to produce the offsprings—the updated species for the next generation. Except for the first generation (the first trial species), selection of the species in the GAs is based on the evaluation of the energy or objective function defined earlier for the SA method. The species with a smaller energy function possesses a greater probability of producing one or more offsprings for the next generation. The set of all the possible species that we examine during the optimization process is called the *population*. One must specify the population's size at the beginning of the optimization process.

The GA is not sensitive to the initial guesses (the initial population of the species) for the parameters to be optimized. Therefore, the first population of the species may be generated randomly in the ranges over which the parameters to be optimized are expected to vary. Of course, if one has some additional insights into the spatial distributions of the parameters to be optimized, they are also used for generating more accurate initial species and their population.

Using the population of the species, we use a model for numerical simulation of the phenomenon in the porous medium for which there are some data. For example, if the data are the time-dependent pressures at one or more production wells in an oil reservoir, we solve the equation for the pressure transient analysis, in order to compute the time-dependent pressures at the production wells. Then, the next species is selected based on the evaluation of the energy function. There are four common selection techniques used in the GAs. We describe one of them, the *binary tournament* selection, as follows.

We set a priori the probability p_s of the selection. The higher p_s, the more likely it is that the GA will eventually yield the true optimal solution. One selects a value of p_s that is high enough to ensure a reasonably accurate solution, but not too high to make the computations prohibitively expensive. One then picks at random two of the species from the population. A random number r, uniformly distributed in (0, 1), is generated. If $r < p_s$, one selects the species that resulted in a smaller energy. Otherwise, the one with the larger energy is picked. Another pair of species is then selected from the population, and the same procedure is repeated. Each pair of the selected species constitutes a *mating pair*. Note that, since the species are chosen at random, any species may be selected numerous times, which is why the population of the selected species generally results in a set with lower energies. Repeating this procedure a large number of times finally yields a set of mating pairs, the size of which is half the population's size. Each mating pair can generate two offsprings during the crossover step. This completes the selection process.

Crossover is achieved when a mating pair produces two offsprings. To do so, the values of the parameters to be optimized are first converted to binary numbers involving 0 and 1. Similar to the selection, there are several types of crossover methods that one may utilize. One may, for example, utilize *uniform crossover*, since it has been shown to encourage the exploration of a robust search domain or population. For each parameter value in its binary representation, the GA selects a 0 and a 1 at random and exchanges their places in the parameter's binary representation. The procedure is then repeated a number of times to generate a new binary representation of that parameter of the offspring. For example, suppose that two of the parameters to be optimized are represented by 01110011010 and 10101100101. Then, one generates, by a uniform crossover, the offsprings 01110100101 and 10101011010. This procedure is repeated for all the parameters in all the mating pairs, resulting at the end in the new species or offsprings (which explains why using a large population of the species is very useful). The crossover step is then completed.

25.3.1.3.2 Mutation

After the offsprings are generated, it is possible that they exhibit some kind of *defect*, which exhibits itself by producing a large energy or the value of the objective function. Such a defect in the GAs is known as mutation. The mutation probability is selected from a Gaussian distribution with zero mean and a given variance (e.g., 0.1). All the binary representations of the parameters are converted back to real numbers, hence generating the new population of the species. Numerical simulation of the phenomenon for which the data are available is then carried out using the new population of the offsprings or species, and the energies are computed for all the species based on the newly calculated properties for which the data are available. This completes one generation of the computations.

25.3.1.3.3 Eliticism

In order to speed up the computations, and to ensure that the true global minimum of the energy will eventually be reached, one also uses *eliticism* that, for every generation, selects those species with the energies of the lowest values and inserts them into the next generation.

Then, the entire procedure, consisting of selection, crossover, mutation, and eliticism, is repeated again, resulting in the second generation. Enough generations are produced until the true optimal solution (in the sense that the minimum of the energy for a species is its true global minimum, not a local one) is obtained.

The efficiency and performance of any GA depend on the numerical values of its parameters, ranging from the population size, to the selection, crossover, and mutation probabilities. This is a virtue of any GA since, by selecting proper (optimal) values of such parameters, the method's efficiency can be greatly increased, while lowering its computational cost. As pointed out earlier, an important advantage of the GA over other optimization techniques is that, it is not sensitive to the initial guesses that one utilizes for the parameters that are to be determined and optimized, such as the spatial distributions of the permeabilities and porosities. Thus, even an arbitrary initial guess may be employed by the GA. The GA *ensures* that practically the entire search domain is tested for optimality, and therefore, the probability of finding the global minimum of the objective function can, in principle, approach 1. Another advantage that the GAs have over many deterministic optimization techniques is that there is no need for calculating any derivative of the energy function, which can be computationally difficult and expensive if the function is complex.

One disadvantage of the GA is that its use can be computationally expensive if computing the energy function is time consuming, so much so that some optimization problems might require many weeks or even months for completion. However, the GA spends up to 99% of the total computation time to evaluate the energy function. Due to this fact, utilizing high-performance computers and massively parallel computational strategies alleviates the problem.

25.3.1.4 Gibbs Sampler

Gibbs sampler (Geman and Geman, 1984) is a special case of the aforementioned Metropolis algorithm. It is a Markov chain Monte Carlo (MCMC) algorithm for computing a sequence of observations that are approximated from a specified multivariate probability distribution (i.e., from the joint probability distribution of two or more random variables), when direct sampling is difficult. The sequence is used to approximate the joint distribution, such as a histogram of the distribution, to approximate the marginal distribution of one of the variables, or some subset of the variables, such as the unknown parameters or latent variables, or to compute an integral, such as the expected value of one of the variables. Typically, some of the variables correspond to observations whose values are known and, hence, do not need to be sampled. Gibbs sampler is commonly used as a means of statistical inference, especially Bayesian inference. It is a randomized algorithm as it makes use of random numbers and, hence, produces different realizations each time it is run. It is an alternative to deterministic algorithms for statistical inference, such as variational Bayes, or the expectation–maximization algorithm.

Lyster and Deutsch (2007) used the method for modeling geological features. The method is similar to the Markov approaches (see later), and different realizations are obtained by resampling the values at each node in an iterative fashion until convergence is achieved. It is, therefore, extremely time consuming.

25.3.1.5 Markov Random Fields

The Markov random-field model (Besag, 1974; Tjelmeland, 1996) utilizes constraints by formulating high-order spatial statistics and enforcing them in the simulated domain using a Metropolis–Hastings algorithm. The algorithm is an MCMC method for obtaining a sequence of random samples from a probability distribution for which direct sampling is difficult. For a good exposition to the method, see Chib and Greenberg (1995). The sequence can be used to approximate the distribution (i.e., to generate a histogram) or to compute an integral, such as an expected value. The Metropolis–Hastings and other MCMC algorithms are generally used for sampling from multidimensional distributions, especially when the number of dimensions is high.

Tjelmeland and Eidsvik (2004) used a sampling algorithm that incorporates an auxiliary random variable. The method suffers from the same computational problems described earlier, namely, that although the Metropolis–Hastings algorithm always converges in theory, it may not do so in a reasonable time.

25.3.2 Sequential Algorithms

Let us now describe the sequential algorithms for the MPS simulations.

25.3.2.1 Single Normal Equation Simulation

As described earlier, the main problem with the original MPS method developed by Guardiano Srivastava (1993) was the need to scan the entire TI for simulating each grid block or node. To overcome the problem, Strebelle (2002) proposed an innovative algorithm whereby the TI is scanned once and all the conditional probabilities for a given pixel's configuration—the template—are stored in a dynamic search tree. Then, there is no need to rescan the entire TI to simulate a new node or template, as one can directly use the tree structure to retrieve the conditional probabilities. The method, popularly referred to as the single normal equation simulation (SNESIM), follows the framework of the traditional sequential algorithms based on a random path described earlier and utilizes the original data and the previously simulated (reconstructed) nodes or grid blocks. The main difference between the traditional methods and the SNESIM algorithm is that the latter uses statistics inferred from the TI, instead of a variogram.

The SNESIM method must be used with categorical TIs. One can, of course, divide a continuous TI into categories (Strebelle and Zhang, 2005). In that case, however, the method becomes very computer memory demanding, if the number of the categories is large, making the method inefficient and slow.

A variation of the SNESIM method is what is called the improved parallel multiple-point algorithm, or IMPALA, using a list approach. In this method (Straubhaar et al., 2011), a structure list is used for storing the data, instead of the search tree in the SNESIM. Since, compared with a tree, a list is much less demanding computationally, the method improves upon the SNESIM. It is particularly useful when one has large TIs that contain large numbers of categories. It can be shown that the size of the tree grows exponentially with the TI complexity, whereas the size of the list grows only linearly. Another advantage of the IMPALA is that it is possible to efficiently parallelize the list, whereas doing so for a tree is very difficult.

25.3.2.2 Integrated Methods

Integrated methods combine several approaches. For example, Ortiz and Deutsch (2004), under the assumption of independence of the data sources, integrated the indicator method with the MPS simulation. Hence, instead of using a TI, the MPS properties are obtained directly from the available HD, such as variograms, and are then integrated with the results of indicator Kriging. Then, a value is drawn from the new distribution; see also Ortiz and Emery (2005) and Hong et al. (2008) for more details. Such methods are usually not very accurate for a highly heterogeneous porous media, because the realizations generated by them are strongly influenced by the initial results of the indicator Kriging.

25.3.2.3 Direct Sampling

Mariethoz et al. (2010) and Mariethoz and Renard (2010) proposed a method that consists of sampling of the TI, conditioned to a given pattern or data event. The data event does not need to have the same shape or the same number of neighbors for each simulated node or grid. Since the TI is sampled directly, there is no need to construct a CCDF, as there is no need to store the MPS. The TI is sampled by defining a distance between the data event searched for and the one sampled. Using various definitions of the distance allows dealing with categorical, continuous, or multivariate cases.

In practice, at each simulated node or grid block, a neighborhood is selected and a data event defined. A data event is a set of data at a particular point or grid block that may change during the course of the simulation, hence the name "event." Then, the TI is searched according to the data event, and the similarity distances are calculated. As soon as the first matching data event in the TI is identified, which corresponds to a distance under a given threshold for acceptance, the value of the central node of the data event in the TI is accepted and attributed to the simulation grid. If the algorithm identifies a pattern that is similar to the TI up to a given threshold, the search is stopped. Otherwise, the most similar pattern is selected, and its central node is inserted in the simulation grid. The method has some important advantage over what has been described so far. One is its very low computer memory requirement. Another advantage is that it is relatively efficient.

Mariethoz and Kelly (2011) proposed a variation of the method by using specific measures of the distance between data events, which allows using and combining elementary TIs to define the desired spatial patterns.

25.3.2.4 Cumulants Approach

Dimitrakopoulos et al. (2010) proposed a simulation method based on computing the cumulants. The approach represents an extension of those based on the variograms and accounts for higher-order statistics beyond two-point ones. It has the distinct advantage that the cumulants are directly inferred from the data, rather than from a TI. Dimitrakopoulos et al. (2010) showed that the choice of the cumulant depends on the geological process, anisotropy, and pattern redundancy.

Computer programs for calculating the higher-order cumulant were developed by Mustapha and Dimitrakopoulos (2010a), and utilized by Mustapha and Dimitrakopoulos (2010b) for the modeling of complex spatially distributed natural systems.

The algorithm first computes high-order statistics from the data. It resorts to using a TI, only if not enough replicates could not be identified to determine the conditional probabilities. A shortcoming of the method is related to selecting the spatial cumulants. It is different for each type of geological structure with no general strategy as to how to select it.

25.3.2.5 Markov-Mesh Model

Daly (2004) and Daly and Knudby (2007) developed an algorithm called Markov-mesh method (MMM) in which a raster path is utilized for simulating and reconstructing the target system, an idea borrowed from texture synthesis. First, a casual template is put on the simulation grig node, and then the conditional probabilities are computed for the sequential nodes along the raster path. Parra and Ortiz (2011) used a similar methodology and obtained accurate results. Conditioning of the MMM to hard and soft data, however, is problematic due to the use of a raster path, making it difficult to reproduce continuity of the model near the HD.

25.3.3 Pattern-Based Algorithms

Pixel-based algorithms described so far encounter difficulties in preserving the continuity of the geological structures under study. To address this difficulty, several pattern-based simulation and reconstruction methods have been developed. Such methods do not simulate one pixel at a time, but an entire patch (represented by a grid block). An important property of the pattern-based simulation methods is their ability for preserving the continuity and overall structure of the TI. In what follows, we describe briefly several of such methods.

25.3.3.1 Simulation of Pattern

Simulation of patterns, or SIMPAT, was introduced by Arpat and Caers (2007) to address some of the limitations of SNESIM. The method uses the TI for determining the conditional probabilities and, therefore, the final pattern that should be attributed to a data event location. First, the TI is scanned with a given template and stored in a pattern data base. Then, the locations to simulate (reconstruct) are selected according to a random path. At each node, the data event is identified. If it is empty in the sense of containing no HD, then a patch (say, a portion with the size of a grid block) from the TI is selected randomly. Otherwise, according to the available known nodes and their distances to all of the patterns in pattern database, the most similar pattern is attributed to the data event. Then, the next node in the random path is simulated. The process continues until all the nodes have been visited. The results are very promising, but due to a high computational cost, SIMPAT is not practicable for 3D applications.

25.3.3.2 Filter-Based Simulation

As pointed out in the last section, a major drawback of SIMPAT is its computational cost, because for each node, one needs to compare a data event with all the patterns in their data base. One possible solution is to use a redundancy algorithm to reduce both the data event and the comparison for identifying similar patterns. Zhang et al. (2006) proposed a new method, filter-based simulation (FILTERSIM), in which they used a set of six and nine filters in 2D and 3D simulation, respectively, in order to summarize the basic spatial properties of the patterns contained in the TI. This allows one to significantly reduce the dimensionality of the patterns' space and, hence, the computation time. The patterns are first summarized using the predefined linear filters and, according to some similarity criteria, are grouped in distinct clusters. Then, for each cluster, a prototype pattern is computed that represents the average of all the patterns in the cluster. The rest of the algorithm proceeds, at each node, by selecting the most similar prototype and randomly drawing a pattern from

that cluster. The procedure is repeated for all locations that are to be simulated. It is due to the use of a limited number of filters that the computation cost of FILTERSIM is better than SIMPAT's.

The most important shortcoming of FILTERSIM is that it uses a limited set of linear filters that cannot always convey all the information and variability in the TI. Moreover, selecting the appropriate filters and several user-dependent parameters for each TI is an issue that is that common among many MPS methods.

25.3.3.3 GROWTHSIM Algorithm

Eskandari and Srinivasan (2010) proposed a new TI-based algorithm, called GROWTHSIM. The main goal for developing the method was integrating dynamic data into the simulation. The main feature of the method is that it begins the simulation from the given data. The simulated values *grow*—hence the name of the algorithm—from the initial seed locations. The method incorporates an optimal template definition. It is particularly suited for the integration of transient flow and transport data in aquifer or oil reservoir simulations.

25.3.3.4 Simulation Using Wavelet Transformation

Gloaguen and Dimitrakopoulos (2009) used analysis based on wavelet transformations (WTs) in order to simulate both categorical and continuous variables, using TIs. The dimensionality of the TI is reduced, in a manner similar to FILTERSIM. The wavelet bands capture the spatial variability contained in the TI with a limited number of wavelet coefficients that correspond to distinct scales of variability. Then, the wavelet coefficients are used to classify the patterns. Whereas FILTERSIM bases the similarity on the filter scores, the WT-based algorithm bases it on the wavelet coefficients. The algorithm can incorporate both hard and soft data. The shortcoming of the method is that a large number of parameters influence both the quality of the results and the computation time, and thus, the user must tune them in order to achieve accurate results in a reasonable time.

Let us mention that Sahimi and coworkers have made extensive use of the WTs in problems related to characterization and modeling of oil reservoirs and other types of porous media. They include analysis of the well logs and cross-correlations between them (Mehrabi et al., 1997; Dashtian et al., 2011a,b), upscaling of the single-phase permeability (Mehrabi and Sahimi, 1997; Ebrahimi and Sahimi, 2002), upscaling of miscible and immiscible flows in porous media (Ebrahimi and Sahimi 2004; Rasaei and Sahimi, 2008, 2009a,b), and identification of fracture distribution in a heterogeneous porous medium (Sahimi and Hashemi, 2001).

25.3.3.5 Distance-Based Pattern Simulation

Distance-based pattern simulation (DISPAT) is a modification of SIMPAT, introduced by Honarkhah and Caers (2010). It also incorporates some features of FILTERSIM, such as pattern classification and the use of an inner patch. The patterns in the database are represented as points in a Cartesian space, using multidimensional scaling. Next, in a kernel space, the dimensionality of the patterns is reduced significantly, leading to a better classification. Another advantage is that it is possible to expand the patterns' database by creating new patterns similar to the ones that already exist in the database. The rest of the algorithm is similar to FILTERSIM. DISPAT produces acceptable results with reasonable computation time, but is limited in terms of memory requirements when if it is used for very large TIs.

25.3.3.6 Cross-Correlation-Based Simulation

Tahmasebi et al. (2012) and Tahmasebi and Sahimi (2012, 2013) proposed a new methodology based on a cross-correlation function (CCF) along a 1D raster path, referred to as cross correlation-based simulation (CCSIM). We describe briefly the CCSIM method for 2D media; the extension to 3D media will be clear. Let $\mathbf{G}$ represent the computational grid used in the reconstruction, which is partitioned into blocks or templates of size $L_x \times L_y$. Likewise, the TI to be simulated and reconstructed is partitioned into exactly the same number of blocks of the same size $L_x \times L_y$. The blocks of $\mathbf{G}$ and the TI are denoted, respectively, by $\mathbf{T}_{\mathbf{G}}$ and $\mathbf{T}_{\mathrm{TI}}$. We denote by $\mathbf{D}_T(\mathbf{u})$ the *data event* at

position **u** in $\mathbf{T_G}$. Between every two neighboring blocks is an overlap region **O** of size $\ell_x \times \ell_y$, representing $\mathbf{D}_T$, where $\ell_x(\ell_y) = L_x(L_y)$ and $\ell_y(\ell_x) \ll L_y(L_x)$, if **O** is between two templates that are neighbors in the $x(y)$ direction. The purpose of the **O** regions is to preserve the continuity near the common boundary between two neighboring blocks.

As mentioned earlier, the previous MPS methods used a distance function in order to reconstruct and simulate the given TI. In the CCSIM, we use a CCF as the measure of the similarity between the TI and its generated realizations. The method can be used for both unconditional simulations—those that are not required to honor hard, quantitative data—and conditional simulations that must honor HD. So, let us describe both cases.

25.3.3.6.1 Unconditional Simulation

Let TI (x, y) represent the datum at point (x, y) of a TI. Examining the TI, one focuses on a portion $\mathbf{D}_T(\mathbf{u})$ and regenerates it based on the data, such that it matches the corresponding portion in the TI. The CCF, used for to quantifying the similarity between the TS and $\mathbf{D}_T$, is given by

$$\mathcal{C}(i,j) = \sum_{x=0}^{\ell_x - 1} \sum_{y=0}^{\ell_y - 1} \mathrm{TI}(x+i, y+j)\mathbf{D}_T(x,y), \tag{25.5}$$

with $0 \le i < L_x + \ell_x - 1$ and $0 \le j < L_y + \ell_y - 1$. Equation 25.5 indicates that the desired position of (i, j)—the best match with the TI—is one that *maximizes* $\mathcal{C}(i, j)$. Since we do not know a priori the location of maximum of the CCF, we use $1/\mathcal{C}$ and set a threshold $0 \le \delta \le 1$. If $\delta = 0$, the similarity between the **O** regions and the corresponding portions in the TI is perfect, whereas $\delta > 0$ generates an ensemble of realizations that do not match the TI *exactly*. The reconstruction proceeds along a 1D raster path. Suppose, for example, that the 1D raster path is along the vertical (y) direction; see Figure 25.1 for an illustration.

The algorithm begins at the path's origin in **G**—Grid block number 1 at the leftmost bottom of **G** in Figure 25.1—and moves along the path. A realization of the disorder in the TI, equal in size to $\mathbf{T}_{\mathrm{TI}}$, is generated and inserted into the first block, part of which represents the **O** region with the next block. As already mentioned, the purpose of the **O** region is to preserve the continuity near the common boundary between two blocks. Thus, one generates the most accurate realization of the disorder for the next neighboring block along the path, denoted by 2 in Figure 25.1, whose bottom **O** section makes a seamless transition between the two. If several realizations of the disorder have the same degree of similarity with **O**, one of them is selected randomly. The procedure continues until

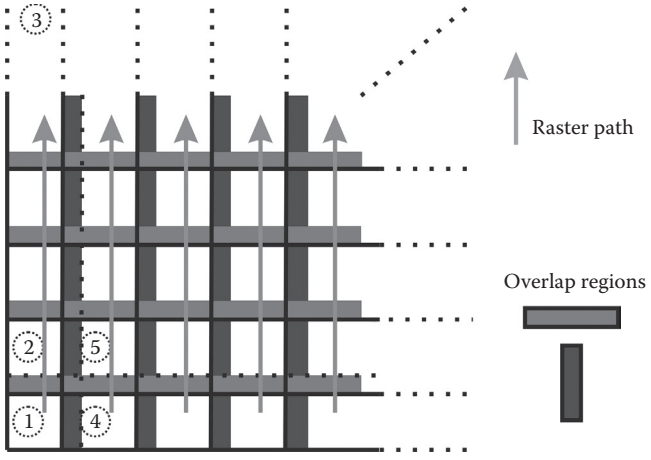

FIGURE 25.1 Schematic of simulation and reconstruction in two dimensions.

reconstruction of the first vertical column of the raster path is finished, and template 3 in Figure 25.1 is reconstructed. The algorithm then moves to the bottom block of the next vertical column of **G**, numbered 4 in Figure 25.1, and uses the same procedure, taking into account its **O** region with the neighboring block, number 1, on the left. The next block, number 5 in Figure 25.1, is more complex as it has two **O** regions, at the bottom and on the left. Thus, the reconstruction is summarized as follows:

1. Generate for the first block of **G** along the raster path a realization of the disorder in the TI, based on TI and constrained by its statistics (such as volume fractions of the phases), or by sampling TI.
2. Compute the CCF between the **O** and the *entire* TI.
3. If $1/\mathcal{C} < \delta$, the realization is accepted. If not, other realizations are generated, or δ is increased somewhat, until $1/\mathcal{C} < \delta$. Typically, one generates 30–50 realizations in order to satisfy the similarity criterion.
4. Fill up the next block with a realization of the disorder, identify the new **O** with the next block to be reconstructed, and repeat steps 1–3. The entire procedure continues until **G** is completely reconstructed.

Use of a raster path has several advantages, as well as a limitation. For example, it is possible to design a parallel algorithm with a raster path. The main drawback of the path is that it is not possible to go back and resimulate or regenerate the discontinuities, particularly around HD. This can, however, be addressed, and we will return to it shortly.

25.3.3.6.2 Conditional Simulation

According to the definition of HD, they do not change at any time and, therefore, the HD event HD_T remains constant during the entire simulation. In conditional simulation, the algorithm tries to identify patterns that are similar to those in the TI and contain the HD. Thus, the algorithm is a two-step process. First, it identifies the patterns that honor the HD. Next, according to the specified threshold δ, the algorithm identifies the patterns that are most similar to the DH_T. Then, one of such patterns is selected at random and inserted into the system.

To improve the continuity of the reconstructed system around the regions that contain HD, one can proceed as follows. One either uses another raster path in a different direction or, alternatively and more rigorously, one may use an adaptive recursive template splitting, summarized in Figure 25.2. For a given threshold δ, the algorithm tries to identify the patterns that honor the HD. If it fails, then HD_T is split into smaller data events (HD_T^s), and the new data events are used for reconstruction of that particular section. The splitting continues until the algorithm succeeds. Clearly, template splitting may happen repeatedly if the TI is highly heterogeneous.

If the size of the TI is not too large, all the computations are carried out in the spatial domain. When the TI is very large, calculations in the Fourier space result in significant savings in the computations (Tahmasebi et al., 2015).

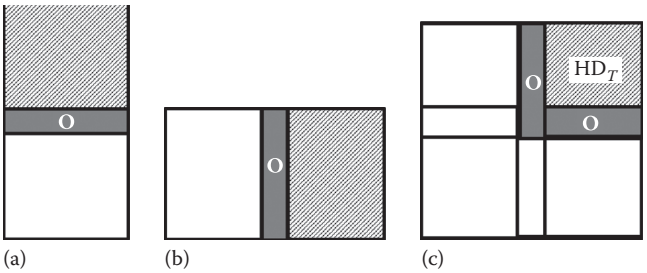

FIGURE 25.2 Adaptive recursive template splitting scheme in order to identify a matching pattern. The O region represents the overlap between (a) two vertical grid blocks on the leftmost side; (b) two grid blocks in the lowest horizontal row of the grid, and (c) between several blocks in inside the grid.

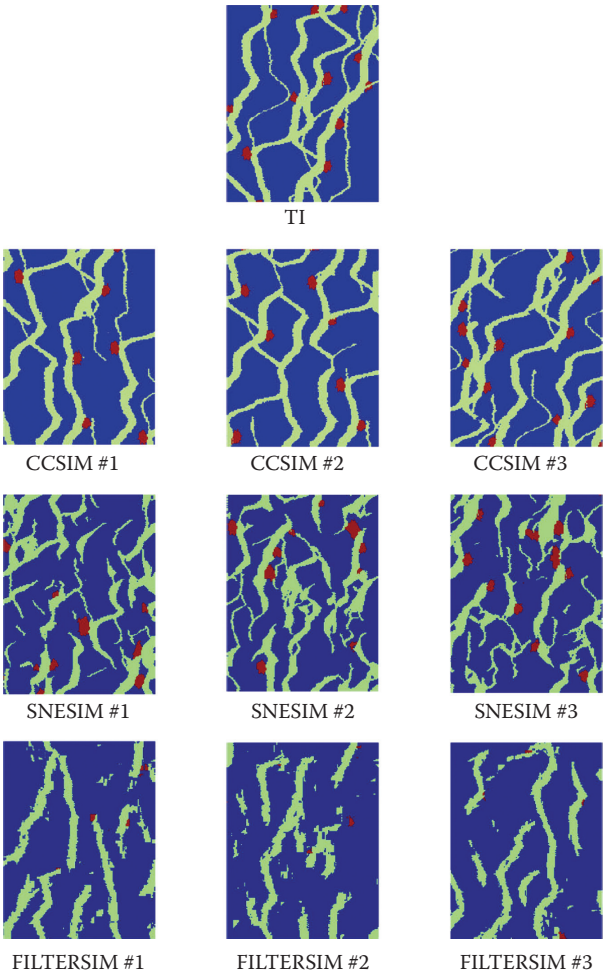

FIGURE 25.3 A training image (TI), shown at the top, and three realizations generated by the CCSIM, SNESIM, and FILTERSIM methods.

As the description of the method makes clear, there is no need to make a large pattern data base, and moreover, the selected pattern is directly inserted in the grid block. Therefore, the CCSIM decreases the computer memory demand significantly. In addition, since the CCSIM uses the overlap regions, it simulates and reconstructs the patterns very quickly.

Let us now present two examples in order to compare some of the MPS methods that are used more frequently. The first example of the TI is shown in Figure 25.3. It represents a 2D heterogeneous reservoir with channeling or fractures with size 195 × 150. The grids used for its simulation and reconstruction are also of the same size. A threshold of $\delta = 0.01$ was used with the CCSIM. Three realizations of the reconstructed TI are also shown in Figure 25.3, generated by the SNESIM, FILTERSIM, and CCSIM. Those generated by the SNESIM do not resemble the TI, while those produced by FILTERSIM do not appear to preserve the continuity of the channels. In contrast, the realizations generated by the CCSIM method are similar to the TI and preserve its continuity everywhere. The computation times were 0.4, 30, and 300 CPU seconds for, respectively, the CCSIM, SNESIM, and FILTERSIM. Thus, not only does the CCSIM do a better job of reconstructing the TI than the other two methods, it is also much more efficient than them.

The second example of a TI is shown in Figure 25.4, with a size 130 × 100. Three realizations were generated by the CCSIM and FILTERSIM algorithms and are also shown in Figure 25.4.

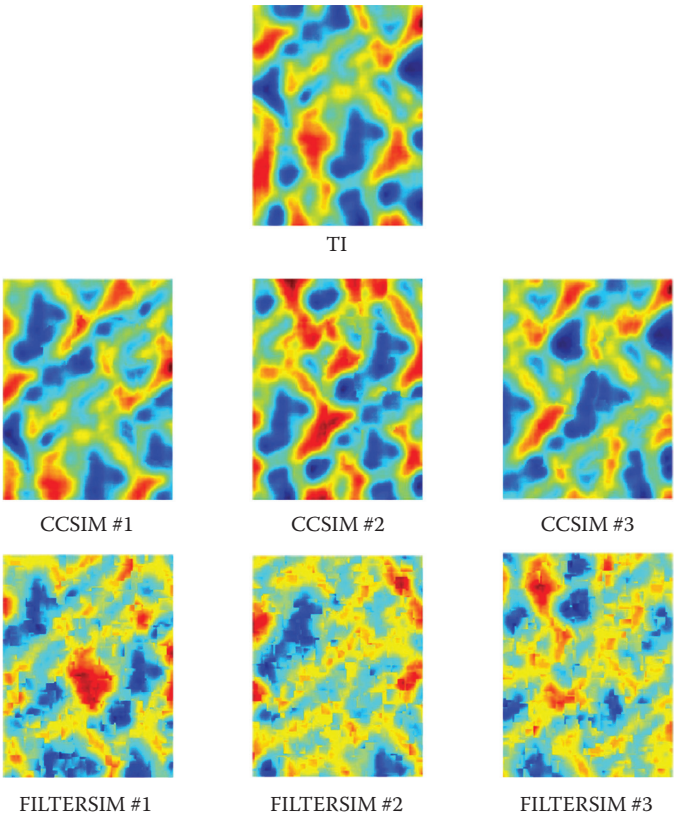

FIGURE 25.4 A training image (TI), shown at the top, and three realizations generated by the CCSIM and FILTERSIM methods.

A threshold of $\delta = 0.01$ was used with the CCSIM. Once again, it is clear that the performance of the CCSIM method is superior over FILTERSIM's. Moreover, the computation times were 0.15 and 50 CPU seconds for, respectively, the CCSIM and FILTERSIM algorithms.

As shown elsewhere, the CCSIM method is equally accurate in 3D. In particular, it has been shown (Tahmasebi and Sahimi, 2012, 2013) that CCSIM is capable of providing plausible solutions to a well-known classical problem: given a single 2D image of a slice of a porous medium, which can be obtained rather easily (as opposed to obtaining 3D image of the entire system, which is very difficult and costly), how can one reconstruct a 3D model for the entire medium? It has been shown in stereology that the solution of the problem is *not* unique. Indeed, CCSIM cannot provide a unique 3D reconstruction of a 3D system, based only on a single 2D image of a slice of a medium, as it is a stochastic method. The CCSIM algorithm does, however, generate an ensemble of plausible solutions, all of which resemble closely the actual 3D system with properties that are very close to the actual 3D porous medium. Many examples of such simulations and reconstruction have been presented elsewhere (Tahmasebi and Sahimi, 2012, 2013).

25.4 SUMMARY

Accurate modeling of complex porous media with realistic structures is a very difficult task that has been studied for a long time. At the same time, having the capability for accurate uncertainty quantification is desirable. As a result, many modeling methods have been developed over the past two decades. Some of the models are based on two-point statistics, such as various variograms that are not, however, capable of reproducing accurately the complex features of porous media and,

in particular, the long-range connectivity of the pore space. Thus, alternative methods have been developed. More advanced approaches are based on MPS, several of which have been developed.

The idea of using a TI in order to carry out geostatistical simulation and reconstruct the TI is simple and appealing. Instead of direct inference of the conditional probabilities from the available data, one can use the TI so that the probability scheme is replaced by patterns. Several algorithms have been proposed to take advantage of this simple concept. By definition, such methods represent multiple-point statistical (MPS) algorithms.

In this chapter, we reviewed the essentials of several two-point and multiple-point geostatistical simulation algorithms. Each MPS algorithm has its individual advantages, as well as shortcomings. For example, the SNESIM algorithm is fast and performs well for modeling categorical images, but it requires very large computer memory when used with large TIs and in particular those with more than four facies. In addition, the SNESIM algorithm cannot model continuous images, and such geological systems as continuous satellite images or thin rock sections. The SIMPAT algorithm can model both categorical and continuous images accurately, but it requires a tremendous amount of computation time.

There are still many issues that must be addressed. For example, the current MPS methods are designed for *stationary* TIs, whereas the properties of many large-scale porous media exhibit nonstationary features. Some progress has recently been made in this direction (Tahmasebi and Sahimi, 2015). In addition, associated with every TI are large uncertainties. Thus, if several TIs are available, it is necessary to design methods that are able to determine which TI(s) to use in a given context.

REFERENCES

Arpat, B., Caers, J., Stochastic simulation with patterns. *Math. Geol.* **39**, 177 (2007).

Asadisaghandi, J., Tahmasebi, P., Comparative evaluation of back-propagation neural network learning algorithms and empirical correlations for prediction of oil PVT properties in Iranian oil fields. *J. Pet. Sci. Eng.* **78**, 464 (2011).

Besag, J., Spatial interaction and the statistical analysis of lattice systems. *J. R. Stat. Soc. Series B* (*Methodological*) **36**, 192 (1974).

Bevilacqua, A., A methodological approach to parallel simulated annealing on an SMP system. *J. Parallel Dist. Comput.* **62**, 1548 (2002).

Borgman, L., Taheri, M., Hagan, R., Three-dimensional frequency-domain simulations of geological variables. In *Geostatistics for Natural Resources Characterization*, G. Verly et al. (Eds.) (Reidel, Dordrecht, the Netherlands, 1984), pp. 517–541.

Caers, J., *Petroleum Geostatistics* (Society of Petroleum Engineers, Houston, TX, 2005).

Caers, J., Journel, A. G., Stochastic reservoir simulation using neural networks trained on outcrop data. In *SPE-ATCE Proceedings*, SPE Paper 49026 (Society of Petroleum Engineers, Houston, TX, 1998).

Caers, J., Ma, X., Modeling conditional distributions of facies from seismic using neural nets. *Math. Geol.* **34**, 143 (2002).

Chib, S., Greenberg, E., Understanding the Metropolis-Hastings algorithm. *Am. Stat.* **49**, 327 (1995).

Chiles, J. P., Delfiner, P., *Geostatistics: Modeling Spatial Uncertainty* (Wiley, New York, 1999).

Chu, J., Journel, A. G., Conditional fBm simulation with dual kriging. In *Geostatistics for the Next Century*, R. Dimitrakopoulos (Ed.) (Kluwer, Amsterdam, the Netherlands, 1993), pp. 407–421.

Cule, D., Torquato, S., Generating random media from limited microstructural information via stochastic optimization. *J. Appl. Phys.* **86**, 3428 (1999).

Daly, C., Higher order models using entropy, Markov random fields and sequential simulation. In *Geostatistics Banaff 2004*, O. Leuangthong and C.V. Deutsch (Eds.) (Springer, Dordrecht, the Netherlands, 2004), pp. 215–224.

Daly, C., Knudby, C., Multipoint statistics in reservoir modeling and in computer vision. In *Petroleum Geostatistics*, Cascais, Portugal (2007).

Dashtian, H., Jafari, G. R., Koohi Lai, Z., Masihi, M., Sahimi, M., Analysis of cross correlations between well logs of hydrocarbon reservoirs. *Transp. Porous Media* **90**, 445 (2011a).

Dashtian, H., Jafari, G. R., Sahimi, M., Masihi, M., Scaling, multifractality, and long-range correlations in well log data of large-scale porous media. *Physica A* **390**, 2096 (2011b).

Davis, M., Production of conditional simulations via the LU decomposition of the covariance matrix. *Math. Geol.* **19**, 91 (1987).
Deutsch, C. V., Annealing techniques applied to reservoir modeling and the integration of geological and engineering (well test) data, PhD thesis, Stanford University, Stanford, CA (1992).
Deutsch, C. V., Journel, A. G., *GSLIB: Geostatistical Software Library and User's Guide*, 2nd edn. (Oxford University Press, New York, 1998).
Deutsch, C. V., Wang, L., Hierarchical object-based geostatistical modeling of fluvial reservoirs, SPE Paper 36514 (1996).
Dimitrakopoulos, R., Luo, X., Generalized sequential Gaussian simulation on group size and screen-effect approximations for large field simulations. *Math. Geol.* **36**, 567 (2004).
Dimitrakopoulos, R., Mustapha, H., Gloaguen, E., High-order statistics of spatial random fields: Exploring spatial cumulants for modeling complex, non-Gaussian and non-linear phenomena. *Math. Geosci.* **42**, 65 (2010).
Ebrahimi, F., Sahimi, M., Multiresolution wavelet coarsening and analysis of transport in heterogeneous media. *Physica A* **316**, 160 (2002).
Ebrahimi, F., Sahimi, M., Multiresolution wavelet scale up of unstable miscible displacements in flow through heterogeneous porous media. *Transp. Porous Media* **57**, 75 (2004).
Eskandari, K., Srinivasan, S., Reservoir modeling of complex geological systems—A multiple-point perspective. *J. Can. Pet. Technol.* **49**, 59 (2010).
Fang, J. H., Wang, P. P., Random field generation using simulated annealing vs. fractal-based stochastic interpolation. *Math. Geol.* **29**, 849 (1997).
Farmer, C. L., Numerical rocks. In *The Mathematical Generation of Reservoir Geology* (Clarendon Press, Oxford, U.K., 1990), pp. 22–33.
Geman, S., Geman, D., Stochastic relaxation, Gibbs distributions and the bayesian restoration of images. *IEEE Trans. Patt. Anal. Mach. Intell.* **6**, 721 (1984).
Gloaguen, R., Dimitrakopoulos, R., Two-dimensional conditional simulations based on the wavelet decomposition of training images. *Math. Geosci.* **41**, 679 (2009).
Goovaerts, P., *Geostatistics for Natural Resources Evaluation* (Oxford University Press, New York, 1997).
Guardiano, F., Srivastava, M., Multivariate geostatistics: Beyond bivariate moments. In *Geostatistics-Troia*, A. Soares (Ed.) (Kluwer Academic, Amsterdam, the Netherlands, 1993), pp. 133–144.
Haldorsen, H. H., Damsleth, E., Stochastic modeling. *J. Pet. Technol.* **42**, 404 (1990).
Hamzehpour, H., Rasaei, M. R., Sahimi, M., Development of optimal models of porous media by combining static and dynamic data: The permeability and porosity distributions. *Phys. Rev. E* **75**, 056311 (2007).
Hamzehpour, H., Sahimi, M., Development of optimal models of porous media by combining static and dynamic data: The porosity distribution. *Phys. Rev. E* **74**, 026308 (2006).
Holden, L., Hauge, R., Skare, O., Skorstad, A., Modeling of fluvial reservoirs with object models. *Math. Geol.* **30**, 473 (1998).
Honarkhah, M., Caers, J., Stochastic simulation of patterns using distance-based method. *Math. Geosci.* **42**, 487 (2010).
Hong, S., Ortiz, J. M., Deutsch, C. V., Multivariate density estimation as an alternative to probabilistic combination schemes for data integration. In *Geostats 2008, Proceedings of the Eighth International Geostatistics Congress*, J. M. Ortiz and X. Emery (Eds.), Vol. 1 (Gecamin Ltda., Santiago, Chile, 2008), pp. 197–206.
Jensen, J. L., Lake, L. W., Corbett, P. W. M., Goggin, D. J., *Statistics for Petroleum Engineers and Geoscientists*, 2nd edn. (Prentice Hall, Amsterdam, the Netherlands, 2000).
Journel, A. G., Geostatistics for conditional simulation of ore bodies. *Econ. Geol.* **69**, 673 (1974).
Journel, A. G., Geostatistics: Roadblocks and challenges. In *Geostatistics—Troia*, Vol. 1., A. Soares (Ed.) (Kluwer Academic, Amsterdam, the Netherlands, 1992), pp. 213–224.
Journel, A. G., Deutsch, C. V., Entropy and spatial disorder. *Math. Geol.* **25**, 329 (1993).
Journel, A. G., Huijbregts, C. J., *Mining Geostatistics* (Academic Press, London, U.K., 1978).
Kirkpatrick, S., Gelatt, C. D., Vecchi, M. P., Optimization by simulated annealing. *Science* **220**, 671 (1983).
Kleingeld, W. J., Lantuéjoul, C., Prins, C. F., Thurston, M. L., The conditional simulation of a Cox process with application to deposits with discrete particles. In *Geostatistics Wollongong 96*, E. Y. Baafi and N. A. Schofield (Eds.) (Kluwer Academic, Amsterdam, the Netherlands, 1997), pp. 683–694.
Lantuéoul, C., *Geostatistical Simulation: Models and Algorithms* (Springer, Berlin, Germany, 2002).
Li, H., Qin, S. J., Tsotsis, T. T., Sahimi, M., Computer simulation of gas generation and transport in landfills. VI. Dynamic updating of the model using the ensemble Kalman filter. *Chem. Eng. Sci.* **74**, 69 (2012).
Li, H., Sanchez, R., Qin, S. J., Kavak, H. I., Webster, I. A., Tsotsis, T. T., Sahimi, M., Computer simulation of gas generation and transport in landfills. V: Use of artificial neural network and genetic algorithm for short- and long-term forecasting and planning. *Chem. Eng. Sci.* **66**, 2646 (2011).

Li, H., Tsotsis, T. T., Sahimi, M., Qin, S. J., Ensembles-based and GA-based optimization for landfill gas production. *AIChE J.* **60**, 2063 (2014).
Lyster, S., Deutsch, C. V., Artifacts near conditioning data in MPS Gibbs sampling. Centre for Computational Geostatistics, Edmonton, Alberta, Canada, Publication Number 9 (2007).
Manwart, C., Hilfer, R., Reconstruction of random media using Monte Carlo methods. *Phys. Rev. E* **59**, 5596 (1999).
Manwart, C., Torquato, S., Hilfer, R., Stochastic reconstruction of sandstones. *Phys. Rev. E* **62**, 893 (2000).
Mariethoz, G., Kelly, B. F. J., Modeling complex geological structures with elementary training images and transform-invariant distances. *Water Resour. Res.* **47**, W07527 (2011).
Mariethoz, G., Renard, P., Reconstruction of incomplete data sets or images using direct sampling. *Math. Geosci.* **42**, 245 (2010).
Mariethoz, G., Renard, P., Straubhaar, J., The direct sampling method to perform multiple-point simulations. *Water Resour. Res.* **46**, W11536 (2010).
Matheron, G., The intrinsic random functions and their applications. *Adv. Appl. Prob.* **5**, 439 (1973).
Mehrabi, A. R., Rassamdana, H., Sahimi, M., Characterization of long-range correlations in complex distributions and profiles. *Phys. Rev. E* **56**, 712 (1997).
Mehrabi, A. R., Sahimi, M., Coarsening of heterogeneous media: Application of wavelets. *Phys. Rev. Lett.* **79**, 4385 (1997).
Mustapha, H., Dimitrakopoulos, R., High-order stochastic simulation of complex spatially distributed natural phenomena. *Math. Geosci.* **42**, 457 (2010a).
Mustapha, H., Dimitrakopoulos, R., A new approach for geological pattern recognition using high-order spatial cumulants. *Comput. Geosci.* **36**, 313 (2010b).
Ortiz, J. M., Deutsch, C. V., Indicator simulation accounting for multiple-point statistics. *Math. Geol.* **36**, 545 (2004).
Ortiz, J. M., Emery, X., Integrating multiple-point statistics into sequential simulation algorithms. In *Geostatistics Banaff 2004*, O. Leuangthong and C. V. Deutsch (Eds.) (Springer, Dordrecht, the Netherlands, 2005), pp. 969–978.
Panda, M. N., Lake, L. W., Parallel simulated annealing for stochastic reservoir modeling. SPE Paper 26418 (1993).
Parra, A., Ortiz, J. M., Adapting a texture synthesis algorithm for conditional multiple point geostatistical simulation. *Stoch. Env. Res. Risk Ass.* **13**, 1 (2011).
Peredo, O., Ortiz, J. M., Parallel implementation of simulated annealing to reproduce multiple-point statistics. *Comput. Geosci.* **37**, 1110 (2010).
Quenes, A., Saad, N., A new, fast parallel simulated annealing algorithm for reservoir characterization. SPE Paper 26419 (1993).
Rasaei, M. R., Sahimi, M., Efficient simulation of water flooding in three-dimensional heterogeneous reservoirs using wavelet transformations: Application to the SPE-10 model. *Transp. Porous Media* **72**, 311 (2008).
Rasaei, M. R., Sahimi, M., Upscaling of the permeability by multiscale wavelet transformations and simulation of multiphase flows in heterogeneous porous media. *Comput. Geosci.* **13**, 187 (2009a).
Rasaei, M. R., Sahimi, M., Upscaling of the geological models of large-scale porous media using multiresolution wavelet transformations. *J. Heat Transfer* **131**, 101007 (2009b).
Reeves, C. R., Rowe, J. E., *Genetic Algorithms Principle and Perspectives: A Guide to GA Theory* (Kluwer Academic, Dordrecht, the Netherlands, 2003).
Romero, C. E., Carter, J. N., Using genetic algorithms for reservoir characterization. *J. Pet. Sci. Eng.* **31**, 113 (2001).
Romero, C. E., Carter, J. N., Gringarten, A. C., Zimmerman, R. W., A modified genetic algorithm for reservoir characterization. SPE Paper 64765 (2000).
Saccomano, A. F., Savioli, G. B., Binder, M. S., Stochastic modeling of rock heterogeneities applying new autocorrelation estimators and simulated annealing. SPE Paper 69654 (2001).
Sahimi, M., *Heterogeneous Materials I*, Springer, New York (2003).
Sahimi, M., *Flow and Transport in Porous Media and Fractured Rock*, 2nd edn. (Wiley-VCH, Weinheim, Germany, 2011).
Sahimi, M., Hashemi, M., Wavelet identification of the spatial distribution of fractures. *Geophys. Res. Lett.* **28**, 611 (2001).
Sanchez, R., Tsotsis, T. T., Sahimi, M., Computer simulation of gas generation and transport in landfills. III: Development of landfills' optimal model. *Chem. Eng. Sci.* **62**, 6378 (2007).
Savioli, G. B., Falcigno, E. D., Binder, M. S., Lake, L. W., Applications of simulated annealing in actual but atypical permeability data. SPE Paper 35345 (1996).

Sheehan, N., Torquato, S., Generating microstructures with specified correlation functions. *J. Appl. Phys.* **89**, 53 (2001).

Skorstad, A., Hauge, R., Holden, L., Well conditioning in a fluvial reservoir model. *Math. Geol.* **31**, 857 (1999).

Srivastava, R., An overview of stochastic methods for reservoir characterization. In *Stochastic Modeling and Geostatistics: Principles, Methods, and Case Studies*, R. L. Chambers (Ed.), Computer Applications, Vol. **3** (AAPG, Tulsa, OK, 1994), p. 380.

Straubhaar, J., Renard, P., Mariethoz, G., Froidevaux, R., Besson, O., An improved parallel multiple-point algorithm using a list approach. *Math. Geosci.* **43**, 305 (2011).

Strebelle, S., Conditional simulation of complex geological structures using multiple-point geostatistics. *Math. Geol.* **34**, 1 (2002).

Strebelle, S., Zhang, T., Non-stationary multiple-point geostatistical models. In *Geostatistics Banaff 2004*, O. Leuangthong and C. V. Deutsch (Eds.), Quantitative Geology and Geostatistics, Vol. **14** (Springer, Dordrecht, the Netherlands, 2005), pp. 235–244.

Tahmasebi, P., Hezarkhani, A., Application of optimized neural network by genetic algorithm. IAMG09, Stanford University, Stanford, CA (2009).

Tahmasebi, P., Hezarkhani, A., Comparison of optimized neural network with fuzzy logic for ore grade estimation. *Aust. J. Basic Appl. Sci.* **4**, 764 (2010).

Tahmasebi, P., Hezarkhani, A., Application of a modular feedforward neural network for grade estimation. *Nat. Resour. Res.* **20**, 25 (2011).

Tahmasebi, P., Hezarkhani, A., Hybrid neural networks-fuzzy logic-genetic algorithm for grade estimation. *Comput. Geosci.* **42**, 18 (2012).

Tahmasebi, P., Hezarkhani, A., Sahimi, M., Multiple-point geostatistical modeling based on the cross-correlation functions. *Comput. Geosci.* **16**, 779 (2012).

Tahmasebi, P., Sahimi, M., Reconstruction of three-dimensional porous media using a single thin section. *Phys. Rev. E* **85**, 066709 (2012).

Tahmasebi, P., Sahimi, M., Cross-correlation function for accurate reconstruction of heterogeneous media. *Phys. Rev. Lett.* **110**, 078002 (2013).

Tahmasebi, P., Sahimi, M., Reconstruction of nonstationary disordered materials and media. *Phys. Rev. E*, in press (2015).

Tahmasebi, P., Sahimi, M., Caers, J., MS-CCSIM: Accelerating pattern-based geostatistical simulation of categorical variables using a multi-scale search in Fourier space. *Comput. Geosci.* **67**, 75 (2014).

Talukdar, M. S., Torsaeter, O., Reconstruction of chalk pore networks from 2D backscatter electron micrographs using a simulated annealing technique. *J. Pet. Sci. Eng.* **33**, 265 (2002).

Talukdar, M. S., Torsaeter, O., Ionnidis, M. S., Howard, J. J., Stochastic reconstruction, 3D characterization and network modeling of chalk. *J. Pet. Sci. Eng.* **35**, 1 (2002a).

Talukdar, M. S., Torsaeter, O., Ionnidis, M. S., Howard, J. J., Stochastic reconstruction of chalk from 2D images. *Transp. Porous Media* **48**, 101 (2002b).

Tjelmeland, H., Stochastic models in reservoir characterization and markov random fields for compact objects, PhD dissertation, Norwegian University of Science and Technology, Trondheim, Norway (1996).

Tjelmeland, H., Eidsvik, J., Directional Metropolis-Hastings updates for posteriors with nonlinear likelihood. In *Geostatistics Banaff 2004*, O. Leuangthong and C. V. Deutsch (Eds.) (Springer, Dordrecht, the Netherlands, 2004), pp. 95–104.

Viseur, S., Stochastic Boolean simulation of fluvial deposits: A new approach combining accuracy with efficiency. In *SPE-ATCE Proceedings*, SPE Paper 56688 (Society of Petroleum Engineers, Houston, TX, 1999).

Ye, H., Lin, Z., Speed-up simulated annealing by parallel coordinates. *Eur. J. Operat. Res.* **173**, 59 (2006).

Yeong, C. L. Y., Torquato, S., Reconstructing random media. *Phys. Rev. E* **57**, 495 (1998a).

Yeong, C. L. Y., Torquato, S., Reconstructing random media. II. Three-dimensional media from two-dimensional cuts. *Phys. Rev. E* **58**, 224 (1998b).

Zhang, T., Switzer, P., Journel, A. G., Filter-based classification of training image patterns for spatial simulation. *Math. Geol.* **38**, 63 (2006).

26 Microbially Induced Carbonate Precipitation in the Subsurface
Fundamental Reactions and Transport Processes

James Connolly and Robin Gerlach

CONTENTS

26.1 Introduction 891
26.2 Biological Processes 893
26.2.1 Alkalinity-Producing Metabolisms in the Subsurface 893
26.2.1.1 Urea Hydrolysis 895
26.2.1.2 Denitrification 895
26.2.1.3 Sulfate Reduction 896
26.2.1.4 Iron Reduction 897
26.2.2 Biofilms 898
26.2.3 Kinetics 899
26.3 Mineral Precipitation Theory 900
26.3.1 Carbonate Minerals and Polymorphs 901
26.3.2 Nucleation 901
26.3.3 Crystal Growth Models and Kinetics 904
26.4 Reactive Transport 908
26.4.1 Solute Transport 908
26.4.2 Biofilm-Catalyzed Reactions 909
26.4.3 Precipitation Reactions 913
26.5 Concluding Remarks 914
26.6 Modeling Notes 915
Acknowledgments 915
Nomenclature 916
References 917

26.1 INTRODUCTION

Many microorganisms are capable of inducing carbonate mineral precipitation under certain conditions. Not to be confused with structured biomineralization in eukaryotes for bones and shells, bacteria can indirectly cause precipitation, being a by-product of alkalinity increasing metabolisms, such as photosynthesis, urea hydrolysis, sulfate reduction, nitrate reduction, and iron reduction. The geologic record holds many examples of microbially produced carbonates, and presently the process is being utilized to manipulate porous media properties (De Muynck et al., 2010; Riding, 2000). Applications in porous media are numerous but can generally be divided into either increasing the material strength or reducing permeability (Phillips et al., 2013). The microbiology

of such systems will be discussed including metabolisms, biofilm concepts, and biological reaction rates, followed by mineral precipitation fundamentals and reactive transport modeling approaches.

Microbial activity can induce a cascade of physical and chemical changes, which can include the shift of carbonate equilibrium chemistry, precipitation, and changes to system hydrodynamics. Changes in hydrodynamics in turn can change the reaction and transport in biofilm- and mineral-affected porous media. Both Darcy-scale and pore-scale reactive transport concepts will be discussed, and classical porous media methodology will be applied to microbially induced carbonate precipitation (MICP) systems.

In the subsurface, microorganisms have a close association with the surfaces of the porous medium they live in making them potentially sensitive to changes to those porous media surfaces. Precipitation can cause physical and chemical changes to the surfaces the microbes are attached to and, as a result, can change the reactive transport behavior in the porous medium. Additionally, precipitation can change the local physical and chemical environments thus altering microbial activity and in mixed microbial communities potentially shifting local populations. As shown in Figure 26.1, many processes can occur during MICP and affect reactive transport, porous media morphology, and biogeochemical conditions. Before precipitation, attached microorganisms can affect flow by the formation of biofilm. Once precipitation commences, additional pore space reduction can occur along with the potential for inactivation of biomass through encapsulation in the precipitate (Al Qabany et al., 2012; Cuthbert et al., 2012; Schultz et al., 2011). Planktonic and attached microbes have the potential to cause precipitation in the bulk fluid. These precipitates can be deposited downstream and cause an additional reduction in porosity and permeability.

The aim of this chapter is to describe the major pore-scale processes associated with MICP and put them in the context of porous media reactive transport modeling approaches. First, MICP is divided into biological, physical, and geochemical subprocesses; their interactions are discussed at the pore scale, and finally it is discussed how these processes and interactions affect local and system-wide reactive transport. The chapter as a whole is intended to serve as an

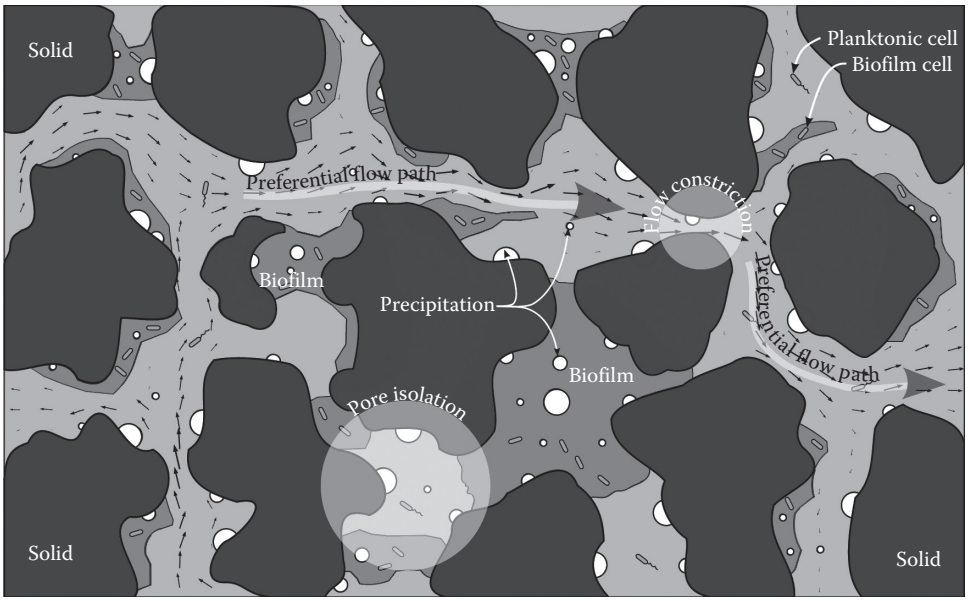

FIGURE 26.1 Fluid flow and reactive processes affecting MICP at the pore network scale. Microbial cells exist either in a freely floating planktonic state or in a biofilm. Precipitation can occur in suspension, in the biofilm or on solid surfaces. Biofilm and precipitates affect local hydrodynamics if they are present in sufficient quantities by blocking pore throats, isolating pores, and constricting flow. Stagnant zones and preferential flow pathways develop leading to pore-scale chemical, physical, and potentially biological heterogeneity.

overview of the current knowledge within the MICP field in regard to pore-scale processes. The processes are represented in equation form where possible to provide mathematical relationships that are useful for modeling.

26.2 BIOLOGICAL PROCESSES

Among the known microbial metabolisms, there are primarily four types that have been associated with significant mineral precipitation in the subsurface through the generation of alkalinity. These mineral precipitation-inducing metabolisms are urea hydrolysis, nitrate reduction, sulfate reduction, and iron reduction (Castanier et al., 1999). Microbial photosynthesis (e.g., in cyanobacteria) is also a significant source of biominerals in nature (e.g., stromatolites [Riding, 2000]). However, the importance of photosynthesis is restricted to the earth's surface because of the requirement for sunlight and will thus not be discussed in this chapter. We do not aim to discuss all types of alkalinity-producing metabolism in this chapter; however, the four that are discussed in detail are likely representative of the most effective ones (DeJong et al., 2010; van Paassen et al., 2010).

26.2.1 Alkalinity-Producing Metabolisms in the Subsurface

Alkalinity is generally defined as the amount of acid that must be added to a solution to decrease its pH to a given level, or alternatively as the ability of a solution to resist a pH decrease (Crittenden et al., 2012). Where the carbonate buffering system dominates, as is the case in most natural waters, alkalinity can be expressed as

$$\text{Alkalinity} = [HCO_3^-] + 2[CO_3^{2-}] + [OH^-] - [H^+]. \tag{26.1}$$

Square brackets indicate molar concentrations. Alkalinity production can then be generalized as any process that results in the consumption of acid equivalents (H^+) or production of base equivalents (OH^- or other anions). In the presence of dissolved inorganic carbon (DIC) and certain cations such as calcium (Ca^{2+}), an increase in alkalinity can induce the precipitation of carbonate minerals such as calcium carbonate ($CaCO_{3(s)}$):

$$Ca^{2+} + CO_3^{2-} \rightarrow CaCO_{3(s)}. \tag{26.2}$$

DIC is the sum of all carbonate species in a solution and can generally be represented as

$$\text{DIC} = [H_2CO_3^*] + [HCO_3^-] + [CO_3^{2-}]. \tag{26.3}$$

$H_2CO_3^*$ denotes the sum of fully protonated carbonic acid and dissolved CO_2. When other ions such as sodium or calcium are abundant, as is often the case in MICP systems, calcium bicarbonate ions ($CaHCO_3^+$), sodium carbonate ions ($NaCO_3^-$), and other similar species may also have to be included. The relative concentration of each of the three pure carbonate species is pH dependent and is determined by the set of equilibrium equations in Table 26.1.

TABLE 26.1
Equilibrium Reactions and pk ($-\log_{10}(k)$) Values for the Carbonate System at 25°C

Reaction	Equilibrium Equation	pk
Water dissociation	$H_2O \leftrightarrow OH^- + H^+$	14
Carbonic acid dissociation	$H_2CO_3^* \leftrightarrow HCO_3^- + H^+$	6.35
Bicarbonate dissociation	$HCO_3^- \leftrightarrow CO_3^{2-} + H^+$	10.33

At a pH value between roughly 6.5 and 10, the DIC is dominated by bicarbonate (HCO_3^-). For this reason, most of the biological and geochemical reactions discussed in later sections of this chapter will be written with DIC as bicarbonate. Although bicarbonate generally dominates DIC at biologically relevant pH values, there will still be a small fraction present as carbonate (CO_3^{2-}), which is the species available for precipitation. It should be noted that equilibrium reactions, and thus the pk ($-\log_{10}(k)$) values in Table 26.1, are dependent on temperature and ionic strength. One example where both ionic strength and temperature must be considered would be a deep brine aquifer that would have elevated temperature and potentially very high ionic strength.

As alkalinity and pH increase, precipitation of carbonate minerals becomes more favorable due to an increase in the carbonate concentration and, as a result, the saturation state. The saturation state (S) is defined as

$$S = \frac{IAP}{k_{sp}}, \tag{26.4}$$

where

IAP is the ion activity product

k_{sp} is the solubility product (Mullin, 2001)

The IAP is simply the product of the activities (here denoted as {x}) of all ions associated with the mineral. Taking calcium carbonate as an example,

$$IAP = \{Ca^{2+}\}\{CO_3^{2-}\}. \tag{26.5}$$

When the IAP is greater than k_{sp} (or $S > 1$), then the solution is supersaturated, and precipitation is possible. Increasing the activity of either calcium or carbonate ions can lead to supersaturation. The use of activity rather than concentration is particularly important when calculating the saturation state because depending on the conditions (e.g., temperature and ionic strength), order-of-magnitude errors are possible (Zhang and Dawe, 1998). Figure 26.2 shows the relationship between

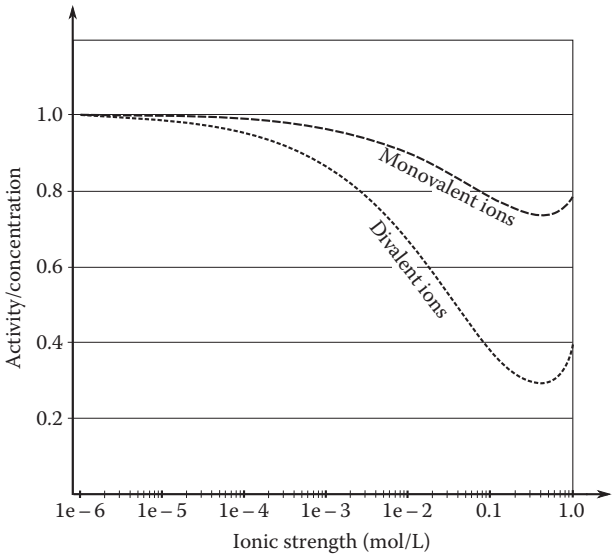

FIGURE 26.2 The ratio of the ionic activity versus concentration (also known as an activity coefficient) for monovalent and divalent ions over a range of ionic strengths. For comparison, seawater has an average ionic strength of approximately 0.7 mol/L. The Davies extension of the Debye–Hückel relationship was used (Davies, 1962). The Pitzer equation should be used at ionic strengths above 0.1 mol/L (Pitzer, 1991) but was not shown here because a more detailed solution chemistry would have to be assumed.

concentration and activity over a range of ionic strengths for divalent and monovalent species. At low ionic strength, the values for ion activity approach the concentrations of the ions (activity coefficient = 1). This approximation cannot be made for high–ionic strength solutions such as seawater or high-salinity brine systems.

26.2.1.1 Urea Hydrolysis

Many heterotrophic soil bacteria have the capability to use urea ($CO(NH_2)_2$) as a nitrogen source (Mobley and Hausinger, 1989; Morsdorf and Kaltwasser, 1989). Urea can be present in the subsurface from animal waste sources or be added directly to engineered environments. Urea must be hydrolyzed in order to be utilized for biomass growth, and many organisms possess enzymes for that purpose. Uncatalyzed urea hydrolysis proceeds slowly, but its rate is greatly increased (by orders of magnitude) by the urease enzyme produced by many organisms (Yingjie and Cabral, 2002). Urease (Dixon et al., 1976; Mobley et al., 1995) catalyzes the hydrolysis of urea to form inorganic carbon and ammonia by

$$CO\left(NH_2\right)_2 + 2H_2O \rightarrow 2NH_3 + HCO_3^- + H^+. \tag{26.6}$$

Urea hydrolysis on its own has no effect on alkalinity, but at circumneutral pH, the ammonia becomes protonated where

$$NH_3 + H^+ \leftrightarrow NH_4^+. \tag{26.7}$$

Combining urea hydrolysis with the subsequent ammonia protonation, the overall reaction becomes

$$CO\left(NH_2\right)_2 + 2H_2O + H^+ \rightarrow 2NH_4^+ + HCO_3^-, \tag{26.8}$$

where one proton is consumed and one bicarbonate ion is produced. Thus, at circumneutral pH, the hydrolysis of one mole of urea increases the alkalinity by 2 mol, effectively increasing the saturation state of carbonate minerals.

Microorganisms can utilize urea hydrolysis in an assimilatory fashion by simply incorporating the ammonium or ammonia into their nitrogen metabolism or in a dissimilatory process where the bacteria gain energy through the formation of a membrane potential (Jahns, 1996). It is also a reasonable theory that dissimilatory urea hydrolysis is a competitive strategy that provides an advantage over non-alkaliphilic organisms. Heterotrophic bacteria in the genera *Sporosarcina* and *Bacillus* have been shown to produce particularly high amounts of urease (Jahns, 1996; Morsdorf and Kaltwasser, 1989). In the case of *Sporosarcina pasteurii*, urease has been shown to comprise approximately 1% of the cell dry weight (Bachmeier et al., 2002), making it a highly effective organism in the context of MICP for engineered purposes in the subsurface where oxygen is present (Al Qabany et al., 2012; Martin et al., 2012; Tobler et al., 2011). Under most conditions, in the presence of sufficient calcium, dissimilatory urea hydrolysis readily induces calcium carbonate precipitation and permeability reduction in a porous medium (De Muynck et al., 2010; Phillips et al., 2013).

26.2.1.2 Denitrification

Denitrification is the reduction of oxidized forms of nitrogen, mainly nitrate (NO_3^-), to nitrogen gas (N_2) and is primarily carried out by heterotrophic bacteria. The overall redox half reaction of denitrification is

$$2NO_3^- + 10e^- + 12H^+ \rightarrow 6H_2O + N_2. \tag{26.9}$$

Denitrification is then coupled to the oxidation of an electron donor such as acetate (CH_3COO^-), and the overall catabolic reaction becomes

$$5CH_3COO^- + 8NO_3^- + 3H^+ \rightarrow 10HCO_3^- + 4N_2 + 4H_2O, \tag{26.10}$$

where alkalinity is generated by the consumption of protons and the generation of bicarbonate. The use of acetate as a carbon source in an engineering setting could be particularly useful because the use of calcium acetate and calcium nitrate accomplishes adding the electron/donor pair necessary for growth and alkalinity production as well as the divalent cation necessary for mineral formation. There are many organic and inorganic electron donors that can be utilized by denitrifying microorganisms. For example, denitrification using hydrogen gas as an electron donor (autohydrogenotrophic denitrification) has been shown to greatly increase alkalinity and to precipitate calcium carbonate in wastewater treatment environments (Lee and Rittmann, 2003).

Mineralization through nitrate reduction has been of recent interest in bioengineering as an alternative to urea hydrolysis (Martin et al., 2013) due to concerns regarding the growth inhibition of ureolytic bacteria in anaerobic environments and potential issues with generating large amounts of ammonium in the subsurface (Martin et al., 2012; Van Paassen et al., 2010). Denitrification is, however, not without complications due to the potential generation of large amounts of nitrogen gas that could cause transient (rather than long-lasting) permeability reduction and the potential formation of nitrous oxide, a strong greenhouse gas. Furthermore, the direct injection of nitrate into the subsurface may face regulatory hurdles because it is a regulated pollutant in much of the world, although balanced addition of nitrate and electron donor could result in very little nitrate remaining after the treatment. Incomplete oxidation of organic electron donors is also possible, potentially causing unwanted by-products.

26.2.1.3 Sulfate Reduction

Bacteria that use sulfate (SO_4^{2-}) as an electron acceptor for respiration, known as sulfate-reducing bacteria (SRB), are capable of increasing alkalinity in anaerobic environments. Sulfate reduction has also been described in *Archaea* (Klenk et al., 1997; Muyzer and Stams, 2008), but in this chapter, the term SRB refers to the broad class of microorganisms that can use sulfate as an electron acceptor. When oxygen or nitrate is not present, mineralization still can occur in the subsurface via sulfate reduction under right conditions (Braissant et al., 2007). As a half reaction, sulfate reduction can be written as

$$SO_4^{2-} + 9H^+ + 8e^- \rightarrow HS^- + 4H_2O. \tag{26.11}$$

The electron donor could be organic or inorganic depending on the specific organism. The reduced sulfur species equilibrium acts similarly to the inorganic carbon equilibrium in that speciation is dependent on pH. At pH values below 7, the dominant species is hydrogen sulfide (H_2S) gas. At pH values between 7 and 13, the dominant species is bisulfide (HS^-), a strong base, and at extremely basic pH values, sulfide (S^{2-}) dominates. In this section, we will assume that these reactions are taking place in an already alkaline environment where bisulfide is the dominant species.

SRBs are a diverse class of microorganisms, many of which are capable of utilizing multiple electron donors and carbon sources (Lengeler et al., 1998). Some SRB species can produce alkalinity and precipitate carbonate minerals on their own. Others enter into symbiotic relationships that form biominerals and yet others decrease alkalinity and cause corrosive environments (Muyzer and Stams, 2008). Both the metabolic potential of the organism and the biogeochemical conditions that surround them dictate how they will affect the mineral saturation states, and this complex interplay cannot be fully covered in this chapter. Rather, this section will primarily deal with the types of systems that are associated with precipitation.

Perhaps the most common example of alkalinity production in nature via sulfate reduction is when it is coupled to anaerobic methane oxidation (Boetius et al., 2000; Milucka et al., 2012). The overall result is the consumption of methane and sulfate and the production of bicarbonate and free sulfides (H_2S or HS^- depending on the pH). At above a pH of 7, the reaction occurs according to

$$CH_4 + SO_4^{2-} \rightarrow HCO_3^- + HS^- + H_2O. \quad (26.12)$$

The resulting increase in alkalinity has been shown to cause precipitation, particularly of carbonate minerals and iron sulfides (Wallmann et al., 2006). Anaerobic methane oxidation has been linked to the formation of modern calcium carbonate deposits in marine environments (Glenn et al., 2007) as well as pore-blocking authigenic carbonates in marine sediments (Wallmann et al., 2006).

Alkalinity generation and precipitation can also be facilitated by SRBs in pure culture by the degradation of organic substances such as carbohydrates and organic acids. As an example, the complete oxidation of acetate (CH_3COO^-) increases alkalinity by producing bicarbonate at circumneutral pH where

$$CH_3COO^- + SO_4^{2-} \rightarrow 2HCO_3^- + HS^-. \quad (26.13)$$

Rather than producing bicarbonate, classes of SRBs, many of which lie in the genus *Desulfovibrio*, are able to gain energy by oxidizing hydrogen gas. Hydrogen oxidation increases alkalinity by consuming a proton where

$$4H_2 + SO_4^{2-} + H^+ \rightarrow HS^- + 4H_2O. \quad (26.14)$$

26.2.1.4 Iron Reduction

Iron-reducing microorganisms represent a potential source of alkalinity production in environments where there is a significant amount of ferric iron (Fe^{3+}). Dissimilatory iron reducers use ferric iron as their terminal electron acceptor reducing it to ferrous iron (Fe^{2+}) coupled with the oxidation of H_2 or organic substrates. Like sulfate reducers, iron reducers are diverse and widely distributed phylogenetically across *Bacteria* and *Archaea* (Fredrickson and Gorby, 1996; Lovley et al., 2004). Species from the genera *Geobacter*, *Desulfuromonas*, and *Shewanella* are representative of the metabolisms discussed in this section. Dissimilatory iron reduction is a particularly complex process because ferric iron exists in many forms and is often poorly soluble in the subsurface (Nevin and Lovley, 2002). This section will not cover iron equilibria and how iron reducers can affect it in detail, but Nevin and Lovely (2002), as well as others, provide a thorough discussion of this topic.

Iron reduction can be represented by the half reaction

$$Fe^{3+} + e^- \rightarrow Fe^{2+}. \quad (26.15)$$

The source of ferric iron and the fate of ferrous iron are highly variable depending on the physical and chemical environments in which the process is taking place. Ferric oxides (Fe_2O_3) and oxyhydroxides (FeOOH) are common in the subsurface but are often not very soluble. Thus, ferric iron reduction requires the use of specialized strategies by the involved microbes, which can include the use of external electron shuttles, chelators, Fe^{3+}-solubilizing agents, and possibly electron flow by direct electrical contact to the iron minerals through filaments (Nevin and Lovley, 2002; Pfeffer et al., 2012). Soluble iron could also be added to a system in an engineered setting. The fate of the reduced iron can be as precipitated pyrite (FeS_2) or magnetite (Fe_3O_4), can remain in the soluble form, or can be oxidized back to ferric iron by either biotic or abiotic reactions (Fredrickson and Gorby, 1996). Ferrous iron can also be precipitated in the form of iron carbonate (e.g., siderite, $FeCO_3$) (Fredrickson et al., 1998).

It has been demonstrated experimentally that iron reduction can increase alkalinity when ferric oxyhydroxide (FeO(OH)) is supplied as the source of soluble oxidized iron (Vile and Wieder, 1993). Using acetate (CH_3COO^-) as the electron donor, net alkalinity will be produced by

$$8FeO(OH) + CH_3COO^- + 15H^+ \rightarrow 8Fe^{2+} + 2HCO_3^- + 12H_2O, \tag{26.16}$$

where protons are consumed and bicarbonate is produced, increasing alkalinity. The formation of bacterial iron carbonates in nature is well documented (e.g., Fredrickson et al., 1998); however, its stimulation for engineered purposes remains relatively unstudied and remains undemonstrated as a viable technology (Stephens and Keith, 2008).

26.2.2 Biofilms

A microbial biofilm consists of a consortium of cells held together by a self-produced matrix that is attached to a surface. The matrix typically consists of biopolymers such as polysaccharides, nucleic acids, and proteins, and is often referred to in general terms as extracellular polymeric substances (EPS) (Characklis and Marshall, 1990; Flemming and Wingender, 2001a). The high surface area of a porous medium can be highly conducive to biofilm growth. Biofilm growth in general, and especially in a porous medium, can be a significant cause of metabolic diversity due to spatially and temporally heterogeneous mass transport (Cunningham et al., 1991; Shafahi and Vafai, 2009) that can cause microenvironments.

Biofilms and planktonic (free-floating) biomass contribute to carbonate precipitation. The ratio of biofilm biomass to planktonic biomass is entirely system dependent, but generally it can be assumed that most of the biomass is acting in an attached state in the subsurface (Costerton et al., 1987; Lappin-Scott and Costerton, 2003; Vandevivere and Baveye, 1992). Even planktonic cells detected in a porous medium will often be detached biofilm clusters (Stoodley et al., 2001). This is in fact an important distinction because at the pore scale, the locations of highest microbial activity and alkalinity generation, thus supersaturation will be most likely localized within biofilm colonies. During the early stages of mineral formation, one would expect nucleation to occur in biofilms, but microbial biofilms, and even the EPS alone, have been shown to affect and in some cases inhibit mineral nucleation and growth significantly (Braissant et al., 2003; Decho, 2010; Dhami et al., 2013; Ercole et al., 2012; Kawaguchi and Decho, 2002; Rodriguez-Navarro et al., 2007). For example, the growth of aragonite has been shown to be inhibited by the adsorption of acidic polysaccharides to crystalline surfaces (Wada et al., 1993).

Along with the physical effects of biofilm growth on mineral formation and reactive transport in a porous medium, there are chemical effects. The chemical effects of biofilm and EPS on mineral precipitation are not fully understood and are likely to vary from system to system; however, there are some concepts that have gained general acceptance. Prokaryotic cells and biopolymers generally have exposed negative charges that are available for cross-linking with divalent cations through electrostatic interaction (Flemming and Wingender, 2001b; Mayer et al., 1999). When divalent cations are present, as they are likely to be in MICP systems, EPS has the tendency to bind these ions potentially affecting crystal nucleation and growth (Kawaguchi and Decho, 2002; Perry et al., 2005). This binding adds structural rigidity to the biofilm by cross-linking the negatively charged EPS polymers (Chen and Stewart, 2002) and lowering diffusivity. Cation binding also affects the polymorphism of minerals. For example, calcite is the most stable form of calcium carbonate at long time scales, but when organic molecules are present, specifically biofilm-associated polymers, other polymorphs (aragonite and vaterite) or amorphous precipitates can be stabilized (Dhami et al., 2013; Rodriguez-Navarro et al., 2007).

26.2.3 Kinetics

Until now, only the existence of the different biogeochemical processes in MICP has been discussed, but in order to truly understand MICP systems, the rates at which these processes take place need to be understood. MICP systems generally have slow, rate-limiting biological reactions followed by fast aqueous inorganic equilibrium reactions. The reactions responsible for producing alkalinity are limited by microbial enzyme rates. For modeling purposes, it is generally assumed that the biological reactions, including those taking place in biofilm, limit overall reaction rates, and all inorganic species equilibrate fast enough to be at equilibrium (Zhang and Klapper, 2010).

The enzyme-catalyzed biological reactions discussed in Section 26.2.1 are usually a chain of many reactions. Nitrate reduction, for example, is a multistep process with each reaction being carried out by a different enzyme possessing different kinetic properties. Even the apparently simple urea hydrolysis system, with the primary reaction being carried out by a single enzyme, can be affected by other reactions that would affect intracellular substrate or product concentrations such as cell membrane transport reactions for urea and ammonia or pH regulation (Jahns, 1996).

Enzymatic reactions are typically a function of reaction substrates, products, temperature, and pH. The most common rate expression is the Michaelis–Menten kinetic model with only substrate concentration being taken into account where

$$\frac{dC_s}{dt} = R_s = R_{max} C_E \frac{C_s}{k_m + C_s}. \tag{26.17}$$

where

C_s is the substrate concentration
R_s is the substrate-dependent reaction rate
R_{max} is a theoretical maximum rate
k_m is a half saturation constant ($C_s = k_m$ at $R_s = 0.5R_{max}$)
C_E is the enzyme concentration

For example, if the Michaelis–Menten kinetic model were applied to urea hydrolysis, C_s would be the concentration of urea, C_E the concentration of urease, and the other kinetic constants would need to be determined through experiments or extracted from the literature taking into account potential pH, temperature, pressure, and ionic strength dependencies. C_E is often assumed to be constant or scaled to the microbial population. It should be noted that above certain enzyme-to-substrate concentration ratios, saturation kinetics with respect to enzyme concentration can also develop. However, such high enzyme-to-substrate concentration ratios are not very likely to occur in porous media systems of relevance to engineers. Simplifications can be made for cases with very high and very low substrate concentrations resulting in *zero-order* and *first-order* relationships with respect to C_s as follows:

$$\text{Zero Order: } R_s = R_{max} \quad \text{for} \quad C_s \gg k_m \tag{26.18}$$

$$\text{First Order: } R_s = \frac{R_{max}}{k_m} C_s \quad \text{and} \quad \frac{R_{max}}{k_m} \equiv k_1 \quad \text{for} \quad C_s \ll k_m. \tag{26.19}$$

In the first-order approximation, R_{max}/k_m is typically combined to form a new variable, the first-order reaction rate constant (k_1), leaving a simple linear relationship. Both enzyme specific rates and rates of overall metabolic activity are commonly expressed in any of the earlier three forms depending on the conditions and application. In substrate-limited systems, it can be more appropriate to use

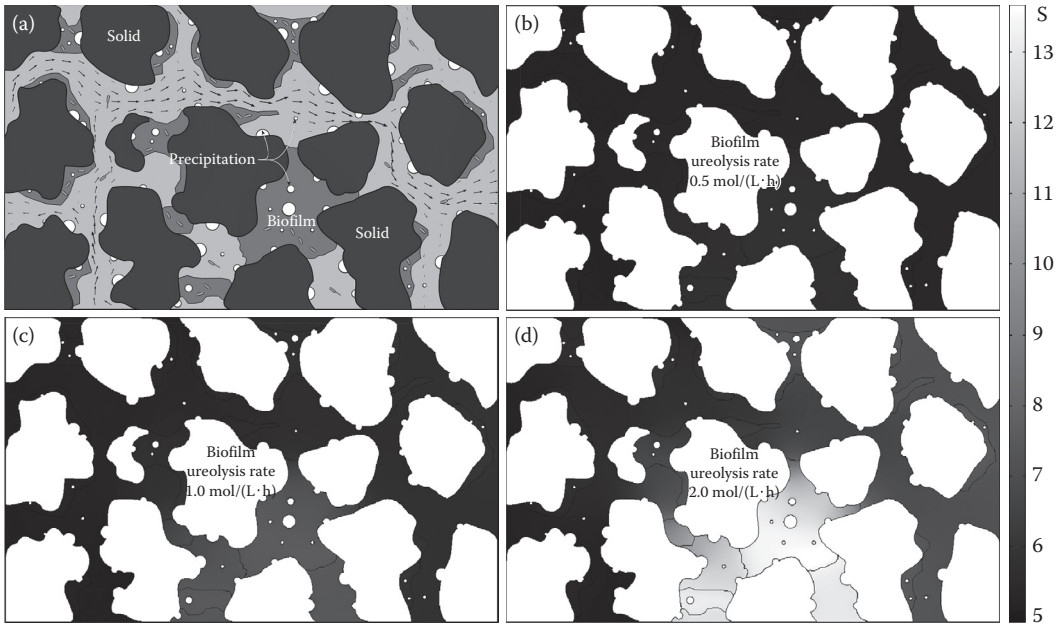

FIGURE 26.3 The theoretical geometry presented in Figure 26.1 (a) was applied to a 2D, steady-state finite element model to demonstrate the effect of alkalinity production in a biofilm on the pore-scale spatially resolved saturation state (S). Panels (b–d) show simulations with varied urea hydrolysis rates of 0.5, 1.0, and 2.0 mol/(L·h) respectively and a constant precipitation rate of 0.001 mol/(m^2·h). In this example, urea hydrolysis occurs only in the biofilm domains, and laminar fluid flow ($Re \ll 1$) is restricted to the liquid domain (no flow inside the biofilm domains). Please refer to Section 26.6 at the end of this chapter for additional information regarding this model.

the first-order approximation because substrate concentrations are low. In other systems, where the substrate concentrations are expected to be higher, a zero-order approximation may be appropriate.

Local reaction rates (and as a result concentrations) are difficult to predict at the pore scale because biofilm specific rates are not well studied. As discussed previously, the majority of the microbiological activity in the subsurface is likely to be attributed to biofilm. Unfortunately, most tabulated kinetic values (R_{max} and k_m) are reported for planktonic systems or for pure enzymes. To accurately predict pore-scale behavior, the volumetric reaction rates (rate per volume of biofilm or per volume of porous medium) must be known, and estimating those rates accurately can be difficult since planktonic or pure enzyme characteristics might not be appropriate for biofilms. Figure 26.3 shows a calculated saturation state distribution in a pore-scale model with ureolytic alkalinity generation. The biovolumetric reaction rate is varied, and the result is a significant change in the calculated heterogeneity of local saturation states. In general, higher biological reaction rates lead to more heterogeneous local concentrations due to mass flux limitations as illustrated in Figure 26.3.

26.3 MINERAL PRECIPITATION THEORY

Precipitation is very effective at blocking pore space in geologic materials. As opposed to pore blockage with biofilm alone, the precipitation of minerals is an attractive strategy to block pores because minerals have the potential to be longer lasting (Ebigbo et al., 2010; Mitchell and Ferris, 2006). The precipitation of carbonate minerals can occur in the subsurface abiotically or through the microbial production of alkalinity as discussed in Section 26.2.1. Biomolecules, even if they are not directly involved in precipitation, have been shown to affect all of the steps involved in

precipitation (Decho, 2010; Kawaguchi and Decho, 2002). In order to understand precipitation, and the effect microbial activity has on it, one must understand abiotic precipitation. The following section presents basic principles of aqueous mineral precipitation processes and theory important in the context of MICP.

26.3.1 Carbonate Minerals and Polymorphs

Carbonate minerals are commonly precipitated when DIC is present in high enough concentration to allow for local or widespread supersaturation with respect to carbonates. Other minerals, such as iron sulfides, phosphates, and silicates, can also precipitate, but carbonates are generally dominant in natural and engineered systems that produce microbially induced precipitates. This is because many microorganisms produce DIC as a metabolic by-product, and divalent cations can be added easily or may already be present. Carbonate precipitation is also comparatively fast (Palandri and Kharaka, 2004) making it an obvious choice in many engineered applications. Nucleation and crystal growth behavior varies between particular minerals, but the specifics pertaining to carbonates will be the focus here. It should be noted that if phosphate is expected in a system, calcium carbonate growth has the potential to be inhibited, and if phosphate is present at a high enough concentration, apatite can be precipitated (Plant and House, 2002).

Carbonates can be either crystalline or amorphous (noncrystalline). Of the crystalline carbonates, there are many types depending on the geochemistry of the environment that they are formed in. If only calcium carbonate is considered, there are three possible polymorphs: calcite, aragonite, and vaterite. Each polymorph is calcium carbonate, but possesses different crystal structure and solubility (Mohamed and Antia, 1998). At room temperature in pure, aqueous environments without microbes, calcite is the most stable polymorph because it has the lowest solubility (Plummer and Busenberg, 1982). The subsurface environment is rarely pure, meaning that trace ions as well as organic and inorganic molecules are present to varying degrees. These impurities change the properties of carbonate minerals that are precipitated. Sparse substitutions by trace metal ions in the crystal lattice of a carbonate crystal can affect the morphology leading to one particular polymorph having many distinct morphologies (Li et al., 2012; Zhang and Dawe, 2000). The precipitation of other carbonate minerals is possible in biologically relevant environments including iron and magnesium carbonates. Carbonates with mixed cationic composition can also form, such as dolomite ($CaMg(CO_3)_2$) (Krause et al., 2012; Sánchez-Román et al., 2011; Vasconcelos et al., 1995).

Polymorphic distribution is affected by biological activity. Multicellular organisms generally control the polymorphism of calcium carbonate shells (e.g., oysters and egg shells) through the use of scaffolding biopolymers and nucleation control. Although it is not as controlled as in multicellular organisms, it has been shown that microbial biofilms change polymorphic composition in a similar way by stabilizing otherwise metastable polymorphs (Rodriguez-Navarro et al., 2007).

26.3.2 Nucleation

Supersaturation with respect to mineral solubility is required for precipitation, but supersaturation does not guarantee precipitation. The formation of thermodynamically distinct phases in a liquid is usually initiated first by nucleation where the rare phase first appears at discrete points. The formation of a nucleus is associated with the system seeking a point of lowest free energy, as proposed by Gibbs (1948). Classical nucleation theory that arose from the work of Gibbs and others was based on condensation of a vapor to a liquid; however, it is commonly extended to crystallization from solutions. The energy difference between a small elementary volume of solid precipitate and the same mass of dissolved molecules, ΔG, can be split into two parts. First, there is a free energy associated with the energy difference between the crystal surface and the bulk crystal lattice that is called the surface free energy, ΔG_s. The second part is the free energy between the bulk crystal lattice and the

dissolved solute called the volumetric free energy, ΔG_v, analogous to a very large crystal particle of infinite radius. The overall free energy can be written as

$$\Delta G = \Delta G_s + \Delta G_v. \tag{26.20}$$

If we assume a spherical crystal geometry of radius r, the total free energy can be written as

$$\Delta G = 4\pi r^2\gamma + \frac{4}{3}\pi r^3 \Delta G_{dv}, \tag{26.21}$$

where
- γ is the unit surface energy
- ΔG_{dv} is a unit volumetric free energy

The surface energy is always positive if ΔG_{dv} is negative so there is a maximum ΔG (ΔG_{crit}) occurring at a radius r_{crit} (see Figure 26.4) such that

$$\Delta G_{crit} = \frac{4}{3}\pi\gamma r_{crit}^2, \tag{26.22}$$

where r_{crit} is the theoretically minimum stable nucleus radius (Mullin, 2001). A nucleus smaller than r_{crit} is most likely to redissolve, and nuclei reaching a size larger than r_{crit} are stable and are more likely to nucleate larger crystals.

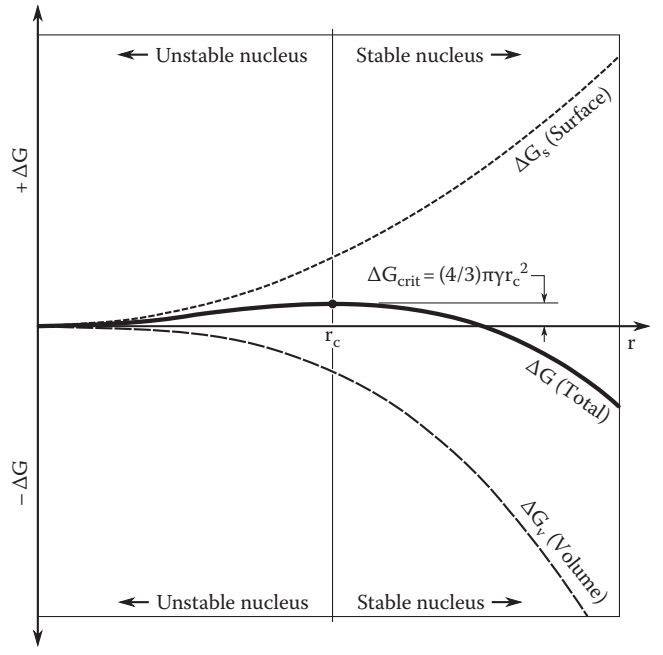

FIGURE 26.4 Critical nucleus size behavior due to a maximum in the total free energy (ΔG) based on Equations 26.20 through 26.22. A small nucleus ($r \ll r_c$) is unstable and is likely to redissolve as relaxation occurs to a lower total free energy. A large nucleus ($r \gg r_c$) is likely to grow in order to reduce total free energy. (From Gibbs, J.W., *The Collected Works of J. Willard Gibbs: Thermodynamics*, Yale University Press, New Haven, CT, 1948; Mullin, J.W., *Crystallization*, 4th edn., Butterworth-Heinemann, Oxford, U.K., 2001.)

The free energy treatment of the nucleation shows the importance of heterogeneities. Any localized perturbation (physical or chemical) to bulk conditions can be either a source or inhibitor of nucleation. Local high concentration locations are more likely to be points of nucleation as systems have a tendency to equilibrate.

Nucleation can happen in two ways: it can occur on surfaces as a result of particles in suspension (heterogeneous nucleation) or it can occur in a perfectly homogeneous liquid (homogeneous nucleation). When considering MICP at the pore scale, the understanding of nucleation is important because it creates the initial conditions for crystal growth. The difficulty for modeling is that nucleation is considered a spatially stochastic process (Gebauer et al., 2008) leading to an uncertainty in the locations and density of nucleation points, and the effects of microbial activity are not well characterized.

The classical approach for homogeneous nucleation is that once a solution is supersaturated, the polymerization of aqueous calcium carbonate occurs randomly and becomes the nucleus precursor (Mullin, 2001). The polymerized aqueous calcium carbonate is termed amorphous calcium carbonate (ACC) and is much different than solid, crystalline phases because it lacks a clear crystal structure. Once an ACC cluster reaches a certain critical size, nucleation occurs, and ordered crystal growth proceeds (Figure 26.4) (Yoreo and Vekilov, 2003). This classical view is useful but neglects some detail that is critical to the understanding of the process in biological systems.

A more modern view of calcium carbonate nucleation has three main differences compared to the classical model. First, ACC forms even in undersaturated solutions and can be more stable than was previously thought (Demichelis et al., 2011; Gebauer et al., 2008; Raiteri and Gale, 2010). Second, there is more than one type of ACC that can be ordered such that different calcium carbonate polymorphs are nucleated (Hasse et al., 2000; Politi et al., 2006). Third, ACC can be metastable even in supersaturated conditions, particularly when magnesium ions are present at certain concentrations (Politi et al., 2010; Radha et al., 2012). The overall impact of these more recent discoveries in carbonate nucleation is a change in the assumed energetics of nucleation. The newer view of calcium carbonate nucleation that includes the existence of metastable prenucleation clusters lowers the energetic boundary (free reaction enthalpy) to precipitation relative to what was previously thought under the classical nucleation model (Gebauer and Cölfen, 2011).

The control of the type of ACC that is present during prenucleation in shell-forming multicellular organisms has been shown to be a mechanism for the control of polymorphic composition (Marin et al., 2008; Weiss et al., 2002). Similarly, it is a reasonable hypothesis that biofilms will affect ACC type and cluster size subsequently changing the nucleation characteristics relative to those that would be expected in the bulk fluid. For example, a number of studies have shown that vaterite and ACC are preferentially formed in some MICP systems (Rodriguez-Navarro et al., 2007; Xiao et al., 2010). Vaterite is the least stable crystalline calcium carbonate polymorph at biologically relevant conditions so its occurrence in MICP systems leads to the conclusion that the bacteria are not only inducing precipitation but also affecting polymorphism by stabilizing otherwise unstable intermediate mineral forms (Rodriguez-Navarro et al., 2007). In many MICP systems, calcite is the only observed calcium carbonate polymorph; however, it is thought that in many cases, vaterite is an intermediary, and calcite develops through the Ostwald rule of stages where more stable phases form via less stable intermediates (Xiao et al., 2010; Yoreo and Vekilov, 2003). Xiao et al. (2010) also present continued evidence for phospholipid cell walls nucleating carbonate minerals, specifically vaterite as a precursor to calcite (also see: Douglas and Beveridge, 1998).

In the subsurface environment, it is reasonable to assume that true homogeneous nucleation is a rare event. Geologic porous media have many of the factors that generally are associated with the existence of heterogeneous nucleation. These factors include the presence of secondary nucleation sites (seed crystals) and rough surfaces (Mullin, 2001). Heterogeneous nucleation requires less free energy change compared to that associated with homogeneous nucleation, allowing nucleation to happen at a lower saturation state. The concentration and distribution

of nucleus-inducing heterogeneities will then also affect precipitation distribution later in the process because nucleation represents the initial condition for precipitation.

There are many factors in nucleation that are difficult to quantitate, and even if they are known, their effect is difficult to predict. The classical nucleation relationship can be described by the Arrhenius expression where

$$R_{nuc} = B\exp\left[\frac{-16\pi\Gamma^3\nu^2}{3k_B{}^3T^3(\ln S)^2}\right]. \tag{26.23}$$

where

B is equal to 1 nucleus per time per volume and simply contains the units of R_{nuc} as in the Arrhenius form (Kashchiev and van Rosmalen, 2003; Mullin, 2001)
Γ is interfacial tension
ν is the molecular volume
k_B is the Boltzmann constant
T is the temperature

Unfortunately, Equation 26.23 does not capture observed nucleation behavior very well leading to a multitude of more complex expressions, many of which are system specific. For a more complete review of mineral nucleation, see Yoreo and Vekilov (2003).

One nearly universal example of a situation where observation does not match classical theory in nucleation is the existence of a lag period between critical supersaturation and nucleation. Observable nucleation does not generally occur at precisely the same time at which the critical supersaturation is reached as predicted by Equations 26.20 and 26.21. A so called induction time, t_{ind}, is required. Many factors affect t_{ind}; however, in general, shorter induction times are associated with higher nucleation and growth rates (Flaten et al., 2010). Similarly, higher supersaturation and the presence of heterogeneous nucleation sites will decrease the induction time. Inverse proportionalities between t_{ind} and R_{nuc} have been proposed such that

$$t_{ind} \propto \frac{1}{R_{nuc}}, \tag{26.24}$$

however their use in predicting subsurface behavior is limited because of the unpredictability of heterogeneous nucleation sites.

26.3.3 Crystal Growth Models and Kinetics

Once nucleation occurs, crystals will grow based on the conditions that exist at the crystal/fluid interface. As in nucleation, there are many molecular scale factors that affect crystal growth. There are thermodynamic controls that limit crystal size and polymorphic composition and kinetic controls due to ion diffusion limitations and surface species equilibrium reactions. Many factors affect crystal growth, but generally, crystal growth is faster with higher supersaturation. The relationship between saturation and crystal growth can be handled a number of ways mathematically. More complete reviews are numerous; however, a complete discussion of basic crystallization can be found in Mullin (2001).

There is no universally accepted mathematical treatment of crystal growth. The general thermodynamics are understood, but the stochastic nature, small scale, and sensitivity to impurities even at extremely low concentration make the quantitative prediction of crystal growth difficult in many systems, including the subsurface environment. At a fundamental level, mineral crystal growth occurs when ions in a supersaturated solution diffuse to a crystal surface and are incorporated into the lattice. Gibbs is credited with providing the current thermodynamic understanding

of crystal growth through the principle of the minimization of system free energy (Gibbs, 1948). Gibbs' theory states that the equilibrium shape of a crystal will be such that it minimizes interfacial energy.

The most basic thermodynamic treatment of crystal growth is the Gibbs–Volmer model, where a thin transition phase on the growing crystal surface is assumed (Volmer and Adhikari, 1926). In this thin transition phase, adsorbed ions lose a degree of freedom and are allowed to diffuse only along the crystal surface before they are incorporated at points of highest energy (e.g., kinks and steps) and grow via layers. The Gibbs–Volmer model is the basis of a number of other models that are useful in the investigation of structural characteristics and mechanisms; however, generally these models fall short of being able to make accurate quantitative predictions especially in complex systems.

Recognizing that crystal growth is a diffusion process, with molecules being required to diffuse to the crystal surface before they can be incorporated, classical work by Nernst and Noyes and Whitney in the late nineteenth and early twentieth centuries (Mullin, 2001) suggests a crystal growth rate of the form

$$\frac{dm}{dt} = \frac{D}{\delta} A(C - C^*). \tag{26.25}$$

The mass growth rate (dm/dt) of a crystal, or collection of crystals, is determined by the molecular diffusion coefficient D, a static boundary layer thickness δ, the crystal/liquid interfacial area A, and the bulk solute concentration C, relative to the theoretical concentration at saturation, C*. Equation 26.25 is valid for a simple system containing a single molecule crystal; however, it requires modification for multicomponent crystals such as carbonates. Equation 26.25 can be split into two parts: molecular diffusion to the surface and reaction at the crystal surface. This division can be written as

$$\frac{dm}{dt} = k_{diff} A(C - C_i) \tag{26.26}$$

and

$$\frac{dm}{dt} = k_{react} A(C_i - C^*) \tag{26.27}$$

where

k_{diff} and k_{react} are diffusional mass transfer and reaction rate coefficients respectively
C_i is the solute concentration at the interface

Typically, reactions 26.26 and 26.27 are combined, and a reaction order term, n_p, is added resulting in

$$\frac{dm}{dt} = k_p A(C - C^*)^{n_p}, \tag{26.28}$$

where k_p is the overall precipitation rate constant. Both k_p and n_p are then determined experimentally. For inorganic salts, n_p is typically between 1 and 2 but should be thought of as a fitting parameter rather than a variable that presents any clear conceptual meaning (Morse et al., 2007). Equation 26.28 requires further modification in multispecies systems where there are multiple concentrations that would affect the precipitation rate. In this case, the saturation, rather than concentration, is used, and Equation 26.28 becomes

$$\frac{dm}{dt} = k_p A(S - 1)^{n_p} \tag{26.29}$$

and serves as the basis of most empirical crystal growth rate models (e.g., Zhong and Mucci, 1989). Dissolution is commonly treated in an analogous fashion. For calcium carbonate, the common rate relationship for dissolution takes the form

$$\frac{dm}{dt} = \left(k_{d1}\{H^+\} + k_{d2}\right) A \left(1 - S\right)^{n_d} \quad \text{for} \quad S < 1 \tag{26.30}$$

(Chou et al., 1989; Compton et al., 1989). k_{d1}, k_{d2}, and n_d are experimentally determined constants. For calcium carbonate dissolution, it was determined that pH plays an important role in addition to the saturation state, S. Thus, an additional rate term is used that is dependent on the bulk proton activity, $\{H^+\}$.

Caution must be used when using empirical precipitation and dissolution relationships and published constants, therein, for pore-scale modeling purposes. Rate constants are typically determined by measuring bulk concentration changes during desaturation over the course of a precipitation event. These concentration measurements are typically taken in well-mixed systems. It may be appropriate to use literature values determined in well-mixed systems for a Darcy scale model (e.g., Ebigbo et al., 2012) because both are volume-averaged approaches, but they might not be appropriate for use in pore-scale models (Miller et al., 2013). In a pore-scale model, crystal growth and dissolution might be better predicted from calculated interfacial concentrations; however, these are unknown in a volume-averaged system, and measured bulk concentrations determine the fitted rate constants. The scarce availability of pore-scale rate constants provides a challenge to using relationships such as Equations 26.29 and 26.30 in pore-scale models. Corrections that account for differing mass transfer characteristics may have to be applied to values that were calculated from experiments in volume-averaged systems in order for them to be used in pore-scale models, potentially reducing their accuracy. Figure 26.5 illustrates the effect of precipitation rate at the pore scale, thereby highlighting the importance of the use of accurate pore-scale rate constants in systems with precipitation.

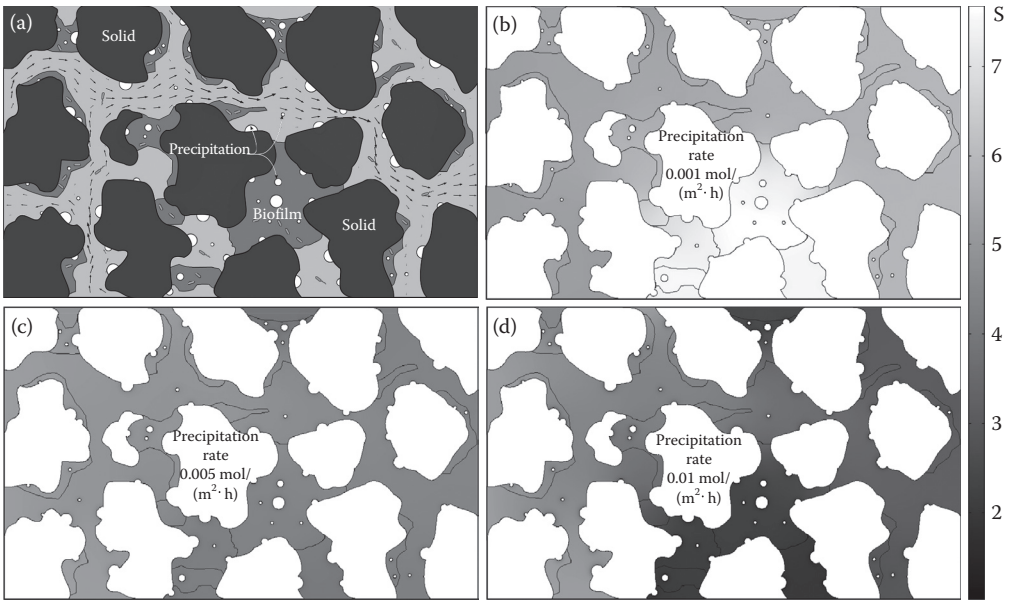

FIGURE 26.5 The theoretical geometry presented in Figure 26.1 (a) applied to a 2D, steady-state finite element model to demonstrate the effect of precipitation rate on pore-scale spatially resolved saturation state (S). Panels (b–d) show simulations with varied precipitation rates of 0.001, 0.005, and 0.01 mol/($m^2 \cdot h$) respectively along with a constant urea hydrolysis rate in biofilm domains of 1.0 mol/($L \cdot h$). Precipitation is modeled as a surface flux of both carbonate and calcium ions at the precipitate boundaries, and laminar fluid flow ($Re \ll 1$) is restricted to the liquid domain (no flow inside the biofilm domains). Please refer to Section 26.6 at the end of this chapter for additional information regarding this model.

Mechanistic approaches to crystal growth can be found in surface complexation models (Heberling et al., 2011; Ruiz-Agudo et al., 2011; Van Cappellen et al., 1993; Wolthers et al., 2012) that lend themselves well to pore-scale models where interfacial surfaces are known (or assumed) and interfacial concentrations can be calculated. Advances in surface-sensitive spectroscopic analysis that were not available to Gibbs and others in the early twentieth century have allowed for an improved understanding of the surface chemistry involved in crystal growth and dissolution. The basic concept behind surface complexation models is that at the crystal/liquid interface, there are water molecules and dissolved ions that form ionic bonds with exposed lattice molecules. These bonded molecules, which are not yet part of the ordered crystal lattice (denoted by > in this text), enter the system of chemical species providing a link between the aqueous chemistry and the crystal surface. Surface complexation has been particularly well studied in carbonates where two classes of hydration species (>CO_3H and >MeOH) have been shown to exist (Morse and Mackenzie, 1990; Nilsson and Sternbeck, 1999; Van Cappellen et al., 1993). Me is any divalent metal such as calcium, magnesium, or a transition metal such as iron. Other surface species such as >$MeCO_3^-$ are also present by complexation with dissolved ions rather than water (Pokrovsky et al., 2000; Ruiz-Agudo et al., 2011).

Taking calcite as an example, the reactions occurring at the crystal surface are found in Table 26.2, which is adapted from Pokrovsky et al. (2000) and Ruiz-Agudo et al. (2011).

Precipitation kinetics can be estimated from surface speciation using an approach first proposed by Nilsson and Sternbeck (1999) and later refined by Ruiz-Agudo et al. (2011), where crystal growth occurs through dehydration and incorporation of either aqueous calcium carbonate ($CaCO_{3(aq)}$) or calcium ions. The adsorption of lattice ions must happen at dehydrated surface sites >CO_3Ca^+, >CO_3^-, >$CaHCO_3$, and >$CaCO_3^-$. Under the conditions studied in Nilsson and Sternbeck (1999) and also by Ruiz-Agudo et al. (2011), which are biologically relevant temperatures and pH, it was determined that adsorption to >$CaHCO_3$ would likely be rate limiting so the two possible rate-limiting precipitation reactions can be written as

$$>CaHCO_3 + CaCO_{3(aq)} \cdot 6H_2O \rightarrow >CaHCO_3 + 6H_2O, \tag{26.31}$$

and

$$>CaHCO_3 + Ca^{2+} \cdot 8H_2O \rightarrow >CO_3Ca^+ + H^+ + 8H_2O. \tag{26.32}$$

$CaCO_{3(aq)}$ or calcium ions approach the surface in a hydrated state, and when they are incorporated in the crystal lattice, they become dehydrated. Equations 26.31 and 26.32 are written such that the molecules that were dehydrated disappear on the right-hand side indicating a flux out of solution (Ruiz-Agudo et al., 2011). The rates of these precipitation reactions can be treated as first order with respect to the

TABLE 26.2
Surface Reactions on a Calcite Crystal and Their Associated Solubility Constants

Surface Reaction	pk (25°C)
>$CO_3H \leftrightarrow CO_3^- + H^+$	5.1
>$CO_3H + Ca^{2+} \leftrightarrow >CO_3Ca^+ + H^+$	1.7
>$CaOH \leftrightarrow >CaO^- + H^+$	12.0
>$CaOH + H^+ \leftrightarrow >CaOH_2^+$	−11.5
>$CaOH + CO_3^{2-} + 2H^+ \leftrightarrow >CaHCO_3 + H_2O$	−23.5
>$CaOH + CO_3^{2-} + H^+ \leftrightarrow >CaCO_3^- + H_2O$	−17.1

">" indicates surface species and all others are aqueous species.

surface concentration of $>CaHCO_3$ (denoted by square brackets in units of mol per surface area) and the activity of the hydrated species being adsorbed. Assuming both reactions from Equations 26.31 and 26.32 are happening at the same time, the overall precipitation rate can be written as

$$\frac{dm}{dt} = k_1\{CaCO_{3(aq)}\}[>CaHCO_3] + k_2\{Ca^{2+}\}[>CaHCO_3]. \tag{26.33}$$

k_1 and k_2 are empirical rate constants, and values for calcite have been estimated to be approximately equal and on the order of 10^8 mol/(L · h) when calculated from measured bulk aqueous activities (Ruiz-Agudo et al., 2011).

26.4 REACTIVE TRANSPORT

Biofilm and MICP have the potential to affect reactive transport in a porous medium greatly. In a homogeneous porous medium, effects include permeability reduction through a decrease in porosity, the formation of isolated pores, and flow channeling that leads to increased dispersion. In a heterogeneous porous medium, biologically mediated effects are less clear and are highly system dependent. The study of pore topology coupled with reaction kinetics and solute transport is essential for a more complete understanding of how physical and chemical mechanisms interact in MICP systems in the subsurface.

26.4.1 Solute Transport

There is a set of dimensionless parameters that are particularly useful in the study of reactive transport in the subsurface. Here we will discuss them in relation to MICP systems, but for a more complete analysis of their meanings, many reviews are available in the chemical engineering and porous media literature (e.g., Bird et al., 2006). There are five rates that we are concerned with in MICP systems. These rates are (1) the solute transport rate due to advection, (2) the solute transport rate due to diffusion, (3) the precipitation rate, (4) the biomass growth rate, and (5) catabolic conversion rates leading to alkalinity production. Note that the biomass growth rate is loosely proportional to the amount of biofilm present in the pore space. Similar to high precipitation rates, high biofilm growth rates correlate with more porous media blockage due to the presence of biofilms. Ratios of these five rates relative to each other or relative to a length scale (such as the pore diameter, biofilm thickness, or discretization dimension) describe system behavior and are the basis for a number of useful dimensionless parameters discussed in this section.

The Reynolds number (Re) is an important parameter in the characterization of the hydrodynamics in a porous medium. Re is the ratio of inertial forces to viscous forces and can be written as

$$\mathrm{Re} = \frac{vL}{\upsilon}, \tag{26.34}$$

or specifically for a porous medium made up of spherical grains of diameter d, Equation 26.34 becomes

$$\mathrm{Re} = \frac{v\phi d}{\upsilon(1-\phi)} \tag{26.35}$$

where

v is the average pore fluid velocity
L is the characteristic length scale
υ is the kinematic viscosity
ϕ is the porosity

Viscous forces generally dominate in the subsurface because of slow velocities and small length scales; however, in an engineered setting, areas around injection points may have very high Re depending on the system.

There is an interplay between Re and biofilm growth. In higher Re flow, biofilm is exposed to higher shear forces and is therefore more susceptible to physical detachment (Stoodley et al., 2001). Biofilms grown in high shear environments are generally stronger and thinner, presumably to counteract the higher shear forces. In contrast, biofilms grown in low shear environments are generally less dense and occupy more pore space (Teodósio et al., 2011).

Pore-scale hydrodynamics also affect chemical gradients. Fast fluid flow causes fast convective solute transport that facilitates faster reaction rates. When considering the balance between solute transport (both convective and diffusive) and reaction rates at the pore scale in MICP systems, one must recognize that there are three types of reaction: (1) reactions occurring in mobile pore fluid, (2) reactions occurring within a biofilm or in immobilized pore fluid, and (3) surface reactions at the precipitate/fluid or precipitate/biofilm interface. Reactions occurring in mobile pore fluid are the most straightforward to quantify. These include reactions for chemical equilibria and planktonic biological reactions; rates measured in a laboratory setting and found in the literature are likely to be appropriate for direct application. Equilibrium reactions, especially in aqueous carbonate chemistry, are much faster than the biological reactions (Zhang and Klapper, 2010, 2011) so it can likely be assumed that, for modeling purposes, they occur instantaneously.

26.4.2 Biofilm-Catalyzed Reactions

Reactions that occur in biofilms are more likely to be limited by mass transport for two main reasons. Biofilm limits both advective and diffusive mass transport and high cell densities can lead to locally high rates of reaction. As Stewart (2003) points out, the diffusive time scale of a solute to the base of a biofilm approximately increases with the square of the biofilm thickness. That is to say, a 100 μm thick biofilm will be 100 times more diffusion limited than a 10 μm thick biofilm and 10,000 times more diffusion limited than a planktonic cell, assuming a diffusion length scale of 1 μm for a single cell. Literature does support the existence of some advection within biofilms that will increase mass transport, but at least some amount of mass transport limitation is inherent in any biofilm system (Pintelon et al., 2012).

Mass transport in precipitation and dissolution surface reactions are often limited by the stagnant layer near the surface often termed the mass transfer resistance layer. In MICP systems, the mass transfer resistance layer becomes difficult to predict because the presence of biofilm can create multiple phase boundaries (biofilm–mineral, mineral–liquid, and liquid–biofilm). Pore-scale information, such as the relative abundance of the various phase boundaries, is important for accurate effective rate predictions in MICP systems because the relative locations of the biofilm that induces precipitation and the growing precipitate become important. Crystals that form and grow within the biofilm matrix may grow at different rates and affect the pore structure differently from crystals attached directly to the porous medium. In MICP systems, both of these precipitation processes are likely to be occurring at the same time.

Simplifying the system and taking microbially induced precipitation as one overall reaction, it can be useful to compare a predicted reaction rate with the rate of mass transport in the form the Damköhler number (Da). Generally, Da is defined as a reaction rate divided by the mass transport rate of the rate-limiting compound (usually the substrate) participating in the reaction. Da can also be thought of as the ratio of the time scales of transport and reaction (Fogler, 2005). This allows for an assessment of whether a system is limited by mass transport or by the reaction rate. The convective Damköhler number can be written generically as

$$\mathrm{Da} = k_{\mathrm{Da}} C_o^{n_{\mathrm{Da}}-1} \tau \tag{26.36}$$

for a reaction of order n_{Da} where k_{Da} is a kinetic rate constant, C_o is a representative concentration (usually the bulk pore water concentration), and τ is a fluid residence time. Da is a useful parameter

to consider for reactions occurring in the bulk pore fluid or when reactions are volume averaged. In more classic chemical engineering reactor design, the calculation of Da allows one to quickly decide if a substrate is being fully utilized in a reactor. If the bulk transport is too high relative to the reaction rate (Da $\ll$ 1), most of the reactant will pass through the reactor without enough time to react. In contrast, the entire reactor volume would not be utilized efficiently if the reaction occurs too quickly relative to bulk transport (Da $\gg$ 1). In porous media systems, when Da is much greater than one for a precipitation reaction, inlet plugging will be expected. However, if Da is less than one, more uniform precipitate deposition is expected but with a lower conversion efficiency of the reactants supplied to the system. Furthermore, Da is not constant temporally or spatially in systems where the reaction causes a change in porosity or the reaction rate changes in space or time. For instance, as porosity decreases due to precipitation and biofilm growth, it is likely that a regime change will occur where the system goes from low Da (reaction rate limited) to high Da (transport limited) behavior (see Figure 26.6). In engineered systems, this transition may mark an important point where control parameters, such as flow rate or reactant concentrations, will need to be adjusted.

The use of the convective Damköhler number (Equation 26.36) is appropriate only if there is minimal diffusion limitation or if effective reaction rates are used, which take into account diffusion limitations. This is because the volume-averaged reaction rates used in the calculation may be inaccurate due to diffusion limitations and locally varying reaction rates. It is reasonable to expect that reactions of interest are limited by diffusion in MICP systems, which are dominated by reactions occurring in biofilms, on surfaces, and in pores with stagnant fluids. There are three primary ways to take the diffusion limitation into account, all of which require the estimation of volume-averaged concentration heterogeneity. Assuming that the reaction rate of interest (i.e., alkalinity production

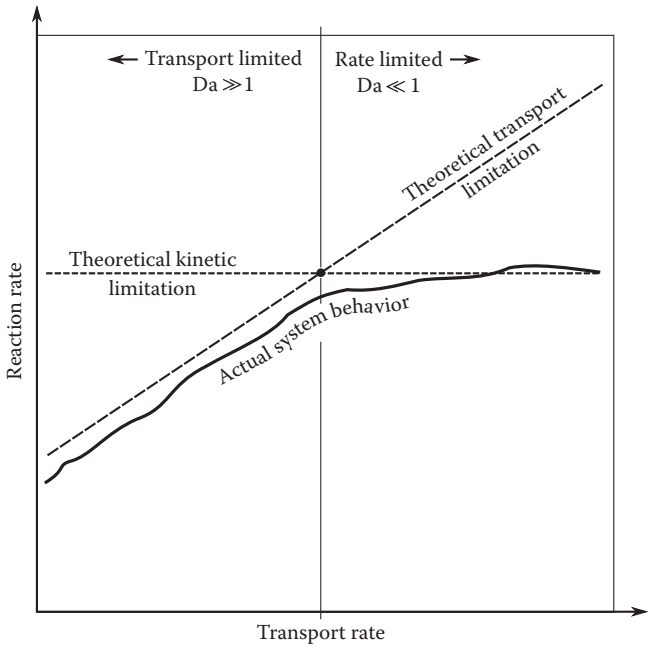

FIGURE 26.6 Expected volume-averaged system behavior in the context of kinetic and transport rate limits. As solute transport is increased, the overall reaction rate will increase until reactions are limited by the reaction kinetics of the system. The shape of an actual system curve is highly dependent on factors such as pore size distribution and concentration dependence on reaction rates, but generally bulk reaction rates will increase with increasing transport rates (i.e., Darcy velocity) until a kinetic limitation is reached. This behavior was shown through pore-scale modeling by Molins et al. (2012).

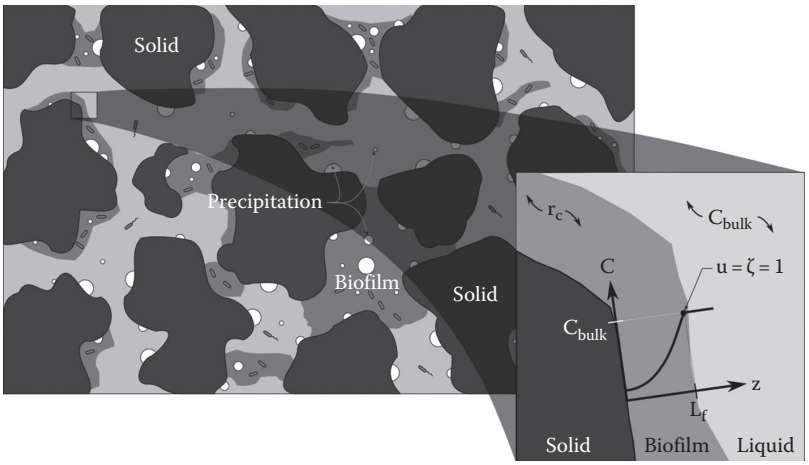

FIGURE 26.7 The assumed biofilm profile geometry for Thiele modulus calculations. The biofilm is assumed to be of a slab geometry with $C = C_{bulk}$ at $z = L_f$. A reaction, r_c is occurring in the biofilm domain only, and the problem is nondimensionalized such that $u = C/C_{bulk}$ and $\zeta = z/L_f$. The assumed profile is put into the context of an assumed pore geometry where L_f can be highly variable highlighting the importance of using caution when using volume-averaged parameters.

and precipitation) is dependent on substrate or product concentrations, rates cannot be constant at the pore scale when concentration heterogeneity exists. Taking diffusion limitation and nonconstant reaction rates into account, actual reaction rates can be significantly different from those predicted from models using bulk pore fluid.

The effect of diffusion limitation can be quantified by calculating an effectiveness factor, η, which is defined as the observed mean rate of reaction, R_{obs}, divided by the rate of reaction that would be predicted if there was no mass transfer limitation (Equation 26.37). The rate predicted as if there was no mass transfer limitation is simply the rate model evaluated at bulk pore fluid conditions, $R_{bulk,}$ so

$$\eta = \frac{R_{obs}}{R_{bulk}}. \tag{26.37}$$

The effectiveness factor can be estimated through the use of the Thiele modulus (h_t), a dimensionless number, which relates diffusion and reaction rates. A brief derivation of the Thiele modulus is useful in the understanding of the assumptions that must be made.

First let us consider a section of biofilm that is attached to an inert porous media grain of the geometry presented in Figure 26.7.

Assume a biofilm that is carrying out a reaction R_c in steady-state conditions. R_c is dependent on the concentration of a solute (C). It is also assumed that the biofilm geometry in the system is well approximated by a slab geometry and that the biofilm is homogeneous. Under these conditions, we can write a mass balance equation

$$D_e \frac{d^2C}{dz^2} = R_c, \tag{26.38}$$

where

D_e is the effective diffusion coefficient of solute C within the biofilm

z is the spatial coordinate normal to the biofilm/liquid and biofilm/support interfaces

We can nondimensionalize concentrations within the biofilm by dividing by the bulk pore water concentration, C_{bulk}, and nondimensionalize the length scale, z, by dividing by the biofilm thickness, L_f, such that $u = C/C_{bulk}$ and $\zeta = z/L_f$.

$$D_e \frac{d^2(uC_{bulk})}{d(\zeta L_f)^2} = R_c. \tag{26.39}$$

By rearranging variables, the general form of the Thiele modulus (h_t) is derived, where

$$\frac{d^2u}{d\zeta^2} = \frac{L_f^2 R_c}{C_{bulk} D_e} = h_t^2 g(u), \tag{26.40}$$

and

$$h_t^2 \equiv \frac{L_f^2 R_{bulk}}{C_{bulk} D_e}. \tag{26.41}$$

g(u) is a function of u (the dimensionless concentration) and is the ratio of the concentration-dependent reaction rate expression, R_c, to the reaction rate evaluated at the bulk concentration, R_{bulk}.

$$g(u) = \frac{R_c}{R_{bulk}}. \tag{26.42}$$

Mass fluxes and concentration profiles can be obtained by solving Equation 26.40. Equation 26.40 is useful in the analysis of h_t for calculating η and characterizing the system with respect to diffusive mass transport.

In order for h_t to be a useful dimensionless descriptor, it must be adjusted so that the dimensionless rate is integrated over the concentration profile. A generalized Thiele modulus, h_t^*, is obtained by

$$h_t^* = h_t \left[2 \int_0^1 g(u) du \right]^{-1/2}. \tag{26.43}$$

Solutions to Equation 26.43 can be found in Table 26.3. If $h_t^* \gg 1$, the representative element of biofilm is diffusion limited, and if $h_t^* \ll 1$, it is limited by the reaction rate. Beyond the simple classification of diffusion limitation or reaction rate limitation, h_t^* can also be used to calculate the effectiveness factor, η, of the biofilm element (Gottifredi and Gonzo, 2005) using

$$\eta = \int_0^1 g(u) d\zeta. \tag{26.44}$$

The zero-order case is solved easily because g(u) = 1 so $\eta = 1$ for $h_t^* \leq 1$. Caution should be used when applying a zero-order model to effectiveness factor calculations. If the biofilm is diffusion limited ($h_t^* > 1$), it is often the case that a zero-order rate model would not accurately represent the system and another rate model may have to be used. As discussed in Section 26.2.3, zero-order rate models are best suited for high substrate concentrations. If a biofilm is limited by diffusion, the deeper region of the biofilm will have very low (or zero) substrate concentration requiring the use of a higher order rate model. Calculating η for a first-order rate model is also straightforward but

TABLE 26.3
Useful Relationships for the Calculation of the Thiele Modulus and Effectiveness Factor for Zero-, First-Order, and Michaelis–Menten (M–M) Rate Models Assuming Boundary Conditions $du/d\zeta = 0$ at $\zeta = 0$ and $u = 1$ at $\zeta = 1$

Rate Model	$R_c =$	$g(u) =$	$h_t^2 =$	$h_t^* =$	$\eta =$
Zero order	R_{max}	1	$\frac{L_f^2 R_{max}}{C_{bulk} D_e}$	$\frac{h_t}{\sqrt{2}}$	1 for $h_t^* \leq 1$
First order	$k_1 C$	u	$\frac{L_f^2 k_1}{D_e}$	h_t	$\frac{\tanh(h_t)}{h_t}$
M–M	$R_{max}\frac{C}{k_m + C}$	$\frac{u(\beta+1)}{(\beta+u)}$	$\frac{L_f^2 r_{max}}{(k_m + C_{bulk})D_e}$	$h_t\left[2(\beta+1)[1-\beta\ln(\beta+1)+\beta\ln\beta]\right]^{-1/2}$	No analytical solution

$\beta = k_m/C_{bulk}$. Note that if $\beta \gg 1$, a first-order approximation is valid, and if $\beta \ll 1$, a zero-order approximation is valid.

requires the calculation of a concentration profile (u as a function of ζ) because u is nonconstant over the integral space and $g(u) = u$. Equation 26.38 can be solved with boundary conditions $du/d\zeta = 0$ at $\zeta = 0$ (no flux at the base of the biofilm) and $u = 1$ at $\zeta = 1$ (bulk concentration applied at the liquid/biofilm interface) to obtain

$$u = \frac{\cosh(h_t \zeta)}{\cosh(h_t)}, \tag{26.45}$$

and

$$\eta = \frac{\tanh(h_t)}{h_t}, \tag{26.46}$$

for a first-order kinetic model.

Calculating h_t^* and η is relatively straightforward for zero- and first-order kinetic models (see Table 26.3) but is more complex for rate relationships such as Michaelis–Menten. Michaelis–Menten effectiveness factors can be estimated numerically or through approximate solutions that are dependent on h_t^2 being very large or very small (Fang and Govind, 2008; Gonzo et al., 2012; Gottifredi and Gonzo, 2005). Another approach is to employ a weighted average of the fluxes that are calculated from zero- and first-order approximations to provide a smooth transition between the regimes without introducing more complicated mathematics (Pérez et al., 2005).

Once η is calculated, its use is straightforward if parameters can be estimated and averaged over a representative volume. If an average biofilm thickness and volume fraction can be estimated, bulk pore water concentrations can be used to estimate the biofilm reaction rate. The correct use of an effectiveness factor can add precision to a volume-averaged model without significantly increasing the computational cost.

26.4.3 Precipitation Reactions

The calculation of an effectiveness factor has been discussed in the context of a biofilm, but the other important reaction of the system, namely, precipitation, also needs attention. The same principles apply, but precipitation reactions occur at a surface rather than within a volume so adjustments must be made. As shown in Figure 26.1, there can be precipitation in three main forms in an MICP system: precipitation can occur (1) in the biofilm matrix, (2) suspended in the liquid phase being transported with the

bulk pore fluid, or (3) attached to the solid porous media grains in direct contact with the bulk pore fluid. The assumption of which type of precipitation dominates a system affects how it should be modeled because it will dictate the degree of diffusion limitation experienced at the precipitate surfaces.

The precipitation reaction models discussed in Section 26.3.3 can be translated into effective rates that can be used in reactive transport modeling similarly to the biofilm-catalyzed reactions; however, some assumptions must be made. Precipitation is a surface reaction, not a reaction that is well approximated over a volume, so the rate of precipitation is proportional to the surface area of the precipitate (see Equations 26.25 through 26.30). It is often most important to know how much pore space is occupied by the precipitated minerals, so additionally, a surface area per volume relationship must be assumed. A surface area (A)-to-volume (V) ratio can be obtained by approximating individual precipitates as spheres of radius, r. Equation 26.27 can then be converted into a volumetric rate where the volume occupied by the number, N, of precipitate particles of radius, r, can be written as

$$\frac{dV}{dt} = \frac{4\pi r^2}{\rho} N k_p \left(S-1\right)^{n_p}, \tag{26.47}$$

where ρ is the precipitate's density. Equation 26.47 can be implemented to calculate the porosity reduction over time in volume-averaged numerical simulations where r and N can be updated at each time step according to a mass balance and physical constraints such as a maximum radius. Note that, if attached precipitates dominate a system, Equation 26.47 still applies, but the surface area term must be divided in half to account for a hemispherical geometry. The approach in Equation 26.47 is best used when discrete (not overlapping) crystals are expected and N (the number of precipitate particles) remains somewhat constant.

The derivation of the precipitation rate model used in Equations 26.29 and 26.47 shows that there is already consideration of the diffusive mass transfer resistance inherent to precipitation reactions (see Equation 26.25). The issue is complicated when additional mass transfer resistance is introduced by the presence of biofilm. k_p is system dependent because the mass transfer portion depends on variables like biofilm thickness and porosity, which can be highly variable from system to system and heterogeneous within a single system. If there is little biofilm in a system, published k_p values, measured in well-mixed batch systems, are more likely to be accurate. When additional mass transfer resistance is expected, it must be taken into account.

26.5 CONCLUDING REMARKS

Pore-scale behavior in MICP systems is important to understand for the accurate predictions of larger-scale process. In this chapter, we have discussed the processes that play a role in increasing alkalinity and ultimately the precipitation of carbonate minerals. The biological and abiotic components of the process on their own are relatively well understood, but their interactions are complex, particularly in the context of porous media systems, which leaves room for future research in the field. Qualitatively, we understand that microorganisms, existing in biofilms, in attached cells, or as free floating planktonic cells, can increase alkalinity as a product of their metabolisms, which can consequently result in carbonate mineral precipitation and porosity reduction. It is known that biologically produced molecules affect the mineralogy of the precipitates; however, in a reactive transport context, this information remains difficult to quantify. The coupled nature of the system where biomass growth and mineral precipitation affect transport, and vice versa, makes it difficult to isolate and study processes independently of each other experimentally. This makes nondestructive analytical techniques and modeling important in future research.

Continuing to make progress in this field will benefit from a multidisciplinary approach with novel methods such as microfluidics (Zhang et al., 2010), confocal microscopy (Connolly et al., 2013; Pitts and Stewart, 2008; Schultz et al., 2011), x-ray microtomography and nanotomography

(Wildenschild and Sheppard, 2013), nuclear magnetic resonance imaging (Fridjonsson et al., 2011; Graf von der Schulenburg et al., 2008; Seymour et al., 2007, 2004), as well as spectroscopic techniques (Dandeu et al., 2006; Nehrke and Nouet, 2011; Ni and Ratner, 2008). Even with quality data from each of these techniques, mathematical models will be essential in order to make predictions about compounds and behavior at spatial and temporal scales currently not observable or measurable. Furthermore, cross-validation between techniques is often best done through modeling.

Modeling studies on MICP systems have been done both at the pore scale (Zhang and Klapper, 2010) and at the continuum scale (Cheng and Cord-Ruwisch, 2014; Ebigbo et al., 2012; Martinez et al., 2014; van Wijngaarden et al., 2010), and the models highlight the need for further experimental characterization and parameter estimation. For example, rate equations can be used to calculate porosity reduction over time, but it is unclear how that porosity reduction is best converted into a permeability reduction. Armstrong and Ajo-Franklin (2011) showed that the commonly used Kozeny–Carman relation provides a poor fit when simple raw permeability reduction data are used but could be refined to provide an acceptable fit when geometric factors were taken into account as measured by x-ray microtomography. In continuum modeling, there is typically little access to accurate geometric descriptors, especially when the pore topology changes over the course of the simulation. Recent advances in high-resolution (≈1 μm) 3D imaging techniques in opaque porous media for the biofilm phase of the MICP system will also help to more fully characterize the system, making it possible for accurate field-scale modeling (Davit et al., 2011; Iltis et al., 2011).

26.6 MODELING NOTES

The pore-scale models shown in Figures 26.3 and 26.5 are intended for illustration purposes only; however, physically relevant equations were solved using tabulated values for chemical constants such as diffusion coefficients and ion dissociation constants. The model was simplified to two dimensions, and the system was assumed to be at steady state with respect to fluid flow, reactive transport, and ion equilibria. Grain diameters are approximately 20 μm, and the pore throats are approximately 5 μm. COMSOL Multiphysics® (Version 4.3a) was used to solve the finite element problem and generate the saturation maps.

Navier–Stokes equations were solved to obtain the flow field with constant velocity defined in the influent regions on the left and zero pressure defined at the effluent regions on the right. Fluid velocities ranged from 0 to 0.5 cm/s in the narrowest pore throat (zero at the solid/liquid and biofilm/liquid interfaces and zero inside the biofilm regions). The average fluid velocity in the fluid domain is 0.024 cm/s. Laminar flow exists throughout the domain. Local ion concentrations were estimated using the Nernst–Planck equation coupled to the Navier–Stokes flow field, and ion equilibrium equations were solved simultaneously. Aqueous equilibrium reactions were modeled with fast-forward and reverse reactions (approximately four orders of magnitude faster than ureolysis or precipitation reactions). Uncharged species, such as urea, followed Fickian diffusion. The total influent DIC is 3 mmol/L, which is in the range of what could typically be found in aqueous environments exposed to the atmosphere. The inlet calcium and urea concentrations were chosen to be equimolar at 100 mmol/L. No chemical species are completely depleted in the domain for this simulation. Precipitation and urea hydrolysis rates are assumed to be constant for illustration purposes; however, they are varied as noted in the figure captions to show the general effect of each.

ACKNOWLEDGMENTS

The authors wish to thank Dr. Logan Schultz, Benjamin Jackson, and Neerja Zambare for reviewing this chapter. The authors were funded by the National Science Foundation through NSF award No. DMS-0934696 and by the US Department of Energy Grant Numbers DE-FG-02-09ER64758, DE-FE0004478 and DE-FE0009599. J.M.C. was also supported by an NSF-IGERT fellowship in Geobiological Systems at Montana State University (DGE-0654336).

NOMENCLATURE

[>X]	Area concentration of a surface species X
{x}	Activity of chemical species x
A	Crystal/liquid interfacial area
ACC	Amorphous calcium carbonate
B	Unit constant from Arrhenius expression
C	Generic concentration variable
C*	Theoretical solute concentration at saturation
C_{bulk}	Bulk pore water concentration
C_i	Solute/crystal interfacial concentration
C_s	General substrate concentration variable
D	Molecular diffusion coefficient
d	Pore diameter
Da	Damköhler number
D_e	Effective biofilm diffusion coefficient
DIC	Dissolved inorganic carbon
EPS	Extracellular polymeric substance
ΔG	Total Gibbs free energy (nucleation)
ΔG_{crit}	Total free energy of a critical nucleus
ΔG_{dv}	Unit volumetric free energy
ΔG_s	Precipitate surface free energy
ΔG_v	Precipitate volume free energy
h_t	Thiele modulus
h_t^*	Generalized Thiele modulus
IAP	Ion activity product
k	Chemical equilibrium dissociation constant
k_B	Boltzmann constant
k_{d1} k_{d2}	Disassociation rate constants
k_{Da}	Damköhler reaction rate constant
k_{diff}	Diffusional mass transfer coefficient
k_m	Michaelis–Menten half saturation constant
k_{nuc}	Nucleation rate constant
k_p	Overall precipitation rate constant
k_{react}	Precipitation reaction rate coefficient
k_{sp}	Mineral solubility product
L	Characteristic length
L_f	Biofilm thickness
m	Mass variable
MICP	Microbially induced carbonate precipitation
n_d	Disassociation rate order (fitting parameter)
n_{Da}	Damköhler reaction order
n_{nuc}	Nucleation rate order
n_p	Precipitation rate order (fitting parameter)
pk	$-\log_{10}(k)$
r	Precipitate radius
R_{bulk}	Rate of reaction as evaluated with bulk conditions
R_c	Concentration-dependent reaction rate
r_{crit}	Radius of a critical nucleus
Re	Reynolds number
R_{max}	Michaelis–Menten maximum reaction rate

R_{nuc}	Volumetric nucleation rate
R_{obs}	Observed mean rate of reaction
R_s	General substrate-dependent reaction rate
S	Saturation state
S_{crit}	Critical supersaturation where nucleation occurs
SRB	Sulfate-reducing bacteria
T	Temperature
t	Time variable
t_{ind}	Nucleation induction time
u	Nondimensionalized concentration variable, C/C_{bulk}
v	Average pore flow velocity
z	Thickness dimension for Thiele modulus calculations
Γ	Interfacial tension
γ	Unit surface free energy
δ	Static boundary layer thickness
ζ	Nondimensionalized spatial variable, z/L_f
η	Effectiveness factor
ν	molecular volume
τ	Hydraulic residence time
υ	Kinematic viscosity
ϕ	Porosity

REFERENCES

Al Qabany, A., Soga, K., Santamarina, C., 2012. Factors affecting efficiency of microbially induced calcite precipitation. *Journal of Geotechnical and Geoenvironmental Engineering* 138, 992–1001.

Armstrong, R., Ajo-Franklin, J., 2011. Investigating biomineralization using synchrotron based x-ray computed microtomography. *Geophysical Research Letters* 38, L08460.

Bachmeier, K.L., Williams, A.E., Warmington, J.R., Bang, S.S., 2002. Urease activity in microbiologically-induced calcite precipitation. *Journal of Biotechnology* 93, 171–181.

Bird, R.B., Stewart, W.E., Lightfoot, E.N., 2006. *Transport Phenomena*, 2nd edn. John Wiley & Sons, New York.

Boetius, A., Ravenschlag, K., Schubert, C.J., Rickert, D., Widdel, F., Gieseke, A., Amann, R., Jørgensen, B.B., Witte, U., Pfannkuche, O., 2000. A marine microbial consortium apparently mediating anaerobic oxidation of methane. *Nature* 407, 623–626.

Braissant, O., Cailleau, G., Dupraz, C., Verrecchia, E.P., 2003. Bacterially induced mineralization of calcium carbonate in terrestrial environments: The role of exopolysaccharides and amino acids. *Journal of Sedimentary Research* 73, 485–490.

Braissant, O., Decho, A.W., Dupraz, C., Glunk, C., Przekop, K.M., Visscher, P.T., 2007. Exopolymeric substances of sulfate-reducing bacteria: Interactions with calcium at alkaline pH and implication for formation of carbonate minerals. *Geobiology* 5, 401–411.

Castanier, S., Le Métayer-Levrel, G., Perthuisot, J.-P., 1999. Ca-carbonates precipitation and limestone genesis—The microbiogeologist point of view. *Sedimentary Geology* 126, 9–23.

Characklis, W.G., Marshall, K.C., 1990. *Biofilms*. Wiley, New York.

Chen, X., Stewart, P.S., 2002. Role of electrostatic interactions in cohesion of bacterial biofilms. *Applied Microbiology and Biotechnology* 59, 718–720.

Cheng, L., Cord-Ruwisch, R., 2014. Upscaling effects of soil improvement by microbially induced calcite precipitation by surface percolation. *Geomicrobiology Journal* 31, 396–406.

Chou, L., Garrels, R.M., Wollast, R., 1989. Comparative study of the kinetics and mechanisms of dissolution of carbonate minerals. *Chemical Geology* 78, 269–282.

Compton, R.G., Pritchard, K.L., Unwin, P.R., 1989. The dissolution of calcite in acid waters: Mass transport versus surface control. *Freshwater Biology* 22, 285–288.

Connolly, J., Kaufman, M.J., Rothman, A., Gupta, R., Redden, G.D., Schuster, M., Colwell, F.S., Gerlach, R., 2013. Construction of two ureolytic model organisms for the study of microbially induced calcium carbonate precipitation. *Journal of Microbiological Methods* 94(3), 290–299.

Costerton, J.W., Cheng, K.J., Geesey, G.G., Ladd, T.I., Nickel, J.C., Dasgupta, M., Marrie, T.J., 1987. Bacterial biofilms in nature and disease. *Annual Review of Microbiology* 41, 435–464.

Crittenden, J.C., Trussell, R.R., Hand, D.W., Howe, K.J., Tchobanoglous, G., 2012. *MWH's Water Treatment: Principles and Design*, 3rd edn. Wiley, New York.

Cunningham, A.B., Characklis, W.G., Abedeen, F., Crawford, D., 1991. Influence of biofilm accumulation on porous media hydrodynamics. *Environmental Science & Technology* 25, 1305–1311.

Cuthbert, M.O., Riley, M.S., Handley-Sidhu, S., Renshaw, J.C., Tobler, D.J., Phoenix, V.R., Mackay, R., 2012. Controls on the rate of ureolysis and the morphology of carbonate precipitated by *S. Pasteurii* biofilms and limits due to bacterial encapsulation. *Ecological Engineering* 41, 32–40.

Dandeu, A., Humbert, B., Carteret, C., Muhr, H., Plasari, E., Bossoutrot, J.M., 2006. Raman spectroscopy—A powerful tool for the quantitative determination of the composition of polymorph mixtures: Application to $CaCO_3$ polymorph mixtures. *Chemical Engineering & Technology* 29, 221–225.

Davies, C.W., 1962. *Ion Association*. Butterworths, Washington, DC.

Davit, Y., Iltis, G., Debenest, G., Veran-Tissoires, S., Wildenschild, D., Gerino, M., Quintard, M., 2011. Imaging biofilm in porous media using x-ray computed microtomography. *Journal of Microscopy* 242, 15–25.

De Muynck, W., De Belie, N., Verstraete, W., 2010. Microbial carbonate precipitation in construction materials: A review. *Ecological Engineering* 36, 118–136.

Decho, A.W., 2010. Overview of biopolymer-induced mineralization: What goes on in biofilms? *Ecological Engineering* 36, 137–144.

DeJong, J.T., Mortensen, B.M., Martinez, B.C., Nelson, D.C., 2010. Bio-mediated soil improvement. *Ecological Engineering* 36, 197–210.

Demichelis, R., Raiteri, P., Gale, J.D., Quigley, D., Gebauer, D., 2011. Stable prenucleation mineral clusters are liquid-like ionic polymers. *Nature Communications* 2, 1–8.

Dhami, N.K., Reddy, M.S., Mukherjee, A., 2013. Biomineralization of calcium carbonate polymorphs by the bacterial strains isolated from calcareous sites. *Journal of Microbiology and Biotechnology* 23, 707–714.

Dixon, N., Gazzola, C., Blakeley, R., Zerner, B., 1976. Metal ions in enzymes using ammonia or amides. *Science* 191, 1144–1150.

Douglas, S., Beveridge, T.J., 1998. Mineral formation by bacteria in natural microbial communities. *FEMS Microbiology Ecology* 26, 79–88.

Ebigbo, A., Helmig, R., Cunningham, A.B., Class, H., Gerlach, R., 2010. Modelling biofilm growth in the presence of carbon dioxide and water flow in the subsurface. *Advances in Water Resources* 33, 762–781.

Ebigbo, A., Phillips, A., Gerlach, R., Helmig, R., Cunningham, A.B., Class, H., Spangler, L.H., 2012. Darcy-scale modeling of microbially induced carbonate mineral precipitation in sand columns. *Water Resources Research* 48, W07519.

Ercole, C., Bozzelli, P., Altieri, F., Cacchio, P., Del Gallo, M., 2012. Calcium carbonate mineralization: Involvement of extracellular polymeric materials isolated from calcifying bacteria. *Microscopy and Microanalysis* 18, 829–839.

Fang, Y.X., Govind, R., 2008. A new Thiele's modulus for the Monod biofilm model. *Chinese Journal of Chemical Engineering* 16, 277–286.

Flaten, E.M., Seiersten, M., Andreassen, J.-P., 2010. Induction time studies of calcium carbonate in ethylene glycol and water. *Chemical Engineering Research and Design* 88, 1659–1668.

Flemming, H.C., Wingender, J., 2001a. Relevance of microbial extracellular polymeric substances (EPSs)—Part I: Structural and ecological aspects. *Water Science and Technology* 43, 1–8.

Flemming, H.C., Wingender, J., 2001b. Relevance of microbial extracellular polymeric substances (EPSs)—Part II: Technical aspects. *Water Science and Technology* 43, 9–16.

Fogler, H.S., 2005. *Elements of Chemical Reaction Engineering*, 4th edn. Prentice Hall, New Jersey.

Fredrickson, J.K., Gorby, Y.A., 1996. Environmental processes mediated by iron-reducing bacteria. *Current Opinion in Biotechnology* 7, 287–294.

Fredrickson, J.K., Zachara, J.M., Kennedy, D.W., Dong, H., Onstott, T.C., Hinman, N.W., Li, S., 1998. Biogenic iron mineralization accompanying the dissimilatory reduction of hydrous ferric oxide by a groundwater bacterium. *Geochimica et Cosmochimica Acta* 62, 3239–3257.

Fridjonsson, E.O., Seymour, J.D., Schultz, L.N., Gerlach, R., Cunningham, A.B., Codd, S.L., 2011. NMR measurement of hydrodynamic dispersion in porous media subject to biofilm mediated precipitation reactions. *Journal of Contaminant Hydrology* 120–121, 79–88.

Gebauer, D., Cölfen, H., 2011. Prenucleation clusters and non-classical nucleation. *Nano Today* 6, 564–584.

Gebauer, D., Völkel, A., Cölfen, H., 2008. Stable prenucleation calcium carbonate clusters. *Science* 322, 1819–1822.

Gibbs, J.W., 1948. *The Collected Works of J. Willard Gibbs: Thermodynamics*. Yale University Press, New Haven, CT.

Glenn, C.R., Filippelli, G.M., Gontharet, S., Pierre, C., Blanc-Valleron, M.-M., Rouchy, J.M., Fouquet, Y. et al., 2007. Nature and origin of diagenetic carbonate crusts and concretions from mud volcanoes and pockmarks of the Nile deep-sea fan (eastern Mediterranean Sea). *Deep Sea Research Part II: Topical Studies in Oceanography* 54, 1292–1311.

Gonzo, E.E., Wuertz, S., Rajal, V.B., 2012. Continuum heterogeneous biofilm model—A simple and accurate method for effectiveness factor determination. *Biotechnology and Bioengineering* 109, 1779–1790.

Gottifredi, J.C., Gonzo, E.E., 2005. On the effectiveness factor calculation for a reaction—Diffusion process in an immobilized biocatalyst pellet. *Biochemical Engineering Journal* 24, 235–242.

Graf von der Schulenburg, D.A., Vrouwenvelderb, J.S., Creber, S.A., van Loosdrecht, M.C.M., Johns, M.L., 2008. Nuclear magnetic resonance microscopy studies of membrane biofouling. *Journal of Membrane Science* 323, 37–44.

Hasse, B., Ehrenberg, H., Marxen, J.C., Becker, W., Epple, M., 2000. Calcium carbonate modifications in the mineralized shell of the freshwater snail *Biomphalaria glabrata*. *Chemistry: A European Journal* 6, 3679–3685.

Heberling, F., Trainor, T.P., Lützenkirchen, J., Eng, P., Denecke, M.A., Bosbach, D., 2011. Structure and reactivity of the calcite-water interface. *Journal of Colloid and Interface Science* 354, 843–857.

Iltis, G.C., Armstrong, R.T., Jansik, D.P., Wood, B.D., Wildenschild, D., 2011. Imaging biofilm architecture within porous media using synchrotron-based x-ray computed microtomography. *Water Resources Research* 47, W02601.

Jahns, T., 1996. Ammonium/urea-dependent generation of a proton electrochemical potential and synthesis of ATP in *Bacillus pasteurii*. *Journal of Bacteriology* 178, 403–409.

Kashchiev, D., van Rosmalen, G.M., 2003. Review: Nucleation in solutions revisited. *Crystal Research and Technology* 38, 555–574.

Kawaguchi, T., Decho, A.W., 2002. A laboratory investigation of cyanobacterial extracellular polymeric secretions (EPS) in influencing $CaCO_3$ polymorphism. *Journal of Crystal Growth* 240, 230–235.

Klenk, H.P., Clayton, R.A., Tomb, J.F., White, O., Nelson, K.E., Ketchum, K.A., Dodson, R.J. et al., 1997. The complete genome sequence of the hyperthermophilic, sulphate-reducing archaeon Archaeoglobus fulgidus. *Nature* 390, 364–370.

Krause, S., Liebetrau, V., Gorb, S., Sanchez-Roman, M., McKenzie, J.A., Treude, T., 2012. Microbial nucleation of Mg-rich dolomite in exopolymeric substances under anoxic modern seawater salinity: New insight into an old enigma. *Geology* 40, 587–590.

Lappin-Scott, H.M., Costerton, J.W. (Eds.), 2003. *Microbial Biofilms*. Cambridge University Press, Cambridge, U.K.

Lee, K.-C., Rittmann, B.E., 2003. Effects of pH and precipitation on autohydrogenotrophic denitrification using the hollow-fiber membrane-biofilm reactor. *Water Research* 37, 1551–1556.

Lengeler, J.W., Drews, G., Schlegel, H.G. (eds.), 1998. Anaerobic energy metabolism. In: *Biology of the Prokaryotes*. Blackwell Science Ltd, Oxford, U.K., pp. 278–326.

Li, W., Chen, W.-S., Zhou, P.-P., Cao, L., Yu, L.-J., 2012. Influence of initial pH on the precipitation and crystal morphology of calcium carbonate induced by microbial carbonic anhydrase. *Colloids and Surfaces B: Biointerfaces* 102, 281–287.

Lovley, D.R., Holmes, D.E., Nevin, K.P., 2004. Dissimilatory Fe(III) and Mn(IV) reduction. *Advances in Microbial Physiology* 49, 219–86.

Martin, D., Dodds, K., Butler, I.B., Ngwenya, B.T., 2013. Carbonate precipitation under pressure for bioengineering in the anaerobic subsurface via denitrification. *Environmental Science & Technology* 47, 8692–8699.

Martin, D., Dodds, K., Ngwenya, B.T., Butler, I.B., Elphick, S.C., 2012. Inhibition of *Sporosarcina pasteurii* under anoxic conditions: Implications for subsurface carbonate precipitation and remediation via ureolysis. *Environmental Science & Technology* 46, 8351–8355.

Marin, F., Luquet, G., Marie, B., Medakovic, D., 2008. Molluscan shell proteins: Primary structure, origin, and evolution. *Current Topics in Developmental Biology* 80, 209–276.

Martinez, B.C., DeJong, J.T., Ginn, T.R., 2014. Bio-geochemical reactive transport modeling of microbial induced calcite precipitation to predict the treatment of sand in one-dimensional flow. *Computers and Geotechnics* 58, 1–13.

Mayer, C., Moritz, R., Kirschner, C., Borchard, W., Maibaum, R., Wingender, J., Flemming, H.-C., 1999. The role of intermolecular interactions: Studies on model systems for bacterial biofilms. *International Journal of Biological Macromolecules* 26, 3–16.

Miller, C.T., Barry, D.A., Katul, G., Rinaldo, A., Wood, B.D., Valdés-Parada, F.J., 2013. Volume averaging: Local and nonlocal closures using a Green's function approach. *Advances in Water Resources* 51, 139–167.

Milucka, J., Ferdelman, T.G., Polerecky, L., Franzke, D., Wegener, G., Schmid, M., Lieberwirth, I., Wagner, M., Widdel, F., Kuypers, M.M.M., 2012. Zero-valent sulphur is a key intermediate in marine methane oxidation. *Nature* 491, 541–546.

Mitchell, A.C., Ferris, F.G., 2006. The influence of *Bacillus pasteurii* on the nucleation and growth of calcium carbonate. *Geomicrobiology Journal* 23, 213–226.

Mobley, H.L.T., Hausinger, R.P., 1989. Microbial ureases: Significance, regulation, and molecular characterization. *Microbiological Reviews* 53, 85–108.

Mobley, H.L.T., Island, M.D., Hausinger, R.P., 1995. Molecular-biology of microbial ureases. *Microbiological Reviews* 59, 451–480.

Mohamed, A.M.O., Antia, H.E., 1998. Lining systems. In: *Geoenvironmental Engineering*. Elsevier, Amsterdam, pp. 371–403.

Molins, S., Trebotich, D., Steefel, C.I., Shen, C., 2012. An investigation of the effect of pore scale flow on average geochemical reaction rates using direct numerical simulation. *Water Resources Research* 48, W03527.

Morsdorf, G., Kaltwasser, H., 1989. Ammonium assimilation in *Proteus vulgaris*, *Bacillus pasteurii*, and *Sporosarcina ureae*. *Archives of Microbiology* 152, 125–131.

Morse, J.W., Arvidson, R.S., Lüttge, A., 2007. Calcium carbonate formation and dissolution. *Chemical Reviews* 107, 342–381.

Morse, J.W., Mackenzie, F.T., 1990. *Developments in Sedimentology 48: Geochemistry of Sedimentary Carbonates*, 1st edn. Elsevier, Amsterdam.

Mullin, J.W., 2001. *Crystallization*, 4th edn. Butterworth-Heinemann, Oxford, U.K.

Muyzer, G., Stams, A.J.M., 2008. The ecology and biotechnology of sulphate-reducing bacteria. *Nature Reviews Microbiology* 6, 441–454.

Nehrke, G., Nouet, J., 2011. Confocal Raman microscope mapping as a tool to describe different mineral and organic phases at high spatial resolution within marine biogenic carbonates: Case study on *Nerita undata* (Gastropoda, Neritopsina). *Biogeosciences* 8, 3761–3769.

Nevin, K.P., Lovley, D.R., 2002. Mechanisms for Fe(III) oxide reduction in sedimentary environments. *Geomicrobiology Journal* 19, 141–159.

Ni, M., Ratner, B.D., 2008. Differentiating calcium carbonate polymorphs by surface analysis techniques—An XPS and TOF-SIMS study. *Surface and Interface Analysis* 40, 1356–1361.

Nilsson, Ö., Sternbeck, J., 1999. A mechanistic model for calcite crystal growth using surface speciation. *Geochimica et Cosmochimica Acta* 63, 217–225.

Palandri, J.L., Kharaka, Y.K., 2004. A compilation of rate parameters of water-mineral interaction kinetics for application to geochemical modeling. U.S. Geological Survey Open File Report, Virginia.

Pérez, J., Picioreanu, C., van Loosdrecht, M., 2005. Modeling biofilm and floc diffusion processes based on analytical solution of reaction-diffusion equations. *Water Research* 39, 1311–1323.

Perry, T.D., Klepac-Ceraj, V., Zhang, X.V, McNamara, C.J., Polz, M.F., Martin, S.T., Berke, N., Mitchell, R., 2005. Binding of harvested bacterial exopolymers to the surface of calcite. *Environmental Science & Technology* 39, 8770–8775.

Pfeffer, C., Larsen, S., Song, J., Dong, M., Besenbacher, F., Meyer, R.L., Kjeldsen, K.U. et al., 2012. Filamentous bacteria transport electrons over centimetre distances. *Nature* 491, 218–221.

Phillips, A.J., Gerlach, R., Lauchnor, E., Mitchell, A., Cunningham, A.B., Spangler, L., 2013. Engineered applications of ureolytic biomineralization: A review. *Biofouling* 29, 715–733.

Pintelon, T.R.R., Picioreanu, C., van Loosdrecht, M.C.M., Johns, M.L., 2012. The effect of biofilm permeability on bio-clogging of porous media. *Biotechnology and Bioengineering* 109, 1031–1042.

Pitts, B., Stewart, P., 2008. Confocal laser microscopy on biofilms: Successes and limitations. *Microscopy Today* 16, 18–22.

Pitzer, K.S., 1991. Ion interaction approach: Theory and data correlation. In: Pitzer, K.S. (Ed.), *Activity Coefficients in Electrolyte Solutions*. CRC Press, London, pp. 75–153.

Plant, L., House, W., 2002. Precipitation of calcite in the presence of inorganic phosphate. *Colloids and Surfaces A: Physicochemical and Engineering Aspects* 203, 143–153.

Plummer, L.N., Busenberg, E., 1982. The solubilities of calcite, aragonite and vaterite in CO_2–H_2O solutions between 0 and 90° C, and an evaluation of the aqueous model for the system $CaCO_3$–CO_2–H_2O. *Geochimica et Cosmochimica Acta* 46, 1011–1040.

Pokrovsky, O.S., Mielczarski, J.A., Barres, O., Schott, J., 2000. Surface speciation models of calcite and dolomite/aqueous solution interfaces and their spectroscopic evaluation. *Langmuir* 16, 2677–2688.

Politi, Y., Batchelor, D.R., Zaslansky, P., Chmelka, B.F., Weaver, J.C., Sagi, I., Weiner, S., Addadi, L., 2010. Role of magnesium ion in the stabilization of biogenic amorphous calcium carbonate: A structure–function investigation. *Chemistry of Materials* 22, 161–166.

Politi, Y., Levi-Kalisman, Y., Raz, S., Wilt, F., Addadi, L., Weiner, S., Sagi, I., 2006. Structural characterization of the transient amorphous calcium carbonate precursor phase in Sea Urchin Embryos. *Advanced Functional Materials* 16, 1289–1298.

Radha, A.V., Fernandez-Martinez, A., Hu, Y., Jun, Y.-S., Waychunas, G.A., Navrotsky, A., 2012. Energetic and structural studies of amorphous $Ca_{1-x}Mg_xCO_3 \cdot nH_2O$ ($0 <= x <= 1$). *Geochimica et Cosmochimica Acta* 90, 83–95.

Raiteri, P., Gale, J.D., 2010. Water is the key to nonclassical nucleation of amorphous calcium carbonate. *Journal of the American Chemical Society* 132, 17623–17634.

Riding, R., 2000. Microbial carbonates: The geological record of calcified bacterial-algal mats and biofilms. *Sedimentology* 47, 179–214.

Rodriguez-Navarro, C., Jimenez-Lopez, C., Rodriguez-Navarro, A., Gonzalez-Muñoz, M.T., Rodriguez-Gallego, M., 2007. Bacterially mediated mineralization of vaterite. *Geochimica et Cosmochimica Acta* 71, 1197–1213.

Ruiz-Agudo, E., Putnis, C.V., Rodriguez-Navarro, C., Putnis, A., 2011. Effect of pH on calcite growth at constant a_{Ca2+}/a_{CO32-} ratio and supersaturation. *Geochimica et Cosmochimica Acta* 75, 284–296.

Sánchez-Román, M., McKenzie, J.A., de Luca Rebello Wagener, A., Romanek, C.S., Sánchez-Navas, A., Vasconcelos, C., 2011. Experimentally determined biomediated Sr partition coefficient for dolomite: Significance and implication for natural dolomite. *Geochimica et Cosmochimica Acta* 75, 887–904.

Schultz, L., Pitts, B., Mitchell, A.C., Cunningham, A.B., Gerlach, R., 2011. Imaging biologically induced mineralization in fully hydrated flow systems. *Microscopy Today* 19, 12–15.

Seymour, J.D., Codd, S.L., Gjersing, E.L., Stewart, P.S., 2004. Magnetic resonance microscopy of biofilm structure and impact on transport in a capillary bioreactor. *Journal of Magnetic Resonance* 167, 322–327.

Seymour, J.D., Gage, J.P., Codd, S.L., Gerlach, R., 2007. Magnetic resonance microscopy of biofouling induced scale dependent transport in porous media. *Advances in Water Resources* 30, 1408–1420.

Shafahi, M., Vafai, K., 2009. Biofilm affected characteristics of porous structures. *International Journal of Heat and Mass Transfer* 52, 574–581.

Stephens, J.C., Keith, D.W., 2008. Assessing geochemical carbon management. *Climatic Change* 90, 217–242.

Stewart, P.S., 2003. Diffusion in biofilms. *Journal of Bacteriology* 185, 1485–1491.

Stoodley, P., Wilson, S., Hall-Stoodley, L., Boyle, J.D., Lappin-Scott, H.M., Costerton, J.W., 2001. Growth and detachment of cell clusters from mature mixed-species biofilms. *Applied and Environmental Microbiology* 67, 5608–5613.

Teodósio, J.S., Simões, M., Melo, L.F., Mergulhão, F.J., 2011. Flow cell hydrodynamics and their effects on *E. coli* biofilm formation under different nutrient conditions and turbulent flow. *Biofouling* 27, 1–11.

Tobler, D.J., Cuthbert, M.O., Greswell, R.B., Riley, M.S., Renshaw, J.C., Handley-Sidhu, S., Phoenix, V.R., 2011. Comparison of rates of ureolysis between *Sporosarcina pasteurii* and an indigenous groundwater community under conditions required to precipitate large volumes of calcite. *Geochimica et Cosmochimica Acta* 75, 3290–3301.

Van Cappellen, P., Charlet, L., Stumm, W., Wersin, P., 1993. A surface complexation model of the carbonate mineral-aqueous solution interface. *Geochimica et Cosmochimica Acta* 57, 3505–3518.

Van Paassen, L.A., Daza, C.M., Staal, M., Sorokin, D.Y., van der Zon, W., van Loosdrecht, M.C.M., 2010. Potential soil reinforcement by biological denitrification. *Ecological Engineering* 36, 168–175.

Van Wijngaarden, W.K., Vermolen, F.J., van Meurs, G.A.M., Vuik, C., 2010. Modelling biogrout: A new ground improvement method based on microbial-induced carbonate precipitation. *Transport in Porous Media* 87, 397–420.

Vandevivere, P., Baveye, P., 1992. Saturated hydraulic conductivity reduction caused by aerobic bacteria in sand columns. *Soil Science Society of America* 56, 1–13.

Vasconcelos, C., McKenzie, J.A., Bernasconi, S., Grujic, D., Tiens, A.J., 1995. Microbial mediation as a possible mechanism for natural dolomite formation at low temperatures. *Nature* 377, 220–222.

Vile, M.A., Wieder, R.K., 1993. Alkalinity generation by Fe(III) reduction versus sulfate reduction in wetlands constructed for acid mine drainage treatment. *Water, Air and Soil Pollution* 69, 425–441.

Volmer, M., Adhikari, G., 1926. Proof and measurement of the diffusion of adsorbed molecules on surfaces of solid bodies. *Zeitschrift fur Physikalische Chemie-Stochiometrie und Verwandtschaftslehre* 119, 46–52.

Wada, N., Okazaki, M., Tachikawa, S., 1993. Effects of calcium-binding polysaccharides from calcareous algae on calcium carbonate polymorphs under conditions of double diffusion. *Journal of Crystal Growth* 132, 115–121.

Wallmann, K., Aloisi, G., Haeckel, M., Obzhirov, A., Pavlova, G., Tishchenko, P., 2006. Kinetics of organic matter degradation, microbial methane generation, and gas hydrate formation in anoxic marine sediments. *Geochimica et Cosmochimica Acta* 70, 3905–3927.

Weiss, I.M., Tuross, N., Addadi, L., Weiner, S., 2002. Mollusc larval shell formation: Amorphous calcium carbonate is a precursor phase for aragonite. *The Journal of Experimental Zoology* 293, 478–491.

Wildenschild, D., Sheppard, A.P., 2013. X-ray imaging and analysis techniques for quantifying pore-scale structure and processes in subsurface porous medium systems. *Advances in Water Resources* 51, 217–246.

Wolthers, M., Nehrke, G., Gustafsson, J.P., Van Cappellen, P., 2012. Calcite growth kinetics: Modeling the effect of solution stoichiometry. *Geochimica et Cosmochimica Acta* 77, 121–134.

Xiao, J., Wang, Z., Tang, Y., Yang, S., 2010. Biomimetic mineralization of $CaCO_3$ on a phospholipid monolayer: From an amorphous calcium carbonate precursor to calcite via vaterite. *Langmuir: The ACS Journal of Surfaces and Colloids* 26, 4977–4983.

Yingjie, Q., Cabral, J.M.S., 2002. Properties and applications of urease. *Biocatalysis and Biotransformation* 20, 1–14.

Yoreo, J. De, Vekilov, P., 2003. Principles of crystal nucleation and growth. *Reviews in Mineralogy and Geochemistry* 54, 57–93.

Zhang, C.Y., Kang, Q.J., Wang, X., Zilles, J.L., Müller, R.H., Werth, C.J., Muller, R.H., 2010. Effects of pore-scale heterogeneity and transverse mixing on bacterial growth in porous media. *Environmental Science & Technology* 44, 3085–3092.

Zhang, T.Y., Klapper, I., 2010. Mathematical model of biofilm induced calcite precipitation. *Water Science and Technology* 61, 2957–2964.

Zhang, T.Y., Klapper, I., 2011. Mathematical model of the effect of electrodiffusion on biomineralization. *International Journal of Non-Linear Mechanics* 46, 657–666.

Zhang, Y.P., Dawe, R., 1998. The kinetics of calcite precipitation from a high salinity water. *Applied Geochemistry* 13, 177–184.

Zhang, Y.P., Dawe, R.A., 2000. Influence of Mg^{2+} on the kinetics of calcite precipitation and calcite crystal morphology. *Chemical Geology* 163, 129–138.

Zhong, S., Mucci, A., 1989. Calcite and aragonite precipitation from seawater solutions of various salinities: Precipitation rates and overgrowth compositions. *Chemical Geology* 78, 283–299.

"… continues the tradition of the first two editions in providing a comprehensive review in each of a number of areas of research into the complex phenomena that comprise transport in porous media. … The editor has drawn once again from the deep international reservoir of porous media expertise. The breadth of the contributions, all gathered in one place, provides a valuable resource for researchers at any stage of their research careers."

—Robert McKibbin, Massey University, Albany, New Zealand

"… provides an excellent, up-to-date treatise on the theoretical aspects of single and multiphase flows in porous media. … The sections dealing with thermal transport of simple and complex fluids in porous media together with geological applications will serve well not only the sophisticated practitioner but also the interested beginner in the area of porous media transport."

—Dr. Jacob Masliyah, University of Alberta, Edmonton, Canada

"The book offers an excellent overview of the latest theories on flow, transport, and heat-exchange processes in porous media. It provides a sound basis for students and scientists from various disciplines to gain a profound insight into topical porous-media applications. The contributing authors are all renowned experts in their fields."

—Rainer Helmig, University of Stuttgart, Germany

"This third edition is truly a tour de force of the ideas that account for the vigorous growth of the field. … Professor Vafai created an exceptional reference for the field."

—Adrian Bejan, J. A. Jones Distinguished Professor, Duke University, Durham, North Carolina, USA

"The third edition is certainly not a simple rewrite or superficial update of previous chapters and topics. Many of the authors are different and various topics have been added, with most or all contributions very much geared toward the current state of the art and its application across disciplinary boundaries, including industry."

—Martinus Th. van Genuchten, Federal University of Rio de Janeiro, Brazil and Utrecht University, The Netherlands

"This book presents the most interesting leading-edge topics on porous media. You will find what you need in this book when you begin a frontier research about transport phenomena in a porous medium."

—Peixue Jiang, Tsinghua University, Beijing, China

"This text will make a valuable addition to most researchers' bookshelves and will most likely stimulate further research efforts in porous media theory."

—J. H. Cushman, President, International Society for Porous Media and University Distinguished Professor, Purdue University, West Lafayette, Indiana, USA

K13996

CRC Press
Taylor & Francis Group
an informa business
www.crcpress.com

6000 Broken Sound Parkway, NW
Suite 300, Boca Raton, FL 33487
711 Third Avenue
New York, NY 10017
2 Park Square, Milton Park
Abingdon, Oxon OX14 4RN, UK

ISBN: 978-1-4398-8554-3
90000
9 781439 885543